نقابة المهندسين الأردنيين
Jordan Engineers Association



JIChEC IX

2021 / 10 / 14 - 12

Le Royal Hotels and Resorts, Amman - Jordan

ISBN: 2020/3/1033
ISSN: 2707-7942

Jordan International Chemical Engineering Hybrid Conference, IX, JChEC09

Introduction

At the end of JIChEC09 and on behalf of the Organizing Committee, it is our delight to thank all participants in this event held during 1-3 December, 2020 in Amman, Jordan It was our great pleasure and privilege to welcome you during the conference days in which 40% of the presentations were face-to-face and 60% were online. Actually, we succeeded to make hybrid presentations in the same session. In addition, our conference hosted leading scientists from the academia and industry from 27 countries, who discussed the latest developments in chemical engineering and promises. We feel that this event was an exciting opportunity for chemical engineers who were seeking to meet after long periods of lockdown due to COVID-19 troubles all over the world.

The manuscripts submitted to JIChEC09 were about 130, and we accepted about 120 papers including 8 keynote speeches. These papers will be listed in this proceeding according to their theme's arrangement in the first invitation. Some of these papers are submitted to the sponsoring journals found in the following list:

1- Science of Total Environment
2- Canadian Journal of Chemical Engineering
3- Desalination and water treatment
4- Arabian Journal for Science and Engineering
5- Jordan Chemical Engineering

The Canadian Journal of Chemical Engineering will publish a special issue under the title:

Feature papers from JIChEC09. Accepted papers in these journals will be also published in this proceeding if we get their permission.

The conference link:

http://jeaconf.org/JICHEC

For more information, please visit the conference website, and send us by email any comment.

Sincerely yours,

Prof. Zakaria Al-Qodah

Chairman, JIChEC09

Organizing Committee

Chairman	Prof. Zakaria Al-Qodah	Al-Balqa Applied University	Zak@bau.edu.jo
Vice Chairman	Dr. Ziad Abu El-Rub	German Jordanian University	ziad.abuelrub@gju.edu.jo
Member	Prof. Ahmad Shawaqfeh	Al-Balqa Applied University	shawaqat@bau.edu.jo
	Prof. Adnan Al-harahshah	Mutah University	adnan@mutah.edu.jo
	Prof. Marwan Batiha	Al-Hussein Bin Talal University	mmbatiha@ahu.edu.jo
	Prof. Mohammad Al-Harahsheh	Jordan University of Science and Technology	msalharahsheh@just.edu.jo
	Prof. Mohammad Al-Hwaiti	Jordan Phosphate Mines Co	mohhwaiti@jpmc.com.jo
	Prof. Reyad Shawabkeh	University of Jordan	rshawabk@ju.edu.jo
	Prof. Waid Omar	Al-Balqa Applied University	waid.omar@bau.edu.jo
	Dr. Emad El Qada	Mutah University	elqadae@mutah.edu.jo
	Dr. Habis Alzoubi	Al-Hussein Bin Talal University	HabisAl-Zoubi@ahu.edu.jo
	Dr. Hussam Khasawneh	Al-Balqa Applied University	H.khasawneh@bau.edu.jo
	Dr. Ibrahim Suleiman	Al-Balqa Applied University	Dr.ibrahim.suleiman@bau.edu.jo
	Dr. Linda Al-Hmoud	University of Jordan	l.alhmoud@ju.edu.jo
	Dr. Nidal M. Hussein	University of Petra	nidal.hussein@uop.edu.jo
	Eng. Emad Taha Talafeha	Arab Potash Company	Emad.t@arabpotash.com
	Eng. Khaled Ananzeh	Jordan Engineers Association	kananzeh@yahoo.com
	Eng.Mohammad Swaiseh	Jordan Engineers Association	mohammad_swesa@yahoo.com
	Eng. Omar Alabadleh	Jordan Engineers Association	O.alabadleh@JEA.ORG.JO
	Eng. Rose Smadi	Amman Chamber of Industry	rose@aci.org.jo
	Eng. Yacoub Banitaha	Jordan Petroleum Refinery	Yacoub.banitaha@jopetrol.com.jo
Coordinator	Eng. Ibrahim Abu Sbaih	Jordan Engineers Association	jichec@jea.org.jo

Keynote Speeches

Ceremony Day: Tuesday, 12-10-2021

Keynote Speech (I)	In Hall	Scale removal from gas and oil wells	Prof. Ibnalwaleed Husein	Qatar
Keynote Speech (II)	Online	Eco-Friendly Fungal Treatment and AOPs for Efficient Removal of Pharmaceuticals in Urban and Hospital Wastewaters	Prof. Damia Baecelo	Spain
Keynote Speech (III)	Online	The impact of two seas canal on Dead Sea Chemical Industries	Prof. Abdelaziz Khlaifat	Jordan

Second Day: Wednesday, 13-10-2021

Keynote Speech (I)	In Hall	The emerging potential of triply periodic minimal surfaces (TPMS) applications in water and wastewater treatment	Prof. Hassan Arafat	UAE
Keynote Speech (II)	Online	Advanced polymers	Prof. João B. P. Soares	Canada
Keynote Speech (III)	Online	The future of the Dead Sea	Prof. Ibrahim Oroud	Jordan

Third Day: Thursday, 14-10-2021

Keynote Speech (I)	Online	Bioprocesses for the conversion of carbon dioxide and other industrial gases to bioproducts	Prof. Christian Kennes	Spain
Keynote Speech (II)	Online	Process mass and heat transfer	Prof. Yunus Cengel	Turkey
Keynote Speech (III)	Online	Chemical and Bio-Pharmaceutical field	Shakeel H. Kadri	USA

Photos from the conference







Themes table

Theme	Pages
Theme 1 Biochemical Engineering and Biotechnology	1-99
Theme 2 Chemical Engineering Kinetics	100-165
Theme 3 Chemical Process Modeling, Simulation and Control	166-251
Theme 4 Chemical Process Safety	252-337
Theme 5 Desalination and Sustainable Water Treatment	338-456
Theme 6 Energy First Renewable Energy and Conventional Resources for Chemical Industries	457-524
Theme 7 General Chemical Engineering	525-601
Theme 8 Heat And Mass Transfer in Chemical Processes	602-747
Theme 9 Nanotechnology Application in Chemical Engineering	748-840
Theme 10 Potentials And Challenges of Local Industrial	841-874
Theme 11 Chemical Engineering and The Dead Sea	875-922
Theme 12 Sustainable Environmental Management	923-1096

Papers table

paper	speaker	page
Biologically production of organic fertilizer (compost) from rise husk	Iman H. Gatea	2
Characterization of inclusions complex's d-glucosamine derivatives with B-CD	Hocine Bouleghlem	9
Effect of Melittin for honey bee Apis mellifera in some pathogenic parasites in vitro	Fayhaa Abbood Mahdi Al-Nadawi	22
Effect of pre-treatment of wheat straw and sludge digestion on biogas yield production	Arwa Al-Da'asen	30
Investigation of the Relationship Between the Digested Sludge Dewatering and Microbial Activity Improved by Chemical Pretreatments	I.Kadri	31
Production of Biodiesel Using Alkaline Based Catalysts from Extracted Jatropha Oil in Yemen: A Case Study	Abdulbari A. Ahmad	49
Studies on Uses of Renewable Energy and Renewable and Alternative Sources of Energy in Heavy and Integrated Industries in Egypt	Mohammed Hamada Ali Ahmed	58
Synthesis of New Compound (Chalcone) Derivative from Pyrimidine and Studying of Antimicrobial to this Compound	Aseel Fadhil kareem	67
Theoretical Investigation of Recovery of Bioactive Compounds from Food Wastes through Supercritical CO2 Extraction	Yaprak Özbakır	71
Thermoelectric Performance of Ni, Co, and Fe Nanoparticles Intrinsically Doped into Their Metal Borates Glassy Matrices	Isam M. Arafa	81
An equilibrium Ab initio atomistic thermodynamics study of 〖CH〗_4 and 〖CO〗_2 adsorption on the α-quartz (001) surface	Ibrahim A. Suleiman	101
Carbon monoxide desorption and reduction behaviors of graphitic carbon nitride supported nickel catalysts and their performance in CO methanation	Khairul Naim Ahmad	106
Kinetics of toluene dry reforming reaction using Jordanian kaolinite as a catalyst	Ziad Abu El-Rub	116
Methylene Blue Active Substances (MBAS-SDBS) Contaminants Removal by Natural Zeolite, Adsorption Isotherm, Kinetic and Thermodynamic Studies	Aymen A.Awad	117
Preliminary Evaluation of Piston Reactor Technology for Methane Reforming Reactions	Ma'moun Al-Rawashdeh	118

Pyrolysis of High-Density Polyethylene: I. Kinetic Study	Mohammed Al-Yaari	129
Spray-Drying Synthesis of Oxidative Coupling of Methane Catalysts: Inclusion of SiC to the Support	Shekhar R. Kulkarni	141
Synthesis and Characterization of Fluoroperovskite Kznf3 Compounds	Bahia Messai	144
Ultrasound Effect on 5-CQA and Tryptophan Reaction: Assessment of The Reaction Kinetics and Product's Physicochemical Characteristics	Anna Maria Menelaou	152
Application of RSM modelling to synthetic Gemini surfactant (SGS) corrosion inhibition of carbon alloy C1010 in acidic environment	Shamsuddeen A. Haladu	167
Design of Deep Eutectic Solvents: Selecting Constituents Based on Molecular Structure	Ahmad Alhadid	178
Optimization Design of Optimal Parameters in the Denitrification reactor	Meriem Bouteraa	179
Pascal Triangle from Neutronics to Genomics	Wajdi Mohamed Ratemi	186
Predictive RSM and Artificial Neural Network (ANN) Models for Cr(VI) Adsorption onto CoAl Based Layered Double Hydroxide Composites	Nabeel Jarrah	198
Robust MBPC control tuning using Multi-objective Evolution Algorithm for a Distillation Column	Haitham Osman	199
Solubility Modelling of Polyphenols in Supercritical Carbon Dioxide and Modifier using Cubic Plus Association Model	Azizul Azri Mustaffa	215
Theoretical Investigations on The Optimal Topology of Crude Oil Desulfurization Process	Said Al Rabadi	233
Population Balance Modelling for Characteristics of Bubble Breakup and Coalescence Dispersions	Siti Aslina Hussain	234
Optimization of Supercritical Carbon Dioxide Extraction of Phenolic Compounds from Algerian Plant (Peganum harmala Seeds) using Box-Behnken Design based Multi-response Analysis	Sarra Melloul	244
Complacency, Our Worst Enemy: A Recipe for Disaster	German Luna-Mejías	253
Encoded Safety Instructions	Shehab Al-Sohpany	259
Heavy Metal-Contaminated Water Treatment Using Low-Cost Adsorbents	Mohammed Abualreesh	267
Prediction of Compressive Strength of Concrete from Early Age Test Result Using Design of Experiments (RSM)	Salem Alsanusi	297

Process Safety Near Misses are Warning Signs for a Major Incident	Rajender Dahiya	305
Protection Layers Integrity Management, an Illusion?	Rajender Dahiya	318
Solar panel technology using nanotechnology	Eyad AlRashaideh	335
Study of the Impact of the Tube Configurations on the Local Heat Transfer Coefficient in a Bubble Column Reactor with Heat Exchanging Tubes	Abdulrazaq Alzamily	336
Using Reason's Swiss Cheese Model to Investigate 2005 Bp Texas City Refinery Explosion Accident in Terms of Occupational Psychology and Ergonomics	Malik M. S. Salhab	337
A Facile Synthesis of Magnesium Oxide Nanoparticles and Their Performance as an Efficient Nano-Adsorbent for Removal of Organic Pollutants from Aqueous Media	Rowaida M. Fahmy	339
Application of the Experimental Design Methodology for the Optimization Activated Carbon's Preparation from Vegetable	H. boulika	360
Effective Wastewater Treatment using Advanced Oxidation Process Combined with Magnetic Nanoparticle Setup	Mohammad Alwaqfi	361
Humic Acid Removal from Aqueous Stream Using Calf Bones Charcoal as a Green Sorbent: A Reversible Process	Seyedeh Parvin Moussavi	369
methanation of carbon dioxide using local low-cost catalyst	Rawan Alyasoury	383
Reuse of Treated Carwash Wastewater by Using Natural Zeolite	Sagheer Onaizi	417
The Corrosion and Sedimentation Status of Drinking Water in Iran's Distribution Network: A Systematic Review	Seyedeh Parvin Moussavi	426
The Role of Cofactor Addition on Flocculation and Deflocculation Behaviors of Fines Flocculation Using a Cofactor and Polyethylene Oxide Retention Aid	Mohammad Raji Abdallah Qasaimeh	438
Removal of heavy metals contaminants from wastewater using petroleum coke bottom ash	Batoul Rhamtalla	456
A case for microbial fuel cell as sustainable wastewater treatment technology with co-generation of electricity : a Saudi Arabia perspective	Nuhu Dalhat Mu'azu	458

Advanced Air Dehumidification Membranes for Energy Efficient Membrane-Based Air-Cooling	Ahmed Abdala	471
Co-combustion characteristic of Malaysian low rank coal and oil palm biomass char derived from tube furnace and microwave irradiation pyrolysis technique	Siti Shawalliah Idris	489
Experimental investigation of the impact of tubes arrangement on local heat transfer coefficient in mimicked Fischer-Tropsch fluidized bed reactor	Zahraa W. Hasan	490
Low-tar, highly-burnable gas production from the gasification of pelletized palm empty fruit bunch	Nur Hanina Malek	491
Paraffin-coated superhydrophobic sand mulches for controlling water evaporation from irrigated soils in arid regions	Adair Gallo Junior	506
Process Evaluation of Heavy Hydrocarbons Autothermal Reforming	Fernanda Tavares	508
Sustainable Portable Solar-Thermal Desalination Unit	Mohamad Hammoud	514
Total safety operation management (TSOM) & business continuity management (BCM) of fire, life safety design aspect	Jalal R. Omar	524
APC Plants Zero Liquid Discharge (ZLD) Case Study	Ala'a Omari	526
COVID-19 effect on health and safety of workers in the workplace: A case study in Jordan	Heba Alzaben	540
Green Hydrogen (New Vision for Clean Energy)	Raudh Jamal Raheem	541
Impacts of Non-Pharmaceutical Interventions (NPIs) on the Trends of COVID 19 Pandemic in selected MENA Region Countries	Nidal M. Hussein	546
Institutional Performance Development in the Water Sector of Jordan	Mohammed Al-Waqfi	564
The reality of threats to security and safety in environment of Gaza Strip	Mohammed M. A. Al-Mougher	576
Development of New Electrode for Phosphoric Acid Fuel Cell	Mohammad Ali Freij	600
CO2 capture by kaolinite based geopolymer	sabreen Mheidat	601
A Review on Dissolution Behaviour of Multi-Component Dnapls	Praveengouda Patil	603

Evaluation of Mechanical and Thermal Properties of Carrageenan/Hydroxypropyl Methyl Cellulose Hard Capsule	Nur Amalina Ramli	623
Experimental Investigation on The Performance of Phase Change Material (PCM) Incorporated with Solar Water Heating System	Obada Dwekat	644
Experimental Study of Hydrodynamic Behavior with Mono-particles of Glass Beads in Three Phase Fluidized Bed Reactor-Part I	Omar S. Mahdy	659
Heat Exchange in the Processes of Welding of Rails and Hardening of Railway Wheels	Vladimir Saranchin	675
Hot air drying of celery: Drying kinetics, pretreatment effect and color changes	Ilknur Kucuk	685
Performance Evaluation of Triple Concentric Tube Heat Exchanger Using [EMIM][BF4] Ionic Liquid and MWCNT/[EMIM][BF4]	Basma A. Abdulmajeed	693
Polymeric Heat Exchangers in Seawater Desalination – Impact of Surface Characteristics and Process Conditions on Cleanability	Hendrik Kiepfer	712
Review of Multicomponent Adsorption and Isotherms for Multicomponent Adsorption	Amrutha	727
Testing and Commissioning of a Cold Inflow Free Chimney Dryer	Hooi Kim Phang	728
Environmentally Safe Microwave Heating of Non-Polar Materials	Vladimir Saranchin	738
An iron rotating disk for the elimination of hexavalent chromium ion from industrial wastewaters; putting it to work	Mohammed S. El-Ali Al-Waqfi	749
Carbon nano-dots from natural resources as optical sensors for iron ions/Fe3+: a review	Marah Daraghmah	759
CO2 capture by graphene-based nanocomposites: effects of oxygen and nitrogen contents	Sagheer A. Onaizi	774
Co-catalyzed with MIL-47 (V) metal organic framework and carbon nanotubes for an enhanced Mgh2 hydrogen sorption performance	Atikah Kadri	790
Evaluation of corrosion and scaling in Khoms Power Plant	Abdulhamid. Elwaer	804
Fairdeal's Introduces Innovative Waste Management Solutions Based on Nano Engineering	Abdalla Al Jedayeh	805
Optimization of the Templated Synthesis of Lithium Iron Phosphate Nanowires	Kian Hong Gan	806

Sulphonated MIL-101(Cr): Microwave Responsive Catalyst for Fructose Dehydration into Platform Chemicals	Noor Aljammal	818
Synthesis of Ag Nanoparticles Loaded Nanotio2 Catalyst Using Mechanical Ball Milling for Phenol Photodegradation	Mohammad Ashraf Ali	820
Tools of Material Engineering for Designing Membrane Materials with Desire Features	Joanna Kujawa	831
Ultimate eradication of the ciprofloxacin antibiotic from the ecosystem by nanohybrid go/o-cnts	Ahmad Rafiq Muosa Mohammad	840
A review on the size reduction technology using mechanochemistry approach	Mohammad Alrbaihat	842
Sequential Extraction of Rare Earth Elements from Phosphogypsum	Ahlam Waleed Hunaihen	852
Dead sea brine water chemical and physical stratification features influenced by the continuous drop in sea level	Tayel El-Hasan	876
Selective Recovery of Lithium from Dead Sea End Brines Using UBK10 Ion Exchange Resin	Sewar Aljarrah	898
Simple Correlation for Predicting Gypsum Deposition from Brine Solutions	Hosni Ezuber	906
Algerian Contaminated Groundwater Treatment by Using Acacia Gum: Organic Pollution Removal	Rania Remmani	924
Application of sentinel 2 to evaluate colored dissolved organic matter algorithms for inland water bodies in Jordan	Nidal M. Hussein	933
Conversion of Oil Palm Empty-Fruit Bunches Waste to Activated-Carbon Using Superheated Steam	Nur A'ina Shafiqa Wakari	948
Dynamic Mechanical Analysis and Morphological Study of Composites of Polyvinyl Chloride - Date Palm Leaf Fiber	Abir Berkouk	960
Evaluation of the Anti-inflammatory Activity of Polyphenols from Algerian Monovarietal Olive Oil Mill Wastewaters	Zakia Guebudji	961
Groundwater Hydrogeochemical and Quality Appraisal for Agriculture Irrigation in Greenbelt Area, Iraq	Eman Sh. Awad	967
Lead Ions Removal in Simulated Industrial Wastewater by Using Activated Carbon Produced From Heavy Oil Fly Ash	Waleed Mohammed Abood	989
Lighting Up the Future New Technologies for Smart Devices	Abdelhadi Benabdessadok	998

Nutrients Recovery from Hybrid Adsorbents Through the Application as Slow-Release Fertilizer: A Mini-Review	Nurliyana Nasuha Binti Safie	1008
Photodegradation of Methylene Blue by Carbon Nanodots Synthesized from Olive Solid Wastes	Shadi Sawalha	1018
Recovery of Glass Fibers from End-of-Life Wind Turbine Fiber Composite Wastes Through Pyrolysis Process	Salman Raza Naqvi	1033
Regeneration of CO2 Loaded 2-(Diethylamino)ethanol using Organic Solvent and Waste Heat	Madhusree Kundu	1044
Sentinel 2 Analysis of Turbidity Retrieval Models in Inland Water Bodies: The Case study of Jordanian Dams	Nidal M. Hussein	1066
Pyrolysis of High-Density Polyethylene: II. Artificial Neural Networks Modeling	Ibrahim Dubdub	1084

Theme 1: Biochemical Engineering and Biotechnology

Biologically production of organic fertilizer (compost) from rise husk

Iman H. Gatea [1,*], Hisham K. Auda [1], Abeer S. Alhendi [2] , Shahad Sh. Sabir [1] and Jumana A Murad [1]

[1] Ministry of science and technology \ Environment and water directorate\Iraq \Baghdad
[2] Quality Control Department/General Company for Grain Trade/ Ministry of Commerce\ Iraq \Baghdad
***** *Corresponding author: eman77aa@yahoo.com; Tel.: 964-07806862838.*

Abstract: The compost material in the present study depicted change in composition of rice husk during three month of experiment. The morphological appearance and characterization of the compositing rice husk depicted change in color, structure, and odor. Present study also recorded physical characteristic features of rice husk after addition of chicken droppings as nitrogen source. The results revealed that, the ratio between carbon to nitrogen gradually decreases during the experiment period, reaching at the end of the treatment 14.5. It was also noticed that the pH level decreases during the first two-thirds of the day, then increases to reach 8.4 after 45 days, to reach the degree of parity in the final product. The experiment showed an increase in the total number of microorganisms during the experiment, which confirms the availability of all the important elements to feed them in the mixture used and the decrease in the number of bacteria, coliform and its effect on its transformation into the formula that makes it safe for use as a fertilizer for soil and improving its characteristics.

Keywords: compost; rice husk; fertilizer; bacteria

1. Introduction

Recycling is the process of recycling and using waste, whether domestic, industrial or agricultural, in order to reduce the impact of this waste and its accumulation on the environment, this process is done by classifying and separating the waste on the basis of the raw materials in it and then recycling each material separately.

The systems and means of recycling agricultural waste to maximize its utilization depending on the type of waste and available technologies and the purpose of recycling these wastes between biological methods of adapting microorganisms to convert these organic wastes into products with economic feasibility, mechanical methods for producing supplies for homes, clubs and industry, chemical methods for the production of paper and compounds [1] Chemical intermediates, physical methods such as pressing, grinding and capping for ease of use, and others for the production of handmade products and others. Advances in biotechnology science have led to the adaptation of microorganisms to convert organic compounds and waste into economical products while preserving the environment from pollution, as well as exploiting the ability of these micro-organisms to produce food, feed, bio-energy and intermediate compounds and purify wastewater, in addition to resisting the negative impact of these microbes to preserve human health and sources of wealth .Composting is a natural biological process which involves the aerobic decomposition of organic materials under controlled conditions [2]. Rice husk is the remains of the rice plant after harvesting and separating the grains from it. The amount of rice straw produced annually is about 6 million tons, most of which are found in the governorates of Dewaniya and AL-Najaf , and farms benefit from only about 17% of the total of these wastes. As the problem of pollution resulting from agricultural waste represents 40%

at the time of the emergence of the black cloud, although it can be used in a very large way in many industries. However, a vast proportion of this rice straw is subjected to open-field burning which is hazardous for the environment. Rice straw possesses various several characteristics that make it an ideal feedstock for value-added products such as animal feed, bioethanol, lignocellulose enzyme, and bio-compost. To make the process of lignin and cellulose degradation economically viable, inoculation with lignocellulolytic microorganisms may prove beneficial [3].

Organic matter plays an important role in solving the problems of all types of lands. With regard to sandy lands, it increases the cohesion of the land, increases its ability to hold water, and increases its content of nutrients necessary for plant growth [4]. As for calcareous lands, adding organic matter leads to an improvement in its natural properties, especially the problem of crust formation. The rice straw is chiefly composed of cellulose (32–47%), hemicellulose (19–27%) and lignin (5–24%) [5].Due to the microbial dissolution of the organic matter and the absorption of particles of large molecular weight onto the granules, the addition of organic matter to heavy clay lands leads to their disintegration, improving their natural properties and raising its fertility. The burning of agricultural waste, especially rice straw, during the months of September and October of each year causes an acute air pollution crisis. Allergic diseases increase by 10 to 15% and the increase in chest sensitivity from 8 to 10%. Smoke also leads to sensitivity in the mucous tissues lining the eye. As a result of the plankton associated with black cloud smoke, the risk increases, which lead to the occurrence of eye inflammation. The problem increases as a result of the resulting smoke for burning organic and inorganic materials, it contains about 11 carcinogenic substances. The burning of rice straw is in itself a waste of the value of industrial and food wealth from this agricultural wealth represented by about 3 million tons of straw. Hence, the present study was formulated to produce organic fertilizer by aerobic a decomposition of rice husk as organic materials and chicken droppings mixture under controlled conditions.

2. Materials and Methods

2.1.1. Source of Plant Materials

The raw rice husk (RRH) was obtained from local rice mill, (Alnajaf provinces) after processing.

2.1.2. Compost of Rice Husk

RRH was milled into smaller size and composting process was carried out in experimental trays with the dimension of 1.5 _ 1.5 _ 1.0 m. A layer of small stones was spread to a height of 3 cm above, where a layer of agriculture soil was added to a height of 5 cm. Six kilograms of rice husk and tow kilograms chicken droppings mixture in treatment ratio of 3:2 was filled in the treatment area. After mixing all the inputs, watering was done with sterilized water to maintain moisture. The compost material was stirred periodically once every 14 days to allow more aeration inside the material. The level of moisture was maintained at 60% by adding water at different levels of composting. The substrate was allowed to compost for 3 months and analysed periodically.

2.2. Physico-Chemical and biological Properties

The compost samples were grounded after drying, for chemical analysis of organic carbon, nitrogen, phosphorus,C\N ratio and potassium and other metals depending on [6].

Fungi total count: Potato Dextrose Agar (PDA) used to isolate fungi from compost

Bacterial total count: Nutrient agar used to isolate bacteria isolate.

3. Results and Discussion

Rice (Oryza sativa L) is one of the most consumed grains after wheat worldwide The production quantity of 2015, 2016, and 2017 were 200, 43, and 100 thousand tons

respectively, and Yassamine rice presented 97%, 99%, and 78% respectively [7] . A previous study on composting of chicken manure and rice husk which was carried out for a period of three months reported lower nutrient content and high C:N and C:P ratios at the first 15 days of experiment . The change in colour from yellow to dark brown colour was well observed after 30 days. As shown in table (1), primary mixture used for the composting process contained 68% of total carbon, 0.52% of total nitrogen (N), 0.23% of phosphorus (P), and 0.35% of potassium (K). The moisture content 17.5, with a neutral PH (7.0). Should get due attention while recommending the compost to be mature and safe for soil application. During the first 15 days of composting (initial pH-7.0) in the earliest stage, the pH value decreasedto 6.25 due to production of organic acids by microorganisms fermentation . The lignin component of the rice straw is decomposed into fulvic acid and humic acids by lignocellulolytic fungi, by humification process, which finally makes the substantial proportion of soil organic matter [8] Thereafter , the pH began to rise and reached 8.4 at the thermophilic period. The increase in the acidity value may be due to the production of ammonia due to the degradation processes.Results presented in table (1) revealed a remarkable change was observed in electrical conductivity, ranged between 2.32 to 0.28 dSm-1, and was far below the safe limit of 3 dSm-1 . On day 90, The N content improved and P and K showed an increasing due to mineralization. Previous studies suggested that microorganism processed waste material contains high concentration of exchangeable K due to enhanced microbial and enzymatic activity during the microbial composting process, which consequently enhances the rate of mineralization [9]. It was observed through Table 2 that the number of bacteria and fungi increased during the incubation period, which had a major role in the biological breakdown of residues and cellulosic materials into other compounds of interest to the soil. Many lignocellulolytic bacteria were used for compost making from agricultural waste [10, 11].

Fungus is widely used for composting of lignocellulosic waste because they are filamentous and have the ability to produce prolific spores that can invade substrates quickly. Fungal culture was used for the composting of rice straw which is one of the waste products from rice field [12].The milled rice husk was reduced to a brown crumpled and compact value-added composted biofertlizer with a high carbon and nitrogen content as shown in figure 2. The color changes of the compost help in evaluation of compost maturity in the field in a swift and convenient manner.



Figure 1.Stages of rice husks formation in one of the mills in the Najaf branch from paddy and rice



Figure 2.Field experience of biological treatment of agricultural residues and method of sample collection

Table 1. Physico-Chemical biological Properties of biocopst

Parameter	Unit	15	30	45	60	90
Moisture content	%	17.5	43	42	45	45
pH		7.0	6.25	8.4	7.4	7.20
Conductivity	ds\m	2.32	2.00	1.43	0.39	0.28
Total carbon	%	68	66	46	34	25
Total nitrogen	%	0.52	0.75	1.25	1.62	1.72
Total phosphor	%	0.23	0.37	0.55	0.60	0.64
Total potassium	%	0.35	0.40	0.44	0.56	0.67
Total Zink	ppm	185	187	183	180	181
Total copper		48	49	47	45	44
Total Cadmium		1.59	1.61	1.58	1.55	1.56
Total Lead		76	74	75	72	71
Total Nickel		38	39	38	35	36
Total Crum		29	30	28	26	27

Table 2. biological Properties of biocopst

Microorganisms	Unit	Sample 1	Sample 2	Sample 3	Sample 4	Sample 5
Fungi total number	Cfu\gm\ ml	500	510	515	525	530
Bacterial total count	Cfu\gm\ ml	6030	8390	8420	8580	8650
Coliform bacteria	Cfu\gm\ ml	890	540	324	NC	NC

4. Conclusions

This research received no external funding .It was an attempt to compost rice husk with microbial cultures and evaluate its efficiency in improving the soil nutrient status which has a role in increasing the agricultural yield. The value of rice husk can be explored by biological conversion of cellulose to a valuable material. It can be made on the farm at very low cost and can be used as organic fertilizer to mitigate its open-field burning.

Acknowledgements: The authors would like to express profound gratitude to Environment and Water Directorate in Ministry of Science and Technology, for financial and technical supports. We also thank the General Company for Grain Trade for providing us with rice husks.

References

1. Sukumaran RK, Surender VJ, Sindhu R, Binod P, Janu KU, Sajna KV, Rajasree KP, Pandey A (2010) Lignocellulosic ethanol in India: prospects, challenges and feedstock availability. Bioresour Technol 101:4826.
2. Epstein, E. (1997). The science of composting. Boca raton, CA: CRC
3. Maki, M.L.; Idrees, A.; Leung, K.T.; Qin, W. **2012**, Newly Isolated and Characterized Bacteria with Great Application Potential for Decomposition of Lignocellulosic Biomass. Mol. Microbiol. Biotechnol.
4. Antil, R., Raj, D., Abdalla, N. and Inubushi, K. (2014). Physical, chemical and biological parameters for compost maturity assessment: A review. In: Maheshwari D. (Eds) Composting for Sustainable Agriculture. Sustainable Development an Biodiversity, Vol 3. Springer, Cham.
5. Garrote G, Dominguez H, Parajo JC (2002) Autohydrolysis of corncob: study of non-isothermal operation for xylooligosaccharide production. J Food Eng 52:211–218.
6. Sequi, P.; De Nobili, M.; Leita, L.; Cercignani, G. A new index of humification. Agrochemica 1986, 30, 175–179.
7. Alhendi, A.S., S.H. Al–Rawi and A.M. Jasim. 2019. Effect of moisture content of two paddy varieties on the physical and cooked properties of produced rice. Braz. J. Food Technol. 22: e2018184.
8. Huang H L, Zeng G M, Tang L, Yu H.Y, Xi H M, Chen Z M, Huang G H (2008) Effect of biodelignification of rice straw on humification and humus quality by Phanerochaete chrysosporium and Streptomyces badius. Int Biodeter Biodegrad 61:331-336
9. Suthar, S. Nutrient Changes and Biodynamics of Epigeic Earthworm Perionyx Excavates (Perrier) during recycling of some agriculture wastes. Bioresour. Technol. 2007, 98, 1608–1614.

10. Premalatha, N.; Gopal, N.O.; Arul Jose, P.; Anandham, R.; Kwon, S.W. 2015, Optimization of cellulase production by Enhydrobacter sp. ACCA2 and its application in biomass saccharification. Front. Microbiol., 6, 1046.
11. Bui, H.B. Isolation of cellulolytic bacteria, including actinomycetes, from coffee exocarps in coffee-producing areas in Vietnam. Int. J. Recycl. Org. Waste Agric. 2014, 3, 48.
12. Kausar, H.; Sariah, M.; Mohd Saud, H.; Zahangir Alam, M.; Razi Ismail, M. 2010 Development of Compatible Lignocellulolytic Fungal Consortium for Rapid Composting of Rice Straw. Int. Biodeterior. Biodegrad.,

Characterization of inclusions complex's *d*-glucosamine derivatives with *B*-CD

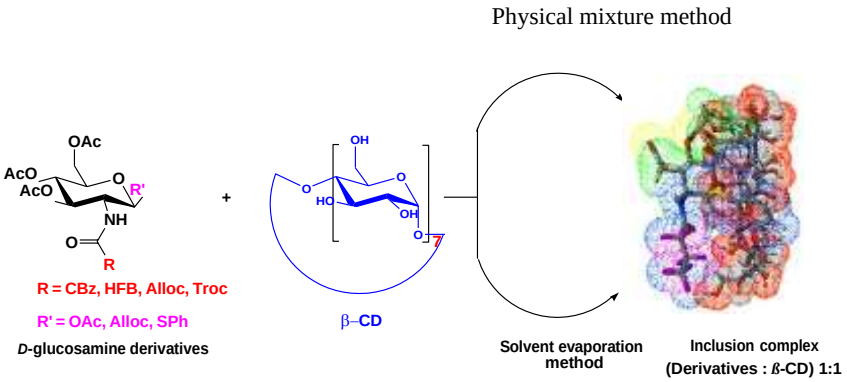
Hocine Bouleghlem [1,2,*] , Salima Zidane [2] and Nour-Eddine Aouf [1]

[1] Organic chemistry laboratory Applied (LCOA), Group of Chemistry Bioorganique Faculty of Science, Department ofChemistry. University Badji-Mokhtar 23000 Annaba, Algeria ;

[2] Department of chemistry, Faculty of Science, University Mohamed Boudiaf- 28000, M'sila, Algeria;

* *Corresponding author: hocine.bouleghlem@univ-msila.dz; Tel.:+ 2137914845.*

Abstract: In this Work, we were interested on the synthesis of *D*-glucosamine derivatives. Within two steps; Acylationof the 1,3,4,6-tetracetyl-amino-2-deoxy-*β*-*D*-glucosamine hydrochloride (2) and the regioselective substitution by thiophenol. Given that this compound has very poor aqueous solubility and to ameliorate this, we have synthesized an inclusion complex between derivative (5) and *β*-CD, the preparation of the complex was carried out by two different methods (Physical mixture method and Solvent evaporation method).The results of this work were confirmed by structural characterization by spectroscopic methods ^{19}F NMR, ^{1}H NMR and IR.Finally we studied the solubility of derivative (5) in an aqueous solution containing various concentrations of *β*-CD by UV-Visible spectroscopy which wasdeducted enhancement of the derivative (5) solubility in the presence of *β*-CD.



Keywords: *β*-CD, *D*-glucosamine hydrochloride; *D*-glucosamine derivatives; inclusion complex; solubility; cavity.

1. Introduction

D-glucosamine (1) and 1,3,4,6-tetracetyl-amino-2-deoxy-*β*-*D*-glucosamine hydrochloride (2) are key carbohydrate building blocks in animals, to a more limited extent in microorganisms, and little or none in plants. (1) or (2) are the major components in polysaccharides and proteoglycans such as chondroitin sulfate, heparin, hyaluronic acids, chitosan and chitin [1], and are components in bacterial capsules [2]. Glucosamine is widely used as a nutritional supplement in particular for the treatment of arthritis.

Glucosamine derivatives have also attracted a considerable amount of interest, both as biologically active compounds, and as cell permeable forms of (1) and (2). The glucosamine derivatives (Figure

1) have shown a range of activities, including antitumor [3], antibacterial [4, 5], anti-inflammatory [6], anti-thrombotic activity [7]. *O*-Acetylatedglucosamine derivatives are rapidly hydrolyzed by intracellular esterases, and therefore can be used as cell permeable sources of aminosugars in the absence of active transport. Peracetylated 2-azidoacetyl-*D*-glucosamine was developed byBertozzi R .C as a probe for intracellular protein incorporation [8], and has been used extensively in the study of dynamicand static glycosylation [9,10]; a variety of other per-*O*-acetyl derivatives have been reported that presumably similarly aspro-drug forms of the sugar derivative [11]. Because of the importance of such derivatives, solubility has been a recurringissue. The 1,3,4,6-tetracetyl-amino-2-deoxy-*β*-*D*-glucosamine hydrochloride (2) itself has limited aqueous solubility (50mg/ml), but most derivatives of interest have negligible aqueous solubility, requiring sometimes significant DMSO concentrations for biological studies. In addition, many derivatives have ampihillic character, and can show surfactant properties [12] that can interfere with the interpretation of certain biological studies. Relatively few attempts at finding a water soluble formulation have been reported. Starting from this definition, the host–guest type is extensively discussed in literature covering a large field of applications [13]. For example, cyclodextrins (CDs), among host molecules, are reported to occupy an important place in the field of inclusion phenomena [14,15]. CDs are cyclic *D*-glucose, hexa-, heptaor octasaccharides that have been widely used for the formulation of poorly soluble drugs and probes (Figure 2) [16]. Thehydrophobic cavity is capable of hosting a hydrophobic guest, while the peripheral hydroxyl groups provide excellent water solubility. They are notably non-toxic, and a variety of cyclodextrin-based drug formulations are currently marketed [17]. Thus, use of CDs is one of several technologies available to improve the solubility of poorly
water-soluble drugs (Diclofenac®, Naringenin®, Quercetin® and Rutin®)[18-22]. The most remarkable property of Cyclodextrin s is their ability to modify the physicochemical characteristics of molecules that are accommodated within their internal cavity to form the so-called inclusion complexes [23, 24]. We report herein a study of the complexation of asmall panel of derivatives in *β*-CD.

The possibility of modulating the activity of a molecule by introducing one or more fluorine atoms is operated in medicinal chemistry and this explains the large effort expended in the last fifteen years to design fluorine reagents [25,26].

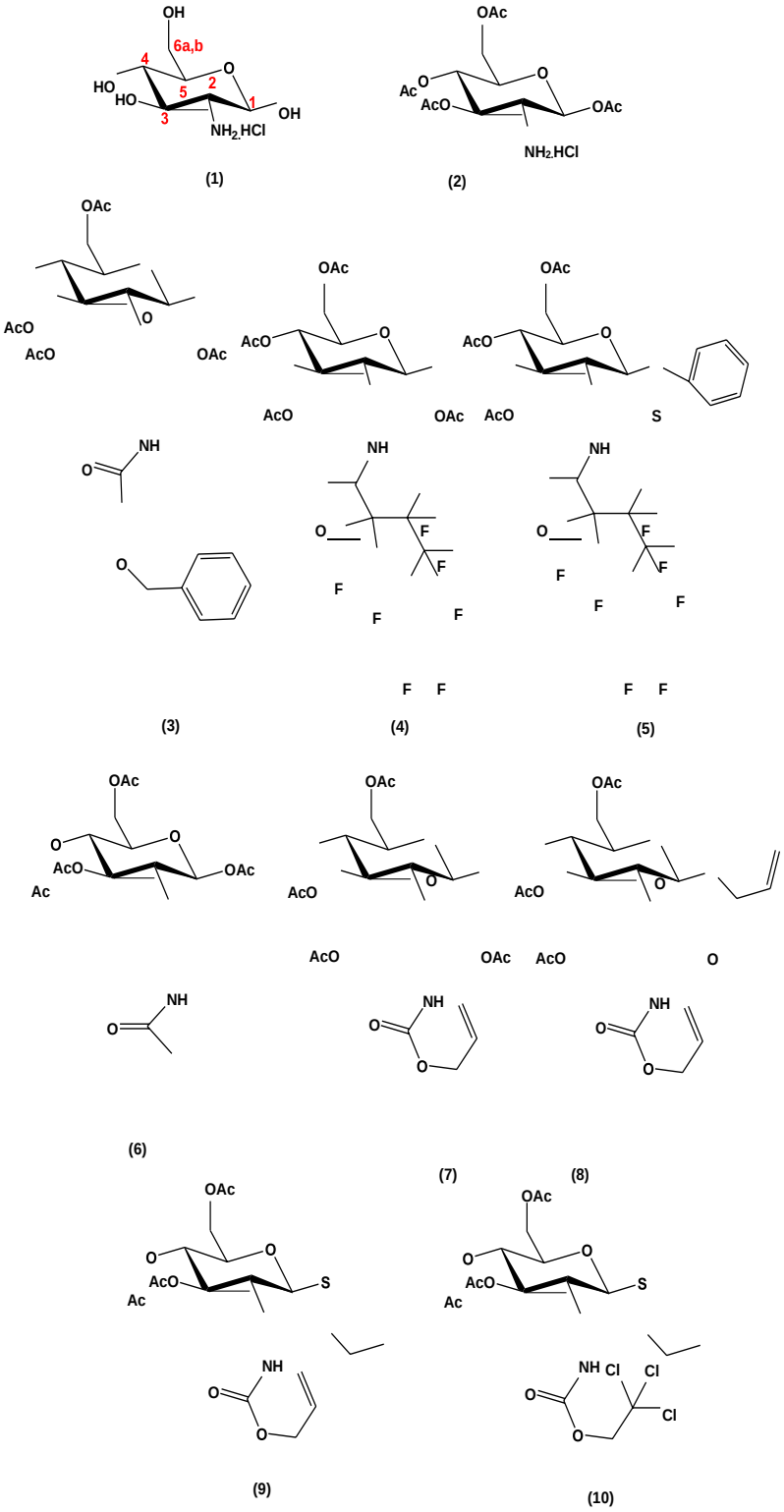


Figure.1. Chemical structure of the derivatives of Glucosamine.

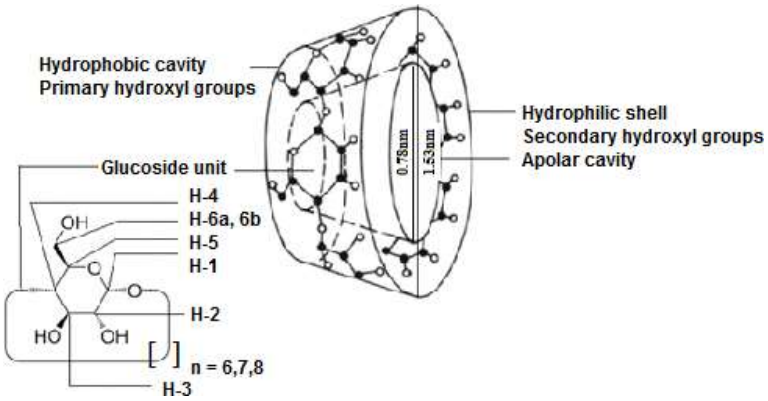


Figure 2. β-Cyclodextrin structure, with representations of its size and position of hydroxyl groups andrepresentation of the glucoside unit.

The studies on supramolecular chemistry give a broad idea of intermolecular interactions where covalent bonds are not likely to form between the interacting species. Thus, most of these interactions have been performed by host-guest interactions. Among the host molecules, cyclodextrin seems to be the most promising to form inclusion complexes, especially with various guest molecules with suitable polarity and dimensions [27,28].Among the various physico-chemical properties of this molecule, Indeed Derived (5) is a substance soluble in organic solvents but very sparingly soluble in water [29]. The most important property of CDs is their ability to modify the physicochemical and biological characteristics of drugs. Their cavity can establish interactions through intermolecular forces with molecules, ions or radicals, acting as a host substance [30, 31]. CDs are widely used in various fields of pharmaceutical industry, stabilization of drugs, additives in the biotechnology and analytical methods…etc. CDs increase the water solubility of poorly soluble drugs and improve their bioavailability. Light thermal and oxidative stability of actives can be improved through the formation of CD complexes [32, 33]. The truncated cone structure of CDs, which are open at both ends, enables the inclusion of a wide variety of organic molecules apolar in their central cavities. Host-guest complexes or molecule-CD complexes also known as inclusion complexes or inclusion compounds, result from the association between host molecules (CDs) and encapsulated molecules [34]. The formation of a complex in an aqueous solution takes place when water molecules are removed from the apolar cavity of CDs (*which are in an energetically disadvantageous environment due to the nature of the polar-polar interaction*) and substituted for a guest molecule or lipophilic group with polarity, size and shape compatible with that of the CD structure. This process is energetically favorable and contributes to an increase in complex stability, because it causes changes in enthalpy (ΔH) and a reduction in the total energy of the system [35]. Furthermore, other forces are involved in the formation and stabilization of inclusion complexes, such as Van Der Waals interactions (*dipole-dipole interaction and dispersion forces like force of London LDF*) [36], between guest molecule and CD hydroxyl groups, hydrophobic interactions, release of deformation energy from the macromolecular ring of CDs, and steric effects. The complexes formed are soluble active ingredients, that they will be more stable in more solutions. They easily dissociate to release the guest molecule [37]. Since both Derived (5) and *β*-CD have a special place and many applications, the the aim of the present research was to prepare and characterize the inclusion compound Derived (5)-*β*-CD.

2. Materials and Methods

2.1 General Methods

Reactions were carried out under argon atmosphere. Solvents were dried according to established procedures by distillation under argon from an appropriate drying agent.

2.2 Chemicals

Products: 98% Sodium hydroxide NaOH , 37% hydrochloric acid HCl , *β*-Cyclodextrin (β-CD) , 99%, silica gel, sulfate sodium (Na_2SO_4), sodium bicarbonate (Na_2CO_3) DMAP (4-Dimethylaminopyridine), Pyridine, anhydride heptafluorobutyric(HFBA), 98 % sulfuric acid H_2SO_4, NaCl Sodium chloride, Thiophenol (PhSH), Boron trifluoride diethyl etherate ($BF_3.OEt_2$).

2.3 Solvents

Methanol 99 %, Ethanol 99.8 %, Dichloromethane, distilled water, hexane, Acetone, petroleum ether (PE), ethyl acetate (EtOAc).

2.4 Characterization methods

Thin layer hromatography (TLC) was performed on Merck 60 F354 (Art. 5554) silica plates.

NMR: The NMR spectra were recorded with a Bruker (Forward) to 300 MHz for ^{1}H NMR, 300 MHz for ^{13}C NMR and 300 MHz for ^{19}F NMR. Tetramethylsilane (TMS) is used as internal reference. Chemical shifts for spectra in D_2O, $CDCl_3$, MeOH d^4 or DMSO-d^6 are given in ppm. NMass spectrometry: high-resolution mass spectrometry electrospray ionization HRMS (ESI): These spectra were recorded using the GCT device waters and using methane as reagent gas, exact mass measurement (*accuracy < 1ppm for m/z < 900 Dalton*). Infrared Spectroscopy: Infrared spectroscopy were recorded on a Nicolet Magna-IR 550 FT-IR –thermo scientific- IS50-NIR-spectrometer (*Fourier Transform Infrared*) (Madison, Wiscosin, USA), in the range of 500 - 4000 cm^{-1}. Absorption Spectra: UV-Vis spectroscopy (*Perkin Elmer UV-Vis lambda 10*) with 1 mm quartz cells was used for all spectroscopic studies. A wavelength absorption profile was obtained in the range of 200 - 400 nm. Spectroscopic analyses were realized by the " Organic Chemistry Laboratory 2 - Glycosciences of CNRS-U.C.B.L. 5246 ICBMS and Laboratory automatic and process engineering LAGEP , CNRS UMR 5007,.Claude Bernard University Lyon 1 (Lyon, France).

2.5 Preparation of β-Cyclodextrin

β-Cyclodextrin was dissolved in 5mL distilled water and sonicated for 15minutes with Cole Parmer Ultrasonic equipment 8891 (Illinois, USA). The concentration of this solution was (17.025mg, 15µM).

2.6 Preparation of the Derived (5)-β-CD Inclusion Complex

2.6.1.Methods

2.6.1.1 Physical mixture method

The required molar (1:1) quantities of the Derived (5) and *β*-CD were weighted accurately and mixed together thoroughly in a mortar, with vigorous trituration for about 10 minutes. These mixtures were then passed through sieve №. 44, and finally stored in airtight containers till further use [38].

2.6.1.2 Solvent evaporation method

In this technique, a required mole of *β*-CD was dissolved in hot distilled water (60°C). Next, Derived (5) was dissolved in methanol at 30°C and was added drop wise into the first solution, with continuous stirring for one hour. The complexes formed were filtered and dried under a vacuum. Then the prepared solid mass was stored in desiccators under vacuum to a constant weight. The dried products were removed, pulverized, and passed through sieve №. 100 [39].

2.6.1.3 Phase solubility studies

The phase solubility studies were performed according to the method reported by Higuchi and Connors [40]. The excess amount of Derived (5) (30mg, 4.8145mmol/L) was added to 20 mL of the aqueous solution (methanol / water) (2/8) containing various concentrations in *μ*M (0, 15, 30 and 45) of *β*-CD in a series of stoppered conical flask and the mixtures were shaken at 25°C for 24 h on a rotary flask shaker. After equilibration, the solutions were filtered immediately using a 0.45 *μ*m nylon disk filter (*Millex-HV, Millipore*). The filtered samples were suitably diluted and assayed.

3. Results and Discussion

Chemical shift changes in the ^{1}H NMR spectra were used to monitor the complex formation process. The hydrogen atoms located in the interior of the cavity (H-3 and H-5) get considerably shielded by the guest molecule, whereas the hydrogen atoms on the outer surface (H-1, H-2, H-4 andH-6a, H-6b) remain unaffected or experiences a marginal shift.

Table 1 and **Table 2** show the chemical shifts and their changes upon complexation for the Derived (5) protons, where $\Delta\boldsymbol{\delta} = \boldsymbol{\delta}_{\textbf{(complexed)}} - \boldsymbol{\delta}_{\textbf{(free)}}$.

Table 1. Chemical shifts δ(ppm) for the protons of *β*-CD free and in inclusion complex.

***β*-CD / (1:1 complex)**			
***β*-CD protons**	$\delta_{(free)}$	$\delta_{(complex)}$	**Changes Δ*δ***
H-1	4.896	4.890	-0.006
H-2	3.378	3.226	-0.152
H-3	3.707	4.150	+0.443
H-4	3.146	2.041	-1.105
H-5	3.590	3.908	+0.318
H-6a,H-6b	3.476	3.475	-0.001

Table 2. Chemical shifts δ (ppm) for the protons of the Derived (5) free and in inclusion complex

	***β*-CD / (1:1 complex)**		
Derived (5) protons	***δ* (free)**	***δ* (complex)**	**Changes Δ*δ***
H-1	5.201	5.200	-0.001
H-2	4.560	3.226	-1.334
H-3	5.280	4.150	-1.130
H-4	4.650	2.041	-2.609
H-5	4.780	3.908	-0.872
H-6a,H-6b	4.343	3.477	-0.866
Ar	7.501	7.550	+0.049
CH_2-Ph	3.705	3.710	+0.005
AcO	2.100	2.100	0.000

As it can be seen from **Table 1** and **Table 2**, for binary complex (1:1), Δδ ppm values for H-3 and H-5 were changed and this suggested that there was association as well as complexation of Derived (5) with *β*-CD.

3.1. Fluorine nuclear magnetic resonance (19F NMR) spectroscopy

^{19}F NMR was made to follow the chemical shifts of CF_2 and CF_3 groups in Derived (5) and compare it with the Derived (5)-*β*-CD complex, the characteristic resonance of (CF_3, CF_2 and CF_2 groups by ^{19}F NMR, are situated in the range of -80 to -120 ppm. The results obtained are summarized in **table 3**, calculating Δ*δ* certifies the chemical shifts of CF_2 and CF_3 groups by adding *β*-CD, where it is noted that after inclusion of the fluoro groups of Derived (5) the peaks become less shifted. So we can say that, this shift provides the indication for the formation of the inclusion complex between *β*-CD and Derived (4).

Table 3. Chemical shifts δ (ppm) for the fluorine of Derived (5) free and in inclusion complex.

	***β*-CD / (1:1 complex)**		
Derived (5) fluorines	***δ* (free)**	***δ* (complex)**	**Changes Δ*δ***
CF_2	-121.1	-121.6	-0.5
CF_2	-127.2	-127.8	-0.6
CF_3	-80.7	-82.1	-1.4

Table 4. Derivatives who have a possibility to formed an inclusion complexes with *β*-CD

D-glucosamine derivatives		Exact Mass (g/mol)	Chemical shift (Δδ) Changes of the	(Δδ) Changes of the	Complex formation with
№	Chemical Formula		H-3	H-5	*β*-CD
3	$C_{22}H_{27}NO_{11}$	481.16	-0.020	-0.179	
4	$C_{18}H_{27}F_7NO_{10}$	543.10	-0.010	-0.080	Yes
5	$C_{22}H_{22}F_7NO_8S$	593.10	+0.443	+0.318	
6	$C_{16}H_{23}NO_{10}$	389.13	-0.150	-0.258	
7	$C_{18}H_{25}NO_{11}$	431.14	0.000	0.000	No
8	$C_{19}H_{27}NO_{10}$	429.16	-0.015	-0.195	
9	$C_{18}H27NO_9S$	433.14	-0.431	-0.702	yes
10	$C_{17}H_{24}Cl_3NO_9S$	523.02	-0.393	+0.137	

The complexation-induced chemical shift of H-3 and H-5 protons of β-CD are those expected as a result of interaction with those protons of the Deriveds of the D-glucosamines which are oriented towards the β-CD cavity, thus confirming a Deriveds 3,4,5,6,8,9 and 10 / β-CD.

3.2. Characterization of the Reactants and the Inclusion Compound Derived (5) β-CD by Infrared

Figure 8. Shows infrared spectra for the reagents β-CD and Derived (5) and Derived (5)-β-CD (1:1) inclusion complex.

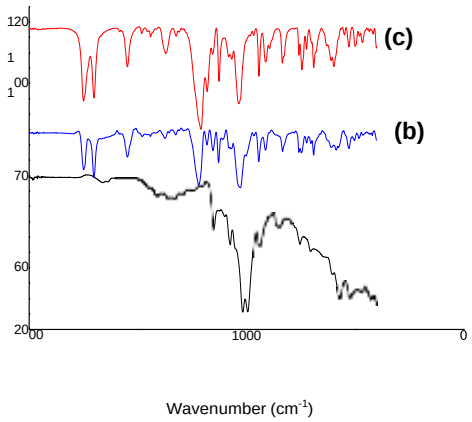


Figure 8. The Fourier transform-infrared (FTIR) spectra in the range of 500 at 4500cm-1 of: (a) β-CD; (b) inclusion complex of Derived(5)-β-CD and (c) Derived (5).

The presence or absences of characteristic peaks associated with specific structural groups of the molecules were noted. The frequencies for β-CD observed at ν of cm−1 (3394.30, 2924.70, 1157.61, and 1031.20) which corresponds to the symmetric and ant-symmetric stretching of ν[OH], ν[CH2], ν[C–C] and bending vibration of ν[O–H] respectively Table 4.

Table 4. Comparison between the intensity of principals groups of β-CD in β-CD free and in the inclusion complex.

Functional Group	Wavenumber (cm^{-1})		Changes Δ ν
	β **-CD**	**Inclusion complex**	
$\nu[OH]_{(symmetric\ and\ antisymmetric)}$	3394	3400	+6
$\nu[CH_2]$	2924	2924	0
ν[C–C]	1157	1160	+3
$\nu[O–H]_{(Bending\ Vibration)}$	1031	1030	-1

Meanwhile, vibrations for Derived (5) were recorded at 690 -740cm−1, 1000-1400 cm−1, 1400-1600 cm−1 and 690-710 cm−1 for respectively: ν[-C-S-] group, vibration of the groups ν [C-F], vibrational stretching of ν[-C=CAromatic] and ν[Ar monosubstituted] (Table 5).

Table 5. Comparison between the intensity of Derived (5) and the complex of the Derived (5)-*β*-CD

Functional Group	Wavenumber (cm^{-1})		Changes Δ ν
	Derived (5)	**Inclusion complex**	
ν[C-S]	691	690	-1
ν[C-F]	1120	1110	-10
$\nu[Ar]_{\underline{monosubstituted}}$	699	700	-1
$\nu[C=C]_{\ Aromatic}$	1490	1492	+2

In Table 3 and table 4 the wavenumber, and changes on complexation to the functional groups of β-CD and Derived (5) are presented, where Δν = ν(complexed) - ν(free).

The tables 4 and 5 have shown the difference in wavenumbers between β-CD and the inclusion complex; and between Derived (5) and inclusion complex respectively. Both tables (4 and 5) show some increase and decrease in intensity changes. The increment is due to the insertion of the C=CAromatic ring part and the chain of the (-C3F7) part into the electron rich cavity of β-CD and will increase the density of electron cloud, which will lead to the increase in wavenumber Δν > 0. The decrease in the wavenumber Δν < 0 between the inclusion complex and its constituent molecule is due to the changes in the microenvironment (microphenomenon) which lead to the formation of hydrogen bonding and the presence of Van Der Waals forces during their interaction to form the inclusion complex. On the other hand, the IR spectrum of physical mixtures imitated the characteristic peaks of β-CD and O-AcGlucosamine (5), which can be regarded as a simple superimposition of those host and guest molecules. Thus, the IR spectra significantly prove the formation of the Derived (5)-β-CD inclusion complex.

Furthermore, the absorption bands 1440, 1374, and 1341 cm−1 of the β-CD disappear (Figure 8(a)), meanwhile the infrared spectrum for Derived (5) show an intense absorption band at 1400.60 cm−1 (Figure 8(b)), it is observed in the Derived (5) inclusion complex (at 3490.00 cm−1) (Figure

8(c)), which is an indication of the formation of the inclusion complex.

3.3. Absorption Spectra

Absorption spectra were used to study the solubility of Derived (5) in presence of different concentration of β-CD, we observed that the solubility of Derived (5) increase by a factor of6 when the concentration of β-CD increase 0.10mmol/L, **figure 9** show this. The solubility curve showed an AN type solubility curve for the β-CD. These relationships indicate that ligand solubilization is proportionally less effective at higher concentration; these indicate that water soluble complex is being formed with solubilities higher than that of the un complexed substrate.

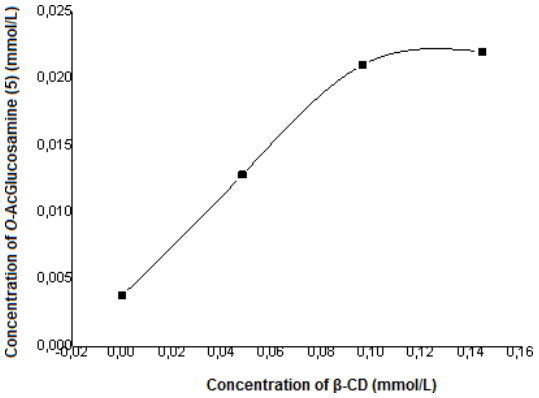


Figure 9: Phase solubility diagram of the Derived (5) in the presence of various concentrations of β-CD at25 °C.

On the other hand, absorption spectra of Derived (5)-β-CD (complex in liquid phase) were taken into consideration, it was recorded that β-CD has almost no absorption throughout thewavelength 200-400 nm; hence, inclusion complex had an increased intensity at all points ofwavelength by the increase of β-CD concentration and that may be due to the inclusion phenomena between β-CD and Derived (5). (**Figure 10**)

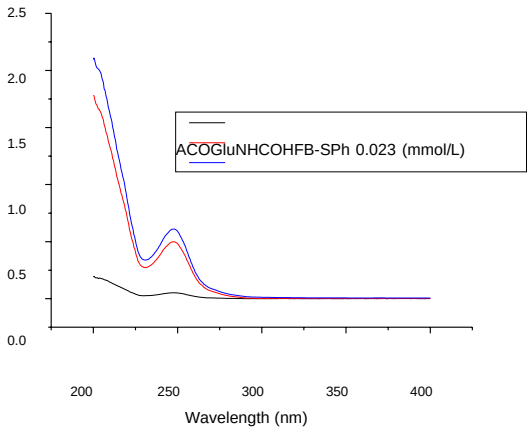


Figure 10. Absorbance against Derived (5) in the presence of various concentrations of β-CD at 25 °C: (a)1:0, (d) 1:1, (c) 1:2, (d) 1:3.

4. Conclusion

A novel inclusion complex was successfully synthesized, and characterized using FTIR,^{1}H NMR, ^{19}F NMR and ultraviolet-visible Derived(5)-*β*-CD. The ^{19}F NMR analysis clearly indicated the formation of complex; Also ^{1}H NMR yielded a good indication of complex formation because of band stretching and change in peak intensity observed for the complex.IR study confirms the formation of the inclusion compound by the disappearance of peaks and the appearance of new peaks which characterizes the inclusion complex. Because of thegood results obtained in the case of complexation between Derived (5) and *β*-CD we finalizedour work by a study which measured the solubility of Derived (5) in a *β*-CD aqueous solutionat different concentrations. From the solubility curve, it was deduced that the solubility of Derived (5) is enhanced by the concentration of *β*-CD, the solubility curve showed AN type for the *β*-CD.

References

1. Hirano, S. Chitin biotechnology applications. Biotechnol Annu Rev,**1996**, *2*, 237–258.
2. Haltiwanger, R. S.; Busby, S. Li Grove, K.; Mason, D.; Medina, L.; Moloney, D.; Philipsberg, G.; Scartozzi, R. O-glycosylation of nuclear and cytoplasmic proteins: regulation analogous to phosphorylation. *Biochem Biophys Res Commun*, **1997**, *231*(2), 237–242.
3. Zhang, L.;. Wan-shun, L.; Bao-qin, H.; Yan-Fei, P.; Dong-feng, W. Antitumor activities of*D*-glucosamine and its derivatives**,** *J Zhejiang Univ Sci B*, **2006**, *7*(8), 608–614.
4. Gale, G.R. Antimicrobial properties of certain glucosamine derivatives, *Can. J. Microbiol*.,**1964**,*10*(6),887– 896.
5. Helmoz R.; Appelt, J.S.; Oliveira, R. C. V.; Santos, O.E. D.; Rodrigues, M. Z.; Santos, E. F.H.; and Líria C.R. Synthesis and Antimicrobial Activity of Carbohydrate BasedSchiff Bases: Importance of Sugar Moiety, *Int. J. Carbohydr. Chem.*, **2013**, 2013, 1–5.
6. Chiu, H.W.; Li, L.H.; Hsieh, C.Y.; Rao, Y. K.; Chen, F.H.; Chen, A.; Hua, K.-F. Glucosamine inhibits IL-1β expression by preserving mitochondrial integrity and disrupting assembly of the NLRP3 inflammasome. *Scientific Reports*, **2019**, *9*(1) 5603– 6516.
7. Posakony, J.J.; Ferré-D'Amaré, A. R. Glucosamine and Glucosamine-6-phosphate Derivatives: Catalytic Cofactor Analogues for the glm S Ribozyme, *J. Org. Chem*. **2013**, 78, 10, 4730-4743
8. Boyce, M.; Carrico, I. S.; Ganguli, A. S.; Yu, S.H.; Hangauer, M. J.; Hubbard, S. C.; Bertozzi, C. R.Metabolic cross-talk allows labeling of *O*-linked-N-Acetylglucosamine-modified proteins via the*N*-acetylgalactosamine salvage pathway. *Proc. Natl. Acad. Sci. U.S.A*, **2011**, 108(8), 3141–3146.
9. Gao, Y.; Wells, L.; Comer, F.I.; Parker, G.J.; and Hart, G.W.Dynamic *O*-glycosylation of nuclear and cytosolic proteins: cloning and characterization of a neutral, cytosolic beta-*N*-acetylglucosaminidase fromhuman brain, *J Biol Chem*, **2001**, 276, 9838–9845.
10. Paul,R.; Wratil, S.R.; Barbara, S.; Guido, K.; Christoph, K.; Werner, R.; Athanassios, G.; and Long, D.N.A novel approach to decrease sialic acid expression in cells by a C-3-modified N-acetylmannosamine, *J Biol Chem*, **2014**, 289(46), 32056–32063.
11. Srinivasa-Gopalan, S.; Mark, B.; Jones, M.; Adam Meledeo, C. T.; Campbell, S.S. Choi.; Kaoru, H.P.; Gomutputra, A. S.; Tim Gilmartin, S. R.; Head, K. J.; Yarema.T. Targeting glycosylation pathways and thecell cycle: sugar-dependent activity of butyrate-carbohydrate cancer prodrugs, *Chem. Biol*., **2006**,*13*(12),1265–1275.
12. Inmaculada, A.; Ruth, H.; and Angeles, H,. Chitosan Amphiphilic Derivatives. Chemistry and Applications. *Current Organic Chemistry*, **2010**, *14*, 308–330.
13. Bishop, R, Supramolecular Host–Guest Chemistry of Heterocyclic V-Shaped Molecules. *Top.*

Heterocycl.Chem. **2009**, *18*, 75–102.

14. Jansook, P.; Kurkov, S. V.; Loftsson, T, Cyclodextrins as solubilizers: formation of complex aggregates. *J.Pharm. Sci*. **2010**, 99, 719–729.
15. Szejtli, J, Introduction and General Overview of Cyclodextrin Chemistry. *Chem. Rev*. **1998**, *98*, 1743– 1754.
16. Lafontaine-Lacasse, M.; Doré, G.; Picard, F, Hexosamines stimulate apoptosis by altering Sirt1 action andlevels in rodent pancreatic *β*-cells. *J Endocrinol* , 2011,208(1),41–49.
17. Janisse Crestani, D.M.; Tércio Elyan, A. M.; Francisco, V.; Humberto Gomes F, Cyclodextrins and ternary complexes: technology to improve solubility of poorly soluble drugs. *Braz. J. Pharm. Sci*., **2011**,*47*, 665–681.
18. Semalty, A.; Semalty, M.; Singh, D, Development and physicochemical evaluation of pharmacosomes of diclofenac. *Acta Pharm*, **2009**, *59*, 335–344.
19. Semalty, A.; Tanwar, Y.S, Preparation and characterization of cyclodextrin inclusion complexes for improving solubility and dissolution of nimesulide. *World J Pharm Sci*, **2014**, *2*(1), 72–78.
20. Semalty, A.; Tanwar, Y.S.; Semalty, M, Preparation and characterization of cyclodextrin inclusion complex of naringenin and critical comparison with phospholipid complexation for improving solubility and dissolution. *J Thermal Anal Calorim*, **2014**,*115*(3), 2471–2478 .
21. Singh, D.; Rawat, M.S.M.; Semalty, A, Quercetin-Phospholipid Complex: An Amorphous PharmaceuticalSystem in Herbal Drug Delivery. *Curr Drug Discov Tech*, **2012**, *9*(1), 17–24.
22. Singh, D.; Rawat, M.S.M.; Semalty, A, Rutin-phospholipid complex: an innovative technique in novel drug delivery system- NDDS . *Curr Drug Deliv* , **2012**, 9(3),305–314.
23. Loftsson, T.; Brewster, M.Pharm, Pharmaceutical Applications of Cyclodextrins. Drug Solubilization andStabilization. *Tech*,1997,5, 26–34.
24. Tsai, Y.; Tsai, H.; Wu, C.; Tsai, F, Preparation, Characterisation and activity of the inclusion complex of paeonol with *β*-Cyclodextrin. *Food Chem*, **2010**, *120*,837–841.
25. Meanwell, N. A. Fluorine and fluorinated motifs in the design and application of bioisosteres for drug design. *J. Med. Chem.* **2018**, *61*, 5822–5880 .
26. Richardson P. Applications of fluorine to the construction of bioisosteric elements for the purposes of noveldrug discovery. *Expert Opin Drug Discov*. **2021**, *10*,1-26.
27. O. Huber ; J. Szejtli, Proceedings of the Fourth International Symposium on Cyclodextrins, Munich, WestGermany, *Springer Science*, *Business Media*, **1988**, *1*, 20–22,
28. Szente, L;. Szejtli. J, Highly soluble cyclodextrin derivatives: chemistry, properties, and trends in development. *Dvanced Drug Delivery Reviews*, **1999**, *36*(1),17–28.
29. Connors, K.A, The Stability of Cyclodextrin Complexes in Solution. *Chem Rev*, **1997**, *97*, 1325–1358.
30. Rojas-Mena, A.R.; López-González. ; Rojas-Hernández, H. A, Preparation and Characterization of Holmium-Beta-Cyclodextrin Complex. *Advances in Materials Physics and Chemistry*. **2015**, *5*(3), 87– 94.
31. De-Miranda.J.C.; Azevedo-Martins. T.E.; Veiga.F.; Ferraz. H.G, Cyclodextrins and ternary complexes: technology to improve solubility of poorly soluble drugs, *Braz. J. Pharm. Sci*, **2011**, *47*(4),656– 681.
32. Eid, E.; Abdul, A.; Suliman, F.E.A.; Sukari, M.A.; Rasedee, A.; Fatah, S.S, Characterization of the inclusion complex of zerumbone with hydroxypropyl-*β*-cyclodextrin. *Carbohydr. Polym.* **2011**,*83*,1707– 1714.
33. Jug, M.; Kosalec, I.; Maestrelli, F.; Mura, P, Preparation and solid-state characterization of
34. bupivacaine hydrochloride cyclodextrin complexes aimed for buccal delivery, *J. Pharm. Biomed. Anal*. **2011**, *54*,1030 –1039.
35. Sambasevam, K.P.; Mohamad, S.; Sarih, N.M.; Ismail, N.A, Synthesis and characterization of the

inclusioncomplex of *β*-Cyclodextrin and azomethine. *International Journal of Molecular Sciences.* **2013**, *14*(2),3671 – 3682.

36. Ceborska, M.; Szwed, K.; Asztemborska, M.; Wszelaka-Rylik, M.; Kinga Suwińska, E. K.Chemical, Study of β-cyclodextrin inclusion complexes with volatile molecules geraniol and *α*-terpineol enantiomers in solid state and in solution, *Physics Letters*. **2015**,*641*,44 – 50.
37. Martin Del Valle, E.M, Cyclodextrins and Their Uses: *A Review. Process Biochemistry*. **2004**, 39,1033 – 1046.
38. Martinez, G. ; Gamez, M.A, Cyclodextrins: Inclusion Complexes with Polymers. *Revista Iberoamericanade Polymers*. **2007**, *8*, 300 – 312.
39. Ghosh . A; Biswas . S; Ghosh .T, Preparation and Evaluation of Silymarin *β*-Cyclodextrin MolecularInclusion Complexes, Young Pharm. **2011**, *3*(3): 205–210.
40. Singh, D.; Rawat, M.S.M. Quercetin-Phospholipid Complex: An Amorphous Pharmaceutical System inHerbal Drug Delivery**,** Curr Drug Disc Tech. 2012,9,17 – 24.
41. Higuchi, T, Phase Solubility Techniques. *Advanced Analytical Chemistry of Instrumentation*, **1965**, *4*,117-212.

Effect of Melittin for honey bee *Apis mellifera* in some pathogenic parasites in vitro

Fayhaa Abbood Mahdi Al-Nadawi

Quality Assurance and university performance dep., Al-Mustansyriah University, Iraq
**Corresponding author: lneadawi@uomustansiriyah.edu.iq*

Abstract: The results showed that *Entamoeba histolytica* was killed when the concentration of 0.6 µg / micromole was 280000 amoeb / ml and killing 70%. When the concentration was 0.8 micrograms / micromole, the kill rate was 380000 amoeba / l and a 90.5% killing rate. The percentage of *Giardia* was 3 000 (6000) parasites / mL at the first concentration 0.6 µg / micromole, and 60% at concentration 0.8 micromole / micromole was 7000 parasites / mL. The percentage of killing was 80%. *Trichomonas vaginalis* . The concentration of 0.6 µg / micromole was dependent on parasite movement of 85%. The percentage of the last concentration is 90% and the killing rate is by the concentration of venom on the parasite.

Keyword: *Apis mellifera* ,*Trichomonas vaginalis*, The concentration ,venom

1. Introduction

Recently, the study of biological antibacterial materials has attracted great attention from medical and pharmaceutical researchers, leading us to study new species, which have few side effects on human health and environment. Germs cannot develop immunity against them.

These biological compounds are old sophisticated weapons. A number of animal venoms such as (cobra, scorpion and frogs) have shown antibacterial properties(1). They were later used as pharmaceutical preparations for their effective role as the primary immune response mechanism(2). These ancient materials were isolated from the kingdoms and people of living beings (3). The honey bee *Apis mellifera* is an economic insect beneficial to humans and the environment, easy to breed, its various products are beneficial in terms of food and medicine, especially the honey bees, which was used by ancient Egyptians, Indians and Greeks to treat various diseases. (4) The bee poison is currently used in Complementary medicine, For blood clotting, analgesic, anti-inflammatory and as a treatment for some chronic diseases such as tendonitis and scleroderma (5, 6).

Studies on bee venom began in the late 19th century (7), known as antimicrobial peptides (AMPs), a unique and varied group of molecules divided into subgroups based on the composition and structure of amino acids, varying in length and effect. , Is composed of 12-50 amino acids, whose molecular mass is less than 10 kilo Dalton, whose net positive charge is as acidic as 2 þ -7 þ, because there is a surplus of the essential acids (Arginine, lysine and Histidine). These compounds contain a high water content of up to 80%, which is liquid, transparent, colorless, with pungent odor, water-soluble taste and some acids, resistant to alkaloids, 1.13, pH 5.5 (10, 11) , These aquatic compounds react with bacterial membranes as part of the mechanism of their effect (12). These substances show some advantages that are encouraged to be used as alternatives to traditional medicines for their speed of action and not to develop resistance against the target organism(13) These compounds have high toxicity against positive and negative bacteria Gout, fungi, metazones and cancer cells (14).

Melittin is the most representative bio peptide antibiotic in the antibacterial compounds (8), consisting of 26 aquatic amino acids (Arginine, Lysine, Lysine, Arginine), its molecular weight 846.462, which represents 40-50% of the dry weight produced by it The honey bee *A. mellifera* (10) of the acid and alkaline gland, in the Venom Sac venom sac located at the end of the last ventricular loop of the worker, is used to defend itself and the cell from the enemies by means of the stinging machine. Poison in the body of the victim through it (15, 16).

Many human parasites are infected with amoeba, the condition of the tissue *Entamoeba histolytica*, causing the disease Amebiasis Amebeasis or Amoebic dysentery. This parasite is spread among poor strata of society, malnutrition or possibly unhealthy conditions. The most important places in tropical and subtropical regions (17). According to the Health World Organization, amoeba parasites cause more than 100,000 deaths per year, the second most common type of malaria.(18) Amoebic liver abscess (Amoebic liver abscess) is the condition of the primary parasite. Protozoa requires the mucous medium of the intestine to spread to other members of the body such as the liver. *Giardia lamble* Giardia is one of the two laryngeal lupus epidemiologists and causes giardic diarrhea. It has two parallel pylori vegetarians (20), containing two nuclei and four lactates, which have a macrophagic phase in the external environment (21), the infectious stage when it is eaten with Contaminated food and water, digested by gastric acid in the intestinal cavity leading to release from the sac to two vegetative stages that multiply by bilateral (22,23). *Trichomonas vaginalis* parasite is one of the parasitic parasites that have a single stage, affecting this vaginal parasite in females and urethra Males, the parasite is infected about (25) m Lyon pregnant women (24).

Due to the lack of studies on this subject, bee venom was selected as a biological compound against the parasites *Entamoeba histolytica, Giardia lamble* and *Trichomonas vaginalis*. The aim of the study was to measure the effect of bee venom by collecting local bee strains and testing its effectiveness on the parasites above and comparing the results with the effect Pure poison imported from the company Segma.

2. Materials and methods of work

Leophilized bee venom and Fetal bovine serum were obtained from Sigma (Minnesota, USA) and Lichrosol (Merck com.,Germany,).

The local bee venom consists of (15) *A. mellifera* bees (the cell consists of two types of Iraqi and Italian bee breeds) from the saplings of the Faculty of Agriculture - University of Baghdad - Jadriya - Baghdad. Form BV0508, early in the morning, put the device in the entrance of the cell and when passing through the bees will be exposed to the electrical current, as it descends the machine sting and fall venom to the glass plate at the base of the device, take the glass board and scrape the venom, the device is used on another cell to get More venom, kept in a poisonous pyramid after being scrapped in special containers at a temperature of 4 M 0 until purification ((25.

Dissolve the raw venom crystals that weigh 100 mg in 4 ml of Lichrosol. The solution is placed in the centrifuge for 20 minutes at a temperature of 4 ° C at 12,000 cycles / minute. The floating solution shall be taken and placed in the centrifuge again and under the same conditions, and the precipitate shall be neglected. The floating liquid shall be passed on a membrane filter with a pores of 0.22 m until it is used.

Preparation of solutions Stock solution

(25) mg of each venom imported from Sigma bee venom (SBV) and from the local bee venom (LBV) toxin purified in 1 ml of PBS solution. Both samples are performed in the same conditions These are the two fundamental solutions.

Protein calibration (calibration):

The proteins were measured according to method (27), where a standard series of Fetal bovine serum (FBS) was obtained with concentrations of 0.6 '0.8 µg / µm in the same saline solution (PBS) used to dissolve the toxin.

The primary solutions of the samples (SBV) and 50-fold (LBV) on the gel electrophoresis are measured. The absorbance was measured with a 565 nm wave of ELISA for all samples. The concentration of the protein in the SBV and LBV samples was determined by projection on the standard curve of a series of increasing concentrations of Embryonic Cow Serum (FBS).

Parasite *Entamoeba histolytica*

The *E. histolytica* parasite was obtained from the patients' stool samples of Kadhimiya Teaching Hospital. After testing for the laboratory diagnosis, mucosal mucus samples were selected as an ideal source for the abundance of parasites of the parasite Trophozoite. Contents Except for the protoplasm (24). The middle is the center of Lock-Egg Di phase: media according to Brand et. al. (28). In order to control the biomaterial density of the lamipa grown in glass, the blood cell count and the 1% Iocene dye were used based on the non-permeability of the Iosine dye to the living parasite cell. The amoeba was used with a density of 400 000 amps / liter and 95% vitality. It was selected by adding 1 ml from the amoeba farm to the seed medium (LE) to a test tube.

The first group was treated with a concentration of 0.6 micrograms / micromole. The second group was treated with a concentration of 0.8 µg / micromole. The third group remained without treatment (control treatment). The tubes were gently pumped to distribute the mixture equally to the plant medium of the ameba. In the incubator at a temperature of 38 ° C for 2 hours, the tubes were taken and the percentage of the parasite was estimated.

$$\text{Amoeba kill precent} = \frac{the\ numbeof\ Amoeba\ dyed\ by \text{eosin}}{total\ number\ of\ Amoeba} x100$$

Parasite *Giardia lamble*

Samples were collected from the liquid stool of the patients of the Kadhimiya Teaching Hospital. After direct examination and confirmation of the infection, the bag was purified based on Sheffield and Bjorvatan (30). The cells of the sac were counted by means of the haemocytometer 105 cell / ml. The stool specimen was planted after the preparation of the gerardia parasite medium (HSP-1) as follows:

Take 1 mL of the 105-cell suspension into the center of the plant and add 3 ml of serum to the medium with two active antibodies penicillin and streptomycin. The 3-day-long incubation tubes were incubated at Candel Jar for a period of three days. A routine check was performed on the third day. A drop of the implant was placed on a glass slide. The lid was examined on a 400x and 1000x optical microscope. The Trophozoite was found in small numbers. . The first group was treated with a concentration of 0.6 micrograms / micromel. The second group was treated with a concentration of 0.8 µg / micromel. The third group remained without treatment (control treatment). The tubes were gently pumped to distribute the mixture equally to the embryonic medium of the parasite. In the incubator at a temperature of 38 ° C for 2 hours, the tubes were taken and the percentage of the parasite was estimated.

$$\text{Percentage of dead parasite} = \frac{the\ numbeof\ parasite\ dyed\ by\ \text{eosin}}{total\ number\ of\ parasite} x100$$

Parasite *Trichomonas vaginalis*

Vaginal Parasites were obtained by taking swabs from the Alawiya and Ibn Al-Baladi Hospital of women with vaginal itching and suffering from vaginal discharge, consultation with the specialist and after laboratory diagnosis. moist swab was placed in the middle of the sperm called Diamond (31) after the parasite identified 102 organisms / ml (32) was taken swab and planted at 5 ml from the center of the Diamond. Fetal bovine serum, a 56 μm dose for 30 minutes, preserves the serum at 20 ° C. Add the swab to 5 ml of the center of the plant plus 0.5 ml of F. b. S and incubate at 35 ° C for 72 hours and examine after 4, 6, 7 days after incubation and note vaginal trigeminal movement.

The first group was treated with a concentration of 0.6 micrograms / micromole. The second group was treated with a concentration of 0.8 μg / micromole. The third group remained without treatment (control treatment). The tubes were gently pumped to distribute the mixture equally for the implant medium. In the incubator at a temperature of 38 ° C for 2 hours, the tubes were taken and the percentage of the parasite was estimated.

$$\text{Percentage of dead parasite} = \frac{the\ numbeof\ parasite\ deyed\ by\ \text{eosin}}{total\ number\ of\ parasite} x100$$

3. Results and Discussion

The results showed in Figure (1) that *Entamoeba histolytica* was killed in the form of (2) when the concentration of 0.6 μg / micromole was 280000 amoeb / ml and killing 70%. When the concentration was 0.8 micrograms / micromole, the kill rate was 380000 amps / l and a 90.5% killing rate. The percentage of *Giardia* was 3 000 (6000) parasites / mL at the first concentration 0.6 μg / micromole, and 60% at concentration 0.8 micromole / micromole was 7000 parasites / mL. The percentage of killing was 80%. *Trichomonas vaginalis* (4) The concentration of 0.6 μg / micromole was dependent on parasite movement of 85%. The percentage of the last concentration is 90% and the killing rate is by the concentration of toxin on the parasite.

Male Bradford et. al. [27] mentioned These peptide compounds, extracted from a wide range of organisms, have inhibitory activity against microbes, which act as a key to disrupting the cell surface. In some cases, their entry affects calcium levels within these microbes, as well as their effect on mitochondrial function , Stimulating self-induction and thus necrosis and apoptosis. There is compelling evidence that the Melittin compound is able to penetrate through cell membranes in a non-selective manner by stimulating the formation of pores and openings. It also analyzes primitive and eukaryotic cells (33), the method responsible for the degradation of blood cells and macrophages (34) (35) and against the cancer cells (36).

Melittin was killed by *leishmania*. (37) Melittin hybrid -Cecropin recently showed a significant inhibitory activity against *leishmania* stages with slight effect against host cells of the parasite (38, 39) and even inside The cells of the animals experiment, giving way to a wide Further research and future studies, that support the side to take advantage of these vital compounds, as alternate of these chemical compounds that are used to treat diseases caused these microbes and parasites, as well as cancers, with side effects on human health in general and his animals.

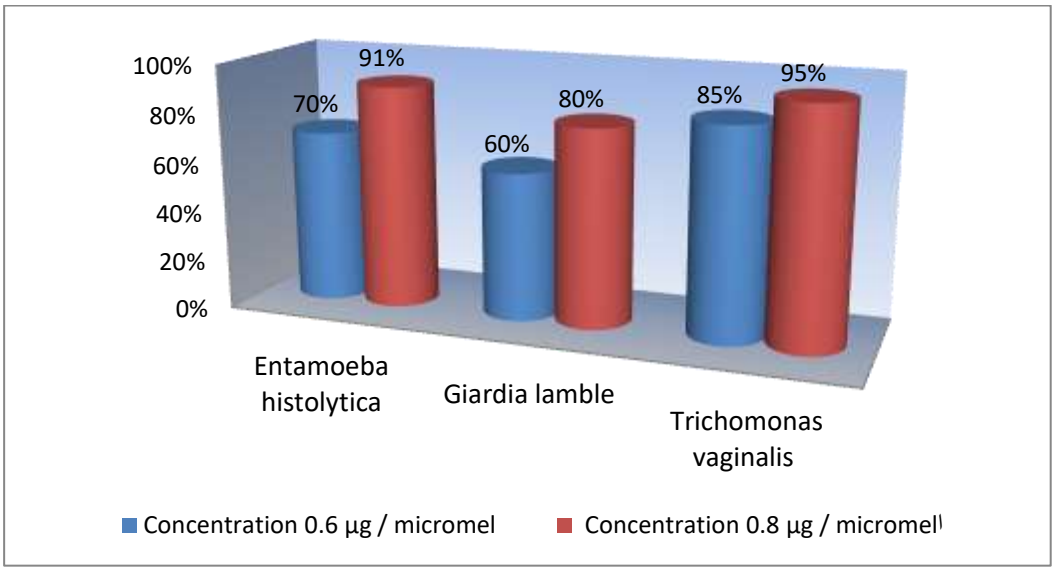


Figure 1: Percentages for the killing of parasites *Entamoeba histolytica*, *Giardia lamble* and *Trichomonas vaginalis* with concentrations (0.6), 0.8 µg / micromole in the name of honey bees in vitro.

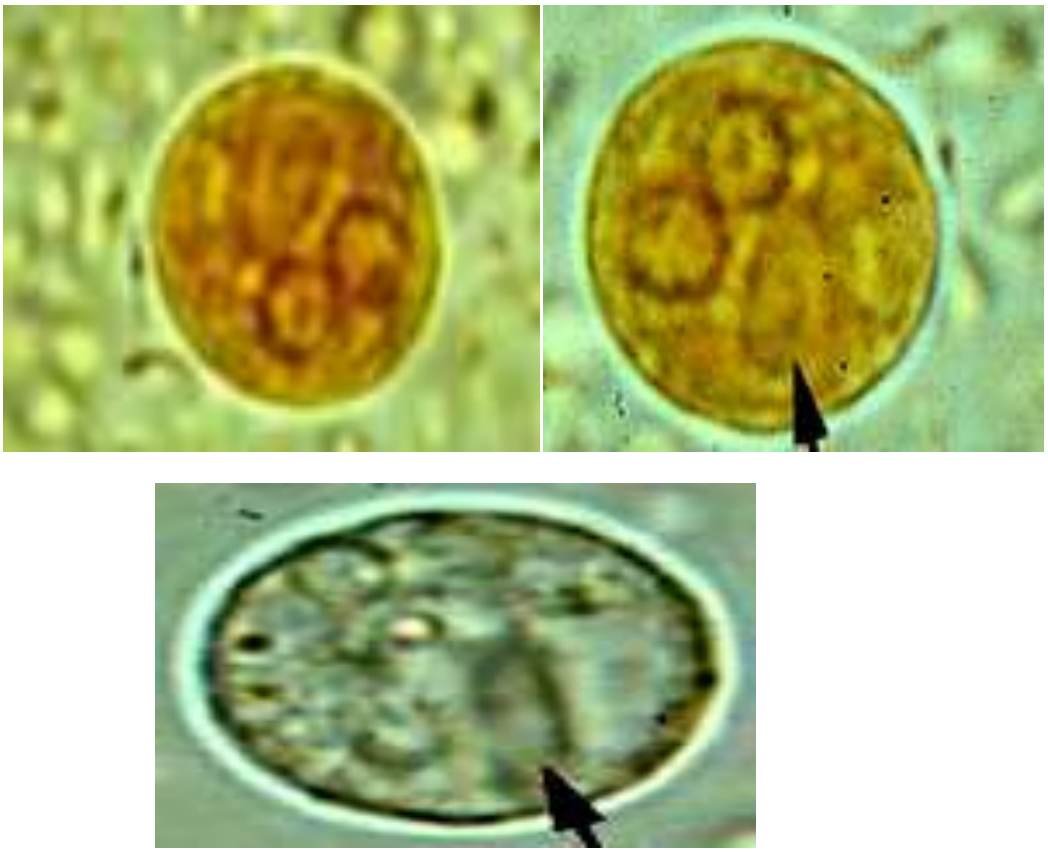


Figure2: (*Entamoeba histolytica*) parasite

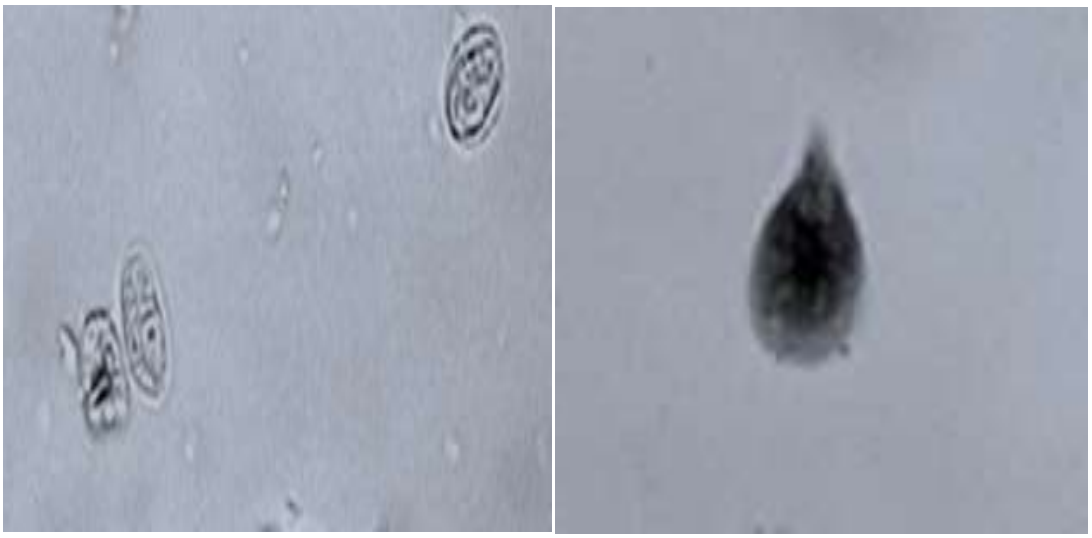


Figure3: *Giardia lamble* parasite

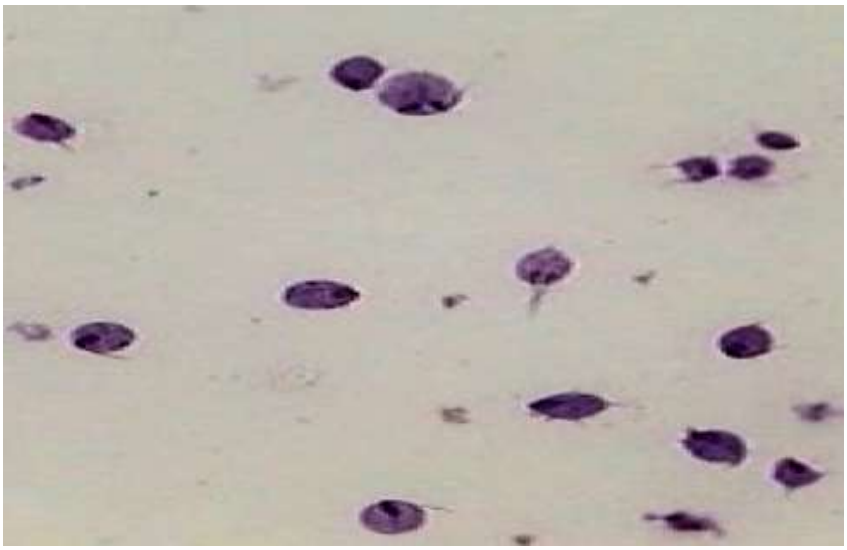


Figure 4: *Trichomonas vaginalis* parasite

References

1. Talan D.A. (1991). Antibacterial activity of crotalid venoms against oral snake flora and other clinical bacteria. J. Infect. Dis. 164: 195-198.
2. Moerman L. ; Bosteels,S.; Noppe,W.; Willems,J.; Clynen,E.; Schoofs, L.; Thevissen, K. ; Tytgat, J. ;Van Eldere, J.; Van der Walt, J.; and Verdonck, F.(2002). Antibacterial and antifungal properties of helical, cationic peptides in the venom of scorpions from southern Africa. European Journal of Biochemistry 269: 4799-4810.
3. Andreu,A., Rivas L.(1998). Animal antimicrobial peptides: an overview Biopolymers, 47 : 415–433.
4. Beck B.F.(1997). In The Bible of Bee Venom Therapy Silver Spring, MD: Health ResourcesPress.
5. Beck B.F. (1935) In Bee Venom Therapy: Bee Venom, Its Nature and Its Effect on Arthritic and Rheumatoid Conditions (Appleton-Century-Crofts.

6. Son DJ, Lee JW, Lee YH, Song HS, Lee CK and Hong JT.(2007). Therapeutic application of anti-arthritis, pain-releasing and anti-cancer effects of bee venom and its constituent compounds. Pharmacol Ther. 115:246–270.
7. Langer J. (1897). Ueber das Gift unserer Honigbiene. Naunyn Schmiedebergs Arch. Pharmacol. 38, 381-396.
8. Yeaman, M.R.; Yount, N.Y. (2003)Mechanisms of antimicrobial peptide action and resistance.*Pharmacol. Rev. 55*, 27–55.
9. Hancock, R.E.W.and Diamond, G.(2000) The role of cationic antimicrobial peptides in innate host defences.Trends Microbiol., 8 : 402–410.
10. Habermann E. Bee and wasp venoms. Science 1972;177(4046):314-322.
11. Raghuraman H., Chattopadhyay A. Orientation and dynamics of melittin in membranes of varying composition utilizing NBD fluorescence. Biophys. J. 2007;92:1271–1283. doi: 10.1529/biophysj.106.088690.
12. Teixeira,C.,Vale,N.,Pérez,B.,Gomes,A.,Gomes,J.R.B.,andGomes,P. (2014).“Recycling”classicaldrugsformalária. *Chem. Rev.* 114, 11164–11220.doi: 10.1021/cr500123g
13. Bechinger, B. (1997).Structure and functions of channel-forming peptides: magainins, cecropins, melittin and alamethicin J. Membr. Biol., 156: 197–211.
14. Hoskin D.W., Ramamoorthy A. (2008). Studies on anticancer activities of antimicrobial peptides. Biochim. Biophys. Acta1778:357–375. doi: 10.1016/j.bbamem.2007.11.008
15. Snodgrass R.E. (1984) .In Anatomy of the honey bee (Cornell University Press.
16. De Lello E. Adnexal (1971) Glands of the sting apparatus of bees: Anatomy and histology, I (Hymenoptera: Colletidae and Andrenidae). J. Kans. Entomol. Soc; 5-13.
17. Haque, R., Ali, I.K. Akther, S,and petri,W.A. (1998). Comparison of PCR. Iso enzyme analysis and antigen detection for diagnosis of *Entamoeba histolytica* infection J .Clin Microbial 36: 449-452.
18. WHO/World Health Organization .(1997).Amoebiasis weekly epidemiology records 72:97-100, Genev, Switzerland.
19. Samuel, L., Syanley, J., Sharon, L., and Reed,(2001).Microbes and microbial toxin paradigram for microbia mucosal interactions VL. *Entamoeba histolytic* parasite host interaction -Am.SPhy. Gastroin testinal Liver physiol 2806:49-1054.
20. Fanbert,F.(1991). Immune response to Giardia doudenalis. Clin.Microbial Rev;13(1):35-54 Table of Contents.
21. Espelage, W., Heiden, M.; Stark,K. and Alpers, K. (2010).Characteristis and risk factors for symptomatic *Giardia lamblia* in fection in Germany ,BioMed cent. Publ Health,10:41-49.
22. Eckmann ,L.(2003)Mucosal defenses against *Giardia* parasite Imminol 25:259-270.
23. Manning, G.Reiner, D.S., Lauwaet, T ., Dacre, M., Smith, A.Zhai, Y. Svard, S. and Gilln,F. D. (2011) .The minimal kinome of *Giardia lamblia* illuminates early kinase evolution and unique parasite biology .Genom .Biol. 12: 66-85.
24. World Health Organization .(2012). Global prevalence and incidence of selected curable sexually transmitted infection -2008.
25. Vasily N. and Krylov O. (2003).Physiologycail aspects of the technology of bee venom industrial production. Mellifera 3: 62-66.
26. 26-Zhou J.; Zhao. J. ;Zhang, S. ; Qi, Y. ; Xue, X.; Li, Y, ;Wu, L. ;Zhang, J. ;Chen, F. ;Chen, L. (2010). Quantification of melittin and apamin in bee venom lyophilized powder from *Apis mellifera* by liquid chromatography–diode array detector–tandem mass spectrometry. Anal. Biochem. 404: 171-178.

27. Bradford,S.M.G, and Kulkami ,M.M. (2010).Interactions of antimicrobial with Leishmania and Trypanosomaes and their functional role in host parasitism .Experimental parasitology 126 (3):397-405.
28. Brand ,I. Von, Rees , C.R. ; Jacobs ,L and Reardon, I.V. (1943).Studies on reducing substances and gas formation in culture of *Entamoeba histolytic* and Single species of symbiotic bacteria , Am. J.H y g. 37:310-319.
29. Deshmuk ,S.D. and Borle ,M.N.(1975).Studies on the insecticidal properties of indigenous plant products S. Indian J. Enthno pharmacology, 37(1):11-18.
30. Sheffield, H.G. and Bjorvatan . B. (1977)Ultra structure of the cyst of *Giardia lamblia*. A m. J. Trop.Med.Hyg.26(1):23-30.
31. Diamond ,L.S.(1957).The establishment of various trichomonads of animals and man in axenic culture. J. parasitology 43(4):48-49.
32. Levi,M.H. Torres ,I.Pina,C. and Klein, R.S. (1997). Comparison of the In pouch TV. culture system and Diamond's modified media for detection of *Trichomonas vaginalis* .J.Clin. Micro,35(12):3300-3310.
33. Raghuraman,H.,andChattopadhyay,A.(2007).Melittin:amembrane-active peptide with diverse functions. *Biosci.Rep.* 27, 189–223.doi:10.1007/s10540- 006-9030-z
34. Blondelle, S. E ;Houghten, R.A.(1991). Hemolytic and antimicrobial activities of twenty-four individual omission analogues of melittin .Biochemistry 30:4671-4678.
35. Lazarev ,V.N. ;Partenova,T.M ;Gularyan,S.K. ;Misyurina,O.; Yu,; Akopian, t..A.;Govorun,V.M.(2002).Indduced by chlamydia trachomtis and Mycoplasma haminis in hela cell line. Int.J. Antimicrob .Agents 19:133-137.
36. Winder, d. ;Gunzburg, W. H. ;Erfle ,V. ; Salmons, B.;(1998).Expression of antimicrobial peptides has an antitumor effect in human cells .Biochem .Biophys. res .Commun 242:608-612.
37. Pereira, A. V.; Barros, G.D.; Pinto ,E .G ; Tempone, A.G,Orsi, R.O; Santos ,L. D.; Jr , C.R.S; Pimenta, D.C ;and Barraviera,B.(2016) Melittin induces in vitro death of Leishmania (Leishmania) infantum by triggering the cellular innate immune response.. Journal of Venomous Animals and Toxins includingTropical Diseases (2016) 22(1):1-8. DOI 10.1186/s40409-016-0055-x.open access.
38. Luque -Ortega,J.r. ;Saugar ,J.M.,Chiva,C.,Andreu,D., Rivas,I .(2003) .Identification of new Leishmanicidal peptide lead structures by automated real-time monitoring of changes in intracellular ATP .Biochem.J.375:221-230.
39. Alberola J, Rodríguez A, Francino O, Roura X, Rivas L, Andreu D. (2004).Safety and efficacy of antimicrobial peptides against naturally acquired Leishmaniasis.Antimicrob Agents Chemother.;48(2):641–3.

Effect of pre-treatment of wheat straw and sludge digestion on biogas yield production

Arwa Al-Da'asen [1] Adnan Al-Harahsheh [2], and Mohammad Al- Hwaiti [3,4,*]

[1] Engineering Collage, Al-Hussein Bin Talal University, Ma'an, Jordan

[2] Chemical Engineering Department, Faculty of Engineering Mutah University, Alkarak, Jordan

[3] Dept.of Mining Engineering, Engineering Collage, Al-Hssein Bin Talal University, Ma'an, Jordan

[4] Director of research & Business Development unit/Jordan phosphate Mines Company, Jordan

**Corresponding authors: adaaseen@yahoo.com; adnan@mutah.edu.jo; mohhwaiti@gmail.com ; Tel: +962772942727; +962777383614; +962795082009*

Abstract: Biogas is a source of biomass energy that is produced from degradation of organic matter throughthe anaerobic digestion process. The main objective of this study is to investigate and improve biogas production from wheat straw (WS), cow manure inoculum (CMI), and sludge using anaerobic co-digestion processes. Batch reactor and various pre-treatments process including sulphuric acid, hydrothermal treatment, process temperature, and pH were assessed. The results showed that highest biochemical methane potential of treated WS (TWS) and sludge of about 314.94 ml CH_4/gVS_{add} followed by thermophillic anaerobic digestion experiment of 232.23 ml CH_4/gVS_{add}, hydrothermally TWS and sludge mixture of 182.11 ml CH_4/gVS_{add} and then untreated WS (UWS) & sludge mixing (50:50) of about 145.02 ml CH_4/gVS_{add}. Moreover, the volatile organic solids decreased in the co-digestion of the three substances by 66.86%, and its consumption for digestion with CMI was improved, which indicates the potential of WS as a pillar for further digestion as well as for biogas production. Mesophilic conditions is more preferred and stable than thermophillic conditions but the latter is faster rate of digestion and shorter retention time process inside the reactor. The pH of biomass mixture was found to be reducing during the process of anaerobic digestion. The study recommended monitoring and controlling the pH enhanced the production of biogas.

Keywords: Biogas; Anaerobic digestion; Wheat straw; Pre-treatment; pH; Temperature

Investigation of the Relationship Between the Digested Sludge Dewatering and Microbial Activity Improved by Chemical Pretreatments

I. Kadri [1, *], R. Zamouche-Zerdazi [1, *] and, O. Achouri[1], M. BencheikhLehocine[1]

**Corresponding author: kadri_imene@yahoo.com ; Tel.: +23165533193*

Abstract: The digested sludge from the anaerobic digestion process of multitude fractions solid is partially stabilized but has a more or less liquid character. Efficient dewatering can significantly reduce the volume of these digestates, reduce the storage or conditioning cost, while achieving a better stability of these products.Although anaerobic digestion can reduce the total amount of solid fraction introduced, the final product is generally more difficult to dewater. This study will attempt to clarify the factors influencing the dewatering of this type of sludge while focusing on the digestion process and mainlythe microbial activity.The digestion process efficiency is generally conditioned by the operating conditions imposed to quote the ratio Inoculum / substrate, the conditions of incubation and particularly the substrate composition , the improvement of the process performances , is always directed towards the substrate hydrolysis, generally complicated, by the pretreatments which can juggle between thermal,chemical or mechanical pretreatments, inducing an microbial activity improvement and thus an increase in the biogas production.In the present study sludge dewatering was studied for co-digested sludge recovered from batch reactors incubated under thermophilic conditions, treating food waste in its raw state and after chemical pretreatment with 3% oxygenated water, while using a co-substrate, orange peels, a variation in the volume of substrate and co-substrate were required in these reactors.The centrifugal dewatering efficiency was estimated by measuring the solid cake while characterizing the digested sludge by mineralization rate, amount of protein and polysaccharides, viscosity, capillary suction time and morphological characteristics.A solid cake varying between 12.10 -13.74 % and between 14.46 - 66.80 % was quantified after centrifugation for digested sludge using raw substrate and chemically pre-treated substrate respectively.

Keywords: Digested sludge, Dewatering, Pretreatment, Microbial activity, Biogas.

1. Introduction

Wastewater treatment produces large quantities of sludge, and these sludges have negative effects on the environment, requiring their treatment, as their treatment was a major challenge and is equivalent to 65% of the total cost of the plant ((1), (2)).

Anaerobic digestion (AD), with its four steps of hydrolysis, acidogenesis, acetylogenesis and methanogenesis (3) is one of the most common and approved methods for the treatment of all types of solid waste including sludge recovered from wastewater treatment plants (4). Anaerobic digestion has also a very important advantage which is the production of energy rich biogas (55-70% methane) (5).

The sludge recovered from AD requires dewatering to reduce its volume in order to improve active (burning) or agricultural (spreading) recovery and to improve the other management steps (storage and transport).

To improve this treatment process, several pre-treatments are practiced and are divided between thermal, chemical or mechanical treatments. (6). These pretreatments allow to reduce the size of the particles constituting the waste, because too large sizes make more difficult the organic matter fragmentation in the step of the hydrolysis what slows down the development of the subsequent phases in the process of the AD. A minimum size gives the particles a more adequate specific surface for the microorganism's action during the organic matter transformation.

Several studies have investigated the effect of these pretreatments on the improvement of AD performance, mainly biogas production ((7), (8)), but few studies have focused on the pretreatments effect on the digested sludge dewatering, since the sludge properties directly control the dewatering process.

Several works have also studied the operating conditions effect of the digesters, on the characteristics of the digested sludge and thus their aptitude for dehydration. Lawler et al (1986) (9), note a very slight increase in the specific filtration resistance (SFR) and capillary suction time (CST) with the increase of the residence time in the digester. Novak et al. (1988) (10), record higher SFR for anaerobically digested sludge than for conventional activated sludge. They also show a significant increase in SRF at low temperatures, or with dry matter input to the digester. Houghton et al. (2000) (11) observed no relationship between the measurement of capillary suction time (CST) and retention time in their digester.

In the present study the suitability of digested sludge for dewatering will be studied not in relation to the digester operating conditions but rather to the digestion process itself and the microorganism's activity (anaerobic heterotrophs), which will be enhanced by pretreatments applied to the substrate upstream of the AD.

The effect of pretreatments on the sludge characteristics recovered after biological treatment under anaerobic conditions will be zoomed, in while trying to understand the relationship between the performance improvement of anaerobic digestion (microbial activity) and the morphological characteristics as well as the composition of the digested sludge, then the pretreatments effect on the dewatering performance carried out by the centrifugation technique.

The sludge centrifugal dewatering was studied for co-digested sludge recovered from batch reactors incubated under thermophilic conditions, treating food waste (FW) in its raw state and after chemical pretreatment with 03% of hydrogen peroxide, while using a co-substrate, orange peels (OP), a variation of the ratios of substrate and co-substrate were varied in these reactors while fixing all the other operating conditions to mention, the ratio of substrate inoculum, pH, incubation temperature, pre-treatment conditions, shape and capacity of the digesters.

2. Materials and Methods

2.1 The different measuring devices and Experimental design of the dehydration technique The measures established during this study aim to monitor:

- The morphological presentation of the sludge recovered from the different reactors is mainly estimated by the capillary suction time (CST), an investigation method conceived by Gale and Beskerville in 1968 (12), corresponding to the time taken by a sludge to travel a fixed distance in a filter paper, it is a simple and fast method to characterize the dehydratability ofthe sludge (13), and thus their presentation during the treatment of the different wastes underdifferent presentations, The suction time is measured by a CST meter AQUALYSE, the viscosity measured by a viscosimeter type SNB digital, to have an idea on the state of microbial flocs presentation during treatment, the increase of this parameter can be caused by the release of the flocs extracellular constituents in case of a stress or of the constituents of the microorganisms

in case of microbial lysis and finally the microscopic visualizations in the colored state (Gram and methylene blue staining) by an optical microscope INFINITY,OPTECH.

The recovered sludge composition, measuring mainly the suspended solids and volatile solidsin suspension (TSS/TVS) estimated by the vacuum filtration technique, the conductivity, salinity and pH measured respectively by a multi-parameter WTW, Multi 3420 and a JENWAY pH-meter (3505) and their compositions in The extracellular polymeric substances(EPS), the estimation of these polymers must be imperatively started by their extraction fromthe microbial flocs, which is carried out in order to quantify proteins, polysaccharides and humic substances, while avoiding a cellular lysis . The EPS bound in the flocs notably by divalent cations were extracted by the ion exchange resin method proposed by Frolund et al (14), where a volume V0 of sludge is taken from each reactor (V0= 0. $1*10^{-3}$/TVS), This volume is chosen according to the concentration of TVS of the sample, it varied between 4.21and 6.8 mL for the fourteen reactors, these volumes are then preserved at 4°C in crushed ice,in order to avoid a cellular lysis and thus a release of intracellular polymers. Prior to EPS extraction, the collected V0 volume of slurry was thickened by centrifugation for 15 min at 4000 rpm, the purpose of which is to separate the soluble exopolymers present in the supernatant, and stored in a stoppered vial surrounded by crushed ice (15). The ionic resin (DOWEX 50 x 8 Na+, 20-50 mesh, Fluka) was subjected to conditioning prior to extraction (6 g resin + 20 mL 0.2 M NaCl) under agitation for 01 hour (16). Extraction was carried outunder agitation, an ice bath maintained at a constant solution temperature around 4 °C. In thebeaker containing the resin and NaCl solution, the centrifuged sludge was added. The sludgeis kept in contact with the ion exchange resin for 02 hours at a temperature of 4 °C and under agitation 600 rpm (16). This step allows solubilizing the EPS. The decantation for 5 min at 4°C, which follows, allows the recovery of only the supernatant which is centrifuged at 4000rpm for 15 min at 4°C. The centrifugation supernatant then contains the EPS that were initially bound to the biological aggregates (15). After this extraction, an assay of proteins and polysaccharides was carried out by UV-Visible spectrophotometry, JASCO V-630 ,usingthe classical methods of Lowry (protein assay) and Dubois (polysaccharide assay). The Lowry method (17), is based on two chemical reactions, the first is the Biuret reaction wherethe peptide bonds of the proteins react with copper sulfate in alkaline medium followed by the second reaction which is only the reduction of the phosphomolybdic-phosphotungstic reagent (Folin-Ciocalteu) by the protein complex previously formed. A blue coloration is theresult of these reactions, the absorption being measured at 750 nm, the standard protein usedas reference was bovine serum albumin (BSA) prepared at concentrations between 20 and 200 mg. L^{-1} for calibration. The determination of polysaccharides was performed by the Dubois method (18). This method is based on the reaction of carbohydrates with sulfuric acid.The product formed combines easily with phenol and gives a pink coloration. The absorbanceis measured at a wavelength of 485 nm. This method is very sensitive as it can detect amountsof carbohydrate up to 1 µg. The standard molecule used for the realization of the calibrationcurve was glucose at concentrations between 10 and 100 mg. L^{-1}.

- The dewatering yield of the different sludge recovered after centrifugation, recalling first thatthe dewatering of sludge is carried out in the present study by centrifugation on a laboratoryscale after a thickening step carried out in a cone for 2 hours of time, forming a bed of concentrated sludge in the lower part of the cone, generally this time can reach 24 hours in industrial thickeners (19). A laboratory electric centrifuge (ROTOFIX 32) with a rotor radiusof 19 cm, with a rotation speed between 600 -4000 rpm and a time limit of 99 minutes was used, a speed of 2900 rpm, a time of 30 minutes and a volume of thickened sludge of 04mL were set in this study, these parameters were optimized in previous work not presented in thisstudy. The yield is estimated by two quite close answers, the dryness which represents the mass percentage of dry

matter contained in the sludge after dewatering (19), using only a desiccator and an oven at 105 ° C and the percentage of cake which is calculated by the following formula: Cake % = p2-p0/p1-p0 where p2 , p1 , p0 , are respectively the weight ofthe crucible with dewatered and dried sludge at 105°C; the weight of the crucible with dewatered and wet sludge and the weight of empty crucible.(20)

- The microbial activity constituting these sludges recovered from the different reactors estimated mainly by the yield of the anaerobic digestion of the authors of this biodegradation, these measurements will be more detailed in the later part.

2.2 Anaerobic digestion experience

As underlined in the introduction, the objective of this study is to explore the effect of the improvement of the activity of the microorganisms implemented during the anaerobic digestion of a food waste on the dehydration of the sludge recovered after the digestion, an activated sludge which is mainly constituted of a fraction of the waste not biodegraded or resistant to the biodegradation, of a complex microbial community mainly heterotrophs dominating in number and in mass, the products of the various metabolisms as well as a good fraction of water varying from 90 to 95% because of the degree of important porosity in the flocs which constitute them, on the other hand the digested sludge or digestates resulting from the methanization of the mixed sludge, leads to the production of digested sludge (digestate) partially stabilized more or less liquid especially according to the water content of the sludge introduced in the methanizer and of the biogas, gaseous mixture saturated in water at the exit of digester is composed of approximately 50 % to 70 % of methane (CH_4), 20 % to 50 % of carbon dioxide (CO_2) and some trace gases (NH_3, N_2, H_2S) (21).

The improvement of the activity of the biomass was based not on the variation of the conditions of operation fixed in the different digesters (discontinuous systems) to quote the temperature of incubation, the ratio Inoculum/substrate (I/S), the type of substrate, the pH, the time of stays or incubation and the intensity of mixing, but on the presentation of the substrates destined to this mode of biological treatment, which are generally classified as complicated and difficult to biodegrade, samples of food waste (FW) mixed with a co-substrate orange peel (OP), of different concentrations were placed in bottles (BMT-Test) in the presence of inoculum (sludge recovered from the return line in a municipal wastewater treatment plant).

Two experimental companions were carried out during this study, incubating in batch reactors of 250mL capacity, the ground food waste, in its raw state in the first seven reactors (ADR0-ADR7) and inthe other seven incubating, the food waste chemically pretreated using hydrogen peroxide at 03% (ADRP0-ADRP7), the feeding conditions with a fixed ratio (I/S) of 0. 5 mg TVS. mg COD^{-1} in the fourteen different reactors incubated in 55°C thermopyles conditions in MEMMERT type incubationchambers, are grouped in Table 01.

Recalling, that the Co-digestion can be a combination of liquid / liquid, solid / solid or liquid / solid co-products. This technology is an attractive option for improving the yields of anaerobic digestion of waste due to the positive synergies established in the digestion medium (positive interactions between co-products can result in anaerobic co-digestion). Co-digestion has several advantages overAD from a single product. The main advantage of Co-digestion resulting from the association of several co-products is the increase in the methane yield of the biogas produced during the process, this increase in yield is due to the balance of nutrients obtained by the association of several co- products, the nutrient inputs improve the organic matter content of the digester.

The main objective of co-digestion in this study by the use of orange peelings (OP) is to maintain thestability of the process. This process stability includes the correct functioning of the reaction

medium(alkaline power, inhibition, equilibrium in C / N ratio, adjustment of the dryness rate, etc.). Stable anaerobic digestion results in a good methane yield from the biogas produced during the process. (22)

10 mL of a nutrient solution was also introduced in the fourteen reactors in order to stimulate biodegradation, the composition of this solution is well detailed in table 02.

The evaluation of the improvement brought by the chemical pretreatment on the biodegradability of these wastes (improvement of the activity) and their methanogenic potential by considering the thermophilic conditions, was evaluated by measuring the quantity of biogas produced, the abatement efficiency of the carbon load evaluated by the chemical oxygen demand of the soluble fraction (CODs) and the fraction in suspension evaluated by the abatement of the suspended solids (TSS) and of the volatile solids in suspension (TVS).

Table 1. Incubation conditions in the different batch digesters

AD conditions	Thermophilic condition			
I/S Ratio	0.5 mg TVS. mg COD^{-1}			
	Without chemical pretreatment of FW			
	Sludge	FW fraction	OP fraction	Nutriment
ADR0	+	0	0	+
ADR 1	+	0.9	0.1	+
ADR 2	+	0.8	0.2	+
ADR 3	+	0.7	0.3	+
ADR 4	+	0.6	0.4	+
ADR 5	+	0.5	0.5	+
ADR 6	-	1	0	+
ADR 7	-	0	1	+
	With chemical pretreatment of FW			
ADRP0	+	0	0	+

ADRP1	+	0.9	0.1	+
ADRP2	+	0.8	0.2	+
ADRP3	+	0.7	0.3	+
ADRP4	+	0.6	0.4	+
ADRP5	+	0.5	0.5	+
ADRP6	-	1	0	+
ADRP7	-	0	1	+

Table 2. Composition of the nutriment solution (23)

Nutriments	Concentration ($g.L^{-1}$)
$FeCl_3.4H_2O$	2
$CaCl_2.6H_2O$	2
$MnCl_2$	0.318
$CuCl_2$	0.024
$ZnCl_2$	0.051
H_3BO_3	0.051
$NiCl_2.6H_2O$	0.051
EDTA	1.001
HCl	1 ml
NH_4Cl	1.401
KH_2PO_4	1.250
MgSO4.7H_2O	0.510
$CaCl_2$	0.041
NO_3Na	2.001

3. Results and Discussion

The extracellular polymeric substances (EPS) in microbial flocs can have several sources to mention, a microbial source, the release of compounds by microorganisms in order to restore a balance of concentrations across the cell membrane (24), microbial metabolism where more than 1000 compounds are involved in the formation of metabolites (24), microbial lysis (25), where the composition of the EPS will be directly linked to the bacterial species present , and an environmental source: linked to the biosorption of organic molecules from the reaction medium (26). The composition of the EPS is the result of different processes and varies enormously in the literature in quantity and quality. EPS can represent up to 60% of the organic fraction of sludge, while cellula

biomass represents only up to 20% (27), EPS may also contain low molecular weight groups such as divalent cations. These groups can alter or change the structure and physicochemical properties of EPS. According **to** Hong Liu et al (28), extracellular polymeric substances (EPS) are metabolic products that accumulate on the surface of bacterial cells (29). They form a protective layer for the cells against the harsh external environment, and also serve as carbon and energy reserves during starvation. EPS have been found to be crucial for flocculation ((27), (30)) and dewatering (31) of activated sludge, as well as for the microstructure of methanogenic granular sludge.

An improved activity by the hydrolysis of the organic loads after a mechanical pretreatment (the grinding of FW) and a chemical treatment, in the AD of the various samples will certainly have aneffect on the microbial metabolisms ingesting a more significant production of these EPS and thus amore important aggregation causing a trapping of the bound water in this very complex matrix inwhich the microorganisms are immobilized, and thus a limitation or not of the dehydration stagewhich follows this mode of biological treatment of these FW mixed at different ratios with the OP. Also recalling that free and bound water are considered the main types of water in a sludge, free waternot associated with solid particles and not affected by capillary force represents the largest part of thesludge and the easiest to remove by the various processes of dewatering, on the other hand boundwater which is defined as the sum of pore water, surface water and internal water. Interstitial water isa water trapped in the crevices and interstitial spaces of flocs and organisms, Surface water, areretained on the surface of solid particles by adsorption and adhesion and Internal water, water inbacterial cells and bound chemically / physically in the sludge, bound water represents a very smallproportion is considered the most difficult to remove ((32), (33)).

It should be noted that all measurements and dewatering experiments were performed just after reaching the steady state, a preservation at 4°C is sometimes used before proceeding with the analysis,the time needed to record a plateau in biogas production (reaching the steady state) was on average 14 hours for the non-pretreated FWs (ADR1-ADR7) and 08 hours for the pre-treated FWs (ADRP1-ADRP7). A mineralization (MR) varying between 50.60 and 53.67 % was reached for the first sevenreactors and between 53.26 and 54.08 % for the other seven, the mineralization rates are quite close despite the fact that the residence times differ by 06 hours, this is due to the improved activity of themicroorganisms following the pretreatments applied.

What was noticed initially in the different reactors that the salinity and consequently the conductivityin all the reactors containing the substrate either in their raw or pretreated state are almost constant, this lets us think that the increase of the viscosity (table 3 and 4) is due to the release of the constituentsof the EPS in the interstitial liquid of the sludge, on the other hand the decrease will be caused by theentrapment of these constituents in the solid matrix, it is also noted that a neutral pH is recorded in the fourteen reactors.

Table 3. Characterization of digested sludge using raw FW (ADR)

AD reactors (KW raw substrate)	**ADR0**	**ADR 1**	**ADR 2**	**ADR 3**	**ADR4**	**ADR 5**	**ADR 6**	**ADR 7**
Characterization of digested sludge								
CST (s)	162	151	128	159	166	103	123	98
CSTs. 10^{-4} ($s.L.mg^{-1}$)	41.7	39.2	38	44.7	44.5	24.8	31.0	31.2
Conductvity ($ms.cm^{-1}$)	6.20	4.80	7.95	6.66	6.83	6.58	7.21	5.72
Salinity (%)	3.4	3.9	3.2	3.7	3.8	3.7	3.9	3.3
T (°C)	27.9	27.1	27.3	27.7	26.3	25.3	26.6	26.6
pH	7.17	7.27	7.19	7.14	7.23	7.13	7.07	7.20
TSS ($mg.L^{-1}$)	38840	38510	33680	35570	37250	41390	39630	31400
TVS ($mg.L^{-1}$)	23700	17860	15480	17570	17420	19300	18360	14560
MR %	38.98	53.62	54.03	50.60	53.23	53.33	53.67	53.63
Polysaccharides ($mg.L^{-1}$)	39.83	46.97	75.03	46.12	66.37	44.54	53.47	49.33
Protein ($mg.L^{-1}$)	121.33	88.88	88.44	81.77	27.77	76.77	40.22	26.55
Ratio protein/polysaccaride	3.04	1.89	1.17	1.77	0.41	1.72	0.75	0.53
Viscosity (pas .s)	6.5	9.4	2.5	7	8.9	3	4.3	2.3
Dewatering efficiency of digested sludge								
Dryness (%)	-	3.64	1.73	3	3.24	2.06	2.35	4.01
Solid cake (%)	15.12	14.68	14.46	15.30	66.80	14.94	15.48	15.12
Microbial activity of different sludge								

Biogas production (mL/g TVS)	-	1214	552.5	1238.33	656.69	1476	636	1365
Abatement of organic loa dexpressed in CODs (%)	-	87.5	26.35	75	33.33	82.85	30.71	71.42
Abatement of organic loa dexpressed in TS (%)	-	61.42	55.06	38.54	22.75	45.36	34.52	56.89
Abatement of organic loa dexpressed in TVS (%)	-	77.64	17	37.93	38.95	60.30	14.28	44.33

Table 4. Characterization of digested sludge using chemically pretreated FW substrate (ADRP)

AD reactors (KW pre-treated substrate)	**ADRP0**	**ADRP1**	**ADRP 2**	**ADRP 3**	**ADRP 4**	**ADRP 5**	**ADRP 6**	**ADRP 7**
Characterization of digested sludge								
CST (s)	185	143	185	176	131	133	144	142
CSTS. 10^{-4} ($s.L.mg^{-1}$)	53.1	36.2	46.5	39.3	35.9	34.1	34.5	35.9
Conductvity (ms/cm)	4.35	7.35	6.09	6.43	6.78	6.43	7.07	5.97
Salinity (%)	1.4	4	3.3	3.5	3.7	3.4	3.8	3.2
T (°C)	28.7	19.6	19	19.8	19.7	19.5	20.3	20.2
pH	7.52	6.87	7.63	6.99	6.80	6.88	6.92	7.09
TSS ($mg.L^{-1}$)	34820	39480	39760	44760	36460	38920	41720	39490
TVS ($mg.L^{-1}$)	16220	18190	18540	20850	16740	17980	19260	18170

MR %	53.41	53.92	53.26	53.34	54.08	53.39	53.83	53.98
Polysaccharides (mg .L^{-1})	33.24	34.70	30.43	44.79	46.23	44.70	50.30	43.50
Protein (mg .L^{-1})	133.11	92.55	94	120	189.22	89.1	99	90.88
Ratio protein/polysaccaride	4.004	2.66	3.08	2.67	4.09	1.99	1.96	2.08
Viscosity (pas .s)	2.1	2.6	6.6	6.7	4.1	5.2	4	4.8
Dewatering efficiency of digested sludge								
Dryness (%)	0.59	0.45	3.06	3.15	2.42	2.9	2.67	2.44
Solid cake (%)	12.80	12.12	12.40	14.32	12.10	12.99	12.91	13.74
Microbial activity of different sludge								
Biogas production (mL/g TVS)	-	1113.82	1289.03	973.88	1274.58	1709.22	810.09	959.70
Abatement of organic load expressed in COD_s (%)	-	60.86	75.65	61.11	77.27	88.46	57.27	80.77
Abatement of organic load expressed in TS (%)	-	31.20	26.22	18.57	68.96	33.54	29.80	22.43
Abatement of organic load expressed in TVS (%)	-	54.68	51.83	41.39	65.38	61.75	30.52	46.86

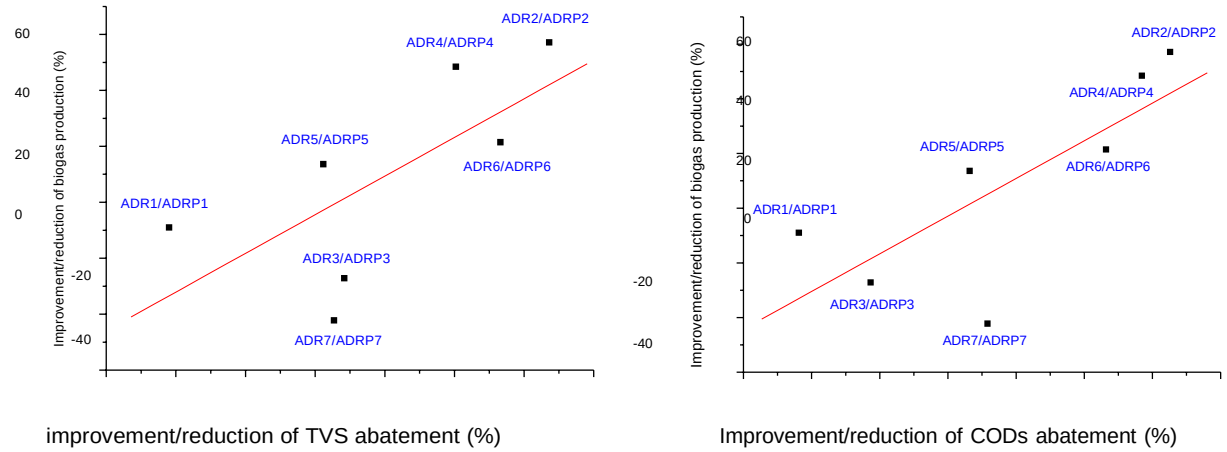


Figure 1. Variation of biogas production as a function of the variation of COD and TVS abatementafter application of chemical pretreatment

It should be noted that a clear improvement in the microbial activity of anaerobic heterotrophs is well recorded in the majority of the reactors after chemical pretreatment, noted mainly in the increase of biogas production, reaching 57.17% (for ADR2 and ADRP2 reactors) and the abatement of carbonaceous load reaching 65.16% and 67.2% expressed in CODs and TVS respectively and for thesame reactors (**Figure 01 /02**). The variation of biogas production is positively correlated with the variation of CODs and TVS abatement with correlation coefficients of 0.762 and 0.688 respectively,following the applied chemical pretreatment. Will this improvement in activity have a direct effect on the sludge characteristics and therefore on the dewatering performance or may other factors interact.

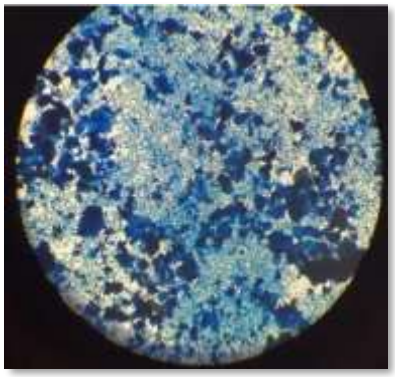
In all the different reactors using the pre-treated substrate, there was a reduction of the solid cake, therefore a reduction of the dehydration performance, a reduction that varies between 6.4 and 81. 88%, from the first observation we can confirm what was initially introduced, but why there was evena reduction of the solid cake despite the fact that in some cases there was no improvement in activity(case for example of ADR3/ADRP3 reactors), for this a monitoring of other CST parameters, viscosity, composition in EPS, microscopic visualizations have been carried out. Note that the drynessvalues recorded have known a growth and a decrease contrary to what was recorded for the solid cake.

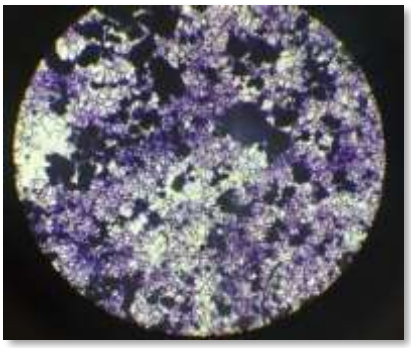
Since these sludges are quite loaded, dilutions of 1/10 with distilled water were made when measuringCST and the realization of microscopic visualizations.

The CST measurements are largely influenced by the TSS concentration of the samples; a correctioncan be made by dividing the recorded CST values by the TSS (CSTS) (34). The correction was moreadvocated in the present study. Recalling, that small values of this parameter correspond to good aggregation and the opposite leads to an increase in CSTs values.

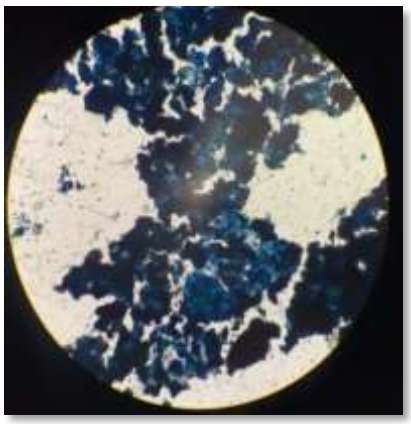
The visualizations established after staining with methylene blue and Gram staining show a clear improvement in the aggregation of microbial flocs from the sludge after using the pretreated FW, **Figure 02** for example presents the microscopic visualizations of the digestates recovered from the reactors (ADR 4 /ADRP 4) after staining with methylene blue and Gram staining and a magnification x 20. These visualizations clearly show a good aggregation caused by a good production of EPS allowing the collision of the flocs, in these reactors an improvement of 48.47 % in the production of biogas and a reduction of 81.88 % of the solid cake are recorded, this was well confirmed by the CSTs where this parameter decreased from 44.5 to 35.9 s (aggregation), and also well confirmed by the viscosity which decreased from 8.9 to 4.1 pa .s, affirming the imprisonment of the EPS in the solid matrix.

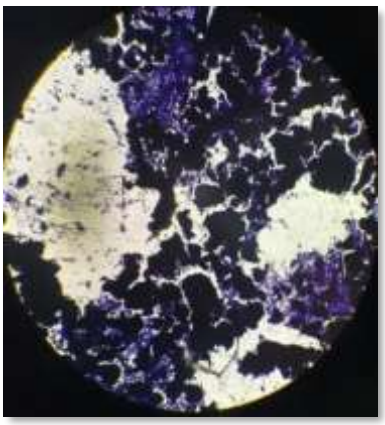
These conclusions were confirmed and generalized in all reactors since the values of CSTs and viscosity are in agreement, when CSTs decreases affirming aggregation, viscosity decreases affirming entrapment of EPS, and when CSTs increases affirming deflocculation, viscosity increases due to the release of EPS constituents (**Table 03 and 04**).





Methylene blue stain **ADR 4** **Gram stain**





Methylene blue stain **ADR 4** **Gram stain**

Figure 2. Example of microscopic visualizations of the reactors (ADR 4 /ADRP 4), methylene blue staining and Gram staining (magnification x 20)

Quantification of the EPS as well as their polysaccharide and protein compositions in the sludge recovered from the reactors was carried out, several studies have examined the effect of EPS on dewatering or according to Xu Zhou, et al (35) , The impact of EPS on sludge dewatering depends on the content of EPS. The relatively lower dewatering of sludge is correlated with higher concentration of EPS and that sludge with low EPS content had higher dewatering due to the fact that water is strongly retained by two types of interactions between water molecules and EPS, electrostatic interactions and hydrogen bonds, the latter are particularly present in polysaccharides and hydrogen bonds contribute to the tertiary structure of proteins (16) . The increase of soluble proteins and polysaccharides in solution has been shown to cause the decrease of sludge dewatering, according to Dong-Qin He et al (36), generally, proteins are considered to play a more important role in sludge flocculation and dewatering than polysaccharides. Therefore, a quantification of these two parameters was established in order to link the dewatering performance of our different digestates with the

concentrations of EPS and more specifically of polysaccharides and proteins.

It should be noted that the composition of polysaccharides and proteins can be influenced by the composition of the samples (ratio between FW/OP) which differs from one reactor to another. What was noticed is that the ratio between the concentration of proteins and polysaccharides has clearly increased in all the reactors that have undergone pretreatment of FW (**Table 3 and 04**), this explains the decrease in solid cake (**Table 03 and 04**), although the performance of AD has not always improved following the pretreatment of FW, this may be caused by the production of other byproducts slowing down or inhibiting the various stages of AD.

Chudoba, (1985) (37) also suggested that the formation and excessive accumulation of EPS in the culture medium may be responsible for a decrease in the specific rates of substrate degradation due to the covering of the cells by these constituents, and perhaps this is the situation encountered in some of our reactors where the performance of AD has been reduced, despite the fact that there has been a clear production of EPS.

The decrease of the solid cake is positively correlated with the increase of the protein/polysaccharide ratio with a correlation coefficient of 0.597 (**Figure 03**), the applied pretreatment allowed to fractionate the particles creating active sites favorable to establish different bonds and thus to trap more water, the fraction of bound water is seen to increase thus limiting the dehydration

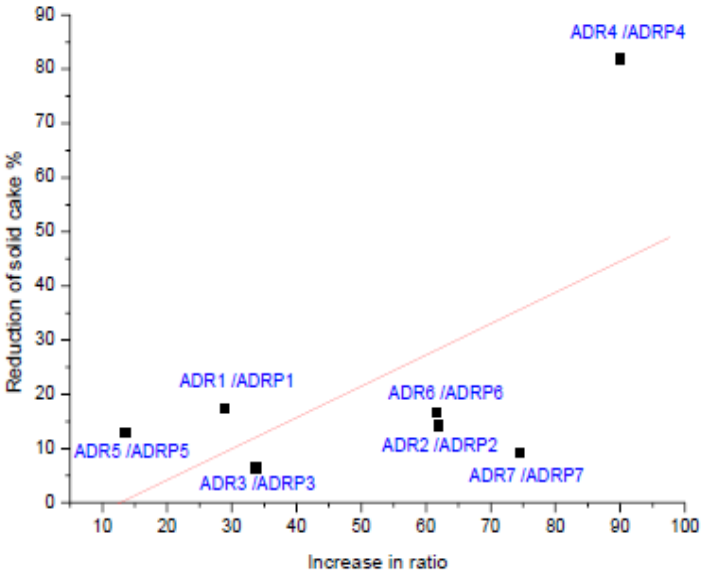


Figure 3. The reduction of the solid cake (%) as a function of the Protein/Polysaccharide ratio

4. Conclusions

To fully understand the effect of pretreatments in anaerobic digestion of a solid waste in its solid or liquid form on the dewatering performance of the recovered digestate, several experiments must be conducted, and several types of pretreatments must be tested, This was well emphasized in the present study using chemical pretreatment, that the effect on dewatering performance is quite apparent despite the fact that the dewatering technique used in the present study is considered among the most efficient dewatering techniques but the most energy consuming between 30-60 KWh/TMS (38) .

The main goal of the pretreatments is to improve the biogas production and thus an energy gain that can be directed in the improvement of the dewatering performances which is seen to be influenced by this approach applied upstream of the AD.

In order to consolidate and confirm all the interpretations put forward in the present study, it is necessary to redo this study on a variety of substrates and a variety of pretreatments applied separately or in combination, but the hydrolysis step must be thoroughly explored and directly linked to the dewatering performance.

References

1. Keke Xiao, Yan Zhou , «protein recovery from sludge: a review , cleaner production 249, 10march 2020
2. Xu Zhou, Guangming Jiang, Qilin Wang And Zhiguo Yuan, «a review on sludge conditioning bysludge pretreatment with a focus on advanced oxidation, RSC advances, 2014, 4, 50644.
3. Barbara Ruffino , Giuseppe Campo , Giuseppe Genon , Eugenio Lorenzi , Daniel Novarino ,Gerardo Scibilia , Mariachiara Zanetti« improvement of anaerobic digestion of sewage sludge in a
4. wastewater treatment plant by means of mechanical and thermal pre-treatments : performance, energyand economical assessment" , bioresource technology (2015).
5. Cuihong Zhou, Xintong Huang, Meng Zeng « experimental continuous sludge microwave system to enhance dehydration ability and hydrogen production from anaerobic digestion of sludge "journal of environmental scieces(2017).
6. Lise Appels , Jan Degrève , Bart Van Der Bruggen , Jan Van Impe , Raf Dewil «influence of low temperature thermal pre-treatment on sludge solubilisation, heavy metal release and anaerobic digestion " , bioresource technology 101 (2010) 5743–5744.
7. Lise Appels , Jan Baeyens , Jan Degre`Ve , Raf Dewil « principles and potential of the anaerobic digestion of waste-activated sludge " progress in energy and combustion science 34 (2008) 770–773.
8. Shuzo Tanaka, Toshio Kobayashi, Ken-Ichi Kamiyama , Ma. Lolita , Signey Bildan «effects of thermochemical pretreatment on the anaerobic digestion of waste activated sludge "*war. sci. tech.* 35, (1997).
9. In Wook Nah, Yun Whan Kang, Kyung-Yub Hwang And Woong- Ki Song « mechanical pretreatment of waste activated sludge for anaerobic digestion process "wat. res. 34, (2000).
10. Lawler D.F., Chung Y.J., Hwang S-J., Hull B.A., 1986, «Anaerobic digestion: effects on particle size and dewaterability", Journal Water Pollution Control Federation, 58(1986).
11. Novak J.T., Goodman G.L., Pariroo A., Huang J-C, «The blinding of sludges during filtration", Journal Water Pollution Control Federation, 60 (1988).
12. J. I. Houghton, J. Quarmby , T. Stephenson « the impact of digestion on sludge dewaterability " trans icheme, vol 78, part b, march 2000.

13. R.S. Gale, R.C. Baskerville, «Capillary suction method for determination of the filtration properties of a solid/liquid suspension, Chem. Ind., 9 (1967) 355–356.
14. R. Zamouche-Zerdazi, M. Bouteraa, S. Hallel, M.Bouhamla, M. Bencheikh Lehocine, A.H Meniai I«mpact of clear waters parasites on the biological wastewater treatment" , Desalination and Water Treatment , 213 (2021) 106–116
15. Bo Frolund, Rikke Palmgren, Kristian Keiding And Per Halkj Nielsen «extraction of extracellular polymers from activated sludge using a cation exchange resin » wat. res. vol. 30, no. 8,(1996)
16. Anthony Massé « bioréacteur a membranes immergées pour le traitement des eaux résiduaires urbaines: spécificités physico-chimiques du milieu biologique et colmatage « l'institut national des sciences appliquées de toulouse (2015).
17. Ana Catalina Avella Vasquez. «Substances polymériques extracellulaires dans les procédés de traitement des eaux usées. Institut national polytechnique de lorraine, 2010. Français
18. Lowry, O.H., Rosebrough, N.J., Farr, A.L., Randall, R.J., «protein measurement with the folin phenol reagent. j. biol. chem. (1951.)
19. Dubois M, Gilles Ka, Hamilton Jk, Rebers Pa, Smith F. «colorimetric method for determination of sugars and related substances. anal chem(1956)
20. degrémont . «mémento technique de l'eau (1951)
21. Swaib Semiyagaa, Mackay A. E. Okureb, Charles B. Niwagabaa, Philip M. Nyenjea, Frank Kansiimec « optimisation of centrifuge operating conditions for dewatering physically conditioned faecal sludge from urban slum " environmental technology & innovation 8november (2017).
22. Julian Tosoni. « Compréhension des facteurs de contrôle des performances de la déshydratation mécanique des boues résiduaires en filtre-presse. Autre. Université Blaise Pascal - Clermont-FerrandII,2015. Français
23. F. Xu, Y. Y. Y. Li, X. Ge, L. Yang, and Y. Y. Y. Li, « Anaerobic digestion of food waste – challenges and opportunities," *Bioresour. Technol.*, vol. 247, no. September, pp. 1047–1058, Jan. 2017.
24. Achouri.O, A. Panico, M. Bencheikh-Lehocine, K. Derbal, F. Pirozi Effect of Ch«emical Coagulation Pretreatment on Anaerobic Digestion of Tannery Wastewater," *J. Environ. Eng.*, 2017.
25. Daigger, G.T.et Grady, C.P.L., (1982). «The dynamics of microbial growth on soluble substrates.Wat.Res. 16: 365-382.
26. Chudoba, J., (1985). «Inhibitory of refractory organic compounds produced by activated sludge microorganisms on microbial activity and flocculation.Wat.res.19, 197.
27. Sponza DT. (2002) « Extracellular polymer substances and physicochemical properties of flocs in steady- and unsteady-state activated sludge systems. Process Biochemistry, 37, 983-998.
28. Frolund B., Palmgren R., Keiding K.et Nielsen P. (1996) «Extraction of extracellular polymers fromactivated sludge using a cation ion exchange resin. Water Research, 30, 1749-1758.
29. Hong Liu, Herbert H.P. Fan .« extraction of extracellular polymeric substances (eps) of sludges. journal of biotechnology 95 (2002)
30. Morgan, J.W., Forster, C.F., Evison, L.M., 1990. «A comparative study of the nature of biopolymers extracted from anaerobic and activated sludges. water res. 6, 743–750
31. Rudd, T., Sterrit, R.M., Lester, J.N., 1984. « Complexation of heavy metals by extracellular polymers in the activated sludge process. j. water poll. control fed. 56 (12), 1260– 1268
32. Nielsen, P.H., Frølund, B., Keiding, K., 1996. «Changes in the composition of extracellular

polymeric substances in activated sludge during anaerobic storage. appl. microbiol. biotech. 44 (6), 823–830.

33. Chih Chao Wu, Chihpin Huang And D. J. Lee « bound water content and water binding strength on sludge flocs " wat. res. .32,)1998(
34. Hua Wei, Boqiang Gao, Jie Ren, Aimin Li, Hu Yang "«Coagulation/flocculation in dewatering of sludge: a review "water research 143 (2018)
35. X. Huacheng, H. Pinjing, Y. Guanghui, S. Liming, «Effect of ultrasonic pretreatment on anaerobic digestion and its sludge dewaterability, J. Environ. Sci., 23 (2011) 1472–1478.
36. Xu Zhou, Guangming Jiang, Qilin Wang and Zhiguo Yuan . A review on sludge conditioning by sludge pretreatment with a focus on advanced oxidation RSC Adv., 2014, 4
37. Dong-Qin He, Ying-Jie Zhang, Chuan-Shu He, Han-Qing Yu . Changing profiles of bound water content and distribution in the activated sludge treatment by NaCl addition and pH modification. Chemosphere 186 (2017)
38. Chudoba, J., (1985). «Inhibitory of refractory organic compounds produced by activated sludge microorganisms on microbial activity and flocculation.Wat.res.19, 197-200.
39. Jérémy Olivier "études des filtres a bandes pour la déshydratation mécanique des boues residuaires urbaines" l'université de Pau et des pays de l'Adour 2003.

Production of Biodiesel Using Alkaline Based Catalysts from Extracted Jatropha Oil in Yemen: A Case Study

Abdulbari A. Ahmad [1,4,*], Marwan Alraggad [1,2], Hani A. Dammag [3], Ghaleb A. Ghaleb [4]

[1] Inter-Islamic Network on Water Resources Development and Management 70 Ahmed Tarawneh st. Jubeiha Amman 11941, Jordan.

[2] Water, Energy and Environment Center, University of Jordan, Amman 11942, Jordan

[3] Department of chemical Engineering, Faculty of Science, Sana's University. Yemen.

[4] Department of Chemical Engineering, Faculty of Engineering, Hodeidah University, Yemen.

**Corresponding author: alborani_75@yahoo.co.uk; Tel.: (00962)-777583910*

Abstract: This research work is about the production of biodiesel from extracted Jatropha oil in Yemen. Jatropha Curcas was chosen because it is not edible therefore, it will not pose a problem to human food competition. Biodiesel production has been identified as a non-toxic, biodegradable fuel, obtained from renewable sources. In Yemen, Jatropha Curcas has grown successfully using primary treated wastewater in Taiz and Hodeidah. Biodiesel production processes using Jatropha oil have been characterized using alkali-based catalysts. The extracted oil was characterized and used to produce biodiesel on a laboratory scale by alkali catalyzed trans-esterification with methanol using 1% NaOH as the catalyst, ratio of methanol to oil 6:1, reaction temperature 60 ^{o}C, and reaction time one hour. The biodiesel yield of this process was about 93.65%. In this study, 4.68 kg of Jatropha seeds were weighed and the oil was extracted mechanically is 1.3 liter. The properties of produced biodiesel were measured and compared to the properties of fossil diesel and they were within the acceptable range of ASTM specifications standard for biodiesel and diesel fuel.

Keywords: Jatropha Curcas; Catalysts; Transesterification; Biodiesel Production

1. Introduction

Yemen, as one of the poorest developing countries in the Middle East, has been facing an unstable political situation since 2011 accompanied by repeated waves of economic crises. The conflict in 2015 was by far the worst with a complete lack of fossil fuel supply to many major cities. Diesel fuel is the only fuel used to run standby and emergency power stations inside cities, thus resulting in a complete blackout in these cities. Biodiesel is the most promising alternative to diesel fuel especially if it can be produced from renewable sources [1]. With a promise of energy independence and decreased environmental impact, the popularity, production, and use of biodiesel have seen a great increase in recent years. Not only has biodiesel been proved safe and biodegradable, but it also aids in the reduction of harmful air pollutants released during the combustion of conventional fuels. Biodiesel production is alternative fuel that can be used directly without any modified by diesel engine. Because it has similar properties to diesel fuel, biodiesel can be blended at any ratio with diesel fuel [2].

Among the various vegetable oil sources, non-edible oils are suitable for biodiesel production. Because edible oils are already in demand and are too expensive than diesel fuel. Among the non-edible oil sources, Jatropha Curcas is identified as a potential biodiesel source and comparing with other sources, which has added advantages as rapid growth, higher seed productivity, suitable growth in tropical regions, and subtropical of the world.

Jatropha Curcas is one of the plants belonging to the Euphorbiaceae family, that produces a high amount of oil from its seeds. This is a non-edible oil-bearing plant widespread in arid, semi-arid, and tropical and subtropical regions of the world. Jatropha is a drought-resistant perennial tree that grows in marginal lands and can live over 50 years. The oil content in Jatropha seed is reported to be in the ranges from 30 to 50 % by weight of the seed and ranges from 45 to 60 % weight of the kernel itself [3]. Jatropha seeds are quite oily. They can yield anything between 25 % to 40 % of their weight as

oil. This vegetable oil is rich in oleic acid and linoleic acid, both of them unsaturated fats. The in-depth composition of fatty acids is mentioned in Table 1. Biodiesel produced from edible oils has low free fatty acid, whereas biodiesel from non-edible oil sources has higher free fatty acid (FFA) [4].

Table 1. Chemical properties and chemical composition of Jatropha oil [5,6]

Chemical properties of jatropha oil	
Item	Value
Acid Value	38.2
Saponification value	195.0
Iodine Value	101.7
Viscosity (at 31°C), Centistokes	40.4
Density (g/cm³)	0.92
Chemical composition of Jatropha oil	
Fatty acid	Composition (as percent of total oil)
Oleic acid	43
Linoleic acid	36
Palmitic	13
Stearic	6
Palmit oleic	0.4

The production of this fuel can be encouraged at the grassroots level to aid ordinary Yemen to use biodiesel as a fuel alternative. This will fill the gap and more importantly relieve pressure on crude oil as the dominant fuel in the running of equipment [7]. The aim of this work was to production of biodiesel from extracted Jatropha oil as available in Hodeidah city in Yemen, characterization of biodiesel, and comparable to diesel fuel.

2. Materials and methods

2.1 Seed preparation

Jatropha Curcus fruits used in this study were collected from different locations in Taiz city, Yemen which is located in the Bani Hamad district. After the fruits were collected, it was sun-dried for two days and removed the external shell of the fruits to reach the seeds (Figure 1). Thereafter seeds were sun-dried for two days to reduce their moisture, liquefies the oil, and improve the extraction.



Figure1. Seeds from Jatropha fruits

2.2 Oil extraction

In this study, 4.68 kg of seeds were weighed and the oil was extracted mechanically using a Jatropha oil press machine. The extracted oil was allowed to settle under gravity for 24 hours. Then solid impurities were removed by filtration. The percentage yield was calculated using the following Equation.

$$\% \text{ Yield} = \frac{\text{Weight of oil}}{\text{Weight of sample}} * 100\% \quad (1)$$

2.3 Characteristics of the Jatropha oil

The oil extracted from the Jatropha seeds was characterized and its physicochemical parameters were determined to be sure that it would be suitable for biodiesel production.

2.3.1 Saponification value determination

A known quantity of oil was refluxed with the amount of ethanolic potassium hydroxide solution, after Saponification, the remaining KOH was estimated by titrating against a standard acid. Based on the method [8], 2.0 (g) of the oil was placed in a 250 ml conical flask and 25 ml of 0.5 N ethanolic and potassium hydroxide solution was added. A reflux condenser was attached and the flask content was refluxed for 30 min on a water bath with continuous swirling until it simmered. The excess potassium hydroxide was titrated against 0.5 N hydrochloric acid using phenolphthalein indicator while still hot. The saponification value was then calculated using the following Equation.

$$\text{Saponification value} = \frac{(\text{B1}-\text{R1})*28.05}{\text{Weight of oil sample}} \quad (2)$$

where B1 and R1 are the volumes of hydrochloric acid used for blank and sample titrations respectively.

2.3.2 Iodine value determination

Hanus method was used for the determination of the iodine value of extracted jatropha oil and biodiesel. This was carried out by placing 0.1 g of the oil in a 250 ml conical flask, add 10 ml of anhydrous chloroform followed by the addition of 30 ml of Hans solution. The content was mixed and placed in a drawer for exactly 30 min. Thereafter, potassium iodide solution (10 ml of 15 % weight volume) was added to the flask in order to wash down any iodide at the stopper that was used for the flask. The entire content was titrated against 0.14 M $Na_2S_2O_3$ until the solution turned light yellow. After that, 2 ml of 1% starch indicator was added and the titration continued until the blue color formed finally disappeared. A blank determination was carried out under the same condition, and the titer values were recorded. The saponification value was then calculated using the following Equation.

$$\text{Iodine value} = \frac{(B2-R2)*Normality\ of\ Na2SO3*12.69}{Weight\ of oil\ sample} \quad (3)$$

Where B2 and R2 are the volumes of $Na_2S_2O_3$ used for blank and sample titrations respectively.

2.3.3 Free Fatty Acid

4.0 g of the oil was placed in a 250 ml conical flask and warmed. 25 ml of methanol was added with thorough stirring, followed by two drops of phenolphthalein indicator and a drop of 0.14 N of sodium hydroxide solution. The content was titrated until a permanent light pink color, which persisted for one minute, was obtained. The endpoint was thus recorded. The Free Fatty Acid (FFA) value was calculated using the following Equation.

$$\text{Free Fatty Acid} = \frac{\text{Titre value}*\text{N}*28.2}{\text{Weight of oil sample}} \quad (4)$$

where N is the normality of NaOH

2.3.4 Acid value

The acid value of the oil extracted from the Jatropha seeds was determined using the following Equation.

$$\text{Acid value} = \text{FFA} * 1.99 \quad (5)$$

2.3.5 Trans-esterification process

Transesterification-ion reaction is carried out in a batch reactor which was done under the following optimal conditions. Sodium hydroxide concentration 1%, reaction temperature 60 °C, reaction pressure one atm, reaction time one hour, and the molar ratio of methanol to oil 6:1. Figure 2 shows the biodiesel production process flow chart. The step-by-step approach used in the production of biodiesel is as follow:

- Two gram of sodium hydroxide was weighed and placed in a round bottom flask.
- 50 grams of methanol of 99.5 % purity having density 0.791 g/cm³ was poured in the same round bottom flask, covered well by aluminum foil, and placed on stirring hot plate, mixed until sodium hydroxide was completely dissolved in methanol.
- 200 mL of Jatropha oil was measured and poured into a 250 ml conical flask and heated to a temperature of 60 °C to drive off moisture and stirred vigorously.
- Once 60 °C was reached, the methanol-sodium hydroxide mixture was added to the oil in the flask, covered well by aluminum foil, and stirred vigorously for 60 minutes using a magnetic stirrer.
- After completion of the transesterification process, the mixture was allowed to settle under gravity for 25 minutes in a separating funnel.
- The biodiesel was then poured into a separate beaker, while the lower layer (which comprises glycerol and soap) was collected from the bottom of the separating funnel.
- Warm water was then used to wash the biodiesel to remove any excess glycerol and soap that remain in the funnel. This process was continued until the clear water become below the biodiesel in the separating funnel.
- The washed sample was dried by placing it on a hot plate and excess water still in the biodiesel was removed.
- The quantity of biodiesel collected was measured and recorded.
- Finally, the separated biodiesel is taken for characterization.

2.4 Characterization of the biodiesel product

The biodiesel produced after the trans-esterification process was carried out was characterized to obtain its physicochemical parameters as outlined below.

2.4.1 Flash point

150 ml conical flask was filled to a certain level with the biodiesel and heated at a slow constant rate on a hot plate. The flash point was taken as the lowest temperature when the application of the test flame caused the vapour above the biodiesel sample to ignite (Ahmed et al 2016).

2.4.2 Pour point

A cylindrical test tube was filled with the produced biodiesel to a certain level and attached to a wooden clamp bearing a thermometer. The sample was left to cool less than 0°C in an ice bath. Thereafter, it was removed and tilted on the clamp and the setup was observed at intervals. The lowest temperature at which the product was observed to flow was recorded as its pour point.

2.4.3 Cloud point

A cylindrical tube was filled with the biodiesel to a certain level and clamped with a wooden clamp bearing thermometer. The sample was left to cool below 0ºC in an ice bath until its color appearance turned white/cloudy. The temperature at which this cloudy appearance color occurred was recorded as the cloud point of the biodiesel.

2.4.4 Viscosity

The produced biodiesel sample was poured into a long-necked funnel with a finger placed at its bottom. A timer was set and started as the finger was released. When the sample ran off completely, the timer was stopped. The analysis was repeated four times and the average time was taken. The viscosity was thereby calculated using the readings taken.

2.4.5 Density

A conical flask was weighed and filled to a volume of 15 ml with the biodiesel. The weight of the glass and the biodiesel was measured also. The weight of the biodiesel was determined, and the density was calculated as mass per unit volume.

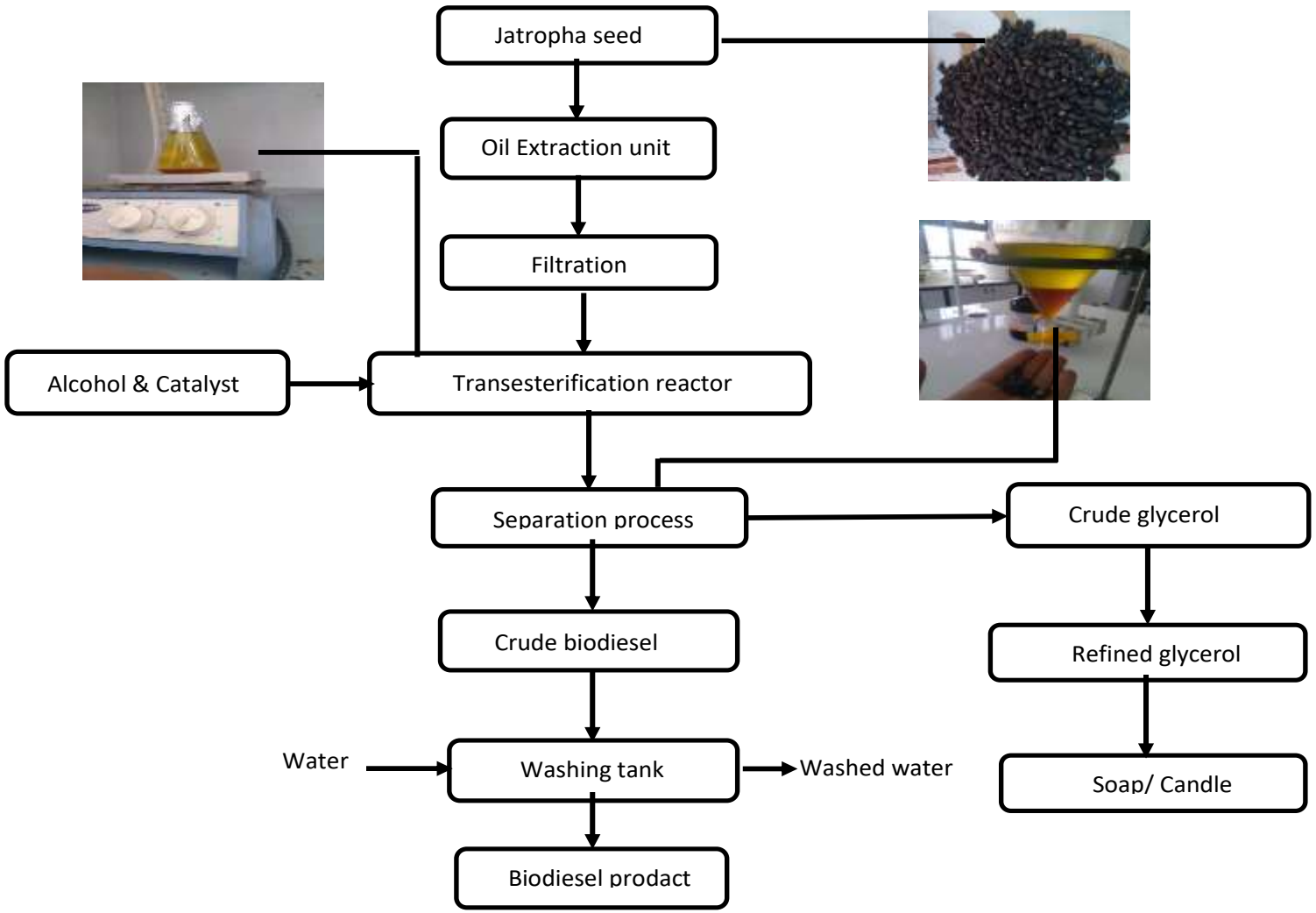


Figure 2. Biodiesel production flow diagram.

3. Results and Discussion

The results of this research will be discussed under the following groups of solution:

- Yield of extracted oil.
- Analysis of the Jatropha oil sample.
- Analysis of the result from the characterization of the biodiesel produced.
- Production and yield of biodiesel.

3.1 Yield of extracted oil

The yield of oil extracted from Jatropha seeds was 28%.

$$\text{Yield } (\%) = \frac{1.310 \text{ kg}}{4.680 \text{ kg}} * 100 = 28\% \qquad (6)$$

3.2 Analysis of extracted Jatropha oil

The results of the acid value, iodine value, free fatty acid content, saponification value, specific gravity, moisture content density, and kinematic viscosity at 25 ºC of extracted Jatropha oil are shown in Table 2. The various properties of the extracted Jatropha oil used are within the range of the standard in Table 3. As observed, the saponification value of the Jatropha oil is 115.83 this is within the standard range given in Table 3. this property is very important because if it is quite high the formation of soap will be more prevalent instead of the desired biodiesel. Another important property is the moisture content, Table 2 shows of the value is 0.20. If the moisture content of the Jatropha oil sample is too high, soap formation will be more and there will be problems with the separation of the by-product (Glycerin). Free fatty acid (FFA) level and pH are also very important parameters, more glycerin will be formed if the pH is too high. the two properties are within the range of the standard as seen in Table 2. Table 2 shows the acid value and % FFA of the extracted were found to meet the required specifications. The properties of raw Jatropha oil obtained from Yemen in this research work were found to be nearly the same as those described in the literature [9].

Table 2. Properties of the extracted Jatropha oil used for biodiesel production.

Properties of extracted Jatropha oil	Value
Acid value (NaOH mg/g)	4.37
Saponification value (NaOH mg/g)	115.83
Iodine value (mg/g)	119.1
Free fatty acid (NaOH mg/g)	2.3
Moisture content %	0.2
Density at 25 ºC (g/cm^3)	0.912
Specific gravity at 40 ºC	0.921
Kinematic viscosity at 40 ºC (mm^2/s)	3.44
Pour point	-6
Cloud point	-2
pH	6

3.3. *Characterization of the biodiesel produced*

Table 3 shows the physical and chemical properties of biodiesel production from extracted Jatropha oil in Yemen were studied. The properties measured were compared with the ASTM specifications, the standard of biodiesel, and diesel fuel. The cetane index of biodiesel from Jatropha oil with methanol was found to be within the ASTM specified limit. So, the result showed that a molar ratio of 6:1 using for the production of biodiesel from Jatropha oil was suitable for the engine. The higher cetane index of biodiesel compared to diesel fuel was indicated that a high potential for engine performance. Generally, diesel engines will run with values between 45 and 55 [10], the biodiesel produced has a value of 50, which is well within range; it is hence suitable to run in diesel engines. The biodiesel has a higher flash point of 120 °C as compared to that of the petrol-diesel (flash point

of 50). This makes biodiesel production is safe for use, loading, and storage. Also, the fuels at the lower flash point highly dangerous if it is not correctly stored and used. The viscosity is an important parameter in fuel because it affects the atomization of the fuel being injected into the engine combustion chamber. The higher viscosity, the larger the propensity of the fuels to cause problems such as blockage of engine components. Table 3 shows that the viscosity of the biodiesel produced is within the range as given by ASTM standards for biodiesels. The density is important to factor for good engine performance; the higher the density, the more problematic it becomes to pump the fuel. The cloud point and pour point of the biodiesel produced within the standard for biodiesel fuel. According to Table 3, Jatropha oil is suitable for producing biodiesel, all the properties of the produced biodiesel compare very well with ASTM standards.

Table 3. Characterization of the biodiesel produced from extracted Jatropha oil, and comparison with standard of biodiesel and diesel fuel.

Property	Present study	ASTM D 6751 standard for biodiesel fuel	ASTM D 975 standard for diesel fuel
Cetane index	50	48 to 65	40 to 55
Flash point (°C)	120	100 to 170	60 to 80
Fire point	130	-	-
Density (g/cm^3)	0.873	0.88	0.85
Kinematic viscosity at 40 °C (mm^2/s)	3.88	1.9 to 6.0	1.3 to 4.1
Pour point (°C)	-1	-15 to 16	-35 to -15
Cloud point (°C)	2	-15 to 16	-3 to 12
Free fatty acid (NaOH mg/g)	0.2065	-	-
Saponification value (NaOH mg/g)	109.23	370 Max	-
Iodine value (mg/g)	105.3	120 Max	-
Acid value (NaOH mg/g)	0.413	0.8 Max	0.50

3.4. Production and yield of biodiesel

After ascertaining that the extracted Jatropha oil was suitable for biodiesel production, it was employed in a trans-esterification reaction for the process which was carried out using the optimum conditions, the methanol to oil molar ratio 6:1, alkali catalyst load of 2 g, reaction time of 60 min, reaction pressure one atm and reaction temperature of 60 ºC and the results of the trans-esterification processes. The chemical reaction that yielded the biodiesel was carried out under standard conditions. The required mol of the catalyst (NaOH) was used so as to prevent emulsification. The yield of biodiesel produced in this experiment was 93.65%. Glycerin which is the by-product of the chemical reaction can be sold to pharmaceutical companies since it is used to produce valuables such as creams and toothpaste.

4. Conclusion

In the investigation, it has been confirmed that extracted jatropha oil in Yemen can be used as a resource to obtain biodiesel. The results show that alkaline-catalyzed transesterification is promising for the production of biodiesel on an industrial scale. Processes for the production of biodiesel have no need for special equipment or scarce chemicals. The effects of different parameters such as reactant ratio, temperature, time, and catalyst concentration on the biodiesel yield were analyzed. The best combination of the parameters was found as a 6:1 molar ratio of methanol to oil, 1.0 % Sodium Hydroxide (NaOH) catalyst, 60 ºC of reaction temperature, and one hour of reaction time. This optimum condition yielded 93.65 % of biodiesel from extracted jatropha oil. The characterization of the biodiesel produced from Jatropha oil with methanol was found to be within the ASTM specified limits, with better engine performance, and emission than the diesel fuel.

Acknowledgment

The corresponding author gratefully acknowledges the fellowship from the Institute of International Education-Scholar Rescue Fund (IIE-SRF).

References

1. Al-attab, K.; Wahas, A.; Almoqry, N.; Alqubati, S. Biodiesel production from waste cooking oil in Yemen: a techno-economic investigation. *Biofuels* (2017), *8* (1), 17-27.
2. Reşitoğlu, İ. A.; Altinişik, K.; Keskin, A. The pollutant emissions from diesel-engine vehicles and exhaust aftertreatment systems. *Clean Technologies and Environmental Policy* (2015), *17* (1), 15-27.
3. Jain, S. The current and future perspectives of biofuels. In *Biomass, Biopolymer-Based Materials, and Bioenergy* (2019), (495-517). Woodhead Publishing.
4. Ehsan, M.; Chowdhury, M. T. H. Production of biodiesel using alkaline based catalysts from waste cooking oil: a case study. *Procedia Engineering* (2015), *105*, 638-645.
5. Raja, S. Antony. "Biodiesel production from jatropha oil and its characterization." Res J Chem Sci 1 (2011): 81-87.
6. Achten, W. M.; Verchot, L.; Franken, Y. J.; Mathijs, E.; Singh, V. P.; Aerts, R.; Muys, B. Jatropha bio-diesel production and use. *Biomass and bioenergy* (2008), *32* (12), 1063-1084.
7. Folaranmi, J. Production of biodiesel (B100) from Jatropha oil using sodium hydroxide as catalyst. *Journal of Petroleum Engineering* (2012), *2013*.
8. Ahmed, F.; Giwa, S. O.; Ibrahim, M.; Giwa, A. Production of biodiesel from Jatropha curcas seed oil using base catalysed transesterification. *International Journal of ChemTech Research* (2016).
9. Abdullah, M. E.; Ahmad, K. A.; Hassan, N. A.; Ambak, K. B.; Musbah, A.; Usman, N.; Bakar, S. K. B. A. Extraction techniques and industrial applications of jatropha curcas. *Jurnal Teknologi* (2016), *78* (7-3).
10. Knothe, G.; Krahl, J.; Van Gerpen, J. *The biodiesel handbook*. Elsevier (2015).

Studies on Uses of Renewable Energy and Renewable and Alternative Sources of Energy in Heavy and Integrated Industries in Egypt

Mohamed Hamada Ali Ahmed[1,]*, Mohamed Elsayed Mohamed Abdel karim [2] and Ahmed Ali ,Ibrahim Kabosh[3]

[1] Section Head of Technical office & PM (NIC);
[2] Laboratory & QC Manager (NIC);
[3] Laboratory & QC Engineer (NIC).

***** *Corresponding author: m.hamada@elnahdacement.com; Tel.:+201002138815*

Abstract: This research study in the field of Energy generation and consumption in heavy industries with the aim of reducing the energy consumption and the combustion emissions to help in reducing the use of fossil fuels such as Coal, Gas or fuel oil and saving fossil CO2 emissions, which is a worldwide goal," by using a by-products of one the integrated industry (sugar production factories). This research study give a study and plan for using an alternative fuel, ideally at least "replacement about20% alternative fuels from the total cement plant fuel consumption" due to plant needs to improve the fossil fuel consumption, its process efficiency and reduce emissions.

This paper represent a case study for one of Egyptian cement plants, meeting the ISO standard and reducing its fuel consumption met the factory needed to reinvent its manufacturing process. to reduce the cost of "energy consumption" and the reduction of "combustion emissions" in the cement production, as developing Projects for the use of alternative Fuels is of outmost importance With the aim of reducing the use of fossil fuels and its harmful emissions.

The research project team was asked to achieve these progresses without any initial costs after applying using coal as main fuel on 2015 & to develop a plan for using an alternative fuel, ideally at least "replacement about20% alternative fuels from the total plant fuel consumption" The plant needed the fuel to improve its efficiency and reduce emissions "due to the government's environmental obligation and for complying with the requirements of ISO 50001:2011*"

This is our case study in which we discovered a new biomass fuel to be available applying in the nearest future in wide range in cement industry & power plants.

Keywords: alternative fuel ; cement plants ; environmental solutions ; biomass fuel

1. Introduction

Energy generation for industrial uses (especially thermal energy & electrical energy) constantly grapple with controlling the emissions levels and fuel consumption for power generation units.
Running an efficient plant means getting the most out of fuel source. Expanding environmental regulations worldwide have brought the need for reductions in greenhouse gases such as carbon dioxide (CO2), sulfur dioxide (SO x), and nitrogen oxides (NO x), among others.

The problems of fuel efficiency and pollution also are faced by smaller generators, including industrial facilities that produce their own power. In some cases, addressing the issue requires an overhaul of the way a facility generates its electricity or thermal power.

Otherwise, to reduce the "energy consumption" & the ―combustion emissions‖ in heavy industries & large power plants such as the cement production factories, developing researches for the use of such alternative Fuels is of outmost importance.

Global cement production has increased more than 30-fold since 1950, and almost four-fold since 1990, with much more rapid growth than global fossil energy production in the last two decades. Since 1990 this growth is largely because of rapid development in China, where cement production has grown by a factor of almost 12, such that 73% of global growth in cement production since 1990 occurred in China.

The Cement Sustainability Initiative (CSI**) has published the ―Getting the Numbers Right‖ (GNR) report for 2015. Consolidating information from 939 cement manufacturing facilities (such as integrated cement plants and grinding centers) show, that the use of such alternative Fuels have been increased from 2% in 1990 to almost 16% in 2015.

Alternative Fuels, such as refuse derived ***or biomass derived Fuels are widely used in the Cement & Lime Industry. With the use of such alternative Fuels, the Industry is reducing the use of fossil fuels such as Coal, Gas or fuel oil and saving fossil CO^2 emissions. There are two aspects of cement production that result in emissions of CO2. First is the chemical reaction involved in the production of the main component of cement, clinker, as carbonates (largely limestone, CaCO3) are decomposed into oxides (largely lime, CaO) and CO2 by the addition of heat. Stoichiometry directly indicates how much CO2 is released for a given amount of CaO produced. Recent estimates are that these so-called

‗process‘ emissions contribute about 5% of total anthropogenic CO2 emissions excluding land-use change (Boden et al., 2016****). The second source of emissions is from the combustion of fossil fuels to generate the significant energy required to heat the raw ingredients to well above 1400°C, and these ‗energy‘ emissions, including those from purchased electricity, could add a further 60% on top of the process emissions (IEA, 2016*****). Total emissions from the cement industry could therefore contribute as much as 8% of global CO2 emissions.

The cement industry is one of the oldest in Egypt. The sector began operating in 1911—the country has several shale and limestone quarries to provide the raw materials for cement production—and Egypt is among the 15 largest producers of cement worldwide, with more than 20 operating plants.

Definitions:

* ISO 50001:2011 is a standard for energy management from the International Organization of Standardization (ISO). The standard, according to ISO, ―specifies requirements for establishing,

implementing, maintaining, and improving an energy management system, whose purpose is to enable an organization to follow a systematic approach in achieving continual improvement of energy performance, including energy efficiency, energy security, energy use, and consumption.
** The Cement Sustainability Initiative (CSI), part of the World Business Council for Sustainable Development, has brought together a global group of large cement producers who promote the business case for sustainable and environmentally sound cement development. CSI said the use of alternative fuels in cement manufacturing facilities it studied jumped from just 2% in 1990 to about 16% in 2015, during a period in which global cement production rose almost 400%, in large part due to the rapid pace of construction in developing nations over the past 30 years.

*** Refuse-derived fuels (RDFs) (which can be further specified into tire-derived fuels (TDF) from used tires, or solid recovered fuels (SRF), usually commercial and industrial waste) and biomass-derived fuels are being more widely used in the cement industry, particularly as producers look to reduce emissions and move away from coal, natural gas, or fuel oil to power their kilns.
**** Scholarly articles for Boden et al., 2016,Global carbon budget 2016 - Le Quéré .

***** IEA – International Energy Agency

The International Energy Agency works with countries around the world to shape energy policies for a secure and sustainable future.

2. Materials and Methods

A. Discovery of (dried sugar beets' pulp) as a new Alternative Fuel*

Our proposal was based on a technology to use one of sugar industry byproduct (dried sugar beets' pulp) *Figure 1. (a)* In a pellets form as alternative fuel to replace fossil fuels in the cement rotary kilns.

One of the main features of these pellets is that it can be co-ground with coal or pet coke on a conventional coal mill; this allows pellets to be blended with conventional fuels, milled on an existing mill, transported to combustion point using existing fuel transport systems and combusted using existing combustion processes which means complete homogenization of the fuel mix which lead to the stability of kiln operation. In other words (dried sugar beets' pulp) it can be used with existing equipment without the needs to invest in new technology (Zero cost).

B. Use of (Sugar cane Bagasse) as a Bio Mass Alternative Fuel

For different causes will be shown below we also try to use one other sugar industry byproduct (Sugar cane Bagasse) *Figure 1. (b)* in a straw form as alternative fuel to replace fossil fuels in the cement rotary kilns same as it have been used in the internal steam power plants in sugar factories to produce high pressure steam which passed through turbine to generate electricity & low pressure steam which is used in industrial processes.

Also the main features of this straw is that it can be co-ground with coal or pet coke on a conventional coal mill, this allows pellets to be blended with conventional fuels, milled on an existing mill, transported to combustion point using existing fuel transport systems and combusted using existing

combustion processes which means complete homogenization of the fuel mix which lead to the stability of kiln operation.

Due high Running costs which is represented in the Prices of dried sugar beets' pulp in the local market in Egypt compare with the prices of bagasse nowadays we tried to use bagasse in its original shape to avoid the problems of heterogeneity of the mix (coal & alternative fuel) and side effect of this on the stability of kiln operation, we planned to use a separate bin for the raw Sugar cane Bagasse (before grinding with coal) to adjust the percent of mix. & separate bin for the pulverized mix. (After grinding & before dosing to kiln) or using a separate unit to turn Bagasse in pellets form *Figure 2. (a)* Same as the unit which use to produce dried sugar beets' pulp *Figure 2. (b)* .Till the prices changed to be the same up on the offers for the required quantities & quality in the future.



(**a**) (**b**)

Figure 1. (**a**) Sample of Sugar dried beet pulp; (**b**) Sample of Sugar cane Bagasse.



(**a**)

It is installed close to the drying unit

Output of the pelleting unit :	24 T/H
Dry substance at outlet of cooler :	90 % DS
Specific weight of dried pulp :	220 kg/m3
Residual moisture of dried pulp :	max 10 %
Saturated steam pressure :	2 – 3 bar g
Diameter of pellets :	8 mm
Temperature of pellets a outlet of the cooler over temperature of cooling air :	+ 5°C
Addition of steam at 2 bar gauge :	1200 kg/h
Working device : 3 pelleting presses working, 1 in standby	

	Pellets
Unit output per press	12 T/H
Number of presses running (one stand by)	3

(**b**)

Figure 2. (**a**) Production process of bagasse pellets; (**b**) Sample data of production unit of dried beet pulp.

Short description of Project Goals:

1- Minimize energy consumption (traditional fuel) & fuel combustion emissions.

2- Using about 20 % Alternative Fuels from the total plant fuel consumption due to the Environmental obligation & complying with the requirements of ISO 50001:2011
3- Employ one of byproduct of the food industries as sustainable fuel replacing fossil fuels in the combustion process realizing reduction in the fuel costs in addition to reduction of CO2 emissions up to 35 %.
4- Saving the cost of supply & installation of a new plant to use RDF, SRF or TDF as an alternative fuel.
5- Facing the problem of lack of the common alternative fuel (RDF, SRF or TDF) in Egypt.
6- Saving the traditional fuel sources.
7- Tendency to "zero carbon" to maintain the climate.

The Steps to implement by:

1- Collecting data and scientific research published locally and internationally related to the subject of the study.
2- Finding the places where the samples are collected determined whether biomass samples or different plants that include the sugar cane and sugar beet areas as the farms & factories in upper & Lower Egypt.
3- Collected samples & prepared samples mixtures are classified and identified, then dried and grinded, then packed in plastic bags until chemical analyzes are done with co-operation of labs of a cement production plant.
4- After making chemical analyzes of samples and the various experimental tests are performed using modern devices, after that make the report about the results
5- Statistical analyzes can be carried out by the statistical programs on the results.
6- By perpetration & co-operation with a cement production plant & sugar co we can try to make an industrial test with 10 -20 % from the used fuel tonnage. If possible.
7- After that we can make the report about the results with the cement production plant.

3. Results and Discussion

- **For Type no. 1of Alternative is biomass fuel (dried sugar beets' pulp)** The residual sugar beet fiber, remaining after sugar extraction, is then; it is dried and pressed in the form of pellets to produce a highly nutritious animal feed supplement. This is available to farmers and feed producers as eight millimeters diameter ―Animal Feed Pellet‖, containing an array of naturally occurring valuable ingredients, with a sugar content of 2.5% and a moisture content of 11%.We use dried sugar beets' pulp in the form of organic pellets with size ϕ 6 mm to 8mm with length 7cm to 10 cm in laboratory experimental trial & we have the analysis as shown in Table.1

- **For Type no.2 of Alternative is biomass fuel (Sugar cane Bagasse)** As we mentioned before, Sugar cane Bagasse is a byproduct from sugar industry in the form of organic straw with size thickness 1 mm to 3mm with length 1cm to 3 cm. We use Sugar cane Bagasse in laboratory experimental trial & we have we have the analysis as shown in Table.2

Table 1

- Carbohydrate : 69.51 %
- Portion : 10.26 %
- Fat : 2.435 %
- Fibers : 9.11 %
- Net Calorific value : 3500 kcal/kg
- Ash Content : 3 %
- Volatile content : 80 %
- Moisture : ≤ 12 %

Table 2

- Cellulose : 32- 48 %
- Hemi-cellulose : 19-24 %
- Lignin : 23-32 %
- Net Calorific value : 3600 kcal/kg
- Ash Content : 2.3 %
- Volatile content : 94 %
- Moisture : ≤ 15 %

To make an industrial trail experiment using about 50 tons of mixed sample manufactured by third party







Figure 3, 4, 5. Production unit by third party & photos of the mixed sample

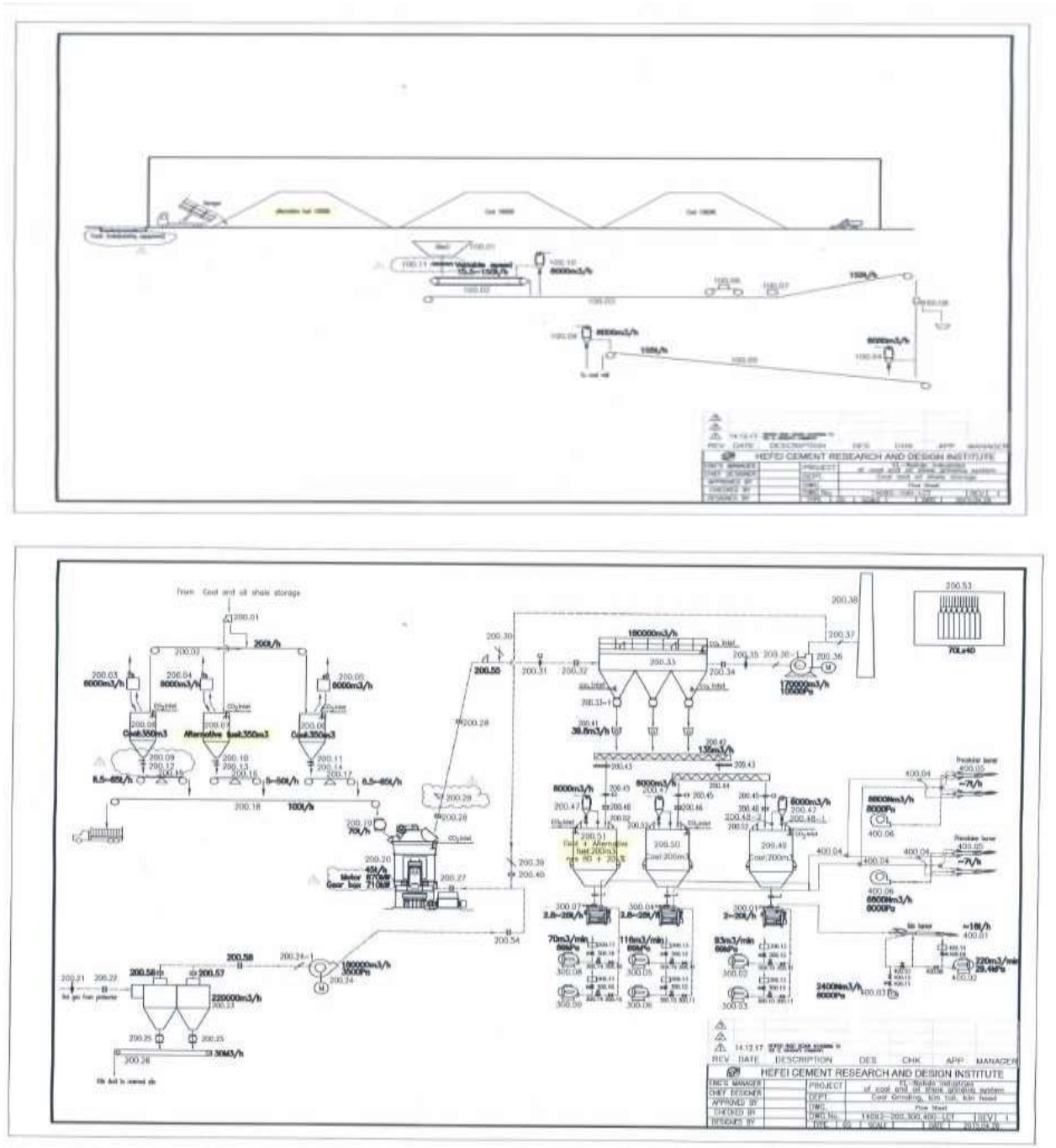


Figure 6, 7. Flow sheets of Coal & alternative fuel unit in cement plant.

- Design, equipment supplying & installation costs are neglected due to using the existing coal system (handling, grinding & dosing plant).Storage area for biomass quantities is available in site.

- The Lab. Devices using for analysis are available.

- Equipment operating & maintenance costs are neglected due to using the existing coal system (handling, grinding & dosing plant).

Acknowledgments: Technical Problems which might occur:

To avoid the problems of heterogeneity of the mix (coal & alternative fuel) and side effect of this on the stability of kiln operation, we used separate bin for the raw dried sugar beets' pulp (before grinding with coal) to adjust the percent of mix. & separate bin for the pulverized mix. (After grinding & before dosing to kiln).

4. Conclusions

This is may be a new technology in usage of alternative fuels which can meet requirement of applying the replacement of fossil fuels with alternative fuels in wide range in Egypt, which essentially based up on how we can provide the required quantities we need from the sugar Companies taking into account how to search for new solutions that help in the challenges of the century such as climate change and global warming.

This was our case study to look for new industrial solutions to help meet the challenges of the century such as climate change and global warming. Where we discovered new biomass fuel that may be applied in the near future in a wide range of cement and power plants.

This type of fuel may help reduce the cost of thermal energy, help in saving the strategic reserve of fossil fuels and contribute to a clean and non-polluting environment for human life and other living organisms which we hope to lived all.

References

Books & researches:

[1] Naganuma H. Ikeda N. Ito T. Matsuura M. Nunome Y. Ueki Y. Yoshiie R. Naruse I. " Reduction mechanisms of ash deposition in coal and/or biomass combustion boilers," *Fuel*, 106 , 2013, pp. 303-309.

[2] Mylläri F., Karjalainen P., Taipale R., Aalto P., Häyrinen A., Rautiainen J., Pirjola L., Hillamo R., Keskinen J. and Rönkkö T, "Physical and chemical characteristics of flue-gas particles in a large pulverized fuel-fired power plant boiler during cocombustion of coal and wood pellets," Combustion and Flame. 176,2017,pp. 554-566.

[3] Wienese, A. " Boilers, boiler fuel and boiler efficiency," Proc. S. Afr. Sug. Technol. Ass.,2001, pp.275-281.

[4] Tomohiro Oda, Shamil Maksyutov , and Robert J. Andres "The Open-source Data Inventory for Anthropogenic CO2, version 2016 (ODIAC2016): a global monthly fossil fuel CO2 gridded emissions data product for tracer transport simulations and surface flux inversions" Earth Syst. Sci. Data, 10, 87–107, 2018 https://doi.org/10.5194/essd-10-87-2018 © Author(s) 2018. This work is distributed under the Creative Commons Attribution 4.0 License.

[5] R.Saidur E.A.AbdelazizaA.DemirbasbM.S.HossainaS.Mekhilefc, A review on biomass as a fuel for boilers, Copyright © 2011 Elsevier Ltd

[6] Bagasse ,From Wikipedia, the free encyclopedia.

links:

[7] https://ar.scribd.com/doc/106999553/The-Handbook-of-Biomass-Combustion-and-Co-Firing-2008

[8] http://wood-pellet-line.com/make-biomass-pellets-from-sugarcane-bagasse/

[9] https://www.google.com.eg/search?q=Sugar+cane+straw&hl=en&tbm=isch&tbo=u&source=univ&sa=X&ved=0ahUKEwjvkvPt8NnaAhVBtBQKHcXoC1MQsAQIQA&biw=1440&bih=794#imgrc=utVfrJeUchMB_M:

[10] https://www.sciencedirect.com/science/article/pii/S0926669015304301

[11] http://www.biofuelmachines.com

[12] http://www.nile-sugar.com/arabic/products.aspx

[13] https://www.youtube.com/watch?v=ejr-63IlyPc

[14] https://www.youtube.com/watch?v=FKXotVOMFWk

Newspaper & articles:

- WORLD CEMENT magazine:

[15] Dec 2015, pages 47 -50 (alternative fuel solutions)-

[16] Nov 2017, pages 47 - 50 (keep your powder dry), pages 51-53(from road to recycle)

[17] Dec 2017, pages 34 -38 (from local to global)

- CEMENT BUILDING MATERIALS REVIEW magazine:

[18] Jun 2015, pages 28 -30 (losing the link to fossil fuel cuts costs, provide new alternatives), pages 31-52 (storage of fuels)

[19] Sept 2017, pages 66-70 (municipal solid waste as alternative fuel resource)

- GOLBAL CEMENT magazine:

[20] Sept 2017, pages 34-35 (energetic use of scrap tyers has been restricted: cement plants have to switch fuels)

Synthesis of New Compound (Chalcone) Derivative from Pyrimidine And Studying of Antimicrobial to this Compound

Aseel Fadhil kareem

Department of Pharmaceutical Chemistry, College of Pharmacy, University of Babylon, Iraq.

Abstract: In this research paper, can prepare anew chalcone compound from pyrimidine derivative due to have shown important in biologicals pharmacological effect is in addition to have a great important in ((antifungal, antimicrobial , anti-inflammatory, antioxidant and anticancer However, most of Chalcones have been wide ared in a recent years and futures by researchers for a new drug.

Keywords: chalcone ; pyrimidine ; Biological activity.

1. Introduction

chalcones are one of the classes of (Flavonoid)[1-2] in plants, [Clasien-Schmidt Condensation][3] is one of the variety methods of synthesis of chalcons these have known with another name as (benzyl acetophenone or benzylidene acetophenone)[4], which found in foods)[5]& (glucoside phloridzin)[6].

This compounds have been awide range of Pharma Cological & medicinal effects[7] as well as significant as antifungal & antibacterial activity. Chalcones are study an potential antitumor agents[8-9] pyrimidline is an organic compound (Heteocyclic aromatics, it have two nitrogen atoms in the positions (one & three) in addition to carbon atoms[10], can prepared in the laboratory by condensation (carbonyls with amines). It have been awid spectrum in biological activity, enoms[11] and drug metabolism[12]. However, pyrimidines known in the medicinal fields due to base in (cytosine, thymine & ura cil) ,DNA&RNA[13].

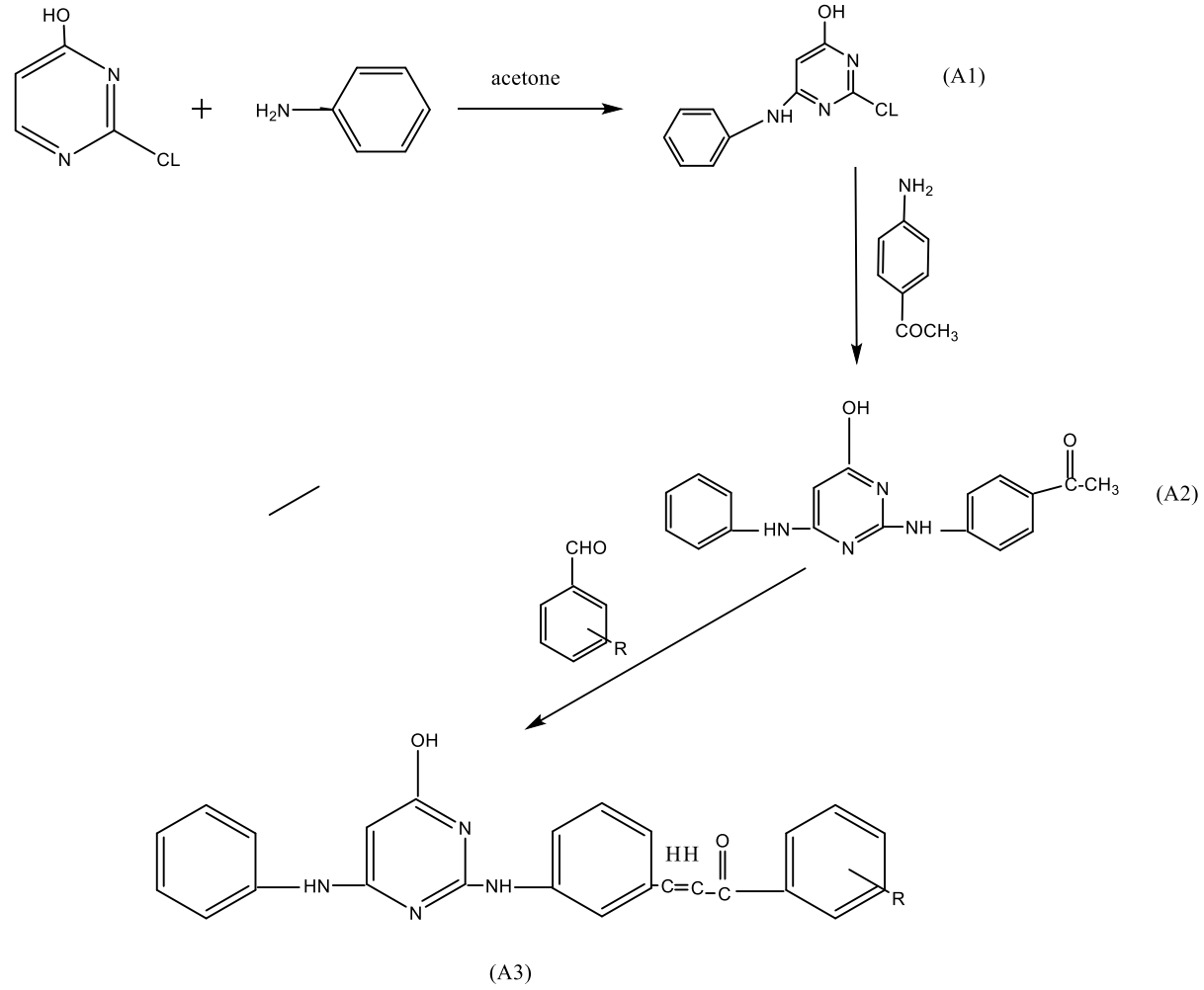
2. Materials and Methods

2.1 Chemical Study

(15mmol) of P-amino aceto Phenone was dissolved in Suitable solvent with (A1) Compound and with Some of aromatic aldehyde (15mmole), then added with constant stirring at($25C^0$), added KoH(10%) solution to reaction mixture with Stirred for (24)h at ($25C^0$) , finally the mixture was added into crushed ice and neutralized with (HCl) solutions the product separated and filtered, then washed by water, dried and recrystallized by ethanol absolute to give chalcone as in Scheme(1).
Note : All the reactions were monitored using by thin layer chromatography (TLC).

2.2 Biological Activity

the synthesized new compound (A3)) was screened by antibacterial against two types of Gram (positive & negative) bacteria as (*Bacillus sub de caly Eilis* , *Staphylococcus aureus*, *Escherichia colil* and *Pseudomonas aeruginosa*) and fungal as (*Percillium Chrysogenum* & *Aspergilus niger*) at three different concentration (lo, 25&35) mg/ml^{-1} and dissolving with (DMSO) as a solvent the Biological activity was measured bog (mm) minimum inhibition.

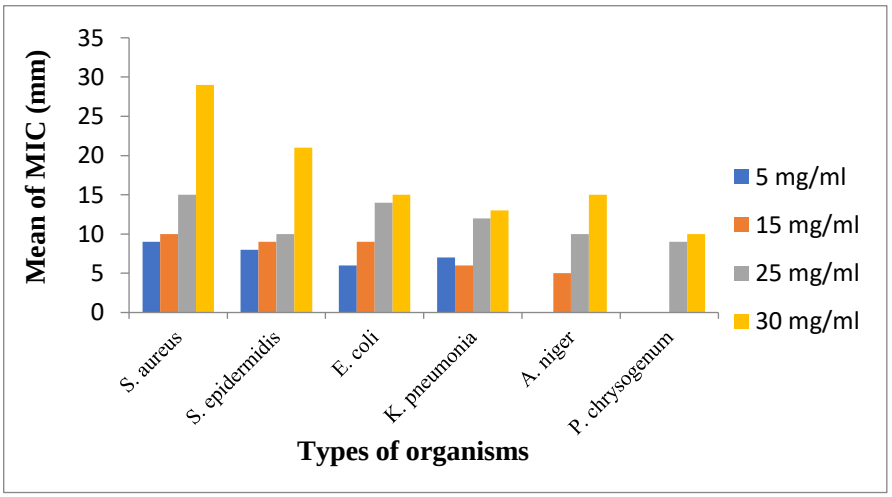


R :- 4- NO2 , 4- Cl

Figure 1. Preparation of (Chalcone) compound.

Table 1. Biological Activity to (A3) comp0und against Bacteria & Fungai.at (10,25&35)mg/ml^{-1}.

isolates .No.		G^+		G^-			Fungai
		S.a	***E.C***	***P.a***	***P.C***	***A.n***	
1	10	9	6	7	-	-	
	15	10	11	10	5	2	
	29	22	13	12	10	9	
2	9	9	7	7	3	-	
	12	11	10	9	7	-	
	30	20	14	12	13	11```	
3	8	8	8	8	-	-	
	10	9	10	8	5	3	
	32	22	17	15	12	9	
4	15	11	11	9	2	2	
	14	12	13	13	7	4	
	35	25	18	12	14	10	



3. Results and Discussions

- Table (1) Biological activity against (43) Compound att bacteria and fungalo
- gainst at (10, 25835) mg/ml
- figure(1) Mean of inhibition zon(mm) of (chalcone) (93) Compound at different
- Conc
- Photo (1): Antibacterial Activity at conc(35) mg/min
- Photol 2) : Antifungal Activity at conc (35) mg/ mit

Results and Discussions : This compound (a3) (Chalcone) has ahigh af level of biological activity towards all bacterial especially at concentration (35mg/mi), due to can ability to damaged of the well of cell and can be inhibition the function of the cell because Cchalcomen) was containing to two rings which increase from activity in addition to heterocyclic atoms .

4. Conclusion

chalcone (a3) compound was found to bat to be active against two types of bacterial Cat SE) and show best activity at (35) ng lint at all types of bacterial comparable activity with fungal - since upon to the type of substituents of the teratyeti atomsu

References

1. *Ni, L.*; Meng, C-Q.; Sikorski, J.A. Recent advances in therapeutic chalcones. Expert opina Ther. pat, 2004, 14, 1669-1691. [Cross Ref] –
2. Sahu) Nike; Balbhadra, SS.; Choudhary, J.; Kohli, Dovo Exploring pharmacological significance of Chalcone scaffoldo. A review. Curr. Medlochem2 de 19, 209-225. [Cross Ref] [PubMed]
3. Patil, C. Boj Mahajan, s. kij katti, S.A., Jo pharm. Sci Resol, 11-22, 2009 –*M.N.*Cífford, J. Sci Food Agric; 80:1|26-1137,
4. 2*00*0.
5. *C. Ar* Calliste, J. C. Lebail, p. Trouilas, C. Pouget, C. Habrioud, S.A. Chulia, L.Jo Duroux, Res; 21: 3949-3956, - 200l.
6. S S. Mokle, MA. S*ay*eed, Kothawarand chopde Into J. Chem. Sci. 261, *96, 2004*
7. & Hsieh HK Tsao LT and wang JP. Je pharm- Pharmacon 521*63, (20*00)
8. M. Liu, po Wilairat and L.M. Go, J. Med ochem, 4*454443)* (2001)
9. MurciaALeal, S.*M.; Roa, M.V.1 N*agles, Ej. Munoz Castro, Ars Hurtaelo, J.J. vil (23) (*8*), (2018).
10. N. A. Al - Masoudi, .ASalih*NoA*bdul Karim, A. J. Isso, Capannecou que, Heteroatian Chem. 22, 44 50, (2011)
11. Timo Cocco, C. Conginio, Lillia, Bioorg. Med-Chemia 14,66-872, (2006).
12. Yamanari, Mo Kida, A. fusuhiro, M-kita, S. Kaszaki, I norg.chem. Acta, 332,115-122,*(2007),*

Theoretical Investigation of Recovery of Bioactive Compounds from Food Wastes through Supercritical CO_2 Extraction

Yaprak Özbakır *

Department of Chemical Engineering, Faculty of Natural Sciences and Engineering, Uskudar University, Turkey;

***** *Corresponding author: yaprak.ozbakir@uskudar.edu.tr; Tel.: (+90)216 400 2222.*

Abstract: Extraction of phenolic compounds (PCs) from an eggplant peel pellet with a diameter of 0.5 cm and 5 cm-height using $scCO_2$/ethanol mixture with 16 mol % ethanol in a 30 ml tubular extraction vessel in batch mode was investigated through simulations. Partial differential equations representing mass transfer within the pellet phase and in the external $scCO_2$/ethanol mixture phase were developed and solved using finite difference method in Matlab. Effect of temperature (40-60 °C) on the extraction of PCs at 150 bar, and that of pressure (150-250 bar) on their extraction at 60 °C as well as pellet porosity (0.1-0.5) and pellet size (0.5-1.9 cm) on the extraction times were investigated. It was found that the increase in temperature and pressure slightly decreased the extraction times, and 40 °C at 150 bar was suggested as the optimum conditions. In addition, the model was used to predict mass transfer coefficients for the extraction of PCs from the pellet. The values in the range from $5x10^{-6}$ m/s to $1x10^{-5}$ m/s was determined to be optimum mass transfer coefficients for the extraction at 60 °C at 150 bar.

Keywords: Supercritical CO_2 extraction; agri-food waste; eggplant peel; phenolic compounds; mass transfer; mathematical modeling.

1. Introduction

Eggplant is among the most widely consumed vegetables. It has received a great interest as functional food in recent years due to its reported nutritional and economic values. [1, 2]. Eggplant is characterized for its high phenolic content that is considered as one of the most important contributor compound to reduce the risk of noncommunicable disesases and certain types of cancer [1, 3-5]. It is classified as one of the top 10 vegetables rich in powerful antioxidants; they exhibit a number of biological effects such as hepato-protective and hypolipidemic activities [2]. Eggplant is rich in polyphenols, approximately 75 % of eggplant polyphenols present in the peel which might be extracted as value-added ingredients [1, 4]. The recovery of these functional ingredients from eggplant peels would add value to the industrial waste in formulation of food products for fortification with those compounds [2]. Thus, the recovery of antioxidant phenolic compounds from natural substances has gained considerable interest in recent years due on the one hand to their beneficial effects on health and on the other hand to the carcinogenic effect of synthetic antioxidants [6].

Extraction is the first step in the recovery of these bioactive compounds from the waste. Extraction of phenolic compounds from the agro-industrial by-products can be achieved by several ways such as the traditional methods such as Soxhlet, steam distillation and cold maceration; however, low efficiency of extraction is the main drawback of these techniques due to prolonged heat treatment which brings about the degradation of thermo-sensitive compounds and also induces high consumption of energy, time, and solvent [6-9]. Recently, supercritical fluid extraction (SFE) has been applied in food technology for processing and extraction of phenolic compounds as the new

emerging green technology which has overcome these challenges enabling high extraction efficiency, short extraction time, and high quality of the final product at lower temperature, enhanced kinetics and less energy/solvent consumption. CO_2 is the most commonly used solvent in SFE due to its low critical point (31.2 °C and 73.8 bar), environmentally friendly features and low cost [10]. Small amounts (5-18 %) of polar solvents such as ethanol, methanol, water, among others, can also be used as modifiers to alter the solvating power of CO_2 and to increase the extraction efficiency of high polar compounds [11, 12].

SFE offers further several advantages as compared to the other techniques. First, since SFE is usually conducted at mild temperatures (however, above the critical temperature of the solvent), the degradation of heat-sensitive compounds can be prevented. Next, high pressures above the critical pressure of the extraction solvent at which SFE is performed increases the solvent density and diffusion coefficient; thereby, the solvation power is increased, and a faster extraction is attained [12]. Also, SFE enables the extraction solvent/modifier to separate from the extract simply through the expansion of the fluid in the extraction vessel outlet through an expansion valve, which causes the stream to separate into a gaseous stream enriched in CO_2 and a liquid stream which is enriched in modifier. This allows the recovery and reusing of the extraction solvent [12-15].

An understanding of the kinetics of supercritical extraction of phenolic compounds and modeling of the process is necessary to provide insight into scale-up and optimization of recovery of bioactive compounds from agri-food waste. However, to the best of our knowledge, the modeling of the kinetics of extraction of phenolic compounds from the eggplant peel has not been studied, and therefore, there is a need for the mathematical modeling of this process. In this study, we aim to investigate the recovery of phenolic compounds from the eggplant peels through supercritical fluid extraction using CO_2, and to develop partial differential equations representing mass transfer in the supercrtical extraction of PCs from the peels and to solve them using numerical techniques. The extraction vessel and sample geometry was such that the derived differential equations were sufficiently well representative of the extraction process inside the vessel and the boundary conditions were well-defined. The model was used to predict mass transfer coefficient in batch mode as well as extraction time. The effects of a range of operating conditions on the extraction were investigated through simulations.

2. Materials and Methods

Extraction of PCs from eggplant peels using $scCO_2$/ethanol mixture with 16 mol % ethanol in the 30 ml tubular extraction vessel was investigated through the simulations. To obtain peels with well-defined shapes and sizes, the preparation of eggplant peels in the form of cylindrical pellets by a mechanical force, in subsequent to the drying and powderizing steps is suggested. Mathematical model for the mass transfer of the PCs from the pellet phase to the external $scCO_2$/ethanol mixture phase was developed and solved using FDM in Matlab. The simulations were performed for the cylindrical pellets with a 5 cm-height and a 0.5 cm-thick in a 30 ml high pressure tubular vessel at 60 °C and 150 bar. In addition, extraction of PCs from the pellets at 60 °C and the pressures of 200 bar and 250 bar and at varying operating temperatures in the range from 40 °C to 60 °C at 150 bar were investigated.

2.1. Mass Transfer Model

Extraction of PCs from the peel pellet in a batch vessel was considered by two cases: in a perfectly mixed vessel and in stationary $scCO_2$. In the former case, it is considered that the pellet is placed in a perfectly mixed vessel, and PCs are transferred from the surface of the pellet into the

$scCO_2$ in the vessel, which results in no concentration gradient throughout the fluid phase around the pellet, and it yields infinitely large mass transfer coefficient. In the latter case, the vessel is filled with stationary $scCO_2$, and PCs in the pellet diffuses into $scCO_2$ in the vessel and a flow around the pellet occurs by natural convection due to temperature gradient that exists in the fluid in the vessel. The concentration of PCs smoothly decreases as the distance from the surface of the pellet increases, which results in a concentration gradient of PCs in the bulk $scCO_2$ phase. In this case, mass transfer coefficient is considered to be in between two extreme cases ranging from zero to infinitely large mass transfer coefficient depending on the convective currents in the system. The extraction in stationary $scCO_2$ with negligible convective currents around the pellet surface yields negligibly small mass transfer coefficient, and increases depending on the convective currents in the system. A number of values were used in the simulations to predict a reasonable range for the mass transfer coefficient for the extraction in batch mode.

2.1.1. Mathematical Modeling of Supercritical Fluid Extraction

Mass transfer in the pellet phase and $scCO_2$ phase were described by a partial differential equation. For the pellet phase, one-dimensional diffusion of PCs through the radial direction in the pellet was modeled based on Fick's second law. Gallic acid was assumed to be the primary phenolic compound present in the peel [16], and initial concentration of phenolic compounds in the pellet was calculated based on the gallic acid. For the $scCO_2$ phase, it was assumed that it does not initially contain any PCs, and the mass transfer of PCs by convection from the pellet surface to the $scCO_2$ phase was considered. Figure 1 shows side view and top vies of a cylindrical pellet as well as one-dimensional extraction of PCs in the pellet. The partial differential equation obtained from a mass balance in a differential volume element in the pellet is given by;

$$D_e \frac{\partial^2 C_A}{\partial r^2} + \frac{D_e}{r}\frac{\partial C_A}{\partial r} = \frac{\partial C_A}{\partial t} \qquad (1)$$

where C_A is concentration of PCs in the pellet, (M), D_e is effective diffusion coefficient, (m^2/s), and t is time, (s), and r is the direction that diffusion occurs in the pellet, (m).

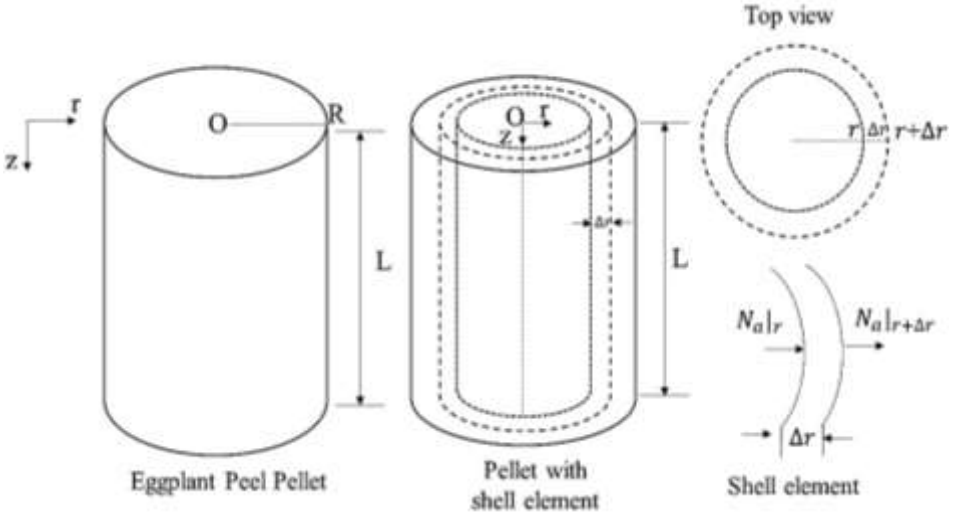


Figure 1. Side view and top view of cylindrical magnified pellet.

The initial and boundary conditions are given by;

Initial Conditions:

$$\text{at} \quad t = 0 \quad C_A(r,0) = C_{A,i} \tag{2}$$

where $C_{A,i}$ is the concentration of pure gallic acid at the initial conditions.

Boundary Conditions: $t > 0$

$$\text{at } r = 0 \quad \frac{\partial C_A}{\partial r} = 0 \tag{3}$$

$$\text{at } r = R \quad \frac{\partial (C_b V)}{\partial t} = K_x (C_{A,s} - C_b) A \tag{4}$$

$$\text{at } r = R \quad D_e \frac{\partial (C_A A)}{\partial r} = K_x (C_b - C_{A,s}) A \tag{5}$$

where C_b is concentration of gallic acid in the bulk in the vessel (M), $C_{A,s}$ is concentration of gallic acid on the pellet surface (M), V is the vessel volume (m^3), A is the lateral surface area of the pellet (m^2), and K_x is the mass transfer coefficient (m/s).

Eq.2 indicates that the gallic acid concentration is assumed to be initially uniform throughout the pellet volume with a concentration of $C_{A,i}$. This is fixed by the density of pure gallic acid at the given conditions. Zero mass flux of gallic acid by diffusion is assumed at the centerline (see Eq. 3) due to symmetry boundary condition. Mass flux of gallic acid from the pellet surface to the $scCO_2$ is defined by convection. Eq.4 shows that the convective mass flux of gallic acid at the pellet surface is equal to rate of increase of gallic acid in the fluid phase, and Eq.5 indicates that the diffusive mass flux of gallic acid at the pellet surface is equal to the convective mass flux of gallic acid. The Finite difference method was used to solve the governing equations. The equations and boundary conditions were approximated by a point-wise discretization scheme divided into equal small regions with increments of r in the pellet for the solution of Eq. 1. These were transformed into discretized equations at each nodal point to obtain a set of algebraic equations that involve the unknown values at the grid points. The algebraic equations were solved and external mass transfer coefficient values for each case were regressed in Matlab.

Fluid properties and diffusion coefficient are essential to predict extraction times. Considering porosity and tortuosity of the pellets, effective diffusivity was used and it was calculated using the binary diffusivity coefficient (D_{12}), overall porosity and tortuousity of the pellet (Eq. 6). The binary diffusion coefficient of gallic acid in $scCO_2$/ethanol mixture (m^2/s) was taken from the literature [13]. The binary diffusion coefficients at corresponding operating conditions are tabulated in Table 1 and Table 2.

$$D_e = \frac{D_{12} \times \varepsilon}{\tau} \qquad \tau = \frac{1}{\varepsilon} \tag{6}$$

Table 1. Diffusion coefficients of gallic acid in $scCO_2$/ethanol mixture with 16 mol % ethanol at 60 °C and at varying pressures from 150 to 250 [13].

T (°C)	P (bar)	D_{12} (m^2/s)
60	150	5.2×10^{-9}
	200	4.4×10^{-9}
	250	4.2×10^{-9}

Table 2. Diffusion coefficients of gallic acid in $scCO_2$/ethanol mixture with 16 mol % ethanol at 150 bar and at varying temperatures from 40 to 60 °C [13].

P (bar)	T (°C)	D_{12} (m^2/s)
150	40	3.7×10^{-9}
	50	4.4×10^{-9}
	60	5.2×10^{-9}

3. Results and Discussion

The effects of various process parameters including mass transfer coefficient, temperature and pressure as well as the pellet porosity, tortuosity and thickness on the extraction time of gallic acid from the eggplant peel pellets were individually investigated. The effect of mass transfer coefficient on the extraction time of gallic acid from the pellet with the diamater of 0.5 cm and a height of 5 cm was investigated for a broad range of values from $1x10^{-7}$ m/s to $1x10^{-3}$ m/s. Figure 2 shows that the extraction with high value of K_x reduces the extraction time, while the values from $5x10^{-6}$ to $1x10^{-3}$ m/s approach a limiting value for the percentage extraction at which the percentage extraction remains constant. It can be said that the mass transfer is predominantly controlled by diffusion after this limiting value and gallic acid molecules which reach the pellet surface are readily swept away from its surface. Figure 2 suggests that the mass transfer coefficient in the batch mode might be between $5x10^{-6}$ m/s and $1x10^{-5}$ m/s, and the optimum mass transfer coefficient was chosen as $1x10^{-5}$ m/s.

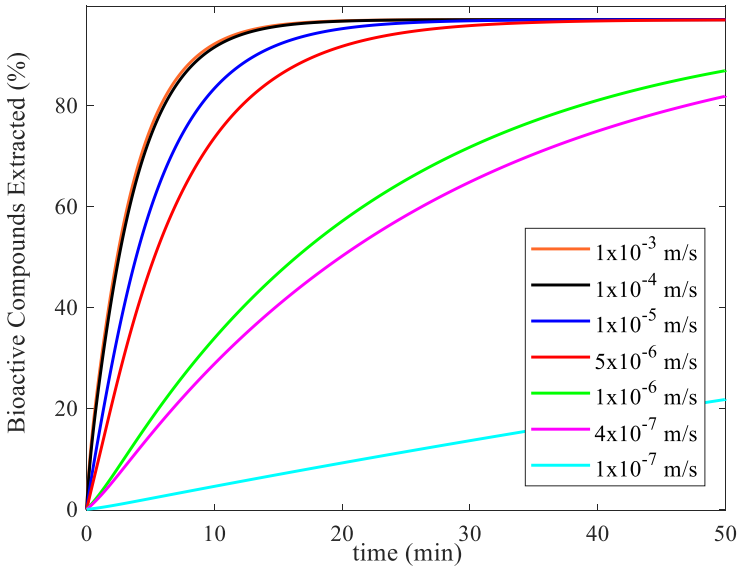


Figure 2. Effect of Mass Transfer Coefficient on Extraction Time ($D_{12} = 5.2 \times 10^{-9}$ m^2/s)

The extraction of gallic acid from the pellet at 60 °C at 150 bar with the mass transfer coefficient of $1x10^{-5}$ m/s resulted in the concentration profile inside the pellet from the center to the surface, shown in Figures 3 and 4. The figure refers that the gallic acid in the pellet is transferred by diffusion through the pellet to its surface, while at the surface; the gallic acid is removed via convective mass

transfer assisted by the $scCO_2$ around the pellet to the vessel. Hence, the gallic acid concentration decreases faster on the gel surface, and the concentration of the gallic acid in the bulk increases with time.

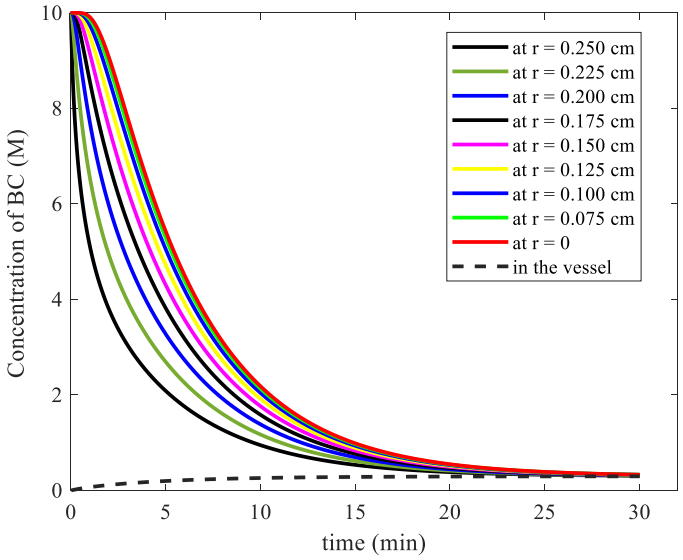


Figure 3. Time variation of concentration of gallic acid inside the pellet and in the vessel (Kx = $1x10^{-5}$ m/s and $D_{12} = 5.2 \times 10^{-9}\ m^2/s$)

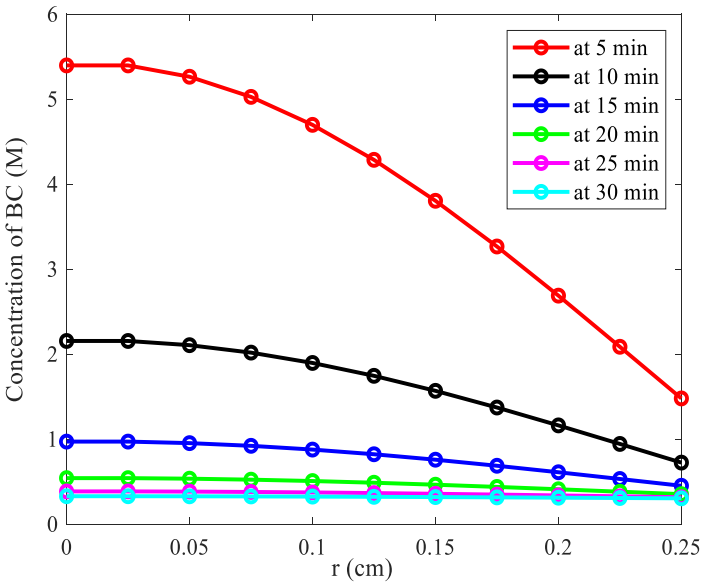


Figure 4. Time variation of concentration of gallic acid inside the pellet and in the vessel (Kx = $1x10^{-5}$ m/s and $D_{12} = 5.2 \times 10^{-9}\ m^2/s$).

Figure. 5 shows the percentage removal of gallic acid over the extraction time at varying operating temperatures of 40 °C, 50 °C and 60 °C. It is found that temperature did not significantly affect the extraction time. It is slightly higher at elevated temperatures since the diffusivity of CO_2 increases with temperature. Additionally, the increase in temperature could also accelerate mass transfer and improve the extraction yield. Furthermore, Figure 6 indicates that the increase in pressure from 150 bar to 250 bar at 60 °C slightly decreased the percentage extraction of gallic acid. The optimum

conditions for the extraction of the gallic acids from the 0.5 cm-thick and 5-height pellet is suggested to be 40 °C at 150 bar.

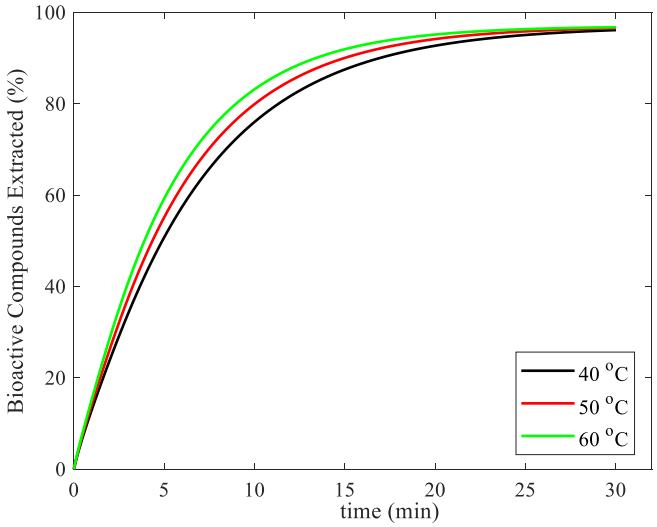


Figure 5. Effect of temperature on percentage removal over time in the pellet (Kx = 1x10^{-5} m/s and D_{12} = 5.2×10^{-9} m^2/s).

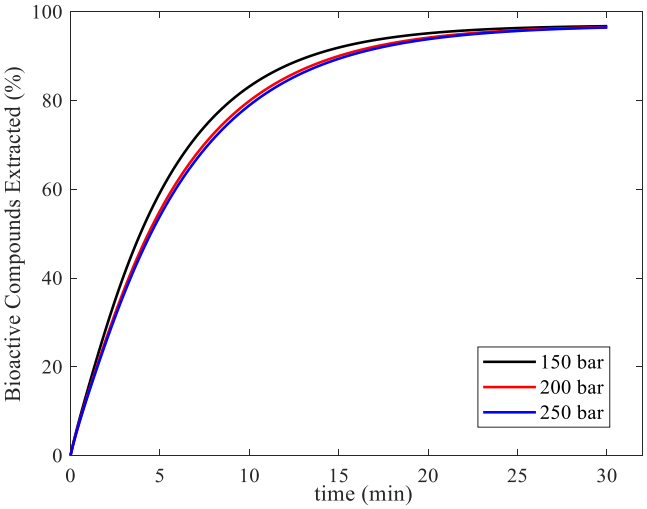


Figure 6. Effect of pressure on percentage removal over time in the pellet (at 60 °C Kx = 1x10^{-5} m/s and D_{12} = 5.2×10^{-9} m^2/s).

Next, effective diffusivity in the porous materials is directly related to binary diffusion coefficient of solvent and material overall porosity, while it is inversely related to the pellet tortuosity. Effect of these parameters on the extraction time was investigated, individually. The effect of effective diffusivity on percentage extraction of gallic acid was investigated through the pellet porosities from 10 % to 30 %, and the corresponding effective diffusivities were calculated using Eq. 6. Figure 7 demonstrates that the higher diffusivity yields faster extraction. In other words, the higher the diffusivity, the shorter time needs to reach the maximum yield. In contrast the lower diffusivity due

to lower porosity values, the more time for extraction and to reach the maximum value of extraction a phenol compounds.

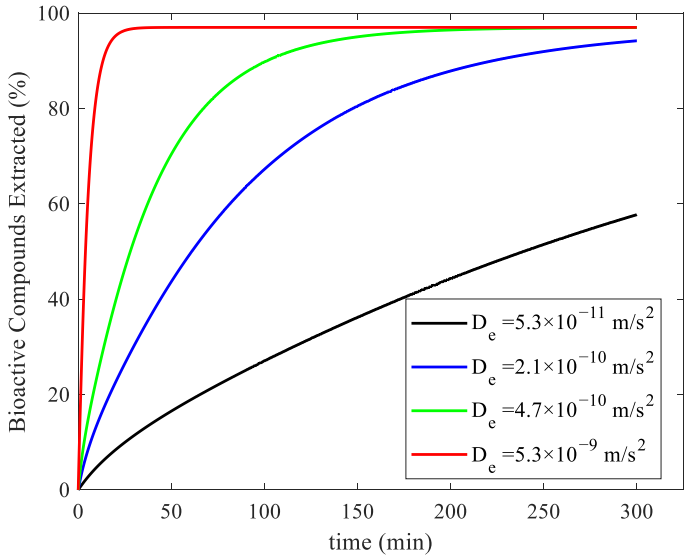


Figure 7. Time variation of concentration of gallic acid inside the pellet and in the vessel (Kx = 1x10^{-5} m/s)

The size of pellet body is one of the most important parameters affecting the extraction times.

Figure 8 shows the effect of pellet thickness on the extraction time. As expected, the pellets with larger diameters need longer times due to larger amount of gallic acid in the matrix. Extraction occurs in a shorter time in thinner pellets, whereas it takes a longer time in thicker pellets. Almost 40 % of gallic acid could be extracted from the pellet with 1.9 cm thickness, whereas approximately 95 % of gallic acid in the pellets with 0.5 cm diameter was extracted.

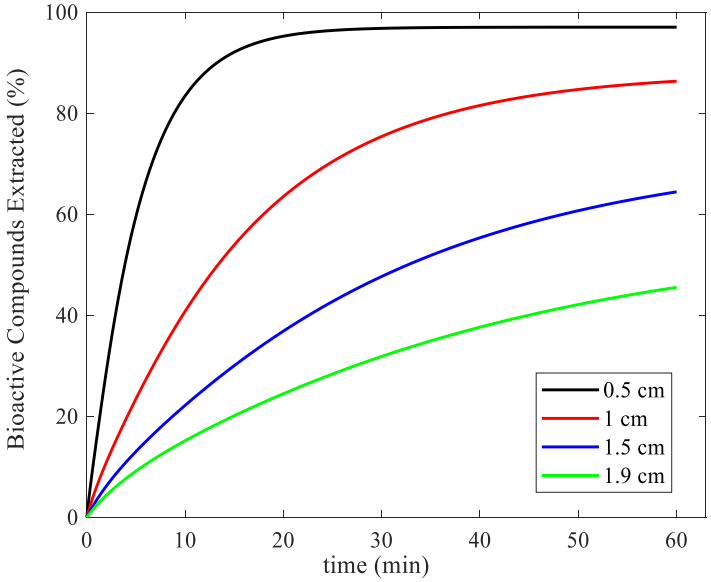


Figure 8. Effect of pellet diameter on gallic acid extraction in the vessel (Kx = 1x10^{-5} m/s and $D_{12} = 5.2 \times 10^{-9}$ m^2/s).

Furthermore, extraction of the pellet with the diameter of 0.5 cm and the height of 5 cm in the vessels with varying sizes were invidiually simulated. The vessels with a diameter of 2 cm and varying height in the range from 1 cm to 10 cm, and the vessels varying diameters in the range from 0.52 cm to 2 cm and a height of 10 cm were selected for the extraction. Figure 9 and 10 demonstrates that the vessel size slightly changes the time for the extraction. The vessel with a 2 cm diameter and 10 cm height can be suggested for faster extraction of the pellet (0.5 cm-diameter x 5 cm-length).

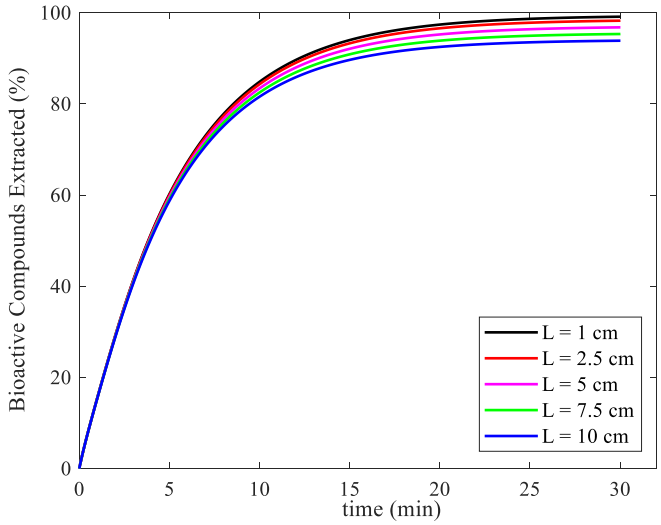


Figure 9. Effect of vessel size on extraction pellet in the vessel (D = 0.5 cm and H = 5 cm, Kx = 1x10^{-5} m/s and $D_{12} = 5.2 \times 10^{-9}$ m^2/s).

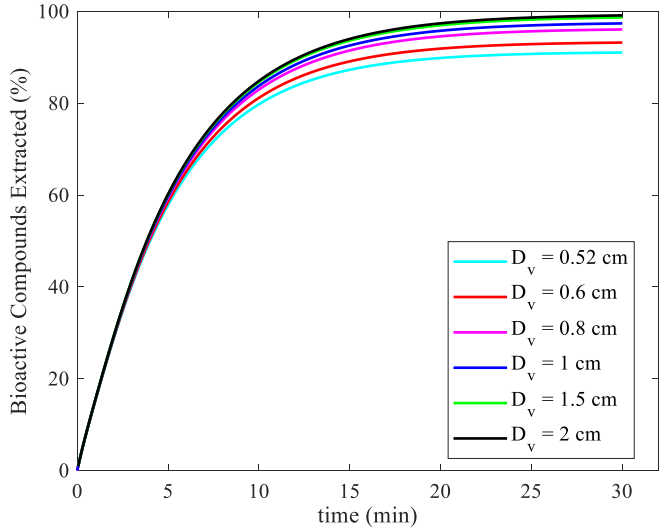


Figure 10. Effect of vessel size on extraction pellet in the vessel (D = 0.5 cm and H = 5 cm, Kx = 1x10^{-5} m/s and $D_{12} = 5.2 \times 10^{-9}$ m^2/s).

4. Conclusions

Supercritical extraction of phenolic compounds using $scCO_2$/ethanol mixture from the cylindrical eggplant pellet in batch mode was investigated through simulations. Partial differential equations representing mass transfer within the pellet phase and in the external $scCO_2$/ethanol mixture phase were developed and solved using FDM in Matlab. Effect of temperature and pressure on the extraction

of PCs as well as pellet porosity and pellet size on the extraction times were investigated. The optimum conditions for the extraction of the gallic acids from the 0.5 cm-thick and 5-height pellet was suggested to be 40 °C at 150 bar, and the values in the range from $5x10^{-6}$ m/s to $1x10^{-5}$ m/s was determined to be optimum mass transfer coefficients for the extraction at 60 °C at 150 bar.

References

1. G. Niño-Medina, V. Urías-Orona, M.D. Muy-Rangel, J.B. Heredia, Structure and content of phenolics in eggplant (Solanum melongena) - a review, South African Journal of Botany 111 (2017) 161-169.
2. S. Ferarsa, W. Zhang, N. Moulai-Mostefa, L. Ding, M.Y. Jaffrin, N. Grimi, Recovery of anthocyanins and other phenolic compounds from purple eggplant peels and pulps using ultrasonic-assisted extraction, Food and Bioproducts Processing 109 (2018) 19-28.
3. Y. Noda, T. Kneyuki, K. Igarashi, A. Mori, L. Packer, Antioxidant activity of nasunin, an anthocyanin in eggplant peels, Toxicology 148 (2000) 119-123.
4. N.-N. Condurache , C. Croitoru, E. Enachi, G.-E. Bahrim, N. Stănciuc, G. Râpeanu, Eggplant Peels as a Valuable Source of Anthocyanins: Extraction, Thermal Stability and Biological Activities, Plants 10 (2021) 577.
5. M. Kazemi, F. Khodaiyan, S.S. Hosseini, Eggplant peel as a high potential source of high methylated pectin: Ultrasonic extraction optimization and characterization, LWT 105 (2019) 182-189.
6. S. Amrouche, F. Mohellebi, R. Derriche, Extraction of phenolic compounds from algerian Inula viscosa (L.) Aiton leaves: kinetic study and modeling, Separation Science and Technology 55 (2020) 3161-3174.
7. O.R. Alara, N.H. Abdurahman, C.I. Ukaegbu, Extraction of phenolic compounds: A review, Current Research in Food Science 4 (2021) 200-214.
8. S.G. Jahromi, Extraction techniques of phenolic compounds from plants, Plant physiological aspects of phenolic compounds (2019) 1-18.
9. J.F. Osorio-Tobón, Recent advances and comparisons of conventional and alternative extraction techniques of phenolic compounds, Journal of Food Science and Technology 57 (2020) 4299-4315.
10. İ. Şahin, Y. Özbakır, Z. Inönü, Z. Ulker, C. Erkey, Kinetics of supercritical drying of gels, Gels 4 (2018) 3.
11. L.M. de Campos, F.V. Leimann, R.C. Pedrosa, S.R. Ferreira, Free radical scavenging of grape pomace extracts from Cabernet sauvingnon (Vitis vinifera), Bioresource Technology 99 (2008) 8413-8420.
12. A.M. Farías-Campomanes, M.A. Rostagno, J.J. Coaquira-Quispe, M.A.A. Meireles, Supercritical fluid extraction of polyphenols from lees: overall extraction curve, kinetic data and composition of the extracts, Bioresources and Bioprocessing 2 (2015) 45.
13. J. Leite, A.L. Magalhães, A.A. Valente, C.M. Silva, Measurement and modelling of tracer diffusivities of gallic acid in liquid ethanol and in supercritical CO2 modified with ethanol, The Journal of Supercritical Fluids 131 (2018) 130-139.
14. Y. Özbakır, C. Erkey, Experimental and theoretical investigation of supercritical drying of silica alcogels, The Journal of Supercritical Fluids 98 (2015) 153-166.
15. Y. Özbakır, Z. Ulker, C. Erkey, Monolithic composites of silica aerogel with poly(methyl vinyl ether) and the effect of polymer on supercritical drying, The Journal of Supercritical Fluids 105 (2015) 108-118.
16. M. Kadivec, M. Kopjar, D. Znidarcic, T. Požrl, Potential of eggplant peel as by-product, Acta Alimentaria 44 (2015) 126-131.

Thermoelectric Performance of Ni, Co, and Fe Nanoparticles Intrinsically Doped into Their Metal Borates Glassy Matrices

Isam M. Arafa*, Mazin Y. Shatnawi, Yousef N. Obeidallah

Department of Applied Chemistry, Faculty of Science and Arts, Jordan University of Science and Technology, P.O. Box 3030, Irbid 22110, Jordan.

* *Corresponding Author: isamaraf@just.edu.jo ; Fax: 962-2-7201071*

Abstract: Here, we present our current attempt to intrinsically dope Ni^0, Co^0, and Fe^0 nanoparticles within Ni^{II}-, Co^{II}-, and Fe^{II}-borate glassy matrices, respectively. The system is prepared by one-pot reaction of the desired M_T^{II} salt with excess $NaBH_4$ through an *in situ* reduction and hydrolysis processes to afford metallic $\mathbf{M_T^0}$ nanoparticles dispersed into the $\mathbf{M_T\text{-}BO_3}$ matrix. The composition and structural characteristics of these $\mathbf{M_T^0}$:$\mathbf{M_T\text{-}BO_3}$ materials were identified by thermal oxidation, ATR-IR, X-Ray diffraction, and magnetic techniques as glassy/amorphous borate matrices containing magnetic nanoparticles. The electrical conductivity (**σ**) of cold-pressed discs of these metal-doped composites shows that they behave as nonohmic semiconductors within the temperature range of $303 \leq T \leq 373$ K. However, their thermal conductivity (**κ**) occurs through phonon lattice vibration dynamics rather than electronic. The **σ/κ** ratio shows a steep nonlinear increase from 9.4 to 270 KV^{-2} in Ni^0:Ni-BO_3. In contrast, a moderate-weak increase is observed for Co^0:Co-BO_3 and Fe^0:Fe-BO_3 analogs. The obtained materials are examined for thermoelectric (TE) applications by determining their Seebeck coefficient (S) power factor (PF), figure of merit (ZT), and conversion efficiency (η%). All the TE data shows that the Ni^0:Ni-BO_3 (S, 80 μVK^{-1}; PF, 259 $\mu Wm^{-1}K^{-2}$; ZT 0.64; η, 2.56%) is a better TE semiconductor than the other two M_T^0: M_T-BO_3. This finding shows that Ni^0:Ni-BO_3 is a promising candidate to exploit low-temperature waste heat from body heat, sunshine, and small domestic devices for small-scale TE applications.

Keywords: metal borates, metal nanoparticles, thermoelectricity, waste heat harvesting,

1. Introduction

The constant rising demand for energy can be managed by resorting to renewable energy sources, including solar photovoltaic (**PV**), thermoelectric (**TE**), geothermal, and wind [1-27]. Global reports show that about 65% of the produced energy is wasted as heat from industrial plants, fuel engines, domestic appliances, solar thermal radiation, and other heat sources. In this term, wasted heat can be utilized by converting into DC current through thermoelectric (**TE**) phenomenon, which is generally governed by Seebeck coefficient (S), figure of merit (**ZT**), power factor (**PF**), and conversion efficiency (**η**%), Equations 1-4, where the temperature gradient (**ΔT)**

$$\Delta V = - S (\Delta T) \quad (1)$$

$$ZT = (S^2 * \sigma / \kappa) T \quad (2)$$

$$PF = S^2 * \sigma \quad (3)$$

$$\eta\% = (\Delta T/T_h) [(1 + ZT_{avg})^{1/2} -1]/ [(1 + ZT_{avg})^{1/2} + T_c/T_h]\% \quad (4)$$

is directly related to the induced DC thermal voltage **(ΔV)** as described by Seebeck, Equation 1. Although TE technology is direct, simple, and environmentally friendly, its slow progress over the past few decades is partly due to the lack of efficient TE semiconductors and the poor conversion efficiencies ($\eta < 5\%$) in comparison with solar PV technology [4-7,11-15,20-23]. Nevertheless, current research in this field is unfolding on utilizing solar thermal energy to build solar-based TE systems [24,25]. However, for TE technology to be practically viable and competitive with PV technology for harvesting solar energy, the TE semiconductors should exhibit ZT values ≥ 1 or PF ≥ 4 mW/m.K^2 [3,4,7,11-15].

On the other hand, the success of this technology relies on obtaining p-type and n-type TE semiconductors characterized by narrow bandgap exhibiting sufficiently high **σ** and **S** values while displaying low **κ** [3-7,11-19,20-23]. The *interrelation between* **σ** and **κ** has been the subject of several theoretical and experimental studies [3,4,16,21,22]. Recent reports showed that the microstructure of TE materials and morphology (texture, crystallinity, dimensionality) significantly affect the transport of charge carriers and phonon scattering. Different authors showed that S, and σ can be enhanced by extrinsic doping, low dimensional structure, and increase of charge carrier concentration while suppressing κ through the formation of point defects, nano-scaled particles, grain boundary scattering, phonon-glass electron crystals, formation of nanocomposites, and sublattice structures [4,6,7,20-23]. In this respect, polycrystalline materials with large-sized grain (> 2 mm) offer transport pathways for electrons, still cannot scatter phonons efficiently at the interfaces, resulting in increasing both σ and $\kappa_{lattice}$ as well. On the contrary, nanoscale grain particles (<500 nm) scatter phonons to maintain a low $\kappa_{lattice}$ while σ increases, thus enhancing ZT values.

To date, the quest for new inorganic semiconductors for TE applications continues to focus on binary and ternary metal chalcogenides (Bi_2Te_3, Bi_2Se_3, PbTe, SnSe, $MoSe_2$/MoS_2…), metal oxides ($LaMo_8O_{14}$, ZnO, $Na_xCo_2O_4$, $Ca_3Co_4O_9$, $CaMnO_3$, $SrTiO_3$, In_2O_3), but to a much lesser extent on borides (ZrB_2, HfB_2), and lead-based perovskites ($CH_3NH_3PbI_3$) [3,8-19,22,26,27]. The highest PF value of 2.8 mW/m.K^2 at 773 K was reported for n-type SnSe semiconductors. In this context, metal borates (**M-BO$_3$**), borides (**M-Bs**), and borohydrides (**M-BHs**) of p-, d-, and f-block elements have become in the spotlight as solid-state materials [26-45]. The borates offer exceptional optical and thermal properties that permit their wide applications in nonlinear optics, radiation shield, vitro-ceramics, ferroelectric, and wide-band semiconductors. In this respect, the boron oxide/borate network matrices are known to accommodate different kinds of additives, including metallic elements and metal oxides where the frameworks are made of $[BO_4]_{tetrahedral}$ and $[BO_3]_{triangular}$ structural units. However, the structural/ thermal properties of M-Bs allow their employment as hard refractory (TiB_6), hard magnets ($Nd_2Fe_{14}B$), battery electrodes, conducting ceramics (ZrB_2, HfB_2), and superconducting (MgB_2) materials [26-34]. Meanwhile, solid-state M-BHs continue to attract attention as H-storage materials in solid fuels, electrolytes in batteries, and luminescence and magnetic applications [35-42]. Given these characteristics, M-BO_3, M-Bs, and M-BHs are anticipated to play a key role in the future's sustainable energy. Although M_T-Bs and M_T-BO_3 tend to form thermally stable materials, their utilization in TE applications is limited [26,27].

Our current research is directed towards the synthesis and applications of materials that possess the potential to convert low-temperature heat ($303 \leq T \leq 373$ K) resulting from body heat, sunshine, and domestic devices for small-scale TE applications. This pursuit reports a one-pot synthetic method to dope metal nanoparticles into their metal borates intrinsically. In this work, we report the production of Ni^0, Co^0, Fe^0 metallic nanoparticles incorporated into their metal borates by sonicating a reaction mixture of the desired transition metal salt and $NaBH_4$ in nonaqueous DMF/MeOH media through reduction and hydrolysis. The individual products were characterized by thermo-oxidative, vibrational spectroscopy (**ATR-IR**), X-Ray diffraction (**P-XRD**), and magnetic (**μ_{eff}**) techniques. The

thermal (**κ**), electrical (**σ**) conductivities, and the corresponding TE parameters (**S, PF**, **ZT, η%)** were evaluated at ambient conditions.

2. Materials and Methods

All chemicals and solvents were reagent grade and used as received unless otherwise stated ($NiCl_2·6H_2O$, Aldrich; $CoCl_2·6H_2O$, Scharlau; $FeSO_4·7H_2O$, Codex; $NaBH_4$, Aldrich). Before each preparation, the transition metal salts were soaked in absolute alcohol for ~10 min., decanted, and dried. This step helps to minimize the presence of water in the reaction system. Thermal-oxidation was performed in a muffle furnace (open-air, steps of 100 ºC, 25 < T < 1100 ºC. The P-XRD was performed on a RIGAKU (Cu_α λ= 1.5408 Å, 40 kV, 40 mA, K-β filter, scintillation counter, scan speed = 3.00 deg./min. sampling width: 0.0200 deg, Scan range 2 θ = 5.00-90.00 deg.) and analyzed by RIGAKU curve-fitting software. The ATR-IR spectra were recorded using a Bruker ATR-IR spectrometer (Alpha, OPUS-7.5.1.8; range: 4000-400 cm^{-1}; resolution: 4 cm^{-1}; scans: 24). The magnetic measurements were performed on a Sherwood static magnetic susceptibility balance. The TE characteristics of the products were performed on cold-pressed circular discs (10 ton/cm^2, 2 min., radius = 6.51 mm, area, $\pi r^2 = 1.33 \times 10^{-4}$ m^2, thickness 1-1.1 mm) of 0.500 g of dry fine samples, sandwiched between two polished brass electrodes. The lower brass disc was gradually heated, and ΔT between the two brass discs was monitored using a digital K-type thermocouple. The developed voltage (ΔV) was monitored as a function of (ΔT) in the range of 303-373 K using a digital K-type multimeter and thermocouple. Thermal conductivity was evaluated from the heat flux (Q, w) passing from the hot disc to the cold disc through discs. Electrical conductivity (**σ,** Sm^{-1}) was determined for nonohmic behavior by plotting Ln I *vs*. Ln V where the intercept gives Ln G (conductance, G = A * σ/ L).

2.1 One-Pot Synthesis of Intrinsically Doped M_T^0:M_T-BO_3 Composites:

2.1.1 Ni^0:Ni-BO_3

In a closed flask, a freshly prepared solution of $NaBH_4$ (1.513 g, 40 mmol) in 50 mL of methanol was dropwise added within 15 min. to a solution of $NiCl_2·6H_2O$ (2.377 g, 10 mmol) in 50 mL of DMF. The reaction mixture was sonicated for 90 min. at ~70 °C. The obtained precipitate was filtered off, washed with distilled water and acetone, dried in an oven (80 °C, 12 hrs.), and stored under vacuum for further analysis. Yield = 56%; Color/State: lustrous black solid. Density of the cold-pressed disc: 2.72 g/cm^3. **ATR-IR**: 3350 (br, υ_{O-H}); 1383, 1318 (s, $\upsilon_{asyB-O3}$); 1260 (s, $\upsilon_{asyB-O4}$); 970 (m, $\upsilon_{symB-O3}$); 893, (m, $\upsilon_{symB-O4}$); 629, 587, 521 (s, δ_{B-O-B}) cm^{-1}.

2.1.2 Co^0:Co-BO_3

The same reaction steps and workup procedure were employed using $CoCl_2·6H_2O$ (2.379 g, 10 mmol) and $NaBH_4$ (1.513 g, 40 mmol). Yield = 59%; Color/State: lustrous black solid. Density of the cold-pressed disc: 2.24 g/cm^3. **ATR-IR**: 3237 (br, υ_{O-H}); 1346 (s, $\upsilon_{asyB-O3}$); 1262(m, $\upsilon_{asyB-O4}$); 963 (m, $\upsilon_{symB-O3}$); 861(m, $\upsilon_{symB-O4}$); 628, 586, 518 (s, δ_{B-O-B}) cm^{-1}.

2.1.3 Fe^0:Fe-BO_3

A solution of $FeSO_4·7H_2O$ (2.78 g, 10 mmol) in 100 mL of H_2O: DMF (1:1) mixture was reacted with $NaBH_4$ (1.513 g, 40 mmol) in 50 mL methanol in a closed flask. Similar reaction and workup procedures were adopted as described above. $FeSO_4·7H_2O$ was used instead of $FeCl_2·6H_2O$ to minimize the amount of iron oxide byproducts that might form in the process. Yield = 52%; Color / State: lustrous black solid. Density of the cold-pressed disc: 2.76 g/cm^3. **ATR-IR**: 3237 (br, υ_{O-H});

1319 (s, $\upsilon_{asyB\text{-}O3}$); 1261(s, $\upsilon_{asyB\text{-}O4}$); 1064 (s, $\upsilon_{symB\text{-}O3}$); 971(s, $\upsilon_{symB\text{-}O4}$); 689,625, 584,551 (m, $\delta_{B\text{-}O\text{-}B}$) cm^{-1}.

3. Results and Discussion

This study is graphically described in **Figure 1.** It involves the synthesis of M_T^0:M_T-BO_3 composites, formation of cold-pressed disc and testing for TE applications.

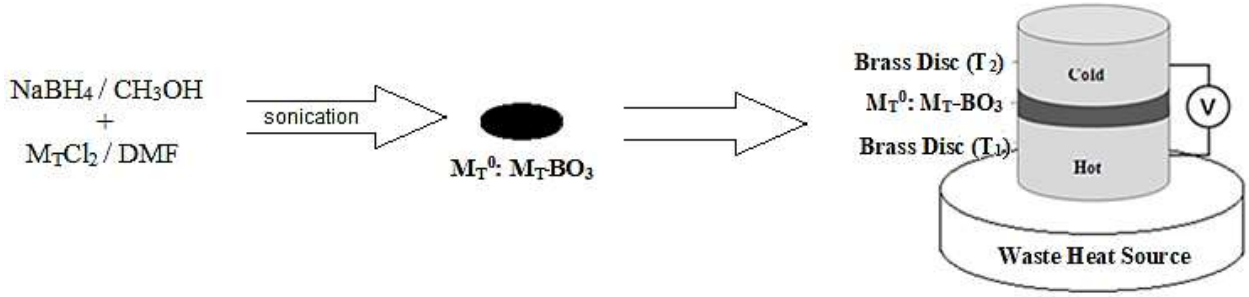


Figure 1: Schematic representation of the synthetic process and TE measurement device.

3.1 Formation and Characterization of M_T^0:*M_T-BO_3* Composites*:*

In this work we report the formation of M_T^0:M_T-BO_3 composites (M_T = Ni, Fe, Co) by mixing the desired metal salt with fourfold excess of $NaBH_4$ in a nonaqueous DMF/MeOH solvent system at ambient conditions, **Equation 5** [38-45]. This process is generally affected by the M_T: BH_4^- ratio, solvent, pH, and slow/rapid mixing of reagents. The reaction proceeds through the formation of unstable $M_T(BH_4)_x$ intermediates that undergo reduction of the ion M_T^{II} ions to yield metallic nanoparticles (M_T^0), and hydrolysis to afford metal borates (M_T-BO_3) which are

$$M_T^{2+}{}_{(sol)} + xBH_4^-{}_{(sol)} \longrightarrow [M_T(BH_4)_x]_{sol} \xrightarrow{H_2O} M_T^0: M_T\text{-}BO_{3(s)} + xH_{2(g)} + BH_{3(g)} \qquad (5)$$

accompanied by the release of hydrogen (H_2) and boranes (BH_3, B_2H_6) [39, 43,45]. To proceed forward, this reaction processes require low reduction potential metal ions such as those used here (Fe^{2+},-0.41; Co^{2+},-0.28; Ni^{2+},- 0.23) and moisture. In this respect, the boron oxide/borate, $B_2O_3/[(BO_2)_2]^{-2}$ network matrices are known to accommodate different kinds of additives, including metallic elements and metal oxides where the frameworks are made of $[BO_4]_{tetrahedral}$ and $[BO_3]_{triangular}$ structural units.

The obtained lustrous black solids are insoluble in common organic solvents. The composition of the obtained composites was determined by thermal-oxidation analysis (*vide infra*, section 3.2). The physicochemical characteristics of these products were established by P-XRD, ATR-IR spectroscopy and magnetic susceptibility techniques. Their thermal (κ) and electrical (σ) conductivities and TE parameters (S, PF, ZT) were evaluated.

3.2 Thermal Oxidation of the Prepared M_T^0:M_T-BO_3 Composites:

This study is designed to gather information about the composition of the obtained materials. Here, the obtained materials were subjected to step-wise pyrolysis in an air draft at the temperature range of 30 < T < 1100 °C, **Equation 6**. The thermal oxidation process proceeds through three overlapping pathways, namely, dehydration (30-250 °C), degradation of the borate

$$M_T^0: M_T\text{-}BO_3.xH_2O \xrightarrow[< 250\ ^oC]{-x\ H_2O} M_T^0: M_T\text{-}BO_3 \xrightarrow[400\text{-}800\ ^oC]{-\ B_2O_3} M_T^0 + M_TO \xrightarrow[> 800\ ^oC]{O_2} M_TO_{\ residue} \qquad (6)$$

matrix (400-800 °C), and oxidation of the of the metallic nanoparticles (800-1000 °C) [31,35,40-42,47]. Typically, the dehydration progress through the condensation of ≡B-OH, leading to ≡B-O-B≡ of higher borate species, which upon further heating (> 400 °C), eliminate B_2O_3 white fumes to ultimately give the corresponding metal oxides (M_T-O). Meanwhile, the reduced metallic nanoparticles (M_T^0) take up oxygen from air to form their oxides [40-42]. The relationship between oxygen adsorption and the different stages of oxidation pathways in metallic nanoparticles and bulk was reviewed by Chernavskii et al [40]. A close analysis of the displayed thermograms below 250 ºC, **Figure 2,** shows that the Fe^0:Fe-BO_3 matrix contains negligible amounts of crystalline water, indicating that it comprises a tetraborate structure, while Co^0:Co-BO_3 and Ni^0:N_i-BO_3 underwent dehydration with mass loss of ~ 11-12% suggesting di-borate matrix. At the 250-800 ºC range, the metal borate matrices decompose in three overlapping steps leading to the elimination of dense white fumes of B_2O_3 / H_3BO_3 leaving behind the metal oxide residues (Fe_2O_3, Co_2O_3, NiO). Upon heating to above 800 ºC, the thermograms show an increase in the mass % where the mass gained represent the oxygen uptake by metal nanoparticles to yield Fe_2O_3 (4.7%), Co_2O_3 (12.0%), and NiO (7.4%) [40-42]. To ensure completion of the thermal oxidation processes, the final residues were treated three times with deionized water and calcined to a constant weight (1100 °C, one hr.), leaving behind their oxide residues (Fe_2O_3, 78.6%; Co_2O_3, 72.0%; NiO, 61.9%) [35,36,38]. The mass (g) and molar amounts (mmol) of structural H_2O, M_T^{II}, B_2O_3, and M_T^0 involved in the above thermal oxidation steps are summarized in **Table 1**. The composition of the obtained M_T^0:M_T-BO_3·xH_2O composites are deduced from their relative molar values.

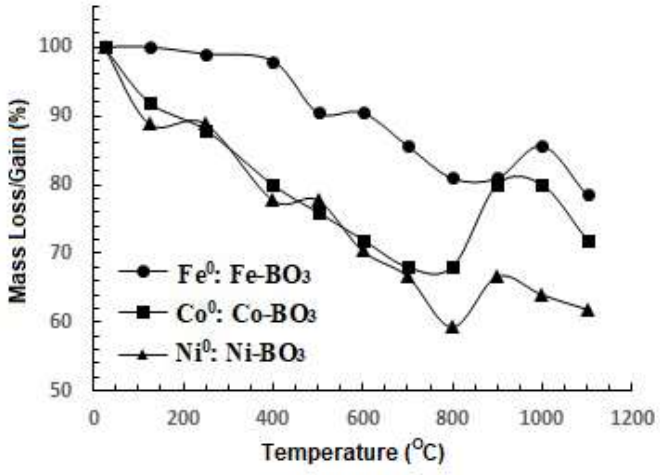


Figure 2: Thermal-oxidation plots of the prepared M_T^0:M_T-BO_3·xH_2O composites.

Table 1: Thermal-oxidation data and the deduced composition of the investigated M_T^0:M_T-BO_3 composites.

Composite [a]	**x H_2O**	**M_T^0**	**M_T^{II}**	**B_2O_3**	**Composition**
	g (mmol) [b]	g (mmol) [c]	g (mmol) [d]	g (mmol) [e]	M_T^0: $M_TO \cdot B_2O_3 \cdot xH_2O$
Fe^0:Fe-$BO_3 \cdot xH_2O$	0.002 (0.1)	0.023 (0.41)	0.099 (1.78)	0.038 (0.55)	Fe^0: $4FeO \cdot B_2O_3 \cdot 0.5H_2O$
Co^0:Co-$BO_3 \cdot xH_2O$	0.025 (1.4)	0.071 (1.21)	0.060 (1.02)	0.054 (0.78)	$2Co^0$: $3CoO \cdot 2B_2O_3 \cdot 3H_2O$
Ni^0:Ni-$BO_3 \cdot xH_2O$	0.027 (1.5)	0.061 (1.04)	0.084 (1.43)	0.071 (1.02)	$2Ni^0$: $3NiO \cdot 2B_2O_3 \cdot 3H_2O$

[a.] Mass of Fe (0.210 g), Co- (0.225 g), and Ni- (0.240 g) composites subjected to thermal oxidation.
[b.] Calculated from the dehydration processes (< 250 °C).
[c.] Deduced from the oxygen uptake to afford the most stable oxides.
[d.] It was calculated from the mass residues difference at 1100 °C representing the total metal oxides and mass of M_T-O due to oxidation of M_T^0.
[e.] Mass of boron oxide matrix was estimated from the thermal curve between 250-800 °C.

3.3 ATR-IR Spectroscopy of the Prepared M_T^0:M_T-BO_3 Composites:

The structural characteristics of $[B_2O_3]$ and borates network matrices can be deduced from their FT-IR spectra [48]. It is typically revealed in their asymmetric and symmetric vibrational ($\nu_{asym\ B\text{-}O}$, $\nu_{sym\ B\text{-}O)}$ and bending ($\delta_{asym\ B\text{-}O\text{-}B}$, $\delta_{sym\ B\text{-}O\text{-}B}$) frequencies of the $[BO_4]_{tetrahedral}$ and $[BO_3]_{triangular}$ structural units. The recorded ATR-IR spectra of the given M_T^0:M_T-BO_3 in **Figure 3** carry diagnostic evidence that permitted the interpretation of relevant structural information. The ATR-IR data and their tentative assignments are given in the experimental section. In all cases, the broad features in the range 3350-3237 cm^{-1} ($\upsilon_{O\text{-}H}$) are assigned to terminal OH groups, while the medium-weak intense bands in 2071-2073 cm^{-1} range suggest the presence of bridging OH units. The asymmetric (υ_{asy}) and symmetric (υ_{sym}) stretching frequencies of triangular structural $[BO_3]$ units are observed at 1387-1318 and 1064-970 cm^{-1}, respectively. However, The υ_{asy} and υ_{sym} stretching frequencies of the tetrahedral units $[BO_4]$ are observed at 1262-1260 and 971-861 cm^{-1} ranges, respectively. Furthermore, the medium intensity low energy bands in the 689-518 cm^{-1} region are attributed to the bending frequency of B-O-B ($\delta_{B\text{-}O\text{-}B}$).

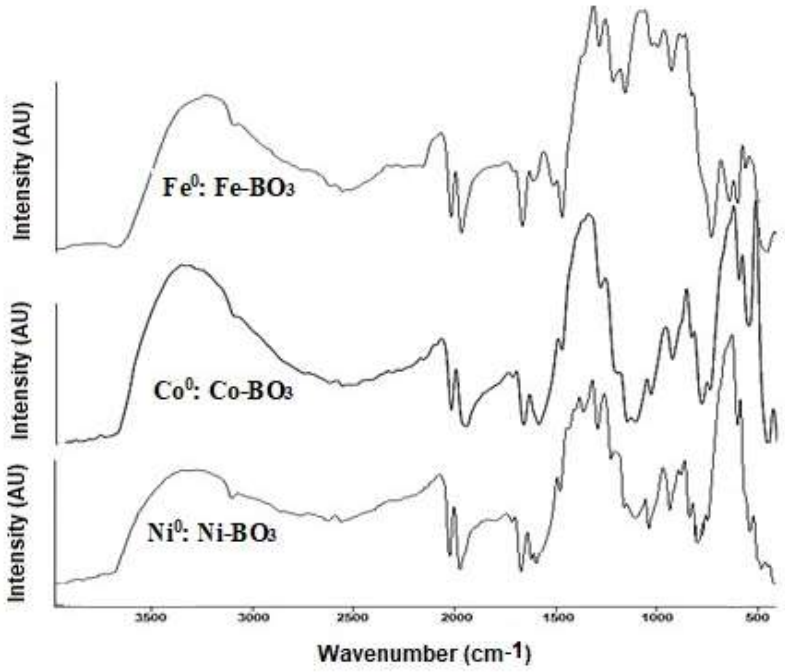


Figure 3: ATR-IR spectra of the prepared M_T^0:M_T-BO_3 composites (M_T = Ni, Fe, Co).

3.4 Powder X-Ray Diffraction of the Prepared M_T^0:M_T-BO_3 Composites:

The p-XRD profiles of the prepared composites were analyzed for phase identification of the intrinsic dopants metallic (M_T^0) and metal oxide (M_T-O) particles dispersed in the borate matrix [35,41,43-45,47]. A first look at these profiles in **Figure 4** shows that their structures vary from highly amorphous as seen in Fe^0:Fe-BO_3 and Co^0:Co-BO_3 to predominantly crystalline Ni^0:Ni-BO_3. However, the broad common features observed in all cases are attributed to the borate matrix. A close inspection of the diffraction patterns of Ni^0:Ni-BO_3 shows that it displays broad diffraction pattern superimposed on a featureless diffraction background of the borate matrix, suggesting

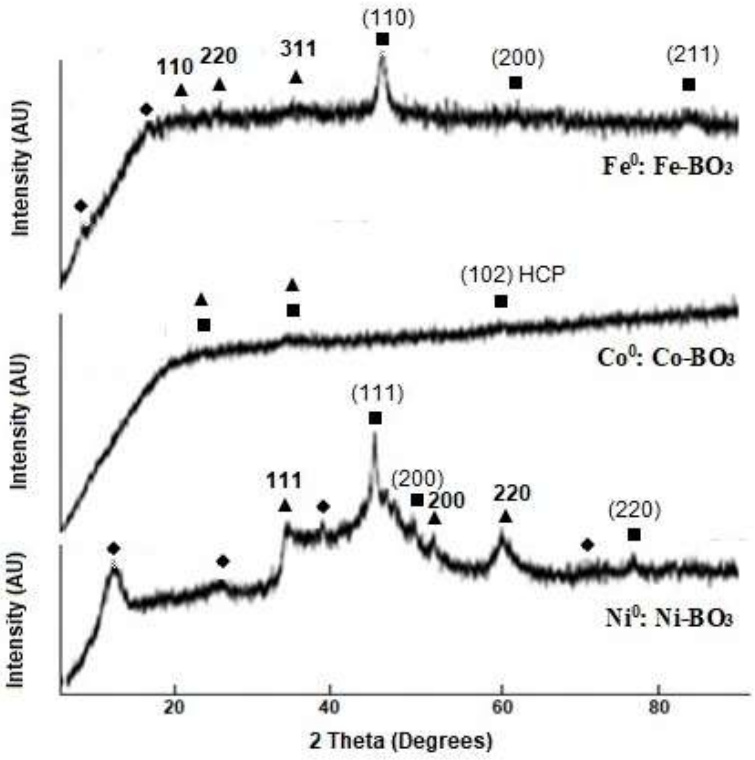


Figure 4: P-XRD profiles of the prepared M_T^0:M_T-BO_3 composites (■ = M_T^0, ▲ = M_T-oxide, ♦ = M_T-oxyhydroxide.

vitreous lattice structures. Nevertheless, the co-existence of multi structural phases for Ni^0, NiO and borate implies that they exhibit clear tendencies to form an amorphous glassy structure upon vitrification/devitrification processes bearing in mind the thermal stability of the materials [35,36,40]. The diffraction patterns show sharp peaks due to metallic Ni^0 (44.4°, 51.7°, 77.1°), which belongs to 111, 200, and 220 planes, respectively, of the common FCC metallic nickel, **Table 2**. The peaks due to NiO are seen at 33.6, 37.5, 45.9, 60.9°, while the low diffraction peak at 12.7° indicates the presence of appreciable amounts of nickel oxyhydroxide phase. On the contrary, the Fe^0:Fe-BO_3 and Co^0:Co-BO_3 composites exhibit amorphous structures with broad

Table 2: P-XRD data for the investigated M_T^0:M_T-BO_3 composites (M_T = Ni, Fe, Co).

Composite [a]	Diffraction Angle 2 θ (degrees) [a]	Crystallinity % [b]	d-Spacing (Å) [c]	Grain Size (nm) [d]
Fe^0: Fe-BO_3	7.9, 15.7, 18.3, 21.6, 25.0, 36.3, **44.3**, **61.4, 84.7**	~ 4%	2.04	6.4
Co^0: Co-BO_3	9.5, 24.3, **36.8** (broad), 61.5	~ 1 %	2.44	7.7
Ni^0: Ni-BO_3	12.7, 22.4, 33.6, 37.5, **44.4**, 45.9, 49.4, **51.7**, 60.9, **77.1**	~ 45%	2.04	24.1

a. Diffraction peaks due to metallic particles are shown in bold.
b. Estimated from the area under the diffraction peaks.
c. Calculated from **$n\lambda = 2d \sin\theta$.**
d. Calculated from Scherer formula (**$t = K\lambda / \beta \cos\theta$**).

features at 2θ of 44.3° and 36.8° attributed to Fe^0 BCC and Co^0 HCP crystal classes, respectively. A further look at the diffraction patterns of Fe^0:Fe-BO_3 show peaks due to Fe^0 nanoparticles at 44.3°, 61.4°, 84.7° arising from 110, 200, and 211 BCC Miller planes, whereas FeO shows low-intensity peaks at 18.3°-25.0° and 36.3° due to low diffraction planes of 220/202 and 311, respectively. The low-intensity diffraction peaks at 7.9° and 15.7° indicate the presence of small amounts of oxyhydroxide species. Further examination of the diffraction patterns of Co^0: Co-BO_3 composite shows that Co^0 and CoO phases are masked by that of the borate matrix, indicating they are deeply impregnated in the B_2O_3 matrix. However, the tiny broad diffractions at 24.3°, 36.8° and 61.5° arising from HCP crystal type of Co^0, however, the low peaks (24.3°, 36.8°) overlap with those arising from CoO.

The diffraction data are summarized in **Table 2**. The crystalline phase in the structure was estimated from the area under the broad peaks in the P-XRD profiles. The corresponding interspatial distances (d-spacing) were calculated from the position of the most intense peak as given by Bragg's Law (**$n\lambda = 2d \sin\theta$**) where n, λ, and θ are the diffraction order, wavelength of the X-ray beam, and diffraction angle, respectively. The interspatial distances were found to range from 2.04 to 2.47 Å. Furthermore, the crystallite size (t) was calculated as described in the Scherer formula (**$t = K\lambda / \beta \cos\theta$**) where K (Scherer constant, 0.95), λ (wavelength of the X-Ray), θ (Bragg's angle of the most intense peak) and β (peak width at half-height in radians). It is clear from the crystallite/grain size in **Table 2** that the prepared M_T^0:M_T-BO_3 are nano-scaled particles in the range of 6.4-26.2 nm.

3.5 Magnetic Characteristics of the Prepared M_T^0:M_T-BO_3 Composites

The static magnetic susceptibility (χ_g, cm^3g^{-1}) of the prepared composites was performed at room temperature. The total magnetic moment (μ_{eff}) per molecular formula for Fe^0:Fe-BO_3, Co^0:Co-BO_3, and Ni^0:Ni-BO_3 were found to be 33.28, 25.49, and 12.88 BM, respectively, **Table 3**. The effective moment per magnetic site in these multi-magnetic center systems was deduced by dividing the total magnetic moment by the number of magnetic sites due to M_T^0 and M_T^{II} as deduced from the thermal oxidation data (Fe^0 + Fe^{II}, 33.28/5 = 6.66; Co^0 + Co^{II}, 25.49/5 = 5.10; Ni^0 + Ni^{II},12.88/5 = 2.58 BM).

Applying the semiempirical scaling laws of μ_{eff} of clusters per magnetic site, we conclude that the magnetic centers in Fe^0:Fe-BO_3 and Co^0:Co-BO_3 reveal ferromagnetic characteristic interactions, while the Ni^0:Ni-BO_3 shows antiferromagnetic interactions [50,51]. The difference may be attributed to the preferred coordination geometry of these ions, where the Fe^{II} and Co^{II} centers strongly prefer the octahedral geometry while the Ni^{II} in nickel glasses coexist in both octahedral (O_h) and tetrahedral (T_d) structural units.

Table 3: Magnetic susceptibility (χ_g), effective (μ_{eff}) and spin magnetic moments (μ_{spin}), and clustering of the investigated M_T^0:M_T-BO_3 composites (M_T = Ni, Fe, Co).

Composite [a]	**χ_g (10^6)** (cm^3g^{-1}) [a]	**χ_m** [a]	**μ_{eff}** (BM) [b]	**μ_{eff}** per mag. site (BM) [b]	**μ_{spin} / d^n** (BM) [c]	**Magnetic interaction**
Fe^0: 3Fe-BO_3	1100	0.464	33.28	6.66	4.89 / d^6	ferromagnet
Co^0: Co-BO_3	507	0.272	25.49	5.10	3.87 / d^7	ferromagnet
Ni^0: Ni-BO_3	130	0.0695	12.88	2.58	2.83 / d^8	antiferromagnet

a. χ_m represents the molar magnetic susceptibility [$\chi_m = \chi_g$* M.wt], diamagnetic contribution is neglected. Average molecular mass as calculated from thermo-oxidative data. $2Ni^0$: $3NiO{\cdot}2B_2O_3{\cdot}3H_2O$ (534.7 g/mol); Fe^0: $4FeO{\cdot}B_2O_3{\cdot}0.5H_2O$ (421.6 g/mol); $2Co^0$: $3CoO{\cdot}2B_2O_3{\cdot}3H_2O$ (435.7 g/mol).

b. μ_{eff} is the effective magnetic moments [$\mu_{eff} = 2.83 (\chi_m * T)^{1/2}$] at 298 K.

c. $\mu_{spin} = g[S (S + 1)]^{1/2}$, g is the gyromagnetic ratio = 2.0023, S total spin.

3.6 Electrical and Thermal Characteristics of the investigated M_T^0:M_T-BO_3 Composites

3.6.1 Electrical Conductivity (σ)

The electrical current (**I**) that develops between the hot and cold brass discs across the prepared composites was examined by plotting their I-V curves, **Figure 5.** The observed nonlinear curves indicate that the conduction in these composites is not purely electronic but being influenced by different possible factors such as temperature, induced ionization, phonon migration, and induced ionic conduction [52-54]. This nonohmic trend is generally encountered in diodes, thermistors, heated filaments, and photovoltaic cells. Recently, Katsufuji et al. addressed the nonlinear behavior of resistance in various disordered systems and reported that the resistivity decreases as a function of current density /electric field but does not rely on the temperature or the materials. They discussed their observation in the light of the percolation conduction theory in disordered systems [53].

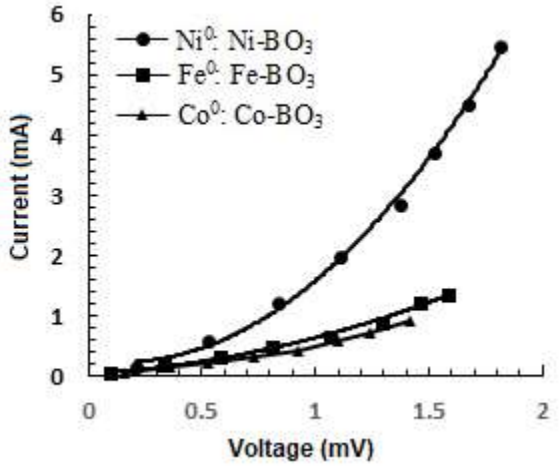


Figure 5: I - V Plots for the examined M_T^0:M_T-BO_3.

Here, the nonlinearity of the I-V curves was analyzed by taking the logarithmic form as described by **Equation 7** and **8**, where I, V, α, and G are the current, voltage, ohmicity, and conductance (G = σ x area/thickness), respectively [54]. The **α** can be estimated from the slope of Ln (I) - Ln (V) linear plots**,** where the obtained values (**α** = 1.76 - 1.23) show substantial deviation

$$\mathbf{I = V^{\alpha} * G} \quad \textbf{(7)}$$

$$\mathbf{Ln(I) = \alpha\ Ln(V) + Ln(G)} \quad \textbf{(8)}$$

from unity (α = 1) of pure electronic conduction, thus indicating higher ionic/mass diffusion in Ni^0:Ni-BO_3, **Table 4**. The **σ** values of the investigated M_T^0:M_T-BO_3 composites show semiconducting behavior, where Ni^0:Ni-BO_3 shows distinctly higher conductivity values than the other two M_T^0:M_T-BO_3 composites. The values of **σ** are further investigated as a function of temperature and was found to increase linearly (**σ *vs.* T** plots), **Figure 6.** The slope of **σ *vs.* T** plots displays a steep linear increase in the case of Ni^0:Ni-BO_3 (σ = 14.7-40.5 Sm^{-1}), while a gradual increase is observed in the case of Fe^0:Fe-BO_3 (σ = 7.0-11.5 Sm^{-1}), and Co^0:Co-BO_3 (σ = 5.3-8.6 Sm^{-1}). This trend is attributed to the increasing concentration/mobility of ion /mass diffusion.

Table 4. Electrical and thermal conductivity data for the investigated M_T^0:M_T-BO_3 composites.

Composite [a]	**α** [b] ohmicity	**σ** [c] Sm^{-1}	κ_{tot} [d] $WK^{-1}m^{-1}$	κ_{el} [f] $mWK^{-1}m^{-1}$	**σ /κ** [e] KV^{-2}
Fe^0: Fe-BO_3	1.25	7.0-11.5	1.56-0.18	0.05-0.10	4.5-64.0
Co^0: Co-BO_3	1.23	5.3-8.6	1.24-0.16	0.04-0.08	4.3-53.8
Ni^0: Ni-BO_3	**1.76**	**14.7-40.5**	**1.57-0.18**	**0.11-0.37**	**9.4-270**

[a.] M_T^0:M_T-BO_3 disc, 10 ton/cm^2, radius = 6.51 mm, area, $\pi r^2 = 1.33 \times 10^{-4}$ m^2, thickness 1-1.1 mm.
[b.] α = 1 for ohmic behavior.
[c.] σ (303 ≤ T ≤ 373 K) typical values semiconductors are in the range of 10^{-6}-10^4 S m^{-1}.
[d.] κ (303 ≤ T ≤ 373 K), κ = Q / [(**Δ**T/L) ⁎A]

e. The relative contribution of σ to κ (303 ≤ T ≤ 373 K).
f. κ_{el} were calculated from Wiedemann–Franz law (κ_{el} = L σ T), L = 2.44 × 10^{-8} WΩK^{-2}.

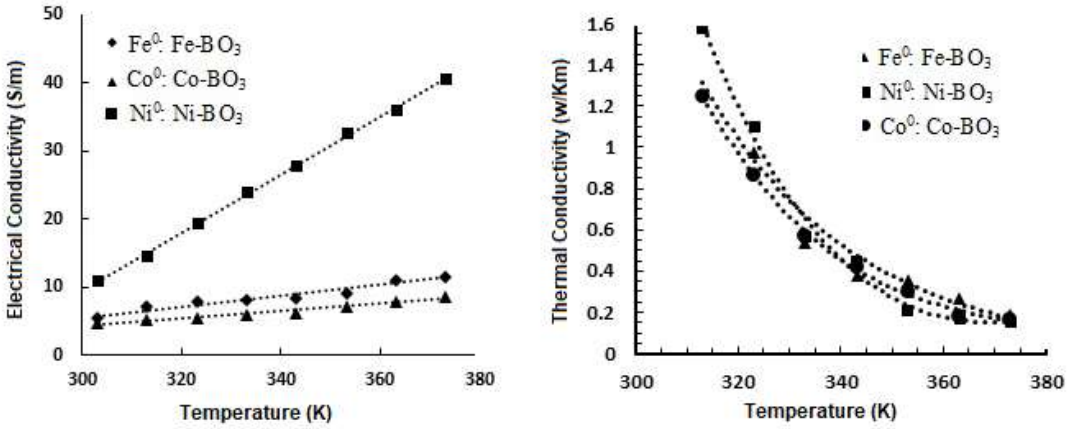


Figure 6: Plots of **t**he electrical (**σ**) and thermal (**κ)** conductivities of the prepared M_T^0:M_T-BO_3 composites as a function of temperature.

3.6.2 Thermal conductivity (κ)

The thermal conductivity (**κ,** $WK^{-1}m^{-1}$), **Table 4,** was determined by measuring the heat flux (**Q**) crossing from the hot brass block to the cold brass block through the M_T^0:M_T-BO_3 composites discs in the temperature range of 303 ≤ T ≤ 373 K as depicted in **Equation 9 (**ΔT = T_{hot}-T_{cold} K; L, thickness in m; A, area in m^2). The ***κ*** values for the given composites slightly vary (1.24-1.57 $WK^{-1}m^{-1}$) at 310 K but nonlinearly decrease to converge to a common point as they

$$\boldsymbol{\kappa = Q / [(\Delta T/L) * A]} \qquad \textbf{(9)}$$

approach 373 K (~0.18 $WK^{-1}m^{-1}$), indicating that κ is inversely proportional to T, **Figure 6**. These values are lower than that reported for wurtzite ZnO (50 $WK^{-1}m^{-1}$ at room temperature), bulk ZnO (~100$WK^{-1}m^{-1}$), and porous ZnO (9.65 $WK^{-1}m^{-1}$) [3,8,9]. However, the thermal conductivity ($\boldsymbol{\kappa}_{total}$) in TE semiconductors involves multi-transport pathways comprising of two components, namely, an electronic ($\boldsymbol{\kappa}_{el}$) owing to charge carrier migration and phonon scattering ($\boldsymbol{\kappa}_{lat}$) due to lattice vibration [4,55]. The κ_{el} is influenced by charge carrier concentration, mobility, the e^- / h^+ ratio, bipolar interactions, and scattering mechanisms similar to σ, while κ_{lat} is generally influenced by lattice dynamics, **Equation 10** [4,55,56]. Fortunately, κ_{el} can be approximated from the σ values as described by the universal Wiedemann–Franz law (**$\boldsymbol{\kappa_{el}}$ = L σ T)** where L is the Lorenz number (2.44 × 10^{-8} WΩK^{-2}). Although this law is best applicable to conductors, it is widely employed for semiconductors as well [4,55]. The calculated κ_{el} data in **Table 4** demonstrates that

$$\boldsymbol{\kappa_{total} = \kappa_{el} + \kappa_{lat}} \qquad \textbf{(10)}$$

the κ_{el} contribution to κ_{total} is small, indicating that the thermal conduction occurs essentially through lattice vibration where $\boldsymbol{\kappa_{total} \approx \kappa_{lat}}$. In other words, the thermal energy transport mechanism in the investigated composites is phononic rather than electronic. Here, we can conclude that the nano-sized

M_T^0:M_T-BO_3 composites favor phonon scattering at the interfacial boundary of the amorphous/vitreous glassy structures. This conclusion is consistent with early reports on amorphous/ glassy semiconductors, where they exhibit low **κ** in comparison with crystalline semiconductors [55,56].

Given that the **σ/κ** ratio plays a vital role in the estimation of TE efficiencies as described ZT (ZT = $(\sigma/\kappa)*S^2*T$), where a high **σ/κ** ratio is desirable for applications in TE materials. In this study, the **σ/κ** ratio was plotted as a function of temperature, **Figure 7**. Interestingly, the nonlinear plot shows a rapid **σ/κ** increase from 9.4 to 270 KV^{-2} in the $303 \leq T \leq 373$ K range in the case of Ni^0:Ni-BO_3 while a moderate-weak increase is observed for Fe^0:Fe-BO_3, and Co^0:Co-BO_3. The **σ/κ** quantitative data in the low and high-temperature ranges are listed in **Table 4**.

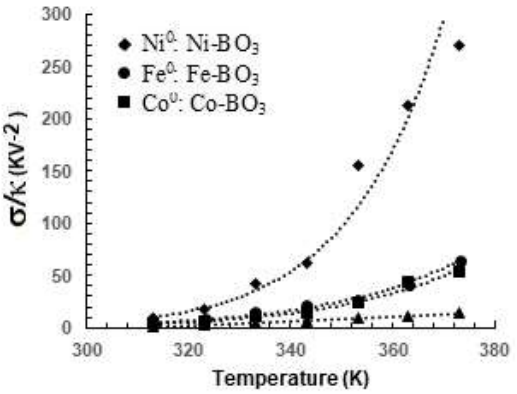


Figure 7: Plots of the σ/κ as a function of T (K).

3.7 Thermoelectric Characteristics of the investigated M_T^0:M_T-BO_3 *Composites*

The key parameters generally used to characterize TE semiconductors include three parameters, **S**, **PF**, and **ZT,** *where their interrelations* have been the subject of several theoretical and experimental studies [3,4,16,21,22]. Here, it should be emphasized that the temperature limitation, $303 \leq T \leq 373$, in this investigation is governed by the thermo-oxidative stability and our intention to prepare and examine semiconductors for waste heat-current conversion produced by body heat, sunshine, and domestic devices for small-scale TE applications. The S values were evaluated from the slope of their ΔV *vs.* ΔT plots, where a slight deviation from linearity is observed, **Figure 8**. Examination of these data shows that Ni^0:Ni-BO_3 exhibits higher S values (60-80 μVK^{-1}) at any specified temperature than the other two composites (Fe^0:Fe-BO_3, 30-52; Co^0:Co-BO_3, 27-42 μVK^{-1}), **Table 5**. These S coefficients are further analyzed by plotting the individual S values as a function of temperature where the linear **S *vs.* T** plot shows positive S values indicating p-type semiconductors in which the + holes are the primary charge carriers [26,27,35,36]. The obtained S values are lower than those reported for n-type ZnO (-200 μVK^{-1}) and nano-porous ZnO (-279 μVK^{-1}) at room temperature where the major carriers were electrons [8,9].

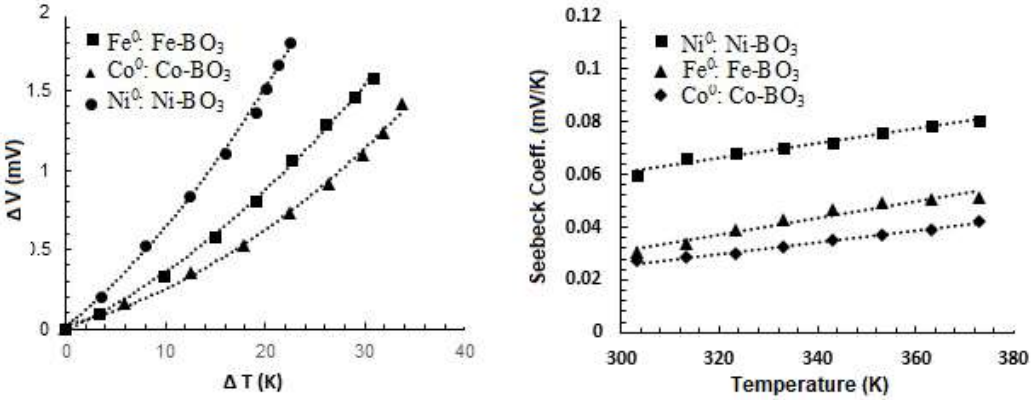


Figure 8: ΔV *vs.* ΔT plots and S dependence on temperature for the examined M_T^0:M_T-BO_3 Composites

Table 5. Thermoelectric parameter data for the investigated M_T^0:M_T-BO_3 Composites

Composite [a]	**S** (μVK^{-1}) [a]	**PF** ($\mu Wm^{-1}K^{-2}$) [b]	**ZT** (10^{-2}) [c]	**η %** [d]
Fe^0: Fe-BO_3	30 - 52	4.9 - 31.1	0.12 – 6.4	0.33
Co^0: Co-BO_3	27 - 42	3.4 - 15.2	0.08 - 3.5	0.19
Ni^0: Ni-BO_3	60 - 80	39.6 - 259	0.76 – 64.4	2.56

[a.] Seebeck factor, the range represents the values at 303 & 373 K, respectively.
[b.] $PF = \sigma * S^2$, the range represents the values at 303 K & 373 K, respectively.
[c.] $ZT = (\sigma/\kappa)*S^2*T$, the range represents the values at 303 K & 373 K, respectively.
[d.] Thermoelectric efficiency, $\eta\ \% = (\Delta T/T_h)\ [(1 + ZT_{avg})^{1/2} -1]/\ [(1 + ZT_{avg})^{1/2} + T_c/T_h]\%$

The performance of the investigated semiconductors for TE applications is further evaluated by examining their power factor ($PF = \sigma * S^2$**),** the figure of merit ($ZT = (\sigma/\kappa)\ S^2\ T$), and conversion efficiency (η %)**.** **Figure 9** depicts the observed linear plots of **PF *vs.* T** for the investigated M_T^0:M_T-BO_3 composites where the PF is practically very sensitive to temperature increase in Ni^0:Ni-BO_3 but weakly affected in the case of Fe^0:Fe-BO_3, and Co^0:Co-BO_3. Given the trend in S *vs.* T plots where all the three M_T^0: M_T-BO_3 show almost similar increases, the difference in the PF can be attributed mainly to σ. The recorded PF values of Ni^0:Ni-BO_3 (259 $\mu Wm^{-1}K^{-2}$) are higher than those reported for oxide semiconductors, while the other two composites (Fe^0:Fe-BO_3, 31.1; Co^0:Co-BO_3, 15.2) exhibit similar PF values [8-10].

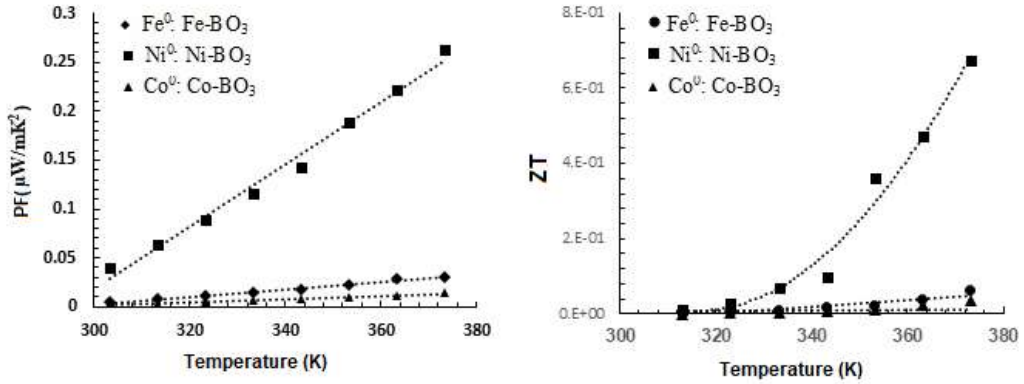


Figure 9: Power factor (PF) dependence on temperature for the obtained M_T^0: M_T-BO_3 Composites.

However, the ZT plots in **Figure 9** show a nonlinear increase in the case of Ni^0:Ni-BO_3 while Fe^0:Fe-BO_3 and Co^0:Co-BO_3 exhibit linear trends with relatively small temperature dependence. Interestingly, extrapolation of the ZT *vs.* T plot of Ni^0: Ni-BO_3 shows that it approaches the value ZT = 1 which allows its feasible application at about 400-450 K. In this respect, the TE conversion efficiency (**η%**) can be calculated from average ZT values in the specified temperature range, **Equation 4.** The **η** efficiency values for the investigated composites show that Ni^0:Ni-BO_3 (2.56%) is a far better TE material than the other two M_T^0:M_T-BO_3 (0.19-0.33%).

4. Conclusions

Our findings show that Ni^0:Ni-BO_3 is a promising candidate to convert low-temperature waste heat to electric current resulting from body heat, sunshine, and domestic devices for small-scale applications at ambient conditions. Although the ZT values of the Ni^0:Ni-BO_3 are less than those reported for the present late metal chalcogenides, it is advantageous for its simple preparation at ambient conditions and bench-top handling. Given the fact that TE measurements are sensitive to moisture, impurities, particle-particle interactions, and grains orientation within the examined cold-pressed discs, the reported TE values were found to be reproducible within 5-7%. In general, the S, PF, and ZT values for Ni^0:Ni-BO_3 (S, 80 μVK^{-1}; PF, 259 $\mu W\ m^{-1}\ K^{-2}$; ZT 0.64; η, 2.56%) were higher than those for the other two M_T^0:M_T-$(BO_2)_2$ investigated in this study. Furthermore, comparing the TE values of n-doped ZnO nanoparticles at 375 K (S, -279 μVK^{-1}; PF, 59 $\mu W\ m^{-1}K^{-2}$; ZT ~0.075) shows that the Ni^0:Ni-BO_3 offer a promising p-type candidate for TE applications. Our future endeavor is to investigate the influence of magnetic polarization and cold press compression on the TE behavior of Ni^0:Ni-BO_3.

Funding: The authors highly appreciate the support of the Deanship of Research at Jordan University of Science and Technology (Grant No. 20200017).

Acknowledgments: The authors highly appreciate the full support of the Jordan University of Science and Technology. The authors acknowledge no conflict of interest.

References:

1. J.Y. Tsao, E.F. Schubert, R. Fouquet, M. Lave, The electrification of energy: Long-term trends and opportunities, MRS Energy Sustain. A Rev. J., 5:7 (2018) 1–13. DOI:10.1557/mre.2018.

2. E. Kabir, P. Kumar, S. Kumar, A.A. Adelodun, K.H. Kim, Solar energy: Potential and future prospects, Renew. Sustain. Energy Rev., 82:1 (2018) 894-900.
3. X.-L. Shi, J. Zou, Z.-G. Chen, Advanced Thermoelectric Design: From Materials and Structures to Devices, Chem. Rev., 120 (2020) 7399. DOI: 10.1021/acs.chemrev.0c00026
4. D. Beretta, N. Neophytou, J.M. Hodges, M.G. Kanatzidis, D. Narducci, M. Martin- Gonzalez, M. Beekman, B. Balke, G. Cerretti, W. Tremel, A. Zevalkink, A.I. Hofmann, C. Müller, B. Dörling, M. Campoy-Quiles, M. Caironi, Thermoelectrics: From history, a window to the future, Mater. Sci. Eng.: R: Reports, 138 (2019) 100501, doi: 10.1016/j.mser.2018.09.00
5. Z. Zhang, B. Wang, J. Qiu, S. Wang, Roll-to-roll printing of spatial wearable thermoelectrics, Manuf. Lett.**,** 21 (2019) 28 DOI: 10.1016/j.mfglet.2019.07.002
6. X. Shi, J. Yang, J.R. Salvador, M. Chi, J.Y. Cho, H. Wang, S. Bai, J. Yang, W. Zhang, L. Chen, Multiple-filled skutterudites: high thermoelectric figure of merit through separately optimizing electrical and thermal transports. J. Am. Chem. Soc. 133:20 (2011) 7837–46. DOI: 10.1021/ja111199y.
7. H. Lipeng, H. Wu, T. Zhu, C. Fu, J. He, P. Ying, X. Zhao, Tuning multiscale microstructures to enhance thermoelectric performance of n-type bismuth-telluride-based solid solutions. Adv. Energy Mater 5 (2015) 1500411. DOI: 10.1002/aenm.201500411
8. R.V.R. Virtudazo, Q. Guo, R. Wu, T. Takei, T. Mori, An alternative, faster and simpler method for the formation of hierarchically porous ZnO particles and their thermoelectric performance. RSC Adv. 7 (2017) 31960-68. DOI: 10.1039/C7RA05067D
9. X. Wu, J. Lee, V. Varshney, J.L. Wohlwend, A.K. Roy, T. Luo, Thermal Conductivity of Wurtzite Zinc-Oxide From First-Principles Lattice Dynamics--a Comparative Study With Gallium Nitride Sci Rep. 6 (2016) 22504. DOI:10.1038/srep22504
10. K. Koumoto, R. Funahashi, E. Guilmeau, Y. Miyazaki, A. Weidenkaff, Y. Wang, C. Wan, Thermoelectric Ceramics for Energy Harvesting. J. Am. Ceram. Soc., 96 (2013) 1–23. DOI:10.1111/jace.12076.
11. J. Liang, S. Yin, C. Wan, Hybrid Thermoelectrics, *Annu. Rev. Mater. Res.* 50 (2020) 319. DOI: 10.1146/annurev-matsci-082319-111001.
12. S. Yazdani, M.T Pettes, Nanoscale self-assembly of thermoelectric materials: a review of chemistry-based approaches, Nanotechnology 29: 43 (2018) 432001, DOI: 10.1088/1361-6528/aad673.
13. Y.Y. Li, Y. Du, Y.C. Dou, K.F. Cai, J.Y. Xu, PEDOT-based thermoelectric nanocomposites—A mini-review. Synth. Met. 226 (2017) 119–28. DOI: 10.1016/j.synthmet.2017.02.007
14. J.L. Blackburn, A.J. Ferguson, C. Cho, J.C. Grunlan, Carbon-nanotube-based thermoelectric materials, and devices. Adv. Mater. 30:11 (2018) 1704386. DOI: 10.1002/adma.201704386
15. Y. Du, K.F. Cai, S. Shen, Facile preparation, and characterization of graphene nanosheet/polyaniline nanofiber thermoelectric composites. Funct. Mater. Lett. 6:5 (*2013*)1340002. DOI: 10.1142/S179360471340002X
16. Y. Zhang, Y.-J. Heo, M. Park, S.-J. Park, Recent Advances in Organic Thermoelectric Materials: Principle, Mechanisms and Emerging Carbon-Based Green Energy Materials, Polymers 11 (2019) 167-89; DOI:10.3390/polym11010167.
17. G. Kim, K.P. Pipe, Thermoelectric model to characterize carrier transport in organic semiconductors. Phys. Rev. B 86 (2012) 6709–17.
18. C.Y. Gao, G.M. Chen, Conducting polymer/carbon particle thermoelectric composites: Emerging green energy materials. Compos. Sci. Technol. 124 (2016) 52–70. DOI:10.1016/J.COMPSCITECH.2016.01.014

19. K. Kanahashi, M. Ishihara, M. Hasegawa, H. Ohta, T. Takenobu, Giant power factors in p- and n-type large-area graphene films on a flexible plastic substrate. npj 2D Mater Appl. 3 (2019) 44. DOI:10.1038/s41699-019-0128-0
20. G. Zhang, Y.-W. Zhang, Thermoelectric properties of two-dimensional transition metal dichalcogenides. J. Mater. Chem. C 5 (2017) 7684–98. DOI:10.1039/C7TC01088E
21. D. Li, Y. Gong, Y. Chen, J. Lin, Q. Khan, Y. Zhang, Y. Li, H. Zhang, H. Xie, Recent Progress of Two-Dimensional Thermoelectric Materials Nano-Micro Lett.**,** 12 (2020). DOI: 10.1007/s40820-020-0374-x
22. Z-Hua Ge, L-Dong Zhao, D. Wu, X. Liu, B.-Ping Zhang, J.-Feng Li, J. He, Low-cost, abundant binary sulfides as promising thermoelectric materials, Materials Today, 19: 4 (2016) 227-239, https://doi.org/10.1016/j.mattod.2015.10.004.
23. P. Mangelis, P. Vaqueiro, A.V. Powell, Improved Thermoelectric Performance through Double Substitution in Shandite-Type Mixed-Metal Sulfides, *ACS Appl. Energy Mater. 3*: 3 (2020) 2168-74. DOI: 10.1021/acsaem.9b02272
24. H. Xi, L. Luo, G. Fraisse, Development and applications of solar-based thermoelectric technologies, Renew. Sustain Energy Rev. 11:5 (2007) 923-36. DOI:10.1016/j.rser.2005.06.008
25. Y. Tao, X. Wang, X. Li, A. Q. Yan, S. Ramakrishna, J. Xu. "Ultra-high Seebeck coefficient and low thermal conductivity of a centimeter-sized perovskite single crystal acquired by a modified fast growth method." *Journal of Materials Chemistry C* 5, 5 (2017): 1255-60.
26. T. Mori Thermoelectric and magnetic properties of rare earth borides: Boron cluster and layered compounds J. Solid State Chem. 275 (2019) 70-82. DOI:10.1016/j.jssc.2019.03.046.
27. T. Mori and T. Tanaka, Thermoelectric properties of homologous p-and n-type boron-rich borides. J. Solid State Chem. 179: 9 (2006) 2908-15. DOI:10.1016/j.jssc.2006.03.030
28. G. Akopov, L.E. Pangilinan, R. Mohammadi, R.B. Kaner, Perspective: Super-hard metal borides: A look forward, APL Mater. 6 (2018) 070901. DOI:10.1063/1.5040763
29. A.-M. Zieschang, J.D. Bocarsly, J. Schuch, C.V. Reichel, B. Kaiser, W. Jaegermann, R. Seshadri, B. Albert, Magnetic and Electrocatalytic Properties of Nanoscale Cobalt Boride, Co_3B Inorg. Chem. 58: 24 (2019) 16609–17, DOI.org/10.1021/acs.inorgchem.9b02617
30. P.R. Jothi, K.Y. Boniface, P.T. Fokwa, A Simple, General Synthetic Route toward Nanoscale Transition Metal Borides, Adv. Mater., 30 : 14 (2018) 1704181, DOI.org/10.1002/adma.201704181.
31. J. Ptačinová, M. Drienovský, M. Palcut, R. Čička, M. Kusý, M. Hudáková Oxidation stability of boride coatings, Kovove Mater. 53 (2015) 175–86, DOI: 10.4149/km 2015 3175.
32. B. Jiang, H. Song, Y. Kang, S. Wang, Q. Wang, X. Zhou, K. Kani, Y. Guo, J. Ye, H. Li, Y. Sakka, J. Henzie, Y. Yusuke. A mesoporous non-precious metal boride system: synthesis of mesoporous cobalt boride by strictly controlled chemical reduction. Chem. Sci., 11 (2020) 791-96. DOI: 10.1039/C9SC04498A
33. A.K. Iyer, Y. Zhang, J.P. Scheifers, B. P.T. Fokwa, Structural variations, relationships and properties of M_2B metal borides, J. Solid State Chem., 270 (2019) 618-35. *DOI:* 10.1016/j.jssc.2018.12.014
34. K. S.-Alcántara, J.R. T. García. Metal Borohydrides beyond Groups I and II: A Review. Materials (Basel). 14: 10 (2021) 2561. doi:10.3390/ma14102561
35. M. Paskevicius, L.H. Jepsen, P. Schouwink, R. Černý, D.B. Ravnsbæk, Y. Filinchuk, M. Dornheim, F. Besenbacher, T.R. Jensen, Metal borohydrides and derivatives – synthesis, structure and properties, Chem. Soc. Rev., 46 (2017) 1565-34. https://DOI.org/10.1039/C6CS00705H

36. W. Lohstroh, M. Heere, Structure and Dynamics of Borohydrides Studied by Neutron Scattering Techniques: A Review, J. Phys. Soc. Jpn., 89 (2020) 051011. DOI: 10.7566/JPSJ.89.051011
37. B. Richter, J.B. Grinderslev, K.T. Møller, M. Paskevicius, T.R. Jensen, From Metal Hydrides to Metal Borohydrides, Inorg. Chem. 57 (2018) 10768. DOI: 10.1021/acs.inorgchem.8b01398.
38. M. Y. Hassaan, H. A. Saudi, Hossam M. Gomaa, Ammar S. Morsy, Optical Properties of Bismuth Borate Glasses Doped with Zinc and Calcium Oxides, J. Mater Appl. 9:1 (2020) 46-54. doi.org/10.32732/jma.2020.9.1.46
39. J. Song, Z. Huang, Y. Qin, X. Li, Thermal Decomposition and Ceramifying Process of Ceramifiable Silicone Rubber Composite with Hydrated Zinc Borate Materials (Basel), 12:10(2019) 1591. doi: 10.3390/ma12101591
40. P. A. Chernavskii, Nick Peskov, A. V. Mugtasimov, V. V. Lunin, Oxidation of metal nanoparticles: Experiment and model, RUSSIAN J. Phys. Chem. B, 1:4 (2007) 394-411. DOI: 10.1134/S1990793107040082
41. P. Song, D.-sheng Wen, Z. X. Guo, T. Korakianitis, Oxidation investigation of nickel nanoparticles, Phys. Chem. Chem. Phys. 10:33 (2008), 5057-65, DOI: 10.1039/b800672e
42. D. Wen, P. Song, K. Zhang, J. Qian, Thermal oxidation of iron nanoparticles and its implication for chemical-looping combustion, J. Chem. Tech. Biotech. 86: 3 (2011) 375-80. doi.org/10.1002/jctb.2526
43. G.N. Glavee, K.J. Klabunde, C.M. Sorensen, G.C. Hadjipanayis, Borohydride Reduction of Nickel and Copper Ions in Aqueous and Nonaqueous Media. Controllable Chemistry Leading to Nanoscale Metal and Metal Boride Particles. Langmuir 10 (1994) 4726—30. DOI:10.1021/la00024a055
44. J.D. Kennedy, The Polyhedral Metallaboranes. Part II. Metallaborane Clusters with Eight Vertices and More, *Prog. Inorg. Chem.*, 34 (2007) 211-434.

DOI: 10.1002/9780470166352.ch4

45. E.A. Sterling, J. Stolk, L. Hafford, M. Gross, Sodium Borohydride Reduction of Aqueous Silver-Iron-Nickel Solutions: A Chemical Route to Synthesis of Low Thermal Expansion–High Conductivity Ag-Invar Alloys, Metall. Mater. Trans. A, 40A (2009) 1701-09, DOI: 10.1007/s11661-009-9859-4
46. H. Braunschweig, C. Kollann, D. Rais, Transition-Metal Complexes of Boron—New Insights and Novel Coordination Modes *Angewandte Chemie, Int`l Ed.,* 45: 32 (2006), 5254-74. DOI:10.1002/anie.200600506
47. D. Acosta, E.E. Gonzo, H.A. Destéfanis, Borane-Tetrahydrofurane Complex Reduction of Nickel and First Transition Metals in Tetrahydrofurane Media: Controllable Chemistry Leading to Nanoscale Metal and Metal Boride Particle. Mod. Res. Catal., 5 (2016), 19-30. DOI:/10.4236/mrc.2016.51003
48. L. Jun, X. Shuping, G. Shiyang, FT-IR and Raman spectroscopic study of hydrated borates, Spectrochimica Acta Part A: Molecular and Biomolecular Spectroscopy, 51: 4 (1995) 519-32, DOI: 10.1016/0584-8539(94)00183-C.
49. N.V. Belkova, I.E. Golub, E.I. Gutsul, K.A. Lyssenko, A.S. Peregudov, V.D. Makhaev, O.A. Filippov, L.M. Epstein, A. Rossin, M. Peruzzini, E.S. Shubina, Binuclear Copper(I) Borohydride Complex Containing Bridging Bis(diphenylphosphino) Methane Ligands: Polymorphic Structures of $[(\mu_2\text{-dppm})_2Cu_2(\eta^2\text{-}BH_4)_2]$ Dichloromethane Solvate, *Crystals 7:* 10 (2017) 318, DOI:10.3390/cryst7100318
50. C. Li, J. Zhang, W. Zhang, Y. Tang, B. Ren, Y. Hu, First-principle study of structural, electronic, and magnetic properties of (FEC)n (n = 1–8) and (FEC)8TM (TM = V, Cr, Mn, and Co) clusters. Sci Rep 7 (2017) 17516. doi.org/10.1038/s41598-017-17834-9

51. Y-W. Jun, J-W. Seo, J. Cheon, Nanoscaling laws of magnetic nanoparticles and their applicabilities in biomedical sciences, Acc. Chem. Res. 41:2 (2008) 179-89. DOI: 10.1021/ar700121f.
52. W. Ślubowska, K. Becmer, T.K. Pietrzak, J.L. Nowiński, M. Wasiucionek, J.E. Garbarczyk. The charge storage capacity of all-glass heterogeneous materials based on phosphate and vanadate glasses. Solid State Ionics **302** (2017) 98-101.
53. T. Katsufuji, H. Ikeda, M. Ashizawa, M. Oike, T. Kajita, Nonlinear Behavior in the Electrical Resistance of Strongly Correlated Insulators, J. Phys. Soc. Jpn., 89 (2020) 044702-5. https://doi.org/10.7566/JPSJ.89.044702
54. I.M. Arafa, H. El-Ghanem, R. Al-Shalabi, Formation, Characterization and Electrical Conductivity of Polycarbosilazane-Cu(II), -Ni(II) and -Cr(III) Chloride Metallopolymers, J. Inorg. Organomet. Polym.13 (2003) 69-86. DOI:10.1023/A:1024172613900.
55. M.A. Zoui, S. Bentouba, J.G. Stocholm, M. Bourouis, A Review on Thermoelectric Generators: Progress and Applications, Energies 13 (2020) 3606-37. doi:10.3390/en13143606
56. S. Wang, J. Yang, T. Toll, J. Yang, W. Zhang, X. Tang, Conductivity-limiting bipolar thermal conductivity in semiconductors, Sci. Reports, 5 (2015) 10136. DOI: 10.1038/srep10136

Theme 2: Chemical Engineering Kinetics

An equilibrium Ab initio atomistic thermodynamics study of CH_4 and CO_2 adsorption on the α-quartz (001) surface

Ibrahim A. Suleiman [1,*], Reyad Shawabkeh [2] and Ibnelwaleed Hussein [3]

[1] Al-Balqa Applied University, Faculty of Engineering Technology, Chemical Engineering Department, Amman 11134, Jordan;
[2] Chemical Engineering Department, University of Jordan, Amman, Jordan;
[3] Gas Processing Center, College of Engineering, Qatar University, Doha, Qatar;
***Corresponding author: dr.ibrahim.suleiman@bau.edu.jo/dr.ibrahim.suleiman@gmail.com; Tel.: +962 79 727 8894.*

Abstract: For the purpose of enhancing the gas recovery via injecting CO_2 into quartz, the stability of various structures of adsorbed CO_2 and CH_4over the α-quartz (100) surface were theoretically investigated using ab initio atomistic thermodynamics. The results showed that among all CH_4/ α-quartz (001) investigated structures, the 1 ML-1B forms the most stable configuration beyond $\Delta\mu_{CH_4} = -0.15$ eV. For CO_2 the first stable structure with 1/2 ML forms at $\Delta\mu_{CO_2} = -0.22$ eV. In contrast to methane, quartz intake of CO_2 increases with increasing the pressure to 1 ML, where beyond $\Delta\mu_{CO_2} = -0.12$ eV, the 1 ML coverage at B1 site structure shows the highest stability among all CO_2/ α-quartz (001) configurations.The calculated phase diagram illustrates that CO_2 adsorption is more favorable than CH_4 over the surface.

Keywords: EGR; atomistic thermodynamics; methane; CO_2.

1. Introduction

Enhanced gas recovery (EGR) technology utilizes CO_2 gas in large scales. The CO_2 gas is injected in near-drained wells in order to recover residual hydrocarbons; in the meantime, CO_2 is sequestrated in the reservoir rock [1, 2].

It is believed that there is a competitive adsorption between CO_2 and methane with the reservoir sedimentary rock materials, which mainly composed of α-quartz. Sun et al [3], showed that in a binary mixed system of CO_2 and methane, CO_2 is more preferentially adsorb to the α-quartz surface than CH_4. They referred that to the strong interactions between the CO_2 species and the hydrophilic part on the surface.

In a previous density functional theory (DFT) investigation [4] the binding energies of CO_2 and CH_4 on the α-quartz (001) at various coverages were calculated. It was illustrated that CO_2 can replace methane on the α-quartz surface, leading to a better extraction of methane.

Zhang et al [5] in their experiment showed that the CO_2 Langmuir adsorption isotherm on α-quartz fits the experimental results, when a monolayer of gas molecules is formed at the maximum gas concentration. At higher pressure levels (~200 bar) and at temperature range of (313 -353) K, the surface hydroxylation degree contributes significantly to CO_2 adsorption selectivity.

This study benefits from the previous DFT results [4] to calculate the surface free energy phase diagrams of pure CO_2 and CH_4 on the α-quartz (001). The temperature and pressure were incorporated with the phase diagram to anticipate the stability of the investigated structure at certain T and p conditions.

2. Materials and Methods

The relative stabilities of the α-quartz (001) surfaces in contact with gaseous CO_2 and CH_4 environments have been investigated using the ab initio atomistic thermodynamic technique. The concentration of gaseous species is implicitly included in the carbon dioxide and methane chemical potential term. The expression of the free energy, γ^{ads}, is given by [6, 7]:

$$\gamma^{ads} = \frac{1}{A}[N_i E_b - N_i \Delta\mu_i(T, p)] \quad (1)$$

Where E_b is the binding energy, $\Delta\mu_i$ and N_i are the chemical potential and number of adsorbed species *i* on the surface, respectively.

Assuming that the surrounding gaseous atmosphere forms an ideal-gas-like reservoir, then $\Delta\mu_i$ as a function of temperature, T, and pressure, p, can be obtained using the formula [6, 7]:

$$\Delta\mu_i(T,p) = \mu_i(T,p^o) + \frac{1}{2}kT\ln\left(\frac{p}{p^o}\right) \quad (2)$$

where k is the Boltzmann constant, and $\mu_i(T,p^o)$ is the chemical potential of species i evaluated at temperature T and pressure p^o, which can be calculated using the equation:

$$\mu_i(T,p^o) = \left[\left(H_i(T,p^o) - H_i(0\ K,p^o)\right) - \frac{T}{2}\left(S_i(T,p^o) - S_i(0\ K,p^o)\right)\right] \quad (3)$$

Where H, the enthalpy, and S, the entropy, can be obtained from thermodynamic tables. More details about the technique can be found in refs.[6-10].

3. Results and Discussion

Using ab initio atomistic thermodynamics, the surface energy phase diagrams of CH_4 and CO_2 over the $\alpha-\text{quartz}(001)$ surface were calculated. The adsorption systems and their associated binding energies are listed in Table (1) [4], and schematics of the investigated configurations are shown in Figure (13) in reference (4).

The surface energy phase diagram of $CH_4/\alpha-\text{quartz}(001)$ is shown in Figure (1). For a dilute methane environment, the clean $\alpha-\text{quartz}(001)$ surface was found to be the most stable structure. Increasing the concentration of methane beyond the value -0.15 eV of $\Delta\mu_{CH_4}$, the 1 ML-A1 configuration becomes the most stable and for the remaining range of $\Delta\mu_{CH_4}$. This is consistent with the results of Sun et al [3] which shows that as pressure increases at 323 K, a one single layer forms a tight adsorption of CH_4 on the nanopore surface. However, to observe this structure at 300 K, the phase diagram suggests that the pressure of methane has to exceed 10^{11} bar. This is expected due to the low binding energy value between CH_4 species and the surface. In order to stabilize this structure at lower pressures, lower temperatures are required. The phase diagram anticipates that at $T = 100$ K, the 1 ML-A1 structure can be observed at $p = 1 - 10^2$ bar within the range $-0.12 < \Delta\mu_{CH_4} < -0.1$ eV.

Table 1: Energetics Obtained for Different Locations and Coverages of CH_4 and CO_2 on the reconstructed $\alpha - quartz(001)$ Surface [4]

System	$CO_2/\alpha - quartz(001)$ Binding Energy (eV)	$CH_4/\alpha - quartz(001)$ Binding Energy (eV)
1/4 ML-A1	-0.210	-0.130
1/2 ML-A1	-0.220	-0.140
3/4 ML-A1	-0.150	-0.140
1 ML-A1	-0.110	-0.150
1/4 ML-A2	-0.140	-0.120
1/2 ML-A2	-0.160	-0.130
3/4 ML-A2	-0.080	-0.140
1 ML-A2	-0.040	-0.140
1/4 ML-B1	-0.180	-0.090
1/2 ML-B1	-0.210	-0.110
3/4 ML-B1	-0.200	-0.120
1 ML-B1	-0.180	-0.130
1/4 ML-B2	-0.090	-0.080
1/2 ML-B2	-0.100	-0.090
3/4 ML-B2	-0.110	-0.110
1 ML-B2	-0.100	-0.120

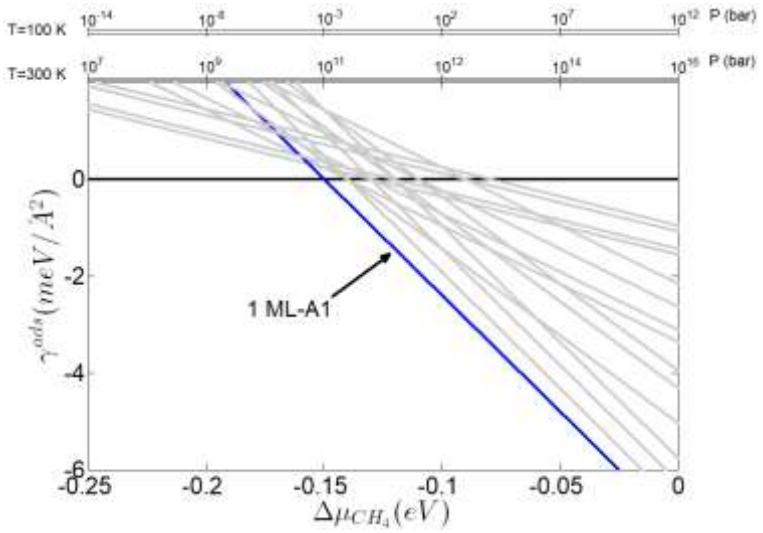


Figure 1: Surface free energy for various $CH_4/\alpha - quartz(001)$ structures as a function of methane chemical potential. The corresponding pressure is given for the temperatures 100, 300 K.

The surface energy phase diagram of $CO_2/\alpha - quartz(001)$ shows various stable structures at different ranges of $\Delta\mu_{CO_2}$, as illustrated in Fig. 2. The clean $\alpha - quartz(001)$ surface appears to be the most stable at $\Delta\mu_{CO_2} < -0.22$ eV. Beyond this value and in the range of $-0.22 < \Delta\mu_{CO_2} < -0.16$ eV, the 1/2 ML-A1 configuration becomes the most stable structure. The 3/4 ML-B1 shows more stability at the range of $-0.16 < \Delta\mu_{CO_2} < -0.12$ eV. Beyond the value $\Delta\mu_{CO_2} = -0.12$ eV, the 1 ML-B1 configuration becomes the most stable among all investigated structures. This is in agreement with the results of Sun et al. [3] which suggest that quartz gets almost saturated rapidly as the pressure of CO_2 increases to 7.4 MPa, then the CO_2 content increases slightly when the applied pressure of CO_2 ranges between 7.4 and 20 MPa. However, the phase diagram in Figure 2 shows that there are three stable configurations for $CO_2/\alpha - quartz(001)$ instead of two.

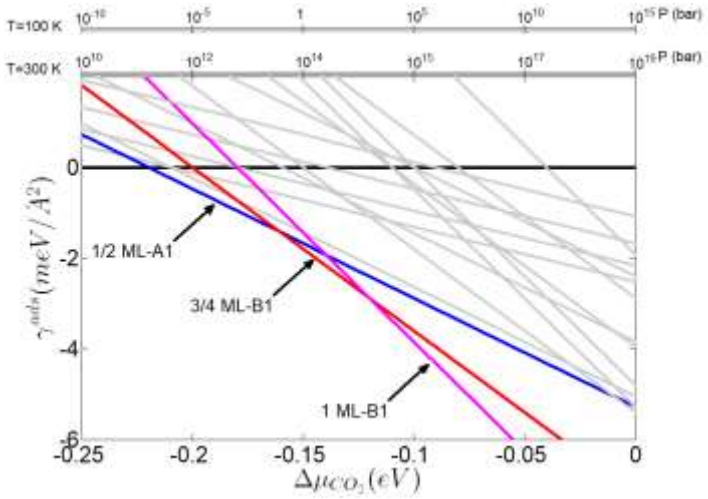


Figure 2: Surface free energy for various $CO_2/\alpha-quartz(001)$ structures as a function of carbon dioxide chemical potential. The corresponding pressure is given for the temperatures 100, 300 K.

Comparing between Figs. 1 and 2, the $CO_2/\alpha-quartz(001)$ system becomes more stable than the clean surface at $\Delta\mu_{CO_2} = -0.22$ eV with 1/2 ML coverage, whereas the most stable 1 ML $CH_4/\alpha-quartz(001)$ structure becomes more favorable at at $\Delta\mu_{CH_4} = -0.15$ eV. The lower chemical potential value as well as the lower coverage of carbon dioxide explain why its adsorption is more favorable than methane over $\alpha-quartz(001)$. However, for a better understanding of competitive adsorption between CO_2 and CH_4, a 2-D free energy phase diagram should be calculated for CO_2/CH_4 co-adsorped systems at different coverages.

The wettability of the rock is one of major factors that would affect the adsorption of CO_2 and CH_4; therefore, studying the adsorption of these species over wet surfaces could help understanding such processes. Studying the thermodynamic stability of co-adsorbed CO_2 and CH_4 over $\alpha-quartz(001)$ systems will be of great benefit to explain the competitive adsorption between these molecules [3]. Finally, high pressure values, could lead to changes in the lattice parameters, which would affect the results above slightly, since it did not change the type of the lattice. Levien et al [11] shows that the Si-quartz structure becomes more like Ge-quartz structure at pressure of 61.4 kbar, which has smaller pore sizes. This might affect the stability of the abovementioned configurations, and studying the adsorption of CO_2 and CH_4 over a Ge-quartz structures will be very helpful to understand the behavior of these systems under high pressure environments.

4. Conclusions

Ab initio atomistic thermodynamics was used to investigate the stability of pure CO_2 and CH_4over α-quartz adsorption systems as part of enhancing the gas recovery process. Among all CH_4/ α-quartz (001) configurations, the 1 ML-A1 is the most stable structure. The CO_2/ α-quartz (001) systems forms various stable structures depending on the concentration of gaseous CO_2 environment. The 1/2 ML-A1 configuration forms the most stable structure at lower pressure values, whereas at higher pressures the 1ML-B1 system is the most stable.

To stabilize the CO_2 and CH_4 over α-quartz (001) at room temperature, high pressures are required. However, at such high pressure values, Si-quartz transforms to Ge-quartz structure which affects the porosity of the rock. If lower pressures are available, then lower temperatures will help to stabilize the abovementioned configurations.

References

1. Oldenburg, C. M.; Pruess, K.; Benson, S. M., Process modeling of CO2 injection into natural gas reservoirs for carbon sequestration and enhanced gas recovery. *Energy Fuels* **2001,** *15*, 293-298.
2. Rani, S.; Padmanabhan, E.; Prusty, B. K., Review of gas adsorption in shales for enhanced methane recovery and CO2 storage. *J. Pet. Sci. Eng.* **2019,** *175*, 634-643.
3. Sun, H. Y.; Sun, W. C.; Zhao, H.; Sun, Y. G.; Zhang, D. R.; Qi, X. Q.; Li, Y., Adsorption properties of CH4 and CO2 in quartz nanopores studied by molecular simulation. *Rsc Adv.* **2016,** *6*, 32770-32778.
4. Carchini, G.; Hussein, I.; Al-Marri, M. J.; Shawabkeh, R.; Mahmoud, M.; Aparicio, S., A theoretical study of gas adsorption on alpha-quartz (001) for CO2 enhanced natural gas recovery. *Appl. Surf. Sci.* **2020,** *525*, 10.
5. Zhang, C.; Kaluvan, S.; Zhang, H. F.; Wang, G. A.; Zuo, L., A study on the Langmuir adsorption for quartz crystal resonator based low pressure CO2 gas sensor. *Meas.* **2018,** *124*, 286-290.
6. Suleiman, I. A.; Radny, M. W.; Gladys, M. J.; Smith, P. V.; Mackie, J. C.; Kennedy, E. M.; Dlugogorski, B. Z., Chlorination of the Cu(110) Surface and Copper Nanoparticles: A Density Functional Theory Study. *J. Phys. Chem. C* **2011,** *115*, 13412-13419.
7. Suleiman, I. A.; Radny, M. W.; Gladys, M. J.; Smith, P. V.; Mackie, J. C.; Kennedy, E. M.; Dlugogorski, B. Z., Thermodynamic stability and structure of cuprous chloride surfaces: a DFT investigation. *PCCP* **2015,** *17*, 7038-7045.
8. Peljhan, S.; Kokalj, A., Adsorption of Chlorine on Cu(111): A Density-Functional Theory Study. *J. Phys. Chem. C* **2009,** *113*, 14363-14376.
9. Rogal, J.; Reuter, K.; Scheffler, M., CO oxidation at Pd(100): A first-principles constrained thermodynamics study. *Phys. Rev. B* **2007,** *75*, 205433.
10. Stampfl, C.; Soon, A.; Piccinin, S.; Shi, H.; Zhang, H., Bridging the temperature and pressure gaps: close-packed transition metal surfaces in an oxygen environment. *J. Condens. Matter Phys* **2008,** *20*, 184021.
11. Levien, L.; Prewitt, C. T.; Weidner, D. J., STRUCTURE AND ELASTIC PROPERTIES OF QUARTZ AT PRESSURE. *Am Min* **1980,** *65*, 920-930.

Carbon monoxide desorption and reduction behaviors of graphitic carbon nitride supported nickel catalysts and their performance in CO methanation

Khairul Naim Ahmad [1], Fairous Salleh [2], Wan Nor Roslam Wan Isahak [1,*], Muhammad Rahimi Yusop [2], Masli Irwan Rosli [1] and Mohd Ambar Yarmo [2]

[1] Department of Chemical and Process Engineering, Faculty of Engineering and Built Environment, Universiti Kebangsaan Malaysia, 43600 UKM Bangi, Selangor, Malaysia;
[2] Department of Chemical Sciences, Faculty of Science and Technology, Universiti Kebangsaan Malaysia, 43600 UKM Bangi, Selangor, Malaysia;
***** *Corresponding author: wannorroslam@ukm.edu.my; Tel.: +603 8921 6424.*

Abstract: In this study, a nickel catalyst supported on graphitic carbon nitride (g-C_3N_4) was prepared by a simple impregnation method. The Ni/g-C_3N_4 desorption and reduction behaviors with carbon monoxide (CO) were investigated by temperature programmed desorption (TPD) and reduction (TPR). The as-prepared Ni/g-C_3N_4 catalyst was also characterized by X-ray diffraction (XRD), N_2 physisorption, and X-ray photoelectron spectroscopy (XPS). It is found that the utilization of g-C_3N_4 as a catalyst support enhances the complete reduction of Ni species and CO desorption. This can be attributed to the role of g-C_3N_4 support as reducing agent for Ni as well as its basicity owing to the richness of nitrogen functional group. The good performance of Ni/g-C_3N_4 catalyst towards CO methanation can be ascribed to the improvement in adsorption and activation of CO molecules on the active sites and number of surface basic sites.

Keywords: graphitic carbon nitride; nickel-based catalyst; temperature-programmed desorption; temperature-programmed reduction; CO methanation; surface basicity

1. Introduction

Graphitic carbon nitride (g-C_3N_4) has been regarded as a promising material in various applications, most notably as a metal free catalyst in photocatalysis [1,2] and as a catalyst support in electrocatalysis [3] and hydrogenation reactions [4,5]. It has a similar structure to graphene, with carbon and nitrogen are bonded strongly together in the form of s-triazine or heptazine aromatic rings [6]. Owing to that, g-C_3N_4 has the advantages such as good thermal and chemical stability, as well as tunable electronic structure [5]. As a catalyst support, g-C_3N_4 possesses nitrogen-rich basic sites and modifiable surface area and pore volume, which can provide high dispersion to metal nanoparticles [7,8]. Additionally, g-C_3N_4 can be simply synthesized by thermal polymerization of organic precursors containing carbon and nitrogen such as urea [9] and melamine [10].

Since the first discovery by Sabatier and Senderens in 1902 [11], CO methanation has been extensively studied in recent years due to the great interest in production of synthetic natural gas (SNG). CO methanation reaction is the hydrogenation of CO to CH_4 (Equation 1), which is the main component in SNG. It is well known that nickel (Ni) is considered the most practical catalyst material for CO methanation owing to its high activity and low cost. However, traditional Ni catalysts often suffer from deactivation at elevated reaction temperature due to the high exothermicity of the reaction [12]. Therefore, the effects of supports, promoters, and preparation methods have been studied in order to improve the activity and stability of Ni-based catalyst.

$$CO + 3H_2 \rightarrow CH_4 + H_2O, \qquad \Delta H_r^\circ = -206\ \text{kJ/mol} \tag{1}$$

There are several studies regarding the application of g-C_3N_4 as the catalyst support. Chen et al. [5] and Park et al. [4] have successfully prepared the mesoporous g-C_3N_4 supported Iron catalyst for the Fischer Tropsch synthesis (FTS). Chen et al. [5] discussed the role of nitrogen-containing base of g-C_3N_4 support in Fe/g-C_3N_4 catalyst towards the high performance in FTS. Furthermore, Park et al. [4] reported the presence of g-C_3N_4 facilitates the reduction of iron oxide to a more reduced form.

Carbon monoxide is a very reactive molecule and has been utilized as a feedstock in many chemical reactions. Apart from that, CO is also regarded as a strong reducing agent aside from classical reducing agents such as hydrogen and metal hydrides [13]. Abu Tahari et al. [14] have investigated the comparison of reduction behavior between reductant CO and H_2 in the reduction process of iron oxide, They found that CO is faster reducer at lower temperature of reduction , whereas H_2 is a good reductant in completing the reduction. As for methanation catalysts, it is interesting to study the behavior of CO molecules either in reduction or adsorption-desorption on the surface of catalysts since CO is one of the reactants.

In recent study, a nickel supported on graphitic carbon nitride (Ni/g-C_3N_4) was synthesized by a facile impregnation method. The desorption and reduction by carbon monoxide were studied by temperature-programmed desorption (CO-TPD) and reduction (CO-TPR), and the characterization was conducted by X-ray diffraction (XRD), N_2 adsorption-desorption, and X-ray photoelectron spectroscopy (XPS) analyses. The performance of CO methanation was determined using temperature-programmed experiment under atmospheric condition.

2. Experimental Section

2.1. Preparation of catalyst

Bulk g-C_3N_4 powder was prepared by heating melamine (Sigma Aldrich, 99%) in a furnace at 500°C for 1 h with temperature ramp 5°C/min. The Ni/g-C_3N_4 catalyst is synthesized by incipient wetness impregnation method. Appropriate amounts of Nickel (II) nitrate hexahydrate (Sigma Aldrich, 99%) and as prepared g-C_3N_4 were dissolved in water and stirred for 4 h under room temperature. Then, the solution is heated at 80°C to evaporate the remaining water before being dried in an oven overnight. Later, the sample underwent calcination under air atmosphere at 450°C for 5 h. The amount of active metal loading in the catalyst is 10wt% of nickel.

2.2. Catalyst characterization

The X-ray diffraction (XRD) patterns of the of the samples were analyzed by a Bruker D8 Advance X-ray diffractrometer with radiation source Cu Kα (λ = 0.15406 nm) operating at 40 kV and 40 mA. The 2θ diffraction angle was measured from 5° to 80° at a scan rate 0.25°/s. Nitrogen adsorption-adsorption isotherms of the catalysts were obtained at 77K (liquid nitrogen) using a Micromeritics Tristar II Plus 3030KR. The Brunauer-Emmett-Teller (BET) surface area and Barrett-Joyner Halenda (BJH) pore diameter and volume were determined from the isotherms of each sample. X-ray photoelectron spectroscopy (XPS) measurement was performed using a Kratos Axis Ultra DLD with Al Kα radiation (1486 eV) as excitation source. All XPS binding energies were referred to C 1s at 284.5 eV. The temperature programmed reduction (TPR) and desorption (TPD) of carbon monoxide were conducted using a Micromeritics Autochem II 2920 Plus Chemisorption Analyzer instrument with thermal conductivity detector (TCD). In TPR experiment, a gas mixture of 10% CO in N_2 was introduced to 50 mg of sample at flow rate 20 ml/min. The sample was heated up to 800°C and CO consumption was recorded using TCD. Prior to TPD measurement, 50 mg of sample was reduced by hydrogen up to 400°C. After cooling down to 50°C, CO gas was introduced to the sample for 1 h with flow rate 30 ml/min until the saturation was reached. Subsequently, the He gas is used to purge excess CO adsorbed on the sample before being heated up to 800°C at heating ramp of 10°C/min.

2.3. CO methanation performance assessment

The CO methanation performances were performed in a fixed-bed quartz tubular reactor with an internal diameter of 6 mm. The experiments were conducted under a temperature-programmed

experiment mode using a chemisorption analyzer equipped with an online MKS Cirrus 2 quadrupole mass spectrometer. Prior to the experiment, 50 mg of the catalyst was placed in the reactor and activated at 400°C in an H_2/N_2 mixture gas. After the system was cooled to 100°C in N_2, a mixture gas with molar percentage H_2/CO/He = 60/20/20 was fed into the reactor. The catalytic tests were conducted from 100 to 600°C with a linear rate of 10°C min^{-1} under atmospheric pressure. The effluent gas of the reactor was analyzed and recorded online by a mass spectrometer (MS). The MS signals of the ions (*m/z* = 2, 15, 29, and 44) corresponding to H_2^+, CH_4^+, $CO^{+\cdot}$ and CO_2^+ were monitored continuously. The calibration of MS signals was performed using standard mix gases of specified concentration. The CO conversion (X_{CO}) and CH_4 selectivity (S_{CH4}) were calculated by the following formulas:

$$X_{CO}(\%) = \frac{n_{CO,in} - n_{CO,out}}{n_{CO,in}} \times 100\% \quad (2)$$

$$S_{CH_4}(\%) = \frac{n_{CH_4,out}}{n_{CO_X,in} - n_{CO,out}} \times 100\% \quad (3)$$

where $n_{a,in}$ and $n_{a,out}$ are the molar flow rates (mol s^{-1}) of CO and CH_4 in the feed and effluent gases, respectively.

3. Results and Discussion

3.1. CO-TPD

In order to evaluate the CO adsorption type and basic strength of Ni/g-C_3N_4, CO-TPD was performed, and the profiles are displayed in Figure 1. The desorption peaks at different temperatures specifies the different types of adsorbed CO species with different adsorption capabilities and reactivity potentials. It is observed that no CO desorption peak is detected in pure Ni sample, indicating that Ni has no interaction with CO. In contrast, Ni/g-C_3N_4 catalyst shows three desorption peaks at high temperature region (507°C, 586°C and 739°C) which correspond to the desorption of strongly adsorbed CO. This can be explained by the interaction of Ni and g-C_3N_4 support leads to enhanced CO adsorption and activation on the active sites of Ni/g-C_3N_4 catalyst in comparison to unsupported Ni catalyst [15]. Moreover, the CO desorption peaks shown in Ni/g-C_3N_4 sample can also indicate the presence of surface basicity on the catalyst surface. It is known that g-C_3N_4 support material contains three types of basic sites which originated from nitrogen functional groups such as Brönsted basic nitrogen, Lewis basic nitrogen and H-bonding motif [5,16].

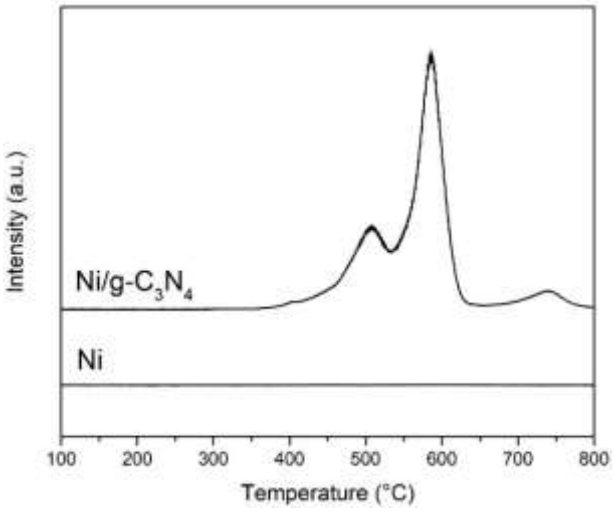


Figure 1. CO-TPD profiles of as-prepared Ni/g-C_3N_4 catalyst and pure Ni.

3.2. CO-TPR

CO-TPR was carried out to analyze the reduction behavior of Ni/g-C_3N_4 and NiO catalysts in CO atmosphere [17]. Figure 2 shows the TPR patterns of the catalysts under 10% CO reductant. For NiO, there is a main peak at ca. 420°C which shows a very high consumption of CO due to the combination of partial reduction of NiO to Ni (Equation 4) and Boudouard reaction (Equation 5) with reduced metallic Ni as the catalyst [18]. According to Sakai et al. [19], carbon deposition occurs when metallic Ni starts to form after the reduction of NiO. The second lower intensity peak at ca. 460°C is attributed to complete reduction of NiO. Meanwhile, the Ni/g-C_3N_4 catalyst shows higher temperature peak at ca. 440°C, signifies the delay of the NiO reduction and Boudouard reaction. However, the NiO reduction in Ni/g-C_3N_4 catalyst is completed at lower temperature (ca. 460°C) compared to unsupported nickel (ca. 580°C), demonstrated the positive effect of g-C_3N_4 support towards metal reducibility. Interestingly, it is observed the negative peak at ca. 582°C in Ni/g-C_3N_4 catalyst indicating the CO is produced at this temperature. This probably originates from reverse Boudouard reaction (Equation 6) where CO_2 that is produced from Equation 4 and 5 would react with deposited carbon to form CO.

$$NiO + CO \rightarrow Ni + CO_2 \quad (4)$$

$$2CO \rightarrow CO_2 + C \quad (5)$$

$$CO_2 + C \rightarrow 2CO \quad (6)$$

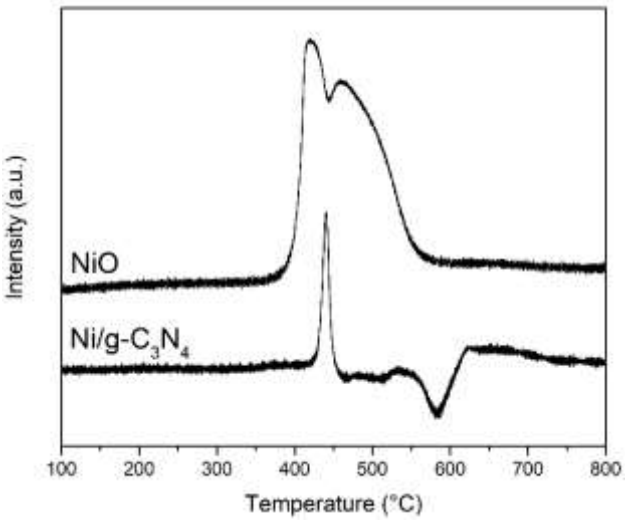


Figure 2. CO-TPR profiles obtained of as-prepared Ni/g-C_3N_4 and pure NiO samples.

3.3. Crystallinity study

The XRD patterns of g-C_3N_4, Ni/g-C_3N_4 and NiO are shown in Figure 3. In g-C_3N_4 sample, there are two diffraction peaks at 13.1° and 27.5° that correspond to the in-plane packing and interlayer stacking structure in g-C_3N_4 [20]. The Ni/g-C_3N_4 fresh catalyst demonstrates the peak at 27.5° which consistent with g-C_3N_4 support, but with lower intensity. This shows that the existence of Ni species inhibits the crystal growth of g-C_3N_4. Furthermore, the peak at 13.1° is very weak and almost not visible due to introduction of Ni reduces the hole-to-hole distance of repeated triazine pores [21]. It is observed the diffraction peaks at 37.3°, 43.3°, 62.9°, 75.8° and 79.5° correspond to reflections of NiO phase (PDF no. 03-065-6920, ICDD). These peaks are less crystalline than pure NiO, demonstrating good dispersion of Ni NPs on the g-C_3N_4 support. Interestingly, highly crystalline

diffraction peaks of metallic Ni are also detected, reflected by the peaks at 44.5°, 51.8° and 76.3° (PDF no. 01-087-0712, ICDD). This phenomenon can be explained by some of NiO species have been partially reduced to Ni during calcination, where the g-C_3N_4 support has acted as reducing agent [4]. The crystallite size calculated from Scherer in Table 1 indicates that the utilization of g-C_3N_4 support results in reduction in NiO crystallite size by half, demonstrating good dispersion of Ni particles on the support.

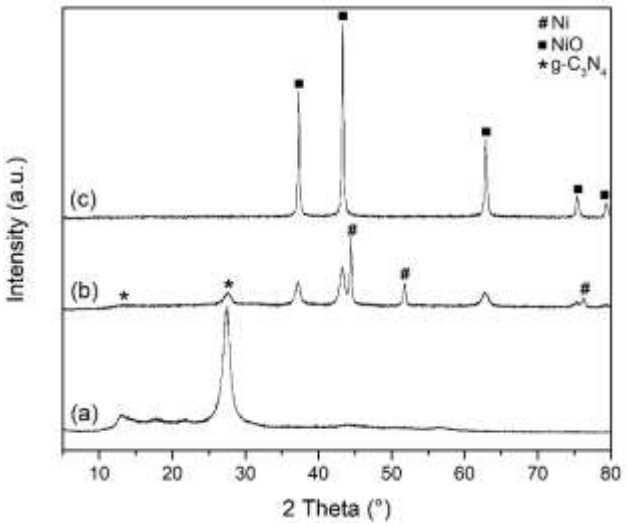
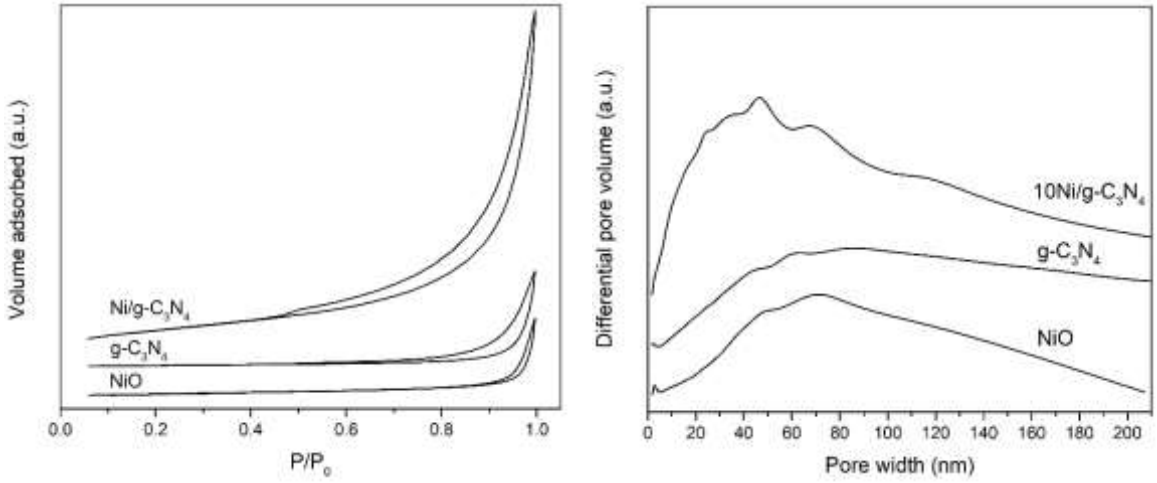


Figure 3. XRD patterns of (a) g-C_3N_4, (b) Ni/g-C_3N_4 and (c) NiO.

3.4. N_2 physisorption

The nitrogen adsorption-desorption isotherms of Ni/g-C_3N_4, g-C_3N_4 and NiO are displayed in Figure 4(a). The catalysts show the type IV isotherms and H3 hysteresis loops, which is typical for mesoporous materials. The pore size distribution profiles in Figure 4(b) shows that pore width of Ni/g-C_3N_4 catalyst became smaller which can be ascribed to the pore filling of g-C_3N_4 support by Ni species. Table 1 summarize the surface area, average pore size and average pore volume of the catalysts. The BET surface areas of g-C_3N_4 support and Ni/g-C_3N_4 catalyst are 5.25 m^2/g and 36.39 m^2/g, respectively. It was found the surface area of Ni-based catalyst increases by seven-fold when bulk g-C_3N_4 is used as support. This suggests that the bulk g-C_3N_4 has undergone thermal exfoliation during the calcination pre-treatment process to form thin sheets [22]. Hence, the large surface area of Ni/g-C_3N_4 catalyst may be one of the factors that influence the amount of basic sites for CO desorption during TPD analysis.



(**a**) (**b**)

Figure 4. (**a**) N_2 adsorption-desorption isotherms and (**b**) pore size distribution of the as-prepared samples.

Table 1. Textural properties of the catalysts.

Catalyst	Specific surface area [1] ($m^2\ g^{-1}$)	Average pore volume [2] ($cm^3\ g^{-1}$)	Average pore diameter [3] (nm)	NiO crystallite size [4] (nm)
$g\text{-}C_3N_4$	5.3	0.021	27.3	-
NiO	5.7	0.011	23.8	36.5
$Ni/g\text{-}C_3N_4$	36.4	0.100	16.0	17.0

[1] Calculated from BET equation. [2] BJH desorption pore volume. [3] BJH desorption average pore diameter. [4] Average Ni crystallite diameter calculated using Scherer equation from NiO(200) plane from XRD.

3.5. XPS analysis

XPS was performed to analyze the surface composition and chemical states of as-prepared $Ni/g\text{-}C_3N_4$ sample. Figure 5 presents the XPS spectra of C 1s, N 1s, and Ni 2p in the catalyst. The XPS spectrum of C 1s (Figure 5(a)) can be deconvoluted into four peaks: the peak at 284.5 eV is attributed to adventitious carbon, whereas the peaks 285.8 and 287.5 eV are assigned to C–N=C and $C–(N)_3$ groups of $g\text{-}C_3N_4$ support [23]. The N 1s spectrum in Figure 5(b) is deconvoluted into two peaks centered at approximately 398.5 and 400.2 eV which correspond to C–N=C and $N–(C)_3$ groups, demonstrating the characteristics of graphitic structure of $g\text{-}C_3N_4$. [24,25]. Figure 5(c) illustrates the Ni 2p XPS spectrum which describes the chemical states of nickel present on the surface. The peaks ($Ni\ 2p_{3/2}$) at approximately 852, 854.5, and 856.2 eV with their respective doublets ($Ni\ 2p_{1/2}$) can be assigned metallic Ni, NiO, and Ni_2O_3 phases. The formation of small amount of Ni reduced phase confirms the occurrence of partial reduction of NiO by $g\text{-}C_3N_4$ support during calcination process.

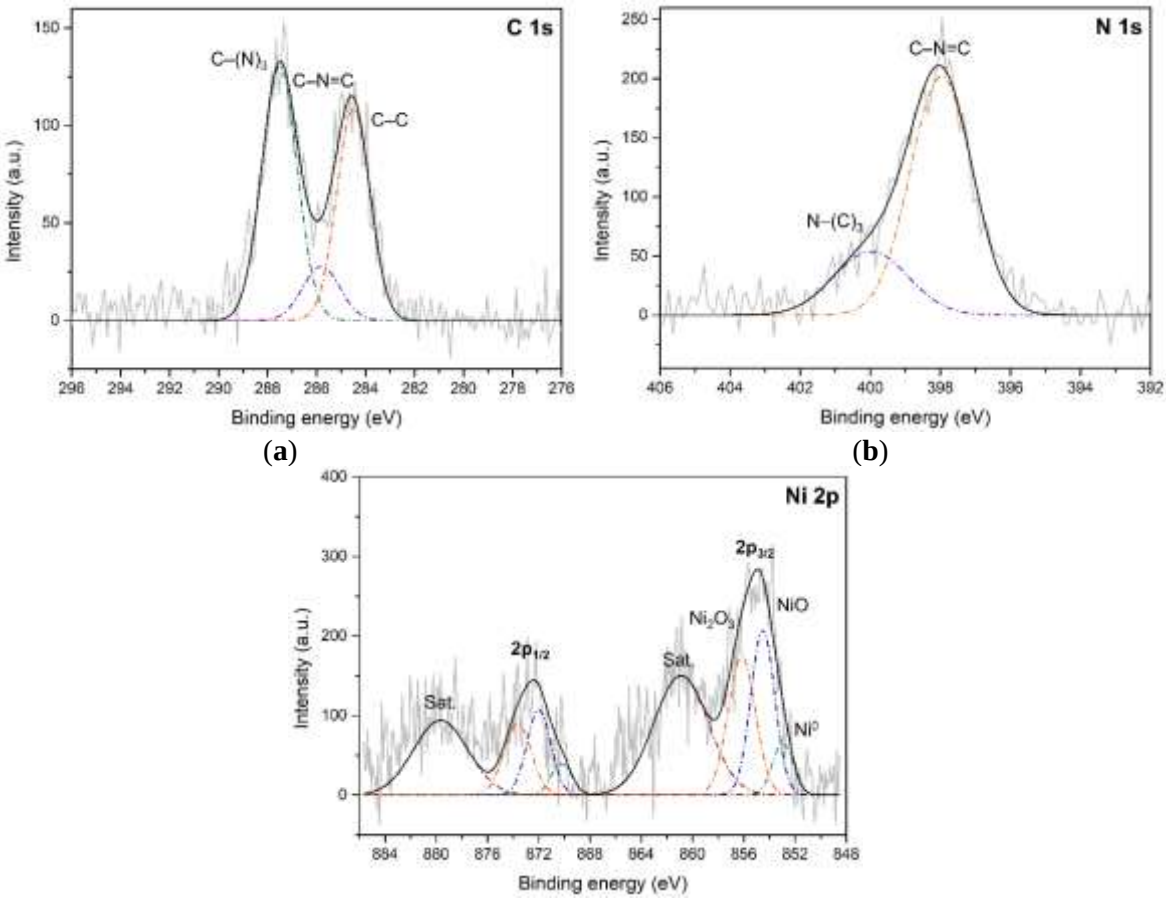


Figure 5. XPS spectra of (**a**) C 1s, (**b**) N 1s, (**c**) Ni 2p for as-prepared Ni/g-C_3N_4 catalyst.

3.6. CO methanation on Ni/g-C_3N_4 catalyst

The performance of the Ni/g-C_3N_4 catalyst for CO methanation is displayed in Figure 6, where (a) and (b) correspond to CO conversion (X_{CO}) and CH_4 selectivity (S_{CH4}), respectively. Below 300°C, there is no significant change in X_{CO}, indicating less activity of the catalyst at a low reaction temperature. As the temperature rises above 300°C, the values of X_{CO} starts to increase exponentially until the maximum CO conversion is achieved at 79.7% with S_{CH4} of 73.9% at 375°C. The catalytic performance of Ni/g-C_3N_4 is comparable to conventional Ni/Al_2O_3 catalyst as reported by Gao et al with X_{CO} value at approximately 80% at 375°C [26]. The good catalytic activity of Ni/g-C_3N_4 can be attributed to the improved CO adsorption and activation on the active sites as well as the presence of basic sites on the catalyst surface, which is beneficial for CO methanation. Although the conversion of CO is maximum at this temperature, the selectivity towards formation of CH_4 is lowered due to the formation of other side product such as CO_2 from water-gas shift reaction (Equation 7). Furthermore, the presence of strong interaction between CO molecules and active metal in CO-TPD analysis that leads to the occurrence of side reaction, resulting in the decline of CH_4 selectivity [27]. Raising the temperature beyond 385°C is unfavorable for CO methanation due to the high exothermicity of the reaction as X_{CO} decrease drastically to 16% at 450°C.

$$CO + H_2O \rightarrow CO_2 + H_2 \quad (7)$$

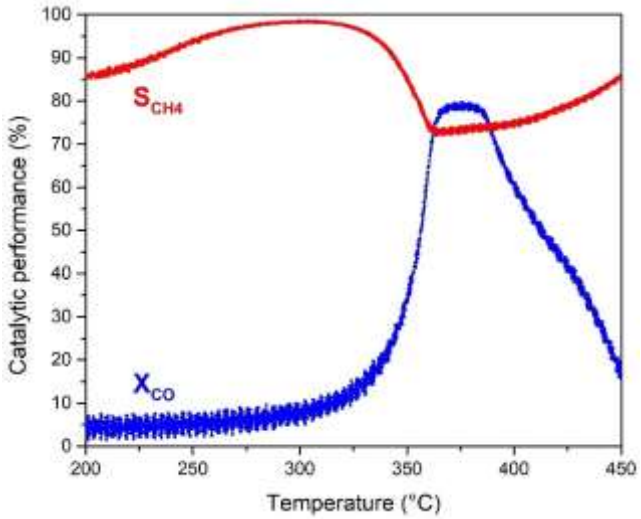


Figure 6. Catalytic performance of Ni/g-C_3N_4 catalyst for CO methanation

4. Conclusions

The CO desorption and reduction behavior of Ni/g-C_3N_4 were investigated using TPD and TPR techniques and characterized by XRD and N_2 physisorption. The findings in this study revealed the addition of g-C_3N_4 support to Ni-based catalyst improved the complete reduction by CO at lower temperature than pure NiO. Furthermore, Ni/g-C_3N_4 catalyst demonstrated the strong desorption of CO on the active sites of the catalyst which can be attributed to the increase in basic sites. In terms of CO methanation performance, Ni/g-C_3N_4 exhibits good catalytic activity with 79.7% CO conversion and 73.9% CH_4 selectivity. The good performance of Ni/g-C_3N_4 catalyst can be ascribed to the enhanced of CO adsorption and activation on the active sites as well as surface basicity.

Funding: This research was funded by Universiti Kebangsaan Malaysia (UKM) under research grant DIP-2018-021.

Acknowledgments: The authors wish to thank the Universiti Kebangsaan Malaysia for funding this project and the Centre of Research and Innovation Management (CRIM) UKM for the use of the instruments.

References

1. Hu, S.; Li, F.; Fan, Z.; Wang, F.; Zhao, Y.; Lv, Z. Band gap-tunable potassium doped graphitic carbon nitride with enhanced mineralization ability. *Dalt. Trans.* ***2015***, *44*, *1084–1092.*
2. Liu, X.; Ji, H.; Wang, J.; Xiao, J.; Yuan, H.; Xiao, D. Ozone treatment of graphitic carbon nitride with enhanced photocatalytic activity under visible light irradiation. *J. Colloid Interface Sci.* ***2017***, *505*, *919–928.*
3. Mansor, N.; Miller, T.S.; Dedigama, I.; Jorge, A.B.; Jia, J., Brázdová, V.; Mattevi, C.; Gibbs, C.; Hodgson, D.; Shearing, P.R.; Howard, C.A.; Corà, F.; Shaffer, M.; Brett, D.J.L.; McMillan, P.F. Graphitic Carbon Nitride as a Catalyst Support in Fuel Cells and Electrolyzers. *Electrochim. Acta* ***2016***, *222*, *44–57.*
4. Park, H.; Youn, D.H.; Kim, J.Y.; Kim, W.Y.; Choi, Y.H.; Lee, Y.H.; Choi, S.H.; Lee, J.S. Selective Formation of Hägg Iron Carbide with g-C3N4 as a Sacrificial Support for Highly Active Fischer-Tropsch Synthesis. *ChemCatChem* ***2015***, *7*, *3488–3494.*
5. Chen, Z.; Zhang, J.; Zheng, S.; Ding, J.; Sun, J.; Dong, M.; Abbas, M.; Chen, Y.; Jiang, Z.; Chen, J. The texture evolution of g-C3N4 nanosheets supported Fe catalyst during Fischer-Tropsch synthesis. *J. Mol. Catal. A* ***2018***, *444*, *90–99.*

6. Martha, S.; Nashim, A.; Parida, K.M. Facile synthesis of highly active g-C3N4 for efficient hydrogen production under visible light. *J. Mater. Chem. A* ***2013****, 1, 7816–7824.*
7. Wang, L.; Wang, C.; Hu, X.; Xue, H.; Pang, H. Metal/Graphitic Carbon Nitride Composites: Synthesis, Structures, and Applications. *Chem. – An Asian J.* ***2016****, 11, 3305–3328.*
8. Ye, T.; Durkin, D.P.; Banek, N.A.; Wagner, M.J.; Shuai, D. Graphitic Carbon Nitride Supported Ultrafine Pd and Pd–Cu Catalysts: Enhanced Reactivity, Selectivity, and Longevity for Nitrite and Nitrate Hydrogenation. *ACS Appl. Mater. Interfaces* ***2017****, 9, 27421–27426.*
9. Safaei, J.; Mohamed, N.A.; Mohamad Noh, M.F.; Soh, M.F.; Ludin, N.A.; Ibrahim, M.A.; Wan Isahak, W.N.R.; Mat Teridi, M.A. Graphitic carbon nitride (g-C3N4) electrodes for energy conversion and storage: a review on photoelectrochemical water splitting, solar cells and supercapacitors. *J. Mater. Chem. A* ***2018****, 6, 22346–22380*.
10. Li, Y.; Wang, M.-Q.; Bao, S.-J.; Lu, S.; Xu, M.; Long, D.; Pu, S. Tuning and thermal exfoliation graphene-like carbon nitride nanosheets for superior photocatalytic activity. *Ceram. Int.* ***2016****, 42, 18521–18528.*
11. Sabatier, P.; Senderens, J.B. New synthesis of methane. *C. R. Hebd. Seances Acad. Sci.* ***1902****, 134, 514–516.*
12. Cao, H.-X.; Zhang, J.; Guo, C.-L.; Chen, J.G.; Ren, X.-K. Highly dispersed Ni nanoparticles on 3D-mesoporous KIT-6 for CO methanation: Effect of promoter species on catalytic performance. *Chinese J. Catal.* ***2017****, 38, 1127–1137.*
13. Tsygankov, A.A.; Makarova, M.; Chusov, D. Carbon monoxide as a selective reducing agent in organic chemistry. *Mendeleev Commun.* ***2018****, 28, 113–122.*
14. Abu Tahari, M.N.; Salleh, F.; Tengku Saharuddin, T.S.; Dzakaria, N.; Samsuri, A.; Mohamed Hisham, M.W.; Yarmo, M.A. Influence of hydrogen and various carbon monoxide concentrations on reduction behavior of iron oxide at low temperature. *Int. J. Hydrogen Energy* ***2019****, 44, 20751–20759.*
15. Ping, D.; Dong, X.; Zang, Y.; Feng, X. Highly efficient MOF-templated Ni catalyst towards CO selective methanation in hydrogen-rich reformate gases. *Int. J. Hydrogen Energy* ***2017****, 42, 15551–15556.*
16. Thomas, A.; Fischer, A.; Goettmann, F.; Antonietti, M.; Müller, J.-O.; Schlögl, R.; Carlsson, J.M. Graphitic carbon nitride materials: variation of structure and morphology and their use as metal-free catalysts. *J. Mater. Chem.* ***2008****, 18, 4893–4908.*
17. Abu Tahari, M.N.; Salleh, F.; Tengku Saharuddin, T.S.; Samsuri, A.; Samidin, S.; Yarmo, M.A. Influence of hydrogen and carbon monoxide on reduction behavior of iron oxide at high temperature: Effect on reduction gas concentrations. *Int. J. Hydrogen Energy* ***2021****, 46, 24791–24805.*
18. Mohammadzadeh Valendar, H.; Rezaie, H.; Samim, H.; Barati, M.; Razavizadeh, H. Reduction and carburization behavior of NiO-WO3 mixtures by carbon monoxide. *Thermochim. Acta* ***2014****, 590, 210–218.*
19. Sakai, N.; Chida, T.; Tadaki, T. Reduction of Nickel Oxide with Carbon Monoxide Accompanied by Carbon Deposition. *Kagaku Kogaku Ronbunshu* ***1988****, 14, 368–373.*
20. Gu, Q.; Gao, Z.; Zhao, H.; Lou, Z.; Liao, Y.; Xue, C. Temperature-controlled morphology evolution of graphitic carbon nitride nanostructures and their photocatalytic activities under visible light. *RSC Adv.* ***2015****, 5, 49317–49325.*
21. Das, D.; Banerjee, D.; Mondal, M.; Shett, A.; Das, B.; Das, N.S.; Ghorai, U.K.; Chattopadhyay, K.K. Nickel doped graphitic carbon nitride nanosheets and its application for dye degradation by chemical catalysis. *Mater. Res. Bull.* ***2018****, 101, 291–304.*
22. Niu, P.; Zhang, L.; Liu, G.; Cheng, H.-M. Graphene-Like Carbon Nitride Nanosheets for Improved Photocatalytic Activities. *Adv. Funct. Mater.* ***2012****, 22, 4763–4770.*
23. Shi, L.; Liang, L.; Ma, J.; Wang, F.; Sun, J. Enhanced photocatalytic activity over the Ag2O–g-C3N4 composite under visible light. *Catal. Sci. Technol.* ***2014****, 4, 758–765.*
24. Ahmad, K.N.; Anuar, S.A.; Wan Isahak, W.N.R.; Rosli, M.I.; Yarmo, M.A. Influences of Calcination Atmosphere on Nickel Catalyst Supported on Mesoporous Graphitic Carbon Nitride Thin Sheets for CO Methanation. *ACS Appl. Mater. Interfaces* ***2020****, 12, 7102-7113.*

25. Mohamed, M.A.; M. Zain, M.F.; Jeffery Minggu, L.; Kassim, M.B.; Saidina Amin, N.A.; W. Salleh, W.N.; Salehmin, M.N.I.; Md Nasir, M.F.; Mohd Hir, Z.A. Constructing bio-templated 3D porous microtubular C-doped g-C3N4 with tunable band structure and enhanced charge carrier separation. *Appl. Catal. B Environ.* ***2018****, 236, 265–279.*
26. Gao, J.; Jia, C.; Li, J.; Zhang, M.; Gu, F.; Xu, G.; Zhong, Z.; Su, F. Ni/Al2O3 catalysts for CO methanation: Effect of Al2O3 supports calcined at different temperatures. *J. Energy Chem.* ***2013****, 22, 919–927.*
27. Tao, M.; Meng, X.; Lv, Y.; Bian, Z.; Xin, Z. Effect of impregnation solvent on Ni dispersion and catalytic properties of Ni/SBA-15 for CO methanation reaction. *Fuel* ***2016****, 165, 289–297.*

Kinetics of toluene dry reforming reaction using Jordanian kaolinite as a catalyst

Ziad Abu El-Rub *, Rajwa Abu Hassan and Rami Alnajjar

Pharmaceutical and Chemical Engineering Department, German Jordanian University, Amman, 11180, Jordan

***** *Corresponding author: ziad.abuelrub@gju.edu.jo.com; Tel.: +962-64294412.*

Abstract: Tar and carbon dioxide removal is an important research topic that contributes to improving quality of the producer gas and enhancing efficiency of the gasification technology. This work aimed to study the raw Jordanian kaolinite as a potential catalyst for the removal of tar produced in biomass gasification processes. The crushed and sieved material to 0.5 mm was characterized by TGA, BET and XRF analyses. Furthermore, the catalytic activity of kaolinite for tar removal was measured by finding the apparent first-order kinetic parameters of the dry reforming reaction of the toluene model tar component in the temperature range of 750-900 °C under atmospheric pressure of carbon dioxide and nitrogen. It was found that both dry reforming and thermal cracking reactions occurred simultaneously. Furthermore, the raw kaolinite achieved significant tar removal (80% at 900°C), with activation energy and frequency factor of 209 kJ/mol and 5.86×10^9 s^{-1}, respectively. Capitalizing on its catalytic activity in the raw or modified form and its high efficacy as a fluidized bed material, kaolinite can have great potential in primary and secondary tar reduction measures.

Keywords: toluene; dry reforming; kaolinite; catalyst; biomass; gasification.

Methylene Blue Active Substances (MBAS-SDBS) Contaminants Removal by Natural Zeolite, Adsorption Isotherm, Kinetic and Thermodynamic Studies

Aymen A. Awad[1], Raha M. Kharabsheh[2], Bashar Alsmadi[3], Mohammad A. Alhusban[4], Kamel Alzboon[5]

1+4Middle East University, Faculty of Engineering - Civil Engineering Department Amman, Jordan

2Doctorate program engineering and management, Polytechnic University of Madrid, Spain

3 Jordan University – Civil Engineering Department – 5 Al-Balqa Applied University

** Corresponding author: aawad@meu.edu.jo, 00962797980703*

Abstract: Removal of surfactants from contaminated wastewater is highly recommended particularly in water poor countries such as Jordan. Jordan's annual renewable water resources are less than 100 m3 per capita, which is below the threshold of 500 m3 per capita which defines severe water scarcity [1]. Zeolite is a natural substance originates in Jordan with a high quantities and one of the most adsorbent material used for removal of different liquid solid waste contaminants. This research was carried out to study and investigate the adsorption capacity of natural zeolite to eradicate the (MBAS-SDBS) from contaminated carwash wastewater effluents using a batch-sorption experiment, the effects of different parameters on the sorption processes were tested and studied, such as sorbent contaminants concentration, contact time and acidity (pH). It was found that the optimal conditions of removal are as following: contact time is one hour, experimental temperature is 250C, adsorbent dose of 1gram with optimal removal efficiency percent is 93.2 % and the uptake capacity is 0.885 mg/g. The physical and chemical adsorption isotherms were applied such as Langmuir, Frenudlich and Pseudo Second Order models, the results showed that the first order Langmuir model correlation coefficient R2 is 99% compared to the second, third, fourth Langmuir order with R2 =95.4%, 96.4%, 96.6% respectively. Freundlich isotherm were also investigated with R2 equals 98.8%, and finally the Pseudo–model showed that the best fit for the adsorption process with R2 = 99.9% using adsorbent dose of 0.1, 0.5 and 1.0 grams of zeolite dosage.

Keywords: Natural Zeolite, Activated Carbon, Methylene Blue Active Substances MBAS, Dedecyl benzene sulfonate SDBS, Pseudo-Model, Langmuir Model.

Preliminary Evaluation of Piston Reactor Technology for Methane Reforming Reactions

Ma'moun Al-Rawashdeh*, Aya Abusrafa, Mary Anna Katebah, and Patrick Linke.

Department of Chemical Engineering, Texas A&M University at Qatar, Education City, Doha, Qatar

***** *Corresponding author: mamoun.al-rawashdeh@qatar.tamu.edu; Tel.:+97444230439*

Abstract: The chemical industry is under immense pressure to find ways to reduce its carbon emission and develop more sustainable processes. The price of renewable electricity has sharply reduced over the past years. This drives the industry to explore it for powering their energy-intensive unit operations and achieving process intensification. One promising option in this direction is the Piston Reactor Technology. It is based on the idea of repurposing a conventional automotive engine, but now to produce chemicals - the exhaust gases here would become valuable products. Advantages of such a technology include very high temperature and pressure conditions at short residence times with rapid quenching to preserve the metastable desired products, besides it is simple and compact reactor design. Exploring and developing a new reactor technology is far from trivial and it is resource-intensive. In this work, we developed three separate tools to assess this reactor technology for industrially important methane reforming reactions. These tools include process design and techno-economic analysis; a reactor model based on a zero-D thermodynamic piston model; and a piston reactor experimental station needed for validation and demonstration. Preliminary results from these studies and how they are linked to evaluating this technology will be presented.

Keywords: Reactor engineering; Process intensification; Piston reactor; Techno-economic; Methane reforming.

1. Introduction

The chemical industry is under immense pressure to find ways to reduce its carbon emission and develop more sustainable processes. The price of renewable electricity has sharply reduced over the past years driving many companies to explore it for powering their energy-intensive unit operations [1]. Besides, it is an opportunity to achieve process intensification if the electricity is introduced in anon-conventional manner. For example, conventional steam methane reforming could be 100 times smaller when replaced by electric heating elements directly integrated with the required heterogeneous catalyst [2]. Electrification of the chemical industry is a rapidly growing field and will remain as such in the coming period.

The piston reactor technology is an emerging concept that offers a simple, safe, and compact medium for carrying out chemical reactions [3]. This reactor is very similar to the traditional internal combustion engine. A gas or gas-liquid stream can be injected into a cylindrical volume that is compressed via a reciprocating piston as shown in Figure 1.(i). Very high pressures of hundreds of bars and high temperatures even above 1500 K, can be realized for very short pulses of time typically in the milliseconds range. In some special design, sub-millisecond pulses with 3000 bar, and 4000 Khave been claimed that is never realized by conventional chemical reactors as shown in Figure 1.(ii).Moreover, chemical reactions can be quickly heated and quenched in less than a second due to the nature of the chemical reactor operation in which heating and

cooling are realized by adiabatic compression and expansion, respectively. This simplifies the process up and down streams. Last, thevery small reaction volume pulses at a very high frequency allow a high production rate with a smallreactor volume. Due to all of these unique technical capabilities, conducting chemical reactions in a reciprocating compression reactor opens a new realm for exploration, process intensifications, and innovation. Piston reactors have been studied for various applications including syngas production bymethane or natural gas partial oxidation, and steam methane reforming. Besides, it is also used to synthesis nanoparticle, produce nitric oxide, synthesize ammonia, acetylene, sulphur, and methanol,amongst others [3].

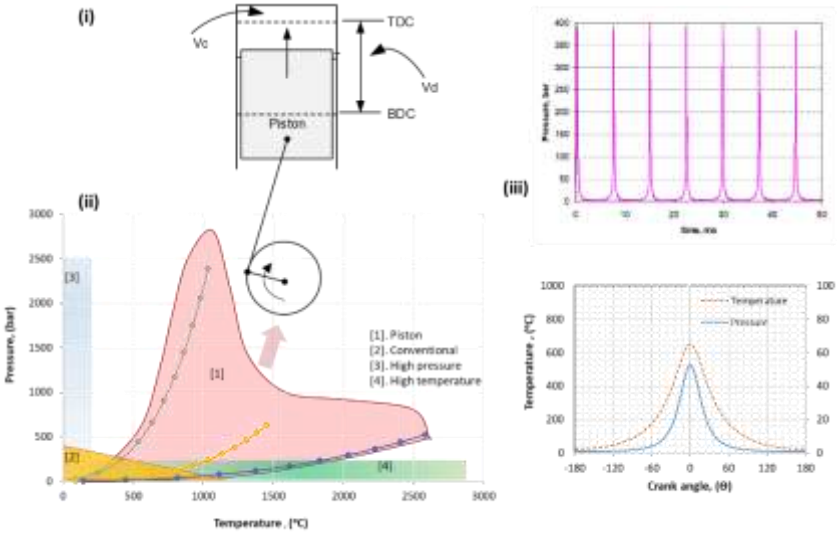


Figure 1. Schematic of a piston reactor (i), and operating temperature and pressure window compared to other reactors (ii), and the periodic operation shown for multiple cycles and a single cycle with the temperature profile (iii).

Methane is a strategic feedstock for the production of many basic chemicals. Current industrial routes to convert methane start with one of the methane reforming reactions to make either hydrogen or syngas depending that depends on the final application. These reactions emit around 8 to 14 kg of CO2/kg of H2 depending on the technology used. However, they are highly optimized technologies and have very competitive production costs which make them difficult to compete with. Reforming reactions are mainly that of steam methane reforming (SMR) which react methane with water and used mainly to maximize the amount of hydrogen produced, and it is endothermic. The second is partial oxidation of methane (POX) which reacts with methane and oxygen, has a lower H2 to CO ratio, and is exothermic.

The most studied application for the piston reactor so far is that of POX followed by SMR. Themain focus of those earlier works was mainly at the reactor level. These include (i) proof of concept that the reaction is proceeding, (ii) understand how to optimize and improve the reaction performance, and (iii) overcoming one of the technical challenges faced by the reactor such as lubrication, leakages, and blocking of the reactor. However, developing and innovating a new reactor technology requires accounting for other equally important factors beyond the reactor level. They should include the effect of the separation train, utilities used, and the heat integration network. These are essential to better

define the expected production cost, emissions, and the limitations and opportunities for making such a process more competitive. Besides, guiding the experiments at the laboratory scale.

This work is based on establishing three separate tools and then combines them to evaluate the piston reactor technology for the methane POX and SMR reforming reactions. The first of these tools is the process design and techno-economic analysis. It clarifies, quantifies and compares, the piston reactor process flow diagram and metrics to its respective conventional technology. The second tool is the piston reactor model. It provides the mass and energy balance needed to supports the process level design, supports scale-up, and enables comparing the reactor metrics to its respective conventional technology. Moreover, the reactor model will be valuable to guide experimental work. The last tool is an experimental piston reactor testing station. It is used for validation, exploration, and demonstration. All of these tools belong to an ongoing research project and the preliminary data from these three tools will be presented and demonstrated here. The interaction between these tools and how they support the overall objective to assess this reactor technology will be presented.

2. Materials and Methods

2.1. Process design and techno-economic analysis

Standard steady-state processes for methane POX and SMR for hydrogen production are designedas benchmarks to assess the performance of the piston reactor-based processes shown in Figure 2. The flowsheets are simulated in AspenPlus software using the HYSPR thermodynamic property package. For the conventional routes, the reforming reactors are modeled as adiabatic RGibbs reactors, whereas the WGS reactors are modeled as REquil. To model the air separation unit (ASU), an input output model was used with power consumption of ~0.35 kWh/Nm^3 oxygen [4]. Heat Integration Pinch Analysis was conducted to enhance heat recovery in the systems and produce electricity from the excess heat generated in the processes [5] . To meet the energy demands, a heat exchanger network (HEN) is designed for each process. In the economic analysis, capital and operating costs of the processes are calculated assuming a plant lifetime of 20 years. These were used to estimate a hydrogen production cost for each process. As shown in Figure 1, process flowsheets are designed for the piston-reactor based POX process. The performance of the piston reactor in the simulations is described using an input-output.model.

The piston reactor model is based on experimental laboratory studies reported in the literature for the reaction. Mass and energy balances around the piston reactor are estimated from thezero-D thermodynamic model developed in this work. The hydrogen production capacity in the pistonreactor process is considered to be the same as the conventional one.

2.2. Zero-D piston reactor model

The piston reactor performance is predicted using a zero-dimensional thermodynamic model. The simulation comprises of compression and expansion strokes, beginning at the bottom dead center (BDC) with the valves closed. The crankshaft is then rotated fully until the exhaust valve’s opening time. The model represents a single-cylinder piston reactor with a variable volume profile according to the piston’s geometrical dimensions. The model takes into account the time/crank angle changes of temperature, pressure, volume, in addition to species’ concentrations. The spatial gradients in the piston chamber are not considerd in the model. The temperature rise is predicted based on the conservation of energy applied around the cylinder volume [6]. Concentration variations, as a result of chemical reactions during the compression-expansion strokes, are calculated based on time-dependent kinetic models from the literature. Kinetics for the partial oxidation reaction is predicted by a combined reaction scheme for

methane steam reforming by Xu and Froment [7] and complete methane combustion by Trimm and Lam [8]. The model is discretized into short time steps. A set of differential equations representing the energy and mass balances are simultaneously solved for each step using a built-in MATLAB ODE45 integrator. A reference case in the literature is used to validate the model [9]. Total heat release is calculated in order to quantify the energy produced in the reaction. This energy comprises of mechanical work, heat losses, and process heat released with the effluent stream. The power produced per cycle, amajor product of piston-reactor systems, is calculated by estimating the area beneath the pressure-volume curve. Heat losses through the walls of the piston reactor are calculated using Hohenberg et al.'s empirical convective heat transfer correlation [10]. The energy remaining leaves the system in the hot exhaust gases. Inlet temperature, pressure, RPM, feed composition, and compression ratio are all investigated to elucidate a feasible operating window to carry out the proposed reactions. Similarly, aconventional plug flow reactor (PFR) model was developed to benchmark the piston reactor in terms ofconversion and productivity.

2.3. Piston reactor experimental testing station

An experimental testing station is currently under commissioning at Texas A&M Univerity at Qatar. It will be used for validation, exploration, and demonstration purposes of the piston reactor technology. This facility is operational but not yet ready to carry out chemical reactions. The station consists of a commercial internal combustion engine (single piston) that is being repurposed as a piston reactor; an electric motor is used to drive and maintain the piston RPM at the target value; an in-cylinder pressure sensor is used to precisely monitor the pressure profile during compression and expansion strokes; a torque meter is used as well for monitoring purposes. In addition, the system contains other components as gas cylinders, piping, flow meters, ventilation system, and the automation and control system. At this stage, the RPM, and gas flow rate are varied and the in-pressure cylinder is being recorded and compared to the pressure profile as predicted by the zero-D piston reactor model

3. Results and Discussion

3.1. Process design and techno-economic analysis

A process flowsheet for a conventional POX reactor technology is developed as shown in Figure2. This process was designed to maximize the amount of produced hydrogen. For the piston reactor, the process flowsheet was developed differently. One of the main differences is that air is used rather than pure oxygen as the oxidant for the POX [3]. Since air used directly in the piston reactor for methane to syngas production, the process does not include an air separation unit. After cooling the produced syngas, water is separated from it, and the mixture is routed to a membrane separation unit. Hydrogen is separated before the water gas shift (WGS) reactions to shift the equilibrium in the right direction and increase the conversion of CO to hydrogen. This resulted in a 10% increase in hydrogen production. The WGS reactors, incinerators, and PSA units are modeled such that they operate at the same conditions as the conventional case. A membrane system is used for the first hydrogen separation, as it is a more suitable separation technology for nitrogen-rich syngas. Similar to the conventional case, a 2-step PSA process operating at 23 bar and 25 ºC is used to ensure the purity of hydrogen is realized. Tail gas from the second PSA gets mixed with the second membrane's retantate, after which it gets pressure-reduced, and treated in the catalytic incinerator. Similar process flow sheets are developed for SMR.

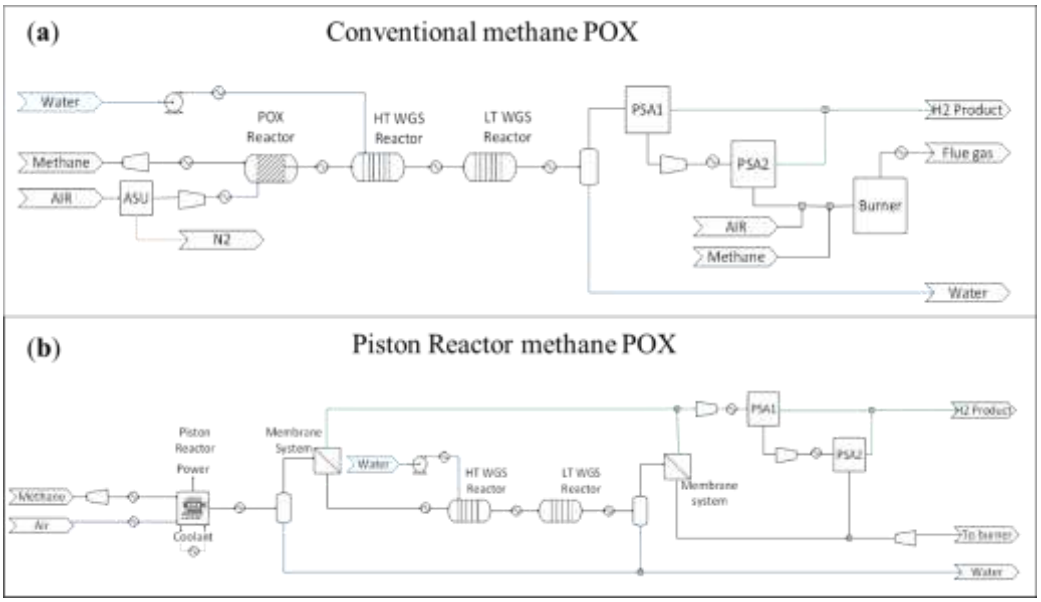


Figure 2. Process flow diagram of two processes: (**a**) conventional methane POX process; (**b**) Piston reactor methane POX.

Heat integration and economic analyses were performed on all the processes. For comparison purposes, all the processes were designed with a hydrogen production capacity of 500 metric tons/day. Afterward, different key process metrics are calculated as shown in Table 1. The metrics of POX and SMR for the conventional reactor technology are presented. The reported metrics match those mentioned in the literature which validated the approach used here. The process metrics of the piston

reactor processes are calculated in the same manner. When compared versus the conventional basis, all processes were self-sufficient concerning heating and power requirements. However, the piston reactor process utilizes more methane feed due to the lower methane conversion, and water production by hydrogen combustion in the reactor.. In addition to operating the reactor on air rather than oxygen, larger feedstock requirements in the piston reactor process lead to a a hydrogen production cost that is approximately 2.5 times higher than the conventional process. Higher CO2 emissions are observed inthe piston reactor process comarped to the conventional one due to the larger amounts of methane feed.The POX piston reactor-based process has large amounts of excess heat that can be used for capturingand storing a portion of the released carbon dioxide to lower the emissions. Relative to the base case,around 30% less CO2 can be emitted when using the process's excess heat for carbon capture and storage.

Although the results showd that the piston reactor technology is not as competitive in terms of hydrogen production cost, the excess heat available in the process result in lower CO2 emissions compared to the conventional process. It is worth mentioning that the above conclusion is reached for one condition from the piston reactor. In case the piston reactor is optimized, the process metrics will change. All of the above findings make clear suggestions on what needs to be aimed at for the piston reactor process to be more competitive. Also, determins the experimental targets that should be aimed at. For example, avoid using air and use oxygen instead which eliminates all of the nitrogen that flows throughout all of the separation trains. Operate the piston reactor at higher inlet and outlet pressures. Currently, the piston reactor operates at atmospheric inlet pressure while all separation is conducted atmuch higher pressure which requires using of compressors that constitute a major part of the cost. And,maximize the methane conversion and amount of hydrogen produced by optimizing the piston reactorconditions. All of these findings would not have been feasible without doing this type of activity.

Table 1. Comparison between SMR and POX for conventional reactors
(MT:Metric ton. Methane price: $3.9/MMBtu)

Parameter	Unit	SMR	POX
H2 Produced (Plant capacity)	MT per day	500	500
Natural Gas Demand	MT NG/ MT H2	3.0	3.0
Water Demand (WGS)	MT H2O/ MT H2	8.8	5.1
Oxygen Demand	MT O2/ MT H2	-	3.1
CO2 Emitted	MT CO2/ MT H2	8.2	8.2
Power demand	MWh/ MT H2	0	0
Heating utilities	MWh/ MT H2	0	0
CAPEX	$/MT H2	272	417
OPEX	$/ MT H2	804	887
Hydrogen production cost	$/ MT H2	1,076	1,304

3.2. Piston reactor benchmarking based on Zero-D piston reactor model

A case study of an industrial steam reformer was simulated using a conventional PFR model. The operating conditions typically used in industrial steam reformers were adopted from the open literature [11]. Numerical simulations were run using the kinetic model developed by Xu and Froment [7]. Afterward, the same kinetics were used in the piston reactor model. The performance was

validated versus reported experimental data for POX reaction using the piston reactor [12]. After that, a parametric study was carried out to identify the conditions needed to achieve hydrogen productivity similar to the PFR reactor model. Figure 3 shows some of the results from these parametric studies for the SMR case. By increasing the intake temperature, the methane conversion, hence hydrogen production is significantly increased. The latter shows good agreement with thermodynamic studies, suggesting that high temperatures favor the highly endothermic methanation reaction in steam reforming. To achieve the same hydrogen production rate of 30.15 mol/ (m3. s) as that of PFR, the piston reactor needs to operate at Tintake = 820 K and N=1000 RPM. This is 310K lower than the PFR case which minimizes the preheating energy requirements. Besides, the amount of catalyst needed in the piston reactor is more than 1000 times less when compared to the conventional reactor. When the piston reactor was simulated with an intake temperature of 1130 K (similar to the PFR) and 5000 RPM, the hydrogen production rate achieved would be approximately five-folds higher compared to the PFR case.

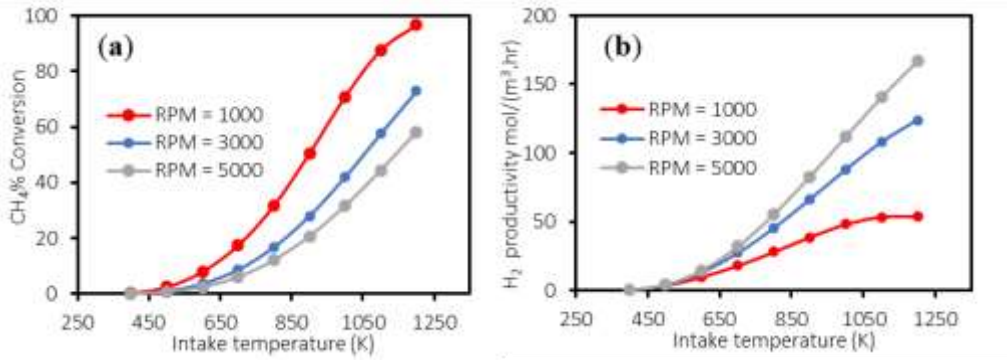


Figure 3. Effect of intake temperature (400-1200K) and speed (100-300 RPM) on (a) methane conversion and (b) hydrogen production rate at 1 bar pressure for SMR process.

These initial studies show great potential for the piston reactor technology in contributing toenergy minimization, compact design, and having a reactor that is driven by renewable electricity. Although a quick screening and benchmarking tool was developed and demonstrated in this work, two challenges are limiting the direct utilization of these findings. The limited validity of the kinetic models which are based on fixed-bed reactor technology for narrow operating windows, and the use of heterogeneous catalysts which is still a challenge to handle in the piston reactor.

In addition to comparing the performance metrics to conventional reactor technology, the developed model was used successfully providing the full mass and energy balance around this reactor as shown in Figure 4. This is essential information when doing process techno-economic evaluation. When reviewing the literature, this type of data seems scarce as most work focuses on some aspects but not the full evaluation. This demonstrates the great potential of the approach proposed in this article to combine multiple tools simultaneously right from the start of the development.

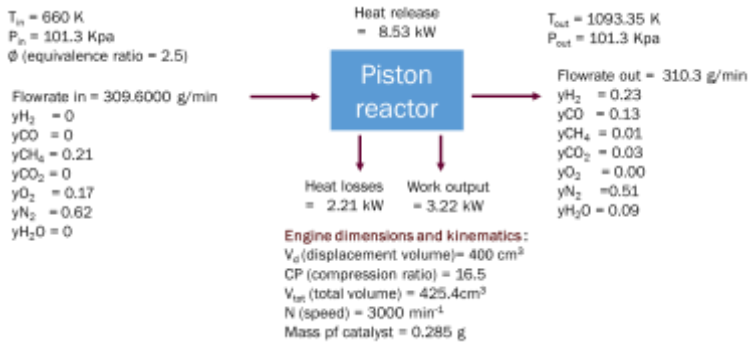


Figure 4. An example of the mass and energy balance from the piston reactor model for POX of methane is provided to the process techno-economic study part.

3.3. Piston reactor experimental testing station

An image of the piston reactor setup under commissioning is shown in Figure 5. The piston reactor used here is a repurposed single-piston ICE engine. Designing, commissioning, and operating such an experimental facility is not straightforward. This is mainly due to the highly multidisciplinary nature of this reactor, and the fact that it is a repurposed engine that is fully optimized for that purpose and not to produce chemicals. For example, there is no guarantee or knowledge available on what is a safe operating window for this device regarding the inlet/outlet temperature and pressure. However,for such an exploration stage this is an acceptable decision. There are other piston reactor designs available that can be used to overcome some of the limitations of this ICE base design if needed [3].



Figure 5. Image of the experimental setup that shows the piston reactor (a repurposed single-cylinderICE engine) and the electric motor that drives it.

Monitoring the reaction performance in the piston chamber is an essential task but also a challengingone due to the limited space available. The best option to opt for is to use an in-cylinder piezoelectric pressure sensor. In this case, it will be placed in the same location as that of the spark plug. The obtainedpressure profile is used to validate the piston reactor thermodynamic model. Such a validation enables predicting the temperature profile which is the essential parameter to simulate any reaction performance in such a reactor type as demonstrated in the previous section.

Figure 6 shows the pressure profile obtained using the mentioned experimental setup at different RPM and flow rates with nitrogen gas. For two of the conditions, the pressure at the piston inlet valve increased (marked with * in the figure). This indicates an overflow to the piston at that given RPM. An increased inlet pressure increases the peak pressure which is observed in the presented data. For the other conditions, equal or underflow has been observed. When operating in the underflow condition, the pistoninlet pressure is reduced and as a result, the peak pressure is also reduced. This is evident when observingthe results at a given RPM and reducing the flow rate as in the case of 1500 RPM.

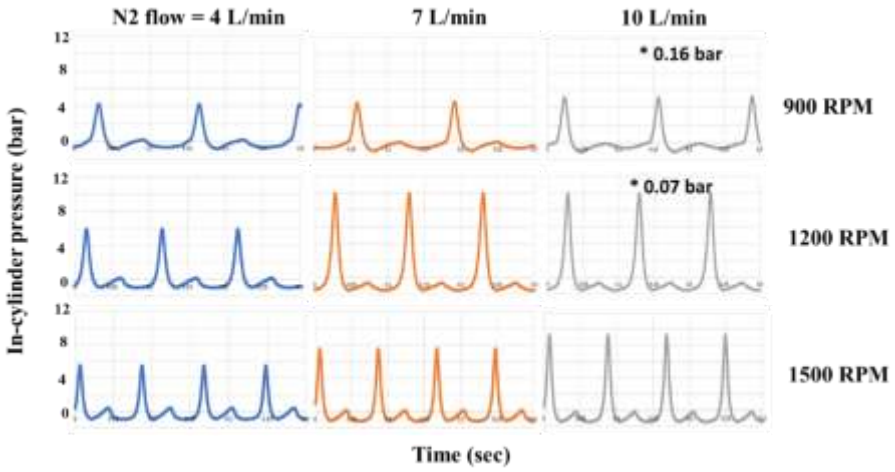


Figure 6. In-cylinder pressure measurements at different inlet gas flow rates and RPM of the piston reactor. The two conditions marked with * have an inlet gauge pressure larger than zero.

4. Conclusions

This work aims to evaluate the potential of the piston reactor technology for two industrially important methane reforming reactions, the partial oxidation for methane and the steam methane reforming. This work presents the development of three separate tools and how they are used for this evaluation. Process flow diagrams are designed for the two reactions using the piston reactor technology and benchmarked against the conventional process routes. Under the tested conditions, results showed that the piston reactor is not competitive in terms of production cost mainly due to the use of air instead of oxygen, the low-pressure operation, and the low obtained methane conversion. Besides, this study was not done at optimized piston reactor conditions. However, the key outcome was in identifying the process design choices, operating conditions, and target conversions that are needed to make this technology more competitive. The second developed tool was the zero-D piston thermodynamic model. It proofs valuable to benchmark the reactor metrics versus conventional flow reactors and shows the compactness of the piston reactor. Additionally, this model provided a complete mass and energy balance that are essential for techno-economic studies. Such data were difficult to find in the open literature. Moreover, this simple reactor model is a promising option for early-stage screening of chemical reaction candidates and guiding essential but expensive experimental work. The last tool presented which is still under commissioning was the piston reactor experimental testing station. Some light was shed on how such an experimental facility looks like and presented one of the key monitoring sensors in this setup which is the in-cylinder pressure sensor. The results presented here are preliminary ones as this is research in progress. However, the presented tools and how they are linked together showed new insights that can hider the development of this reactor technology which would be not possible to identify if each tool was developed and presented separately. The entire presented work has two main assumptions that still need to be experimentally validated. The limited validity of the kinetic models which are based on fixed-bed reactor technology that has a very narrow operating window. And the use of heterogeneous catalyst which is still a challenge to handle in the piston reactor.

The combination of very high temperatures and pressures attained in short pulses is a unique feature of the piston reactor technology that hardly can be achieved by other chemical reactors. Piston reactor has a significant potential to produce high value-added chemicals and a breakthrough in energy efficiency, lower cost, modularity, portability, and safety. This technology is in its early stage of development and requires interdisciplinary effort to solve the faced technical challenges. This work paves the way toward the exploration and development of this promising but less explored reactor technology.

Funding: This work was made possible by funding from Qatar National Research Fund (QNRF) project number NPRP12S-0304-190222 and co-funding by Qatar Shell Research and Technology Center (QSRTC). The statements made herein are solely the responsibility of the author(s).

Acknowledgments: NA

References

1. Renewable Power Generation Costs | IRENA. *Renewable Power Generation* Costs in 2019; **2020**.
2. Wismann, S. T.; Engbæk, J. S.; Vendelbo, S. B.; Bendixen, F. B.; Eriksen, W. L.; Aasberg-Petersen,K.; Frandsen, C.; Chorkendorff, I.; Mortensen, P. M. Electrified Methane Reforming: A Compact Approach to Greener Industrial Hydrogen Production. *Science (80-.).* **2019**, 364 (6442), 756–759. https://doi.org/10.1126/science.aaw8775.

3. Ashok, A.; Katebah, M.A.; Linke, P.; Kumar, D.; Arora, D.; Fischer, K.; Jacobs; T., Al-Rawashdeh,
4. M. Review of Piston Reactors for the Production of Chemicals. *Reviews in Chemical Engineering*,
5. **2021**. accepted
6. Jakobsen, D.; Åtland, V. Concepts for Large Scale Hydrogen Production. **2016**. Master Thesis 145.
7. Smith, R., Chemical Process Design and Integration. *Chichester. ed. Wiley*. **2008**
8. Gossler, H.; Deutschmann, O. Numerical optimization and reaction flow analysis of syngas production via partial oxidation of natural gas in internal combustion engines. *International Journal of Hydrogen Energy*, **2015**, 40, 11046–11058. https://doi.org/10.1016/j.ijhydene.2015.06.125
9. Xu, J.; Froment, G.F.; Methane steam reforming, methanation and water-gas shift: I. Intrinsic
10. kinetics. *AIChE Journal*. **1989**, 35, 88–96. https://doi.org/10.1002/aic.690350109
11. Trimm, D.; Lam, C.-W. The combustion of methane on platinum-alumina fibre catalysts- I. *Chemical Engineering Science*. **1980**, 35.
12. Hegner, R.; Atakan, B. A polygeneration process concept for HCCI-engines – Modeling product gas purification and exergy losses. *International Journal of Hydrogen Energy*. **2017**, 42, 1287–1297. https://doi.org/10.1016/j.ijhydene.2016.09.050
13. Hohenberg, G.F. Advanced approaches for heat transfer calculations. *SAE Technical Papers*. **1979**, 2788–2806. https://doi.org/10.4271/790825
14. Elnashaie, S. S.; Uhlig, F. Numerical techniques for chemical and biological engineers using MATLAB®: A simple bifurcation approach. *Springer Science & Business Media*. **2007**.
15. Goßler, H. Partial Oxidation of Natural Gas in a Piston Engine: Modeling and Simulation. Diss. Karlsruhe Institute of Technology, 2014.

Pyrolysis of High-Density Polyethylene: I. Kinetic Study

Mohammed Al-Yaari [1,*], Ibrahim Dubdub [2]

[1] Chemical Engineering Department, King Faisal University, P.O. Box 380, Al-Ahsa 31982, Saudi Arabia; malyaari@kfu.edu.sa
[2] Chemical Engineering Department, King Faisal University, P.O. Box 380, Al-Ahsa 31982, Saudi Arabia; idubdub@kfu.edu.sa
***** *Corresponding author: malyaari@kfu.edu.sa; Tel.: 00966135898583.*

Abstract: This work presents a comprehensive kinetic study of the thermal decomposition of high-density polyethylene (HDPE) to obtain the triple kinetic parameters of the reaction rate equation. Thermogravimetric analysis (TGA) tests were performed at four different heating rates (5, 10, 20, and 40 K/min) under nitrogen environment covering the temperature range of 298 – 900 K. Results showed that as the heating rate increases the pyrolysis characteristic temperatures are shifted to higher temperatures. Three integral isoconversional (model-free) methods, namely Flynn-Wall-Ozawa (FWO), Kissinger-Akahira-Sunose (KAS), and Starink models were used to best fit the experimental TGA data to obtain the activation energy of the HDPE pyrolysis. High-efficient values of activation energy (273±1 kJ/mol) were obtained by all models. In addition, Coats-Redfern was used to best find the most controlling reaction mechanism and the third-order reaction (F3) mechanism was reported as the most suitable one. Then, the values of the pre-exponential factor have been obtained by the three used models. This work clearly defines a step-by-step procedure to obtain the kinetic parameters (activation energy, and pre-exponential factor) and to determine the most suitable reaction mechanism of the pyrolysis of biomass.

Keywords: Pyrolysis; High-density polyethylene (HDPE); Activation energy; Thermogravimetric analysis (TGA); Isoconversional models; Reaction mechanism

1. Introduction

Although massive plastic wastes are being generated, the annual rate of the recycled plastic is very low [1] compared with the plastic production rate due to some limitations. Thus, most of the plastic waste is either incinerated or disposed in landfills [2,3] which results in serious environmental issues.

Municipal plastic waste (MPW) contains around: 22.7 wt% low-density polyethylene (LDPE), 17.8 wt% high-density polyethylene (HDPE), 19.6 wt% polypropylene (PP), 10.7 wt% polyvinyl chloride (PVC), 11.9 wt% polystyrene (PS), 8.1 wt% polyethylene terephthalate (PET), and 9.2 wt% other plastics. However, these compositions may change from one place to another [4].

Due to its moderate operating temperatures, wide range of application, and clean products, pyrolysis is a preferable option to recover energy from MPW as chemicals and fuels [5-9]. Therefore, extensive work has been performed to obtain the kinetic parameters of the pyrolysis of pure and mixed plastics.

Wu et al. [10] obtained the kinetic parameters of the HDPE pyrolysis using thermogravimetric analysis (TGA) data at different heating rates (1, 2, 5.5 K/min). The pyrolysis reaction was reported as a single-stage reaction and the triple kinetics parameters were reported as: (Pre-exponential factor (A)= $9.3x10^{13}$ (min^{-1}), the reaction order (n) =0.74, and the activation energy (E= 233 kJ/mol)).

Later, Conesa et al. [11] studied the thermal decomposition of HDPE isothermally and non-isothermally using TGA at different heating rates (5, 25, 50 and 100 K/min). The values of the activation energy were reported between 185 to 221.5 kJ/mol.

Aboulkas et al. [12] obtained the values of the activation energy of the pyrolysis of HDPE by Friedman, Kissinger-Akahira-Sunose (KAS) and Flynn-Wall-Qzawa (FWO) isoconversional methods at different heating rates (2, 10, 20, 50 K/min). Values were reported between 238 and 247 kJ/mol.

Chin et al. [13] investigated the pyrolysis HDPE using TGA under argon environment flowing at 100 cm3/min at different heating rates (10, 20, 30, and 50 K/min) covering the temperature range of 323–1173 K. The activation energies were found between 242.13 and 278.14 kJ/mol.

Diaz Silvarrey and Phan [2] developed a kinetic model for the pyrolysis of HDPE using TGA data. All experiments were conducted under N_2 environment at different heating rates (5, 10, 20 and 40 K/min) and covering the temperature range of 303 and 973 K. Four models, namely KAS, Málek, Friedman, and linear model fitting, were applied to obtain the kinetic parameters of the reaction. Activation energy values ranging between (202.40 ± 9.47 by KAS method) and (375.59 ± 39.69 by Friedman method) were reported.

Khedri and Elyasi [14] used four iso-conversional models (Friedman, FWO, Ozawa, and KAS) to obtain the kinetic parameters of HDPE pyrolysis using isothermal and non-isothermal TGA data at different heating rates (40, 45, 50, and 55 K/min). The reported values of activation energy varied heavily with the conversion. While the kinetic parameters obtained by Ozawa, FWO, and KAS models increased gradually as conversion increased, the values obtained by Friedman model, especially below 15% conversion, were different.

Although a good amount of work on the pyrolysis of HDPE has been conducted, there is a need to design a clear algorithm to obtain the reaction parameters to be followed. Therefore, this work aims to obtain the triple kinetic parameters (activation energy, pre-exponential factor, and reaction mechanism) of the pyrolysis of HDPE using TGA at different heating rates (5, 10, 20, and 40 K/min). Three integral isoconversional models have been used. In addition, a robust step-by-step procedure to obtain the kinetic parameters has been clearly defined.

2. Materials and Methods

2.1. Material Characterization

HDPE samples, obtained from Ipoh SY Recycle Plastic, Malaysia, have been characterized by the proximate and ultimate analysis techniques before the experimental tests. Both characterization techniques were performed using PerkinElmer Simultaneous Thermal Analyzer 6000, and PerkinElmer 2400 Series II CHNS Elemental Analyzer, USA, respectively. Details of both analyses are reported elsewhere [15] and analysis data are presented in Table 1.

Table 1. Proximate and ultimate analysis of HDPE samples

Proximate Analysis, wt%			**Ultimate Analysis, wt%**			
Moisture	**Volatile**	**Ash**	**C**	**H**	**N**	**S**
0.405	99.377	0.218	82.77	16.92	0.00	0.29

2.2. Thermogravimetric Experiments

Pellets of HDPE sample were ground by a grinding mill to produce polymer powder with an average particle size of 0.7 mm. polymer sample of 10 mg was used throughout this investigation. Thermogravimetric analysis (TGA) was performed using the PerkinElmer thermogravimetric analyzer (TGA-7), produced by PerkinElmer, Waltham, MA, USA, with a high precision weighing balance. TGA experiments were conducted under nitrogen (99.999%) gas flowing at 100 cm^3/min at four different heating rates (5, 10, 20, and 40 K/min).

2.3. Kinetic Theory

A rate of reaction (r) of most of the kinetic processes can be expressed as follows:

$$r = \frac{d\alpha}{dt} = K(T)f(\alpha) \qquad (1)$$

For non-isothermal pyrolysis, equation (1) can be expressed as:

$$r = \beta\frac{d\alpha}{dT} = K(T)f(\alpha) \qquad (2)$$

where:

α : is the reaction conversion defined as: $\alpha = \frac{w_o - w}{w_o - w_f}$;

w_o : is the weight of the HDPE sample at the beginning of each experiment (mg);

w : is the weight of the HDPE sample at time t (mg);

w_f : is the weight of the HDPE sample at the end of each experiment (mg);

t : is time (min);

K : is the reaction rate constant (min^{-1});

T : is temperature (K);

$f(\alpha)$: is the conversion-dependent term;

β : is the heating rate (K/min), and it is defined as: $\beta = \frac{dT}{dT}$;

If the reaction rate constant is assumed to obey Arrhenius relationship, equation (2) becomes:

$$\beta\frac{d\alpha}{dT} = A\exp\left(-\frac{E}{RT}\right)f(\alpha) \qquad (3)$$

where:

A : is the pre-exponential factor (K^{-1});

E : is the activation energy (kJ/mol);

R : is the universal gas constant (8.314 J/mol K).

Equation (3) can be rearranged and expressed as follows:

$$g(\alpha) = \int_0^{\alpha}\frac{d\alpha}{f(\alpha)} = \frac{A}{\beta}\int_{T_o}^{T}\exp\left(-\frac{E}{RT}\right)dT \qquad (4)$$

where:

$g(\alpha)$: is the integral form of the reaction model based on the reaction mechanism;

T_o : is the initial temperature of the HDPE pyrolysis (K).

The expression of $g(\alpha)$ is presented in Table 2 for the main reaction models including reaction-order models (F1, F2, and F3), diffusion models (D1, D2, and D3), nucleation models (A2, A3, and A4), geometrical contraction models (R1, R2, and R3), and power law models (P2, P3, and P4).

Table 2. Solid-state thermal reaction mechanism

Reaction mechanism	Symbol	$g(\alpha)$
First order reaction model	F1	$-\ln(1-\alpha)$
Second order reaction model	F2	$(1-\alpha)^{-1}-1$
Third order reaction model	F3	$[(1-\alpha)^{-1}-1]/2$
One-dimensional diffusion model	D1	α^2
Two-dimensional diffusion model	D2	$(1-\alpha)\ln(1-\alpha)+\alpha$
Three-dimensional diffusion model	D3	$[1-(1-\alpha)^{1/3}]^2$
Two-dimensional nucleation model	A2	$[-\ln(1-\alpha)]^{1/2}$
Three-dimensional nucleation model	A3	$[-\ln(1-\alpha)]^{1/3}$
Four-dimensional nucleation model	A4	$[-\ln(1-\alpha)]^{1/4}$
One-dimensional contraction model	R1	α
Contracting cylinder contraction model	R2	1-$(1-\alpha)^{1/2}$
Contracting sphere contraction model	R3	1-$(1-\alpha)^{1/3}$
Power law model II	P2	$\alpha^{1/2}$
Power law model III	P3	$\alpha^{1/3}$
Power law model IV	P4	$\alpha^{1/4}$

To obtain the reaction triple kinetic parameters (*E*, *A*, and reaction mechanism), TGA experimental data should be modelled based on equation (4). Different models are existing and can be used. In this work, three well-known isoconversional models, namely FWO, KAS, and Starink, will be used to obtain *E*, and *A*, the reaction mechanism will be obtained by a famous non-isoconversional model (Coats-Redfern). Their equations, derived/approximated from equation (4) are listed in Table 3.

In this work, using TGA data, activation energy at different conversions will be obtained by three isoconversional models. Then, the average activation energy values at 15 different reaction mechanisms obtained by Coats-Redfern model will be compared with those obtained by the isoconversional models to determine the most suitable reaction mechanism. Based on the nominated reaction mechanism, the average value of the pre-exponential factor can be calculated using isoconversional models. However, a linear relationship between *ln A* and *E* at different conversion is expected [16].

Table 3. Equations of the used models

Model	Equation	
1. Isoconversional Models		
Flynn-Wall-Qzawa (FWO)	$ln(\beta) = ln\ \frac{A\ E}{R\ g(\alpha)} - 5.331 - 1.052\frac{E}{RT}$	(5)
Kissinger-Akahira-Sunose (KAS)	$ln\left(\frac{\beta}{T^2}\right) = ln\ \frac{A\ R}{E\ g(\alpha)} - \frac{E}{RT}$	(6)
Starink	$ln\left(\frac{\beta}{T^{1.92}}\right) = Con. - 1.0008\frac{E}{RT}$	(7)
2. Non-isoconversional Model		
Coats-Redfern	$ln\left[\frac{g(\alpha)}{T^2}\right] = ln\left[\frac{A\ R}{\beta\ E}\right] - \frac{E}{RT}$	(8)

3. Results and Discussion

3.1. Thermogravimetric Analysis

The thermogravimetric (TG) and the derivative thermogravimetric (DTG) curves of the pyrolysis of HDPE at different heating rates (5, 10, 20, and 40 K/min) are shown in Figures 1 and 2, respectively. Like other plastics [17,18], the thermal decomposition of HDPE has a single inverted S-shape indicating a single reaction during the pyrolysis and occurs within the temperature range of 600 K to almost 800 K. As shown in both figures, complete decomposition has been observed and attributed to the negligible ash content as revealed by the proximate analysis.

The characteristic temperatures of the HDPE pyrolysis are presented in Table 4. As the heating rate increases these temperatures are shifted to higher temperatures (i.e., faster heating indicates lower mass loss) as shown in Figure 1. On the other hand, faster heating resulted in larger mass loss rate and thus larger peak values as shown in Figure 2.

Table 4. Characteristic temperatures of the pyrolysis of high-density polyethylene (HDPE)

Heating Rate (K/min)	Onset (K)	Peak (K)	Endset (K)
5	603	733	753
10	613	743	763
20	623	753	773
40	633	763	783

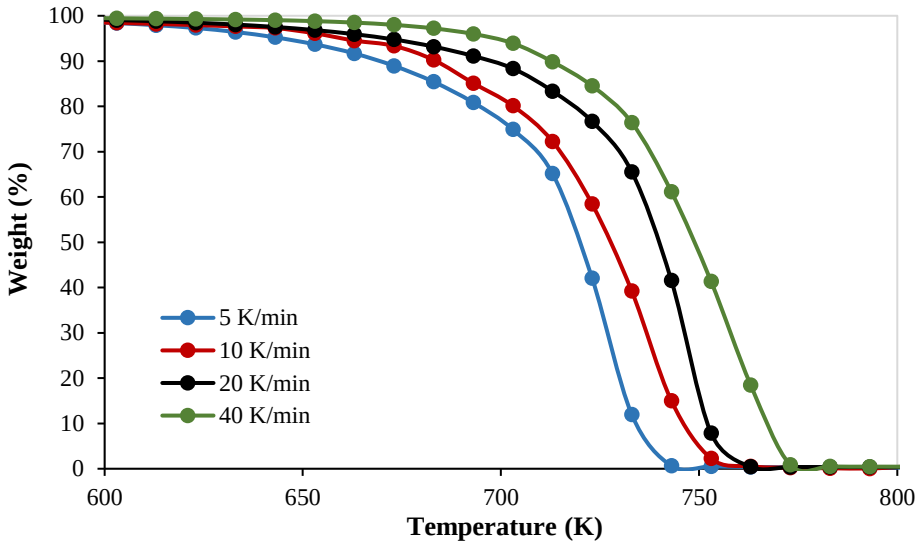


Figure 1. Thermogravimetric (TG) curves of the pyrolysis of high-density polyethylene (HDPE).

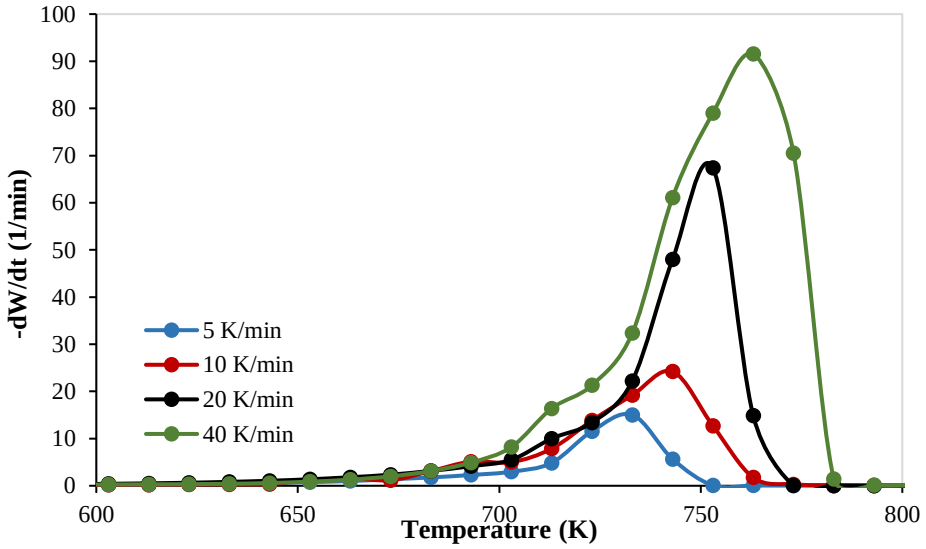


Figure *2*. Derivative thermogravimetric (DTG) curves of the pyrolysis of HDPE.

3.1. Kinetic Analysis Based on the Isoconversional Methods

To obtain the value of the main kinetic parameter (activation energy) of the HDPE pyrolysis, three integral isoconversional models, namely FWO, KAS, and Starink, have been used. Efficient linear regression of the TGA data at four different heating rates was obtained for all models (R^2>0.96) as shown in Figure 3 and Table 5 according to equations (5-7). Based on these equations, the activation energy values at different conversions can be obtained from the slope of the trendline of the fitted data. These values are presented in Table 5 and Figure 4.

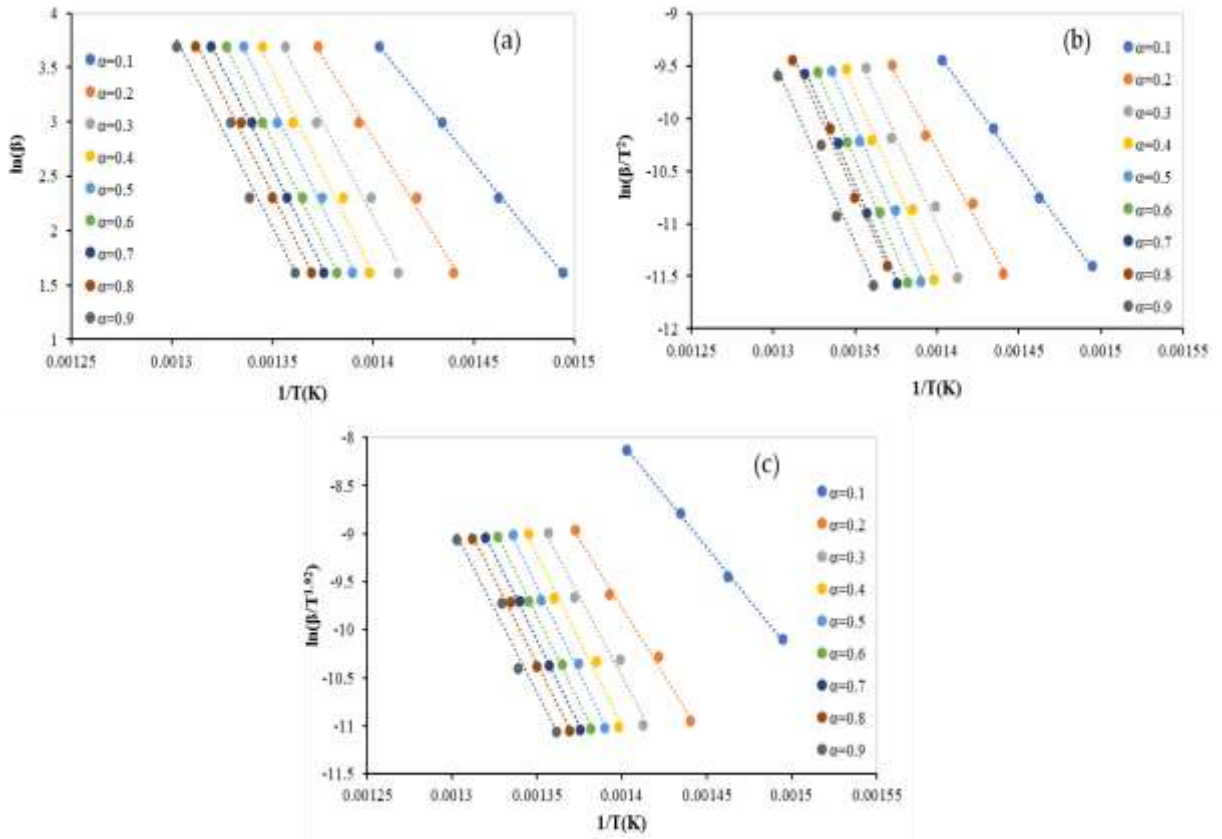


Figure 3. Linear regression lines of HDPE pyrolysis by: (a) FWO; (b) KAS; (c) Starink.

Table 5. Activation Energy values obtained by isoconversional models.

Conversion	FWO		KAS		Starink	
	E (kJ/mol)	R^2	E (kJ/mol)	R^2	E (kJ/mol)	R^2
0.1	181	0.9993	179	0.9992	180	0.9992
0.2	234	0.9929	235	0.9921	235	0.9921
0.3	276	0.9822	278	0.9807	278	0.9807
0.4	292	0.9853	295	0.9841	295	0.9842
0.5	296	0.9948	299	0.9944	300	0.9944
0.6	297	0.9992	300	0.9991	301	0.9991
0.7	294	0.9990	297	0.9989	298	0.9989
0.8	290	0.9949	287	0.9947	294	0.9945
0.9	287	0.9720	289	0.9696	288	0.9697
Average	**272**	**0.9910**	**273**	**0.9903**	**274**	**0.9903**

>0.99 The average values of the obtained activation energy by FWO, KAS, and Starink models were 272 kJ/mol, 273 kJ/mol, and 274 kJ/mol with regression coefficients of 0.991, 0.9903, and 0.9903, respectively. The very close values indicate a very accurate experimental

data. In addition, as the conversion increases from 0.1 to 0.4, the activation energy value increases as well and remain almost constant at high conversion (0.5-0.9). The obtained values are in a good agreement with some published data [2,11-14,19].

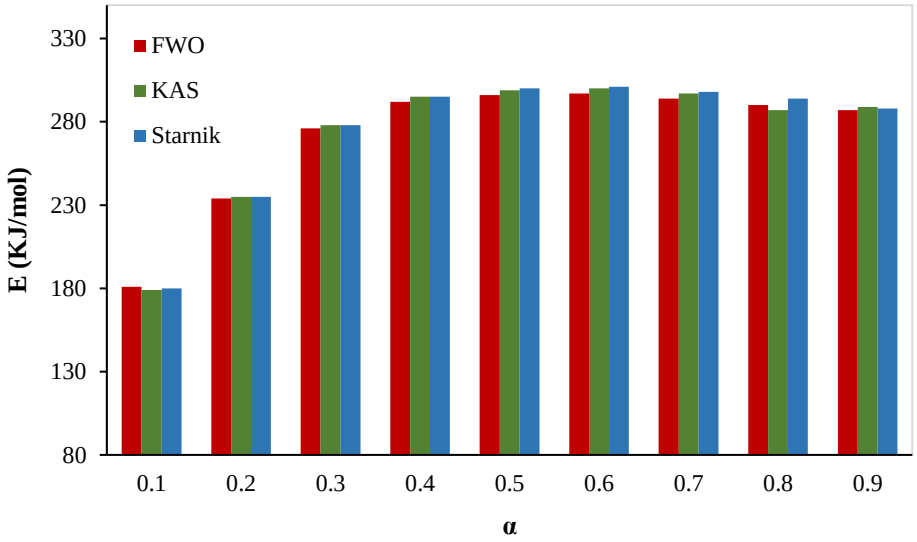


Figure 4. Dependence of activation energy on conversion.

3.2. Estimation and Verification the Reaction Mechanism

To find the reaction mechanism, Coats-Redfern model has been used (equation 8). By plotting $\ln(g(\alpha)/T^2)$ against 1/T for 15 different solid-state reaction mechanisms, presented in Table 2, linear relationships can be obtained and thus the value of the activation energy can be calculated from the slope. The activation energy values obtained by the Coats-Redfern model at different heating rates are presented in Table 6.

Then, the average values of activation energy obtained by Coats-Redfern model are then compared with the average value of the activation energy obtained by the isoconversional models (273±1 kJ/mol) to find the most suitable reaction mechanism. As shown in Table 3, the average value of the activation energy for the third-order reaction (F3) mechanism (262.5 kJ/mol) was the closest value to that obtained by the isoconversional methods. Therefore, it can be concluded that the most appropriate reaction mechanism of the HDPE pyrolysis is F3.

After that, the pre-exponential factor (A) can be obtained by all isoconversional models after substituting $g(\alpha) = [(1-\alpha)^{-1} - 1]/2$ and find the intercept. The obtained values are presented in Table 7.

Figure 5 presents very precise linear relationships between the pre-exponential factor and activation energy as expressed in equation 10 (R^2>0.995) which further confirms the suitability of the proposed reaction model (third-order reaction model).

Table 6. Activation Energy values obtained by Coats-Redfern model.

Reaction Mechanis	5 K/min		10 K/min		20 K/min		40 K/min		Average Value	
	E (kJ/mol)	**R^2**	**E (kJ/mol)**	**R^2**	**E (kJ/mol)**	**R^2**	**E (kJ/mol)**	**R^2**	**E (kJ/mol)**	**R^2**
F1	122	0.9926	195	0.9905	162	0.9961	241	0.9955	**180**	**0.993675**
F2	141	0.9889	250	0.98	184	0.9929	299	0.9882	**218.5**	**0.9875**
F3	162	0.9849	314	0.9684	208	0.9891	366	0.9788	**262.5**	**0.9803**
D1	222	0.9963	312	0.9977	297	0.9985	396	0.9985	**306.75**	**0.99775**
D2	233	0.9954	339	0.9961	309	0.9979	425	0.9981	**326.5**	**0.996875**
D3	244	0.9943	370	0.9938	323	0.9972	459	0.9972	**349**	**0.995625**
A2	55	0.9911	92	0.9894	75	0.9955	114	0.995	**84**	**0.99275**
A3	33	0.9891	57	0.988	46	0.9947	72	0.9945	**52**	**0.991575**
A4	22	0.9863	40	0.9862	32	0.9938	51	0.9939	**36.25**	**0.99005**
R1	105	0.9959	150	0.9975	142	0.9984	192	0.9984	**147.25**	**0.99755**
R2	113	0.9943	172	0.9947	152	0.9974	215	0.9976	**163**	**0.996**
R3	116	0.9938	179	0.9934	156	0.997	223	0.997	**168.5**	**0.9953**
P2	46	0.9949	69	0.9971	65	0.9982	90	0.9981	**67.5**	**0.997075**
P3	27	0.9935	42	0.9966	39	0.9978	56	0.9979	**41**	**0.99645**
P4	18	0.9914	29	0.9959	27	0.9974	39	0.9975	**28.25**	**0.99555**

Table 7. Pre-exponential factor of the pyrolysis of HDPE.

Conversion	ln (A), ln (min^{-1})		
	FWO	**KAS**	**Starink**
0.1	35.18	20.93	22.44
0.2	44.29	30.51	31.11
0.3	51.24	37.76	38.36
0.4	53.98	40.59	41.20
0.5	54.74	41.37	41.98
0.6	55.03	41.65	42.26
0.7	54.77	41.36	41.98
0.8	54.42	40.13	41.59
0.9	54.34	40.85	41.46
Average	**50.89**	**37.24**	**38.04**

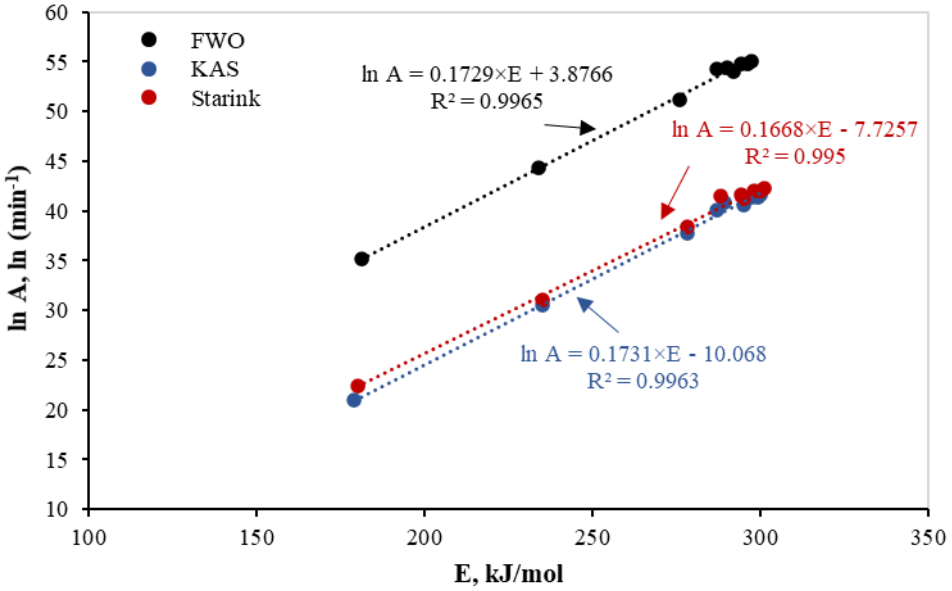


Figure 5. Selected reaction mechanism suitability

4. Conclusions

In this work, the pyrolysis of HDPE at different heating rates (5, 10, 20, and 40 K/min) has been investigated. Thermogravimetric experiments were conducted to obtain the TGA data from which kinetic parameters and reaction mechanism/s can be determined.

TG and DTG curves of the HDPE pyrolysis at different heating rates had similar trends (single inverted S-shape) which implies a single reaction takes place within the temperature range of 600 K and almost 800K. In addition, characteristic temperatures were shifted to higher temperatures as the heating rate increased.

Activation energy values at different reaction conversion were obtained efficiently (R^2>0.95) by three famous integral isoconversional models, namely FWO, KAS, and Starink. Very close average values (273±1 kJ/mole) were calculated by all models which indicates accurate experimental data. Furthermore, the most suitable reaction mechanism has been determined by Coats-Redfern model and results revealed that the HDPE pyrolysis obeys the third-order reaction (F3) mechanism. Then, the pre-exponential factor was obtained. Moreover, the relationship between the linear relationship between pre-exponential factor and activation energy confirms the suitability of the proposed reaction mechanism (F3).

This work clearly defines a step-by-step procedure to obtain the kinetic parameters (activation energy, and pre-exponential factor) and to determine the most suitable reaction mechanism of the pyrolysis of any biomass material.

Author Contributions: Both authors contributed significantly to the completion of this article and have read and agreed to the published version of the manuscript.

Funding: This research and the APC were funded by the Deanship of Scientific Research at King Faisal University, Saudi Arabia, under the Research Group Support Track (Grant No. 17122013).

Acknowledgments: The authors acknowledge the Deanship of Scientific Research at King Faisal University (KFU) in Al-Ahsa for the financial support under the Research Group Support Track (Grant No. 17122013).

Conflicts of Interest: The authors declare no conflict of interest.

References

1. Thompson, R. C.; Moore, C. J.; Fvom Saal, F. S.; Swan, S. H. Plastics, the environment and human health: current consensus and future trends. Philos. *Trans. R. Soc. Lond. B. Biol. Sci.* **2009,** 364, 2153-2166. https://doi.org/10.1098/rstb.2009.0053
2. Diaz Silvarrey, L.S.; Phan, A.N. Kinetic study of municipal plastic waste. *International Journal of Hydrogen Energy* **2016**, 41, 16352-16364. https://doi.org/10.1016/j.ijhydene.2016.05.202
3. Miskolczi, N.; Bartha, L.; Dea´k, Gy. Thermal degradation of polyethylene and polystyrene from the packaging industry over different catalysts into fuel-like feed stocks. *Polymer Degradation and Stability* **2006**, 91, 517-526. https://doi.org/10.1016/j.polymdegradstab.2005.01.056
4. Cardona, S.C.; Corma, A. Tertiary recycling of polypropylene by catalytic cracking in a semibatch stirred reactor. *Appl. Catalysis B.* **2000**, 25, 151-162. https://doi.org/10.1016/S0926-3373(99)00127-7
5. Arandes, J.; Abajo, I.; Lopez-Valerio, D.; Fernandez, I.; Azkoiti, M. J.; Olazar, M.; Bilbao, J. Transformation of several plastic wastes into fuels by catalytic cracking. *Ind. Eng. Chem. Res.* **1997**, 36 (11), 4523-4529. https://doi.org/10.1021/ie970096e
6. Lu, J. S.; Chang, Y.; Poon, C. S.; Lee, D. J. Slow pyrolysis of Municipal Solid Waste (MSW): a review. *Bioresource Technology*. **2020**, 312, 123615. https://doi.org/10.1016/j.biortech.2020.123615
7. Kaminsky, W.; Schlesselmann, B.; Simon, C. M. Thermal degradation of mixed plastic waste to aromatic and gas. *Poly. Degrad. and Stab.* **1996**, 53, 189-197. https://doi.org/10.1016/0141-3910(96)00087-0
8. Aguado, J.; Serrano, D.P.; San Miguel, G.; Castro, M.C.; Madrid, S. Feedstock recycling of polyethylene in a two-step thermo-catalytic reaction system. *J. Anal. Appl. Pyrolysis* **2007**, 79, 415–423. https://doi.org/10.1016/j.jaap.2006.11.008
9. Rasul Jan, M.; Shah, J.; Gulab, H. Catalytic conversion of waste high-density polyethylene into useful hydrocarbons. *Fuel* **2013**, 105, 595–602. https://doi.org/10.1016/j.fuel.2012.09.016
10. Wu, C.H.; Chang, C.Y.; Hor, J.L.; Shih, S.M.; Chen, L.W.; Chang, F.W. On the Thermal Treatment of Plastic Mixture of MSW: Pyrolysis Kinetics. *Waste Management* **1993**, 13, 221-235. https://doi.org/10.1016/0956-053X(93)90046-Y
11. Conesa, J.A.; Marcilla, F. R.; Caballero, J.A. Thermogravimetric studies on the thermal decomposition of polyethylene. *Journal of Analytical and Applied Pyrolysis* **1996**, 36, 1-15. https://doi.org/10.1016/0165-2370(95)00917-5
12. Aboulkas, A.; El harfi, K.; Bouadili, K.A. Thermal degradation behaviors of polyethylene and polypropylene. Part I: Pyrolysis kinetics and mechanisms. *Energy Conversion and Management* **2010**, 51, 1363-1369. https://doi.org/10.1016/j.enconman.2009.12.017
13. Chin, B.L.F.; Yusup, S.; Al Shoaibi, A.; Kannan, P.; Srinivasakannan, C.; Sulaiman, S.A. Kinetic studies of co-pyrolysis of rubber seed shell with high density polyethylene. *Energy Conversion and Management* **2014**, 87, 746–753. https://doi.org/10.1016/j.enconman.2014.07.043
14. Khedri, S.; Elyasi, S. Kinetic analysis for thermal cracking of HDPE: A new isoconversional approach. *Polymer Degradation and Stability* **2016**, 129, 306-318. https://doi.org/10.1016/j.polymdegradstab.2016.05.011
15. Dubdub, I.; Al-Yaari, M. Pyrolysis of mixed plastic waste: I. Kinetic study. *Materials* **2020**, 13, 4912. https://doi.org/10.3390/ma13214912
16. Chen, R.; Li, Q.; Zhang, Y.; Xu, X.; Zhang, D. Pyrolysis kinetics and mechanism of typical industrial non-tyre rubber wastes by peak-differentiating analysis and multi kinetics methods. *Fuel* **2019**, 235, 1224–1237. https://doi.org/10.1016/j.fuel.2018.08.121
17. Dubdub, I.; Al-Yaari, M. Pyrolysis of low-density polyethylene: kinetic study using TGA data and ANN prediction. *Polymers* **2020,** 12, 891. https://doi.org/10.3390/polym12040891
18. Al-Yaari, M.; Dubdub, I. Application of artificial neural networks to predict the catalytic pyrolysis of HDPE using non-isothermal TGA data. *Polymers* **2020,** 2, 1813. https://doi.org/10.3390/polym12081813

19. Chan, J. H.; Balke, S.T. The thermal degradation kinetics of polypropylene: part iii. Thermogravimetric analyses. *Polymer Degradation and Stability* **1997**, 57, 135-149. https://doi.org/10.1016/S0141-3910(96)00160-7

Spray-Drying Synthesis of Oxidative Coupling of Methane Catalysts: Inclusion of SiC to the Support

Gontzal Lezcano, Vijay K. Velisoju, Shekhar R. Kulkarni, and Pedro Castaño*

KAUST Catalysis Center (KCC), King Abdullah University of Science and Technology (KAUST), Thuwal, 23955-6900, Saudi Arabia.

***** *Corresponding author: pedro.castano@kaust.edu.sa;*

Abstract: Oxidative Coupling of Methane (OCM) is a promising single-step route to convert natural gas to high-value C_2 chemicals. The Mn-Na-W/SiO_2 catalyst can be identified as a benchmark based on the balanced conversion-selectivity displayed in the literature. However, the support can further be improved from thermal stability point of view for a highly exothermic reaction like OCM. The current work outlines a novel SiC-SiO_2 support synthesized by spray drying. The SiC-containing catalyst displayed enhanced metal-support interactions that prevent complete oxidation of the support among others. A combined effect of spray drying and inclusion of SiC resulted in a uniform Mn-Na-W catalyst that shows excellent long-term stability for over 70 h run and sustained activity with 70% C_2 selectivity as compared to the SiC-free catalyst that shows noticeable deactivation.

Keywords: oxidative coupling of methane, silicon carbide, spray drying, natural gas to chemicals

1. Introduction

The oxidative coupling of methane (OCM) is an interesting catalytic route for the single-step production of high-value chemicals like ethane and ethylene through a highly exothermic reaction [1]. OCM, thus offers a possibility of utilizing the vast natural gas resources for direct chemical production. The trimetallic Mn-Na-W, supported on silica is the preferred catalyst in literature due to high C_2 yields (ethane + ethylene) [2]. Inclusion of SiC in the support can, however, improve the thermal stability of the support/catalyst on account of high thermal conductivity, as welldemonstrated in the literature for other exothermic reactions [3]. In the present work, two catalysts are compared: conventional Mn-Na-W/SiO_2 prepared by wetness impregnation method and the novel Mn-N-W/SiC-SiO_2 synthesized by spray drying.

2. Materials and Methods

The SiO_2-based Mn-Na-W catalyst was prepared by wetness impregnation method with an aqueous solution of sodium tungstate dihydrate, manganese acetate tetrahydrate and sodium oxalate at 80 ºC. The nominal metallic composition of 2 wt% Mn, 1.6 wt% Na and 3.1 wt% W was chosen as reported by Vamvakaros et al. [4]. Water was evaporated by drying at 100 ºC overnight and the dry samples were subsequently calcined in air at 800 ºC for 6 h with a ramp of 10 ºC min^{-1}.

The novel catalyst (SD SiO_2-SiC) is prepared by spraying a homogeneous slurry containing the precursor metal salts, Ludox silica solution (40 wt.% in water) and non-porous silicon carbide powder. The atomized droplets are dried in a chamber at around 200 °C by hot air. The catalyst was calcined under identical conditions as of the SiO_2 support. The nominal metal loading for both the catalysts is maintained the same to study the effect of support modification on their performance.

Both the catalysts (fresh and spent) were subjected to a detailed characterization of BET, XRD, TPR. SEM, XPS and Raman spectroscopy. The catalytic tests were performed using a lab scale fixedbed quartz reactor (inner diameter 2 mm, length 300 mm). Around 50 mg of sieved catalyst (150 - 300 µm) were loaded onto a 100 mm long coarse SiC bed that ensures the catalyst bed lies on the isothermal zone of the reactor. The molar composition of the feed was CH_4:O_2:N_2 2.5-3.3:1:3.3-3.5

where the main role of N_2 was to avoid hotspots and potential thermal runaway. The reaction productions were analyzed online in a GC.

3. Results and Discussion

For both the catalysts, as seen in Figure 1, the observed CH_4 conversions are noteworthy only above 750 °C. A remarkable exponential increase in CH_4 conversion is observed as temperatures were raised beyond 750 ºC for both the catalysts, reaching around 33 % at 800 ºC. The thermal conversion can be neglected on the account of meagre contributions for runs without the catalyst (blank). Assuming the overall conversion of CH_4 follows a first order reaction, pseudo-activation energies could be estimated by combining the rate law with the conservation equation of an integral fixed-bed plug-flow reactor. Figure 1 (b-c) are the Arrhenius plots for the IMP SiO_2 and SD SiO_2-SiC catalysts, respectively, from which pseudo-activation energies presented in Figure 1 (d) have been derived. The pseudo-activation energy of the spray-dried catalyst (166 ± 11 kJ mol^{-1}) happens to be lower than that of the impregnated catalyst (197 ± 6 kJ mol^{-1}), in line with the higher conversions presented in Figure 1 (a). Hence, the pseudo-activation energies reveal the higher activity of the SD SiO_2-SiC catalyst as compared to the impregnated SiO_2 catalyst.

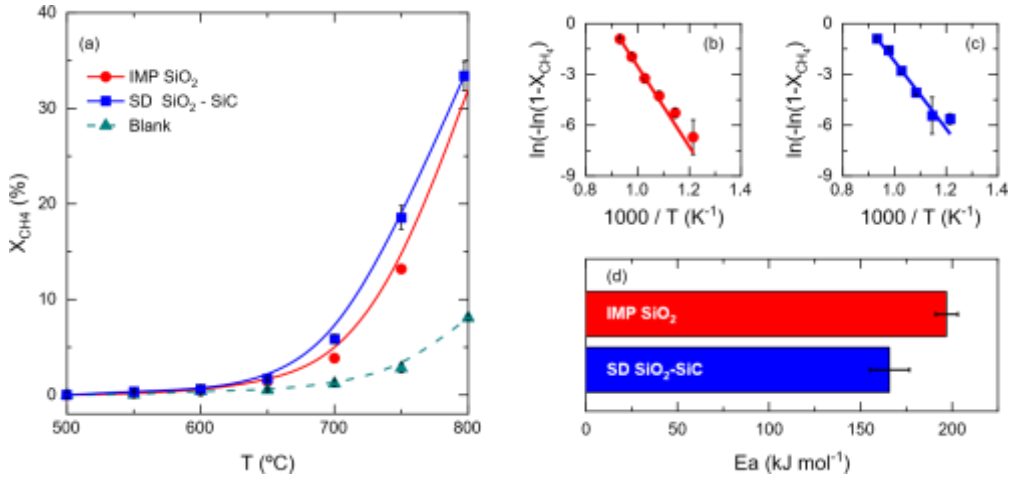


Figure 1. (a) Effect of temperature on CH_4 conversion at W/F_0 = 4.42 g_{cat} h $molC^{-1}$ and feed molar ratio CH_4:O_2:N_2 = 3.3:1:2.7. Arrhenius plots for (b) IMP SiO_2, (c) SD SiO_2-SiC and (d) estimated pseudo-activation energies of the catalytic and thermal conversions.

The time on stream performance of the two catalysts was tested at 800 °C for over 70 hours (not shown). The silica-based catalyst showed a progressive deactivation from an initial methane conversion of ~20% to ~13% after 70 h operation. The spray-dried catalyst, however, showed a steady methane conversion around 20%. Both the catalysts, though, retained the remarkable C_2 selectivity of ~70% over the entire test duration. The highest C_2 yields recorded were ~22% & 20.4% for the SD SiO_2-SiC & IMP SiO_2 respectively, showing the superior performance of the novel catalyst for OCM.

4. Conclusions

The novel, hybrid, spray-dried support of SiC-SiO_2 is able to surpass the performance of silicabased benchmark from the literature for the same active phase composition of Mn-Na-W. Addition of SiC enables the exothermic reaction heat to be dissipated effectively from the active sites and preventing metal sintering that could result in catalyst deactivation over longer run lengths, as observed with the SiO_2-supported catalyst.

References

1. T. Karsten, V. Middelkoop, D. Matras, A. Vamvakeros, S. Poulston, N. Grosjean, B. Rollins, F. Gallucci, H.R. Godini, S.D.M. Jacques, A.M. Beale, J.-U. Repke, Multi-Scale Studies of 3D Printed Mn–Na–W/SiO2 Catalyst for Oxidative Coupling of Methane, Catalysts. 11 (2021) 290.
2. https://doi.org/10.3390/catal11030290.
3. D. Kiani, S. Sourav, J. Baltrusaitis, I.E. Wachs, Oxidative Coupling of Methane (OCM) by SiO2-Supported Tungsten Oxide Catalysts Promoted with Mn and Na, ACS Catal. 9 (2019) 5912– 5928. https://doi.org/10.1021/acscatal.9b01585.
4. M. Liao, Y. Chen, Z. Cheng, C. Wang, X. Luo, E. Bu, Z. Jiang, B. Liang, R. Shu, Q. Song, Hydrogen production from partial oxidation of propane: Effect of SiC addition on Ni/Al2O3 catalyst, Appl. Energy. 252 (2019) 113435. https://doi.org/10.1016/j.apenergy.2019.113435.
5. A. Vamvakeros, S.D.M. Jacques, V. Middelkoop, M. Di Michiel, C.K. Egan, I.Z. Ismagilov, G.B.M. Vaughan, F. Gallucci, M. Van Sint Annaland, P.R. Shearing, R.J. Cernik, A.M. Beale, Real time chemical imaging of a working catalytic membrane reactor during oxidative coupling of methane, Chem. Commun. 51 (2015) 12752–12755. https://doi.org/10.1039/c5cc03208c.

Synthesis and Characterization of Fluoroperovskite $Kznf_3$ Compounds

Bahia Messai * and Rachid Makhloufi

Applied Chemistry Laboratory, Exact and Natural and Life Sciences Faculty Materials Science Department, Mohamed Khider University of Biskra BP145 (7000), Algeria
Bahia Messai, Department of Materials Science, , Mohamed Khider University of Biskra, Algeria.
***** *Corresponding author: bahia.messai@univ-biskra.dz*

Funding information
This research received no external funding.

Abstract: This study was largely part of a research axis whose objective was to synthesis, structural and physical characterization and develop a material from the fluoroperovskite $KZnF_3$, which is a solid solution by liquid (soft chemistry). The synthesized phases were characterized by X - Ray Diffraction (XRD) and Fourier Transform Infrared Spectroscopy (FTIR) and by Particle size analysis.The complete description of the X-ray diffraction pattern was made by the Rietveld technique, including the background, shape, position, and intensities of the diffraction patterns observed using the structural model using the CIF file. The parameters of the model have been refined by least squares technique to obtain as good a match as possible between the observed and calculated diffractogram. To conclude, a brief discussion of the results obtained was made.

Keywords: $KZnF_3$; XRD, Refinement; FullProf, FTIR; Co-precipitation.

1. Introduction

Ternary fluorides are, in a wide field, good or even excellent ionic conductors at high temperature and have better stability in ambient air. [1-6]

The perovskite structure is named after the mineral $CaTiO_3$. Many oxides of the general formula ABO_3, for example $LiNbO_3$ and $BaTiO_3$ adopt this structure, as do ABF_3 fluorides. Materials of perovskite structure with the chemical formula ABX_3 ($X = F^-, O^{2-}, S^{2-}, Cl^-, Br^-$…) are extremely attractive from a fundamental and technological point of view because they present a great variety. Electrical, magnetic, and structural properties, which are, in many cases, sensitive to external disturbances such as pressure or temperature. Most of these systems do not correspond with the ideal cubic perovskite structure, but undergo phase transitions that lower the overall symmetry of the crystal. [2-5]

Fluoroperovskite have the general formula ABF_3 where A is generally an alkali metal (eg: Li, Na, K, Rb) and B is an alkaline earth metal (Be, Mg, Ba, Sr) or a transition metal (Zn, Cu, Co, Cd, Ni, Fe, Mg, V). [2, 3]

The ideal perovskite structure is of simple cubic symmetry and can be described in the space group Pm3m. This "ideal" structure is rarely encountered, and one example is strontium titanate SrTiO3. [4]

The mineral $KMgF_3$ was discovered in Utah (USA) in the form of rounded blue-gray grains. There is a distortion of the cubic perovskite structure with lattice parameters a = 3.988 Å; of

space group Pm3m. (Z = 1) induced by two independent tiltings of the MgF_6 octahedral; this results in a significant deviation from the linearity of the Mg-F-Mg angle. [5]

The first investigations on the powder diagram of $KZnF_3$ showed that its structure is of cubic symmetry, with lattice parameters a = 4.055 Å; space group Pm3m.

The mineral $KNiF_3$, present in the form of white rounded grains. There is a distortion of the cubic perovskite structure with lattice parameters a = 4.012 Å; of space group Pm3m.

Regarding the synthesis by chemical route, there are different techniques for preparing powders which can be separated into two categories depending on whether the synthesis is carried out by solid route (ceramic method) or by liquid route (soft chemistry). [7]

By solid route: This is the basic synthesis method in solid-state chemistry. It makes it possible to prepare powders. The ceramic technique is characterized by the fact that the solid reagents are not brought to their melting temperature and the reactions take place in the solid state throughout the synthesis. [8]

Liquid: Liquid processes allow obtaining powders with a homogeneous chemical distribution, formed of small grains and having a narrow particle size distribution. [9] In this work, deals with Synthesis and characterization of compounds of the fluoroperovskite $KZnF_3$.

2. Materials and Methods

2.1 Materials

Co-precipitation makes it possible to obtain precursor products by simultaneous precipitation of two cations M and M ′ (M being an alkali and M ′ an alkaline earth metal or a transition metal).

This method consists of using solutions of metal chloride added to a solution of KF. During co-precipitation, as many $KZnF_3$ are formed as there are limiting reagents in solution (the K^+ and Zn^{2+} ions), so the excess reagents will remain in the form of an ion in solution. Will filter.

$$3KF + ZnCl_2 \longrightarrow KZnF_3 + 2K^+ + 2Cl^- \qquad (R1)$$

There are several liquid synthesis processes; we present the co-precipitation process that we want to use to synthesize the materials studied in this work.

In this work, we will present the experimental protocol for the synthesis of the fluoroperovskite phase $KZnF_3$ by co-precipitation taking advantage of the complexing effect of F^- fluoride ions in solution.

2.2.1 Solution

This method consists of using the complexing power of F^- fluoride ions in solution. For reasons of time and availability of X-ray diffraction analysis, we have limited ourselves only to the synthesis of the two pure phases $KZnF_3$. Approximately 15 g of sodium fluoride KF, 13.63 g of zinc chloride $ZnCl_2$ are dissolved in an aqueous solution. The solution is heated to 80 °C with stirring. The solution is cooled and filtered through a Buchner funnel. The product obtained is dried in an oven at 120 °C.

2.2.2 Analytical methods

After the presentation, we will present, in this work, the characterization of the $KZnF_3$ Fluoroperovskite phase by X-ray powder diffraction (DRX).

X-ray crystallographic analysis on powder is a very convenient method to know the various phases of a mixture, their proportion, their crystalline structure, and to determine their domain of

existence. Powder synthesis was also followed by X-ray diffraction (XRD). The diffraction patterns are carried out using a Bruker D8 diffractometer installed at the University of Mohamed Khider Biskra. Monochromatic X-ray radiation is produced by a copper anticathode (wavelength of the CuKα line, λ = 1.5418 Å) and the diffractograms are recorded at room temperature, the diffraction angle 2θ varies between 10 ° and 90 °.

The result obtained clearly confirms the formation of the $KZnF_3$ fluoroperovskite phase by the co-precipitation method. The powder obtained is well crystallized and identical to that indexed

The complete description of the X-ray diffraction pattern was made by the Rietveld technique, including the background, shape, position, and intensities of the diffraction patterns observed using the structural model using the CIF file. The parameters of the model have been refined by least squares technique to obtain as good a match as possible between the observed and calculated Diffractogram. To conclude, a brief discussion of the results obtained was made.

$$R_B = \frac{\sum_N |I_{obs} - I_{cal}|}{\sum_N I_{obs}} \quad (1)$$

where R_B is the Bragg factor.

$$I_k = \sum I_k^{cal}\ \Omega_{ik} \frac{y_i - y_{ib}}{y_{ic} - y_{ib}} \quad (2)$$

We also use the "R -structure factor" defined by

$$R_F = \frac{\sum_N \left| I_{obs}^{\frac{1}{2}} - I_{cal}^{\frac{1}{2}} \right|}{\sum_N I_{obs}^{\frac{1}{2}}} \quad (3)$$

The R_B is probably the best criterion for judging the quality of the refinement. On the other hand, the value R_{wp} is dominated by the profile function and it is not very sensitive to the structural parameters, it is therefore preferable to use it to judge the profile. Among the other factors used, we can also mention.

$$\chi^2 = \frac{\sum w_i \left[y_i - (1/c) y_{ic} \right]^2}{(N - P + C)} \quad (4)$$

$$R_{exp} = \frac{R_{wp}}{\sqrt{x^2}} = \left[\frac{(N - P + C)}{\sum_i w_i y_i^2} \right]^{1/2} \quad (5)$$

Where N, P and C are respectively the number of information items used, the number of refined parameters and C the number of constraints.

Figures and tables

By co-precipitation of an aqueous solution containing the F^- ions (KF solution) and an aqueous solution containing the Zn^{2+} ions, a white powder is obtained after filtration and drying. This powder is characterized by DRX. The diffractogram obtained is illustrated in figure 1.

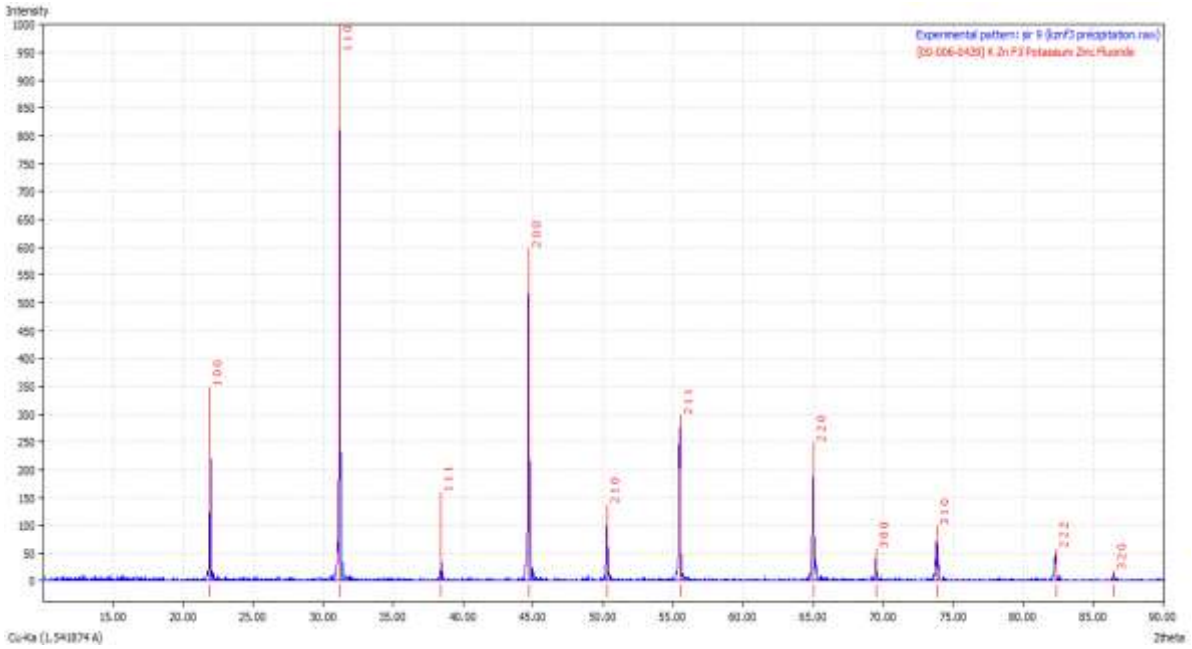


Figure 1. Powder diffractogram of the $KZnF_3$ composition prepared by co-precipitation

Figure 2A-C presents the refinement pattarns of the synthesized $KZnF_3$ nanopowders. Initially, the refinement procedures were carried out following the adoption of various needed information and the structure of $KZnF_3$ is described in cubic form (Figure 2 (C)) where the centers of the faces are occupied by the atoms of F and all summits by K and the centers of mesh occupied by the atoms of
Zn.

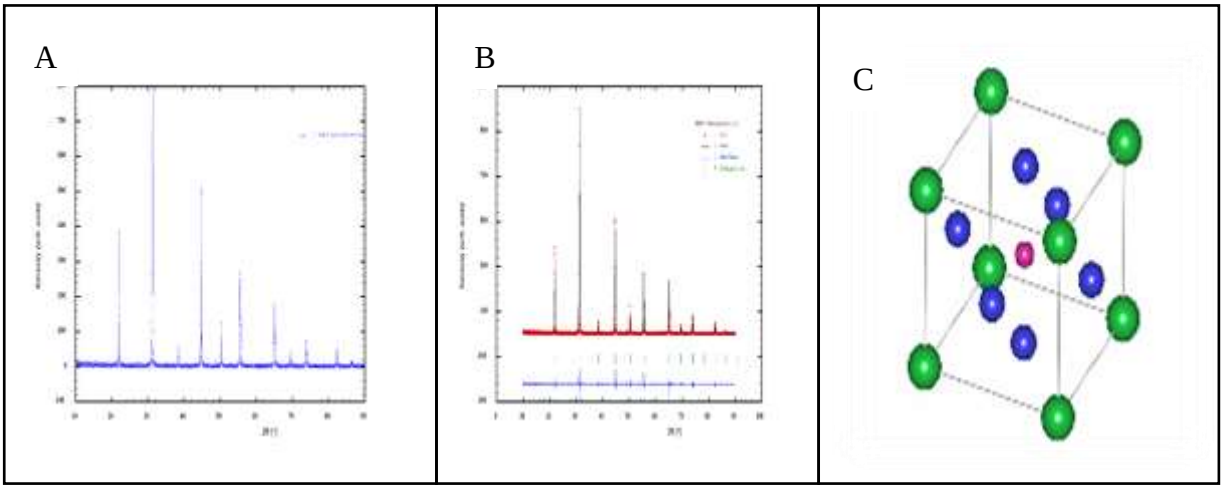


Figure 2. (A) Powder diffractogram of the $KZnF_3$ composition prepared by co-precipitation, (B) Rietveld diagram resulting from the refinement of the structure of the compound $KZnF_3$, (C) Representation of the structure of $KZnF_3$

Fourier transform infrared spectroscopy (FTIR) is based on the absorption of infrared radiation by the material analyzed.

In inorganic solids, the study of infrared absorption phenomena makes it possible to identify certain groups, in our case the vibration bungs of the $KZnF_3$ structure, provides structural information from their vibrational properties. The Fourier transform infrared spectroscopy study was carried out on the powder. The spectrum obtained is illustrated in figure 3.

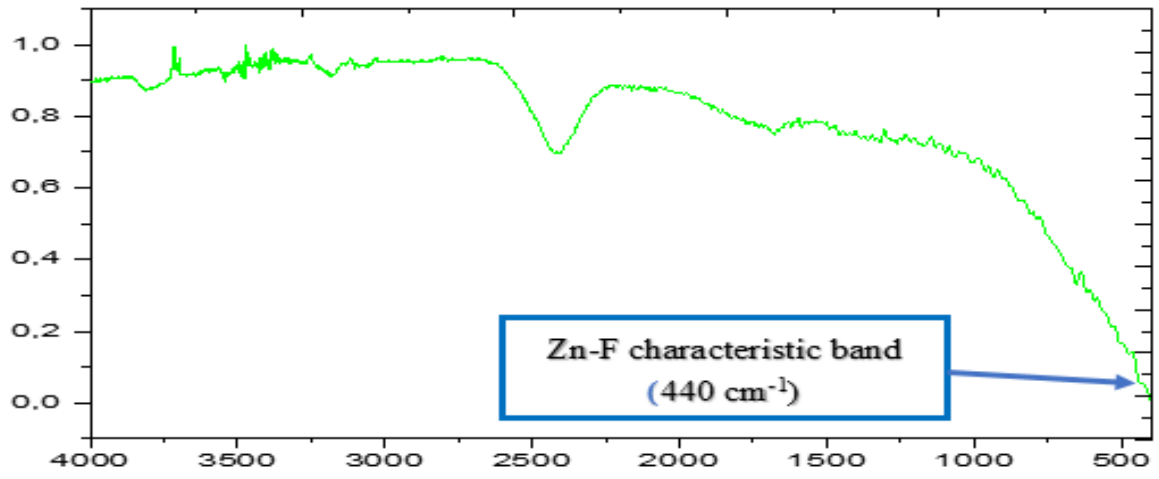


Figure 3. Infrared spectrum of the co-precipitated $KZnF_3$ phase

Figure 4 summarize the results of the particle size analysis of the $KZnF_3$ composition (co-precipitation route). Concerning the $KZnF_3$ powder prepared by co-precipitation, the size distribution of the grains is almost homogeneous around 1.5 µm. The distribution around 15 µm can be attributed to an agglomeration of the grains

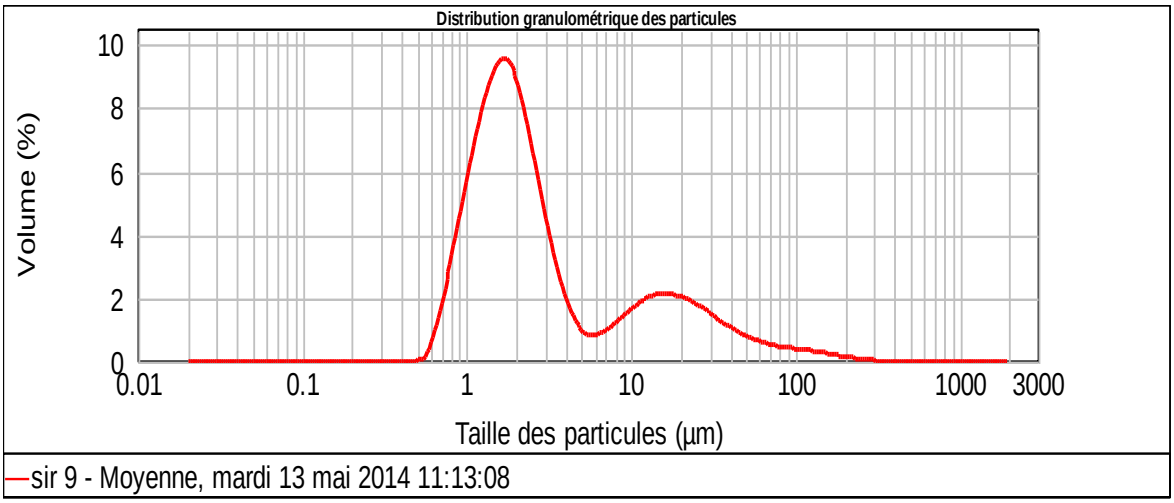


Figure 4. Particle size distribution of the co-precipitated $KZnF_3$ powder

Table 1 shows all the radio-crystallographic characteristics, the acquisition conditions and the structural refinement parameters of the new $KZnF_3$ phase.

Table 1. Refined structural parameters listed for $KZnF_3$

Lattice parameter (Å)	**Angle (°)**	**Volume (Å³)**	**Space group**	**Atomic position (x, y, z)**
a=b=c= 4.0566	α=β=γ= 90	V=66.7554	P m-3m	K 0.000 0.000 0.000 Zn 0.500 0.500 0.500 F 0.500 0.500 0.000

Abbreviations: FTIR, Fourier transform infrared spectroscopy; XRD, X-ray powder diffraction.

3. Discussion

The result obtained clearly confirms the formation of the $KZnF_3$ fluoroperovskite phase by the co-precipitation method. The powder obtained is well crystallized and identical to that indexed, Rietveld structure refinements for the synthesized nanopowders were fulfilled with

FullProf software packages and high quality collected XRD data in order to determine the fractional phase components percent as well as the various crystallographic properties. Including the structure information of the identified phases which are obtained from the cif files, the background that is identified as a linear interpolation of adjusted selected points, the peak profile function which is defined as pseudo-Voigt (pV), and the determined instrumental resolution function (IRF). The IRF details were returned through employing the WinPlotr program using a detected XRD pattern from a reference specimen (Cu) with the same identified measurement conditions.

The structural refinement of the new $KZnF_3$ phase (Figure 2 (B)) was carried out using the Rietveld software using the Full Prof Program. With several refinement cycles, the refinement confidence factors stabilize. We may make the following results:

1. R_p= 16.7.
2. R_{wp}= 24.6.
3. R_{exp}= 19.65.
4. χ^2= 1.56.

4. Conclusions

This study was largely part of a research axis whose objective was to develop a material from the Fluoroperovskite $KZnF_3$ family, which is a solid solution by liquid (soft chemistry).

Zinc fluoride is an alkaline earth mineral; ions were partially, of the same charge and of very similar ionic radius, which made it possible to form the $KZnF_3$ phase.

The solid solution, which was synthesized by the soft chemistry method known as co-precipitation. The formation of the perovskite phase was used the complexing power of F^- fluoride ions in solution with the metals preceding and results in the pure $KZnF_3$ phase.

The synthesized phases were characterized by X-ray diffraction (XRD). The perovskite phase of $KZnF_3$ crystallizes in the system and adopts the same crystal structure favors the co-precipitation method. Furthermore, the crystallite size values obtained from Rietveld refinements showed the opposite trend of the WH values. The modified tolerance factor values were extremely close to unity, indicating a strong perovskite structure

The results of infrared spectroscopy confirm formation of the $KZnF_3$ fluoroperovskite phase, in fact, the zinc atoms being heavier and consequently the characteristic band of vibration (Zn-F) shifts towards the low values of wavenumber (frequency, vibration energy).

Acknowledgements: The authors are grateful to professor SOLTANI Ibrahim for the analysis Fourier transform infrared spectroscopy (FTIR).

Nomenclature

Symbols

CIF	Open data base
a, b, c	lattice parameter (Å)

Greek letters

θ	equilibrium contact angle (°)
Å	angstrom
α, β, γ	angle (°)

Subscripts	
g	gas phase
l	liquid phase
Dimensionless numbers	
N	the number of points of the refined part of the diagram
P	the number of adjusted parameters
C	the number of constraints applied

References

1. N. H. Andersen, J. K. Kjems, W. Hayes, *Solid State Ionics*, **1985**,143,145.
2. J. C. Gâcon, A. Gros, H. Bill and, J. P. Wicky, *Journal of Physics and Chemistry of Solids*, **1981**, 587,593.
3. N. J. M. Le Masson, A. P. Vink, P. Dorenbos, A. J. J. Bos, C. W. E. VanEijk, J. P.Chaminade, *Journal of Luminescence*, ,**2003**, 175,183.
4. R. D. Shannon, *Acta crystallogr*. A32, **1976**, 751,
5. E.C.T.Chao and al., Neighborite, $NaMgF_3$, *a new minral from the green river formation, south Ouray, Utah . American Mineralogis*t, **1961**, 379.
6. K. Adamkovičová and al. *ThermochimicaActa*, **1994**,23,26.
7. S. Rey, *thèse doctorat*. Institut National des sciences Appliquées de Lyon, **1986**.
8. P. Boch, Frittage et microstructure des céramiques. *Matériaux et Processus Céramiques. Paris: Editions Hermès Sciences Publications*, **2001**, 20, 21.
9. P. Colomban, *Ceramics International*, **1989**,15-23.

Ultrasound Effect on 5-CQA and Tryptophan Reaction: Assessment of The Reaction Kinetics and Product's Physicochemical Characteristics

Anna Maria Menelaou , Konstantina Parmaxi and Patroklos Vareltzis *

Department of Chemical Engineering, Laboratory of Food Industry Technology and Agricultural Industries, Aristotle University of Thessaloniki, 54124 Thessaloniki, Greece

***** *Corresponding author: pkvareltzis@cheng.auth.gr, Tel: +306989510191*

Abstract: Chlorogenic acid and tryptophan can react under certain conditions and produce a red pigment with potential application in the food industry. In literature, the shortest reaction time reported is 24h. The main goal of this research effort is to reduce the reaction time by means of ultrasound and to evaluate the reaction kinetics. Experiments were also performed to determine the physicochemical properties of the product for potential use as a colour additive in the food industry. The main experimental and analytical methods used are ultrasound, spectrophotometry, HPLC and colourimetry. Application of ultrasound accelerated the reaction considerably, since a 98% conversion of 5-CQA was achieved in 8.5h. The global order of the reaction was found equal to 2, while the order of tryptophan equal to 0. Increasing reaction temperature from 40 to 73°C led to increased reaction rate but also to discoloration of the final product. The product of the reaction exhibited remarkable stability when treated under extreme temperature conditions, did not show any antimicrobial activity in relation to the pure 5-CQA, however it had the ability to slow down the oxidation and preserve the colour of the test food for a longer period compared to sodium nitrite.

Keywords: Chlorogenic acid; tryptophan; ultrasound; reaction kinetics; red colour pigment.

1 Introduction

Chemical interactions between phenolic compounds and proteins, can form a green or brown colour in food products during their processing [1]. Therefore, such interactions are the focal point of experimentation in the food area. Chlorogenic acids, are the esters of caffeic and quinic acid [2]. They are biologically important phenolic compounds produced by plants and are mostly present in certain fruits, vegetables, and plant species, such as coffee beans, sweet potato leaves, eggplant etc. [3]. According to previous studies, there are many advantageous health benefits linked to the CGA family, including hepatoprotective and choleretic activities, antioxidant, antiviral, antibacterial, anti-cancer and anti-inflammatory properties, reduction of the risk of cardiovascular disease, of the relative risk of diabetes type 2 and Alzheimer's disease [2].

The reaction between 5-CQA and amino acids, commonly leads to greening of the mixtures. The green colour is attributed to the result of the formation of benzacridine dye. An exception to this was the formation of a red colour in a reaction between 5-CQA and tryptophan (TRP). The appearance of this red pigment was connected to the indole portion of tryptophan. According to previously stated methods, the reaction between 5-CQA and TRP can be performed in two different ways. As Vercruysse (2019) suggests, the reaction can be completed within 24hr, after the final mixture is kept at 37°C. More specifically, 5-CQA 1mM stock solution has been prepared by dissolving 5-CQA in methanol and then diluting it to the final concentration with 100mM acetate buffer (pH=6.5), so the final concentration of methanol is 10% v/v. Tryptophan (TRP) stock solution in a final concentration

of 7mM has been prepared by dissolving TRP in 50mM Na_2CO_3 solution. This particular mixture required overnight standing at room temperature, to achieve complete dissolution. The final reaction mixture consists of 1mM 5-CQA, 10mM Na_2CO_3, and 7mM TRP. The authors conducted experiments for different TRP concentrations (0-7mM) to examine the effect of the concentration on the end product's colour. It was concluded that, as the concentration increased, the red colour became more intense, while for low concentrations the product displayed a brown colour [1].

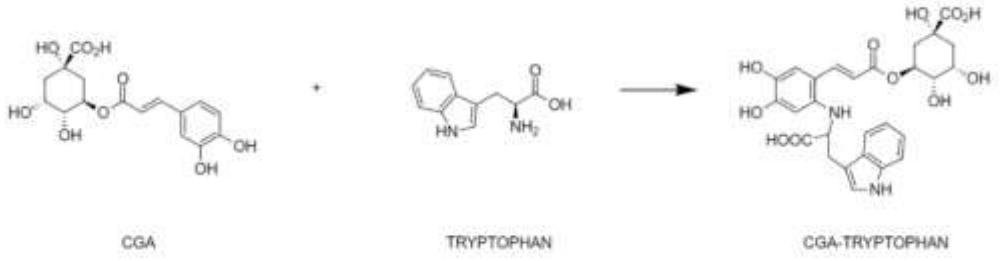


Figure 3: Reaction scheme between CGA and TRP [1]

Moccia et al (2021) stated that the reaction can be carried out with a different method. In this method, aqueous solutions of TRP (28-140mM) were mixed with aqueous solutions of 5-CQA 28mM. In this case, the pH is being adjusted to 9 with 0.1M NaOH, which is added at the beginning of the reaction, after 10 minutes and then after 30 minutes. The mixture was left under vigorous stirring for 64hr. The experiments were aimed at making red powder that can be used in food formulations mainly as a colourant. The stability of the colour was checked under various temperature and pH conditions while at the same time, the powder was introduced in various foods in order to verify its suitability. In this article, the researchers concluded that this dye is a promising alternative for red colouring for food [4].

The reaction scheme between CGA and tryptophan proposed by Vercruysse (2019) is depicted in Figure 1 [1]. Another possible mechanism is proposed by Xue et al (2020), where soy protein isolates-cyanidin-3-galactoside conjugates were produced via a free radical mechanism induced by ultrasound [5]. Sonochemistry is being used in many cases the recent years to reduce the chemical reaction times. Ultrasonic treatment has become a popular method, due to its multiple advantages including reduced energy requirements, waste prevention, improvement in mass transfer which in turn can speed up a chemical reaction [6]. Ultrasound has been introduced to batch and large-scale reactors in order to intensify various chemical and biological processes in terms of reaction rates and mass transfer [7]. The chemical and physical effects of ultrasound cannot result from the direct interaction of sound waves with matter, but rather they are caused by the cavitation phenomena that occur. There are four basic types of cavitation: acoustic, hydrodynamic, optical, and particle cavitation. Through acoustic cavitation, power ultrasound promotes and enhances chemical and physical changes. When the bubbles formed through cavitation collapse, they cause very high instantaneous temperatures and pressures. Cavities first grow in size until the maximum of the negative pressure is reached, and in the succeeding compression cycle they contract and collapse, producing shock waves that have a magnitude of several thousand atmospheres [8]. When bubble collapse, the implosion releases enormous amounts of energy and produces intense local heating, high pressures, and very short lifetimes. These so called “hot spots” have temperatures of about 5000°C and pressures of about 1000 atm [9].

The aim of this research work was to speed up the reaction between 5-CQA and tryptophan by applying ultrasound and study its kinetics. Experiments were then conducted to investigate the effect of temperature on the reaction. Furthermore, the product of the reaction was tested for its physicochemical properties, such as stability against heat treatment, anti-oxidative and antimicrobial properties. Finally, its potential role as a food colourant instead of nitrites was explored.

2 Materials and methods

2.1 Chemicals

5-CQA (chlorogenic acid, CAS: 327-97-9), TRP (L-tryptophan, CAS: 73-22-3), methanol HPLC grade (CAS: 67-56-1), glacial (acetic acid, CAS: 64-19-7), sodium acetate (CAS: 6131-90-4), sodium carbonate (CAS: 497-19-8) were purchased from Merck KGaA (Germany) and they were all of analytical grade.

2.2 General experimental methods

5-CQA concentration during the reactions was followed by high performance liquid chromatography. HPLC analyses were performed on a Knauer Smartline HPLC instrument equipped with a UV/Vis detector (λ = 280nm) using a Eurospher II 100-5 C18P column (150 × 4 mm with precolumn). 2% acetic acid with water was used as the eluent B and acetonitrile HPLC was used as the eluent A at a total flow rate of 1,0 ml/min. The gradient that was used is described in *Table* . Analytical grade 5-CQA standard (purity 98%) was used for constructing the calibration curve.

Table 1: Gradient of eluents A and B for 5-CQA determination

Time (min)	Eluent A (%)	Eluent B (%)	Flow rate (ml/min)
0	100	0	1,0
4	85	15	1,0
20	60	40	1,0
40	45	55	1,0

Colour development (product of reaction) was followed by UV/vis on a Spectrometer Helios Gamma (ThermoScientifc, USA) at a wavelength of 540nm, where absorbance maximum was observed after scanning the product in the range 400 to 700nm. The same wavelength for absorbance maximum was also observed by Moccia et al (2021) [4]. Samples at regular intervals were taken out of the sonication bath, cooled down to room temperature under running tap water and were diluted by equal volume of ultra-pure water in order for the readings of the spectrophotometer to be within its linear range. Colourimetric measurements were made with a ColourLite sph870 (ColourLite GmbH, Germany) spectrophotometer with the proper attachment for measuring liquid samples.

2.3 Reaction of 5-CQA with TRP

The reactants were prepared according to previously reported procedures with slight modifications [1]. Specifically, TRP 7mM solution was prepared by dissolving TRP in 50mM aqueous Na_2CO_3 solution under constant stirring at room temperature for 5min. 5-CQA 1mM solution was prepared by dissolving 5-CQA in methanol and then diluting it with acetate buffer 100mM (pH=6,5) to the final concentration. Subsequently, the final reaction mixture consists of 1mM 5-CQA, 7mM TRP and 10mM Na_2CO_3, which results from the mixing of a proper amount of 5-CQA solution and TRP

solution. The mixture was placed in an ultrasonic bath (FALC LBS1, 200W, 50kHz) at 40ºC, while samples were analyzed by UV–vis spectroscopy and HPLC for 8.5hr at regular intervals. To establish the effect of temperature on the final product the reaction was also performed at 63 ºC and 73ºC. Different TRP concentrations (6mM-14mM) were also tested in order to investigate the effect of TRP concentration on the kinetics.

2.4 Stability of 5-CQA-TRP red product

The product of the reaction was freeze-dried, and a red powder was collected (ca. 0.05g). The powder was redissolved in 10mL ultra-pure water by vortexing for 1 min and subjected to extreme temperature conditions to test its stability. Aliquots of the red pigment (~4-5mL) in a glass screw-top vial were subjected to different heat treatments: a) water bath at 100ºC for 20 minutes, b) freezer at -18ºC overnight, c) ultrasound, at 40ºC for 15 minutes and d) microwave at 700 W for 2 minutes. Colour was measured after each treatment with a ColourLite sph870 (ColourLite GmbH, Germany) spectrophotometer.

2.5 Antimicrobial action of product

Samples of pure 5-CQA and product of the reaction 5-CQA-TRP at concentrations of 5000 ppm were tested for their antimicrobial activity against various bacteria shown in *Table* . The methods of agar well diffusion and minimum inhibitory concentration using microplate were used. The agar well diffusion method is a qualitative technique as it is not possible to accurately control the agar diffusion conditions. The agar plate surface was inoculated by spreading the microbial inoculum over the entire agar surface. Then, a hole with a diameter of 8 mm was punched aseptically with a sterile tip, and 50 µL of the antimicrobial agent solution was introduced into the well. Then, agar plates were incubated under suitable conditions depending upon the test microorganism and the inhibition of microbial growth was observed over time [10] . The potential resistance shown in the agar diffusion method was confirmed by the method of broth dilution to determine the minimum inhibitory concentration using a microplate [11].

Table 2: Bacteria stems that were used to test anti-microbial action of the red pigment

Bacteria type	Stem 1	Stem 2
Salmonella	*S.* Typhimurium *DT120*	*S.* Typhimurium ATCC 14028
Listeria monocytogenes	ATCC 7644	CIP 103575
Escherichia coli	ATCC 11303	ATCC 16628
Staphylococcus aureus	ATCC 25923	DSM 102262
Enterococcus faecalis	N39	N54

2.6 5-CQA-TRP red product as a food colourant in sausages

Three cooked pork sausages were prepared following the recipe of Herrmann, Granby & Duedahl-Olesen, (2015) with some modifications [12]. Specifically, freshly purchased pork loin from a local vendor was trimmed of any visible fat, minced, and mixed with the additives (Primo Kitchen Equipment, 550W). Minced meat (70%), tap water (28%), salt (2%) and 100ppm nisin as an antimicrobial agent were the common ingredients for all preparations, while sodium nitrite 150ppm

and the product of 5-CQA-TRP reaction (90mg dissolved in the tap water) were added to separate mixtures and blended under cold conditions till all ingredients were evenly distributed. Samples were prepared in triplicates. The mixtures were packed into plastic cylindrical cases and boiled for 30min at 90ºC followed by immediate cooling in ice-water bath. Final weight of each sausage was 80gr. The sausages were placed at refrigerating temperature and daily measurements were taken to determine the oxidation level of each sausage during the 8-day refrigerated storage. Oxidation was followed by TBARs according to Lemon's method as modified by Vareltzis, Hultin, & Autio, 2008 [13].

2.7 Determination of myoglobin forms

Oxidation of myoglobin and colour change in the sausages was followed by measuring the oxymyoglobin (OxyMb) concentration in the samples spectrophotometrically. For the experiment performed, 2 g of minced meat were weighed and placed in a test tube. 20 mL of phosphate buffer (0.04 M and pH=6.8) were added to the tube. Homogenization followed and the sample was placed in centrifuge vials. The centrifugation took place for 30 minutes at 4000 rpm (Orto alresa, Madrid-Spain). For isolation, the supernatant was filtered to remove suspended particles. Finally, the absorption of the filtrate at specific wavelengths (503, 525, 557, 582nm) was measured and the percentage contents of the myoglobin forms were calculated according to Tang et al (2004) [14].

3 Results and discussion

3.1. Reaction Kinetics

The concentration of the reactant 5-CQA was followed by HPLC. The first samples analyzed were the reactants separately, i.e., pure 5-CQA dissolved in methanol and TRP in Na_2CO_3. 5-CQA was detected giving one single peak (Appendix, Figure 8). TRP was also detected under these specific chromatographic conditions. In Appendix Figure 9, the chromatograms of 25, 50 and 100ppm TRP solutions are shown, with a retention time around 6.1 min.

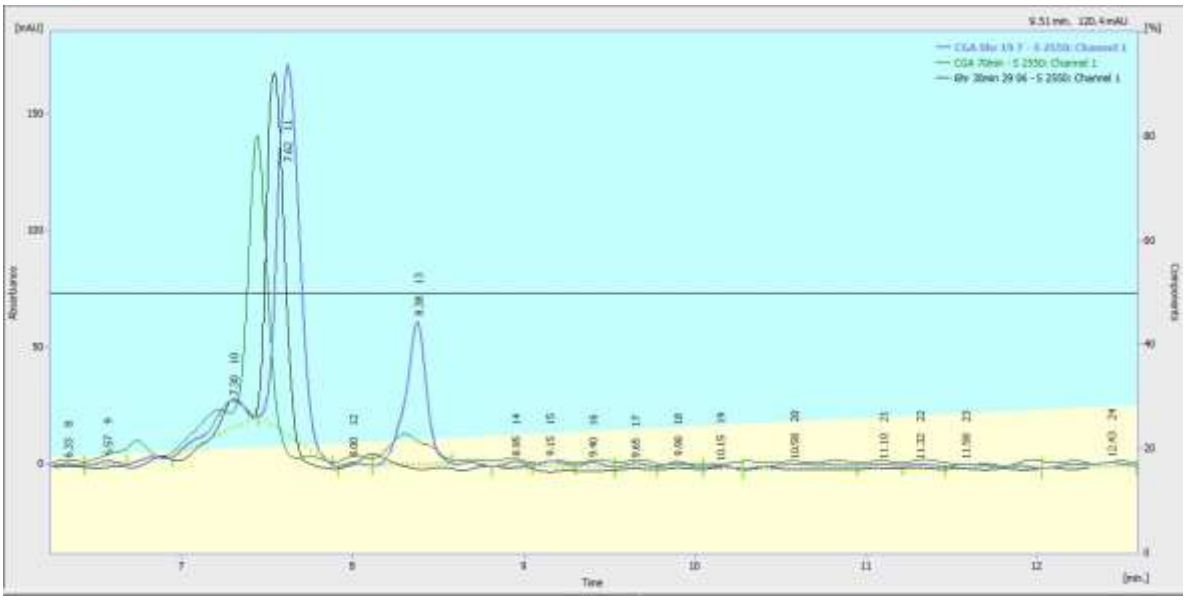
Measurements were taken during the reaction resulting in two peaks appearing in the chromatogram. Indicatively, in Figure 2a the chromatograms of the reactant mixtures at t=0min, t=70min and t=390min are shown. The first peak has a retention time very close to the retention time of TRP (Figure 2a). At t=70min the area of the first peak slightly decreases compared to t=0min, while at t=390min the area has increased again. Consequently, it is assumed that the total area of that peak is the sum of the area of the red pigment's peak which increases with time and the area of TRP's peak, which decreases with time. Improvement of the chromatographic conditions, such as change in the gradient, mobile phase composition and/or flow rate might contribute to improving the resolution and separation of the two peaks, but it was out of the scope of this manuscript. The second peak was identified as the second reactant, 5-CQA. During the reaction, the 5-CQA peak was decreasing, and it was not detectable after 6.5hours (Figure 2a).

The development of red colour during the reaction between 5-CQA and TRP was followed spectrophotometrically at 540nm, and the results are presented in Figure 2b. Observing Figure 2b it seems that for the first three hours the absorption increases rapidly. Progressively, it slows down ending up in a plateau. Based on these observations it is concluded that the reaction ends at about 8,5h where the absorbance at 540nm stabilizes. This constitutes almost a 3-fold reduction in reaction time reported in literature and can be attributed to the enhanced mixing, mass transfer and the local "hot spots" that are created by the application of ultrasound [9]. It can also be seen that initially the reaction rate is higher while it gradually decreases until it stabilizes at the end of the reaction.

It also seems that 5-CQA concentration decreases sharply with the onset of the reaction, while after 130 minutes reaches a plateau, at the same time that the absorption of the product is increased. This type of behavior matches a typical second order reaction. Practically after 6.5h 5-CQA

concentration in the reaction mixture remained constant ($1.7x10^{-5}$ mol/Lt), which translates to 98% conversion taking into account that initial concentration Co=0.001 mol/Lt. It is possible that the remaining 5-CQA continues to react, since the color stabilizes after 8.5hours. However, we were not able to determine that analytically due to the HPLC method detection limitation. Another possible explanation could be given by the work of Yao et al (2010), where it was shown that *cis*-double bonds could be quantitively converted to the corresponding *trans*-forms under sonication even at low temperatures (0^oC) [15]. This conversion is possible to facilitate the increase in conjugation of double bonds over time, and therefore the intensity of the red color.

a



b

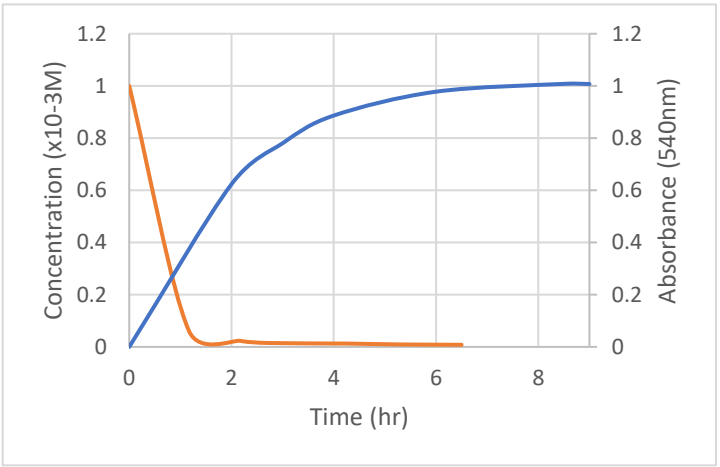


Figure 2: a) HPLC (280nm) Comparative chromatograms at different time points (0min (purple), 70min (green), 390min (black) showing the difference in peak surfaces over time b) Concentration of 5-CQA and absorbance of the reaction product over time

In order to determine the order of the reaction, hypotheses were made and with the help of the experimental results these hypotheses were rejected or confirmed. Specifically, the first hypothesis was that the reaction follows first order kinetics, and the second hypothesis was that it follows second

order kinetics. First order kinetics can be described by equation 3.1, and the results are shown in Figure 3a.

$$\ln\left(\frac{C_A}{C_{Ao}}\right) = -kt \qquad (3.1)$$

If this assumption was correct, then the data of the two axes should have a linear dependence. Instead, a curve is formed in Figure 3a, so it is concluded that this hypothesis cannot be confirmed.
It is now assumed that the reaction is a second order one which is described by the equation 3.2 [16]:

$$\ln(C_A) = \ln(C_{Ao}) + kt \qquad (3.2)$$

The second hypothesis seems to be correct since, as shown in Figure 3b, there is a linear dependence as predicted by the equation 3.2. Thus, it is concluded that the reaction is a second order for 5-CQA and the reaction rate constant equals to 323,03 ($M^{-1}min^{-1}$) or 5,38 ($M^{-1}sec^{-1}$).

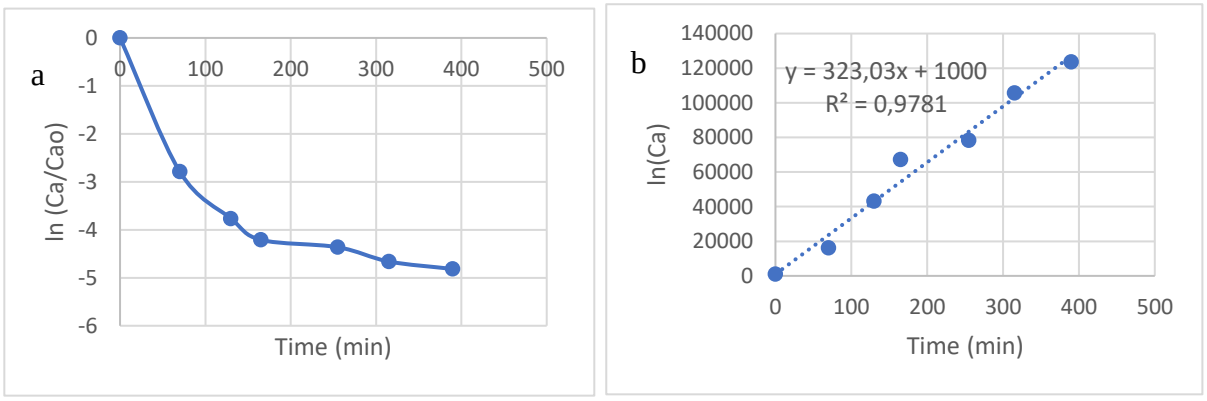


Figure 3: (a) reaction rate calculated as first order reaction and (b) reaction rate calculated as second order reaction

To further investigate the reaction order, experiments with various concentrations of the reactants were performed. The reaction mixtures prepared as described in 2.3 were placed in the ultrasonic bath at 40°C. During the reaction, measurements were taken using HPLC which aimed at monitoring the reaction process and more specifically at the degree of conversion of the reactant (5-CQA). Applying the Method of Initial Rates to Second Order Reactions given by Eq. (3.3), the order of the reaction for each of the reactants is calculated separately. Results are presented in Table 3.

Table 3: Initial Rate Method results

[A] (mM)	**[B] (mM)**	**r (M min^{-1})**
1	7	1,34x10^{-5}
0,5	7	2,43x10^{-6}
1	14	1,06 x10^{-5}

*A= 5-CQA B=TRP

$$\frac{r_1}{r_2} = \frac{k[A]_1^n[B]_1^m}{k[A]_2^n[B]_2^m} \qquad (3.3)$$

By solving Eq 3.3 it is concluded that the reaction is second order in A and zero order in B. Therefore, the global order for the reaction is second order. Then the reaction constant is calculated, according to the results from the HPLC and thus Table 4 is formed. More specifically, the rate constant is calculated for each time point and the final result is obtained as the average of the individual constants. To verify that the reaction order is 2, initially the rate constants were calculated for a first order reaction (n=1). Table 4 clearly shows that first order kinetics cannot be applied in this case. The average rate constant k for a second order reaction (n=2) is calculated equal to 315.68$M^{-1}min^{-1}$, which is very close to the k value calculated by equation 3.2 (323.03 $M^{-1}min^{-1}$).

Table 4: Rate constant calculation

t (min)	$[C_A]$ (M)	k (min^{-1}) n=1	k (M^{-1} min^{-1}) n=2
70	6,15 x10^{-5}	0,0398	217,71
130	2,31 x10^{-5}	0,0289	324,45
165	1,49 x10^{-5}	0,0255	401,49
255	1,27 x10^{-5}	0,0171	303,60
315	9,46 x10^{-6}	0,0148	332,421
390	8,09 x10^{-6}	0,0123	314,41
Average		-	315.68

3.2. Effect of different TRP concentrations

The experiments have been chosen to take place for tryptophan concentrations from 6mM-14mM because according to the literature concentrations lower than 6mM give brown colour [1]. Since in literature the molar ratio of the two reactants is 1:7 (CGA:TRP), the product of that reaction was used as a measure for comparison for the products of the other reactions with different molar ratios. As shown in Figure 4, the most concentrated (dark) red colour is observed when the concentrations of 5-CQA and TRP are 1mM and 7mM (sample 1) respectively. The highest colour difference (ΔE) was observed for samples 4, where TRP had twice the initial concentration of sample 1 and sample 5, where CGA had half the concentration of the sample 1 (Table 5).

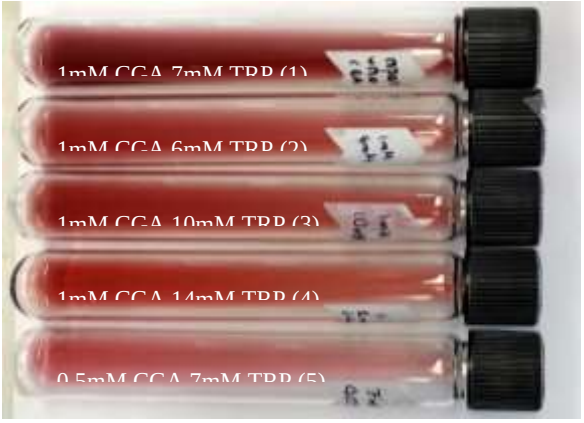


Figure 4: Colour development for different CGA and TRP concentrations after 8.5h of reaction

Table 5: Colourimetric results for samples with different concentration of reactants (samples 1-5, average of 3 readings)

Sample	L*	a*	b*	ΔE
1	25.14	50.21	40.20	-
2	38.28	59.73	52.58	20.41
3	35.76	59.70	53.93	19.79
4	39.58	65.98	63.76	31.82
5	54.17	57.14	30.81	31.29

3.3. Temperature effect on the reaction

After the reaction rate constant was defined, tests were performed at three different temperatures (40ºC, 63 ºC, 73 ºC), in order to determine the temperature dependence. It was observed that with increasing temperature the reaction time decreased significantly. At 40 ºC the reaction takes place in 8.5 hours, at 63 ºC at 5.5 hours and at 73 ºC in just 3 hours. However, with increasing temperature, the colour changed gradually from red to brown (Figure 5). This may be due to adverse reactions that may occur at higher temperatures or possibly the destruction of one or both of the reactants upon exposure to those temperatures. Cuq and Cheftel (1983) reported a marked decrease of free tryptophan at pH 6.5 starting at 90ºC with a calculated activation energy of 78920 Joule/mol [17]. Considering that the reaction takes place under ultrasound treatment, this activation energy is expected to decrease leading to even higher percentage of free tryptophan destruction. It has been reported that 5-CQA in alkaline environment undergoes isomerization and transformation even at room temperature [18]. Moreover, the increase in heating time of 5-CQA solution caused an increase in the amounts of caffeic acid, quinnic acid and cis-caffeic acid [9]. To verify the colour change the samples were measured with a colourimeter to and the results are presented in the Table 6.

Table 6: Results from colourimetry measurements *at different temperatures (average of 3 readings)*

Temperature (ºC)	Colour	L*	a*	b*
40	Red	22,20	47,87	33,42
63	Light Red	26,59	45,91	35,84
73	Brown	25,31	28,56	36,51

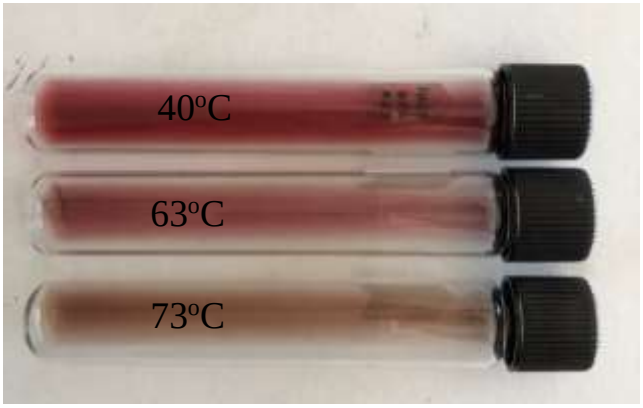


Figure 5: Colour development at 40, 63 and 73ºC

3.4. Heat stability of the red pigment product

Exposure to high temperatures leads to degradation and that poses a major critical issue of natural pigments restricting their use to foodstuffs that are not subjected to heat treatment [19]. As described in 2.4, the red pigment was subjected to various heat treatments. The colour difference (ΔE) between the untreated and treated samples was 3.91±0.11, 1.35±0,09, 2.52±0,18 and 19.12±1,23 for heating, freezing, sonication and microwave treatments, respectively. It is noted that the red pigment exhibits a remarkable stability to different sources of heating at neutral pH conditions. Similarly, Moccia et al observed that the red 3-CQA-TRP product had a minimal pH dependence and proved stable for at least 3 h at 90 ◦C, both at pH 3.6 and 7.0 [4]. This represents an advantageous property that could allow to significantly expand the range of applications of this colourant within the food industry.

3.5. Antimicrobial action of products

Reaction product did not exhibit any significant anti-microbial action. 5-CQA on its own is a known antimicrobial agent [20]. However, when it reacts with tryptophan (98% conversion) there is a negligible amount of 5-CQA remaining in the final product.

3.6. 5-CQA-TRP red product as a food colourant in sausages

Cooked pork sausages were stored at refrigerating temperatures and were monitored for colour and oxidation stability during storage and compared to samples prepared with the addition of sodium nitrite. Colour was followed by measuring the OxyMb content of the samples and spectrophotometrically at 422nm, where it exhibited maximum absorbance for both the nitrite salt sample and the red pigment sample. Analyzes to determine the percentage content of myoglobin and its forms were performed using the equations proposed by Tang (2004) [14]. In Figure 6a, it is observed in all three samples that the %oxyMb value falls sharply on the second day of storage. The sample that did not contain additives shows the largest drop in %oxyMb. It is also observed that on the remaining days of storage, the percentage of oxymyoglobin in the samples with the additives decreases slowly and at a similar rate, maintaining to a large extent their original colour.

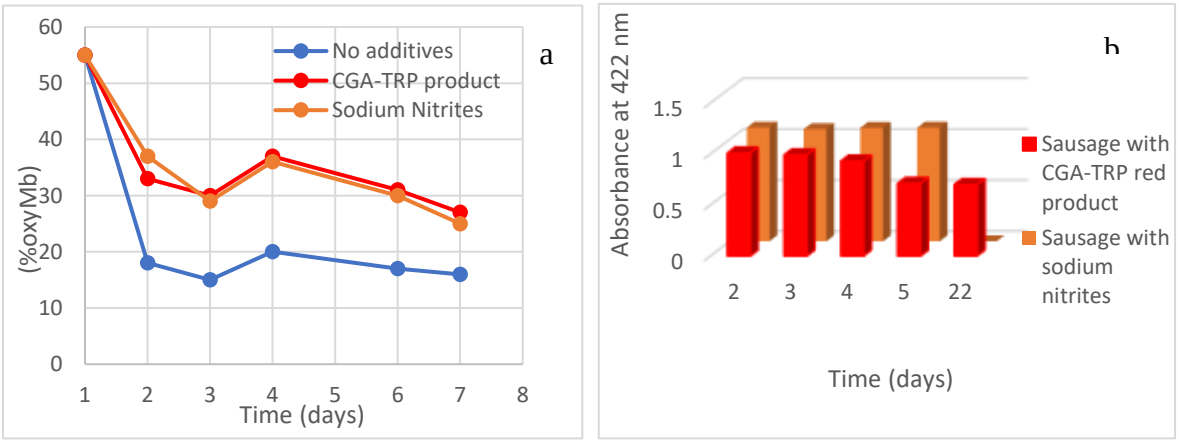


Figure 6: (a) OxyMb content of samples during storage and (b) Absorbance at 422nm during storage6

The spectrophotometric analysis of the samples was performed on the 2nd to the 5th day of their preparation and on the 22nd day of storage at a wavelength of 422 nm which corresponds to the pink-

violet colour. In the sausage containing the product from the 5-CQA-TRP reaction, there is a decrease in absorption at this wavelength over time, while the colour of the sausage fades slowly. On the 22nd day it is observed that it still absorbs at a wavelength of 422 nm and that its absorption decreased slightly compared to the 5th day. This was also verified visually in the sausage. As for the sausage that contained sodium nitrite, its absorption is constant for the first 5 days at 422 nm, but on the 22nd day there is a visual alteration acquiring a gray colour accompanied by no absorbance at 422nm (Figure 6b).

3.7. Antioxidant properties of the 5-CQA and TRP reaction product as a food additive

The results above are promising regarding the potential application of the reaction product as a food colourant, especially since it compares favorably to nitrite salts. Therefore, another important parameter that should be compared was its anti-oxidant properties. Figure 7 depicts the formation of secondary oxidation products during refrigerated storage of the cooked pork sausages, as measured by TBARs. The sample without additives from the second day began to show a higher concentration of μmolMDA / kg than the other two sausages containing additives, while showing visual signs of oxidation (discolouration). The addition of nitrites and the red pigment considerably retarded the lipid oxidation of the cooked sausages during the storage period in a similar manner. On days 3 through 8 the samples with the addition of the 5-CQA-TRP product exhibited significantly lower oxidation than the control (no additives) sample ($p<0.05$). The antioxidant activity of nitrıtes was expected, since their addition to meat products significantly slows down the oxidation of lipids [21]. Phenolic compounds according to various studies also slow down the oxidation of lipids. Specifically, Papuc. C et al. (2017) argue that polyphenols can inhibit the oxidative degradation of lipids and proteins, thus maintaining the odor and improving the colour stability of meat [22]. Maqsood and Benjakul (2010) also studied the effect of phenolic compounds on ground beef and observed a lower concentration of μmolMDA / kg [23]. This effect was also investigated by Liu et al. (2015), who found that, in all meat samples with added phenolic compounds, lipid peroxidation was significantly delayed [24]. Regarding the 5-CQA-TRP product, no studies have been performed to confirm their inhibitory effect on lipid oxidation.

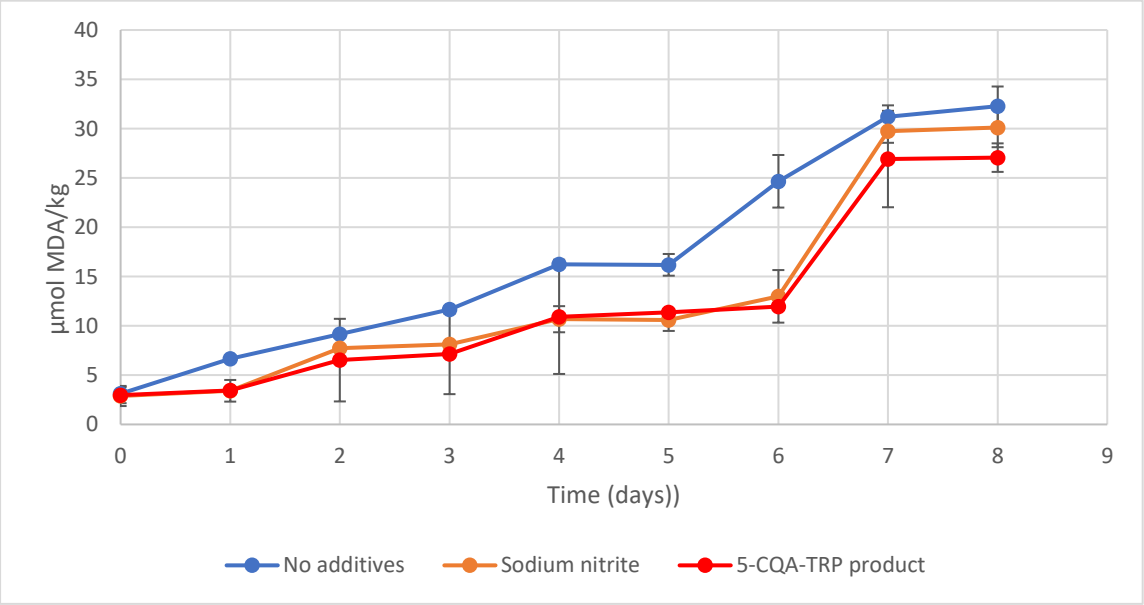


Figure 7: Oxidation of cooked pork sausages during storage

4 Conclusions

Natural red pigments currently used in the food industry suffer from a main disadvantage, i.e. susceptibility to heat degradation. The reaction product between 5-CQA and tryptophan is a promising alternative. In this work, it is reported for the first time a significant decrease in reaction time from 24-64h to 8.5h by means of ultrasonication. The global reaction order was estimated at 2, with 5-CQA order being equal to 2 and tryptophan's 0. The reaction constant was also calculated (k=323.03 M-1min-1). The red pigment had no significant antimicrobial properties. However, it exhibited antioxidant properties similar to those of sodium nitrite as measured by both secondary oxidation products and colour stability of Frankfurt-type sausages (OxyMb content), and most importantly showed remarkable heat stability. The latter property broadens the spectrum of its potential applications in the food industry.

References

1. Vercruysse, KP.: Preliminary observations on the interactions between chlorogenic acid and select amino acids. ChemRxiv. Cambridge: Cambridge Open Engage (2019). D O I: 10.26434/chemrxiv.8311481.v1
2. Wianowska, D., Gil M.: Recent advances in extraction and analysis procedures of natural chlorogenic acids. Phytochem Rev. 2019 Feb;18(1):273–302.
3. Lu ,H., Tian, Z., Cui, Y., Liu, Z., Ma ,X..: Chlorogenic acid: A comprehensive review of the dietary sources, processing effects, bioavailability, beneficial properties, mechanisms of action, and future directions. Comprehensive Reviews in Food Science and Food Safety. 2020 Nov;19(6):3130–58.
4. Moccia, F., Martín, MÁ., Ramos,S., Goya ,L., Marzorati, S., DellaGreca, M., et al. : A new cyanine from oxidative coupling of chlorogenic acid with tryptophan: Assessment of the potential as red dye for food coloring. Food Chemistry. 2021 Jun;348:129152.
5. Xue F, Li C, Adhikari B. Physicochemical properties of soy protein isolates-cyanidin-3-galactoside conjugates produced using free radicals induced by ultrasound. Ultrasonics Sonochemistry. 2020 Jun;64:104990.
6. Schiel, MA., Chopa, AB., Silbestri, GF., Alvarez, MB., Lista, AG., Domini, CE.. : Use of Ultrasound in the Synthesis of Heterocycles of Medicinal Interest. In: Green Synthetic Approaches for Biologically Relevant Heterocycles [Internet]. Elsevier; 2015 [cited 2021 May 12].p.571–601. Available from: https://linkinghub.elsevier.com/retrieve/pii/B9780128000700000219
7. Gogate, PR. : Cavitational reactors for process intensification of chemical processing applications: A critical review. Chemical Engineering and Processing: Process Intensification. 2008 Apr;47(4):515–27.
8. Gogate ,PR., Tayal, RK., Pandit, AB. : Cavitation: A technology on the horizon. Current Science. 2006;91(1):13.
9. Dawidowicz, AL., Typek, R.: The influence of pH on the thermal stability of 5-O-caffeoylquinic acids in aqueous solutions. Eur Food Res Technol. 2011 Aug;233(2):223–32.
10. Magaldi, S., Mata-Essayag, S., Hartung de Capriles, C., Perez, C., Colella, MT., Olaizola, C., et al. : Well diffusion for antifungal susceptibility testing. International Journal of Infectious Diseases. 2004 Jan;8(1):39–45.
11. CLSI : Methods for Dilution Antimicrobial Susceptibility Tests for Bacteria that Grow Aerobically, Approved Standard, 9th ed., CLSI document M07-A9. Clinical and Laboratory Standards Institute, 950 West Valley Road, Suite 2500, Wayne, Pennsylvania 19087, USA, 2012).
12. Herrmann, SS., Granby, K., Duedahl-Olesen, L.: Formation and mitigation of N-nitrosamines in nitrite preserved cooked sausages. Food Chemistry. 2015 May;174:516–26.

13. Vareltzis, P., Hultin, HO., Autio, WR.: Hemoglobin-mediated lipid oxidation of protein isolates obtained from cod and haddock white muscle as affected by citric acid, calcium chloride and pH. Food Chemistry. 2008 May;108(1):64–74.
14. Tang, J., Faustman, C., Hoagland, TA. Krzywicki Revisited: Equations for Spectrophotometric Determination of Myoglobin Redox Forms in Aqueous Meat Extracts. Journal of Food Science. 2006 May 31;69(9):C717–20.
15. Jun Hong Yao, Yusheng Chen, Yi Pang, : Application of Sonochemistry in the Isomerization of Carbon-Carbon Double Bonds. Wiley Online Library. 2010 Aug.; https://doi.org/10.1016/j.ultsonch.2020.104990
16. Ancheyta Juárez, J. : Chemical reaction kinetics: concepts, methods, and case studies. Hoboken, NJ: John Wiley & Sons, Inc; 2017. 1 p.
17. Cuq, JC., Cheftel, JC.: Tryptophan degradation during heat treatments: Part 1—The degradation of free tryptophan. Food Chemistry. 1983 Jan;12(1):1–14.
18. Clifford, M.: Characterisation of chlorogenic acids by simultaneous isomerisation and transesterification with tetramethylammonium hydroxide. Food Chemistry. 1989;33(2):115–23.
19. Fernández-López, JA., Angosto, JM., Giménez, PJ., León, G.: Thermal Stability of Selected Natural Red Extracts Used as Food Colorants. Plant Foods Hum Nutr. 2013 Mar;68(1):11–7.
20. Zhao, M., Wang, H., Yang, B., Tao, H.: Identification of cyclodextrin inclusion complex of chlorogenic acid and its antimicrobial activity. Food Chemistry. 2010 Jun;120(4):1138–42.
21. Majou, D., Christieans, S.: Mechanisms of the bactericidal effects of nitrate and nitrite in cured meats. Meat Science. 2018 Nov;145:273–84.
22. Papuc, C., Goran, GV., Predescu, CN., Nicorescu, V., Stefan, G.: Plant Polyphenols as Antioxidant and Antibacterial Agents for Shelf-Life Extension of Meat and Meat Products: Classification, Structures, Sources, and Action Mechanisms: Polyphenols extending meat shelf-life. Comprehensive Reviews in Food Science and Food Safety. 2017 Nov;16(6):1243–68.
23. Maqsood, S., Benjakul, S.: Preventive effect of tannic acid in combination with modified atmospheric packaging on the quality losses of the refrigerated ground beef. Food Control. 2010 Sep;21(9):1282–90.
24. Liu, F., Xu, Q., Dai, R., Ni, Y : Effects of natural antioxidants on colour stability, lipid oxidation and metmyoglobin reducing activity in raw beef patties. Acta Sci Pol Technol Aliment. 2015;14:37–44. doi: 10.17306/J.AFS.2015.1.4.

APPENDIX

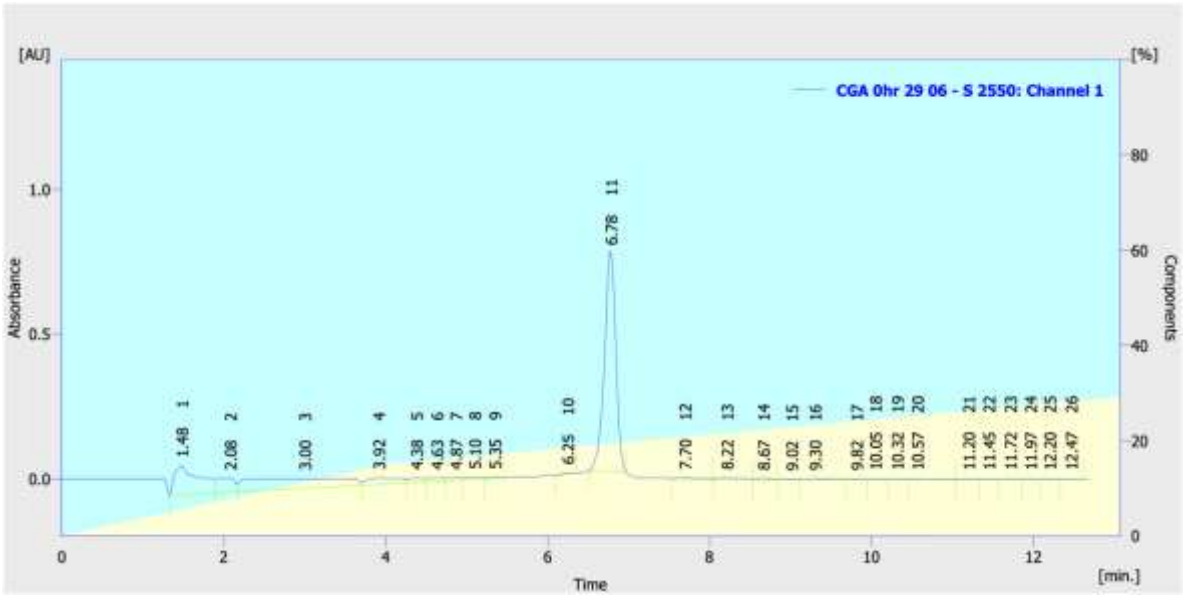


Figure 8: *Pure 5-CQA chromatogram*

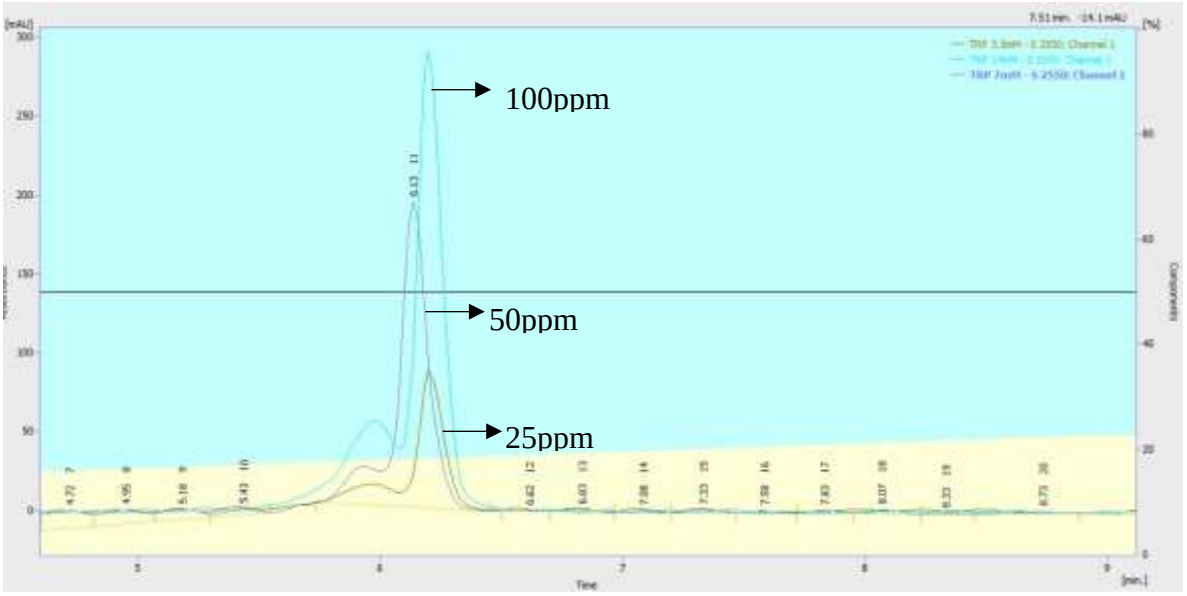


Figure 9: Comparative chromatogram of TRP at different concentrations

Theme 3 : Chemical Process Modeling, Simulation and Control

Application of RSM modelling to a synthetic gemini surfactant (SGS) corrosion inhibition of carbon steel C1010 in acidic environment

Nuhu Dalhat Mu'azu[1]*, Shamsuddeen A. Haladu[2]; Ayman Alradi[1], Mustafa Almohammedali[1], Yaqoob Aljasir[1] and Yazeed Alkhathami[1]

[1] Department of Environmental Engineering, College of Engineering, Imam Abdulrahman Bin Faisal University, P.O Box 1982 ,31451 Dammam, Saudi Arabia.

[2] Department of Basic Engineering Sciences, College of Engineering, Imam Abdulrahman Bin Faisal University, P.O Box 1982 ,31451 Dammam, Saudi Arabia

**Corresponding author: nmdalhat@iau.edu.sa; dalhat@gmail.com; Tel.: (+966507532689)*

Abstract: In this work, response surface methodology (RSM) modelling technique was applied to assess the potentials of a synthetic gemini surfactant (SGS) as a corrosion inhibitor for carbon steel in strong acidic environment. Under faced centered central composite design (CCD), the influence of operating temperature (25-65°C), exposure period (2-48 hours) and inhibitor concentration (C=0.01, 0.0055 and 0.1 mM) on the steel weight loss, corrosion rate and inhibition efficiency where modelled, evaluated, and optimized. High RSM predictive models were developed for the investigated response (R^2 =0.9930-0.9999) with significant models' fitness (p-values <0.0001). The operational parameters significantly, influence on the corrosion of the carbon steel which increases with temperature and exposure time while higher the SGS inhibitor concentration significantly slowed down the corrosion. The optimal experimental conditions were obtained at 45 ^{o}C, exposure time 48 and 0.1 mM SGS concentration, yielding high inhibition efficiency of 92%, weight loss of 0.34 g and low corrosion rate of 0.003 mm/year. This study demonstrates the suitability of application of RSM modelling technique for evaluation of corrosion inhibitors under aggressive environments

Keywords: Response surface methodology, corrosion protection, weight loss, statistical analysis, corrosion modelling; ANOVA

1. Introduction

Corrosion of pipes is a global problem that greatly affect economics of majority of industries, with estimated cost reaching billions of dollars globally (Prasad et al., 2020; Verma et al., 2021). One of the most effective approaches to combat these problems is through using chemical additives (inhibitors) that serve as protective films to metals and alloys to prevent or control the extent of the damaging effects (AbdelRaheem et al., 2020; Verma et al., 2021). A number of synthetic chemical materials such as copolymers, organophosphonates, poly(maleic acid), polyphosphates, and poly(acrylic acid) have been developed and successfully tested and deployed as anti-corrosion agents (AbdelRaheem et al., 2020; Haladu et al., 2019; Verma et al., 2021). Saudi Arabia is a top destination for desalination and oil markets, with vast water and oil distribution networks spanning thousands of kilometers (Prasad et al., 2020). Additionally, KSA has extreme weather conditions that can aggravate chemical reactions that lead to substantial corrosion of the pipe distribution network integrity via corrosion. Thus, identifying sustainable and cost-effective corrosion inhibitors will help several

industries to mitigate harmful effects of corrosion. Different types of gemini surfactants have been reported to demonstrate high potentials for metals corrosion inhibition in different aggressive environments (Du et al., 2018; Heakal and Elkholy, 2017; Mao et al., 2021; Mobin et al., 2017). Recently, applications of response surface methodology (RSM) modelling technique has attracted increased interest in corrosion studies (Oyekunle et al., 2019; Wang et al., 2021), yet despite its numerous potential merits, its adoption in corrosion studies is still rare. In this study, RSM modelling technique was implemented for evaluation and optimization of influences of operational parameters on the corrosion inhibition efficacy of a synthetic gemini surfactant (SGS) on carbon steel (carbon steel C1010) via weight loss bench scale experiments.

2. Materials and method

2.1. Synthesis of Gemini surfactant (SGS)

The SGS used is shown in Figure 1. It was synthesized by reacting 1,6-dibromohexane with N,N-dimethyldodecylamine in acetonitrile at 80 °C for 24 h. The residue was recrystallized from ether and dried under vacuum.

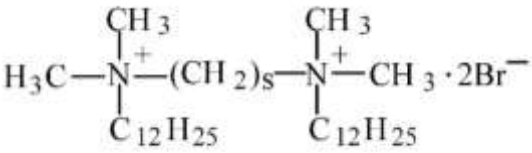


Figure 1: Chemical structure of the gemini surfactant

2.2. RSM experiments design matrix and modeling

Weight loss experiments as good indicator of material corrosion, is usually, the initial step of testing any corrosion inhibitor in corrosion studies (Guo et al., 2020). This owes to the fact that weight loss experiment is a simple effective way to detect corrosion which is usually provides clue to determine deterioration of pipelines materials and efficacy of protection that could be provided by an inhibitor. As such, in this study, response surface methodology (RSM) modeling approach was implemented for evaluating the corrosion inhibition efficacy of the SGS (due to its numerous advantages of RSM) on carbon steel C1010 in acidic solution via weight loss bench scale experiments. To achieve that, a three factors faced centered central composite design (CDD) was adopted to investigate the influence of temperature (A=25-65°C), exposure time (B=2-48 hours) and SGS inhibitor concentration (C=0.01-0.1 mM) on R1=Weight loss, R2= Corrosion rate(mm/year) and R3= Inhibition efficiency (%). The levels of the operational paraneters and coding for RSM modeling are provided in Table 1. For a k number of factors experiments, the faced centered CCD adopted involved three types of required experiments; 3k factorial, 2k axial and k central runs (star points) that are replicated required for estimation of the experimental variability and repeatability necessary to determine the curvature of the model as well as the model's error (Ait-Amir et al., 2020; Myers et al., 2016). Additionally, the adopted CCD is advantigous over other types of the CCD as in such a design the "star points" are located at the center of each face of the factorial space (i.e $\alpha = \pm 1$), fewer factor levels (as low as 3 compared to 5) and also available data for factorial or resolution V design can be augmented with star

points to transformed into the dsedign (Ait-Amir et al., 2020; Myers et al., 2016). The required seventeen (17) corrosion tests are given in Table 2. Design-Expert version 9 was used for fitting the obtained corrosion

Table 1: Investigated operational conditions and their levels

Run#	Independent variable			Responses		
	A	B	C	Weight loss (R1) (g)	Corrosion rate (R2) (mm/year)	Inhibition efficiency (R3) (%)
1	25	2	0.01	0.012	4.434	0.000
2	65	2	0.01	0.179	66.433	28.107
3	25	48	0.01	0.169	2.605	60.932
4	65	48	0.01	6.354	98.232	0.592
5	25	2	0.1	0.009	3.339	23.729
6	65	2	0.1	0.099	36.621	60.369
7	25	48	0.1	0.134	2.069	68.966
8	65	48	0.1	2.219	34.304	65.286
9	25	25	0.055	0.079	2.335	65.060
10	65	25	0.055	1.417	42.054	66.128
11	45	2	0.055	0.043	16.140	51.151
12	45	48	0.055	0.572	8.839	74.925
13	45	25	0.01	0.549	16.303	49.592
14	45	25	0.1	0.321	9.515	70.581
15	45	25	0.055	0.424	12.247	62.133
16	45	25	0.055	0.413	12.594	61.059
17	45	25	0.055	0.388	11.532	64.345

Table 2: Faced-centred central composite (FC-CCD) experimental design and results for Carbon steel C1010 corrosion inhibition tests

data into the generalized RSM polynomial function given equation 1, the analysis of variance (ANOVA) as well as the optimization study.

$$y = \beta_0 + \sum_{i=1}^{k} \beta_i x_i + \sum_{i=1}^{k} \beta_i x_i^2 + \sum_{i=1}^{k-1} \sum_{j=2}^{k} \beta_{ij} x_i x_j + \varepsilon \qquad (1)$$

Factor		Lower level (-1)	Mid-level (0)	High-lower (+1)
A	Temperature (°C)	25	45	65
B	Exposure time (mg/L)	2	25	48
C	Inhibitor concentration (mM)	0.01	0.055	0.1

where y= developed model predicted response (R1, R2 or R3); β_{ii}, β_{ij}, β_i, β_0, are the developed model's coefficients; x_j , x_i, = operational conditions.

2.3. Corrosion inhibition experiments

The seventeen (17) weight loss corrosion tests were undertaken at different operational conditions (Table 2) which were set based on preliminary experiments. Carbon steel C1010 coupons used were submerged in glass bottles containing 100 mL of 1 M H_2SO_4 acid at different SGS concentrations, temperature, and exposure time as per the adopted design. Each of the seventeen samples was run in duplicate. At the end of each experiment, the weight difference before and after submerging the metal coupons in the acid solution was measured as the weight loss in g (R1). The rate of corrosion (R2) and percent inhibition efficiency (R3) was calculated using the equation 2 and 3, respectively:

$$R2\ (mm/yr) = 87.6 \times (R1/rAT) \quad (2)$$

R3 □□□□□□□□υ□□□□□υ□υ□□x 100 (3)

where: D = density of metal (g/cm^3); A = sample area (cm^2); T = metal sample exposure time (in hours); υ□□= weight loss of coupon sample in blank solution (i.e., without inhibitor); □υ= weight loss (mg) of coupon sample in solution with inhibitor

3. Results and discussions

3.1. Development SGS corrosion inhibition models' and their validations

The best fitted polynomial corrosion inhibition models R1, R2 and R3 given in equation 4, 5 and 6 were obtained via regressing the experimental data the coded operational variable (+1, 0, +1 as per Table 1) using equation 1, respectively. The R2 model required square root experimental data transformation to get the best fitted regression coefficients. The difference between these models' predictions and the corresponding actual experimental values (i,e, the residuals) given in Table 3, clearly, indicate goodness of the developed models. This is further corroborated by the high values of regression coefficients of R^2 (0.9979, 0.9999 and 0.9930), respectively (Lukman et al., 2014).

Similarly, all the requirements for other parameters such as CV, measures of precision adequate as well as all three(3) model's terms and lack-of-fit established at 5% (i.e., p-value < 0.05 and p-value >0.05 in Table 3, respectively) were adequately, met(Anderson and Whitcomb, 2016). This implies the high quality of the SGS corrosion inhibition models as well as their appropriateness of the design space navigation for drawing vital inferences regarding the SGS inhibition potentials based on the studied responses (Mu'azu et al., 2019). The ANOVA presented in Table 4 established the significant effects of all the investigated experimental operational parameters was established (Anderson and Whitcomb, 2016; Mu'azu et al., 2019). As the results given in Table 2 the single (B and C), binary (AB and AC), squared terms (A^2 and B^2) and cubic ABC terms were all major sigficant terms for all the responses (R1, R2 and R3). Meanwhile, were significant for R1 and R3 while not been associated with R3. These models are reduced RSM models that included model's terms that are directly, significant or insignicant terms B2, A2B2 for R2 and R3 A, BC, B2, A2B for R3 that were added to met RSM hierachical requirements as they indirectly had impact on their respective models (Anderson and Whitcomb, 2016; Mu'azu et al., 2021). Intrestingly, the best fitted models for all the three models needed to include the A, B, C, AB, AC, BC, A^2, B^2, ABC, A^2B, A^2C, AB^2 and A^2B^2 terms with only R1 having all theses terms been significant

$$R1 = 0.419 + 0.669A + 0.264B - 0.114C + 1.0017AB - 0.522AC - 0.5108BC + 0.328A^2 - 0.111B^2 - 0.502ABC + 0.8079A^2B - 0.417A^2C + 0.3968AB^2 + 0.510A^2B^2 \quad (4)$$

$$(Sqrt(R2) = 3.480 + 2.480A - 0.522\ B - 0.477C + 0.306AB - 0.713AC - 0.232BC + 0.525A^2 + 0.014B^2 - 0.257ABC + 0.608A^2B - 0.349A^2C + 0.395AB^2 + 0.520A^2B^2 \quad (5)$$

$$R3 = 62.51 + 0.5338A + 11.89B + 10.49C - 16.08AB + 8.16AC + 2.11BC + 3.08A^2 + 0.5257B^2 + 6ABC - 1.46A^2B + 5.58A^2C - 0.4582AB^2 - 25.18A^2B^2 \quad (6)$$

Table 3: Experimental vs Models' RSM predictions

Run#	R1=Weight loss			R2=Corrosion Rate			R3=Inhibition efficiency		
	Actual	Predicted	Residual	Actual	Predicted	Residual	Actual	Predicted	Residual
1	0.0435	0.0435	0	4.02	4.02	0	51.15	51.15	0
2	0.012	0.0119	0	2.11	2.11	0	0.12	0.12	0
3	0.0987	0.0987	0	6.05	6.05	0	60.37	60.37	0
4	2.22	2.22	0	5.86	5.86	0	65.29	65.29	0
5	6.35	6.35	0	9.91	9.91	0	0.59	0.59	0
6	0.1338	0.1338	0	1.44	1.44	0	68.97	68.97	0
7	0.4243	0.419	0.0053	3.5	3.48	0.0182	62.13	62.51	-0.3793
8	0.5493	0.5334	0.0159	4.04	4.04	0	49.59	49.59	0
9	1.42	1.42	0	6.48	6.48	0	66.13	66.13	0
10	0.0787	0.0786	0	1.53	1.53	0	65.06	65.06	0
11	0.4126	0.419	-0.0064	3.55	3.48	0.0674	61.06	62.51	-1.45
12	0.1685	0.1685	0	1.61	1.61	0	60.93	60.93	0
13	0.3205	0.3047	0.0159	3.08	3.08	0	70.58	70.58	0
14	0.179	0.1791	0	8.15	8.15	0	28.11	28.11	0
15	0.009	0.009	0	1.83	1.83	0	23.73	23.73	0
16	0.3885	0.419	-0.0305	3.4	3.48	-0.0856	64.34	62.51	1.83
17	0.5718	0.5718	0	2.97	2.97	0	74.92	74.92	0

Table 4: Analysis of variance (ANOVA) for Developed RSM Models for Carbon steel C1010 corrosion inhibition tests

Source	R1		R2		R3	
	F-value	p-value	F-value	p-value	F-value	p-value
Model	5842.83	< 0.0001	1115.13	0.0009	226.26	0.0007
A	1784.80	< 0.0001	2013.89	0.0005	0.2030	0.7378
B	278.14	0.0005	89.40	0.0110	100.69	0.0038
C	52.13	0.0055	74.45	0.0132	78.48	0.0055
AB	16003.44	< 0.0001	122.65	0.0081	737.10	0.0002
AC	4349.57	< 0.0001	665.63	0.0015	189.99	0.0015
BC	4161.35	< 0.0001	70.30	0.0139	12.66	0.0625
A^2	307.66	0.0004	54.22	0.0179	4.06	0.0998
B^2	35.35	0.0095	0.0376	0.8641	0.1182	0.4483
ABC	4033.23	< 0.0001	86.78	0.0113	102.64	0.0037
A^2B	2082.18	< 0.0001	96.91	0.0102	1.21	0.4363
A^2C	555.41	0.0002	32.01	0.0299	17.75	0.0414
AB^2	502.37	0.0002	40.84	0.0236	0.1197	0.7963
A^2B^2	392.03	0.0003	14.95	0.0608	76.37	0.0012

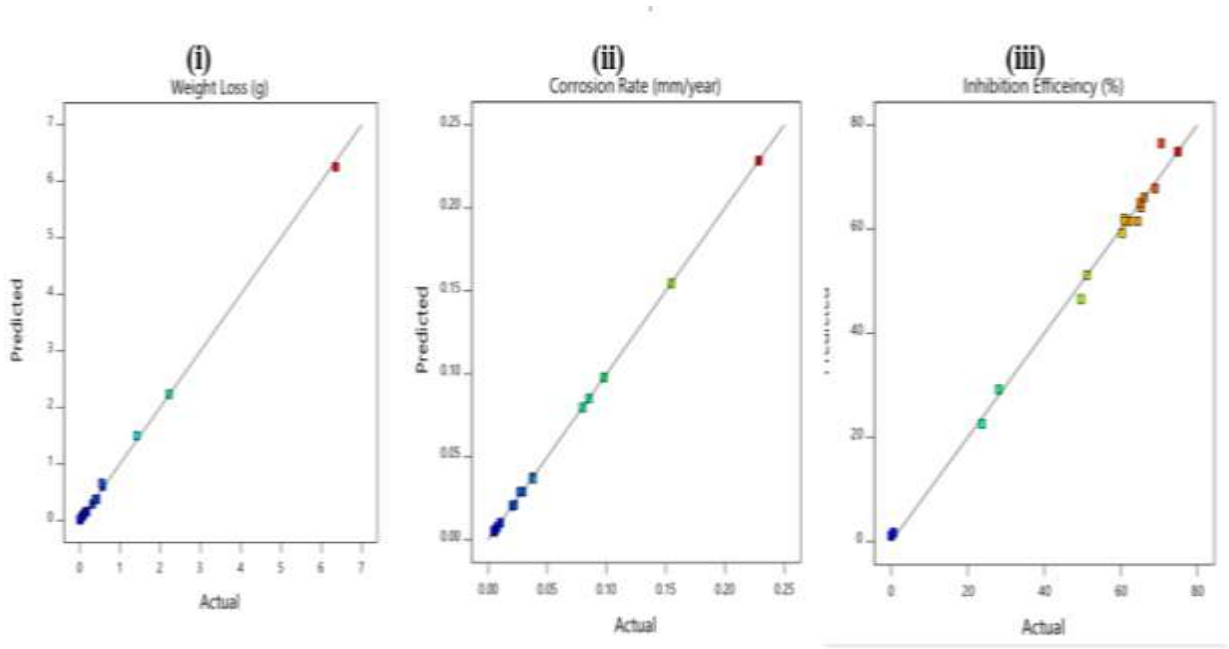


Figure 2: Experimental vs predicted results for (i) weight loss (ii) corrosion rate and (iii) inhibition RSM models

3.1.1 Effect of operation conditions on Measured Corrosion Responses.

The dependencies of R1, R2 and R3 on A, B and C are visaully, depicted in 3D and corresponding contours Figures 3, 4 and 5, respectively. Figure 3i and 3ii show a strong positive correlation of temperature and exposure time on the carbon steel weight loss, respectively. Meanwhile, the SGS

inhibitor concentration yielded a negative correlation with the weight loss while maintaining a strong intractive relation with the other two parameters as manifested in the $p<0.05$ for AB, AC and BC in the ANOVA in Table 4. This implies that, as the lost in the steel wieght increases with increase in both factor A and C which became agrrievated when the SGS concentration decreases. Consequently, the observed highest lost in the steel weight (*6.354 g)* was observable when the A=65 ^{o}C, B= 48 hours and C=0.01 mM (Table and Figure 3).

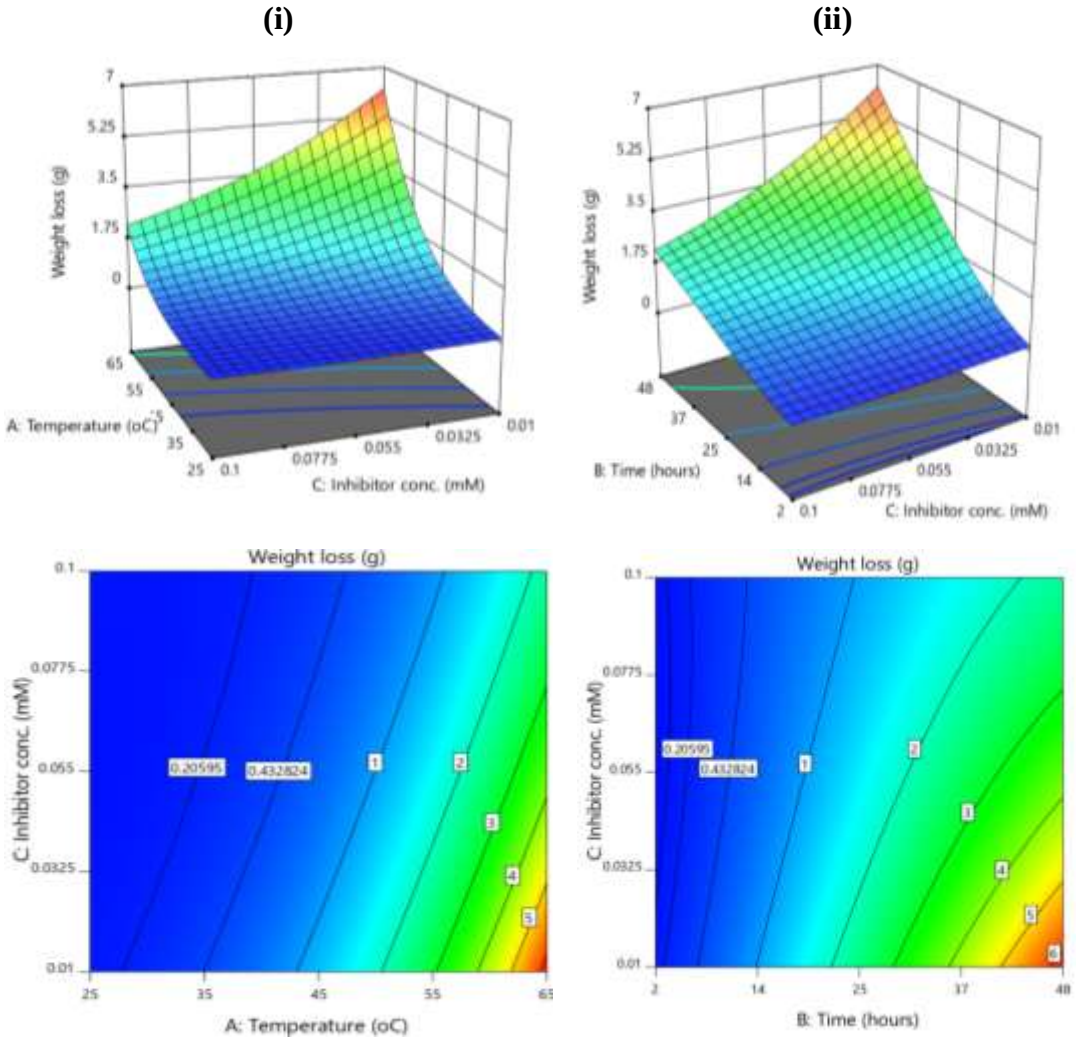


Figure 3: Effect of different operating conditions on Carbon steel C1010 weight loss

Comparable trends were obtained for the corrosion rate model (i.e., R2) as presented in Figure 4 with the worst rate also occuring A=65 ^{o}C, B= 48 hours and C=0.01 mM.

There was initial reduction in the R2 when the exposure time was increased between 2 to 25 hours, especially at higher inhibitor concentration (0.1 mM). Afterwards, the rate of corrosion started to deteriorate, reaching the worst scenario at the highest exposure duration. Meanwhile, at lower temperature range of 25 to 35 ^{o}C, both the weight loss and corrosion rate variability were insignificant regardless of the SGS concentration. On the other hand, as the inhibitor concentration was increased,

there is clear manifestations of decline in R1 and R2, implying the better performance of the SGS towards steel protection

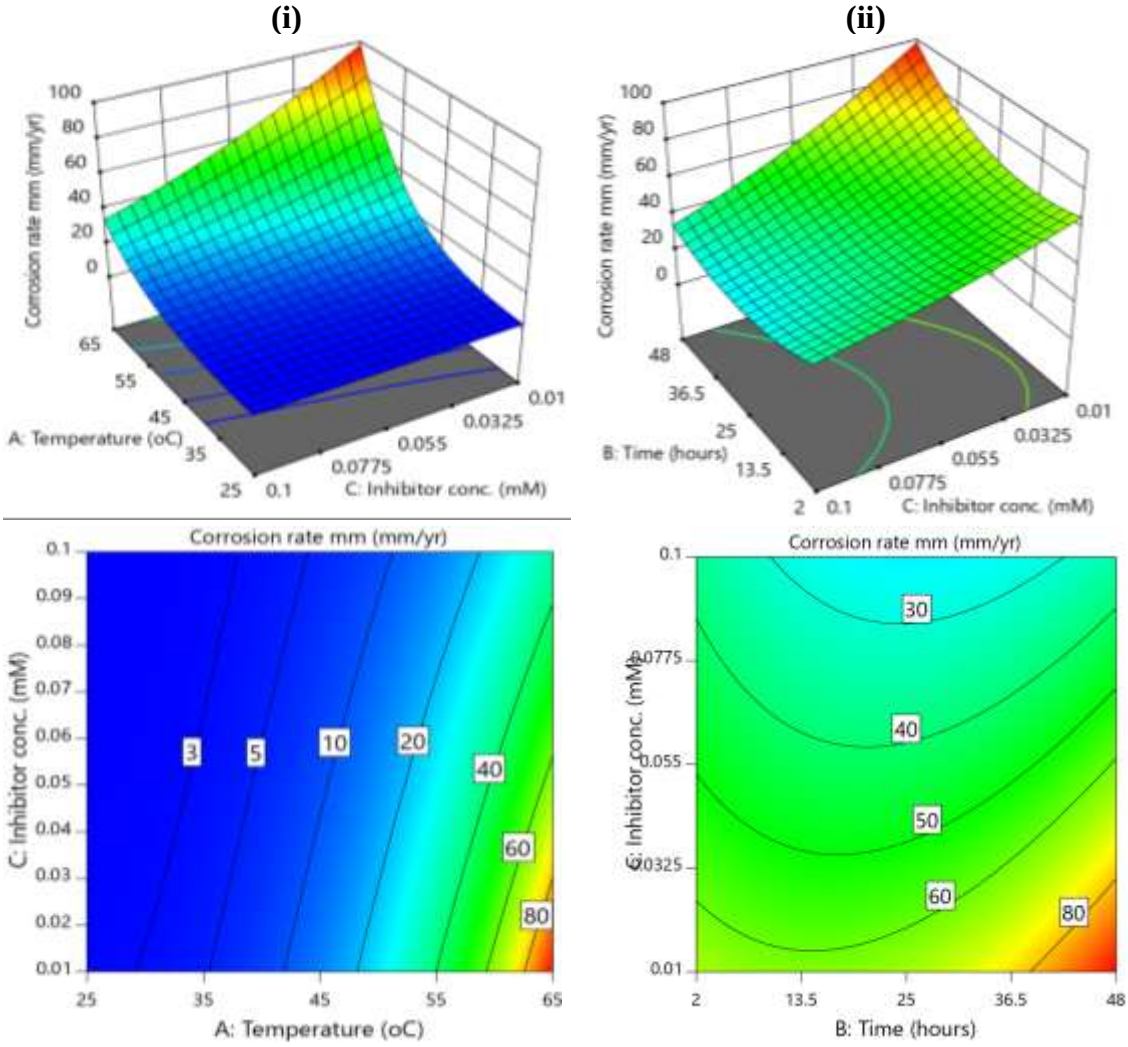


Figure 4: Effect of operating conditions on Carbon steel C1010 corrosion rate

Contrastingly, the dependency of SGS inhibition efficiency on temperature and time as shown in Figure 51 and 5ii, repsectively, show a different picture. The R3 initially, improved when both temperature and time were increased, reaching peak value (74.9%) around the central region when C= 0.01 mM). Thereafter, as both factors were increased, the R3, continously, reduced reaching the initial observed values at highest level of all the factors.

3.2 Numerical optimization of SGS inhibition

The numerical optimization of SGS corrosion inhinition of the steel carbon was undertken using Design Expert 9 desirability function under different optimization scenario as per Mu'azu el al (Mu'azu et al., 2021) The optimal experimental conditions with the highest desirability of 92.8% was

obtained at 45 °C, exposure time 48 and 0.1 mM SGS concentration of inhibitor, yielding high inhibition efficiency of up to 92%, weight loss of 0.34 g and low corrosion rate of 0.003 mm/year.

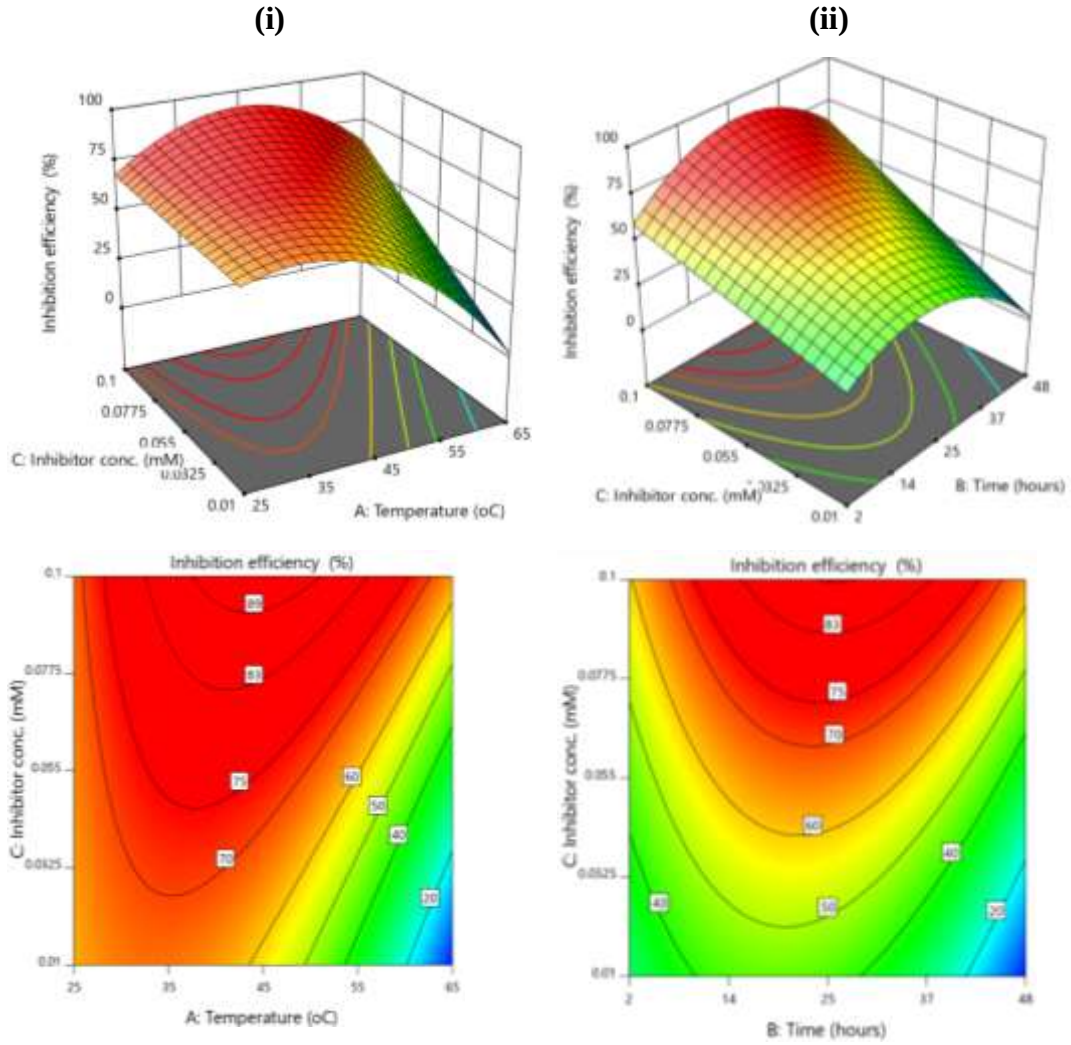


Figure 5: Effect of operating conditions on polymer inhibition efficiency

4. Conclusions

Response surface methodology (RSM) modelling technique was applied for assessing the potentials of a synthetic gemini surfactant (SGS) as a corrosion inhibitor for carbon steel in 1 M sulfuric acid under faced centered central composite design (CCD). The influence of operating temperature, exposure period, and inhibitor concentration on the steel weight loss, corrosion rate and inhibition efficiency where modelled, evaluated, and optimized. High RSM predictive models were developed for the investigated response (R^2 =0.9930-0.9999) with significant models' fitness (p-values <0.0001). The operational parameters significantly influence the corrosion of the carbon steel, which increases with temperature and exposure time, while higher SGS inhibitor concentration significantly slowed down the corrosion. The optimal experimental conditions were obtained at 45 °C, exposure time 48 and 0.1 mM SGS concentration, yielding high inhibition efficiency of 92%, weight loss of 0.34 g and low corrosion rate of 0.003 mm/year. This study demonstrates the suitability of application of RSM modelling technique is evaluation of corrosion inhibitors under aggressive environments.

References

1. AbdelRaheem, S.K., Ali, I.H., Ebraheem, S.A.M., Chung, I.-M., Mohamed, S.K., 2020. Exploring the corrosion inhibition effect of two hydrazone derivatives for mild steel corrosion in 1.0 M HCl solution via electrochemical and surface characterization studies. Int. J. Electrochem. Sci 15, 9354–9377.

2. Ait-Amir, B., Pougnet, P., El Hami, A., 2020. 6 - Meta-Model Development, in: El Hami, A., Pougnet, P.B.T.-E.M.S. 2 (Second E. (Eds.), . ISTE, pp. 157–187. https://doi.org/https://doi.org/10.1016/B978-1-78548-190-1.50006-2

3. Anderson, M.J., Whitcomb, P.J., 2016. RSM simplified: optimizing processes using response surface methods for design of experiments. Productivity press.

4. Du, J., Chen, Q., Liu, Q., Hu, X., 2018. Synthesis of a Novel Gemini Cationic Surfactant and Its Inhibition Behaviour and Mechanism Study on 2024 Al-Cu-Mg Alloy in Acid Solution. Int. J. Corros. 2018, 9890504. https://doi.org/10.1155/2018/9890504

5. Guo, W., Umar, A., Zhao, Q., Alsaiari, M.A., Al-Hadeethi, Y., Wang, L., Pei, M., 2020. Corrosion inhibition of carbon steel by three kinds of expired cephalosporins in 0.1 M H2SO4. J. Mol. Liq. 320, 114295.

6. Haladu, S.A., Umoren, S.A., Ali, S.A., Solomon, M.M., Mohammed, A.R.I., 2019. Synthesis, characterization and electrochemical evaluation of anticorrosion property of a tetrapolymer for carbon steel in strong acid media. Chinese J. Chem. Eng. 27, 965–978. https://doi.org/10.1016/j.cjche.2018.07.015

7. Heakal, F.E.-T., Elkholy, A.E., 2017. Gemini surfactants as corrosion inhibitors for carbon steel. J. Mol. Liq. 230, 395–407. https://doi.org/https://doi.org/10.1016/j.molliq.2017.01.047

8. Lukman, S., Bukhari, A., Al-Malack, M.H., Mu'Azu, N.D., Essa, M.H., 2014. Geochemical modeling of trivalent chromium migration in saline-sodic soil during Lasagna process: Impact on soil physicochemical properties. Sci. World J. 2014. https://doi.org/10.1155/2014/272794

9. Mao, T., Huang, H., Liu, D., Shang, X., Wang, W., Wang, L., 2021. Novel cationic gemini ester surfactant as an efficient and eco-friendly corrosion inhibitor for carbon steel in HCl solution. J. Mol. Liq. 117174.

10. Mobin, M., Aslam, R., Aslam, J., 2017. Non toxic biodegradable cationic gemini surfactants as novel corrosion inhibitor for mild steel in hydrochloric acid medium and synergistic effect of sodium salicylate: Experimental and theoretical approach. Mater. Chem. Phys. 191, 151–167. https://doi.org/https://doi.org/10.1016/j.matchemphys.2017.01.037

11. Mu'azu, N.D., Jarrah, N., Zubair, M., Manzar, M.S., Kazeem, T.S., Al-Harthi, M., 2019. Evaluation of novel Mg/Al/Ni-BaFe ternary layered hydroxides uptake of methyl orange dye from water. Korean J. Chem. Eng. 36, 2008–2022. https://doi.org/10.1007/s11814-019-0384-x

12. Mu'azu, N.D., Zubair, M., Ihsanullah, I., 2021. Process Optimization and Modeling of Phenol Adsorption onto Sludge-Based Activated Carbon Intercalated MgAlFe Ternary Layered Double Hydroxide Composite. Mol. . https://doi.org/10.3390/molecules26144266

13. Myers, R.H., Montgomery, D.C., Anderson-Cook, C.M., 2016. Response surface methodology: process and product optimization using designed experiments. John Wiley & Sons, New York,

New York.

14. Oyekunle, D.T., Oguntade, T.I., Ita, C.S., Ojo, T., Orodu, O.D., 2019. Corrosion inhibition of mild steel using binary mixture of sesame and castor oil in brine solution. Mater. Today Commun. 21, 100691. https://doi.org/10.1016/j.mtcomm.2019.100691

15. Prasad, A.R., Kunyankandy, A., Joseph, A., 2020. Corrosion Inhibition in Oil and Gas Industry: Economic Considerations. Corros. Inhib. Oil Gas Ind. 135–150.

16. Verma, C., Abdellattif, M.H., Alfantazi, A., Quraishi, M.A., 2021. N-Heterocycle Compounds as Aqueous Phase Corrosion Inhibitors: A Robust, Effective and Economic Substitute. J. Mol. Liq. 117211.

17. Wang, D.-Y., Nie, B.-L., Li, H.-J., Zhang, W.-W., Wu, Y.-C., 2021. Anticorrosion performance of grape seed proanthocyanidins extract and Tween-80 for mild steel in hydrochloric acid medium. J. Mol. Liq. 331, 115799. https://doi.org/https://doi.org/10.1016/j.molliq.2021.115799

Design of Deep Eutectic Solvents: Selecting Constituents Based on Molecular Structure

Ahmad Alhadid [1,*], Liudmila Mokrushina [2], and Mirjana Minceva [1]

[1] Technical University of Munich, Biothermodynamics, TUM School of Life Sciences, Germany
[2] Friedrich-Alexander-Universität Erlangen-Nürnberg (FAU), Separation Science & Technology, Germany
** Corresponding author: ahmad.alhadid@tum.de*

Eutectic systems can offer a wide range of new green and sustainable designer solvents for diverse applications. Deep eutectic solvents (DES) are a new class of solvents obtained by mixing two or more solid compounds, usually inexpensive, natural, and biodegradable, forming a eutectic mixture with a melting temperature significantly lower than that of the pure components. So far, constituents selection and their ratio are made by trial and error. The large depression in the melting temperature at the eutectic point is due to low melting enthalpy values of constituents or significant negative deviation from ideal solution behavior.[1] We aim to understand the correlation between the molecular structure of constituents, their melting enthalpy, and non-ideality in the liquid solution to facilitate the design of new and novel DES.

The melting enthalpy of pure substances depends on the intermolecular interactions in the crystal lattice and the crystal structure. Group contribution methods usually fail to provide satisfactory predictions for the melting enthalpy, as the crystal structure is not considered. In contrast, the melting entropy of a substance is well-correlated with molecular structure. We propose an approach to select DES constituents based on their melting entropy predicted from the molecular structure.[2] We found that constituents with rigid molecular structures form DES with lower eutectic temperatures than those formed by constituents with flexible molecular structures.

Further, we investigated the effect of the molecular structure of the constituents on the intermolecular interactions in the liquid phase of DES. We have depicted that the hydrogen bonding interactions in DES with rotationally symmetrical hydrogen bond donors are stronger than those with asymmetrical analogs. Therefore, designing new DES with a significant depression in the mixture's melting temperature can be achieved by selecting rotationally symmetrical constituents. The selection strategy proposed in this work allows apriori design of new and improved DES, based only on the molecular structure of constituents.

References

1. Alhadid, A.; Mokrushina, L.; Minceva, M., 2019. Modeling of Solid–Liquid Equilibria in Deep Eutectic Solvents: A Parameter Study. Molecules 24 (12), 2334.
2. Alhadid, A.; Mokrushina, L.; Minceva, M., 2020. Design of Deep Eutectic Systems: A Simple Approach for Preselecting Eutectic Mixture Constituents. Molecules 25 (5), 1077.

Optimization Design of Optimal Parameters in the Denitrification reactor

Meriem Bouteraa [*], Rania Zamouche-Zerdazi ,Mossaab Bencheikh-Lehocine,

Process Engineering Faculty, Environmental Engineering Department, University of Constantine 3, Ali Mendjeli Nouvelle Ville, Constantine, Algeria.

***** *Corresponding author: meriem_bouteraa@yahoo.fr; Tel.: +213549684821*

Abstract: The effects of operational parameters such as temperature, ratio initial S_0/X_0, and pH value on heterotrophic denitrification were evaluated. When sodium acetate was used as the sole carbon source, complete denitrification was achieved in a short time without emitting nitrite (NO2). Complete denitrification was carried out at low S_0X_0 ratios (0.1 or 0.2) and at neutral pH 7 as well as a temperature between 20 and 30C. This data on denitrification performance and its relationship to the dynamics of functional genes under various operating circumstances might help with NO_2 mitigation methods for wastewater treatment systems.

Keywords: dénitrification biologique; température; S_0/X_0;pH.

1. Introduction

Since the 1970s, nitrate poisoning of both surface and ground water has been a hot topic across the world, and it has grown into a significant environmental concern.Nitrogen-containing substances discharged into the environment can cause significant issues, such as river eutrophication. [1–4]. Because nitrate in the gastrointestinal system can be converted to nitrite ions, water quality might deteriorate and pose a health risk [5–7]. Furthermore, nitrate and nitrite have the ability to produce N-nitrous compounds, which are carcinogens [8]. Anthropogenic sources of nitrate in surface and ground water include nitrogenous fertilizers, animal wastes, septic systems, and other nitrate sources associated with urban growth [9–12]. In the treatment of residential and complicated industrial wastewaters, biological nitrate reduction is frequently employed [13–18].

It can harm children and animals, as well as induce eutrophication of aquatic bodies [19]. The worldwide drinking water quality requirements for nitrate (NO_3) have been reduced to 50 mg/L as a "recommended" level and 50–100 mg/L as a "acceptable" level, which translates to 11.3–22.6 mg/L when stated as NO_3–N [20].

Because removing nitrate from water is difficult and not possible using traditional water treatment procedures (coagulation, filtration, and disinfection), extra approaches are necessary to get nitrate-free water. Abiotic (physicochemical) or biological techniques might be used to remove nitrate from water. [21] Ghafari et al. The drawbacks of several abiotic approaches for removing nitrate from water and producing a brine solution were listed, whereas the biological method treats nitrate and transforms it to harmless nitrogen gas. In this sense, microbial treatment (denitrification) is recognized as the most ecologically friendly technique of nitrate removal from water. Furthermore, of the several procedures used to remove nitrate from water, denitrification has been recorded as the most cost-effective [22, 23]. The full reduction of nitrate (NO_3) to nitrogen gas (N_2) is achieved in this approach using the four reduction stages indicated in Eq. (1) [21]. In parenthesis, the oxidation state of the nitrogen atoms for each chemical is listed.

$$NO_3^- \rightarrow NO_2^- \rightarrow NO \rightarrow N_2O \rightarrow N_2 \quad (1)$$

The objective of this study is presented experimental data on the biological mechanisms of nitrate elimination. Allowed the factors that control the denitrification nitrate concentration, pH, temperature and $S0/X_0$ ratio.

2. Materials and Methods

2.1 batch reactor

The cultures are carried out in a batch reactor with capacities of 1L (Figure 1) containing our synthetic medium (Table 1) loaded with sodium acetate as the carbon source used, they are subsequently inoculated with activated sludge. The anaerobic is carried out by bubbling nitrogen through until the solution is completely deoxygenated, a magnetic bar placed inside the reactor to stir.

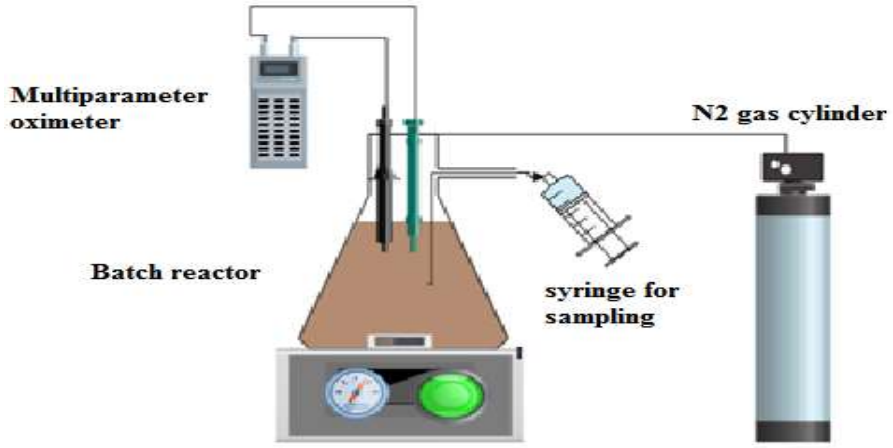


Figure 1. Experimental setup in a barch reactor

2.2 Enrichment of the bacterial-denitrifying consortium

To promote the growth of denitrifying microorganisms, and to fuel systems, many research works in the literature use an effluent [24] .It is advisable to respect the C: N: P ratio of 100: 5: 1 in order to favor an efficient growth of anoxic bacteria in the basin, to prepare a synthetic effluent. In addition, traces of minerals must also be present in the effluent in order to ensure proper development of the biomass. Tables III show: composition of the culture medium and their concentrations, in g / L, previously used for the preparation of synthetic effluents during various studies in the literature

Table 1. Composition of the wastewater culture medium [24]

Compound	Concentration	Compound	Concentration
KH_2PO_4	1,00 g/L	NaCl	1,00 g/L
K_2HPO_4	1,00 g/L	$MgSO_4$	0,20 g/L
KNO_3	1,00 g/L	$CaCl_2$	0,02 g/L
Solution TE	1,00 ml/L		
Composition of the trace solution of TE elements			
HCl 37%	6,76 Ml/L	$ZnCl_2$	0,070 g/L
$FeCl_2.4H_2O$	1,5 g/L	$NiCl_2.6H_2O$	0,025 g/L
H_3BO_3	0,06 g/L	$CuCl_2.2H_2O$	0,015 g/L
$MnCl_2.4H_2O$	0,10 g/L	$NaMoO_4.2H_2O$	0,025 g/L
$CoCl_2.6H_2O$	0,12 g/L	EDTA	5,2 g/L

3. Results and Discussion

3.1 Effect of temperature on denitrification

Like any factor influencing gas diffusion and substrate solubility, temperature affects the rate of denitrification. It is also a parameter very influencing biological processes and microbial activity.

The temperature of the water in the treatment facilities is mainly reacted by the temperature of the ambient air. However, under identical climatic conditions, thermal differences are often observed between installations. They are explained by energy losses during the transit of the raw effluent through the collection network and within the installation itself. Any change in temperature has an immediate impact on the activity of the biomass.

Temperature is an environmental parameter that controls the denitrification process by influencing the metabolism and availability of nitrate and carbon sources [25, 26].

Temperature generally affects enzyme activity, so low temperatures lead to slower enzyme levels and subsequently influence metabolic rates [25].

In this part of our study we carried out experiments on the effect of temperature on denitrification, we set two important parameters $S_0/X_0 = 2$, pH = 7, and vary the temperature values from 15 °C up to 30 °C

The results of this part show in the figures 2**.**

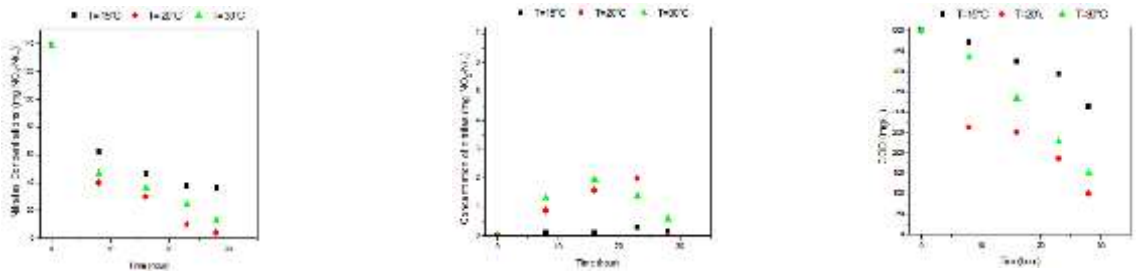


Figure 2. Effect of temperatures on (a) nitrate reduction, (b) nitrate formation and (c) COD degradation,

Figure 2 indicates the temperature effect is an environmental parameter on the performance of denitrification. Overall, the transformation efficiency trend was similar at 20–30 °C, except at 15 °C figure 2 (a, b and c). NO_3 tended to increase with increasing temperatures, but there were no significant differences between the values. The nitrate removal efficiencies were 74.36% (15 °C), 97.16% (20 °C) and 90.64% (30 °C), for the degradation of organic matter 37.44% (15 °C), 80% (20 °C) and 70% (30 °C) .At 15 ° C all the NO_3-N eliminated (74.36 %) was completely reduced to N_2 gas, and other nitrogen compounds such as NO_2-N were not detected . However, by-products of the denitrification process (NO_2-N) were detected at 20–35 °C. These results indicate that too high a temperature can lead to a high build-up of nitrites. Similar results have been reported that nitrite and other nitrogen sources such as N_2O could accumulate at higher temperatures [27].

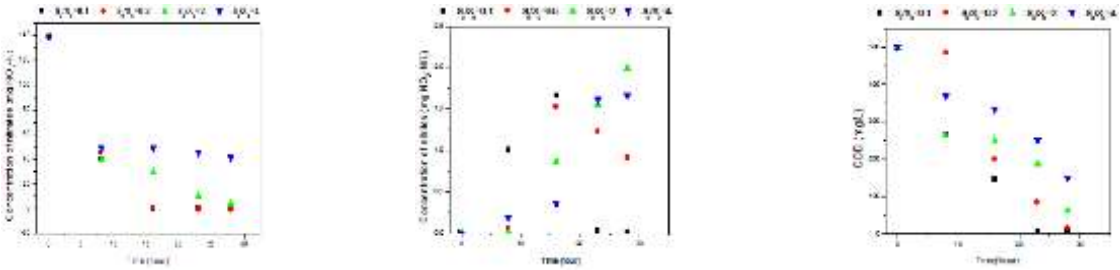
So we conclude that the ideal temperature for denitrification is 20 to 30 °C [28].

3.2 Effect of the S_0/X_0 ratio on denitrification

Many authors have demonstrated the importance of the initial conditions in biodegradation tests, more particularly the initial ratio between the substrate and the biomass concentration, noted S_0/X_0.

In general, for a batch culture, the initial concentration of substrate (S_0) represents a source of carbon and energy for biosynthesis and other energy purposes, while the initial concentration of biomass (X_0) is a source of use of the substrate. Batch culture can be initiated at any desirable S_0/X_0 ratio by changing S_o to a constant X_0, or by varying X_0 to a constant S_0. It seems certain that the S_0/X_0 ratio reflects the initial energy level of the batch culture. There is strong evidence that this ratio will directly affect the growth patterns of microorganisms [29].Indeed, this ratio influences both the metabolic processes involved during degradation, the identification of kinetic parameters as well as the dissociation of easily and slowly biodegradable compartments [30].

There are two important ratios in the treatment of strong denitrification and weak initial S_0/X_0 ratio of 0.1, 0.5, 2, and 4 mgCOD /mgMVS.



(a) **(b)** **(C)**

Figure 3. Effect of S_0/X_0 variation on nitrate reduction with sodium acetate as carbon source

We notice that the reduction of almost complete nitrates for the S_0/X_0 ratios were 0.1 and 0.5 unlike for the 2 and 4 ratios (Figure 3a) with their efficiency percentages of 99.99%, 99.05%, 97.16 % and 70.29%, respectively. And for the degradation of organic matter we reach percentages 99.38%, 96.96%, 80% and 70% (Figure 3b), these values indicate that the effect of S_0/X_0 is important to eliminate all nitrates in the middle.

Chudouba et al [31] indicates that with a higher initial S_0/X_0 ratio, the onset of delayed phases of about 1 day was detected. This is the time needed to multiply.

On the other hand with a low S_0/X_0 ratio, the substrates were removed very quickly and learns less time than high ratio, indicating the absence of cell multiplication.

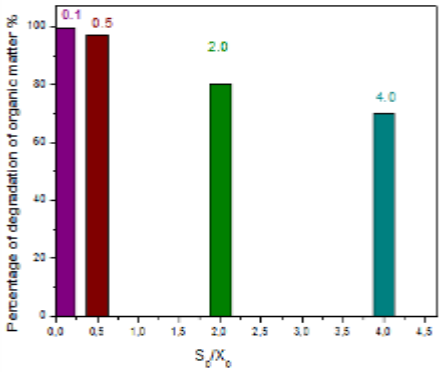


Figure 4. The percentages for the reduction of COD as a function of the S_0/X_0 ratio

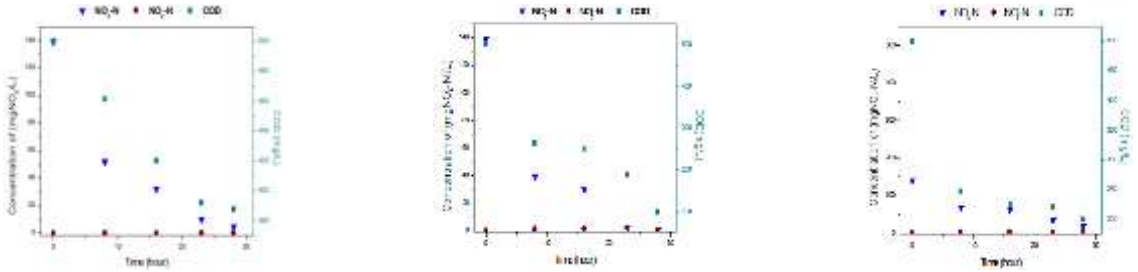
3.3 Effect of pH on denitrification

As we have already mentioned previously the pH is an important factor which limits denitrification. First we followed the bacterial growth in three culture media with different initial pH (5, 7 and 9) this was done by adding HCl (1M) to ensure acidity and NaOH (1M) for basicity. The results of this experiment show in Figures 5.

In the experiments where the activated sludge and the synthetic solution were acclimatized to pH 5, 7 and 9, denitrification was not inhibited and total nitrogen removal occurred in about 23 h. Figures 5(a, b and c) are profiles of nitrate, nitrite and COD for pH 5, 7 and 9.0, respectively.

These three profiles represent two significant changes with increasing pH: increasing peak nitrite concentration and increasing nitrate and COD reduction rate. In addition, in Figures 5 (a and b) there

is some reduction of nitrite before all nitrate is reduced, while in Figure 5c no reduction of nitrite occurs. Until all nitrate is reduced. Figures 5(a - b) clearly show that denitrification of 138.88 mg/L of NO_3-N is possible at solution pH values of 5.7, while denitrification at this concentration was not possible at pH 9.



(a) **(b)** **(C)**

Figure 5. Nitrates, nitrites and COD denitrification profile (a, b and c) with controlled pH (5.7 and 8), respectively.

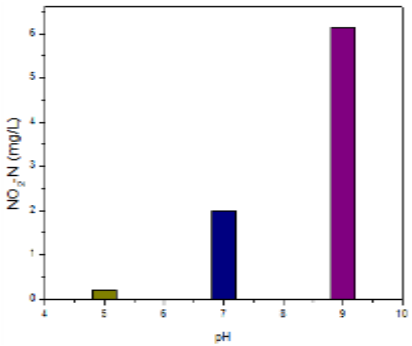


Figure 6. Maximum accumulation of nitrite during denitrification with pH control.

In Figure 6, the maximum nitrite concentration as a function of pH has been plotted. It was observed that the maximum concentration of nitrite in the batch reactors increased from 0.196 mg NO_2-N/L at pH 5, 1.99 mg NO_2-N/L at pH 7, 6.13 mg NO_2-N/L at pH 9.0.

Operation of denitrification reactor under different pH has shown that at high pH, nitrite can accumulate. This long-term effect of pH on nitrite accumulation during denitrification is mainly attributed.

A simplified stoichiometry for the energy-producing part of the denitrification reaction, using sodium acetate as an electron donor, the production of hydroxide (OH) ions is responsible for the increase in pH.

$$2CH_3COONa + 8NO_3^- \rightarrow 8NO_2^- + 4CO_2 + 2H_2O + 2OH^- + 2Na^+ \qquad (2)$$

The production of hydroxide ions (OH) is responsible for increasing the pH. Neutral to alkaline pH (7–8) is considered the most optimal for denitrification [32,33] .Changing the pH from this range decreases the denitrification efficiency of bacteria. Guo et al. (2018) [34] reported that pH levels above 8.75 or below 6.25 negatively impacted the efficiency of TN elimination by E. cloacae. Strong alkaline or acidic conditions have also been shown to be harmful to the growth of A. Junii [25]. Saleh-lakha et al (2009) [25] reported that pH 5 has a negative effect on the denitrification capacity of Ps. Mandelli. However, it has been observed that few species also perform denitrification at higher pH.

For example, Halomonas campestris and Aeromonas perform heterotrophic nitrification - aerobic denitrification at pH 9 and pH 11 respectively.

4. Conclusions

The pollution of aux by nitrates in Algeria is an alarming problem, this is due to the intensive use of nitrogen fertilizers as well as the poor training of our farmers who use the fertilizers in excess of the needs of the plants. Over the years, this unabsorbed excess will be found either in rivers (rivers, lakes, etc.) or in groundwater.

Water pollution by nitrates causes nuisances on nature (eutrophication) and more particularly on human health (methaemoglobinemia).

Our work was focused on the study of denitrification by the use of a mixed culture of microorganisms collected in the IBN ZIAD Constantine wastewater treatment plant in a batch reactor using a single carbon source. We have studied the influence of different physicochemical parameters that can have an inhibiting or accelerating effect on the biodegradation of nitrates.

The degradation of nitrates using sodium acetate is complete and does not stop at the nitrite stage of which the formation of the latter is only an intermediate stage. The ideal temperature for denitrification is T [20-30] ° C. The S_0/ X_0 ratio is a parameter affecting denitrification while a weight ratio equal to 0.1 is optimal to achieve better denitrification with sodium acetate as the carbon source and for a neutral pH.

Funding: "This research received no external funding"

Acknowledgments: The wastewater treatment plants at « IBN ZIAD», Constantine in Algeria, are all acknowledged for providing sludge for the experiments.

References

1. Fennesy, M.S.; Cronk, J.K. The effectiveness and restoration potential of riparian ecotones for the management of nonpoint source pollution, particularly nitrate, Crit. *Rev. Environ. Sci. Technol* 1997, 27, 285–317.
2. Lillie, R.A.; Barko, J.W. Influence of sediment and groundwater on the distribution and biomass of *Myriophyllum spicatum* L. in Devil's lake, Winconsin, *J. Freshw. Ecol* 1990,5, 417–426.
3. Rodgers, S.J.; McFarland,D.G.; Barko ,J.W. Evaluation of the growth of Vallisneria Americana Michx. In relation to sediment nutrient availability. *Lake Reservoir Manage* 1995. 11 ,57–66.
4. Mackie,G.L. Applied Aquatic Ecosystem Concepts, Kendall/Hunt Publishing Company. *Dubuque, Iowa*, 2001.
5. Dorshemier, W.T.; Drewery, C.B.; Fritishch ,D.P.; Williams ,D.E. Removing nitrate from ground water. *Water Eng. Manage*1997, 144, 20–24.
6. Sedlak ,R.; Phosphorous and Nitrogen Removal from Municipal Wastewater. Principle and Practice, XIII, Lewis Publishers, *Boco Raton, FL* 1991, 224.
7. Fonseca, A.D.; Crespo ,J.G.;.Almeida, J.S.; Reis ,M.A. Drinking water denitrification using a novel ion exchange membrane bioreactor. *Environ. Sci. Technol* 2000,34, 1557–1562.
8. Forman,D.; Nitrate exposure and human cancer. in: I. Bogardi, R. Kuzelka (Eds.), Nitrate Contamination, RD NATO ASI Series, vol. G30, Springer- Verlag, Berlin, Heidelberg, Germany, 1991.
9. Ford, M.; Tellam, J.H. Source, type and extent of inorganic contamination within the Birmingham urban aquifer system, United Kingdom. *J. Hydrol* 1994, 156, 101–135.
10. Lerner,D.N.; Yang ,Y.; Barrett ,M.H.; Tellam ,T.H. Loading of Nonagricultural Nitrogen in Urban Water, in Impacts of urban growth on surface and groundwater quality,Ellis J.B. (Ed.).; Publisher:IAHS Publ. 2A, IAHA Press, Willingford, UK, 1999; pp. 117–123.
11. Wakida, F.T.; Lerner ,D.N. Non-agricultural sources of groundwater nitrate: a review and case study. *Water Res*2005, 39 ,3–16.
12. Aslan ,S.; Cakici ,H. Biological denitrification of drinking water in a slow sand filter. *J. Hazard. Mater2007,* 148 , 253–258.

13. Delanghe, B.; Nakamura,F.; Myoga ,H., Magara ,Y., Guibal ,E. Drinking water denitrification in a membrane bioreactor. *Water Sci. Technol*1994,30, 157–160.
14. Lemmer ,H.; Zaglauer ,A.;. Neef ,A.; Meier ,H.; Amann ,R.; Denitrification in a methanol fed fixed bed reactor. Part 2: Composition and ecology of the bacterial community in the biofilms. *Water Res*1997, 31, 1903–1908.
15. Sozen ,S., Orhon ,D. The effect of nitrite correction on the evaluation of the rate of nitrate utilization under anoxic conditions. *J. Chem. Technol. Biotechno*1999, 74, 790–800.
16. Kesseru ,P.; Kiss ,I.; Bihari ,Z.; Polya'k ,B. Biological denitrification in a continuous-flow pilot bioreactor containing immobilized *Pseudomonas butanovora* cells. *Biores. Technol*. 2003,87,75–80.
17. Dong, X.; Tollner ,E.W.; Evaluation of Anammox and denitrification during anaerobic digestion of poultry manure. *Biores. Technol*2003, 86,139–145.
18. Gabald'on ,C.; Izquierdo ,M.; Mart. Soria V.; Marzal ,P.; Penya-roja ,J.M.; Hornos F.J.A. Biological nitrate removal from wastewater of a metalfinishing industry. *J. Hazard. Mater2007* ,148,485–490.
19. G´alvez ,J.M.; G´omez, M.A.; Hontoria, E.; Gonz´alez-L´opez, J. Influence of hydraulic loading and air flowrate on urban wastewater nitrogen removal with a submerged fixed-film reactor. *J. Hazard. Mater*2003, 101,219–229.
20. Brons ,H.J.; Zehnder ,A.J.B. Aerobic nitrate and nitrite reduction in continuous cultures of *Escherichia coli* E4, Arch. *Microbiol*1990 ,153,531–536.
21. Ghafari ,S.; Hasan ,M.;. Aroua ,M.K. Bio-electrochemical removal of nitrate from water and wastewater—a review. *Bioresour. Techno2008,* 99,3965–3974.
22. Szekeres ,S.; Kiss ,I.; Kalman ,M.; Soares ,M.I.M. Microbial population in ahydrogen-dependent denitrification reactor,*Water Res*2002, 36,4088–4094.
23. Soares ,M.I.M. Biological denitrification of groundwater. *Water Air Soil Pollut*2000, 123, 183–193.
24. Cheurfi, W., utilisation de bacteries prelevees dans la station d'epuration d'el menia constantine pour la denitrification.
25. Saleh-lakha, S. and al. Effect of pH and Temperature on Denitrification Gene Expression and Activity in Pseudomonas mandelii. 2009, 75(12), pp.3903–3911.
26. Holtan-Hartwiga, L.,P.Dorschb & Bakkenb, L.R.Low temperature control of soil denitrifying communities : kinetics of N_2O production and reduction. *Soil Biology Biochemistry*2002, 34, 1797–1806.
27. Lee, Y.; Choi,H. ; Cho,K.S.Effects of carbon source , C / N ratio , nitrate , temperature , and pH on N 2 O emission and functional denitrifying genes during heterotrophic denitrification emission and functional denitrifying genes during heterotrophic denitrification. *Journal of Environmental Science and Health, Part A*2018, 54,1–14.
28. Foglar, L.; Briški, F. Wastewater denitrification process - The influence of methanol and kinetic analysis. *Process Biochemistry*2003, 39,95–103.
29. Liu, Y. Bioenergetic interpretation on the so /x0 ratio in substrate-sufficient batch culture. *Wat. Res*1996, 30,2766–2770.
30. Zamouche, R. Study and modeling of dysfunction in biological purification systems. Salah Boubnider ,constantine 03. 2017
31. Chudoba, P.; Capdeville, B.; Chudoba, J.Explanation of biological s/xo ratio in batch cultivation. *Wat.Sci.Tech*1992, 26,3, 743–751.
32. Wang, X.M.W.J.L. Nitrate removal from groundwater using solid-phase denitrification process without inoculating with external microorganisms2013,955–960.
33. Yang, L.; Ren, Y.; Zhao, S. Isolation and characterization of three heterotrophic nitrifying-aerobic denitrifying bacteria from a sequencing batch reactor. *Annals of Microbiology*2016, 737–747.
34. Guo, Y.; Yang,R.; Zhang, Z., Wang, X. ; Chen,S. Synergy of carbon and nitrogen removal of a co-culture of two aerobic denitrifying bacterial strains, Acinetobacter sp. GA and Pseudomonas sp. GP. *Royal society of chemistry* 2018.21558–21565.
35. Ren, Y. . Yang, L..Liang, X. Bioresource Technology The characteristics of a novel heterotrophic nitrifying and aerobic denitrifying bacterium , Acinetobacter junii YB. *Bioresource technology*2014, 171,1–9.

Pascal Triangle from Neutronics to Genomics

Wajdi Mohamed Ratemi

Nuclear Engineering Department, University of Tripoli, and Libyan Atomic Energy Establishment, Tripoli, Libya

*****Corresponding author: wmratemi@gmail.com ; w.ratemi@uot.edu.ly ; w.ratemi@aee.gov.ly ; Tel.: 218926175485*

Abstract: This paper has two folds objective. firstly, the author introduces a mathematical polynomial expansion (Ratemi 1996). This expansion has revealed a new mathematical form for the classical inhour equation which is a well known equation for nuclear reactor kinetics. The polynomial form of the inhour equation represents the characteristic equation for the mathematical model of a nuclear reactor. The model, called Coefficient Based Model (CBM) has the solution with the advantage of avoiding the numerical stiffness in calculation associated with the varying time constants involved in nuclear reactor kinetics, as well as when coupling kinetics with thermohydraulic. Secondly, a special form of the introduced expansion represents a binomial expansion of $(x+y)^n$. The coefficients of such expansion generate the very well known Pascal's triangle. Again, the author (Ratemi 2010) extended the expansion to multinomial expansion of the form $(x+y+z+w+\cdots)^n$. This in turn introduces a generalization of Pascal's triangles (GPTs). Some applications ranging from coin tossing, dice tossing, radioactive decay, combinatorics, probability distribution functions , minimal cut sets for fault tree analysis, and DNA sequencing analysis are highlighted. Further explorations of the GPTs application to other disciplines, such as the field of chemical science and engineering are encouraged .

Keywords: Pascal's triangle; generalized Pascal triangles; nuclear reactor kinetics; combinatorics; probability distribution functions; Genome's Tagging; Fault tree analysis

1. Introduction

This paper will be presented as an invited talk. It highlights some of the author's research activities which is considered to add modest contribution in nuclear reactor kinetics, and in number theory, and in field theory and polynomials. Regarding nuclear reactor kinetics, a new presentation to existing famous classical nuclear reactor inhour equation appearing in literature , in textbooks as well as papers, [1-7] is presented. For the second contribution, the famous classical Pascal's triangle [8-13] has been generalized by the author to a simple generalization of nth order, where The classical Pascal's triangle is represented as a 2nd order of the generalization.

The triggering event to both researches was a home work assignment by the author to his students in a class of nuclear reactor kinetics. It is simply, related to mathematical expansion of the form of the inhour equation for six groups of delayed neutrons. The outcome of the expansion was about six pages of rigorous mathematical representation of the expansion. The author raised a question: Is there a way to represent this expansion in a simpler form?. The research revealed the answer [14], yes. The new compact form of the inhour equation , the inhour polynomial [15] represents a characteristic equation of a nuclear reactor model, hence a compact mathematical form of a nuclear reactor model follows up, called the Coefficient Based Model, CBM, of a nuclear reactor[16]. The solution of this model has the advantage of overriding the associated numerical stiffens with the classical representation because of varying system time constants kinetically, as well as in system's coupling of kinetics and thermohydraulic. Some other authors cited this work in literature [17-21].

As stated earlier regarding the answer to the question of finding a compact form for the expansion of the inhour equation, the author devised a special expansion form, later named as the Guelph expansion[22]. This expansion has, for a special case (single n-roots), the binomial expansion form $(\omega + y)^n$, the associated binomial coefficient of this expansion generates the very well known Pascal's triangle. The author extended the binomial expansion to a multinomial expansion of the form: $(\omega + y + z + w + \cdots)^n$, and the generated multinomial coefficients generates the Generalized Pascal Triangls GPTs. Such coefficients are generated by the author's proposed Embedded Pascal Triangles (EPTs) method [23]. An algorithm is developed to generate such coefficients and generates the corresponding multinomial expansion [24]. Later on, the author simplified the method for generating GPTs via the method of Staircase Horizontal Vertical, SHV, [25]. Pascal's triangle carries many secretes in it [26,27], such as Fibonacci numbers, Sierpinski's triangle, binomial coefficients, and applications in combinatorics, and probabilities (coin tossing) stochastic modeling (radioactive decay). It seems obvious, that extension and generalization into GPTs, reveals applications such as multinomial distribution functions, dice tossing [24], Genomic analysis[24,28], fault tree analysis [29], and possible nuclear reactions, such as nuclear radioactive decay which can be considered as a stochastic process. It is worthwhile, to further explore the GPTs,
and the corresponding multinomial distribution functions to other disciplines of which could be the field of chemical science, and engineering.

2. Guelph expansion and nuclear reactor kinetics

2.1. A question triggerring the research

The initiating trigger to this research was a home work assignment to my students in the class of nuclear reactor kinetics course, it is simply expanding the classical inhour equation for six groups of delayed neutrons (n=6) which is given by:

$$\rho = \Lambda\omega + \sum_{i=1}^{n} \frac{\beta_i \omega}{\omega + \lambda_i} , \qquad (1)$$

Where, ρ is the reactivity, β_i is the ith delayed neutron fraction, λ_i is the ith group precursors decay constant, and ω is the roots of the equation, representing the reciprocal of system time constants. The answer was a report of about six pages of rigorous expansion. The question raised by the author, is it possible to represent the answer into a compact mathematical form, the answer indeed was yes.

2.2. Devising the mathematical tool

In analyzing the expansion, it is seen that the term $\prod_{i=1}^{n}(\omega + \lambda_i)$ needs further mathematical manipulations. The investigation resulted the following expansion [14,15, 22]:

$$\prod_{i=1}^{n}(\omega + \lambda_i) = \sum_{k=0}^{n} \omega^{n-k} \sum_{T_{nk}} \lambda \ldots^{k} \ldots \lambda \qquad (2)$$

Where $\sum_{T_{nk}} \lambda \ldots^{k} \ldots \lambda$ denotes the sum of the products of each and every possible combinations of k elements of the set $\lambda_1, \ldots, \lambda_n$. The number of such combinations is in fact the binomial coefficient given by:

$$T_{nk} = \binom{n}{k} = \frac{n!}{k!(n-k)!} \qquad (3)$$

2.3. The inhour polynomial

Expanding eq.(1), one gets:

$$(\Lambda\omega\text{-}\rho) \prod_{i=1}^{n}(\omega + \lambda_i) + \beta_1 \prod_{i\neq 1}^{n}(\omega + \lambda_i) + \beta_2 \prod_{i\neq 2}^{n}(\omega + \lambda_i) + \cdots \beta_n + \beta_1 \prod_{i\neq n}^{n}(\omega + \lambda_i) = 0 \qquad (4)$$

Applying the Guelph expansion tool; eq.(2) for expanding the π-terms, and with further mathematical manipulations, one gets the new compact form of the inhour polynomial which is given by:

$$F(\omega) = \sum_{m=0}^{n+1} A_m \omega^m = 0 \qquad (5)$$

Where,

$$A_m = \Lambda \sum_{\binom{n}{k}} (\lambda \ldots^{k} \ldots \lambda) + \sum_{i=1}^{n} \beta_i \sum_{\binom{n-1}{k-1}} (\lambda \ldots^{k-1} \ldots \lambda)_{\neq i} - \rho \sum_{\binom{n}{k-1}} (\lambda \ldots^{k-1} \ldots \lambda) \quad , \qquad (6)$$

and m=n+1→ 0 , k=0 →n+1, with one to one correspondence. Equivalently, eq.(6) can be represented in terms of the universal abc-values [15] as: $A_m = \Lambda a_m + b_m + \rho c_m$.

Since β's , and λ's are values depending on the fuel used in the reactor, therefore, the abc- values are universal values depending on the type of fuel fueling the reactor, and can be calculated for U, Th, and Pu fueled reactors. Table 1 presents the Universal abc-values for U235 fueled reactors. Whereas, fig.1, and fig.2 present a quantitative and qualitative graphical representation of the inhour polynomial for six groups of delayed neutrons, respectively.

Table 1. The universal abc-values for U235-fueled reactors [16]

a0	0	0
a1	$\lambda_1\lambda_2\lambda_3\lambda_4\lambda_5\lambda_6$	4.3359e-005
a2	$\lambda_1\lambda_2\lambda_3\lambda_4\lambda_5 + \lambda_2\lambda_3\lambda_4\lambda_5\lambda_6 + \lambda_1\lambda_3\lambda_4\lambda_5\lambda_6 + \lambda_1\lambda_2\lambda_4\lambda_5\lambda_6 + \lambda_1\lambda_2\lambda_3\lambda_5\lambda_6 + \lambda_1\lambda_2\lambda_3\lambda_4\lambda_6 + \lambda_1\lambda_2\lambda_3\lambda_4\lambda_5$	0.0055
a3	$\lambda_1\lambda_2\lambda_3\lambda_4 + \lambda_1\lambda_2\lambda_3\lambda_5 + \lambda_1\lambda_2\lambda_3\lambda_6 + \lambda_2\lambda_3\lambda_4\lambda_5 + \lambda_2\lambda_3\lambda_4\lambda_6 + \lambda_2\lambda_3\lambda_5\lambda_6 + \lambda_3\lambda_4\lambda_5\lambda_6 + \lambda_1\lambda_3\lambda_4\lambda_5 + \lambda_1\lambda_3\lambda_4\lambda_6 + \lambda_1\lambda_3\lambda_5\lambda_6 + \lambda_1\lambda_4\lambda_5\lambda_6 + \lambda_1\lambda_2\lambda_4\lambda_5 + \lambda_1\lambda_2\lambda_4\lambda_6 + \lambda_1\lambda_2\lambda_5\lambda_6 + \lambda_1\lambda_2\lambda_3\lambda_5 + \lambda_1\lambda_2\lambda_3\lambda_6 + \lambda_1\lambda_2\lambda_4\lambda_5$	0.1832
a4	$\lambda_1\lambda_2\lambda_3 + \lambda_1\lambda_2\lambda_4 + \lambda_1\lambda_2\lambda_5 + \lambda_1\lambda_2\lambda_6 + \lambda_1\lambda_3\lambda_4 + \lambda_1\lambda_3\lambda_5 + \lambda_1\lambda_3\lambda_6 + \lambda_1\lambda_4\lambda_5 + \lambda_1\lambda_4\lambda_6 + \lambda_1\lambda_5\lambda_6 + \lambda_2\lambda_3\lambda_4 + \lambda_2\lambda_3\lambda_5 + \lambda_2\lambda_3\lambda_6 + \lambda_2\lambda_4\lambda_5 + \lambda_2\lambda_4\lambda_6 + \lambda_2\lambda_5\lambda_6 + \lambda_3\lambda_4\lambda_5 + \lambda_3\lambda_4\lambda_6 + \lambda_3\lambda_5\lambda_6 + \lambda_4\lambda_5\lambda_6$	1.7761
a5	$\lambda_1\lambda_2 + \lambda_1\lambda_3 + \lambda_1\lambda_4 + \lambda_1\lambda_5 + \lambda_1\lambda_6 + \lambda_2\lambda_3 + \lambda_2\lambda_4 + \lambda_2\lambda_5 + \lambda_2\lambda_6 + \lambda_3\lambda_4 + \lambda_3\lambda_5 + \lambda_3\lambda_6 + \lambda_4\lambda_5 + \lambda_4\lambda_6 + \lambda_5\lambda_6$	5.3707
a6	$\lambda_1+\lambda_2+\lambda_3+\lambda_4+\lambda_5+\lambda_6$	4.6049
a7	1	1.0

b0	0	0
b1	$\beta_1(\lambda_2\lambda_3\lambda_4\lambda_5\lambda_6) + \beta_2(\lambda_1\lambda_3\lambda_4\lambda_5\lambda_6) + \beta_3(\lambda_1\lambda_2\lambda_4\lambda_5\lambda_6) + \beta_4(\lambda_1\lambda_2\lambda_3\lambda_5\lambda_6) + \beta_5(\lambda_1\lambda_2\lambda_3\lambda_4\lambda_6) + \beta_6(\lambda_1\lambda_2\lambda_3\lambda_4\lambda_5)$	3.6736e-006
b2	$\beta_1(\lambda_2\lambda_3\lambda_4\lambda_5 + \lambda_2\lambda_3\lambda_4\lambda_6 + \lambda_2\lambda_3\lambda_5\lambda_6 + \lambda_2\lambda_4\lambda_5\lambda_6 + \lambda_3\lambda_4\lambda_5\lambda_6) + \beta_2(\lambda_1\lambda_3\lambda_4\lambda_5 + \lambda_1\lambda_3\lambda_4\lambda_6 + \lambda_1\lambda_3\lambda_5\lambda_6 + \lambda_1\lambda_4\lambda_5\lambda_6 + \lambda_3\lambda_4\lambda_5\lambda_6) + \beta_3(\lambda_1\lambda_2\lambda_4\lambda_5 + \lambda_1\lambda_2\lambda_4\lambda_6 + \lambda_1\lambda_2\lambda_5\lambda_6 + \lambda_1\lambda_4\lambda_5\lambda_6 + \lambda_2\lambda_4\lambda_5\lambda_6) + \beta_4(\lambda_1\lambda_2\lambda_3\lambda_5 + \lambda_1\lambda_2\lambda_3\lambda_6 + \lambda_1\lambda_2\lambda_5\lambda_6 + \lambda_1\lambda_3\lambda_5\lambda_6 + \lambda_2\lambda_3\lambda_5\lambda_6) + \beta_5(\lambda_1\lambda_2\lambda_3\lambda_4 + \lambda_1\lambda_2\lambda_3\lambda_6 + \lambda_1\lambda_2\lambda_4\lambda_6 + \lambda_1\lambda_3\lambda_4\lambda_6 + \lambda_2\lambda_3\lambda_4\lambda_6) + \beta_6(\lambda_1\lambda_2\lambda_3\lambda_4 + \lambda_1\lambda_2\lambda_3\lambda_5 + \lambda_1\lambda_2\lambda_4\lambda_5 + \lambda_1\lambda_3\lambda_4\lambda_5 + \lambda_2\lambda_3\lambda_4\lambda_5)$	3.3387e-004
b3	$\beta_1(\lambda_2\lambda_3\lambda_4 + \lambda_2\lambda_3\lambda_5 + \lambda_2\lambda_3\lambda_6 + \lambda_2\lambda_4\lambda_5 + \lambda_2\lambda_4\lambda_6 + \lambda_2\lambda_5\lambda_6 + \lambda_3\lambda_4\lambda_5 + \lambda_3\lambda_4\lambda_6 + \lambda_3\lambda_5\lambda_6 + \lambda_4\lambda_5\lambda_6) + \beta_2(\lambda_1\lambda_3\lambda_4 + \lambda_1\lambda_3\lambda_5 + \lambda_1\lambda_3\lambda_6 + \lambda_1\lambda_4\lambda_5 + \lambda_1\lambda_4\lambda_6 + \lambda_1\lambda_5\lambda_6 + \lambda_3\lambda_4\lambda_5 + \lambda_3\lambda_4\lambda_6 + \lambda_3\lambda_5\lambda_6 + \lambda_4\lambda_5\lambda_6) + \beta_3(\lambda_1\lambda_2\lambda_4 + \lambda_1\lambda_2\lambda_5 + \lambda_1\lambda_2\lambda_6 + \lambda_1\lambda_4\lambda_5 + \lambda_1\lambda_4\lambda_6 + \lambda_1\lambda_5\lambda_6 + \lambda_2\lambda_4\lambda_5 + \lambda_2\lambda_4\lambda_6 + \lambda_2\lambda_5\lambda_6 + \lambda_4\lambda_5\lambda_6) + \beta_4(\lambda_1\lambda_2\lambda_3 + \lambda_1\lambda_2\lambda_5 + \lambda_1\lambda_2\lambda_6 + \lambda_1\lambda_3\lambda_5 + \lambda_1\lambda_3\lambda_6 + \lambda_1\lambda_5\lambda_6 + \lambda_2\lambda_3\lambda_5 + \lambda_2\lambda_3\lambda_6 + \lambda_2\lambda_5\lambda_6 + \lambda_3\lambda_5\lambda_6) + \beta_5(\lambda_1\lambda_2\lambda_3 + \lambda_1\lambda_2\lambda_4 + \lambda_1\lambda_2\lambda_6 + \lambda_1\lambda_3\lambda_4 + \lambda_1\lambda_3\lambda_6 + \lambda_1\lambda_4\lambda_6 + \lambda_2\lambda_3\lambda_4 + \lambda_2\lambda_3\lambda_6 + \lambda_2\lambda_4\lambda_6 + \lambda_3\lambda_4\lambda_6) + \beta_6(\lambda_1\lambda_2\lambda_3 + \lambda_1\lambda_2\lambda_4 + \lambda_1\lambda_2\lambda_5 + \lambda_1\lambda_3\lambda_4 + \lambda_1\lambda_3\lambda_5 + \lambda_1\lambda_4\lambda_5 + \lambda_2\lambda_3\lambda_4 + \lambda_2\lambda_3\lambda_5 + \lambda_2\lambda_4\lambda_5 + \lambda_3\lambda_4\lambda_5)$	0.0058
b4	$\beta_1(\lambda_2\lambda_3 + \lambda_2\lambda_4 + \lambda_2\lambda_5 + \lambda_2\lambda_6 + \lambda_3\lambda_4 + \lambda_3\lambda_5 + \lambda_3\lambda_6 + \lambda_4\lambda_5 + \lambda_4\lambda_6 + \lambda_5\lambda_6) + \beta_2(\lambda_1\lambda_3 + \lambda_1\lambda_4 + \lambda_1\lambda_5 + \lambda_1\lambda_6 + \lambda_3\lambda_4 + \lambda_3\lambda_5 + \lambda_3\lambda_6 + \lambda_4\lambda_5 + \lambda_4\lambda_6 + \lambda_5\lambda_6) + \beta_3(\lambda_1\lambda_2 + \lambda_1\lambda_4 + \lambda_1\lambda_5 + \lambda_1\lambda_6 + \lambda_2\lambda_4 + \lambda_2\lambda_5 + \lambda_2\lambda_6 + \lambda_4\lambda_5 + \lambda_4\lambda_6 + \lambda_5\lambda_6) + \beta_4(\lambda_1\lambda_2 + \lambda_1\lambda_3 + \lambda_1\lambda_5 + \lambda_1\lambda_6 + \lambda_2\lambda_3 + \lambda_2\lambda_5 + \lambda_2\lambda_6 + \lambda_3\lambda_5 + \lambda_3\lambda_6 + \lambda_5\lambda_6) + \beta_5(\lambda_1\lambda_2 + \lambda_1\lambda_3 + \lambda_1\lambda_4 + \lambda_1\lambda_6 + \lambda_2\lambda_3 + \lambda_2\lambda_4 + \lambda_2\lambda_6 + \lambda_3\lambda_4 + \lambda_3\lambda_6 + \lambda_4\lambda_6) + \beta_6(\lambda_1\lambda_2 + \lambda_1\lambda_3 + \lambda_1\lambda_4 + \lambda_1\lambda_5 + \lambda_2\lambda_3 + \lambda_2\lambda_4 + \lambda_2\lambda_5 + \lambda_3\lambda_4 + \lambda_3\lambda_5 + \lambda_4\lambda_5)$	0.0265
b5	$\beta_1(\lambda_3 + \lambda_4 + \lambda_5 + \lambda_6) + \beta_2(\lambda_1 + \lambda_3 + \lambda_4 + \lambda_5 + \lambda_6) + \beta_3(\lambda_1 + \lambda_2 + \lambda_4 + \lambda_5 + \lambda_6) + \beta_4(\lambda_1 + \lambda_2 + \lambda_3 + \lambda_5 + \lambda_6) + \beta_5(\lambda_1 + \lambda_2 + \lambda_3 + \lambda_4 + \lambda_6) + \beta_6(\lambda_1 + \lambda_2 + \lambda_3 + \lambda_4 + \lambda_5)$	0.0273
b6	$\beta_1 + \beta_2 + \beta_3 + \beta_4 + \beta_5 + \beta_6$	0.0065
b7	0	0

c0	c1	c2	c3	c4	c5	c6	c7
-a1	-a2	-a3	-a4	-a5	-a6	-a7	0

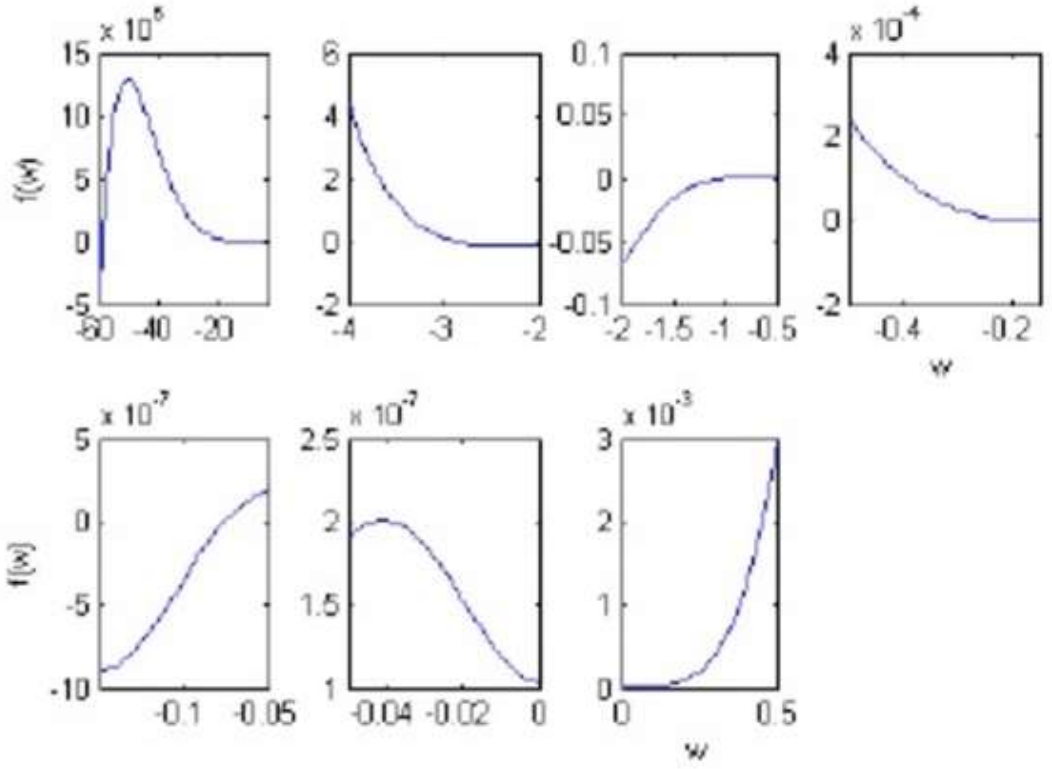


Figure 1. Quantitative behavior for the inhour polynomial equation (ρ=0.1$)[16]

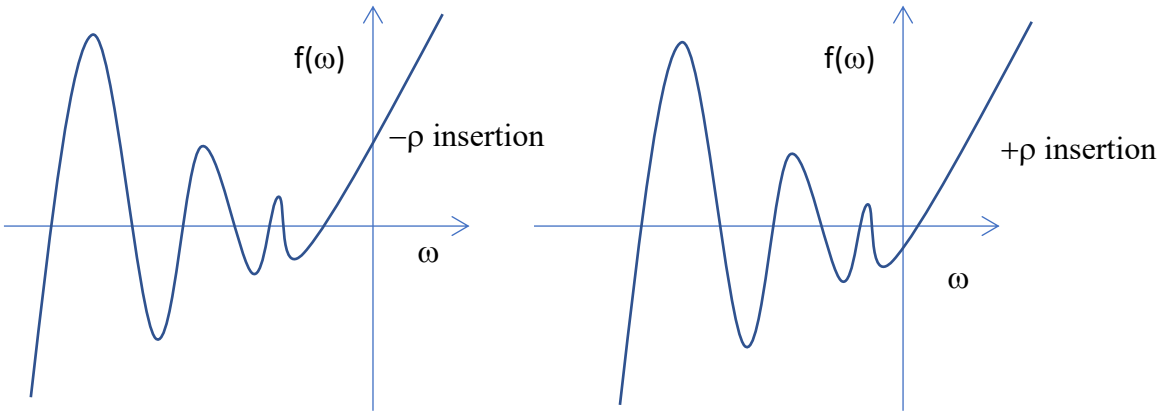


Figure 2. Qualitative behavior for the inhour polynomial equation [15]

2.4. The CBM- reactor equation

Equation (4) represents the characteristic equation of nuclear reactors, hence the corresponding nuclear reactor model presented in a compact form is given by:

$$\sum_{m=0}^{n+1} A_m \frac{d^m P}{dt^m} = 0 \qquad (7)$$

Where, P the nuclear reactor power, t is the time, A_m as given above. This is referred to as Coefficient Based Model, CBM, of nuclear reactors.

2.5. Guelph expansion for roots finding and coefficient building of polynomials

A close examination to the expression of the Guelph expansion eq.(2), and the inhour polynomial eq.(5), shows that knowing the roots of a polynomial, one can generate the coefficients of that polynomial, and vise versa, if one knows the coefficients of the polynomial, one can solve system of nonlinear equations for its roots [24, 30]

$$\sum_{k=0}^{n} \omega^{n-k} \sum_{T_{nk}} \lambda \ldots^{k} \ldots \lambda \; = \sum_{k=0}^{n} A_{n-k} \omega^{n-k} = 0 \qquad (8)$$

with

$$A_{n-k} = \sum_{T_{nk}} \lambda \ldots^{k} \ldots \lambda \qquad , k = 0,1,2,3, \ldots n \qquad (9)$$

Eq.(9) states that knowing the roots of a polynomial, one can generate its coefficients through the sum of the corresponding combinations of the negative roots specific to that coefficient. Similarly, knowing the coefficients, one can solve a system of nonlinear equation specified by eq.(9).

Example: If roots are 3, 2, then n=2 , and k=0, 1, 2

$A_{2\text{-}0} = \sum_{\binom{2}{0}=1} \lambda \ldots^{0} \ldots \lambda \; = 1$, $A_{2\text{-}1} = \sum_{\binom{2}{1}=2} \lambda \ldots^{1} \ldots \lambda \; =$ -3-2 = -5,

$A_{2\text{-}2} = \sum_{\binom{2}{2}=1} \lambda \ldots^{2} \ldots \lambda \; = (-3)(-2) = +6$, Then, $A_2 = 1$, $A_1 =$ -5, $A_0 = 6$

Therefore, the polynomial has the form: ω^2-5$\omega^2 + 6 = 0$.

On the other hand, knowing the coefficients: $A_2 = 1, A_1 =$ -5, $A_0 = 6$, one needs to solve system of 2-equations: -5 = -λ1-λ2, and $6 = (-\lambda 1)(-\lambda 2)$, solving these equations yields $\lambda 1 = 3$, and $\lambda 2 = 2$.

A projection of eq.(8) on eq.(5) with its auxiliaries, with its roots r's, yields :

$$\sum_{k=0}^{n+1} \omega^{n+1-k} \sum_{T=\binom{n+1}{k}} r \ldots^{k} \ldots r =$$

$$A_m = \sum_{\binom{n}{k}} \left(\lambda \ldots^{k} \ldots \lambda\right) + \frac{1}{\Lambda} \sum_{i=1}^{n} \beta_i \sum_{\binom{n-1}{k-1}} \left(\lambda \ldots^{k-1} \ldots \lambda\right)_{\neq i} - \frac{\rho}{\Lambda} \sum_{\binom{n}{k-1}} \left(\lambda \ldots^{k-1} \ldots \lambda\right) =$$

$$A_m = a_m + \frac{b_m}{\Lambda} + \frac{\rho}{\Lambda} c_m = \sum_{T=\binom{n+1}{k}} r \ldots^{k} \ldots r \quad , \; m=n+1 \rightarrow 0 \quad , k=0 \rightarrow n+1, \qquad (10)$$

with $A_{n+1} = 1$, one can solve for the roots, r's, knowing the coefficients A_m's (universal abc-values specific for the type of fuel , type of reactor; fast or thermal, Λ, and the inserted reactivity , ρ (control rod movement, or boric acid insertion). Furthermore, eq.(10) indicates that knowing the time constants of the system, one can determine the reactivity of the system.

2.6. Authors citing the author's research (related to reactor kinetics:the inhour polynomial)

The work presenting the inhour polynomial which was published in the journal of Annals of nuclear energy in April, 1998 [15] has been cited by other authors, naming few:
Labarrios, and Paredes in their work: A new formula of neutron multiplication during startup of PWR[17], and Li, Chen, Zhang, and Chen in their study of A new formula of neutron multiplication

during startup of PWR [18], Aboanber for An efficient analytical form for the period-reactivity relation of beryllium and heavy-water moderated reactors[19], and in the PhD. dissertation of Erik Wallerbos titled:Reactivity effects in pebble-bed type nuclear reactor[20], and Paredes, Labarrios, and Diaz in their work on the inhour equation based on P1 approximation of neutron transport equation [21].

3. Pascal's triangle, and its generalization

3.1. Guelph expansion and the classical Pascal's triangle

The previously introduced Guelph expansion equation , eq.(2), for mono lambdas (single valued), λ, can be presented as:

$$\prod_{i=1}^{n}(\omega+\lambda_i) == \sum_{k=0}^{n}\omega^{n-k}\sum_{T_{nk}}\lambda\ldots^{k}\ldots\lambda = (\omega+\lambda)^n = \sum_{k=0}^{n}\omega^{n-k}\binom{n}{k}\lambda^k \qquad (11)$$

The binomial coefficient $T_{nk}=\binom{n}{k}$ (for n=0, 1, 2, 3,….., and k=0, 1, 2, 3,…n) generates what is known to the most of the western world as Pascal's triangle, in China as Yang Hui's triangle, and in Iran as Khayyam's triangle [8,9]. The elements of Pascal's triangle are generated by the binomial coefficients:

$$T_{nk}=\binom{n}{k}=\frac{n!}{(n-k)!k!}\quad,\ n=0,1,\ 2,\ 3\ldots\ ,\text{and}\ \ k=0,1,\ 2,\ 3\ldots,n \qquad (12)$$

They are given in Table 2.

Table 2. Pascal's Triangle

n / k	0	1	2	3	4	…..
0	1					
1	1	1				
2	1	2	1			
3	1	3	3	1		
4	1	4	6	4	1	
…..						

Furthermore, as eq.(11) suggests, it represents binomial expansion. In an x-y notation eq.(11) is rewritten as:

$$(x+y)^n=\sum_{k=0}^{n}\binom{n}{k}x^{n-k}y^k\quad, \qquad (13)$$

where, $\binom{n}{k}x^{n-k}y^k$ presents the binomial probability distribution function.

3.2. The Generalization of Pascal's triangles

The author suggests extension of the binomial expansion, $(x+y)^n$, into a multinomial expansion, $(x+y+z+w+r+s+t+\cdots..)^n$ [23,24]. The expansion in x_i - notation is given by:

$$\left(\sum_{i=1}^{I}x_i\right)^n=\sum_{\substack{k\\k'\\k''\\\vdots\\k^{(I-2)}}}\binom{n}{k}\binom{k}{k'}\binom{k'}{k''}\ldots\binom{k^{(I-3)}}{k^{(I-2)}}x_1^{n-k}x_2^{k-k'}x_3^{k'-k''}\ldots x_{I-1}^{k^{(I-3)}-k^{(I-2)}}x_I^{k^{(I-2)}} \qquad (14)$$

Where, $k,k',k'',k''',\ldots,k^{(I-2)}$ take on the values $k=0,\ldots,n;\ k'=0,\ldots,k;\ k''=0,\ldots k';\ k'''=0,\ldots,k'';\ldots\ldots;\ k^{(I-2)}=0,\ldots,k^{(I-3)}$.

The addends of eq.(14) represents the multinomial probability distribution function. The coefficients in the summation term of eq.(14) represents the elements of the Generalized Pascal's Triangles, GPTs.

3.2.1. Embedded pascal's Triangles (EPTs) method for generating GPTs

Such elements of Pascal's triangles can be generated using the Embedded Pascal Triangles , EPTs , method suggested by the author [23]. Table 3 presents the EPTs- method for generating a generalized Pascal triangles. The method is simply developed by laying out the classical Pascal's triangle vertically(1st raw of each patch in grey background), then for higher order triangles, a horizontally laid out Pascal triangle of the associated elements (elements in white background cells) are consecutively multiplied with the above celled Pascal elements. This then produces the required elements of the higher order elements of Pascal's triangle (the raw below the white cells).

Table 3. EPTs method for generating the elements of GPTs [23]

Expansion	Embedded Pascal's Triangles (white background) and Polynomial Coefficients																			
$(x+y)^0$	1																			
$(x+y+z)^0$	1																			
$(x+y+z+w)^0$	1																			
$(x+y)^1$	1	1																		
$(x+y+z)^1$	1	1	1																	
$(x+y+z+w)^1$	1	1	1	1																
$(x+y)^2$	1	2	1																	
$(x+y+z)^2$	1	1	1	1	2	1														
	1	2	2	1	2	1														
$(x+y+z+w)^2$	1	1	1	1	1	1	1	2	1											
	1	2	2	2	1	2	2	1	2	1										
$(x+y)^3$	1	3	3	1																
$(x+y+z)^3$	1	1	1	1	2	1	1	3	3	1										
	1	3	3	3	6	3	1	3	3	1										
$(x+y+z+w)^3$	1	1	1	1	1	1	1	2	1	1	1	1	1	2	1	1	3	3	1	
	1	3	3	3	3	6	6	3	6	3	1	3	3	3	6	3	1	3	3	1
$(x+y)^4$	1	4	6	4	1															
$(x+y+z)^4$	1	1	1	1	2	1	1	3	3	1	1	4	6	4	1					
	1	4	4	6	12	6	4	12	12	4	1	4	6	4	1					
$(x+y+z+w)^4$	1	1	1	1	1	1	1	2	1	1	1	1	1	2	1	1	3	3	1	1	4	6	4	1
	1	4	4	4	6	12	12	6	12	6	4	12	12	12	24	12	4	12	12	4	1	4	6	4	1

An algorithm, has been developed to generate the elements of the Generalized Pascal's triangles, as well as, expressing the full expansion of the multinomials in its most general form presented by eq.(14) [24].

3.2.2. Staircase Horizantal Vertical (SHV) method for generating GPTs

Ratemi [25] suggested an easier alternative method for generating different orders of GPTs. The method starts with 1, from which one can generate all orders of Pascal's triangles, where the very famous classical Pascal's triangle is considered to be of order two, and its elements present the coefficients of a binomial expansion, $(x+y)^n$. Hence, the generated 3rd order Pascal's triangle represents the coefficients of trinomial expansion, $(x+y+z)^n$, and the 4th order Pascal's triangle represents the coefficients of quadrinomial expansion, $(x+y+z+w)^n$,etc. The method is named Staircase Horizontal Vertical , SHV method. The name of this method retains the old Chinese name

staircase mount Mero, and adding Horizantal for displaying the elements of Pascal's triangle under the steps of the staircase, and multiplying those elements by vertically aligned columns of a related matrix, the Wterloo Numbers [31], generated from the classical Pascal's triangle by pulling up all elements of a classical Pascal's triangle to start from the first raw by ones.
The Waterloo Matrix is given by the shaded area of Table 4:

Table 4. The Waterloo Matrix [31]

n / k	0	1	2	3	4	5	…..
0	1	1	1	1	1	1	
1	1	2	3	4	5	6	
2	1	3	6	10	15	21	
3	1	4	10	20	35	56	
4	1	5	15	35	70	126	
5	1	6	21	56	126	252	
…..							

The following figure, Fig.3 presents the explained method for generating different orders of GPTs. Starting with the expansion of 0-variables this corresponds to the expansion of $(0)^n$ which has a value of 1 for n=0, hence Pascal's triangle of order 0 is 1, (see Fig. 3 (a)). To generate the next monomial expansion of the form$(x)^n$, one draws one step and lay out the value of 1 corresponding to n=0, and to generate the other elements for n=1, 2, 3,….etc., one multiplies the element corresponding to n=0 by the elements of the first column of Waterloo matrix $W1 = [1\ 1\ 1\ 1\ 1\ 1\ \ldots\ \ldots]'$, consecutively. Therefore, Pascal's triangle of order 1 is a column of 1's, (see Fig. 3 (b)). Next, to generate the coefficients of a binomial of the form$(x+y)^n$, one lays out, horizontally, all of the 1's of the previous monomial expansion under a staircase of a one step size (corresponding to the numbers of the 1st column of the Waterloo matrix) , then, to complete for the rest of the elements, one multiplies those laid out elements for each step by the columns of the Waterloo matrix in a consecutive manner, i.e.; first step by $W1 = [1\ 1\ 1\ 1\ 1\ \ldots\ \ldots]'$, 2nd staircase step by $W2 = [1\ 2\ 3\ 4\ 5\ \ldots\ \ldots]'$, 3rd staircase step by $W3 = [1\ 3\ 6\ 10\ 15\ \ldots]'$, 4th staircase step by $W4 = [1\ 4\ 10\ 20\ \ldots]'$, … , etc.
Hence, one gets the classical Pascal's triangle which is of order 2, (see Fig. 3 (c)). Now, to generate the coefficients of trinomials of the form$(x+y+z)^n$, one draws a staircase of varying step width, i.e.; one element width, two elements width, three elements width, etc. Such width size of the staircase steps corresponds to the elements of the 2nd column of the Waterloo matrix $W2 = [1\ 2\ 3\ 4\ 5\ \ldots]'$. Next, one lays out the previously generated binomial coefficients under the steps of the new staircase (bolded numbers in Fig.3 (d)). Finally, to complete the rest of the elements, one multiplies those laid out elements for each step by the elements of the columns of the Waterloo matrix in a consecutive manner, i.e.; W1, W2, W3, W4, etc. The full coefficients of the trinomial expansion corresponding to planar Pascal's triangle of order 3 are depicted in Fig.3 (d). To get further expansions, one follows the same algorithm.

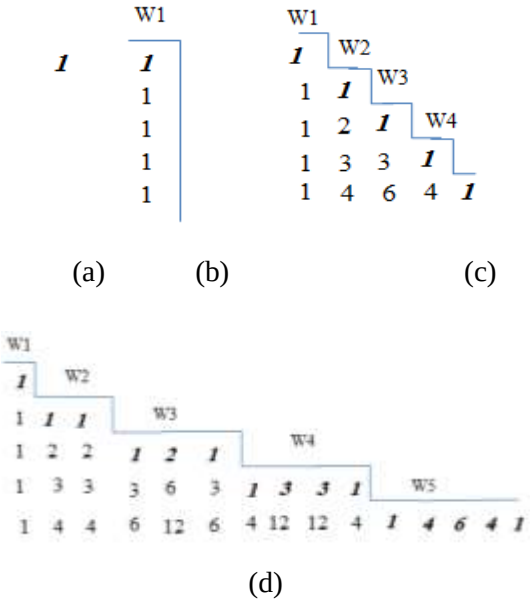


Figure 3. The Staircase Horizontal Vertical (SHV) method for generating different orders of Pascal's triangles for: (**a**) zeronomials $(0)^n$, (**b**) monomials $(x)^n$, (**c**) binomials $(x+y)^n$, and (**d**) trinomials$(x+y+z)^n$ [25].

3.3. Some applications

Typical application of Pascal triangle is calculating the probabilities of tossing coins either from the elements of classical Pascal's triangle (the 2nd order), or from the binomial probability distribution function ,eq.(13), by replacing x and y by Head, H, and Tail, T, respectively, with n representing the number of tossing [32]. If the number of faces increases to 4, then one can use quadrinomial expansion $(x+y+z+w)^n$, and the associated 4th order Pascal's triangle of the GPTs for analyzing the probabilities associated with it. An example for n=4 is presented in Table 5 in a tabular for the generated 4th order pascal elements along with the associated probabilities. If one replaces $x, y, z,$ and w by 4 DNA nucleotides A, T, C and G with a strand length of n, then the probabilities presented in Table 5 represent the associated probabilities of the 4 DNA-strand sequencing [24]. That is the probability for a sequence of {A A A A} is 0.00390625 as it is read from the table(1st raw), and that of a sequence {A T C G} is 0.09375 (15th raw).

Table 5. Detailed tabular coding of the expansion of $(x + y + z + w)^4$ and the probabilities corresponding to the coefficients [24]

n	k	k'	k''	T_{nk}	$T_{kk'}$	$T_{k'k''}$	Coefficients $T_i=T_{nk}T_{kk'}T_{k'k''}$	Terms of the expansion: $x^{n-k}\ y^{k-k'}\ z^{k'-k''}\ w^{k''}$	Probability $P_i=T_i/\Sigma_i T_i$
4	0	0	0	1	1	1	1	x^4	0.00390625
	1	0	0	4	1	1	4	x^3y	0.015625
		1	0	4	1	1	4	x^3z	0.015625
			1	4	1	1	4	x^3w	0.015625
	2	0	0	6	1	1	6	x^2y^2	0.023438
		1	0	6	2	1	12	x^2yz	0.046875
			1	6	2	1	12	x^2yw	0.046875
		2	0	6	1	1	6	x^2z^2	0.023438
			1	6	1	2	12	x^2zw	0.046875
			2	6	1	1	6	x^2w^2	0.023438
	3	0	0	4	1	1	4	xy^3	0.015625
		1	0	4	3	1	12	xy^2z	0.046875
			1	4	3	1	12	xy^2w	0.046875
		2	0	4	3	1	12	xyz^2	0.046875
			1	4	3	2	24	xyzw	0.09375
			2	4	3	1	12	xyw^2	0.046875
		3	0	4	1	1	4	xz^3	0.015625
			1	4	1	3	12	xz^2w	0.046875
			2	4	1	3	12	xzw^2	0.046875
			3	4	1	1	4	xw^3	0.015625
	4	0	0	1	1	1	1	y^4	0.00390625
		1	0	1	4	1	4	y^3z	0.015625
			1	1	4	1	4	y^3w	0.015625
		2	0	1	6	1	6	y^2z^2	0.023438
			1	1	6	2	12	y^2zw	0.046875
			2	1	6	1	6	y^2w^2	0.023438
		3	0	1	4	1	4	yz^3	0.015625
			1	1	4	3	12	yz^2w	0.046875
			2	1	4	3	12	yzw^2	0.046875
			3	1	4	1	4	yw^3	0.015625
		4	0	1	1	1	1	z^4	0.00390625
			1	1	1	4	4	z^3w	0.015625
			2	1	1	6	6	z^2w^2	0.023438
			3	1	1	4	4	zw^3	0.015625
			4	1	1	1	1	w^4	0.00390625

Ratemi, in another study [28], explored tagging of the complete DNA sequence of the Hepatitis B Virus genome, using the tagger $T(n, k, k', k'')$.

In another study [29], the author employed the EPTs method for identifying the minimal cut sets (82 of them) for fault tree analysis of a system's vacuum loss fault of two identical loops. The system is modeled with a multinomial expansion of 18 variables representing the basic events, and since a combination of two events (one from each loop) will suffice to bring the system into halt, one raises the multinomial to power of 2; that is: one has to expand the following multinomial $(x_1 + x_2 + x_3 + \cdots + x_{18})^2$.

3.4. Authors citing the author's research (related to multinomial expansion: GPTs)

Similarly, the work related to the author's research on the Generalization of Pascal's triangles, GPTs, and the related multinomial expansion has been cited by some other authors, namely by; Mina Mohammadi-Kambs in studying DNA Molecular Recognition Specificity: Pairwise and in Competition as a PhD Dissertation [33]. Y. Sun , referenced the work in their introduction of the technique of second-order corrected likelihood for nonlinear models with fixed effects [34]. Also,

Sun, and Dhaene referenced the work in their study of Second-order corrected likelihood for nonlinear panel models with fixed effects [35].

4. Conclusions

In this invited talk, the author introduces a polynomial expansion tool to serve for compacting a long expansion. The application of this tool named as the Guelph expansion leads to presentation of a new form of the very well known inhour equation in nuclear reactor kinetics. With such new presentation as a polynomial inhour equation, a coefficient-based model (CBM) for nuclear reactors is presented. It turns out that a special form of the Guelph expansion represents a binomial expansion, the coefficients of which is called the binomial coefficient and it represents the vey well famous Pascal' triangle. The devised Guelph expansion serves as well as a tool to generate the coefficients of any polynomial knowing its roots, and it serves as well the reversable process; finding the roots of any polynomial knowing its coefficients. The binomial expansion is extended into multinomial expansion, leading to a generalization of Pascal's triangles, GPTs, where two methods for generating such GPTs; namely the EPTs, and the SHV methods were introduced. Different applications were highlighted, and the research is open for further explorations in other fields and disciplines, chemical science and engineering can be one of them.

References

1. D.L.Hetrick , Dynamics of Nuclear Reactors, Chicago 1971.
2. James J. Duderstadt, and Louis J. Hamilton, Nuclear Reactor Analysis, John Wiley& Sons, Inc.,1976, p.244.
3. Roger A. Rydin, Nuclear Reactor Theory and Deign, PBS series in Reactor physics,
4. Samuel Glasstone, and George C. Bell, Nuclear Reactor Theory, 1st ed., ANS, 1970.
5. Jeffery Lewins, Nuclear Reactor Kinetics and Control, 1st ed., Pergamon, 1978
6. Milton S. Ash, Nuclear Reactor Kinetics, 2nd ed., McGraw-Hill Co., 1979.
7. J. A. Bernard and L. W. Hu, "Dynamic period equation: Derivation, relation to inhour equation, and precursor estimation," in IEEE Transactions on Nuclear Science, vol. 46, no. 3, pp. 433-437, June 1999, doi: 10.1109/23.775559.
8. T. M. Green, Recurrent sequences and Pascal's triangle, Math. Mag. vol.41, no.1, pp. 13-21, 1968.
9. Paul F. Kisak, "A History of Mathematics", CreateSpace Independent Publishing Platform, Paperback, p.50, 2015.
10. K. J. Smith, "Pascal's triangle," The Two-Year College Mathematics Journal, vol. 4, no.1, 1973, pp. 1-13.
11. A. W. F. Edwards, Pascal's Arithmetical Triangle: The Story of a mathematical idea, The John Hopkins University Press, 2002.
    P. Hilton and J. Pedersen, "Looking into Pascal's triangle: combinatorics, arithmetic, and geometry," Math. Mag., vol.60, no.5, 1987, pp.305-316.
12. Tony Colledge, "Pascal's triangle: Teachers' Guide," paperback, Tarquin Publications, 1992.
13. Hans Lausch and Wilfried Nöbauer (editors), "Algebra of Polynomials," North-Holland Publishing Company, 1973, pp.1-46.
14. W.M.Ratemi, Special mathematical expansion for polynomials, Unpublished work. Personal communication, 1996.
15. W.M. Ratemi, AE Eshabo, New form of the Inhour equation and its universal ABC-values for different reactor types , Annals of Nuclear Energy, Volume 25, Issue 6, April 1998, Pages 377-386.
16. Wajdi M. Ratemi, Reactor Kinetics Revisited: A Coefficient Based Model (CBM), In Proceedings of International Conference on Power Generation Systems& Renewable Energy Technologies (Pgsret), Islamabad, Pakistan, Editors: Khan, Syed, and Chohan , Publisher: University of engineering and Technology , International Islamic University(IIU), Nov.29-Dec.2,2010 pp.147-162.

17. MA Polo-Labarrios, G Espinosa-Paredes , Numerical analysis of startup PWR with fractional neutron point kinetic equation Progress in Nuclear Energy, 2012 – Elsevier
18. H Li, W Chen, F Zhang, Z Chen, A new formula of neutron multiplication during startup of PWR, Progress in Nuclear Energy, 2010 - Elsevier
19. AE Aboanber , An efficient analytical form for the period-reactivity relation of beryllium and heavy-water moderated reactors, Nuclear engineering and design, 2003 – Elsevier.
20. Erik Johannes Maria Wallerbos, Reactivity effects in pebble-bed type nuclear reactor, PhD dissertation , Delft University of Technology, The Netherlands, June, 1998.
21. G. Espinosa-Paredes, M. A. Polo-Labarrios and D. Suescún-Díaz, INHOUR EQUATION BASED ON P1 APPROXIMATION OF NEUTRON TRANSPORT THEORY, ARPN Journal of Engineering and Applied Sciences, VOL. 16, NO. 1, JANUARY 2021.
22. W. M. Ratemi and H. Abdulla, "The Guelph expansion: a mathematical expansion for polynomial expansion," in: Abstracts of International Conference on Mathematical Sciences, Istanbul, 2009, p. 381.
23. W. M. Ratemi, "Embedded Pascal's triangles for polynomial expansion," in: Abstract of The 19th International Workshop on Matrices and Statistics ,5-8 June 2010, Shanghai Finance University, Shanghai, China, 2010, pp. 45-46.
24. Serge B. Provost and Wajdi M. Ratemi, "Polynomial expansions via embedded Pascal's triangles," Acta et Commentationes Universitatis Tartuensis de Mathematica, vol. 15, no. 1, 2011. (Available online at www.math.ut.ee/acta/).
25. Wajdi Mohamed Ratemi, A Generalization of Planar Pascal's Triangle to Polynomial Expansion and Connection with Sierpinski Patterns, International Journal of Mathematical, Computational, Physical, Electrical and Computer Engineering, Vol: 10, No: 2, 2016, pp.15-20
26. ed.Ted, https://ed.ted.com/lessons/the-mathematical-secrets-of-pascal-s-triangle-wajdi-mohamed-ratemi
27. Amara, https://amara.org/en/videos/00EH5XoZslyF/info/the-mathematical-secrets-of-pascals-triangle/
28. Wajdi M. Ratemi,TAGGING OF GENOMES USING EMBEDDED PASCAL TRIANGLES EXPANSION, Universal Journal of Mathematics and Mathematical Sciences,Volume 5, Issue 2, Pages 121 - 132 (April 2014).
29. Wajdi Mohamed Ratemi , Embedded Pascal Triangles and Its Application for Minimal Cut Sets of Fault Tree Analysis, Middle-East J. Sci. Res., 13 (Mathematical Applications in Engineering): 90-96, 2013.
30. Ratemi, W.M., 2010. R-transforms for polynomial expansion and root extraction. Abstract-International Conference on Analysis and Applications (ICAA2010). Sultan Qaboos University, Muscat, Oman, pp: 52.
31. Wajdi Mohamed Ratemi, and Otman Basir, "Waterloo Numbers and Their Relation to Pascal Triangle and Polygons, " The Aligarh Bulletin of Mathematics, vol. 33, no. 1-2, pp. 39-53, 2014.
32. Stefan Hollos and J. Richard Hollos, Coin Tossing: The Hydrogen Atom of Probability, Abrazol Publishing, 2019
33. Mina Mohammadi-Kambs, DNA Molecular Recognition Specificity: Pairwise and in Competition, PhD Dissertation, natural science-technical faculty of the University of Saarland, Saarbrücken, Germany, 2019.
34. Y. Sun , Second-order corrected likelihood for nonlinear models with fixed effects, KU Leuven, Faculty of Economics, Discussion Paper Series, DPS16.06, MAY 2016.
35. Yutao Sun, and Geert Dhaene, Second-order corrected likelihood for nonlinear panel models with fixed effects, researchGate, 2017, ResearchGate https://www.researchgate.net/publication/315663135

Predictive RSM and Artificial Neural Network (ANN) Models for Cr(VI) Adsorption onto CoAl Based Layered Double Hydroxide Composites

Nuhu Dalhat Mu'azu [1] and Nabeel Jarrah[2,*]

[1] Department of Environmental Engineering, Imam Abdulrahman Bin Faisal University, 31451 Dammam, Saudi Arabia;

[2] Department of Chemical Engineering, Mutah University, 61710 Karak 61710, Jordan;

[*] *Corresponding author: nmdalhat@iau.edu.sa; dalhat@gmail.com; aljarrahn@mutah.edu.jo ; Tel : +966507532689*

Abstract: Excellent prediction of thermodynamics data is of paramount importance in adsorption studies. In this study, the adsorptive performance of CoAl-LDH and its bentonite-CoAl intercalated (Bentonite-CoAl-LDH) for removal of Cr(VI) from water were modelled using artificial neural network (ANN) based algorithms and response surface methodology (RSM) and compared based coefficient of determination (R^2) and root mean square error (RMSE). The adsorbents uptake capacities for Cr(VI) well fitted quartic RSM polynomial models (R^2 = 0.997). The Cr (VI) uptake capacity improved with increasing Cr(VI) initial concentration and initial pH while increasing the operational temperature increase tended to decrease with temperature 25ºC, pH 2 and 126 mg/L initial Cr(VI) concentration optimal conditions based on desirability function analysis. Levenberg-Marquardt ANN algorithms (ANN-LMA) converges faster and better compared to other tested ANN based models providing better fits R^2 of 0.993 and 0.992 (RSME = 4.089 and 4.99), for thermodynamics data compared to the RSM models (R^2 = 0.872 and 0.979 and RMSE = 20.5 and 8.0), respectively. The ANN-LMA models indicated a consistent and an insignificant decline their predictions potentials under different data set. This suggest that the ANN-LMA models are more reliable in capturing Cr(VI) adsorption data for LDHs nanocomposites heavy metals uptake.

Keywords: Response surface methodology; artificial neural network; adsorption modeling; adsorption thermodynamics; layered double hydroxides; chromium heavy metal; water and wastewater treatment.

Robust MBPC control tuning using Multi-objective Evolution Algorithm for a Distillation Column

Haitham Osman

Department of Chemical Engineering, College of Engineering, King Khalid University, Abha 61411, Saudi Arabia.

**Corresponding author: haman@kku.edu.sa, Tel: +966569537424*

Abstract: In this article, the implementation of the Multi-objective Evolution Algorithm (MOEA) for tuning Model Base Predictive Control (MBPC) to control the distillation at model uncertainty is presented. Control performance and stability objective functions are considered to tune and optimise the controller to overcome the implications of model mismatch. Initially, a step response is applied to the distillation column, and then a successful step response model is developed, this approximate model is used by the MBPC control system to control the top and bottom composition of the distillation column. To overcome the drawback of the conventional optimization algorithms trapping into the local optimum, MBPC is optimised by MOEA with the objective frameworks of robust control performance and stability. the results showed that NSGA-II algorithm is successfully tuned MBPC at 20% model uncertainty in the time delay to control the distillation column by using the sensitivity and complementary sensitivity function. these robust functions are combined and tested with the two control error functions (MSE and IAE) as objective functions. MSE combined objective function show supremacy to IAE in terms of finding a larger number of optimum tuning parameters solutions.

Keywords: Model mismatch; NSGA; Evolution Algorithm; distillation column; Model based predictive control.

1. Introduction

MBPC originally referred to a control algorithm that directly applies a process model, to forecast the future response of the controlled plant and take suitable action by optimization of the control cost function. This kind of advanced control device is commonly used in the chemical and petrochemical industry.

Qin and Badgwell (2003) stated that the majority of MBPC applications (67 per cent) are in the field of refining, the initial technology segment of MBPC.

The key distinction between MBPC models is the type of model used for process modeling and the formulation of the cost-function that must be minimized. When there are no mismatches between the process and the model, there are enough conditions to assure the controller's accuracy and reliability.

Otherwise, it is essential to have bounded uncertainties in the controller synthesis to maintain stability, which is difficult or impossible to be measured analytically(Mayne 2001).

Dynamic Matrix Control (DMC) is one of the most popular MBPCs. Over the last decays, a significant range of DMC control modeling and tuning techniques have been proposed, beginning with a formal tuning technique given by Cooper et al. where the model is very similar to the mechanism only.(Dougherty and Cooper 2003).

(Rippon et al. 2019)suggest an optimized tuning approach based on particle swarm optimization, in which the Morari resiliency index and the condition number are introduced as performance metrics.

Furthermore, (Tran, Özkan, and Backx 2012)determined the tuning parameters were by looking for an optimal bandwidth that offered a balance between robustness and nominal efficiency .Recently,

Júnior, Martins and Kalid represented the tuning question as a two-degree optimisation (2-DOF) dilemma (Júnior, Martins, and Kalid 2014). This approach is often used to produce stronger closed-loop responses, calculated by over-shot, setting times and performance swings with parametric uncertainties decided by the operator(He et al. 2015).

Garriga and Soroush (2010) investigated different strategies and available tuning recommendations for model predictive control. Nagrath et al. (2000) used a default prediction horizon value of 10 for DMC monitoring a state space image of a continuous stirred tank reactor (CSTR) with excellent results.

A generalized predictive control is used with Artificial neural network to determine the optimal injection rates during the CO_2 injection process by (Hajisalehi, Salahshoor, and Sefat 2014),More recently (Santander, Elkamel, and Budman 2019)applied dynamic nonlinear optimization algorithm (REMPC) to improve the economic performance of parallel reactions system the algorithmisshowntomaintainstabilityinthepresenceofmodelparameters mismatch.

The top and bottom composition control of the distillation column can be a major challenge due mainly to the control loop interactions and nonlinearity of the process. One means of understanding this problem is to build a process model as the distillation column dynamics can be quite complex. In generating such a model for the purposes of process simulation, a number of general assumptions are introduced to simplify the mathematical modelling. Typical assumptions include constant relative volatility,

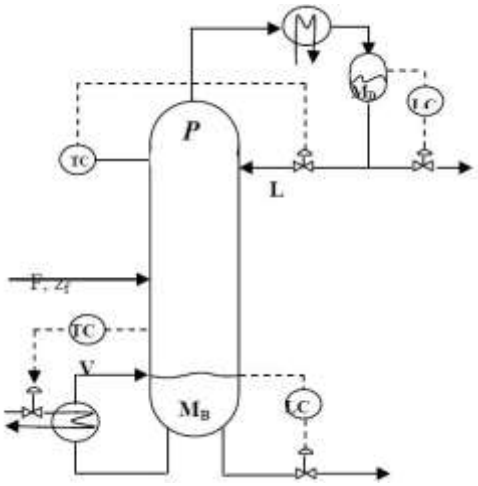


Figure 1: A typical distillation column with LV configuration

Negligible vapour holds up, total condenser, constant boil-up rate, and perfect top and bottom control level

Another of the primary explanations for using MOEA to optimize MBPC tuning parameters is that in the case of MBPC constraints and/or a nonlinear process, the optimization problem is becoming non-convex, allowing the standard optimization algorithm to converge to a local optimum, resulting in weak MPC tuning and deterioration. The process of optimizing the MPC tuning parameters is nonlinear, and it is challenging to solve using a numerical solution in the case of optimum system design techniques (for example, using LQC, H2 and H control design). Indeed, there is hardly an empirical approach to the specific issue that the designer wants to tackle. The analytical approach becomes more complicated, particularly as the size of the process plant increases. Because of the above, the usage of MOEA with a robust stability and performance objective functions is regarded as

a promising strategy in this paper for optimizing and tuning the MPC parameters to control the distillation column in the presence of high model volatility or mismatch.

2. Methodology

2.1Mathematical Model for the Distillation Column

The development of the dynamic model of the distillation column is based on the dynamic continuity equations of mass and energy balance on each stage..

The simple three-stage distillation column considered by Skogestad (1997)to which separates a two-component mixture of water and methanol figure 1 is used in this paper. The column separates a binary mixture with a relativity volatility of 1.0 and has two theoretical stages and total condensation in stage 3 at the top. Although a more complex distillations column model could be utilised, this model is sufficient complex to demonstrate the implementation aspects of MBPC.

The feed enters at the second tray of the distillation and the component balance can be written as follows:

$$M_2 \frac{dx_2}{dt} = Fz_f + V_1 y_1 - L_3 X_3 - V_2 y_2 - L_2 X_2 \quad \text{Feed stage} \qquad (1)$$

Where, F is the Feed rate [kmol/min] with z_f feed composition [mole fraction]. t is the time,L is the reflux flow [kmol/min],V and $V_1$are the boil-up flow [kmol/min], the subscript is the number of the stage(1 for the bottom,3 for the top). X and y are the liquid and vapour composition [mole fraction] respectively. M is the liquid hold-up [kmol] (M_B for re boiler, M_D for condenser hold up). D and B is the distillate (top) and bottoms product flow rate respectively [kmol/min].

The component balance for the condenser at stage 3 can be modelled (in *[kmol/min*])as follows:

$$M_3 \frac{dx_3}{dt} = V_2 y_2 - L_3 X_3 - D\ X_3 \quad \text{Condenser} \qquad (2)$$

Where$D$ is the distillate (top) flow rate [kmol/min], X_3or X_D is the distillate composition while X_1*or* $X_B$is the bottom production composition.

The Re-boiler is stage one of the distillation column and the component balance can be modelled as follows:

$$M_1 \frac{dx_1}{dt} = L_2 X_2 - V_1 y_1 - B\ X_1 \quad \text{Re-boiler} \qquad (3)$$

These equations are first order nonlinear ordinary differential equations. The differential equations can be solved numerically by integrating forward in the time. At the outset initial conditions should be specified, next all differential equations are calculated from the material and energy balance at the current time, then each equation is integrated to the next time step.

For the integration procedure, the Euler method can be used. It offers ease of implementation and low computation time. It can be highly effective at solving such equations, especially when the model does not include a description of vapour hydraulic and pressure dynamic effects.

More precise algorithms are available and widely used such as Runge Kuttaand LSODE(Hindmarsh 1980),but are more computationally expensive. However, the computational

speed of computers has dramatically increased, making systems that were considered difficult and times consuming to solve now quite feasible.
Using a Taylor series to linearise the previous material balance equations at steady state conditions yields the following model in the linear form:

$$M_i \frac{dx}{dt} = A\Delta x + B\Delta u + E\Delta f \qquad (4)$$

By assuming of $V=V_1, L=L_3$, $V_2=V, L_2=L+F, D=V-L$, and $B=L+F-V$, the linear model for the condenser (stage3) can be written after a little manipulation as follows:

$$M_3 \frac{dx}{dt} = V(\Delta y_2 - \Delta x_3) + (y_2 - x_3)\Delta V \qquad (5)$$

The Relative Gain Arrays (RGA) forms the basis for selecting the optimum configurations which is described by Shinskey et al. (Shinskey 1984). The options include selection s from *L*, *V*, *D*, *B*and their ratios.

From the 25 possible control configurations there are actually only 4 schemes that offer acceptable input-output combinations. The most common schemes in practical industrial application are *LV, DV, LB,*and*L/V-D/B*. Table A1 in the appendix presents the configuration for those schemes:

The *LV* configuration is the most common configuration in industry (row 1 table1). Its main advantage is the manipulated variables directly affect the compositions with high interaction.In this control structure the reflux flow rate L and the boil up manipulator V (the 'primary' control manipulators) are used to control the output compositions X_B and $X_D$respectively. The reflux drum and the reboiler hold-ups (the 'secondary' output) are usually controlled by the distillate flow rate D and the bottoms flow rate B.

2.2 Model Based Predictive control

The basic idea behind MBPC is that the potential control action is calculated by minimizing a quadratic objective feature that reduces and balances the error between the expected result and the reference signal against a term relevant to the control action's rate of change. Model predictive control is also known as receding (moving) horizon control, especially in the field of electrical engineering. Mayne and Michalska et al.(Mayne and Michalska 1990) showed that receding horizon control provides a stable closed loop system when applied to process with significant time delay. MBPC consists of four basic elements: a model of the process, The goal defined by the objective function, optional constraints on the system and the control variables, and the optimisation procedure. The model should give a good description of the system and may be black-box (e.g. time series, state space or nonlinear such as Artificial Neural Network (ANN)),Grey-box (e.g. hybrid or fuzzy logic) or a white box model (e.g. a first principle model).

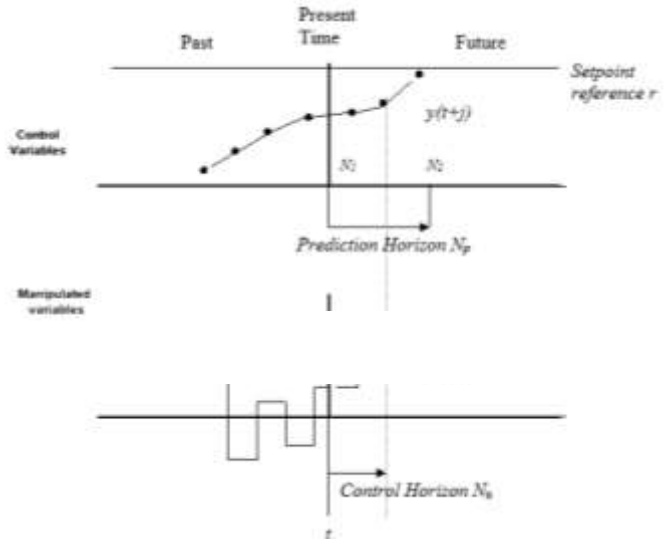


Figure 2: Moving horizon concept of Model Base Predictive Control(MBPC).

The above diagram Figure 2 demonstrates the receding horizon strategy where *y (t)* represents the output signal; *u(t)* is the input signal, and *r(t)* the process setpoint. At every sampling interval the control signal is calculated by minimising the objective function by searching for a sequence of control changes between time zero and N_{u-1}:

$$J = \sum_{i=N_1}^{N_2} (y(t+i) - r(t+i))^2 + \lambda \sum_{i=0}^{Nu} (\Delta u(t+i-1))^2 \qquad (6)$$

The variable *r(t+i)* is the setpoint at the time *t+i*, and *u(t+i-1)* is the control signal, the output signal *y(t+i)* represents the *i* step a head prediction, The values N_1 and N_2 are the minimum and the maximum of the prediction horizons respectively (hence, $Np = N_2 - N_1$), and *Nu* denotes the control horizon,Δ is the difference operator ($1-z^{-1}$) and the parameter λ represents the control

To solve the cost function for the desired control move, the *j*-step predictions of the future process output are required. For convenience the MBPC cost function can be expressed in the matrix vector notation as follows:

$$J = (y-r)^T (y-r) + \lambda (u_t - u_{t-1})^T (u_t - u_{t-1}) \qquad (7)$$

Where $y=[y(t+N_1) \ ..y(t+N_2)]^T$is the output vector, $r=[r(t+N_1)r(t+N_2)]$ the setpoint vector, $u_t$is a vector of the calculated future control moves and u_{t-1} is the past control value.

The minimum solution of the cost function is obtained by differentiating the cost function with respect to Δu (t), and then at the minimum, the gradient is equal to zero. Setting the equation to zero and rearranging gives the control law in the following form:

$$\Delta u = (G^T G + \lambda I)^{-1} G^T (r - f) \qquad (8)$$

Where:

$$G = \begin{bmatrix} g_{N_1} & 0 & 0 & .. \\ g_{N_1+1} & g_{N_1} & 0 & .. \\ .. & .. & .. & .. \\ g_{N_2} & g_{N_2-1} & .. & g_{N_2-N_u+1} \end{bmatrix} \quad And \quad f = [f_{N_1} \dots f_{N_2}]$$

G is a square matrix, which contains the step-response coefficients of the model and is of dimension $(N_2\text{-}N_1\text{+}1)$ by N_u.

2.3 Tuning the Parameters of MBPC to Control distillation column

The tuning parameters for GPC are N_1, N_2, N_u and λ (the start of prediction horizon, end of prediction horizon, control horizon and weighting for the control moves).

The dimension of the *G* matrix (from the equation 3.12)is that of the control horizon and *G* must be inverted to calculate the future control moves. The computation effort increases as the control horizon N_u increases.

The greatest difficulty in tuning MBPC is the specification of the weighting parameters, but with appropriate choice, they give the MBPC the capability to stabilise non-minimum phase systems, nonlinear systems and open loop unstable systems.

Shridhar and Cooper (1997)developed an extension of a SISO (Single Input Single Output) tuning strategy, to use an MPC tuning formula for tuning multivariable DMC and GPC.The significant contribution of their work was the derivation of a novel analytical expression that computes the move suppression coefficient for MIMO DMC. However, their approach is limited to unconstrained MPC. Moreover, it requires representation of the process by a First order Plus Dead Time (FOPDT) model. The main drawback of this approach is that it is not applicable for higher order and/or unstable systems.

Exadaktylos and Taylor (2010) proposed multi-objective performance optimisation utilizing the goal attainment method. (Sawulski and Ławryńczuk 2018)published a detailed comparison of a few heuristic optimisation algorithms, discussing the usage of the Particle Swarm Optimisation (PSO) process, the firefly algorithm, the gray wolf optimiser, and the Java algorithm used by Ramasamy et al. (2019) and Júnior, Martins, and Kalid (2014)

2.4 Non-dominated Sorting Genetic Algorithm (NSGA-II) application to MBPC

Deb (1999)created NSGA, a Multi-objective Genetic Algorithm in which a rating selection approach is used to emphasize existing non-dominated solutions and a niche method is used to preserve diversity in the population figure 3. The algorithm is divided into two parts: fitness assignment and fitness sharing.The full description of the algorithm is presented in appendix 1, the algorithm is used with another clustering technique to avoid the loss of the optimum solutions from the previous generations.

The main difference between NSGA-II and NSGA is NSGA-II combines the previous non-dominated sorting population with the current one, and then performs crowding distant sorting to reject some members that are lying on the more crowded area.

The implemented NSGA-II has the following parameters, which are used in all simulations in this paper: the Population size is set to be 100 individuals, the length of the chromosome is 32, the probability of the crossover (P_c) is 95% and the Mutation probability (P_m) is 5%, sharing factor is set to one. The simulation is stopped after 30 generations

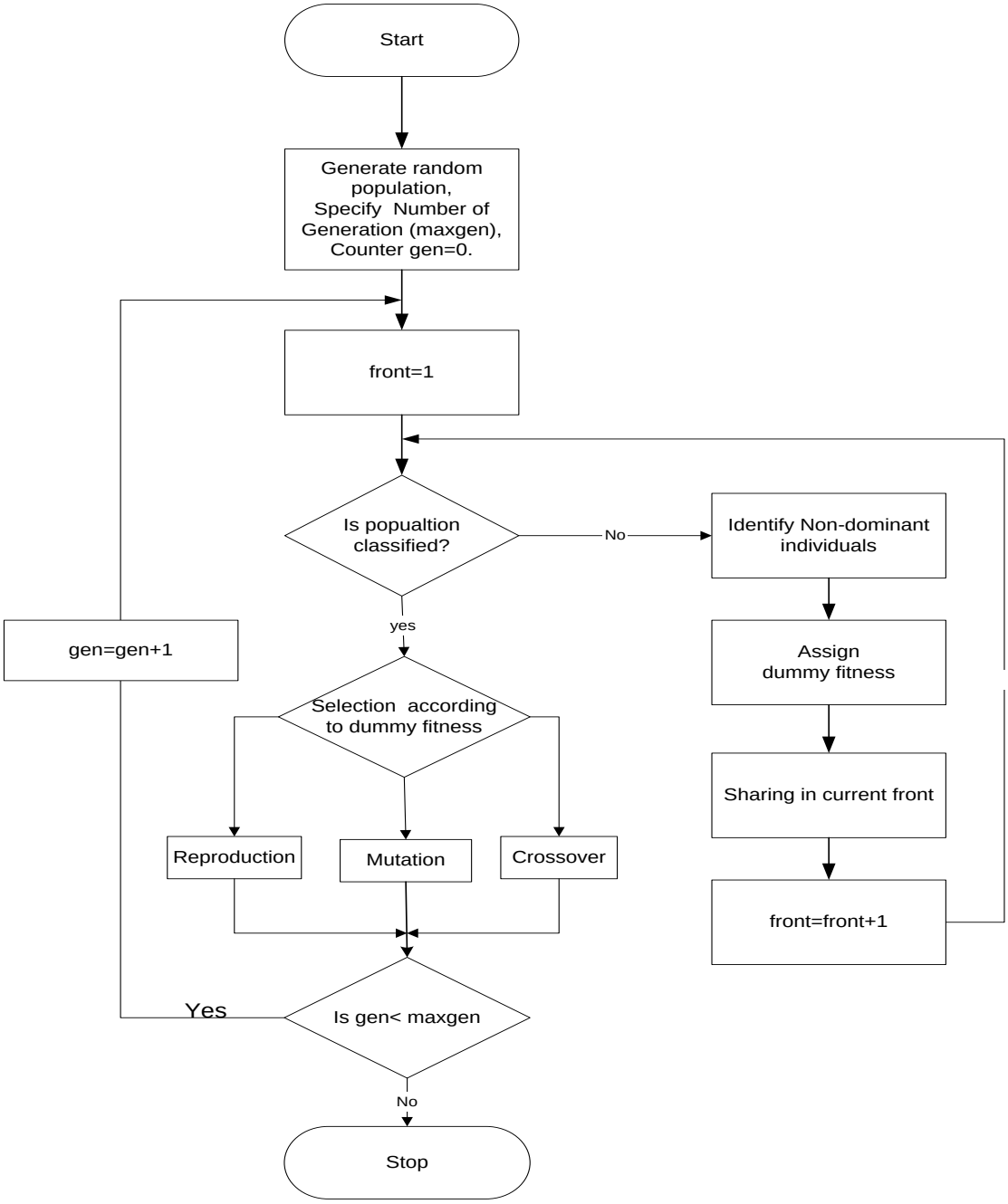


Figure 3: Flow chart of the Non-dominated Sorting Genetic Algorithm NSGA(Deb, Pratap, and Agarwal 2002; Zitzler and Thiele 1999)

2.5. Multi-objective function for robust control performance and stability

2.5.1 Stability and performance in MBPC

The process model which drives the controller is usually not an exact description of the real process.It is therefore important to investigate the influence of modelling errors on the properties of the closed loop system.

A closed loop structure is said to be stable if it retains those properties despite process variations. The stability and efficiency of a closed-loop device are two important properties to consider, and there are two types of robustness to consider: robust stability and robust performance. The term "robust stability" refers to the closed loop structure being consistent even though the model used for system architecture differs from the farm. Robust performance guarantees that the closed loop's performance stays within the prescribed limits even though the process varies from its model.The origins of robust control go back to Nyquist analysis, which revealed that a trade-off between performance and stability in control system design when modelling error is considered. This formed the basis of all robust control studies to date. Some primary concepts need to be defined before deriving the relationship between robust stability and performance.

Firstly, if the control system is closed loop stable when applied to a nominal process model then it satisfies 'nominal stability'. The extension of this idea yields the fact that the controller satisfies robust stability if it stable when applied to any member of the family of the processes. Similar definitions can be made for 'nominal performance' and 'robustness performance'.

Secondly, the combination of all uncertainty bounds along with the process model response builds a 'family' Γ of possible process plants. This can be written in terms of additive uncertainty bounds $l_a(j\omega)$ as follows:

$$l_a(j\omega) = p(j\omega) - \tilde{p}(j\omega) \qquad (8)$$

Where $p(j\omega)$ is any process model in the family Γ, and $\tilde{p}(j\omega)$ is the nominal process model. This allows the family of plants described by the disc in Figure 3.3 to be defined algebraically by:

$$\Gamma = \left\{ p : \left| p(j\omega) - \tilde{p}(j\omega) \right| \le \tilde{l}_a(j\omega) \right\} \qquad (9)$$

Where $l_a(\omega)$ is the additive uncertainty disc radius, in other words the difference in frequency response between the nominal process and a member of the family of the process measured by the additive uncertainty $l_a(\omega)$ bound.

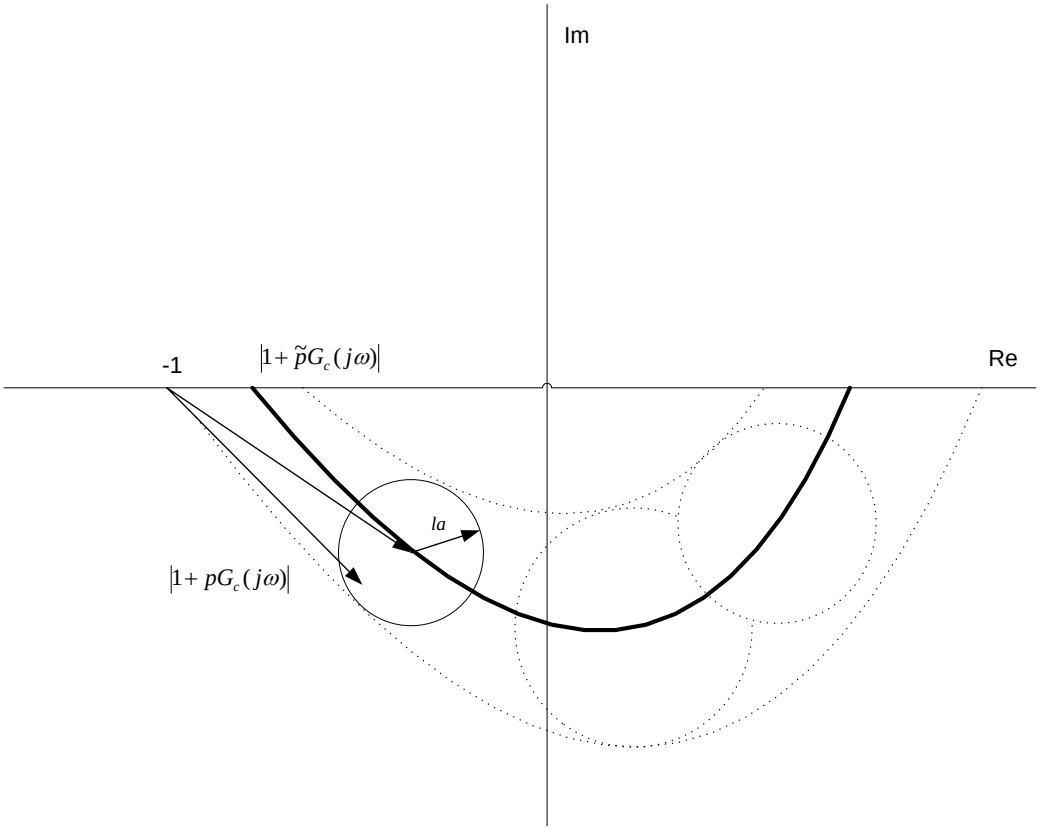


Figure 4: The Nyquist diagram of the robust stability

2.5.2 Robust Stability

Robustness is a highly desirable property for process control systems. In general, the control system results in robust closed loop stability if the closed loop is stable even if there is a difference between the model used by the controller and the actual process structure.

It can be seen from Figure 4 that if the Nyquist stability criterion is to hold, the distance from the (-1, 0) point to any point on the polar plot of the system $\tilde{p}G_c$, must be greater than the additive uncertainty at any frequency:

$$|1+\tilde{p}(j\omega)G_c(j\omega)| > \bar{l}_a(j\omega) \qquad \forall\omega \qquad \forall p \in \Gamma \tag{10}$$

Since $\bar{l}_a(\omega) = \left|G_c(j\omega)\,\tilde{p}(j\omega)\right|\bar{l}_m(j\omega)$, this helps to write equation 10 in terms of the multiplications uncertainty description,

$$|1+\tilde{p}(j\omega)G_c(j\omega)| > \left|G_c(j\omega)\,\tilde{p}(j\omega)\right|\bar{l}_m(j\omega) \qquad \forall\omega \tag{11}$$

Rearranging in terms of the complementary of the sensitivity function yields:

$$1 > \frac{\left|G_c(j\omega)\,\tilde{p}(j\omega)\right|}{\left|1+G_c(j\omega)\tilde{p}(j\omega)\right|}\bar{l}_m(j\omega) = \left|\tilde{\eta}(j\omega)\right|\bar{l}_m(j\omega) \qquad \forall\omega \tag{12}$$

Rearranging again, gives:

$$\left|\tilde{\eta}(j\omega)\right|\bar{l}_m(j\omega) < 1 \qquad \forall\omega \tag{13}$$

This can be expressed in H-infinity norm as follows:

$$\left\|l_m\eta\right\|_\infty < 1 \tag{14}$$

Robust stability imposes a bound on the infinity-norm of the complementary function η weighted by the multiplicative uncertainty l_m. The calculation of the complementary sensitivity for MBPC is a straightforward procedure in the MATLAB environment and the smaller the value, the larger is the robust stability of the closed loop system.

2.5.3 Robust Performance

Robustness Performance can be defined as the sensitivity of the performance of the closed loop system to process changes. Hence, the lower the sensitivity is, the larger is the robust performance.

Two theoretical measures are designed to predict control performances are the H_2 and H_∞performance objectives. The H_2 performance objective aims to minimise the Integral of Square Error (ISE) between the process output and the setpoint. It is sometimes referred to as linear Quadratic (LQ) control. The use of the LQ fits into the predictive control philosophy and the resulting optimisation problem is often intractable.

The H_∞performance objective aims to minimise the maximum absolute error that can result from an input to the process over all frequencies. This resulting optimisation problem is much more tractable and can be expressed in terms of the sensitivity function (Morarri and Zafiriou, 1989).
The min max performance objective in terms of the weighted sensitivity function where *w* represents a performance weight gives:

$$\min_{Gc}\left\|\varepsilon w(j\omega)\right\|_\infty = \min_{Gc}\sup_\omega\left|\varepsilon w(j\omega)\right| \tag{15}$$

By assuming the performance objective at a particular frequency has a consistent value,

$$\sup_\omega\left|\varepsilon w(j\omega)\right| = k \tag{16}$$

Across the whole frequency range, the individual consistent solutions can be absorbed into the performance weight. This gives:

$$\left|\varepsilon\right| = \left|w(i\omega)\right|^{-1} \qquad \forall\omega \tag{17}$$

That can be written in the infinity norm as follows:

$$\left\|\varepsilon w\right\|_\infty = 1 \tag{18}$$

By extending this concept to the complete family of plants yields the fact that the performance requirements must be achieved for the worst-case process. Rewriting equation 18 by considering the family of processes gives:

$$\min_{p\in\Gamma}\left\|\varepsilon w(j\omega)\right\|_\infty = \min_{p\in\Gamma}\sup_\omega\left|\varepsilon w(j\omega)\right| < 1 \tag{19}$$

This means robust performance can be achieved by minimising the infinity norm of the sensitivity function weighted by the input of the disturbance *w*.
From Figure 4 for robust stability to be justified:

$$\left|1+ pG_c\right| - \left|1+ \tilde{p}G_c\right| - \left|\tilde{p}G_c\right|\bar{l}_m \qquad \forall p \in \Gamma \tag{20}$$

Rearranging this criterion by expressing the terms of the sensitivity function and the complementary of the sensitivity function:

$$\left|\varepsilon\right| \le \frac{\left|\tilde{\varepsilon}\right|}{1-\left|\tilde{\eta}\right|\bar{l}_m} \qquad \forall \qquad p \in \Gamma \tag{21}$$

This relationship places upper limits on the sensitivity functions for any process in the family of plants. This can be arranged in the following form:

$$\left|\tilde{\eta}\bar{l}_m\right| + \left|\tilde{\varepsilon}w\right| < 1 \forall \omega \tag{22}$$

This means that the condition for robust performance also implies robust stability.

3. Results and Discussion

3.1 Step Response Modelling and simulation of the distillation column

MBPC control required an accurate model of the process to produce acceptable performance, hence, the step tests with small amplitude are introduced to the open loop to build a relationship between the input and the output variables. This data is crucial to determine the transfer functions describing the distillation column.

The basic procedures for obtaining step response model is to introduce a step input to each manipulated variable of the plant and record the open loop response of each output variable until all the output variables are settled at constant values.

A first order transfer function is described by three parameters: the time constant (the time required by output to rise 63.2% of its final value), the gain (the ratio of output to input change), and the time delay in multiples of sampling time for a discrete time representation.

Step response testing has many drawbacks in the real world. For example, it is undesirable to apply in industry, as it will be disruptive to normal plant operation. This could result in increasing the operating costs and reducing profitability, but nevertheless it is used quite commonly. Table1 shows the linear approximation of the process obtained fromstep response test model distillation column resulted in the following transfer function model.

Table 1: The transfer functions for the *LV* configuration

	Step Test up		Step Test down		Average	
	X_D	X_B	X_D	X_B	X_D	X_B
Reflux L	$\frac{2.5e^{-1.1s}}{5.1s+1}$	$\frac{0.854e^{-1.1s}}{4.1s+1}$	$\frac{0.933e^{-1.1s}}{5.5s+1}$	$\frac{0.2567e^{-1.1s}}{3.2s+1}$	$\frac{1.67e^{-1.1s}}{5.3s+1}$	$\frac{0.553e^{-1.1s}}{3.65s+1}$
Boil up V	$\frac{-0.225e^{-1.1s}}{2.95s+1}$	$\frac{-0.87e^{-1.1s}}{4.8s+1}$	$\frac{-0.211e^{-1.1s}}{2s+1}$	$\frac{-0.887e^{-1.1s}}{3.8s+1}$	$\frac{-0.547e^{-1.1s}}{3.75s+1}$	$\frac{-0.878e^{-1.1s}}{4.3s+1}$

3.2 Step response of the feed disturbance

For feed disturbance modelling, the step test in the feed is introduced up and down (of 50% and -50%), from a feed of 1 kg/min to 1.5 kg/min for the step up and from 1 kg/min to 0.5 kg/min for the step down. The following disturbance model is built from the step test in Table 2:

Table 2: The disturbance model of the step test

	Step Test up		Step Test down		Average	
	X_D	X_B	X_D	X_B	X_D	X_B
Feed Disturbance	$\frac{1.8e^{-1.1s}}{2s+1}$	$\frac{1.68e^{-1.1S}}{1.7s+1}$	$\frac{0.19e^{-1.1s}}{1.3s+1}$	$\frac{1.3e^{-1.1s}}{1.9s+1}$	$\frac{1.67e^{-1.1s}}{5.3s+1}$	$\frac{0.553e^{-1.1s}}{3.65s+1}$

3.3 NSGA-II tuning for MBPC with ISE and the control variance objective functions

In this paper, the application of 'SCMPCNL' MATLAB™ file developed by Maciejowski (2001) which designs an MBPC controller for constrained distillation column using quadratic programming QP is considered. This form of MBPC type is known as Quadratic Dynamic Matrix Control (QDMC). The advantage of this version lies on the capability to use a SIMULINK™ process plant model that can include nonlinear dynamics. The MBPC objectives are to bring the distillate output XD and the bottom composition XB to the setpoint of 0.95 and 0.05 respectively. The MBPC control is tuned using the NSGA-II algorithm. NSGA-II is used to overcome the problem of Simple genetic algorithm trapping in the local optimum. as Osman et al. show that the SGA is unable to stabilised the MBPC at high model uncertainty NSGA was successfully found the tuning parameters which stabilise MBPC(Osman 2017).

The NSGA-II implemented in this paper has the following parameters: The Population size is set to be 100 individuals, the length of the chromosome is 32, the probability of the crossover (Pc) is 95% and the Mutation probability (Pm) is 5%, sharing factor is set to one. Initially the objective functions for the NSGA-II.The simulation is stopped after 30 generations. The following results in Figure 5 are obtained.

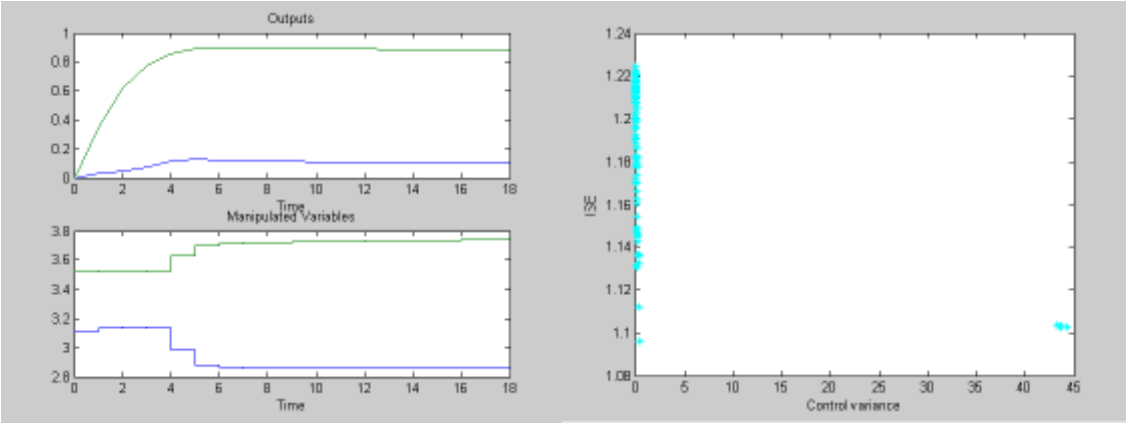


Figure 5 Simulation of NSGA using ISE and the control variance objective functions.

Figure 5 shows that the Pareto Optimum Front (POF) is not well constructed as a large gap in the middle of the POF is due to high value of the sharing factor. Moreover, the MBPC tuning variables resulted in only one pair of tuning parameters producing good performance and stability

3.4 NSGA-II tuning for MBPC with three objective functions:(IAE, Sensitivity function, and complementary of sensitivity function) and (ISE Sensitivity function, and complementary of sensitivity function).

The previous distillation step response control model is used for the MBPC controller with a 20% model mismatch in the time delay. The aim is to demonstrate by simulation the benefits of the use of three objective functions to stabilise MBPC when controlling the distillation column. Two sets of runs were performed to compare the NSGA-II with three objective functions, IAE, Sensitivity function and Complementary of Sensitivity function with MSE, Sensitivity function and Complementary of Sensitivity function. The two NSGA simulations are terminated after the 30th generation. The main problem of MOEA is that there no guarantee that the good solutions are saved until the last generation. Deb et al. solved this problem when byproposing elitism NSGA -II(Deb, Mohan, and Mishra 2003).

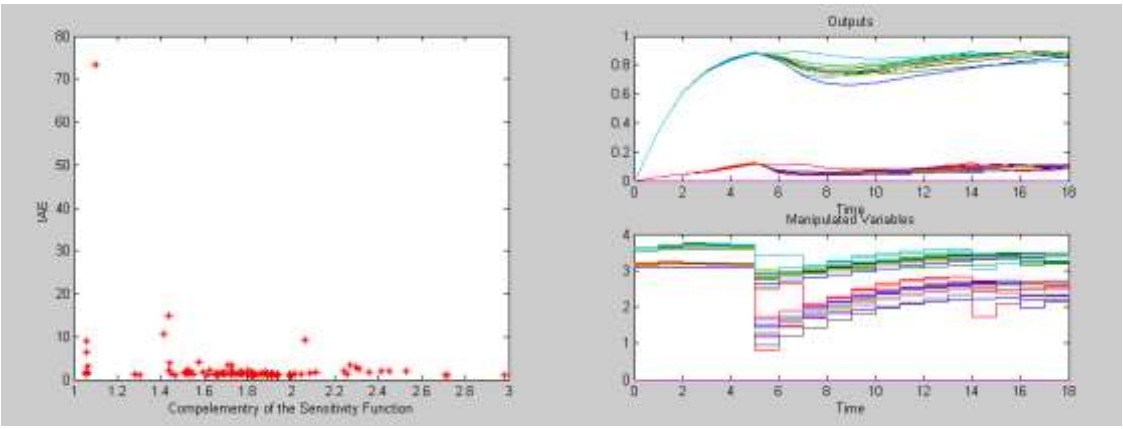


Figure 6: IAE, Sensitivity function and Complementary of Sensitivity function

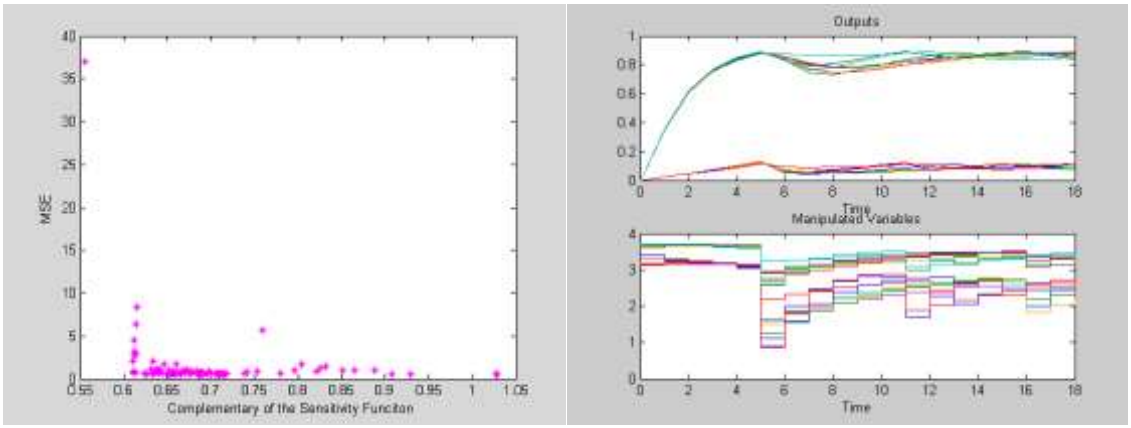


Figure 7: MSE, Sensitivity function and Complementary of Sensitivity function

It can be seen from Figure 6and Figure 7that MSE objective function slightly outperforms the IAE in the shape and limits of Pareto front, where MSE possess a well-distributed Pareto Optimum Front (POF) and less random sets. In addition, the POF of the MSE have a lower complementary function value. This can be noticed clearly in the simulation results of the control output of MSE in terms of producing better tuning values that give better tracking of the setpoint and reduced overshoot compared to the IAE. NSGA II with elitism is a promising optimisation technique in difficult search space due to its ability to keep the optimum non-dominated front until the last generations. Osman et al. optimise the MBPC tuning parameters for the Combustion Boiler Process using the NSGA-II the LQC objective function at high model uncertainty(Osman 2017; Osman 2014).

In line with other researchers' findings, Nafsun and Yusoff (2011)discovered that a mismatch in process gain has a much greater impact on MPC efficiency than a mismatch in time constant or time delay. Badwe et al. (2010)demonstrated that an underestimated (negative uncertainty) in the time delay mismatch will contribute significantly to oscillatory behavior, potentially leading to instability. Overestimation (positive uncertainty) in the time delay, on the other side, makes the controller tentative, resulting in an over-damped response

4.Conclusion

The NSGA-II has been implemented successfully for tuning MPC to regulate the top and bottom compositions of the distillation column at the model mismatch of up to 20% in the time delay.

Despite the MBPC model's linearity, it has been demonstrated that the proposed objective functions successfully optimized the model-based predictive control for the distillation column's nonlinear process. Additionally, they can provide several solutions that aid in the creation of the control at model uncertainties, in contrast to other traditional optimization approaches.

A comparison of these two sets of objective functions (IAE, Sensitivity, and complementary function) and (MSE, Sensitivity, and complimentary function) found that MSE outperformed IAE in terms of finding a well-distributed Pareto Front.

Funding: “This research was funded by DEANSHIP OF SCIENTIFIC RESEARCH, KING KHALID UNIVERSITY, grant number R.G.P.1/283/42”

References

1. Badwe, Abhijit S, Rohit S Patwardhan, Sirish L Shah, Sachin C Patwardhan, and Ravindra D Gudi. 2010. "Quantifying the impact of model-plant mismatch on controller performance." Review of. *Journal of Process Control* 20 (4):408-25.
2. Deb, K, A Pratap, and S Agarwal. 2002. "Meyarivan TJItoec." Review of. *A Fast and Elitist Multiobjective Genetic Algorithm* 6:182-97.
3. Deb, Kalyanmoy. 1999. "Multi-objective genetic algorithms: Problem difficulties and construction of test problems." Review of. *Evolutionary computation* 7 (3):205-30.
4. Deb, Kalyanmoy, Manikanth Mohan, and Shikhar Mishra. 2003. Towards a quick computation of well-spread pareto-optimal solutions. Paper presented at the International Conference on Evolutionary Multi-Criterion Optimization.
5. Dougherty, Danielle, and Doug Cooper. 2003. "A practical multiple model adaptive strategy for single-loop MPC." Review of. *Control engineering practice* 11 (2):141-59.
6. Exadaktylos, Vasileios, and C James Taylor. 2010. "Multi-objective performance optimisation for model predictive control by goal attainment." Review of. *International Journal of Control* 83 (7):1374-86.
7. Garriga, Jorge L, and Masoud Soroush. 2010. "Model predictive control tuning methods: A review." Review of. *Industrial & Engineering Chemistry Research* 49 (8):3505-15.
8. Hajisalehi, MH, K Salahshoor, and MH Sefat. 2014. "A New Methodology for Simulation and Optimization of CO2 Sequestration in a Saline Aquifer Using Artificial Neural Network and Model Predictive Control Approach." Review of. *Energy Sources, Part A: Recovery, Utilization, and Environmental Effects* 36 (3):336-46.
9. He, Ning, Dawei Shi, Jiadong Wang, Michael Forbes, Johan Backstrom, and Tongwen Chen. 2015. "User friendly robust MPC tuning of uncertain paper-making processes." Review of. *IFAC-PapersOnLine* 48 (8):1021-6.
10. Hindmarsh, Alan C. 1980. "LSODE and LSODI, two new initial value ordinary differential equation solvers." Review of. *ACM Signum Newsletter* 15 (4):10-1.
11. Júnior, Gesner A Nery, Márcio AF Martins, and Ricardo Kalid. 2014. "A PSO-based optimal tuning strategy for constrained multivariable predictive controllers with model uncertainty." Review of. *ISA transactions* 53 (2):560-7.
12. Mayne, David Q. 2001. "Control of constrained dynamic systems." Review of. *European Journal of Control* 7 (2-3):87-99.
13. Mayne, DQ, and Hi Michalska. 1990. An implementable receding horizon controller for stabilization of nonlinear systems. Paper presented at the 29th IEEE Conference on Decision and Control.
14. Nafsun, AI, and N Yusoff. 2011. "Effect of model-plant mismatch on MPC controller performance." Review of. *Journal of Applied Sciences* 11 (21):3579-85.
15. Nagrath, Deepak, Vinay Prasad, B Wayne Bequette, and HP Isermann. 2000. Model predictive control of open-loop unstable cascade systems. Paper presented at the Proceedings of the 2000 American Control Conference. ACC (IEEE Cat. No. 00CH36334).
16. Osman, Haitham. 2014. LQ evolution algorithm optimizer for model predictive control at model uncertainty. Paper presented at the 2014 14th International Conference on Control, Automation and Systems (ICCAS 2014).
17. Osman, HM. 2017. "Optimizing Model Base Predictive Control for Combustion Boiler Process at High Model Uncertainty." Review of. *Chemical and biochemical engineering quarterly* 31 (3):313-24.

18. Qin, S Joe, and Thomas A Badgwell. 2003. "A survey of industrial model predictive control technology." Review of. *Control engineering practice* 11 (7):733-64.
19. Ramasamy, Valarmathi, Rakesh Kumar Sidharthan, Ramkumar Kannan, and Guruprasath Muralidharan. 2019. "Optimal tuning of model predictive controller weights using genetic algorithm with interactive decision tree for industrial cement kiln process." Review of. *Processes* 7 (12):938.
20. Rippon, Lee D, Qiugang Lu, Michael G Forbes, R Bhushan Gopaluni, Philip D Loewen, and Johan U Backström. 2019. "Machine Direction Adaptive Control on a Paper Machine." Review of. *Industrial & Engineering Chemistry Research* 58 (26):11452-73.
21. Santander, Omar, Ali Elkamel, and Hector Budman. 2019. "Robust economic model predictive control: disturbance rejection, robustness and periodic operation in chemical reactors." Review of. *Engineering Optimization* 51 (5):896-914.
22. Sawulski, Jakub, and Maciej Ławryńczuk. 2018. Optimisation-based tuning of dynamic matrix control algorithm for multiple-input multiple-output processes. Paper presented at the 2018 23rd International Conference on Methods & Models in Automation & Robotics (MMAR).
23. Shinskey, FG. 1984. "Distillation Column Control." In.: McGraw Hill New York.
24. Shridhar, Rahul, and Douglas J Cooper. 1997. "A tuning strategy for unconstrained SISO model predictive control." Review of. *Industrial & Engineering Chemistry Research* 36 (3):729-46.
25. Skogestad, Sigurd. 1997. "Dynamics and control of distillation columns: A tutorial introduction." Review of. *Chemical Engineering Research and Design* 75 (6):539-62.
26. Tran, Quang N, Leyla Özkan, and ACPM Backx. 2012. "Mpc tuning based on impact of modeling uncertainty on closed-loop performance." Review of.
27. Zitzler, Eckart, and Lothar Thiele. 1999. "Multiobjective evolutionary algorithms: a comparative case study and the strength Pareto approach." Review of. *IEEE transactions on Evolutionary Computation* 3 (4):257-71.

Appendix

Table A1: The feasible control schemes for Dual composition distillation column

	Controlled outputs		Manipulated inputs	
Scheme	X_B	X_D	M_D	M_B
L-V	*L*	*V*	*D*	*B*
D-V	*D*	*V*	*L*	*B*
L-B	*L*	*B*	*D*	*V*
L/V-D/B	*L/V*	*D/V*	*D*	*B*

Solubility Modelling of Polyphenols in Supercritical Carbon Dioxide and Modifier using Cubic Plus Association Model

Chew Yi Min [1] and Azizul Azri Mustaffa [2,*]

[1] School of Chemical and Energy Engineering, Faculty of Engineering, Universiti Teknologi Malaysia, 81310 UTM Johor Bahru, Johor, Malaysia.

[2] Process Systems Engineering Centre (PROSPECT), Research Institute for Sustainable Environment (RISE), Universiti Teknologi Malaysia, 81310 UTM Johor Bahru, Johor, Malaysia.

***** *Corresponding author: azizulazri@utm.my; Tel.: +60162195295.*

Abstract: Solubility modelling of solutes in supercritical carbon dioxide ($scCO_2$) with modifiers is essential for optimization of separation process. In this study, the purpose is to develop solubility modelling of polyphenols (cinnamic acid, salicylic acid and ferulic acid) in mixtures of $scCO_2$ and ethanol at different temperatures and pressure using Cubic Plus Association equation of state (CPA EOS) through solid vapor equilibrium (SVE). Parameter regression of k_{ij} is conducted using fminsearch optimization tools in MATLAB by fitting it with binary mixtures solubility data. In order to have a model over a wide range of temperature and pressure, regressed k_{ij} are presented as a function of pressure and temperature. Polyphenol solubility is investigated using CPA EOS with the k_{ij} function at pressures ranging from 8 to 40 MPa and temperature between 308 to 323 K for the three component, polyphenol-CO_2-modifier systems. Optimum condition in SFE is determined using CPA EOS for solubility of ferulic acid. The overall average absolute relative deviation is 5.4% and solubility prediction using modelling closely agreed with experimental data by representing temperature and pressure effects properly. In general, this work suggests that CPA EOS using function k_{ij} is useful for solubility modelling of polyphenols in $scCO_2$ and modifier with reasonable accuracy over pressure and temperature ranges evaluated.

Keywords: Cubic plus association; solubility modelling; polyphenols; modifier; supercritical fluid extraction

1. Introduction

Polyphenol represents a diverse ubiquitous class of compounds present in most fruits, herbs and vegetables as secondary plants metabolites. Polyphenols are very important functional foods in our nutrition. The current contribution of polyphenols is focused on their bioavailability, antioxidative and anticarcinogenic properties. At the present time, several studies and research have been conducted to investigate the positive health effect of polyphenols and the classification of polyphenols [1].

The importance of polyphenols with antioxidant and antimicrobial activity as well as increment of demands to obtain functional foods have encouraged a quick expansion of research studies for extraction of polyphenols. In order to acquire polyphenols for research purposes, many extraction methods have been applied such as Soxhlet extraction, microwave-assisted extraction, ultrasonic-assisted extraction, and supercritical fluid extraction. The extraction method must be fast, eco-friendly, non-toxic, low cost and easy to handle. The supercritical fluid extraction (SFE) process has been extensively investigated and chosen to be an alternative in the isolation of polyphenols.

Supercritical fluid extraction has been widely utilized because it is a clean and environmentally friendly processing technique. Health and safety benefits are the main consideration of SFE which are non-cancerogenic, non-toxic, non-flammable and thermodynamically stable. Supercritical carbon dioxide ($scCO_2$) is used as the extracting agent in SFE. However, supercritical carbon dioxide is a weak extracting solvent for polar polyphenols due to its non-polarity. Therefore, polar modifier is added to increase the polarity of carbon dioxide and the solubility of the solute in the supercritical solvent. The knowledge of the solubility of solids involved in supercritical fluids is essential for evaluating the feasibility and for establishing optimum operating conditions.

Due to the limitations of measuring the solubility in SFE such as time constraints and high costs of experimental, solubility modelling has been widely considered and developed by fitting it with existing solubility data at different temperature and pressure. Those solubility models include empirical models, kinetic models, and equation of state models. Solubility models are important as they are alternatives to predict the behavior and the solubility of solutes at different operating conditions for optimization of separation processes without conducting the real experiments.

Thermodynamic modelling which can predict not only the solubility but also the phase behavior of the system has great importance due to the high pressure and the importance of intermolecular forces at high pressure in SFE. Among the thermodynamic models, Peng-Robinson equation of state (PR EOS) and Soave-Redlich-Kwong equation of state (SRK EOS) are the most common model used to describe the system at high pressure and give a good qualitative and quantitative picture of phase behavior in SFE [2]. However, with the addition of modifiers in SFE, PR EOS and SRK EOS do not account for strong associating interaction between modifiers and solute polyphenols such as hydrogen bonding, thus resulting in inaccurate results [3]. Bitencourt et al. [4] have shown good results in the solubility of caffeic acid in supercritical carbon dioxide and ethanol using Cubic Plus Association equation of state (CPA EOS). CPA EOS consists of the combination of a cubic equation Soave-Redlich-Kwong, and the association term proposed by Wertheim perturbation theory.

The main objective of this study is to develop a solubility modelling to estimate the solubility of polyphenols in modifiers and supercritical carbon dioxide using Cubic Plus Association (CPA) using solid vapor equilibrium (SVE). The solubility modelling of Cubic Plus Association can be used to determine the optimum condition in SFE with maximum solubility of polyphenol.

2. Methodology

The polyphenols solubility in the supercritical carbon dioxide and modifier can be calculated using solid vapor equilibrium (SVE) [5]. The solubility of polyphenol is calculated as:

$$y_1 = \frac{P_1^{sub}}{P}\frac{1}{\varphi_1^V}\exp\left(\frac{V_1^S(P - P_1^{sub})}{RT}\right) \tag{1}$$

where y_1 is the solubility of polyphenol, φ_1^V is the fugacity coefficient of polyphenol at sublimation pressure, V_1^S is the molar volume of polyphenol, P_1^{sub} is the sublimation pressure of polyphenol, P is the operating pressure, T is the operating temperature, R is the gas constant.

The fugacity coefficient of polyphenol, φ_1^V is calculated using Cubic Plus Association modelling [6]. The modelling can be expressed in terms of pressure as a sum of the SRK EOS and the contribution of the association term.

$$P = \frac{RT}{V_m - b} - \frac{\alpha(T)}{V_m(V_m + b)} - \frac{1}{2}\left(\frac{RT}{V_m}\right)\left(1 + \frac{1}{V_m}\frac{d\ lng}{d\left(\frac{1}{V_m}\right)}\right)\sum_i x_i \sum_{Ai}(1 - X_{Ai}) \tag{2}$$

where T is the operating temperature, P is the operating pressure, V_m is the molar volume, X_{Ai} is the fraction of A-sites of molecule *i* that are not bonded with other active sites, x_i is the mole fraction of component *i*, α is the pure component energy parameter, b is the co-volume pure component parameter, ρ is the molar density. The letters *i* and *j* are used to index the molecules, whereas the letters A and B indicate the bonding sites on a given molecule.

The fugacity coefficient with CPA for the solubility of polyphenol in SFE is calculated using the following equation [6]:

$$RT\ ln\varphi_i = \left(\frac{\partial A^r}{\partial n_i}\right)_{T,V,n} - RT\ lnZ \tag{3}$$

$$A^r(T,V,n) = A^r_{SRK}(T,V,n) + A^r_{assoc}(T,V,n) \tag{4}$$

where A^r is the residual Helmholtz energy for the mixture, Z is the compressibility factor, V is the total volume of the system, φ_i is the fugacity coefficient of component i.

X_{Ai} is calculated from the association strength between two sites belonging to two different molecules by solving the following set of equations [6]:

$$X_{Ai} = \frac{1}{1 + (\frac{1}{V_m}) \sum_j x_j \sum_{Bj} X_{Bj} \Delta^{AiBj}} \quad (5)$$

where B_j indicates summation over all sites.

Δ^{AiBj} is the association strength between site A on molecule i and site B on molecule j is given by [6]:

$$\Delta^{AiBj} = g(V_m)^{ref} [\exp (\frac{\in^{AiBj}}{RT}) - 1] b_{ij} \beta^{AiBj} \quad (6)$$

where $\in^{AiBj}$ and β^{AiBj} are the association energy and volume of interaction between site A of molecule *i* and site B of molecule *j*, respectively.

$g(V_m)^{ref}$ is the contact value of the radial distribution function for reference fluid. In CPA, the radial distribution function derived from the Carnahan Starling EOS which is given by [6]:

$$g(V_m)^{ref} = \frac{1}{1 - 1.9 \frac{b}{4V_m}} \quad (7)$$

The pure component energy parameter, α in the SRK term is given by a Soave-type temperature dependency:

$$\alpha(T) = a_0[1 + c_1(1 - \sqrt{T}_r)]^2 \quad (8)$$

where T_r is the reduced temperature $(\frac{T}{T_c})$, a_0 *and* c_1 are additional parameters in the SRK term.

The extension of CPA to binary pair in polyphenol-CO_2-modifier system requires mixing rules for the CPA pure component parameters (a_0, $c_1, b, \in^{AiBj}$, β^{AiBj}). The parameters of the physical terms (a_0, c_1, b) for binary pair are calculated employing van der Waals mixing rules, fitting a binary interaction parameter, k_{ij} which required the parameter regression. The energy and volume association parameters of binary pair ($\in^{AiBj}$, β^{AiBj}) are calculated by CR1 combining rules.

$$a = \sum_i^n \sum_j^n x_i x_j (a_i a_j)^{0.5} (1 - k_{ij}) \quad (9)$$

$$b = \sum_i^n x_i b_j \quad (10)$$

$$\in^{AiBj} = \frac{\in^{AiBi} + \in^{AjBj}}{2} \quad (11)$$

$$\beta^{AiBj} = \sqrt{\beta^{AiBi} \beta^{AjBj}} \quad (12)$$

The overall research methodology to develop Cubic Plus Association modelling with solid vapor equilibrium for estimation of the solubility polyphenols in supercritical carbon dioxide and modifier is divided into 5 stages as shown in Figure 1.

2.1. Stage 1: Development of Database for Modelling

The data collection consists of four important parts which are selection of polyphenols, selection of modifier, collection of experimental data and physical properties of all components (Polyphenol-CO_2-modifier). All the input data are collected and stored in Microsoft Excel.

In the selection of polyphenols, the properties of each type of polyphenol and their importance are considered. The type of polyphenols chosen is phenolic acid because it consists of both carboxylic acid group and phenolic hydroxyl which are considered as association sites and all the association

sites will be considered in CPA. Among the various type of phenolic acids, salicylic acid, cinnamic acid and ferulic acid are selected due to their importance in application [7].

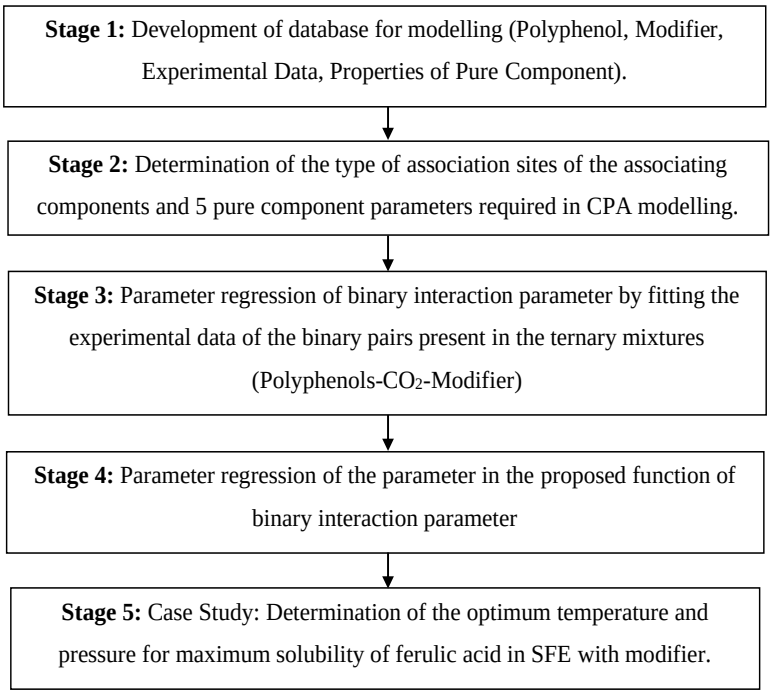


Figure 1. Overall flow chart for research methodology

The selection of modifiers is highly dependent on the properties of the desired components to be extracted which is polyphenol. The polar modifier is selected to increase the polarity of supercritical carbon dioxide because polyphenol is a polar compound. In this study, the selected polar modifier is ethanol due to its high miscibility with carbon dioxide and lower toxicity.

Experimental data of each binary pair in ternary system consisting of polyphenol, carbon dioxide and modifier are required in this study. The type of polyphenols and modifiers as well as the operating conditions of the experiment are collected from the literature. For cinnamic acid, the experimental solubility data for both binary and ternary systems are extracted from literature [8]. For salicylic acid, the experimental solubility data in binary and ternary systems are extracted from the literature [9, 10]. In SFE of ferulic acid, the experimental solubility data are obtained from the literature [3, 11]. The experimental solubility data are used for regression of binary interaction parameter, k_{ij} using CPA.

Physical properties required for calculation of polyphenol solubility using CPA are determined including molar volume, sublimation pressure, critical temperature, critical pressure, van der Waals volume and sublimation pressure for all components involved in polyphenol-CO_2-modifier system. The properties of all the components are extracted from the literature search or Design Institute for Physical Properties database (DIPPR) [12] whereas sublimation pressure is calculated using the method proposed by Mackay, Bobra [13] due to its accuracy and simplicity [14] as shown by Equation (13).

$$\ln P = -(4.4 + \ln T_B)\, x \left[1.803 \left(\frac{T_B}{T} - 1\right) - 0.803 \ln\left(\frac{T_B}{T}\right)\right] - 6.8 \left(\frac{T_M}{T} - 1\right) \quad (13)$$

where T_B is boiling temperature, T_M is melting temperature, P is sublimation pressure and T is temperature.

2.2. Stage 2: Determination of the Number of Association Scheme and Pure Component Parameters

Before determining the CPA pure component parameter, it is important to identify the association scheme of all components. Polyphenols, carbon dioxide and modifiers are identified as either an associating or non-associating compounds by determining the functional group of the components. The compounds with functional groups of acid, alcohol and amine are identified as associating

compounds. For the associating compounds, their number of association schemes are determined as proposed by Huang and Radosz [15]. The association scheme is identified by determining the number of proton donors and proton acceptors in the component.

CPA modelling has five pure compound parameters which are three for non-associating compound ($a_0,\ c_1, b$) and two additional parameters for associating compound ($\in^{AiBj},\ \beta^{AiBj}$). For non-associating compounds, there are only three pure compound parameters ($a_0,\ c_1, b$) that can obtain with conventional method using critical data and acentric factors. These are defined as follows:

$$a_0 = \frac{0.42748R^2T_C^2}{P_C} \tag{14}$$

$$b_i = \frac{0.08664RT_C}{P_C} \tag{15}$$

$$c_1 = 0.48 + 1.574w - 0.176w^2 \tag{16}$$

where a_0, c_1 and b are the pure component parameters in SRK term, T_C is the critical temperature, P_C is the critical pressure, R is the universal gas constant and *w* is the acentric factor.

For associating compounds, there are two additional association parameters which are association energy and volume ($\in^{AiBj},\ \beta^{AiBj}$). For CPA modelling, the pure components parameters are usually estimated by fitting vapor pressure and liquid density [6]. However, in this work, the data are unavailable for both vapor pressure and liquid density. The pure component parameters in SRK term ($a_0,\ c_1, b$) are calculated by applying the critical properties and van der Waals volume as shown in Equation (17) to (19) [7]. This method is suitable to calculate the pure components parameters for phenolic acids. The association energy and volume parameters ($\in^{AiBj},\ \beta^{AiBj}$) are extracted from the literature search for all the associating components in polyphenol- CO_2- modifier system.

$$a_0 = 0.2267 + 24.38\frac{T_C^2}{P_C} \tag{17}$$

$$b = -2.328\ x10^{-5} + 1.884(Vw) \tag{18}$$

$$c_1 = -3.557 + (6.289\ x\ 10^{-3})T_C \tag{19}$$

where a_0, c_1 and b are the pure component parameters in SRK term, T_C is the critical temperature, P_C is the critical pressure, Vw is the van der Waals volume.

After obtaining CPA pure component parameters, for multicomponent mixtures, energy and volume of the physical term and association parameter of the mixture ($a_0,\ c_1, b, \in^{AiBj},\ \beta^{AiBj}$) is calculated by using mixing rules and combining rules as shown in Equation (9) to (12).

2.3. Stage 3: Parameter Regression of Binary Interaction Parameter

CPA modelling used in polyphenol-CO_2-modifier system comprises of three binary interaction parameters, k_{ij}. The binary interaction parameters are estimated for all the binary pairs involved in the ternary system of polyphenol (1) – CO_2 (2) – modifier (3) at different temperatures and pressures.

The values for k_{ij} are regressed by fitting the experimental solubility data of the binary or ternary system of polyphenol-CO_2-modifier in the CPA. For binary pair of polyphenol-CO_2, k_{12} was regressed by fitting the binary mixture experimental solubility data of polyphenol and CO_2. Due to lack of the solubility data for the polyphenol-modifier system, k_{13} between polyphenol and modifier is regressed by fitting the ternary experimental solubility data [16]. The binary interaction parameter of CO_2-modifier system, k_{23} is extracted from the literature [4]. This is because there is no vapor-liquid data at the required temperature and pressure. The regression is performed in MATLAB using the fminsearch in the optimization toolbox [17]. The binary interaction parameters are regressed by minimizing the objective function (OF 1).

$$OF\ 1 = \sum_i^{NP}(\frac{y_i^{exp} - y_i^{calc}}{y_i^{exp}})^2 \tag{20}$$

where NP is the number of data used in regression, y_i^{exp} is the experimental solubility data, y_i^{calc} is the calculated solubility using modelling, *i* is the index for the components.

During parameter regression, the input data from Stages 1 and 2 are included in MATLAB. The method used for CPA modelling which is important to calculate the fugacity coefficient of polyphenol is based on literature [18, 19]. CPA based on the method used and objective function are presented in MATLAB. The initial guess value of k_{ij} and OF 1 tolerance are set in the optimization toolbox. By substituting k_{ij}, fugacity coefficient of polyphenol is calculated, and the solubility of polyphenol can be calculated as shown in Equation (1). The binary interaction parameters for each binary pair are obtained for different temperatures and pressure. Figure 2 shows the flow chart for parameter regression of k_{ij}.

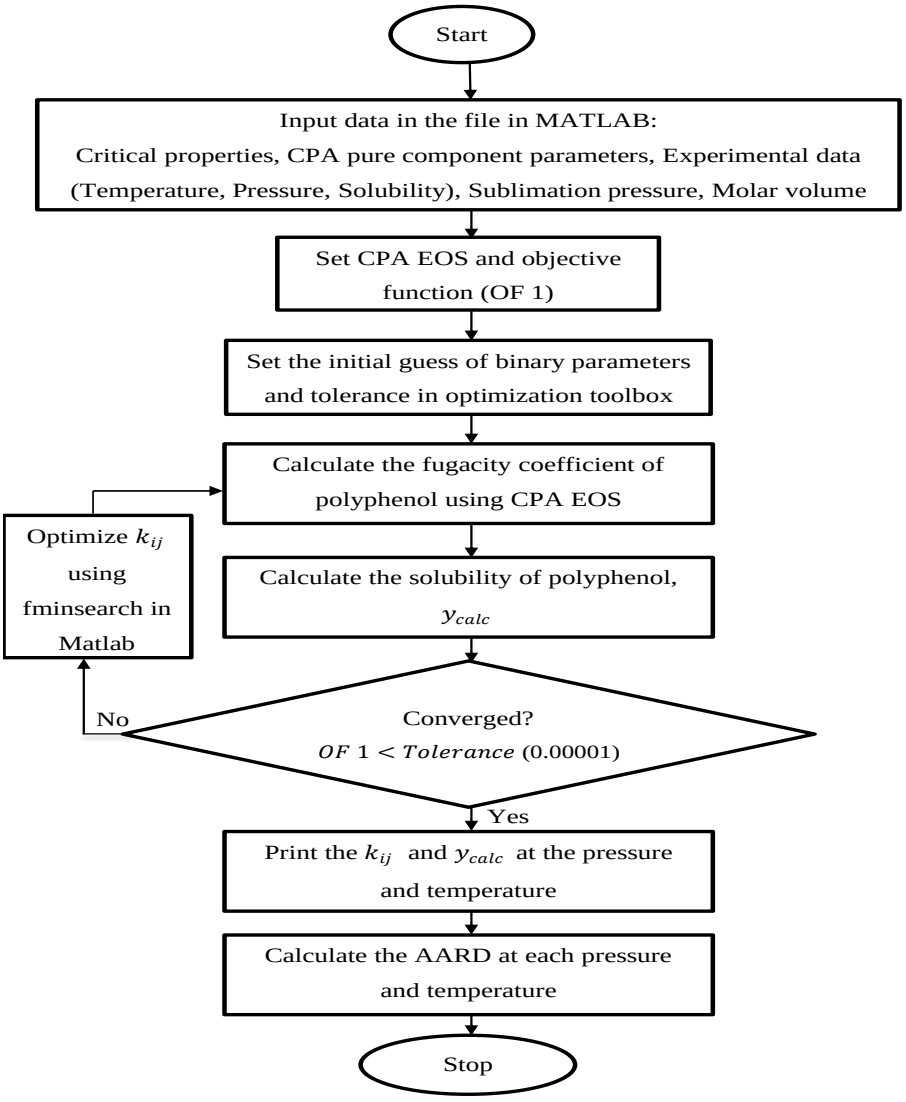


Figure 2. Flow chart for parameter regression of k_{ij}

After the regression, the average absolute relative deviation (AARD) is computed to analyze the deviation between the experimental training set and the solubility data predicted from the modelling.

$$AARD = \frac{100}{NP}\sum_{i}^{NP}\frac{y_i^{exp} - y_i^{calc}}{y_i^{exp}} \tag{21}$$

where NP is the number of data used in regression, y_i^{exp} is the experimental solubility data, y_i^{calc} is the calculated solubility using modelling, i is the index of components.

2.4. Stage 4: Parameter Regression of Parameter in Function of Binary Interaction Parameters

The regressed k_{ij} in Stage 3 is only specific at a certain temperature and pressure. To increase the application range for temperature and pressure, it is important to have a model function to predict the values of k_{ij} at specific range of temperatures and pressures.

The function for k_{ij} is proposed based on the trend of k_{ij} with temperature and pressure by plotting the graph of temperature and pressure against k_{ij} and determine whether k_{ij} of each binary pair is dependent on temperature and pressure. The possible k_{ij} functions are proposed as shown below.

$$k_{ij} = xP + yT + z \tag{22}$$

$$k_{ij} = wT^2 + xP + yT + z \tag{23}$$

$$k_{ij} = qP^2 + xP + yT + z \tag{24}$$

where T is temperature, P is pressure and w, q, x, y and z are parameters which are determined by regression using the optimization toolbox in MATLAB.

The parameters in the function are regressed by minimizing the objective function (OF 2).

$$OF\ 2 = \sum_{i}^{NP} \left(\frac{k_{ij}^{exp} - k_{ij}^{calc}}{k_{ij}^{exp}}\right)^2 \tag{25}$$

where NP is the number of data used in regression, k_{ij}^{exp} is the binary interaction parameter from Stage 3, k_{ij}^{calc} is the calculated binary interaction parameter using proposed function.

Figure 3 illustrates the flow chart for parameter regression of parameters in the proposed function.

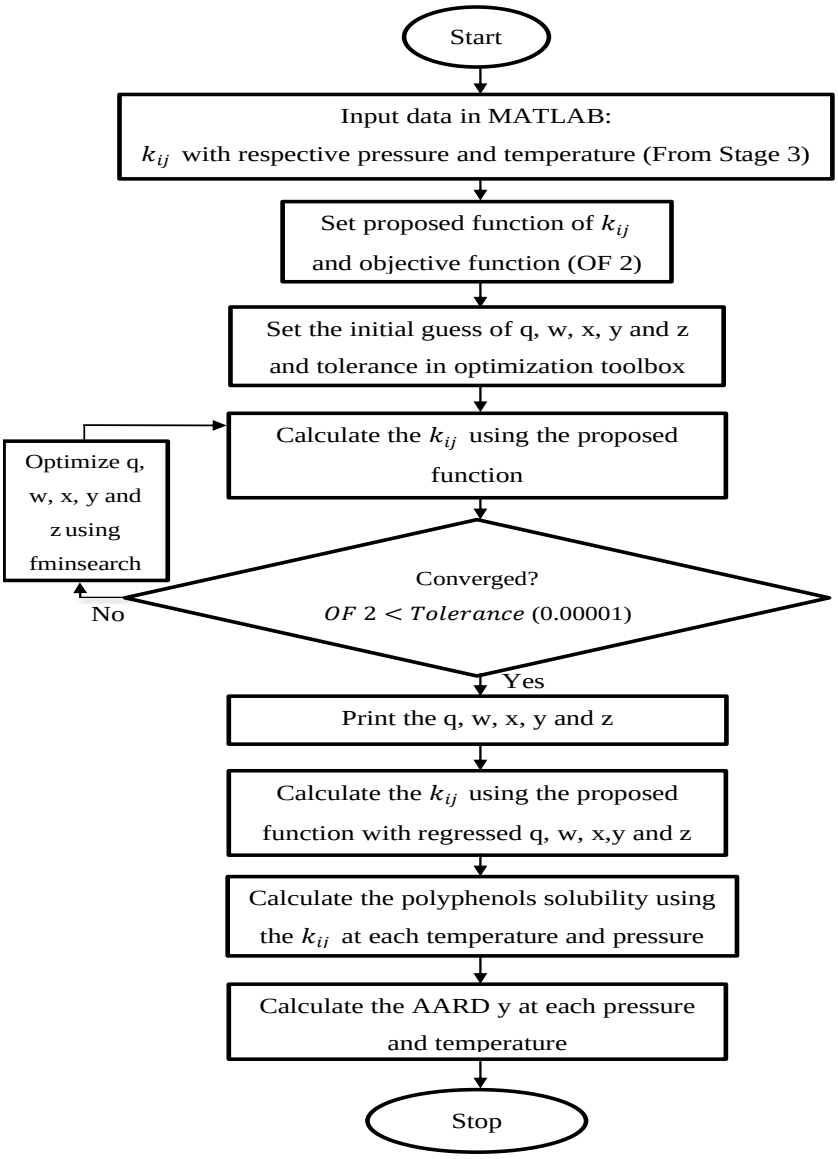


Figure 3. Flow chart for parameter regression of parameter in the proposed function

For modelling validation, the solubility of polyphenols calculated using the modelling is compared with the experimental test set by plotting a graph of experimental solubility data against the calculated solubility data.

2.5. Stage 5: Case Study

A case study is conducted to show the steps of determining the solubility of ferulic acid in SFE by using the CPA modelling at different temperatures and pressures. Selection of optimum temperature and pressure is conducted by determining the maximum solubility within the pressure and temperature range. Figure 4 shows the flow chart for the calculation of polyphenol solubility.

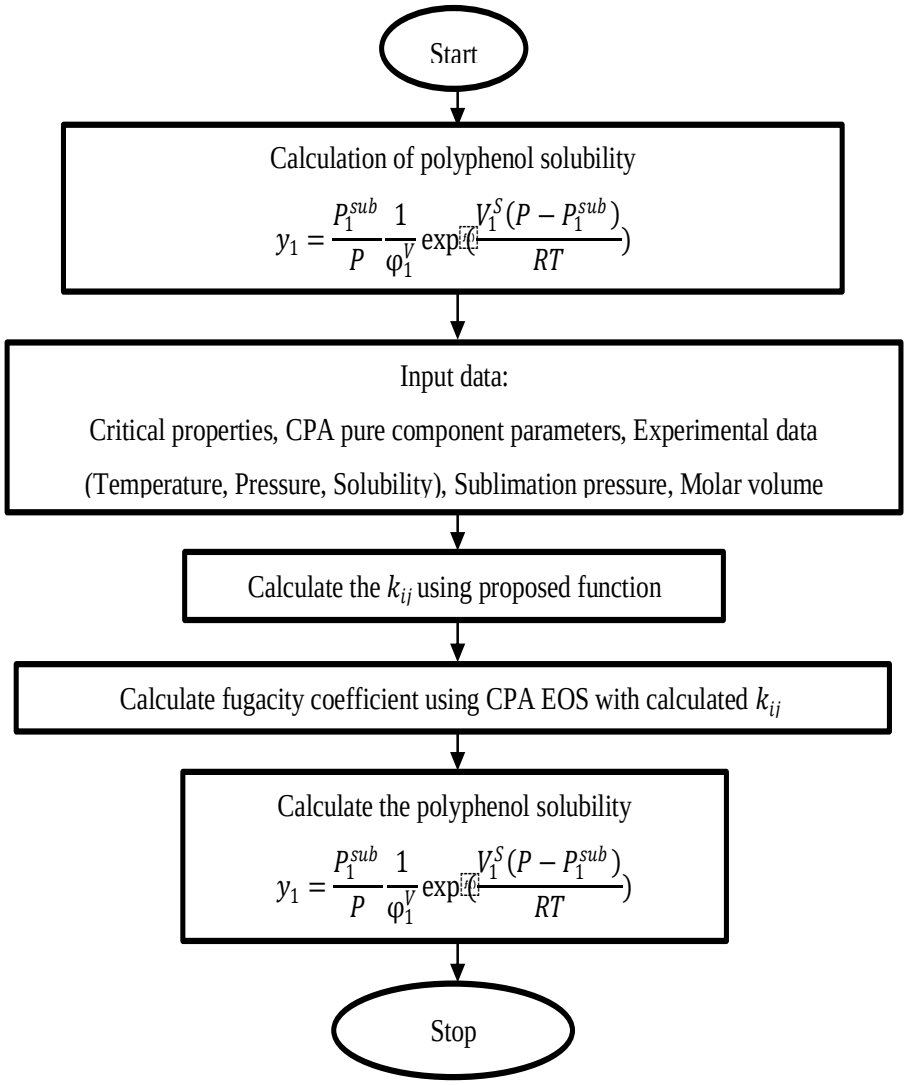


Figure 4. Flow chart for the calculation of polyphenol solubility

After obtaining the solubility of ferulic acid at different temperature and pressure using modelling, the effect of temperature and pressure on the solubility of ferulic acid is observed by plotting the graph of temperature and pressure against solubility of ferulic acid. The optimum temperature and pressure are selected with the maximum solubility.

3. Results and Discussion

Critical properties, molar volume, van der Waals volume, boiling and melting temperature required for CPA are recorded in Table 1.

Table 1. Pure component physical properties

Components	Carbon Dioxide	Ethanol	Cinnamic acid (CA)	Salicylic acid (SA)	Ferulic acid (FA)
Molar Volume (m^3/kmol)	0.0197	0.05862	0.118	0.134	0.1766
Critical Temperature (K)	304.2	514.0	797.0	739.0	834.4
Critical Pressure (MPa)	7383	6137	3494	5112	3813
Boiling Temperature (K)	194.69	351.44	573.15	529.00	623.24
Melting Temperature (K)	26.58	159.05	406.15	431.75	421.36
Van der Waals volume (m^3/mol)	$1.97x10^{-5}$	$3.19\ x10^{-5}$	$8.10\ x10^{-5}$	$7.13\ x10^{-5}$	$1.07\ x10^{-4}$

The properties of cinnamic acid, salicylic acid, carbon dioxide and ethanol are extracted from Design Institute for Physical Properties (DIPPR) database [12]. For phenolic acids, there is a limited amount of thermophysical properties data and sublimation pressure. For ferulic acid, the properties are calculated using Marrero & Gani group contribution method due to the lack of experimental values [20]. The molar volume of ferulic acid is taken from the literature [3]. For cinnamic acid, molar volume is extracted from the literature [21]. The molar volume of salicylic acid is taken from the literature [22]. Van der Waals volume of phenolic acids are extracted from literature [7].

Carbon dioxide is assumed as non-associating components while polyphenols and modifiers are treated as associating compounds. The pure component parameter for carbon dioxide and ethanol are extracted from literature [6]. For phenolic acids, the pure component parameters of the physical term ($a_0,\ c_1, b$) are calculated based on Equation (17) to (19). The association parameters ($\epsilon^{AiBj},\ \beta^{AiBj}$) for phenolic acids are extracted from the literature [23]. The results of the association scheme and pure component parameters are presented in Table 2.

Table 2. Association scheme and CPA pure component parameter

Compound	Association Group	Association Scheme	a_0 ($\frac{Pam^6}{mol}$)	b ($\frac{m^3}{mol}$)	c_1	ϵ^{AiBj} ($\frac{J}{mol}$)	β^{AiBj}
Carbon dioxide	-	-	0.3500	$2.72\ x10^{-5}$	0.7600	-	-
Ethanol	OH	2B	0.8672	$4.91\ x10^{-5}$	0.7369	21532	0.0080
Salicylic acid (SA)	OH, COOH	2B	2.8712	$1.11\ x10^{-4}$	1.0906	10000	0.0603
Cinnamic acid (CA)	OH, COOH	2B	4.6989	$1.29\ x10^{-4}$	1.4553	19100	0.0016
Ferulic acid (FA)	OH, COOH	2B	4.7181	$1.78\ x10^{-4}$	1.6904	21400	0.0030

3.1. Parameter Regression of k_{ij}

The prediction of polyphenol solubility in polyphenol – CO_2– modifier by using SVE in CPA requires three binary interaction parameters, k_{ij}. Parameter regression of k_{ij} is conducted by fitting the experimental solubility data of the binary pair. The result for the regressed k_{ij} of each binary pair at different temperatures and pressures are presented in Tables 3, 4 and 5. Experimental solubility training data are compared to the CPA predicted results by reporting AARD for every single operational condition. Each component is represented with the specific index number where cinnamic acid (1), carbon dioxide (2), ethanol (3), salicylic acid (4) and ferulic acid (5).

Table 3. Binary interaction parameter for cinnamic acid - CO_2 (k_{12}) and cinnamic acid – ethanol (k_{13})

Temperature (K)	Pressure (MPa)	k_{12}	AARD y (%)	Temperature (K)	Pressure (MPa)	k_{13}	AARD y (%)
308	13	0.272	0.857	308	11	0.575	0.085
308	15	0.274	0.296	308	15	0.442	0.091
308	18	0.274	0.609	308	18	0.396	0.011
318	13	0.270	0.353	318	11	0.652	0.027
318	15	0.275	0.013	318	15	0.503	0.019
318	18	0.276	0.927	318	18	0.423	0.042
328	13	0.259	0.624	328	11	0.602	0.009
328	15	0.272	0.344	328	15	0.460	0.057
328	18	0.278	0.361	328	18	0.399	0.073

Table 4. Binary interaction parameter for salicylic acid - CO_2 (k_{42}) and salicylic acid – ethanol (k_{43})

Temperature (K)	Pressure (MPa)	k_{42}	AARD y (%)	Temperature (K)	Pressure (MPa)	k_{43}	AARD y (%)
308	15	0.052	0.394	308.15	8.7	-1.330	0.016
308	20	0.053	0.378	308.15	13.0	-1.105	0.107
308	24	0.049	0.559	308.15	15.6	-1.024	0.106
318	15	0.056	0.592	318.15	12.7	-1.116	0.046
318	20	0.055	0.718	318.15	13.9	-1.047	0.483
318	24	0.055	0.367	318.15	15.7	-0.953	0.501
328	15	0.057	0.113				
328	20	0.057	0.021				
328	24	0.056	0.276				

Table 5. Binary interaction parameter for ferulic acid - CO_2 (k_{52}) and ferulic acid – ethanol (k_{53})

Temperature (K)	Pressure (MPa)	k_{52}	AARD y (%)	Temperature (K)	Pressure (MPa)	k_{53}	AARD y (%)
313	20	0.232	0.4297	313	20	-0.343	0.0026
313	30	0.215	0.6947	313	30	-0.338	0.0466
313	40	0.211	1.3306	313	40	-0.229	0.0234
323	20	0.238	0.7702	323	20	-0.462	0.0229
323	30	0.228	09844	323	30	-0.471	0.0043
323	40	0.222	0.2815	323	40	-0.286	0.0790
333	20	0.247	0.6816				
333	30	0.229	0.2633				
333	40	0.223	1.1376				

Solubility of polyphenols in SFE will be affected by various process parameters such as temperature, pressure, type and concentration of modifier, extraction time and CO_2 flow rate. Therefore, the regressed k_{ij} can only be used to determine the solubility of polyphenols in SFE within the same operating conditions as the experimental conditions. The SFE operating conditions of the experimental solubility from the literature are shown in Table 6.

Table 6. SFE operating condition of the experimental solubility data

Systems	CA-CO_2-Ethanol	SA-CO_2-Ethanol	FA-CO_2-Ethanol
Temperature range (K)	308 - 328	308.15 - 318.15	313 - 323
Pressure range (MPa)	11 – 18	8.7 - 15.7	20 – 40
CO_2 flow rate (L/min)	0.1 – 0.4	20 – 25	0.4
Extraction time (min)	80	120	90
Modifier concentration (%)	5.0	7.0	5.0

Based on the result of the regression of k_{ij} in binary pairs, the regressed k_{ij} for polyphenol-modifier pair by fitting the polyphenol-CO_2-modifier systems are observed to be large and negative for salicylic acid and ferulic acid by using CPA. The large and negative k_{ij} for polyphenol-modifier system indicates the strong associating interaction between polyphenol and modifier [24]. Similar results of negative polyphenol-modifier interaction parameters have been reported in several studies [16, 24]. These results suggest the accuracy of CPA as the polyphenols have a polar group (-COOH) which will interact strongly with the polar group in modifier (- OH). Therefore, the interaction of polyphenol and modifier is stronger and resulting in higher solubility in polyphenol-CO_2-modifier systems.

A good description of the binary pairs is achieved with low AARD which is from 0.0026% to 1.3326% using CPA with the regressed k_{ij}. The calculated solubility of binary pair suggests CPA using solid vapor equilibrium provided good prediction using the parameters obtained by fitting the binary phase equilibrium data.

3.2. Parameter Regression of Parameter in Proposed Function

In order to use the CPA modelling within a wide range of temperature and pressure, function k_{ij} dependent on temperature and pressure are proposed as shown in Equation (22) to (24). The function k_{ij} is dependent on pressure and temperature because based on the k_{ij} from parameter regression in Stage 3, k_{ij} changes linearly with temperature and pressure or changes polynomial in second order with temperature and pressure. Figures 5, 6 and 7 show the three examples of trend of k_{ij} with temperature and pressure.

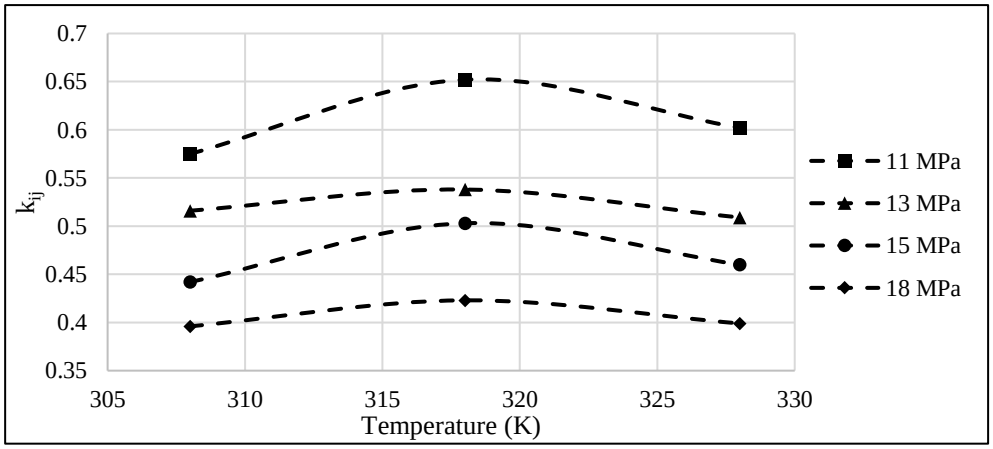


Figure 5. Trend k_{13} versus temperature

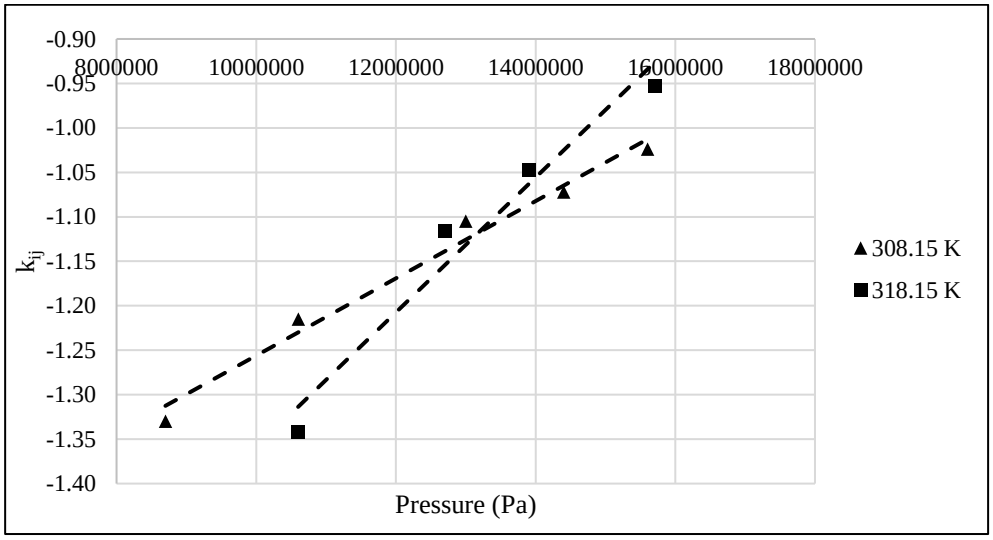


Figure 6. Trend k_{43} versus pressure

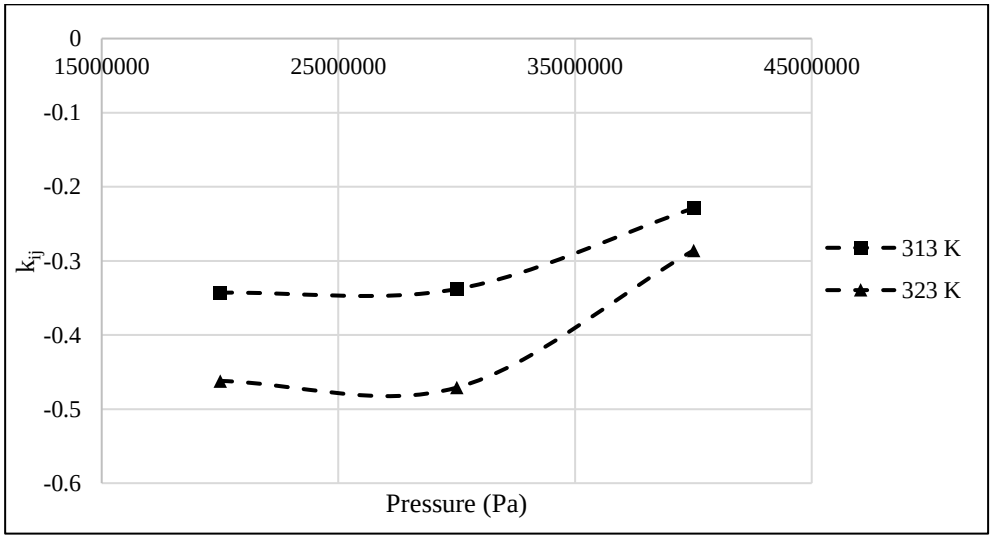


Figure 7. Trend k_{53} versus pressure

Table 7. Parameters in proposed function of binary function parameter in each binary system

Components		k_{ij}					**AARD**
		w	**q**	**x**	**y**	**z**	**(%)**
CA-CO_2	12	-	-	$1.7193118x10^{-9}$	-0.00018344	0.3041948	5.41
SA-CO_2	42	-	-	$-1.7771x10^{-10}$	0.000266739	-0.026882	2.10
FA-CO_2	52	-	-	$-1.0166154x10^{-9}$	0.00068323	0.0370368	6.16
CA-Ethanol	13	-0.00047	-	$-2.9432428x10^{-8}$	0.29971887	-46.82482	2.57
SA-Ethanol	43	-	-	$5.6779964x10^{-8}$	-0.00158875	-1.363904	7.96
FA-Ethanol	53	-	$7.45018x10^{-16}$	$-3.7451012x10^{-8}$	-0.0103	3.323914	3.56
CO_2-Ethanol	23	-	-	-	0.000301	0.0407	14.8

[1] Cinnamic acid (CA), Salicylic acid (SA), Ferulic acid (FA)

Upon obtaining the parameters in function k_{ij}, the solubility of polyphenols in the binary pairs is determined using the k_{ij} calculated from the proposed function k_{ij} and AARD is determined to compute the deviation between the experimental training data and the solubility data from the modelling of the binary pairs. Table 7 shows the function k_{ij} of each binary pair in polyphrnol-CO_2-modifier system.

All the function k_{ij} are obtained by using Equation (22) except function k_{13} and function k_{53} which using Equation (23) and (24) respectively. This is because the trend of regressed k_{ij} in Stage 3 shows a linear trend with temperature and pressure as shown in Figure 6. However, the trend of k_{13} shows a second order polynomial trend with increasing temperature and trend of k_{53} shows a second order polynomial trend with increasing pressure as shown in Figure 5 and 6 respectively.

The function k_{ij} in each binary pair correlated the experimental data well with reasonable AARD for the polyphenol solubility ranging from 2.10% to 14.8%. Hence, the functions k_{ij} of the binary pair are used to calculate k_{ij} for determination of polyphenol solubility in polyphenol-CO_2-modifier system of SFE. Figures 8, 9 and 10 show the correlation of solubility calculated using CPA and function k_{ij} in the system with the experimental training data.

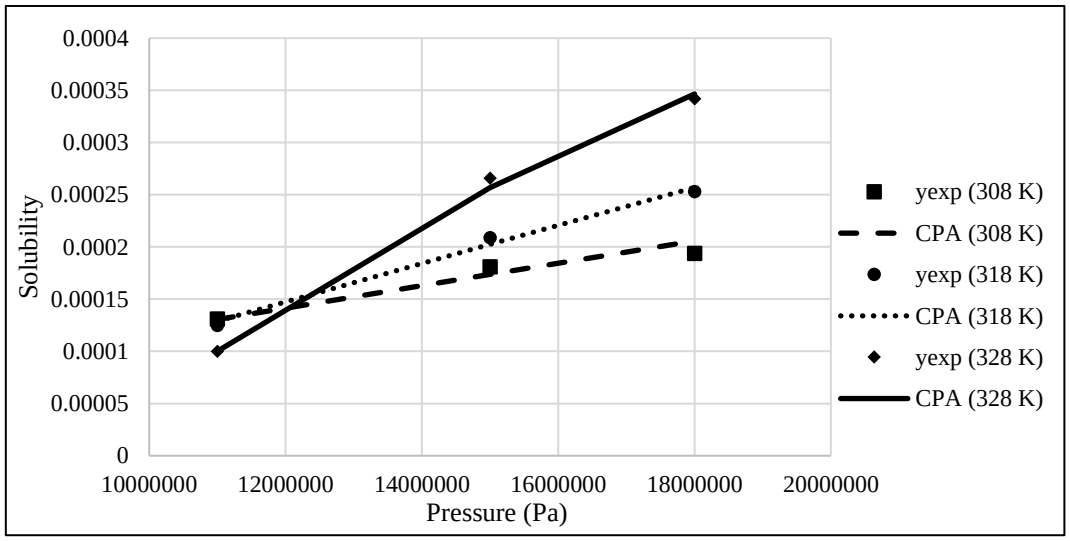


Figure 8. Correlation of cinnamic acid solubility calculated using CPA with experimental solubility data

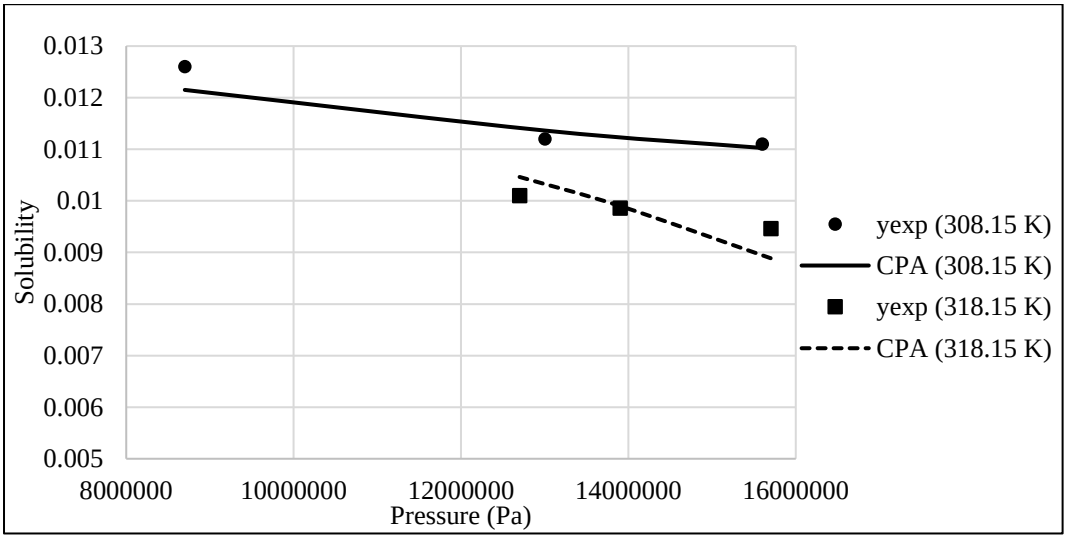


Figure 9. Correlation of salicylic acid solubility calculated using CPA with experimental solubility data

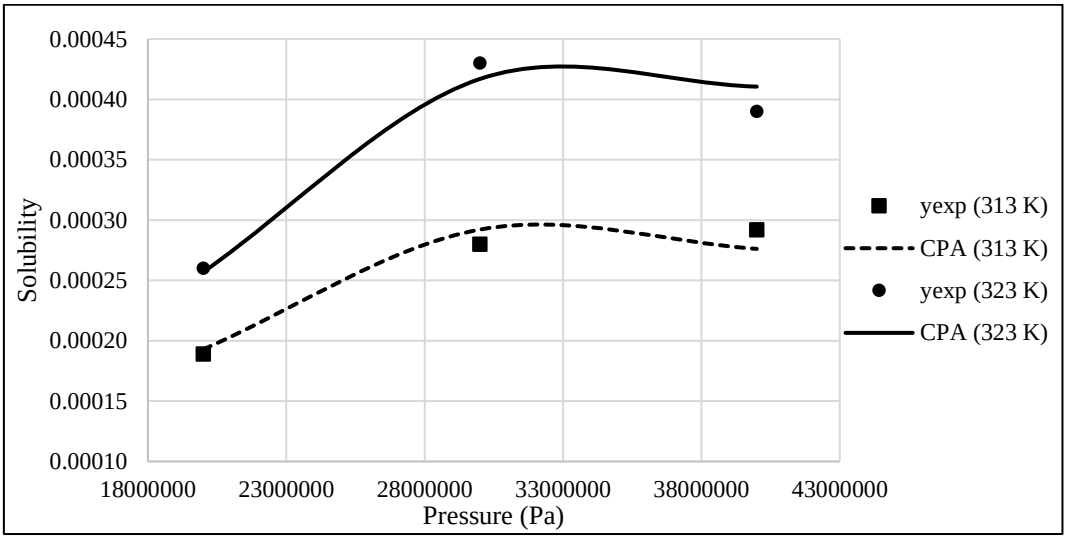


Figure 10. Correlation of ferulic acid solubility calculated using CPA with experimental solubility data

Figures 8, 9 and 10 suggest that CPA demonstrated good capability to correlate the experimental solubility data of polyphenols. The graph of calculated polyphenol solubility using CPA represent the pressure and temperature effect properly with the experimental solubility data. AARD is calculated to compute the deviation between the experimental solubility data used and solubility data calculated from modelling using the function k_{ij} in polyphenol-CO_2- modifier system as shown in Table 8.

Table 8. AARD and condition of ternary system

Solute	Solvent	Modifier	Temperature (K)	Pressure (MPa)	AARD (%)
Cinnamic acid	Carbon dioxide	Ethanol	308-328	11-18	2.45
Salicylic acid	Carbon dioxide	Ethanol	308.15-318.15	8.7-15.7	7.88
Ferulic acid	Carbon dioxide	Ethanol	313-323	20-40	3.71

From Table 8, it can be observed that reasonably good agreement between experimental training data and calculated has been achieved with AARD ranging from 2.45% to 7.88%. CPA consider the associative interactions such as hydrogen bonding which take place between the polyphenols and modifier.

3.3. Modelling Validation

Modelling validation is conducted to study how accurately the solubility of polyphenols in supercritical carbon dioxide with modifier could be predicted using CPA with solid vapor equilibrium and the function k_{ij}. The calculated solubility data using the modelling are compared against the experimental solubility data where these data are not used in the regression step to validate the reliability of the developed modelling as shown in Figure 11.

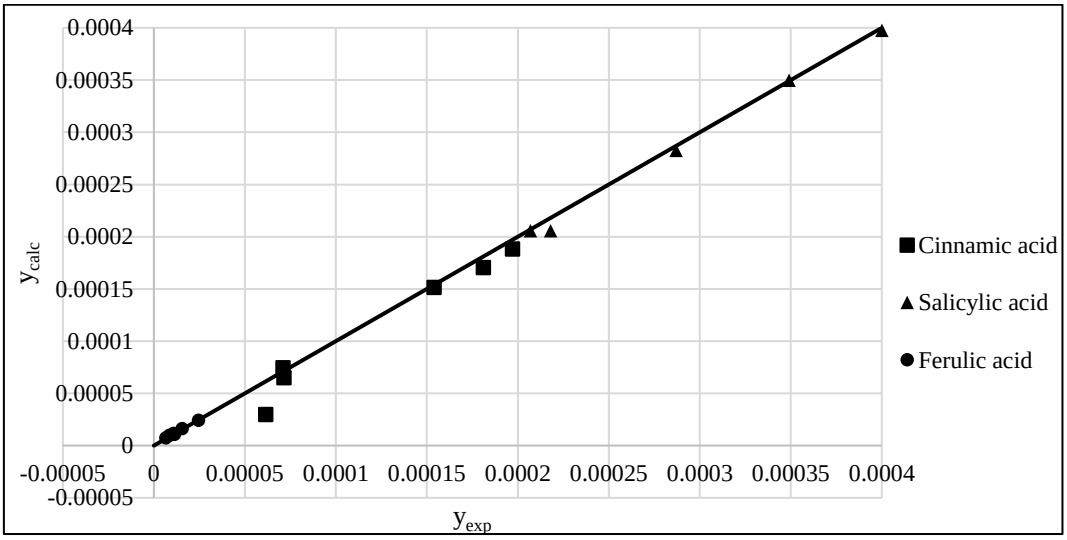


Figure 11. Comparison between calculated and experimental solubility data

Figure 11 shows the linear plot of the experimental solubility data against the calculated solubility data which all the points fall on the diagonal line. This suggests CPA modelling has good accuracy for the prediction of polyphenols solubility within the specific condition range.

3.4. Case Study

In this case study, the solubility of the ferulic acid in supercritical carbon dioxide with ethanol is predicted at different temperatures and pressures using the modelling with the regressed parameters within the condition range. Figure 12 shows the optimization graph for the solubility of ferulic acid.

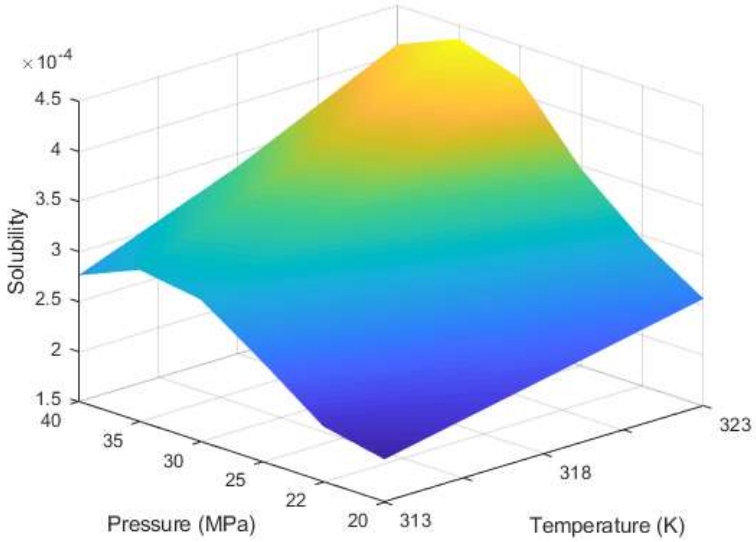


Figure 12. Optimization graph for solubility of ferulic acid

Figure 12 shows the solubility of ferulic acid increases with the increase of pressure and temperature. However, after the optimum point of pressure, the solubility of ferulic acid decreases. Based on Figure 12, the highest point which is the optimum condition for maximum solubility is obtained. The optimum condition is at a temperature of 323 K with the pressure of 35 MPa using 5% ethanol as a modifier.

The changing of polyphenol's solubility in supercritical carbon dioxide with ethanol with changing temperature and pressure are exhibited towards two factors which are the solvating power of supercritical carbon dioxide which is affected by density which demonstrates an increasing trend with increasing temperature. At a constant temperature, the density of supercritical carbon dioxide increases with increasing pressure, and this induces higher solvating capacity in supercritical carbon dioxide.

The description of solubility of ferulic acid in the case study shows the accuracy of CPA to describe the influence of temperature and pressure on polyphenols solubility in supercritical carbon dioxide with ethanol. In this case study, CPA can be used for the prediction of polyphenol solubility in supercritical carbon dioxide with ethanol to determine the optimum condition for maximum solubility in SFE.

4. Conclusions

A Cubic Plus Association (CPA) solubility modelling with solid vapor equilibrium (SVE) has been developed to estimate the solubility of polyphenols in carbon dioxide and modifier for SFE. Based on this study, several objectives have been achieved. The regressions of binary interaction parameters show low deviation between experimental and calculated values. The function of binary interaction parameters dependent on temperature and pressure for each binary pair are proposed by fitting the regressed interaction parameters. The main objective of the case study is to present the guideline by using the developed modelling to determine the optimum condition in SFE and it can help another researcher to extend the proposed modelling for a larger polyphenol and modifier database in the future. In general, CPA with solid vapor equilibrium demonstrated a high accuracy to predict the solubility data of polyphenols in supercritical carbon dioxide with modifier at a wide range of pressure and temperature evaluated and able to represent the effect of temperature and pressure on the solubility of polyphenols properly. The generated model parameters can serve as a guideline for other researchers to predict the solubility of certain polyphenols in SFE with modifiers at different temperature and pressure and determine the optimum condition with maximum solubility data in SFE without conducting real experiments.

Acknowledgments: The authors gratefully acknowledge the help and support provided by Professor Georgios M. Kontogeorgis and Associate Professor Liang Xiao Dong from Technical University of Denmark. This work was funded by the Malaysian Ministry of Higher Education under Fundamental Research Grant Scheme (FRGS/1/2020/TK0/UTM/02/92).

References

1. Bayir, A.G., A.N. Aksoy, and A. Kocyigit. The Importance of Polyphenols as Functional Food in Health. Bezmialem Science. (2019).7(2): p157-164. https://doi.org/10.14235/bas.galenos.2018.2486.
2. McHugh, M., and V. Krukonis. Supercritical fluid extraction: principles and practice. Elsevier. (2013)
3. Bitencourt, R.G., F.A. Cabral, and A.J.A. Meirelles. Ferulic acid solubility in supercritical carbon dioxide, ethanol, and water mixtures. The Journal of Chemical Thermodynamics. (2016). 103: p. 285-291. https://doi.org/10.1016/j.jct.2016.08.025.
4. Bitencourt, R.G., et al. Solubility of caffeic acid in CO2 + ethanol: Experimental and predicted data using Cubic Plus Association Equation of State. The Journal of Supercritical Fluids. (2018). 138: p. 238-246. https://doi.org/10.1016/j.supflu.2018.04.008.
5. Murthy, K., and B. Manohar. Modelling solubility of phenolics of mango ginger extract in supercritical carbon dioxide using equation of state and empirical models. Journal of Food Science and Technology. (2014). https://doi.org/10.1007/s13197-014-1667-1.
6. Kontogeorgis, G.M. and G.K. Folas. Thermodynamic models for industrial applications: from classical and advanced mixing rules to association theories. John Wiley & Sons. (2009). https://doi.org/10.1002/9780470747537
7. Mota, F.L., et al. Aqueous Solubility of Some Natural Phenolic Compounds. Industrial & Engineering Chemistry Research. (2008). 47(15): p. 5182-5189. https://doi.org/10.1021/ie071452o.

8. Guo, L., et al. Solubility of cinnamic acid in supercritical carbon dioxide and subcritical 1,1,1,2-tetrafluoroethane: Experimental data and modelling. Fluid Phase Equilibria. (2019). 480: p. 66-80. https://doi.org/10.1016/j.fluid.2018.10.009.
9. Ravipaty, S., K. Koebke, and D. Chesney. Polar Mixed-Solid Solute Systems in Supercritical Carbon Dioxide: Entrainer Effect and Its Influence on Solubility and Selectivity. Journal of Chemical and Engineering Data - J CHEM ENG DATA. 53. (2007). https://doi.org/10.1021/je700486g.
10. Ke, J., et al. Solubilities of salicylic acid in supercritical carbon dioxide with ethanol cosolvent. The Journal of Supercritical Fluids. (2009). 9(2): p. 82-87. https://doi.org/10.1016/S0896-8446(96)90002-9.
11. Sovová, H. Solubility of ferulic acid in supercritical carbon dioxide with ethanol as cosolvent. Journal of Chemical & Engineering Data. (2001). 46(5): p. 1255-1257. https://doi.org/10.1021/je0101146.
12. Thomson, G. The DIPPR® databases. International journal of thermophysics. (1996). 17(1): p. 223-232. https://doi.org/10.1007/BF01448224.
13. Mackay, D., et al. Vapor-pressure correlations for low-volatility environmental chemicals. Environmental Science & Technology. (1982). 16(10): p. 645-649. https://doi.org/10.1021/es00104a004.
14. Sodeifian, G., R. Detakhsheshpour, and S.A. Sajadian. Experimental study and thermodynamic modeling of Esomeprazole (proton-pump inhibitor drug for stomach acid reduction) solubility in supercritical carbon dioxide. Journal of Supercritical Fluids. (2019). 154. https://doi.org/10.1016/j.supflu.2019.104606.
15. Huang, S.H. and M. Radosz. Equation of state for small, large, polydisperse, and associating molecules. Industrial & Engineering Chemistry Research. (1990). 29(11): p. 2284-2294. https://doi.org/10.1021/ie00107a014.
16. Huang, Z., et al. Solubility of Aspirin in Supercritical Carbon Dioxide with and without Acetone. Journal of Chemical & Engineering Data. (2004). 49(5): p. 1323-1327. https://doi.org/10.1021/je0499465.
17. Kloc, A.P., et al. Phase equilibrium measurements and thermodynamic modeling of {CO2 + diethyl succinate + cosolvent} systems. Fluid Phase Equilibria. (2019). 502. https://doi.org/10.1016/j.fluid.2019.112285.
18. Kontogeorgis, G.M., et al. An equation of state for associating fluids. Industrial & engineering chemistry research. (1996). 35(11): p. 4310-4318. https://doi.org/10.1021/ie9600203.
19. Liang, X. Numerical aspects of phase equilibrium calculations with the cubic and association models. Industrial & Engineering Chemistry Research. (2018). 57(42): p. 14273-14285. https://doi.org/10.1021/acs.iecr.8b03956.
20. Marrero, J., and R. Gani. Group-contribution based estimation of pure component properties. Fluid Phase Equilibria. (2001). 183-184: p. 183-208. https://doi.org/10.1016/S0378-3812(01)00431-9.
21. Cháfer, A., et al. Trans-Cinnamic Acid Solubility Enhancement in the Presence of Ethanol as a Supercritical CO2 Cosolvent. Journal of Chemical & Engineering Data. (2009). 54(8): p. 2263-2268. https://doi.org/10.1021/je900154x.
22. Lim, J., et al. Solubility of salicylic acid in pure alcohols at different temperatures. The Journal of Chemical Thermodynamics. (2013). 57: p. 295-300. https://doi.org/10.1016/j.jct.2012.09.006.
23. Bitencourt, R.G., et al. Prediction of solid solute solubility in supercritical CO2 with cosolvents using the CPA EoS. Fluid Phase Equilibria. (2019). 482: p. 1-10. https://doi.org/10.1016/j.fluid.2018.10.020.
24. Huang, Z., et al. Modeling aspirin, and naproxen ternary solubility in supercritical CO2/alcohol with a new Peng–Robinson EOS plus association model. The Journal of Supercritical Fluids. (2007). 43(2): p. 259-266. https://doi.org/10.1016/j.supflu.2007.05.011.

Theoretical Investigations on The Optimal Topology of Crude Oil Desulfurization Process

Said Al Rabadi [1,*]

[1] Department of Chemical Engineering, Al Balqa Applied University;
Corresponding author: said.alrabadi@bau.edu.jo ; Tel.:+962 777 201 726.

Abstract: This study evaluates a low cost and efficient topology designed for the immobilization of harmful Sulfur compounds' content of crude oil feed stock in refinery process. Theoretical investigations simulate the reduction of Sulfur content to a target limit of less than 15 ppm in the product fuels, to achieve a better combustion of low Sulfur product fuel and to enhance emissions control. The conventional Hydro-desulfurization (HDS) using Hydrogen under prevailing conditions (temperature, pressure, Hydrogen amount) is investigated. Principally feasible HDS is restricted to Sulfur content of less than 3 wt. % and is operated under high reaction temperatures and pressures, additionally pertinent eco- & economical regulations must be considered for better marginal performance, massive Hydrogen amounts and highly active catalysts are required. Additionally, a generic concept of oxidative desulfurization (ODS) is provided, which will be applicable over relatively higher Sulfur contents (more than 8 wt. %), with different kinds of oxidants in mainly liquid phase and under mild operating conditions, to effectively attain the low Sulfur product fuels. Thus, the major implementation of the aspired results is assigned to the relevant fields; process engineering, production control, automotive and environment technology.

Keywords: HDS; ODS; Simulation, Hydrocarbon Loss.

Population Balance Modelling for Characteristics of Bubble Breakup and Coalescence Dispersions

Nur Khairunnisa Abd Halim [1], Siti Aslina Hussain [1,*], Mus'ab Abd. Razak [1] and Mohd Amirul Syafiq Mohd Yunos [2]

[1] Department of Chemical and Environmental Engineering, Universiti Putra Malaysia, 43400 Serdang, Selangor, Malaysia;
[2] Plant Assessment Technology, Industrial Technology Division, Malaysian Nuclear Agency, bangi 43000 Kajang, Selangor, Malaysia;
***** *Corresponding authors: aslina@upm.edu.my; Tel.: +603-97696292*

Abstract: The characteristics of different-sized bubbles in multiphase assembly are critical for determining interfacial area, as well as mass and heat transfer efficiency. However, due to breakup and coalescence phenomenon caused by the sparging gas and increasing gas volume fraction, leads to homogeneous flow pattern with broader bubble size distribution and uneven distributed gas content over the cross section. This paper focus on to model of two-phase flow in bubble column considering non-drag forces and polydisperse flow using Eulerian two-fluid approach and Multiple Size Group (MUSIG) model. The superficial gas velocities used for the simulations were 0.0125 and 0.0627 m/s which were considered as homogeneous and heterogeneous regime, respectively. To simulate the system, the disperse phase with different sizes are divided into several groups. The bubble breakup and coalescence of bubble fractions in each group was solved using Luo and Svendsen breakup model and Prince and Blanch coalescence model with interphase transfers related to drag and lift forces. The homogenous MUSIG model using ANSYS CFX 2019 R3 has been validate against experimental data performed using high-speed camera. As a result, mesh size of 4 mm is the best size to performed for simulating using experimental data. Throughout the comparisons of velocity profiles, gas holdup and axial liquid velocity with experimental data are provided, attesting the validity and accuracy of model as well as the broadening of their applicability are discussed.

Keywords: Bubble column; Computational fluid dynamics; Multiple size group, Gas hold-up, Axial liquid velocity

1. Introduction

The chemical, petrochemical, bioprocessing and pharmaceutical sectors have allegedly utilized bubble column reactor. The general concept of bubble column is where the gas phase is distributed into a fluid continuous phase in the form of bubbles. The regime inside the bubble column is either homogenous, transitional or heterogenous, depending on superficial velocities, column dimensions and method of gas injection [1.2]. In vertical reactor, the flow regimes are found to be dependent on the void fraction of the gaseous phase, which is observed range of bubble sizes as the void fraction increases. Dispersed homogeneous flow with low volume fractions of gas are mainly monodispersed, however an increase of gas volume fraction causes bubble breakup and coalescence, resulting in larger bubble size distribution. The former involves the gas hold-up which has been stated to be the most significant design requirement in biphasic bubble columns [3,4]. A thorough understanding of fluid dynamics is necessary, and the latter would be quite beneficial in many industrial applications. Hence, the biphasic flow needs closure terms in interphase momentum transfer equations that operate specifically on phase physical properties, velocity profiles and turbulence coefficients [3].

Many researchers have utilized Computational Fluid Dynamics (CFD) approaches to model the flow morphology of gas-liquid phase in bubble column reactor. The Euler-Euler technique often used to simulate two-fluid flow compared to Euler-Lagrange or Volume-of-Fluid (VOF) method as it requires less computational time and not required high-end computational power. However, the reliability of the results has been questioned as it is not representing the actual system. The failure to account for several significant non-drag forces, such as turbulent dispersion, lift and wall lubrication

is one of the reasons for the difference between experimental work and simulation forecast. Among the forces, the bubble lift forces were discovered to change sign as the bubble size varies due to radial separation of small and large bubbles, as well as the subsequent coalescence of large bubbles moving towards the column center forming slugs.

An adequate attempt in modelling multiphase flow development have been made by considering all these phenomena. The process of bubble coalescence and breakup necessitates the use of Population Balance Equation (PBE), which enables for the computation of evolved bubbles into N-classes and combined with a two-fluid model. The homogenous MUSIG approach assumes all bubble travels in one single velocity field while inhomogeneous MUSIG approach involves multiple momentum equations, making the approach computationally costly. Frank et al. [5] has applied inhomogeneous MUSIG model by using multi-fluid Eulerian approach to facilitate the prediction of radial demixing of different-sized bubbles. The disperse phase is characterized by dividing evolved bubbles into N inhomogeneous velocity groups and each group is further divided into M bubble size classes. Similarly, Krepper et al. [6] has tested an inhomogeneous MUSIG model for simulating a gas-liquid phase, claiming that 2-3 subgroups are sufficient to simulate fluid dynamics. On the other hands, Xu et al. [7] have implemented both homogeneous and inhomogeneous MUSIG models to simulate the gas bubble phase in bubble column. It was found that both models provide comparable results to the experimental data. Different models for bubble forces, bubble breakage and coalescence were analyzed, as well as the necessity of considering bubble induced turbulence. A validation on closure models, which define multiphase flows in a wide range can be found in recent work [7-10]. By conducting experimental and numerical research on rectangular bubble column, Ziegenhein et al. [8] highlighted the potential value of considering lateral forces, including lift and wall forces. They discovered that a comprehensive set of forces needed to be considered. These forces may also affect the stability of homogeneous bubbly flow, as well as the transition between the homogeneous and heterogeneous regimes [11]. In addition, Braga Viera et al. [12] have demonstrated the applicability of bubble induced turbulence models including a source term for kinetic energy and turbulent dissipation in their recent work.

In light of this, the goal of this research is to make an attempt to incorporate the population balance model in simulation with appropriate modelling of coalescence and breakup processes in gas-liquid bubbly flow, with a focus on industrial applications. To account for the bubble size distribution in a gas-liquid flow, the MUSIG model has been implemented in CFX 2019 R3 software. The development of flow pattern has been studied for two different inlet gas superficial velocity. The model's predictions are then compared to the experimental data.

2. Multiple Size Group (MUSIG) Model Description

The MUSIG model was proposed to deal with multiphase polydispersed flows. The varying sizes of dispersed phase interact with one other through breakup and coalescence mechanisms, shows one of the characteristics of polydispersed multiphase flow. Population balance is a well-known approach for determining a polydispersed phase's size distribution, including breakup and coalescence effects. The population balance approach can be included into three-dimensional CFD calculations using the MUSIG framework.

2.1. Population Balance Equation

In bubbly flow, the population balance modelling is used to calculate the size distribution of the dispersed phase and account for breakage and coalescence effects. The population balance equation can be written as

$$\frac{\partial n_i}{\partial t} + \nabla \cdot \left(\mathrm{u}_g n_i\right) = B_B - D_B + B_C - D_C, \tag{1}$$

where n_i represents the number of density of size group i, and B_B, D_B, B_C and D_C respectively represent the birth rate and death rate due to breakup and coalescence of bubbles. The left side depicts the spatial and temporal growth of a bubble class, while the right side simulates the interchange of

classes caused by bubble breakup and coalescence. The density of bubbles n_i is said to be proportional to the gas volume fraction α_g which can be expressed by

$$\alpha_g f_i = n_i V_i, \tag{2}$$

where f_i denotes the volume fraction of bubbles in group i, and V_i is the volume of bubble in group i. Individual models for each of the breakup and coalescence processes are required because they are dependent on the mechanisms and are sensitively related on the presence of turbulence level, surfactants and other factors [12].

2.2. Size Fraction Equation

The derivation of the size fraction equation utilised by the MUSIG model, as well as the default discrete formulation in ANSYS CFX are briefly described for coherence purpose. A transport equation for the bubble number concentration in each size group N_i is defined by discretizing Equation (1) into bins, or size groups

$$\begin{gathered}\frac{\partial N_i}{\partial t} + \nabla\vec{x} \cdot (\vec{x} N_i) = \\ \int_{m_{i-1/2}}^{m_{i+1/2}} B_C(m)dm - \int_{m_{i-1/2}}^{m_{i+1/2}} D_C(m)dm + \int_{m_{i-1/2}}^{m_{i+1/2}} B_B(m)dm - \int_{m_{i-1/2}}^{m_{i+1/2}} D_B(m)dm,\end{gathered} \tag{3}$$

where m_i defines as the mass of bubbles of size group i and N_i defines the number of concentration of size group i

$$N_i\,(t) = \int_{m_{i-1/2}}^{m_{i+1/2}} n(m)dm, \tag{4}$$

According to user guide [13], $m_i N_i = \rho_i r_i$ and $B_{Bi} - D_{Bi} + B_{Ci} - D_{Ci} = S_i$, thus integration of Equation (3) over the group size dimension and multiplication with m_i give

$$\frac{\partial(\rho_i r_i)}{\partial t} + \frac{\partial}{\partial x^i}\left(\rho_i r_i U_i^i\right) = S_i, \tag{5}$$

while the size fraction of the size group i is denoted as $f_i = r_i / r_d$, thus the size fraction equation used by the MUSIG model can be written as

$$\frac{\partial}{\partial t}(\rho_i r_d f_i) + \frac{\partial}{\partial x^i}\left(\rho_i r_d U_i^i f_i\right) = S_i, \tag{6}$$

Therefore, the homogeneous MUSIG model can be further simplified by assuming that all size groups have the same density ρ_d and velocity U_d^i

$$\frac{\partial}{\partial t}(\rho_d r_d f_i) + \frac{\partial}{\partial x^i}\left(\rho_d r_d U_d^i f_i\right) = S_i, \tag{7}$$

2.3. Bubble Breakup and Coalescence

The model developed by Luo and Svendsen [14] is used for the bubble's breakup in turbulent dispersion. The model is based on isotropic turbulence theories and assumes binary breakup of the bubbles. A dimensionless variable indicating the sizes of bubbles and drops can be defined as follows for binary breakage

$$f_{BV} = \frac{V_i}{V} = \frac{d_i^3}{d^3} = \frac{d_i^3}{d_i^3 + d_j^3}, \tag{8}$$

where d_i and d_j are diameters of small bubbles in the binary breakage of larger bubble with diameter d. The fracture of volume fraction has a range of values between 0 and 1. The breakup rate of bubbles of volume sizes of $V_i\ (= V_{f_{BV}})$ from volume V_j can be calculated as

$$\frac{\Omega(V_j : V_i)}{(1-\alpha_g) n_j} = C\left(\frac{\epsilon}{d_j^2}\right)^{1/3} \int_{\xi_{min}}^{1} \frac{(1+\xi)^2}{\xi^{11/3}} exp\left(-\frac{12 c_f \sigma}{\beta \rho_l \epsilon^{2/3} d_j^{5/3} \xi^{11/3}}\right) d\xi, \tag{9}$$

here $\in$ signifies rate of energy dissipation per unit of liquid mass, ξ is the dimensionless size of eddies in the inertial subrange of isotropic turbulence, c and β values are to be 0.923 and 2, respectively which are determined from fundamental consideration of bubbles breakage in turbulent dispersion system. The coefficient of surface area c_f is said to be as

$$c_f = \left[f_{BV}^{2/3} + (1 - f_{BV})^{2/3} - 1\right], \tag{10}$$

Therefore, the equation of birth rate of group i as a result of the disintegration larger bubbles and the equation of death rate of group i as a result of the disintegration into smaller bubbles can be written as

$$B_B = \sum_{j=i+1}^{N} \Omega(V_j : V_i) n_j, \tag{11}$$

$$D_B = \Omega_i n_i;\ \Omega_i = \sum_{k=1}^{i} \Omega_{ki}, \tag{12}$$

The Prince and Blanch model [15] implies that the coalescence of two bubbles takes place in three stages. The first stage is the bubbles collide within each other and trap a layer of liquid film between them. Next, the liquid film then drains until it reaches a critical thickness separating the bubbles. The last stage is where the film ruptures and the bubbles coalesce. There are many factors that may cause collisions between bubbles; however, turbulence is the only cause that is considered in the present model. According to Prince and Blanch [15], the coalescence rate when turbulent collide is define as

$$\chi = \theta_{ij} exp\left(-\frac{t_{ij}}{\tau_{ij}}\right), \tag{13}$$

where t_{ij} is the time required for coalescence while τ_{ij} is the actual contact time during the collisions. As the collision between bubbles happen, a small circular layer of liquid formed. The capillary forces that entrapped the liquid film causes it to be thinning film of radius R and thickness h. Oolman and Blanch [16] has derived a thinning formula of equal size bubbles in stagnant liquid

$$\frac{-dh}{dt} = \left\{\frac{8}{R^2 \rho_L}\left[h^2\left(\frac{2\sigma}{r_b} + \frac{A}{6\pi h^3}\right)\right]\right\}^{1/2}, \tag{14}$$

The time necessary for two bubbles with diameters d_i and d_j, respectively to coalesce is estimated numerically by Prince and Blanch [15] after solving the following equation

$$t_{ij} = \left\{\left(\frac{d_{ij}}{2}\right)^3 \frac{\rho_L}{16\sigma}\right\}^{1/2} ln\left(\frac{h_0}{h_j}\right), \tag{15}$$

where h_0 and h_j is the initial film thickness and the critical film thickness when rupture occurs, respectively. Prince and Blanch [15] ran few experiments using air-water system and have determined the values for h_0 and h_j to be 1×10^{-4} m and 1×10^{-8} m, respectively. The turbulent contributions to collision frequency, θ_{ij} for two bubbles is modelled as

$$\theta_{ij} = \frac{\pi}{4}\left[d_i + d_j\right]^2 \left(\boldsymbol{u}_{ti}^2 + \boldsymbol{u}_{tj}^2\right)^{1/2}, \tag{16}$$

where the turbulent viscosity, $\boldsymbol{u}_t$ [13] is defined as

$$\boldsymbol{u}_t = 1.4\ \in^{1/3} d^{1/3}, \tag{17}$$

Due to the coalescence of group k and group l bubbles, the birth rate and the death rate of group i can be written as

$$B_C = \frac{1}{2}\sum_{k=1}^{N}\sum_{l=1}^{N} \chi_{i,kl} n_i n_j, \tag{18}$$

$$D_C = \sum_{j=1}^{N} \chi_{ij} n_i n_j, \tag{19}$$

3. Experimental Setup

Experiments are carried out in a 0.2 m diameter of rectangular-shaped bubble column at atmospheric pressure for two values of superficial gas velocity, 0.0125 $m \cdot s^{-1}$ and 0.0627 $m \cdot s^{-1}$. The schematic diagram of the bubble column is shown in Figure 1. The initial liquid height is set at 1.0 m and the net liquid flow is zero. The overall column height is measured around 10 diameters for the column to be able to operate at high gas volume fractions. A high-speed video imaging is used to determine the flow regime and characterize bubbles. For this experiment, MEGA SPEED model CMOS MS30KG of high-speed camera has been used for recording fast moving objects at frame rate of 1000 frames per second (fps). The camera is positioned at three different heights of the bubble column: at the top, middle and bottom. The recording starts once the gas enters the column filled with liquid pool through the sparger. The flow velocity of resulting images of bubbles are calculated by measuring the displacement of each bubble in each frame that gas been labelled for tracking. Current models were validated using these data. The experimental facility is described in detail in Yunos et al. [17].

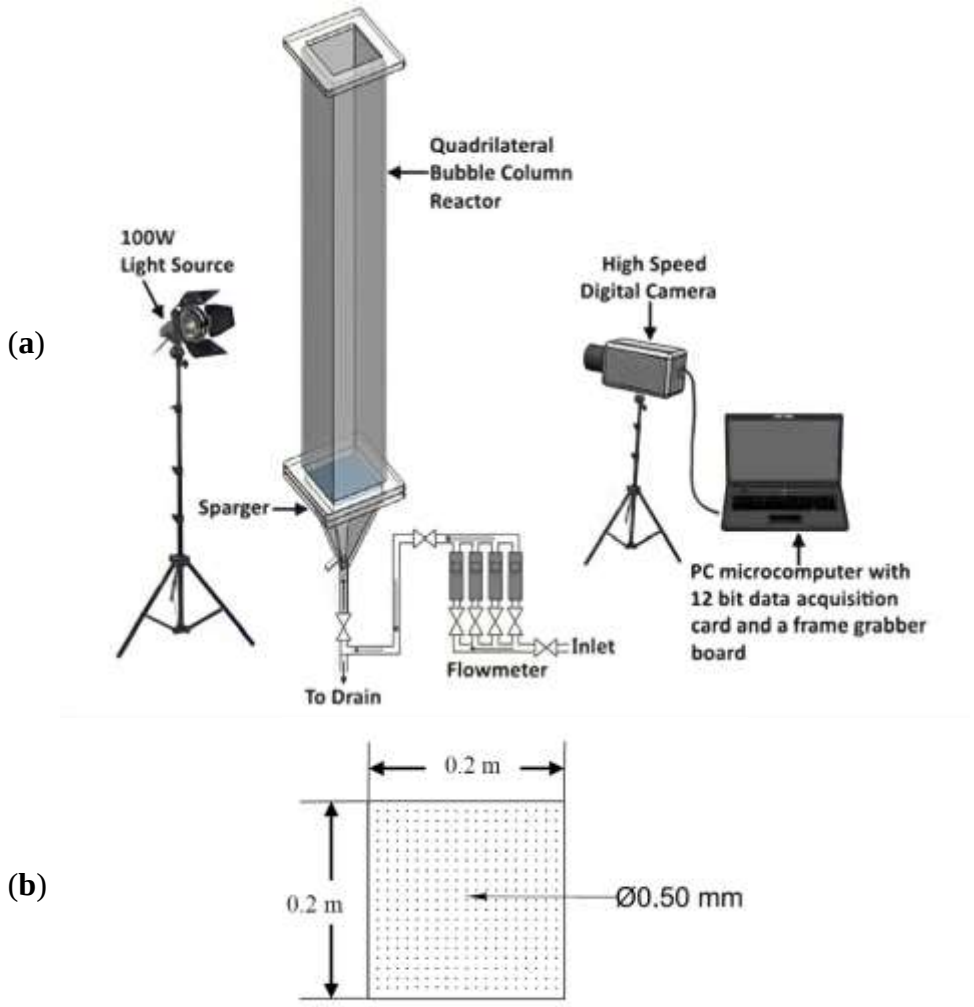


Figure 1. Schematic diagram of (**a**) bubble column using high-speed video imaging [17] and; (**b**) sparger configuration.

4. Numerical Setup

The numerical calculations were run on a 3D geometry through the use of the commercial computational fluid dynamics code ANSYS CFX 2019 R3. The air and water used in the experimental work are set as dispersed and continuous phase respectively. The initial liquid height is set at 1.0 m,

similar to the experimental observations. The inlet geometry of the experimental setup consisted of sparger plate with 361 holes with hole diameter of 0.5 mm. The MUSIG model coupled with population balance method with the breakup [14] and coalescence [15] has been implemented to account for bubble size distribution in the gas-liquid mixture.

The experimental observation of average bubble diameter for gas superficial velocity 0.0125 m/s and 0.0627 m/s is 4 mm and 6 mm respectively, thus bubble is ranging from 1 mm to 10 mm diameter divided into 10 classes in this current study. The population balance model was used to determine the outcome of the discrete bubble sizes that were set. To reduce cost and computational time, it was assumed that each bubble class travels at the same mean velocity. Thus, there are 10 continuity equations for the gas phase and 1 continuity equation for the liquid phase. It was also under impression that the number of classes needed to describe by appropriate distribution by dividing the bubble diameters equally into 5, 10 and 15 size groups. It was demonstrated that employing the given bubble size groups, there was no discernible change ($\pm$2%) in the anticipated maximum bubble Sauter mean diameter. The maximum Sauter mean bubble diameter was estimated by maximum difference of 3% for the segmentation into 10 size group, which gave similar outcome by Ekambara et al. [12]. Due to the computational resources and time constraints, it was determined that dividing the bubble sizes into 10 size groups was sufficient, and all remaining computational results are based on this discretization.

The CFX 2019 R3 was used to solve the coupled sets of governing equations for the mass and momentum balances of both dispersed and continuous phases. Pressure-based solver is used for the algorithms of the pressure-velocity procedure. The time step is set at 5000 steps at 1×10^{-5} s. The gas velocity magnitude and the average volume fraction have been quantified at the inlet while a relative average static pressure of zero is set at the outlet. The backflow hydraulic diameter of 0.2 m is specified according to the width of the column. For initialization section, the parabolic liquid velocity profile and average volume fraction of gas are defined as initial conditions. All operating, boundary and physical conditions are summarized in Table 1. All numerical works are run isothermally at atmospheric air of 25 ℃, hence heat and mass transfer effects are neglected.

Table 1. Summarization of all conditions used on the simulation work.

	Conditions
Column dimensions	0.2 m × 0.2 m × 2.0 m
Gas phase (air)	25 ℃
Liquid phase (water)	25 ℃
Inlet gas superficial velocity	0.0125 m/s and 0.0627 m/s
Inlet liquid superficial velocity	0.0 m/s, the stagnant liquid level is maintained at 1.0 m
Outlet condition	Pressure outlet
Wall condition	Non-slip
Pressure-velocity coupling	Coupled
Bubble diameter	1 mm – 10 mm
Multiphase model	Eulerian two-phase
Viscous model	Standard k-ε
Surface tension	0.07 N/m
Time step	5000 steps at 1×10^{-5} s

5. Result and Discussion

The CFD simulations are run using the coupled two-fluid and population balance model for solving Sauter-mean diameter of bubble, radial profile of the gas volume fraction and liquid velocities from the experimental conditions reported by Yunos et al. [17]. It is to be noted that this work is a continuing work of investigation on hydrodynamics analysis of the same model and sparger design which has been run previously involving monodispersed flow [18]. In this work, the values of

superficial gas velocity and bubble diameter are specified. All simulations are carried out for superficial gas velocity of 0.0125 m/s and 0.0627 m/s for one design of sparger.

In previous work involving monodisperse flow [18], a constant bubble diameter of 0.004 m is specified at sparger inlet, which is clearly a simplification. In actuality, the sparger may produce a range of bubble size distribution, which might have a substantial impact on simulation results. The bubble size distribution at the sparger, on the other hand, is rarely accessible because it is difficult to measure. For this modelling purposes, the bubble diameters were divided into 10 bins with diameters ranging from 0 to 10 mm. The simulation findings are compared to the data from the experiments. The CFD simulation used the experimental distribution as the beginning condition, and the equivalent distribution along the height of the column was anticipated. Figure 2 shows the comparison on experimental and the calculated average bubble size distribution along the column height for a superficial gas velocity U_g = 0.0125 m/s and U_g = 0.0627 m/s. Both figures appear to have almost identical distribution at small bubble size distribution (d_B < 5 mm), implying that the bubble contact processes have no substantial effect for the fluid system and the gas flow rates investigated.

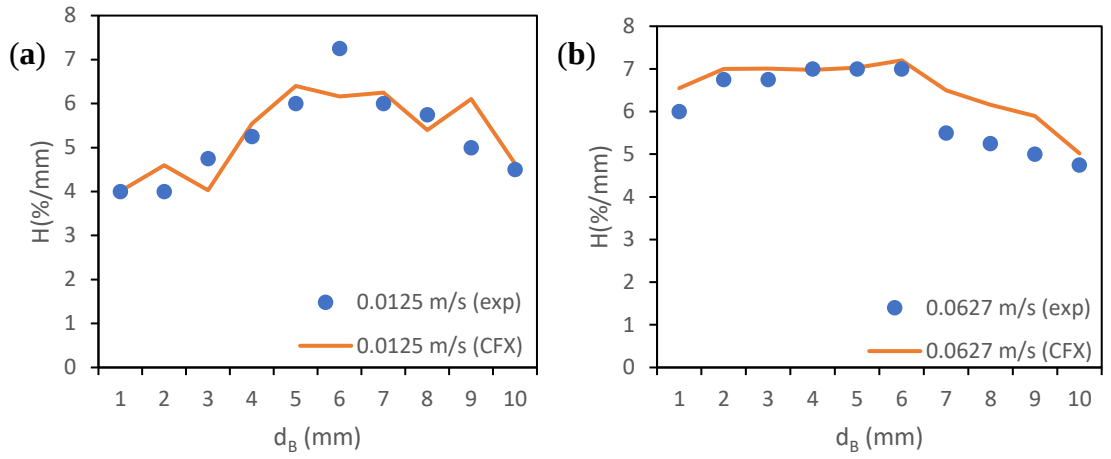


Figure 2. Comparison on average bubble size distribution above gas sparger for superficial gas velocity (**a**) 0.0125 m/s and (**b**) 0.0627 m/s of experimental data to CFD predictions.

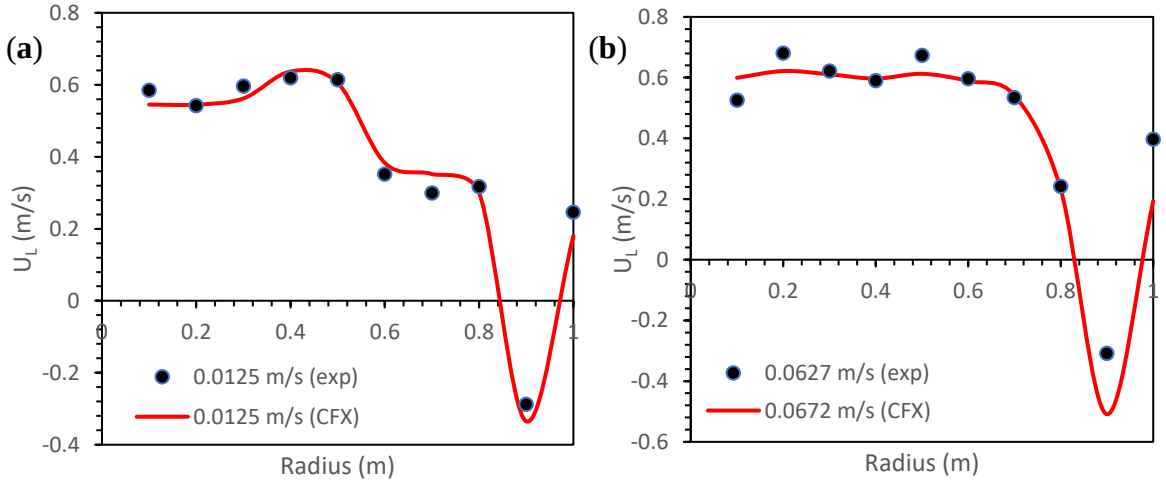


Figure 3. Comparison experimental mean axial liquid velocity along the column radius to CFD predictions for superficial gas velocity of (**a**) 0.0125 m/s and (**b**) 0.0627 m/s.

Figure 3 shows the comparison of the axial velocity of liquid phase in experimental work and numerical predictions along the column radius. The computed values are in good agreement with the

experimental findings, which used high-speed camera to determine axial velocity of the liquid phase. The liquid circulation into the bubble column is well predicted by the CFD simulation too.

The effect of the superficial gas velocity in relation to the column cross section on the overall gas holdup in the bubble column reactor is shown in Figure 4. Figure 4 (a) shows how the contours signifies the overall gas holdup affected by both superficial gas velocities. Clearly, the values of holdup increases as the superficial gas velocity increases. As the experimental data is compared to the simulation predictions in Figure 4 (b), it is discovered that the CFD code calculates the gas hold-up satisfactorily in the homogeneous regime, but underestimates it in the heterogeneous regime, where the model assumptions of equal bubble velocity and low gas flow rates do not hold true. The figure shows the effect of average void fraction, i.e., the gas holdup highlights how the interplay of polydispersity and non-drag forces, particularly the lift force, influences the void fraction profile. The smaller bubbles clump together near the column walls, while larger bubbles congregate around the center of the column. A solid peaking profile of the void fraction can be obtained if the exact amount of void fraction profiles of large bubbles for different superficial gas velocity are employed in the simulations. Conversely, if the number of large bubbles is underestimated, the void fraction will be overly flat. This emphasizes the understanding the correct bubble size distribution in order to create accurate void fraction calculations in bubble column.

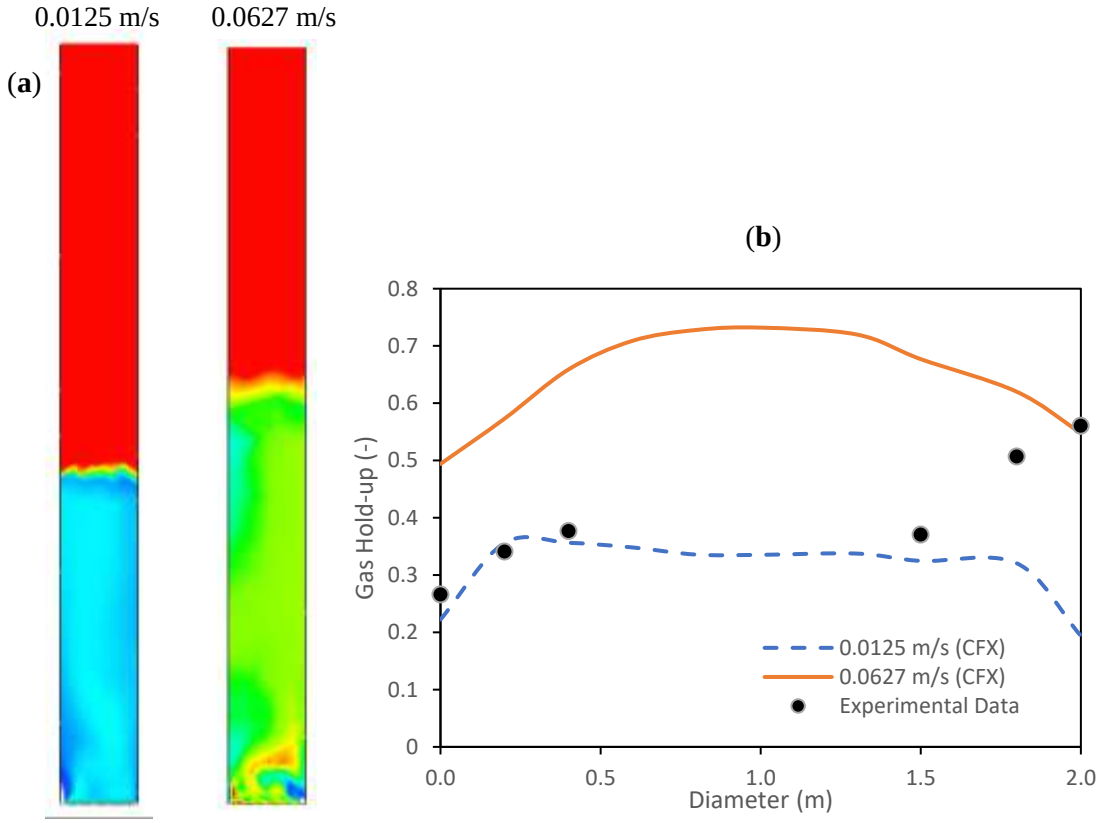


Figure 4. Comparison experimental overall gas holdup values to CFD predictions: (**a**) contour plot; (**b**) graphical plot

6. Conclusions

The effects of population balance combined with breakup and coalescence model on the hydrodynamics of bubble columns have been considered. The average bubble density transport equation was formulated and applied for the gas-liquid bubbly flows in the CFD code CFX 2019 R3 to calculate the spatial and temporal geometrical changes of the gas bubbles, as well as to demonstrate

the use of the population balance technique. A detail comparison of the CFD simulation and the experimental setup has been presented and it shows that the bubble size distribution, axial liquid velocity and gas hold-up may be accurately anticipated at the homogeneous regime. Better models of bubble interaction are required in order to expand the validity of CFD codes to additional flow regimes and incorporate systems with various physical features. Experiments paired with CFD simulations would yield universally valid correlations between configurable parameters and variant liquid phase physical properties. Clearly, a more sophisticated measurement of the bubble size distribution would be required to apply in future investigation of vertical gas-liquid flow.

Funding: This research is carried out as part of current research projects funded by Universiti Putra Malaysia under project number GP-IPS/2017/9573900.

Acknowledgments: The authors gratefully acknowledge the staffs of Department of Chemical and Environmental Engineering, Universiti Putra Malaysia and Industrial Technology Division, Malaysian Nuclear Agency for their support and supervision.

References

1. Kantarci, N.; Borak, F.; Ulgen, K.O. Bubble column reactor. *Process Biochemistry* **2005**, *40*(7), 2263 – 2283.
2. Khan, K.I. Fluid dynamic modelling of bubble column reactor. *PhD Thesis (March)* **2014.**
3. Syed, A.H.; Boulet, M.; Melchiori, T.; Lavoie, J. CFD simulation of an air-water bubble column: Effect of Luo coalescence parameter and breakup kernels. *Frontiers in chemistry* **2017**, *5*, 68.
4. Wagh, S.M.; Ansari, M.E.A.; Kene, P.T. Axial and radial gas holdup in bubble column reactor. *Bulletin of the Korean Chemical Society* **2014**, *35*(6), 1703 – 1705.
5. Frank, T; Zwart, P.J.; Shi, J.; Krepper, E.; Lucas, D.; Rohde, U. Inhomogeneous MUSIG model – a population balance approach for polydispersed bubbly flows. *Proceedings of the International Conference "Nuclear Energy for New Europe 2005"* **2005**, 1 – 14.
6. Krepper, E.; Lucas, D.; Frank, T.; Prasser, H.M.; Zwart, P.J. The inhomogeneous MUSIG model for the simulation of polydispersed flows. *Nuclear Engineering and Design* **2008**, *238*(7), 1690 – 1702.
7. Xu, L.; Yuan, B.; Ni, H.; Chen, C. Numerical simulation of bubble column flows in churn-turbulent regime: comparison of bubble size models. *Industrial & Engineering Chemistry Research* **2013**, *52*(20), 6794 – 6802.
8. Ziegenhein, T.; Rzehak, R.; Krepper, E.; Lucas, D. Numerical simulation of polydispersed flow in bubble columns with the inhomogeneous mutli-size-group model. *Chemie Ingenieur Technik* **2013**, *85*(7), 1080 – 1091.
9. Liao, Y. Update to the MUSIG model in ANSYS CFX for reliable modelling of bubble coalescence and breakup. *Applied Mathematical Modelling* **2020**, *81*, 506 – 521.
10. Gaurav, T. Numerical investigations bubble column equipped with vertical internals in different arrangements. **2018**.
11. Ziegenhein, T.; Lucas, D.; Besagni, G.; Inzoli, F. Experimental study of the liquid velocity and turbulence in a large-scale air-water counter-current bubble column. *Experimental Thermal and Fluid Science* **2020**, *111*, 109955.
12. Ekambara, K.; Dhotre, M.T.; Joshi, J.B. CFD simulations of bubble column reactors: 1D, 2D and 3D approach. *Chemical Engineering Science*, **2005,** *60*(23), 6733 – 6746.
13. Ansys, C.F.X. Ansys CFX-solver theory guide. *ANSYS CFX Release* **2009**, *15317*, 724 – 746.
14. Luo, H.; Svendsen, H.F. Theoretical model for drop and bubble breakup in turbulent dispersions. *AlChE Journal* **1996**, *42*(5), 1225 – 1233.
15. Prince, M.J.; Blanch, H.W. Bubble coalescence and break-up in air-sparged bubble column. *AlChE Journal* **1990**, *36*(10), 1485 – 1499.
16. Oolman, T.O.; Blanch, H.W. Bubble coalescence in stagnant liquids. *Chemical Engineering Communications* **1986**, *43*(4-6), 237 – 261.
17. Yunos, M.A.S.M,; Halim, N.K.A.; Hussain, S.A. Investigations of bubble size, gas hold-up, and bubble rise velocity in quadrilateral bubble column using high-speed camera. *Am. J. Eng. Technol.*

Soc. **2017**, 1 – 18.

18. Abd Halim, N.K.; Hussain, S.A. CFD analysis of phase holdup behaviour in a gas-liquid in a gas-liquid bubble column. *Journal of Applied Science & Process Engineering* **2021**, *8*(1), 738 – 749.

Optimization of Supercritical Carbon Dioxide Extraction of Phenolic Compounds from Algerian Plant (Peganum harmala Seeds) using Box-Behnken Design based Multi-response Analysis

Sarra Melloul [1,] *, Raouf Zehioua[1] and Abdeslam-Hassen Meniai[1]

[1] Université Constantine 3 Salah Boubnider

***** *Corresponding author: sarramelloul@live.fr; Tel.: +213793176164.*

Abstract: The present study considered the extraction of phenolic compounds such as total phenolic, flavonoids from seeds of a natural local plant, namely Peganum harmala, by means of a supercritical fluid extraction (SFE) using carbon dioxide. A Box-Behnken statistical design was used to investigate the effect of operating parameters like pressure, temperature and particle size at a fixed supercritical CO_2 flow rate of 50 g min^{-1} for an extraction time of 180 min. A maximum total phenolic content (TPC) of 79.04 mg GAE/g E was obtained at 100 bar and 35°C for a particle size of 0.9 mm, whereas a total flavonoid content of 7.10 mg QE/g E was obtained still at 35°C and for a particle size of 9 mm but at a pressure of 170.7 bar.

Keywords: Carbon dioxide; Phenolic compounds; Box-Behnken.

1. Introduction

In fact medicinal plants are often used in traditional herbal medicine and have shown to be an important natural source of bioactive molecules, particularly for natural antioxidants. This has led to the development of biomedical research basing on the search and test of new bioactive compounds.

In recent years, there has been a growing demand for the exploitation of natural plants, especially in the pharmaceutical and food industry. This has been encouraged by the development of performing oil extraction processes like the supercritical fluid extraction which has found wide applications in these industrial fields. It has been introduced as an alternative to conventional extraction techniques that require great amounts of solvents that must be eliminated from the extract to avoid harmful consequences on human health and the environment [1]. Carbon dioxide at supercritical conditions is the most commonly used due to its clear advantages like its abundance, low cost, low critical properties, no environmental impact, etc. [2].

Therefore in this perspective it is aimed to examine the properties of a local natural plant known as Peganum harmala. It belongs to zygophyllaceae family made of about 27 genera and 285 species[3]. Peganum harmala is also commonly known as “Syrian rue”, “African rue”, or just as “Harmal”. It is a wild growing flowering plant, highly present in North Africa, in Mediterranean, middle and far East countries like southern parts of Iran, Pakistan and India [4], [5]. It is also present in countries like America and Australia [3], [5]. Its fame is mainly due to its exceptional composition in alkaloids and their various interesting biological activities [4], [6]. Several studies have illustrated different pharmacological activities like antioxidant [7], [8], antibacterial [9], anti-inflammatory properties [8], antihistaminic, anti-tubercular activities, anti-nociceptive effects [7], [8], leukemic healing. In addition, it has been reported that this plant has hypoglycemic effect, antifungal[8] and antiviral effects[10], [11]. It is a potential source of pigments and essential oils potentially of interest to food, pharmaceutical, and cosmetic industries[12], hence the need of the performing supercritical carbon dioxide technique to extract phenolic compounds such as total phenolic, flavonoids and tannin from natural local plant seeds.

An optimization has been carried out in order to determine the best total phenolic compound and flavonoid as well as the corresponding operating conditions like pressure, temperature and particle size, by means of a Box-Behnken statistical design, at a fixed CO_2 flow rate and extraction time.

2. Materials and Methods

2.1. Plant material

Peganum Harmala L. seeds were collected last May harvest from Oum Bouaghi, an eastern region of Algeria. In order to remove all impurities they were washed, dried and then ground into particles of reduced sizes and the obtained powder was sieved by means of a vibrating sifter to recover the three particle diameters classes of 0.5, 0.7 and 0.9 mm.

2.2. Chemicals and reagents

The used chemicals were all of a reagent grade and were supplied by different companies: Methanol, Aluminum trichloride ($AlCl_3$), Quercetin and Sodium carbonate (Na_2CO_3) by Sigma-Aldrich; Gallic acid and Folin-Ciocalteau by Biochem Chemopharma; Carbon dioxide (CO_2) with 99.99% purity was supplied by Air Liquide, Algeria.

2.3. Methods

2.3.1.Supercritical CO_2 extraction

A supercritical fluid extraction machine (Separex-4219) supplied by Separex (Champigneulles, France) was used. For each experimental run a mass of 50 g of crushed Peganum Harmala leaves were introduced into a 50 mL stainless steel cylindrical vessel the ends of which are protected by filter mesh screens to prevent any particles entrainment by supercritical phase. The duration of each run was around 3 hours, using supercritical CO_2 at different conditions of temperature and pressure.

2.3.2. Determination of extract properties

- Total phenolic content

Total phenolic contents (TPC) were determined by the Folin-Ciocalteau method [13]. Extract volumes of 0.5 mL of different dilutions were mixed with 2.5 mL of 0.2 N Folin-Ciocalteau reagents for 5 min before the addition of 2.0 mL of 75 g/L sodium carbonate. The absorbance of reaction was measured at 760 nm after 2 h of incubation at room temperature .

- **Flavonoid content**

The determination of total flavonoids contents (TFC) was carried out by the method of aluminum trichloride ($AlCl_3$) [14]. It was used to quantify the flavonoids in different extracts. $AlCl_3$ formed a yellow complex with flavonoids and absorbed in the visible range at 430 nm. An extract volume of 1 mL was added to 1 mL of $AlCl_3$ in a 2% methanol solution. After 10 min of incubation at 37°C in dark, the absorbance was read at 430nm.
A calibration curve was obtained under the same operating conditions using quercetin in a concentration range varying from 0 to 70 µg / mL. The total flavonoid content of the analyzed seed extracts was expressed in milligram equivalent of quercetin per gram of extract (mg EQ /gE).

2.3.3. Experimental design

Box-Behnken design was applied to optimize the the phenolic compounds content of Peganum harmala oil. Three main factors, namely particle size (x_1), temperature (x_2) and pressure (x_3), varying in ranges of [0.5, 0.9 mm], [35, 55°C] and [100, 300 bar], respectively, were considered as the system variables in order to investigate their effects on the oil extraction yield.
The experimental results of the Box-Behnken design were fitted with a second-order polynomial equation expressed as follows:

$$y = a_0 + a_1x_1 + a_2x_2 + a_3x_3 + a_{12}x_{12} + a_{13}x_{13} + a_{23}x_{23} + a_{11}x_1^2 + a_{22}x_2^2 + a_{33}x_3^2 \qquad (2)$$

with y denoting the estimated response, x_1 the particle diameter, x_2 the temperature and x_3 the pressure are the independent parameters, a_0 the constant coefficient, a_1, a_2, and a_3 the linear

coefficients, a_{12}, a_{13}, and a_{23} the interaction coefficients and a_{11}, a_{22}, and a_{33} the quadratic coefficients.

Table 1: The level of variables chosen for the Box–Behnken design

Variables (coded)	-1	0	1
x_1 (mm)	0.5	0.7	0.9
x_2 (°C)	35	45	55
x_3 (bar)	100	200	300

3. Results and Discussion

3.1. Supercritical CO2 extraction

Different oil extracts obtained by means of the supercritical carbon dioxide extraction was obtained with different yield values, depending on the set operating conditions. This can be regarded as a very important result since the operating parameters can be manipulated according to the desired extract composition and extraction yield.

3.2. Box-behnken design model and statistical analysis:

3.2.2 TPC and TFC

Regression Equations in Uncoded Units for the TPC and TFC have been developped and are expressed by Equations 1 and 2 respectively. The predicted results obtained using these equations are shown in Table 2.

$$TPC = -3{,}6 - 117\,d + 6{,}65\,T - 0{,}668\,P + 291{,}0\,d^2 - 0{,}0399T^2 + 0{,}001153\,P^2 - 6{,}08\,d\,T + 0{,}064\,d\,P + 0{,}00272\,T\,P \quad (1)$$

$$TFC = 3{,}70 + 13{,}7\,d - 0{,}355\,T + 0{,}0428\,P + 12{,}63\,d^2 + 0{,}00873\,T^2 - 0{,}000082P^2 - 0{,}628\,d\,T - 0{,}0155\,d\,P - 0{,}000027\,TP \quad (2)$$

- Total phenol content

The quantitative analyses of total phenols were determined from the equation of the linear regression of the calibration curve of Figure 1 where Gallic acid was used as standard. The obtained values are expressed in mg EGA / g E and are shown in Table 2 where it can be seen that the total polyphenol contents of the various extracts varied between 21.90 ± 1.24 and 66.50 ± 0.66 mg EGA / g E. The latter value *i.e*. the highest one was obtained for a particle size of 0.9 mm and at 45°C and 100 bar. From these results it can be deduced that the phenolic content in the obtained extracts depends upon the operating conditions of the supercritical carbon dioxide extraction, which have a great influence on the composition of the extracted oil.

- Total flavonoid content

The flavonoid levels of the extracts were calculated from the calibration curve shown in Figure 2 plotted using quercetin as a standard. They are expressed in terms of mg QE / g E as shown in Table 2 and where the results show that the total flavonoid contents were almost constant just varying between 4.254 and 4.39 under the majority of the adopted operating conditions. However they showed important variations under few conditions like (0.9 mm, 35 ° C and 200 bar), (0.5 mm, 55°C and 200 bar) and (0.9 mm, 45°C and 300 bar), with a TFC 7.56, 6.22 and 2.90 mg QE / g E respectively. This may be explained by the effect of the interactions between the operating conditions on the extracted

oil composition. For some operating conditions these effects may cancel each other contrary to others where one or more may be dominant.

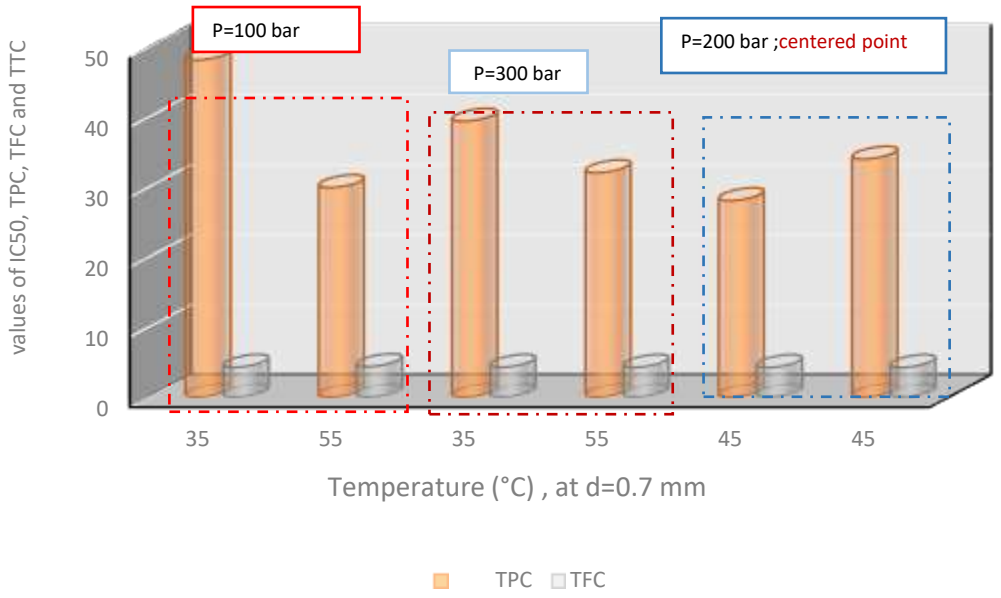
Table 2. Experimental design results for IC50, TPC, TFC and TTC

	D	T	P	TPC (mg GAE/g E)		TFC (mg QE/g E)	
	mm	°C	bar	experimental	predicted	experimental	predicted
1	0,5	35	200	28.80 ± 2.73	26.04	4.32 ± 0.019	4.52
2	0,9	35	200	59.69 ± 1.01	62.12	7.56 ± 0.83	7.03
3	0,5	55	200	39.66 ± 2.46	37.23	6.22 ± 0.31	6.75
4	0,9	55	200	21.90 ± 1.24	24.67	4.45 ± 0.05	4.24
5	0,5	45	100	52.11 ± 3.44	52.39	4.37 ± 0.016	3.83
6	0,9	45	100	66.50 ± 0.66	61.60	4.25 ± 0.056	4.45
7	0,5	45	300	37.01 ± 1.81	41.92	4.26 ± 0.016	4.06
8	0,9	45	300	56.52 ± 3.60	56.23	2.90 ± 0.150	3.44
9	0,7	35	100	48.17 ± 2.39	50.64	4.29 ± 0.011	4.62
10	0,7	55	100	29.94 ± 1.66	32.08	4.38 ± 0.016	4.40
11	0,7	35	300	39.42 ± 1.66	37.28	4.30 ± 0.016	4.29
12	0,7	55	300	32.07 ± 2.00	29.59	4.28 ± 0.014	3.95
13	0,7	45	200	28.08 ± 0.94	29.87	4.258 ± 0.013	4.26
14	0,7	45	200	34.02 ± 1.57	29.87	4.265 ± 0.016	4.26
15	0,7	45	200	27.50	29.87	4.258	4.26

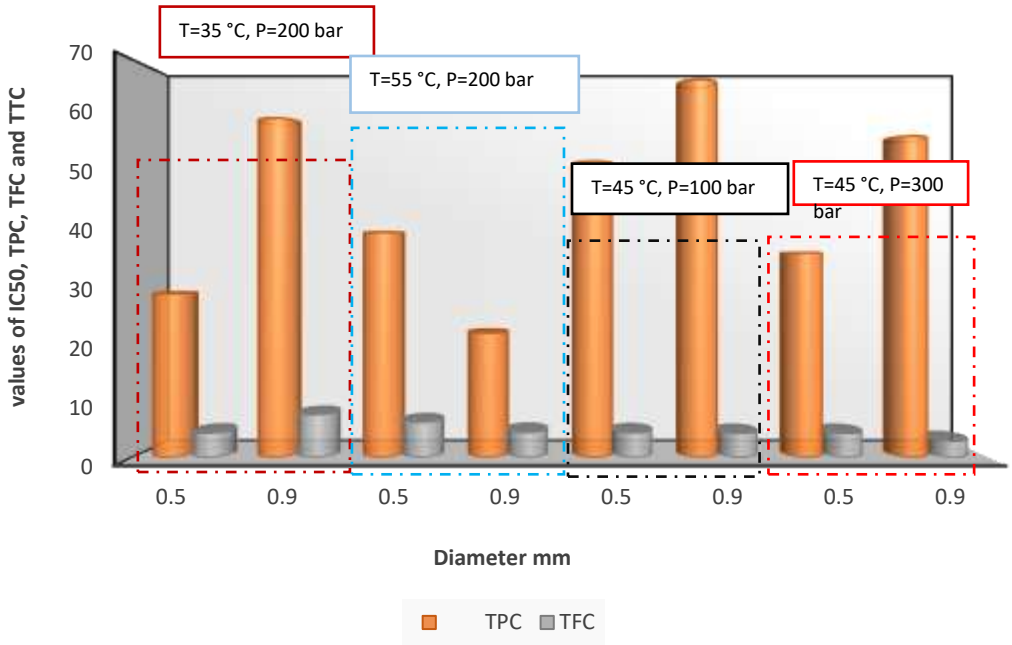
TPC (Total Phenolic Content), GAE (Gallic Acid Equivalent), TFC (Total Flavonoid Content), QE (Quercetin Equivalent),

Figures 1(a) & (b) show the effects of the operating parameters on TPC and TFC of the Peganum Harmala oil extracts. Figure an 1(a) show that for a fixed particle size of 0.7 mm and at a pressure of 100 bar an adverse effect on the TPC was observed when the temperature varied from 35 to 55°C, *i.e.* the TPC decreased. This can be explained by the fact that the prevailing operating conditions of pressure and temperature may correspond to the retrograde zone characterized by a decrease of the oil with an increase of the temperature. Also from the same figure 1(a) and for a particle size of 0.7 mm, a negative effect of temperature on the results was observed since the increase of temperature from 35 to 55°C led to a decrease in polyphenols content.

From Figure 1(b) it can be seen that the TPC increased when the pressure value decreased to the lowest value of 100 bar at 45 °C, when the particle size increased from 0.5 to 0.9 mm. Moreover, the highest TPC value was observed for the largest particle sizes of 0.9 mm at 45 °C and 100 bar. This may be regarded as an unusual behaviour since the mass transfer is enhanced with small particle sizes which do provide a larger mass transfer area.



(a)



(b)

Figure 1. Effect of operating parameters on TPC and TFC of supercritical extracts of Peganum Harmala.

3.2.3. Analysis of Variance

The statistical analysis of the model was performed in the form of analysis of variance (ANOVA) and the results are shown in the following figure:

Table 4: Analysis of variance results for the quadratic models

	TPC (GAE/ g E)		TFC (QE/ g E)	
Model	11,10	0,008	5,03	0,045
Linear	10,35	0,014	0,50	0,696
d	11,50	0,019	0,00	0,999
T	14,33	0,013	0,52	0,502
P	5,22	0,071	0,99	0,366
Square	14,24	0,007	7,28	0,028
d*d	20,46	0,006	3,09	0,139
T*T	2,57	0,170	9,24	0,029
P*P	20,06	0,007	8,08	0,036
2-Way Interaction	8,70	0,020	7,32	0,028
d*T	24,60	0,004	20,67	0,006
d*P	0,27	0,624	1,26	0,312
T*P	1,23	0,318	0,01	0,925
R-sq	95,16%		90,06%	
R-sq(adj)	86,45%		72,16%	

This analysis includes the Fisher's test. The F test makes it possible to compare, for a fixed risk in advance, the Fobs calculated in the previous table with an F (critical) read from the Fisher-Snedecor table with (p-1) and (n - p) degrees of freedom. F-values obtained for TPC and TFC were 11.10 and 5.03 respectively and were greater than the tabulated F (for risk 0.05, $F_{0.05}(9, 5) = 4.77$) [15], [16]. Therefore it was confirmed that the model was a good predictor of the experimental results

For the significance of the factors in the model, it should be checked that $p < 0.05$ for each factor [17].

For TPC, and TFC, It was found that the predicted values matched the experimental values reasonably well with R2 = 95.16%, 90.06 % respectively.

Adjusted R2 (Adj-R2) is also a measure of goodness of fit, but it is more suitable for comparing models with different numbers of independent variables. It corrects R2-value for the sample size and the number of terms in the model by using the degrees of freedom in its computations. If there are many terms in a model and not very large sample size, Adj-R2 may be smaller than R2. For the present case Adj-R2 values were 86.45 and 72.16 %, respectively, indicating that there was a good agreements between the experimental and predicted values of oil extraction yield.

A large value of R^2 does not necessarily imply that the regression model is a good one. Because R^2 always increases as we add terms to the model, regardless of whether the additional variable is statistically significant or not. Thus, it is possible for models that have large values of R^2 to yield poor predictions of new observations or estimates of the mean response [15] .

3.3. Optimization of the oil extraction yield

The main objective of using experimental design in the present work is to obtain the optimal values of the operating variables to give a maximum response.

An optimum condition for the supercritical CO_2 extraction of the bioactive compounds from Peganum harmala seeds was determined to obtain maximum total phenolic and flavonoid of the extracts. The

second order polynomial models developed in this study were used for each response in order to obtain specified optimum conditions.
The analysis of the model of Peganum harmala and the technical statistical resolution in the Minitab 16 software, provided the values of 100 bar, 35°C and 0.9 mm, for the pressure, temperature and particle size, respectively, for a maximum oil extraction yield value of 79.04 mg GAE/g E %.

However, for the TFC, an optimum value of 7.10 mg QE/g E was obtained at a pressure of 170.7 bar but still at a temperature and a particle size of 35°C and 0.9mm, respectively.

4. Conclusion

The present study has shown carbon dioxide supercritical extraction can be used to valorize natural plants like Peganum harmala, present in abundance in nature, with no cost, no environmental impact, etc. It may also be an important source of oil characterized by an important antioxidant potential that can be exploited in many applications in the agro-food and pharmaceutical industrial fields.

The adopted approach had the merit to consider two aspects: (i) an experimental work based on the supercritical fluid extraction technology; (ii) a modeling and optimization part based on a Box-Behnken statistical design to investigate the effect of the considered operating parameters (pressure, temperature and particle size).

in the present study, the optimization of the quality of the extracted oil with respect to the targeted properties like the total phenol content, was considered.

The use of the Box-Behnken statistical design, led to reasonable results compared to the experimental values. Numerically the determined optimal extraction conditions were a pressure of 100 bar, a temperature of 35 °C and particle size of 0.9 mm for an optimum total phenolic content around 79.04 mg GAE/g E. whereas a total flavonoid content of 7.10 mg QE/g E was obtained still at 35°C and for a particle size of 0.9 mm but at a pressure of 170.7 bar.

References:

[1] L. Nahar et S. D. Sarker, « Supercritical Fluid Extraction in Natural Products Analyses », in *Natural Products Isolation*, vol. 864, S. D. Sarker et L. Nahar, Éd. Totowa, NJ: Humana Press, 2012, p. 43-74. doi: 10.1007/978-1-61779-624-1_3.

[2] M. Herrero, J. A. Mendiola, A. Cifuentes, et E. Ibáñez, « Supercritical fluid extraction: Recent advances and applications », *J. Chromatogr. A*, vol. 1217, nº 16, p. 2495-2511, avr. 2010, doi: 10.1016/j.chroma.2009.12.019.

[3] M. Kchaou *et al.*, « Chemical Composition and Biological Activities of Zygophyllum album (L.) Essential Oil from Tunisia », p. 12, 2016.

[4] A. e A. Isabela *et al.*, « Chemical study of Peganum harmala seeds », *Afr. J. Biotechnol.*, vol. 18, nº 21, p. 462-471, mai 2019, doi: 10.5897/AJB2019.16762.

[5] M. Kumar, S. Joshi, V. Kulkarni, et C. Savant, « Phytochemical screening and evaluation of analgesic, anti-inflammatory activities of Peganum harmala Linn., seeds in rodents », *J. Appl. Pharm. Sci.*, p. 052-055, 2015, doi: 10.7324/JAPS.2015.50510.

[6] L. M. I. Hassani et M. El Hadek, « Analyse de la composition de l'huile de *Peganum harmala* L. *(Zygophyllaceae)* », *Acta Bot. Gallica*, vol. 146, nº 4, p. 353-359, janv. 1999, doi: 10.1080/12538078.1999.10515822.

[7] R. A. Kaskoos, « Physico-chemical Parameters, Phytochemical Screening and Antioxidant Activity of Seeds of Peganum harmala Collected from Iraq », *Asian J. Biomed. Pharm. Sci.*, p. 5, 2014.

[8] A. Dube, P. Misra, T. Khaliq, S. Tiwari, N. Kumar, et T. Narender, « Therapeutic Potential of Harmala (Peganum harmala L.) Seeds with an Array of Pharmacological Activities », in *Nuts*

and Seeds in Health and Disease Prevention, Elsevier, 2011, p. 601-609. doi: 10.1016/B978-0-12-375688-6.10071-4.

[9] I. Apostolico *et al.*, « Chemical Composition, Antibacterial and Phytotoxic Activities of Peganum harmala Seed Essential Oils from Five Different Localities in Northern Africa », *Molecules*, vol. 21, nº 9, p. 1235, sept. 2016, doi: 10.3390/molecules21091235.

[10] S. K. Marwat et F. ur Rehman, « Medicinal and Pharmacological Potential of Harmala (Peganum harmala L.) Seeds », in *Nuts and Seeds in Health and Disease Prevention*, Elsevier, 2011, p. 585-599. doi: 10.1016/B978-0-12-375688-6.10070-2.

[11] Jinous Asgarpanah, « Chemistry, pharmacology and medicinal properties of Peganum harmala L. », *Afr. J. Pharm. Pharmacol.*, vol. 6, nº 22, juin 2012, doi: 10.5897/AJPP11.876.

[12] S. Tahrouch, S. Rapior, L. Mondolot-Cosson, L. A. Idrissi-Hassani, et J. M. Bessière, « PEGANUM HARMALA : SOURCE COMBINEE D'AROMES ET », *Rev. Biol. Biotechnol.*, vol. 2, p. 33-37, 2002.

[13] E. M. A et H. S. J, « ANTIOXIDANT AND FREE RADICAL SCAVENGING ACTIVITY OF FEIJOA SELLOWIANA FRUITS PEEL AND LEAVES », *Pharmacologyonline*, Iran, p. 1: 7-14, 2008.

[14] T. Bahorun *et al.*, « Oxygen species scavenging activity of phenolic extracts from hawthorn fresh plant organs and pharmaceutical preparations. », *Arzneimittelforschung.*, vol. 46, nº 11, p. 1086-1089, 1996.

[15] D. C. Montgomery, *Design and analysis of experiments*, Eighth edition. Hoboken, NJ: John Wiley & Sons, Inc, 2013.

[16] C.-H. Dong, X.-Q. Xie, X.-L. Wang, Y. Zhan, et Y.-J. Yao, « Application of Box-Behnken design in optimisation for polysaccharides extraction from cultured mycelium of Cordyceps sinensis », *Food Bioprod. Process.*, vol. 87, nº 2, p. 139-144, juin 2009, doi: 10.1016/j.fbp.2008.06.004.

[17] J. P. Maran, S. Manikandan, B. Priya, et P. Gurumoorthi, « Box-Behnken design based multi-response analysis and optimization of supercritical carbon dioxide extraction of bioactive flavonoid compounds from tea (Camellia sinensis L.) leaves », *J. Food Sci. Technol.*, vol. 52, nº 1, p. 92-104, janv. 2015, doi: 10.1007/s13197-013-0985-z.

Theme 4: Chemical Process Safety

Complacency, Our Worst Enemy: A Recipe for Disaster

German Luna-Mejías *

LUPATECH LTD; Canada (www.lupatechltd.ca)
** Corresponding author: german.luna@lupatechltd.onmicrosoft.com; Tel.: + 1 403-6713878.*

Abstract: Layer of Protection Analysis (LOPA) is a semi-quantitative method for risk reduction and it uses typical factors to establish the frequency of initiating events happening and the probability of failure of safeguards; conditional modifiers or enablers also contribute to this equation. LOPA modifiers/enablers are diverse and depend on the operating scenario and conditions. Exposure time for people in the impacted area may be considered. Other factors such as human error and adverse weather conditions, etc. are also used. There are others that are not so obvious such as the probability of a hidden valve failure, etc. Operational experience can also be used to calculate these factors, but with great caution. In this paper, a misuse of LOPA modifiers is presented to raise awareness of the potential complacency but user. ASME Code, and API Standards 520/521 define pressure protection strategy even material of construction may theoretically resist more than design pressure. Material resistance should not be used for overpressure protection. Using LOPA pressure modifier factor in the calculation may lead to reach Target Frequency without even consider safeguards. Existing safeguards may not be validated to save some money, resulting in a facility poorly protected. A well-trained facilitator and team are a must to prevent this from happening.

Keywords: process safety; LOPA; process hazard analysis; overpressure; risk; complacency

1. Introduction

After the sadly-remembered events of Bhopal, Piper Alpha and others and the release of API 750 and OSHA 1910.119; Process Safety Management (PSM) became more prominent and important as business were required to properly manage their industry in regards of using hazardous chemicals. Outside of US, other organizations had issued similar documents with the same objective: "make the world a safer place".
Unfortunately, regulations equivalent to OSHA are not mandatory in some countries.

PSM is system for managing the integrity of operating systems and processes that handle hazardous substances, to prevent unplanned releases of hazardous materials or energy which could lead serious or catastrophic incident or accident.

To address Process Safety Management, there are several risk studies that come into play, being the most commons: Hazard and Operability studies (HAZOPs), Layers of Protection Analysis (LOPA), among others.

Once a HAZOP study is completed, a more detailed analysis may be required to ensure integrity and reliability of the safeguards. Here is when the Layers of Protection Analysis (LOPA) came into the game: "Layer of protection analysis (LOPA) is a simplified method of risk assessment that provides the much-needed middle ground between a qualitative process hazard analysis and a traditional, expensive quantitative risk analysis"[1]

One big difference between the HAZOP approach and the LOPA approach for Process Safety is the use of Conditional Modifiers and/or Enablers. A misuse of the LOPA modifiers/enablers may impact the validity of the LOPA and move the company or organization into safety "quicksand" which is also a "a feeling of quiet pleasure or security, often while unaware of some potential danger, defect, or the like"[2] called complacency.

There are two major areas in LOPA where "complacency" may occur: a) reliability of the safety systems and b) incorrect use of modifiers/enablers.
An example of the first follows:

[1] CCPS: Guidelines for Enabling Conditions and Conditional Modifiers in Layer of Protection Analysis
[2] Merriam-Webster Dictionary definition of complacency

"A refiner with maintenance cost limitations, decided to postpone the *required inspection* of the PVRVs on their crude tanks based on the following: "this is heavy crude, how this tank is going to overpressure? let's delay the maintenance a couple of years as nothing had happened since we started (10 years)."
During LOPA maintenance's crew did not mention it and it was assumed that PVRV was under its regular inspection cycle. Therefore, during LOPA no action was described as there were enough safeguards.

PVRV was stuck close (for overpressure) and one day hot diluent was injected into the crude tank (normal but not frequent operation) and without a pressure protection device, tank got damaged" Was an error of the LOPA or the LOPA facilitator? Of course not, it was complacency: "nothing has happened in the last 10 yrs., let's wait two more years for maintenance" Sadly, there are many, many cases like this in the industry.

The second case, is the objective of this paper: inadequate use of LOPA modifiers

2. Overpressure and Overpressure Protection

Merriam-Webster defines "overpressure" as pressure significantly above what is usual or normal.

For the purpose of this paper, overpressure is the pressure a vessel or equipment can reach, or be exposed to, above design pressure. In Process Safety additional qualification is added: "which may cause extensive damage of equipment, facilities and harm people." Therefore, overpressure protection is required.

The primary parameter used to characterize a pressure vessel is the maximum allowable working pressure (MAWP). The MAWP is the maximum allowable pressure at the top of the vessel at design temperature. Also, the design temperature for which the MAWP is set at is called the Maximum Allowing Working Temperature (MAWT). Operating temperature will affect the MAWP. Another parameter that cannot be exceed is the MDMT (Minimum Design Metal Temperature) which will also impact the MAWP; any of these 3 factors must not be exceeded during normal operating conditions. MAWP is defined by manufactures as per ASME Code [1].
Overpressure protection is considered the last line of defense against possible catastrophic failure of pressure equipment. The function of overpressure protection is to: Protect people, prevent unsafe operation of pressure equipment, protect equipment from failure due to overpressure, prevent loss of production. Overpressure protection strategy is defined by API Standards 520/521 [2,3]
In general terms, overpressure protection is required if the pressure at which a vessel or equipment can be exposed may exceed MAWP. Setting of the relief device may deviate from MWAP only if some conditions apply:[3]

2.1. Maximum allowable set pressure: 100% of MAWP for single relief.
2.2. Maximum allowable set pressure: 105% of MAWP for multiple reliefs.
2.3. Maximum allowable relief pressure: 110% of MAWP for single relief (non-fire)
2.4. Maximum allowable relief pressure: 116% of MAWP for multiple reliefs
2.5. Maximum allowable relief pressure: 121% of MAWP for fire sizing

Each scenario must be studied carefully for proper calculation of the relief system and guarantee adequate protection.

3. HAZOP Overpressure Protection

Overpressure is one of the worst-case scenarios for HAZOP and Pressure Safety Valves (PSV's) are key safeguards for protection. When a relief device has not been sized to account for a scenario, it cannot be relied upon to provide protection during an emergency event.

Two outcomes may happen from an overpressure event: a leak or a rupture. As it is difficult to judge which one will happen with the HAZOP tools; it is recommended to consider the worst of the scenarios (conservative approach) and properly document all existing safeguards. There is a "false

[3] API Standard 521: Pressure-relieving and Depressuring System (6th Edition, Jan 2014)

believe" that a leak cannot be catastrophic… in 1991, 2/3 of an Alkylation unit was seriously damaged because of a leak.[4]

The selection of the worst-case scenario will determine safeguards needed, here the expertise and knowledge of the team members is paramount. Once a HAZOP study is completed, quite often we ask ourselves: Is that enough? Do we have enough safeguards? These questions may be answered in a LOPA study.

4. LOPA Overpressure Protection

LOPA is a method used to evaluate high-consequence scenarios determining if the combination of probability of occurrence and severity of consequences meets a company's risk tolerance: "Beginning with an identified accident scenario, LOPA uses simplifying rules to evaluate initiating event frequency, independent layers of protection, and consequences to provide an order-of-magnitude estimate of risk.

4.1. Concepts

From the scenario evaluated in the HAZOP that has shown a high risk or high severity consequence, a LOPA study is recommended and a PSV is required. The case will be built and credit will be given to the existing PSV for overpressure protection if the PSV is sized for the scenario under evaluation. If there is no evidence of PSV sized for the scenario, no credits in the LOPA should be taken and a recommendation must be written.

LOPA credits are based on a factor called PFD (Probability of failure on Demand). The Probability of Failure on Demand (PFD) is a measure of the effectiveness of a safety function. It expresses the likelihood that the safety function does not work when required to.

Performance of PSVs as Independent Layer of Protection (IPL) must be carefully reviewed as operation may be impacted by the nature of the process and by the frequency and quality of the maintenance. Traditionally for a "clean service" (which means not subject to corrosion, plugging, fouling, freezing) and a well-maintained PSV a PFD of 0.01 can be used. If the service is considered "dirty" factor will drop to 0.1 (one order of magnitude). If PSV is well-know to have maintenance issues, a new PFD should be calculated (using maintenance data from the facility) before using it in the LOPA calculation. Another option is to install a new PSV sized for the worst-case scenario.

4.2. Modifiers

Layer of Protection Analysis (LOPA) is a tool for analyzing and assessing scenario risk. LOPA has grown in popularity in the time since the publication of the CCPS Concept Book, Layer of Protection Analysis: Simplified Process Risk Assessment, in 2001 [4]

One big difference between the HAZOP (PHA) approach and the LOPA approach for Process Safety is the use of Conditional Modifiers and/or Enablers. Enabling conditions are associated with the part of an incident sequence leading up to a release of hazardous material or energy, whereas conditional modifiers are probabilities generally associated with the post-release part of an incident sequence [5].

Enablers (Enabling condition) refers to a condition that makes the initiating event of a scenario possible. It is not the failure of a protection layer, but is must be active in order for the scenario to proceed to a loss event (consequence). By the other hand, the best example of conditional modifier is the presence of personnel during the consequence event, presence of people will not stop or allow the event to continue but rather mitigate people exposure to consequence.

Conditional modifiers and/or enabling conditions are not required in every LOPA. Experienced facilitator will recommend the path forward based on the scenario and the Process being studied.

4.3. Vessel Material of Construction as conditional Modifier

LOPA is a simplified semi-quantitative method using a conservative approach, which gives the user the option of selecting the PFD (Probability of Failure on Demand) of the IPLs based on their own experience and from technical data.

Modifiers must be used with extreme care to ensure their proper and adequate use; as their over-use may create a false sensation of safety; organization may drive into a safety's quicksand.

[4] German Luna-Mejías, Alkylation Fire Memorandum, January 1991. PDVSA Cardon Refinery

Some Engineering companies use LOPA modifiers for overpressure based on the pressure at which the vessel may be exposed in the event of a failure of a system; some other include modifiers based on pressure and construction materials. The use of these LOPA modifiers may give the user the false sensation of safety (complacency) based on because of construction materials, it will be less likely to fail.

These factors vary between 0.1 and 0.001 depending on a factor called PR (Pressure Ratio) which is the ratio between the maximum pressure the vessel can be exposed to and the MAWP. These factors are based on two potential outcomes: a) leaks: for PR below 2.0 and b) rupture for PR above 3.

ASME Code [1] states that overpressure protection is needed above MAWP and recommends to use API STD 521 guidelines; so, no factors are to be considered based on fabrication of the corresponding vessel. Then what is the correct approach?

Consider a scenario where an event leading to overpressure is possible; from the HAZOP it was considered: single fatality because the pressure level is not so high and the impact radius will not affect more than one person. Indirectly, the HAZOP already considered in the consequence the PR; later on, LOPA is performed and PR factor is used as a modifier; also, occupancy is included as a modifier; the frequency of the initiating event is included in the equation and the result is that the Mitigated Frequency (MF) is equal or below the Tolerable Frequency (TF); as a result, no verification of the other safeguards (if any) neither the existing PSV (required by Code). This may be a case of complacency: false sensation of safety.

The example presented above is the typical case of "double dipping": reducing the severity of the consequence and use modifiers to reduce the likelihood of the same event, to give the users -that may not be properly trained in PSM- a false sensation of safety.

It is not just the mathematical calculation; it is the need for the facilitator and team members to understand what are they doing and why. The facilitator is responsible for using the methods, factors, etc. correctly while the team is responsible for speaking-out the true and operational concerns during the study.

5. Use of QRA in the LOPA

In the CCPS book **[x]** the use of some forms of QRA (Quantitative Risk Assessment) in the LOPA are allowed specially when some scenarios are difficult to address in terms of Initiating event and/or consequences.

Caution must be exercised if using QRA for the consequence to ensure additional modifiers are not been added to the LOPA if they are already considered when calculating the QRA. If QRA considers blast impact based on PR; then LOPA modifiers (PR related) are already incorporated in the calculation of the severity and cannot be used -again- in the LOPA. Couple of cases are presented for clarification:

5.1. Case 1:

Initiating event: Pressure control loop failure, closing the valve.
Consequences: Overpressure of vessel; leaks or rupture; loss of containment; fire; hazards to people.
Using QRA it is found that most likely event will be a single fatality due to blast ratio based on PR; and TF is 0.0001.

LOPA calculation:
Initiating event: 0.1
Presence of people: 0.1
PSV: 0.01 (sizing to be confirmed)
RRF: 1.
As a result of this evaluation, a proper verification of the PSV will be performed; no further safeguards are required.

5.2. Case 2:

Initiating event: Pressure control loop failure, closing the valve.
Consequences: Overpressure of vessel; leaks or rupture; loss of containment; fire; hazards to people.
Using QRA it is found that most likely event will be a single fatality due to blast ratio based on PR; and TF is 0.0001.

LOPA calculation:
Initiating event: 0.1
Presence of people: 0.1
PR modifier: 0.01
RRF: 1.

As a result of this evaluation, no PSV verification will be performed; no further safeguards are required. Team driving into "quicksand"
Using PR factors in LOPA without verifying the PSV sizing "because it is not needed" or because "it will increase the scope of the project" is wrong. That is why we still have many PSM accidents; seems that we have not learn the lesson or people at high levels in the organization do not understand Process Safety rather "money talks"
All these described here take us to the OSHA guidelines: "a team of experts" Are the team of experts in the room? Is the facilitator capable to understand the differences and guide the team? Not everybody can facilitate a HAZOP or LOPA study, rules need to be known, but process too.

6. Conclusions

6.1. Using factors in LOPA to estimate the severity and at the same time, using them as modifiers is not correct and user can get into safety "quicksand"
6.2. No rules from ASME Code neither API Standard 521 allow for additional pressure protection based on vessel design and construction materials.
6.3. If using QRA for estimating the severity for the LOPA, caution must be exercise not to re-use modifiers already accounted for in the calculation.
6.4. A leak in a process plant, depending on operating conditions can produce disastrous effects regardless of the Pressure Ratio (P/MAWP)
6.5. Using 3rd party guidelines for LOPA evaluation without proper knowledge or reason is complacency.
6.6. A well-trained facilitator in HAZOP & LOPA with broad knowledge of the process is a must to reduce the risk of misusing LOPA modifiers.

7. Recommendations

7.1. Use of PR factors as modifiers in the LOPA are not recommended as there is a potential for complacency and false sensation of safety (reduced number of safeguards are required).
7.2. Using 3rd party factors for LOPA without proper evaluation or analysis is dangerous and complacent.
7.3. Ensure HAZOP/LOPA facilitation is managed by a well-trained facilitator with Process knowledge to ensure the best guidance to team members.

References

1. ASME, "Boiler and Pressure Vessel Code (BPVC) Section VIII Rules for Construction of Pressure Vessels. Division 1." (BPCV-VIII-1-2021); 2021
2. American Petroleum Institute, API Standard 520 "Sizing, Selection, and Installation of Pressure-relieving Devices, Part I-Sizing and Selection" 9th Edition; July 2014.
3. American Petroleum Institute, API Standard 521 "Pressure-relieving and Depressuring Systems" 6th Edition; January 2014.
4. Center for Chemical Process Safety (CCPS), "Layer of Protection Analysis – Simplified Process Risk Assessment" New York, 2021

5. Center for Chemical Process Safety (CCPS), "Guidelines for Enabling Conditions and Conditional Modifiers in Layer of Protection Analysis" New York, 2013

Encoded Safety Instructions

Shehab Al-Sohpany

Safety Consultant-Yemen
***** *Corresponding author: Sohpani@gmail.com; Tel.: 00 967 775100120.*

Abstract: this paper aims to make systematic study of "Encoded safety instruction" (Encoded abbreviations that indicate descriptive information Which helps descripting wide aspects of hazards & safety to the targeted beneficiary) By analyzing all its figures and evaluate its effectiveness and efficiency. And setting up recommendations to solve its weaknesses. which represents the main root Couse of accidents due to the ignorance on its meaning as a communication method from the beneficiary perspective. And according to my research I found a shocking result which is The problem is in the instructions itself! and the responsibility of that is mostly on the Creator/designer/issuer/manufacturer of the Hazardous factors due to the unsuitable and ineffective clarifying methods of the hazards and safety instructions to the users or consumers according to Right to know role "Don't tell me what I can't understand" it's the supplier responsibility to "tell me what I can understand".

Keywords: Encoded Safety Instructions; Safety instructions; Safety signs; Hazard communication; Hazard identification; Safety Standards.

1. Introduction

Safety and Hazard identification failure and ignorance considered as the main root cause of chemical and Hazardous substance accidents, injuries, losses and disasters. Despite of many legislations and standards that imposes & obligates the clear specifying of Hazards and safety instructions throughout all chemical activities. Thus, most firms in complied in setting up these instructions as an encoded communication system like signs, symbols, colors, texts, shapes, and codes designed and published by variant standardization's organizations and accredited by many and different regions and countries. With an assumption that all personals and users will understand and should commit to its meaning and react according to it.

But that led me to wonder… Could instruction- itself -is a part of the problem? Is it Because of its complexity, diversity, differences, complications with others, language boundaries, and its requires capabilities of both physical and knowledge?

Because of that I felt the importance and necessity to study and analyze the root's roots which led to inability to react, not understand/misunderstand, decommitment, lake of usage and ignorance of hazards & safety instructions. From the targeted Recipient/users needs, ability/characters.

Through this paper I have summarized most important figures related to this important subject due to the originality of this subject and the lake and rare of studies and scholars in this field and in safety field in general. Supporting my climes and results with global and local statics (in Yemen).

Therefore, this paper has been carefully written in an interactive & unique style to insure "you can understand what I say", finally this paper includes many recommendations which- in my opinion- may help solving this issue.

1.1. The purpose of Encoded safety instructions:

a. Legal requirement.
b. Easy to understand.
c. Globally Recognized.
d. Ensuring Safety.
e. Quality standards.
f. Describe Specifications.
g. Protecting Resources.
h. Minimizing Risks.
i. Costumers Care goal.
j. Efficient investment.
k. Environment friendly.
l. Accident management.
m. Avoiding claims.



Figure (1)

1.2. Encoded safety instructions clarify:

Regulatio ns	Standards	Guides	Specificatio ns	Requireme nts	Identificati on	Rules	Actions	Usage
Hazards	Safety	Precautio ns	Marking	Emergenc y	Treatment	Disposal	PPE	Accridatio n

1.3. Encoded safety instructions as a communication method:

As any communication method in has the same systematic prosses as followed:

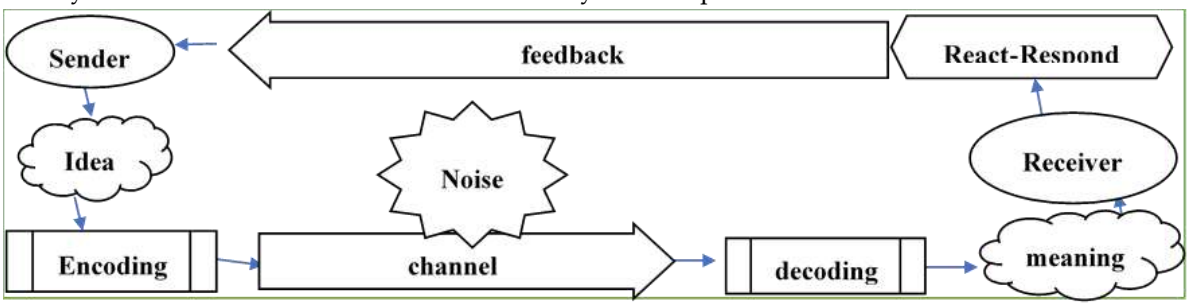


Figure (2)

a. **The sender**: the owner of data which needed to be transferred to the receiver. - in this case the manufacturer responsible of specify Hazard and safety instruction(massage) to the user (receiver).example: Toxic.
b. **Encoding:** the way that massage is physically designed to be transmittable- example:
c. **Channel:** the prosses of transmitting the coded message to the receiver. Example: paper label on can.
d. **Decoding:** the process of decoding the massage by the receiver- in this case the receiver must identify or recognize the meaning of that symbol which means can contains Toxic substance
e. **Noise:** any disturbance between sender and receiver may affect the effectiveness of the massage- Example: bad printing- the label is so small- the label fainted.
f. **The feedback:** the reaction of the receiver – in this case by not swallow the content.

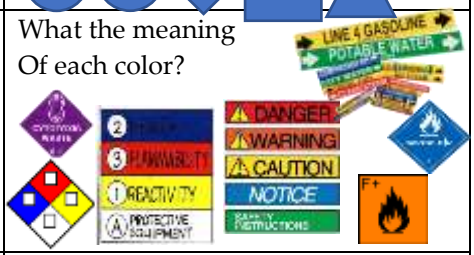
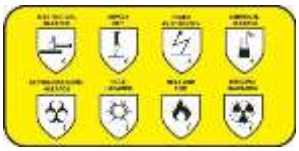
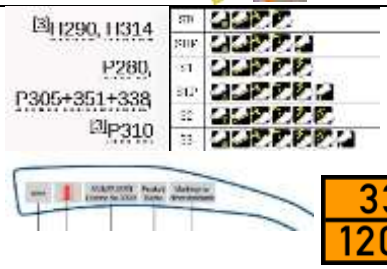
- **Note1**: both sender and receiver have the same knowledge of the code.
- **Note2**: if the receiver is blind, how could he identify the hazard of can's content?!

- **Note3**: what would happen If the encoded massage was Text (Toxic) and the receiver cannot read.
- **Note4**: English man bough a can with this warning text (خطر سام عند الابتلاع).
- **Note4**: what would a normal consumer do if the can has this encoded instruction GHS (S24/35/40)?

The receiver must study the receiver ability to understand the coded system before Encoding.

1.4. The main encoded instructions types:

Table (1)

type	Weaknesses/not suitable for	Example
Text	Takes plenty of size- language differences- illiteracy- vision disabilities-	Danger- خطر
Letters	Needs advanced knowledge- vision disabilities- language differences	COR- EHS- TWA+TWAEV- W LD50+ LC50 -LEL+LFL
logos	Needs advanced knowledge- vision disabilities- language differences	
Symbols	Needs knowledge- vision disabilities- not unified- physical requirements.	
Shape	Needs knowledge- vision disabilities- not unified- physical requirements.	
Colors	Needs knowledge- vision disabilities- not unified- physical requirements.	What the meaning Of each color? 
Sound sirin	Needs knowledge- Hearing disabilities- not unified - physical requirements.	Fire- tsunami-biohazards- che nuclear- earth quick- naval horn 
Light	Needs knowledge- vision disabilities- not unified- physical requirements.	
Tools	Needs knowledge- needs resources- physical requirements.	
Codes	Needs very advanced knowledge - language - illiteracy- vision disabilities- children – needs a decoding guide.  	

1.5. The issuers of the encoded instructions:

Countless standardizations organization works to create each own systems mostly located in Europe and Germany, UK, USA , japan and Canada (the most advanced and industrial countries) therefore many systems were issued, thou there is a global approach select a globally unified systems and institution. Like the will known ISO, unfortunately this strategic goal facing a lot of difficulties and may not see light soon. Currently there are some leading and worldly recognized institutions such as:



Figure (3)

1.6. Ideal encoded instruction specifications.

g. Minimal physical requirements.
h. Effective and efficient.
i. Unified globally.
j. Using more than one type in the same code.
k. Overtaking illiteracy-language- Educational barrios.
l. Can be used with people with disabilities.
m. Get advantage of currant advance Technologies.
n. I prefer using English letters and numbers because its advantages and wide spread.

- **Note1**:most of instructions types requires vision abilities.
- **Note2**: most safety instructions are used to identify hazards, only a handful of them clarify requirements (GHS), specifications and rating (DOT), personal protective equipment (HIMS) and firefighting instructions (HAZCHEM).[see resource]
- **Note3:** there are NO encoded system guides to Exposure, spillage, disposal or First medical instructions.

2. Materials and Methods:

2.1. Systemic study of designing:

I have studied the method of designing currant Encoded safety instructions and analyzed the main figures of its process and fundamentals.

2.2. Comparative study of different systems and issuers:

I have studied many issuers and their Encoded systems Which are uncountable due to the huge numbers and variety of specializations, Therefor I focused on the most16 most used [Reference a].

2.3. Statics indicators:

1. I must clarify that I couldn't find same previous research in this field, in spite of that many studies of uncertainty of awareness, hazard identification/assessment of spectacular of some systems has been issued, see references, that indicates that there is an obvious issue in currant systems worldwide.
2. Within my activities as a safety Trainer, I have studied the level of awareness of different encoded systems as a pre-training questionnaire for the training course " the International systems, guidance and standards of describing Hazardous substances" -that I created- and executed in many places.
3. I selected 7 main Samples to be analyzed which comprehended all levels of spatializations as follows:

Table (2)

N	Spatiality level	Required knowledge	Target	N Samples
1.	Level 1	Very high	Chemical collage -Sanaa UNV	60
2.	Level 2	high	Civil defense authority -Sanaa	50
3.	Level 3	moderate	5 Pharmatical &Chemical industry Co	40
4.	Level 4	Essentials	10 Medical students and graduates	100
5.	Level 5	fundamentals	5 Workers in many fields	100
6.	Level 6	basic	Normal unemployed people	50
Total				400

4. I gathered the pre-training questionnaire results – each has a score of 100%- and divided to the whole samples number.
5. I selected the highest 10% scores of each level samples to analyze the most recognized coded types (except sounds).
6. The results of this simple statics as follows:

Table (3)

N	level	score	10% of the high score results due to types awareness rate (1 for best)									
		average	text	letters	logos	symbol	shape	color	light	codes	avg	rate
1.	Level 1	22%*	1**	2	2	1	1	2	2	3	1.7	B
2.	Level 2	6%	3	3	3	3	3	2	2	3	2.75	E
3.	Level 3	25%	1	1	2	1	2	1	1	2	1.37	A
4.	Level 4	12%	1	3	2	2	3	2	2	3	2.25	C
5.	Level 5	9%	1	3	3	2	3	2	2	3	2.37	D
6.	Level 6	12%	2	3	2	2	3	2	2	3	2.37	D
average		14.3%	1.5	2.66	2.33	2.5	2.5	1.8	1.8	2.83		
Rate A for best type			A	D	C	E	E	B	B	F		

*** Colors grades (Highest- high- midrate- low- very low)**

**** Number grade 1=best,2=mid,3=worst.**

2.4. Global statics of abilities:

2.4.1. I focused on special characters necessary to use the encoded instructions such as:
   a. Illiteracy statics.
   b. Disabilities statics.
   c. English language knowledge statics.

2.4.2. Evaluating, Compering and analyzing of global population capabilities of using and understanding encoded safety instruction's systems.

3. Results and Discussion

3.1. Results:

3.1.1. According to field study:

1. Levels (1,3,4,5) has most score because= High education+ good English skills.
2. Level (1) has a good score because= specialized high education+ good English.
3. Level (3) has highest score because= Training+ experience +high education+ English.
4. Level (4,6) has moderate score because= high education +moderate English.
5. Level (6) has poor score because= moderate education+ poor English+ poor training.
6. Level (2) has the worst score because= poor Education/training/English +high rate of corruption (fact).
7. **Extra variables:**

a. Private sectors are better than public sector.
b. Young age persons are better than old ones.
c. English skills is a primary factor and a necessity to understand most types of instructions.
d. specialized education has to be developed.
e. Experience and Training is considered the best way to understand the instructions.

8. **Most effective types:(from the best to worse)**

a. Text: as long as people can read it.
b. Colors: Easy+ needs to be united.
c. Lights: easy+ simple.
d. symbols: Easy+ needs to be united and simplified.
e. Shapes: Easy+ needs to be united and simplified.
f. Litters & logos: needs special knowledge.
g. Codes: needs advanced training and knowledge and experience, and the result justifies the poor existence of standards in the 3rd world which leads to highest rate of accidents and losses.

- **Note**: Beirut harper catastrophe 2020 root cause is "the Non- compliance to storage standards"

9. **As a general result 14%** of the most famous and wide used encoded safety inspections were Recognized only!
10. the studied simples were educated and physically in good capabilities, and they score 14% only, what would the score be in case of illiterate people or with disabilities!

3.1.2. Global statics [see references b]:

1. Global population statics is (7.2 billion) [1].
2. Global statics of populations with disabilities indicates in percentage that: 17% with vision disabilities – 6% with Hearing disabilities- 2.8% with communication disabilities- approximately 1 Billion humans 1/7 with some type and range of disabilities [2].
3. 13.7% of people can't read at all[3], 100 million in Arab world![1]
4. 0.1% of people only speaks English! Which is the most industrial and scientific language [4]
5. 70% of illiterate adults are females and only 1 of 5 girls join the school [3]
6. Only 65 million high educators [4] = 0.1% of global population

3.1.3. Evaluating studied systems sample requirements:

I have estimated – in percentage- the capabilities required to understand the types of encoded safety instructions as follows:

- 95% present of encoded instructions abilities.
- present of encoded instructions the ability to read.
- 75% present of encoded instructions requires English language skills.
- 50% present of encoded instructions requires specialized education and training.

3.1.4. Comparing and analyzing the data in 3.1.2 and above data:

Table (4)

Disability	% (3.1.2)	Un Capable people	Sys types req	Capable people	% Globally
Vision	17%	1.2 b	95% requires vision	6b	83%
Hearing	6%	432 m	5% requires hearing	6.77 b	93%
Reading	13.7%	1 b	85% requires reading	6.2 b	87.3%
English	99.9%	7.19 b	75%requires English	72 m	0.1%
Education	95%	6.55 b	50% requires education	360 m	5%
Capable people how can Use all types because they got all requirements (globally)				242,593 persons	0.00337%
				1 person of 29,679 People *	

- Further studies required to local statics according to each region sub statics and data.

3.2. Discussion:

- **Extremely low awareness and knowledge of Encoded safety instructions worldwide.**
- **Extremely low awareness and knowledge of Encoded safety instructions in Yemen due to:**

a. low effectiveness of the high and specialized educational system.
b. Low level of English language and high rate of illiteracy.
c. Low public awareness due to poor media activities.
d. Poor training and capacity building activities.
e. The absence of local legislations and standards and accreditation of spectacular systems.
f. The absence of Scientific Research and development activities.
g. Extremely high Corruption in public sector.

- **Obvious poor study of based on receiver's methods in encoded safety instructions designing.**
- **The verity of issuers and different types of encoded safety makes it difficult to identify.**
- **The absence care of populations with disabilities needs.**

4. Conclusions

The importance to develop two major fields:

a. Encoded instruction Development:

1. Carful study to the receiver specifications when designing encoded instructions.
2. Developing the encoded instructions to be usable by people with disabilities.
3. Global effort to Create Unified authority responsible of developing Unified systems and standards.
4. Building a unified system to help responding to accidents &exposure and guides medical care workers to correct treatment protocols.
5. Get advantage of currant new communication & technologies.

b. General awareness:

1. The necessity of Improving Occupational health and safety field.
2. Unification and adaption of unified systems Locally and Regionally.
3. Governments should Enable, encourage and develop its national experts & professionals in this field.
4. Developing Educational, Training, Research, and awareness Institutions to help teaching and understanding these coded instructions.
5. Media has to be focus to spread safety general knowledge.
6. Support translation of international guides and standards.

Acknowledgments: To Ms Wafaa Al-Sohpany (my sister) for academic Review and To Jordanian Engineers association- jeaconf- JIChEc team to motivate preparing this paper and their assistance.

References

a. Issuers and standards:

n	Encoded	Issuer	website
1.	ISO 7010	International standardization organization	www.iso.org
2.	NFPA704	National fire protection agency	www.nfpa.org
3.	ADR	Euro agreement dangerous goods on road	www.hsa.ie
4.	GHS	Globally harmonized system	www.osha.gov
5.	HIMS	Hazardous identification system	www.unece.org
6.	HAZCHEM	Hazardous chemical – UN	www.hazchem.ie
7.	DOT	Department of transportation- USA	www.transportation.org
8.	WHMIS	Workplace hazardous materials info-sys	www.whmis.org
9.	HIN	Hazard identification number	www.ilo.com
10.	CE	Europe union standard	www.ec.eropa.eu
11.	ASTM	American society for testing materials	www.astm.org
12.	DIN	German institute for Standardization	www.din.de
13.	ANSI	The American National Standards Institute	www.ansi.org
14.	BSI Group	British standard institute	www.bsigroup.com
15.	CAS number	Chemical abstract service	www.cas.org
16.	UN number	United nations identification number	www.unece.org

b. Study data source:

1. www.wikipedia.com
2. www.diabled-world.com
3. www.unesco.org
4. www.ourworlddata.com

Heavy Metal-Contaminated Water Treatment Using Low-Cost Adsorbents

Mohammed Abualreesh *, Ahmad Abukhashabeh and Suhaib Hameedi

Freelancer – Water and Wastewater Treatment Technologist
***** *Corresponding author: mohammed.processengineer@gmail.com , Tel.:+970-59-5058395.*

Abstract: Presence of heavy metals in water is important issue due to toxicity and environmental impact. Heavy metals are removed from water by many techniques such as chemical precipitation, membranes, ion exchange, electrodialysis and adsorbents. In this assay project, adsorbents are discussed in details. Type of adsorbent, pH, initial concentration and temperature affect the performance of heavy metal removal. Optimum removals of heavy metals by adsorbents are noticed at acidic medium such as Pb (II) at pH of 5. Adsorption of heavy metals by clays is a function of temperature. Adsorption by bentonite is endothermic while adsorption by China Clay and Wollastonite are exothermic. Maximum adsorption of Hg (II) was observed to be 815 mg / g by chitosan adsorbent. The optimum pH for the removal of Pb (II) was 5 in which around 85 mg/g removal capacity was achieved by calcined phosphate. Zn (II) was removed by bentonite by the capacity 53 mg/g. Activated carbon is widely used for the adsorption. Many attempts are carried out to prepare activated carbon from organic rich material. Sewage sludge is one the raw materials for activated carbon preparation. Maximum adsorption by sewage sludge based activated carbon was 175 mg/g of mercury optimized at pH of 5. Chemical activation of activated carbon improves the surface area and heavy metal removal efficiency.

Keywords: Water; heavy metals; adsorbent; activated carbon; lead; zinc; mercury; adsorption.

1. Introduction

Wastewater treatment is now days an important and great issue in the world because of high demands for water. However; disposal of untreated wastewater causes environmental impact due to the absence of toxics and/or pathogens. One of the critical issues for the treatment of wastewater is removal of heavy metals. The presence of heavy metals in water supplies may cause adverse effects on health, environmental toxicity, and affect the aesthetic quality of water environment [1]. Metal discharges to the environment not only cause acute toxicity to aquatic organisms, microorganisms, and plants, but also strongly reduce microbial activity, which adversely affects biological wastewater treatment plants [2]. Heavy metals in water are ions of transition elements in the periodic table such as iron, chromium, zinc, cadmium, copper, cobalt, nickel, and other elements. Some heavy metals are micronutrients such as zinc, copper, selenium and iron and are only toxic at high concentrations, but other heavy metals including lead, arsenic, cadmium, chromium, nickel and mercury are toxic even at very low concentrations [3]. However; heavy metal removal is challenging because the quality of heavy metal-contaminated wastewater is not almost stable from source to other due to the variety of industrial and human applications. For example, contents of heavy metal of battery manufacturing plant wastewater are different from that of electroplating plant. Also, the content of heavy metals is different from plant to another plant.

2. Heavy Metals Present in Water, and Sources

Heavy metals are present in water and/or wastewater in different concentrations. Due to the environmental pollution in the natural water bodies such as sea and rivers, and soils by heavy metals, it is important to carry out for the frequent sampling and analyzing for the concentrations of heavy metals in water prior to water treatment. Heavy metals present in the industrial wastewater and sewage wastewater which cause toxicity for microorganisms necessary for biological treatment of sewage wastewater.

Heavy metals present in water are iron (Fe), zinc (Zn), chromium (Cr), cadmium (Cd), mercury (Hg), lead (Pb), copper (Cu), manganese (Mn), arsenic (As), nickel (Ni) and cobalt (Co). Researchers are interested in various heavy metals especially, Co, Pb, As, Cd, Cr, Hg and Ni due to their high degree of toxicity relative to others.

Heavy metal-water pollution is caused by both natural and anthropogenic sources [3]. Natural sources include mobilization of naturally occurring heavy metals from earth crust due to volcanic activity or weathering of rocks from where they are released into water sources. Anthropogenic sources include non-ferrous metal ore mining and smelting, electroplating, industrial activities, organic wastes, refuse burning, transport and power plants [3]. The largest sources of Cu are tap water and roofs. For Zn the largest sources are galvanized material and car washes [4]. In the case of Ni, the largest sources are chemicals used in the wastewater treatment plant and drinking water itself. Regarding to the Hg, the most dominant emission source is the amalgam in teeth [4]. Regarding to the Pb, Cr and Cd, where sources are more poorly understood, the largest contributors for all are car washes [4]. Here table 1 summarizes the reasons of presence of heavy metals.

Table 1. Reasons of presence of heavy metals in water and/or wastewater [5]

Heavy metal	Reason of presence
Arsenic (As)	• In groundwaters, where there are sulfide mineral deposits and sedimentary deposits deriving from volcanic rocks, the concentrations can be significantly elevated. • Found in diet, particularly fish and shellfish.
Cadmium (Cd)	• Originally, used in steel and plastic factories. • Used in batteries. • Contamination from fertilizer and local air pollution.
Chromium (Cr)	• Leaching of chromium from chromium – zinc plated taps.
Copper (Cu)	• Corrosion of pipes, valves, and fittings. • Copper sulfate pentahydrate is sometimes added to the surface water for the control of algae.
Iron (Fe)	• Corrosion of steel and cast iron pipes. • Use of iron coagulants.

Heavy metal	Reason of presence
	• Generally, it is not of health concern, but may affect acceptability of drinking water.
Lead (Pb)	• Principally, used in the production of lead-acid batteries. • Organolead compounds 'tetraethyl and tetramethyl lead' are used as anti-knock and lubricant agents in petrol.
Mercury (Hg)	• Mercury is used in the electrolytic production of chlorine gas. • Used is dental amalgam.
Nickel (Ni)	• Mainly used in the production of stainless steel and nickel alloys. • Released from chromium – nickel plated taps and fittings.
Uranium (U)	• Result of leaching from natural deposits where uranium is widespread in nature, occurring in granites and various other minerals. • Release in mill tailings. • Emission from nuclear plants. • Combustion of coal and other fuels contaminated with uranium. • Use of phosphate fertilizers that contain uranium.
Zinc (Zn)	• Diet is the principal source of zinc. • Dissolution of zinc from pipes in taps, pipes and fittings.

2.1. Industrial Wastewater Sources

Environmental pollution by heavy metals always raises fingers against plants. Electroplating and metal surface treatment processes generate significant quantities of wastewaters containing heavy metals (such as cadmium, zinc, lead, chromium, nickel, copper, vanadium, platinum, silver, and titanium). Also, conversion-coating, anodizing-cleaning, milling, printed circuit board (PCB) manufacturing, and etching are considered [6]. The wood processing industry, where a chromated copper-arsenate wood treatment produces arsenic-containing wastes, is also included [6]. Inorganic pigment manufacturing producing pigments that contain chromium compounds and cadmium sulfide; petroleum refining which generates conversion catalysts contaminated with nickel, vanadium, and chromium; and photographic operations producing film with high concentrations of silver and Ferro cyanide [6]. All of these generators produce a large quantity of wastewaters, residues, and sludges

that can be categorized as hazardous wastes requiring extensive waste treatment (Sorme and Lagerkvist, 2002).

2.2. Sewage - Households Sources

Heavy metals-contaminated wastewater categorized as "***households***" include emissions from food, amalgam, detergents, pipes (taps), drinking water, and artist paints. Drinking water itself includes some metals. Some of the drinking water piping networks is copper material of construction where the corrosion of these pipes causes drinking water contamination by Cu [4]. Food contains some heavy metals, e.g. the essential Cu and Zn. Detergents contain small amounts of heavy metals. Artist paints in the colors of yellow–red can contain Cd [4]. Amalgam, consisting mainly of Hg, Ag, Cu and Zn, is slowly released from fillings in teeth. However; the emissions of Cu and Zn are negligible in comparison to other sources [4].

3. Health Effects of Heavy Metals and Standard Limits

Heavy metals become toxic when they are not metabolized by the body and accumulate in the soft tissues. Heavy metals may enter the human body via food, water, air, or absorption through the skin in agriculture, manufacturing, pharmaceutical, industrial, or residential settings. Industrial exposure is common in adults. Ingestion is the most common route in children. Children may develop toxic levels from normal hand-to-mouth activity (ie, coming in contact with contaminated soil or eating objects that are not food such as dirt or paint chips). Heavy metals cause serious health effects, including reduced growth and development, cancer, organ damage, nervous system damage, and in extreme cases, death. Wastewater regulations were established to minimize human and environmental exposure to hazardous chemicals.

3.1. Maximum Contamination Level (MCL)

The maximum contamination level standards, for heavy metals, were established by United States Environmental Protection Agency (USEPA). MCL standards for heavy metals are summarized in table 2.

Table 2. The MCL standards for the most hazardous heavy metals (Babel and Kurniawan, 2003)

Heavy metal	Toxicities	MCL (mg/l) / [µg/l]
Arsenic (As)	Skin manifestations, visceral cancers, vascular disease	(0.05) / [50]
Cadmium (Cd)	Kidney damage, renal disorder, human carcinogen	(0.01) / [10]
Chromium (Cr)	Headache, diarrhea, nausea, vomiting, carcinogenic	(0.05) / [50]
Copper (Cu)	Liver damage, Wilson disease, insomnia	(0.25) / [250]
Nickel (Ni)	Dermatitis, nausea, chronic asthma, coughing, human carcinogen	(0.20) / [200]
Zinc (Zn)	Depression, lethargy, neurological signs and increased thirst	(0.80) / [800]
Lead (Pb)	Damage the fetal brain, diseases of the kidneys, circulatory system, and nervous system	(0.006) / [6]
Mercury (Hg)	Rheumatoid arthritis, and diseases of the kidneys, circulatory system, and nervous system	(0.00003) / [0.03]

3.2. World Health Organization (WHO)

WHO organization reported characteristics of heavy metals, presence, sources, health effects, concentration limits, and possible treatment technologies. Table 3 summarizes the health guideline of heavy metals in water reported by WHO.

Table 3. Health guideline of heavy metals reported by WHO [5]

Heavy metal	Concentration limit guideline (µg/l)	Health effect
Cadmium (Cd)	3	• Accumulation of Cd in kidneys and has a long biological half-life in humans of 10 – 35 years. • Carcinogenic by inhalation route.
Chromium (Cr)	50	• Chromium (VI) causes human carcinogen. • Stomach upsets and ulcers. • Convulsion. • Kidney and liver damage.
Copper (Cu)	2000 (2 mg/l)	• Gastrointestinal effects. • Wilson diseases. • Metabolic disorders of copper homeostasis.
Iron (Fe)	300 (0.3 mg/l)	• No health concern. • Only, affect the acceptability of drinking water.
Lead (Pb)	10	• Infants and children are considered to be the most sensitive. • Neurodevelopmental effects. • Impaired renal function. • Hypertension. • Impaired fertility and adverse pregnancy outcomes. • Cardiovascular diseases. • Increase in systolic blood pressure.

Heavy metal	Concentration limit guideline (µg/l)	Health effect
Mercury (Hg)	6	• Hemorrhagic gastritis. • Colitis. • Ultimate damage of the kidney.
Nickel (Ni)	20	• Carcinogenic to humans (group 1 & group 2).
Uranium (U)	30	• Nephritis.
Zinc (Zn)	3000 (3 mg/l)	• No health concern. • Only, affect the acceptability of drinking water.

4. Treatment Technologies

Heavy metals can be absorbed by living organisms. Once they enter the food chain, large concentrations of heavy metals may accumulate in the human body. If the metals are ingested beyond the permitted concentration, they can cause serious health disorders [6]. Therefore, it is necessary to treat metal-contaminated wastewater prior to its discharge to the environment. Heavy metal removal from inorganic effluent can be achieved by conventional treatment processes such as chemical precipitation, ion exchange, and electrochemical removal.

4.1. Chemical Precipitation

Chemical precipitation is the most widely used for heavy metal removal from inorganic effluent. The conceptual mechanism of heavy metal removal by chemical precipitation is presented in Eq. (1)

$$M^{2+} + 2(OH)^{-} \leftrightarrow M(OH)_2 \downarrow \quad (1)$$

Adjustment of pH to the basic conditions (pH 9–11) is the major parameter that significantly improves heavy metal removal by chemical precipitation. Lime and limestone are the most commonly employed precipitant agents due to their availability and low-cost in most countries [6]. Lime precipitation can be employed to effectively treat inorganic effluent with a metal concentration of higher than 1000 mg/l [6]. Other advantages of using lime precipitation include the simplicity of the process, inexpensive equipment requirement, and convenient and safe operations. However, chemical precipitation requires a large amount of chemicals to reduce metals to an acceptable level for discharge. Other drawbacks are its excessive sludge production that requires further treatment, slow metal precipitation, poor settling, the aggregation of metal precipitates, and the long-term environmental impacts of sludge disposal (Aziz et al., 2008).

There are other precipitant rather than lime. Sulfides are other precipitant selected. Table 4 summarizes the comparison in removal efficiency between different precipitants.

Table 4. Heavy metal removal using chemical precipitation [7]

Species	Initial metal concentration	Precipitants	Optimum pH	Removal efficiency (%)
Zn^{+2}	32 mg/l	CaO	9 – 10	99 – 99.3
Cu^{+2}, Zn^{+2}, Cr^{+3}, Pb^{+2}	100 mg/l	CaO	7 – 11	99.37 – 99.6
Cu^{+2}, Zn^{+2}, Pb^{+2}	0.018, 1.34, 2.3 mM	H_2S	3	100, >94,>92
Cr^{+3}	5363 mg/l	CaO and MgO	8	>99
Hg^{+2}	65.6, 188 mg/l	1,3-benzendiamidoethaneethiolate	4.7 and 6.4	>99.9
CuEDTA	25,50,100 mg/l	1,3,5-hexahydrotriazinedithiocarbamate	3	99,99.3,99.6

4.2. Ion Exchange

Ion exchange is another method used successfully in the industry for the removal of heavy metals from effluent. An ion exchanger is a solid capable of exchanging either cations or anions from the surrounding materials. Commonly used matrices for ion exchange are synthetic organic ion exchange resins. Ion-exchange processes have been widely used to remove heavy metals from wastewater due to their many advantages, such as high treatment capacity, high removal efficiency and fast kinetics [7]. Ion-exchange resin, either synthetic or natural solid resin, has the specific ability to exchange its cations with the metals in the wastewater. Among the materials used in ion-exchange processes, synthetic resins are commonly preferred as they are effective to nearly remove the heavy metals from the solution (Alyüz and Veli, 2009). The most common cation exchangers are strongly acidic resins with sulfonic acid groups (-SO_3H) and weakly acid resins with carboxylic acid groups (-COOH). Hydrogen ions in the sulfonic group or carboxylic group of the resin can serve as exchangeable ions with metal cations. As the solution containing heavy metal passes through the cations column, metal ions are exchanged for the hydrogen ions on the resin with the following ion-exchange process:

$$nR{-}SO_3H + M^{n+} \rightarrow \left(R{-}SO_3^-\right)_n M^{n+} + nH^+ \quad (2)$$

$$nR - COOH + M^{n+} \rightarrow \left(R - COO^-\right)_n M^{n+} + nH^+ \quad (3)$$

The disadvantage of this method is that it cannot handle concentrated metal solution as the matrix gets easily fouled by organics and other solids in the wastewater [6]. Moreover; ion exchange is nonselective and is highly sensitive to the pH of the solution. Table 5 describes the results of efficiency of heavy metal removal of clinoptilolite ion-exchanger resin as an example.

Table 5. Selective heavy metal uptake using clinoptilolite ion-exchange resin [7]

Species	Operation styles	Initial metal conc. (mg/L)	Optimum pH	Adsorption capacity (meq/g)	Removal efficiency (%)	Clinoptilolite (g/L)
Pb^{2+}	Fixed-bed and batch operation	2072	4.0	0.21–1	NA	20–40
Pb^{2+}	Batch experiments	1036	4.0	NA	55	20
Ni^{2+}	Fluidized bed process	2900	NA	0.5–1.77	NA	50
Ni^{2+}	Batch experiments	25	7.0	0.11	93.6	15
Zn^{2+}	Batch experiments	65.4–654	5.0	2.237 ± 0.15	100	25
Pb^{2+}	Batch experiments	162.65–400	4.0	1.361, 1.372	NA	0.52–4.17

4.3. Membranes

Membrane filtration has received considerable attention for the treatment of inorganic effluent, since it is capable of removing not only suspended solid and organic compounds, but also inorganic contaminants such as heavy metals. Depending on the size of the particle that can be retained, various types of membrane filtration such as ultrafiltration, nanofiltration and reverse osmosis can be employed for heavy metal removal from wastewater.

4.3.1. Ultrafiltration

Ultrafiltration (UF) is a membrane technique working at low transmembrane pressures for the removal of dissolved and colloidal material. Since the pore sizes of UF membranes are larger than dissolved metal ions in the form of hydrated ions or as low molecular weight complexes, these ions would pass easily through UF membranes.

Ultrafiltration (UF) utilizes permeable membrane to separate heavy metals, macromolecules and suspended solids from inorganic solution on the basis of the pore size (5–20 nm) and molecular weight of the separating compounds (1000–100,000 Da).

Using the amicon-generated cellulose YM10 was used as the ultrafilter. About 100% and 95 % rejection were achieved at pH ranging from 8.5 to 9.5 for Cu (II) and Zn (II) ions, respectively [6]. Table 6 summarizes heavy metal removal performance by the miceller enhanced ultrafiltration (MEUF) and polymer enhanced ultrafiltration (PEUF).

Table 6. Heavy metal removal by MEUF and PEUF [7]

UF type	Membrane	Surfactant/complexing agent	Heavy metal	Initial concentration	Optimum pH	Removal efficiency (%)
MEUF	Ceramic	Dodecylbenzenesulfonic acid, dodecylamine	Pb^{+2}, AsO^{-4}	4.4 – 7.6 mg/l	7.47	Pb: >99%, As: 19%
MEUF	Polysulfone	Sodium dodecyl sulfate (SDS)	Cd^{+2}, Zn^{+2}	50 mg/l	NA	92 – 98
MEUF	Amicon regenerated cellulose	Sodium dodecyl sulfate (SDS)	Cd^{+2},Zn^{+2}	0.5 mM	NA	99
MEUF	Polycarbonate	Sodium lauryl ether sulfate	Ni^{+2}	0.2 mM	7	98.6
PEUF	Polyethersulfone	polyethyleneimine (PEI)	Cu^{+2},Ni^{+2}	50 mg/l	pH > 6 , pH > 8	94, 100
PEUF	Polyethersulfone	Carboxy methyl cellulose	Cu^{+2},Cr^{+3},Ni^{+2}	10 mg/l	7	97.6, 99.5, 99.1
PEUF	AMICON 8400	Sodium polyacrylate, PEI	Cr (III),Cr (VI)	5, 50 mg/l	6 – 7, 5- 6	82 – 100
PEUF	Ceramic	Poly(acrylic acid) sodium	Cu^{+2}	160 mg/l	5.5	99.5
PEUF	Polysulfone	Poly (ammonium acrylate)	Cd (II)	112.4 mg/l	6.32	99

4.3.2. Reverse Osmosis (RO)

The reverse osmosis (RO) process uses a semi-permeable membrane, allowing the fluid that is being purified to pass through it, while rejecting the contaminants. RO is one of the techniques able to remove a wide range of dissolved species from water. It accounts for more than 20% of the world's desalination capacity. RO is an increasingly popular wastewater treatment option in chemical and environmental engineering. Using appropriate RO systems to remove heavy metals have been investigated, but these have yet to be widely applied.

Cu^{+2} and Ni^{+2} ions were successfully removed by the RO process and the rejection efficiency of the two ions increased up to 99.5% by using Na_2EDTA [7]. Dialynas and Diamadopoulos applied a pilot-scale membrane bioreactor system in combination with RO and they found heavy metal removal efficiencies were very high. The major drawback of RO is the high power consumption due to the pumping pressures, and the restoration of the membranes.

4.3.3. Nanofiltration (NF)

Nanofiltration (NF) is the intermediate process between UF and RO. NF is a promising technology for the rejection of heavy metal ions such as nickel, chromium, copper and arsenic from wastewater [7]. NF process benefits from ease of operation, reliability and comparatively low energy consumption as well as high efficiency of pollutant removal. Figoli. (2010) studied the removal of pentavalent arsenic from synthetic water by two commercial NF membranes (NF90 and N30F) [7]. It was found that an increase of pH and a decrease of operating temperature and arsenic (As) feed concentration led to higher (As) removal for both membranes. Among the parameters affecting the (As) rejection, feed concentration plays a key role for the production of a permeate stream.

In recent years, Murthy and Chaudhari devoted a lot in the removal of heavy metal ions using NF membrane. They reported the application of a thin-film composite polyamide NF membrane for the rejection of nickel ions from aqueous wastewater [7]. The maximum observed rejection of nickel is found to be 98% and 92% for an initial feed concentration of 5 and 250 mg/l, respectively. They investigated the binary heavy metals (cadmium and nickel) separation capability of a commercial NF membrane from aqueous solutions (Murthy and Chaudhari, 2009). The maximum observed solute rejection of nickel and cadmium ions is 98.94% and 82.69%, respectively, for an initial feed concentration of 5 mg/L.

Table 7 shows the efficiency of heavy metal removal between different membranes.

Table 7. A list of some selected examples of heavy metal removal by RO, NF and NF+RO [7]

Membrane	Heavy metal	Initial metal Conc.	Removal efficiency (%)
RO	Cu^{2+}, Ni^{2+}	500 mg/L	99.5
RO	Cu^{2+}	20–100 mg/L	70–95
RO	As	<500 μg/L	As(V) 91–99, As(III) 20–55
RO	Ni^{2+}, Zn^{2+}	Ni^{2+}: 44–169	99.3
		Zn^{2+}: 64–170 mg/L	98.9
NF	Cu^{2+}	10 mM	47–66
NF	Cr(VI)	NA	99.5
NF	Cu^{2+}	0.47 M	96–98
RO + NF	Cu^{2+}	2 g/L	>95
RO + NF	Cu^{2+}	15 mg/L	95–99

4.4. Electrodialysis (ED)

Electrodialysis (ED) is a membrane separation in which ionized species in the solution are passed through an ion exchange membrane by applying an electric potential. The membranes are thin sheets of plastic materials with either anionic or cationic characteristics. When a solution containing ionic species passes through the cell compartments, the anions migrate toward the anode and the cations toward the cathode, crossing the anion-exchange and cation-exchange membranes. Figure 1 shows the principles of electrodialysis. Some interesting results were reported by Tzanetakis [6], who evaluated the performance of the ion exchange membranes for the electrodialysis of Ni (II) and Co (II) ions from a synthetic solution. Two cation-exchange membranes, perfluorosulfonic Nafion 117 and sulfonated polyvinyldifluoride membrane (SPVDF) were compared under similar operating conditions. By using perfluorosulfonic Nafion 117, the removal efficiency of Co (II) and Ni (II) were 90% and 69%, with initial metal concentrations of 0.84 and 11.72 mg/L, respectively.

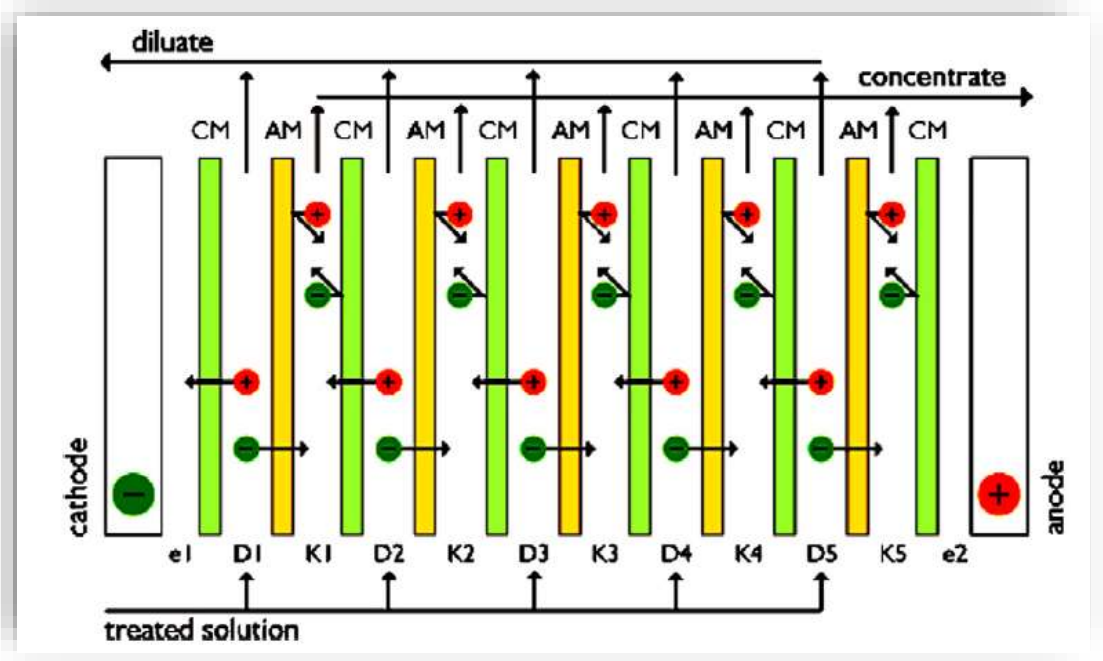


Figure 1. Electrodialysis principles. CM – cation-exchange membrane, D – diluate chamber, e1 and e2 – electrode chambers, AM – anion exchange membrane, and K – concentrate chamber [6]

5. Comparison Between Different Treatment Methods

The treatments from heavy metals are not limited to the previous methods mentioned. Others are employed such as aeration, coagulation, biological process, and adsorption. In this project (sections 5 and 6), treatment using adsorption, especially low-cost adsorbent, are described in details. Table 8 summarizes the comparison between different treatment methods.

Table 8. The main advantages and disadvantages of various physic-chemical methods for the treatment of heavy metal in wastewater [6]

#	Treatment method	Advantages	Disadvantages
1	Chemical precipitation	Low capital cost, simple operation	Sludge generation, extra operational cost for sludge disposal
2	Adsorption with new adsorbents	Low-cost, easy operating conditions, having wide pH range, high metal-binding capacities	Low selectivity, production of waste products
3	Membrane filtration	Small space requirement, low pressure, high separation selectivity	High operational cost due to membrane fouling
4	Electrodialysis	High separation selectivity	High operational cost due to membrane fouling and energy consumption
5	Photocatalysis	Removal of metals and organic pollutant simultaneously, less harmful by-products	Long duration time, limited applications

6. Results and Discussion

6.1. Heavy Metal Removal Using Adsorption

Adsorption is a mass transfer process by which a substance is transferred from the liquid phase to the surface of a solid, and becomes bound by physical and/ or chemical interactions [6]. Various low-cost adsorbents, derived from agricultural wastes, industrial by-products, natural materials, or modified biopolymers, have been recently developed and applied for the removal of heavy metals from metal-contaminated wastewater. Technical applicability and cost-effectiveness are the key factors that play major roles in the selection of the most suitable adsorbent to treat inorganic effluent.

Activated carbon (AC) adsorbents are widely used in the removal of heavy metal contaminants. Its usefulness derives mainly from its large micropore and mesopore volumes and the resulting high surface area. A large number of researchers are studying the use of AC for removing heavy metals (Jusoh et al., 2007; Kang et al., 2008). Nowadays, the depleted source of commercial coal-based AC results in the increase of price. To make progress in heavy metals adsorption to AC without the expense of decline in the pollutants adsorption, additives and AC composite could be an option.

Consequently, many researches are carried out for naturally low-cost adsorbent. In this assay project, some of low-cost adsorbent are discussed and described. Zeolite, chitason, calcined phosphates and clays are described as definitions, how manufactured and heavy metal removal performance at different conditions through section 6. Sewage sludge – based activated carbon is described in more details in section 7.

6.1.1. Chitosan

Chitosan and its derivatives are examples of value-added materials. The molecular structure of chitosan is similar to cellulose [8] as shown in figure 2. They are produced from chitin shown in figure 3, which is a natural carbohydrate polymer found in the skeleton of crustaceans, such as crab, shrimp. Chitosan is a polymer obtained from deacetylation of chitin [9]. It is made by treating shrimp and other crustacean shells with the alkali sodium hydroxide. Here, figure 2 and 3 show the molecular structure of chitosan and chitin, respectively.

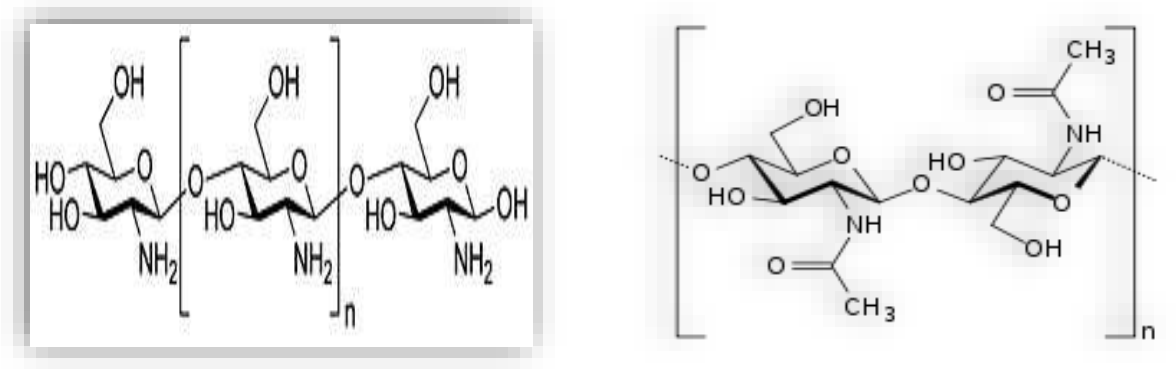


Figure 2. Molecular structure of chitosan

6.1.1.1. Preparation of Chitosan [9]

Shrimp shell waste materials are collected. Shrimp shells are scraped free of loose tissue, washed with cold water and dried in sun for 2 days. Chitin is extracted from shrimp shell. The process mainly involved the following steps:

De-mineralizations of shells

In this step, the shells are suspended in 4% HCl at room temperature in the ratio of 1: 14 (w/v). After 36 hours, the shells are quite squashy and are rinsed with water to remove acid and calcium chloride.

De-proteinization of shells

The demineralized shells are then treated with 5% NaOH at 90°C for 24 hours with a solvent to solid ratio of 12: 1 (v/w). The residue is then collected and washed to neutrality in running tap water then it was dried in sun and the product is chitin. The preparation of Chitosan is simply deacetylation of chitin. Removal of acetyl groups from the chitin is achieved by using 70% NaOH solution with a solid to solvent ratio of 1: 14 (w/v) at room temperature for 72 hours. The mixture is stirred after some times for homogenous reaction. The resulting chitosans are washed to neutrality in running tap water and rinsed with distilled water. Then filtered and dried in sun.

6.1.1.2. Heavy Metal Removal Performance

Various researches on chitosan have been done in recent years. In 1988, the utilization of chitosan for cadmium removal was intensively investigated [8]. Also, it was demonstrated that an adsorption capacity of 5.93 mg of Cd^{+2}/g of chitosan was achieved at a pH range of 4.0–8.3 and that the presence of ethylene diamine tetra acetic acid (EDTA) significantly decreased the cadmium removal by chitosan since EDTA, a stronger chelating agent than chitosan, suppressed the metal uptake by chitosan [8].

It was found that the maximum adsorption capacities of chitosan for Hg^{+2}, Cu^{+2}, Ni^{+2}, and Zn^{+2} were 815, 222, 164, and 75 mg/g, respectively [8]. It was reported that an adsorption capacity of 273 mg of Cr^{+6} / g of chitosan was achieved at pH of 4.0 [8]. Regarding to the copper, 1 gram of chitosan could adsorb 4.7 mg of Cu^{+2} noticed at pH of 6.2 [8]. It was reported that pH of 5.5 was found to be optimum for copper removal and about 13 mg of Cu^{+2} could be adsorbed by 1 g chitosan at equilibrium condition. Table 9 shows the performance of different heavy metal removal by chitosan and its derivatives.

Table 9. Adsorption capacities (mg/g) of chitosan for various heavy metals [8]

Material		Cr^{+6}	Ni^{+2}	Pb^{+2}	Hg^{+2}	Zn^{+2}	Cu^{+2}	Cd^{+2}	Pt^{+6}	pH
Chitosan								5.93		4 – 8.3
					815	75	222			
					430					
		273								4.0
			2.4	16.36	51.55		16.80	8.54		
							4.7			6.2
							13			5.5
Chitosan beads								250		
Non-crosslinked chitosan		80					85			
Crosslinked chitosan		50					86			
Crosslinked chitosan	GD*								280	
	GD*						60			6
	EC**						62			6
	EGDE***						46			6

* Glutaraldehyde

** Epichlorohydrin

*** Ethylene glycol diglycidyl ether

6.1.2. Calcined Phosphate (CP)

Calcined phosphate (CP) has been studied for the removal of heavy metals as heterogeneous catalyst. The abundance of natural phosphate, its low price, its non-aggressive nature towards the environment and the results obtained in this study, classifies the calcined natural phosphate as a new competitor of some well-known adsorbents for wastewater treatment.

According to figure 5, the adsorption capacities obtained at pH 5 are 85.6, 29.8, and 20.6 mg/g for Pb^{+2}, Cu^{+2} and Zn^{+2}, respectively (A. Aklil, M. Mouflih, S. Sebti 2004). However; the dominant mechanism, at pH 2 and 3, is the dissolution of CP and precipitation of a fluoropyromorphite for lead and the formation of solid-solution type fluorapatite for copper.

6.1.2.1. Preparation of Calcined Phosphate

Aklil carried out for the preparation of calcined phosphate and studied the performance of heavy metal removal. Phosphate rock used by Aklil came from an extracted ore in Khouribga, Morocco. The fraction of 100–400 μm grain size was washed with water, calcined at 900 °C for 2 h, washed again, calcined at 900 °C for 0.5 h and ground (63–125 μm). The structure of calcined phosphate (CP) is similar to that of fluorapatite ($Ca_{10}(PO_4)_6F_2$). The CP shows low surface area (1 – 2 m^2 / g) together with a low total pore volume (0.007 cm^3 / g) [1].

6.1.2.2. Performance of Heavy Metal Removal by Calcined Phosphate

Aklil studied the performance of heavy metal removal. For the determination of adsorption characteristics of Pb^{+2}, Cu^{+2}, and Zn^{+2} ions in the CP, the initial concentrations of the metal ions were varied between 5 and 140 mg / L while the dry phosphate weight of the adsorbent was kept constant at 0.5 g / L at pH 5 [1]. Lead was observed with highest adsorption capacity among other heavy

metals. Figures 4, 5 and 6 show the performance of heavy metal removal by CP (A. Aklil, M. Mouflih, S. Sebti 2004).

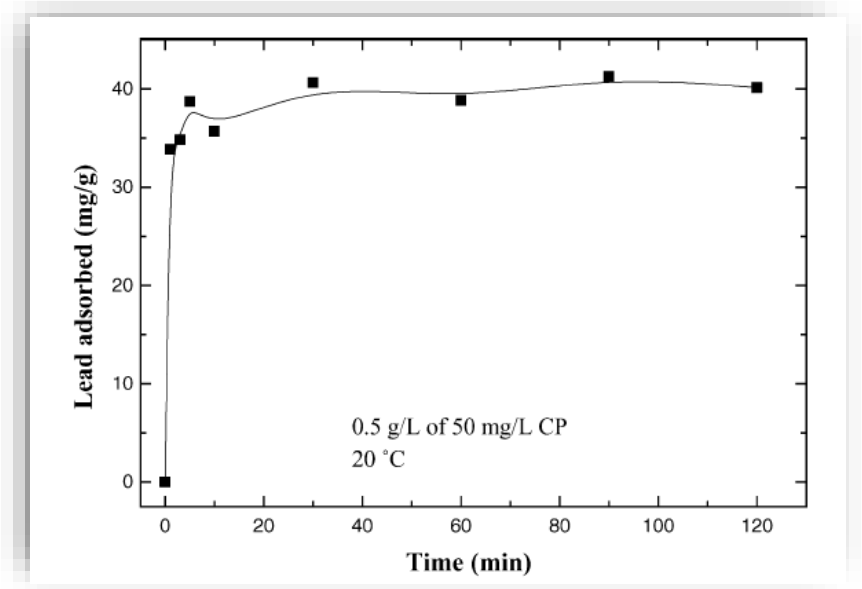


Figure 3. Kinetic curve of lead sorption on CP ([Pb^{+2}] = 50 mg / L, (amount of CP = 1g/L and pH 5)) [1]

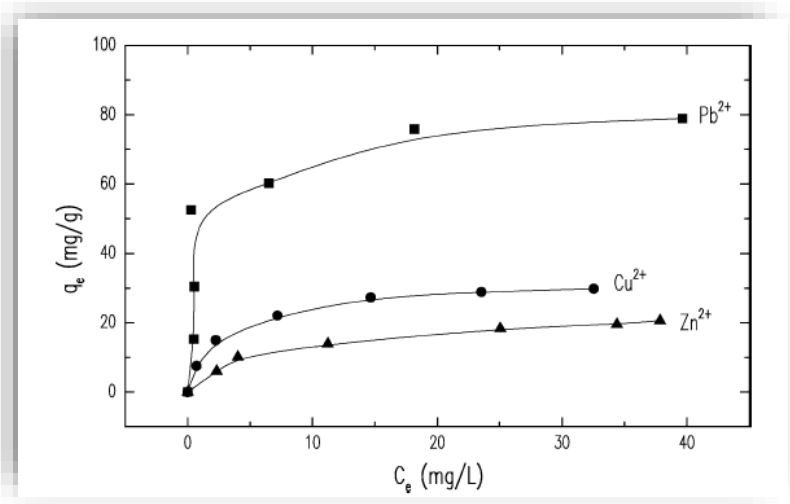


Figure 4. Isotherms of the adsorption of lead, copper, and zinc onto CP (amount of CP = 0.5 g / L and pH 5) [1]

Noting that Ce (mg / L) is equilibrium concentration, and qe (mg / g) is the amount of adsorption per unit mass at equilibrium.

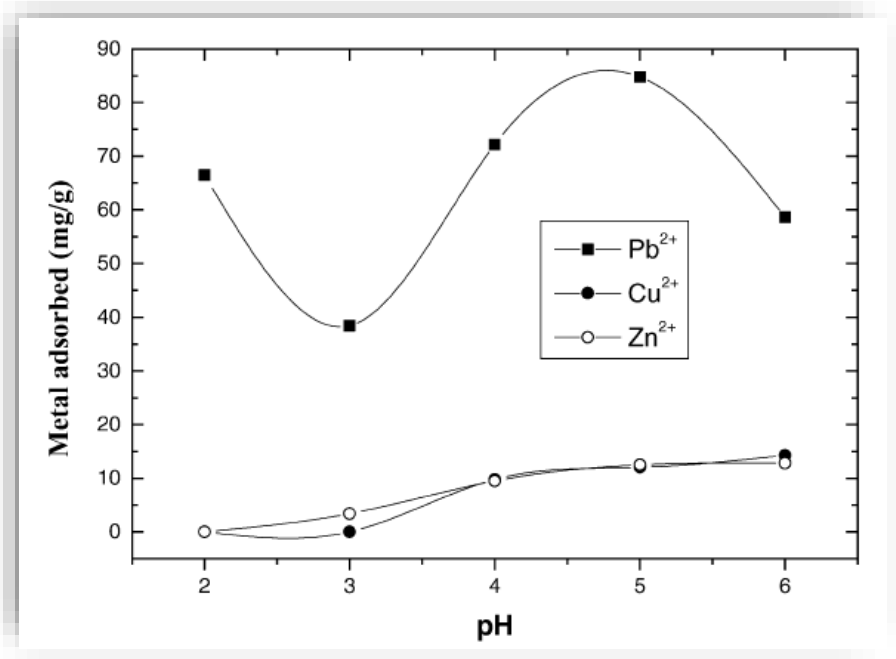


Figure 5. Adsorption of lead, copper, and zinc on CP at different pH ($[Pb^{+2}]$ = 100 mg / L, $[Cu^{+2}]$ = $[Zn^{+2}]$ = 50 mg / L, and amount of CP = 1g / L [1]

6.1.3. Zeolite

Zeolites are microporous, aluminosilicate minerals commonly used as commercial adsorbents. Natural zeolites gained a significant interest among scientists due to their ion-exchange capability to preferentially remove unwanted heavy metals. Large deposits of natural zeolites are available in many countries such as Greece, UK, Italy, Mexico, Iran, and Jordan.

Zeolites consist of a wide variety of species such as clinoptilolite and chabazite [8]. Among the most frequently studied natural zeolites, clinoptilolite was shown to have high selectivity for certain heavy metal ions such as Pb^{+2}, Cd^{+2}, Zn^{+2}, and Cu^{+2} [8]. Approximately 1.4 mg/g of Pb^{+2} and 1.2 mg/g of Cd^{+2} were removed [8].

It was also reported that conditioning of zeolites with NaOH solution improved removal efficiency. Chabazite and clinoptilolite treated with sodium hydroxide performed best with Pb^{+2} and Cd^{+2} exchange capacity exceeding 100 mg/g [8]. The two zeolites were evaluated with respect to their performance for treating effluents contaminated with Pb^{+2}, Cd^{+2}, Cu^{+2}, Zn^{+2}, Ni^{+2}, and Co^{+2}. It was reported that both the zeolites exhibited 100% removal efficiency at the metal concentration of 10 mg/l. It was reported that dissolved Pb and Cd were effectively removed in the acidic pH range. Tables 10, 11, and 12 show the performance of heavy metal removal by different zeolites.

Table 10. Metal uptake by clinoptilolite at different temperatures and particle size [8]

Particle size of clinoptilolite (μm)	Pb^{2+} [a]		Cd^{2+} [a]	
	25 °C	50 °C	25 °C	50 °C
<600	1.31	1.41	1.06	1.20
160–600	1.29	–	1.02	–
600–1000	1.28	1.31	1.01	1.12
1000–2000	1.27	1.29	0.98	1.08

[a] Pb^{2+} and Cd^{2+} taken at equilibrium (meq/g).

Table 11. Adsorption capacities (mg/g) of zeolites for some heavy metals [8]

Material	Cd^{+2}	Cr^{+3}	Cr^{+6}	Co^{+2}	Ni^{+2}	Zn^{+2}	Cu^{+2}	Pb^{+2}
Clinoptilolite	2.40	0		1.42	0.48	0.50	1.64	1.60
	1.20							1.40
	70							62
	3.70		2.40	1.50	0.90	2.70	3.80	6
Chabazite	137							175
	6.70		3.60	5.80	4.50	5.50	5.10	6
Chabazite–phillipsite		7.10						
		0.25			0.56	0.04	0.37	

Table 12. Summary of column runs for Ni^{+2}, Zn^{+2}, Cu^{+2}, Cr^{+3}, and Fe^{+2} uptakes by Jordanian zeolites [8]

Heavy metal	Ni^{+2}	Zn^{+2}	Cu^{+2}	Cr^{+2}	Fe^{+2}
Efficiency %	29.60	2.20	22.70	19.70	3.10

6.1.4. Clays

It is widely known that there are three basic species of clay: smectites (such as montmorillonite), kaolinite, and micas [8].

It was found that the adsorption capacity of Pb^{+2} and Cd^{+2} is greater on montmorillonite (Pb: 0.68, Cd: 0.72 mg/g) than on kaolinite (Pb: 0.12, Cd: 0.32 mg/g) [8]. It was also indicated that the presence of cationic surfactant reduces the uptake of both ions, while the anionic surfactants enhance their removal.

It was found that the Zn^{+2} is adsorbed in larger amounts than Cd^{+2} due to the fact that zinc has higher ionic potential than cadmium. Therefore, Zn^{+2} adsorption was favored over Cd^{+2} by cationic interchange. It was reported that an adsorption capacity of 1.25 mg of Zn^{+2}/g was achieved by kaolinite and that the maximum removal efficiency was found to be at pH of 8.0 [8].

Adsorption capacity by clays is affected by temperature either exothermic or endothermic (tables 13 and 15). Tables 13, 14, and 15 show the adsorption capacity of different heavy metal ions by different clays, and the effect of different temperatures.

Table 13. Adsorption capacity of China clay and wollastonite for Pb^{+2} at different temperatures [8]

Type of adsorbent	Temperature (°C)	Adsorption capacity (mg/g)	ΔG° (kJ/mol)	Remarks
China clay	20	0.411	-8.08	ΔH° (kJ/mol) = -77.95 kJ/mol
	30	0.395	-4.53	
	40	0.346	-3.07	
Wollastonite	20	1.680	-2.36	ΔH° (kJ/mol) = -16.40 kJ/mol
	30	1.290	-1.58	
	40	1.100	-1.05	

Table 14. Adsorption capacities (mg/g) of clay for different heavy metals [8]

Material	Cu^{+2}	Pb^{+2}	Cd^{+2}	Zn^{+2}	Cr^{+6}	Sr^{+2}	pH	Remarks
Montmorillonite		0.68	0.72					
			4.78	4.98				
Kaolinite				1.25			8.0	
		0.12	0.32					
		1.41						
Illite		4.29						
Bentonite			11.41	4.54				
					0.57			
						32.94		
				52.91				
		20					3.4	
Fly ash – wollastonite	1.18							
Sarooj clay (Samir I. Abu-Eisha)				17			7	Maximum adsorption capacity (Qe)
			20				5	
		45					5	

Table 15. Adsorption capacity of bentonite for hexavalent chromium at different temperatures [8]

Temperature (°C)	Adsorption capacity (mg/g)	ΔG° (kJ/mol)	Remarks
20	0.33	-0.24	ΔH° (kJ/mol) = + 5.62 kJ/mol Maximum adsorption at pH = 2 by bentonite
30	0.45	-0.44	
40	0.57	-0.64	

6.1.5. Miscellaneous Adsorbents and Comparisons

Many attempts were carried out to figure out the removal performance from natural available materials.

Old newspaper pulp, chemically treated by disodium hydrogen phosphate (Na_2HPO_4), was tested for the removal of Cd (II) (Mona Ossman). Maximum adsorption capacity of Cd onto treated newspaper pulp (TNP) was 10 mg/g at pH of 6 shown in figure 7 [10].

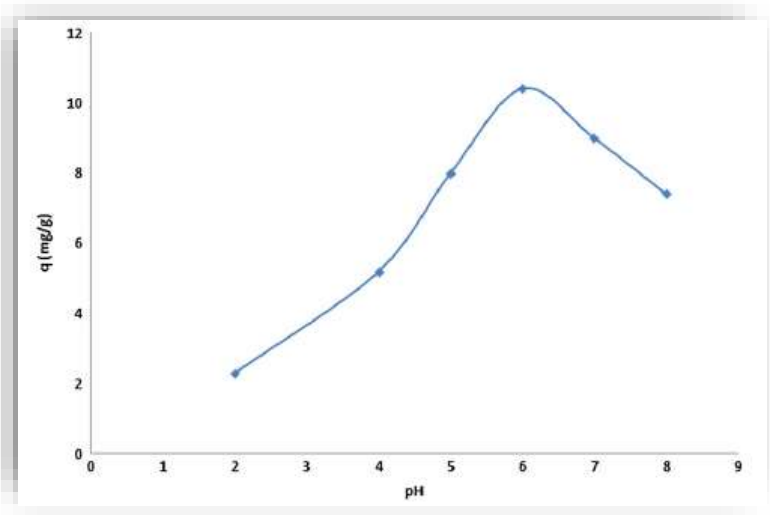


Figure 6. Effect of pH of the solution on adsorption of Cd(II) onto TNP. At an initial concentration of 30 mg/L and TNP dosage of 0.33 g/L at 22°C [10]

Activated carbons are widely usually used for the removal of heavy metals. However; due to high price of commercial activated carbons, many attempts were carried out for the production of activated carbons from naturally available organic matters to test heavy metal removal. Metal oxides also were tested, and results were reported (table 16). Biomasses and agricultural wastes, either activated or non-activated, had good results (tables 17 and 22). Industrial wastes have shown good removal performance (table 18).

Table 16. Adsorption capacities (mg/g) of natural oxides for some metals [8]

Material	Cd^{+2}	Pb^{+2}	Cr^{+6}	pH
Aluminum oxide			11.7	4
	31	33		
Ferric oxide	72	230		

Table 17. Unmodified/modified agricultural waste utilized for removal of heavy metals by adsorption. CSC: coconut shell charcoal, PSA: phosphoric acid-activated pecan shell carbon, PSC: carbon dioxide-activated pecan shell carbon, PSS: steam-activated pecan shell carbon [11]

Species	Type of adsorbent	Optimum dose (g/L)	Initial metal concentration (mg/L)	Optimum pH	Adsorption capacity (mg/g)	Retail price (US$/kg)	ΔH° (kJ/mol)	ΔG° (kJ/mol)	ΔS° (kJ/mol)	References
Cr(VI)	As-received CSC	24	20	6.0	2.18	0.25	NA	NA	NA	Babel and Kurniawan (2004b)
	CSC coated with chitosan	18	20	4.0	3.65	0.25				
	H_2SO_4-treated CSC	15	20	6.0	4.05	0.25				
	HNO_3-treated CSC	12	20	4.0	10.88	0.25				
Cd(II)	Cocoa shell	5	28.10	2.0	4.94	NA	NA	NA	NA	Meunier et al. (2003)
Cr(III)		5	13.00	2.0	2.52					
Cu(II)		5	15.88	2.0	2.87					
Ni(II)		5	14.68	2.0	2.63					
Zn(II)		5	16.35	2.0	2.92					
Cu(II)	Pecan shell	1	500	3.6	95.0	NA	NA	NA	NA	Shawabkeh et al. (2002)
Ni(II)	Orange peel	20	1000	6.0	158.0	NA	10.37	−9.49	−0.06	Ajmal et al. (2000)
	Parthenium	1	70	5.0	54.35	NA	NA	NA	NA	Kadirvelu et al. (2002)
Ni(II)	Orange peel	1	25	6–8	6.01	NA	NA	NA	NA	Annadurai et al. (2002)
Cu(II)		1	25	6–8	3.65					
Zn(II)		1	25	6–8	5.25					
Cr(VI)	Sawdust	2.4	100	2.0	15.82	NA	NA	−2.02	NA	Dakiky et al. (2002)
Cr(VI)	Maple sawdust	50	10	5.0	5.1	NA	NA	NA	NA	Yu et al. (2003)
Zn(II)	PSA	10	32.70	NA	13.9	NA	NA	NA	NA	Bansode et al. (2003)
Cu(II)		10	31.75		6.84					
Zn(II)	PSC	10	32.70		6.62					
Cu(II)		10	31.75		0.001					
Zn(II)	PSS	10	32.70		7.38					
Cu(II)		10	31.75		18.1					

Remarks: *NA: Not available.

Table 18. Removal of heavy metals by adsorption using industrial by-products. NA: Not available [11]

Species	Type of adsorbent	Optimum dose (g/L)	Initial metal concentration (mg/L)	Optimum pH	Adsorption capacity (mg/g)	Retail price (US$/kg)	ΔH° (kJ/mol)	ΔG° (kJ/mol)	ΔS° (kJ/mol)	References
Ni(II)	Red mud	7	400	9.0	160	NA	NA	NA	NA	Zouboulard Kydros (1993)
	Fly ash	1	50	8.5–9.0	NA	NA	NA	NA	NA	Mavros et al. (1993)
Zn(II)	Green sands	40	100	5.5–6.0	32.46	NA	+15.76	−12.66	+0.168	Lee et al. (2004)
Cu(II)	Blast-furnace slag	NA	214.63	7.5	133.35	NA	NA	NA	NA	Dimitrova (1996)
Ni(II)		NA	205.45	7.5	55.76					
Zn(II)		NA	220.40	9.0	103.33					
Cu(II)	Iron slags	2	200	3.5–8.5	88.50	NA	NA	NA	NA	Feng et al. (2004)
Pb(II)		2	200	3.5–8.5	95.24					
Cu(II)	Steel slags	2	200	5.2–8.5	16.21	NA	NA	NA	NA	
Pb(II)		2	200	5.2–8.5	32.26					
Ni(II)	Activated slag	10	250	4.0	30		+9.28	−18.50	0.091	
Cu(II)	(batch studies)	20	500	5.0	29		+17.99	−15.02	0.108	
Ni(II)	Activated slag	NA	248	NA	66	0.038	NA	NA	NA	Gupta (1998)
Cu(II)	(column studies)	NA	248	NA	38		NA	NA	NA	
Cd(II)	Bagasse	10	14	6.0	2.0	NA	−9.39	−4.95	+14.55	Gupta et al. (2003)
Ni(II)	Fly ash	10	12	6.5	1.70		−12.19	−5.44	+20.89	
Ni(II)	Magnetite	1	20	5.5–6.0	18.43	NA	NA	NA	NA	Ortiz et al. (2001)
Cr(VI)	Bagasse	4	100	6.0	0.03	NA	NA	NA	NA	Rao et al. (2002)
	Fly ash	4	90	6.0	0.01					
Ni(II)	Bagasse	10	90	8.0	0.001					
	Fly ash	10	100	8.0	0.0002					
Ni(II)	Fly ash type	20	25	8.0	1.16					
Cu(II)	Seyitomer	20	25	7.0	1.25					
Ni(II)	Fly ash type	20	25	8.0	0.99	NA	NA	NA	NA	Bayat (2002)
Cu(II)	Afsin-Elbistain	20	25	7.0	1.35					
Cr(VI)	Hydrous titanium oxide	20	0.1	1.5	30.0	NA	NA	NA	NA	Ghosh et al. (2003)

Table 19. Heavy metal uptake by natural materials through adsorption. SDS: sodium dodecyl sulfate [11]

Species	Type of adsorbent	Optimum dose (g/L)	Initial metal concentration (mg/L)	Optimum pH	Adsorption capacity (mg/g)	Retail price (US$/kg)	ΔH° (kJ/mol)	ΔG° (kJ/mol)	ΔS° (kJ/mol)	References
Cr(VI)	NaCl-treated zeolite	9	20.0	4.5	3.23					Babel and
	As-received zeolite	27	20.0	4.5	1.79	0.75	NA	NA	NA	Kurniawan (2003b)
Zn(II)	Natural zeolite	10	65.4	6.5	13.06	NA	NA	NA	NA	Perić et al. (2004)
Cu(II)		10	64.3	5.5–6.5	25.04					
Cd(II)	Na-Montmorillonite	1274	112.0	5.5	5.20	NA	NA	NA	NA	Abollino et al. (2003)
Cr(III)		1274	52.0		5.13					
Cu(II)		1274	63.5		3.04					
Ni(II)		1274	58.7		3.63					
Zn(II)		1274	65.4		3.61					
Ni(II)	HCl-treated clay	10	85	6.2	80.9	NA	NA	NA	NA	Vengris et al. (2001)
Cu(II)		10	90	6.2	83.3					
Zn(II)		10	85	6.2	63.2					
Cu(II)	SDS-modified	2.5	2857.5	4.0	16.13	NA	+7.05	−9.66	+9.09	Lin and Juang (2002)
Zn(II)	montmorillonite	2.5	2943.0	4.0	13.27		+7.39	−9.17	+6.39	
Cd(II)	Kaolinite	20	200	6.0	3.04	NA	NA	NA	NA	Ulmanu et al. (2002)
Cu(II)		20	200	6.0	4.47					
Cd(II)	Bentonite	20	200	6.0	9.27					
Cu(II)		20	200	6.0	18.16					
Cd(II)	Diatomite	20	200	6.0	3.24					
Cu(II)		20	200	6.0	5.54					
Cr(III)	Bentonite	10	20	5.0	4.29	NA	NA	NA	NA	Chakir et al. (2002)
	Perlite	10	20	5.0	1.4					

Table 20. Heavy metal uptake by natural materials through adsorption [11]

Species	Type of adsorbent	Optimum dose (g/L)	Initial metal concentration (mg/L)	Optimum pH	Adsorption capacity (mg/g)	Retail price (US$/kg)	ΔH° (kJ/mol)	ΔG° (kJ/mol)	ΔS° (kJ/mol)	References
Cu(II)	Kaolinite	5	20	4.0	1.9	NA	NA	NA	NA	Arias et al. (2002)
	Kaolinite-HA	5	20	4.0	4.8					
Cd(II)	Kaolinite	5	20	4.0	3.7					
	Kaolinite-HA	5	20	4.0	8.6					
Cd(II)	Kaolinite	20	100	6.5	0.75	NA	NA	NA	NA	Chantawong et al.
	Ball clay	20	100	6.5	2.24					(2003)
Cr(III)	Kaolinite	20	100	4.0	1.81					
	Ball clay	20	100	4.0	3.60					
Cu(II)	Kaolinite	20	100	5.0	0.76					
	Ball clay	20	100	5.0	1.60					
Ni(II)	Kaolinite	20	100	6.0	0.003					
	Ball clay	20	100	6.0	0.41					
Zn(II)	Kaolinite	20	100	6.5	1.80					
	Ball clay	20	100	6.5	2.88					
Ni(II)	Natural	10	100	6.0	19.3	NA	NA	NA	NA	Álvarez-Ayuso and
Cu(II)	vermiculite	10	100	5.0	26.0					García-Sánchez (2003)
Ni(II)	Exfoliated	10	100	6.0	5.91					
Cu(II)	vermiculite	10	100	5.0	8.60					
Cu(II)	Kaolinite	10	3159	NA	10.79	NA	+39.52	−4.61	+0.117	Yavuz et al. (2003)
Ni(II)		10	1010	NA	1.70		+37.27	−5.42	+0.107	
Co(II)		10	1000	NA	0.92		+21.52	−5.51	+0.054	
Mn(II)		10	1029	NA	0.45		+36.73	−6.69	+0.101	
Cr(VI)	Pyrite fines	20	100	5.0–6.5	10.00	NA	NA	NA	NA	Zoubulis et al. (1995)
Cd(II)	Glauconite	2	5	4.0–6.5	4.10	NA	NA	NA	NA	Smith et al. (1996)
Zn(II)		2	5	4.0–6.5	1.37					
Cr(VI)	Wollastonite	20	10.4	2.5	0.52	NA	NA	NA	NA	Sharma (2003)

Remarks: *NA: Not available.

Table 21. Miscellaneous low-cost adsorbents for metals decontamination using adsorption [11]

Species	Type of adsorbent	Optimum dose (g/L)	Initial metal concentration (mg/L)	Optimum pH	Adsorption capacity (mg/g)	Retail price (US$/kg)	ΔH° (kJ/mol)	ΔG° (kJ/mol)	ΔS° (kJ/mol)	References
Cu(II)	Coal	10	100	4.0	1.62	NA	NA	NA	NA	Karabulut et al. (2000)
Zn(II)		10	100	4.0	1.20					
Zn(II)	Coal	5	500	6.0	27.2	NA	NA	NA	NA	Solé et al. (2003)
Cu(II)	Sludge	1.2	38.1	4.0	9.50	NA	NA	NA	NA	Calace et al. (2003)
Cd(II)			67.4	4.0	10.23					
Ni(II)	Sludge-ash	1	5.1	>8.0	0.32	NA	+30.45	−31.12	0.20	Weng (2002)
Cd(II)	Anaerobic sludge	20	200	6.0	5.82	NA	NA	NA	NA	Ulmanu et al. (2002)
Cu(II)		20	200	6.0	0.25					
Cd(II)	Sewage sludge	10	40	5.5–6.0	16	NA	NA	NA	NA	Zhai et al. (2004)
Ni(II)		20	30	5.5–6.0	9					
Cd(II)	Coffee	10	200	7.0–9.0	39.5	NA	−4.66	NA	NA	Boonamnuayvitaya
Cu(II)	residue-clay		50	7.0–9.0	31.5					et al. (2004)
Zn(II)			250	7.0–9.0	13.4					
Ni(II)			100	7.0–9.0	11.0					
Cr(III)	Milled peat	NA	200	4.0	14.04	NA	NA	NA	NA	Dean et al. (1999)
Cr(VI)		NA	200	2.0	30.16					
Cu(II)	Calcined	1	50	5.0	29.8	NA	NA	NA	NA	Aklil et al. (2004)
Zn(II)	phosphate	1	50	5.0	20.6					

Remarks: *NA: Not available.

Table 22. Summary of highest reported adsorption capacities of low-cost adsorbents and activated carbon. GAC: Granular activated carbon [11].

Source of adsorbent	Type of adsorbent	Adsorption capacity (mg/g)						References
		Cd(II)	Cr(III)	Cr(VI)	Cu(II)	Ni(II)	Zn(II)	
Agricultural waste	Hazelnut shell			170				Kobya (2004)
	Orange peel					158		Ajmal et al. (2000)
	Citric acid-modified soybean hull				154.9			Marshall et al. (1999)
	Jackfruit	52.08						Inbaraj and Sulochana (2004)
Industrial by-products	Red mud					160		Zouboulis and Kydros (1993)
	Blast-furnace slag				133.35		103.33	Dimitrova (1996)
	Titanium oxide			30				Ghosh et al. (2003)
Natural materials	HCl-treated clay				83.3	80.9	63.2	Vengris et al. (2001)
Miscellaneous adsorbent	Wool			41.15				Dakiky et al. (2002)
	Coffe residue-clay	39.5			31.5			Boonamnuayvitaya et al. (2004)
	Coal						27.2	Solé et al. (2003)
	Calcined phosphate				29.8			Aklil et al. (2004)
Activated carbon	GAC type			145				Sharma and Forster (1996)
	Filtrasorb 400		30					Park and Jung (2001)
	HNO_3-treated ACF	146						Rangel-Mendez and Streat (2002)
	GAC type C						20	Leyva-Ramos et al. (2002)

6.2. Heavy Metal Removal Using Sewage Sludge – Based Activated Carbon

Activated carbon is widely used in heavy metal removal from water and wastewater. Activated carbon is a carbonaceous material with a high degree of porosity and an extended particulate surface area [12]. Activated carbon is prepared from organic-rich materials, wastes and/or biomasses. Sewage sludge is one of the wastes rich in organic material convertible into activated carbon.

Sewage sludge can be defined as the residue generated from the treatment of wastewater [12]. Sludge types are principally primary sludge and secondary sludge. Secondary sludge (biological sludge) is the sludge generated from biological treatment in wastewater treatment plants (WWTPs) wasted from secondary settling tank. Table 23 explains the composition of sewage sludge.

Table 23. Typical composition and properties of sewage sludge – adapted by Metcalf and Eddy, Inc.et at., (2003) from EPA (1979) [12]

Item / sludge	Untreated primary		Digested primary		Activated range
	Range	Typical	Range	Typical	
Total dry solids (TS), %	2 – 8	5	6 – 12	10	0.83 – 1.16
Volatile solids (VS), %	60 – 80	65	30 – 60	40	59 – 88
Grease and fats (% of TS)					
• Ether soluble	6 – 30	-	5 – 20	18	-
• Ether extract	7 – 35	-	-	-	5 – 12
Protein (% of TS)	20 – 30	25	15 – 20	18	32 – 41
Nitrogen (N, % of TS)	1.5 – 4	2.5	1.6 – 6	3	2.4 – 5
Phosphorous (P_2O_5, % of TS)	0.8 – 2.8	1.6	1.5 – 4	2.5	2.8 – 11
Potash (K_2O, % of TS)	0 – 1	0.4	0 – 3	1	0.5 – 0.7
Cellulose (% of TS)	8 – 15	10	8 – 15	10	-
Iron (not as sulfide)	2 – 4	2.5	3 – 8	4	-
Silica (SiO2, % of TS)	15 – 20	-	10 – 20	-	-
Organic acids (mg/L as HAc)	200 – 2000	500	100–600	3000	1100 – 1700

6.2.1. Preparation of Activated Carbon From Sewage Sludge

Preparation of activated carbon technique is almost common for various organic-rich materials including sewage sludge. Activated carbon is mainly prepared by carbonization and activation. The activation technique is categorized into physical and chemical activation.

6.2.1.1. Carbonization of Sewage Sludge

Carbonization comprises heating the carbonaceous (organic-rich) materials to temperature ranges of 500 – 800 ^oC under inert atmosphere [12]. Optimum carbonization was observed at 850 ^oC (Jeyasee, Lu and Zhai). Carbonization of 550 – 650 ^oC formed macro-porous structure of the adsorbent (Lu et al. 1995). However; at 700 ^oC, micro-pores and meso-pores were formed after the preparation of the adsorbent [12]. While at higher temperature micro-pores were destroyed, and meso- and macro-pores were formed (Chiang et al., 2001). Tables 24, 25 and 26 show the characteristics of the adsorbent at different carbonization conditions.

Table 24. Pore structure characteristics and pH values of some of the SBAs produced by carbonization [12].

Reference	Sludge type	Carbonization conditions			BET surface area (m^2 / g)	Micropore volume (cm^3 / g)	pH
		Temperature (°C)	Time (h)	Heating rate (°C / min)			
Bagreev et al. (2001)	T	950	1	10	122	0.051	11
Bandosz and Block (2006), Seredych and Bandosz (2007)	D M WWTP	950	0.5	10	141	0.058	10.9
Jeyaseelan and Lu (1996)	D M	850	2	20	101	NA	NA
Lu et al. (1995)	AN	850	2	20	100	NA	NA
Rio et al. (2004, 2005)	M WWTP VL	1000	1	20	96	0.036	10.6
Seredych and Bandosz (2006)	WWTP	950	0.5	10	103	0.043	10.9
Zhai et al. (2004)	M WWTP	900	1.17	NA	359	0.153	NA

AN: anaerobically digested; D: dewatered; M: municipal/urban; NA: not available; T: fertilizer derived from municipal sludge; VL: viscous liquid sludge; WWTP: wastewater treatment plant.

Table 25. BET surface area of SBAs prepared from blends of sludge with other feedstocks [12]

Reference	Sludge type	Carbonization conditions		Post-carbonization treatment	BET surface area (m^2 / g)
		Temperature (°C)	Time (h)		
Ansari et al. (2005)	D WWTP	950	1	H_2O	94
	70 % Po, 30 % D WWTP	950	1	H_2O	948
Bandosz and block (2006)	50 wt % WO, 50 wt % D M WWTP	950	1	None	100
Seredych and Bandosz (2006)	50 wt % WO, 50 wt % WWTP	650	0.5	None	108
	50 wt % WO, 50 wt % WWTP	950	0.5	None	192
	WWTP	650	0.5	None	93
	50 wt % WO, 50 wt % WWTP	650	0.5	H_2O – 3	199
Sioukri and Bandosz (2005)	D WWTP	950	1	None	98
	50 wt % CAC, 50 wt % D WWTP	950	1	None	1023

Reference	Sludge type	Carbonization conditions		Post-carbonization treatment	BET surface area (m^2 / g)
		Temperature (^oC)	Time (h)		
CAC: commercial activated carbon; D: dewatered; M: municipal/urban; Po: polymer (not sludge); WO: waste oil; H_2O: soaked in water; H_2O – 3: soaked in water for 3 days; WWTP: wastewater treatment plant.					

Table 26. Effect of HCl washing on properties of SBAs produced by carbonization [12]

Reference	Sludge type	Carbonization conditions			Post-carbonization treatment	BET surface area (m^2 / g)	Micropore volume (cm^3 / g)	pH
		Temperature (^oC)	Time (h)	Heating rate (^oC / min)				
Bagreev et al. (2001)	T	400	0.5	10	HCl	41	0.084	7.72
		400	0.5	10	HCl	17	0.063	NA
Bagreev et al. (2001)	T	800	1	10	None	104	0.107	11.2
		800	1	10	HCl – 3	193	0.113	4.0
Rose et al. (2006)	D A M WWTP	700	0.5	15	None	13	0.04	8.2
		700	0.5	15	HCl	188	0.22	3.4
Rose et al. (2007)	D Ax L M WWTP	700	0.5	15	None	49	0.08	10.2
		700	0.5	15	HCl	428	0.55	2.7
A: aerobically digested; Ax: extended aeration sludge; D: dewatered; L: sludge treated with lime; M: municipal/urban; T: fertilizer derived from municipal sludge; WWTP: wastewater treatment plant.								

6.2.1.2. Physical Activation of Sewage Sludge

Physical activation is processed by oxidizing gas such as CO_2, steam, or air at 700 – 1100 ^oC (Byrne and Marsh). Activation by CO_2 is more competitive than steam if temperatures is excess of maximum of 800 ^oC [12].

6.2.1.3. Chemical Activation of Sewage Sludge

Chemical activation entails mixing carbonaceous materials with an active reagent and then heating in an inert atmosphere. Chemical activation improves for higher surface area and pore structure of sewage sludge based activated carbons (SBAs). Chemicals widely used are KOH, NaOH, $ZnCl_2$, H_2SO_4 and H_3PO_4. Chemical activation by KOH was found to be the most effective technique for the production of excess of 1800 m^2 / g [12].

6.2.2. Performance of Sewage Sludge Activated Carbon (SBAs) on Heavy Metal Removal

Carbonized activated carbon from sewage sludge was found to be the most effective for the removal of Cu^{+2} [12]. Despite its low surface area, 63 m^2/g, Cu^{+2} removal was 277 mg/g by sewage sludge activated carbon carbonized at 800 ^oC (Rio). SBAs still attained higher Cu^{+2} removals than

commercial activated carbon (CAC) (Seredych and Bandosz). SBAs activated by $ZnCl_2$ were observed more effective in the removal of Hg than either that carbonized, H_2SO_4 activated or H_3PO_4 (Zhang et al. 2005). Table 27 compares the heavy metal removal performance by different sewage sludge treatment [12].

6.2.3. Iron Oxide Coated Sewage Sludge Activated Carbon (SBAs)

The municipal sewage sludge was modified with iron oxide employed in metal ions removal. The surface modification method was proposed and the effect of parameters in the preparation was studied. The iron oxide coated sludge had higher surface area, pore volume and iron content, compared to uncoated sludge (Thapanapong Phuengprasop 2011) [13].

6.2.3.1. Preparation [13]

The municipal sewage sludge was collected and treated at a specified pretreatment temperature for 3 h before coating. The amount of 5 g sewage sludge was added to 10mL of solution containing 2.0 g Fe $(NO_3)_3 \cdot 9H_2O$ (2.77%, w/v, Fe). The pH of the mixture was adjusted to the desired value with NaOH. The mixture was stirred for 1 h, dried at 105 ◦C for 20 h and then washed with de-ionized water to remove unattached oxide until the pH of the runoff water

Table 27. Metal cation uptake of SBAs [12]

Reference	Sludge type	Carbonisation conditions		Activation conditions			Post-treatment	BET surface area (m^2/g)	pH	Cation	Conc. in sol^n (mg/l)	Uptake	Cation	Conc. in sol^n	Capacity	% of CAC	Cation	Conc. in sol^n	Uptake	% of CAC
		Temperature (°C)	Time (h)	Reagent	Temperature (°C)	Time (min)														
Bouzid et al. (2008)	M WWTP	Not carbonised		Air	600	120	None	51	NA	Cu^{2+}			Cu^{2+}	Lang	5.7 mg/g	6				
Gasco et al. (2005b)	A M	450	1		Not activated		None	NA	6.3	Na^+	10,500	76.8% of sol^n	Mg^{2+}	1350 mg/l	42.8% of sol^n		K^+	380 mg/l	66.0% of sol^n	
	A M	Not carbonised		H_2SO_4	450	60	None	NA	5.1	Na^+	10,500	69.7% of sol^n	Mg^{2+}	1350 mg/l	44.8% of sol^n		K^+	380 mg/l	57.8% of sol^n	
Kang et al. (2006)	PaM WWTP	400	1	KOH	700	60	4%NaOH_W H_2O	1002	NA	Cr	1.0	0.2 mg/l	Cu^{2+}	1 mg/l	1.1 mg/g		Cd^{2+}	1 mg/l	1 mg/g	
Martin et al. (2002b)	2° D WWTP	Not carbonised		H_2SO_4	700	30	HCl	253	4.3				Cu^{2+}	50 mg/l	15 mg/g	300	Cd^{2+}	50 mg/l	40 mg/g	800
Mendez et al. (2005)	A WWTP	450	1	O_2/N_2	275	240	None	102	7.8				Fe^+	100 mg/l	65.0% of sol^n					
	AN WWTP	450	1	O_2/N_2	275	240	None	105	7.7				Fe^+	100 mg/l	99.7% of sol^n					
Mendez and Gasco (2005)	AN WWTP	650	2		Not activated		None	NA	8.2	Na^+	500	19.0% of sol^n	Mg^{2+}	200 mg/l	65.0% of sol^n		K^+	500 mg/l	17.8% of sol^n	
	AN WWTP	650	2		Not activated		50% HNO_3	NA	8.2	Na^+	500	26.1% of sol^n	Mg^{2+}	200 mg/l	78.0% of sol^n		K^+	500 mg/l	18.3% of sol^n	
Pan et al. (2003)	D 1° M WWTP	Not carbonised		Air	700	180	None	11	NA				Cu^{2+}	Lang	4.1 mg/g					
Rio et al. (2004, 2005b)	M WWTP VL	600	1		Not activated		None	59	8.9	Cu^{2+}	100	78.6 mg/g	Cu^{2+}	Lang	155 mg/g					
	M WWTP L VL	600	1		Not activated		None	33	12.4	Cu^{2+}	100	121.1 mg/g	Cu^{2+}	Lang	238 mg/g					
	M WWTP VL L	800	1		Not activated		None	63	12.5	Cu^{2+}	100	131.8 mg/g	Cu^{2+}	Lang	277 mg/g					
Rio et al. (2005b)	M WWTP VL	Not carbonised		H_2SO_4	600	180	NA	353	5.9	Cu^{2+}	100	83 mg/g								
Rio et al. (2006a)	M WWTP, VL	600	1	Steam	760	30	None	226	8.0				Cu^{2+}	Lang	146.9 mg/g	81				
Seredych and Bandosz (2006)	50 wt.% WO,	650	0.5		Not activated		None	108	9.4	Cu^{2+}	50	50 mg/g	Cu^{2+}	Lang-Frlh	69.7 mg/g					
	50 wt.% WWTP	950	0.5		Not activated		None	192	10.4	Cu^{2+}	50	45 mg/g	Cu^{2+}	Lang-Frlh	47.1 mg/g					
	WWTP	650	0.5		Not activated		None	93	10.2	Cu^{2+}	50	52 mg/g	Cu^{2+}	Lang-Frlh	63.5 mg/g					
	WWTP	950	0.5		Not activated		None	103	10.9	Cu^{2+}	50	24 mg/g	Cu^{2+}	Lang-Frlh	34.0 mg/g					
Zhai et al. (2004c)	M	Not carbonised		$ZnCl_2$	850	NA	HCl	550	NA				Ni^{2+}	Lang	9.1 mg/g	611	Cd^{2+}	Lang	16.7 mg/g	150
Zhang et al. (2005)	M	650	1		Not activated		None	137	NA	Hg(II)	80	42 mg/g								
	M	Not carbonised		H_3PO_4	650	60	NaOH	289	NA	Hg(II)	80	97 mg/g								
	M	Not carbonised		$ZnCl_2$	650	60	HCl	555	NA	Hg(II)	80	127 mg/g								

Abbreviations: 50%HNO_3 – digested in 50% nitric acid; Conc. in sol^n – initial concentration of adsorbate in solution used to assess uptake; Lang – uptake calculated from the adsorption isotherm with the Langmuir equation; Lang-Frlh – uptake calculated from the adsorption isotherm with the Langmuir-Freundlich equation. For all other abbreviations please refer to previous tables.

was constant (pH 7–8). The solid was dried at 105 °C for 24 h and finally stored in a capped bottle for further use. The effects of pretreatment temperature, pH of ferric solution and amount of ferric nitrate were studied. The effect of coating parameters was evaluated by comparing the adsorption capacity for Cu (II) ions of the adsorbents obtained from different preparation conditions.

6.2.3.2. Heavy Metal Removal Performance [13]

The suitable pH is 7 for the removal of Cd (II) and Ni (II), 6 for Cu (II), and 5 for Pb (II) [13]. Maximum adsorption capacity of Cu (II), Cd (II), Ni (II) and Pb (II) was 17.3, 14.7, 7.8 and 42.8 mg/g, respectively [13]. Figures 8 and 9 show the efficiency of heavy metal removal by iron coated sewage sludge adsorbent.

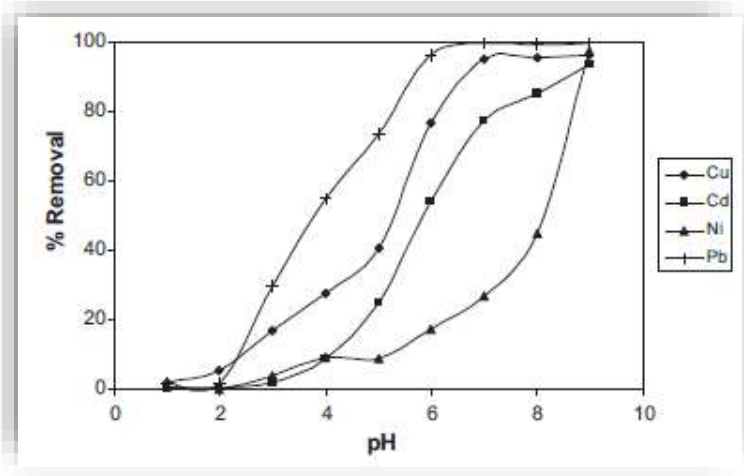


Figure 7. Effect of pH of metal solutions on removal efficiency
(concentration 30mgL^{-1} Pb(II), 30mgL^{-1} Ni(II), 20mgL^{-1} Cu(II) and 20mgL^{-1} Cd(II); adsorbent dose 1 g L^{-1}) [13]

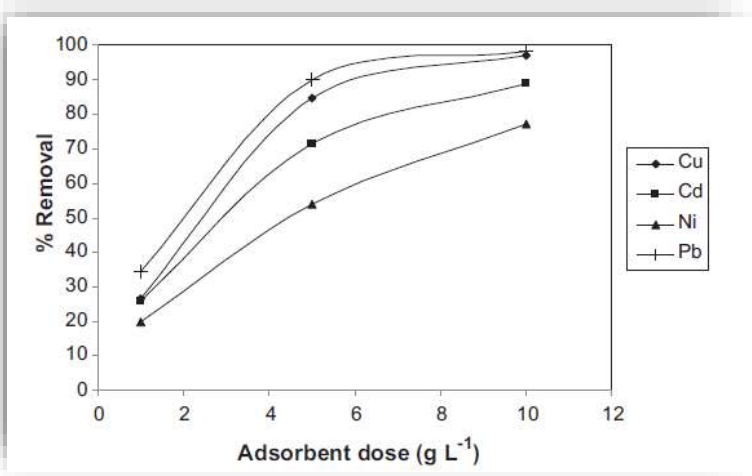


Figure 8. Effect of adsorbent dose on removal efficiency (concentration: 48mgL^{-1} Cu(II), 30mgL^{-1} Cd(II), 20mgL^{-1} Ni(II) and 99mgL^{-1} Pb(II); pH 5 for Cu(II), Cd(II), Ni(II) and pH 4 for Pb(II)) [13]

6.2.4. Miscellaneous Sewage Sludge Activated Carbon (SBAs)

Removal of mercury by sewage sludge activated by $ZnCl_2$ was observed higher than that by sulfuric and phosphoric acids optimized at pH of 5 as shown in figures10 and 11

.

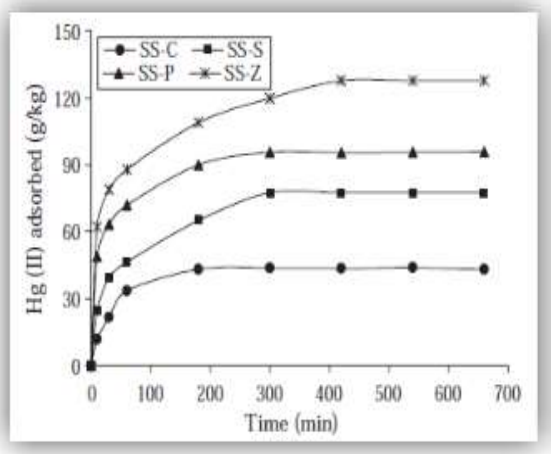


Figure 9. Hg(II) removal by various SS carbons as a function of contact time. Initial Hg(II) concentration 80 mg/L, pH = 5.0, temperature = 25 °C [14]

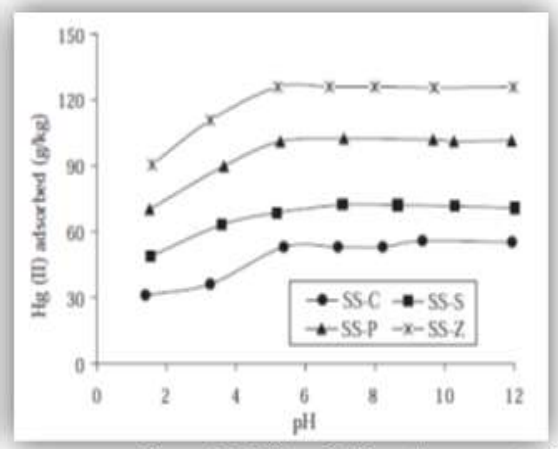


Figure 10. Effect of pH on the removal of Hg(II) by various SS adsorbents. Initial Hg(II) concentration = 80 mg/L, contact time = 7 h, temperature = 25 °C [14]

SS-C: inactivated sewage sludge carbon; SS-S: H_2SO_4 activated SS carbon; SS-P: H_3PO_4 activated SS carbon; SS-Z: $ZnCl_2$ activated SS carbon.

F. Rozad reported the removal capacities 175.4, 64.1, 30.7 and 15.4 mg/g of Hg, Pb, Cu and Cr, respectively [15]. Also, it was reported that $ZnCl_2$ activated sewage sludge followed by pyrolysis (AS) had the removal capacity of heavy metals much greater than only pyrolyzed sewage sludge (PS) as shown in figures 12 and 13.

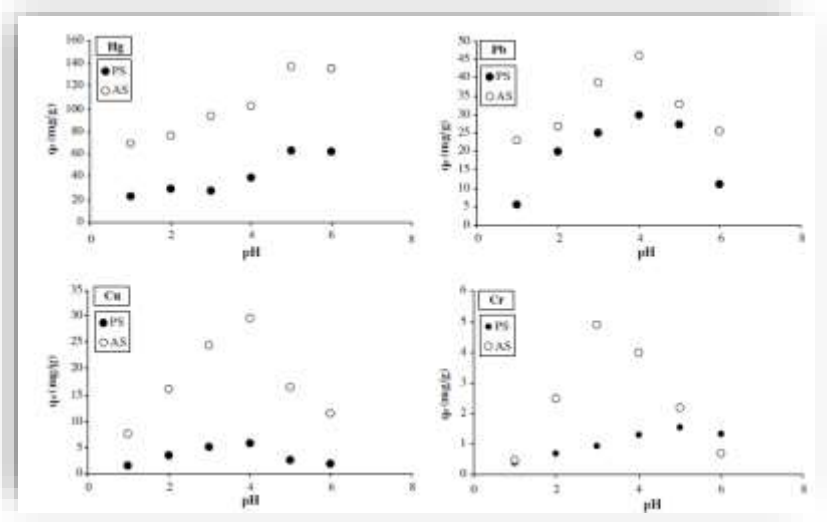


Figure 11. Effect of pH on the adsorption of metal ions onto PS and AS adsorbents [15]

AS: $ZnCl_2$ activated sewage sludge followed by pyrolysis.PS: single pyrolyzed sewage sludge.

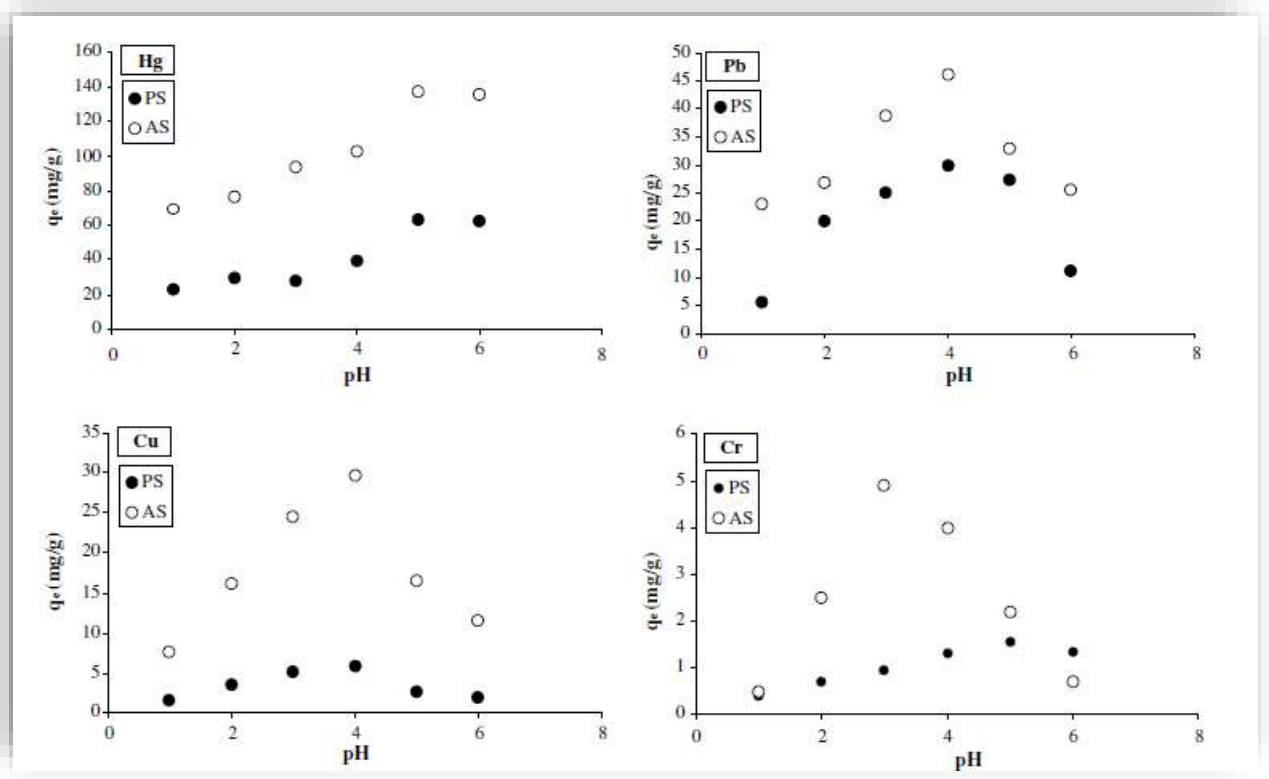


Figure 12. Effect of pH on the adsorption of metal ions onto PS and AS adsorbents [15]

4. Conclusions

Heavy metals-contaminated water has a great negative effect on health. Most of literatures reported that the sources of heavy metals are from industrial applications. Also, other human activities have potential. Many techniques of heavy metal removal from water were studied such as chemical precipitation, membranes, ion exchange, coagulation and adsorption. Adsorption is currently more widely tested and proposed for the purpose of treatment from heavy metals. Commercial activated carbon is used for the treatment in wide range, and it achieved great results in treatment. However; its disadvantages are its expenses and transportation since activated carbon manufacturers are centralized and distributors are available over the world. Thus, many attempts are carried out to study the removal of heavy metals by low-cost adsorbent because of low cost and abundance. Chitosan, clays, zeolites, phosphates and activated carbon form organic wastes are under researches and studies. Sewage sludge is one of organic wastes. Sewage sludge activated carbon adsorbent reported heavy metal removal better than commercial activated carbon.

Acknowledgments: It is highly full of appreciation to Jordan Association of Engineers for arranging this conference and accepting this paper work. It is highly acknowledgment to the colleagues; Mr. Ahmed Abukhashabeh and Suhaib Hameedi who assisted to prepare this paper. In addition, it is a great appreciation to the staff of Chemical and Petroleum Engineering Department of the United Arab Emirates University who supported to do such a valuable and strategic research for the enhancement of water pollution control.

References

1. A. Aklil, M. Mouflih, S. Sebti, *Removal of heavy metal ions from water by using calcined phosphate as a new adsorbent*, Journal of Hazardous Materials A112 (2004) 183–190.
2. Gökhan Ekrem Üstün, *Occurrence and removal of metals in urban wastewater treatment plants*, Journal of Hazardous Materials 172 (2009) 833–838.
3. Saeed ur Rehman, *Production of activated carbon from sewage sludge for the removal of lead from water*, A Thesis Presented to The Faculty of The American University of Sharjah, College of Engineering, Master of Science in Chemical Engineering.
4. L. So¨rme, R. Lagerkvist, *Sources of heavy metals in urban wastewater in Stockholm*, The Science of the Total Environment 298 (2002) 131–145.
5. *Guidelines for drinking-water quality - 4th ed*, World Health Organization 2011.
6. M.A. Barakat, *New trends in removing heavy metals from industrial wastewater*, Arabian Journal of Chemistry (2011) 4, 361–377.
7. Fenglian Fu, Qi Wang, *Removal of heavy metal ions from wastewaters: A review*, Journal of Environmental Management 92 (2011) 407 – 418.
8. Sandhya Babel, Tonni Agustiono Kurniawan, *Low-cost adsorbents for heavy metals uptake from contaminated water: a review*, Journal of Hazardous Materials B97 (2003) 219–243.
9. V. C. Renge, S. V. Khedkar, Shraddha V. Pande, *Removal of heavy metals from wastewater using low cost adsorbents : a review*, Science Reviews and Chemical Communication.: 2(4), 2012, 580-584, ISSN 2277-2669.
10. Mona E Ossman, Moustapha S Mansour, *Removal of Cd (II) ion from wastewater by adsorption onto treated old newspaper: kinetic modeling and isotherm studies*, International Journal of Industrial Chemistry 2013, 4:13.
11. Tonni Agustiono Kurniawan, Gilbert Y.S. Chan, Wai-hung Lo, Sandhya Babel, *Comparisons of low-cost adsorbents for treating wastewaters laden with heavy metals*, Science of the Total Environment 366 (2006) 409– 426.
12. K.M. Smith, G.D. Fowler, S. Pullket, N.J.D. Graham, *Sewage sludge-based adsorbents: A review of their production, properties and use in water treatment applications*, water research 43 (2009) 2569 – 2594.
13. Thapanapong Phuengprasop, Jarinya Sittiwong, Fuangfa Unob, *Removal of heavy metal ions by iron oxide coated sewage sludge*, Journal of Hazardous Materials 186 (2011) 502–507.
14. Fu-Shen Zhang, Jerome O. Nriagua, Hideaki Itoh, *Mercury removal from water using activated carbons derived from organic sewage sludge*, Water Research 39 (2005) 389‑395.
15. F. Rozada, M. Otero, A. Mora´n, A.I. Garcıa, *Adsorption of heavy metals onto sewage sludge-derived materials*, Bioresource Technology 99 (2008) 6332‑6338.
16. I. Heidmann, W. Calmano, Separation and Purification Technology 61 (2008) 15.
17. C. Phalakornkule, S. Polgumhang, W. Tongdaung, B. Karakat, T. Nuyut, Journal of Environmental Management 91 (2010) 918.
18. T. O¨lmez, Journal of Hazardous Materials 162 (2009) 1371.
19. S.S. Hamdan, M.H. El-Naas, J. Ind. Eng. Chem. (2013), http://dx.doi.org/10.1016/j.jiec.2013.11.006

Prediction of Compressive Strength of Concrete from Early Age Test Result Using Design of Experiments (RSM)

Salem Alsanusi*

Civil Engineering Department, Faculty of Engineering, University of Benghazi, Benghazi, Libya
**Corresponding author: salem.alsanusi@uob.edu.ly*

Abstract: Response Surface Methods (RSM) provide statistically validated predictive models that can then be manipulated for finding optimal process configurations. Variation transmitted to responses from poorly controlled process factors can be accounted for by the mathematical technique of propagation of error (POE), which facilitates 'finding the flats' on the surfaces generated by RSM. The dual response approach to RSM captures the standard deviation of the output as well as the average. It accounts for unknown sources of variation. Dual response provides a more useful model of overall response variation. In our case, we implemented this technique in predicting compressive strength of concrete of 28 days in age. Since 28 days is quite time consuming, while it is important to ensure the quality control process. This paper investigates the potential of using design of experiment to predict the compressive strength of concrete at 28th day. Data used for this study was carried out from experiment schemes at university of Benghazi, civil engineering department. A total of 114 sets of data were implemented. ACI mix design method was utilized for the mix design. No admixtures were used, only the main concrete mix constituents such as cement, coarse-aggregate, fine aggregate and water were utilized in all mixes. Different mix proportions of the ingredients and different water cement ratio were used. The proposed mathematical models are capable of predicting the required concrete compressive strength of concrete from early ages

Keywords: Mix proportioning; response surface methodology; compressive strength; optimal design

1. Introduction

Concrete is the most widely used structural material for construction today. Traditionally, concrete has been fabricated from a few well-defined components; Cement, water, fine aggregate, coarse aggregate, etc. In concrete mix design and quality control, the strength of concrete is regarded as the most important property. The design strength of concrete normally represents by 28 days strength .In case of construction work 28 days is considerable long period of time. Due to some experimental errors in mix design, the test results fail to achieve the designed strength, then repetition of the entire process becomes necessary, which can be costly and time consuming. Data used for this study was carried out from experiment schemes at University of Benghazi, civil engineering department. A total of 114 sets of data were implemented. ACI mix design method was utilized for the mix design. No admixtures were used, only the main concrete mixes constituents such as cement, coarse-aggregate, fine aggregate and water were utilized in all mixes. Different mix proportions of the ingredients and different water cement ratio were used. The proposed mathematical models are capable of predicting the required concrete compressive strength of concrete from early ages.

Proportions of the ingredients and different water cement ratios in estimating the strength at an early age of concrete were investigated. A rapid and reliable concrete strength prediction would be a great significance. A special type of response surface problem called a (RSM) is implemented. Using polynomial regressions, the DOE approach permits calculation of the response surfaces for the parameters under study over the experimental domain. Because of the high complexity of the relation

between the compressive strength and component composition of concrete, conventional regression analysis could be insufficient to build an accurate model. This paper investigates the potential of using design of experiments (DOE) to predict the compressive strength of concrete at 28th day as the response. Response surface method (RSM) opens new possibilities in the classification and generalization of available experimental results to estimate concrete strength from the mix components. This work presents and examines the mix proportioning of ordinary concrete using RSM technique to optimize the mixture proportions and development of mathematical model for desired properties of concrete compressive strength in terms predictable and increase the efficiency of the prediction [1].

2. Experimental Program

Locally produced Ordinary Portland Cement (OPC) was used. The coarse aggregate was 19 to 25 mm in maximum size crushed stone. No admixtures or additives were used in this study, only the ordinary constituents of concrete were used. Specimens were cured in water for 3, 7,and 28 days. A total of 114 sets of data were used to analyze the behavior of the concrete with time. Mix design according to (ACI 211.1-91) was used for the mix design. The concrete compressive strength after 28 day was obtained from standard cubes. The statistical analysis was performed using the computer software (Minitab). Computing the statistical information of the data like the mean, standard deviation and the correlation coefficient between the variable was present at Tables 1 and 2. [2].

Table 1. Descriptive Statistics Information's

Variable	Quantity	Mean	StDev	Min.	Max.
W/C	Water cement ratio	0.60	0.10	0.40	0.90
W	Wight of water, Kg	209.56	15.3	185.0	230.0
C	Wight of cement, Kg	356.28	55.0	250.0	513.0
CA	Wight of coarse aggregate Kg	1109.90	240.1	480.0	1401.0
FA	Wight of fine aggregate Kg	697.50	175.2	470.0	1119.0
fc`7	concrete compressive strength at 7 day Mpa	25.27	6.20	10.40	39.60
fc`28	concrete compressive strength at 28 day Mpa	34.81	7.20	16.40	49.20

Table 2. Correlation Between the Variables Used for Analysis

	W/C	W	C	CA	FA	fc`7
W	0.52					
C	-0.85	-0.08				
CA	0.02	-0.61	-0.32			
FA	0.16	0.61	0.09	-0.95		
fc`7	-0.63	-0.63	0.38	0.50	-0.62	
fc`28	-0.64	-0.57	0.37	0.35	-0.46	0.84

3. **Methodology**

Response surface methodology (RSM) consists of a set of statistical methods that can be used to develop, improve, or optimize products [3]. (RSM) used to optimize one or more responses, or to meet a given set of specifications (e.g., a minimum strength specification). There are three general steps that comprise (RSM): experiment design, modeling, and optimization [4]. Concrete is a mixture of several components; water, cement, fine and coarse aggregates. Various chemical and mineral admixtures, as well as other materials such as fibers, also may be added. Choosing the design correctly will ensure that the response surface is fit in the most efficient manner. MINITAB provides central composite and Box-Behnken designs [3]. Consider a concrete mixture consisting of q component materials (where q is the number of component materials). Two approaches can be applied to concrete mixture, the mathematically independent variable approach, and optimization the mathematic model. The steps which were followed in this methodology in shown in figure 1.

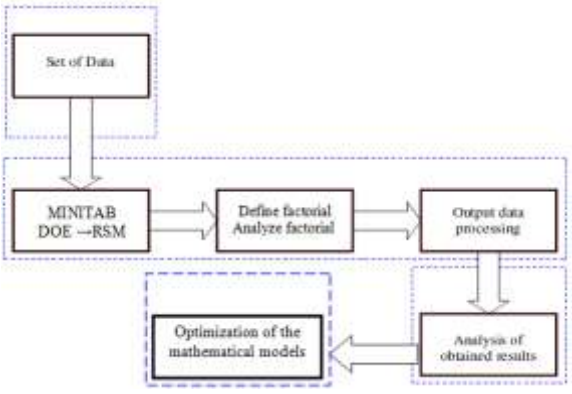


Figure 1. The research diagram

The empirical models are fit to the data, and polynomial models (linear or quadratic) typically are used. The general case of the full quadratic model for k =3 as an example for independent variables is shown as [3]:

$$y = b_0 + b_1x_1 + b_2x_2 + b_3x_3 + b_{22}x_1x_2 + b_{33}x_1x_3 + b_{23}x_2x_3 + b_{11}x_1^2 + b_{22}x_2^2 + b_{33}x_3^2 \quad (1)$$

In equation (1), the ten coefficients are represented by the b_k and e is a random error term representing the combined effects of variables not included in the model. The interaction terms ($x_i x_j$) and the quadratic terms (x_i^2) account for curvature in the response surface. The central composite design (CCD), an augmented factorial design, is commonly used in product optimization [2]. The design consists of 2k factorial points representing all combinations of coded values $x_k = \pm 1$, 2*k axial points at a distance $\pm\alpha$ from the origin, and at least 3 center points with coded values of zero for each x_k . The value of α usually is chosen to make the design rotatable, but there are sometimes valid reasons to select other values shown in Fig. 2.

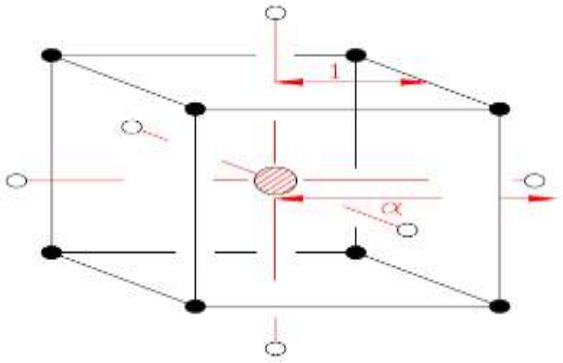


Fig. 2 Schematic of a central composite design for three factors

Optimization may be performed using mathematical or graphical (contour plot) approaches. Numerical optimization requires defining an objective function that reflects the levels of each response in terms of minimum (zero) to maximum (one) desirability (D) which is [5]:

$$D = \frac{(w_1 \times d_1 + w_2 \times d_2 + \cdots w_n \times d_n)}{n} \qquad (2)$$

Several types of desirability functions can be defined. Common types of desirability functions are shown in Fig.3.

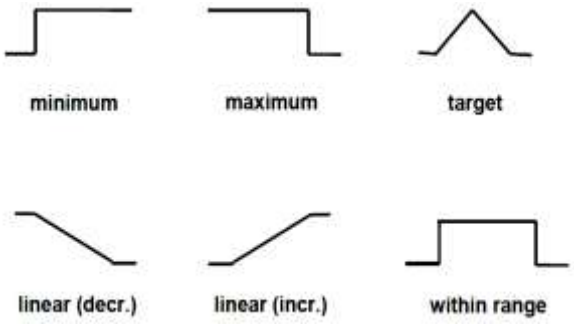


Figure 3. Examples of desirability functions

When the model was completed, sets of tested data are used to determine the accuracy of regression for comparisons between the predicted compressive strength and the true compressive strength. The best performances (observations) are selected according to several criteria. The chosen criteria are defined as follows:

1. Mean Absolute Percentage Error MAPE%

$$MAPE\% = \frac{100}{n} \sum_{i=1}^{n} \left| \frac{x_i - y_i}{x_i} \right| \qquad (3)$$

2. Coefficient of Efficiency E

$$E = 1 - \left(\frac{\sum_{i=1}^{n} (x_i - y_i)^2}{\sum_{i=1}^{n} (x_i - \bar{x})^2} \right) \quad (4)$$

4. Development of Mathematical Model

In a mixture experiment, the response is observed at all mixture design points and the effects of components and interactions between components are investigated simultaneously. However, in concrete mixture design, certain mixture design points are not possible and must be omitted. Therefore, a flattened simplex-centroid mixture experiment design was adopted [4]. Concrete cubes were fully compacted on a vibrating table, moist cured for 24 h_r, and then cured in water at 20°C until testing at 3, 7, and 28. Therefore, there were 114 training data covered six different levels of strength, about 15, 20, 25, 30,35and 40 MPa. It may be certain that these will form a fairly representative group covering all the ranges of practical use for concrete mixtures and will present the rather complete and independent information required for such an evaluation. The results of the compressive strength tests were subjected to polynomial regression using a computer program (MINITAB) [6]. Two polynomials were tried to represent the measured compressive strength data for five component contents and a 7-day age. The best fit for the compressive strength was obtained with a lowest absolute percentage error (MAPE %) and high coefficient of efficiency (E). The summary of the results were present in Tables 3 and 4, scatter diagrams showing at Figure 4.

Usually some of the terms are not significant, the full quadratic model and for each coefficient, calculate the t-statistic for the null hypothesis that the coefficient is equal to zero.

The Model (1) in terms of Mix components:

$$fc`28 = -42261 + 179962\,{}^{W}/_{C} - 446w + 312C - 20FA - 37500({}^{W}/_{C})^2 + w^2 - 311\,{}^{W}/_{C} - 163({}^{W}/_{C})(C) - 4({}^{W}/_{C})CA - 4({}^{W}/_{C})FA \quad (5)$$

Table 3. Mixture Experiment Summary Statistics for fc`28 day MPa Strength for Model (1)

Variable	Mean	StDev	Min	Max	95%
FIT1	34.67	6.76	17.08	43.25	CI
fc`28	34.67	7.35	16.40	49.20	33.46
MAPE%=		6.42			-
E=	0.85				36.15

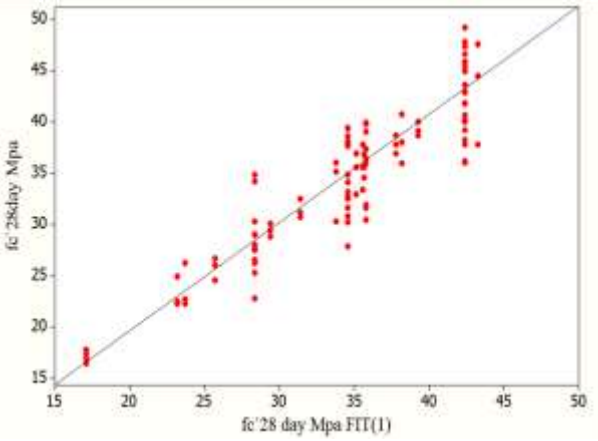


Figure 4. Measured and predicted compressive strength of model 1

The Model (2) figure 5 in terms of Mix components and the concrete compressive strength of fc`7 day:

$$fc`28 = -6684 + 58900.7\frac{w}{c} - 180.8w + 99.9c - 11.1CA + 9.4FA + 5.4fc`_{7day} - 12266.1\left(\frac{w}{c}\right)^2 + 0.5w^2 - 0.1c^2 - 99.6\left(\frac{w}{c}\right)w - 54.3\left(\frac{w}{c}\right)c - 1.7\left(\frac{w}{c}\right)CA - 1.1\left(\frac{w}{c}\right)FA - 5.6\left(\frac{w}{c}\right)fc`_{7day} - 0.1w \times c + 0.1w \times CA \qquad (6)$$

Table 4. Mixture Experiment Summary Statistics for fc`28 MPa Strength for Model (2)

Variable	Mean	StDev	Max	Min	
FIT 2	34.70	6.96	45.64	15.97	95%CI
Fc`28	34.70	7.30	49.20	16.40	33.46-36.15
MAPE %	4.87				
E	0.91				

It can be seen that, the MAPE % for the results is rather low, and the E for the models are so high as to provide accurate predictions. In other words, the models are good in generalization and close to the observed value within the range of 95% confidence interval. However, there is uncertainty in the fitted functions, because they are estimated from a sample of data. The uncertainty provided is for a 95 percent confidence interval.

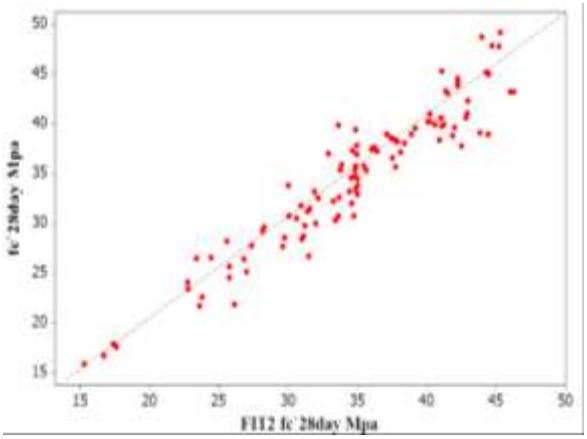


Figure 5. Measured and predicted compressive strength of model (2)

5. Optimization

Numerical optimization using desirability functions can be used to find the optimum mixture proportions in this situation. A desirability function must be defined for each response (property) [6]. The desirability function takes on values between 0 and 1, and may be defined in several ways. A several targets were optimizing for 28 fc` concrete compressive strength to find out the proper mix component meet the target. In this study, the overall desirability D was defined as the geometric mean of the individual desirability functions d_i over the feasible region of mixtures. Numerical optimization for model (1) gave the following best settings for this concrete mixture as shown in Table 5.

Table 5. Numerical Optimization for Model (1)

The fc` 28 target	W/C	W	C	CA	FA
20	0.46	230	512.8	1401	1119
25	0.69	185	513	480	1117
30	0.70	185	250	1394	480
35	0.70	185	250	1397	480
40	0.69	185	513	480	1114
45	0.69	185	513	480	1113

6. Summary and Conclusions

Data used for this study was taken from experiment results. Total 114 sets of data were used to analyze the behavior of the concrete with time. ACI mix design method was used for the mix design process. Concrete compressive strength was defined as the strength obtained from standard cubes (150mm) no admixtures or additives were use. Different mix proportions of the ingredients and different w/c ratio were used to study the variations; the following points were drawn from this study:

1. The statistical error analysis shows the adequacy of the model obtained and also that the terms added to the model have significant effects on the response variable. For both of the models, values of (E) are 0.85 and 0.91 for the first and second models. Therefore, it can be said that the models established for compressive strength are adequate. In both of the models, the MAPE% is

in reasonable agreement with the prediction for compressive strength (MAPE% is 6.7% and 4.5%). This indicates that the amounts of results obtained from the models are appropriate.

2. The models are reasonable in generalization and close to the observed value within the range of 95% confidence interval.
3. Based on the data obtained from the RSM models, high correlations between the compressive strength and the component composition of concrete can be developed using the generalization capabilities. Such a model can be efficiently used for simulating the compressive strength.
4. The importance of the influence of mix constituents on the strength of concrete was approved. Two mathematical models for the prediction of concrete compressive strength at the age of 28 was proposed and developed (using RSM) from the knowledge of the mix constituents, and strength at the ages of 7 days.
5. Practical approach has been described for prediction of 28-day compressive strength of concrete and the proposed technique can be used as a reliable tool for assessing the design strength of concrete from quite early test results. This will help in making quick decision for accidental poor concreting at site and to reduce delay in the execution time of large civil construction projects.

References

1. Hasan. M and Kabir, " Prediction of compressive strength of concrete from early age test result",4th Annual Paper Meet and 1st Civil Engineering Congress, 2011, 22-24, Dhaka, Bangladesh ISBN: 978-984-33-4363-5.
2. M. Sayed-Ahmed1, "Statistical Modeling and Prediction of Compressive Strength of Concrete" Concrete Research Letters, 2012, Vol. 3(2).
3. M. J. Simon, "Concrete Mixture Optimization Using Statistical Methods: Final Report" FHWA Office of Infrastructure Research and Development, 6300 Georgetown Pike, 2003, McLean, VA 22101.
4. M. T. Cihan et al., "Response surfaces for compressive strength of concrete", Construction and Building Materials 40, 2013, 763–7740.
5. Murali. and Kandasamy, " Mix proportioning of high performance self-compacting concrete using response surface methodology", Journal of Civil Engineering (IEB), 2009,37 (2) ,91-98.
6. Myers, R. H., and Montgomery, D. C. "Response surface methodology", 1995, Wiley, New York.

Process Safety Near Misses are Warning Signs for a Major Incident

Rajender Dahiya [1,*], Priyal Dahiya [2,*]

[1] Professional Process Safety Engineer, Senior Technical Services Manager – Loss Control
AIG PC Global Services, Inc./ A member company of American International Group, Inc. (AIG), Houston, Texas USA
[2] Mechanical Engineering, University of Texas, Austin, Texas USA
**Corresponding authors: rajender.dahiya@aig.com ; priyal@utexas.edu*

Abstract: "Near misses" are warning signs about weaknesses in a process safety management program or human performance and can be precursors to a high potential incident. Repeatedly, case studies have shown how deadly incidents could have been prevented if process safety near misses were captured and investigated. The Chemical Safety Board (CSB) demonstrates the importance of investigating near misses through its own investigative reporting, also demonstrating how deadly incidents could have been prevented. [1] In the majority of these cases, process safety near misses were ignored or not taken seriously due to poor process safety culture or poorly implemented process safety management programs.This paper covers the importance of implementing a Process Safety Near Miss (PSNM) incident investigation and learning process into safety management programs and how process safety near misses can be used to help prevent major disasters. Emphasis is given to reporting and investigating near misses.Through practical examples, the author explains pertinent gaps, industry best-practices, and learning for reporting and investigating process safety near misses. Real life examples from a variety of high hazard industries are presented to call attention to opportunities for improvement, including well-tested tips for developing or updating an existing incident investigation program. Industry best-practices presented articulate how to develop the criteria for reporting process safety near misses, investigate root causes for their potential consequences, and develop recommendations that can help prevent potentially serious incidents by implementing actions to improve a process safety program.The paper concludes by explaining how a well-written and implemented process safety management program in general, and the incident investigation program in particular, plays a vital role in preventing major incidents.

Keywords: Process Safety Near Miss, Incident Reporting and Investigation

1. Introduction

Failure to identify the hazards and manage the risks of highly hazardous materials and processes is one of the primary root-causes of an incident, and failure to learn from the past incidents is the leading cause of the recurrence of incidents.

Investigations of process safety incidents reveal that there were numerous precursors, which if captured/taken care of, could have prevented most of the major incidents.

The purpose of an incident reporting and investigation process is to identify the root causes of an incident and provide recommendations to prevent a recurrence. The first and foremost important step in this process is to report an incident, only then can there be an investigation and lessons learned to prevent similar or higher potential incidents. There are several areas of improvement for making use of process safety near miss incidents to incorporate in the reporting process and investigation before a major incident hit.

Furthermore, a strong corporate safety culture and a competent workforce is critical for developing and implementing user friendly and fit-for-purpose processes and tools.

2. Why do we keep repeating major incidents?

Investigation outcomes of major incidents have been consistent for decades and validate that the causes and consequences are often identical in spite of enormous overall development in tools and technologies.

Commonalities in past incidents clearly indicate that there are continuing gaps in the learning process. There were several precursors before those incidents, and most importantly all incidents were preventable. These precursors were either ignored altogether or not taken seriously. About two dozen incident investigation reports were reviewed and found that in more than 70% of the investigations, the most common primary causes of incidents were:

- Management failure to identify the hazard and/or mitigate the risk of hazardous processes or materials.
  - A poorly done hazard study such as HAZID, PHA, or LOPA is one of the leading causes of the failure.

- Management failure to maintain the integrity of safety critical systems and equipment.
  - In the majority of the incidents, safety barriers were either bypassed, disabled or not maintained due to inadequate management programs and / or poor process safety culture.

- Management failure to learn from the past incidents.
  - Learning from PSNM incidents is a proactive approach for incident prevention. Whereas, learning from incidents is a reactive approach for preventing the recurrences of incidents. However learning from both can prevent the incidents.

It has been learned that inadequate or poorly implemented management systems, poor process safety culture, and lack of process safety competency are the key components of the learning failure. Each of these components, alone or in combination, were unable to identify the hazards and manage the risks by maintaining the integrity of safety critical equipment and systems.

The focus of this paper is on learning from process safety near miss incidents. The learning gaps and industry best practices are described in the following sections of this paper.

3. What is a process safety near miss incident?

OSHA defines a near miss as an incident in which no property was damaged and no personal injury was sustained, but where, given a slight shift in time or position, damage or injury easily could have occurred. A process safety near miss is an event that presents an opportunity to learn valuable information that may prevent future incidents, without the accompanying severe consequence of a true process safety incident [2]. These incidents are warning signs / weak signals / precursors of a high potential incident.

The following incidents / events are commonly considered as process safety near misses by leading industries [3];

a. Safe operating limit excursions – operations upsets
b. Demands on safety systems – safety systems activated
c. Safety system failure on demand
d. Safety system test failures
e. Pressure safety valve (PSV) pre-pop test failures
f. Any significant non-reportable release of a hazardous substance
g. Primary containment inspection or testing results outside acceptable limits

Safety systems examples: Safety Instrumented Systems (SIS), Mechanical Shutdown Systems e.g., emergency shut down (ESD), Pressure Relief Devices such as pressure safety value (PSV) or rupture discs (RD).

4. Why investigate process safety near miss incidents?

Several deadly incidents could have been prevented if the process safety near misses were captured and investigated. These near misses are warning signs/weak signals/precursors for a high potential incident.

Process safety near miss incidents provide an early warning about the weaknesses in the management program and human performance required to maintain the integrity of process equipment and physical barriers. Identifying the warning signs and addressing their root causes can definitely prevent high potential incidents.

Since there is no loss, risk improvement will normally cost much less than an incident with severe consequences. In most cases, root causes of a PSNM can be fixed with minimal resources such as extra training for employees, changing the preventive maintenance (PM) and inspection frequency, changing the material of construction, updating or developing a specific procedure, increasing the administration authority control etc.

"There's an old saying that if you think safety is expensive, try an accident. Incident cost a lot of money. And, not only in damage to plant and in claims for injury, but also in the loss of the company's reputation."– Dr Trevor Kletz.

The Chemical Safety Board (CSB) and other third party investigation reports of major incidents pointed out that there were several PSNM before the incident which were either ignored or learning not applied. If those PSNM were investigated and learning implemented, could have prevented the deadly incidents.

5. How can process safety near miss investigations prevent major incidents?

The following examples describe how investigating a PSNM and addressing its root causes can prevent a major incident.

Example 1: Safe operating limit excursion – operations upsets

A process with a runaway reaction hazard with an auto trip safety system, which was set at 355^0F, was bypassed; the board operator controlled the process which reached 372 ^{0}F, 17^0F above its trip set point. The trip system was in bypass mode for more than 7 years, so the unit did not trip automatically. This event was documented in the logbook like other process data / parameters. It was not discussed in any meeting and no concerns were raised. No incident was submitted. This was the third incident in the last year with that DCS operator. There may be more such incidents on other shifts. The DCS operator and operation supervisors were not sure what is wrong in this case and why it is an incident when there is no injury, no loss, and the unit was not shutdown. On the other hand, they think this demonstrates that the operators are competent to manage the emergency operations. Job well done! However, they do not understand the potential risk associated with this incident. This is also a normalization of deviation and the company is very fortunate not to face an accident so far.

Actual Consequences of this incident: None. No injury, damage or production loss.

Potential consequences: A runaway reaction with potential catastrophic vessel rupture, explosion and fire with severe consequences.

What is the potential risk of not investigating this incident?

Runaway reaction incidents are not uncommon. Knowingly or unknowingly, the site management is operating the reactor at a very high and unacceptable risk due to lack of critical protection layers. Considering the repeat excursions, a runaway reaction is highly likely with severe consequences.

This is a repeat incident with no losses or unit shutdowns so far. There is a likelihood that next time this excursion may not be controlled and brought back to safe operating limit due to several reasons such as; operator errors, fatigue, ignored alarms, alarm failure, alarm bypassed, control system malfunction, final element (valves) failure, etc.

How this incident investigation can prevent a major incident?

Considering the high potential consequences, this incident should be a candidate for detailed root cause analysis (RCA). The investigation will not only point at the weaknesses in the barriers and human interface but also identify the missing barriers or unidentified hazards or underestimated / unmitigated risks.

The investigation team should identify at least the following system causes:

1. Management failure to maintain the integrity of critical safeguards.

Considering the potential consequences, this risk should be one of the highest risks at the site and be taken seriously.

a. The trip system was bypassed for more than 7 years. There was no documentation for bypassing this critical barrier such as safety bypass or management of change.
b. Operation, maintenance and process safety staff were not aware of this change.
c. No one questions the "trip window" RED on the DCS for 7 years.
d. Emergency operating procedures recertification and operator training could have captured it. Operating procedures review process and training is not effective.
e. Maintenance could not capture it during the preventive maintenance and testing of this critical safety system in 7 years. Maintenance program is not effective.

2. Management failure to identify the hazards and manage the risks.

a. Poor PHA quality. This was not captured during last PHA revalidations. Since there was no MOC for the trip bypass, credit for this barrier was taken and risk was considered acceptable which was not true.
b. This is one of the highest consequence scenarios and must be evaluated well. This may be a candidate for a more detailed risk study. Any changes or bypasses must be escalated to the plant manager for approval.
c. No process safety key performance indicators (KPI). KPIs could have raised the alarm of the repeat incidents.
d. Process safety audit is ineffective.
e. Process safety near miss are not defined and included in the investigation procedure
f. Lack of training and competency

There were several opportunities to detect this deficiency as mentioned above. Examples of good process safety culture and practices are:

a. Process safety near miss incidents are reviewed in daily management meetings.
b. A list of safety critical equipment is maintained up to date.
c. Written safety critical systems bypass program with strict control, approval process and audit.
d. Plant supervision review the critical alarms in the control room.

A quality incident investigation should reveal all these weaknesses in the management systems and process safety culture. If all the findings are addressed, then the incidents can definitely be prevented.

Example 2: Safety device test failure – pressure safety valve (PSV)

A PSV failed the pre pop shop test during the company's preventive maintenance program. Since there are no actual consequences of this incident, normally it is repaired and reinstalled. However, this failure is giving a warning sign that this PSV could have failed while in service leading to severe losses. This is a PSNM incident and should be reported for investigation.

Actual consequences: None. PSV pre-pop test failure in the shop.

Potential consequences: This PSV may fail while in service. Vessel burst, explosion and fire, severe losses.

What is the potential risk of not investigating this incident?

This PSV may not function at its set pressure while in service due to several reasons. The vessel may get overpressure and fail catastrophically with explosion, fire or toxic release with serious consequences.

How this incident investigation can prevent a major incident?

Considering the high potential consequences, this incident should be a candidate for root cause analysis. The potential root causes of the PSV test failure include but are not limited to:

a. Incorrect type of PSV.
b. Incorrect materials of construction.
c. Type of service – clean or dirty.
d. Operating conditions.
e. Lack of maintenance and testing.

The following actions are potential solutions to address the root causes;

a. Change PSV type.
b. Change material of construction.
c. Increase maintenance testing.
d. Add a rupture disc – upstream.

Examples of good process safety culture and practices are:

a. A written PSV testing procedure.
b. Competent person review the test records.
c. Fail test reported and investigated.
d. Fail test valve testing frequency reduced to half.
e. Audit the testing records.
f. Tracked KPIs.

The cost and resources to address the root causes of PSV test failure are negligible compared to an incident with severe consequences.

Disclaimer: The root causes and consequences and actions listed in the examples 1 and 2 are for illustration purpose only. In case of any such incidents, conduct your own root cause investigation and write actions for preventing the recurrences.

Similarly, other process safety near miss investigations can reveal management system weaknesses. Addressing these gaps can improve the risk and reduce the likelihood of incidents.

6. Incident investigation and learning process

The purpose of an incident investigation is to identify the root causes of an incident and provide the recommendations to prevent the recurrence of similar incidents. This process is comprised of five key steps as given in Figure 1.



Figure 1: Incident Investigation and Learning Process

The first two steps in the investigation process are critical for any incident however, emphasis is on the process safety near miss incidents. Subsequently, the learning process is same for all types of incidents.

The continuing learning gaps and best industry practices with learning for each step are provided in the following sections.

1.1 Incident Reporting

The first and foremost important step is to report an incident, only then can there be an investigation and lessons learned. Incidents such as fire, explosion, injuries, toxic release etc. are normally reported and investigated as per the company policy and to meet regulatory requirements. However, process safety near misses are not always reported. There may be several reasons for not reporting these incidents, including company safety culture, inadequate or complex processes, a lack of effective communication and awareness, etc.

Many of the world class companies in various sectors have defined what constitutes a process safety near miss for their company as well as implemented the reporting and investigation requirements for PSNMs through their corporate policies and programs. However, there are still a number of industries that are either not reporting process safety near misses or the process is not implemented effectively. What matters the most is how effectively the investigation and learning process is implemented, not just checking the box of reporting. This is the challenge Process Safety leaders are facing to make this program effective.

1.1.1 Most Common Gaps

Reporting requirements of process safety near miss incidents such as operations upsets, challenges to safety systems, safety system failure on demand, failure of safety systems during testing, etc., are not included in the company policy and procedures.

Not all process safety near miss incidents are reported due to poor process safety culture, inadequate and complex reporting processes, or a lack of training and awareness.

No key performance indicators and not audited.

1.1.2 Best Industry Practices

The incident investigation policy, procedures, and eTools are developed and updated to include reporting requirements of process safety near miss incidents.

Walk the Talk (importance of PSNM reporting) by site supervision. The operation manager and plant manager review the shift logbook and questions the operator about process safety near misses in addition to production, injuries and other unit related items.

An agenda item in the daily plant meeting.

Incident reporting requirement is built in to the relevant documents and audited regularly. Incidents and related documents are given below:

Incident	Document	Implementation
• **Safe operating limit excursions – operations upsets** • **Demands on safety systems – safety systems activated** • **Safety system failure on demand**	• Operating procedures: SOP / EOP • Operator training • Shift handover procedure • Shift logbook / report	• Training and awareness to management and operations personnel. • Regular compliance audit
• **Safety system test failure** • **PSV pre-pop test failures**	• Safety system testing procedure • Safety system test form • Work order	• Training and awareness to management and operations / maintenance personnel • Regular compliance audit

All employees are trained and made aware of the importance of reporting these incidents through various training and safety meetings. Management walk the talk approach is very effective to encourage employee participation for reporting all incidents.

1.1.3 Learning

It has been learned that before any major incident there were several precursors which were not reported, therefore not investigated. These precursors, if reported and investigated, could have prevented several major incidents.

A simple reporting process, an effective training program, a good safety culture, management commitment, and employee involvement drives continuous improvement for the reporting of all process safety incidents.

1.2 Incident Investigation

All reported incidents are investigated by using various techniques depending on the severity of the consequences. A critical step in this process is to categorize the incident for its level of investigation depending on the actual and potential consequences.

Low consequence incidents are given less effort and the resources end up with generic low risk recommendations, whereas higher consequence incidents are given more focus, more detailed investigations, and the recommendations may lead to major changes in the processes, plant, or people.

1.2.1 Most Common Gaps

Incidents are investigated based on their actual consequences, which may be none or very low, and may have very severe potential consequences. In such cases, normally a less detailed investigation technique is used such as "5 WHY", and the incident is potentially closed with generic, low impact recommendations.

Incidents are not investigated to the root cause level, even when a root cause analysis tool is used. The most common causes are poorly done investigation due to lack of competency, poor safety culture, or a complex investigation process/tool. Consequently, incident investigations are closed by listing the immediate or contributing causes rather than root causes.

1.2.2 Best Industry Practices

Near misses and minor incidents are investigated for actual as well as potential consequences using root cause analysis techniques. The level and details of investigations are based on the potential consequences, not the actual because potential consequences for a low actual consequence incident may be a disaster.

Refer to example 1 in section 5, operating outside the safe operating limit (SOL) has no actual consequences, if controlled, but may have very severe potential consequences such as runaway reaction, vessel rupture, equipment failure etc. if not controlled.

A well written procedure and a user friendly tool are used to conduct an investigation. Trained and competent teams in a good safety culture conduct and deliver high quality investigations and reports which help in preventing the recurrence of incidents.

1.2.3 Learning

Simple user friendly tools and techniques, well trained investigation teams, and good safety culture will produce a high quality investigation with true root causes or management system causes.

Without discovering the root causes, the recurrence of incidents cannot be prevented. This omission is one of the major causes of learning failure.

1.3 Recommendations

Writing and implementing specific recommendations which address the root causes of an incident is critical for a successful learning process. Generic recommendations do not address the root causes and are not measurable.

Example 3: A small fire occurred on an operating gas platform due to a hot work activity. There were several permit violations including: using a contractor's permit, no gas testing, flammable

materials were not removed, drains were not covered, etc. The root cause of this fire was the management failure to implement the hot work permit system. The recommendations should address this root cause but management fired the contractor and disciplinary action was taken against the operator and the investigation was closed. The root cause still exists and the same unsafe practices may continue until a serious incident occurs.

1.3.1 Most Common Gaps

Generic recommendations are written based on the immediate or contributing causes, not the root causes. In the above example, recommendation to remove the contractor and action against the operator addresses the immediate and contributing causes.

If the root causes are identified, then irrelevant or generic recommendations are written which are easy to close but do not address the root causes. "Improve operating procedures and retrain employees" is an example of a generic recommendation for a tank overfill incident.

1.3.2 Best Industry Practices

Specific recommendations are written which address the root causes and are auditable.

Specific recommendation example for a tank overfill incident: "Update tank operating procedure to include causes and steps taken by the operator to prevent tank overfill. Retrain operators on the procedure changes."

1.3.3 Learning

Specific recommendations addressing the root causes, if implemented effectively, could have prevented the recurrence of major incidents. Poor process safety culture and competency gaps are the leading causes of poorly written recommendations.

A well written recommendation could be "Add a redundant level transmitter with a pump trip at HI-HI level on all tanks storing hazardous materials. This recommendation should be implemented corporate-wide."

1.4 Action Tracking

The quality of action implementation is one of the major challenges for learning. Various action tracking tools are used for tracking the actions to closure. Well designed and implemented tools are very efficient and user friendly with auto tracking features.

1.4.1 Most Common Gaps

1.4.1.1. *Central tracking system:*

complex systems that are not designed and implemented effectively are a data dump. As a result, actions are not entered into this tool and are tracked individually on spreadsheets which are not auto tracked and do not provide summary reports for management review. In some tools, the important features such as action source, action priority, current status summary etc., are missing.

Some companies have a central action tracking tool which was designed by a large team of individuals from both the company and the vendor. Although years and millions of dollars were spent, the central action tracking tool became a data dump. The causes of the failure are incompetent teams who were unable to set the right expectations and did not involve the end users. The second cause of failure is the lack of effective training for end users.

1.4.1.2. *Individual tracking systems:*

these systems are developed in isolation by an individual and lack auto tracking features and may not provide the status of actions and summary report for management review. It is highly likely that

individually tracked action may quickly become difficult to track due to manual tracking by emails or paper copies.

1.4.1.3. *Implementation verification:*

actions are closed by using a check box approach which does not meet the intent of the recommendation. Quality of the action implementation is not verified by another competent person.

Example of a recommendation without verification: "Add a 30 minute fire watch to a hot work permit as a result of a fire incident." This action was closed by adding this requirement on the permit form only but the procedure and training was not updated.

1.4.2 Best Industry Practices

A simple, user friendly tool is designed as per the company requirements by input from the end users. It is rolled out effectively through face to face and hands on initial training with periodic need based refresher training. The tool imports the actions from other tools and has all tracking features including action priority, current status, due date, accountability, and can produce summary reports with graphics for management review.

A well designed spreadsheet tracks the actions and produces summary reports for management review. Changes and modification can be made easily such as adding a new column for filtering the high priority actions.

Actions are resolved by the assigned person and verified for effective implementation by another competent person. Without this verification step, the action cannot be closed.

Actions are reviewed by the management.

1.4.3 Learning

Companies should develop or update their procedures and then design the action tracking tools to meet the necessary requirements. The tools should be need based, and not what the vendor wants to sell. Complex tools fall in the data dumps and employees keep using their paper copies for tracking actions in isolation, leading to the failure of the overall learning process.

A poorly implemented action is another leading cause of learning failure. Lack of competency, economic reasons, and safety culture force an action to close without proper verification. Checking a box methodology still prevails.

1.5 Learning Sharing and Implementation

Learning from incidents is not limited to incident investigation and closing the actions at the plant level. If the lessons learned are not shared within or outside the company due to a lack of effective learning process, then this causes the total failure and defeats the overall incident investigation objective. Learning can be more effective if imbedded into corporate policies, engineering and design standards, and operating management systems. It is critical to identify and eliminate the communication and implementation gaps in these processes and systems in order to prevent the recurrences of major incidents. Figure 2 below illustrates the learning cycle for prevention of recurring incidents.

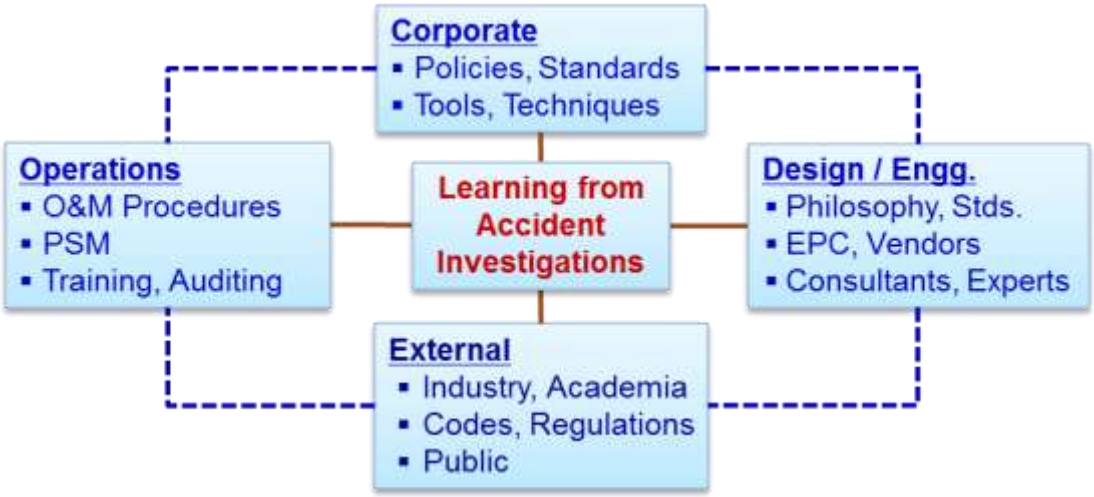


Figure 2: Learning cycle for prevention of recurrences of incidents

1.5.1 Most Common Gaps

Lessons learned are applied at plant level but not communicated or incorporated in the following management systems due to a poor process safety culture and a subpar learning process:

- Corporate policies and standards for company-wide implementation.
- Engineering and design standards for future projects and modifications.

Lessons learned are incorporated in design standards, but not implemented in design due to project cost control, poorly done hazard studies, or poor safety culture.

Lessons learned are implemented in designs and installed safety systems, but bypassed or not maintained in the operations stage due to lack of any one or combination of the following: effective maintenance practices, safety bypass programs, process safety competency, safety culture, etc.

1.5.2 Best Industry Practices

A one page incident summary with causes, consequences and actions to prevent the recurrences is shared across the corporation and discussed in various meetings. A monthly process safety beacon issued by CCPS is one of the best examples. [4]

Learning is communicated and implemented effectively and verified by a competent person. Learnings are incorporated in corporate policies, design standards, and operating management systems across the company.

Example of a fully implemented recommendation from a tank fire incident caused by tank overfill: "Add a redundant level transmitter with pump trip at HI-HI level at all tanks storing hazardous materials." Corporate philosophy for tank operation was updated, the requirement was added in design standards for future projects and modifications, site operating / maintenance procedures and training were updated, affected people were trained.

1.5.3 Learning

Strong corporate safety culture, robust management programs, management commitment and employee involvement are the key components for the communication and effective implementation of the learning process. Furthermore, continuous performance measurements will improve corporate memory of learning from incidents.

Learning from PSNM is a proactive approach for incident prevention whereas learning from incidents is a reactive approach for recurrences of incidents.

7. Conclusion

Process safety near miss incident reporting requirements should be ingrained in all relevant documents and audited for compliance. Consistent and fit-for-purpose management systems, simpler processes and tools, a good process safety culture, and a competent workforce all work hand in hand to prevent the failure to learn from past incidents.

Conducting gap assessments in process safety management systems and developing strategic action plans can help in improving the overall learning process. A good start can be analyzing recommendations from third parties, corporate audits, inspections, and incident investigations.

In a poor corporate safety culture, management programs and processes are poorly developed and implemented, documents and activities are manipulated, and the priority is production over safety. After any major incident, people tend to forget the lessons or the drive to implement learnings. As repeatedly stated by the late Dr. Trevor Kletz, "organizations have no memory, only people have", it is therefore imperative that process safety experts have memory and apply the learning to prevent the recurrence of similar major incidents.

References

1. U.S. Chemical Safety Board. Accessed at www.csb.gov
2. Process Safety near Misses in Dow Chemical: A Proactive Program to Improve Process Safety Performance - AIChE Spring Meeting and Global Congress on Process Safety, April 3, 2012
3. American Petroleum Institute, ANSI/API Recommended Practice 754, Process Safety Performance Indicators for the Refining and Petrochemical Industries, Second Edition, Washington D.C., 2016.
4. Process Safety Beacon – American Institute of Chemical Engineers, Center for Chemical Process. https://www.aiche.org/ccps/search/beacon

The views expressed in this work by the author(s) are his/her/their own and do not necessarily represent those of American International Group, Inc. (AIG) or any of its subsidiaries, business units or affiliates. Persons should always seek the advice of counsel or a professional insurance broker before purchasing any insurance product or services.

This document is for general informational purposes only, and has been compiled from sources believed to be reliable. The information herein does not address every possible loss potential, law, rule, regulation, practice or procedure. No warranty, guarantee, or representation, either expressed or implied, is made as to the correctness or sufficiency of the information herein. Reliance upon, or compliance with, anything stated herein in no way guarantees any result, including without limitation the fulfillment of your obligations under your insurance policy or as may otherwise be required by any laws, rules or regulations. No responsibility is assumed for the discovery and/or elimination of any hazards that could cause incidents, injury or damage. The information contained herein should not be construed as financial, accounting, tax or legal advice and does not create an attorney-client relationship.

American International Group, Inc. (AIG) is a leading global insurance organization. Building on 100 years of experience, today AIG member companies provide a wide range of property casualty insurance, life insurance, retirement solutions, and other financial services to customers in more than 80 countries and jurisdictions. These diverse offerings include products and services that help businesses and individuals protect their assets, manage risks and provide for retirement security. AIG common stock is listed on the New York Stock Exchange.

Additional information about AIG can be found at www.aig.com | YouTube: www.youtube.com/aig | Twitter: @AIGinsurance www.twitter.com/AIGinsurance | LinkedIn: www.linkedin.com/company/aig. These references with additional information about AIG have been provided as a convenience, and the information contained on such websites is not incorporated by reference into this document.

AIG is the marketing name for the worldwide property-casualty, life and retirement, and general insurance operations of American International Group, Inc. For additional information, please visit our website at www.aig.com. All products and services are written or provided by subsidiaries or affiliates of American International Group, Inc. Products or services may not be available in all countries and jurisdictions, and coverage is subject to underwriting requirements and actual policy language. Non-insurance products and services may be provided by independent third parties. Certain property-casualty coverages may be provided by a surplus lines insurer. Surplus lines insurers do not generally participate in state guaranty funds, and insureds are therefore not protected by such funds.

© American International Group, Inc. All rights reserved.

Protection Layers Integrity Management, an Illusion?

Rajender Dahiya, CSP, MIChemE [1] and Priyal Dahiya [2,*]

[1] Professional Process Safety Engineer , Senior Technical Services Manager – Loss Control
AIG PC Global Services, Inc./ A member company of American International Group, Inc. (AIG) ,
Houston, Texas USA

[2] Mechanical Engineering , University of Texas, Austin, Texas USA

**Corresponding authors: rajender.dahiya@aig.com ; priyal@utexas.edu*

Abstract: Illusions about protection layer integrity can leave a facility exposed to loss. It doesn't have to be that way.Trending scenarios where employees experienced an illusion of process safety were identified as the author conducted risk assessments and interacted with site managers at complex high-hazard oil and chemical processing plants. In each of these scenarios, robust safety systems with multiple layers of protection were in place, yet because of gaps in operating management systems and process safety knowledge of the workforce, the facility remained exposed to potential loss. Similarly, the author observed that some organizations believe that a process hazard analysis (PHA), once completed, provided a backdrop of safety. This perception is yet another illusion. PHA alone is not intended to guarantee safe operations. A robust integrated management system and a strong process safety culture are essential for safe operations.These findings raise the question, "How do we know if the systems in place are effective and the process safety culture is sufficient?" This question can be answered in one of two ways: 1) proactively, where gaps or opportunities for improvement are identified before a loss or 2) through a reactive approach in which gaps in the safety systems are realized after a loss as a lesson learned, often a costly one.In this paper, the author identifies real-life examples of "illusion" and explains how a proactive approach to identifying gaps in management programs, employee competency and safety culture can help to ensure layer of protection integrity. Emphasis is given to the integrity of maintenance programs, operating discipline, training, and risk-modeled exercises. The author also shares several surprises that were revealed during the fact-checking discussions along-side relevant industry best practices. The paper concludes by explaining how a well-written and implemented management program in general, and the inspection, testing and preventive maintenance program in particular plays a vital role in maintaining the integrity of the protection layers that can help to prevent potentially serious and major process incidents.

Keywords: protection layers integrity, safety critical, incident prevention

1. Introduction

The purpose of the protection layers (PL) is to either prevent or mitigate a potential incident. These protection layers are typically independent of the basic process control systems (BPCS) and act when the BPCS are unable to prevent the escalation. These safety systems can be either automatic or manual or in combination. A combination of management programs, tools, techniques, and human actions are required to maintain the integrity and availability of these critical systems.

Failure to maintain the integrity of safety systems is one of the primary root causes of major incidents.

In this paper, the author shares numerous industry best practices that may be helpful.

For the purpose of this paper, world class operators (companies) are those – small or large – that have implemented very strong management programs, a competent (trained and experienced)

workforce and go beyond the minimum requirements of local codes, regulations and manufacturer's recommendations. The practices that world class companies put into place beyond what is minimally required are often then identified as "best industry practices" and shared with peers in that industry.

In this paper, it is presumed that the hazards identification and risk management steps are completed, and adequate safeguards are installed. The scope is limited to the integrity, availability, and operability of these safety critical systems during the operation phase of the facility.

Note: the terms "protection layers", "safety systems", "safeguards", and "safety barriers" are used interchangeably across various industries and also in this paper.

2. Protection Layers – Life Cycle

The Hazard identification and risk assessment (HIRA) process starts early in the project design and engineering stages and continues throughout the lifecycle of the project employing various techniques and tools. These may include hazard identification studies (HAZID), PHA, layer of protection analysis (LOPA), quantitative risk assessment (QRA) etc. Protection layers or safeguards designed to prevent an incident or mitigate the consequences of an incident are identified during this process.

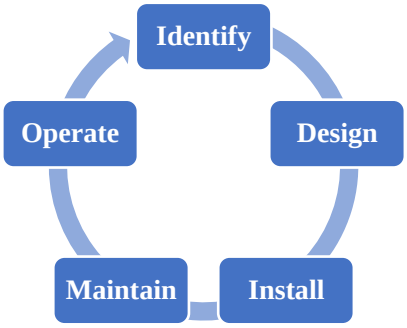


Figure 1: Protection Layers Lifecycle

The HIRA process is mandatory and critical to demonstrate that all potential hazards are identified and risks managed using a hierarchy of controls and the facility is safe to operate. These identified safeguards are then designed, installed, and tested for the proper functioning and the project is handed over to Operations. Responsibility then becomes that of the plant management to operate and maintain the equipment and systems as described in design specifications, and as per licensor, vendor, codes, and industry best practices. Figure 1: Protection Layers Lifecycle.

The following scenarios demonstrate how knowingly or unknowingly, the integrity of the safeguards can deteriorate with time. This integrity deterioration can lead to a facility operating at a higher and potentially unacceptable level of risk.

2.1 Design Stage – Acceptable Risk

Figure 2. Design Stage - Risk Management illustrates how risks from identified potential hazards are managed through adequate safeguards to an acceptable level as per corporate risk criteria. This is normally the case when the site is built and handed over to Operations. The expectation is to then keep the protection layers intact during the operating stage. For companies who maintain the facility as it was designed, the protection layers can stay in place "as is" and the plant operates within an acceptable level of risk.

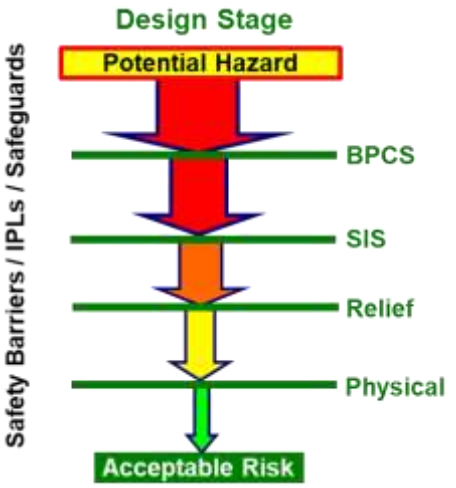


Figure 2: Design Stage – Risk Management

2.2 Operation Stage – An Illusion!

A well-designed and protected facility does not typically stay the same after the design stage. Safety systems can become disabled, degraded, or bypassed. See Figure 3. Over time, gaps in the protection layers develop. In this case, knowingly or unknowingly, the facility is operating at a higher, potentially unacceptable risk. And management may be unaware this is occurring.

It is commonly heard from the management personnel that "My plant is built to codes and we are following the codes." No doubt, meeting code requirements is a must; however, codes are a minimum requirement to operate a facility. Industry Best Practices and Recognized and Generally Accepted Good Engineering Practices (RAGAGEP) can further help in minimizing incidents and losses.

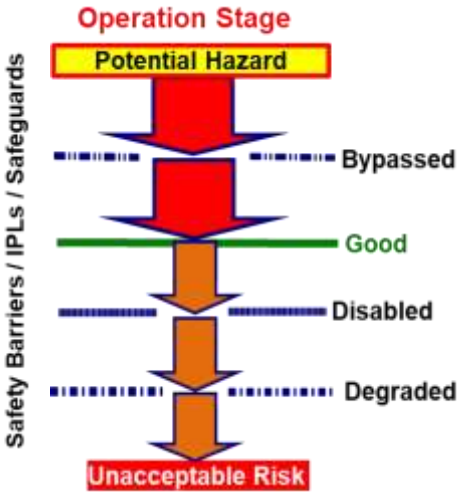


Figure 3: Operation Stage – Risk Management

For the scenario depicted in Figure 3, it can be seen that one "Good Safeguard" can prevent an incident, but only if it is an independent protection layer (IPL). However, to reach the point where 75% of the safeguards were not maintained, many warning signs must have been neglected. There are several proactive actions that can help minimize the potential for this type of scenario: identifying process weaknesses by investigating process safety near miss (PSNM) incidents, auditing, training, management reviews, key performance indicators (KPI), emergency operating drills, and more. Plant management should know the current state of the risk through documentary proof.

The root causes of these weaknesses are discussed in the following sections.

2.3 Reactive Approach – An Incident

Management failure to maintain the integrity of safety systems is one of the primary root causes of major incidents, and management failure to learn from the incidents is the root cause of repeat incidents. Figure 4 - Swiss Cheese Model demonstrates a scenario where all preventive and mitigative safeguards failed, and an incident occurred. There were opportunities to identify these gaps in protection layer integrity through warning signs and weak signals. This is the reactive approach of risk management and it does not stop with one incident. Following an incident, complacency continues, the incident reoccurs, and a vicious cycle begins. This scenario explains the results of weaknesses in the management programs to maintain the integrity of safeguards - one of the leading causes of major incidents and their recurrences due to reluctancy after a reactive approach. The holes in the safeguards represent a failure mode and indicate weaknesses in the management program and / or human performance. Thus, through robust ITPM practices, the size of the holes can be minimized and, sometimes, certain failure modes (holes themselves) can be eliminated through engineering.

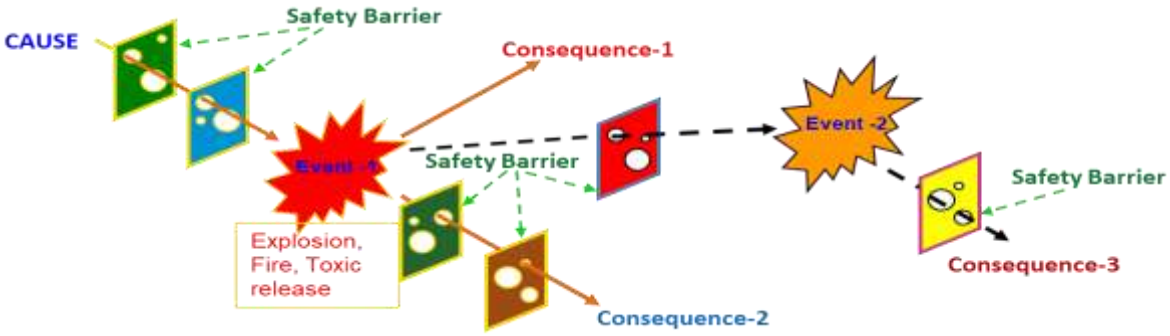


Figure 4: Incident Scenario

The management system weaknesses and their causes are explained in the following sections.

3. Walkthrough Process

This section is based on author's personal experience derived from loss control discussions with site management and employees of several large and complex high hazard industries including oil refineries, chemicals, petrochemicals and gas processing plants, oil terminals, medium and small size chemical batch process and midstream operations. Some of the sites visited were world class leading industries with best practices in loss prevention and risk management. However, those also have improvement opportunities that are also highlighted in this paper. The improvement opportunities identified in this paper are from all kind of industries mentioned above. The best practices shared are learned from the leading industries, insurance brokers and insurance risk engineers, US Chemical Safety Board (CSB), industry organizations such as American Institute of Chemical Engineers (AIChE), Center for Chemical Process Safety (CCPS), Institution of Chemical Engineers (IChemE), American Petroleum Institute (API) and other web resources. The following sections will cover high level questions and deep dive to reveal the gaps in the management programs and human performance required to maintain the integrity and availability of protection layers.

3.1. High Level Screening Questions (Conference Room)

To start, the facility manager and/or discipline managers are asked high-level questions found in Table 1. All "YES" answers were verified in detail. The findings often surprised the site management.

Table 1: High Level Questions				
Site Discipline Manager's Answer	**Process Safety Management (PSM) Covered Sites**			**Non-PSM**
Questions	**World Class**	**Large and Complex**	**Small-Medium**	**Low Hazards**
Do you know and understand the facility's hazards?	YES 100%	YES 100%	YES 100%	Yes 100%
The answer is a big "YES" by all site managers with full confidence.				
Are those hazards identified and risks managed adequately?	YES 100%	YES 100%	YES 100%	Yes >90%
The answer is a big "YES" by PSM covered facilities and >90% by others. In most cases PHA is the answer. However, poor quality PHAs are not uncommon in which either the risks are not assessed or managed adequately.				
Are there management systems in place to maintain the safeguards?	YES 100%	YES 100%	YES >80%	Yes >50%
The confidence starts to diminish as the questioning moves towards documentation. The common answer is the PM program however, there are gaps.				
Is there documented evidence to demonstrate that all safeguards are maintained and available – fully functional and the current level of your facility's risk is tolerable?	YES 100%	YES >90%	YES <60%	Yes <50%
More than 60% of the time, documentary proof could not be made available due to inadequate and inconsistent management programs.				
Does the management system in place adhere to the RAGAGEP as a minimum requirement?	YES 100%	YES >70%	YES <30%	Yes <5%
Mid and small size PSM covered facilities think they adhere but in reality, NO, they do not. Most programs of the large site's adhere but not all.				
Is documented evidence externally verified and benchmarked with peers?	YES >90%	YES <30%	YES <5%	No
Most PSM covered sites employ a third party for audits; very few companies benchmark against their peers.				
Note: The values reported in Table 1 are based on author's estimates based on experience.				

All the YES answers are reviewed further and verified in more detail by reviewing the management programs, records, interviewing personnel, and physical check in the field. Most common findings are discussed in the following sections.

3.2. Process Safety and Process Engineering

Process engineering and process safety personnel normally own the hazard identification and risk assessment process. They are accountable for communicating the outcomes of the hazard studies to the affected personnel and monitoring the integrity, availability, and operability of the safeguards.

Process Safety is also responsible for educating the management and workforce about process risks and the management of those risks. The answer to the following question was verified in detail.

Question 3. Are all hazards identified and the risks acceptably managed?

Answer: The response of most of the process safety / engineering manager(s) is YES.

The following gaps were identified during discussions, document reviews, site visit, and interviews.

3.2.1 Most common findings

- Lack of process safety competency throughout – management to staff level.
- Poorly done hazard studies, particularly PHA.
- No formal process to communicate PHA outcomes to affected personnel.
- PHA report is not made available to affected personnel for reference.
- Current process safety information (PSI) such as C&ED, safety interlock list, piping and instrumentation drawings (P&IDs), interlock loop drawings are not readily available and / or not referenced.
- Lack of understanding of the purpose of a safety bypass.
- Production and personnel safety are still a priority due to poor process safety culture.

Illusion: Management assumes that relevant staff are trained in process safety management. However, in more than 50% of the cases, only a 45-60-minute computer-based (CBT) PSM training that covers all 14 OSHA PSM elements is provided to management and employees. Therefore, a process safety training and competency program is implemented however, not effective due to the inadequacy of the training. In a few instances board operators have never seen a PHA report.

3.3. Integrity of Safeguards – Inspection, Testing and Preventive Maintenance (ITPM)

Inspection and maintenance are responsible for maintaining the integrity of all safety systems. The answer to the following question was verified in detail.

Question 1. Are all safety critical systems (safeguards) maintained as per manufacturer's recommendations, local codes and RAGAGEP?

Answer: The response of most of the inspection and maintenance manager(s) is YES. The most common answer is that all safety systems are inspected, tested, and maintained but there are no test records.

The following gaps were identified during discussions, document reviews, site visit, and interviews.

3.3.1. Most Common Findings

a. No list of safety critical equipment and devices.
b. Inadequate maintenance procedures.
c. Inspection and testing methods are not written.
d. No formal maintenance training program.
e. Incomplete or no records of inspection and testing.
f. Required PSI not available – C&ED, P&IDs and interlock loop drawings.
g. Inadequate or indecisive KPIs.
h. No or poorly audited program(s).

3.3.2. Most Common Findings – World Class Companies

a. Lacking current and consistent PSI.

b. Incomplete testing records.
c. Lacking data analysis, learning and continuous improvement.
d. Shallow internal audit. Checkbox approach still prevails.
e. Deficient benchmarking with other sites or peer companies.
f. Instrumented safety systems test failures are not investigated.

Illusion: Management assumes that all safety systems are maintained. Yet in the majority of the cases where formal inspection, testing and a preventive maintenance program were implemented and audited, no or only basic findings were reported. In more than 50% of the cases, there was no list of safeguards and test records were either incomplete or not documented at all.

3.4. Availability and Operability – Operations and Process Control

Operations, process engineering and process control personnel are responsible for ensuring the availability, accessibility, and operability of safety barriers. The answer to the following question was verified in detail.

Question 2. Are all safety critical systems (safeguards) available and operable?

Answer: The response of most of the operations/process manager(s) is YES.

The following gaps were identified during discussions, document reviews, site visit, and interviews.

3.4.1 Most common findings

- Availability – Safety Bypass
  - Inadequate formal safety bypass program – procedure, permit, log, audit, KPIs.
  - In most cases, consequences of safety bypass, and interim measures sections are either missing from the bypass permit or poorly completed.
  - Incomplete bypass permits signed off by the approvers.
  - Missing duration of bypass.
  - Permits active for several month after reinstating the safeguard.

- Operability – Training and Accessibility
  - Users are not trained when to use the ESD and what happens when it is activated. This requirement is not documented in operating procedures.
  - Missing C&ED or shutdown keys.
  - Inconsistency between the critical interlocks in the field and operating procedure.
  - The ESD button is not installed at a safe location or is not accessible.
  - ESD button is not visible, no, or poor labeling.

3.4.2 Most Common Findings – World Class Companies

- Bypassed without appropriate equivalent interim measures. In most cases, critical safeguard (IPL) is bypassed without assessing the risk of the bypass and providing equivalent temporary measures.
- More than 50% of the closed bypass permits reviewed were found incomplete and signed off by multiple level of authorities.
- PHA/LOPA and C&ED are not referred to understand the consequences of bypass.

Illusion: Management assumes that there is a formal safety bypass program implemented and audited periodically with minor findings. However, in more than 70% cases, a bypass permit is used just to get management approval (signature) to bypass a safeguard. The consequences of the bypass and interim measures are either not on the permit or poorly articulated. Interestingly, due to lack of

process safety competency and poor process safety culture, management signs these permits without ensuring that the process meets the intent. In this case, bypass simply means safeguard is disabled.

4. Example – Disabled Safeguard (IPL)

The following example describes how a critical safeguard was disabled for 7 years and was not be captured by any of the various programs and activities due to ineffective and inconsistent management programs and poor culture. If all the required activities were performed per corporate policies, then how is it that such a big gap in front of everyone's eyes could not be recognized and fixed in 7 years??? Many new sets of eyes have come to this place in those years.

During the plant control room visit, a visual alarm (RED Window) was observed on the distributed control system (DCS) screen. After discussions with the board operator and site management, the following observation and facts were identified.

- A process with a runaway reaction hazard with an auto trip safety system, which was set at 355^0F, was disabled; the board operator controlled the process which reached 372 ^{0}F, 17^0F above its trip set point.
- The trip system was in disabled mode for more than 7 years, so the unit did not trip automatically. This event was documented in the logbook like other process data / parameters. It was not discussed in any meeting and no concerns were raised. No incident was submitted.
- This was the third incident in one year with that particular board operator. There may be more such incidents on other shifts.
- The board operator and operation supervisors don't understand what went wrong in this case and why a controlled temperature runaway event was considered an incident when there is no injury, no realized loss, and the unit was not shutdown. On the other hand, they think this demonstrates that the operators are competent to manage the emergency operations. In other words, "Job well done!" However, they do not understand the potential risk associated with this incident. This is also a normalization of deviation and the company is very fortunate not to face an accident so far.

Considering the high potential consequences, this incident (PSNM) should be a candidate for a detailed root cause analysis (RCA). The investigation will not only point at the weaknesses in the barriers and human interface but also identify missing barriers, unidentified hazards or underestimated / unmitigated risks.

The team performing the investigation would be expected to identify the following system causes, at a minimum:

- **Management failure to maintain the integrity of critical safeguards.**

Considering the potential consequences, this risk should be one of the highest risks at the site and be taken seriously.

a. The trip system was disabled for more than 7 years. There was no documentation for disabling this critical barrier such as safety bypass or management of change.
b. Operation, maintenance, and process safety staff were not aware of this change.
c. No one questions the "trip window" RED on the DCS for 7 years.
d. Annual emergency operating procedures recertification and operator training could have captured it. The operating procedure review process and training was not effective.
e. Maintenance could not capture it during the preventive maintenance and testing of this critical safety system in 7 years. The maintenance program was not effective. This critical barrier was not in the list. In realty, there was no formal list of safety critical equipment (SCE).

- **Management failure to identify the hazards and manage the risks.**

f. This was not captured during the last PHA revalidations. Since there was no MOC or bypass, credit for this barrier was taken and risk was considered acceptable which was not true. A senior operator must have raised the alarm in PHA. This is an example of a poor quality PHA.
g. This is one of the highest consequence scenarios and must be evaluated well. This may be a candidate for a more detailed risk study. Any change or bypass must be escalated to the plant manager for approval.
h. There were no process safety key performance indicators (KPI). KPIs could have raised the alarm to the repeat incidents.
i. Several audits were performed during this time. No one questioned this disabled trip system in DCS or asked for the SCE list and testing records. The auditing process was ineffective.
j. Process safety near miss were not defined and included in the investigation procedure. Therefore, they were never reported and investigated.
k. Ineffective training and competency of site management and employees. In this case, training was more important for management personnel than shop floor staff.

All operation, maintenance and engineering activities mentioned above are performed as planned. There were several opportunities to detect this deficiency. The management programs, procedures and practices were ineffective individually as well as inconsistent and lacked integration.

- PHA, P&ID, C&ED, MOC were inconsistent as well as ineffective individually. Competency of PHA team and process safety culture was deprived.
- DCS, EOP, Training, EOP Recertification, shift handover, operations upset reporting, were not consistent as well as not effective individually and in combination.
- Inspection and maintenance programs were inadequate.

Examples of good process safety culture and practices are:

e. Management should enquire about PSM activities along with production and personnel safety.
f. Process safety is given the priority by management and transfer downward.
g. Process safety near miss incidents are reviewed in daily management meetings.
h. Plant supervision to review the critical alarms in the control room.

The root causes of this failure are lack of process safety competency and poor process safety culture misalignment between site management and shop floor employees.

The example shows a fragmented and ineffective management system; however, an integrated management system could have identified, and the problem fixed sooner. A cohesive management system, competent site management and a strong process safety culture is must to identify and eliminate such gaps.

Illusion: What can be a bigger illusion than this as explained in the example? These weaknesses are not uncommon in industries. They exist from high hazard industries to small operations.

5. What is Next

As discussed earlier, management programs and human performance is required to maintain the integrity and availability of safeguards. As a minimum the facility should develop and implement the following processes and programs and document the results.

6. Process Safety Engineering

Process safety team is normally responsible for educating the site personnel about the hazards associated with the plant and ensuring that the integrity and availability of safety systems is maintained, and facility is operated at acceptable risk.

a. Provide adequate initial PSM training to management and employees. Then continue need-based and refresher training for continuous improvement.

b. Educate management about the importance of process safety systems in improving the productivity, safety, and integrity of the plant by preventing untimely shutdown and losses.
c. Define what is critical safety equipment, safeguard, or protection layer. Provide the list to maintenance and operations.
d. Ensure management and employees are trained for maintaining and using the safeguards.
e. Communicate the outcome of hazard studies to management and affected employees.
f. Keep PHA report a living document and educate employees how and when to use it. Make it available to them.
g. Make process safety information available to relevant employees which include at least P&IDs, C&E drawing, shut down keys, safety interlock list, loop drawings.
h. The integrity and availability of safeguards should be audited and any opportunity for improvement should be implemented. Provide need-based training and improve the overall process.
i. The status of all safeguards should be tracked using formal key performance indicators, compare against the goal and review by management. Keep continuous improvement cycle on.

7. Maintenance Management

If one or more of the following programs do not exist, those should be developed and implemented. If all required programs exist, then review them for the effectiveness and improve them per RAGAGEP and industry best practices. Continuous improvement should be an ongoing process. Equally important is that the process be effective.

It doesn't always matter what you do…what matters is how good you do it. To help ensure effectiveness:

Develop/write:

a. A list of all the safeguards. PHA/LOPA reports are the best sources.
b. Performance standards.
c. Preventive maintenance procedures.
d. Inspection and testing methods/procedure.
e. Inspection and testing frequency per manufacturer or risk-based guidelines.
f. Inspection and testing checklist/form. Use a current cause and effect diagram to develop the checklist.
g. Formal ITPM deferral program. Ensure it meets the industry practices, not just a paper copy for signature and records.
h. Formal training program for maintenance employees and contractors. It should include ongoing and refresher training.

Quality assurance:

i. Process to verify each equipment function test results documented and complete. Final sign off by instrument and control, process control and operations.
j. Process to ensure the inspection and test records are reviewed by a competent person.

Review and improve:

k. Process to report test failures as PSNM.
l. Formal audit program consistent with industry best practices.
m. KPIs, track and analyze. Communicate to all affected and review by management.
n. Action tracking program and review by management. Ensure actions are prioritized with due dates. Implement a formal approval process for changing the due date if needed.

o. Formal learning process. Ensure the process is effective for sharing and learning from others. Incorporate lessons learned into the procedures and training program in addition to the toolbox talk.

8. Operations Management

Safety barrier failures to prevent or mitigate an incident do not depend merely on its readiness but also on the correct use and upkeep by operations or other users.

Operations or the other user should ensure that the safeguards are available, accessible and operable. This can be achieved by implementing the following programs.

9. Availability

Safety barriers must be ever ready to perform their function. However, there are circumstances when a safeguard is required to be bypassed. The purpose of safety bypass process is to ensure that the risk of bypassing a safeguard is managed by equivalent interim measures and is restored back to its original operating condition. The intent of the program is not for a worker, to just get approval signatures and file the form. The following steps should be followed to ensure that the risk is managed, and the safeguard is restored in its working condition.

The majority of the facilities have a written safety bypass program and some use temporary MOC for this purpose. There are improvement opportunities in the procedure as well as its implementation. The program should include at least the following.

a. Written procedure, bypass permit and a bypass log. Some companies have a partly or fully electronic bypass management program.
b. Active bypasses are readily available in the DCS in a paper or electronic log.
c. In addition to other requirements, there should be an approval escalation process based on the criticality (for e.g., bypassing an alarm versus safety interlock) and duration of bypass (e.g., SIS bypass allowed for a maximum of 24 hours).
d. Ensure that consequences of bypass, and interim measures are included in the procedure and permit. Refer PHA/LOPA to know the consequences of bypass.
e. Communicating safety bypass should be a mandatory item during shift handover process.
f. Tracking process of transition from bypass to MOC to closure.
g. Before signing, approving authority should ensure that all sections of the permit are correct and complete especially consequences of bypass, and interim measures. These are the most critical steps of bypass and are poorly done.
h. Ensure duration of bypass comply with the procedure.

10. Operability and Accessibility

Most of the instrumented safeguards are interlocked and function automatically. The most common manual safety system is an emergency shut down system (ESD) which is normally hardwired and can be activated from the field (in some cases more than one location) as well as DCS. Following improvements are identified:

a. As mentioned earlier, more than 50% operators do not know when to push the ESD button and what happens after the button is pushed. Even if they know, it is not documented. ESD system criteria should be clearly documented in the operating procedures (emergency procedures) and communicated to the operators (end users) including authority to shut down, when to shut down and what happens afterwards. A Cause and Effects diagram is the most relevant document to help a person understand the logic of the ESD. This diagram should be made available in the DCS. Figure 5 depicts the steps for ESD in a typical high risk process unit with multiple IPLs.

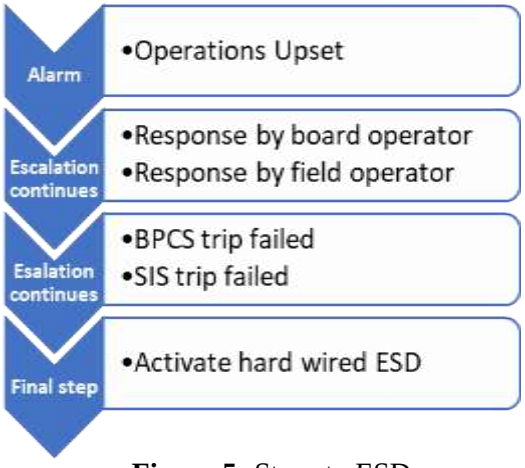


Figure 5: Steps to ESD

b. ESD buttons should be labeled appropriately for identification and visibility. A safety cover should be provided to prevent accidental activation and weather protection if the button is outdoors.
c. The location of ESD button should be at a remote location away from the hazard along the evacuation route. For example, an ESD button could be located on either side of a truck loading rack instead of in the center of the rack next to the loading pump.
d. Operator should sign the testing form for each ESD tested and field verified.

10.1 Process Safety Competency and Culture

10.1.1 Process Safety Competency

Process safety training for management / supervisory level is equally important as the shop floor employees. They are the people who verify and approve all the risk management decisions. Competent management and employees will ensure the quality and completeness of each activity and will prevent the check box mentality. Everyone should be trained as per their roles in PS activities instead of just 45-60 minutes CBT PSM overview. In the earlier example, there were many opportunities to catch the disabled safeguard but lack of PSM competency was one of the root causes. A training matrix should be developed for all affected management personnel and employees.

10.1.2 Process safety culture

One of the leading causes of overlooking the process risks and their management is poor process safety culture. Production is a must but safety first should be the one of the key slogans of the company, posted widely and discussed in meetings. More than that, safety first should be practiced by the management as a role model to help influence shop floor employees. A strong positive top down process safety culture is must for developing and implementing required programs and continuous improvement. Figure 6 demonstrates that a robust management system, competent workforce and a strong process safety culture are the foundation of a safer workplace. In other words, a competent workforce in a good process safety culture will be able to develop and implement a robust management system.

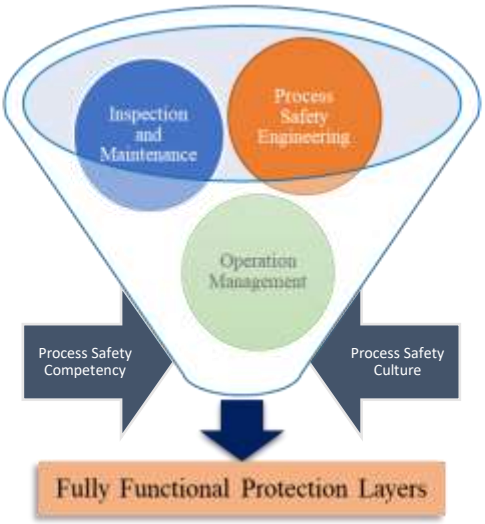


Figure 6: A Safer Workplace

11. Industry Best Practices

Following are some of the industry best practices used in world class and leading industries.

Testing and Maintenance:

a. A formal procedure and testing records. An example of Safety System (SIS) Testing and Inspection Procedure is given in Table 2.

Table 2: Safety System (SIS) Testing and Inspection Procedure – Sample

Scope					
Test frequency	▪ Sensor: XX Months at the maximum ▪ Logic Solver: XX Months at the maximum ▪ Final Element: XX Months at the maximum				
Requirements	Qualifications of persons doing testing and others				
Required documents	P&IDs, C&ED, data sheets, loop drawing, testing sheet, other				
Tools and equipment	As applicable				
Safety requirements	▪ JSA ▪ Gas monitoring ▪ PPE ▪ ……				
Environmental impact	Leak, spill or emission				
Responsibilities	▪ Process control engineer ▪ Instrument and electrical technician ▪ Operator (DCS and Field)				
HIRA	▪ Safety Bypass ▪ Procedure deviation ▪ Risk mitigation plans				
Description of safety function	▪ Description ▪ Critical action ▪ Loop drawing				
Test procedure	All required step including permit to work, safety and test outcomes recorded.				
	▪ Step 1 ▪ Step 2 ▪ ….. and so on			Y	N NA
Findings	All corrective actions documented and communicated to relevant parties.				
Sign-off	Department	Name	Date	Signature	
	▪ Process Control ▪ Maintenance ▪ Operations				

b. Testing failures and challenges to safety systems are investigated as a process safety near miss incident. The ITPM frequency is changed in case the SIS or PSV fail the test. (for e.g., 5 years to 2.5 years).

c. A formal ITPM deferral program and deferred equipment listed as overdue. ITPM completed at the earliest opportunity.

Safety Bypass Management

a. Some facility's policy is not to bypass a Safety Trip and ESD system, instead shutdown the unit and fix the problem. This is possible mostly in smaller units with batch processes or individual units not impacting the entire site.

b. Safety bypass approval escalation process based on the risk level and duration of the bypass. The duration of SIS bypass can be allowed up to maximum of one shift to 24 hours. Further evaluation and approval escalation are required to extend after 24 hours or use an MOC.
c. Electronic reminders for a bypass in every shift especially with newer control systems.
d. Live status of bypass. In modern DCS, active bypasses are visible on the DCS or dedicated SIS console. A list of active bypasses available.
e. An example of Safety System (SIS) Bypass Permit is given in Table 3.

Table 3: Safety System (SIS) Bypass Permit – Sample

Safety System (SIS) Bypass Permit/Approval Form			
Requested By		Unit:	MOC#: (if >24 hrs.)
Date and time start		Date and time end	(Max 24 hrs.)
Device being bypassed			
Bypass description			
Reason for bypass			
Are any other initiators in the system currently bypassed? If yes, list.			
Risk of operating in bypass (mode of failure)			
Mitigation measures	Backup Variable if any: ▪ Description and Tag#: ▪ Trip Point:		
Method of bypassing			
Approval	Name	Date / Time	Extension-Date/Time
Board Operator			
Shift Leader			
Operations Manager			
Installed by			
Removed by			
Verified by			
Note: safeguards other than SIS can be bypassed for longer time as per the procedure. Criteria for approval escalation based on time and criticality of bypass should be documented in the procedure, training and add to this permit accordingly.			

Audits

a. Process safety, ITPM and operations programs are benchmarked with peers and externally verified through auditing.

KPIs

a. Process safety, ITPM and operations KPI tracking and management review and lessons learned shared and incorporated accordingly.
b. Process safety competency and culture are given high priority - management walks the talk.

12. Proactive Approaches

The following are the proactive approaches most closely associated for improving the integrity and availability of protection layers.

12.1 Inspection, Testing and Preventive Maintenance:

In case, ITPM frequency is not met, a formal deferral must be documented and perform missing ITPM at the earliest opportunity. Inspection and testing frequency can be adjusted based on the learning and best practices.

12.2 Incident Investigation and Reporting:

PSNM incidents provide the warning signs about the weaknesses of the safety barriers and management programs. Safety system test failures and safety system challenges are investigated, and lessons learned implemented to prevent the failure on demand. PSNM incidents are investigated for their potential consequences.

12.3 Supervision and Verification:

The verification of work completion is very effective for ensuring the effectiveness of programs and practices. Verification will ensure that the actions completed meet the intent.

12.4 Management Reviews:

Any changes to safety systems which increased the risk to unacceptable level are escalated to the senior management for their review and approval using an appropriate process such as an MOC or bypass. This includes ITPM deferral and / or safety system bypass.

12.5 Drills and Simulations:

Tabletop and Red Tag drills are conducted on all emergency operating procedures (EOP). The critique of the drill is very critical, and the findings must be communicated and incorporated in the relevant procedures and training programs. For example, if an operator action is not performed in the prescribed time and manner as mentioned in PHA then the time assumption should be updated in the next PHA accordingly.

12.6 Process Safety Audits:

An effective audit will identify these gaps if done correctly in many ways such as deep dive to verify the list of SCE is current, ITPM records are up to date, C&E diagram is current, available, used and consistent with other PSI, DCS alarms and indications are reviewed and verified, and PHA quality.

12.7 Key Performance Indicators:

If correct KPIs are developed, useful data is collected and analyzed, then such weaknesses could be captured sooner depending on the update frequency of KPIs, for example daily or weekly or monthly. These KPIs should be reviewed by the management and accessible to all relevant personnel. In the example above, several repeat operations upsets, repeat PSNM, no ITPM on SCE etc. could have captured in multiple KPIs.

13. Summary and Conclusion

Maintaining protection layer integrity requires 1) a well written and implemented management system 2) competent management and workforce and 3) a strong process safety culture. The first step is documentation of the safeguard. Then only, an inspection and testing and maintenance program can be developed, and employees trained accordingly. Because supervisors, engineers, and senior management make most of the risk management decisions, they need a more comprehensive process safety training than the workforce to implement the management program effectively and efficiently. Process safety near misses are the warning signs for weaknesses in the management program required to maintain the safeguards. This is one of the proactive approaches for identifying the weaknesses of the safeguards. It does not matter how detailed the processes and programs are, if the quality and integrity of these processes and programs are low. Keep in mind the very old saying that is always current: that what is not measured cannot be improved. Good audits can deep dive and verify the consistency in the relevant documents and check the completeness and quality of the activities.

References

1. U.S. Chemical Safety Board https://www.csb.gov/

2. American Petroleum Institute https://www.api.org/
3. Occupational Safety and Health Administration – Process Safety Management
4. https://www.osha.gov/process-safety-management
5. IChemE Safety Centre https://www.icheme.org/knowledge/safety-centre/
6. AIChE-CCPS. Guidelines for Defining Process Safety Competency Requirements. https://www.aiche.org/ccps/resources/publications/books/guidelines-defining-process-safety-competency-requirements

The information, suggestions and recommendations contained herein are for general informational purposes only. This information has been compiled from sources believed to be reliable. Risk Consulting Services do not address every possible loss potential, law, rule, regulation, practice or procedure. No warranty, guarantee, or representation, either expressed or implied, is made as to the correctness or sufficiency of any such service. Reliance upon, or compliance with, any recommendation in no way guarantees any result, including without limitation the fulfillment of your obligations under your insurance policy or as may otherwise be required by any laws, rules or regulations. No responsibility is assumed for the discovery and/or elimination of any hazards that could cause accidents, injury or damage. The information contained herein should not be construed as financial, accounting, tax or legal advice and does not create an attorney-client relationship.

This document is not intended to replace any recommendations from your equipment manufacturers. If you are unsure about any particular testing or maintenance procedure, please contact the manufacturer or your equipment service representative.

Solar panel technology using nanotechnology

Eng. Eyad AlRashaideh ,Eng. Doaa Shaheen

The introduction

The sun is a gift from God. It is one of the available and renewable sources to all human beings. The sun is clean energy that is free of any emissions that may be caused by other ways to obtain energy as it is in the non renewable energy. Solar energy has been exploited since ancient times. Over time people invited different technologies to take advantage of this energy. One of the most important technologies that has been developed in the solar energy is the manufacture of solar panels. The development of solar panels passed through several stages to increase the efficiency and to exploit most of the solar radiation falling on it.

The Components of the Solar Panel and the Technology

The solar panel consist of several layers of solar cells that makes it tolerate with the surrounding conditions such as high temperatures, humidity and dust.... etc.

it consists of (Aluminum Frame , Tempered Glass , Encapsulant Material EVA , photovoltaic Solar cell , Insulating Back sheet and Junction Box)

The purpose of this research is to focus on the manufacture of the front face-the glass part- to deliver as much solar radiation as possible to the solar cell.

The main problem

The main problem is the dust on solar panels, which reduces its efficiency. The dust on solar panels is one of the most important problems facing solar systems projects. It reduces the efficiency of the panel by preventing all solar radiation from reaching the solar cell.

Solve the problem

According to previous research on the use of nanotechnology in the manufacture of some materials, nanotechnology may be used in the main part, which is glass. Nanotechnology restores the polymerization of the material particles, so it may be possible to make glass with a cohesive force that is closer to zero and the angle of the solar panels will be as much dust as possible. This will improve the quality of the solar plane and will increase the access of solar radiation to the cells.

Study of the Impact of the Tube Configurations on the Local Heat Transfer Coefficient in a Bubble Column Reactor with Heat Exchanging Tubes

Abdulrazaq Nadhim Alzamily, Abbas J. Sultan, Amer Aziz Abdulrahman, Laith S. Sabri *

Department of Chemical Engineering, University of Technology, Baghdad, Iraq

***Corresponding authors: che.19.23@grad.uotechnology.edu.iq, Abbas.J.Sultan@uotechnology.edu.iq, 80004@uotechnology.edu.iq , Laith.S.Sabri@uotechnology.edu.iq*

Recently, energy consumption has become a primary global concern because of a rising oil demand and oil reserves reduction. Hence, there is an urgent need to search for clean alternative energy sources to cover this energy shortage. Among these alternative sources is the Fischer-Tropsch process that can convert synthesis gas in the presence of catalyst into clean liquid fuels and chemicals. The preferred reactor for the Fischer Tropsch process is the bubble column reactor due to its advantages over other multiphase reactors. The Fischer Tropsch process involves a high exothermic reaction. Therefore, a bundle of cooling tubes is inserted inside this reactor to remove the excess heat and maintain the desired temperature of the reaction. Therefore, the present work investigates the influence of vertical tubes and their arrangement on the local heat transfer coefficient under different operating conditions. The experiments of this study were conducted in a Plexiglass column with an inner diameter of 0.13 m and a height of 1.83 m. Two types of arrangements of tubes (triangle and square pitch) were examined under a wide range of superficial gas velocities in different axial and radial positions using an advanced heat transfer technique. The outcomes of current and previous studies will further improve the fundamental understanding of the effect of vertical tubes and their arrangement on the local heat transfer coefficient. It also provides the essential knowledge to the design, scale-up, and simulations. The results and findings of this study will be presented on conference day.

Using Reason's Swiss Cheese Model to Investigate 2005 Bp Texas City Refinery Explosion Accident in Terms of Occupational Psychology and Ergonomics

Malik M. S. Salhab*

Director of The National Palestinian Center of Occupational Safety, Health & Environmental Protection (COSHEP)
MSc. OSHE/GradIOSH/ACIEH/AIIRSM / Palestine Polytechnic University
Corresponding author: malek@ppu.edu

Abstract: BP explosion which happened on the 23rd of March 2005 in a section of the refinery concerning a raffinate splitter tower within the isomerization (ISOM) unit and the related blowdown system, which left 15 killed persons and around 180 injured besides large financial losses.The accident chronology was analyzed, and there were many root and immediate causes to this accident which were modelled using Reason's Swiss Cheese Model for accidents investigations.Root causes such as the absence of programs for controlling major hazards and risks, poor safety culture and leadership, lack of resources to prevent major accidents, budget cuts, impaired process safety performance, absence of an effective reporting and learning culture, incidents investigations were not carried out perfectly and if so, appropriate corrective action was not taken. On the other hand, immediate causes were operators' fatigue, and the absence of a fatigue remedy policy, the poor design of the control displays and meters (poor ergonomics), faulty gauges and level meters, operator's errors, deviation from safe start-up procedures.Safety culture, climate and safety leadership were found to affect employees' attitude, perception and behaviour, in addition to human factors and ergonomics which contributed to the BP explosion accident will be discussed in this presentation as means of preventing major accidents.

Theme 5: Desalination and Sustainable Water Treatment

A Facile Synthesis of Magnesium Oxide Nanoparticles and Their Performance as an Efficient Nano-Adsorbent for Removal of Organic Pollutants from Aqueous Media

Ayman A. Ali, Sayed A. Shama, Abdel-Azem M. El-Sharkawy and Rowaida M. Fahmy*

Chemistry Department, Faculty of Science, Benha University, Benha City, Egypt.

**Corresponding author: rowaidamahmmoud@yahoo.com (R. M. Fahmy); Tel. +201004149108*.

Abstract: Herein, the fabricated magnesium oxide (MgO) nanoparticles were synthesized utilizing auto-combustion method and different fuels (ascorbic acid, urea, and valine). The obtained products (MA, MU and MV samples) were obtained after the annealing at 600°C for 2h.The synthesized MgO nanoparticles were investigated by X-ray diffraction, High-resolution transmission electron microscopy, Fourier transform infrared spectroscopy, Field-emission scanning electron microscopy, thermal analysis and BET method. The crystallite sizes, particle size and surface area of the obtained samples were determined. The synthesized products were used as an adsorbent for organic dyes from water. The adsorption capacity of the calcined magnesium oxide nano-adsorbent was tested utilizing various factors. The models of adsorption isotherm and adsorption kinetics were used for the explanation of the removal process over the fabricated magnesium oxide nano-adsorbent. Besides, the thermodynamics parameters were calculated for the removal process of the selected organic dyes using the obtained MgO nano-adsorbent.

Keywords: auto-combustion method; magnesium oxide nanoparticles; Adsorption; Morphology

1. Introduction

Today dyes, highly colored organic compounds, find widespread applications in industries like textile, food, leather tanning, paper, coloring products, printing, light-harvesting solar cells, plastics, photoelectrochemical cells, pharmaceutical and cosmetics. However, large usage of these organic dyes leads to their release as effluents that eventually contaminate drinking water sources making water pollution increasingly serious and hampering the ecological system [1, 2].Sunset and Tartrazine dyes are examples for the food industry due to their color but the higher amount of these dyes inside water leading to the pose mutagenic and carcinogenic effects and other health problems such as skin eczema, migraine, thyroid cancer, lupus, infertility, etc. Dye containing wastewater treatment has become essential nowadays because of the health problems, toxic effects of pathogens and the hazards of wastewater pollution on humans, agriculture and animals[3]. Wastewater treatment at the personal and government level must be taken into account to protect the environment from pollution involve physical, chemical, and biological procedures for water purification from various contaminants[4, 5].

Various methods of treatment for dye removal are being implemented to decrease their impact on the environment. These methods include adsorption, coagulation, photo-catalytic degradation, microbial decomposition, wet air oxidation, flocculation, sono-chemicaland electrochemical methods. Among various methods of dye removal, adsorption has been reported to be the most effective, attractive and favorable method that provides promising results due to low cost, simplicity of design, recycling of adsorbent, high efficiency and nonexistence of harmful residues[6-14]. Nano-sized metal oxides (simple and composite) have received tremendous attention for applications in wastewater treatment because they have large specific surface areas and high surface reactivity,

which endows them with a high affinity for various aqueous contaminants. Furthermore, metal oxide nanoparticles have gained significant interest among scientists as potential adsorbents for the removal of dyes from wastewater as they are generally nontoxic and easy to prepare[15]. Among all known metal oxide nanoparticles, magnesium oxide MgO has become a distinctive material because it's inexpensive, non-toxic, stable, and has been utilized as an ideal adsorbent for wastewater remediation [2, 16-18].

Various methods can be fabricated metal oxide in the form of simple and composite with nano-sized such as combustion method [14, 19-24], sol-gel method [25, 26], precipitation method [27, 28], etc. The aim objective of this study is the synthesis of MgO nanoparticles via the auto-combustion method using different fuels. The obtained magnesium oxide nanoparticles were investigated using various tools and the calcined magnesium oxide nano-adsorbent was utilized in the removal of Sunset and Tartrazine dyes from aqueous media.

2. Experimental

2.1 Materials and reagents

All chemicals and reagents were of analytical grade and used directly without further purification. Magnesium nitrate ($Mg(NO_3)_2.6H_2O$, 98.5%), Sunset yellow FCF (SSD: $C_{16}H_{10}N_2Na_2O_7S_2$, 99%), Tartrazine FD&C Yellow 5 (TZD: $C_{16}H_9N_4Na_3O_9S_2$, 99%) were purchased from Sigma–Aldrich Chemical Company. Ascorbic acid ($C_6H_8O_6$, 98%), urea (CH_4N_2O, 99.5%), valine ($C_5H_{11}NO_2$, 98%), hydrochloric acid (HCl, 30-34%) and sodium hydroxide (NaOH, 99%) were purchased from El Nasr pharmaceutical chemical company. The chemical structure of the organic dyes was displayed in Figure 1.

2.2 Synthesis of magnesium oxide nanoparticles via auto-combustion method:

In simple procedures, magnesium nitrate hexahydrate was dissolved in 25 mL bidistilled water. The obtained solution was mixed with the solution (25 mL) of the calculated number of moles for the selected fuels (urea, valine and ascorbic acid), separately. Equations No. 1-3 explained the combustion reaction between magnesium nitrate and the selected fuels according to the principles of the combustion method. The solutions were ignited at 250 ^oC for 15 minutes to produce pale brown and white powders. The obtained powder was calcined at 600 ^oC for 2 h in a muffle furnace to get the crystalline magnesium oxide nanoparticles. The sample names of the as-fabricated and calcined magnesium oxide were labelled as (MU, MV and MA) and (MU6, MV6 and MA6) using urea, valine and ascorbic acid fuels in the preparation method, respectively. Table 1 displayed the sample names and compositions of the starting materials for the synthesis of magnesium oxide nanoparticles using the auto-combustion method.

$$3Mg(NO_3)_2.6H_2O + 5CH_4N_2O = 3MgO + 8N_2 + 5CO_2 + 28H_2O \quad (1)$$

$$2Mg(NO_3)_2.6H_2O + C_6H_8O_6 = 2MgO + 28N_2 + 40CO_2 + 50H_2O \quad (2)$$

$$27Mg(NO_3)_2.6H_2O + 10C_5H_{11}NO_2 = 27MgO + 32N_2 + 50CO_2 + 217H_2O \quad (3)$$

2.3 Characterization

The morphology of the calcined product was investigated using a Field emission scanning electron microscope (FE-SEM, Zeiss Sigma 500 VP). The morphology and particle size of the annealed samples were revealed using Highresolution transmission electron microscope HR-TEM (model Tecnai G20, FEI, Netherland) at an electron voltage of 200 kV. The thermal analysis (TG, DTA and DTG) were used to test the as-synthesized products (MU, MV and MA samples) and carried out under air gas atmosphere using a thermal analyzer instrument (Shimadzu; model TA-60WS) with a heating rate of 10 $^oC\ min^{-1}$ from 25 ^oC to 700 ^oC. The obtained phase of the as-prepared

and calcined samples was confirmed by measuring the XRD pattern analysis (18 KW diffractometer: Bruker; model D 8 advance) with monochromatic Cu-Ka radiation, 1.54178 (A^o) in the angular range of 10-70° with step size 0.02^o (2Θ) and scan step time 0.4 (s). The as-synthesized and annealed products were measured using an FTIR spectrometer (ThermoFisher; model Nicolet iS10) from 4000 to 400 cm^{-1}. The adsorption processes were investigated using a Jasco UV-Vis spectrophotometer (Jasco; model V 670).The specific surface area, total pore volume and mean pore radius of the obtained samples after the calcination at 600 ^{o}C were calculated from nitrogen adsorption isotherms at 77 K using a conventional volumetric apparatus and the Brunauer Emmett Teller method (NOVAtouch type and model Nova 2200e)

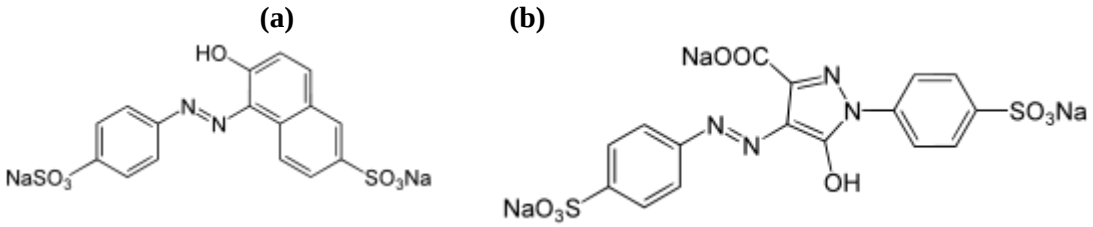


Figure1. Chemical structure of (a) Sunset dye; (b) Tartrazine dye.

Table1. The sample names and compositions of the starting materials for the synthesis of magnesium oxide nanoparticles using auto-combustion method.

No.	Sample names	Mg^{2+}, mole	Type of fuel	Fuel, mole
1	MU	0.03	urea	0.05
2	MV	0.02	valine	0.01
3	MA	0.27	Ascorbic acid	0.01

3. Result and discussion

3.1 Characterization of magnesium oxide nanoparticles

The thermogravimetric analysis provides information on the stability and composition of a sample. It monitors its performance concerning temperature in a specific atmosphere, recording the sample's weight loss when exposed to a combination of temperature, heating rate and reaction atmosphere[29].Figure 2(a, b and c) displays the TGA, DT and DTG curves of the magnesium oxide (MU, MV and MA samples) under an air atmosphere, in which the temperature was increased from 30 ◦C to 700 ◦C at a heating rate of 10 ◦C/min, respectively. DTG curves of MU, MV and MA samples appeared two broad peaks. The first peak appeared in the range of 30-200 °C (~105 °C), 30-200 °C (~95 °C) and 30-200 °C (~75 °C) for MU, MV and MA samples, respectively. The second peak appeared in the range of

350-475 °C (~410 °C and 450 °C), 280-480 °C (~310 °C, 370 °C and 450 °C) and 300-540 °C (~450 °C) for MU, MV and MA samples, respectively. It explains that the degradation of the as-prepared magnesium oxide in two steps in the temperature range of 30-700 °C.

TGA curves of MU, MV and MA samples showed the degradation of the asprepared magnesium oxide in two steps and the total mass loss percentages were found to be in the range of 82 %, 48.5 % and 42.5 %, respectively. The first step in TGA curves occurred in between 25-200°Cfor MU, MV and MA samples, in which the mass loss percentages were found to be40 %, 10 %, 7 %, respectively. It was mainly attributed to the liberation of the adsorbed water molecules on the surface of the synthesized magnesium oxide [30].The second step occurred between 200 °C and 500-600°Cfor MU, MV and MA samples. The mass loss percentages were found to be 42 %, 38.5% and 35.5 % for MU, MV and MA samples, respectively. It is attributed to the removal and decomposition of the excess of carbon ashes, fuels and magnesium nitrate[31] in the samples and/or attributed to dehydroxylation of $Mg(OH)_2$ to MgO [9]. TGA curves of MU, MV and MA samples agree with the DTG curves for the decomposition of the asprepared magnesium oxide in the two steps in the range of 30 °C to 500-600 °C, fabricating the white and crystalline magnesium oxide nanoparticles. According to TGA and DTG curves, the fine and crystalline magnesium oxide nanoparticles were fabricated after the calcinations in the temperature range of 500-600 °C [32, 33].Figure 2(a, b and c) showed the DTA curves of the as-prepared of magnesium oxide (MU, MV and MA samples), appeared one endothermic and one exothermic peaks for all samples. The endothermic peaks in the DTA curves of MU, MV and MA samples appeared in the range of 30-200 °C (at 95 °C and 105 °C), at 100 °C and a small peak at 75 °C, respectively. It indicated the dehydration of the MU, MV and MA samples and the removal of water and hydroxides groups on the surface of the as-fabricated MgO samples. The exothermic peaks in the DTA curves of MU, MV and MA samples appeared in the range of 400-470 °C (at 425 °C and 455 °C), 340-420°C (at 380 °C) and a small peak at 450 °C, respectively. It indicated the dehydroxylation of the MU, MV and MA samples and the removal and degradation of magnesium hydroxides to obtain the white and fine crystalline magnesium oxide nanoparticles from the as-fabricated samples. It means that the starting of the formation of the magnesium oxide in the temperature range of 450500 °C.

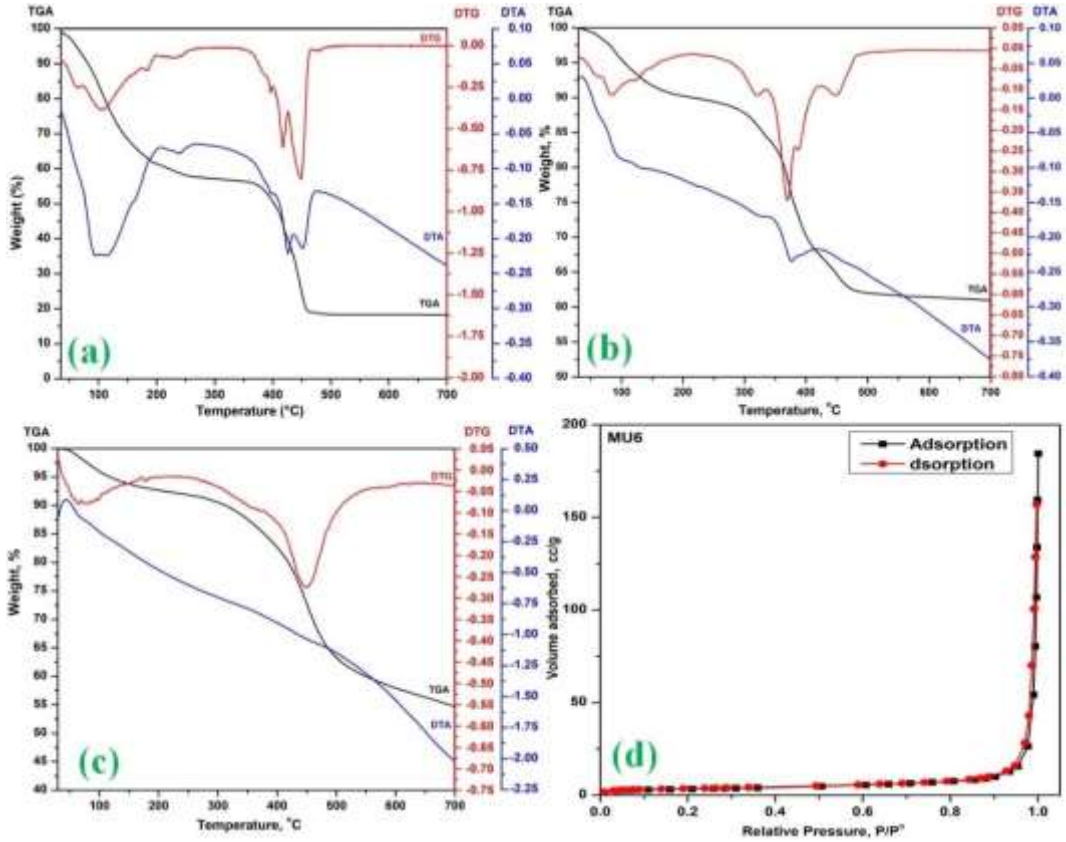


Figure2. Thermal analysis (TGA, DTA and DTG curves) of the as-synthesized magnesium oxide (a) MU; (b) MV; (c) MA samples and (d) N_2 adsorption-desorption isotherms of MU sample.

Adsorption-desorption isotherms of the fabricated and calcined magnesium oxide nanoparticles (MU6 sample) are appeared in Figure 2(d). The appeared isotherm of the synthesized MU6 sample is related to type IV of Brunauer's categorization. The isotherm type appeared that the fabricated oxide can be indicated to the presence of mesopores materials according to the obtained morphology feature. It can be attributed to the formation of slit-like pores of the synthesized magnesium oxide surface. The surface area determined by the Brunauer–Emmett–Teller method and the N_2 gas adsorption/desorption isotherms were performed at 77 K. BET surface area, average pore diameter and total pore volume of the fabricated magnesium oxide nanoparticles (MU6 sample) estimated to be 11.35 m^2/g, 30.1 nm, 0.0853 cc/g, respectively[28, 34, 35].

The powder XRD analyses were performed in the 2θ range between 20°and 70° for both the as-prepared samples and the annealing ones as shown in Figure 3(a and b). In Figure 3(a), the XRD patterns of as-prepared MU, MV and MA samples displayed the strong peaks, which can be indexed to the hexagonal structure of magnesium hydroxide structure according to the card No. 84-2163.After the ignition of the samples at 600 for 2h °C, no characteristic peaks for magnesium oxide were detected, suggesting that the obtained product was the magnesium hydroxides nanoparticles. In Figure 3(b), the XRD patterns of annealed MgO showed three major and strong peaks at 2θ = 36.8°, 42.8° and 62.2°, which can be indexed to the lattice planes of (111), (200) and (220), respectively. It represented the formation of the cubic structure of MgO crystals according to card No. 711176. Furthermore, no characteristic peaks from other crystalline impurities were detected, suggesting that the product was pure and crystalline MgO nanoparticles[36]. The diffraction peaks were very sharp, which indicating that the magnesium oxide nanoparticles were well crystallized [37]. The average crystallite size of the particles was determined from the XRD pattern, by using the Debye–

Scherrer's equation: $D = K\lambda/\beta\cos\theta$. The D, K, θ, λ and β parameters are the crystallite size (nm), constant, Bragg diffraction angle, X-ray wavelength and FWHM (full-width half maxima) of the diffraction peaks, respectively. The average crystallite sizes for magnesium nanoparticles (MU6, MV6 and MA6 samples) were found to be 62, 28 and 21nm respectively, as calculated from Debye–Scherrer equation[38].

The as-prepared and annealed samples were characterized by FTIR spectroscopy as shown in Figure 3(c and d). The spectra were measured over the range of 400 – 4000 cm^{-1} to determine the functional groups inside the synthesized samples which confirm the structure of the obtained magnesium oxide nanoparticles.

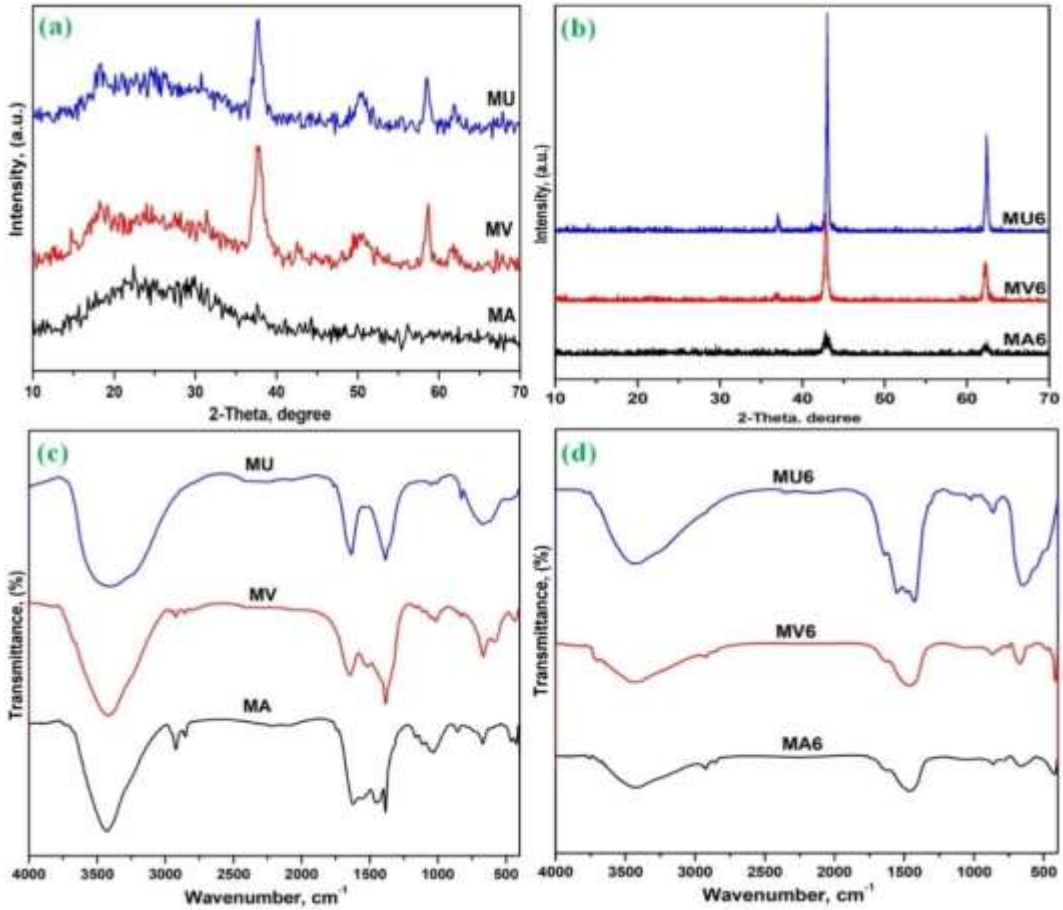


Figure 3. XRD patterns and FTIR spectra of (a and c) as-prepared MgO nanoparticles; (b and d) annealed MgO nanoparticles.

In all spectra, there were strong broad bands around 3500 cm^{-1}, related to the presence of the O-H stretching vibrations due to the existence of a surface hydroxyl group and the adsorbed H_2O molecules on the surface of magnesium oxide samples[39, 40]. Besides, the bands around 1620-1650 cm^{-1} were harmonized to the vibrational modes of the bending of the hydroxide groups on the magnesium oxide surface for all the synthesized samples. The bands near 14901500 cm^{-1} and 670-680 cm^{-1} are linked to the stretching vibration of Mg-O and Mg-O-Mg deformation. The bands at 1020-1050 cm^{-1} and 2850-2950 cm^{-1} are related to the C-O, C-N and C-H with the fabricated samples. The bands observed at 423/450/431 cm^{-1} and 422/416/480 cm^{-1} for the as-prepared and calcined samples are confirm to the presence of Mg-O stretching vibration modes inside the lattice of the magnesium oxide nanoparticles[41].

Figure 4 exhibits the HR-TEM and FE-SEM micrographs and EDX spectrum of annealed magnesium oxide nanoparticles (MU6 sample). Figure 4(a-d) exhibits the HR-TEM micrographs of the MU6 sample and the morphology appeared the completed and uncompleted spherical shape and the cubic structure of the synthesized magnesium oxide. The particle diameter of the fabricated magnesium oxide (MU6 sample) was determined from the TEM micrographs, and it was found to be 70 nm, which reflected the presence of the dense agglomerations of the synthesized magnesium oxide nanoparticles using the combustion method. Also, the morphology of the annealed MU6 sample was investigated using FESEM as shown in Figure 4(e-h). SEM micrographs of the fabricated MU6 sample appeared a uniform spherical and cubic shape with hard agglomeration. Elemental analysis of the MU6 sample was studied utilizing the EDX technique as appeared in Figure 4(i). The EDX spectrum had confirmed the formation of pure MgO nanoparticles by the observation of peaks for only Mg and O and the absence of any other contaminating elements.

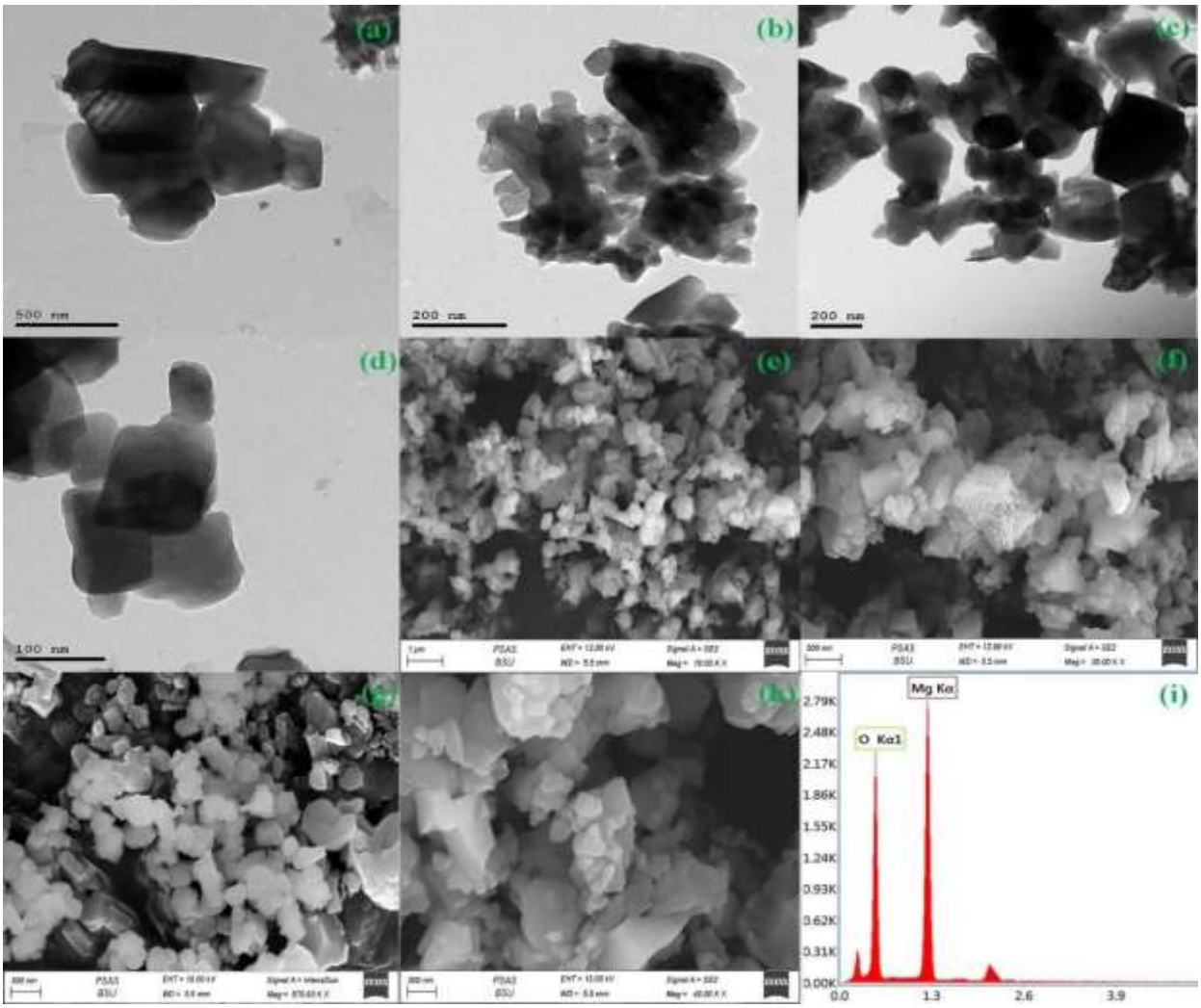


Figure 4. (a-d) HR-TEM micrographs; (e-h) FE-SEM micrographs at different magnification power ;(i) EDX spectrum of annealed MU6.

3.2 Batch adsorption

Sunset (SSD) and Tartrazine (TZD) solutions were prepared, and their pH was adjusted to the target value (2–9) with 0.1 M HCl and NaOH. Certain dosages of MgO nanoparticles were added to each and then the mixture was shaken at a constant temperature for a specified duration. The MgO was removed by centrifugation to obtain a clear filtrate. The adsorption efficiency of MgO nanoparticles was examined through different parameters like initial concentration of dyes, pH, temperature, contact time and absorbent dosage. The concentrations of Sunset (SSD) and Tartrazine (TZD) dyes in the filtrates were determined according to the Beer-Lambert law by recording the absorbance of the solution at 482 and 427 nm, respectively using double beam UV/Vis spectroscopy. The quantity of Sunset (SSD) and Tartrazine (TZD) dyes adsorbed by using the synthesized MgO nanoparticles at the state of equilibrium at time t are q_t (mg/g) using Equation (1).The removal percentage (RP, %) of (SSD) and(TZD) dyes adsorbed by MgO nanoparticles from the aqueous solution was obtained by using Equation (2)[38].

$$q_t = (C_0 - C_t)(V/m) \quad (1)$$

$$RP, \% = (C_0 - C_t)/C_0 \times 100 \quad (2)$$

Where C_0, C_t and C_e (mg L^{-1}) are the initial dye concentration, the concentration at time t and concentration of the dyes at equilibrium state, respectively, whereas the mass of the dyes is m (g) and V (mL) is the solution volume. The study of initial dye concentration is studied by varying the concentration of the dyes from 50 to 300 mg L^{-1}. The rapid adsorption took place in the first 30 min. Then the adsorption rate decreased gradually, and the adsorption reached equilibrium. This is because at a low adsorbate/adsorbent ratio, the number of sorption sites in the MgO nanoparticles but as the ratio increases the adsorption sites are saturated, resulting in to decrease in the sorption efficiency. At high initial concentration, the gradient between the solution sample and the center of the particle enhances dye diffusion through the film surrounding the particle and in the porous network of MgO nanoparticles

The pH of the dye solution plays an important role in the whole adsorption process. The adsorption capacity of the synthesized magnesium oxide adsorbent decreased as the rise of the pH in the range 2-9 at room temperature as displayed in

Figure 5(a). The adsorption amount of Sunset (SSD) and Tartrazine (TZD) dyes over the fabricated magnesium oxide was slightly decreased by the raising of pH. The removal percentages of Sunset (SSD) and Tartrazine (TZD) dyes on the synthesized magnesium oxide were found 96 % and 92 % at pH=2 after 24 h. The adsorption experiments were carried out for different contact times with a fixed adsorbent dose (0.05 g) at pH=2 and room temperature as shown in Figure 5(b). It was observed that the uptake of the Sunset (SSD) and Tartrazine (TZD) dyes (C_i= 100 mg L^{-1}) increased with time. The extent of adsorption was rapid in the initial stage and becomes slow in later stages basically due to saturation of the active site on the fabricated magnesium oxide surface following by very slowly adsorption after 300 min. According to Figure 5(b), the adsorption capacity of Sunset (SSD) and Tartrazine (TZD) dyes on the fabricated magnesium oxide (MU6 sample) were found to be 46.6 mg/g and 43 mg/g after 300 min, respectively. The dependence of dye adsorption on MgO nanoparticles dosage was studied by varying the amount of MgO nanoparticles (10, 25, 50, 75 and 100 mg), keeping other parameters constant (pH =2, contact time =300 min and room temperature) for Sunset (SSD) and Tartrazine (TZD) dyes (C_i= 100 mg L^{-1}) as shown in Figure 5(c). The removal efficiency of Sunset (SSD) and Tartrazine (TZD) dyes increased with the increase in the magnesium oxide dosage. It is due to the greater surface area of the fabricated magnesium oxide (MU6 sample) with more functional groups consequent to the increase in the amount of MgO adsorbent and the number of exchangeable sites for adsorption and saturation which occur as a result of the nonavailability of exchangeable sites on the selected adsorbent. Various initial concentrations of the Sunset (SSD) and Tartrazine (TZD) dyes (50-300 mg/L) were used for the investigation of the adsorption capacity of the selected dyes on 0.05 gram of the MU6 sample at pH=2 and 300 min. The extracted data from the relation showed the adsorption capacity increased until became constant after 150 mg/L. The maximum value of the adsorption capacity was found at 52 mg/g and 51 mg/g for 300 min for Sunset (SSD) and Tartrazine (TZD) dyes, respectively as shown in Figure 5(d).

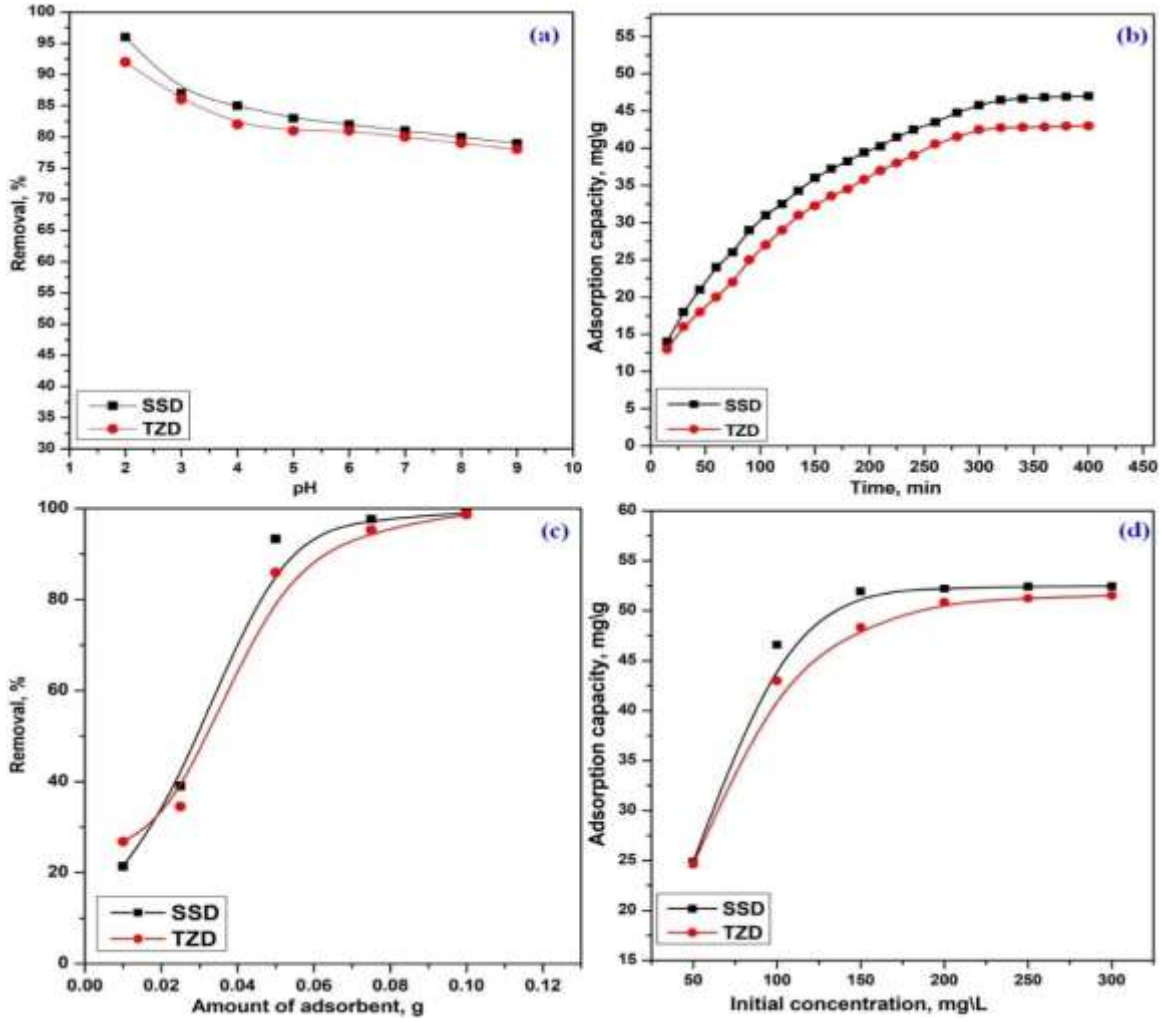


Figure 5. Effect of (i) pH; (ii) time, (iii) adsorbent dose ; (iv) initial dye concentration for the removal of the (SSD) and (TZD) dyes on the MU6 sample.

3.3 Adsorption isotherms

The models of the adsorption isotherm were examined by investigating the relationship between the determined adsorption capacities of the synthesized magnesium oxide nanoparticles with the various initial concentration of the Sunset (SSD) and Tartrazine (TZD) dyes (Ci=50-300 mg/L). The extracted data from the relation shows the adsorption capacity increased until became constant after 150 mg/L. The maximum value of the adsorption capacity was found at 52 mg/g and 51 mg/g for 300 min for Sunset (SSD) and Tartrazine (TZD) dyes, respectively. Langmuir, Freundlich and Temkin isotherm models are used for the explanation of the determined data using different equilibrium concentrations of Sunset (SSD) and Tartrazine (TZD) dyes (50-300 mg/L) using 0.05 gram of MU6 sample at pH=2, room temperature and 300 min as appeared in Figure 6(a-c). The plots of Langmuir (Ce/qe &Ce), Freundlich (ln qe & ln Ce) and Temkin (qe & ln Ce) models are appeared in Figure 6(a-c) according to equations No. 3-5, respectively[12, 38, 42].

$$\frac{C_e}{q_e} = \frac{1}{K_L\, q_m} + \frac{C_e}{q_m} \qquad (3)$$

$$\ln q_e = \ln K_F + \frac{1}{P} \ln C_e \qquad (4)$$

$$q_e = G \ln K_T + G \ln C_e \qquad (5)$$

Ce is the equilibrium concentrations of Sunset (SSD) and Tartrazine (TZD) dyes in solution (mg/L), qe is the equilibrium adsorption capacity of Sunset (SSD) and Tartrazine (TZD) dyes using magnesium oxide adsorbent, K_L is the Langmuir parameter (L/mg), q_m is the maximum quantity of adsorbed solute to adsorbent (mg/g). K_f is the Freundlich constant (mg/g), (1/P) is the heterogeneity factor, G is constant (G= RT/b), K_T (L/g) is Temkin equilibrium binding constant due to the maximum binding energy and b is related to the heat of adsorption. From the Langmuir isotherm, the equilibrium parameter can calculate from $R_L=1/(1+W)$, $W= K_L C_o$ and the R_L values explain the nature of the adsorption process (if the values of R_L in between 0-1, the adsorption process is favorable). From the Freundlich isotherm, the maximum adsorption capacity can calculate using the relation: $q_m= K_f/C_o^P$. If the value of P: 1<P<10, this indicates a favorable adsorption process. From Temkin isotherm can determine from: G =RT/b, Where R is the universal gas constant, and T is the absolute temperature in Kelvin[12].

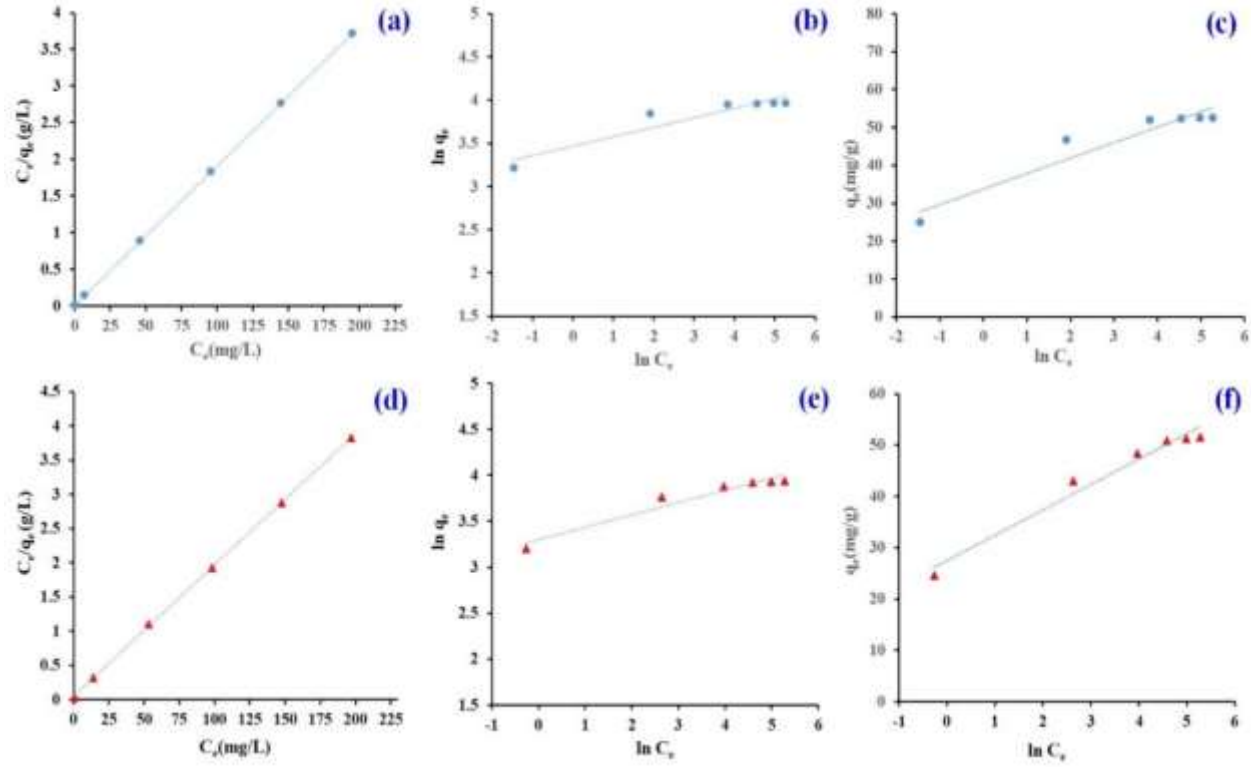


Figure 6. (a and d)The Langmuir;(b and e) Freundlich ; (c and f) Temkin for removal of the Sunset (SSD) and Tartrazine (TZD) dyes using the fabricated magnesium oxide nanoparticles (MU6 sample).

Table 2 summarized the factors were extracted from Langmuir, Freundlich and Temkin models. From the R^2 values, the Langmuir isotherm model is better fitting than the other isotherms. It reflects that the uptake of the Sunset (SSD) and Tartrazine (TZD) dyes using the magnesium oxide nano-adsorbent as monolayer without any interaction between adsorbed molecules. Besides, the determined adsorption capacity from Langmuir isotherm was determined to be 53 mg/g and 52 mg/g which are

closed with the experimental values: 52 mg/g and 51 mg/g for the Sunset (SSD) and Tartrazine (TZD) dyes, respectively. The values of R_L were found in the range of 0.00194-0.01155 and 0.00813-0.04686 for the adsorption of the Sunset (SSD) and Tartrazine (TZD) dyes on the MU6 sample, respectively, which is related to the initial concentration 50-300 mg/g. It explains that the adsorption of the Sunset (SSD) and Tartrazine (TZD) dyes on the MU6 sample is a favorable process. From the Freundlich isotherm, the K_f is the Freundlich constant found to be 32.021 and 27.11 mg/g for the Sunset (SSD) and Tartrazine (TZD) dyes, respectively. From the extracted data of Temkin isotherm, the heat of adsorption (G) has the value (0.597.2 KJ/mole and 0.493 KJ/mole for SSD and TZD dyes, respectively) and it appeared the weak interaction force between the Sunset (SSD) and Tartrazine (TZD) dyes and the magnesium oxide surface. The values of the Temkin constant (G) were found to be 4.079J/mol and 4.942 J/molfor SSD and TZD dyes, respectively.

Table 2. The extracted parameters from Langmuir, Freundlich and Temkin isotherms for MgO adsorbent (MU6 sample).

Adsorption isotherm	Parameter	SSD	TZD
Langmuir parameters	K_L (L/mg)	1.712	0.407
	$q_{m\ (cal)}$ (mg/g)	52.632	52.083
	R_L	0.00194-0.01155	0.00813-0.04686
	R^2	0.9996	0.9998
	$q_{m(exp)}$ (mg/g)	52	51
Freundlich parameters	K_F [(L/mg)(L/mg)$^{1/p}$]	32.021 55.288 9.174	27.11 55.257 7.441
	$q_{m\ (cal)}$ (mg/g) p(L/mg)		
	R^2	0.887	0.9449
	$q_{m(exp)}$ (mg/g)	52	51
Temkin parameters	K_T (L/g) d (J/mol)	3930.897 597.176	258.572 492.948
	G	4.079	4.942
	R^2	0.915	0.972

3.4 Adsorption kinetics

The study of adsorption kinetics describes the solute uptake rate and evidently, this rate controls the residence time of adsorbate uptake at the solidsolution interface including the diffusion process. The adsorption study was tested using the pseudo-first-order model, pseudo-second-order model and intra-particle diffusion as shown in equations No. 6-8. The experiments are examined at time intervals varied from 0 to 400 min at a constant temperature, 50 milligrams of MU6 sample and 100 mg L^{-1} of both Sunset and Tartrazine dyes by keeping other parameters constant as shown in Figure 7(a-c)[12, 38, 42].

$$\log(q_e - q_t) = \log q_e - \frac{K_1}{2.303} \quad (6)$$

$$\frac{t}{q_t} = \frac{1}{K_2 {q_e}^2} + \frac{t}{q_e} \quad (7)$$

$$q_t = K_{IPD} t^{0.5} + Z \quad (8)$$

q_e and q_t are the amounts of Sunset (SSD) and Tartrazine (TZD) dyes adsorbed (mg/g) at equilibrium and time t (min), respectively, t (min) is contact time, and k_1 is the pseudo-first-order rate constant of adsorption (min^{-1}), k_2 (g/mg. min) is pseudo-second-order rate adsorption constant, k_{IPD} is intraparticle diffusion constant (mg/g. $min^{0.5}$). Z is constant and it gives an idea about the thickness of the boundary layer (mg/g).

From Table 3 and depending on the R^2 values, the pseudo-second order model is the better fitting than the pseudo-first order for the removal of the Sunset (SSD) and Tartrazine (TZD) dyes on the MU6 nano-adsorbent. The removal of Sunset (SSD) and Tartrazine (TZD) dyes over magnesium oxide nanoparticles followed the pseudo-second order model. The values of the estimated adsorption capacity (56.1 mg/g and 53.4 mg/g) agree with the experimental data: 52 mg/g and 51 mg/g for the Sunset (SSD) and Tartrazine (TZD) dyes, respectively.

Figure 7(c) appeared the intraparticle diffusion model and the determined values from linear relation: K_{IPD}= 2.14 and 2.1 and Z=8.15 and 5.75 mg/g for Sunset (SSD) and Tartrazine (TZD) dyes, respectively. The experimental plots didn't pass the origin, and it is reflected that the intraparticle diffusion model was not the only model for the explanation mechanism of the removal of the Sunset (SSD) and Tartrazine (TZD) dyes using magnesium oxide nano-adsorbent.

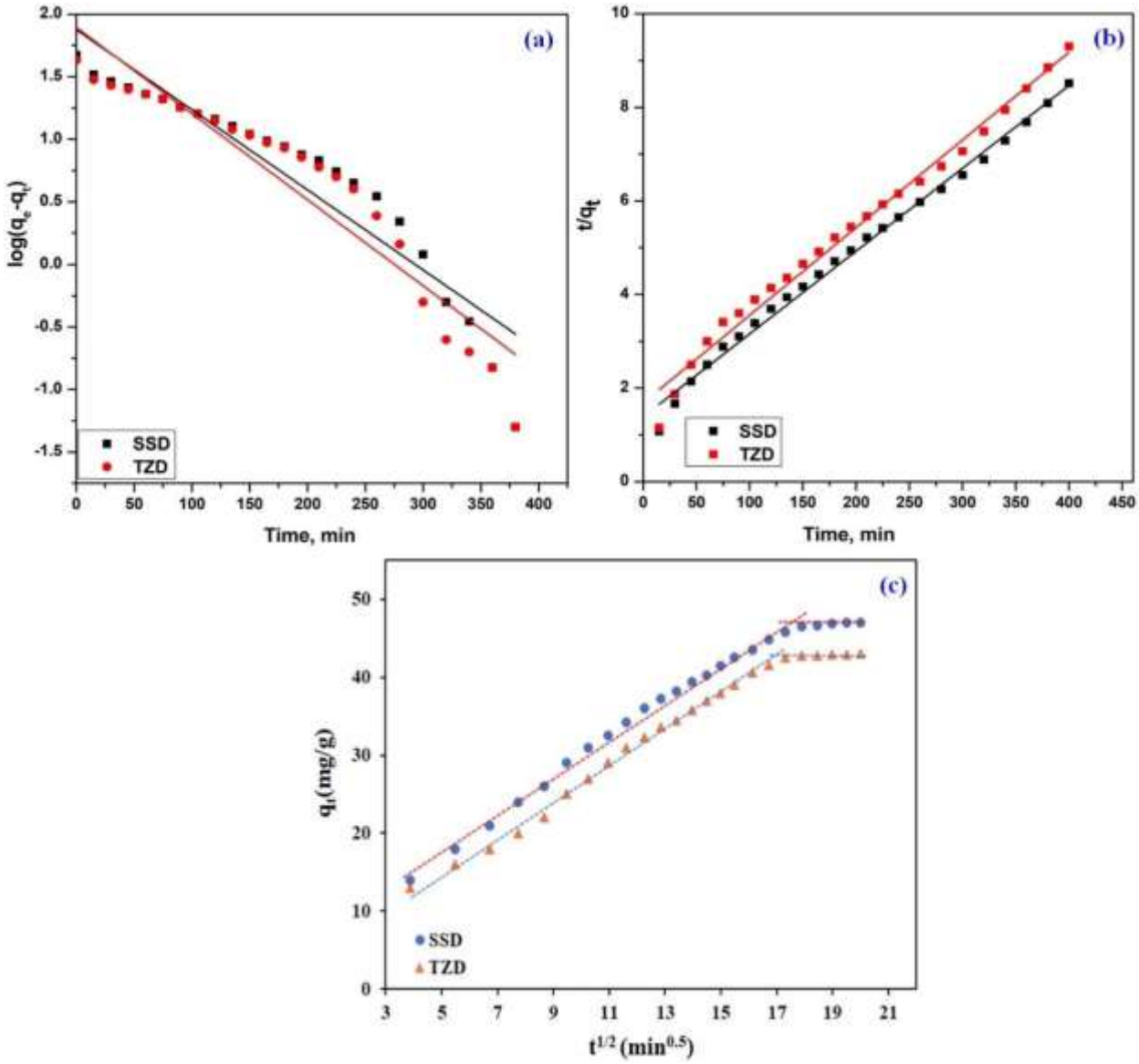


Figure7. (a) Pseudo-first order model; (b) Pseudo-second order model; (c) Intra-particle diffusion model for removal the Sunset (SSD) and Tartrazine (TZD) dyes using MU6 sample.

Table3. Kinetic parameters for adsorption of (SSD) and (TZD) dyes using magnesium oxide adsorbent (MU6 sample).

Kinetic parameters	Parameter	SSD	TZD
Pseudo- first order	$K_1(min^{-1})$	0.0147	0.0153
	$q_{m\ (cal)}$ (mg/g)	75.277	62.230
	R^2	0.885	0.907
	$q_{m\ (exp)}$ (mg/g)	46.60	43.00
Pseudo- second order	K_2(g/mg.min)	0.00023	0.00019
	$q_{m\ (cal)}$ (mg/g)	56.507	53.36
	R^2	0.993	0.988
	$q_{m\ (exp)}$ (mg/g)	46.60	43.00
Intra-particle diffusion	KIPD (mg/g min0.5)	2.14	2.10
	Z (mg/g)	8.15	5.75
	R^2	0.9941	0.9953

3.5 Effect of temperature and thermodynamic studies

The effect of temperature on the adsorption process was investigated in the temperature range of 308-319 K, separately for the removal of 100 mg/L of the Sunset (SSD) and Tartrazine (TZD) dyes using 0.05 g of MU6 sample. The data appeared that the adsorption capacity decreased slowly with raise in the solution temperature for the removal of Sunset (SSD) dye on the MU6 sample as exhibited in Figure 9(a). This indicates that the removal of Sunset (SSD) dye on the synthesized MgO adsorbents was an exothermic process. The increase of temperature of the removal of Sunset (SSD) dye was due to the increase of the moving of Sunset (SSD) dye in the boundary layer around for the MU6 sample and the thickness and mass transfer resistance of adsorbate in the boundary layer was increased. This leads to an increase in the mobility of the dye molecules with the rise of temperature from the surface of magnesium oxide to the bulk of the solution. The data showed that the adsorption capacity increased slowly with raise in the solution temperature. For the removal of Tartrazine (TZD) using the MU6 sample as exhibited in Figure 9(a), this indicates that the removal of Tartrazine (TZD) on the synthesized MgO nanoparticles was an endothermic process. The increase of temperature of the separation process was due to a decrease in the thickness of the boundary layer surrounding the MU6 sample and the mass transfer resistance of adsorbate in the boundary layer was decreased. This leads to an increase in the mobility of the molecules of Tartrazine (TZD) dye with the rise of temperature.

The effect of temperature on the removal of Sunset (SSD) and Tartrazine (TZD) dyes using MgO nano-adsorbent was examined in the temperature range

(308-319) K. The values of ΔH^o, ΔS^o and ΔG^o parameters were calculated using Van't Hoff equation as shown in equation No.(9) [12, 38].The experimental data appeared in Figure 7(b). The values of Gibbs free energy (ΔG^o) of the removalof Sunset (SSD) and Tartrazine (TZD) dyes using 0.05 g of MU6 sample calculated from equation No. (10)[12, 42].

$$\ln K_c = \frac{\Delta S^\circ}{R} - \frac{\Delta H^\circ}{RT} \qquad (9)$$

$$\Delta G^\circ = \Delta H^\circ - T\Delta S^\circ \qquad (10)$$

ΔH^o and ΔS^o are enthalpy change,entropy change. The k_c (equilibrium constant: L/g) values were calculated from q_e/C_e. T is the temperature in Kevin (k) and R is the gas constant. The plot of $\ln(k_c)$ against 1/T appeared a straight line as shown in Figure 9(b) with slope ($-\Delta H^o/R$) and intercept ($\Delta S^o/R$). Table 4 summarized the experimental parameters for the removal of Sunset (SSD) and Tartrazine (TZD) dyes using MU6 adsorbent.

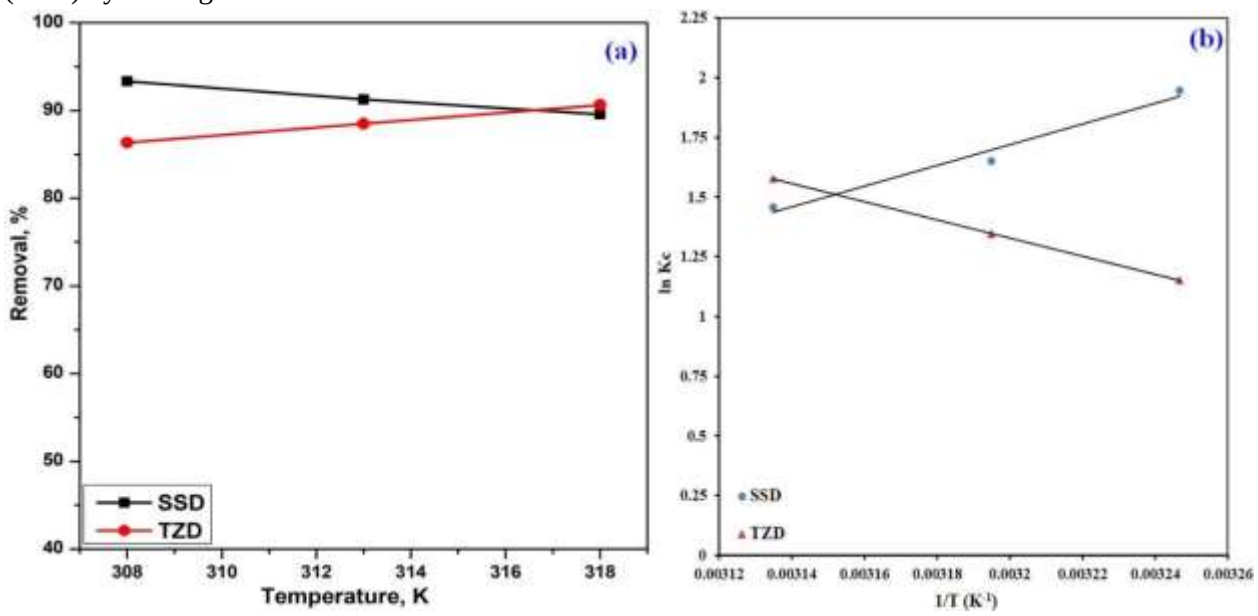


Figure 8. (a) Effect of temperature; (b) Van't Hoff relation for the removal of the Sunset (SSD) and Tartrazine (TZD) dyes using MU6 sample.

The removal of Sunset (SSD) dye on the synthesized MgO adsorbents were an exothermic process due to the value of ΔH^o (-36.077). The value of ΔH^o was lower than 40 KJ/mol, the removal of Sunset (SSD) dye on the synthesized MgO adsorbents dye was a physisorption process. ΔS^o had a negative charge that means a decrease in the degree of freedom of solution for the adsorption process. The negative values of ΔG^o reflected that the adsorption process was spontaneous. Also, the values ΔG^o increased with the increase of temperature that means the adsorption of Sunset (SSD) dye on the synthesized MgO adsorbents was unfavorable at high temperatures. Besides, the removal of Tartrazine (TZD) using the MU6 sample was an endothermic process due to a positive charge of the ΔH^o. The value of ΔH^o (cal. 31.650 KJ/mol), the adsorption of Tartrazine (TZD) using the MU6 sample dye was a physisorption process. ΔS^o had a positive charge that means an increase in the degree of freedom of solution for the removal process of Tartrazine (TZD) using the MU6 sample. The negative values of ΔG^o reflected that the adsorption process was spontaneous. The values of the ΔG^o parameter decreased with the increase of temperature and it means that the removal of Tartrazine (TZD) using the MU6 sample was more favorable at high temperatures[12, 38, 42].

Table4. Thermodynamic parameters for the adsorption of (SSD) and (TZD) dyes using magnesium oxide adsorbent (MU sample).

Dyes	**Thermodynamic parameters**		
	ΔGº	ΔHº	ΔSº
	(KJ/mol)	(KJ/mol)	(KJ/mol)
SSD	-4.922	-36.077	-0.101
	-4.416		
	-3.81		
TZD	-2.946	31.650	0.112
	-3.508		
	-4.182		

3.6 Comparative study

The adsorption capacities of magnesium oxide nano-adsorbents compared with other adsorbents reported in the literature and utilized for the removal of Sunset (SSD) and Tartrazine (TZD) dyes. These collection data have been outlined in Table 5. The collected data appeared that MU6, MV6 and MA6 samples can be used for the removal of Sunset (SSD) and Tartrazine (TZD) dyes from aqueous media [43-50].

Table 5. The adsorption capacities of magnesium oxide nano-adsorbents (MU6, MV6 and MA6) compared with other adsorbents.

Absorbent	Dye	Adsorption, capacity, mg/g	References
Sawdust	TZD	4.71	43
Chitosan	TZD	350	44
Chitin	TZD	30	44
Polyaniline/sawdust	TZD	2.47	45
CuO/activated carbon	TZD	58.8	46
MU6	TZD	52	This study
MV6	TZD	73	This study
MA6	TZD	68	This study
CdTN-AC	SSD	61.31	47
$Cd(OH)_2$-NW-AC	SSD	76.92	48
Ag-NP-AC	SSD	37.04	48
activated carbon	SSD	22.2	49
ZnO-NPs-AC	SSD	142.85	50
MU6	SSD	51	This study
MV6	SSD	72.44	This study
MA6	SSD	70.6	This study

4. Conclusions

Magnesium oxide (MgO) nanoparticles were fabricated utilizing the autocombustion method and different fuels following by the annealing at 600 °C for 2 h. The synthesized magnesium oxide nanoparticles were examined by X-ray diffraction, High-resolution transmission electron microscopy, Fourier transform infrared spectroscopy, Field-emission scanning electron microscopy, thermal analysis and BET mothed. The crystallite sizes, particle size and surface area of the obtained magnesium oxide nanoparticles (MU6 sample) were calculated to be 62 nm, 70 nm and 11.35 m^2/g. The synthesized products are used as an adsorbent for removal of the Sunset (SSD) and Tartrazine (TZD) dyes from water. The maximum adsorption capacities of the synthesized magnesium oxide nanoparticles (MU6, MV6 and MA6 samples) were determined to be 52/73/68 mg/g and 51/72.44/40.6 mg/g for the removal of the Sunset (SSD) and Tartrazine (TZD) dyes, respectively. From the collected data, Langmuir isotherm model and pseudosecond-order model are better fitting than the other models for the removal of SSD and TZD dyes on the MU6 nano-adsorbent. The removal of Sunset dye on the synthesized MgO adsorbents was an exothermic, physisorption and spontaneous process. According to the ΔG^o values, the adsorption of SSD dye on the synthesized MgO adsorbents is unfavorable at high temperatures. The removal of Tartrazine dye on the synthesized MgO adsorbents was an endothermic, physisorption and spontaneous process. According to the ΔG^o values, the adsorption of TZD dye on the synthesized MgO adsorbents is favorable at high temperatures.

References

1. Siddhartha, B.; Naba, K.M.; Jan, P.; Václav,S.; Pavel, K., Dyes and their removal technologies from wastewater: A critical review IN Intelligent Environmental Data Monitoring for Pollution Management, Elsevier, 2021,pp.127160.
2. Ting,G.; Chaoke,B., Facile fabrication of MgO/graphene oxide composite as an efficient adsorbent for rapid removal of aqueous organic dyes: Performance evaluation and mechanistic investigation, J. Phys. Chem. Solids, 2021,158, p.110251.
3. Varsha,S.; Philipp,M.; Yogesh,C.S.; Mika,S., Synthesis and application of polypyrrole coated tenorite nanoparticles (PPy@ TN) for the removal of the anionic food dye 'tartrazine'and divalent metallic ions viz. Pb (II), Cd (II), Zn (II), Co (II), Mn (II) from synthetic wastewater, RSC Adv., 2015,5,pp. 80829-80843. [4] Taiba,N.; Tayyiba,D., The role of some important metal oxide nanoparticles for wastewater and antibacterial applications: A review, Environ. Chem. Ecotoxicol., 2021,3,pp.59-75.
4. Gabrie,B., Wastewater microbiology, 3rd ed., John Wiley & Sons, 2005, PP.211-371.
5. Sushmita,B.; Mahesh,C.C., Adsorption characteristics for the removal of a toxic dye tartrazine from aqueous solutions by a low cost agricultural by-product, Arabian J. Chem., 2017,10, pp. S1629-S1638.
6. Shri, T.V.; Ranjani, V.; Y.,A. N.; B., K. C., Kinetics and thermodynamics of reactive and vat dyes adsorption on MgO nanoparticles, Chem. Eng. J., 2012,198,pp.1-10.
7. You, L.;Tengchao,W.; Shaoshuai,Z.; Yanling,Z.; Lulu,Y.; Ruijiang, L., Adsorption and electrochemical behavior investigation of methyl blue onto magnetic nickel-magnesium ferrites prepared via the rapid combustion process, J. Alloys Compd., 2021 ,885,p.160969.
8. Barsharani,P.; Tanaswini,P.; Tapas,R.S., An efficient and comparative adsorption of Congo red and Trypan blue dyes on MgO nanoparticles: Kinetics, thermodynamics and isotherm studies, J. Magnes. Alloy.,2021,9 pp.478-488. [10] Candelaria,T.T.; Angel,V.O.; Ángel, D.G., Adsorption of Azo-Anionic Dyes in a Solution Using Modified Coconut (Cocos nucifera) Mesocarp: Kinetic and Equilibrium Study, Water, 2021,13,p.1382.
9. **Mostafa,**Y.N.; **Ayman,**A.A.; **Alaa,**S.A., A facile Pechini sol–gel synthesis of TiO_2/Zn_2TiO_2/ZnO/C nanocomposite: an efficient catalyst for the photocatalytic degradation of Orange G textile dye, RSC Adv., 2017,7,pp.30411-30421.
10. Ayman,A.A.; Sayed,A.S.; Alaa,S.A.;Sahar,R.E., Synthesis and characterization of ZrO_2/CeO_2 nanocomposites for efficient removal of Acid Green 1 dye from aqueous solution, Mater. Sci. Eng. :B, 2021,269,p.115167.
11. Ayman,A.A.; Ibrahim, S. A., Alaa, S. A.; Mai, M. G., Auto-combustion Fabrication and Optical Properties of Zinc Oxide Nanoparticles for Degradation of Reactive Red 195 and Methyl Orange Dyes, J. Inorg. Organomet. Polym Mater., 2021,31,pp.3780-3792.
12. Ayman,A.A.; Ezzat,A.E.; Nasrallah,M.D., Auto-combustion fabrication, structural, morphological and photocatalytic activity of CuO/ZnO/MgO nanocomposites, Mater. Chem. Phys., 2021,270, p.124762.
13. Timir,H.M.; G.K.P.; Beer, S., Jayadev A.; A.R. S.; Ramanuja V., Nanocrystalline zinc oxide for the decontamination of sarin, J. Hazard. Mater., 2009,165,pp.928-932.
14. Xiaogang,Z.; Ming,H.; Yaohui,Y.; Xiaojing,F.; Yong,L.; Jing,W., One-pot synthesis of sandwich-like MgO@ Carbon with enhanced sorption capacity of organic dye, Chem. Eng. J., 2018,334,pp.1399-1409.
15. Mengqing,H.; Xinlong,Y.; Xiaoyan,H.; Jiajin,Z.; Rui,F.; Min, Z., i. science, Ultra-high adsorption capacity of MgO/SiO_2 composites with rough surfaces for Congo red removal from water, J. Colloid Interface Sci., 2018,510, pp.111-117. [18] Yanyan,P.; Zhuwu,J.; Liangjie,Y., Facile synthesis of MCM-41/MgO for highly efficient adsorption of organic dye, Colloids Surf. A Physicochem. Eng. Asp, 2019,581,p.123816.

16. Ibrahim,.S.A.; Sayed,A.S.; Hassan,.A.D., Ayman,A.A., Low temperature combustion synthesis of $CoxMg1-xAl_2O_4$ nano pigments using oxalyldihydrazide as a fuel, Mater. Chem. Phys., 2011,125, pp.326-333.
17. Ayman,A.A.; Ezzat,E.F.; Ibrahim,.S.A., Near-infrared reflecting blue inorganic nano-pigment based on cobalt aluminate spinel via combustion synthesis method, Dyes Pigm., 2018,158,pp.451-462.
18. Ayman,A.A.; Ibrahim,.S.A., Sol-gel auto-combustion fabrication and optical properties of cobalt orthosilicate: Utilization as coloring agent in polymer and ceramic, Mater, Chem. Phys., 2019,238,pp.121888-121902.
19. Ibrahim,.S.A., Sayed.A.S.; Mahmoud,M.M.; Hassan,.A.D.; Ayman,A.A.,
20. Synthesis and spectral characterization of $Co_xMg1-xAl_2O_4$ as new nano-coloring agent of ceramic pigment, Spectrochim. Acta A Mol. Biomol. Spectrosc., 2009,74, pp.665-672.
21. Mauskar,S.; K.V. Karthik, R. Ravishankar, K.S. Anantharaju, H. Nagabhushana, K. Jeetendra, Y.S. Vidya, L. Renuka, Synthesis of ZnO, MgO and ZnO/MgO by Solution Combustion Method: Characterization and Photocatalytic Studies, Mater. Today: Proc., 2017,4, pp.11791-11798.
22. Balakrishnan, G.; Velavan, R.; Khalid ,M.B.; Emad,H.R., Microstructure, optical and photocatalytic properties of MgO nanoparticles, Results Phys., 2020,16,p.103013.
23. Yuncheng, C.; Dan, W.; Xiwei, Z.; Wei, W.; Fatang, T.; Jianguo, C.; Xueliang, Q.; Xiaolin, Qiu., Sol-gel preparation of Ag-doped MgO nanoparticles with high efficiency for bacterial inactivation, Ceram. Int., 2017, 43, pp.10661072.
24. Hakimeh, M.; Abolghasem, D., Microwave Assisted Sol-Gel Synthesis of MgO Nanoparticles and Their Catalytic Activity in the Synthesis of Hantzsch 1,4Dihydropyridines, Chin. J. Catal., 2012, 33, pp.1502-1507.
25. Sadegh, Y.; Behrooz, G.; Mohammad, T.; Alireza, A., Optical properties of MgO and $Mg(OH)_2$ nanostructures synthesized by a chemical precipitation method using impure brine, J. Alloys Compd., 2017, 711, pp. 521-529.
26. Mehran, R.; Majid, K.; Behzad, N., Preparation of nanocrystalline MgO by surfactant assisted precipitation method, Mater. Res. Bull., 2011,46, pp. 16321637.
27. Jingyuan, X.; Elizabeth, F.K.; Veera, M.B.; Sean, X.Li.; Wen, C. L., Production and characterization of cellulose nanofibril (CNF) from agricultural waste corn stover, Carbohydr. Polym.,2018,192, pp. 202-207.
28. Baixiong, L.; Cong, L.; Lina, Z.; Zhiping, L.; Mengjie, K.; Xingyu, H., Fabrication of three-dimensional ordered macroporous/mesoporous magnesium oxide for efficient cadmium removal, Ceram. Int., 2021, 47, pp. 22830-22838. [31] Masahiro, S.; Rika, K.; Toru, M.; Wataru, U., Preparation and formation mechanism of three-dimensionally ordered macroporous (3DOM) MgO, $MgSO_4$, $CaCO_3$, and $SrCO_3$, and photonic stop band properties of 3DOM $CaCO_3$, J. Solid State Chem., 2011, 184, pp. 2299-2305.
29. Chunhui. F.; Yingchao, Z., Adsorption isotherms, kinetics and thermodynamics of nitrate and phosphate in binary systems on a novel adsorbent derived from corn stalks, J. Geochem. Explor., 2018, 188, pp. 95-100.
30. Nasmi, H. S.; Wardana, I.N.G.; Irawan, Y.S.; Siswanto, E., Characterization of the chemical, physical, and mechanical properties of NaOH-treated natural cellulosic fibers from corn husks, J. Nat. Fibers, 2018,15, pp. 545-558.
31. Lunhong, A.; Haitao, Y.; J., Sacrificial template-directed synthesis of mesoporous manganese oxide architectures with superior performance for organic dye adsorption, Nanoscale, 2012,4, pp. 5401-5408.
32. Anne, M. R.; Ki-Joon, J. Jeffrey, J. U., Size-dependent CO_2 capture in chemically synthesized magnesium oxide nanocrystals, J. Mater. Chem., 2011,21, pp. 11486-11491.

33. Amr, F.; Saad, E.H.; Ebrahim, S.; Mohammed, F. H., Photocatalytic degradation of real textile and tannery effluent using biosynthesized magnesium oxide nanoparticles (MgO-NPs), heavy metal adsorption, phytotoxicity, and antimicrobial activity, J. Environ. Chem. Eng., 2021, 9, p.105346.
34. Tatenda, C. M.; Karthigeyan. A.,Heavy metal ion effluent discharge containment using magnesium oxide (MgO) nanoparticles, Mater. Today. Proc., 2017,4, pp. 9-18.
35. Ayman, A.A.; Sahar, R.E.; Sayed, A.S.; Talaat, Y.M.; Alaa, S.A., Fabrication and characterization of cerium oxide nanoparticles for the removal of naphthol green B dye, Desalin. Water Treat., 2020, 204, pp. 124-135.
36. Daniel, S.; Shoba, U., Research, Synthesis, characterization and adsorption behavior of MgO nano particles on Rhodamine B dye, J. Chem. Pharm. Res., 2015, 7, pp. 713-723.
37. Songnan, L., Combustion synthesis of porous MgO and its adsorption properties, Int. J. Ind. Chem., 2019, 10, pp. 89-96.
38. Jing, F.; Linyi, Z.; Yuting, W.; Bowen, L.; Xiaofeng, H.; Zhuangjun, F.; Yueming, R.; Yanzhuo, L.; Milin, Z.; Dan, C., Synthesis of high surface area, mesoporous MgO nanosheets with excellent adsorption capability for Ni (II) via a distillation treating, J. Colloid Interface Sci., 2015, 438, pp. 259-267.
39. Ayman, A.A.; Ibrahim, S. A.; Esraa, M. E., Auto-combustion Synthesis and Characterization of Iron Oxide Nanoparticles (α-Fe2O3) for Removal of Lead Ions from Aqueous Solution, J. Inorg. Organomet. Polym., 2021, 31, pp. 384-396. [43] Sushmita, B.; Chattopadhyaya, M.C., Adsorption characteristics for the removal of a toxic dye, tartrazine from aqueous solutions by a low cost agricultural by-product, Arabian J. Chem., 2017, 10, pp. 1629-1638.
40. Guilherme, L.D.; Mery, L.G.V.; Luiz, A. A. P., Kinetics and Mechanism of Tartrazine Adsorption onto Chitin and Chitosan, Ind. Eng. Chem. Res., 2012, 51, pp. 6862-6868.
41. Ansari, R.; Mohammad, B. K.; Ali, F.; D., Application of polyaniline nanolayer composite for removal of tartrazine dye from aqueous solutions, J. Polym. Res., 2011, 18, pp.1931-1939.
42. Azadeh, J. R., Compounds, Synthesis of copper oxide nanoparticles on activated carbon for pollutant removal in Tartrazine structure, j. compos. comps., 2020,2, pp. 99-104.
43. Ghaedi, M.; Hekmati, J.A.; Khodadoust, S. Sahraei, R.; Daneshfar, A.; Mihandoost, A.; Purkait, M.K., Cadmium telluride nanoparticles loaded on activated carbon as adsorbent for removal of sunset yellow, Spectrochim. Acta, Part A, 2012, 90, pp. 22-27.
44. Ghaedi, M., Comparison of cadmium hydroxide nanowires and silver nanoparticles loaded on activated carbon as new adsorbents for efficient removal of Sunset yellow: Kinetics and equilibrium study, Spectrochim. Acta, Part A, 2012, 94, pp.346-351.
45. Helen, O.O.; Francis, K. E.; Kovo, G.A.; Jude, C.N.; Amarachi, G.O., Adsorption of tartrazine and sunset yellow anionic dyes onto activated carbon derived from cassava sievate biomass, Appl. Water Sci., 2021, 27, p.11.
46. Maghsoudi, M.; Ghaedi, M.; Zinali, A.; Ghaedi, A.M.; Habibi, M.H., Artificial neural network (ANN) method for modeling of sunset yellow dye adsorption using zinc oxide nanorods loaded on activated carbon: Kinetic and isotherm study, Spectrochim. Acta, Part A, 2015, 134, pp.1-9.

Application of the Experimental Design Methodology for the Optimization Activated Carbon's Preparation from Vegetable waste - Physicochemical characterizations

H. boulika [1], M. el hajam [1,2], M. hajji nabih [1], N. idrissi kandri [1], A. Zerouale [2]

[1] Signals, Systems and Components Laboratory (SSC), Faculty of Sciences and Techniques, Sidi Mohammed Ben Abdellah University, Route Imouzzer, BP2202, Atlas, FEZ, Morocco

[2] Processes, Materials and Environment Laboratory (PME), Faculty of Sciences and Techniques, Sidi Mohammed Ben Abdellah University, Route Imouzzer, BP2202, Atlas, FEZ, Morocco

Nowadays, the process of adsorption of pollutants holds a place of choice for the cleaning of the environment. The search for new adsorbent materials, using natural resources, is in permanent growth. The preparation of activated carbon, from vegetable wastes, is topical due to their abundance and their low cost. The transformation of these wastes into activated carbon gives rise to new techniques of improvement to better control the whole factors influencing the process of this transformation.

The objective of this work is the preparation of activated carbon from a vegetable waste and its optimization by a process developed with the help of Experimental design Methodology. The use of experimental design by varying several factors influencing the adsorption capacity of the prepared activated carbon is detailed. The activated carbon prepared on the basis of the optimal parameters was characterized by several analytical methods including; scanning electron microscopy, X-ray diffraction, thermogravimetric analysis and infrared spectroscopy. Complementary analyses were also carried out such as specific surface area by acetic acid adsorption, BOEHM surface functions, zero charge pH, and iodine value.

The results obtained indicate that this material prepared at 420°C has an iodine value of 824.85 mg/g, which makes it competitive with other activated carbons cited in the literature.

Keywords: Activated carbon, Experimental design,Iodine value, Preparation, Vegetable waste.

Effective Wastewater Treatment using Advanced Oxidation Process Combined with Magnetic Nanoparticle Setup

Ihab H. Alsurakji [1,*], Amjad El Qanni [2,*], Emad Salahat [1], Abdelkareem Arman[1], Mohammad Abuabiah [3], Waleed Abuzaina [3]

[1] An-Najah National University, Department of Mechanical Engineering, Nablus 7, Palestine;
[2] An-Najah National University, Department of Chemical Engineering, Nablus 7, Palestine;
[3] An-Najah National University, Department of Mechatronics Engineering, Nablus 7, Palestine;
[*]*Corresponding authors*: *isurakji@najah.edu;; a.elqanni@najah.edu; Tel.: +970594545128; +97059581448*

Abstract: Industrial organic wastewater effluents affect our ecosystem, especially when discharged without any treatment. Nowadays, advanced oxidation process (AOP) is considered one of the most conventional treatment techniques. It mainly depends on producing hydroxyl radicals (·OH) in presence of an oxidizing agent and/or bulk or nanoparticles which must have high sorption affinity and photocatalytic activity to speed up the treatment process. In this study, a magnetic iron oxide (Fe_3O_4) nanoparticle was used along with hydrogen peroxide (H_2O_2) and sodium persulfate ($Na_2S_2O_8$) for comparison purposes. This magnetic nanoparticle (MNC) has a high surface-area-to-volume ratio and is magnetic in nature which can be recovered by a magnetic field for further cycles of treatment and regeneration once needed. To the best of our knowledge, there is no continuous industrial process for such a treatment. Thus, a bench-scale setup that provides continuous wastewater flow was built which mainly depends on using four stages mechanism and recovering MNC using the magnetic field. This study should help in quantifying the efficiency, performance, and give insights regarding its feasibility towards wastewater treatment on an industrial scale. Hence, design and automated controlling parameters, optimal operating conditions, and economical descriptions were addressed in this work.

Keywords: Advanced oxidation process (AOP); sodium persulfate ($Na_2S_2O_8$); hydrogen peroxide (H_2O_2); magnetic nanoparticle (MNC); (Fe_3O_4) nanoparticle material; chemical oxygen demand (COD).

1. Introduction

The global population and industrial sectors are increasing rapidly nowadays, therefore solid waste and wastewater effluents are dramatically increasing. Therefore, residential building wastes must be considered through population growth. Hence, environmental institutions and governmental organizations shall constitute laws that restrict effluent resources by limiting their discharge, and by treating domestic and industrial wastewater. Generally, the sources of such effluents come from hospital discharges, landfill leachates, slaughterhouses, textile industry, livestock, and aquaculture [1-4]. Remarkably, those effluents are rich in chemical, colors, organic pollutants, and dyestuffs [5]. For instance, slaughterhouse wastewater effluents are a vital source of colored wastewater. The Palestinian Central Bureau of Statistics (PCBS) found that 17 slaughterhouses in Palestine; 11 in the West Bank and 6 in the Gaza Strip [6]. Thus, pollution prevention, solid waste management, and wastewater treatment are a must in Palestine to keep a clean and sustainable environment.

One of the most effective processes for treating wastewater is the advanced oxidation process (AOP), with the principle of oxidizing most of the organic pollutants. This technology has a conventional method for treating through producing hydroxyl radicals ($^{\cdot}OH$) that attack the organic pollutants or sulfate radical-based AOPs which are sufficient for degrading refractory organic pollutants. Moreover, $^{\cdot}OH$ can be gained using hydrogen peroxide (H_2O_2) along with other metal oxide-based catalysts that speed up the reaction rate of AOP [1, 7].

There are different treatment techniques used in AOPs. For instance, Fenton technique, which depends on producing $^{\cdot}OH$ removal from the reaction of (H_2O_2) with iron-based catalyst, since this mixture between Fe^{+2} and H_2O_2 is called Fenton's reagent [8], and the chemical reactions that represent $^{\cdot}OH$ are:

$$Fe^{+2} + H_2O_2 \rightarrow Fe^{+3} + HO^- + HO^{\cdot} \quad (1)$$

$$Fe^{+3} + H_2O_2 \rightarrow Fe^{+2} + FeOOH^{+2} \quad (2)$$

$$FeOOH^{+2} \rightarrow OH_2^{\cdot} + Fe^{+2} \quad (3)$$

Nanoparticle technology is emerging as one of the most interesting technologies for enhancing wastewater treatment. Literature review reveals that metal-oxide-based nanoparticles have unique properties in comparison with their counter parts for energy and environmental applications [9-12]. Owing to their nano-size, exceptional high. surface area to volume ratio, and easily manipulated surface make nanoparticles suitable as nanoadsorbents and nanocatalysts [13]. However, one of the critical challenges for this technology is the use of nanoparticles in continuous modes. Herein, in this study the investigation of the use of magnetic iron oxide nanoparticles, magnetite (Fe_3O_4) for degrading synthetic wastewater exemplified by crystal violet (CV) model molecule within a continuous in-house prototype. In addition, two different oxidation agents, hydrogen peroxide (H_2O_2) and sodium persulfate ($Na_2S_2O_8$), were also used to mimic the AOP process and to compare their degradation degree of CV model molecule at different initial concentration. At the end, optimal design parameters were estimated to give a comprehensive process description and thus promote its feasibility.

2. Materials and Methods

2.1. Dye model molecule

Synthetic wastewater samples were prepared using a crystal violet (CV) model dye molecule which could mimic colored and textile wastewater effluents [5]. This molecule has been purchased from Sigma-Aldrich and used without any further treatment. Table 1 and Figure 1 show the CV dye properties and its structure, respectively.

Table 1. Crystal violet model molecule properties.

Items	Specifications
Chemical formula	$C_{25}N_3H_{30}CL$
Molecular weight (MW)	407.98 $g.mol^{-1}$
Max wavelength (λ_{max})	590 nm
Purity	98%

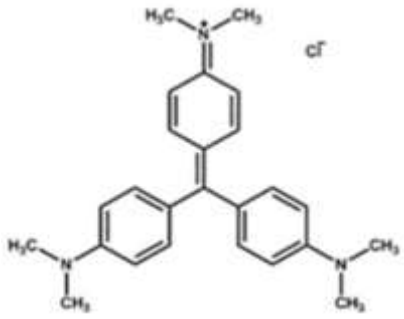


Figure 1. Crystal violet chemical structure [5].

A stock of 200 ppm of CV dye solution was prepared by dissolving a specified amount of CV in 20 mL of deionized water (DW) and subsequently diluted to the required concentration; 30 ppm. The concentration of 200 ppm dye was prepared by using the following equation:

$$\mathrm{C} = \frac{\mathrm{m}}{\mathrm{pu} \times \mathrm{V}} \tag{4}$$

where C is the CV dye concentration (ppm), pu is the purity of the CV dye, m is the desired mass of the CV dye (mg), and V is the volume of the DW (L). Applying equation 4 yields the desired mass of CV dye which is equal to ~ 4.0 mg which means diluting 4.0 mg of the CV dye with 0.02 L of DW producing 200 ppm CV dye concentration. The dilution equation can be described as:

$$\mathrm{V_1\,M_1} = \mathrm{V_2\,M_2} \tag{5}$$

where $\mathrm{V_1}$ is the volume needs to be diluted (L), $\mathrm{M_1}$ is the dye concentration before dilution (ppm), $\mathrm{V_2}$ is the desired volume (L) which is equal to 0.02 L, and $\mathrm{M_2}$ is the desired CV dye concentration (ppm) which is equal to 30 ppm. Applying equation 5, yields $\mathrm{V_1}$ equal to 0.003 L which means using 0.003 L from the 200 ppm CV dye solution and adding 0.017 L DW producing a dye solution with concentration of 30 ppm and volume of 0.02 L.

To determine the calibration curve of UV-Vis absorbance of CV concentration, the absorbance of the CV aqueous solution at different known concentrations was determined using UV-Vis spectrophotometry (Genesys 10S, Thermo Scientific Instruments Canada Inc., Mississauga, ON) at a wavelength of 590 nm. Three trials were performed at same ambient room temperature, constant pH which was around 6.0, and different initial concentrations varied from 10 to 30 ppm. A well-fitted regression equation for the calibration curve, $C = 10.582 \times Abs$, was obtained with a linear regression coefficient, $R^2 > 0.99$, where C is the CV concentration in ppm and Abs is the absorbance. Subsequently, the absorbance of the CV aqueous solution that had been degraded after the reaction was measured and the final concentration was calculated using the calibration curve equation.

2.2. Magnetite nanoparticles and oxidation reagents

Commercial magnetite (Fe_3O_4) nanoparticles used in the experiments as well as the oxidation agents are listed in Table 2. Worth mentioning that two different oxidation agents, H_2O_2 and $Na_2S_2O_8$, were used for comparison purposes.

Table 2. List of chemicals and reagents

Chemical/Reagent	Chemical formula	Purity	Vendor
Commercial magnetite	Fe_3O_4	--	Sigma-Aldrich (Haifa) via local
Hydrogen peroxide	H_2O_2	30 % (w/w)	sub-vendor BioTech Medical
Sodium persulfate	$Na_2S_2O_8$	98 %	Supplies (Ramallah, Palestine)

2.3. Optimization of oxidation agent amounts

In real industrial process shaking time and/or reaction residence time is a challenging parameter. Therefore, to optimize the amounts of H_2O_2 and $Na_2S_2O_8$ oxidation agents with mixing time, three runs were conducted by mixing 30 ppm of CV dye solution with Fe_3O_4 nanoparticles and H_2O_2 agent. A shaker device (Grant OLS200 Orbital Shaking Water Bath, Grant Instruments, Cambridge, UK) was used at constant speed of 40 rpm. Other experimental conditions were: pH at around 6.0, constant room temperature, and constant dose of Fe_3O_4 nanoparticles around $0.1g/10mL$ CV dye.

2.4. Optimization of mixing speed

Mixing the dye model molecule with the oxidation agent along with the nanoparticles were investigated using two methods. First one was by using the shaker device (see section 2.3) and the other one was by using four-blades mixing impeller. Four runs were performed to find the optimal mixing type and speed. In a typical run, 30 ppm of CV dye solution mixed with Fe_3O_4 nanoparticles in a ratio of 0.1g/10mL dye at constant pH (~6.0) and H_2O_2 agent amount which was 4mL/10mL dye.

3. Magnetic nanoparticles-assisted setup

Figure 2 shows a schematic diagram of the bench-scale setup that provides continuous wastewater treatment flow and in-house built prototype. It mainly consists of the following; i) one pre-treatment storage cylinder of 1800 *mL* capacity, ii) three cylinders for wastewater treatment of 600 *mL* each, iii) piping system, valves, couplers, pump, magnet, mixers, and bearings, iv) control unit including power supply, motors, boost, Arduino, and relays, v) chemicals including magnetite nanoparticle, H_2O_2, and $Na_2S_2O_8$ agents.

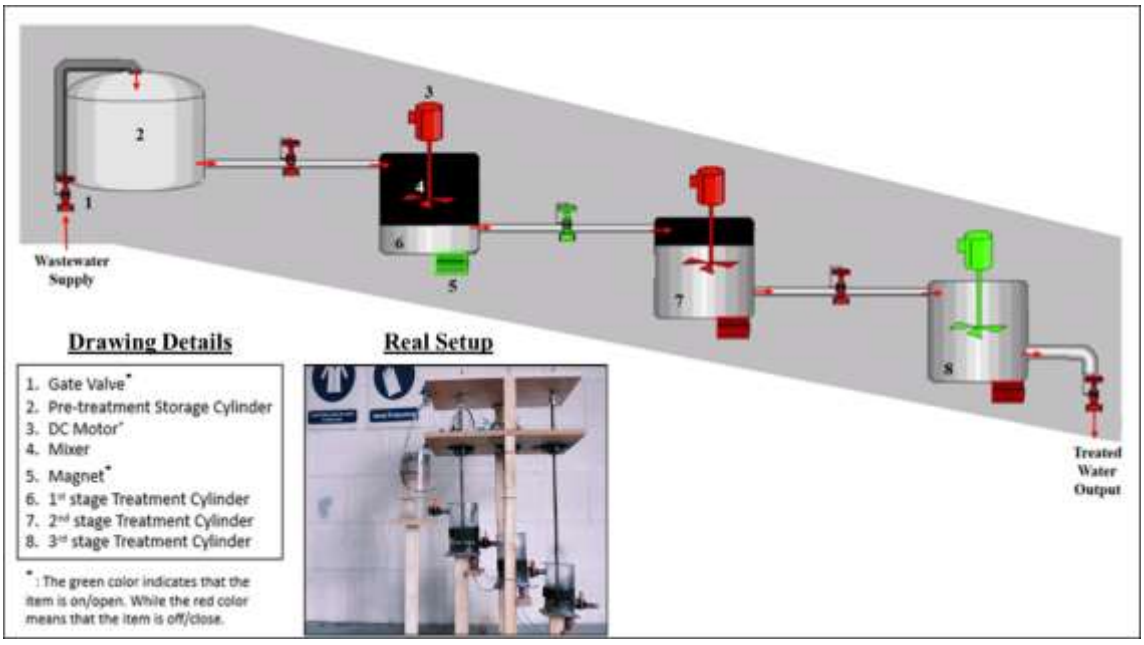


Figure 2. Schematic diagram of the magnetic wastewater treatment setup (drawn by using the Wondershare EdrawMax Software Version 10.5.2) and in-house built prototype.

4. Results and Discussion

4.1. Adsorption along with AOP treatment process

Adsorption and AOP for CV dye model molecule stock solution with different initial concentrations were performed using the in-house built prototype in presence of Fe_3O_4 nanoparticles. Table 3 shows the treatment cycles that were performed by using both oxidation agents H_2O_2 and $Na_2S_2O_8$ alongside the amount of the nanoparticles for each cylinder, the amount of each oxidation agent, the mixing duration, and the initial and final concentrations. The total volume of the prepared dye was 1800 *mL*, and thus 600 *mL* was delivered to each cylinder benefiting from gravity-transfer. As seen, the experimental conditions allowed to fully treat the stock solution of 30-200 ppm of CV, as pure effluents were obtained upon treatment as also shown in Figure 3. However, less amount of $Na_2S_2O_8$ was needed for this process in comparison with H_2O_2. More explanation of this observation will be elaborated in section 4.2.

Table 3. The result of treating of CV dye model molecule solution by using H_2O_2 and $Na_2S_2O_8$ agents.

Agent	Cycle	Amount of Catalyst (g/cylinder)	Amount of Agent (ml/cylinder)	Mixing Time (min/cylinder)	Initial Concentration (ppm)	Final Concentration (ppm)
H_2O_2	1	6	240	10	30	0
	2	6	240	10	30	0
	3	6	240	10	30	0
$Na_2S_2O_8$	1	6	180	10	30	0
	2	6	180	10	30	0
	3	6	180	10	30	0
	1	6	180	10	120	0
	2	6	180	10	120	0
	3	6	180	10	120	0
	1	6	180	10	200	0
	2	6	180	10	200	0
	3	6	180	10	200	0

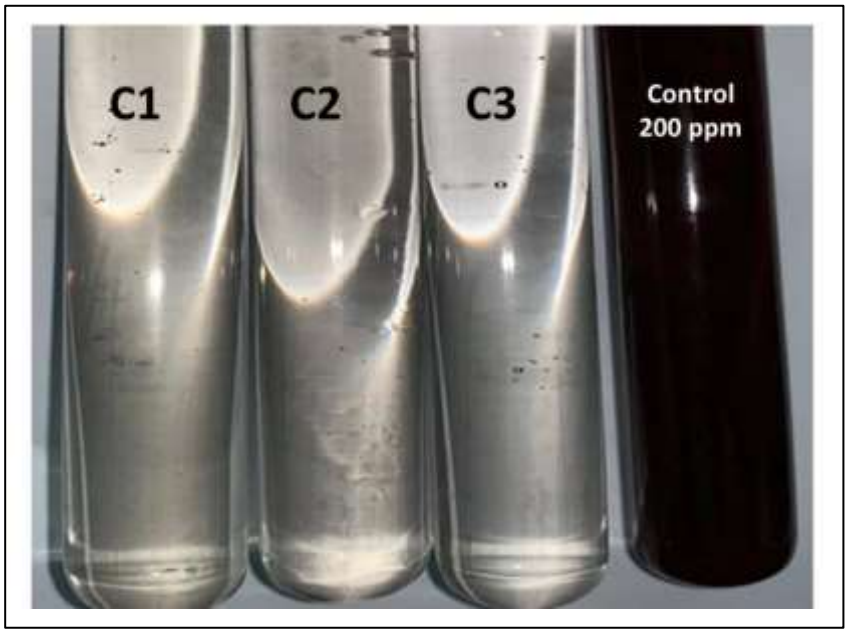


Figure 3. Pure effluents upon treating 200 ppm CV dye model molecule solution using $Na_2S_2O_8$ oxidation agent in presence of Fe_3O_4 nanoparticles.

4.2. Optimal oxidation agent amounts

Table 4 shows the results of the three optimization runs regarding the oxidation agent amounts. As seen, as the amount of H_2O_2 agent is increased the shaking time decreased, as well as the final concentration of the CV dye. The same scenario is noticed for $Na_2S_2O_8$. However, the degradation degree of CV molecule is way bigger in presence of $Na_2S_2O_8$ in comparison with H_2O_2. For instance, the final concentration of CV molecule was dropped to 1.6 ppm and 9.5 ppm in presence of 2 *mL* of $Na_2S_2O_8$ and H_2O_2, respectively. This could be attributed to the stability of each oxidation agent. Since this process is an advanced oxidation process, sulfate-radical-based ($SO_4^{-\bullet}$) is a powerful oxidizing agent than OH-radical-based ($OH^{-\bullet}$). As indicated by Hung et al., 2016, the persulfate anion is thermodynamically more stable than H_2O_2 [14].

Table 4. Optimization results of H_2O_2 and $Na_2S_2O_8$ amounts with mixing time.

Agent	Run	Initial Concentration (ppm)	Amount (mL)	Shaking Time (min)	pH	Final Concentration (ppm)
H_2O_2	1	30	0	60	6	30.0
	2	30	2	60	6	11.2
	3	30	4	30	6	9.5
$Na_2S_2O_8$	1	30	0.5	30	6	4.1
	2	30	1	30	6	1.9
	3	30	2	30	6	1.6

4.3. Optimal mixing speed

This is a vital parameter for the continuous process as the target is to avoid nanoparticles agglomeration as well as the suspension. Thus, Table 5 shows the runs' parameters and the results for optimal mixing type and speed. Noticeably, as the four-blade impeller (conventional mixer) speed increases the final concentration of the dye decreases. As seen, the optimal speed could be in range 300-400 rpm to achieve maximum degradation percentage (64-82 %). Worth mentioning that at this speed range the nanoparticles stayed dispersed neither suspended nor precipitated during the whole time within the experimental runs. Hence, four-blade impeller with a speed of (300-400 rpm) has been chosen for the prototype experiments.

Table 5. The results of optimizing the mixer type and parameters.

Run	Initial Concentration (ppm)	Shaker Speed (rpm)	Four-Blade Impeller Speed (rpm)	Final Concentration (ppm)
1	30	40	--	9.5
2	30	--	200	25.0
3	30	--	300	10.7
4	30	--	400	5.5

4.4. Process Description and Cost estimation

Four 1800 *mL* CV dye samples were prepared at different dye concentrations. Each sample was divided into three 600 *mL* batches passed through three cylinders by using a 16 *mm* ID manual gate valve. The process itself is unique which intended to treat the samples continuously through three stages. A hydrostatic pump of 1.0 *mL/sec* capacity is used for pumping the wastewater effluent into the pre-treatment storage cylinder. Each of the other three cylinders contained a mixer (four-blade impeller) which is used for mixing the sample with 6.0 *g* of Fe_3O_4 nanoparticles for 10 *min*. Initially, the first gate valve between the pre-treatment storage cylinder and the first cylinder is fully opened until a quantity of 600 *mL* is transferred. Then, 10 *min* mixing is conducted for the wastewater and the nanoparticles. Thereafter, a magnetic mechanism is turned on and all nanoparticles were grasped due to their magnetism characteristics. The grasping process lasts for three minutes while the second gate valve is fully closed. While the magnetic mechanism in the first cylinder is still on, the second gate valve is fully opened. Herein, 600 *mL* is transferred between first cylinder and the second one. Same scenarios are repeated for the second and the third cylinders. Interestingly, the three wastewater treatment cylinders were mounted on a wood stand which was designed in a way that allowed gravity-transferred between stages (Figure 2).

A magnetic mechanism was used for generating an electrical magnetic field in order to attract the Fe_3O_4 nanoparticles from the treated wastewater. It consists of a cupper coil wrapped around a steel rod and connected to a power supply. The electrical magnetic field has a proportional relation with the current value and the coil length. Three runs were performed by using the steel rod which has

length of 7 *cm* and 1.4 *cm* in diameter, the power supply has a voltage of 12-*Volt* (DC) and a current of 10 *A*, and varying coil length. Table 6 shows the effect of the coil length to the magnetic field force. It is worthwhile mentioning that no attraction occurred when 10 *m* coil length was used which means that the electrical magnetic force is not enough for attracting the Fe_3O_4 nanoparticles. Moreover, at 30 *m* length the Fe_3O_4 nanoparticles were attracted while the coil was started to be heated due to high power supply current which means the coil resistance is not enough. Remarkably, run number three represents the selected design parameter.

Table 6. The result of optimizing the electrical magnetic field parameters.

Runs	Coil length (m)	Result
1	10	Not Effective
2	30	Effective with side effect
3	50	Effective without side effect

Nevertheless, for futuristic industrial scale up of such in-house built prototype, Table 7 lists the major components along with the process description and the cost for each element indicating the feasibility of such nonconventional treatment process.

Table 7. Major element items, process description, and cost estimation for the prototype.

Element	Descriptions	Capital Cost ($)
Fiber Glass Cylinders	Four transparent fiberglass cylinders were used, and all of them were equipped with an opening to atmosphere. The first cylinder (pre-treatment storage cylinder) has the largest volume which is 1,500 ml of 10 cm diameter and 20 cm height. The other three-stages-treatment cylinders have smaller volume of 1,100 ml with 10 cm diameter and 15 cm height.	80
Piping system and Valves	A transparent polyethylene pipe of 16 mm diameter was used to allow visual observation of flowing water from one cylinder to another. Five manual gate valves of 16 mm diameter were installed at the entering, bottom side for each cylinder, and at the exit.	10
DC Motor	Three DC motors were installed and each one has a shaft diameter of 0.65 cm and rotates at constant speed up to 400 rpm.	90
Bearing	Six bearings were used in this design. Two bearings were mounted at each shaft to prevent vibration forms due to shaft rotation. The bearing has inner diameter of 1.2 cm.	
Couplers	Three couplers were used to connect the motor shaft with the mixer shaft.	45
Pump	Hydrostatic pump with capacity of 1 mL/sec.	25
Magnet	Three magnets were installed at the bottom of each treatment cylinders. Each magnet consists of 50 meters cupper coil wrapped around a steel rod which has dimension of 1.4 cm in diameter and 7 cm in length. Moreover, 12-volt DC power supply that provides a current of 10-A was connected in series with the magnet.	30
Mixer	Three mixers were used in this design. Each mixer shaft has diameter of 1.2 cm and varying lengths equal to 45, 50, and 65 cm.	25
Power supply	12-Volt DC power supply and current of 3.2 A	10
Boost	Intended to increase voltage which in turn increase the motor rotational speed.	10
Arduino and relays	Used to control mixers and magnets start-stop automatically.	100
Fe_3O_4	In-house prepared nanoparticles	110/1kg
H_2O_2 agent	Locally available (960 ml was used)	25/1L
Wood stand	Holding the whole setup	45
	Total ($)	605

5. Conclusions

Industrial and domestic sectors are in critical needs for emerging technologies for water and wastewater treatment. Herein, the results of this study promote the effectiveness of using magnetite (Fe_3O_4) nanoparticles within a continuous treatment process. In fact, these nanoparticles showed high efficiency and durability along with sodium persulfate ($Na_2S_2O_8$) oxidation agent for treating synthetic aqueous solution for many adsorptions and AOP cycles. This study showed the proof of concept, therefore, futuristics efforts will focus on the reaction kinetics, nanocatalysts sustainability, and synergistic effects upon using different competitive model molecules in the water matrix within a fully automated and modified prototype.

References

1. A. R. Ribeiro, O. C. Nunes, M. F. Pereira, and A. M. J. E. i. Silva, "An overview on the advanced oxidation processes applied for the treatment of water pollutants defined in the recently launched Directive 2013/39/EU," vol. 75, pp. 33-51, 2015.
2. K. Paździor, L. Bilińska, and S. J. C. E. J. Ledakowicz, "A review of the existing and emerging technologies in the combination of AOPs and biological processes in industrial textile wastewater treatment," vol. 376, p. 120597, 2019.
3. L. Bilińska, K. Blus, M. Gmurek, and S. J. C. E. J. Ledakowicz, "Coupling of electrocoagulation and ozone treatment for textile wastewater reuse," vol. 358, pp. 992-1001, 2019.
4. A.-N. Husam, A. J. J. o. W. R. Nassar, and Protection, "Slaughterhouses wastewater characteristics in the Gaza strip," vol. 11, no. 07, p. 844, 2019.
5. N. N. Nassar, N. N. Marei, G. Vitale, and L. A. J. T. C. J. o. C. E. Arar, "Adsorptive removal of dyes from synthetic and real textile wastewater using magnetic iron oxide nanoparticles: thermodynamic and mechanistic insights," vol. 93, no. 11, pp. 1965-1974, 2015.
6. P. Ramallah and B. Localities, "Palestinian Central Bureau of Statistics," ed, 2016.
7. Q. Yang *et al.*, "Recent advances in photo-activated sulfate radical-advanced oxidation process (SR-AOP) for refractory organic pollutants removal in water," vol. 378, p. 122149, 2019.
8. R. Andreozzi, V. Caprio, A. Insola, and R. J. C. t. Marotta, "Advanced oxidation processes (AOP) for water purification and recovery," vol. 53, no. 1, pp. 51-59, 1999.
9. M. Amde, J.-f. Liu, Z.-Q. Tan, and D. J. E. p. Bekana, "Transformation and bioavailability of metal oxide nanoparticles in aquatic and terrestrial environments. A review," vol. 230, pp. 250-267, 2017.
10. P. K. Rai *et al.*, "Nanoparticle-plant interaction: Implications in energy, environment, and agriculture," vol. 119, pp. 1-19, 2018.
11. D. Zu *et al.*, "Oxygen-deficient metal oxides: Synthesis routes and applications in energy and environment," vol. 12, no. 9, pp. 2150-2163, 2019.
12. I. H. Alsurakji, A. El-Qanni, A. M. El-Hamouz, I. Warad, and Y. J. J. o. E. R. T. Odeh, "Thermogravimetric Kinetics Study of Scrap Tires Pyrolysis Using Silica Embedded With NiO and/or MgO Nanocatalysts," vol. 143, no. 9, p. 092302, 2021.
13. P. Xu *et al.*, "Use of iron oxide nanomaterials in wastewater treatment: a review," vol. 424, pp. 1-10, 2012.
14. C.-M. Hung, C.-W. Chen, Y.-Z. Jhuang, and C.-D. J. J. o. A. O. T. Dong, "Fe3O4 magnetic nanoparticles: characterization and performance exemplified by the degradation of methylene blue in the presence of persulfate," vol. 19, no. 1, pp. 43-51, 2016.

Humic Acid Removal from Aqueous Stream Using Calf Bones Charcoal as a Green Sorbent: A Reversible Process

Seyedeh Parvin Moussavi[1], Zakaria Al-Qodah[2] Razieh Ashoori[3] and Milad Mousazadeh[4,5,*]

[1] Department of Renewable Resources, University of Alberta, Edmonton, Canada seyedehp@ualberta.ca
[2] Al-Balqa Applied University, Faculty of Engineering Technology, Department of Chemical Engineering, Amman, Jordan. zak@bau.edu.jo
[3] Department of Environmental Health Engineering, School of Health, Shiraz University of Medical Sciences, Shiraz, Iran. ra.ashoori90@gmail.com
[4] Student research committee, Qazvin University of Medical Sciences, Qazvin, Iran
[5] Department of Environmental Health Engineering, Qazvin university of Medical Sciences, Qazvin, Iran
***** *Corresponding author: m.milad199393@gmail.com; Tel.: +989118557536.*

Abstract: Humic acid (HA) is available in waters as the main organic substance, causing carcinogenic byproducts with chlorination. Therefore, efficient treatment should be used for removing it. Removal of HA with the calf bone char (CBC) in batch reactors was investigated in this study. The influences of pH, a dosage of adsorbent, HA content, and reaction time, were explored. Langmuir ($R2 > 0.943$) model fitted with the equilibrium sorption data. Removal rate was fast in the first 30 minutes, and then decreased until reaching equilibrium. Furthermore, the results showed that as pH decreased, HA adsorption increased. 100% removal efficiency was obtained with 3 g/L CBC in acidic pH, within 180 minutes. As the adsorbent dose was increased, the removal efficiency also increased. In addition, as the initial HA content decreased, HA removal efficiency increased. It is successfully proved that the CBC can be applied as a cost-effective, operative, and reversible adsorbent for HA removal from the aqueous stream. Regeneration of the bone char using 50 mL of NaOH solution (0.1–0.5 M) over 2 h, at constant stirring and temperature (180 rpm and 25 °C) resulted in a HA sorption capacity of 92.4 mg/g.

Keywords: Bone Charcoal; Humic Acid Removal; Adsorbent; Isotherm; Kinetic Study

1. Introduction

These days, providing clean water in developing countries can be regarded as one of the most challenging problems due to population growth and supply scarcity [1]. Natural water resources usually contain different organic and inorganic soluble ions and compounds that are considered as pollutants [2-5]. Among these compounds are Humic substances (HS) which, can be subdivided into three fractions such as humin, humic acids (HA), and fulvic acids. These are the predominant natural organic matters (NOM), in ground water and surface water resources [6, 7]. About 60% of NOM includes HA, and it is widely used in industrial agriculture as a soil supplement. It improves the soil properties and acts as an organic fertilizer that helps for nourishing crops [8, 9]. However, the presence of HA in treated water by chlorination will lead to the formation of toxic compounds. It reacts with the chemicals resulted from the chlorination process and forms some disinfection by-products (DBPs) such as chloroform and dihaloacetonitriles [10]. Such by-products are toxic to both the environment and humans [11]. Thus, HA removal from water is an important and vital subject worldwide [12, 13]. Although conventional processes such as membrane technology [14] ozonation [3] ion exchange [15] adsorption [16] filtration [17] chemical coagulation [18] Electrocoagulation [19] and gas–liquid interface discharge plasma [3] have been employed for HA removal, adsorption seems to be a more affordable one as it is characterized by high yield, scalability, simplicity, and availability of suitable sorbents [9, 20]. Such properties could easily enhance the applicability of this process [21-23]. Literature has shown that several synthetic and natural adsorbents such as activated carbon, carbon nanotubes, and hematite are being applied for HA removal [5, 20, 24]. According to previous application, activated carbon (AC) has been the most common adsorbent that successfully used for water and wastewater treatment. However, the relatively high cost of this adsorbent, and the

restrictions on its broad use have led to the search of more cost effective resources. Recently, Bone charcoal (BC) has been reported as an adsorbent with outstanding physicochemical properties. BC is being studied as an innovative natural adsorbent for the treatment of water and wastewater contaminated with HA. It is found that BC produced by the carbonization process of cow bones possesses 10% carbon and 90% hydroxyapatite [25]. Accordingly, the application of this bone for BC synthesis is a promising strategy for solid waste management and the removal of many hazardous pollutants as it has a very active surface suitable for the adsorption process [26-28].

In addition, it is worthwhile to develop low-cost and effective adsorbents synthesized from biological wastes such as calf bone charcoal (CBC) to remove HA and other pollutants. Accordingly, this approach can be adopted in developing countries, owing to its availability, rapid action, pristine, low-cost, and efficacy for the adsorption of organic compounds including HA. Actually, the potential surface characteristics of CBC are expected to be beneficial for HA adsorption. This water contaminant is chosen in this study due to its solubility and negative effects on ecosystems and living organisms. It should be noted that, there are many research studies that apply the adsorption process of organic compounds using several char types obtained from animal or plant resources. However, the use of CBC to adsorb humic acid and remove it from wastewater has not been reported in the literature. There are few studies assessing regeneration methods. Therefore, the current study aimed at investigating the feasibility of CBC application as a natural adsorbent for the HA removal from the aqueous stream. Furthermore, for extending sorbent useful life and reducing the operating costs, it is possible to use the appropriate eluent for the sorbent regeneration. The cow bone char with better equilibrium sorption capacity were used for performing kinetic batch assays. Desorption studies using NaOH were performed aiming to verify the effectiveness of this eluent in the regeneration of the saturated bone char.

2. Materials and Methods

2.1. Materials

All chemicals required in the assays required for the current study, at analytical grade, were purchased from Merck Company. The fresh femur of the calf was obtained from local livestock slaughterhouses in Yazd City, Iran.

2.2. The adsorbent - calf bone charcoal - preparation

Calf bone waste was exploited for the production of the bio-adsorbent material. First, calf bones were carefully washed with tap water, cleaned from meat, rinsed again with de-ionized water to remove impurities on the surfaces and transferred to the oven at 100˚C for 24 hours to become dry. Afterward, the dried bones were crushed and ignited at 400˚C for three hours in a muffle furnace under oxygen-limited condition. The calcination process was also carried out in the furnace at 800℃ for 30 minutes. The produced bone ash was further triturated by standard ASTM sieves with mesh sizes ranging from 10 to 16 in the ball mill for 20-30 seconds, followed by washing in 0.1 M HCl solution at a concentration of 40 g/L for 1 h. It positively charges surface of the absorbent, enhances the attraction of humic acid ions, but retains the carbon morphology, without changing the mass and chemical composition of the material. Then, it was washed with deionized water three times, for removal the excess of acid present on the surface, and oven dried at 60 °C for 24 h. NaOH solutions, in a range of 0.1 to 0.5 M, used for bone char regeneration studies, were prepared by NaOH (p.a. Merck) dissolution in D.I. water.

2.3. Instrumentation

The surface properties of the prepared CBC were detected with scanning electron microscopy (SEM). Fig. 1 exhibits the SEM image of CBC, which defined an agglomerated structure of CBC. The specific surface area of CBC was measured by the Brunauer-Emmett-Teller (BET) method that was 112 m^2/g; much more efficient than the results of previous works [29, 30]. HA content was determined by a UV spectrophotometer (DR 6000, Hach, Germany). The adsorption assays were performed using the Jar Test. A digital calibrated multi-parameter analyzer (CONSORT C831, Belgium) was employed to measure the pH value of the solutions.

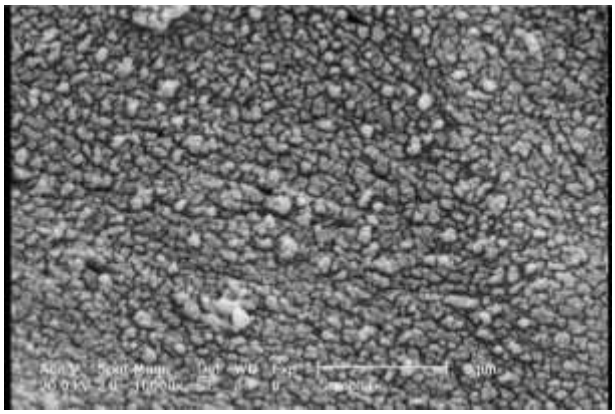


Fig. 1. SEM image of CBC

2.4. Adsorbate - humic acid

A stock solution of HA was prepared by dissolving Merck HA powder in 100 mL sodium hydroxide (0.1 N) solution. The prepared solution was left overnight, and then its volume was increased to 1 L with deionized water. The solution was filtered using a Whitman filter (1.2 µm pore size) to remove any suspended solids. Solutions of 5, 10, 20, and 30 mg/L were prepared by diluting the stock solution with deionized water.

2.5. Experiment methods

The parameters in the current study were pH, HA concentration, adsorbent dose, and reaction time. Experiments were performed in a lab-scale, using 250 mL bottles of HA placed in an incubator with rotating shakers (with agitation 150 rpm). HCl (0.1 N) and NaOH (0.1 N) were used for pH adjustment in the samples. For each sample, a blank sample was prepared for controlling the condition. At the end of each experiment, solutions were filtered with 1.2-µm cellulose acetate filters (Sartorius, Germany) in order to measure the final content of HA.

All assays were run in triplicate to ensure reproducibility. The calibration curve of experimental and blank samples was acquired under similar conditions for finding the appropriate wavelength. Equations (1) and (2) were used to calculate the amount of HA adsorbed on the CBC and the removal efficiency, respectively.

$$q_e = \frac{C_i - C_e}{m} xV \quad (1)$$

$$\%R = \frac{C_i - C_e}{C_i} x100 \quad (2)$$

Where, q_e, the adsorption capacity at equilibrium, mg/g; *Ci*, the initial concentration of HA, mg/L; *R*, is the % Rejection; *Ce*, the equilibrium concentration of HA, mg/L; *V*, volume of the aqueous stream, mL; and *m*, mass of CBC, g.

For the adsorption kinetics studies, pseudo-first-order and pseudo-second-order kinetic models, respectively expressed by Equations (3) and (4) were used [31, 32].

$$\log(q_e - q_t) = \log q_e - (\frac{k_1}{2.303})t \quad (3)$$

$$\frac{t}{q_t} = \frac{1}{k_2 q_e^2} + \frac{t}{q_e} \quad (4)$$

Where q_e was the amount of HA adsorbed onto the CBC at equilibrium (mgg^{-1}); q_t, the amount of HA adsorbed at time *t* (mgg^{-1}); k_1, the rate constants of pseudo-first-order (min^{-1}); and k_2, the rate constants of pseudo-second-order (min^{-1}).

The Langmuir, Freundlich, and Temkin isotherm models were used to fit the adsorption experimental isotherm data obtained from the study. The Langmuir model has been successfully

applied to a wide range of systems that exhibit limiting or maximum adsorption capacities. The linear form of Langmuir isotherm model is expressed as:

$$\frac{C_e}{q_e} = \frac{1}{K_L Q_0} + \frac{C_e}{Q_0} \quad (5)$$

Where q_e is the amount of HA adsorbed onto the CBC adsorbent at equilibrium, mg/g; K_L, is the equilibrium constant, L/mg; and Q_0, is the maximum adsorption capacity, mg/g.

In the Freundlich isotherm, a level of heterogeneity with heterogeneous distribution of heat adsorbed into the surface usually occurs in the adsorption process. The linear form of this model is:

$$\log(q_e) = \log K_F + \frac{1}{n}\log C_e \quad (6)$$

Where K_F is the capacity of adsorption at a unit of concentration, mg/g; and 1/n, represents the adsorption intensity [33, 34].

In addition, the linear form of the Temkin isotherm model is:

$$q_e = B\ln K_T + B\ln C_e \quad (7)$$

Where K_T, and B are Temkin isotherm constants.

The activation energy of the HA adsorption onto CBC can be calculated by the following Eqs (15):

$$k_2 = k_o \exp(\frac{-E}{RT}) \quad (8)$$

and

$$k_p = k^* \exp(\frac{-E}{RT}) \quad (9)$$

where k_2 and k_o are the pseudo-second order constant (g/mg min) and the rate constant of the adsorption process (g/mg min), respectively. On the other hand, k_p is the intraparticle diffusion coefficient (mg/g $min^{1/2}$), k^* is intraparticle diffusion coefficient at infinite temperature or the pre-exponential constant, (mg/g $min^{1/2}$).

The thermodynamic parameters for the adsorption process, the standard free energy ΔG^o, the standard enthalpy ΔH^o and the standard entropy ΔS° were calculated using the following Eqs:

$$\ln K_d = \frac{\Delta S^o}{R} - \frac{\Delta H^o}{RT} \quad (10)$$

where R (8.314 J/mol.K) is the universal gas constant, T (K) is the absolute solution temperature and K_d is the distribution coefficient which can be calculated as shown below:

$$K_d = \frac{C_{Ae}}{C_e} \quad (11)$$

where C_{Ae} (mg/L) is the adsorbed amount at equilibrium and C_e (mg/L) is the equilibrium concentration. Eq. (10) for calculating ΔG° is as follows [35].

$$\Delta G^o = -RT\ln K_d \quad (12)$$

3. Results and Discussion

3.1. Effect of HA content and reaction time

In order to investigate the effect of initial HA concentration on the adsorption rate, equilibrium concentration and equilibrium loading capacity, HA solutions of 5-30 mg/L with constant pH of 4, T of 25 °C, and 3 g/L of adsorbent dose were used. The results, showed in Fig. 2, reveals that the adsorption rate was fast and the equilibrium contact time was about 30 minutes. This indicates that HA and the CBC strongly interacted. It is clear that the fraction of HA in the solution decreases with time for all HA initial concentration. However, the uptake rate of the HA decreases with time until it approaches a pseudo steady state after 60 minutes. It is depicted from Fig. 2 that equilibrium fraction of HA remaining in the solution at 25 °C decreases as the initial HA concentration increases from 5

to 30 mg/l. In addition, the shapes of the curves are similar and seems to be independent on the initial HA concentration. This indicates a monolayer formation of the dye on the external surface [12].

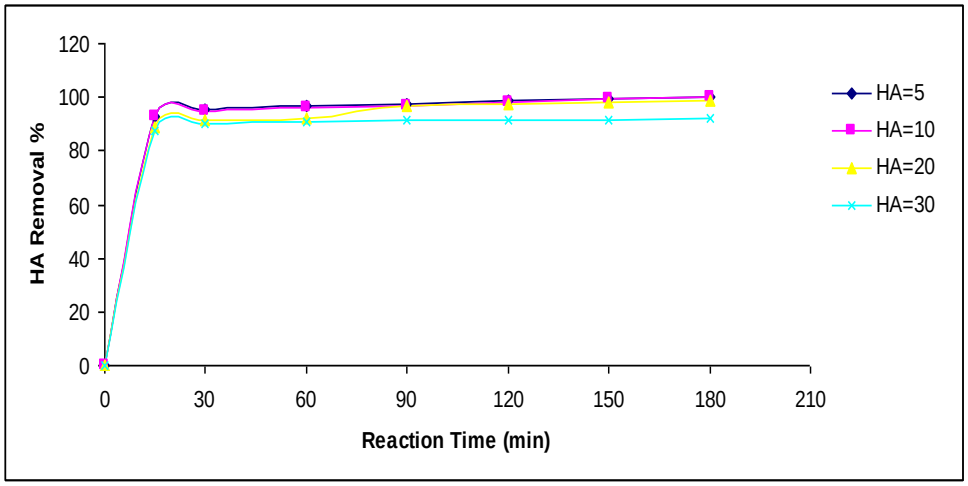


Fig. 2. Effect of reaction time and HA contents on adsorption by CBC (pH: 4, adsorbent dose: 3 g/L)

Accordingly, as HA concentration increases from 5-30 mg/L, the loading capacity of CBC decreases, consequently the removal efficiency decreases from 100- 92.1%. These results are in agreement with those obtained by Moussavi et al. [5], who had observed that by increasing the initial concentration of HA, the removal efficiency decreases. It is shown in Fig. 2 that the optimal reaction time was about 30 minutes where the adsorption rate is too high. After that the adsorption rate shows negligible decrease for all initial concentrations. Dawlet et al. [35] reported that for mercury adsorption the optimal time using sheep bone charcoal extended to 120 minutes, after which it reached equilibrium and decreased afterward.

3.2. Effect of adsorbent dose and reaction time

The variation of HA fraction adsorbed with time at several adsorbent doses with HA content of 20 mg/l; pH 4; reaction time of 180 min and T of 25 ^{o}C. As shown in Fig. 3, in the first 30 min, the C/C_0 decreased significantly because there were more free HA molecules in solution and more active sites on the surface of the adsorbents. It is expected that increase in CBC dosage and thus rise in the number of adsorption sites resulted in enhanced adsorption rate. Afterward, the adsorption rate did not change significantly. Likewise, as can be seen from Fig. 4, the maximum HA adsorption capacity was observed at 4 g/L of CBC. According to Fig. 4, the residual fraction of HA in the solution rapidly decreases from 0.48 to 0.002 as CBC dosage increases from 0.5 to 4 g/L. 98.9% removal efficiency was obtained with 3 g/L CBC in acidic pH, within 180 minutes.

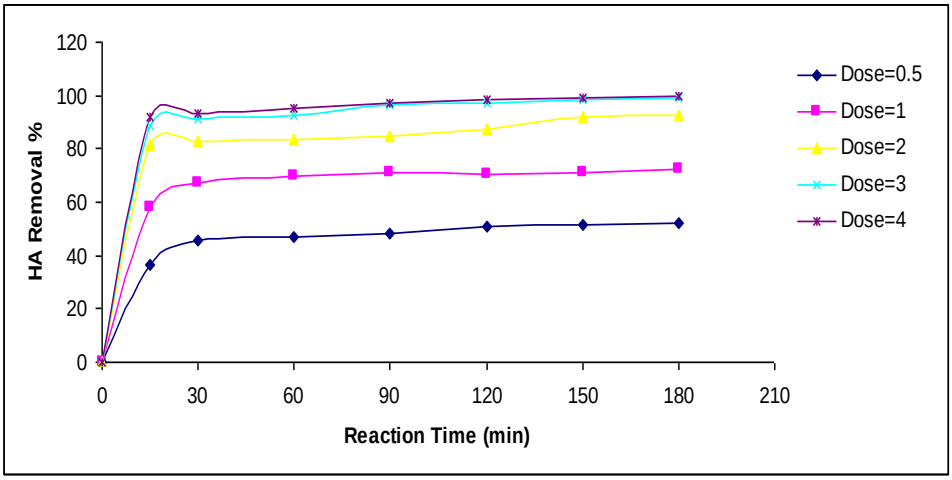


Fig. 3. Effect of reaction time and adsorbent dose on adsorption by CBC (pH: 4, HA content: 20 mg/L)

Similar conclusions were reported by Yu et al. [36]. They observed that in the 60 minute of reaction time, by increasing dual-pore carbon shells dosage, the adsorption of HA increased significantly. The increase in the adsorption capacity may be ascribed to the fact that with an increase in the adsorbent dose, the higher adsorption surface is available for the adsorbed molecules. A previous study reported that increasing the BC dosage resulted in a rapid initial increase in the norfloxacin removal rate [37]. Based on Fig. 4, the highest adsorption capacity of 38.08 mg/g occurred when HA concentration of 20 mg/L, pH of 4, a reaction time of 180 minutes, and an adsorbent dose of 0.5 mg/L.

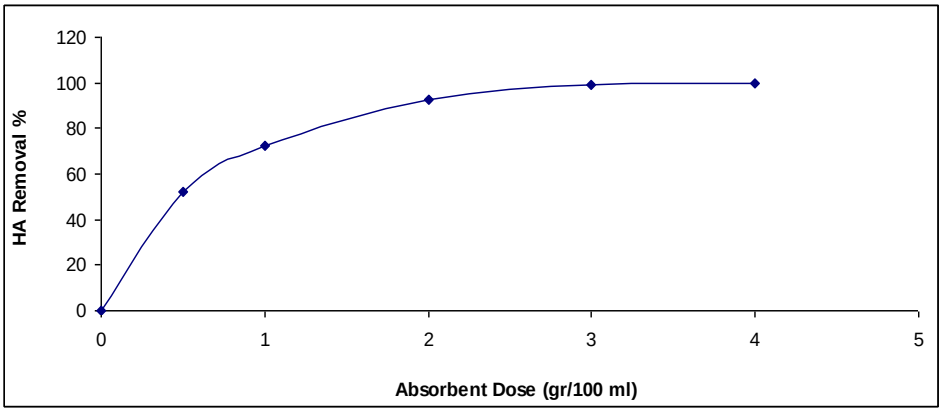


Fig. 4. Effect of adsorbent dose on adsorption by CBC (HA content: 20 mg/L, pH: 4, reaction time: 180 min)

3.3. Effect of solution pH and reaction time

Both adsorption capacity, the adsorbent surface load can be affected by solution pH. Since solution pH affects the interaction between adsorbate and functional groups of adsorbent, it is an important parameter in adsorption process. It is also an important control parameter which affects adsorption level of humic acid molecules on adsorbent surface. To study the effect of pH on adsorption of HA, batch experiments were carried out in different pHs. The effect of the pH on adsorption was studied at three pH values of 4, 7, and 10. As depicted in Fig. 5, as pH decreases from 10-4, adsorption level of humic acid increases and the highest adsorption level is observed in pH of 4. The adsorption capacity of CBC was considerably influenced by the pH value in such a way that the highest removal efficiency achieved in the acidic environment when pH was 4. On the other hand,

the lower removal efficiency was at pH value 10. Similar results were reported in earlier works [30, 35]. However, these results contradict those found in other study [38]. In addition, the findings represented that the maximum adsorption capacity occurred at the pH of 4 and that the adsorption capacity sharply decreased when the pH was increased from 4 to 10. Another significance of humic acid is its size and molecular structure which changes to a spherical shape in low pHs and to a linear or extended structure in high pHs; it may decrease adsorption of humic acids in higher pHs [39-41]. Therefore, size of humic acid macromolecules can be another factor which is related to decreased adsorption capacity in low pH. Considering the results from contact time curve, the highest adsorption level occurs in the first 30 minutes. As time of contact increases more than that, adsorption level doesn't change significantly and stabilizes; therefore, the optimum level can be achieved at 30 minutes. These results reveal that adsorption process of humic acid is very fast using bone charcoal and this phenomenon is related to a large number of vacant surface sites available on adsorbent surface in initial stages of adsorption process. As time passes, gradually the remaining vacant surface sites are toughly occupied by adsorbate because of repulsive forces among molecules of solute on solid and bulk phases [39-42].

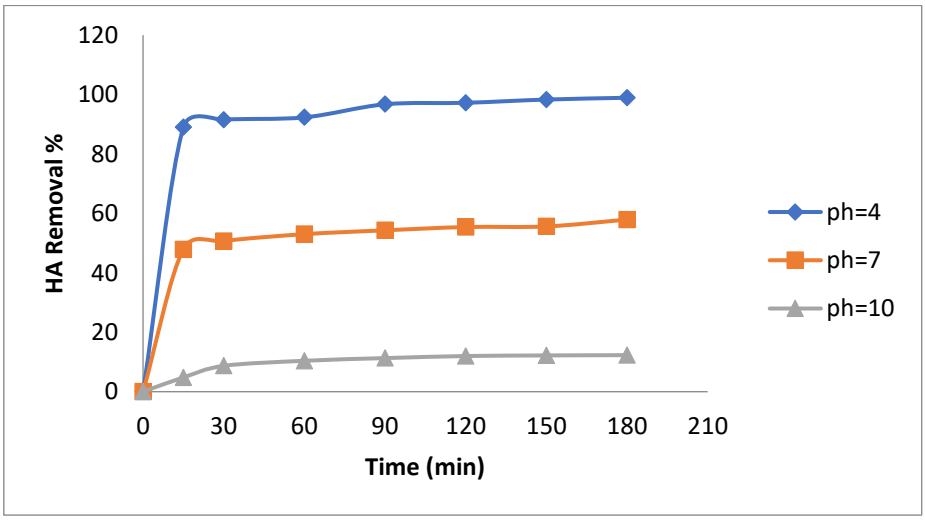
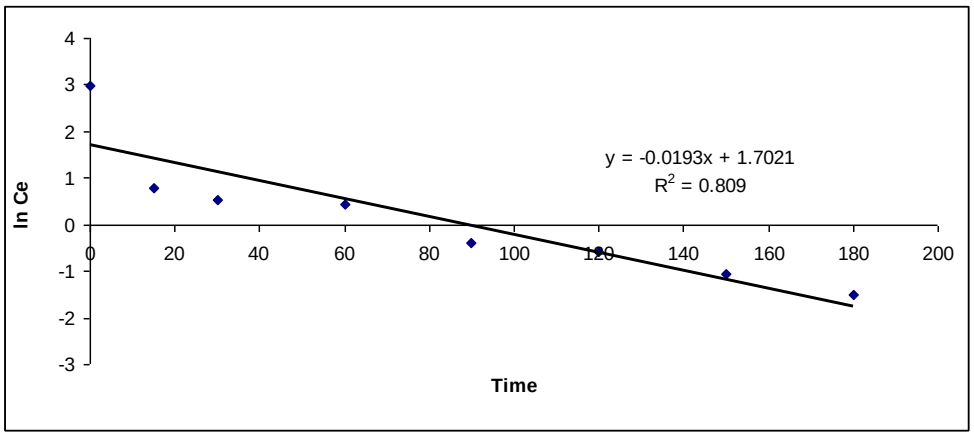


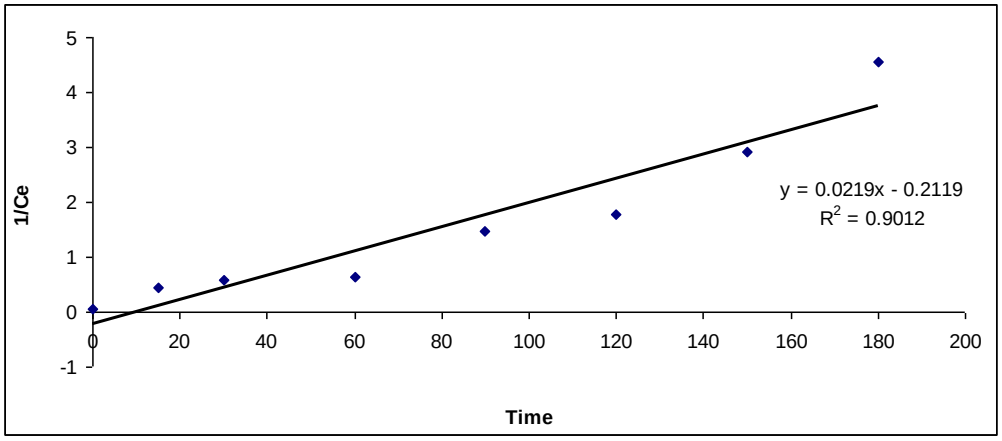
Fig. 5. Effect of reaction time and pH on adsorption by CBC (adsorbent dose: 3 g/L, HA content: 20 mg/L)

3.4. Adsorption kinetics

The effect of reaction time and the initial HA concentration on the adsorption rate, equilibrium concentration and equilibrium loading capacity of HA on CBC are investigated. The results reveal that the amount of HA adsorbed, Q_t, increases with time for all initial HA concentrations. In addition, the uptake rate of the HA decreases with time until it approaches a pseudo steady state value known as the equilibrium loading capacity, Q_e. The contact time needed to reach equilibrium conditions was about 3 h. The kinetic models exploited in this study, help to investigate the adsorption mechanism and the rate-determining steps. Figs. 6a and b show the correlation coefficient (R^2) of the kinetic models for the adsorption of HA into CBC at the pH of 4, HA content of 20 mg/L, and an adsorbent dose of 3 g/L. The kinetic models were performed at 30, 60, 90, and 180 minutes. The results of linear regression analyses were 0.809 and 0.901, corresponding to pseudo-first-order and pseudo-second-order kinetic models, respectively. Accordingly, the kinetic model that best fit the adsorption of HA onto CBC is the pseudo-second-order kinetic model.



(a)



(b)

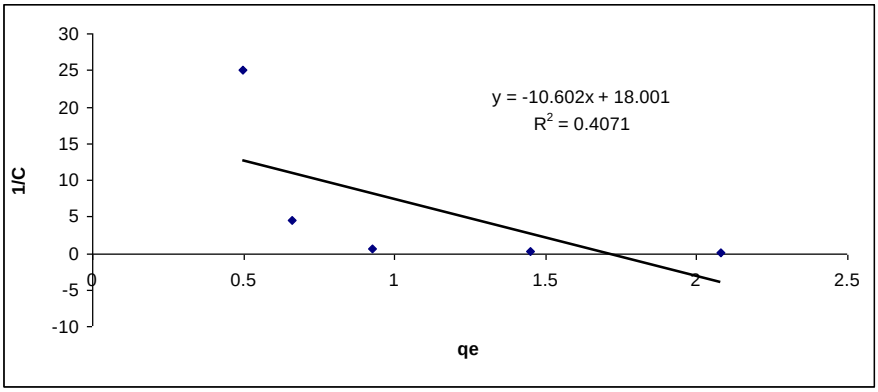
Fig. 6. Correlation coefficient (R^2) of (a) pseudo-first-order and (b) pseudo-second-order (pH=4, HA content= 20 mg/L, adsorbent dose= 3 g/L)

3.5. Adsorption isotherms

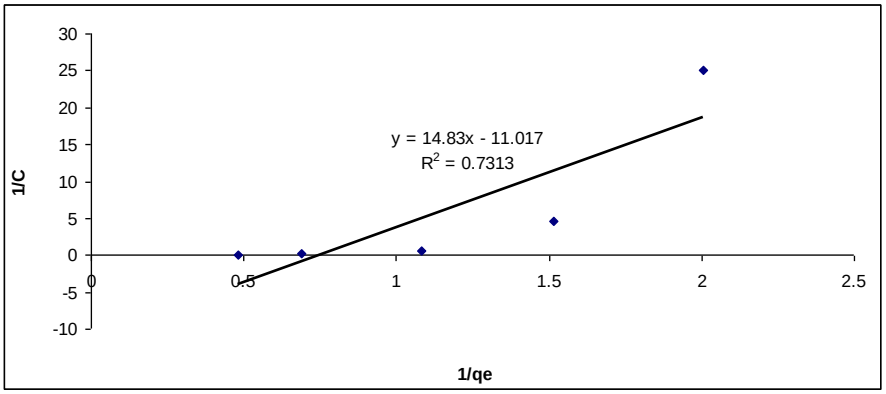
Adsorption isotherms are of utmost importance in order to determine both the adsorption capacity and the adsorption mechanism [31, 43, 44]. In addition, the isotherm models usually show how the adsorbate molecules are distributed between the solution and the adsorbent surface at the equilibrium conditions and the effect of equilibrium concentration on the loading capacity at different temperatures. Three of the most common isotherms are used to explain the relationship between the surface concentration q_e and the equilibrium concentration C_e. These are the Langmuir isotherm, which assumes that equilibrium is attained when a monolayer of the adsorbate molecules saturates the adsorbent, the empirical Freundlich model which is the most important multi-site adsorption isotherm for heterogeneous surfaces, and the Temkin isotherm.

In the present study, the experimental data were fitted by isotherm models of Temkin, Freundlich, and Langmuir. The isotherm correlation coefficients of HA adsorption with CBC are shown in Figs. 7a, b, and c. These experimental data were correlated to these linearized models causing in regression coefficient values of 0.407, 0.731, and 0.943 for Temkin, Freundlich, and

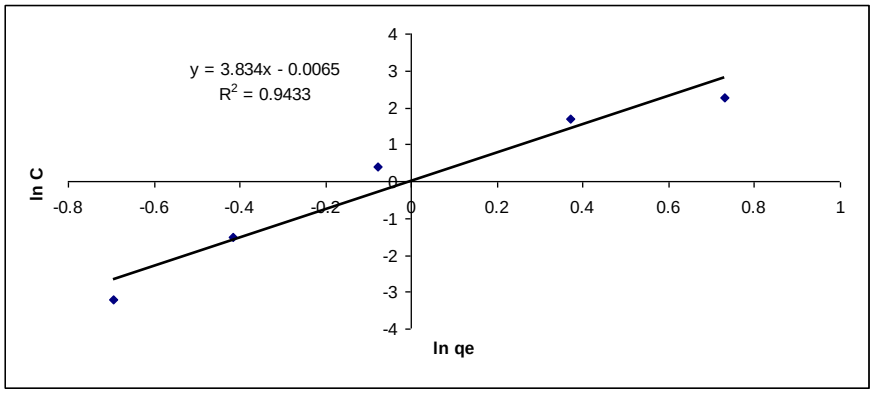
Langmuir isotherms, respectively. The results revealed that the adsorption of HA into the adsorbent follows the Langmuir model. Based on the results, the Langmuir isotherm has the most consistency in HA absorption with CBC (R^2 = 0.943).



(a)



(b)



(c)

Fig. 7. Isotherm models for adsorption at pH=4, 3 g/l of adsorbent: (a) Temkin; (b) Freundlich; (c) Langmuir

3.6. Adsorption thermodynamics

Table 1 presents the variation of the distribution coefficient (K_d), with temperature at four HA initial concentrations of 5, 10, 20 and 30 mg/L. It can be seen in Table 1 that the quantity of HA adsorbed by CBC, C_{Ae} (mg/L) and consequently Q_{max} increases as temperature increases. These results confirms the endothermic nature of the adsorption of HA molecules onto CBC. This can be attributed to the fact that as temperature increases the liquid phase viscosity decreases and consequently the intra-particle diffusion of solute molecules in the pores increases. In addition, Table 1 shows that the values of the distribution coefficient, K_d increases as the temperature increases. However, the values of K_d at 30 mg/L are lower than those at 5 mg/L. This indicates the feasibility of the adsorption process if HA initial concentration is not high.

Table 1. Variation of K_d with temperature for the adsorption of HA onto CBC

C_o (mg/L)	Temperature (K)	C_{Ae} (mg/L)	C_e (mg/L)	K_d
5	298.15	4.985	0.015	332.333
	308.15	4.993	0.007	713.285
	318.15	4.998	0.002	2499
10	298.15	9.96	0.04	249
	308.15	9.99	0.01	999
	318.15	9.997	0.003	3332.333
20	298.15	19.66	0.34	57.823
	308.15	19.845	0.155	128.032
	318.15	19.994	0.006	3332.333
30	298.15	27.51	2.49	11.048
	308.15	28.743	1.257	22.866
	318.15	29.037	0.963	30.152

It was shown above that the experimental results of HA adsorption with CBC were well described with the pseudo-second order model. Accordingly, the activation energy of the adsorption of the HA was calculated using Eq. 8. The value of E was obtained from the slope of the plot lnk2 versus 1/T. At an initial concentration equal 5 mg/l the values of the correlation coefficient, R^2 were above 0.96 and the value of E was 82.11 kJ/mol. Since E is higher than 42 kJ/mol, this indicates that the reaction kinetics between HA and CBC controls the adsorption process [45]. The value of $\ln K_d$ were plotted against 1/T at four different initial HA concentrations as shown in Fig. 8. It reveals that the relationship between $\ln K_d$ and 1/T is linear, and its high correlation coefficient R^2 is about 0.9806. The slopes and intercepts of the lines were used to calculate the thermodynamic parameters of the adsorption process of HA with CBC, ΔH^o, ΔS^o and ΔG^o using equations 10-12. The obtained values at different concentrations and temperatures are shown in Table 2.

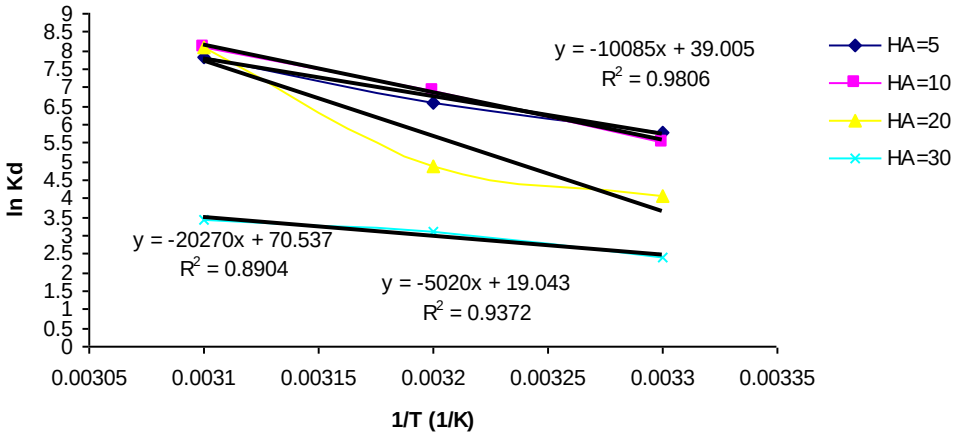


Fig. 8. Variation of thermodynamic parameters with temperature for the adsorption of different concentrations of HA onto CBC

Table 2 depicts that the values of ΔS^o are positive, which indicates the affinity of the CBC adsorbent for HA is a result of the increased randomness at the interface between the solid liquid phases. These results prove feasibility of the process and its spontaneous nature especially with the initial concentration of CBC 10 mg/L. When the CBC concentration is relatively low and the temperature is relatively high, it is highly likely to obtain best results (100% removal).

Table 2. Thermodynamic parameters for adsorption of HA

C0 (mg/l)	ΔHo (J/mol)	ΔSo (J/mol K)	ΔGo (J/mol)		
			298.15 K	308.15 K	318.15 K
5	67467.3	258.4	-9564.7	-12158.7	-14742.7
10	81746.6	295.7	-6412.6	-9373.4	-12339.4
20	51131	193.6	-6605.6	-8526.8	-10464.8
30	65347	234.4	-4434.2	-6883.4	-9227.3

3.7. Reversible process of CBC

In this part of the study, attempt was made to desorb HA from CBC surface at the end of experiment. This will lead to two advantages namely: Regenerating the exhausted CBC to be used many times and to extract the valuable HA molecules to be used in some useful application. This will prove the reversibility of HA adsorption onto CBC. To investigate the reversibility of the process a 50 mL of NaOH solution (0.1–0.5 M) over 2 h, at constant stirring and temperature (180 rpm and 25 °C) was applied for regenerating CBC to a reversible process. First, for saturating the bone char with HA, the samples were placed in contact with 500 mg/L HA solution under mixing, for 4 hours with a solid/liquid ratio of 50 g/L. After that, for fully sorbent saturation, the bone char was placed in contact with a new HA solution, under the same conditions. Then, deionized water was applied to washing and removing the excess of HA on the saturated bone char surface. Thereafter, it was dried at 60 °C for 24 h in an oven and stored. Then, saturated bone char was used for conducting regeneration studies. Approximately 3 g of saturated absorbent was placed in contact with 50 mL of NaOH solution

(0.1–0.5 M) over 2 h, at constant stirring and temperature (180 rpm and 25 °C). Having completed the regeneration process, the bone char samples were washed with deionized water until the stabilization of the pH (around 7), dried at 60 °C for 24 h and applied for new sorption cycles with 5, 10, 20, 30 mg/L HA solutions and solid/liquid ratio of 3 g/L, under constant stirring and temperature (150 rpm and 25 °C). An equilibrium test was also performed, using the best regeneration conditions found in this study. Fig. 9 shows the effect of reaction time and HA contents on adsorption by regenerated CBC. Accordingly, findings indicated that the alteration in degradation efficiency of CBC after the first sorption step and further use after reversibility was insignificant. Hence, the reversible CBC can be used for the treatment of water and wastewater containing HA. Therefore, cost-efficacy and simply reversible without losing its efficiency concerning HA removal, CBC seems to be a promising adsorbent to industrial wastewater treatment that contaminated through HA.

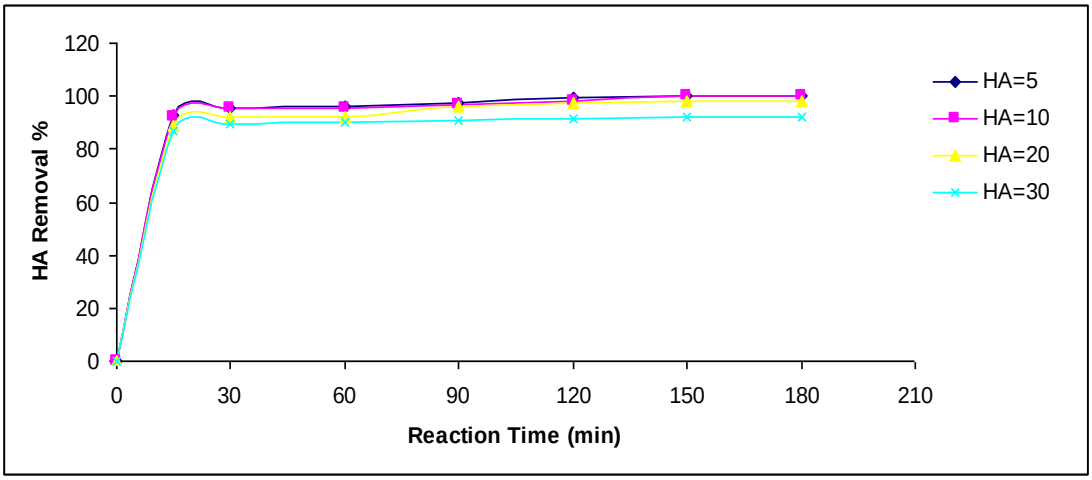


Fig. 9. Effect of reaction time and HA contents on adsorption by regenerated CBC (pH: 4, adsorbent dose: 3 g/L)

4. Conclusions

In summary, calf bone char (CBC) was employed as an efficient, cost-effective, high yield, environmentally friendly, and reversible adsorbent to treat water/wastewater comprising HA. The results revealed that virtually high HA removal from an aqueous stream in short reaction time (30 minutes) was achieved. In the current work, pH of 4 was appropriate for removing HA by CBC. Furthermore, as adsorbent dose increased, HA adsorption capacity also increased, with maximum adsorption at 4 g/L of adsorbent dosage. The Langmuir isotherm has the most consistency in HA absorption with CBC. According to thermodynamic results the reversibility and high adsorption capacity of CBC makes it very promising for HA removal from the aqueous stream. For regenerating the exhausted CBC and using it many times, regeneration of the bone char using 50 mL of NaOH solution (0.1–0.5 M) over 2 h, at constant stirring and temperature (180 rpm and 25 °C) was done. It results in a HA sorption capacity of 92.4 mg/g. This work proved that CBC as an efficient bio-adsorbent overcomes the drawback of common adsorbents such as expensive, harsh availability, low yield, and irreversible. Cost-efficacy and simply reversible without losing its efficiency concerning HA removal, CBC seems to be a promising adsorbent to industrial wastewater treatment that contaminated through HA. As stated by the results and discussions, the following further works can be recommended for the adsorption of HA onto CBC: (I) utilizing CBC for HA adsorption in real HA contaminated wastewater; (II) calculation of the cost of production of CBC; (III) modifying CBC by nano-oxides, and (IV) application of this technology on an industrial scale.

Funding: This research received no external funding.

References

1. M.M. Emamjomeh, H.A. Jamali, Z. Naghdali, M. Mousazadeh, Carwash wastewater treatment by the application of an environmentally friendly hybrid system: an experimental design approach, Desalin. Water Treat, 160 (2019) 171-177.
2. N. Ahmad, H. Sereshti, M. Mousazadeh, H.R. Nodeh, M.A. Kamboh, S. Mohamad, New magnetic silica-based hybrid organic-inorganic nanocomposite for the removal of lead (II) and nickel (II) ions from aqueous solutions, Materials Chemistry and Physics, 226 (2019) 73-81.
3. Y. Cui, J. Yu, M. Su, Z. Jia, T. Liu, G. Oinuma, T. Yamauchi, Humic acid removal by gas–liquid interface discharge plasma: performance, mechanism and comparison to ozonation, Environmental Science: Water Research & Technology, 5 (2019) 152-160.
4. A. Honarbakhsh, M. Tahmoures, B. Tashayo, M. Mousazadeh, B. Ingram, Y. Ostovari, GIS-based assessment of groundwater quality for drinking purpose in northern part of Fars province, Marvdasht, Journal of Water Supply: Research and Technology-Aqua, 68 (2019) 187-196.
5. S. Moussavi, M. Ehrampoush, A. Mahvi, S. Rahimi, M. Ahmadian, Efficiency of multi-walled carbon nanotubes in adsorbing humic acid from aqueous solutions, Asian Journal of Chemistry, 26 (2014) 821.
6. G. Hasani, A. Maleki, H. Daraei, R. Ghanbari, M. Safari, G. McKay, K. Yetilmezsoy, F. Ilhan, N. Marzban, A comparative optimization and performance analysis of four different electrocoagulation-flotation processes for humic acid removal from aqueous solutions, Process Safety and Environmental Protection, 121 (2019) 103-117.
7. M. Molczan, M. Szlachta, Anion exchange pretreatment for the removal of natural organic matter from humic rich water, Water Science and Technology: Water Supply, 11 (2011) 699-710.
8. B. Mansouri, F. Majnoni, S.P. Moussavi, Distribution of mercury in some organs of the Kani Barazan wetland common coot (Fulica atra), Chemistry and Ecology, 30 (2014) 440-445.
9. S. Moussavi, M. Ehrampoush, A. Mahvi, M. Ahmadian, S. Rahimi, Adsorption of Humic Acid from Aqueous Solution on Single-Walled Carbon Nanotubes, Asian Journal of Chemistry, 25 (2013).
10. Y. Zhan, Z. Zhu, J. Lin, Y. Qiu, J. Zhao, Removal of humic acid from aqueous solution by cetylpyridinium bromide modified zeolite, Journal of Environmental Sciences, 22 (2010) 1327-1334.
11. M.M. Emamjomeh, H. Torabi, M. Mousazadeh, M.H. Alijani, F. Gohari, Impact of independent and non-independent parameters on various elements' rejection by nanofiltration employed in groundwater treatment, Applied water science, 9 (2019) 1-10.
12. Y.H. Lin, H.J. Hsien, Characteristics transformation of humic acid during ozonation and biofiltration treatment processes, Water Environment Research, 83 (2011) 450-460.
13. K. Szymański, A.W. Morawski, S. Mozia, Humic acids removal in a photocatalytic membrane reactor with a ceramic UF membrane, Chemical Engineering Journal, 305 (2016) 19-27.
14. J. Lowe, M.M. Hossain, Application of ultrafiltration membranes for removal of humic acid from drinking water, Desalination, 218 (2008) 343-354.
15. W. Wang, J. Cheng, J. Jin, Q. Zhou, Y. Ma, Q. Zhao, A. Li, Effect of humic acid on ciprofloxacin removal by magnetic multifunctional resins, Scientific reports, 6 (2016) 1-10.
16. E. Derakhshani, A. Naghizadeh, Optimization of humic acid removal by adsorption onto bentonite and montmorillonite nanoparticles, Journal of Molecular Liquids, 259 (2018) 76-81.
17. I. Sutzkover-Gutman, D. Hasson, R. Semiat, Humic acid removal by deep-bed filtration and by UF membranes, Desalination and Water Treatment, 31 (2011) 42-53.
18. K. Rucka, A. Solipiwko-Pieścik, M. Wolska, Effectiveness of humic substance removal during the coagulation process, SN Applied Sciences, 1 (2019) 535.
19. H. Rezaei, M.R. Narooie, R. Khosravi, M.J. Mohammadi, H. Sharafi, H. Biglari, Humic acid removal by electrocoagulation process from natural aqueous environments, International Journal of Electrochemical Science, 13 (2018) 2379-2389.
20. F.C. Wu, R.L. Tseng, R.S. Juang, Adsorption of dyes and humic acid from water using chitosan-encapsulated activated carbon, Journal of Chemical Technology & Biotechnology: International Research in Process, Environmental & Clean Technology, 77 (2002) 1269-1279.
21. D.A. Fearing, J. Banks, S. Guyetand, C.M. Eroles, B. Jefferson, D. Wilson, P. Hillis, A.T. Campbell, S.A. Parsons, Combination of ferric and MIEX® for the treatment of a humic rich water, Water Research, 38 (2004) 2551-2558.
22. D. Gümüş, F. Akbal, A comparative study of ozonation, iron coated zeolite catalyzed ozonation and granular activated carbon catalyzed ozonation of humic acid, Chemosphere, 174 (2017) 218-231.

23. J. Wei, B. Gao, Q. Yue, Y. Wang, W. Li, X. Zhu, Comparison of coagulation behavior and floc structure characteristic of different polyferric-cationic polymer dual-coagulants in humic acid solution, Water research, 43 (2009) 724-732.
24. X. Qin, F. Liu, G. Wang, G. Huang, Adsorption of humic acid from aqueous solution by hematite: effects of pH and ionic strength, Environmental Earth Sciences, 73 (2015) 4011-4017.
25. L.R. Brunson, D.A. Sabatini, An evaluation of fish bone char as an appropriate arsenic and fluoride removal technology for emerging regions, Environmental engineering science, 26 (2009) 1777-1784.
26. J.C. Moreno, R. Gómez, L. Giraldo, Removal of Mn, Fe, Ni and Cu ions from wastewater using cow bone charcoal, Materials, 3 (2010) 452-466.
27. S. Mortazavi, G. Asgari, S. Hashemian, G. Moussavi, Degradation of humic acids through heterogeneous catalytic ozonation with bone charcoal, Reaction Kinetics, Mechanisms and Catalysis, 100 (2010) 471-485.
28. C.K. Rojas-Mayorga, D.I. Mendoza-Castillo, A. Bonilla-Petriciolet, J. Silvestre-Albero, Tailoring the adsorption behavior of bone char for heavy metal removal from aqueous solution, Adsorption Science & Technology, 34 (2016) 368-387.
29. F. Granados-Correa, J. Vilchis-Granados, M. Jiménez-Reyes, L. Quiroz-Granados, Adsorption behaviour of La (III) and Eu (III) ions from aqueous solutions by hydroxyapatite: kinetic, isotherm, and thermodynamic studies, Journal of Chemistry, 2013 (2013).
30. M.K. Shahid, J.Y. Kim, Y.-G. Choi, Synthesis of bone char from cattle bones and its application for fluoride removal from the contaminated water, Groundwater for Sustainable Development, 8 (2019) 324-331.
31. Z. Al-Qodah, W. Lafi, Adsorption of reactive dyes using shale oil ash in fixed beds, Journal of Water Supply: Research and Technology—AQUA, 52 (2003) 189-198.
32. Z. Al-Qodah, A. Shawaqfeh, W. Lafi, Two-resistance mass transfer model for the adsorption of the pesticide deltamethrin using acid treated oil shale ash, Adsorption, 13 (2007) 73-82.
33. S. Allen, G. Mckay, J.F. Porter, Adsorption isotherm models for basic dye adsorption by peat in single and binary component systems, Journal of colloid and interface science, 280 (2004) 322-333.
34. S.R. Olsen, F.S. Watanabe, A method to determine a phosphorus adsorption maximum of soils as measured by the Langmuir isotherm, Soil Science Society of America Journal, 21 (1957) 144-149.
35. A. Dawlet, D. Talip, H.Y. Mi, Removal of mercury from aqueous solution using sheep bone charcoal, Procedia Environmental Sciences, 18 (2013) 800-808.
36. H. Yu, Q. Zhang, M. Dahl, J.B. Joo, X. Wang, L. Wang, Y. Yin, Dual-Pore Carbon Shells for Efficient Removal of Humic Acid from Water, Chemistry–A European Journal, 23 (2017) 16249-16256.
37. Y. Feng, Q. Liu, Y. Yu, Q. Kong, L.-l. Zhou, Y.-d. Du, X.-f. Wang, Norfloxacin removal from aqueous solution using biochar derived from luffa sponge, Journal of Water Supply: Research and Technology-Aqua, 67 (2018) 703-714.
38. Y.-N. Chen, L.-Y. Chai, Y.-D. Shu, Study of arsenic (V) adsorption on bone char from aqueous solution, Journal of Hazardous Materials, 160 (2008) 168-172.
39. J. Wang, X. Han, H. Ma, Y. Ji, L. Bi, Adsorptive removal of humic acid from aqueous solution on polyaniline/attapulgite composite, Chemical Engineering Journal, 173 (2011) 171-177.
40. K. Yang, D. Lin, B. Xing, Interactions of humic acid with nanosized inorganic oxides, Langmuir, 25 (2009) 3571-3576.
41. Z. Yue, J. Economy, K. Rajagopalan, G. Bordson, M. Piwoni, L. Ding, V.L. Snoeyink, B.J. Mariñas, Chemically activated carbon on a fiberglass substrate for removal of trace atrazine from water, Journal of Materials Chemistry, 16 (2006) 3375-3380.
42. N.V. Perez-Aguilar, P.E. Diaz-Flores, J.R. Rangel-Mendez, The adsorption kinetics of cadmium by three different types of carbon nanotubes, Journal of colloid and interface science, 364 (2011) 279-287.
43. Z. Al-Qodah, Biosorption of heavy metal ions from aqueous solutions by activated sludge, Desalination, 196 (2006) 164-176.
44. Z. Al-Qodah, A. Shawaqfeh, W. Lafi, Adsorption of pesticides from aqueous solutions using oil shale ash, Desalination, 208 (2007) 294-305.
45. H.M. Zalloum, Z. Al-Qodah, M.S. Mubarak, Copper adsorption on chitosan-derived Schiff bases, Journal of Macromolecular Science, Part A, 46 (2008) 46-57.

Methanation of Carbon Dioxide Using Local Low-Cost Catalyst

Qusai Al-Najdawi , Deema Abu Al-Ruz ,RawanAlyasoury ,Ghadeer Al-Khatib

Al-Balqa'a Applied University Faculty of Engineering Technology Chemical Engineering Department

Dedication

To our unknown soldiers to the watchful eyes, our parents and family the main cause of our ambition and success.
To everyone who taught us a letter, our Teachers, Engineers and Doctors especially Our scientific Father our graduation project Doctor Dr. Ahmad Shawaqfeh the inspirational of the project.
To our friend and all those who had to stand beside us and help us.

Abstract: The mitigation and utilization of greenhouse gases, such as carbon dioxide and methane are among the most important challenges in the area of energy research. Dry reforming of CH_4, which uses both CO_2 and CH_4 as reactants is a potential method to utilize the greenhouse gases in the atmosphere , to supply more clean fuels to meet the increasing demand for liquid and gaseous fuels , to increase the efficiency of energy utilization for fuel and to elimination the pollutants and decouple the link between energy utilization and greenhouse gas emission in end – use system .

Acknowledgment
Dr. Ahmad shawaqfeh for his supervision us, helping and giving us advices and feedbacks about our project.
Dr. maysa'ashawaqfeh for participating in applying accurate procedure.
All Engineers in the Chemical Engineering Department fortheir continued helps and support to us.

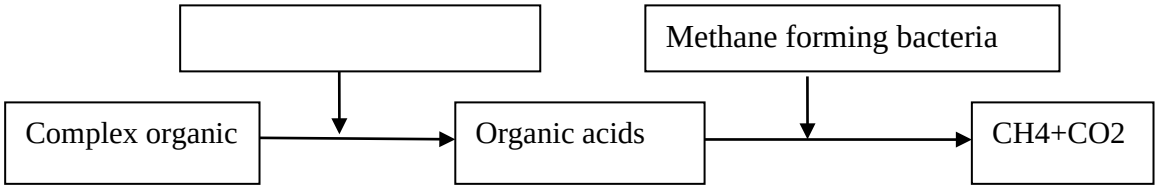
CHAPTER ONE

1.Introduction

The production of methane gas from organic material is not a new process. Volta discovered methane in marsh gas in the eighteenth century, and ideas and experiments on how the process can be used have been going on for the past hundred years. Many ideas and experiments done to how the process can be used and much work has been reported on the application of anaerobic digestion to produce methane from waste. As the energy crisis worsens bioconversion of agriculture, animal, and industrial waste have become increasingly attractive.

Anaerobic fermentation is a biological process in which an organic substrate is first metabolized by non methanogenic organism to produce mainly aorganic acid and carbon dioxide. These acids are then degraded by methanogenic organism to produce methane and carbon dioxide. So the amount of carbon dioxide that produces from the fermentation by organism is more than the amount of methane, carbon dioxide is a greenhouse gas and polluted to the environment on the other hand methane gas can use as a fuel.

Initial word involved the design of single stage digesters. They did not allow for very efficient digestion, since acid forming and methane-forming bacteria differ in their optimum environmental conditions.The growth rate of methane forming bacteria is very low compared to the growth rate of acid forming bacteria. Thus, acid production is usually much faster than the degradation of the acid to methane and carbon dioxide.as a result, the concentration of these acids in the fermenter will increase to levels which inhibit methanogenic bacteria. Acid forming bacteria



Biological wastes are mainly made up of varying ratios of the following compounds: carbohydrate, amino acids, proteins, fatty acids, lipids, alcohols, and a group of nitrogenous compounds originating from living cell

$CH_3COOH \longrightarrow CH_4+CO_2$ 1

$4CH_3OH \longrightarrow 3CH_4+CO_2+2H_2O$ 2

$C6H_{12}O_6 \longrightarrow 3CH_4+3CO_2+70\ Kcal$ 3

Here there is an upgrade procedure from biogas to methane using an extra conversion unit to the bio reactor, the conversion of carbon dioxide to methane is a catalytic reaction that need a catalyst to occur and here local low cost catalyst will use in the experiments. The reaction occur faster with catalyst because they require less activation energy, catalyst may be classified as either:

1. Homogeneous catalyst is one whose molecules are dispersed in the same phase
2. Heterogeneous is one whose molecules are not in the same phase
3. Enzymes and other biocatalyst are often considered as a third category

Our reaction catalyst is known from old research and theses, is well known that supported group (VIII) metals are good catalysts for this reaction giving a high yield of methane. One serious problem is the catalyst deactivation by carbon deposition on the active surface. It has been well established that noble metals (Rh, Ru, Pt) do not suffer the carbon deposition while Ni and Zn are very sensitive to deactivation by coking. The expensive market prices of noble metals render their industrial application quite questionable. Thus, this leads to investigation of supported catalysts consisting of nonnoble metal and promoters in order to obtain a catalyst having a high catalytic activity without suffering the coking deactivation.

Zeolite is micro porous, aluminosilicate minerals commonly used as commercial absorbents and catalysts. Zeolites occurs naturally but are also produced industrially on large scale there are over 200 synthetic zeolites that have been synthesized by a process of slow crystallizationof a silica-alumina gel in the presence of alkalis and organic templates. Many more such structures could theoretically be made.[14] In addition to variations in structures, zeolites can also be made with a variety of other atoms in them to make them chemically interesting and active. Some examples of the so-called heteroatoms that have been incorporated include germanium, iron, gallium, boron, zinc, tin, and titanium.[15] One of the important processes used to carry out zeolite synthesis is sol-gel processing. The product properties depend on reaction mixture composition, pH of the system, operating temperature, pre-reaction 'seeding' time, reaction time as well as the templates used. In sol-gel process, other elements (metals, metal oxides) can be easily incorporated. The silicalite sol formed by the hydrothermal method is very stable. The ease of scaling up this process makes it a favorite route for zeolite synthesis.The procedure that we used to produce our zeolite is alkali hydrothermal activation using sodium hydroxide
Oil shale, also known as kerogen shale, is an organic-rich fine-grained sedimentary rock containing kerogen (a solid mixture of organic chemical compounds) from which liquid hydrocarbons called shale oil can be produced, Oil shale gains attention as a potential abundant source of oil whenever the price of crude oil rises. At the same time, oil-shale mining and processing raise a number of environmental concerns, such as land use, waste disposal, water use, waste-water management, greenhouse-gas emissions and air pollution.
Oil shale in Jordan represents a significant resource. Oil shale deposits in Jordan underlie more than 70% of Jordanian territory. The total resources amounts to 31 billion tons of oil shale. Jordan has significant oil shale deposits occurring in 26 known localities. According to the World Energy Council, Jordan has 8th largest oil shale resource in the world. Geological surveys indicate that the existing deposits underlie more than 60% of Jordan's territory. The resource has been estimated to consist of 40 to 70 billion tons of oil shale, which may be equivalent to more than 5 million tons of shale oil.

In general Jordanian oil shales are of high quality, comparable to the western United States oil shale, although their sulfur content is usually higher. While the sulfur content of the most of oil shales in Jordan varies from 0.3 to 4.3 wt. %, the
JurfedDarawish and the Sultani deposits have sulfur content of 8 and 10% respectively. Sulfur is mostly associated with the organic matter with minor occurrence as pyrite. The moisture content of the oil shale is low (2 to 5.5%). The major mineral components of the Jordanian oil shale are calcite, quartz, kaolinite, and apatite, along with small amounts of dolomite, feldspar, pyrite, goethite, and gypsum. It has also a relatively high metal content.

We used a by-product from oil shale processing which is considered a environmental problems, oil shale ash is usedto produce sodium zeolite, the conversion process of oil shale ash to sodium zeolite

means that the reaction will occur using a very low catalyst comparing with noble metals that have a high cost and by this conversion we clean the environment from the harmful material that produce from oil shale (oil shale ash) and having a useful material like zeolite.

CHAPTER TWO

2.Materials and Methods

Catalyst usually consists of two or more components in which various constituents are assembled in the desired structure and shape. The physico-chemical characteristics (structure, chemical composition, defect groups, and thermal stability) of supports are fundamental aspects to consider in metal-supported catalyst tuning.These characteristics affect the activity, productivity, and lifetime of the final heterogeneous catalyst. The interactions between support and metal were studied by different researchers in many reactions of environmental interest, such as dry reforming, steam reforming, partial oxidation, and autothermal reforming.

2.1 Transition metals as catalysts

Transition metals were thoroughly investigated in many works as active catalysts for CO_2methanationandshowhighcatalyticproperties forCO_2 activation.
Chemisorptionofcarbondioxideontransitionmetalsisspontaneous,whilethesurface structure of the metal strongly affects the thermodynamic of the catalytic process .For example,thebindingenergyofcarbondioxideontheironsurfaceisstrongerthanthatofplatinum, whiletheCO$_2$ dissociationproceedsmoreeasilyonplatinumthanon iron.
Alltheseworksdemonstratethatmetal playsa pivotalroleinCO$_2$ hydrogenation(bothintheactivationandreductionssteps).

2.1.1 Nickel-Based Catalyst:

Nickel based catalysts are commonly studied because of their high activity, low price, and high efficiency in CH_4 production.A lot of supports have been investigated for Ni catalyst since, so well known, the catalyst performance strongly depends upon the nature and properties of the support.Supported Ni catalysts are the most widely investigated materials for CO_2methanation due to their high efficiency in CH_4 production and low cost.

A lot of supports have been investigated for Ni catalyst. The catalyst performance strongly depends upon the nature and properties of the support. Its influence can be generally linked to physico-chemical peculiarities: (i) varying the dispersion of the active phase; (ii) modifying the reducibility of the oxide precursors by tuning the interaction between the active phase and the support. In this work, we will examine the role of the most investigated supports for the methane reaction with CO_2 to CH_4such as: Al_2O_3, zeolites, $SiO_2$with particular emphasis on the role of promoters/modifiers in their catalytic performance in the reaction.

Table 1: Nickel chloride properties

Chemical formula	$NiCl_2$
Molar mass	129.5994 g/mol (anhydrous) 237.69 g/mol (hexahydrate)
Appearance	yellow-brown crystals deliquescent (anhydrous) green crystals (hexahydrate)
Density	3.55 g/cm^3 (anhydrous) 1.92 g/cm^3 (hexahydrate)
Melting point	1,001 °C (1,834 °F; 1,274 K) (anhydrous) 140 °C (hexahydrate)
Solubility in water	*anhydrous* 67.5 g/100 mL (25 °C) [1] 87.6 g/100 mL (100 °C) *hexahydrate* 123.8 g/100 mL (25 °C) [1] 160.7 g/100 mL (100 °C)
Solubility	0.8 g/100 mL (hydrazine) soluble in ethylene glycol, ethanol, ammonium hydroxide insoluble in ammonia, nitric acid

2.1.2 Zinc Based Catalyst:

zinc catalyst to meet your chemical synthesis needs, in addition to the various offerings of zinc reagents and elemental zinc forms such as powder, foil, shot, and mesh. Zinc catalysis finds wide applicability in synthetic chemistry and organic synthesis. a zinc chloride catalyst, acting as a moderate-strength Lewis acid.In addition to ZnCl2, a zinc oxide catalyst can be useful in a variety of catalytic conversions.

Table 2: Zinc chloride properties

Chemical formula	ZnCl2
Molar mass	136.315 g/mol
Appearance	white crystalline solid hygroscopic and very deliquescent
Odor	odorless
Density	2.907 g/cm3
Melting point	290 °C (554 °F; 563 K)[1]
Boiling point	732 °C (1,350 °F; 1,005 K)[1]
Solubility in water	432.0 g/ 100 g (25 °C)
Solubility	soluble in ethanol, glyceroland acetone
Solubility in alcohol	430.0 g/100ml
Magnetic susceptibility (χ)	−65.0·10−6 cm3/mol

2.2 Supports

Catalyst support is the material, usually a solid with a high surface area, to which a catalyst is affixed.The activity of heterogeneous catalysts occurs at the surface atoms. Consequently, great effort is made to maximize the surface area of a catalyst by distributing it over the support. The support may be inert or participate in the catalytic reactions. Typical supports include various kinds of carbon, alumina, and silica.

2.2.1Alumina Support

The Alumina supported catalysts shows a high catalytic activity, although it suffers from severe carbon deposition or poor stability due to the high reaction temperature used. The aim was to develop catalysts able to show both high activity and resistance to carbonaceous deposits.

Table 3: Alumina properties

Chemical formula	Al2O3
Molar mass	101.96 g·mol−1
Appearance	white solid
Odor	odorless
Density	3.987g/cm3
Melting point	2,072 °C (3,762 °F; 2,345 K)[1]
Boiling point	2,977 °C (5,391 °F; 3,250 K)[2]
Solubility in water	insoluble
Solubility	insoluble in diethyl ether practically insoluble in ethanol

2.2.2 Silica support

The numerous SiO_2-based materials used as supports for metal catalyst ,the silica recently found wide application in several processes and reaction .Amorphous pure silica material, well known as mesoporous materials , such as highly ordered hexagonal structure , or large pore size and high specific surface area .The metal particles are smaller when the extent of the Ni(II) phase-silica interface increases.

Table 4: Silica dioxide properties

Chemical formula	SiO_2
Molar mass	60.08 g/mol
Appearance	Transparent solid (Amorphous) White/Whitish Yellow (Powder/Sand)
Density	2.648 (α-quartz), 2.196 (amorphous) $g \cdot cm^{-3}$[1]
Melting point	1,713 °C (3,115 °F; 1,986 K) (amorphous)[1](p4.88) to
Boiling point	2,950 °C (5,340 °F; 3,220 K)[1]
Magnetic susceptibility (χ)	$-29.6 \cdot 10^{-6}$ cm^3/mol
Thermal conductivity	12 (‖ c-axis), 6.8 (⊥ c-axis), 1.4 (am.) W/(m·K)[1](p12.213

2.3 Zeolite

Zeolites are microporous, aluminosilicate minerals commonly used as commercial adsorbents and catalysts. Althoughit is a few negatively charged minerals found in nature but also have a very unique structure,it has large vacant spaces or cages that allow space for large positively charged ions to be attracted to it then trapped and eliminated from the body andthe structure building with silicon block that is electrically neutral and aluminum building carries a negative charge, which creates charged site throughout the entire crystal structure.

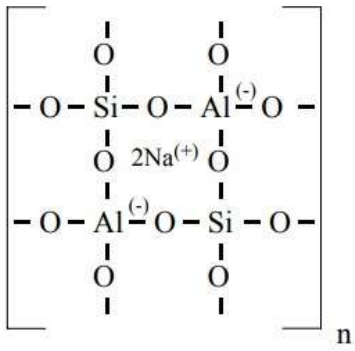


Figure 1: Zeolite Structure

Zeolites have the ability to act as catalysts for chemical reactions which take place within the internal cavities. Essentially, zeolites have two properties which make them particularly suitable as starting materials for the preparation of catalysts:

1- They are cationexchangers, hence it is possible to introduce a large variety of cations with different catalytic properties into their intracrystalline pore system, which in turn offers the opportunity to create different catalytic properties, e. g. in acid- or metal-catalyzed reactions.

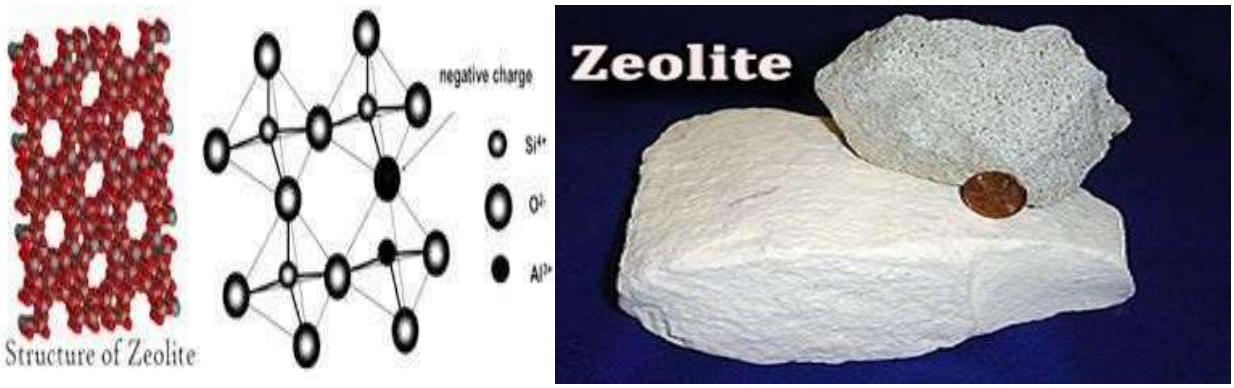


Figure 2:Zeolite shape

2- Zeolites are crystalline porous materials with pore dimensions in the same order as the dimensions of simple molecules; hence they possess molecular sieving properties when the shape and size of a particular pore system exert a steric influence on the reaction, controlling the access of reactants and products.In the case of shape-selective catalysis in zeolites, the combination of both properties exploited to control the selectivity of catalytically conducted reactions.Using zeolites as catalysts have many advantages since can be recovered and recycled with greater ease and low cost, leading to less waste and fewer byproducts, often function with higher activity, may combine several catalytic steps, reduce environment pollution by

substitution of homogeneous catalysts used in the traditional chemical industry (mineral acids, salts, heavy metals).

Zeolites find and increasing application in production of petrochemicals, often replacing environmentally unfriendly catalysts. Zeolite catalysts typically yield fewer impurities, have higher capacity, give greater unit efficiency, and afford higher selectivity. Unlike the more hazardous acid catalysts that have been used in the past, e.g., solid phosphoric acid, hydrofluoric acid, etc., zeolites are non-hazardous and regenerable.
Zeolites occurs naturally but are also produced industrially on large scale There are over 200 synthetic Zeolites that have been synthesized by a process of slow crystallizationof a silica-alumina gel in the presence of alkalis and organic templates.Zeolites are natural volcanic minerals that are mined in certain parts of the world when volcanoes erupt, molten lava and thick ash pour out. Because many volcanoes are located on an island or near an ocean this lava and ash often flows into the sea.

Oil shale ash

Oil shale exists in Jordan with large quantity. It is estimated that 50 billion ton of oil shale can be mined by open pit mined while 25% of this quantity can be extracted as oil. A byproduct from oil shale processing (shown in figure 1) is fly oil shale ash which is considered a environmental problems can be converted into a high-grade zeolite product by alkali hydrothermal activation using sodium hydroxide which is environmentally friend and have a very amazing properties in chemicals and have a lot of usage on of this usage is in our projects we use it as a catalyst and as a support.

Oil shale chemical composition from Jordan Royal Scientific society

Table 5:chemical composition for Jordan oil shale ash

Material	Composition Wt%
SiO2	32.5%
Al2O3	6.5%
Fe2O3	3%
P2O5	4%
CaO	50%
MgO	3.3%
TiO2	.2%
Na2O	.5%

Lime, Silica and alumina together 89% of the total weight of the average samples. There is a potential for low emissions due to the inherent presence of carbonate minerals. Calcium carbonate present in oil shale ash binds sulfur dioxide, and it is not necessary to add limestone for desulfurization:

$$CaCO3 \rightarrow CaO + CO2 \qquad 4$$

$$2CaO + SO2 + O2 \rightarrow CaSO4 \qquad 5$$

Table 6: Properties of Jordanian oil shale

	Number of Drilled Wells	Moisture Content (%)	Ash Content (%)	Sulfur Content (%)	Density (g/cm3)	kcal/ kg	Calorific Value (kj/kg)
EL-Lajjun	135	2.1	54.7	3.1	1.81	1650	6906
Sultani	57	5.5	55.5	2.4	1.96	1526	6380
Jurf Ed-Darawish	50	4.5	58.4	2.4	2.1	1100	4603
Attaraat	41	3.25	53.2	2.6	1.8	1730	7.235
WadiMaghar	21	2.9	57.5	2.6	2.03	1090	4.773
EL-Thamad	12	2.5	54.7	3.2	1.8	1800	6903

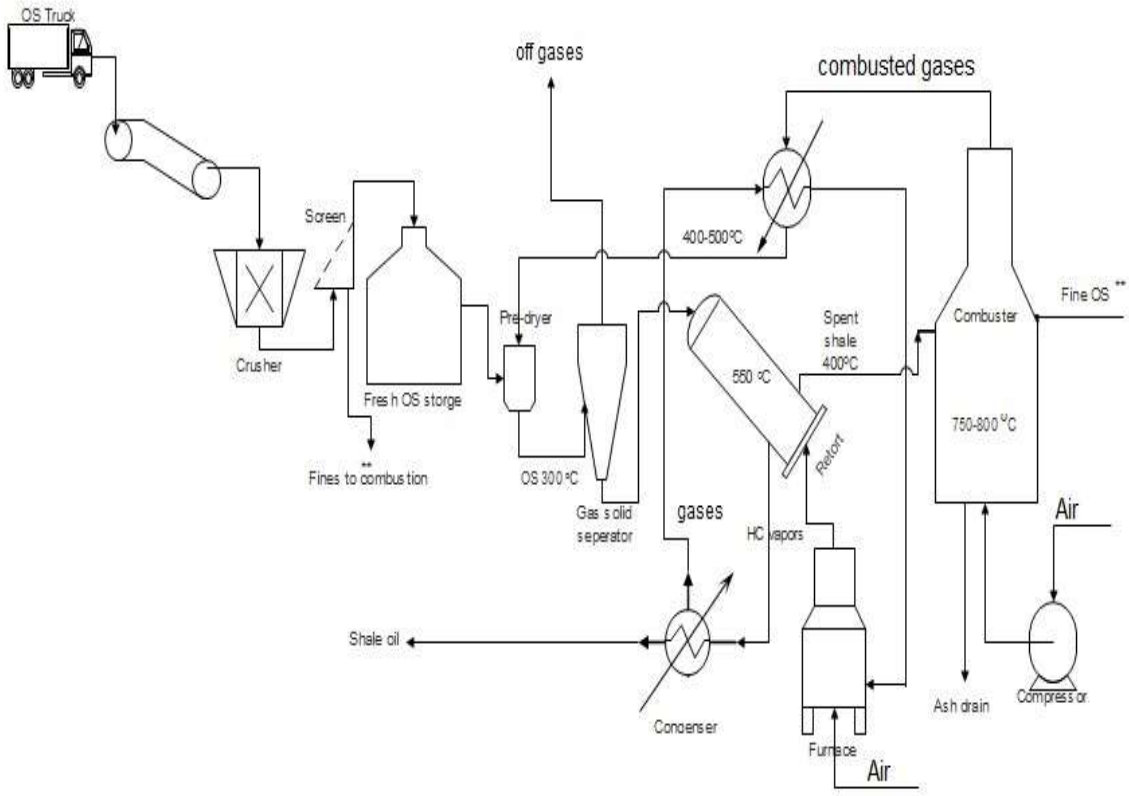


Figure 3: Oil shale process

2.4 Method

An important consideration when designing a catalyst is its preparation method. How the metal is combined with the support can affect the metal dispersion, crystal structure, and allowable metal loading. In this reportfour methodsof preparinga catalyst were discuses.

2.4.1 Impregnation

Also called capillary impregnation or dry impregnation, is a commonly used technique for the synthesis of heterogeneous catalyst. Typically, the active metal precursor is dissolved in an aqueous or organic solution. Then the metal –containing solution is added to a catalyst support containing the same pore, Volume as volume of the solution that was added. Capillary action draws the solution into the pores. Solution added in excess of the support pore volume, causes the solution transport to change from a capillary action process to diffusion process, which is much slower.

The catalyst can be dried and calcinations to drive off the volatile components within the solution , depositing the metal on the catalyst surface , the maximum loading is limited by the solubility of the impregnation compound depends on the mass transfer conditions.within the pores during impregnation and drying.

Impregnation consists in contacting a solid with a liquid containing the components to be deposited on the surface. During impregnation many different processors take place with different rates.

1. Selective adsorption of species (charged or not) by coulomb force, van der Waals forces or H-bonds;
2. Ion exchange between the charged surface and the electrolyte;
3. Polymensation/depolymerisation of the species (molecules, ions) attached to the surface;
4. Partial dissolution of the surface of the solid.
5. The type of product depends on (i) the nature of both reactants (the liquid and the solid surface), and (ii) the reaction conditions. The main parameters affecting the liquid are the pH, the nature of the solvent, the nature and concentrations of the dissolved substances.
6. Impregnation method is simpler that Precipitation since in all precipitations it is essential to carefully control all the details of the process of catalyst preparation including: a- The order and rate of addition of one solution into the other; b- The mixing procedure;

c- The pH and variation of pH during the process d- The
maturation process.

.2 The sol-gel process

The sol-gel process may be described as ”Formation of an oxide network through polycondensation reactions of a molecular precursor in a liquid.”A sol is a stable dispersion of colloidal particles or polymers in a solvent. The particles may be amorphous or crystalline. An aerosol is particles in a gas phase, while a sol is particles in a liquid, A gel consists of a three dimensional continuous network, which encloses a liquid phase, in a colloidial gel, the network is built from agglomeration of colloidal particles. In a polymer gel the particles have a polymeric sub-structure made by aggregates of sub-colloidal particles. Generally, the sol particles may interact by van der Waals forces or hydrogen bonds. A gel may also be formed from linking polymer chains. In most gel systems used for materials synthesis, the interactions are of a covalent nature and the gel process is irreversible. The gelation process may be reversible if other interactions are involved.
The idea behind sol-gel synthesis is to “dissolve” the compound in a liquid in order to bring it back as a solid in a controlled manner.

•Multi component compounds may be prepared with a controlled stoichiometry by mixing sols of different compounds.

•The sol-gel method prevents the problems with co-precipitation, which may be inhomogeneous, be a gelation reaction.

The sol-gel method was developed in the 1960s mainly due to the need of new synthesis methods in the nuclear industry. A method was needed where dust was reduced (compared to the ceramic method) and which needed a lower sintering temperature. In addition, it should be possible to do the synthesis by remote control.
Sol-gel synthesis may be used to prepare materials with a variety of shapes, such as porous structures, thin fibers, dense powders and thin films. If the gel is dried by evaporation, then the capillary forces will result in shrinkage, the gel network will collapse, and a xerogel is formed. If drying is performed under supercritical conditions, the network structure may be retained and a gel with large pores may be formed. This is called an aerogel, and the density will be very low. A record is < 0.005 g/cm3.
A sol which is aliquid suspension of solid particle ranging in size from 1nm to 1 micron, can be optioned by the hydrolysis and partial condensation of a precursor such as an inorganic salts or a metal alkoxide, our particle is mesh 45 so it is larger than the rang that must use in this method.

.3 CP: CO-Precipitation

In chemistry, co precipitation is the carrying down by a precipitate of substances normally soluble under the conditions employed,it involves two distinct processes, namely nucleation and growth. Nucleation requires that the system is far from equilibrium (high supersaturation, or, in the case of ionic species, a solubility product far exceeding the solubility constant of the solid to be precipitated. There are three main mechanisms of co precipitation: inclusion, occlusion, and adsorption:

1- Inclusion: occurs when the impurity occupies a lattice site in the crystal structure of the carrier, resulting in a crystallographic defect, this can happen when the ionic radius and charge of the impurity are similar to those of the carrier.
2- Adsorption: is an impurity that is weakly bound (adsorbed) to the surface of the precipitation.
3- Occlusion: occurs when an adsorbed impurity gets physically trapped inside the crystal site grows.

Co-precipitation is also used as a method of magnetic nanoparticle synthesis and it used mostly in water treatment. There are four steps for this process after adding the anion solution to the cation solution: 1-Nucleation &Growth 2- Precipitation 3Filteration

4- Calcination.

Co-precipitation is an important issue in chemical analysis, where it is often a desirable, but in some cases it can be exploited. Co precipitate is a problem because UN desired impurities often co precipitate with analyte. This problem can often be mitigated by ”digestion” (waiting for the precipitation To equilibrate and form larger purer partials) or by re dissolving the sample and precipitate it again, when you prepare a catalyst the sample must has no impurities so we have to do an extra steps in order to remove the impurities if we need to use this method so we suggested to use more accurate method without any impurities.

.4 Ion Exchange

Ion exchange is an exchange of ion between two electrolytes or between an electrolyte solution and complex. In most cases the term is used to denote the processes of purification ,separation and decontamination of aqueous and other ion-containing solution with solid polymeric or mineralic “ion exchangers’’ .Typical ion exchangers are ion-exchange resins (functionalized porous or gel polymer) zeolites ,montmorillonite ,clay, and soil humus .cation exchangers are exchanger positively charged ions (cation),anion exchangers are exchanger negatively charged ions and amphoteric exchange are able to exchange both cation and anions .This can be dependent on the size of the ions, their change ,or their structure .

Ion exchange is a reversible process, and the ion exchanger can be regenerated or loaded with desirable ions by washing with an excess of these ions. This method is not very well in the project and don’t achieve the aim of the preparation , which is adding catalyst on support structure with no separation under any condition occur, because the ion exchange method is reversible when adding material contain ions

CHAPTER THREE

3. Experimental aspect

3.1 Procedure

Incipient wetness impregnation is the simplest preparation method, allowing for easier control of loading, and no liquid waste generation, this chapter discuss the preparation method for catalysts. here we prepare (Zn/SiO_2 , Zn/Al_2O_3 , Ni/SiO_2 , Ni/Al_2O_3 , Zn/Zeolite , Ni/Zeolite).

The active site is the major section in the catalyst and any impurity can the performance of this site so to protect the activity of the catalyst deionized water is used.

3.1.1 Preparing the deionized water

In our experiments if the water has any ions there may affect the results of impregnation and preparing of the catalyst. Deionized water (*DI water*, *DIW* or *deionized water*), often synonymous with *demineralized water / DM water*, is water that has had almost all of its mineral ions removed, such as cations like sodium, calcium, iron, and copper, and anions such as chloride and sulfate. Deionization is a chemical process that uses specially manufactured ion-exchange resins, which exchange hydrogen and hydroxide ions for dissolved minerals, and then recombine to form water. Because most non-particulate water impurities are dissolved salts, deionization produces highly pure water that is generally similar to distilled water, with the advantage that the process is quicker and

does not build up scale. However, deionization does not significantly remove uncharged organic molecules, viruses or bacteria, except by incidental trapping in the resin. Specially made strong base anion resins can remove Gram-negative bacteria. Deionization can be done continuously and inexpensively using electrodeionization.

An ion-exchange resin or ion-exchange polymer is a resin or polymer that acts as a medium for ion exchange. It is an insoluble matrix (or support structure) normally in the form of small (0.25–0.5 mm radius) microbeads, usually white or yellowish, fabricated from an organicpolymer substrate. The beads are typically porous, providing a large surface area on and inside them. The trapping of ions occurs along with the accompanying release of other ions, and thus the process is called ion exchange. There are multiple types of ion-exchange resin. Most commercial resins are made of polystyrene sulfonate.

There are three types of resin anionic, cationic and mixed resin,we use a mixed bed of ion exchange resin these resin replace the ions that in the water by a hydrogen and hydroxide atoms.Here, we use 400 purlite ion exchange resin its reduce the conductivity of water from 170 micro seminsto 10 micro semins

In a long column put a piece of cotton in the end of them to be sure that there is no particle in the output and closed them, then add a ion exchange resin, then add the water in a very low flow rate in order to have a high residence time and high efficiency of removing ions.



Figure 4: preparing the deionized water.

3.1.2 Preparation of saturated solutions

By searching about the MSDS of nickel chloride we found that it is hazardous in case of skin contact so any one need to work with it they must applied all the safety requirements.

The first step in the impregnation procedure is preparing of the saturated solutions of zinc and nickel components. We don't have nickel as element, we have it as a compound with CL (NiCL2), firstly we prepare a saturated solution, and solubility of $NiCL_2$ (anhydrous) in water is 123.8 g/100ml Sample weight 268g, so we dissolve it in 216.5 ml, the sample is hardly dissolved, so we use stirrer in order to make a saturated solution. The dilution reaction is exothermic while the solution becomes very hot.

When we return to the solution in the next day we saw that the solution is precipitate we guess that because of the low temperature in the night then we use a stirrer in order to insure that the solution is well mixed solution.

Also, we don't have Zinc as element, we have it as a compound with CL ($ZnCL_2$) Firstly we prepare a saturated solution; solubility of $ZnCL_2$ (anhydrous) in water is 432g/100ml. We put 626.485 g $ZnCL_2$ in 145ml, hence exothermic ionization; we use a stirrer to dissolve

3.1.3 preparation of nickel catalyst

We add the nickel into two types of supports Alumina and silica supports.Before using the silica we use the screen analyses in order to use the same particle size and we use the silica that collected in mesh45 **Alumina and silica supported nickel**

1. By taken a 25g of solid sample of AL_2O_3 with 25ml $NiCL_2$ and put them in a clean and dry beaker after that putting them in a water bath with shaking.

i. In parallel to this we add 25g of SiO_2 with 25 ml $NiCl_2$ and put them in a clean and dry beaker after that putting them in a water bath in order to control temperature at desired value and to make shaking

2. The first set temperature in the water bath is T=31 C where the room temperature T=24 C
3. This sample will stay two days in this water bath , the second temp was 37 C , the last temperature was 42 C ,Also two days for all temperatures .
4. Put (Ni/Al_2O_3) and (Ni/SiO_2) samples in a convection oven at 102 C, before putting samples in oven we transfer it from the bickers to ceramic Crucible.
5. After 48 hours, remove the Crucible that includes the impregnated sample from conventional oven and put them in moisture removal condition with silica gel.
6. After some weeks, we take all samples to a furnace to make calcinations at 650C for 5h. In order to made calcination for the sample we went to the al zarqa'a applied university and used there muffle furnace.
7. Wash the samples with 3% HCl each sample by 25 ml HCL

1. Prepare 250 ml of 3% HCl solution by adding 10.88 ml .69 HCl and complete the solution with 239.12 ml water.
8. Re dry the samples in the convection oven at 105 C for 2 hr
9. When they dry wash them by deionized water 25ml for each one and then return them to the oven for 3 hr. and redo this step twice.

3.1.4 Preparation of Zinc catalyst

Before using the silica we use the screen analyses in order to use the same particle size and we use the silica that collected in mesh45

1- By taken a 25g of solid sample of AL_2O_3 with 25ml $ZnCL_2$ and put them in a clean and dry beaker after that putting them in a water bath and make shaking
2- In parallel to this add 25g of SiO_2 with 25 ml $ZnCl_2$ and put them in a clean and dry beaker after that putting them in a water bath in order to control temperature at desired value and to make shaking
3- The first set temperature T=31 C where the room temperature T=24 C 4- This sample will stay two days in this water bath , the second temp was 37 C , the last temperature was 42 C ,Also two days for all temperatures .
5- Put ($ZnCL_2/Al_2O_3$) and ($ZnCL_2/SiO_2$) sample in a convection oven at 102 C, before putting samples in oven we transfer it from the bickers to ceramic Crucible.
6- After 48 hours, we back to the Crucible that includes the impregnated sample from convection oven and we saw that the samples were not dry.
7- We increase the temperature to120 C and left the samples for a day
8- The alumina supported Zinc was dry but the silica was not so we remove the alumina samples andput them in moisture removal condition with silica gel and left the other samples in the oven.

9- After a week the samples were not dry yet but we remove them and put them in a moisture absorbing condition, after some weeks, we take all samples to a furnace to make calcinations at 650C for 5h.

In order to made calcination for the sample we went to the al zarqaa applied university and used there muffle furnace.

10- Wash the samples with 3% HCl each sample by 25 ml HCL
11- Prepare 250 ml of 3% HCl solution by adding 10.88 ml 0.69 HCl and complete the solution with 239.12 ml water.
12- Re dry the samples in the convection oven at 105 C for 2 hr
13- When they dry wash them by deionized water 25ml for each one and then return them to the oven for 3 hr. and redo this step twice.

3.1.5 Compressing and cutting of catalyst.

After preparation of the universal catalysts (Ni/SiO_2) (Ni/Al_2O_3) (Zn/Al_2O_3) (Zn/SiO_2) we compressed the samples into tablets each tablet 1g then we cut it into slices using a knife and in order to find the average particle size and the best size to use we made a screen analyses and in the table below there is the data that we collect

Table 7: Particle Size distribution for catalyst

The mesh size	Ni/Al_2O_3[g]	Ni/SiO_2[g]	Zn/Al_2O_3[g]	Zn/SiO_2[g]
5.6 mm	0	0	32.05	0
4mm	45.09	29.7	7.2	0
2.8	3.645	4.28	0.895	0
2mm	1.180	1.715	0.5	0
1mm	1.6	1.1	0.265	0
500 micro	8.755	0	0	0
125		3.34	3.555	16.28
pan				0
The avg size[mm]	3.245mm	3.38mm	4.77mm	0.125mm
Total weight [g]	60.27	40.135	44.465	16.28



Figure 5: compressing and cutting of catalyst

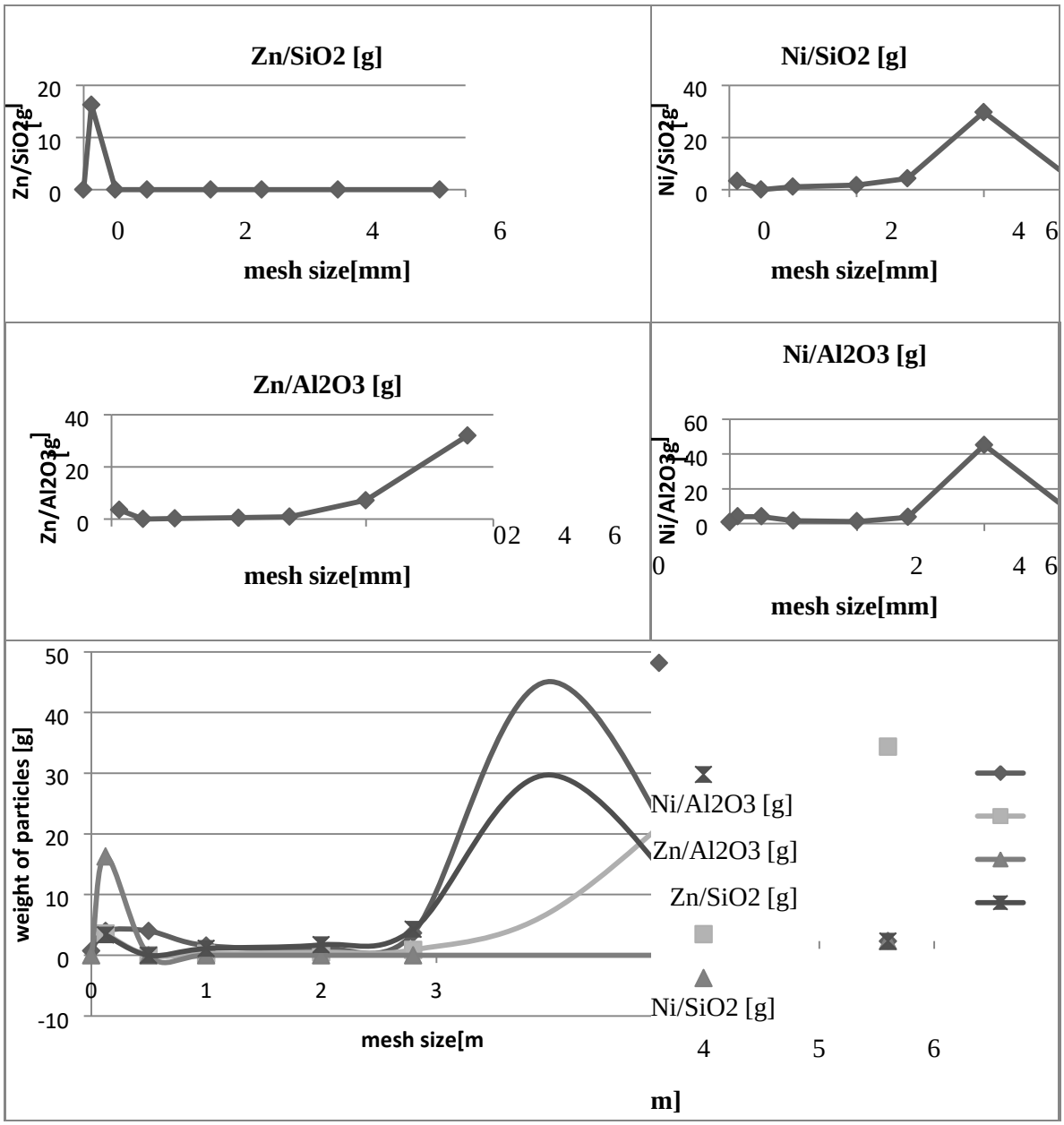


Figure 6:mesh size VS weight of catalyst

3.1.6 Sodium Zeolite preparations.

1- Prepare a solution of sodium hydroxide with 8 Molar concentrations.

In a clear beaker put a (80 g) of sodium hydroxide and dissolve them using 250 ml in a conical flask the dilution.

2- In a large beaker put 50g of oil shale ash and 100 ml of sodium hydroxide.

3- Then the slurry placed to a closed vessel and transfer to a conventional oven at 160 C for 24 hour. Use a tiny flow of nitrogen gas to purge* the gases that produce from the process by removing the air continually from the vessel

4- The slurry removed from the oven and washed several time with deionized water.

5- Filtrate the product using Buchner then dried it at 105C.

6- Store it in a closed container.

*Nitrogen is a clean, dry, inert gas and has long proven effective at displacing oxygen in tanks, hoses, and piping. Blanketing with nitrogen reduce the potential of combustion.



Figure 7: reaction vessel for sodium zeolite preparation in convectional oven



Figure : 8 buchner filtration

3.1.7 Zeolite as a support

1. By taken a 25g of solid sample of zeolite with 25ml $NiCl_2$and 25ml of $NiCl_2$ and put them in a clean and dry beaker after that putting them in a water bath and to make shaking.
2. In parallel to this we add 25g of Zeolitewith 25 ml $ZnCl_2$ and put them in a clean and dry beaker after that putting them in a water bath in order to control temperature at desired value and to make shaking.
3. The first set temperature T=31 C where the room temperature T=24 C 4- This sample will stay two days in this water bath , the second temp was 37 C , the last temperature was 42 C ,Also two days for all temperatures .
4. Put the (Zn/Zeolite) and (Ni/Zeolite) sample in a convection oven at 102 C, before putting samples in oven we transfer it from the bickers to ceramic Crucible.
5. After 48 hours, remove the Crucible that includes the impregnated sample from convection oven.
6. The calcination procedure and washing with HCl was not made.

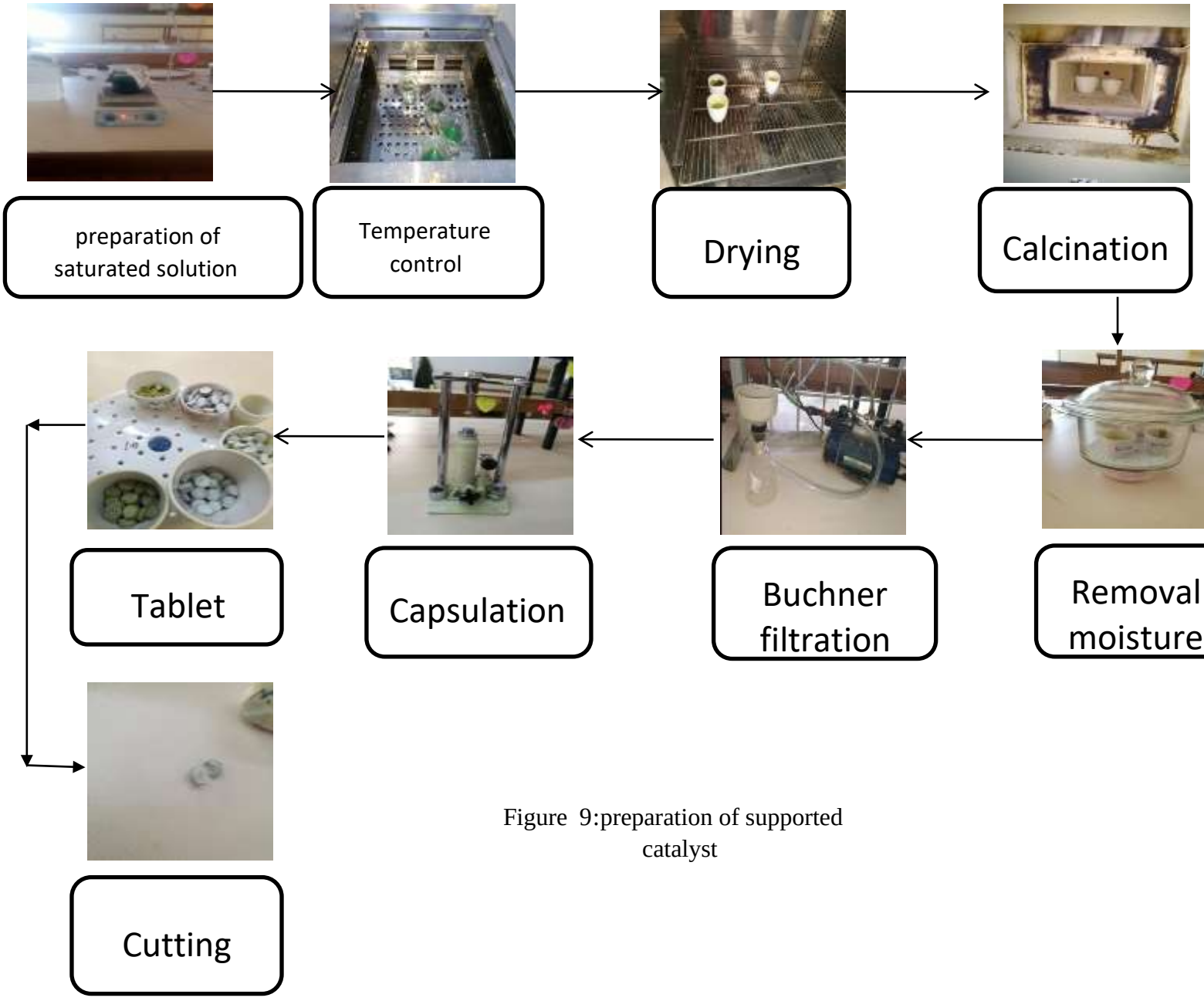


Figure 9:preparation of supported catalyst

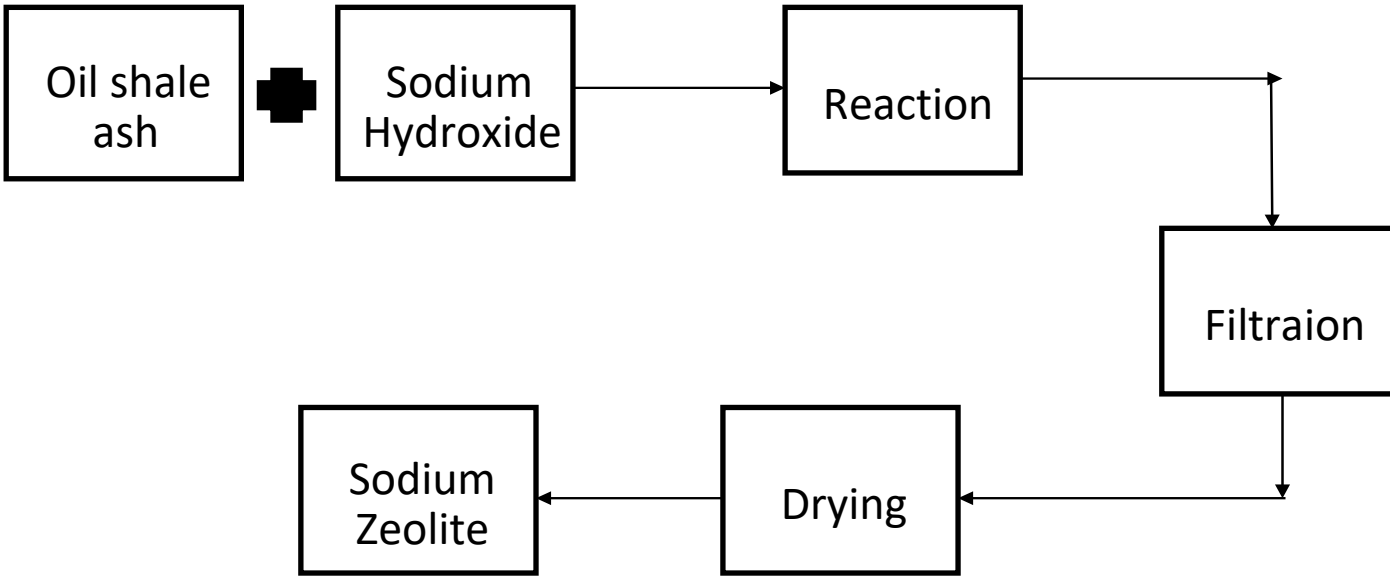


Figure 10:preparation of sodium zeolite

3.2 Improved Fermentation process for production methane

Methane fermentation is a versatile biotechnology capable of converting almost all types of polymeric materials to methane and carbon dioxide under anaerobic conditions. This is achieved as a result of the consecutive biochemical breakdown of polymers to methane and carbon dioxide in an environment in which avariety of microorganisms which include fermentative microbes (acidogens); hydrogen-producing, acetate-forming microbes (acetogens); and methane-producing microbes (methanogens) harmoniously grow and produce reduced end-products. Anaerobes play important roles in establishing a stable environment at various stages of methane fermentation.

Methane fermentation is the consequence of a series of metabolic interactions among various groups of microorganisms. A description of microorganisms involved in methane fermentation, based on an analysis of bacteria isolated from sewage sludge digesters and from the rumen of some animals.

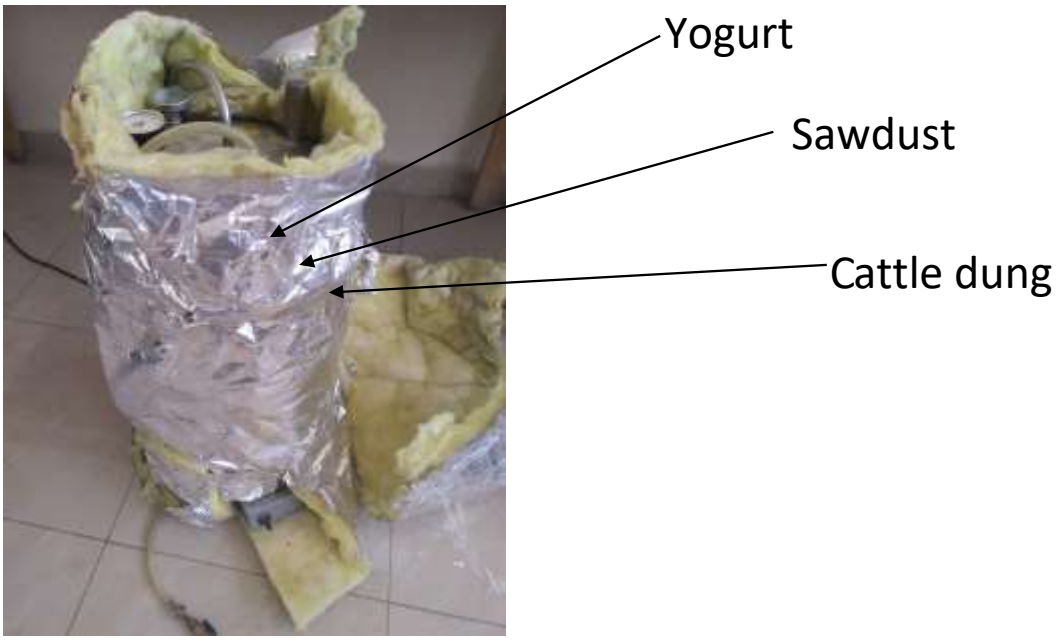


Figure 11: batch fermentation

3.3 silica gel recovery

Silica gel is a granular from silicon dioxide it contain a nano porous and micro structure that can suspended liquids inside it so Silica is a good absorbent that can use to keep the catalyst samples anhydrate in decenter.

There are three types of silica gel (blue, pink and white) when the silica is pink color that mean its saturated with water and regeneration should be doing be putting it in oven at 200C for 1-2 hr. to remove the water molecules that absorbed by its particles and make it active to absorb water, when the silica being in blue color its ready to use, the blue color means that no moisture absorbed by it and it can absorbed now, the white color means that the silica is saturated with water and can't be generated.





Figure 12:silica recovery

CHAPTER FOUR

4. Conversion Unit

The conversion unit consists of four sections (energy source, catalytic reaction section, cooling section and (silica gel and preheating section)),in this unit the methanation reaction occur by using catalyst at 700 C and 1 atm.

4.1 Energy Source

The first section is energy source and the methanation reaction occurs at 700C under atmospheric pressure so the energy source must operate at these conditions.

GBC scientific Equipment PTY LTD VICTORIA/AUSTRALIA is the only available energy source in the laboratory when we calibrate it we found that the controller

(GBC TC 300 Controller) is deactivated so this oven can't be used, the recovery trial for this controller is field so in peace time the task is to found another alternatives to use as an energy source.



Figure 13:PTY LTD VICTORIA/AUSTRALIA

The first alternative after searching about energy source Decson coils was discussed to use around the tube reactor after isolated it, and using thermostat in order to control the temperature but it was not practical because the isolation of the reactor was not professional, so any mistake occurs electrical short.

When the first alternative field the attempt is to change the reactor shape into (U) shaped reactor, these shape is suggested because the chemical engineering department have a muffle furnace that has a hole in its side so it can exploit to put the inlet and outlet pipes in it, but after that we observed that the furnace is not available for students to make their research so this alternative field because the uncooperative department.



Figure 14: MuffleFurnace

The third alternative is 2100 Tube Furnace that has obtained lately we found it in a chemical laboratory it is small and inexpensive furnace ideally suited for chemical and industrial laboratory. So after field of the previous two alternatives this furnace was decided to use because of its ability to operate at very high temperature 1100. During the utilization a lot of problem was faced like: the furnace does not work the cause of this problem noted as defect in thermocouple so we replace the thermocouples by another one.



Figure 15 : The reactor in the furnace



Figure 16 : 2100 Tube Furnace

4.2 Reactor

It is the catalytic reaction section and it is a Fixed-bed reactors, fixed bed reactor have long been used in process industries. They contain catalyst, typically in crushed pellet form, packed in a staticbed. The feed gases are then passed through the bedwhere the reactions are induced as the gases contact the catalyst originally.

Fixed-bed reactors were the only commercially viable reactor type due to technological limitations. However, they alsoPresented drawbacks main in the constraints existing in access to the catalyst material since the gas has to pass over the material the reaction is limited by the available surface area. This problem can be reduced by allowing more than one "bed in the reactor for the gas to pass over, under, and/or through. The catalysts in fixed-bed reactors do not need to be as resilient, as they do not move in the bed, fixedbed

Reactors demand cooling of the bed . If the excess heat is not dissipated from the reactor bed, it could eventually lead to deterioration and deactivation of the catalyst material Fixed-bed reactors can be equipped with internal tubes where a heat transfer fluid, such as boiler feed water, can circulate inside the tubes to control the temperature rise in the reactor.

The reforming reaction was conducted in a fixed bed reactor of stainless steel tube with inner diameter (8mm) at the atmospheric pressure. The catalysts shaped as a plate with average size (2.2mm) are packed in the reaction tube. The amount of (1 g)catalyst resulted in a catalyst bed, the reactor length (300mm) was placed in a horizontal tube furnace and connected to a supply of the reaction gas mixture (methane ,carbon dioxide and steam) , the mixture firstly inter to a moisture absorber section using silica gel with (250mm) length then to a preheating section (100mm),and finally to the catalyst section where the conversion occur, a thermocouple was located outside the reactor wall at the position corresponding to the middle of the catalyst bed, however it was considered as the reaction temperature (650-850 C), after the reaction occur and the product collected there is a cooling section with water.

4.3 silica gel and preheating section

Before the feed gases interring the catalytic reaction section should bath through silica section to remove any moisture, and also it should be pre heated, while the silica section located in the beginning of the furnace so the two tasks occur in one section it is benefit to increase the temperature and arriving conditions of the reaction rapidly.

Calculations:
The length of the reactor= 30cm
The length of silica section(preheating)=10cm
Total length=40cm
The mass needed to packed the total length=38.4g
So for the 10 cm it need9.1 g packed material so we will use 9.1 g in the silica and pre heating section

4.4 cooling section

The end of reactor will be connect with cupper coil immersed in a vessel filled with water to reduce product temperature, the water has to absorbed 4184 Joules of heat for the temperature of 1 Kg of water to increase 1 degree Celsius so it can use in this cooling section because of the highly difference between the specific heat of water and the specific heat of methane, see Appendix 6.3.

4.5 Reactions

The First and most popular path considers of **Co_2** To **Co** which in turn is hydrogenated to **CH_4** by the same mechanism involved in **CO** methanation.
The second includes the direct hydrogenated of **Co_2** to **CH_4** without formation of any **CO** intermediate.

$$Co_2 + CH_4 \leftrightarrow 2CO + 2H_2 \quad \triangle \ \mathbf{H=247Kj/mol} \qquad (6)$$

$$C + 2H2 \leftrightarrow CH4 \quad \triangle \ \mathbf{H=75Kj/mol} \qquad (7)$$

$$2CO \leftrightarrow Co_2 + C \quad \triangle \ \mathbf{H= -171kj/mol} \qquad (8)$$

$$CO + 3H_2 \leftrightarrow CH_4 + H_2 \quad \triangle \ \mathbf{H=206Kj/mol} \qquad (9)$$

$$C + H_2O \leftrightarrow CO + H_2 \quad \triangle \ \mathbf{H= -131Kj/mol} \qquad (10)$$

CHAPTER FIVE

5.Discussion

- Putting the samples in impregnation procedurein a water bath with shaking in order to control temperature at desired value and to the shaking in order to improve the deposition of metals on the support.
- Using nitrogen to purge the oxygen from the system chamber to get anaerobic environment, Anaerobes play important roles in establishing a stable environment at various stages of methane fermentation.

Methane is the major raw material will be used to methanation of co2 by using low cost catalyst .the source of methane in chemical engineering department depend on previous research group, When they failed to achieve their aim, the alternative of the source should be founded .the first

alternative is buy methane jar but it not available In Jordan,so it is very cost .the second alternative is ask help from another university, also it is not achieves.The last solution of the problem is methane fermentation by using organic material, but it need 40days at (32-37)C in vertical closed isolated vessel (bio reactor) to give suitable flow rate,and checking it using gas chromatography if it is containing CH4 or not .but this solution also failed because the project time ended after getting for it , and maybe because we weren't using temperature sensor to control condition in system .After 720 hr. of fermentation we should obtain the data that mention in appendix 6.2 but we don't have these results we guess that the causes of this problem are:

1- The distribution in temperature because we can't do a perfect isolation and use a thermostat or Temperature controller

2- The biogases may be produced but these gases leaked into surround.

3- In theoretical procedure fermentation needs a flipping to occur but we don't do that because the vessel doesn't has a mixer and it is very heavy to mix it manually.

- Using a high ratio steam in the feed in order to reduce the deactivation by carbon formation
- Using silica gel in the feed input in order to remove the moisture.
- prepare the feedby pre heating the gases to increase the temperature before interring the catalyst sectionso when the gases inter the catalyst section it reacted directly

- Carbon formation : increase presser drop , blocks the active surface.carbon deposition may reduce the catalyst performance and it may eventually have to be replaced.
- The formation of $NiAl_2O_4$spinel's has generally been considered to be another route that leads to the deactivation of Ni/Al_2O_3 catalyst during methane reforming reactions. $NiAl_2O_4$ can easily form from a reaction between Ni and Al2O3; however, it is believed that the $NiAl_2O_4$ spinel cannot be easily reduced to a Ni species and thus, it is formation should lower the amount of active Ni.
- Na, Mg, K, make CO_2 absorbed on the Ni catalyst metal surface and decrease the ability of Ni for CH_4formation, but using a support Ni avoid this deactivation. Sulfur we must make desulfurization of the feed stock, but we don't have sulfur in our feed.
- Using the magnetic stirrer when preparing the solutions and using the water bath to control the temperature and prevent re precipitation
- In our first trial to prepare sodium zeolite we prepare the slurry but the oil shale ash that used in these preparation was not ash it was oil shale and put them into a small crucible and closed them using the crucible cap then put them into horizontaltube furnace when we return to them in the morning of the next day we saw unexpected result the crucibles were broken and the furnace was disintegrated, we guess these causes for these result:

During prepared solution from oil ash and NaOH with 8 molar concentration the sample is very corrosive, because the NaOH high concentration. The procedure for production of sodium zeolite side that should put the sample in furnace, the furnace found in the department is tube furnace so the samples put in a furnace horizontally that caused to spill the sample in the furnace that lead to partially melted of the coil.

The corrective action that was done to solve this problem and continue the work on the project asked a help from Araptic Maintenance Company, they reconnect the coil and test it. For more safety we isolated the shell of the furnace by using glass wool

The preventive action that we do: that we prepare the above procedure using a large beaker in a closed vessel and adding a flow rate of nitrogen to purge the gases unfortunately 3 Jars of Nitrogen are overs in 2 days we expected that pressure regulator is not accurate.

CHAPTER SIX

6.Conclusion

- in order to have a homogenous distribution of the catalyst along the reactor length and to increase the surface area of the catalyst we can mix the catalyst with extra amount of support.
- To improve the efficiency of the reaction and increase the reaction conversion we can make a multi section fixed bed.
- The catalytic performance strongly depends upon the nature and properties of the support.
- Impregnation is the best method to prepare catalyst but you have made sure of the metal distribution on the support surface. The better distribution is achieved when another competitive material is used simultaneously during the impregnation process. For example using HCL with different concentrations with metals of Rh or Re will result in better distribution of the metal and maybe the quantity deposited on support surface.
- Capsulation of the catalyst to make more homogenous structure.
- Iron, cobalt, nickel, and copper show high catalytic properties forCO_2 activation. Chemisorption of carbon dioxide on transition metals is spontaneous.

References

1. "Jordan china in $2.5 bn deal for oil shale plant".Fox News. Retrieved 6 November 2013
2. Sciencelab.com, Inc. 14025 Smith Rd. Houston, Texas 77396 US Sales: 1-800-901-7247 International Sales: 1-281-441-4400 Order Online: ScienceLab.com
3. Conversion of oil shale ash into zeolite cadmium and lead removal from waste water, Reyadshawabkeh*, Adnan Al-Harasheh, MalekHami, AbdelazizKhlaifat. Department of chemical engineering , mutah university , AL-Karak 61710, Jordan received 27 january 2003 , revised 3 October 2003 , accepted 8 October 2003 , available online 29 october 2003.
4. Koschany, F.; Schelereth, D.; Hinrichsen, O. On the kinetics of the methanation of carbon dioxide on coprecipitatedNiAl(O)x. Appl. Catal. B Environ. 2016, 181, 504–516.
5. Improved Fermentation Process for Producing Methane from Cheese Whey. :https://digitalcommons.usu.edu/etd Part of theFood Science Commons, and theNutrition Commons
6. Four challenges for nickel steam-reforming catalysts ,jenssehested , haldore A/S , DK-2800 lyngby , Denmark , available online 23 November 2005..

Appendices

A. Material safety data sheet

a. Nickel Chloride

Section 2: Composition and Information on Ingredients

Composition:

Name	CAS #	% by Weight
Nickel chloride	7791-20-0	100

Toxicological Data on Ingredients: Nickel chloride: ORAL (LD50): Acute: 105 mg/kg [Rat].

Section 3: Hazards Identification

Potential Acute Health Effects:
Hazardous in case of skin contact (irritant), of eye contact (irritant), of ingestion, of inhalation. Severe over-exposure can result in death.

Potential Chronic Health Effects:
CARCINOGENIC EFFECTS: IARC Cancer Review: Animal Limited Evidence; Not assigned an overall evalution by IARC. MUTAGENIC EFFECTS: Mutagenic for mammalian somatic cells. TERATOGENIC EFFECTS: Not available. DEVELOPMENTAL TOXICITY: Not available. The substance may be toxic to blood, kidneys, liver, mucous membranes, upper respiratory tract, skin. Repeated or prolonged exposure to the substance can produce target organs damage. Repeated exposure to a highly toxic material may produce general deterioration of health by an accumulation in one or many human organs.

Section 4: First Aid Measures

Eye Contact:

p. 1

Check for and remove any contact lenses. In case of contact, immediately flush eyes with plenty of water for at least 15 minutes. Cold water may be used. Get medical attention.

Skin Contact:
In case of contact, immediately flush skin with plenty of water. Cover the irritated skin with an emollient. Remove contaminated clothing and shoes. Cold water may be used.Wash clothing before reuse. Thoroughly clean shoes before reuse. Get medical attention.

Serious Skin Contact:
Wash with a disinfectant soap and cover the contaminated skin with an anti-bacterial cream. Seek immediate medical attention.

Inhalation:
If inhaled, remove to fresh air. If not breathing, give artificial respiration. If breathing is difficult, give oxygen. Get medical attention.

Serious Inhalation:
Evacuate the victim to a safe area as soon as possible. Loosen tight clothing such as a collar, tie, belt or waistband. If breathing is difficult, administer oxygen. If the victim is not breathing, perform mouth-to-mouth resuscitation. WARNING: It may be hazardous to the person providing aid to give mouth-to-mouth resuscitation when the inhaled material is toxic, infectious or corrosive. Seek medical attention.

Ingestion:
If swallowed, do not induce vomiting unless directed to do so by medical personnel. Never give anything by mouth to an unconscious person. Loosen tight clothing such as a collar, tie, belt or waistband. Get medical attention immediately.

Serious Ingestion: Not available.

b. Zeolite

Section 2: Composition and Information on Ingredients

Composition:

Name	CAS #	% by Weight
Zeolite	1318-02-1 or	100
	68989-22-0	

Toxicological Data on Ingredients: Not applicable.

Section 3: Hazards Identification

Potential Acute Health Effects: Slightly hazardous in case of skin contact (irritant), of eye contact (irritant), of ingestion, of inhalation.

Potential Chronic Health Effects:
Hazardous in case of skin contact (corrosive). Slightly hazardous in case of skin contact (irritant). CARCINOGENIC EFFECTS: 3 (Not classifiable for human.) by IARC. MUTAGENIC EFFECTS: Not available. TERATOGENIC EFFECTS: Not available. DEVELOPMENTAL TOXICITY: Not available.

Section 4: First Aid Measures

Eye Contact:

p. 1

Check for and remove any contact lenses. In case of contact, immediately flush eyes with plenty of water for at least 15 minutes. Get medical attention if irritation occurs.

Skin Contact: Wash with soap and water. Cover the irritated skin with an emollient. Get medical attention if irritation develops.

Serious Skin Contact: Not available.

Inhalation:
If inhaled, remove to fresh air. If not breathing, give artificial respiration. If breathing is difficult, give oxygen. Get medical attention.

Serious Inhalation: Not available.

Ingestion:
Do NOT induce vomiting unless directed to do so by medical personnel. Never give anything by mouth to an unconscious person. If large quantities of this material are swallowed, call a physician immediately. Loosen tight clothing such as a collar, tie, belt or waistband.

Serious Ingestion: Not available.

c. Sodium hydroxide

Section 2: Composition and Information on Ingredients

Composition:

Name	CAS #	% by Weight
Sodium hydroxide	1310-73-2	100

Toxicological Data on Ingredients: Sodium hydroxide LD50: Not available. LC50: Not available.

Section 3: Hazards Identification

Potential Acute Health Effects:
Very hazardous in case of skin contact (corrosive, irritant, permeator), of eye contact (irritant, corrosive), of ingestion, of inhalation. The amount of tissue damage depends on length of contact. Eye contact can result in corneal damage or blindness. Skin contact can produce inflammation and blistering. Inhalation of dust will produce irritation to gastro-intestinal or respiratory tract, characterized by burning, sneezing and coughing. Severe over-exposure can produce lung damage, choking, unconsciousness or death. Inflammation of the eye is characterized by redness, watering, and itching. Skin inflammation is characterized by itching, scaling, reddening, or, occasionally, blistering.

Potential Chronic Health Effects:
CARCINOGENIC EFFECTS: Not available. MUTAGENIC EFFECTS: Mutagenic for mammalian somatic cells. TERATOGENIC EFFECTS: Not available. DEVELOPMENTAL TOXICITY: Not available. The substance may be toxic to mucous membranes, upper respiratory tract, skin, eyes. Repeated or prolonged exposure to the substance can produce target organs damage. Repeated exposure of the eyes to a low level of dust can produce eye irritation. Repeated skin exposure can produce local skin destruction, or dermatitis. Repeated inhalation of dust can produce varying degree of respiratory irritation or lung damage.

Section 4: First Aid Measures

Eye Contact:
Check for and remove any contact lenses. In case of contact, immediately flush eyes with plenty of water for at least 15 minutes. Cold water may be used. Get medical attention immediately.

Skin Contact:
In case of contact, immediately flush skin with plenty of water for at least 15 minutes while removing contaminated clothing and shoes. Cover the irritated skin with an emollient. Cold water may be used.Wash clothing before reuse. Thoroughly clean shoes before reuse. Get medical attention immediately.

Serious Skin Contact:
Wash with a disinfectant soap and cover the contaminated skin with an anti-bacterial cream. Seek medical attention.

Inhalation:
If inhaled, remove to fresh air. If not breathing, give artificial respiration. If breathing is difficult, give oxygen. Get medical attention immediately.

Serious Inhalation:
Evacuate the victim to a safe area as soon as possible. Loosen tight clothing such as a collar, tie, belt or waistband. If breathing is difficult, administer oxygen. If the victim is not breathing, perform mouth-to-mouth resuscitation. WARNING: It may be hazardous to the person providing aid to give mouth-to-mouth resuscitation when the inhaled material is toxic, infectious or corrosive. Seek immediate medical attention.

Ingestion:
Do NOT induce vomiting unless directed to do so by medical personnel. Never give anything by mouth to an unconscious person. If large quantities of this material are swallowed, call a physician immediately. Loosen tight clothing such as a collar, tie, belt or waistband.

Serious Ingestion: Not available.

d. Zinc chloride

Section 2: Composition and Information on Ingredients

Composition:

Name	CAS #	% by Weight
Zinc chloride	7646-85-7	100

Toxicological Data on Ingredients: Zinc chloride: ORAL (LD50): Acute: 350 mg/kg [Rat]. 329 mg/kg [Mouse].

Section 3: Hazards Identification

Potential Acute Health Effects:
Very hazardous in case of skin contact (irritant), of eye contact (irritant), of ingestion, of inhalation. Hazardous in case of skin contact (corrosive, permeator), of eye contact (corrosive). The amount of tissue damage depends on length of contact. Eye contact can result in corneal damage or blindness. Skin contact can produce inflammation and blistering. Inhalation of dust will produce irritation to gastro-intestinal or respiratory tract, characterized by burning, sneezing and coughing. Severe over-exposure can produce lung damage, choking, unconsciousness or death. Inflammation of the eye is characterized by redness, watering, and itching. Skin inflammation is characterized by itching, scaling, reddening, or, occasionally, blistering.

Potential Chronic Health Effects:
CARCINOGENIC EFFECTS: Not available. MUTAGENIC EFFECTS: Classified POSSIBLE for human. Mutagenic for mammalian somatic cells. Mutagenic for bacteria and/or yeast. TERATOGENIC EFFECTS: Not available. DEVELOPMENTAL TOXICITY: Not available. The substance may be toxic to kidneys, pancreas. Repeated or prolonged exposure to the substance can produce target organs damage. Repeated exposure of the eyes to a low level of dust can produce eye irritation. Repeated skin exposure can produce local skin destruction, or dermatitis. Repeated inhalation of dust can produce varying degree of respiratory irritation or lung damage.

Section 4: First Aid Measures

Eye Contact:
Check for and remove any contact lenses. In case of contact, immediately flush eyes with plenty of water for at least 15 minutes. Cold water may be used. Get medical attention immediately.

Skin Contact:
In case of contact, immediately flush skin with plenty of water for at least 15 minutes while removing contaminated clothing and shoes. Cover the irritated skin with an emollient. Cold water may be used.Wash clothing before reuse. Thoroughly clean shoes before reuse. Get medical attention immediately.

Serious Skin Contact:
Wash with a disinfectant soap and cover the contaminated skin with an anti-bacterial cream. Seek immediate medical attention.

Inhalation:
If inhaled, remove to fresh air. If not breathing, give artificial respiration. If breathing is difficult, give oxygen. Get medical attention.

Serious Inhalation:
Evacuate the victim to a safe area as soon as possible. Loosen tight clothing such as a collar, tie, belt or waistband. If breathing is difficult, administer oxygen. If the victim is not breathing, perform mouth-to-mouth resuscitation. WARNING: It may be hazardous to the person providing aid to give mouth-to-mouth resuscitation when the inhaled material is toxic, infectious or corrosive. Seek immediate medical attention.

Ingestion:
Do NOT induce vomiting unless directed to do so by medical personnel. Never give anything by mouth to an unconscious person. If large quantities of this material are swallowed, call a physician immediately. Loosen tight clothing such as a collar, tie, belt or waistband.

Serious Ingestion: Not available.

B. bioreactor literature result

Table 21. Methane production during fermentation of whey containing 2.5% lactose at 37° C by pH controlled batch fermentation.

Time	Lactose	gas-volume	gas-rate	CH_4	CH_4-volume	Alkalinity
(h)	(%)	($m^3 \times 10^{-2}$)	($m^3 \times 10^{-2}/h$)	(%)	($m^3 \times 10^{-2}$)	(mg/L)
0	2.510	0.00	0.00	0.00	0.00	990
20	0.913	0.1239	0.0061	0.00	0.00	3240
30	0.00	0.5785	0.0578	0.00	0.00	3910
42	0.00	0.7049	0.0587	0.00	0.00	4670
50	0.00	0.3945	0.0493	0.00	0.00	5090
61	0.00	0.6431	0.0584	0.00	0.00	5330
90	0.00	0.8969	0.0309	0.00	0.00	5680
102	0.00	0.1172	0.0097	0.00	0.00	5840
120	0.00	0.0281	0.0015	0.00	0.00	6020
144	0.00	0.00	0.00	0.00	0.00	6120
168	0.00	0.00	0.00	0.00	0.00	6190
192	0.00	0.00	0.00	0.00	0.00	6220
216	0.00	0.00	0.00	0.00	0.00	6200
240	0.00	0.00	0.00	0.00	0.00	6240
264	0.00	0.00	0.00	0.00	0.00	6240
288	0.00	0.00	0.00	0.00	0.00	6230
312	0.00	0.00	0.00	0.00	0.00	6240
336	0.00	0.00	0.00	0.00	0.00	6230
360	0.00	0.00	0.00	0.00	0.00	6250
384	0.00	0.00	0.00	0.00	0.00	6280
408	0.00	0.00	0.00	0.00	0.00	6280
432	0.00	0.0451	0.0018	0.952	0.0004	6270
480	0.00	0.1803	0.0037	6.633	0.0189	6340
504	0.00	0.3148	0.0131	25.874	0.0814	6370
552	0.00	1.252	0.0260	55.152	0.6898	6490
					0.7905	

C. Methane Gas Specific Heat

Temperature [K]	Specific heat [kJ/(kgK)]
200	2.087
225	3.121
250	2.156
275	2.191
300	2.226
325	2.293
350	2.365
375	2.442
400	2.525
450	2.703
500	2.889
550	3.074
600	3.256
650	3.432
700	3.602
750	3.766
800	3.923
850	4.072
900	4.214
950	4.348
1000	4.475
1050	4.595
1100	4.708

Reuse of Treated Carwash Wastewater by Using Natural Zeolite

Raha M. Kharabsheh [1], Aymen A.Awad [2], Mohammad A. Alhusban [2,*]

[1] Doctorate program engineering and management, Polytechnic University of Madrid, Spain

[2] Middle East University, [1]Faculty of Engineering -Civil Engineering Department, Amman, Jordan

***** *Corresponding authors: rahamohammed99@gmail.com, Aawad@meu.edu.jo , mhmd.hsbn@hotmail.com*

Abstract: Jordan is the world's second water-poorest country. Treating and reusing of wastewater are significantly important at the national level. This research aims to investigate the using of natural and modified Zeolite for the removal of Methylene Blue Active Substances (MBS) and lead (one of the toxic heavy metals) from wastewater produced in the carwash stations. Five samples were collected from each station. Then, physical and chemical tests were conducted for each sample such as Acidity, Alkalinity, Carbonate Hardness, Total Hardness, Total Solids, Total Dissolved Solids, Total Suspended Solids , Chemical Oxygen Demand , Biochemical Oxygen Demand , Oil and Grease, Heavy Metal, Methylene Blue Active Substance . Raw wastewater was pre-treated starting with a settling step to flotation which precedes sand filtration and finally zeolite batch adsorption process .It was found that the natural zeolite is effective in removal of MBAS by 93.42%. Results showed that as the time elapsed the initial concentration of SDBS (sodium dodecyl benzene sulfonate) which is the main pollutant component of the carwash wastewater was decreased from 2.5 mg/L to 1.25 mg/L at the final step of treatment. Other contaminated were reduced while the process of treatment continued until critical situations which furthermore treatment is not efficient. Using zeolite in removing of with carwash stations contaminants was approved efficient removal by this study. On the other side, this technique is considered as one of the most effective methods to increase water resources.

Keywords: Wastewater; Zeolite; Removal; Hardness; TSS; TDS; COD; BOD and MBAS.

1. Introduction

Jordan is suffered from the water shortage since 40 years. This Middle East country is considered as one of the ten most low water resources countries in the world. According to Douad in 2019, the country has high temperatures and the population growth is increased rapidly, as results more water resources are needed in last decade urgently. This situation in Jordan was due to the increase of population number where the country in 1980 had about two million people while after 40 years; Jordan had about 10 million people. This is because of the natural increase in people and the refugees whom came from neighbouring countries as results of conflicts and wars". In addition, the prices of water are increased from about 70 cents to 1200 cent in the last decade [15].Those factors and others, forces the government and even the private sectors to looking for new water resources. Different and unusual resources are needed in Jordan to lower water deficiency and clean the environment in the same time [2].

Therefore, any attempt to lower; the water deficiency, the cost of production and protection of environment is reflected the strong adopted strategy for both decreasing pollutants and improving water resources. On the other side, it was reported that the carwash stations in Jordan spent about 20 liters/wash higher than what is used in normal situations in other countries, [3].Based on the number of vehicles in Jordan, the total water consumption in carwash stations in Jordan is ($30.5x10^6$ L/day) [16]. However, Jordan has limited projects and attempts on treatment and reusing of the wastewater generated in the carwash stations.

The government steps to enhancing the public awareness on the environmental subjects and following environmental regulations on effluent discharge has resulted in the growth of the number of studies on treating carwash wastewater. Therefore, the present study suggest that treating and reusing of the wastewater produced in the carwash station in Jordan for washing the cars again or irrigation purposes is of most important.

Literature Review

Pak investigated some factors which they affecting the phosphorus and organic materials removals generated from carwash stations in treatment systems by using bio filters. These parameters are representing the operational parameters which including the hydraulic retention time, organic matters, suspended solid and nitrogen loading rate. The results exhibited that a significant removals were attained but the treated water had low organic matters but high phosphorus materials [11]. Hamada suggested a treatment system for reuse the treated wastewater generated from carwash stations using the technology of ultrafiltration membrane with the added of flocculation and activated carbon materials. These material containing different chemical agents indicated an advanced removals of chemical oxygen demand (COD) and turbidity of wastewater [17].Al-Odwa in conducted a research in Kuwait city on the carwash wastewater reclamation depends on the desalination techniques to treat and produce treated water with accepted properties to be fit to use in all industrial applications and activities [4]. Panizza examined the applicability of treatment of wastewater by applying the electrochemical methods to treat the carwash station wastewater. These treatment steps had a combined two-step processes containing an electrochemical anodes technology which was developed for the treatment of carwash wastewater [18].

Bhatti succeeded to reduce water contaminants in carwash wastewater (CWW) by adopted the chemical oxidation methods. The treatment was done on wastewater to decrease water pollution carried out on details with various investigations. The CWW was treated by input the air inside a 5 liters container representing the aeration chamber [5]. As known the WWC has high concentrations of oil and grease which produce high scum during the treatment processes. This scum is removed by decanted it from time to time. During this treatment alum was used as a coagulant in primary treatment steps. The removal percentages were 93% and 97% for the parameters of COD and turbidity, respectively. For further treatment and removals of contaminates, the secondary treatment of carwash wastewater was attained a good results and achieved 71% and 83% reduction in COD and turbidity again by using hydrogen peroxide. Zaneti in Brazil established a treatment plant to develop and treat the wastewater of carwash stations for reuse (reclamation) in commercial car washing. This project confirmed that the proposed innovative process which included — Flocculation-Column Flotation (FCF), filtration, and chlorination approved that this method is effective in removal of contaminates [14]. Lau conducted a research in Malaysia for the treating of CWW by using ultrafiltration and Nano filtration membranes. The plant was consisted of three different types of commercial membranes used to treat CWW effluents. The results reflected a good achievements with respect to the readings of permeate flux, rejection of conductivity, total dissolved solid (TDS), chemical oxygen demand (COD) and turbidity [13].

Awad investigated the adsorption of hexavalent chromium by local Jordanian sand; it was found that the sand as an adsorbent removed this heavy metal up to about 65 % of its initial concentration. Sarkar, et. al., in 2014, conducted a research for treating the wastewater generated from carwash station by using coagulation and activated sludge system. Testing were applied to follow the parameters of acidity (pH) , total solids (TS) , total suspended solids (TSS) , Chemical Oxygen Demand (COD) and Oil and Grease. Results of composite samples treated using coagulants like alum, Fe_2SO_4 and CaCl2 showed a good removal efficiencies and the process adopted was effective for treatment of the raw wastewater[1].Etchepare conducted a research by using a new proposed treatment system consisting from a flocculation-column flotation (FCF), sand filtration and final chlorination steps. The results revealed that the water usage and savings audits of (20 weeks) showed that almost about 70% recovery was possible, and less than about 40 liters of fresh water per wash was attained [14].

Treated wastewater is considered as unusual water resources and could be achieved by different techniques where the reclaimed water is fully characterized by monitoring chemical, physicochemical and biological parameters.

2. Materials and Methods

This research has started with a thorough literature review to identify the gap of knowledge in which it was found a lack of research on treating and reusing of the wastewater generated and produced in the carwash stations in Jordan. Then site visits were conducted to these stations to collect data on the source of the supply water, paths of wastewater, management of wastewater, sampling techniques, preservation, transport, detergents used, the reuse of carwash wastewater, and water consumption. The following sections will discuss the adopted methodology which is including; sampling methods, lab experimental procedures and methods of treatment used.

2.1 Sampling

This study investigated the wastewater generated in five carwash stations in Amman - Jordan. Five samples were collected from each station. Then, tests were conducted for each sample and the average value was taken at a different time of sampling. Figure (1) below shows the water consumption in liters per car per wash in different water wash station in Amman city.

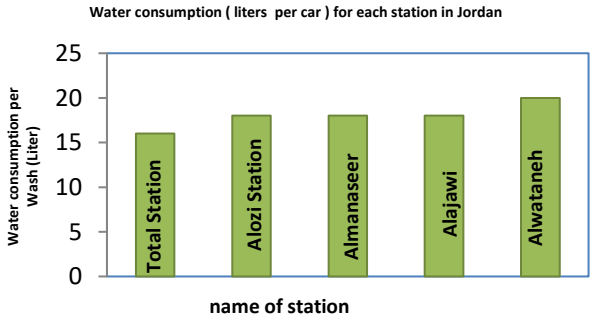


Figure 1. Carwash water consumption for five stations in (liters /car. wash) in Amman city.

2.2 Lab Experimental Procedure and testing methods.

Many parameters were tested and carried out for water samples collected from each carwash station before and after each treatment stage. Those parameters tested are as follows: Acidity (pH), Alkalinity, Carbonate Hardness (CH), Total Hardness (TH), Total Solids (TS), Total Dissolved Solids (TDS), Total Suspended Solids (TSS), Chemical Oxygen Demand (COD), Biochemical Oxygen Demand (BOD), Oil and Grease, Heavy Metal, Methylene Blue Active Substance (MBAS).

Table (1) below shows the selected tests methods used according to standard methods examination with corresponding (ASTM) code.

Table1. Water and Wastewater Standard Methods Examination [13]

No.	Test	ASTM (Method)
1	Chemical Oxygen Demand(COD)	D1252 - 06
2	PH Measurement and Water Conductivity	D5464 - 11
3	Acidity or Alkalinity of Water	D1067 - 11
4	Total Dissolved Solids and Total Suspended Solids in Water	D5907-10
5	Hardness in Water	D1126-12
6	Determining heavy metal Concentration in Water Samples	D3977 - 97
7	Methylene Blue Active Substances(MBAS)	D2330-02

2.3 Proposed Treatment Method

Raw wastewater was pre-treated starting with a settling step which precedes filtration; it aims to enhance the filtration process by removing particulate matter; the water was left to flow through a rectangular basin at a slow enough velocity and left for 24 hours to permit the particulate matter to settle to the bottom of the basin before the water exits the basin. This water was then sent to a flotation and aeration tanks to remove the oil from water. Next, the water continued to enter a sand filtration unit filled with (Swieleh Sand) sand used as a filtration media. This adsorbent media has specifications describe as follows: the gravel particle diameter is 1.5 mm, the sand particle diameter is 0.05 mm, specific gravity is 2.65 and bed porosity is 0.82.

The schematic diagram in figure (2) below represents the suggested wastewater treatment unit for carwash station's water produced in different parts of Amman city. Batch equilibrium technique was used to study the adsorption isotherms lines of MBAS on the synthesized zeolite used as an adsorbent. Different concentrations of zeolite were added (0.1, 0.5 and 1.0 grams) at different temperatures (25, 35 and 45°C) and pH = 6.8 which is the suitable value were most of the research papers adopted. The mixture was shaken at different times (30, 60, 120) minutes, after which it was filtered and the concentration of MBAS+ was determined by spectrophotometers techniques.



Figure 2. Suggested Wastewater Treatment Processes.

3. Results and Discussion

The accuracy and errors in measurements of different parameters are very important. Therefore, to ensure higher accuracy, reliability and reproductively of the estimated and calculated data for the five gas stations at different sites in Amman city, all experimenters were carried out three times at least and then the mean resultant values of the measured parameters are presented and adopted.

3.1 Wastewater Parameters Analysis.

This study has classified and reported the results into three main categories; physical, chemical, and biological parameters. The following section will describe each of these parameters.

Part One: - Chemical Parameters Analysis (Alkalinity, Calcium Hardness, Total Hardness and Chemical Oxygen Demand - COD).

Figure 3, shows that alkalinity is reduced up to (35 %) when the treated water discharged from the treatment unit (i.e. after Zeolite adsorption treatment step). This approved that these consecutive treatment steps are operative in the reduction of solution alkalinity which is expected in physical primary treatment with a highly basic media effluent. The calcium hardness, total hardness and chemical oxygen demand concentrations are reduced slightly about (62%, 52%, 25%) respectively after sedimentation process. This is expected because of all sediments and inorganic matter will settle down and reduced sharply, these results are in consistence with the results attained by a research done by Sepehr [13]. and showed that calcium hardness, total hardness, chemical oxygen demand concentrations reduction percent in the all steps before zeolite treatment steps are (62.3%,57.1%,20%), respectively. While, the reduction removals are (75%, 86%, 67%) respectively percentage reduction after zeolite treatment as it is expected. This may be due to adsorption of salts ions, inorganic matter and chemicals in water by zeolite. These results are in consistence with many researches where done by Aragaw. The results are (70%, 80%, 64%), respectively [19]

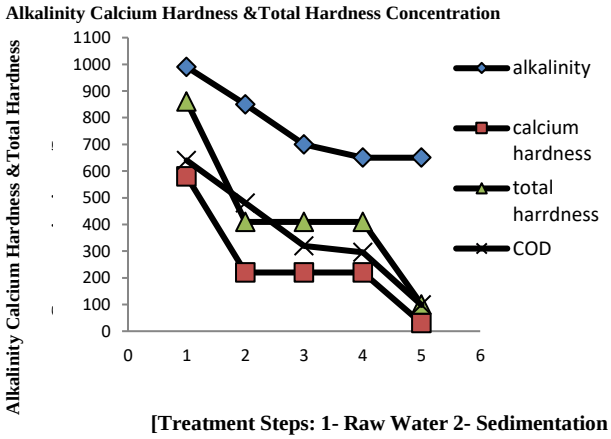


Figure 3. Chemical analysis test results after five treatment steps.

Figure 4, shows the reduction of oil and grease pollutants concentration by which is estimated as (25%) after the floatation process. This is expected because after flotation oils and fats are skimmed and removed by a mechanical skimmer. Moreover, the oil and grease concentration is reduced sharply by (99.6%) of its initial concentration after zeolite adsorption of contaminants, which emphasizes the effectiveness of zeolite treatment for removing the oil and grease from the wastewater. These results are in complying with the results achieved by a research done by Sanghamitra which showed that the oil and grease removals reached to 99% [20]

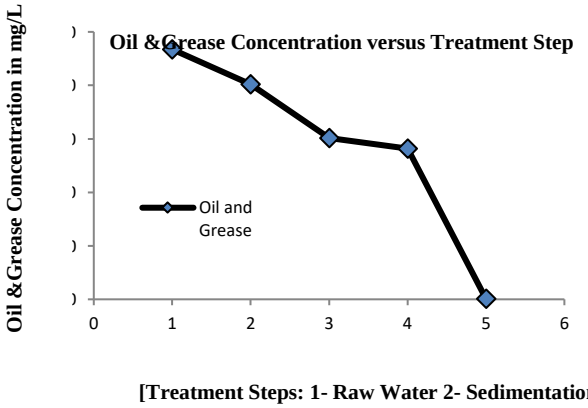


Figure 4. Oil and grease test (mg/L) after five treatment processes

Figure 5, shows that MBAS concentration values after each step in wastewater treatment plant where the concentration is reduced sharply up to removal efficiency of 95.4 % of its initial concentration. The highest removal efficiency has occurred after the zeolite adsorption step which has a high efficiency to adsorb all kind of surfactants. . These results are in revealed the same results as achieved in a research done by Berth which showed that the MBAS removal reached about 94% [21].

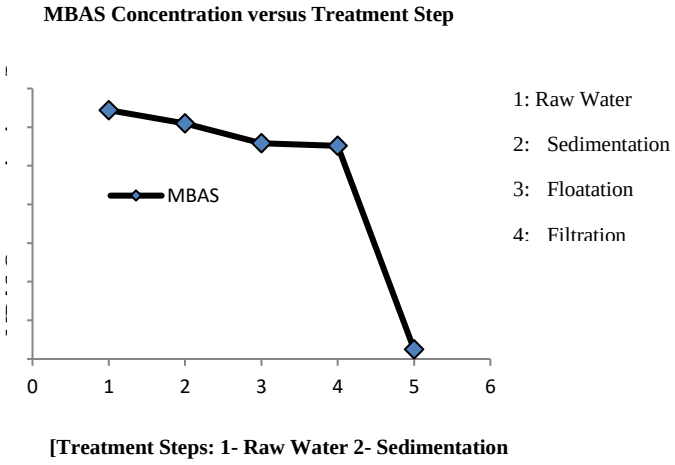


Figure 5. MBAS concentration (mg/L) after five treatment processes

Part Two: - Physical Parameters Analysis (Total Suspended Solids – TSS and Total Dissolved Solids - TDS).

The total suspended solids (TSS) concentration is reduced sharply up to 76% removal efficiency after sedimentation process which is expected due to that all sediments and suspended matter with whether settle down or floated up with the part oil and graces contaminates. On the other hand, the total dissolved solids (TDS) concentration, is also reduced slightly after sedimentation treatment step up to a removal efficiency of 18%, this is clear in Figure 6. These results are in consistence with the research done by kumar the results showed that the TSS, TDS removal reached to76.1 % and 10% respectively [22].

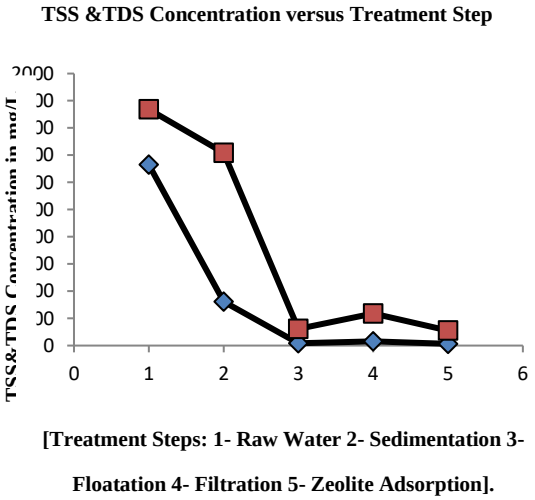


Figure 6. TSS and TDS concentrations (mg/L) after each treatment steps.

Part Three: - Biological Oxygen Demand Analysis (Biological Oxygen Demand – BOD).

The biological oxygen demand (BOD) concentration is reduced slightly about (22%) after each treatment steps as shown in Figure 7. This is expected due to the treatment used here which is a

physical treatment, not biological treatment and the test is done to investigate the ability of zeolite to adsorb chemicals and other pollutants. The results showed that zeolite is highly effective in removing chemicals and solids but slightly effective in removing pathogens. Finally (BOD) removal is reached about 45 % after all treatment steps as shown in Figure 5 below. These results are in consistence with the results achieved in a research done by Makisha where the results showed that the BOD removal reached up to 40% [23].

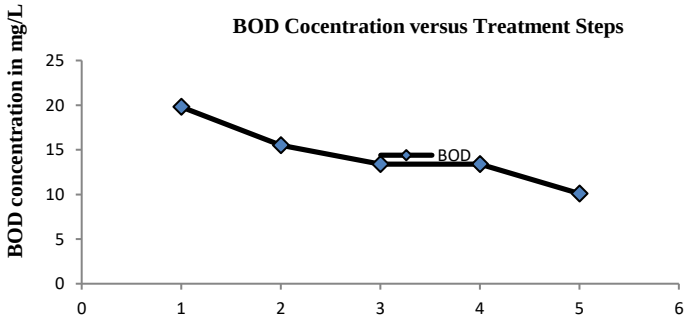


Figure 7. Biological Oxygen Demand (BOD) concentration (mg/L) versus treatment steps.

4. Conclusions

This study demonstrates the treatment and reuse of carwash wastewater in Amman City in Jordan. Based on findings of this research, the treatment technologies could be considered as viable alternative resources to provide with a large amount of water that could be used in carwash again. The treatments were used in this research were found that they are effective in the removal of contaminates with different removal efficiencies. Through the research, it was found that the natural and modified zeolite used to have a high potential for COD, TDS, TSS, total hardness, oil and grease, heavy metals, MBAS removal. The methods were used in the suggested treatment plant described as a less operating and maintenance cost. Hence, the adopted processes for treatment are considered environmental friendly techniques without chemical operation.

Acknowledgments

The authors would like to express their gratitude to the support extended to them throughout this research project by the colleagues and the staff of Jordan University. This research was conducted in part using the resources of the university.

The authors of this article are also grateful to the Middle East University (MEU), Amman, Jordan for the all types of supports and grants to cover the works of this research article.

References

1. Awad, "Adsorption of Hexavalent Chromium Cr(VI) by Using Local Jordanian Sand (LJS) and Iron dust - Sand mixed Adsorbents "Jordan Journal of Earth and Environmental Sciences. Volume (6) Number (1), September (2014) / Dhu al-Hijjah 1435, ISSN 1995-6681.
2. Awad, ,"Utilizing Of Wastewater and Biomass Generated In Jordanian Sewage Treatment Plants" International Journal of Innovative Technology and Exploring Engineering (IJITEE) ISSN: 2278-3075, Volume-9 Issue-1, November 2019
3. A Report for the International Carwash Association, International Carwash Association, Inc. September (2002).

4. Al-Odwani, A., M. Ahmed, and S. Bou-Hamad. "Carwash water reclamation in Kuwait." Desalination 206.1-3 (2007): 17-28
5. Bhatti, Zulfiqar Ahmad; Mahmood, Qaisar; Raja, Iftikhar Ahmad; Malik, Amir Haider; Khan, Muhammad Suleman; Wu, Donglei, "Chemical oxidation of carwash industry wastewater as an effort to decrease water pollution." Physics and Chemistry of the Earth, Parts A/B/C 36.9-11 (2011): 465-469.
6. Dorji, Kinley. "A review on Water Resources and Water Resource Management in Bhutan by Kinley Dorji."
7. Hadadin, Nidal A., and Zeyad S. "Water shortage in Jordan—Sustainable solutions." Desalination 250.1 (2010): 197-202.
8. Hussein, Hussam. "An analysis of the framings of water scarcity in the Jordanian national water strategy." Water international 44.1 (2019): 6-13.
9. Kadirvelu, K., K. Thamaraiselvi, and C. Namasivayam. "Adsorption of nickel (II) from aqueous solution onto activated carbon prepared from coirpith." Separation and purification Technology 24.3 (2001): 497-505.
10. Mazumder, Debabrata, and Somnath Mukherjee. "Treatment of automobile service station wastewater by coagulation and activated sludge process." International Journal of Environmental Science and Development 2.1 (2011): 64.
11. Pak, D., and W. Chang. "Factors affecting phosphorus removal in two biofilter system treating wastewater from car-washing facility." Water science and technology 41.4-5 (2000): 487-492.
12. Sampranpiboon, Panida, Pisit Charnkeitkong, and Xianshe Feng. "Equilibrium isotherm models for adsorption of zinc (II) ion from aqueous solution on pulp waste." WSEAS Transactions on Environment and Development 10 (2014): 35-47.
13. The American Public Health Association, et al. Standard methods for the examination of water and wastewater, (2013)
14. Zaneti, Rafael, Ramiro Etchepare, and Jorge Rubio. "More environmentally friendly vehicle washes: water reclamation." Journal of Cleaner Production 37 (2012): 115-124.
15. NWSJ - Ministry of Water and Irrigation Report, (2016 – 2025).
16. Ministry of transportation report, (2019).
17. Hamada, T., & Miyazaki, Y. (2004). Reuse of carwash water with a cellulose acetate ultrafiltration membrane aided by flocculation and activated carbon treatments. Desalination, 169(3), 257-267.
18. Panizza, Marco, and Giacomo Cerisola. "Applicability of electrochemical methods to carwash wastewaters for reuse. Part 2: Electrocoagulation and anodic oxidation integrated process." Journal of Electroanalytical Chemistry 638.2 (2010): 236-240.
19. Aragaw, T. A., & Ayalew, A. A. (2019). Removal of water hardness using zeolite synthesized from Ethiopian kaolin by hydrothermal method. Water Practice and Technology, 14(1), 145-159.
20. Sanghamitra, P., Mazumder, D., & Mukherjee, S. (2021). Treatment of wastewater containing oil and grease by biological method-a review. Journal of Environmental Science and Health, Part A, 1-19.
21. Baumann, E. R., Hopping, W. D., & Warner, F. D. (1981). Field evaluation of the treatability of type A zeolite in a trickling filter plant. Water Research, 15(7), 889-901.
22. Kumar, P. R., Pinto, L. B., & Somashekar, R. K. (2010). Assessment of the efficiency of sewage treatment plants: a comparative study between nagasandra and mailasandra sewage treatment plants. Kathmandu university journal of science, engineering and technology, 6(2), 115-125.
23. Kulakov, A., & Makisha, N. (2017). Removal of nitrogen and phosphorous from domestic wastewater. In MATEC Web of Conferences (Vol. 112, p. 10019). EDP Sciences.

The Corrosion and Sedimentation Status of Drinking Water in Iran's Distribution Network: A Systematic Review

Seyedeh Parvin Moussavi [1,*], Reza Rostami [2,*], Farideh Malekdar [3]

[1] Department of Renewable Resources, University of Alberta, Edmonton, Canada
[2] Student research committee, Kermanshah University of Medical sciences, Kermanshah, Iran
[3] Department of Chemical and Petroleum Engineering, Chemical Engineering, Sharif University of Technology, Tehran, Iran
** Corresponding authors : seyedehp@ualberta.ca ; rezarostami745@gmail.com ;Tel : +989221106736*

Abstract: Corrosion and sedimentation are important indexes in assessing water quality. The corrosivity and sedimentation make problems in economic, industry, water treatment, water transmission and distribution of water. On the other hand, the presence of an important factor such as corrosiveness can lead to entering byproducts into drinking water and as a result it has hygienic and economic problems such as reducing the pipe lifetime. In the present study, a comprehensive review on the corrosion and sedimentation status of water in all regions of Iran has been carried out according to previous studies. In this study, in addition to water quality, other effective parameters on corrosion and sedimentation have been investigated. In the collected findings, according to the Langelier Saturation Index (LSI), the most corrosive and sedimentation rate were respectively in Qom and Shiraz. The Relative Strength Index (RSI) index shows that the most corrosive and sedimentation rate is respectively in the outlet valve of the refinery in Anzali and Qamsar. For both aggressive corrosive index (AL) and Puckorius Scaling Index (PSI), the most corrosive rate are respectively related to the outlet point of Anzali and Qom refineries and the highest sedimentation rate for both indexes are related to Qamsar.

Keywords: index ; corrosion ; sedimentation ; drinking water ; distribution network

1. Introduction

Considering that it is necessary to have healthy water for community water supply, therefore it is inevitable and necessary to know the factors that endanger the optimal quality of required water in various sectors such as transmission and distribution networks, industrial sectors, etc. The corrosivity phenomenon is one of these problems at the facilities of water treatment and transmission and distribution network [1]. Corrosion is a physical – chemical reaction that is caused by the contact of material with the environment and causes the properties of the materials change. In the field of material engineering, corrosion is the result of electrochemical erosion. In the first type, physical factors such as the collision of suspended solids with water or sewage with the pipe wall is the reason of pipe damage, while the second type is resulted by the formation of an electric cell and also the electrochemical reactions between the material and the environment. The firs type of corrosion is more in metal and nonmetal pipes such as concrete and the second type is more in metal pipes [2]. The internal corrosion of the pipe can be due to several factors such as microbial water quality, physical and chemical quality of water (oxygen concentration, concentration and type of the residual chlorine, the concentration of chlorine, sulfate and calcium ions, water temperature, etc.), PH, hydraulic conditions of water in the pipe (flow velocity) and pipe material [1-4]. It should be noted that the presence of ions such as OH, SiO_3 and CrO_2 in water reduces corrosion [3]. One of the corrosive health problems of byproducts is due to dissolving metals in distribution networks and

house plumbing. Lead, Cadmium, Fe, Zinc, Copper and Manganese are some of these metals. Lead and Cadmium are toxic elements; Fe, Zinc, Copper and Manganese cause aesthetic problems and create problems such as smelling, tasting, color and stains on the toilets [4]. Different methods such as corrosion and stability indexes and Coupon and Marble tests are used to assess the corrosion and sedimentation status of the water. Saturated indexes are most often used by water industry to determine the corrosivity and sedimentation of water and include the Langelier saturation index (LSI), the Rayznr stability index (RSI) and the calcium carbonate (marble) stability test [5].

The adverse economic effects of corrosion are very severe. Although the effects of using products of water corrosion are not well known but there are hidden risks. The damages caused by corrosion in the pipes of the USA water distribution network are estimated to be $700 million [6]. This article aimed to review the corrosion and sedimentation status of drinking water in the distribution network of the country from 1380 to 1395. Despite not all of the relevant conditions were provided, this article was written in the form of a review article in order to have better effects.

2. The method of study

In order to find documentations related to the potential of corrosion and sedimentation of drinking water, the keywords such as sedimentation, corrosion and drinking water were searched in English and Persian in databases such as google scholar, Iran Medex, SID, Pubmed, Scopus. The found titles by the search engine were first examined in terms of relationship to the topic in order to select the useful documentation. The criteria for entering the researches into this study are: 1- using the terms defined for the title, 2- the completeness of the research report, 3- the quantitative research methods, 4- ignoring the repetitive studies, 5- During the years 2002 to 2016.

2.1 The evaluation criteria:

2.1.1 Calculating and interpreting the index of LSI:

$$LSI = pH - pHs$$

In fact PHs is the PH of saturated water of calcite or calcium carbonate and it is calculated using the following equations:

$$pHs = (9.3 + A + B) - (C + D)$$

$$A = (Log10\ [TDS] - 1) / 10$$

$$B = -13.12 * Log10\ (oC + 273) + 34.55$$

$$C = Log10\ [Ca2+\ as\ CaCO3] - 0.4$$

$$D = Log10\ [alkalinity\ as\ Ca\ CO3]$$

In the interpretation of LSI index, there are 3 available states: LSI<0 which shows the tendency of water to dissolve $CaCO_3$, LSI = 0 which shows no water corrosion and sedimentation, and LSI>0 which shows the tendency of water to $CaCO_3$ sequestration [7].

2.1.2 Calculating and interpreting the index of RSI:

$$RSI = 2(pHs) - pH$$

There are interprets for each state of RSI index that include: RSI<6 which indicates the increasing tendency to sedimentation by increasing the index value, 6<RSI<7 which shows the lack of creating protective film due to the formation of calcium carbonate sedimentation and at the end RSI>7 which shows an increase in the mild corrosion in steel pipes [7].

2.1.3 Calculating and interpreting the index of PSI:

$$PSI=2pH_s-pH_{eq}$$

PH_{eq} is the equilibrium PH which is calculated by following equation:

$$pH_{eq} = 1.465\log [Alk]+ 4.54$$

If this index is greater than 6, it indicates the tendency of water to corrode and if this index is less than 6, it refers to the tendency of water to sediment.

2.1.4 Calculating and interpreting the index of AI:

The following relation is used to calculate the (aggressive) corrosive index:

$$AI=\{pH + \log[(A)(H)]\}$$

AI: The aggressive corrosive index
A: Total alkalinity ($CaCO_3$ mg/L)
H: Calcium hardness ($CaCO_3$ mg/L)
The variable values of index of AI as other indexes indicate to different states as follow [7]:

- AI<10: Highly corrosive
- 10<AI<12: corrosive (mild)
- AI>12: non-corrosive

3. Findings and results

3.1 The effective parameters:

The factors and parameters which are used to measure the corrosive properties and sedimentation of water are PH, temperature, total alkalinity, calcium, bicarbonate, chlorine, sulfate and their permissible values in the National Iranian Standard were respectively 6.5 to 9, 23°c, 1500 mg/L, 500 $CaCO_3$ mg/L, 500 $CaCO_3$ mg/L, 200 mg/L, no allowable amount, 400 mg/L and 400 mg/L. It should be noted that in the EPA standard, the PH, total soluble solids, chlorine and sulfate were reported to be 6.5 to 8.8, 500, 250 and 250 mg/L respectively [8-9]. The effective factors measured in various studies have been reported according to table 1.

Table 1. The results of studies in studied cities during recent 15 years.

The summary of study	Sulfate (mg/L)	Chlorine (Mg/L)	Bicarbonate (Mg/L)	Ca^{2+} ($CaCO_3$ mg/L)	T.ALK (Mg/L)	T.H ($CaCO_3$ mg/L)	TDS (Mg/l)	Temperature (°c)	PH	The samples specifications	The aim of study	The writer, year, city
The corrosion index in the water supply network in Tabriz is approximately in the range of partial sedimentation.	-	-	-	82.54	193.44	206	535	21.86	7.88	5 samples of drinking water in different areas	Studying the corrosive factors in water supply network	Asl Hashemi-Tabriz-2011[1]
The water in Kouhdasht has tendency to corrosive properties.	-	-	-	-	-	-	-	-	-	26 samples of drinking water in 12 regions.	Studying the quality of drinking water and determining the potential of corrosion and sedimentation	Ebrahimi-Kohdasht-2013[10]
According to studies, Langelier index, Rayznr's index and aggressive index respectively has a low sedimentation, severe corrosion to low corrosion and low corrosion to medium corrosion.	46	134.3	228.3	19.68	-	104	555.7	34.4	8.24	144 samples of 8 stations	Determining the potential of corrosion and sedimentation	Ahmadpour-Manojan-2010[11]
The corrosion rate and its potential in the water distribution network is higher than the outlet water of refineries and wells. The outlet water in the great refinery of Gilan, the water of wells and water in Anzali distribution network are in the range of medium to high	-	-	-	-	326.2	227	598.9	19.5	7.73	45 samples in 1 year and all seasons	The potential of corrosion or sedimentation of distribution network	Jafri-Anzali-2011[12]
	-	-	-	-	298.6	288	606.7	17.9	7.74		The potential of corrosion or sedimentation of valves in wells	

corrosion, and are corrosive and they are can't sediment.	-	-	-	-	275.3	191	669.2	20.55	7.86		The potential of corrosion or sedimentation of the output of refineries	
The drinking water of Shiraz has a sedimentation potential in most cases and only has the corrosion potential in some slight cases.	-	-	-	82.54	193.44	206	535	21.86	7.88	72 drinking water wells and Doroudzan dam	Determining the potential of corrosion of drinking water	Mazlomi-Shiraz-2009[3]
The quality of water in Boshehr in near to corrosive	58.33	170.34	-	105.24	-	263	586.82	30.6	7.5	11 samples for 1 year from 7 stations	The characteristics of chemical qualities and determining the potential of corrosion	Askari-Boshehr-2015[13]
The quality of water in Miyaneh is more appropriate in terms of AL index than other indexes.	159.06	104.61	387	122.09	323.03	310	797.1	19.1	7.26	56 samples of desired wells in 12 months	Determining the potential of drinking water corrosion	Heybati-Miyaneh-2008[14]
The drinking water in Qamsar has corrosive potential	318.44	163.23	276.8	120.05	226.99	384	1060.8	15.99	7.56	6 wells for supplying drinking water	Determining the potential of drinking water corrosion in Qamsar	Dehghani kashani i-Ghamsar -2003[15]
The results show that the water in cities is near to corrosive	-	-	-	-	-	-	-	-	-	50 points in the distribution network during summer and fall	Determining the corrosion or sedimentation potential of drinking water in distribution network	Piri Alam-Khoramabad -2008[16]
Lots of studied water sources were corrosive and a few of them had sedimentation property	-	-	226.5	100.67	-	-	-	15.48	-	151 samples in 4 times from 39 water supplies in 39 villages	Identifying the quality of corrosion or sedimentation in rural water sources	Rabani-Kashan-2011[17]

Drinking water in Ardebil water supply network tends to some extant to be corrosive	-	-	-	-	225.5	132	-	17.25	7.35	24 samples of 12 divided blocks in the city in 2 stages	Evaluating the quality of drinking water in water distribution network	Mokhtari - Ardabil-2010[2]
The water status in studied sections are in the corrosive area	-	231.2	-	132.29	-	436	1205	-	7.27	100 samples in 12 months	Determining the corrosion and sedimentation potential in water resources	Rezaei Kalantary - Ghom-2013[18]
The water in refineries has good quality against corrosion	-	-	-	-	-	-	-	-	-	Collecting 15 samples of 2 to 3 liters per month during 10 months	Studying the corrosion potential and getting layered of purified water	Hosseinzadeh- Takab-2013[19]
Based on LSI index, water has a little tendency for sedimentation and according to the PSI index, it tends for corrosion	278.9	545	-	73	157.67	399	1589	-	7.88	31 samples in one month of the summer	Evaluating the corrosion potential and water scale in distribution networks	Shams - Tabas-2012[20]
Water has a moderate corrosivity and the measured parameters in this research were in accordance with the Iranian standard and EPA.	-	-	-	-	-	-	-	-	-	Sampling twice a month during 12 month	Determining the potential of water corrosion in water refineries	Fazlzadeh - Ilam-2009 [21]
The quality of drinking water in Sarableh: the water distribution system has a moderate corrosion rate	-	-	-	62	214	-	293	26	7.5	60 samples of water (30 samples in summer, 30 samples in winter)	Evaluating the quality of water in water distribution network	Normoradi-Sarablah-2016 [22]

Studying the corrosion indexes showed that the drinking water in Tabriz is corrosive	-	-	-	107.15	132.45	-	295.1	17.71	7.027	80 samples in 2 seasons od spring and summer	The potential of corrosion and sedimentation of drinking water	Taghipour - Tabriz-2012[23]
Due to the high degree of corrosion, the drinking water sources in Zahedan are harmful	536.62	417.7	252	118.18	318.01	-	279.61	22	7.68	33 samples of water in different places of the city	Studying the corrosive indexes in drinking water resources	Biglari - Zahedan-2016[24]

3.2 The index of LSI:

According to the conducted studies on corrosion and sedimentation of drinking water in different cities, the average rate of Rayznr index is reported as (LSI index) in the figure 1 and showed that Qom has the highest corrosivity of -1.67. And also the most tendencies to sedimentation are related to Shiraz and it is 0.86. Studying the corrosion indexes showed that drinking water in Shiraz has a sedimentation potential in most cases and only in a few cases has small corrosion potential. The results showed that Tabas has the most favorable situation in terms of LSI index. According to the effective parameters in the mentioned formulas and the data obtained from the studied studies which are shown in table 1, the reason of water corrosivity in these cities is based on the Langelier index, the high total soluble solids, the total hardness and calcium rate and finally the low value of PH.

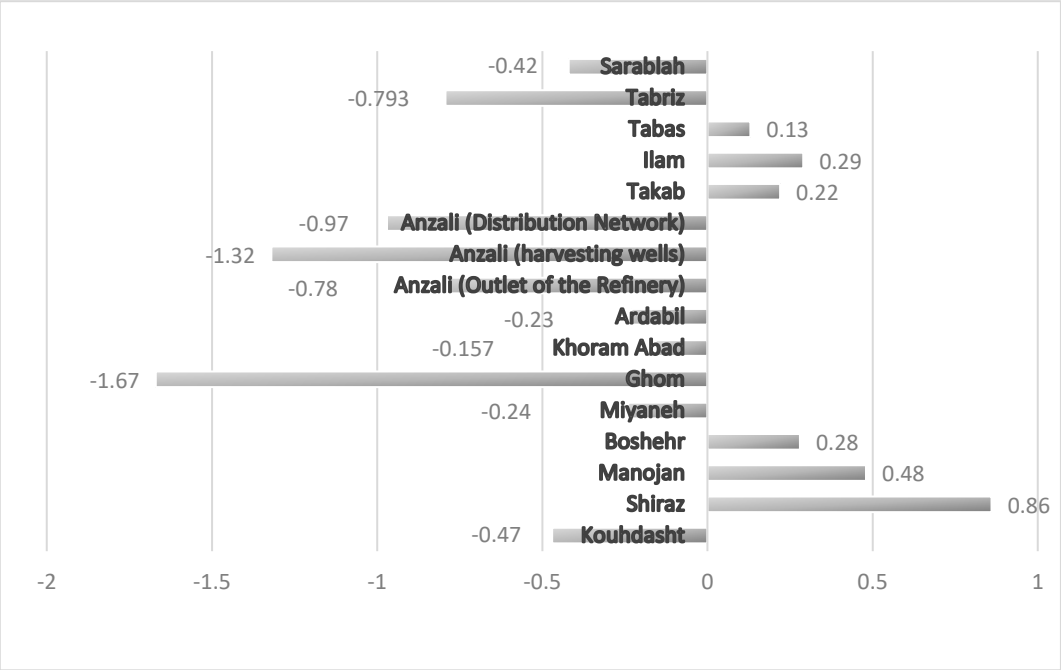


Figure 1. LSI Index Measured in Cities Researched

3.3 The index of RSI:

According to the studies on corrosion and sedimentation of drinking water in different cities of the country, the average rate of RSI index was reported based on the figure 2 (RSI index) and the highest tendency to sedimentation is in Shiraz and it is 5.95. The studies show that Qamsar has the most suitable status for the RSI index. Generally, the results showed that the outlet water of Anzali refinery has the highest corrosion of 11.92. The water supply of the wells and water in Anzali distribution network is in the medium to high range of corrosion. It is not corrosive and it doesn't sediment and the corrosion rate in the water distribution network has more potential in corrosion than the outlet water of the refineries and wells, which can be related to the types of the pipes in distribution network, the water alkalinity and also hardness of water.

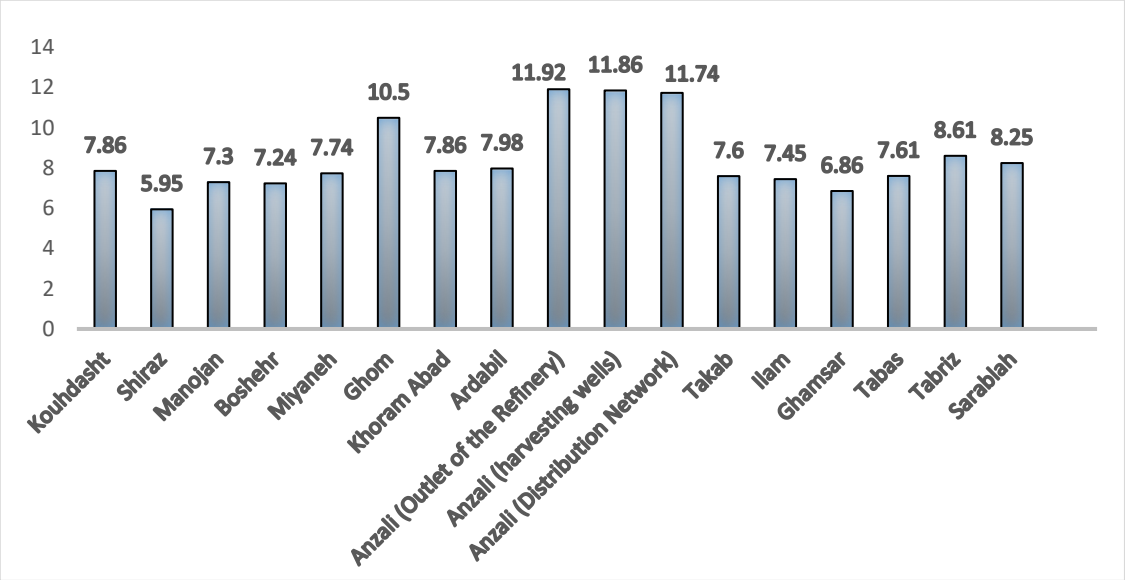


Figure 2. RSI Index Measured in the Cities Explored

3.4 The PSI index:

According to studies on corrosion and sedimentation of drinking water in different cities of the country, the average of PSI index was reported in the figure 3 as PSI index and shows that Qom has the highest corrosion rate of 9.92. The results show that Kouhdasht, Miyaneh and Qamsar have relatively good conditions of the PSI index.

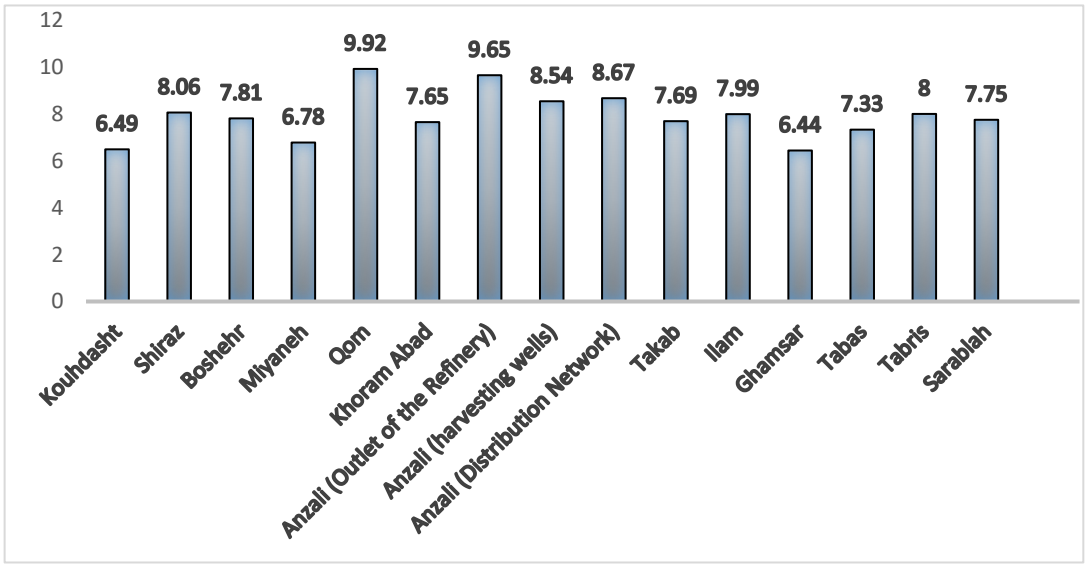


Figure 3. PSI Index Measured in the Cities Researched

3.5 The AI index:

According to the studies on corrosion and sedimentation of drinking water in different cities of the country, the average AI index was reported according to the figure 4 as AI index and shows that Anzali has the highest corrosion of 8.64. And the highest amount of tendency to precipitation was

14.42 and it was in Qamsar. The results showed that Kouhdasht, Miyaneh, Sarableh, Shiraz and Khoram abad have the most favorable conditions of AI index.

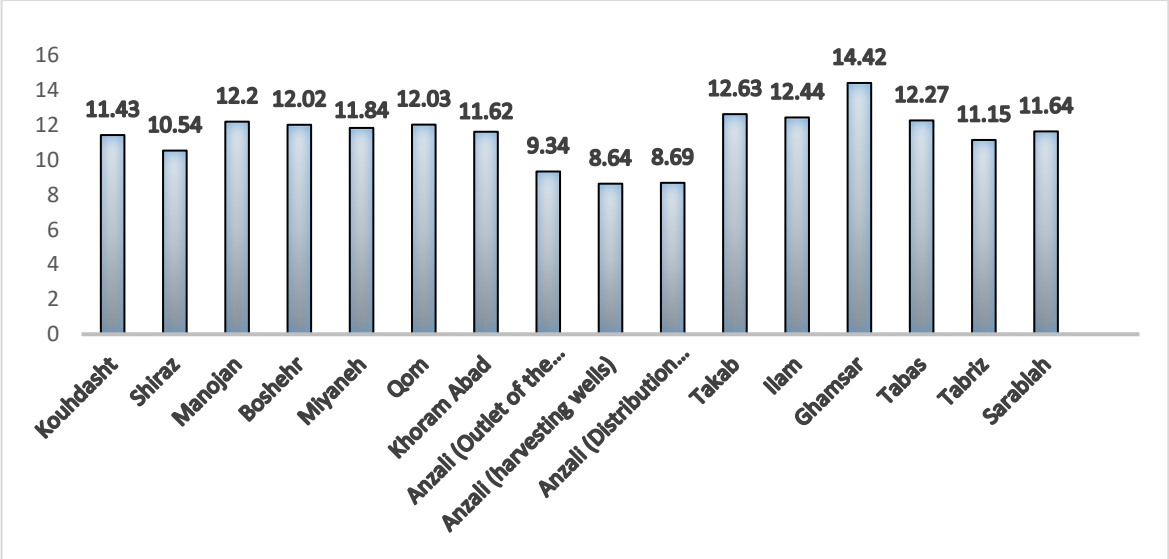


Figure 4. AI Index Measured in the Cities Researched

4. Conclusion

According to the data and results obtained from the study and investigating the articles and references which were mentioned in previous sections, it was estimated that in none of the various cities of the country, water is not completely neutralized and is likely to be minor, moderate or severe in corrosivity or sedimentation. It should be noted that different methods such as adjusting and setting PH in such a way that water is not corrosive and also it is not able to be sediment are used to reduce or modify the sedimentation or corrosivity of water. On the hand, the lower the alkalinity of the water, the PH should be increased to prevent sedimentation and if alkalinity is high, a PH reduction is required. Adding lime or sodium carbonate are some ways to increase alkalinity. Also other methods of corrosion control and sedimentation control are using polyphosphate, sodium silicate and also using metal pipes which their internal and external walls are isolated.

Funding: This research received no external funding.

Reference

1. Asl Hashemi A, Dehghan Zadeh R. Investigation Of Corrosion In Tabriz City Water Supply Network. Application Of The Environmental Chemistry.2011;3(9):5-9. (Persian)

2. Mokhtari S, Aalighadri M, Hazrati S, Sadeghi H, Gharari N, Ghorbani L. Evaluation of Corrosion and Precipitation Potential in Ardebil Drinking Water Distribution System by Using Langelier & Ryznar Indexes. j.health.2010;1(1):14-23.(Persian)
3. Mazlomi S, Babaee A, Fazl Zadeh Doil M, Aboee E, Rabiee Nezhad A, Norozi M, Haj Poorsogh KH. Corrosion And Precipitation Potential Of Drinking Water In The City Of Shiraz. Twelfth National Conference on Environmental Health. Shahid Beheshti University of Medical Sciences. 2009.(Persian)
4. Zhu D, Van Ooij WJ. Corrosion protection of metals by water-based silane mixtures of bis-[trimethoxysilylpropyl] amine and vinyltriacetoxysilane. Progress in Organic Coatings.2004 ;49(1):42-53.
5. Mahvi AH, Dindarlou K, Ali Jamali HA, Alipour V. Corrosion and scaling in Bandar Abbas Pipe water network. Bimonthly Journal of Hormozgan University of Medical Sciences. 2011;14(4):335-40.(Persian)
6. Karbasi A, Nabi Bidhendi Gh. Corrosion in water distribution networks and drinking water quality. Ecology,1995;21(17):24-33.
7. Yousefi Z, Kazemi F, Ali Mohammadpour R. Assessment of scale formation and corrosion of drinking water supplies in Ilam city (Iran). Environmental Health Engineering and Management Journal.2016;15;3(2):75-80.
8. EPA ,2004. Edition of the drinking water standards and health advisories, EPA 822-R-04-005. Office of water protection agency Washington, DC.
9. Industrial research and standard institute of Iran, physical and chemical quality of drinking water. No 1053, fifth edition, Tehran (1997).
10. Ebrahimi A, Kamarehie B, Asgari G, Seid Mohammadi A, Roshanaei G. Drinking Water Corrosivity and Sediment in the Distribution Network of Kuhdasht, Iran. Health system research Journal.2012;8(3):480-6.(Persian)
11. Ahmadpoor A, Zazoli M.A, Ghaneian M.T. Survey of corrosion and scaling potential of drinking water distribution system in Manoojan City in 2010. 14th National Conference on Environmental Health. Shahid Beheshti University of Medical Sciences.2010.(Persian)
12. Jafari M, Fallah F, Hassani A. Investigating the Hygiene of Anzali Drinking Water Resources for Corrosion and Precipitation Potentials Using Corrosion Indexes Journal of Guilan University of Medical Sciences.2011;20(79):90-96.(Persian)
13. Asgari G, Ramavandi B, Tarlaniazar M, Fadaie nobandegani A, Berizie Z. Survey of chemical quality and corrosion and scaling potential of drinking water distribution network of Bushehr city. Iran South Med J.2015;18(2):353-361.(Persian)
14. Heybati B, Mazlomi S, Fazl Zadeh Doil M, Norozi M. Determine the corrosion potential and sedimentation of water in the middle of the year 2008. Twelfth National Conference on Environmental Health. Shahid Beheshti University of Medical Sciences.2009.(Persian)

15. Dehghani kashani A, Asadi M, Golsorkhi M, Amir A. Evaluate the potential of scaling and corrosion in drinking water in 1390-1389 Ghamsar using corrosion indices. Fourteenth National Congress corrosion.2013.(Persian)
16. Pirialam R, Shams khorramabadi G, Shahmansouri M R, Farzadkiya M. Determination of corrosion and sedimentation potential in drinking water distribution system of khorramabad city by corrosion indices and weight loss method. yafte.2008;10(3):79-86.(Persian)
17. Rabbani D, Miranzadeh M B, Paravar A. Evaluating the corrosive and scale-forming indices of water in the villages under the coverage of Kashan rural water and wastewater company during 2007-9. KAUMS Journal (FEYZ). 2011;15(4):382-388.(Persian)
18. Rezaei Kalantary R, Azari A, Ahmadi E, Ahmadi Jebelli M. Quality evaluation and stability index determination of Qom rural drinking water resources. Journal of Health in Field.2013;1(3):9-16.(Persian)
19. Hoseinzadeha E, Yusefzadehc A, Rahimid N, Khorsandie H. Evaluation of corrosion and scaling potential of a water treatment plant. Archives of Hygiene Sciences Volume.2013;2(2):41-47.
20. Shams M, Mohamadi A, Sajadi SA. Evaluation of corrosion and scaling potential of water in rural water supply distribution networks of Tabas, Iran. World Appl Sci J. 2012;17(11):1484-1489.
21. Fazlzadeh Davil M, Mahvi AH, Norouzi M, Mazloomi S, Amarluie A, Tardast A, Karamitabar Y. Survey of corrosion and scaling potential produced water from Ilam water treatment plant. World Appl Sci J.2009;7(11):11-24.
22. Nourmoradi H, Mirbagheri SA, Moradnejadi K, Kazembeigi F, Shamsizad M. Determination of corrosion and scaling levels of drinking water in distribution system: A study in Sarableh city (Ilam), western of Iran. J Bas Res Med Sci.2016;3(3):21-27.
23. Taghipour, H. Shakerkhatibi, M. Pourakbar, M. Belvasi, M. Corrosion and Scaling Potential in Drinking Water DistributionSystem of Tabriz, Northwestern Iran. Health Promotion Perspectives. 2012;2(1):103-111.
24. Biglari, H. Saeidi, M. Rahdar, S. Narooie, M R. Salimi, A. Khaksefidi, R. Alipour, V. Evaluation of corrosion scaling tendency indices in zahedan grand water resources. Iioab Journal.2016;7:523-528.

The Role of Cofactor Addition on Flocculation and Deflocculation Behaviors of Fines Flocculation Using a Cofactor and Polyethylene Oxide Retention Aid

Dr. Mohammad Raji Abdallah Qasaimeh

Umm Al Qura University, Engineering College in Al-Lith, Environmental Engineering Department, Saudi Arabia

**corresponding author : mrqasaimeh@uqu.edu.sa; qasaimeh@hotmail.com; Tel : (+) 966 53864 8076*,

Abstract : For the importance of fines retention in paper sheet and conventional use of cofactor (CF) and Polyethylene oxide (PEO) retention aid, the objective of this work was to investigate the effect of CF additions (C_{CF}) in a wide range on fines flocculation. Results have shown significant enhancements to flocculation and deflocculation and variations in their parameter values with CF addition C_{CF} in a wide range divided into subzones. Resulted floc size (relative to maximum) was found increasing with increases in C_{CF} at low values, reaching maximum in optimum zone, and then decreased to produce small flocs at high (excessive) C_{CF} values. Flocculation rate constant increased with increases in C_{CF} at low values, plateaus in optimum zone, and then significantly increased at high C_{CF} values. Deflocculation occurred in all runs at all C_{CF} values with variable ratio of deflocculation rate constant to flocculation rate constant. This ratio was found about 0.408 when PEO was used alone, decreased with C_{CF} increase to 0.11 in optimum zone, and then increased to 0.56 at some high C_{CF} values. Variations of floc size and of flocculation and deflocculation rate constants in wide C_{CF} range have enriched mills with knowledge useful to many applications and to selections of required characteristics.

Keywords: Polyethylene oxide ; Cofactor Concentration ; Flocculation, Deflocculation ; Rate constants.

1. Introduction

In papermaking, retention aids are used to bridge fines with fibers, fines with fines and retain them into paper sheet. These processes are performed at high shear rates to produce the required flocs that maintain uniform sheets. In previous work, in fines flocculation using a cofactor CF and polyethylene oxide PEO at high effective shear rate, small portion of fines was deposited on fibers, while the majority formed flocs.[5] After equilibrium, flocs started to deflocculate and the deposited fines on fibers started to leave the surfaces.[2, 8, and 9] In flocculation processes using polyelectrolyte retention aids, some ascribed deflocculation to detachments by shear rate and polymer breakages.[10-15] In fines

flocculation with CF-PEO retention aid, the deflocculation cause was related to factors in PEO.[16] To know better the CF-PEO mechanism and the accompanied deflocculation, the dominant factors in retention and their effects have become the interest of this work. Improvement of fines flocculation was the main goal in papermaking and literature work. To improve paper sheet, one work showed two types of Cellulose Nanofibers (CNF) used with a dual system, polyvinylamine (PVA) and cationic starch as reference. CNF addition increased floc stability, minimized overdosing, increased floc size for given PVA dose and improved the wet end in paper machine.[17] We used neutral and high molecular weight PEO as an alternative to cationic retention aids that incorporate with ions;[18,19] thus reduce their performances. In case of PEO, to flocculate some colloids and fines, it requires to have a large coils size (δ) enough to bury the effect of the electrostatic double layer thickness (κ^{-1}) and bridge surfaces,[5] but no bridging will occur with unsatisfied small coil size δ (Figure 1a). To improve its performance, we added a cofactor having a phenol group, [18-20] where number of cofactors are used in papermaking.[21] These cofactors and PEO do not adsorb on most colloids, fines and fibers, but their combinations adsorb and bridge effectively.[22] One particle polymer bridging theory is the transient network mechanism,[23] which was argued by the association-induced polymer bridging proposed by van de Ven, T.G.M. and Alince, B.,[24] who described bridging of fillers using CF-PEO in two ways.[24] In first way, the adsorbed CF segments on PEO coils of size δ expand the PEO coils forming larger CF-PEO complex (of size δ_x), which effectively adsorbs on surfaces and bridges particles. In this state, repulsion among the negative CF segments in the complex stiffens and expands the PEO coils into a size larger than the thickness of the electrostatic double layer κ^{-1}, inducing bridging with two conditions: $\delta_x > 2\kappa^{-1}$ and $\theta(=\Gamma/\Gamma_m) < 1$.[24] Here, (θ) is PEO fractional coverage on the surfaces, (Γ) is PEO quantity covering the surfaces, and (Γ_m) is PEO quantity that maintains the full coverage on surfaces.[25]



-ve

a-) No Bridging b-) Bridging (Floc)

Figure 1 Bridging conditions and PEO induced bridging mechanism.

In second way, the adsorbed CF segments on PEO coils act to reduce the heat of adsorption into adsorption zone facilitating for PEO coil adsorption on the surfaces.[24] This CF-PEO induced bridging (Figure 1b) is also active in fines flocculation,[2, 21] where CF induces PEO coils to adsorb on fines surfaces bridging them although the charges of CF and fines are negative. One significant factor of CF-PEO bridging is PEO coils microstate prior to flocculation (entanglement size δ and configuration); bridging is governed by factors in PEO dissolution unit[5] to satisfy the condition $\delta > 2\kappa^{-1}$.[5, 25] PEO entanglements usually form in early dissolution of PEO granules in water as clear solution,[38] and prepared since larger entanglement is more efficient to bridge particles.[5, 37] Another bridging mechanism is the asymmetric bridging where PEO is used alone with no cofactor. Here PEO adsorbs on one class of fines of Kraft pulp, which acquires the ability to adsorb on other fines and bridge fines with asymmetric bridging mechanism.[8, 26] Abdallah/ Qasaimeh, M.R. et al.[27] studied fines flocculation with PEO alone and with CF-PEO and found several enhancements to flocculation efficiency and to floc sizes with CF-PEO combination; similar results were found in another work [16]. In kinetic view, the fines flocculation using CF-PEO was found applying to Langmuir equation and Smoluchowski isotherm with a rate constant $k_0 (= \frac{4}{3} G_p (a_1 + a_2)^3)$, defined as a collision rate between two spherical particles of radii (a_1) and (a_2) in unit volume at process shear rate (G_p).[5] In fines deposition on a fiber (heteroflocculation) using a polymeric retention aid, the deposition time of fines on fibers (in a unit volume) with dominant attractive van der Waals forces is defined as $t_d (= \frac{1}{\eta\ k_o\ n_{fno}\ N_f})$. Here, (n_{fno}) is the initial number of fines in the suspension divided by maximum number that can deposit on fibers; (N_f) is fibers number; $\eta (= \alpha\ \beta_{fast})$ is deposition (flocculation) efficiency; (α) is capture efficiency; and (β_{fast}) is fast collision efficiency. Similarly, is fines flocculation (homoflocculation) at same micro forces conditions. Fines of radius ( ) will have the rate constant $k_0 = \frac{16}{3} G_p a^3$,[5, 28] and for initial number of fines in a unit volume ( ) and flocculation efficiency η, the time needed to reduce fines number by one half at equilibrium is

half time $t_{1/2}$ $(= \frac{1}{\eta\, k_o\, n})$ based on Smoluchowski theory.[5, 49, and 50] In this work, we ran experiments at constant G_p, constant room temperature (T), constant PEO addition, and flocculation parameters were taken at initial flocculation initial deflocculation after equilibrium, where flocculation rate (r_f) and deflocculation rate (r_d) were measured experimentally. To understand more the PEO induced bridging, we compare its features with ionic bridging features using polyelectrolytes and find the differences. One feature of PEO induced bridging is adsorption of the negative CF-PEO complex on the negative fines, and bridging dependence on the complex expansion, stiffness, and enthalpy reduction into adsorption zone on surfaces,[24] while ionic bridging depends on different charges and on the magnitude of charge differences.[30-34] Second feature is polymer configuration and chain charges. The CF-PEO induced bridging is affected by complex shape and a size that should satisfy $\delta_x > 2\kappa^{-1}$, while optimum performances are at optimum values of factors in PEO preparation and flocculation process. In other hand, ionic bridging is affected by polymer coil configuration, chain charges, and radius of gyration, which varies at various pH levels and affect flocculation rate, efficiency, and floc size,[30, 31] while optimum performances occur below and above the isoelectric point of the flocculants used.[31] Third feature is flocculation efficiency under the effects of hydrodynamic shear rate G_p and colloidal forces. In general, flocculation efficiency η is the ratio of the successful collisions rate (k_{att}) to the total collision rate k_0. In case of no ionic forces, flocculation efficiency equals to collision efficiency (β) and $\eta (= k_{att}/k_o = \beta)$. In case of attractive van der Waals ionic forces, collision efficiency becomes fast (β_{fast}) and $\eta = \beta_{fast}$. In case of repulsive or attractive forces rather than van der Waals, flocculation efficiency $\eta (= \alpha\beta_{fast})$ becomes a function of capture efficiency (α).[35] In CF-PEO induced bridging with $\delta_x > 2\kappa^{-1}$, the effects of electrostatic forces will eliminate except attractive van der Waals, and particles will bridge with $\alpha = 2\theta(1-\theta)$.[36] In general, the attachment rate constant is defined by $k_{att} = \eta\, k_o$ and η value is the case it applies.[35] In flocculation process using the CF-PEO retention aid, the factors affecting flocculation efficiency η were former and process factors. The following former factors: stirring rate and time of PEO granules, PEO concentration, storage time, and delivery shear rate after storage were investigated and found in PEO preparation and delivery units.[5, 37] Increases in former

factor magnitudes caused a decrease in the efficiency η,[5, 37] ascribed to PEO entanglement dissociation into free coils, smaller sizes, and changes in PEO coil configurations.[5]

In other hand, process factors have additional effects to former factors. One process factor is particle type such as fines and fibers, which more likely form aggregates and flocs in water.[39-42] The second is particle concentration (Consistency C) that determines the free spaces among particles, where fiber concentrations higher than the critical fiber concentration (CFC)[4] allow fibers to rotate, collide, and flocculate. The third is PEO quantity Γ used in term of fractional coverage θ,[5, 36] which is a parameter of flocculation efficiency.[38] The fourth is process shear rate G_p, which has a role in particle collisions, attachment, and detachment rate constants. For more, one work claimed formation fiber flocs after a reduction in G_p.[10, 11] In previous work, increases in stirring rate caused flocculation rate r_f, flocculation amplitude (floc size A), and characteristic time of flocculation (τ) to decrease.[43] The fifth is CF addition C_{CF} with respect to fines mass indicates the CF concentration in suspension. The sixth is CF to PEO ratio, a factor indicating the negative charge density (r_{ch}) of CF segment on PEO coils. Usage of CF with PEO showed better performance in flocculation and particle retention.[18-20] Abdallah/ Qasaimeh, M.R. et al.[27] compared fines flocculation using PEO alone with flocculation using CF-PEO and found that flocculation efficiency and floc sizes were enhanced several times with CF usage. Similar results were found in a second work.[16] One important common feature of particle flocculation with PEO alone and with CF-PEO is deflocculation of resulted flocs (transient flocculation). We and some workers in literature reported this behavior.[5, 16, and 44] We recorded the rate r_d and characteristic time of deflocculation (τ_d) when PEO was used alone in asymmetric flocculation, and when CF was used with PEO. In both cases, we ascribed deflocculation cause to PEO and found that increases in CF caused the rates r_f and r_d to increase.[16] In other work, increases in CF addition at constant PEO and moderate C_{CF} values caused increases in A, r_f, and r_d and decreases in τ, confirming CF enhancement to flocculation and deflocculation.[43] Based on Langmuir equation ($r_f = r_{att} - r_{\det}$), where (r_{att}) is the rate of particle attachment and $(r_{\det})$ is the rate of floc detachment, flocs increase with time during flocculation and plateaus at equilibrium ($r_{att} = r_{\det}$), but deflocculation with rate r_d is a contradiction to Langmuir equation.[16, 44] Based on the reported results of flocculation and

deflocculation and on their significant factors in literature, we are looking to study these factors and their effects. In this work, the objectives are to investigate the roles of CF addition C_{CF} on flocculation and deflocculation in a wide range of C_{CF} including excessive additions. Results of this work are expected to explore CF role, CF-PEO induced bridging, guide to future studies on PEO entanglement instability and explore other process factor effects.

2- Materials and Methods

2.1 Materials

The materials were the same used in previous works.[5, 16] Different CF additions C_{CF} (mg/gmfines) at constant PEO (0.08 mg/gm-fines) were added to 0.1% consistency (C) of fines in all runs. The fines were obtained after disintegration and washing of different pulps from Masson Maclaren Mill (Canada). The neutral PEO of 7 million molecular weight (Flocc 999) and the negative phenol material cofactor (Interac 1323) were supplied by I.Q.U.I.P Inc, Canada.[5,16]

2.2 Experimental Setup

This setup is the same used in previous works.[5, 16, 27, 37, and 45] Fines were added to flocculation beaker and flocculation runs were performed at different C_{CF} values. The following parameters: PEO addition, C, Γ, G_p, N, T, and tube shear rate (G_t) were kept constants in all runs, while first run was performed using PEO alone (asymmetric flocculation) and no cofactor $(C_{CF_o}=0)$. The G_t was the shear rate subjected on the fines stream from the beaker passing the transparent tube into the Photometric Dispersion Analyzer (PDA) photo cell to measure flocculation intensity.[46, 47] Amplitude A, flocculation rate r_f, characteristic time of flocculation τ, deflocculation rate r_d, and characteristic time of deflocculation τ_d were estimated in all runs.

.

2.3 Flocculation and Deflocculation Intensity Readings

In each flocculation run, the main PDA output signal, the ratio reading (R) denoting the particle size A [46, 47] was plotted versus the time (t) by a recorder. After the initial steady state of the fines in the beaker, CF followed with PEO was added to the fines and the reading R started to increase with time t, reached maximum at equilibrium, and then started to decrease showing

deflocculation. The resulted curve (Figure 2) shows the maximum R reading (maximum floc size A_m) in arbitrary unit (A.U.) and flocculation and deflocccculation parameters can be measured or estimated experimentally. Initial rate of flocculation $r_f\ (=A_m/\tau)$ in A.U. was the slope of the curve at initial flocculation,[5] where (τ) was the characteristic time of flocculation, the time needed to reach amplitude A_m with the initial rate r_f.[5] The time needed to reach

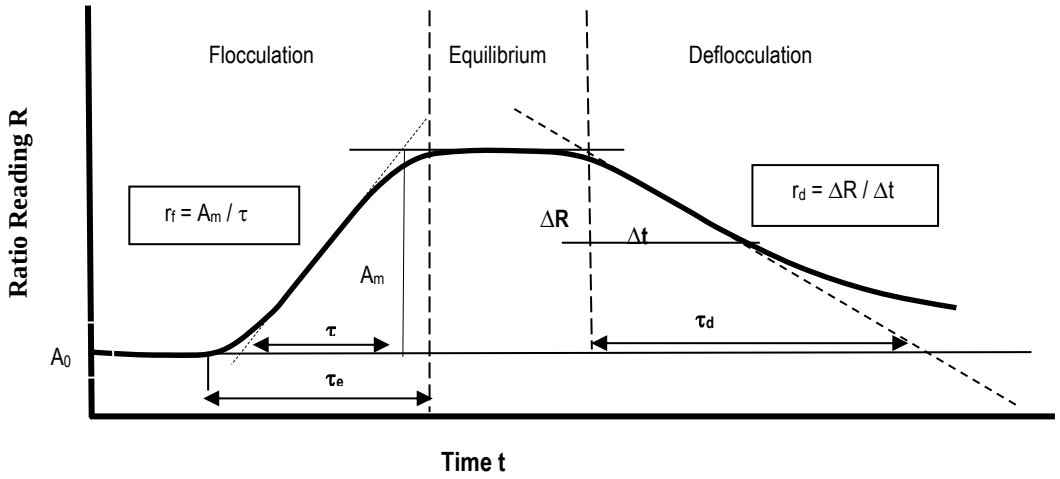


Figure 2 Flocculation and deflocculation intensity readings

equilibrium was equilibrium time (τ_e). The slope of the curve at initial deflocculation was the initial rate of deflocculation $r_d(=A_m/\tau_d)$.[16] The time needed to drop to initial floc size after equilibrium (A_m) with initial rate r_d was the characteristic time of deflocculation (τ_d).[16] The used measuring devices differ between labs in research, but flocculation and deflocculation characteristics remain same, so we evaluated the parameters relative to reference values. So a parameter of value X is related to its optimum value X_{opt} as a relative value $X_r\ (=X/X_{opt})$.

3- Results and Discussion

Number of factors affecting flocculation of fines is mentioned in literature. In this work we chose cofactor role and the effect its quantity C_{CF} on flocculation and deflocculation. Based on our and other previous work on fines flocculation with PEO in literature, showing the necessity of CF addition

with PEO, unwanted results,[5, 16, and 43] and production small flocs at high and excessive C_{CF},[44] we performed in this work number of flocculation runs of fines at different values of C_{CF} in a wide total range $TR\,(=0<C_{CF}<1.2)$. Important parameters in fines flocculation and in deflocculation were found variable with the increase in C_{CF} in TR, and based on the same

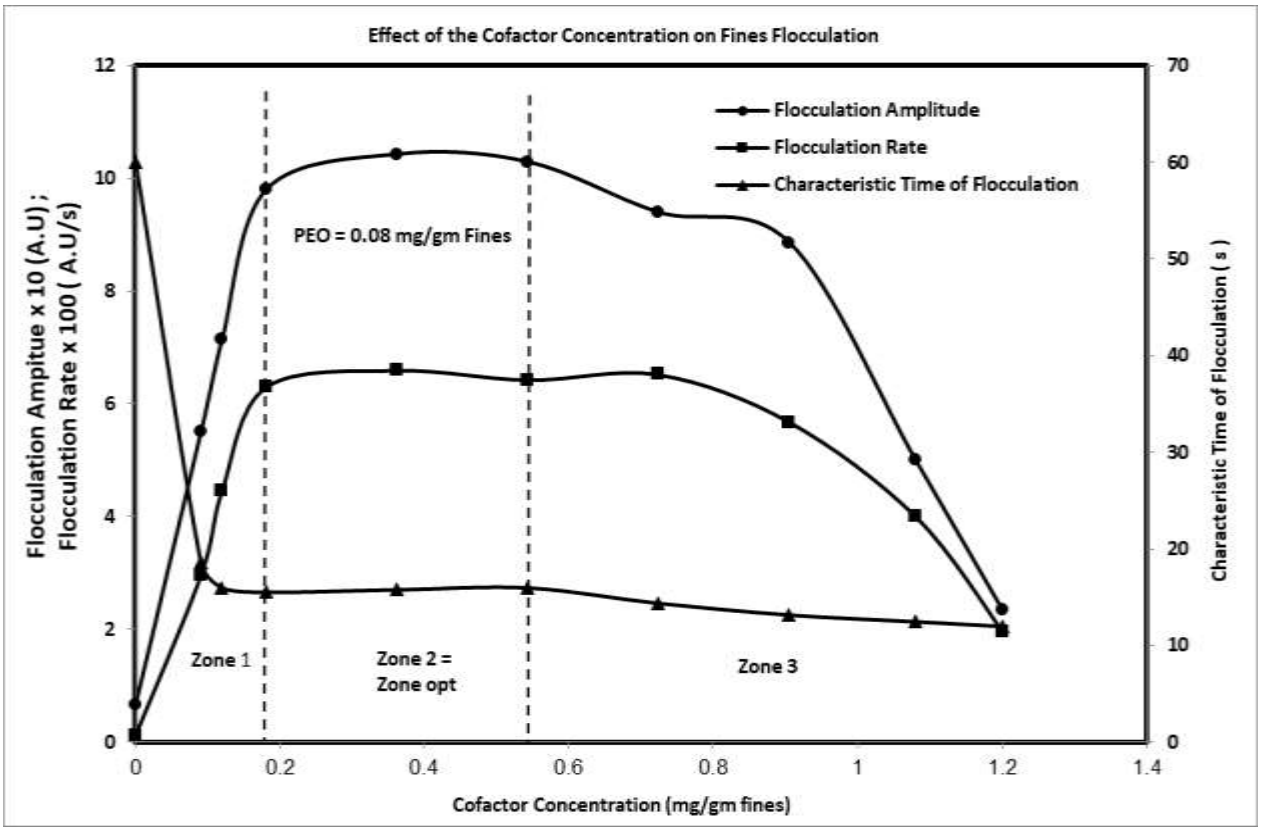


Figure 3 The effect of cofactor concentration on flocculation parameters.

parameter behaviors, this variation divided TR into small zones (Z). These zones were $Z_1\,(=0<C_{CF}<0.18)$, $Z_2\,(=0.18<C_{CF}<0.55)$, $Z_3\,(=0.55<C_{CF}<1.2)$. In flocculation

(Figure 3) and for all runs in TR, the parameters A, r_f, and τ show the following results with

increases in C_{CF}. Floc size A and flocculation rate r_f are significantly increasing in Z_1

(acceleration zone) and reach maximum at C_{CF} = 0.18. The characteristic time τ is drastically

dropping showing fast flocculation, and reaches minimum at C_{CF} = 0.18. In Z_2, the optimum zone (Z_{opt}), the parameters have optimum values (Figure 3) denoted by $A(=A_{opt})$, $r_f(=r_{f\,opt})$ and $\tau(=\tau_{opt})$. In Z_3 (the excessive CF addition zone), the parameters A, r_f, and τ started to decrease with production of small flocs and faster flocculation. These results are in agreement with results by Meng R.Wu and van de Ven.[44] For first run (at C_{CF_o}), the process is asymmetric bridging and smaller flocs and lower r_f are obtained compared with all runs of CF- PEO induced bridging. Deflocculation is also recorded with the increase in ϕ in all runs, showing varied values of r_d, and τ_d, which are in agreement with results of other work.[5, 16, and 43] For changes in CF additions in all runs in TR, we have expressed the values of flocculation parameters in relative forms. We also defined flocculation speed in term of flocculation rate constant $k(=1/\tau)$, where τ is measured experimentally as shown in figure 2. In optimum zone Z_{opt}, flocculation rate constant will be optimum $k_{opt}(=1/\tau_{opt})$. We also defined relative flocculation rate constant $k_r=(k/k_{opt})$ as the rate constant of a run relative to the rate constant at optimum value, giving $k_{r\,opt}(=1)$ in Z_{opt}. Now for a number of flocculation runs using different CF additions C_{CF}, same fines, same retention aids, and keeping C, Γ, G_p, N, T, and G_t constants, the relative k_r for a run at C_{CF} will be $k_r=\frac{k}{k_{opt}}=\frac{\tau_{opt}}{\tau}=\frac{t_{1/2\,opt}}{t_{1/2}}=\frac{(1/\eta\,k_o\,n)_{opt}}{(1/\eta\,k_o\,n)}=\frac{\eta\,n}{\eta_{opt}\,n_{opt}}=\eta_r\,n_r$; where η_r is relative flocculation efficiency and n_r is relative number of particles. Similarly for a run at C_{CF}, the relative floc size for a run is $A_r=(A/A_{opt})$ and $A_{r\,opt}(=1)$ in Z_{opt}.

In this work, we have plotted flocculation size and flocculation rate constant (Figure 4) in relative values as functions of C_{CF}. For first run at C_{CF_o}, $A_r=A_{r0}=0.064$; in Z_1 and Z_3, $A_r<1$; in Z_{opt}, $A_r=A_{r\,opt}=1$; and at $C_{CF}=1.2$, $A_r=0.225$. Similarly is for k_r, n_r, η_r. For first run at C_{CF_o}, $k_{r0}(=0.262)$; for zones Z_1 and Z_3, $k_r=\eta_r\,n_r$; and for zone Z_{opt}, $k_{r\,opt}=\eta_{r\,opt}=1$. For more, we have defined magnification (M) of a parameter as the ratio of its value at two different

runs or cases. Referred to CF role in expanding PEO entanglement to induce PEO bridging, and the effect of excessive CF addition (high C_{CF}) on flocs size, these effects (Figure 4) are likely indicating similar effects on the size of the CF-PEO complex as well. The maximum

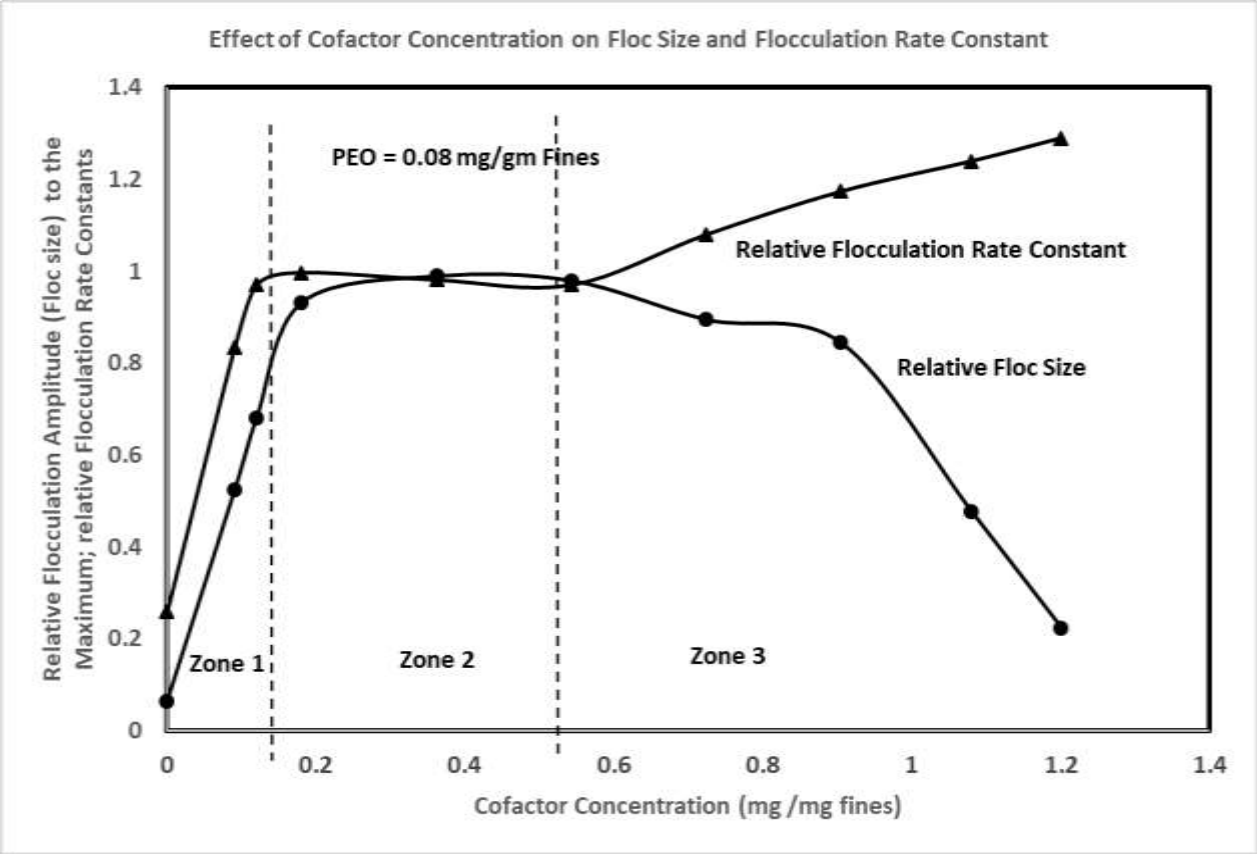


Figure 4 Effect of cofactor concentration on relative floc size and relative flocculation rate constants.

flocs size shown in Z_{opt} is also corresponding to the maximum CF-PEO complex size. These sizes can be expressed in term of magnification, which is most often related to first run where PEO alone was used with no CF addition. One important case is the size magnification of a floc in first run by CF-PEO usage in Z_{opt} (Figure 4) giving $M_{Aopt} = A_{ropt} / A_{r0} = 15.63$. This CF-PEO magnification in Z_{opt} is most likely the image of PEO entanglement size magnification at C_{CFo}. One important result in Z_3 is the relative floc size at $C_{CF} = 1.2$ ($A_r = 0.225$), which has a value larger than the floc size at C_{CFo} ($A_{r0} = 0.064$) and magnification $M_A = 0.225/0.064 = 3.52$. This value indicates that flocculation continues at CF additions larger than $C_{CF} = 1.2$ giving smaller

flocs. In general, floc size magnification in TR are $M_{Aopt}=15.63$ for Z_{opt} and $1<M_A<15.63$ for Z_1 and Z_3. Magnifications at larger CF additions $(C_{CF}>1.2)$ can be studied in future work.

Similarly, we have found the magnification of flocculation rate constant using $M_k\ (=k_r/k_{r0})$ and data from figure (5). In Z_{opt} and with using optimum CF addition, magnification of flocculation rate constant will be $M_k(=1/0.262)=3.82$. In Z_3, flocculation rate constant increases significantly with C_{CF} increase, and at $C_{CF}=1.2$ magnification becomes $M_k\ (=1.31/0.262)=5$.

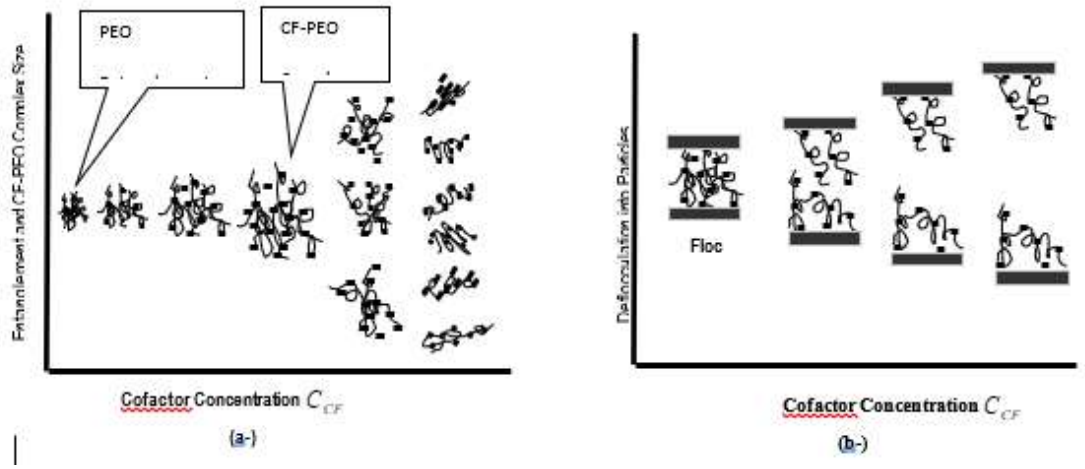


Figure 5 Effect of high cofactor concentration C_{CF} on: (a-) CF-PEO complex size and (b-) deflocculation.

Now from resulted data, increases and decreases in floc size as a function of C_{CF} shown by A_r and M_A are in agreement with decreases and increases in the sizes of floc and complex resulted by Meng. et al..[44] For more, flocs formation and increases in their sizes are ascribed to PEO entanglement expansion due to the increase in the induced repulsion forces by CF segments adsorbed on PEO coils.[24] In this work smaller flocs were resulted at excessive CF addition (high C_{CF}) in Z_3 and in [44] smaller complexes were resulted at high C_{CF}. These two results (Figure 5 a) indicate the PEO entanglement dissociation in suspension ascribed to the decrease in the transient interaction forces among PEO coils,[16] enhanced by repulsion forces increase induced

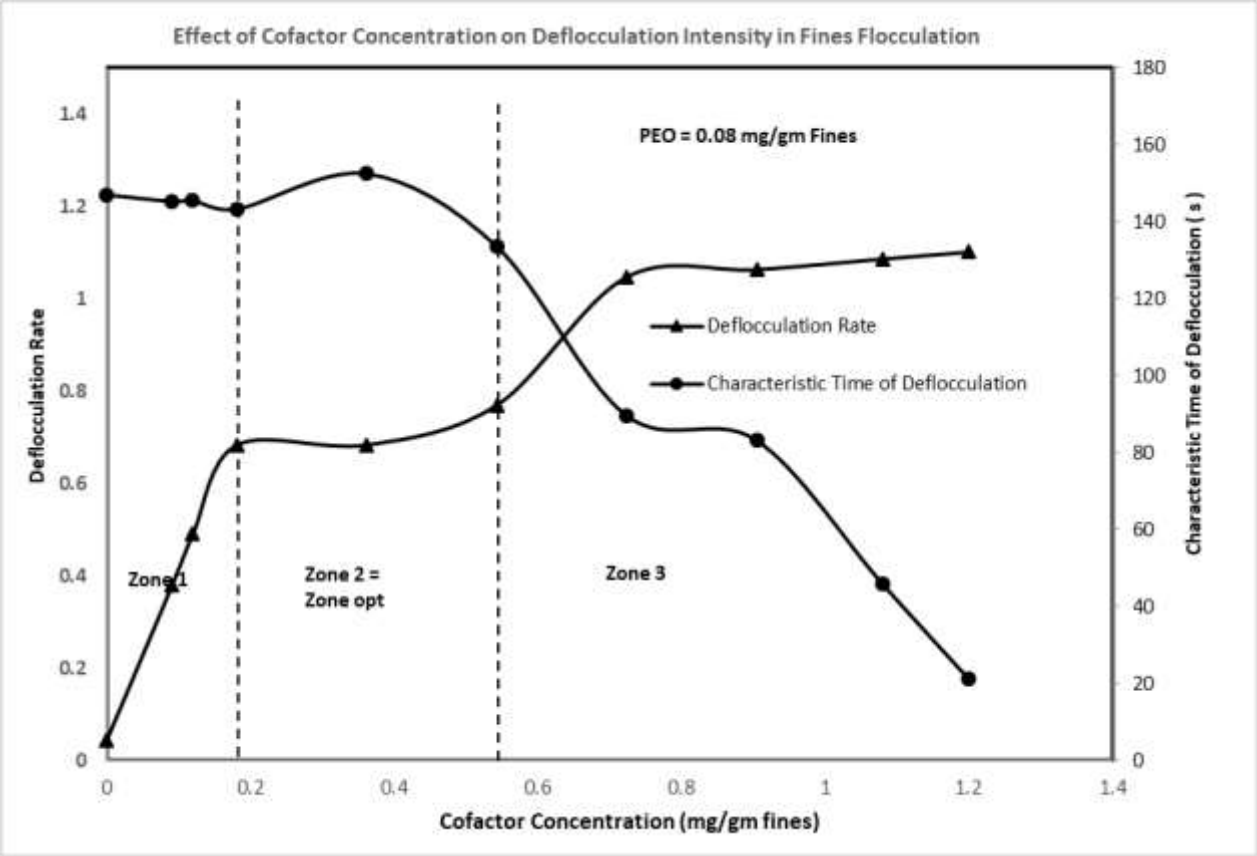


Figure 6 Effect of cofactor concentration on deflocculation dynamics in fines flocculation

by CF segments adsorbed on PEO coils. These resulted small complexes are rich in the adsorbed CF on PEO coils that bridge small fines to produce small flocs. In addition to flocculation, deflocculation has been studied as a function of C_{CF} in TR and both flocculation and deflocculation occurred in the same run having same amplitude. At low CF concentrations in Z_1 and with increases in C_{CF}, results (Figure 6) show significant increase in r_d with slight decrease in τ_d. In optimum zone Z_{opt}, both r_d and τ_d level with increases in C_{CF}. In Z_3, deflocculation rate r_d increases significantly with increases in C_{CF}, while τ_d decreases drastically with increases in C_{CF}. These results (Figure 6) agree with other work in literature, Meng. et al.,[44] and our work.[16] Deflocculation is resulted (Figure 5b) in a manner seemingly similar to CF-PEO complex dissociation in suspension at high C_{CF}, but with some additional repulsion forces coming from the negative fines in a floc. The deflocculated fines are proposed to separate with some CF-PEO complexes flattened on their surfaces.[9, 24, 51, 52] Now, results in this work confirm that deflocculation cause is the transient interacting forces decreasing with time in PEO entanglement in floc. The CF action after adsorption on PEO coils occurs in a number of stages; first it induces repulsion forces among the PEO coils expanding the entanglement. It then induces bridging in flocculation producing flocs. In a floc, the induced repulsion

forces act to add to the decreasing interacting PEO coils along with repulsion among fines, enhancing deflocculation. Similarly at a definite C_{CF}, we have expressed the deflocculation parameters as following: deflocculation dynamic speed as deflocculation rate constant by $k_d\ (=\frac{1}{\tau_d})$; its value relative to optimum value by $k_{d\,r}\ (=\frac{k_d}{k_{d\,opt}}=\frac{\tau_{d\,opt}}{\tau_d})$; and reverse equilibrium rate constant (R_d), the ratio of deflocculation rate constant to flocculation rate constant, by $R_d\ (=\frac{k_d}{k})=\frac{\tau}{\tau_d}=\frac{r_d}{r_f}$ using $k\ (=\frac{1}{\tau})$. We have plotted r_f, r_d, and R_d versus C_{CF} in TR. In all runs at different C_{CF}, the parameter values (Figure 7) can be analyzed by R_d values since R_d is a ratio of deflocculation to flocculation values of these parameters. Results (Figure 7) show R_d values are varying with increases in C_{CF}. At C_{CFo} where PEO is functioning alone, $R_d\ (=0.408)$ has a higher value than its values at small CF additions in Z_1, where R_d is decreasing with increases in C_{CF} that indicate higher deflocculation speed in asymmetric flocculation. In Z_{opt} and with increases in C_{CF}, R_d has a constant minimum value $(R_{d\,opt}=0.11)$, showing a lowest deflocculation speed. In Z_3, values of R_d start to increase drastically with increases in C_{CF} to have the highest value $R_d\ (=0.562)$ at $C_{CF}=1.2$, indicating faster deflocculation in total range TR. As a result, increases in CF addition, C_{CF} is found (Figures 6 and 7) enhancing to deflocculation, whose cause is ascribed to the transient state of PEO coils that confirms results in [16]. For mills, to

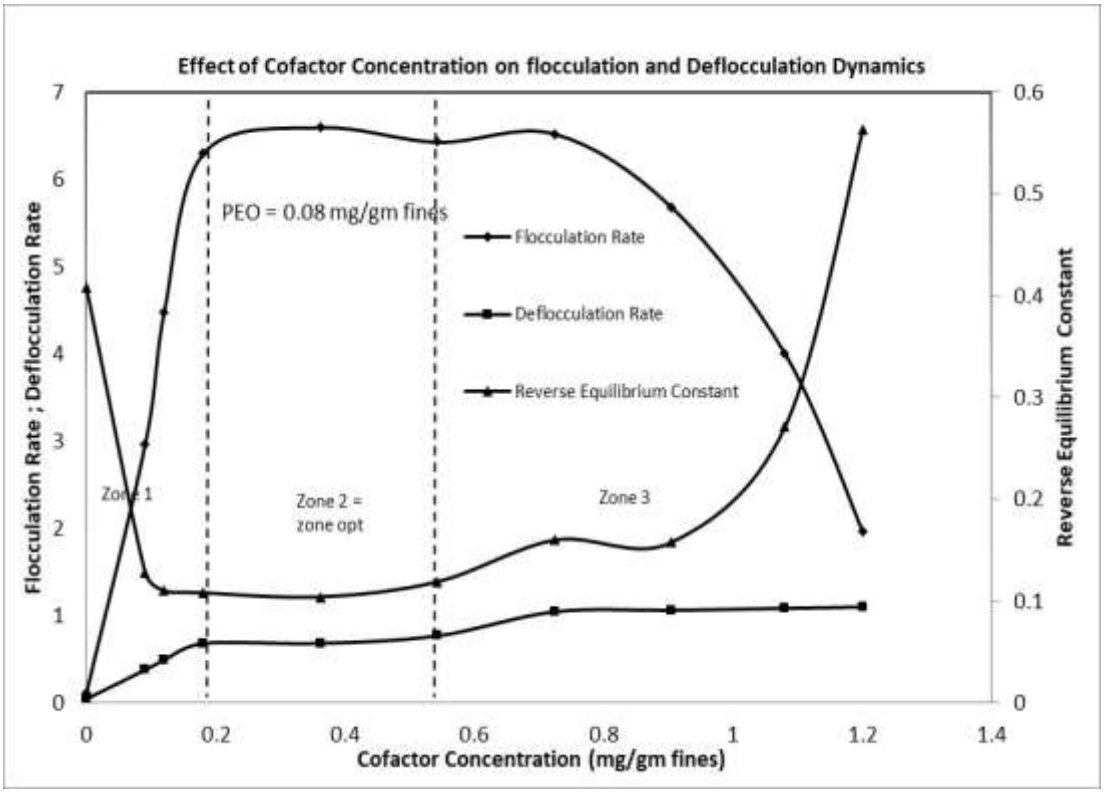


Figure 7 Effect of cofactor concentration C_{CF} on reverse equilibrium constant, the ratio of the deflocculation rate constant to flocculation rate constant.

minimize deflocculation effect and to enhance flocculation, selection of suitable CF additions C_{CF} and knowledge of equilibrium time τ_e, maximum floc size A_m, and operation cost are needed to characterize flocculation process. One characterization method we proposed in previous work,[48] and mill operators can establish a suitable one to optimize their process performance. Another important result in this work is having parameter values, mainly floc size, flocculation and deflocculation rate constants, and reverse equilibrium constant in wide range of CF addition that gives more liable choices in practical operations to choose the CF addition satisfying the requirements.

4- Conclusion

In this work, we have confirmed the CF role in PEO entanglement expansion, production of larger CF-PEO complexes, bridging of fines and flocculation enhancement. We also investigated the role of CF addition at constant PEO in a wide range of CF additions and subdivided the flocculation and deflocculation parameter results in subzones based on similar behaviors. We have proposed relative floc size and investigated the flocculation and deflocculation dynamic speeds in terms of rate constants in a wide range of CF additions. We have found the values of flocculation and deflocculation parameters at small, moderate, and high CF additions in a wide range. These

parameter values have given more liable conditions and choices to perform the wanted operation in optimum performance and avoid the negative operating effects in mills.

Acknowledgment

1. I like to acknowledge Pulp and Paper Research Center/McGill, where these experiments were performed.
2. Dr. van de Ven T.G.M. and Dr. Paris j. for valuable discussions 3- Maclaren Masson Mill and E.QU.I.P Inc for material supply.

References

1. Brecht, W. and Klemm, K. The Mixture of Structures in a Mechanical Pulp as a Key to Knowledge of its Technological Properties, *Pulp Paper Mag. Can.* **1953**, 54(1), 72-80.
2. Norman, B. Papermaking Science and Technology Book 8, Chapter 6, H. Paulapuro (ed.), Fapet, Finland **2008.**
3. Hubbe, M. A., and Wang, F. Where to ad0d retention aid: Issues of time and shear, *Tappi. J.* **2002,** 1(3), 28-33.
4. Hubbe. Flocculation of cellulose fibers, *BioResources* **2007** 2(2), 296-331
5. Abdallah, Mohammad. R. *PhD Thesis,* Chemical Engineering Department, McGill University. Montreal, Canada **2002.**
6. Casey, *J.P. Pulp and Paper Chemistry and Chemical Technology,* 3rd edn., Wiley Interscience, New York, **1979,** P.1593-1607.
7. van de Ven, T.G.M. Particle Deposition on Pulp Fibers, *Nordic Pulp and Paper Research Journal,* **1993,** no.1, P.130-134.
8. Carignan, A., Garnier.G. and van de Ven, T.G.M. The Flocculation of Fines by PEO Cofactor Retention Aid Systems, *J.Pulp and Paper Science,* **1998,** Vol. 24, No.3, P.94-99.
9. van de Ven, T.G.M. Kinetic Aspects of Polymer and Polyelectrolyte Adsorption on Surfaces, *Adv. Colloid Inter. Sci.*, **1994,** 48, P.121-140.
10. Jacquelin, G. Improvement in or Relating to the Method of and Apparatus for Testing Suspensions of Fibers for the Formation of Aggregates, *UK Pat.1*, **1968,** 109, 895.
11. Bjorkman. Break-up of Suspended Fiber Networks, *Nordic Pulp Paper Res.J.* **2003,** 18, 1, P 32-37.
12. Healy, T. W. and La Mer, V.K. The Energetics of Flocculation Redispersion of Polymers, *J Colloid Sci.* **1964**, 19, 4, P 323-332.
13. Spicer, T. P. and Pratsinis, S. E. Sheared Induced Flocculation: The Evolution of Floc Structure and the Shape of the Size Distribution at Steady State, *Water Res.* **1996**, 30, 5, P 10491056.
14. Klomogorov A. N. (1949): On the Breakup of Droplets in Turbulent Flow, *Doklay Akad.*

15. *Nauk SSSR.* **1949**, 66, 5, P 825-828.
16. Higashitani, K., Inada, N. and Ochi, T. Floc Breakup in Contraction Flow to Orifice, Presented at *AICHE Ann.Mtg.*, San Francisco, **1989**.
17. Abdallah Qasaimeh, M.R. (2011): Causes of Transient Flocculation of Fines with Polyethylene Oxide and a Cofactor: Implications for Mill Performance, *Colloids and Surfaces A:*
18. *Physicochem. Eng. Aspects*, **2011,** 386, P 125–130.
19. Noemi Merayo. Ana Balea. Elena de la Fuente. A ´ngeles Blanco. Carlos Negro, Interactions between cellulose nanofibers and retention systems in flocculation of recycled fibers, *Cellulose*, **2017,** 24, P 677-692.
20. Pelton, R.H., Alen,L.H. and Nugent, H.M. Factors affecting the effectiveness of some retention aids in newsprint pulp, *Srensk pappestidn*, **1980**, 9, 251.
21. Pelton, R.H., Allen, L. and Nugent, H.M. Novel dual polymer retention aids for newsprint and ground wood specialties, *Tappi J.*, **1981,** 64, 11, P 89-92.
22. Tay, C.H. and Canley, T.A., presented at *Tappi papermakers conf.*, 1, on Studies on Polyethylene oxide as a Retention Aid in Wood Fiber Systems **1982.**
23. van de Ven, T.G.M. Mechanism of Fines and Filler Retention with PEO/Cofactor Dual Retention Aid Systems, *J.Pulp and Paper Science*, **1997**, 23, 9, P 447-451.
24. Lindström, T. and Glads-Nordmark, G. Flocculation of Latex and Cellulose Dispersion by Means of Transient Polymer Networks, *Colloids Surfaces*, **1984**, 8, 4, P 337-351.
25. Lindström, T. and Glads-Nordmark, G. Network Flocculation and Fractionation of Latex
26. Particles by Means of a Polyethyleneoxide-Phenolformaldehyde Resin Complex, *J.Colloid Interface Sci.* **1984,** 97, 1, 62.
27. van de Ven, T.G.M. and Alince, B. Association-Induced Polymer Bridging: New Insights into the Retention of Fillers with PEO, *J.Pulp Paper Sci.*, **1996,** 22, 7, P 257-263.
28. De Witt, J.A. and van de Ven, T.G.M. The effect of Neutral Polymer and Electrolyte on the Stability of Aqueous Polystyrene Latex, *Adv.Colloid Inter.Sci.* **1992,** 42, 41.
29. van de Ven, T.G.M. and Alince, B. Heteroflocculation by asymmetric polymer bridging, Journal of colloid and interface science, **1996,** 181, P 73-78.
30. Abdallah/Qasaimeh, M.R., Bani Hani, F., Dawagreh, A. M. Neutral Polyethylene Oxide with a Cofactor Recommended for Particle Flocculation, *Brazilian Journal of Chemical Engineering*, **2011,** 28, 3, P 467- 473.
31. Petlicki, J. and van de Ven, T.G.M. Sheared Induced Deposition of Colloidal Particles on Spheroids, *J. Colloid Interface Sci.* **1992,** 148, 14.
32. Varenners, S. and van de Ven, T.G.M. *PhysicoChemical Hydrodynamics* **1987,** 9, 537.
33. Zhen Yang, Bo Yuan, Xin Huang, Junyu Zhoua, Jun Caia, Hu Yang, Aimin Li, and Rongshi Cheng. Evaluation of the flocculation performance of carboxymethyl chitosan-graft-

polyacrylamide, a novel amphoteric chemically bonded composite flocculant, water research **2012,** 46, P 107-114.

34. Zhen Yang, Yabo Shang, Yaobo Lu, Yichun Chen, Xin Huang, Aimin Chen, Yuxiang Jiang, Wei Gu, Xiaozhi Qian, Hu Yang, and Rongshi Cheng. Flocculation properties of biodegradable amphoteric chitosan-based flocculants, *Chemical Engineering Journal* **2011**, 172, P 287-295. [32] Nylund, J., Lagus, O., and Eckerman, C. Character and Stability of Colloidal Substances in Mechanical Pulp suspension, *Colloids Surf. A,* **1994**, 85, 81.
35. Holmbom, B. Dissolved and Colloidal Substances in Papermaking. *Nordisk Forskarkursi Papperskemi*, Ronnige, Sweden, **1995**.
36. Swerin, A., Odberg, L., and Wagberg, L. Preparation and Some Properties of the Colloidal Pitch Fraction from a Thermomechanical Pulp, *Nord. Pulp Pap. Res. J.,* **1993,** 8, 3, 298. [35] van de Ven, T.G.M. Physicochemical and Hydrodynamic Aspects of Fines and Fillers Retention, *Mech. Eng. Publ. Ltd.*, London, **1989,** 1, 471.
37. Hogg, R. Collision Efficiency Factors for Polymer Flocculation, *J.Colloid Interface Sci.*
38. **1984,** 102, 1, P 232-236.
39. van de Ven, T.G.M., Abdallah Qasaimeh, M., Pigeon, C. and Paris, J. PEO-induced Flocculation of Fines: Effect of PEO Dissolution Conditions and Shear History, *Colloids and Surfaces A: Physicochem.Eng. Aspects,* **2004,** 248, P 151-156.
40. Kratochvil, D., Alince, B. and van de Ven, T.G.M. Flocculation of Clay Particles with Poorly and Well Dissolved Polyethylene Oxide, *J. Pulp and Paper Science*, **1999,** 25, 9, P 331-335. [39] Wasser, R.B. Formation aids for paper – An evaluation of chemical additives for dispersing long fibered pulps, *Tappi*, **1978,** 61, 11, P 115-118.
41. Kerekes, R. J. Rheology of fibre suspensions in papermaking: An overview of recent research, *Nord. Pulp Pap Res. J.*, **2006,** 21, 5, P 598-612.
42. Yan, H., and Norman, B. (2006a): Fibre floc behaviour of softwood kraft pulp in flowing suspensions, Nord. Pulp Pap Res. J. 21(1), 24-29.
43. Yan, H., Lindström, T., and Christiernin, M. Fibre length effect on fibre suspension flocculation and sheet formation," *Nord. Pulp Pap Res. J.*, **2006b,** 21, 1, P 30-35.
44. Abdallah/Qasaimeh, M. R., Qasaimeh, Ahmad. and Bani Hani, F. Factors Affecting Fines Flocculation Performance with Cofactor-Polyethylene Oxide, to appear: *Advances in Chemical Engineering and Science (ACES),* **2014,** 4, 1.
45. Meng R.Wu. and van de Ven, T.G.M. Flocculation and Reflocculation: Interplay Between the Adsorption Behavior of the Components of a Dual Flocculant, *Colloids and Surfaces A:Physicochem. Eng. Aspects.*, **2009,** 341, P 40-45.
46. Abdallah Qasaimeh, Mohammad., Bani Hani, Falah., Dawagreh, Abdulkareem., and Ajlouni, Khloud. Neutral Polyethylene Oxide with a Cofactor Recommended for Particle Flocculation,

presented at Zarqa Scientific and Engineering Conference-2, 24-26 Nov, Zarqa Ahli University, Zarqa, Jordan, **2010**.

47. Gregory, J. Turbidity fluctuations in flowing suspensions, *J.colloid Interface Sci., Interface Sci.*, **1984,** 102, 1, P 232-236.
48. Rank Brothers Ltd., Photometric Dispersion Analyzer PDA 2000, Operating Manual., High Street, Bottisham, Cambridge CB5 9DA, England, Telephone (0223) 811369.
49. Abdallah/Qasaimeh, Mohammad. R. Characteristics of Floc: Interplay between Retention Aid and Hydrodynamic Forces Effects in Fines Flocculation, presented at the sixth Jordan
50. International Chemical Engineering Conference (JIChEC06), Holiday Inn Hotel, Amman - Jordan, march 12-14, **2012**.
51. Roger Gaudreault Nicolas Di Cesarea, David Weitzc, Theo G.M. van de Ven. Flocculation kinetics of precipitated calcium carbonate, *Colloids and Surfaces A: Physicochem. Eng. Aspects*, **2009,** 340, P 56–65.
52. B. Alince. Cationic latex as a multifunctional papermaking wet end additive, *Tappi J.* **1999,** 82, 3, P 175-187.
53. Carignan, A., The Influence of Cofactor on the Flocculation Behavior of Polyethylene Oxide, *M. Eng. Thesis*, McGill university, Montreal, Canada, **1996.**
54. Stack, K.R., Dunn, L.A., and Roberts, N.K., Study of the Interaction Between Poly(Ethylene Oxide) and Phenolformaldehyde Resin, *Colloids Surfaces*, **1991**, 61, P 205-218.

Removal of heavy metals contaminants from wastewater using petroleum coke bottom ash

Batoul Rhamtalla *

Department of Chemical Engineering, University of Khartoum

**Corresponding author: batuolnana555@gmail.com*

Abstract: Low cost adsorbent (Petroleum Coke Bottom Ash) was tested for removal of chromium (III) from tannery effluents. All the experiments were carried out in batch process. Influences of adsorbent dosage, contact time, adsorbent particle size, pH and temperature on removal of chromium from effluent was investigated. The adsorption data were tested well by Langmuir isotherm. The maximum removal of Cr (III) was observed at 5g adsorbent dose, 120 minutes of contact time, 150-micrometer particles size, 30 ^{o}C and pH 10. The results indicate that Petroleum Coke Bottom Ash can be used for the removal of chromium (III).

Keywords: tannery effluent; petroleum coke bottom ash; adsorption

Theme 6: Energy First: Renewable Energy and Conventional Resources for Chemical Industries

A Case for Microbial Fuel Cell as Sustainable Wastewater Treatment Technology with Co-Generation of Electricity: A Saudi Arabia Perspective

Nuhu Dalhat Mu'azu *

Department of Environmental Engineering, College of Engineering, Imam Abdulrahman Bin Faisal University, P.O Box 1982 Dammam, 31451, Saudi Arabia

**Corresponding author: nmdalhat@iau.edu.sa; cell: +966507532689*

Abstract: Geographically, Kingdom of Saudi Arabia (KSA) and other GCC countries are amongst nations located in arid region characterized by limited renewable fresh water supplies, acute rainfall scarcity and high temperatures. KSA rely mainly on non-renewable fossils groundwater and energy intensive seawater desalination to meet water their demands. Due to the huge market of desalination compared to other countries, significant portion of KSA energy reserve goes for operating desalination plants. This is worsened by the huge amount needed for operating several waste and wastewater treatment plant across the Kingdom, thereby depleting available funds for maintaining public services. The enormous infrastructural development underway and high population and improved living standard result in ever increasing demands for water and energy (W&E). These necessitate radical change towards adoption of alternative sustainable W&E management strategy for successful achievement of environmental sustainability policy enshrined in VISION 2030. Thus, coupling recycling of huge volume of treated wastewater effluents and tapping alternative energy sources are of paramount importance. Thus, recycling of huge volume of treated wastewater effluents and tapping alternative energy sources are of paramount importance. Considering that the organic material in the wastewater is sources of harvestable bio-energy which can be directly tapped using microbial fuel cell (MFC) technologies while treating the wastewater for various recycle reuse purposes. This approach could reduce complete reliance on conventional energy and water sources with less environmental impacts possessing potentials of upsetting future demands. This paper presents the relevance and case for exploring the MFC technologies for potential use in simultaneous treatment of municipal wastewater and generation of electrical energy in KSA. Currently, MFCs are one of the identified future technologies that have great potential in addressing the water-energy nexus problem in sustainable manner globally. Thus the merits of establishing MFCs technology in KSA for addressing strategic sustainable solutions towards addressing water-energy nexus are explored in order to present the case of advancing MFC capabilities in relation to its associated impending challenges

1. Introduction

By the virtue of its location in hyper-arid region, the Kingdom of Saudi Arabia (KSA) is known to be one of the countries challenged by source of freshwater. This necessitates it major reliance brackish groundwater and exorbitant energy demanding seawater desalination, thereby, depleting the country's major source of revenue, significantly. The current enormous infrastructural development, high population and improved living standard result in ever increasing demands for water and energy (W&E)

calls for significant change in approach to water and energy management strategies. Sustainable development of the KSA no doubt necessitates immediate adoption of policies that support shifting

from traditional complete dependency on non-renewable water supplies and desalination technology for meeting long term demands as enshrined in VISION 2030. Hence, under the current KSA water and energy scenario, harnessing alternative self-sustainable and environmentally friendly technologies for energy generation and wastewater treatment for recycling and reuse has been identified as components of national integrated water management. Wastewater treatments in KSA involve excessive utilization of high amounts of energy and their operating costs are ever increasing. Considering that the organic material in the wastewater is a source of bio-energy which is harvestable is left untapped; though it can provide opportunity for generation of electricity to power the wastewater treatment plants as well as treat wastewater for various recycle reuse purposes. This approach could reduce complete reliance on conventional energy and water sources possessing potentials of upsetting future demands while ensuring less environmental impacts of wastewater management

2. Literature Review

As results of global robust economic and population growth, it is expected in near decades, the global demand for water and energy for serving all sectors will be more than doubled of the recent demand as is the case for KSA [1]. Hence, the unrelenting rapid depletion of fossil fuel resources exacerbated by the environmental concerns emitted from widespread use of fossil fuels, have raised the demand for newer, cleaner and more sustainable sources production of energy and water. Renewable bioenergy is viewed as one of the ways to alleviate the future foreseen energy crisis. Consequently, significant efforts devoted in the last few decades resulted in the emergent of alternative renewable energy production technologies for ensuring sustainable local and global development. An energy producing technology that could meet the current economic and environmental challenges in sustainable manner should be able to produce energy from renewable resources without a net emission of undesirable products is unquestionably the most desired [2, 3]. In that regard, microbial fuel cells (MFCs) technology that convert the energy stored in chemical bonds in organic (and even inorganic) compounds to electrical energy achievable through the microorganisms catalytic biodegradation reactions has received considerable interests among decision makers, industries and researchers in recent years [4-6]. Interestingly, the wastewaters that need to be treated for various reuse purpose to upset the surging domestic and industrial demands are rich in organic compounds, main substrates required for operating MFCs. As the emphasis on today's wastewater management favours environmental friendly treatment with economic energy recovery coupled with less production of wastes, MFCs technology becomes a global attractive future technology for real wastewater treatment plants. This owes to the fact that its vital characteristics render it as a potential player in addressing global water-energy nexus problems in sustainable manner.

2.1 The Microbial Fuel Cell (MFC)

MFC is a technology capable of converting the energy stored in chemical bonds in mainly organic compounds as result of microorganisms' catalytic biodegradation reactions. In doing that, the cell performs two functions simultaneously; producing power and removal of pollutant loading of the same wastewater that need to be treated. Basically, a MFC cell consists of anode, cathode, microbial consortium (attached to the anode), substrate and a conductive electrolyte. The two chambers could be separated by a proton exchange membrane (PEM) to form a dual chamber MFC. Fig. 1 shows a schematic diagram of a typical two-chamber MFC for producing electricity. MFC process involves complex biologically electrochemical reactions. Simply, the process starting from the anode chamber involves oxidation of the organic matter or the substrate by the microbial catalytic degradation under anaerobic condition releasing electrons and protons. The electrons flow to the cathode through the external electric circuit producing electrical power in form of a current. Meanwhile, in the cathode side, oxygen (or other electron acceptor) reacts with electrons and protons to produce water (or other reduced compound). Continuous electron liberations at the anode as well as its consumption for oxygen reduction at the cathode are the defining characteristics of any MFCs.

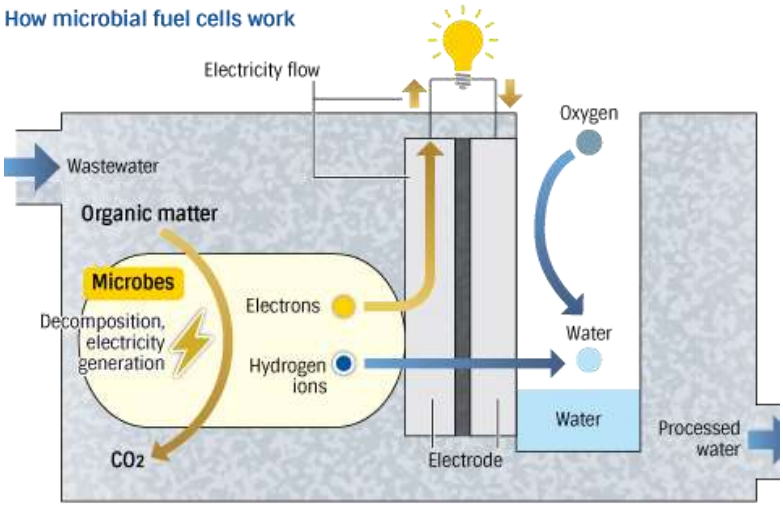


Figure 1: Schematic diagram of a typical two-chamber microbial fuel cell

2.2 Performance Evaluation of MFC Technology

Basically, the performance of MFC technology is determine by considering the two efficiency of parameters related to increase in treated wastewater effluence and efficacy in electricity generation which are calculated as follows

- ✓ *COD and BOD removal Efficiencies***:** The removal of COD and BOD as indication of the wastewater decontamination efficiency of the MFC via equation 1

$$\frac{(C_{influent} - C_{effleunt})}{C_{Influent}} \text{ x } 100\% \quad (1)$$

- ✓ *Electricity Generation Efficiency* are evaluated based on the power output in terms of the normalized power density (NPD), and also columbic and energy efficiencies calculated using equations below
- ✓ *Normalized Power Density (NPD)*: two NDP, normalized to electrode surface area or reactor volume (i.e., power divided by the anode or cathode area or reactor volume) given in equations 2 and 3, respectively, estimates the power output to enable comparisons between different MFCs experimental conditions and reactor configurations.

$$P_{electrode} = \frac{E_{cell}^2}{A_{electrode} R_{ext}}, \text{ W/m}^2 \quad (3)$$

$$P_v = \frac{E_{cell}^2}{v_{reactor} R_{ext}}, \text{ W/m}^3 \quad (4)$$

- ✓ *Columbic Efficiency, CE (ε_{cb}):* depending on the adopted MFC reactor configuration , the CE, i.e., ratio of the total actual coulombs transferred to the anode to the maximum possible, is determined according to either fed-batch mode (equation 5) via integrating the current over time or the equation for MFC continuously flow system (equation 6)

$$\varepsilon_{cb} = \frac{M \int_0^{t_b} I dt}{Fbv_{Anode} \Delta COD}, \% \quad (5)$$

$$\varepsilon_{cb} = \frac{MI}{Fbq \Delta COD} \quad (6)$$

- ✓ *Energy Efficiency (EE)* **(** ε_E **(**:EE calculated as ratio power generated power over the run time to the total heat that is generated from the substrate or organic compound given in equation 7

$$\varepsilon_E = \frac{\int_0^t E_{cell} I dt}{\Delta H m_{added}} \quad (7)$$

2.3 Challenges of Microbial Fuel Cell Technology

Although MFCs have gained global attraction as environmental sustainable technology, nevertheless, their practical implementation is challenged till date [7]. Currently, the technology is

mainly limited to laboratories owing to the scalability bottleneck that surrounds the MFC operations and quantity as well as efficacy of bioelectricity generation. This owes to major factors that limit the operational capabilities of MFCs measured in terms of columbic and pollutant loading removal efficiencies which provided in Figure 2 and discussed below

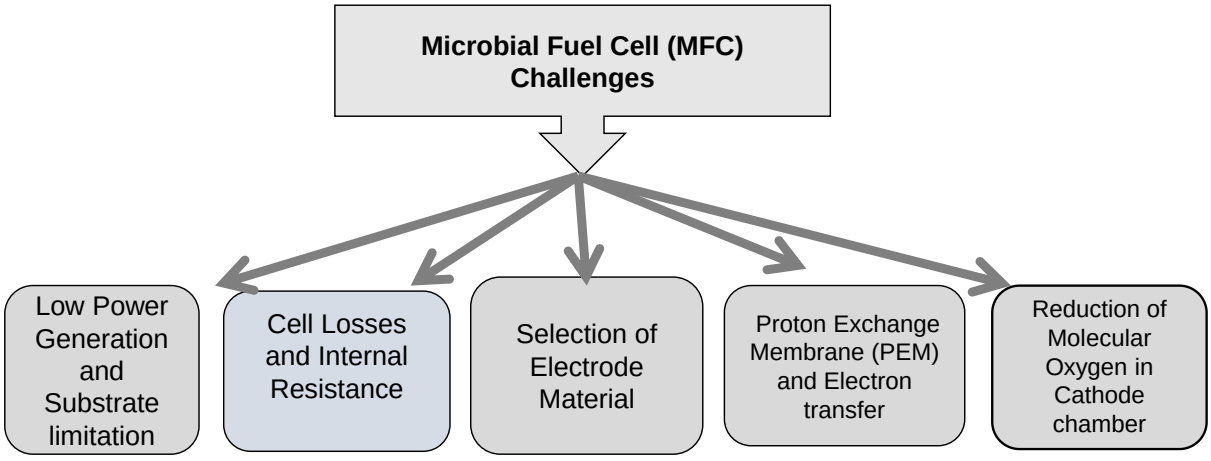


Figure 2: Technical Problems Associated with MFC technology

2.4 Low Power Generation

As the main target of MFC in wastewater treatment is mainly dual benefit of simultaneous pollution reduction/removal and power generation, the most fundamental limitation of the MFC technology is the low power generation as well as the difficulty in ensuring continuity of power generation for overall process economic viability [8]. This could be attributed to several factors such as operating conditions (ionic strength, feeding regime, HRT, substrate, pH, temperature etc.), reactor configuration, electrode material, membrane type, electrode surface area and external resistance[9]

2.5 Cell Losses and Internal Resistance

Irreversible losses that occur in a MFC due to actual cell potential always been lower than its ideal value[10] also limits the performance of MFCs. These losses are as result of three phenomena that take place within the MFC cell namely (i) activation polarization (ii)Ohmic losses and (iii) concentration polarization[10, 11].Table 1 summarizes these losses and respective ways for overcome them. These losses are collectively known to contribute to the "internal resistance" of MFC cell, a key limiting parameter that seriously challenges the energy efficacy of MFCs [12, 13]. This internal resistance is sum total of partial resistances that compose of cathode resistance, resistance for ion transport through the membrane, the anode resistance as well as the electrolyte resistance.

2.6 Electrode Material, Substrate limitation and Electron transfer

Besides getting suitable bacteria and enabling environmental for the bacteria to function well in MFC, the mechanism of electron transmission in MFC is another challenge in the viable MFC

operations. This is hevenly dependent on the selection of appropriate electrode materials as well as availability of suitable substrate in the wastewater. Most of the bacterial species used in MFCs are inactive for electron transmission and in order to overcome that shortcomings, natural and artificial chemicals (called redox mediators) such as thionine, humic acid, neutral red, methyl blue and methyl viologen are used [14]. However, as most of the available mediators are expensive and toxic, they are not attractive in MFCs for energy production [15]. Some microbes are electrochemically active, capable of accepting electrons from an external source or donating electrons to an external object such as an electrode. The availability of these microbes for MFCs eliminate the need for employing expensive or toxic mediators

2.7 Proton Exchange Membrane (PEM)

One of the limiting factors is the Proton Exchange Membrane (PEM) used in two-chamber MFCs. More, the PEM significantly controls internal resistance of the MFCs cells. As such, single chamber or membrane-less MFCs eliminates the cost prohibition of PEM and could yield better performance which renders it attractive [14, 16]. As such for dual-chamber MFC, selection of PEM is crucial. For PEM to be relevant in high energy efficient MFCs operations, it must possess low resistance to proton transfer, allow easy diffusion of oxygen diffusion couples with high bio-fouling resistance and low cost[17].

2.8 Reduction of Molecular Oxygen in Cathode chamber

In MFCs, availability of an electron acceptor is required at the cathode to accept the electrons transferred from the anode to ensure smooth and efficient operation. Molecular oxygen is identified to be the most ideal electron acceptor for MFCs due to its availability, high oxidation potential, low cost and formation of clean product i.e., water. However, for the commonly used low price cathode material (mainly graphite/carbon electrodes), oxygen reduction rate on the surface of these electrodes is very slow which leads to unacceptable high over potential thereby becoming major limiting reaction in MFCs[18, 19]. Using potassium ferricyanide as electron acceptor and non-precious metals such as platinum to catalyzed the cathodic reaction leading to a low cathode overpotential, and allows the MFC to work with high efficiency [8, 20].

Table 1: Major Problems limiting MFC Efficiency, Causes and Possible Solutions [7, 10, 11]

Problem	**Reasons/Causes**	**Ways to overcome**
Activation polarization	dominant at low current densities activation energy that must be overcome by the reacting species Adsorption or desorption of reactant species, transfer of	minimized by adding mediators

	electrons and the nature of the electrode surface	
Ohmic loss	intermediate current densities ionic and electronic conduction	reduced by shortening the distance between the two electrodes, increasing the ionic conductivity of the electrolytes and using membranes with lower resistance
Concentration polarization	High current densities Decay of initial substrate concentration in the bulk fluid and mass transport limitations	Stirring and/or bubbling as well as the MFC design helps to reduce this loss

2.9 Recent Advances in Microbial Fuel Cell

In order to render MFCs operation economical and increased their viability for electricity production, various measures have been investigated by a number researchers to modify MFCs to improve performance, lower material cost and improve power generation[10, 21-24]. These measures include minimizing ohmic losses for improved columbic efficiency, culturing and selection of specialized microbes; using new mediators, catalyst, electrolytes and substrates, membrane type and modifications in the MFC design and configurations (improvement in electrode type, morphology, arrangement, spacing, number, flow mode)[10, 25], operating conditions (ionic strength, feeding regime, retention time, pH, temperature etc.) and external resistance[9] (The efforts of numerous researchers have as such led to the emergence of many variants and modifications of the MFC reactor design and configurations for improved performances which received intensively review recently [8, 21, 26, 27]. Based on different classifications and design criteria, Figure 2 and 3 summarizes and depicts different types of MFC reactor design [21]. Considering that transfer of electrons from bacterial activity to the anode electrode surface significantly limits MFCs performances, ways that enhance bacterial attachment, substrate oxidation and easy electron transfer are desirable for improved MFCs performance [28]. Successive advances in this area showed that some active electrochemically ferrous reducing bacteria (such as Shewanella putrefaciens and Geobacter sulfurrenducens) are capable of transmitting electrons directly to the anode electrode with high efficiency thereby reducing the electron transfer limitations [28-31]. Other studies demonstrated that using different approached could enhanced the performances of MFC, thereby, raising their potentials as future technology

3. Mfc Development and Localization In Ksa

The Kingdom of Saudi Arabia is the major global supplier of energy from its vast fossil oil and gas reserves which are responsible more than 70% of its GDP. Owing to the ever-increasing population, urban development, industrialization and improved living standard, the current scenario of intense reliance on its fossil fuel serves to meet its huge current and future local energy demand is detrimental to jeopardizing its economic and sustainable development. In addition, increasingly larger volumes of wastewaters emanating from domestic, agricultural, and industrial effluents due to the rapid development further necessitate deploying costly and energy-intensive conventional wastewater treatment technologies for environmental pollution control under current scenario. As underscored in earlier, MFCs are one of the future technologies that have great potential of addressing the water-energy nexus problem in sustainable manner; thus, the need to venture into locally developed MFCs technologies cannot be overemphasized. This owes to the fact that, MFCs could only be practically deployable mainly under local environmental settings due to the process dependence on bacterial consortium. Bacterial consortium importations are not practical due to ethical and biohazard risk associated with it. Thus the relevance of feasibility research projects targeting initiating process for the development and establishment MFCs technology which are deployable in KSA under its local environmental settings to ensure that the Kingdom goes in pace with global strategic sustainable development cannot be overemphasized. This will ensure special new microbial colonies are identified using advanced techniques in controlled environments using wastewater from local domestic treatment plant. The most active electrogenic bacteria identified can be isolated and employed under different experimental conditions for highly efficient treatment of municipal wastewater with the production of electricity. This help in advancing the understanding of the applicability of MFC technology in KSA using locally developed electrogenic bacteria

3.1 Socio-Economic Values of MFC Technology in KSA

In relation to strategy spelt out clearly in VISION 2030, a vision which detailed the most ambitious plan for towards transforming KSA into a more sustainable society in terms of self-sufficiency in all sectors socio-economic development, the potential of exploration of MFC in KSA is multi-faceted which can be enumerated the Figure 3 below

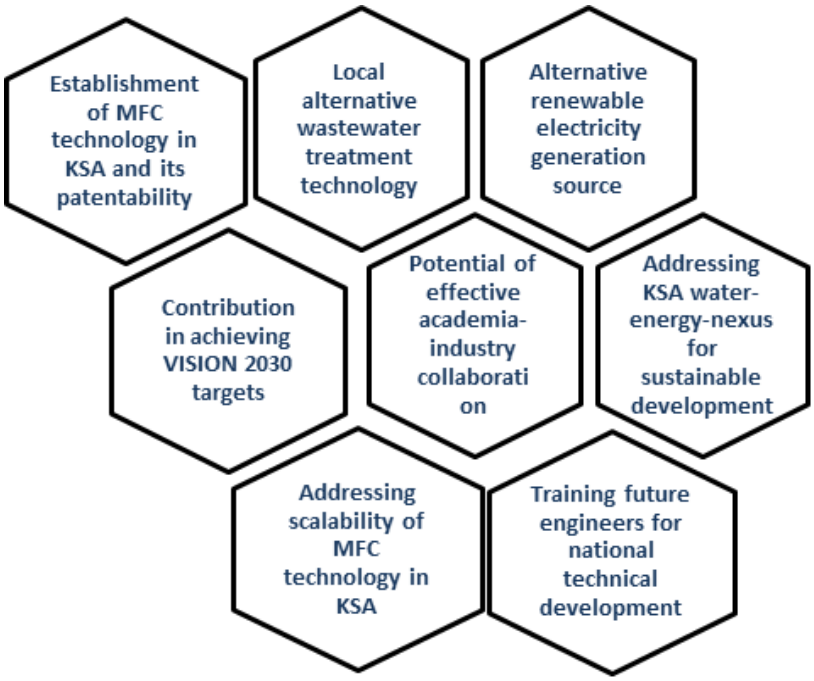


Figure 3: Multifaceted benefits of MFC technology in KSA

This will go directly in line with the strategic scientific approach of the King Abdul Aziz City for Science and Technology (KACST) and Ministry of Education (MOE) towards wastewater treatment and renewable energy generation, thereby underlining the high priority Area of "Energy and Water Technology" which is ranked at the top of the priority list in the Kingdom's Strategic Research Plan

3.2 Relevant of MFC Development and its Localization in KSA

The Kingdom of Saudi Arabia is the major global supplier of energy from its vast fossil oil and gas reserves which are responsible more than 70% of its GDP. Owing to the ever-increasing population, urban development, industrialization and improved living standard, the current scenario of intense reliance on it fossil fuel serves to meet its huge current and future local energy demand is detrimental to jeopardizing its economic and sustainable development. In addition, increasingly larger volumes of wastewaters emanating from domestic, agricultural, and industrial effluents due to the rapid development further necessitate deploying costly and energy-intensive conventional wastewater treatment technologies for environmental pollution control under current scenario. As underscored in the literature review, MFCs are one of the future technologies that have great potential of addressing the water-energy nexus problem in sustainable manner; thus, the need to venture into locally developed MFCs technologies cannot be overemphasized. This owes to the fact that, MFCs could only be practically deployable mainly under local environmental settings due to the process dependence on bacterial consortium. Bacterial consortium importations are not practical due to ethical and biohazard risk associated with it. Thus, establishment MFCs technology which are deployable in KSA under its local environmental settings to ensure that the Kingdom goes in pace with global

strategic sustainable development. Other potential benefits of engaging in research and advancement of MFC as follows

3.2.1. Patentability of MFC in KSA

By achieving the target research objectives, there is great feasibility of implementing the findings in patenting the microbes and the overall MFC under local KSA environmental conditions

3.2.2. Alternative wastewater treatment technology in KSA

The proposed MFC in this work would immensely pave way for exploring an alternative way of wastewater treatment in KSA which has greater potentials in ensuring that the treatment process becomes more sustainable as it would incorporate electricity generation beside the wastewater treatment

3.2.3. Contribution in achieving VISION 2030 targets

Establishment and testing of MFC technology in KSA, will help in meeting VISION 2030, a vision which detailed the plan of the decision makers towards transforming KSA into a more sustainable society in terms of self-sufficiency in all sectors of KSA socio-economic development

3.2.4. Establishment of an alternative energy source to upset wastewater treatment costs

In this manner, establish MFC in KSA have the potential to create more avenues to utilization of treated effluent which could help in higher set targets for better reusing and recycling of treated wastewater. It can be a means for transforming wastewater treatment process technology into commodity capable to generating economic added value with possibility of upsetting some of the wastewater treatment cost. Additionally, localizing the solution by using cheaply and widely available wastewater as the raw materials for generation of may lead to reduction in expenditure associated with the current costly wastewater treatment and electricity consumption from the national grid.

3.2.5. Potential scalability and Academia-industry collaboration

Exploring MFC technology in KSA can open doors for feasibility assessments addressing the scalability issue of the developed MFC. This could enhance transfer of technology from academia to the industry within the Kingdom; thereby supporting cooperation between these two entities as encouraged by the government.

3.2.6. Addressing KSA water-energy-nexus

Potential outputs from MFC research and projects in KSA are expected to uniquely provide an avenue for addressing the water-energy nexus which challenges the Kingdom's sustainable development. It is expected that the development and testing of MFC technology at a local and national level will add value to the KSA quest for alternative innovative sustainable solutions to satisfying water and energy demand. Moreover, there is high potential for rendering KSA to be in the

league of countries having the know-how on MFC which is current believed to be possess the potential of been part of the sustainable solutions to impending water-energy nexus problem.

3.3 Potential Challenges to Establishment of MFC in KSA

Theoretically, MFC has proven to be future technology suitable for production of limitless amount of good electricity output and minimum hazards (production clean byproducts; H_2O and CO_2) from wastewater receiving greater attention [7]. However, as enumerated earlier, their full implementations are yet to come to fruition due several challenges. The major potential challenges to MFC technology in KSA are mainly related to technical feasibility and market penetration as listed below:

- ✓ Lack of knowledge and awareness of about MFC technology as well and its socioeconomic and environmental benefit potentials
- ✓ Difficulty in development of integration methods of MFCs into wastewater treatment plants and usage of multiple units [7]
- ✓ Lack of or adequate implementation legislations and incentives for encouraging stakeholders and investors in renewable energy alternatives
- ✓ Cost competiveness and potential of marketability of MFC bioelectricity in the midst of abundant electricity supply from natural gas and crude oil
- ✓ Acceptance of MFC bioelectricity and lack of knowledge of potential users

3.4 Future Prospects

Despite these challenges, technical advancements in the field of MFCs are proving that MFCs are still future cost-effective technology that could be employed for sustainable conversion of organic waste materials in wastewater to energy for countries like KSA [7]. Moreover, the issue of identification of efficient biocatalysts microbes for improved optimal electricity generation and overall cost-effectiveness and possibility of integrating the MFC-WWTP integration as well as storage devises for storage and distribution according to demand pinned hope for future adoptability of the technology globally.

Acknowledgement: The support provided for this work by King Abdul-Aziz City for Science and Technology (KACST) NSTIP project No. 12-Env2229-46 through Imam Abdulrahman Bin Faisal University, Dammam is appreciated

References

1. A.J. R, Williams CK, Davison BH, G. B, J. C, C.A. E. The path forward for biofuels and biomaterials. Science 2006;484-489.:484-9.

2. Lovley DR. Microbial fuel cells: novel microbial physiologies and engineering approaches. Current Opinion in Biotechnology 2006;17:327-32.
3. Davis F, Higson SPJ. Biofuel cells—Recent advances and applications. Biosensors and Bioelectronics 2007;22:1224-35.
4. Allen RM, Bennetto HP. Microbial fuel-cells: Electricity production from carbohydrates. Applied Biochemistry and Biotechnology ; Vol/Issue: 39-40 1993:Pages: 27-40.
5. Gil G-C, Chang I-S, Kim BH, Kim M, Jang J-K, Park HS, et al. Operational parameters affecting the performannce of a mediator-less microbial fuel cell. Biosensors and Bioelectronics 2003;18:327-34.
6. Moon H, Chang IS, Kim BH. Continuous electricity production from artificial wastewater using a mediator-less microbial fuel cell. Bioresource Technology 2006;97:621-7.
7. Kumar SS, Kumar V, Malyan SK, Sharma J, Mathimani T, Maskarenj MS, et al. Microbial fuel cells (MFCs) for bioelectrochemical treatment of different wastewater streams. Fuel 2019;254:115526.
8. Logan BE, Hamelers B, Rozendal R, Schröder U, Keller J, Freguia S, et al. Microbial fuel cells: methodology and technology. Environmental Science & Technology 2006;40:5181-92.
9. Jadhav GS, Ghangrekar MM. Performance of microbial fuel cell subjected to variation in pH, temperature, external load and substrate concentration. Bioresource Technology 2009;100:717-23.
10. Oliveira VB, Simões M, Melo LF, Pinto AMFR. Overview on the developments of microbial fuel cells. Biochemical Engineering Journal 2013;73:53-64.
11. Logan BE, Regan JM. Electricity-producing bacterial communities in microbial fuel cells. Trends in Microbiology 2006;14:512-8.
12. Kaushik A, Chetal A. Power generation in microbial fuel cell fed with post methanation distillery effluent as a function of pH microenvironment. Bioresource Technology 2013;147:77-83.
13. Jia B, Hu D, Xie B, Dong K, Liu H. Increased power density from a spiral wound microbial fuel cell. Biosensors and Bioelectronics 2013;41:894-7.
14. Mansoorian HJ, Mahvi AH, Jafari AJ, Amin MM, Rajabizadeh A, Khanjani N. Bioelectricity generation using two chamber microbial fuel cell treating wastewater from food processing. Enzyme and Microbial Technology 2013;52:352-7.
15. Kim B, Park H, Kim H, Kim G, Chang I, Lee J, et al. Enrichment of microbial community generating electricity using a fuel-cell-type electrochemical cell. Applied microbiology and biotechnology 2004;63:672-81.
16. Min B, Kim J, Oh S, Regan JM, Logan BE. Electricity generation from swine wastewater using microbial fuel cells. Water Research 2005;39:4961-8.
17. Leong JX, Daud WRW, Ghasemi M, Liew KB, Ismail M. Ion exchange membranes as separators in microbial fuel cells for bioenergy conversion: A comprehensive review. Renewable and Sustainable Energy Reviews 2013;28:575-87.
18. Rismani-Yazdi H, Carver SM, Christy AD, Tuovinen OH. Cathodic limitations in microbial fuel cells: An overview. Journal of Power Sources 2008;180:683-94.

19. Logan BE, Regan JM. Microbial fuel cells-challenges and applications. Environmental Science & Technology 2006;40:5172-80.
20. Franks AE, Nevin KP. Microbial Fuel Cells, A Current Review. Energies 2010;3:899-919.
21. Zhou M, Wang H, Hassett DJ, Gu T. Recent advances in microbial fuel cells (MFCs) and microbial electrolysis cells (MECs) for wastewater treatment, bioenergy and bioproducts. Journal of Chemical Technology & Biotechnology 2013;88:508-18.
22. kumar GG, Sarathi VGS, Nahm KS. Recent advances and challenges in the anode architecture and their modifications for the applications of microbial fuel cells. Biosensors and Bioelectronics 2013;43:461-75.
23. Wei J, Liang P, Huang X. Recent progress in electrodes for microbial fuel cells. Bioresource Technology 2011;102:9335-44.
24. Li W-W, Sheng G-P, Liu X-W, Yu H-Q. Recent advances in the separators for microbial fuel cells. Bioresource Technology 2011;102:244-52.
25. Zhang X, Shi J, Liang P, Wei J, Huang X, Zhang C, et al. Power generation by packed-bed air-cathode microbial fuel cells. Bioresource Technology 2013;142:109-14.
26. Pant D, Van Bogaert G, Diels L, Vanbroekhoven K. A review of the substrates used in microbial fuel cells (MFCs) for sustainable energy production. Bioresource Technology 2010;101:1533-43.
27. Du Z, Li H, Gu T. A state of the art review on microbial fuel cells: A promising technology for wastewater treatment and bioenergy. Biotechnology Advances 2007;25:464-82.
28. Zhuang L, Zhou S, Yuan Y, Liu T, Wu Z, Cheng J. Development of Enterobacter aerogenes fuel cells: From in situ biohydrogen oxidization to direct electroactive biofilm. Bioresource Technology 2011;102:284-9.
29. Biffinger JC, Byrd JN, Dudley BL, Ringeisen BR. Oxygen exposure promotes fuel diversity for Shewanella oneidensis microbial fuel cells. Biosensors and Bioelectronics 2008;23:820-6.
30. Pham CA, Jung SJ, Phung NT, Lee J, Chang IS, Kim BH, et al. A novel electrochemically active and Fe(III)-reducing bacterium phylogenetically related to Aeromonas hydrophila, isolated from a microbial fuel cell. FEMS Microbiology Letters 2003;223:129-34.
31. Liu H, Cheng S, Logan BE. Production of electricity from acetate or butyrate using a single-chamber microbial fuel cell. Environmental Science & Technology 2005;39:658-62.

Advanced Air Dehumidification Membranes for Energy Efficient Membrane-Based Air-Cooling

Abdul Rehman, Omnya Abdalla, and Ahmed Abdala*

Chemical Engineering Program, Texas A&M University at Qatar, Doha, Qatar
* *Corresponding author: ahmed.abdala@qatar.tamu.edu; Tel.: +974-7796-3310*

Abstract: Air cooling based on the isothermal membrane-based air dehumidification is more energy-efficient and economical than the conventional air-cooling processes. However, there are currently no commercial membrane-based air dehumidification systems due to the limitations of current membranes. Membranes for air dehumidification require exceptional separation performance, i.e., water permeance $>10^{-6}$ kmol/s.m^2. kPa and H_2O/N_2 separation factor >1000. In addition, to the excellent separation performance, candidate membranes must possess excellent mechanical reliability and antifouling characteristics. This article discusses the principles and advantages of the membrane-based air-cooling process, analyzes the state-of-the-art air dehumidification membranes' performance, and provides a perspective on the research directions.

Keywords: air-dehumidification, membranes, air-cooling

1. Introduction

Humankind pollution and global warming are factors that led to destruction in the world's climate, making it hotter and more humid [1]. Many countries suffer from high levels of humidity that result in human discomfort and infeasible building durability [2]. Air dehumidification is the process of removing moisture from humid air using various methods. Conventional methods use heating, ventilation, and air-conditioning (HVAC) systems in residential and commercial spaces to overcome these issues. However, these systems consume a vast amount of energy, contributing to 8.5% of the total electricity consumption in 2019 worldwide [3]. Over 90% of HVAC systems cool humid air to its dew point, then to the dew point of the supply air. A highly energy-intensive condensation process extracts the moisture from the air by cooling below the dew points [4]. HVAC systems rely on mechanical vapor compression cycles, which utilize synthetic artificial like hydrofluorocarbons (HFCs) that possess the effects of harmful greenhouses [5]. Another standard method is desiccant absorption, where a desiccant material is used to absorb the moisture from the air to help reduce energy usage. Yet, desiccants cannot absorb all the moisture in humid air due to their limited energy. Another drawback of desiccants is the complex regeneration process of the material and the possible contamination with air; thus, they are not used alone, and they must be coupled with condensing systems [6, 7]. Therefore, energy-efficient air dehumidification technologies are required to compensate for adverse environmental consequences and high-energy consumption.

Researchers have been extensively studying air dehumidification technologies using membranes for their promising efficiency, simple structure, and reliability [8]. Furthermore, the US department of energy classified membrane technology in the area of non-vapor-compression HVAC technology as one of the leading futuristic technologies because it is more environmentally firmly, as it uses less hazardous hydrofluorocarbons and has tremendous capability in reducing energy consumption [9]. According to IPCC, the rising energy demand and CO_2 emissions can be mitigated by utilizing renewable energies, improving energy efficiency, and switching fuel. It was found that the improvement in the energy efficiency sector got the highest share to achieve the needed energy demand and CO_2 emissions reduction in the future [10]. Therefore, using more energy-efficient technologies, i.e., membrane technology, is essential. Air dehumidification membranes work simply, where water vapor is separated from the air through the chemical potential between the feed side and permeate side, primarily arising due to differences in the water vapor partial pressures. In addition, Water vapor molecules migrate through the membrane's pores because they have smaller radii than

other gases, making the separation more feasible [11]. The performance of air dehumidification membranes is usually analyzed through the selectivity and permeability parameters. Permeability is the rate of water vapor transmitted through the membrane per unit area under a given driving force. In contrast, selectivity is the ratio of the permeability constant of the water vapor compared to other gases in the humid air [12]. It is essential to fabricate membranes with improved and outstanding permeability and selectivity to water vapor to enhance the separation performance of air dehumidification membranes.

Park and Jeong prepared a stable organic framework (MOF) ionic liquid (ILs) membranes encapsulated 1-butyl-3-methylimidazolium bromide (C4MIM) (Br) through the ship-in-a-bottle method. Because of encapsulation of ILs membranes, the hydrophilicity of the membranes increased after ((C4MIM) (Br)) encapsulation, demonstrated by the decrease in contact angle from 35° to 29° as shown in Figure 1. Thus, it led to extraordinary high water permeance of 2.36 $\times 10^4$ mol/ m^2 s Pa. Moreover, the encapsulated (C4MIM) (Br) significantly enhanced the H_2O/N_2 separation factor reaching a value of 1560, consistent with the minimum required separation for commercially available air dehumidification membranes. These membranes showed remarkable performances compared to preamble air dehumidification membranes in literature [13].

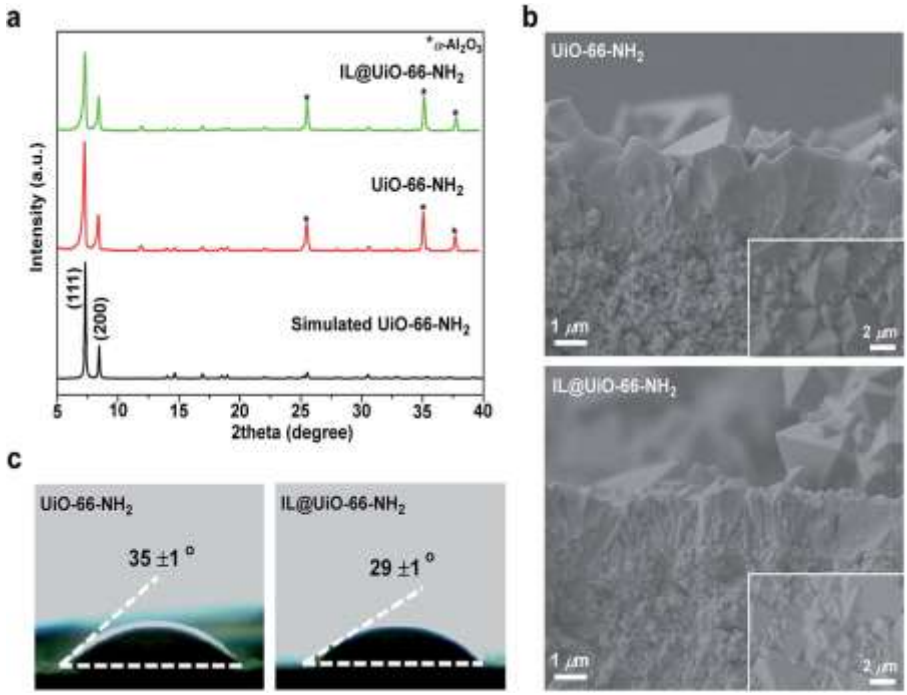


Figure 1. a) XRD Pattern, b)SEM images, and c)water contact angles of UiO-66-NH2 and IL-UiO-66-NH_2 [13]

Another study by Park and Jeong demonstrated partial hydrolysis of f polyimide (PI) membranes using NaOH and NaCOOH to increase the membranes' H_2O/N_2 separation performance. The hydrolysis process resulted in the formation of symmetrically (S-PAA) and asymmetrically (A-PAA) hydrolyzed poly(amic acid) (PAA)/PI membranes. The hydrolysis of PI membranes affected the morphology by forming hydrophilic channels with the PI matrix. As a result, the H_2O/N_2 separation performance was enhanced by increasing the H_2O permeability from ~6400 Barrer to ~11,000 Barrer and H_2O/N_2 separation factor from ~190 to ~ 320, while maintaining the mechanical characteristics of the membrane [14].

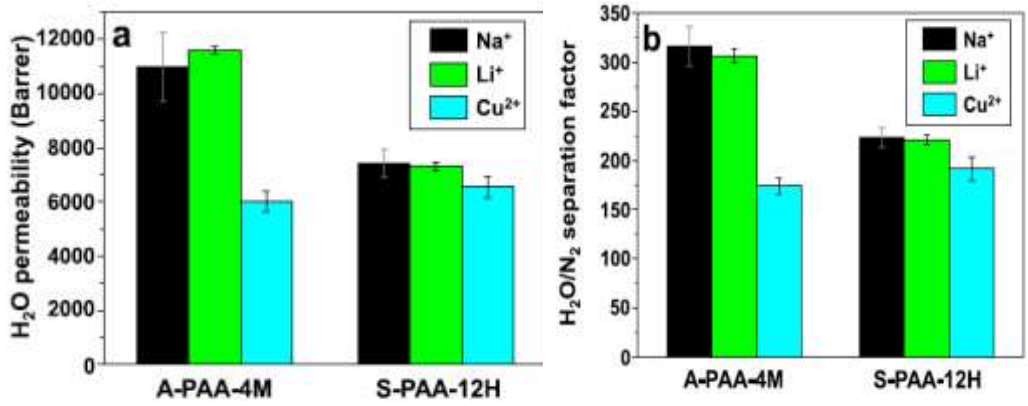


Figure 2. Comparison of H2O/N2 separation performance of PAA with different cations (i.e., Na+, Li+, and Cu2+): (a) H2O permeability and (b) H2O/N2 separation factor [14].

This paper aims to review all the recent advances in membrane technology for air dehumidification applications. This paper will study different parameters that affect the performance of air dehumidification membranes, such as material selection, processing method, and system modules. Moreover, it will highlight any complications with the scalability of such membranes and conclude with future directions and suggestions.

2. Air dehumidification Methods and Processes

The membrane air-dehumidification process can come in several shapes and forms. Still, perhaps the three main categories that each process can be classified into are liquid-desiccant dependent, proton electrolyte-based membrane systems (PEM), and vacuum-based processes.

2.1 Liquid Desiccant Air-Dehumidification

Liquid desiccants are hygroscopic liquids with a high affinity for absorbing water. Lithium chloride, lithium bromide, calcium chloride, and triethylene glycol [15]. Membrane air-dehumidification that utilizes these liquids aims to remove the permeated water moisture in a continuous process. Thus, they require a second inlet of constant circulation of such desiccants. On the plus side, modules that use liquid desiccants can employ hollow fiber membranes and flat sheet membranes, as seen in figure [16].

The main challenge in using liquid desiccants is regenerating desiccants to their dehydrated state so they may be used again. Moreover, most liquid desiccants are toxic in nature, so any possible leakage may harm the air quality output [17].

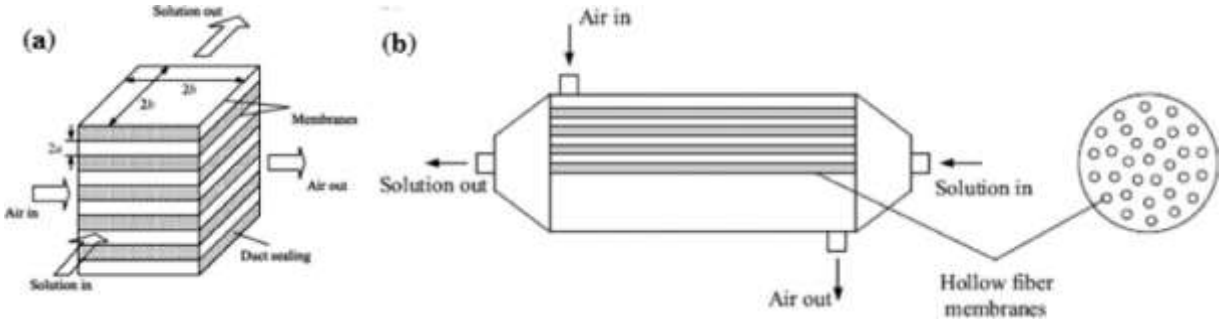


Figure 3. Air-dehumidification module utilizing liquid desiccants while using flat sheet and hollow fiber membranes. Adapted from Qi *et al. [15]*

The performance of these systems yields a relatively low coefficient at less than one where the system efficiency remains a steady high of 70-80% [15, 16].

2.2 Proton Electrolyte Membrane Air-Dehumidification

Proton electrolyte membranes (PEM) aim to produce a driving force based on electrochemistry. The humid air is split into H^+ and O_2 molecules, allowing the proton H^+ to pass through the proton electrolyte membrane. The hydrogen ion reforms to water when the absorbed oxygen from the cathode side interacts in the presence of flowing electrons [18].

The transfer of hydrogen atoms only allows the flow of moisture currents to pass on through. However, an obvious challenge of using PEM membranes for air-dehumidification air cooling concerns fouling. With PEM, the requirement of humid inlet air must be of high quality. Although, if pre-treatment is availed, the selectivity of PEM can be very high. PEMs are more expensive and high maintenance, primarily due to the additional sensitive parts, i.e., cathodes, which may need more frequent attention and repair.

For the system's performance, due to the voltage requirement, the coefficient of performance of PEMs remains as low as 0.33, which does not allow the technology yet to be desirable in an air-cooling operation [18].

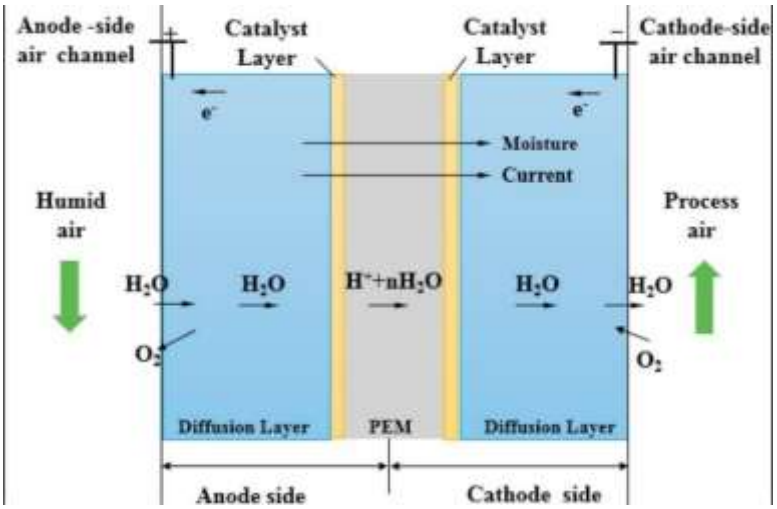


Figure 4. Operation of proton electrolyte membrane for air-dehumidification. Adapted from Qi *et al. [18]*

2.3 Vacuum Air-Dehumidification

The operation of VMD begins with the cooling of warm air via humidification. The cool water reduces the temperature of the warm inlet air, increasing the air water-content. The humid air then enters the membrane dehumidification chamber, where the water/air separation occurs. The permeate water passes through the membrane driven by a pressure gradient created by a vacuum pump. The water vapor then condenses as water and is extracted as pure water. Moreover, the cold dry air exits the dehumidification chamber on the retentate side and can be further humidified to reach the required comfort level. The dehumidification chamber consists of flat sheet membranes. Increasing the number of membrane sheets can lead to higher dehumidification, although with a tradeoff in lower water permeance.

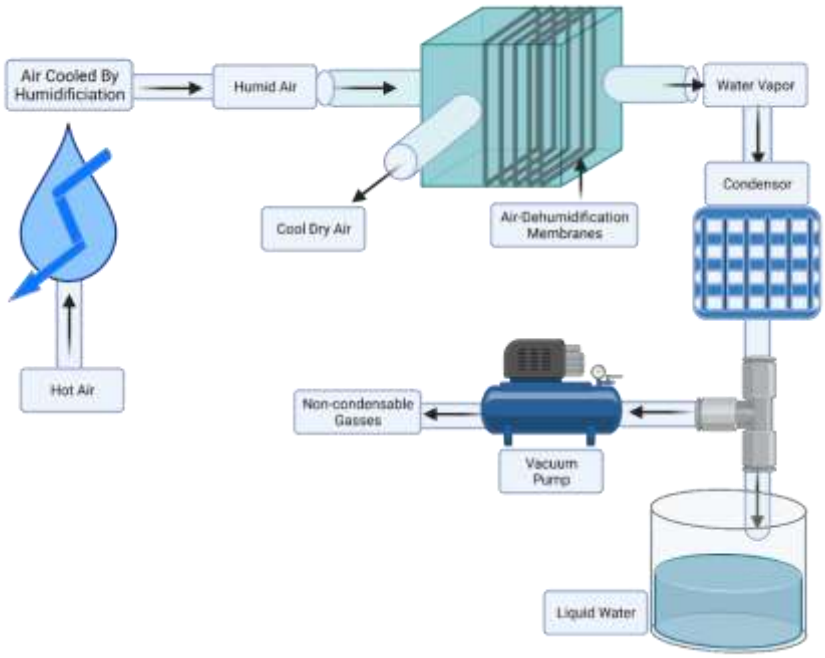


Figure 5. Claridge-Culp-Liu's patented vacuum-based air-dehumidification cooling process.

Alternatively, the air-dehumidification membrane chamber may differ dependent on membrane and system requirements. The modules may be designed for hollow fiber membranes or even incorporate desiccant removal of vapor. The coefficient of performance (COP) for these systems has been reported to reach consistently in the range of 2-3, matching those of modern air-conditioning units, making it an ideal replacement candidate for air-cooling application [19, 20].

The permeance and separation factors are two essential factors that favor air dehumidification membranes as commercially and economically viable. Considering the simplified diagram for the vacuum air dehumidification step in Figure . The work provided by the vacuum pump(s) ($\dot{W}$) and the latent heat removal ($\dot{Q}$) are related to the molar flow rate of water removal ($\dot{N}_{\mathrm{H2O}}$) and therefore are highly dependent on membrane water permeance ($\dot{J}_{H2O}$) and selectivity (water/air separation factor).

$$\dot{J}_{H2O} = \frac{\dot{N}_{\mathrm{H2O}}}{A \cdot (\Delta P_{\mathrm{H2O}})_{lm}} \qquad (1)$$

where $\dot{J}_{H2O}$ is the permeance, A is the area and $(\Delta P_{\mathrm{H2O}})_{lm}$ is the water vapor partial pressure difference across the membrane (logarithmic mean).

$$S = \left(\frac{\dot{N}_{\mathrm{H2O,p}}}{\dot{N}_{\mathrm{H2O},R}}\right)\left(\frac{\dot{N}_{\mathrm{air,R}}}{\dot{N}_{\mathrm{air,P}}}\right) \qquad (2)$$

where S is the separation factor and P and R refer to the permeate (water) and reject (air) streams.

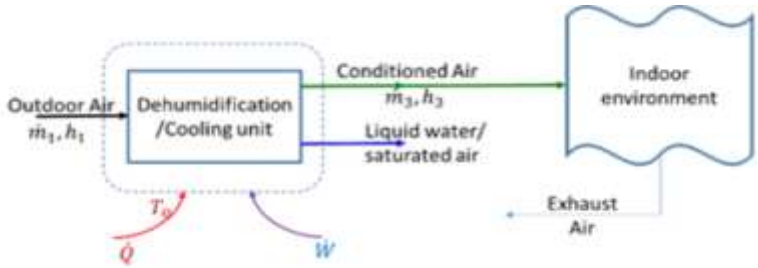


Figure 6. Simplified flow diagram of air-dehumidification

For a typical 3-ton cooling unit, 200 ft3 /min of inlet humid hot air (100° F and 95 RH) is required to be isothermally dried to 30% RH by passing the water vapor through the selective water membrane. The required membrane area estimated as a function of the water permeance across the membrane is shown in Figure 3a.

To limit the size and cost of the process, the commercial practice is to restrict the membrane area to 10 m^2, which requires water permeance of $7x10^{-6}\frac{kmol}{m2.s.kPa}$ $\boldsymbol{s}$. Lower water permeance would require a significantly higher membrane area. For example, the permeance of $1x10^{-6}\frac{kmol}{m2.s.kPa}$ requires 7 times higher membrane area. Moreover, the membrane selectivity significantly affects the fraction of air that crosses (leak through) the membrane and, therefore, the vacuum pump duty. As shown in Figure 3b, the pump duty is only 5% above the duty for an infinitely selective membrane at separation factor $\geq 3x10^3$ and no significant reduction in pump duty results from the increase in separation factor above 10^4.

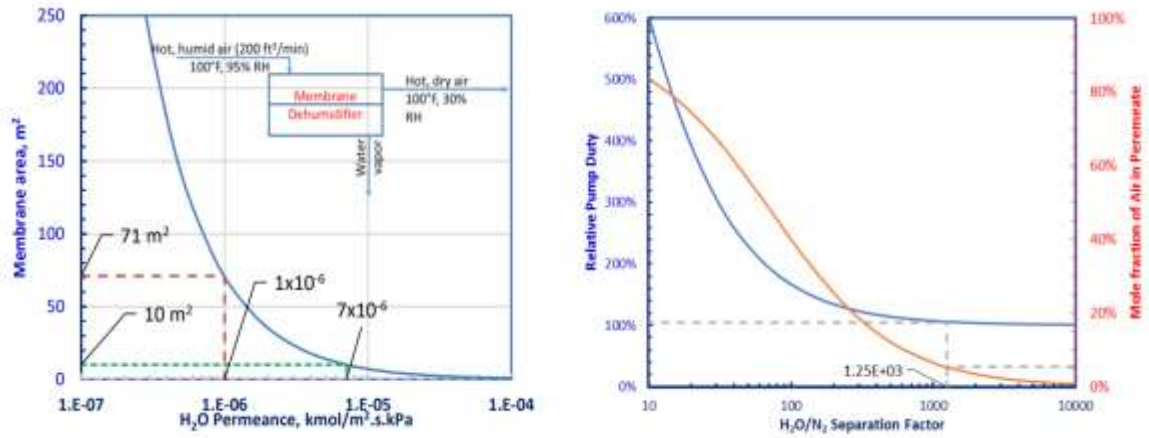


Figure 7. Dependence of (a) relative pump duty on membrane selectivity and (b) required membrane surface area on water vapor permeance. Inlet air at 100°F with 95% RH and outlet air at 100°C and 30% RH.

This analysis indicates, the membrane transport properties (permeance and separation factor) significantly influence the cost (membrane area and vacuum pump size) and energy consumption (vacuum pump duty). Keeping this in mind, the membrane requirements for such a process to be economically and technically feasible are:

- High water vapor permeance of $\geq 7x10^{-6}\frac{kmol}{m2.s.kPa}$
- High selectivity of water vapor versus air (O2 and N2). The targeted separation factor of ≥ 10,000.
- Robust, fouling resistant, and cost-effective.

3. Membranes for Air-Dehumidification

The dehumidification step occurs in the air-dehumidification chamber. Therefore, the overall performance of the process is highly dependent on the performance of the air-dehumidification membranes. These membranes can be classified into organic, inorganic, or composites of each. Within organic and inorganic membranes, mixed matrix membranes and composite membranes may be found. Mixed matrix membranes include inorganic fillers. Moreover, composite membranes may include the fabrication of a membrane using more than one polymer. In contrast, composite membranes between organic and inorganic membranes were also found in the literature.

3.1 Pristine Organic and Inorganic Membranes

Organic membranes can be classified into pristine polymeric membranes and mixed matrix or composite membranes of polymeric membranes. Several studies in this area indicate that organic membranes are inexpensive, easily reproducible, and mechanically robust [4]. Hung and coworkers prepared free-standing graphene oxide framework membranes tuned with different cross-linking agents such as glyoxal (GLX), oxalic acid (OXA), and ethylenediamine (EDA). Performance tests were done by varying the relative humidity from 30 to 90 %. The results significantly improve the water vapor permeability, selectivity, and separation factor at high relative humidity. The GLX-GO membrane demonstrated the optimum selectivity among others with a value of 2.8×10^6 and stability performance that lasted five days [21].

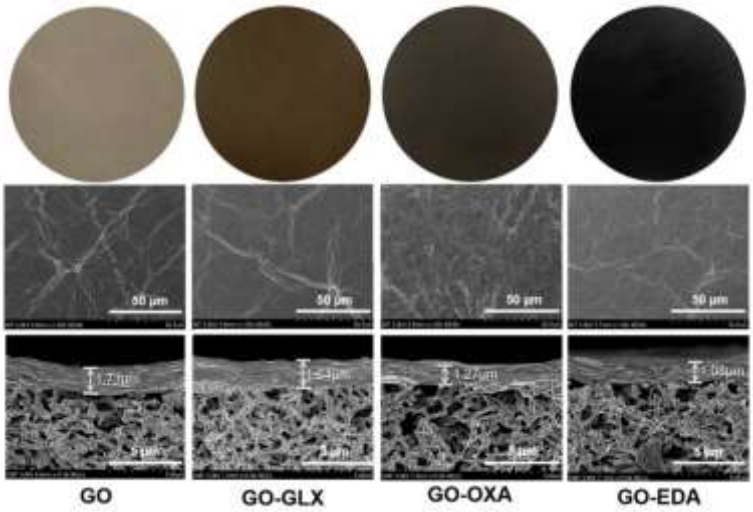


Figure 8. SEM images (surface and cross-sectional views) of the GO-based membranes [21].

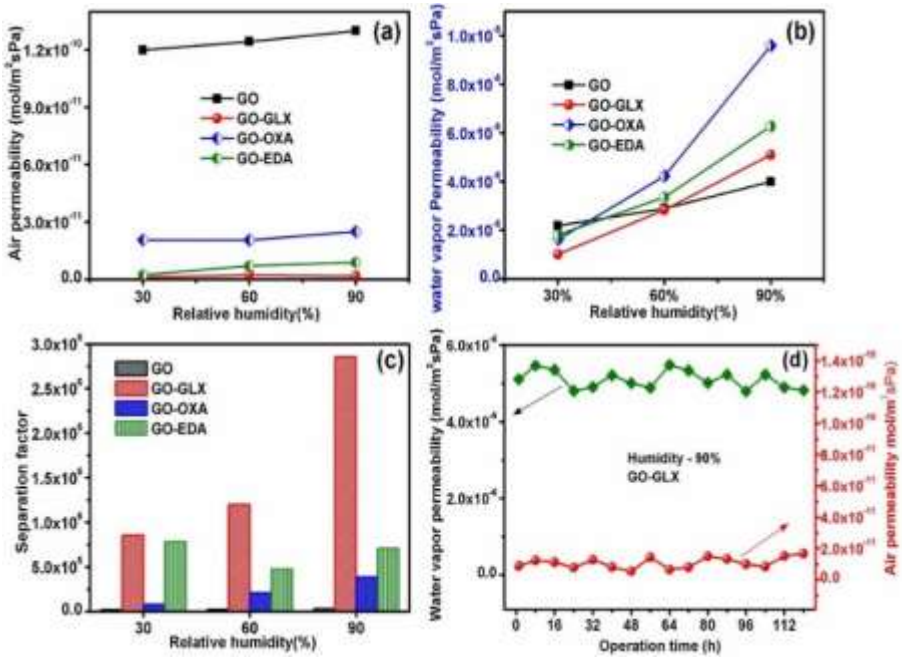


Figure 9. Dehumidification of air streams using GO and cross-linked GO membranes: (a) air permeability, (b) water vapor permeability, (c) separation factor, (d) long-term dehumidification performance [21].

To qualify for large-scale applications, pristine polymeric air dehumidification membranes require further improvement in permeance and selectivity. Moreover, free-standing graphene oxide membranes suffer from defects, scalability, and production; thus, using them as a standalone membrane is very complicated. However, these studies showed that graphene and its derivatives are promising materials with excellent graphene material properties in air dehumidification applications [22].

Table 1. Summary of fabrication and performance of pristine organic and inorganic air-dehumidification membranes

Membrane Details	Fabrication Technique	Membrane Performance				Ref.
		Permeance (GPU)	Permeability (Barrer)	Selectivity	Separation Factor	
• Free-standing GO membrane, Crosslinking OXA EDA • Pristine Inorganic Membrane	Pressure-assisted self-assembly		$1.37x10^{10}$		2.9×10^{6}	[21]
• Graphene Oxide Free Standing Membrane • Pristine Inorganic Membrane	Slurry spread out on a glass bar	$3x10^{4}$	$1.82x10^{5}$	1000 < H_2O/N_2		[22]
• Polyimide Hollowfiber Membrane • Pristine Organic Membrane	Dry-wet spinning process	$1.3x10^{3}$		100-700		[23]

3.2 Mixed-Matrix and Composite Organic Membranes

One way to further enhance air dehumidification polymeric membranes is to incorporate organic and inorganic fillers into the polymer matrix. This combination would reduce the tradeoff between permeance and selectivity and benefit from the favorable properties of polymeric membranes [24]. Organic and inorganic fillers include carbon nanotubes, metal oxides, metal-organic frameworks, metal chlorides, and graphene and its derivatives.

Akhtar and coworkers studied the effect of various inorganic hydrophilic TiO_2 concentrations (0.5wt. % to 20 wt. %) in the performance of polybenzimidazole (PBI) membranes. The prepared membranes were fabricated using solution ring casting, characterized using TEM, FTIR, and EDX. The TEM analysis revealed the TiO_2 structure was preserved after carboxylation, and the filler distribution in the matrix is uniform. A significant improvement in the water vapor permeability and selectivity was achieved with 0.5 wt.% loadings of TiO_2 nanotubes with water vapor permeability and H_2O/N_2 selectivity of 6.8×10^{4} and 3.9×10^{6} Barrer, respectively [25]. Furthermore, pyridine-based polymeric ionic liquids (PIL) membranes were prepared by Deimede and coworkers via solution casting method for dehumidification purposes. The pristine PILs were modified with different inorganic counter anions ($MeSO_4^-$, BF_4^-, and $TFSI^-$) to analyze their effect on the vapor permeance and selectivity of the membranes. Comparing the impact of three anions, PIL-$MeSO_4$ resulted in the best performance in the highest water vapor permeability and H_2O/Gas selectivity with about 1.84×10^{5} Barrer and 2.0×10^{5}, respectively. Compared with existing membranes in literature, these membranes are considered one of the best dehumidification membranes [26].

Metal oxides and most inorganic fillers are very expensive and tend to leach easily. Therefore, researchers are moving towards more economically friendly fillers. Liu and coworkers conducted a study on hollow fiber membranes consisting of polymer hollow fiber composite through a dry-wet spinning process of polyvinyl acetate (PVA) and polyvinylidene fluoride (PVDF), including varying

concentrations of poly(dopamine) (PDA). Variable parameters including treatment or modification time of the membrane. The water vapor permeance results that were the most promising were of the hollow fiber membranes that had gone through 30 minutes of modification process and had the PDA concentrations of 0.1g/L, resulting in ~3000 GPU of water permeance [27].

In another study, Liang *et al.* fabricated thin-film composite (TFC) polydimethylsiloxane (PDMS)/polyacrylonitrile (PAN) hollow fiber membrane coated with an ultrathin (~260 nm) PDMS layer. Unlike other previous work, the pore size of the PAN substrate was about 5.6nm, resulted from the spinning at 60 m/min. The addition of small amounts of PDMS significantly improved the selectivity of the membranes compared to pristine PAN membranes, as shown in Figure 2. The prepared membranes' morphology was also analyzed using FSEM, which confirmed the fabrication of a defect-free membrane with a thin layer of PDMS for the 0.5 wt.% coated membrane illustrated in Figure 3. The same membrane exhibited high gas permeance of about ~280 GPU for N_2 [28].

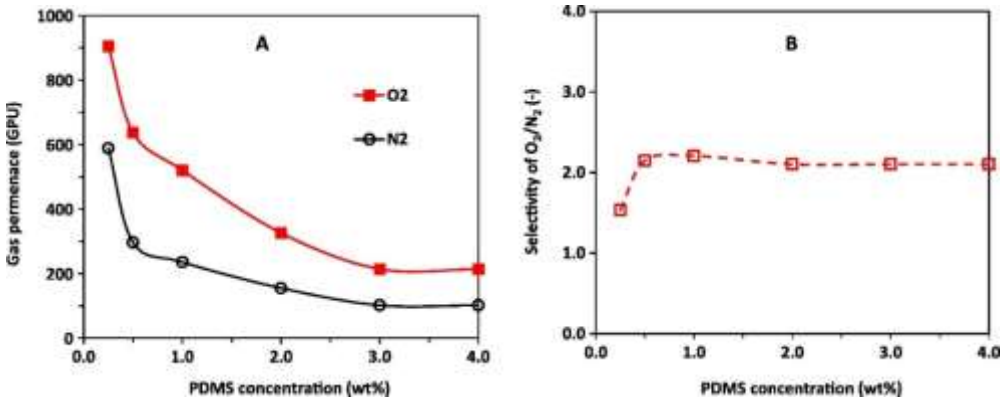


Figure 10. The gas permeation of the PDMS/PAN composite membranes coated with different PDMS concentrations. (A) Effects of PDMS concentrations on gas permeance (B) (A) Effects of PDMS concentrations on O2//N2 selectivity [28]

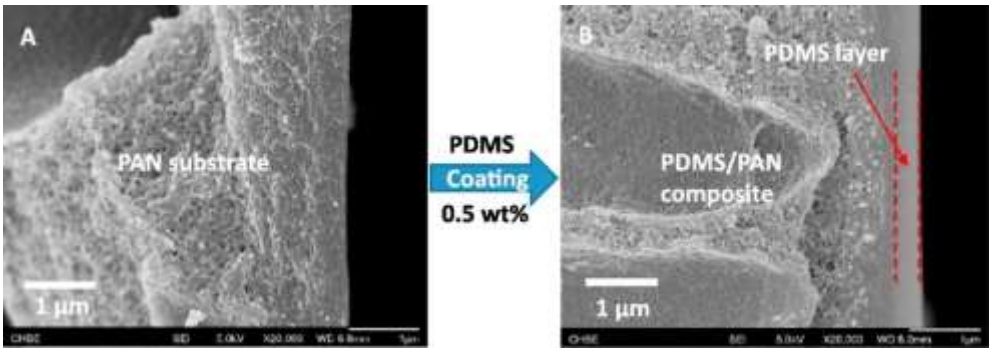


Figure 11. The cross-section morphology of the optimal PDMS/PAN composite hollow fiber membrane. (A) The cross-section image of the PAN hollow fiber substrate, (B) The cross-section image of the optimal composite. [28]

Sijbesma *et al.* investigated the dehydration of flue gas, comparable and analogical to dehumidification of air. They studied the effect of PEEK sulfonation used with polyether block amide (Pebax 1074) to form a composite via block copolymerization. The permeance of Pebax 1074 was around 200000 Barrer, which was doubled once the SPEEK-Pebax 1074 composite was polymerized, yielding permeance of 490000 Barrer. Functionalizing PEEK by sulfonation has a significant impact on its performance, and the block polymerization with Pebax-1074 enhanced the performance of the membrane by over two folds [29]. In a similar study, Akhtar and coworkers investigated using a hydrophilic grade of polyether block amide (Pebax 1657) as support incorporated with graphene oxide as a filler, supported on a polyacrylonitrile flat sheet prepared by dip coating in the Pebax-GO

solution. The composite membrane resulted in high permeance of 196000 Barrer with a selectivity of water/nitrogen of up to 80,000. The optimum incorporation of GO in the Pebax 1657 matrix was deduced to be at 1.5wt%. The single-layer coating performance yielded high permeance, whereas the high selectivity resulted from the five layers of coating [30].

Another investigated organic support included polyethersulfone as a support for a thin film composite with a coating of polyvinyl alcohol (PVA) and a hygroscopic liquid, lithium chloride (LiCl). The lithium chloride coating reduced the contact angle on the surface of the membrane, allowing the membranes active layer to be more hydrophilic. The study lacked results for water-air separation experiments, with neither permeance nor selectivity being shown. Although, water mass flux was shown, depicted in **Figure ,** where the increase if LiCl loading lead to an increase of mass flux. Moreover, the increase of velocity always had the corresponding effect. The maximum mass flux was obtained by 2.5g of LiCl loading with 8g of PVA, resulting in 43.20 g/m^2h. This mass flux number is still relatively low for the application of air-dehumidification air-cooling purposes. [31].

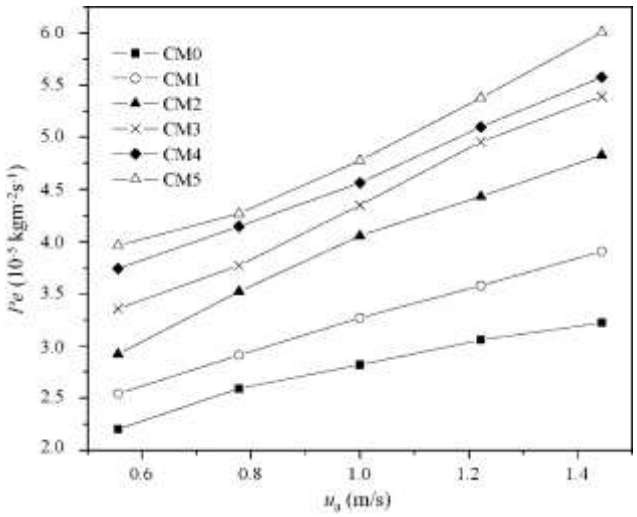


Figure 12. Water mass flux against inlet velocity for membranes with different LiCl loading [31]

Another study using polyethersulfone (PES) as a support was conducted by Ingole *et al.*, where commercial PES was washed and cross-linked with 1 wt.% of a volatile organic monomer, such as 1,3-benzenedithiol (TFC-HF-1), m-phenylene-diamine (TFC-HF-2), piperazine (TFC-HF-3), or 1,3,5-benzene-trithiol (TFC-HF-4). The membrane with the highest roughness, measured by AFM, and the lowest contact angle was the TFC-HF-1, with a roughness of R_{ms} of 20.95 nm and a contact angle of 52.1°.

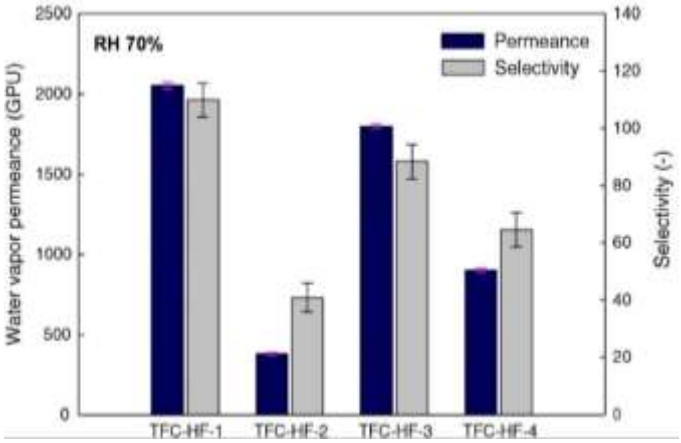


Figure 13. Water vapor permeance and selectivity of TFC membranes studied by Ingole *et al.* Adapted from Ingole *et al. [32]*.

As seen in figure 13, the highest selectivity and permeance of 2054 GPU and 1900 respectively were delivered by the TFC-HF-1 membrane, originally cross-linked with 1,3-benzenedithiol. Whereas the study provides excellent results, it does not show the longevity and sustained performance of the selected membranes. Moreover, the toxic nature of the organic covalent monomers raises a question about their cooling application [32].

Polysulfone was used as a support in multiple studies. In the first study, mixtures of graphene oxide (GO) the titanium oxide (TiO_2) were used as nanofillers embedded into a polysulfone matrix covered with graphene oxide slurry. This TFC produced high permeance of 2500 GPU and a selectivity varying from 900 to 2500 with different nanofiller concentrations [33]. Moreover, the second study that utilized polysulfone as support also used titanium oxide as a filler, although the processed version was carboxylated titanium oxide. The carboxylated titanium oxide is interfacially polymerized with polysulfone, making a membrane with an admirable performance of 1340 GPU and selectivity of 486 [34]. However, the selectivity and permeance performance were not commendable compared to other membranes or even utilizing polysulfone as support.

Although, functionalizing nanofillers and attempting to enhance their properties show the great aspect of their improvement. A third study using polysulfone as support involved the interfacial polymerization of Engelhard titanosilicate (ETS) with hollow fiber PS. The dehumidification performance was quite identical to the previous study involving the TFC of carboxylated titanium dioxide and polysulfone. In the ETS-PS thin film nanocomposite membrane, the selectivity and permeance were 347 and 1377 GPU. The awful similarities can hypothesize that perhaps polysulfone may be the performance limiting factor [35].

Metal-Organic-Frameworks (MOFs) are also carbon-synthetic builds that are increasing in their usage in membrane structures. A recent study utilized hollow zeolitic imidazolate framework-8 (HZIF-8) nanospheres in corroboration with polymer support and interfacial synthesis on the surface of polyacrylonitrile with sodium alginate (SA). The resulting flux was somewhat promising with around 2500 g/m^2h of water [36]. Moreover, the highest permeance of 6000 GPU was achieved with a select 10 weight percent of water in ethanol.

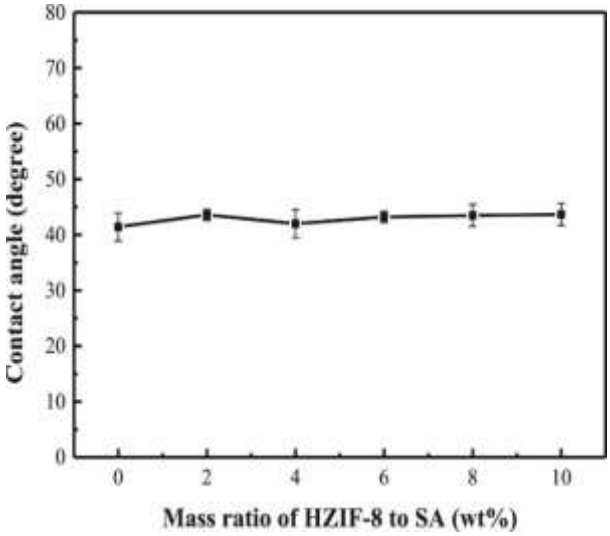


Figure 14. The mass ratio of HZIF to SA in HZIF-8-SA/PAN membranes - Adapted from Cheng *et al. [36]*

As seen in **Figure** the contact angle remained steady around 42° regardless of the loading of HZIF-8. Although the study showed extensive morphological and material characterization studies, the application and testing with water in ethanol instead of air shows a significant flaw in its usage in air-dehumidification and especially for cooling.

Table 2. Summary of fabrication and performance of 2 Mixed-Matrix and Composite Organic Membranes

Membrane Details	Fabrication Technique	Membrane Performance				Ref.
		Permeance (GPU)	Permeability (Barrer)	Flux (g/m^{2}h)	Selectivity	
PVA/PVDF/PDA Hollow fiber composite membrane	Dry-wet spinning process. PVA/PVDF membrane: Coating for 30 to 90 minutes	2898			H_2O/N_2	[27]
PEBAX 1074 - Sulfonated PEEK Composite Block Copolymer Composite	Sulfonation of Commercial PEEK Commercially Acquired PEBAX 1074 Block Copolymerization		SPEEK: 490000 PEBAX 1074: 200000		Water/Flue Gas	[29]
Pebax 1657 - Graphene Oxide Filler Mixed Matrix Membrane	Graphene Oxide prepared by Hummers. Mixed matrix membranes: Dip coating of Pebax 1657	196000	34000		10,000 - 80,000 H_2O/N_2	[30]
Polyether Sulfone + Covalent TFN	Polyether Sulfone: Phase Inversion	2054			119	[32]

Polymer Composite Membrane	Composite: Interfacial Polymerization				H_2O/N_2	
PVA/LiCl on PES support Composite Membrane	Coating PVA casting solution on PES support. Glacial acid used as catalyst.			43.2	H_2O/N_2	[31]
PDMS/PAN Hollow Fiber Membrane Composite	Dry-wet spinning process Dipcoat PAN hollow Fiber membrane in PDMS Spun to 60m/min	800-3700			2.2 O_2/N_2	[28]
Poly (amic acid) (PAA) /PI membranes, Degree of hydrolysis (0, 10,13,17%) Polymer Composite Membrane	Dip coating PI followed by NaOH hydrolysis (Alumina disc supports)		6400~11000		190~320 H_2O/N_2	[14]
Pyridinium-based polymeric ionic liquids/ (MeSO4−, BF4−, TFSI−) Polymer Composite Membrane	Solution casting method		1.84×10^5			[26]
Polybenzimidazole (PBI)/ TiO2 Mixed Matrix Membrane	Ring cast on a silicon wafer		$6.8x10^4$		$3.9x\ 10^6$ H_2O/N_2	[25]
SA-HZIF-8/PAN & SA-ZIF-8 Metal Organic Framework - Mixed Matrix Membrane	HZID-8 prepared through ultrasonic treatment. Substrate: Spin-casting SA solution on PAN substrates. Composite: Interfacial Synthesis via Cross linking			SA-HZIF86/PAN : 2458 SA-ZIF-8: 2136	H_2O/N_2	[36]
Graphene Oxide & Graphene Oxide/TiO2 Filler - TFN on Polysulfone Mixed Matrix Membrane	Interfacially polymerized with Polysulfone	GO-TiO2-PS: 2820 GO-PS: 2500			GO-TiO_2-PS: 910 H_2O/N_2 GO-PS: 2500- 690	[33]
Carboxylated TiO2 filler in TFN on PSF Mixed Matrix and Composite Membranes	Carboxylation of TiO2: Reflux Condenser	1340			486 H_2O/N_2	[34]

	Composite: Interfacial Polymerization					
TFN – ETS -3 Engelhard titanosilicate-4 Polymer Composite Membrane	Interfacial Polymerization	1377			346 H_2O/N_2	[35]

3.3 Mixed-Matrix and Composite Inorganic Membranes

Inorganic membranes have been used in the applications of gas separation for an extended period. They are known for their thermal and chemical stability and outstanding separation abilities due to their crystalline structure with uniform pores [4]. Song and coworkers carried out one of the earliest studies on inorganic membranes for air dehumidification purposes. They fabricated a water vapor permeable membrane by coating a hydrophilic polymer on an alumina support. The best hydrophilic polymer chosen showed the highest water sorption property. The performance of the prepared polymer/alumina membrane was tested by measuring the water permeation ratio considering the feed flow rate and relative humidity. The permeation ratio increased with increasing feed flow rate, however reaching a maximum and then decreasing at high flow rates due to the formation of a water film at the surface of the membrane since the amount of water permeated is less than the amount of water vapor in feed reducing the permeability of the membrane. The results showed that at flow rates of 50 cc/min, 70 cc/min, and 90 cc/min, the water vapor permeation ratios were 45%, 60%, and 25%, respectively, as shown in **Figure** [37].

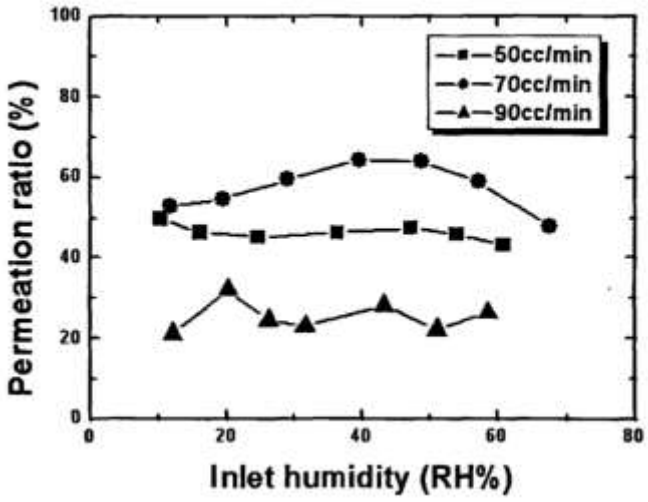


Figure 15. Permeation ratio of the water vapor through the membrane C (coated with G4460 of 0.2wt %) with varying relative humidity of feed stream [37].

Pethukov *et al.* carried out a study involving the fabrication of graphene oxide composite on a porous inorganic alumina substrate. The composite was formed by spin coating a slurry of graphene oxide on the porous alumina substrate. This simplistic method yielded high-performance results, with a water vapor permeance of up to 1.4 m^3/m^2h. Although the method used is straightforward and minimal, it still suffers from limitations and requires many improvements and further investigations. Graphene oxide can have several further improvements and better, more suitable substrates that can be used for investigation [38]. In another study, Bui and coworkers investigated the use of stainless-steel scaffolds as support. The group prepared these membranes by dip coating the stainless-steel scaffold in a series of TiO_2 and polyvinyl alcohol (PVA)/lithium chloride (LiCl) solutions until a clear

coat forms. Distinct concentrations of LiCl (0%, 16.7%, 33.3%, 40% and 50% wt. %) were used. Higher hydrophilicity was observed as the concentration of LiCl increases, implied by the decrease in contact angle from 80º to 45º. Due to improved hydrophilicity, the sorption rate and diffusion rate increased, leading to high water vapor permeation of about 1.35. $\times 10^{-6}$ mol/m^{2}sPa at 90% relative humidity [39].

Tanskyi *et al.* studied the use of zeolite membranes for water vapor separation in membrane dehumidification applications. The studied membranes were prepared by depositing a thin zeolite membrane (< 2μm) on a thin nickel metal sheet (~50μm). The mechanical stability is provided by the zeolitic membrane's metallic nature, which guarantees the ability to work at high pressures, i.e., more than one atmosphere. The optimum results showed effective air permeance of 3x10^{-9} k-mol/kPa-m²-s and average effective water permeance of 5x10^{-6} k-mol/kPa-m²-s resulting in an outstanding membrane selectivity coefficient above 1500 [40].

Table 3. Table 2: Summary of fabrication and performance of Mixed-Matrix and Composite inorganic Membranes

Membrane Details	Fabrication Technique	Membrane Performance					Ref.
		Permeance (GPU)	Permeability (Barrer)	Permeation Ratio (%)	Flux (m^3/m^2h)	Selectivity	
Polyester - Dichloromethane on Alumina Support Inorganic Composite Membrane	Dichloromethane membrane coated with Polyester resin on Alumina Membrane used as a substrate			60			[37]
Graphene Oxide on Aluminum Oxide Support	Spin coating and pressure-assisted filtration				1.4		[38]
TiO2/PVA/LiCl Inorganic Composite Membrane	Dip coating stainless steel scaffold		4.03x10^9				[39]
(C4MIM)(Br)/polycrystalline UiO-66-NH2 MOF membranes Inorganic MMM/Composite	Ship-in-a bottle method	7.01x10^5				312 to 1564 H_2O/N_2	[13]
Zeolite Imadazolate framework ZIF-8 in Silica - Alumina Support Inorganic MMM/Composite	In situ formation Hydrothermal Solvosis Zeolite Crystal growth Silica – Alumina Support	Water: 1.49x10^4 Air: 9.9				>1500 H_2O/N_2	[40]

4. Conclusions and Future directions

In preliminary studies, air-dehumidification air-cooling has shown promise as an alternative to conventional air-conditioning modes while providing incredible energy savings and process sustainability. Air-dehumidification systems such as liquid desiccant-based systems, proton

electrolyte membrane (PEM) air-dehumidifiers, and vacuum-based air-dehumidification systems provide workable models. Based on the coefficient of performance, vacuum-based air-condition provides a COP of up to 3, compared to 1 for desiccant systems and 0.33 for PEMs, making vacuum-based air-dehumidification ideal for air-cooling applications. The membranes used in such a process based on pristine organic and inorganic membranes showed low permeance of ~1000 GPU with similar water/nitrogen selectivity. However, the overall permeance increased two folds by incorporating inorganic fillers such as graphene oxide, titanium dioxide, or SA-ZIF-8. The majority of the membranes ranged in the 1000-4000 GPU, or the order of $1x10^5$ Barrer. The outstanding membranes crossed that threshold were free-standing graphene oxide membranes and Pebax–GO composites, with permeance over $1.96x10^5$ GPU.

Moreover, the water/nitrogen selectivity was almost kept below 1000 for most of the membranes. Polymer composites of SPEEK/Pebax also showed great promise for water/flue gas separation, which should also be investigated for air-dehumidification. Polymeric membranes allow for ease of modification and incorporating nanofillers or using block polymers such as Pebax and SPEEK as active layers for composites tend to show great promise in air-dehumidification. Membranes for air-cooling also are required to be mechanically durable as well as resistant to fouling. Inorganic or organic mixed matrix membranes can be used as a support to a composite active layer, increasing the durability and performance of the membrane while keeping the ease of the fabrication process.

Acknowledgments:

References

1. A. I. Barreca, "Climate change, humidity, and mortality in the United States," Journal of environmental economics and management, vol. 63, no. 1, pp. 19-34, 2012.
2. J. Winkler, J. Munk, and J. Woods, "Sensitivity of occupant comfort models to humidity and their effect on cooling energy use," Building and Environment, vol. 162, pp. 106240, 2019/09/01/, 2019.
3. C. Delmastro, "Cooling," International Energy Agency, 2020.
4. [M. Qu, O. Abdelaziz, Z. Gao, and H. Yin, "Isothermal membrane-based air dehumidification: A comprehensive review," Renewable Sustainable Energy Rev., vol. 82, no. Part_3, pp. 4060-4069, //, 2018.
5. M. F. Lunt, M. Rigby, A. L. Ganesan, A. J. Manning, R. G. Prinn, S. O'Doherty, J. Mühle, C. M. Harth, P. K. Salameh, T. Arnold, R. F. Weiss, T. Saito, Y. Yokouchi, P. B. Krummel, L. P. Steele, P. J. Fraser, S. Li, S. Park, S. Reimann, M. K. Vollmer, C. Lunder, O. Hermansen, N. Schmidbauer, M. Maione, J. Arduini, D. Young, and P. G. Simmonds, "Reconciling reported and unreported HFC emissions with atmospheric observations," Proceedings of the National Academy of Sciences, vol. 112, no. 19, pp. 5927, 2015.
6. K. S. Rambhad, P. V. Walke, and D. J. Tidke, "Solid desiccant dehumidification and regeneration methods—A review," Renewable and Sustainable Energy Reviews, vol. 59, pp. 73-83, 2016/06/01/, 2016.
7. M. Sultan, I. I. El-Sharkawy, T. Miyazaki, B. B. Saha, and S. Koyama, "An overview of solid desiccant dehumidification and air conditioning systems," Renewable and Sustainable Energy Reviews, vol. 46, pp. 16-29, 2015/06/01/, 2015.
8. B. Yang, W. Yuan, F. Gao, and B. Guo, "A review of membrane-based air dehumidification," Indoor and Built Environment, vol. 24, no. 1, pp. 11-26, 2015/02/01, 2013.
9. [9] W. Goetzler, R. Zogg, J. Young, and C. Johnson, "Energy savings potential and RD&D opportunities for non-vapor-compression HVAC technologies," USA: US Department of Energy, Office of Energy Efficiency and Renewable Energy, Building Technologies Office, 2014.
10. I. A. B. Bruckner T., Y. Mulugetta, H. Chum, A. de la Vega Navarro, J. Edmonds, A. Faaij, B. Fungtammasan, A. Garg,, and D. H. E. Hertwich, D. Infield, M. Kainuma, S. Khennas, S. Kim, H.B. Nimir, K. Riahi, N. Strachan, R. Wiser, and X. Zhang,, "Energy Systems. In: Climate Change 2014: Mitigation of Climate Change. Contribution of Working Group III to the Fifth Assessment Report of the Intergovernmental Panel on Climate Change," Cambridge University Press, 2014.

11. B. Zhao, N. Peng, C. Liang, W. F. Yong, and T.-S. Chung, "Hollow Fiber Membrane Dehumidification Device for Air Conditioning System," Membranes, vol. 5, no. 4, 2015.
12. R. Xing, Y. Rao, W. TeGrotenhuis, N. Canfield, F. Zheng, D. W. Winiarski, and W. Liu, "Advanced thin zeolite/metal flat sheet membrane for energy efficient air dehumidification and conditioning," Chemical Engineering Science, vol. 104, pp. 596-609, 2013/12/18/, 2013.
13. S. Park, and H.-K. Jeong, "Highly H2O permeable ionic liquid encapsulated metal-organic framework membranes for energy-efficient air-dehumidification," J. Mater. Chem. A, vol. 8, no. 44, pp. 23645-23653, //, 2020.
14. S. Park, and H.-K. Jeong, "Enhancing air-dehumidification performance of polyimide membranes by generating hydrophilic Poly(amic acid) domains using partial hydrolysis," Journal of Membrane Science, vol. 621, pp. 119006, 2021/03/01/, 2021.
15. M.-G. Ham, W.-J. Jeon, H.-J. Kim, C.-u. Bak, and Y.-D. Kim, "Performance and viability of absorptive dehumidification module using flat-sheet polytetrafluoroethylene/polypropylene composite membranes," Energy Conversion and Management, vol. 205, pp. 112393, 2020.
16. Z. Chen, J. Zhu, H. Bai, Y. Yan, and L. Zhang, "Experimental study of a membrane-based dehumidification cooling system," Applied Thermal Engineering, vol. 115, pp. 1315-1321, 2017.
17. R. Qi, C. Dong, and L.-Z. Zhang, "A review of liquid desiccant air dehumidification: From system to material manipulations," Energy and Buildings, vol. 215, pp. 109897, 2020.
18. R. Qi, D. Li, and L.-Z. Zhang, "Performance investigation on polymeric electrolyte membrane-based electrochemical air dehumidification system," Applied Energy, vol. 208, pp. 1174-1183, 2017.
19. Y. Wang, Y. You, and Z. Zhang, "Experimental Investigations on a Conventional Air- conditioner Working as Air-water Heat Pump," Procedia Engineering, vol. 23, pp. 493-497, 2011/01/01/, 2011.
20. T. Bui, Y. Wong, M. Islam, and K. Chua, "On the theoretical and experimental energy efficiency analyses of a vacuum-based dehumidification membrane," Journal of Membrane Science, vol. 539, pp. 76-87, 2017.
21. W.-S. Hung, Y.-L. Lai, P.-H. Lee, Y.-H. Chiao, A. Sengupta, M. Sivakumar, K.-R. Lee, and J.-Y. Lai, "Tuneable interlayer spacing self-assembling on graphene oxide-framework membrane for enhance air dehumidification," Separation and Purification Technology, vol. 239, pp. 116499, 2020/05/15/, 2020.
22. Y. Shin, W. Liu, B. Schwenzer, S. Manandhar, D. Chase-Woods, M. H. Engelhard, R. Devanathan, L. S. Fifield, W. D. Bennett, B. Ginovska, and D. W. Gotthold, "Graphene oxide membranes with high permeability and selectivity for dehumidification of air," Carbon, vol. 106, pp. 164-170, 2016/09/01/, 2016.
23. N. Tanihara, S. Nakanishi, and T. Yoshinaga, "Gas and Vapor Separation through Polyimide Membranes," Journal of the Japan Petroleum Institute, vol. 59, pp. 276-282, 11/01, 2016.
24. M. A. Aroon, A. F. Ismail, T. Matsuura, and M. M. Montazer-Rahmati, "Performance studies of mixed matrix membranes for gas separation: A review," Separation and Purification Technology, vol. 75, no. 3, pp. 229-242, 2010/11/20/, 2010.
25. F. H. Akhtar, M. Kumar, L. F. Villalobos, H. Vovusha, R. Shevate, U. Schwingenschlögl, and K.-V. Peinemann, "Polybenzimidazole-based mixed membranes with exceptionally high water vapor permeability and selectivity," Journal of Materials Chemistry A, vol. 5, no. 41, pp. 21807-21819, 2017.
26. V. Deimede, D. Vroulias, J. Kallitsis, and T. Ioannides, "Pyridinium based Poly(Ionic Liquids) membranes with exceptional high water vapor permeability and selectivity," Separation and Purification Technology, vol. 251, pp. 117412, 2020/11/15/, 2020.
27. Y. Liu, Y. Wei, J. Su, L. Zhang, X. Cui, and L. Jin, "Surface-modified PVA/PVDF hollow fiber composite membrane for air dehumidification," Journal of Materials Science, vol. 55, no. 13, pp. 5415-5430, 2020/05/01, 2020.
28. C. Z. Liang, and T.-S. Chung, "Robust thin film composite PDMS/PAN hollow fiber membranes for water vapor removal from humid air and gases," Separation and Purification Technology, vol. 202, pp. 345-356, 2018/08/31/, 2018.

29. H. Sijbesma, K. Nymeijer, R. van Marwijk, R. Heijboer, J. Potreck, and M. Wessling, “Flue gas dehydration using polymer membranes,” Journal of Membrane Science, vol. 313, no. 1, pp. 263-276, 2008/04/10/, 2008.
30. F. H. Akhtar, M. Kumar, and K.-V. Peinemann, "Pebax® 1657/Graphene oxide composite membranes for improved water vapor separation," Journal of membrane science, vol. 525, pp. 187-194, 2017.
31. L.-Z. Zhang, Y.-Y. Wang, C.-L. Wang, and H. Xiang, "Synthesis and characterization of a PVA/LiCl blend membrane for air dehumidification," Journal of Membrane Science, vol. 308, no. 1, pp. 198-206, 2008/02/01/, 2008.
32. P. G. Ingole, W. K. Choi, G. B. Lee, and H. K. Lee, "Thin-film-composite hollow-fiber membranes for water vapor separation," Desalination, vol. 403, pp. 12-23, 2017/02/01/, 2017.
33. M. I. Baig, P. G. Ingole, J.-d. Jeon, S. U. Hong, W. K. Choi, and H. K. Lee, "Water vapor transport properties of interfacially polymerized thin film nanocomposite membranes modified with graphene oxide and GO-TiO2 nanofillers," Chemical Engineering Journal, vol. 373, pp. 1190-1202, 2019/10/01/, 2019.
34. M. I. Baig, P. G. Ingole, W. K. Choi, S. R. Park, E. C. Kang, and H. K. Lee, "Development of carboxylated TiO2 incorporated thin film nanocomposite hollow fiber membranes for flue gas dehydration," Journal of Membrane Science, vol. 514, pp. 622-635, 2016/09/15/, 2016.
35. X. An, P. G. Ingole, Won K. Choi, Hyung K. Lee, S. U. Hong, and J.-D. Jeon, "Enhancement of water vapor separation using ETS-4 incorporated thin film nanocomposite membranes prepared by interfacial polymerization," Journal of Membrane Science, vol. 531, pp. 77-85, 2017/06/01/, 2017.
36. X. Cheng, Z. Jiang, X. Cheng, H. Yang, L. Tang, G. Liu, M. Wang, H. Wu, F. Pan, and X. Cao, "Water-selective permeation in hybrid membrane incorporating multi-functional hollow ZIF-8 nanospheres," Journal of Membrane Science, vol. 555, pp. 146-156, 2018/06/01/, 2018.
37. K.-H. Song, J.-W. Seol, S.-S. Kim, and K.-R. Lee, "Dehumidification of Air by the Hydrophilic Composite Membrane using Hydrophilic Polymer on Inorganic Substrate," Journal of Polymer Engineering, vol. 29, no. 1-3, pp. 15-26, 01 Mar. 2009, 2009.
38. D. I. Petukhov, E. A. Chernova, O. O. Kapitanova, O. V. Boytsova, R. G. Valeev, A. P. Chumakov, O. V. Konovalov, and A. A. Eliseev, "Thin graphene oxide membranes for gas dehumidification," Journal of Membrane Science, vol. 577, pp. 184-194, 2019/05/01/, 2019.
39. D. T. Bui, A. Nida, Kim C. Ng, and Kian J. Chua, "Water vapor permeation and dehumidification performance of poly(vinyl alcohol)/lithium chloride composite membranes," Journal of Membrane Science, vol. 498, pp. 254-262, 2016/01/15/, 2016.
40. O. Tanskyi, "Zeolite Membrane Water Vapor Separation for Building Air-Conditioning and Ventilation Systems."

Co-combustion characteristic of Malaysian low rank coal and oil palm biomass char derived from tube furnace and microwave irradiation pyrolysis technique

Siti Shawalliah Idris[1,*], Norazah Abd Rahman[1], Khudzir Ismail[2], Mohammed Faisal Mohammed Yunus[3], Noor Irma Nazashida Mohd Hakimi[3], Hadiyanto Hadiayanto[4]

[1] School of Chemical Engineering, College of Engineering, Universiti Teknologi MARA Malaysia, Shah Alam 40450 Selangor Darul Ehsan, MALAYSIA;

[2] Faculty of Applied Science, Universiti Teknologi MARA Perlis, Arau, 01234, Perlis Indera Kayangan, MALAYSIA;

[3] Sime Darby Plantation Research Sdn Bhd, Carey Island, Selangor, MALAYSIA;

[4] Department of Chemical Engineering, Faculty of Engineering, Universitas Diponogoro, Semarang, INDONESIA;

** Corresponding author: shawal075@uitm.edu.my; Tel.: +603-55436312*

Abstract: Co-utilization of coal and biomass deem to be one of the alternatives to reduce climate changes due to global warming. Despite rapid development in this area, no work has been reported on co-combustion of coal-biomass char blends derived from microwave pyrolysis of oil palm biomass. The oil palm biomasses namely empty fruit bunches (EFB), palm mesocarp fiber (PMF) and palm kernel shell (PKS) were pyrolysed in a tube furnace pyrolysis and microwave irradiation pyrolysis units (1 kW, 2.45 GHz). The biomass chars were then mixed with coal at blend ratios of 0%, 20%, 40%, 50%, 60%, 80% and 100% for combustion analysis using TGA. A weighted sample of 20 ± 0.2 mg was used and for the investigation whereby, the sample was heated in oxidizing atmosphere from temperature of 25°C to 1100°C at heating rates of 20°C/min under non-isothermal conditions. Upon combustion, the biomass char depicts one evolution profile that was similar to that of MB coal. Co-combustion of MB coal with biomass chars had shown synergistic effects occurred for selected blends. Biomass chars produced from microwave pyrolysis of PMF was easily ignited during combustion followed by EFB and PKS. Biomass char derived from EFB showed highest reactivity during combustion followed by PKS and PMF. With regards burnout temperature, EFB has better carbon burnout temperature followed by PMF and PKS. Co-combustion of coal with biomass char produced from microwave irradiation pyrolysis is undoubtedly a new area and will therefore contribute to new knowledge and novelty in this field.

Keywords: oil palm wastes; Mukah Balingian coal; microwave and tube furnace pyrolysis; biomass char and coal combustion; synergistic analysis using thermogravimetric analyzer.

Experimental investigation of the impact of tubes arrangement on local heat transfer coefficient in mimicked Fischer-Tropsch fluidized bed reactor

Zahraa W. Hasan, Abbas J. Sultan, Laith S. Sabri, Jamal M. Ali *

Department of Chemical Engineering, University of Technology, Baghdad, Iraq

*****Corresponding authors: che.19.07@grad.uotechnology.edu.iq, Abbas.J.Sultan@uotechnology.edu.iq, Laith.S.Sabri@uotechnology.edu.iq, 80002@uotechnology.edu.iq*

Abstract: Due to worldwide concern throughout the cost of natural energy sources, a gradually attractive power generation technologies have been developed with Fischer Tropsch (F-T) technology, that facilitates the production of various types of clean, high quality and ultra-clean fuels from coal and natural gas feedstock in presence of a catalyst in an extremely exothermic reaction. Various multiphase reactors would have been used but due to its applications in various processes, fluidized bed reactor is the preferred reactor for carrying out the Fischer Tropsch process's exothermic reaction. A bundle of heat exchanging tubes is inserted inside these reactors to eliminate the excessive heat and preserve the reaction temperature. Therefore, this work is indeed over the first time study and quantify the influence of the presence of vertical tubes and their arrangement (square and triangular-pitch) on the local heat transfer coefficient by using an advanced heat transfer technique in a Plexiglas fluidized bed column with a 0.13 m diameter and a height of 1.83 m with vertical heat exchanging tubes using glass beads as a bed material under different axial and radial positions with a wide range of superficial gas velocities. Moreover, the findings of this study would improve the knowledge of the impact of vertical tubes on heat transfer in such reactors. The data will also be used to verify reactor models and CFD codes and simulations that promote the design and scale-up purposes of such reactor. The results of this work will be presented in detail on the conference day.

Low-tar, highly-burnable gas production from the gasification of pelletized palm empty fruit bunch

Nur Hanina Malek , Rusmi Alias and Syed Shatir A. Syed-Hassan *

School of Chemical Engineering, College of Engineering, Universiti Teknologi MARA, 40450 Shah Alam, Selangor, Malaysia

***** *Corresponding author: shatir@uitm.edu.my; Tel.: +60 3 5543 7957*

Abstract: Gasification is an attractive method to convert lignocellulosic biomass into a combustible gas mixture for electricity and power generation. To control tar concentration in the produced gas to be within the allowable limit of downstream applications, it is important for a gasification system to be integrated with tar removal process. In this study, an integrated gasification system consisting of a downdraft gasifier and a secondary catalytic tar-cracking reactor was designed and tested for the gasification of pelletized oil palm empty fruit bunch. To further purify the producer gas, the system was also integrated with a cyclone, a water scrubber and a carbon-bed filter. Biomass was fed at a rate of 5 kg/h, while the air equivalence ratio (ER) and the gasification temperature was set at 0.1 and 800 °C, respectively. 5 kg of the specially developed low-cost Fe/AC catalyst was utilized in the hot gas catalytic tar-cracking reactor. Results indicate that our integrated gasification system was able to produce a clean burnable gas with lower heating value (LHV) of 9.05 MJ/Nm^3, carbon conversion efficiency (CCE) of 79.4%, cold gas efficiency (CGE) of 89.9%, and H_2 and CH_4 concentration of 29.5% and 10.3%, respectively. The final outlet gas was found to only contain 32.5 mg/Nm^3 of tar, thus suitable for internal combustion engine (ICE) application.

Keywords: gasification; palm empty fruit bunch; biomass; tar removal; carbon-supported catalyst

1. Introduction

Biomass gasification is a promising cost-effective technology for producing highly combustible producer gas for renewable electricity and power generation. The presence of tar in the gasifier outlet imposes a major problem in advanced application of gasification technology [1]. Carcinogenic tar in the form of thick and viscous liquid contains a complex mixture of condensable hydrocarbons including single- to five-rings aromatic compounds, oxygen-containing hydrocarbons and complex polycyclic aromatic hydrocarbons (PAH) [2]. When condensed in the downstream pipeline and equipment, tar causes clogging, fouling and corrosion, leading to equipment malfunction, operational breakdown and inefficient gas utilization [3]. The allowable tar content in the producer gas and the heating value of the gas depends on its downstream application. For example, internal combustion engine (ICE), which is designed to use natural gas (NG) as a fuel, requires gas heating value to be comparable to NG and the gas needs to fulfill the tolerable tar requirement of 100 mg/Nm^3 or lower [4, 5]. The acceptable level of tar concentration in producer gas for different technological applications are listed in Table 1 [6]. Achieving these requirements demands an effective tar removal strategy to be incorporated together with the gasifier design and development.

Table 1. Allowable limit of tar concentration in the producer gas for different power generation applications [6].

Application in industry	Tar acceptance limit (mg/Nm^3)
Compressors	500
Internal combustion engine	100
Gas turbines	5
Fuel cells	<1

Generally, tar removal techniques can be classified into two groups: (i) the primary method which refers to the internal treatment inside the gasifier through adjusting gasification operational parameters or through the addition of catalytic materials in the gasifier bed, and (ii) the secondary method which utilises various post-gasification gas clean up methods which can be further divided into (i) physical (e.g. cyclones, scrubbers, filters and electrostatic precipitators), and (ii) thermal (e.g. catalytic cracking and reforming) processes [7-10]. Considering that tar contains significant amount of energy components, converting it into combustible gaseous products through catalytic tar cracking or reforming, either in-situ or ex-situ, not only helps eliminating the tar and enhances gas quality, but also improves the overall gasification efficiency [11-13].

The selection of catalyst holds the key to developing a reliable and effective catalytic tar cleaning system to be integrated with a biomass gasifier. Various types of catalysts have been reported to be promising for tar cracking and reforming reactions [14-16]. Carbon materials originated from biomass have recently gained popularity as tar cracking/reforming catalyst and catalyst support due to its practicability and economic attractiveness [17-19]. Recently we have shown that, unlike the conventional impregnation method, the stepwise impregnation method allows high loading of metals onto activated carbon without severely deteriorating the porosity of support material and the dispersion of catalytic species [20]. The cheap catalyst produced in this manner was used to catalytically reform tarry bio-oil from the fast pyrolysis of oil palm empty fruit bunch into clean producer gas where the best composition of the burnable product gas was obtained with iron loading of 15 wt% [20].

Extending our previous laboratory-scale findings [20], in this study the previously developed activated carbon-supported iron catalyst (Fe/AC) was tested in a prototype-scale integrated biomass air gasification system (~5kg/hr feeding capacity) combining a downdraft gasifier with a post-gasification multichannel catalytic tar-cracking reactor. The aim of this present study is to prove the possibility of producing a high heating value clean producer gas from the pelletized palm empty fruit bunch by applying only air as a gasifying agent, without any assistance of steam supply. The second aim of this study is to prove that gas quality, carbon conversion efficiency (CCE) and cold gas efficiency (CGE) can be improved at a pilot-scale with the use of the previously developed cheap Fe/AC catalyst with high loading of iron in the secondary catalytic tar-cracking reactor.

2. Materials and Methods

2.1. Biomass

Pelletized palm empty fruit bunch (EFB) in the size range of 30 – 50 mm was obtained from IGN (M) Sdn Bhd in Klang, Malaysia. The proximate and ultimate compositions of EFB pellet are summarized in Table 2. Proximate analysis was performed using a Thermogravimetric Analyser, TGA (Mettler Toledo, United States) for volatile matter and ash content determinations, while the moisture content was determined using an oven dry method following the ASTM E871 standard method (equation 1). The fixed carbon content (FC) was calculated using equation 2.

$$\text{Moisture content (\%)} = \frac{W_1 - W_2}{W_1} \times 100\% \quad (1)$$

where,

W_1 is the initial weight of the sample before heating

W_2 is the final weight of the sample after heating

$$FC = 100\% - M - VM - AC \quad (2)$$

where,

M represents moisture content

VM represents volatile matter

AC represents ash content

The ultimate analysis to determine elemental percentage of carbon (C), hydrogen (H) and nitrogen (N) was carried out using an Elemental Analyser CHNS-O, (FlashEA 1112 Series, United States) following the ASTM D-5291. The elemental oxygen (O) content was obtained by difference using equation 3.

$$\%O = 100 - (\%C + \%H + \%N) \quad (3)$$

where,

%O is the oxygen content (wt%)

%C is the carbon content (wt%)

%H is the hydrogen content (wt%)

%N is the nitrogen content (wt%)

An oxygen bomb calorimeter (Parr Oxygen Bomb Calorimeter, 6400) was used to determine the lower heating value (LHV) of the EFB pellet. By considering only the main elements (C, H, O, and N) in EFB, the molecular formula of the studied biomass sample based on one C atom can be written as $CH_{0.11}O_{1.06}N_{0.01}$.

Table 2. Ultimate and proximate analysis of EFB.

Proximate composition	Moisture content (wt%)	10.77
	Volatile content (wt%)[db]	76.40
	Ash content (wt%)[db]	3.25
	Fixed carbon (wt%)[db]	20.35
Ultimate composition	Carbon (wt%)[daf]	45.76
	Hydrogen (wt%)[daf]	5.11
	Oxygen[*] (wt%)[daf]	48.63
	Nitrogen (wt%)[daf]	0.50
Lower heating value, LHV (MJ/kg)		16.93
Empirical formula		$CH_{0.11}O_{1.06}N_{0.01}$

* Calculated by difference (equation 3)

db Dry basis

daf Dry and ash free basis

2.2. Catalyst

In our previous work [20], a highly micro-porous AC-supported iron catalyst was developed using a novel step-wise impregnation method. The catalyst was used to reform tarry bio-oil for the production of hydrogen-rich clean producer gas at a bench-scale level. Based on the gas composition, the cold gas efficiency and the tar concentration in the producer gas, the most optimum iron loading was found to be at 15 wt%. In this study, the optimized 15 wt% Fe/AC catalyst was used in the secondary catalytic tar-cracking reactor to reduce the tar content in the gas exiting from a downdraft gasifier. The procedures used to prepare the catalyst have already been described in detail in our previous publication [20]. The properties of the catalyst are summarized in Table 3.

Table 3. Summary of the catalyst properties.

Catalyst properties	
Size (mm)	3 - 5
Iron loading (wt%)	15
BET surface area (m^2/g)	997
Micropore surface area (m^2/g)	807
Total pore volume (m^3/g)	0.42
Pore size (Å)	17.00

2.3. Integrated biomass gasification system

A prototype-scale integrated biomass gasification system with a biomass feeding capacity of ~5 kg/hr was set up to include a downdraft biomass gasifier and a multichannel catalytic tar-cracking reactor. To further improve the quality of the gas, the gasification system was also installed with a cyclone, a wet scrubber and a carbon-bed filter. Figure 1 shows the schematic diagram of the

gasification system. The downdraft gasifier was made of stainless steel. The inner diameter of the throat and the cylinder part of the gasifier was 40 cm and 60 cm, respectively, while the total height of the gasifier was 120 cm. The top of the gasifier was directly attached to the mechanical screw feeder which was used to feed the biomass from the hopper into the gasifier. At the bottom of the reactor, a wire mesh was welded to segregate the ash into the ash collector.

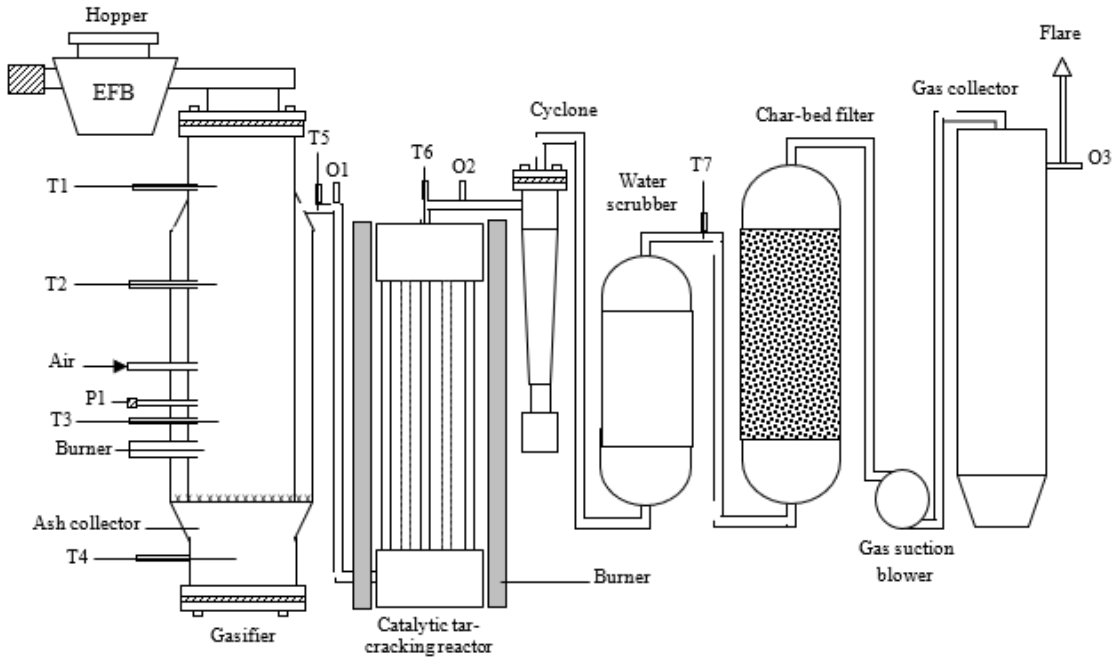


Figure 1 A schematic diagram of the gasification system

A gasifier outlet at the throat of the reactor was connected to the bottom of the catalytic tar-cracking reactor which was made of six stainless steel tubes, each having an inner diameter of 6 cm and a length of 120 cm. Each of the tubes, which was filled with Fe/AC catalyst, was connected to the bottom and the top compartments that provide the producer gas an entrance to and an exit from the catalytic hot gas cleaning unit. A stainless steel cyclone connected to the outlet of the tar cracking unit had an inner body diameter of 30 cm and a total length (body and cone) of 60 cm. A dust collector connected to the cyclone had an inner diameter of 10 cm. The outlet of the cyclone goes to a water scrubber with an inner diameter of 30 cm and a length of 50 cm. A carbon bed filter with a 100 cm length and a 40 cm inner diameter was connected to the water scrubber outlet. It was packed with 3 – 5 mm sized activated carbons (AC) with an average specific surface area of 1055 m^2/g.

Three different thermocouples (T1, T2 and T3) were installed at different positions in the gasifier to continuously monitor the temperature (see Figure 1). T1 is the temperature of the pyrolysis zone of the gasifier, T2 is the oxidation zone temperature and T3 is the reduction zone temperature. A pressure transmitter (P1) with a safety valve was installed close to T3 in order to monitor the pressure

inside the gasifier. Four more thermocouples were placed at the ash collector (T4), the gasifier outlet (T5), the catalytic tar-cracking reactor (T6), and the scrubber outlet (T7).

2.4. Gasification of pelletized palm empty fruit bunch

During startup, about 3 kg of EFB char were loaded into the downdraft gasifier, and the EFB pellets were layered above the char in the gasifier bed. The char bed was ignited using an ignition torch, and diesel from the burner tube and air was introduced to maintain the production of hot flue gas to preheat the reactor. At the same time, the catalytic tar-cracking reactor, which was filled with 5 kg of 15 wt% Fe/AC catalyst, was also heated up externally by a burner. Gasifier and catalytic tar-cracking reactor were insulated with quartz wool to reduce heat loss. Once both reactors achieved and stabilized at the desired temperature of 800°C, EFB pellets from the hopper were gradually fed into the gasifier and air as the gasifying agent was then supplied in controlled amounts for an autothermal operation without other heat supply. Feeding rate of the EFB pellets was regulated at 5 kg/h and air was supplied at an air equivalence ratio (ER) of 0.1. The hot producer gas from the gasifier passed through the catalytic tar-cracking reactor and made contact with the Fe/AC catalyst before entering the cyclone. By passing through a water scrubber, particulate matter, heavy tars and other contaminants are further removed. Although most of the tar compounds are non-soluble in water, water scrubbing the hot producer gas allows tarry vapors to condense into fine aerosols which are readily to be absorbed into water droplets. Carbon-bed filter further cleaned the producer gas before it was collected in a gas collector. The operating conditions of the gasification system are summarized in Table 3. In the present study, the autothermal gasification operation was run up to about two hour of continuous biomass feeding upon achieving a stabilized temperature.

Table 3. Experimental conditions of the gasification of EFB pellets.

Feeding rate of EFB Pellet	5 kg/h
Amount of 15wt% Fe/AC catalyst	5 kg
Temperature in the pyrolysis zone (T1)	450 °C
Temperature in the oxidation zone (T2)	700 °C
Temperature in the reduction zone (T3)	800 °C
Temperature at the ash collector (T4)	800 °C
Temperature at the gasifier outlet (T5)	800 °C
Temperature of the catalytic tar-cracking reactor (T6)	800 °C
Temperature at water scrubber outlet (T7)	Below 100 °C

2.5. Gas and tar analysis

After observing an hour of relatively steady temperature, the producer gas was sampled at three different sampling outlets, i.e., outlet 1 (O1), outlet 2 (O2) and outlet 3 (O3), as shown in Figure 1. Each of the sampling outlets was connected to two solvent traps, each filled with 25% methanol and 75% chloroform. The first solvent traps were immersed in water bath (25°C), while the second traps were placed in the dry ice bath (-20°C). After the second tar traps, gas samples were collected using gas sampling bags. Each sampling took about 10 – 15 minutes to complete. The total tar solution and gas collected were directly weighed after experiment. The gas sample was analyzed using a Finnigan

Trace Gas Chromatograph Ultra, equipped with a molecular sieve column and a thermal conductivity detector (TCD). Tar content was quantified by drying 5 g of solvent containing tar and placed in a 50 mL aluminum tray. The tar sample was dried in an oven maintained at 35˚C for 4 h. The solvent was completely evaporated, and the tar remained on the tray due to its high boiling point. The tray was then cooled in a desiccator to avoid moisture absorption. After the tray was stabilized at room temperature, it was weighed and the tar yield was quantified.

In order to evaluate the performance of the gasification system, the lower heating value (LHV), the carbon conversion efficiency (CCE) and the cold gas efficiency (CGE) were determined using equations 4 – 6:

$$\text{LHV (MJ/Nm}^3) = 0.108\text{H}_2 + 0.126\text{CO} + 0.359\text{CH}_4$$

where,

H_2 is the percentage of hydrogen in the producer gas (vol%)

CO is the percentage of carbon monoxide in the producer gas (vol%)

CH_4 is the percentage of methane in the producer gas (vol%)

$$\text{CCE (\%)} = \frac{\dot{W}_{gas} \times C\%_{gas}}{\dot{W}_{biomass} \times C\%_{biomass}} \times 100 \quad (5)$$

where,

$\dot{W}_{gas}$ is the producer gas production rate (kg/h)

$\dot{W}_{biomass}$ is the biomass feeding rate (kg/h)

$C\%_{gas}$ is the carbon content in the producer gas (wt%)

$C\%_{biomass}$ is the carbon content of EFB biomass (wt%)

$$\text{CGE (\%)} = \frac{\dot{W}_{gas} \times LHV_{gas}}{\dot{W}_{biomass} \times LHV_{biomass}} \times 100 \quad (6)$$

where,

$\dot{W}_{gas}$ is the producer gas production rate (Nm^3/h)

$\dot{W}_{biomass}$ is the biomass feeding rate (kg/h)

LHV_{gas} is the lower heating value of producer gas (MJ/Nm^3)

$LHV_{biomass}$ is the lower heating value of EFB biomass (MJ/kg)

3. Results and Discussion

3.1. Gas composition, gas heating value and gasification efficiency

Under an autothermal operation, where both of the reactors maintained a temperature of 800 °C without any external heat source, the gas was sampled at three different sampling outlets. O1 represents the gas directly produced from the downdraft gasifier where the gas had not gone through additional tar reduction process. O2 was the gas obtained at the outlet of the catalytic multichannel tar-cracking reactor, where its tar content had been further cracked into combustible gaseous products by the assistance of the Fe/AC catalyst. O3 was obtained at the final point where the gas from the

catalytic reactor was submitted to the cyclone and further washed through water scrubbing and passed to the gas filtration bed for further cleaning before being captured in the gas collection system. Mass balances of this process were established based on the total input basis of biomass material and air, and the output of the gasification products.

Figure 2 illustrates the composition of the burnable gas (H_2, CO, CH_4 and C_2) from the samples obtained at different sampling outlets in this study, while Table 4 summarizes the results of this study in terms of gas compositions, LHV, CCE and CGE in comparison with other previous studies on the pilot-scale biomass gasification that utilize air as a gasifying agent. From the total input of biomass of 5 kg/h, gas collected from O1 provided the lowest total combustible gas composition of 36%, indicating that significant amount of volatiles from the decomposition of EFB biomass in the pyrolysis zone of the gasifier were not converted well into light gases in the gasifier. By passing the gas exiting from the downdraft gasifier into the catalytic tar-cracking reactor, the amount of combustible gases increased to about 57%, as can be seen for the results of O2 and O3. These results indicate that the Fe/AC catalyst we previously developed using a novel stepwise impregnation method can be effectively being utilized as a cracking catalyst to crack tar in the biomass producer gas into light gases (R1) especially H_2 whose concentration increased almost triple. A slight decrease in the concentration of CH_4 and C_2-hydrocarbon at O2 and O3 provides an indication that the catalyst might also had cracked these light hydrocarbons into H_2 (R2) in addition to its action on heavier hydrocarbons (R1). Other than that, the presence of catalyst may also promote, to a lesser extent, other reactions such as partial oxidation (R3) and dry reforming to results in the increased CO and H_2 concentration in the product gas.

Tar cracking $$C_nH_m \rightarrow nC + \left(\frac{m}{2}\right) H_2 \quad \text{(R1)}$$

Methane cracking $$CH_4 \rightarrow C + 2H_2 \quad \text{(R2)}$$

Partial oxidation $$C_nH_m + \left(\frac{n}{2}\right) O_2 \rightarrow nCO + \left(\frac{m}{2}\right) H_2 \quad \text{(R3)}$$

Dry reforming $$C_nH_m + nCO_2 \rightarrow 2nCO + \left(\frac{m}{2}\right) H_2 \quad \text{(R4)}$$

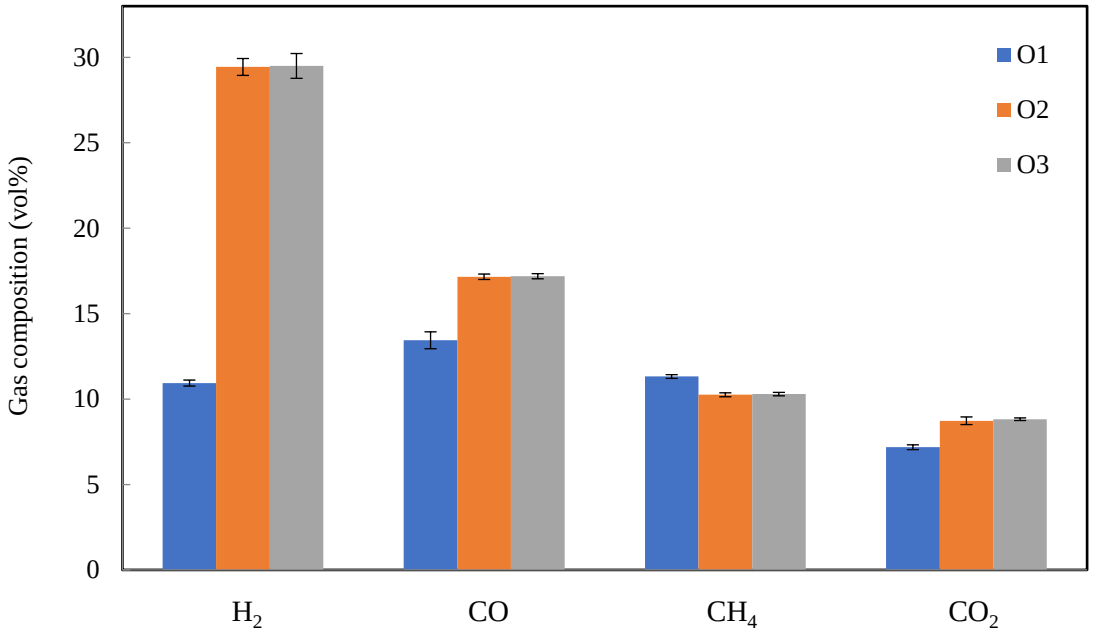


Figure 2 Gas composition (vol%) at O1, O2, and O3

The increase in the composition of burnable gas also resulted in the increase in the lower heating value (LHV) of the gas from 6.94 MJ/Nm^3 (without tar cracking) up to 9.05 MJ/Nm^3 (with tar cracking). Since some tarry vapors remained unconverted in the gasifier, the carbon conversion efficiency (CCE) of the downdraft gasifier was only merely 70%. By combining with the post-gasification processes, the CCE increased up to 79%. Meanwhile, the results also show that the cold gas efficiency (CGE) also increased from 68% to 90% with the integration of post-gasification processes. The almost identical results obtained at O2 and O3, on the other hand, suggest that the catalytic cracking process was more significant in improving the gas quality and gasification efficiency as compared to the physical processes (cyclone, scrubber and gas filter) which can only help reducing the condensable tar and other contaminants (especially particulates) in the product gas but not to increase the burnable gas composition. Comparison of our results with some other past studies on the pilot-scale gasification of biomass, in terms of gas composition, gas heating value and gasification efficiency (Table 4), suggest that our integrated catalytic system for the gasification of EFB pellet can efficiently produce a superior quality gaseous product.

Table 4. Gas composition and gasification efficiency in comparison with other pilot scale studies.

Ref	This study			[21]	[22]	[23]	[24]	[9]
	O1	O2	O3					
Biomass	EFB pellet	EFB pellet	EFB pellet	Rice husk	Corn cob	Waste wood	Pine cone	Olive pits
Temperature (°C)	800	800	800	800	834	907	950	1200
Gas composition (vol%)								
H_2	10.94	29.44	29.50	8.05	17.00	16.30	18.76	10.10

CO	13.44	17.16	17.19	15.41	16.70	21.30	23.62	12.90
CH_4	11.32	10.25	10.29	<2.00	3.10	2.30	1.83	2.50
CO_2	7.18	8.73	8.82	-	6.20	12.40	11.87	10.10
C_2-Hydrocarbon	0.40	0.29	0.25	-	-	0.40	-	0.17
LHV (MJ/Nm^3)	6.94	9.02	9.05	3.13	5.10	5.50	6.06	5.04
Gasification efficiency (%)								
CCE	69.88	79.06	79.41	-	-	-	-	98.27
CGE	67.92	89.39	89.89	72.73	37.00	67.70	78.00	75.00

It is important to note that, in this study, air was the only gasifying agent used to gasify the EFB pellets where the equivalence ratio (ER), defined as the ratio between the actual air-to-fuel ratio to the stoichiometric air-to-fuel ratio for complete combustion of the biomass, was set at 0.1. Steam, which participated in the reactions such as water-gas-shift (R5) and steam reforming (R6) to produce H_2, CO and CO_2 in the gasifier, came mostly from the biomass moisture only. Although many studies in the past favour the use of steam to produce low-tar, hydrogen-rich gas from biomass [25-27], for a large-scale operation, this can be quite expensive since supplying steam requires extensive energy to operate. Using only air as a gasifying agent is sufficient since the heat generated from the reactions of air can supply required energy for endothermic reactions in the gasification [28]. By having the gasifier outlet gas to pass through a catalytic reactor filled with Fe/AC catalyst in this study, we have shown that quite substantial amount of hydrogen (~ 30%) can be generated by the air gasification of biomass.

Water-gas shift reaction $$CO + H_2O \rightarrow CO_2 + H_2$$ (R5)

Steam reforming $$C_nH_m + nH_2O \rightarrow nCO + \left(n + \frac{m}{2}\right) H_2$$ (R6)

3.2. Concentration of tar in the product gas

Figure 3 shows the tar concentration in the producer gas that condensed in a solvent trap containing 25% methanol and 75% chloroform placed in the dry ice bucket (-20°C) at each of the sampling outlets (O1, O2 and O3). In the downdraft gasifier, tarry vapors generated in the pyrolysis/oxidation zone were oxidized or cracked at high temperature into simpler molecule components but still there were heavy tars that remain in the product gas. As is shown in Figure 3, tar concentration at O1 was 614.54 mg/Nm^3, which is simply too high for further downstream applications. However, when the gas from the downdraft gasifier was sent to the catalytic tar-cracking reactor, the tar at O2 was reduced significantly to 71.48 mg/Nm^3 (88% reduction), which is well below the 100 mg/Nm^3 limit of ICE application. Supporting our earlier discussion, this clearly indicate that catalytic cracking by the highly active 15wt% Fe/AC catalyst was efficient to convert high molecular weight tarry materials into combustible light gases through reactions R1 – R4, possibly due to the high loading of well-dispersed iron species on the activated carbon support.

Additional tar cleaning by physical processes, i.e., by the cyclone, the water scrubber and the carbon-bed filter, although did not contribute to better gas composition (as discussed earlier), was

shown to further reduce tar and other contaminants to result in the final product gas at O3 to have only 32.46 mg/Nm^3 of tar, which is equivalent to 95% reduction of tar from the one exiting the gasifier. The insert in Figure 3 compares the appearance of tar solution from the tar trap at O1, O2 and O3. The tar solution from the tar trap at O1 was found to have blackish color due to its high tar concentration of 614.54 mg/Nm^3. When the tar was reduced 71.48 mg/Nm^3 through catalytic cracking, the tar solution from O2 was brownish, indicating that high amount of particulates were still present in the gas. Only after going through physical treatment process through a cyclone, a water scrubber and a carbon-bed filter, these particulates and some more tar were removed to result in the tar solutions to be clear at O3.

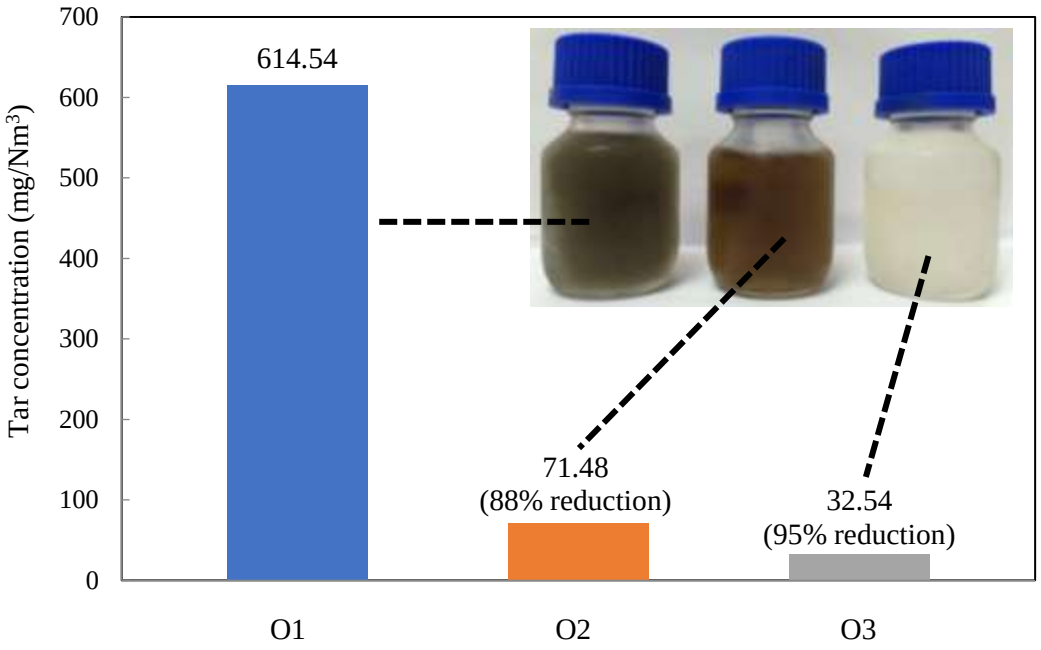


Figure 3 Tar concentration and the tar solvents colour at different sampling point

In the pilot/commercial scale biomass gasification, gas cleaning system is crucially required due to the presence of particulates, tar and other contaminants in the producer gas that reduce its combustibility and gasification efficiency, as well as being detrimental to the downstream pipeline and equipment. Table 5 compares our present study with some of the pilot-scale biomass gasification studies available in the literature. Clearly, tar concentration in the pilot-scale biomass gasification system can be reduced to the minimum level when secondary treatment was introduced at downstream of the gasifier. Conventionally, tar removal with physical processes was preferred in the commercial or pilot-scale gasification system due to its simple operation and setup, but the data in Table 5 shows that tar removal by physical processes alone was not sufficient. The use of thermal and/or catalytic process together with physical process(es) provides better tar reduction results. Overall, the tar reduction strategy applied in our integrated biomass gasification has resulted in the overall performance which is superior to or comparable with other reported studies.

Table 5. Comparisons of tar concentration before and after gas cleaning, gasification operating parameters, and the type of gas cleaning method from the pilot-scale biomass gasification studies reported in the literature.

Biomass	Process parameter	Type of cleaning system	List of cleaning equipment	Tar concentration (mg/Nm^3)	Ref
EFB pellet	Feed rate = 5 kg/h T = 800°C P = 1 atm ER = 0.10	Catalytic & Physical	1. Catalytic tar-cracking reactor (Fe/AC catalyst) 2. Hot gas cyclone 3. Wet scrubber 4. Carbon-bed filter	Before* = 614.54 After** = 32.54	This study
Wood pellet	Feed rate = 45 kg/h T = 807°C P = 1 atm ER = 0.28	Catalytic & Physical	1. Catalytic tar-cracking reactor (AC catalyst) 2. Cyclone 3. Gas cooler 4. Desulfurization tower	Before* = 660.00 After** = 42.00	[28]
Pine sawdust	Feed rate = 70 kg/h T = 760°C P = 1 atm ER = 1.2	Catalytic & Physical	1. Feedstock pre-heating unit and gasifier were designed with insulated layer of refractory jacket that can maintain temperature of 700-800°C during the process. 2. Catalytic bed (modified dolomite catalyst) 3. Purification unit	Before* = 149.85 After** = 57.34	[29]
Waste wood	Feed rate = 10 kg/h T = 810°C P = 1 atm	Physical	1. Wet scrubber 2. Sawdust-filled surge tank 3. Fabric filter	Before* = 2000.00 After** = 201.30	[30]
Cedar wood	Feed rate = 60 kg/h T = 800°C P = 1 atm Air flow rate = 23 Nm^3/h	Physical	1. Gas cooler (2 units) 2. Centrifuge (2 units) 3. Bio-oil scrubber (2 units) 4. Char bed filter (2 units)	Before* = 2530.00 After** = 47.00	[10]
Olive pits	Feed rate = 100 kg/h T = 1200°C P = 1 atm	Thermal & Physical	1. Hot gas cyclone 2. Gas cooler	Before* = 796.00 After** = 32.00	[9]

Air flow rate = 112 Nm^3/h	3. Venturi vortex water gas scrubber 4. Wet electrostatic precipitator (WESP) 5. Demister cyclone 6. Gas suction blower 7. Mesh filter

* Tar concentration at the gasifier exit, before the gas cleaning system

** Tar concentration after the gas cleaning system

4. Conclusions

Pelletized palm empty fruit bunch was successfully gasified to produce clean and highly combustible producer gas using an integrated biomass gasification system comprising a downdraft gasifier and a post-gasification catalytic tar-cracking reactor. The use of the low-cost Fe/AC catalyst with iron loading of 15wt% prepared by a stepwise impregnation technique was very efficient to reduce 88% of the tar content from 614.5 mg/Nm^3 to 71.5 mg/Nm^3, and improve the CCE and CGE from 69.9% and 67.9% to 79.4 and 89.9%, respectively. With the reaction temperature of 800 °C for both gasification and tar cracking, and air equivalence ratio (ER) of 0.1, product gas with an LHV of 9.05 MJ/Nm^3 consisting of 29.5% H_2, 17.2% CO, and 10.3% CH_4 was obtained. The use of additional physical treatments involving a cyclone, a water scrubber and a carbon-bed filter, although did not contribute to the enhancement of gas heating value, managed to further reduce the tar content to 32.5 mg/Nm^3. Although the pilot-scale gasification experiments in this study provided promising prospects, further study with a much longer operation time is needed to observe the long-term performance of the gasification system.

Funding: This work was supported by the Ministry of Higher Education of Malaysia (MOHE) via Fundamental Research Grant Scheme (FRGS/1/ 2017/TK02/UITM/02/24).

Acknowledgments: The authors greatly appreciate the various forms of assistance by Research Management Centre (RMC) of Universiti Teknologi MARA (UiTM).

References

1. J. Ren; Y.-L. Liu; X.-Y. Zhao; J.-P. Cao. Biomass thermochemical conversion: A review on tar elimination from biomass catalytic gasification. *Journal of the Energy Institute* **2020**. *93*, 1083-1098.
2. Y. Qin; A. Campen; T. Wiltowski; J. Feng; W. Li. The influence of different chemical compositions in biomass on gasification tar formation. *Biomass and Bioenergy* **2015**. *83*, 77-84.
3. M. Shahbaz; T. Al-Ansari; M. Inayat; S.A. Sulaiman; P. Parthasarathy; G. McKay. A critical review on the influence of process parameters in catalytic co-gasification: Current performance and challenges for a future prospectus. *Renewable and Sustainable Energy Reviews* **2020**. *134*, 110382.
4. G. Przybyla; A. Szlek; D. Haggith; A. Sobiesiak. Fuelling of spark ignition and homogenous charge compression ignition engines with low calorific value producer gas. *Energy* **2016**. *116*, 1464-1478.

5. P. Raman; N.K. Ram. Performance analysis of an internal combustion engine operated on producer gas, in comparison with the performance of the natural gas and diesel engines. *Energy* **2013**. *63*, 317-333.
6. V.S. Sikarwar; M. Zhao; P. Clough; J. Yao; X. Zhong; M.Z. Memon; N. Shah; E.J. Anthony; P.S. Fennell. An overview of advances in biomass gasification. *Energy & Environmental Science* **2016**. *9*, 2939-2977.
7. S. Lotfi; W. Ma; K. Austin; A. Kumar. A wet packed-bed scrubber for removing tar from biomass producer gas. *Fuel Processing Technology* **2019**. *193*, 197-203.
8. M. Awais; W. Li; A. Arshad; Z. Haydar; N. Yaqoob; S. Hussain. Evaluating removal of tar contents in syngas produced from downdraft biomass gasification system. *International Journal of Green Energy* **2018**. *15*, 724-731.
9. M. Dogru. Experimental Results of Olive Pits Gasification in a Fixed Bed Downdraft Gasifier System. *International Journal of Green Energy* **2013**. *10*, 348-361.
10. S. Nakamura; S. Kitano; K. Yoshikawa. Biomass gasification process with the tar removal technologies utilizing bio-oil scrubber and char bed. *Applied Energy* **2016**. *170*, 186-192.
11. J. Grams; A.M. Ruppert. Development of heterogeneous catalysts for thermo-chemical conversion of lignocellulosic biomass. *Energies* **2017**. *10*, 545.
12. Y. Liu; M. Paskevicius; H. Wang; G. Parkinson; J. Wei; M. Asif Akhtar; C.-Z. Li. Insights into the mechanism of tar reforming using biochar as a catalyst. *Fuel* **2021**. *296*, 120672.
13. L. Cao; I.K.M. Yu; X. Xiong; D.C.W. Tsang; S. Zhang; J.H. Clark; C. Hu; Y.H. Ng; J. Shang; Y.S. Ok. Biorenewable hydrogen production through biomass gasification: A review and future prospects. *Environmental Research* **2020**. *186*, 109547.
14. A. Soomro; S. Chen; S. Ma; W. Xiang. Catalytic activities of nickel, dolomite, and olivine for tar removal and H2-enriched gas production in biomass gasification process. *Energy & Environment* **2018**. *29*, 839-867.
15. C. Quan; S. Xu; C. Zhou. Steam reforming of bio-oil from coconut shell pyrolysis over Fe/olivine catalyst. *Energy Conversion and Management* **2017**. *141*, 40-47.
16. J. Meng; Z. Zhao; X. Wang; J. Chen; A. Zheng; Z. Huang; G. Wei; H. Li. Steam reforming and carbon deposition evaluation of phenol and naphthalene used as tar model compounds over Ni and Fe olivine-supported catalysts. *Journal of the Energy Institute* **2019**. *92*, 1765-1778.
17. S. Zhang; Y. Song; Y.C. Song; Q. Yi; L. Dong; T.T. Li; L. Zhang; J. Feng; W.Y. Li; C.-Z. Li. An advanced biomass gasification technology with integrated catalytic hot gas cleaning. Part III: Effects of inorganic species in char on the reforming of tars from wood and agricultural wastes. *Fuel* **2016**. *183*, 177-184.
18. G. Ravenni; Z. Sárossy; J. Ahrenfeldt; U.B. Henriksen. Activity of chars and activated carbons for removal and decomposition of tar model compounds – A review. *Renewable and Sustainable Energy Reviews* **2018**. *94*, 1044-1056.
19. D. Xu; L. Yang; K. Ding; Y. Zhang; W. Gao; Y. Huang; H. Sun; X. Hu; S.S.A. Syed-Hassan; S. Zhang; H. Zhang. Mini-Review on Char Catalysts for Tar Reforming during Biomass Gasification: The Importance of Char Structure. *Energy & Fuels* **2020**. *34*, 1219-1229.

20. N.H. Malek; S.S.A. Syed-Hassan; S. Zhang; R. Alias; A.R. Mohamad Daud. Hydrogen- and Methane-Rich Clean Producer Gas from the Reforming of Bio-oil with Fe/AC Catalyst Prepared by a Stepwise Impregnation Method. *BioEnergy Research* **In Press**.
21. A.A.P. Susastriawan; H. Saptoadi; Purnomo. Comparison of the gasification performance in the downdraft fixed-bed gasifier fed by different feedstocks: Rice husk, sawdust, and their mixture. *Sustainable Energy Technologies and Assessments* **2019**. *34*, 27-34.
22. L. Martínez; J. Rubiano; M. Figueredo; M. Gómez. Experimental study on the performance of gasification of corncobs in a downdraft fixed bed gasifier at various conditions. *Renewable Energy* **2019**. *148*.
23. M. Simone; F. Barontini; C. Nicolella; L. Tognotti. Gasification of pelletized biomass in a pilot scale downdraft gasifier. *Bioresource Technology* **2012**. *116*, 403-412.
24. E.S. Aydin; O. Yucel; H. Sadikoglu. Experimental study on hydrogen-rich syngas production via gasification of pine cone particles and wood pellets in a fixed bed downdraft gasifier. *International Journal of Hydrogen Energy* **2019**. *44*, 17389-17396.
25. J. Ashok; N. Dewangan; S. Das; P. Hongmanorom; M.H. Wai; K. Tomishige; S. Kawi. Recent progress in the development of catalysts for steam reforming of biomass tar model reaction. *Fuel Processing Technology* **2020**. *199*, 106252.
26. D. Feng; Y. Zhao; Y. Zhang; Z. Zhang; L. Zhang; S. Sun. In-situ steam reforming of biomass tar over sawdust biochar in mild catalytic temperature. *Biomass and Bioenergy* **2017**. *107*, 261-270.
27. R. Jahromi; M. Rezaei; S. Hashem Samadi; H. Jahromi. Biomass gasification in a downdraft fixed-bed gasifier: Optimization of operating conditions. *Chemical Engineering Science* **2021**. *231*, 116249.
28. Y.-S. Jeong; Y.-K. Choi; B.-S. Kang; J.-H. Ryu; H.-S. Kim; M.-S. Kang; L.-H. Ryu; J.-S. Kim. Lab-scale and pilot-scale two-stage gasification of biomass using active carbon for production of hydrogen-rich and low-tar producer gas. *Fuel Processing Technology* **2020**. *198*, 106240.
29. M. Hu; D. Guo; C. Ma; S. Luo; X. Chen; Q. Cheng; M. Laghari; B. Xiao. A novel pilot-scale production of fuel gas by allothermal biomass gasification using biomass micron fuel (BMF) as external heat source. *Clean Technologies and Environmental Policy* **2016**. *18*, 743-751.
30. D.S. Upadhyay; H.V. Makwana; R.N. Patel. Performance evaluation of 10 kWe pilot scale downdraft gasifier with different feedstock. *Journal of the Energy Institute* **2019**. *92*, 913-922.

Paraffin-Coated Superhydrophobic Sand Mulches for Controlling Water Evaporation from Irrigated Soils in Arid Regions

Adair Gallo Junior*, Kennedy Odokonyero, Himanshu Mishra

Interfacial Lab, Water Desalination and Reuse Center, King Abdullah University of Science and Technology (KAUST), Thuwal, 23955-6900, Saudi Arabia

*****Corresponding author: Adair.GalloJunioe@kaust.edu.sa*

Abstract: Irrigated agriculture contributes to 33%–40% of the global food supply, while accounting for only 20% of cultivated land and consuming around 70% of the global freshwater annually[1-3]. Water used in irrigation is majorly lost via plant transpiration, percolation and direct evaporation from the soil surface. Transpiration is directly linked to plant health and cannot be suppressed without compromising yields or growth. Percolation losses can be managed by controlled irrigation. Water evaporation from the topsoil, although contributing to excessive amounts of water loss, particularly in aridlands such as the Middle East, has been overlooked[4]. In response, we developed the superhydrophobic sand (SHS)[5]: a bio-inspired protocol for coating common sand, a widely available resource in arid regions, with a nanoscale layer of paraffin wax. The evaporation losses from topsoil can be dramatically reduced by mulching the soils with a 5–10 mm layer of SHS. As a result of lower evaporation, the soil moisture content increases, leading to better crop performance. Field trials with tomato (*Solanum lycopersicum*), barley (*Hordeum vulgare*), and wheat (*Triticum aestivum*) showed that SHS mulching enhanced yields by 17%–73%[6]. Further details will be presented, such as the methods for coating the sands, the effects on evaporation fluxes as function of SHS thickness, and in-depth results from field trials. SHS mulching could play an important role in enhancing the water usage efficiency of aridland agriculture or afforestation and desert control projects.

Keywords: hydrophobicity, irrigation, water, agriculture, afforestation

References

1. Salmon, J. M.; Friedl, M. A.; Frolking, S.; Wisser, D.; Douglas, E. M., Global rain-fed, irrigated, and paddy croplands: A new high resolution map derived from remote sensing, crop inventories and climate data. *International Journal of Applied Earth Observation and Geoinformation* **2015,** *38*, 321-334.
2. Siebert, S.; Burke, J.; Faures, J.-M.; Frenken, K.; Hoogeveen, J.; Döll, P.; Portmann, F. T., Groundwater use for irrigation–a global inventory. *Hydrology and Earth System Sciences* **2010,** *14* (10), 1863-1880.
3. *HLPE, 2015. Water for food security and nutrition. A report by the High Level Panel of Experts on Food Security and Nutrition of the Committee on World Food Security, Rome 2015.*
4. Gong, D.; Mei, X.; Hao, W.; Wang, H.; Caylor, K. K., Comparison of ET partitioning and crop coefficients between partial plastic mulched and non-mulched maize fields. *Agricultural Water Management* **2017,** *181*, 23-34.

5. Mishra, H.; Reihmer, J.; Gallo Jr., A. Compositions and methods relating to functionalized sands (U.S. Patent and Trademark Office; U.S. Department of Commerce, Provisional Patent Application #62550264; https://patents.google.com/patent/WO2018091986A1/en). 2017.
6. Gallo Jr, A.; Odokonyero, K.; Mousa, M. A.; Reihmer, J.; Al-Mashharawi, S.; Marasco, R.; Manalastas, E.; Morton, M. J.; Daffonchio, D.; McCabe, M. F., Superhydrophobic sand mulches increase agricultural productivity in arid regions. *arXiv preprint arXiv:2102.00495* **2021**.

Process Evaluation of Heavy Hydrocarbons Autothermal Reforming

Fernanda Tavares, Jahirul Mazumder, Marwan Alamro, Mohammed Albuali and Pedro Castano*

Multiscale Reaction Engineering, KAUST Catalysis Center (KCC), King Abdullah University ofScience and Technology (KAUST), Thuwal, 23955-6900, Saudi Arabia;

*****Corresponding author: pedro.castano@kaust.edu.sa; Tel.: +966 (0) 12 808 7324.*

Abstract: Global demand for hydrogen has been increasing every year, and its sustainable production depends on efficient conversion of hydrocarbon feedstock. Although catalytic steam reforming (SR) of hydrocarbons is a cost-effective technology for hydrogen production, it requires high amount of energy. Its combination with partial oxidation (POX) referred as the autothermal reforming (ATR), is an efficient strategy to overcome this drawback. This study focuses on catalytic ATR of heavy hydrocarbons using heptane as a naphtha surrogate. Performance of a highly performing Ni/Al_2O_3 catalysts were compared for both SR and ATR at similar conversion levels. Experimental runs covered a wide range of ATR operating conditions trending towards SR or POX to help in the identification of the most efficient conditions. We show that while higher conversions are reached with ATR, the hydrogen production is lower compared to SR, but with optimal operational conditions high yield of hydrogen can be obtained while sustaining an energy efficient system.

Keywords: hydrogen; energy; petrochemical industry

1. Introduction

Hydrogen is a raw material largely used in the chemical and petrochemical industry [1], where the main applications are related to ammonia and methanol production, oil refining, among other uses [2]. Furthermore, the interest in using hydrogen in fuel cell applications, automobile applications and for the production of electricity has been increasing due to the demand for an environmentally sustainable energy system, since hydrogen burns without emitting any pollutants [3,4] and has a high density, yielding more energy per kg than any other fuel [5], representing a good option as energy carrier.

Several studies have been evaluating hydrogen production process from various sources, as methanol, biomass and natural gas, however, the cost and efficiency for its storage and distribution are currently non-viable, and the use of the actual infrastructures of chemical and refining industries

seems to be the best approach to a gradual transition to a new energy system [1,6]. Particularly, long-chained hydrocarbons, as diesel, gasoline, kerosene and naphtha, present advantages due to the potential of on-site hydrogen generation [7]. Currently, 96% of hydrogen production is achieved employing non-renewable sources, where 48% is from natural gas and 30% from oil reforming; coal gasification represents 18% of the production and other alternative sources as water electrolysis, the final 4% [2]. The main process employed for converting petroleum fuels to hydrogen-rich gas are steam reforming, partial oxidation, dry reforming, autothermal reforming or a combination of two ormore [8], each process presenting advantages and barriers related to operational conditions.

Steam reforming of hydrocarbons is among the most cost-effective routes to obtain hydrogen. Itis also the technology with the highest H_2/CO_2 ratio, with only 0.2 mol of CO_2 produced per mol of H_2. However, it is a very endothermic process with high energy demand that requires very high operating temperatures (500-900 °C). Combining partial oxidation (POX) and steam reforming (SR) processes in a single unit, refer as the autothermal reforming (ATR), is an efficient strategy to overcome this drawback. In ATR, heat produced from exothermic catalytic partial oxidation drives the highly endothermic steam reforming, generally remains as slightly exothermic or thermally neutral, resulting in no need for external heating or cooling source. Because of the presence of water, ATR reaction condition is milder than catalytic partial oxidation as well. As a whole, ATR is the most suitable technique for on-site hydrogen production using heavy hydrocarbon fuels because of its rapid thermal response, relatively high hydrogen yields, and remarkable coke-suppression capability [9].

The scope of this study is to assess the catalytic autothermal reforming of heavy hydrocarbons in terms of H_2 yield and energy efficiency. Effect of equivalence ratio, steam/carbon (S/C) ratio, temperature and space time are evaluated for heptane, a representative of paraffinic content of naphtha, in a flow reactor for assessing the optimal ATR conditions.

2. Materials and Methods

2.1 Materials

Nickel (II) nitrate ($Ni(NO_3)_2.6H_2O$), Cerium (III) nitrate ($Ce(NO_3)_3 \cdot 6H_2O$) and cobalt (II) nitrate ($Co(NO_3)_2 \cdot 6H_2O$) obtained from (Sigma-Aldrich) were used as precursors for Nickel (20%), Cerium(10%) and Cobalt (5%), respectively. Alumina mixed-phase ($\gamma+\alpha$ Al_2O_3) was utilized as support materials. Absolute ethanol and distilled water were applied as a solvent for support and metals solution, respectively.

2.2 Catalyst preparation

The Ni-Ce-Co based-catalyst were impregnated on the support layer using a simple impregnation method, in which a required amount of Ni, Co and Co nitrate were dissolved in 3 ml deionized water and sonicated for 10 min to get a clear solution. Then dropwise of this homogenous solution was added to the supporting solution contained a determined concentration of Al_2O_3 dissolved in 60 ml ofethanol. The formed solution continuously stirred for 1h at RT until the complete evaporation of ethanol and water. Then the obtained gel was dried at 100 °C overnight, followed by calcination at 500 °C for 4h. The calcined samples were crushed and sieved into an average size of (150-300) µm.

The nominal nickel cerium and cobalt loadings of the prepared catalysts were 20, 10 and 5wt%, respectively.

2.3 Catalytic system

The heptane autothermal reforming reactions were carried out in a fixed bed catalytic system. Prior to feedstock injection, the catalyst was reduced in situ under 15 ml/min of H_2 at 700 °C for 90 min. The system is composed of a stainless-steel tubular reactor (length: 30 cm, inner diameter: 8 mm) inside a furnace, to where the liquid reactants (heptane and water) are pumped towards, passing first through an evaporator set to 400 °C and arriving in gas phase at the reactor where they flow over the catalytic bed. In the reactor outlet, the gaseous flow (CO, CO_2, CH_4, H_2, H_2O, and hydrocarbon) will be separated from water and heptane in excess by passing through a condenser. Finally, reaction products are analyzed by gas chromatography. The gas chromatograph is constituted by three independent channels, each equipped with a thermal conductivity detector. The first channel allows separating CO_2, CO, and CH_4; the second one separates hydrogen and helium, and the third one allows to separate heptane and possible lighter hydrocarbons that could be generated due to heptane cracking.

Water and heptane feed are mixed with a gas flow of argon that is used as a carrier and pure oxygen is fed at the top of the reactor. Helium is used as the internal standard for gas analysis.

Operation conditions studied are: P = 1 bar, T = 723 – 923 K, S/C = 3 (mol H_2O /mol C), equivalence ratio = 2 – 5, W/F = 4 – 12 g_{cat} h/ heptane mol.

The heptane conversion is calculated as follow:

$$X_{C_7H_{16}}(\%) = 100 * \frac{F^{in}_{C_7H_{16}} - F^{out}_{C_7H_{16}}}{F^{in}_{C_7H_{16}}}$$

3. Results and Discussion

3.1 Catalytic performance on steam and autothermal reforming of heptane

The Ni-Ce-Co catalyst was tested on steam (SR) and autothermal (ATR) reforming, inconditions reaching 25 ± 2% and 50 ± 2% heptane conversion. Under the same conversion, the products yields could be compared and it is displayed in Figure 1. At both conversion levels evaluated,the trends were the same, with higher amounts of H_2 and less CO_2 and CO being produced for SR while compared to ATR with an equivalence ratio of 4.0. The extent of methanation reaction is also lower for the case of ATR.

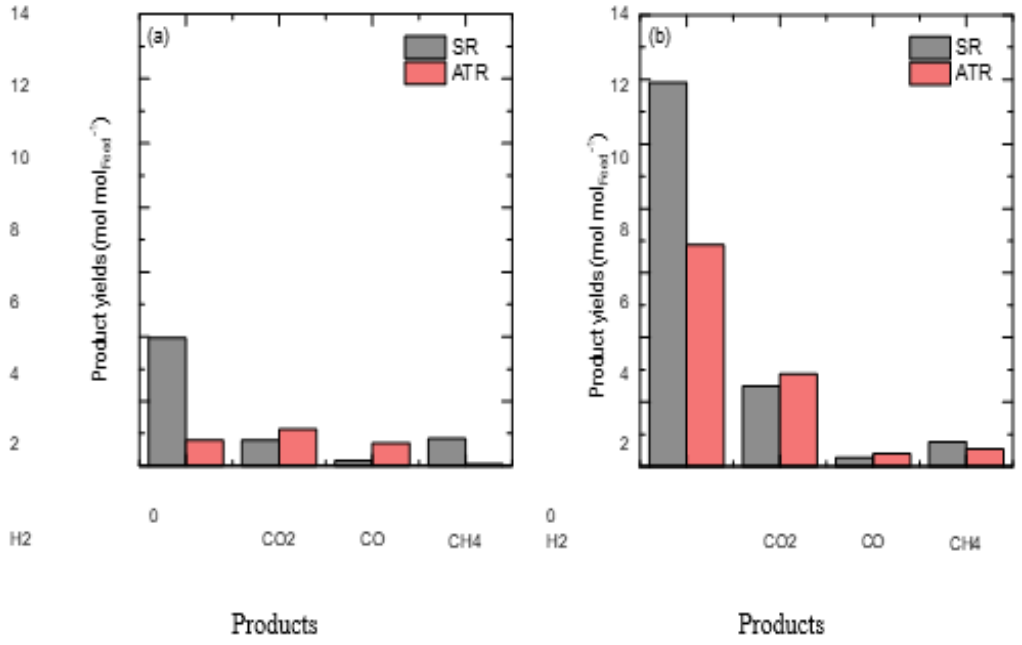


Figure 1. Comparison of steam and autothermal reforming of n-heptane at 500 °C under the similar conversion ranges: (a) 25□ 2% conversion [SR: S/C = 0.8 and W/F = 8 gcat h molFeed- 1; ATR: S/C = 0.8, Equivalence ratio = 4.0 and W/F = 6 gcat h molFeed-1] and (b) 50□ 2% conversion [SR: S/C = 3.0 and W/F = 8 gcat h molFeed-1; ATR: S/C = 0.8, Equivalence ratio =

4.0 and W/F = 12 gcat h molFeed-1].

The effects of water - steam to carbon ratio (S/C), oxygen - equivalence ratio, and temperature were evaluated for ATR and are displayed in Figure 2. We performed the reactions at space time W/F=12 gcat h molFeed-1, where conversion at the standard conditions of 500 °C, S/C of 0.8 and equivalent ratio of 4 is 50%. As shown in (Figure 2 (a), with the increase in space time (W/F) from 6 to 12 gcat h molFeed-1, the conversion of n-heptane is improved from 27 to 51% yielding 8 times higher H2 while almost doubled the CO_2 yields. In the evaluated range, theS/C ratio did not have much effect on heptane conversion, but affected hydrogen yield, presenting a higher value on 1.2 ratio, as can be seen in Figure 2 (b). Figure 2 (c) shows the effect of increasing the equivalence ratio. The equivalence ratio is the ratio of oxygen required for complete combustion to actual oxygen, i.e., at the equivalence ratio of 4.0, the amount of oxygen fed is ¼ of stoichiometric requirement. The conversion decreases with thedecrease of oxygen in the medium, when the reaction is towards steam reforming, along with CO_2 levels, but hydrogen remains almost constant, with an optimal condition observed on ratio 4. The effect of temperature, Figure 2 (d), was pronounced, reaching almost 90% conversion at 700 °C at the standard conditions.

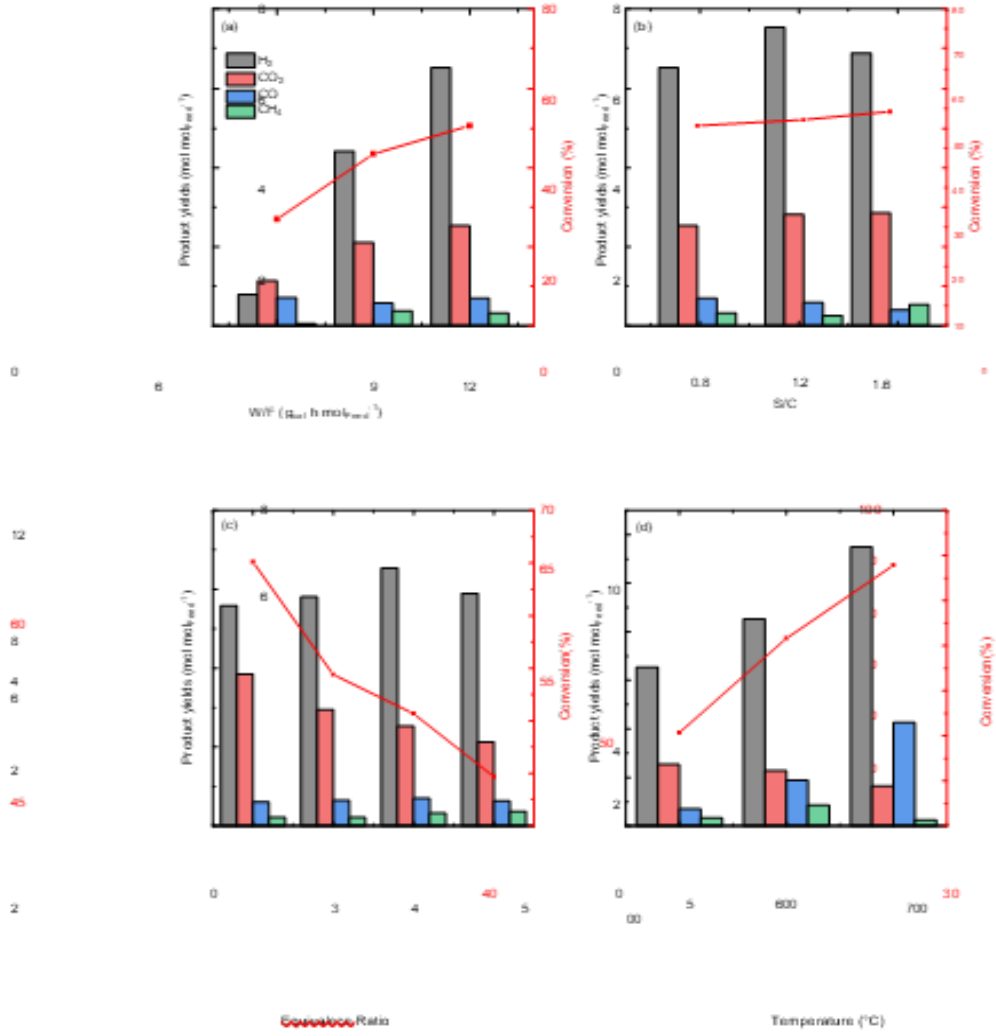


Figure 2. Evaluation of the autothermal reforming of n-heptane at (a) different space times under 500 °C, S/C of 0.8 and equivalence ratio of 4; (b) different S/C ratios at 500 °C, equivalence ratio of 4 and W/F of 12 gcat h molFeed-1; (c) different equivalent ratios at 500 °C, S/C ratio of 0.8 and W/F of 12 gcat h molFeed-1; (d) different temperatures at S/C ratio of 0.8, equivalent ratio of 4 and W/F of 12 gcat h molFeed-1.

4. Conclusions

The optimal operating ranges for the catalytic autothermal reforming of hydrocarbons are experimentally assessed in this study:

- Yields of H2 and CH4 are decreased for ATR while compared to SR at the similar conversion levels.
- Within the studied operating range, the effect of S/C ratio is not pronounced at an equivalence

ration of 4.0 while temperature has a significant impact of conversion and product compositions.

Funding: This research received no external funding.

References

1. F. Melo, N. Morlanés, Study of the composition of ternary mixed oxides: Use of these materials on a hydrogen production process, Catal. Today. (2008). doi:10.1016/j.cattod.2007.12.059.
2. A. Arregi, M. Amutio, G. Lopez, J. Bilbao, M. Olazar, Evaluation of thermochemical routes for hydrogen production from biomass: A review, Energy Convers. Manag. (2018). doi:10.1016/j.enconman.2018.03.089.
3. J.O.M. Bockris, The origin of ideas on a Hydrogen Economy and its solution to the decay of the environment, Int. J. Hydrogen Energy. (2002). doi:10.1016/S0360-3199(01)00154-9.
4. A. Haryanto, S. Fernando, N. Murali, S. Adhikari, Current status of hydrogen production techniques by steam reforming of ethanol: A review, Energy and Fuels. (2005). doi:10.1021/ef0500538.
5. I.K. Kapdan, F. Kargi, Bio-hydrogen production from waste materials, Enzyme Microb. Technol. (2006). doi:10.1016/j.enzmictec.2005.09.015.
6. C.E. Thomas, B.D. James, F.D. Lomax, I.F. Kuhn, Fuel options for the fuel cell vehicle: Hydrogen, methanol or gasoline?, Int. J. Hydrogen Energy. (2000). doi:10.1016/S0360-3199(99)00064-6.
7. L. Li, Z. Shang, Z. Xiao, L. Wang, X. Liang, G. Liu, Steam reforming of n-dodecane over mesoporous alumina supported nickel catalysts: Effects of metal-support interaction on nickel catalysts, Int. J. Hydrogen Energy. 44 (2019) 6965–6977.
8. P.K. Cheekatamarla, C.M. Finnerty, Reforming catalysts for hydrogen generation in fuel cell applications, J. Power Sources. (2006). doi:10.1016/j.jpowsour.2006.04.078.
9. S. Zhang, X. Wang, X. Xu, P. Li, Hydrogen production via catalytic autothermal reforming of desulfurized Jet-A fuel, Int. J. Hydrogen Energy. 42 (2017) 1932–1941. doi:10.1016/j.ijhydene.2016.11.004.

Sustainable Portable Solar-Thermal Desalination Unit

Zaid AlHulaybi [1,*], Mohamad Hammoud[2], Nada S. AlHumaid[2], Amer AlRamdan[2], Sarah M. AlQattan[2], and Ibrahim Dubdub[1]

[1] Chemical Engineering Department, King Faisal University, P.O. Box 380, Al-Ahsa 31982, Saudi Arabia
[2] Chemical engineering graduate, King Faisal University, P.O. Box 380, Al-Ahsa 31982, Saudi Arabia
***** *Corresponding author: zalhulaybi@kfu.edu.sa; Tel.: +966 135897880.*

Abstract: A basic model of a portable sustainable Solar-Thermal Desalination (STD) unit has been designed and built. Optimization for the unit was done. The ability to operate during the absence of sunlight, and its portability make this prototype perfect for emergency uses and for areas where potable water and energy deficiencies are present. The aim is to attain drinkable water from a high Total Dissolved Salt (TDS) concentration water feed (above 30,000 ppm). The desalination process is powered by solar radiation that has been converted to electrical energy (20W solar panel). This energy is stored in a group of batteries. A heater then uses this energy to boil water in a 750 ml tank. Water vapor is then passed through a rolled copper tube to be condensed and transferred to an adjacent tank. The unit can be operated when the batteries are in the process of charging and in the absence of sunlight. Total cost of this design comes at 166 US$. The unit charges to full capacity in 55 minutes. Total heater operation time on a full charge is 1 hour and 15 minutes. Feed boils completely within 50 minutes of heater operation. Further improvements are suggested.

Keywords: Solar energy, Renewable Energy, Sustainability, portable desalination

1. Introduction

The need of fresh water is increased over the years as the market is growing and the population is increasing. The earth is composed of more than 97% of water [1], but most of it is impure water as it is contaminated with chemicals or some harmful organisms. The only nature method to produce fresh water is the water cycle of salty water due to the exposure to solar energy [2]. Fresh water is needed world-wide as salty and contaminated water have biophysiological effects that can lead to morbidity or mortality in some cases. The growth of the population makes the water purifying process challenging. Moreover, fresh water is required for some industrial applications. Generally, producing energy depends highly on water, and most of electricity generation count on it. Therefore, the industry of energy generation has studied the effect of using renewable energy, which have decreased the consumption of water. The dependency on renewable energy can reduce the environmental pollution [1], [3]. Scientists have been inspired by the natural solar system to produce solar desalination, which uses solar energy to purify salty and contaminated water. The system is classified into direct system and indirect system. The main difference is that indirect system uses subsystems other than the solar to collect water after vaporization [1], [4]. Recently, the industry of using renewable energy for desalination has grown and improved. Many researchers and innovators are aiming to study and design systems that can purify water faster, safer, and able to consume minimum amount of energy. This scope of research gets more attention year by year [5].

As most of the earth is covered by impure water, the desalination process becomes necessary and gets lots of attention. World Health Organization (WHO) have approved that the accepted limit of salinity is 500 ppm. Unfortunately, seawater and the water available in the earth have salinity of more than 10,000 ppm [1], [2]. The nature water cycle starts by heating up the salty sea water by the sun. After reaching the boiling point, the water vaporizes. The vapor is condensed and appear as rain after clouds get heavy [1]. The solar desalination system is provided by taking the nature water cycle as a reference. The system is charged by the advantage of manipulating the solar energy. The main power

source should be electric charges travelling through cables. The purification system is provided basically by following the nature water cycle.

In this paper, the main focus is on studying the efficiency of using solar energy to change a battery of a desalination device. By measuring several factors as the charging period, the discharging period, the purification duration, and other, the effectiveness and efficiency can be tested.

2. Materials and Methods

2.1 Literature Review

The earth intercepts a solar power of about 173000 TW. The solar power is larger than the total amount of energy used earth. Thus, solar energy is a dependable source of energy for powering a system that will eliminate the risks and provide safe drinking water. Earlier studies had also developed a number of concepts. One research studied solar panel for water desalination. The difficulty for them was fluctuating of solar panel energy. The findings, on the other hand, revealed the long-term potential of this water purification strategy [6]. Later, it has developed a system where the solar panels power a pump to purify water by radiation [7]. Another modification in water desalination system that was combination of filters and thermal energy [8], while group of research created a distillation unit that uses solar energy to purify water [9]. Then, the performance of 16 solar powered water purification systems were studied. Their research demonstrates that the solar-powered system removes ions from water; chlorine levels are location-dependent. The development of various solar-powered water purification systems is described in this literature, as well as evidence of their feasibility [10].

The thermal method of solar water purification is based on the principle of converting sunlight rays into heat through a thermal heating system. Flat plate collectors, which can generate heat at temperatures as low as 60°C, are frequently used to heat liquids [11]. Solar water disinfection (SODIS), is a type of portable water purification that uses solar energy to disinfect biologically contaminated water. Solar water disinfection usually involves a combination of electricity generated by photovoltaic panels (solar PV), heat (solar thermal), and the collection of solar ultraviolet light. [12]. SODIS is effective in eliminating contaminants and for providing low turbidity water [13]. The advantage of such a system is that the heat can handle wide spectrum of contaminants whether it was microbiological or chemical. Figures 1-3 demonstrates the solar water distillation method [14], a parabolic dish configuration [15], and a “heating coils” configuration [16] respectively. Tables 1-3 show the advantage and disadvantage of the three mentioned configurations.

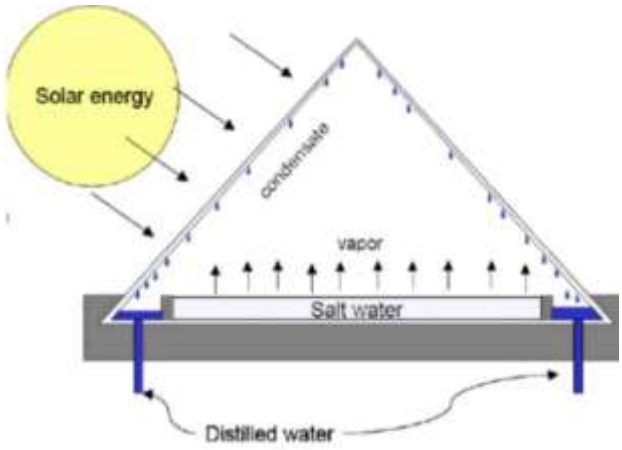


Figure 1. Distillation method

Table 1. The advantages and disadvantages of the system used in the figure above

Advantages	Disadvantages
Condensation is used	It is not portable
Triangle shape	No usage of heating coil

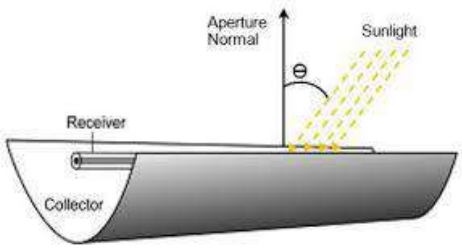


Figure 2. Parabolic dish configuration

Table 2. The advantages and disadvantages of the system used in the figure above

Advantages	Disadvantages
Boiler is used	It is not portable
Batteries are used.	High cost

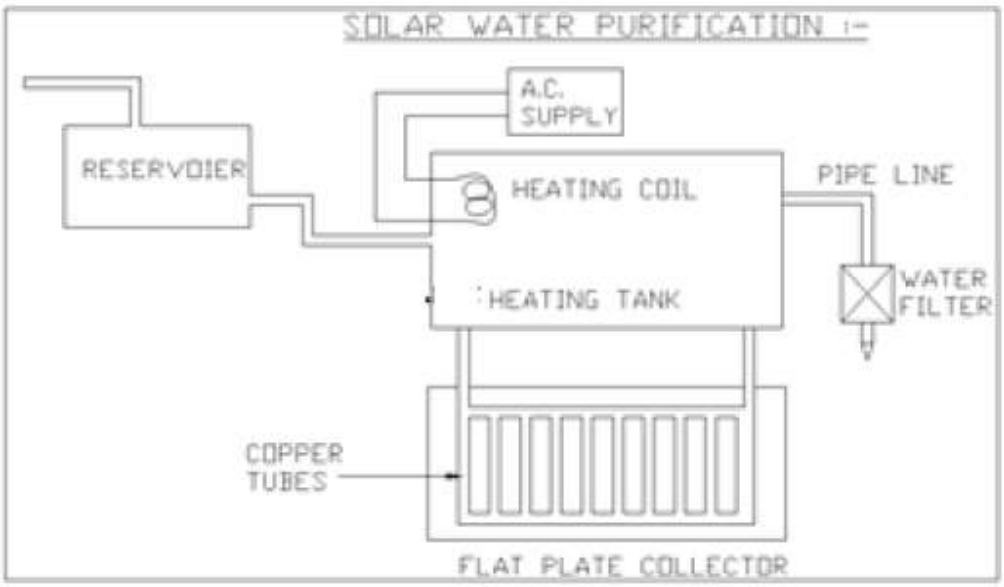


Figure 3. Heating coils solar water purification system

Table 3. The advantages and disadvantages of the system used in the figure above

Advantages	Disadvantages
The design incorporates heating coils within the heating tank, improving the heat supply efficiency for water purification.	No usage of solar panels and batteries

2.2 The Design

2.2.1 Specifications and Requirements

The specifications and requirements that have been taken into account when developing solar-powered water purification system.

1. The system should have a reasonable lifespan
2. The system is powered with renewable energy (sun).
3. The system should have a collection tank that is free of contaminates.
4. The design must be simple to use and produce a sufficient amount of distilled water.
5. The system must be portable.
6. Conductivity, Total Organic Carbon (TOC), pH, Total Dissolved solids (TDS) and other parameters must comply with the World Health Organization (WHO) regulations and recommendations.

2.2.2 Functional Decomposition

The process of breaking down a complex process into smaller, simpler parts is known as functional decomposition. A black box model reveals how energy, material, or signals are converted to achieve a desired result as shown in Figure 4.

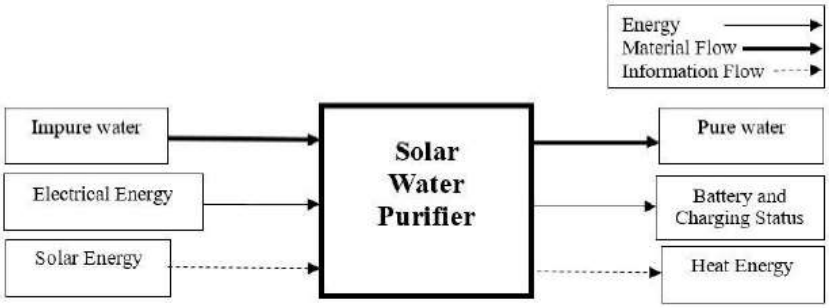


Figure 4. Black box model of the system

System Components:

1. Heating tank made of stainless steel with heating coil at the bottom of the tank
2. Collection tank made of plastic
3. Copper coil tube
4. Solar panels
5. Batteries
6. Battery casing components
7. Battery controller

3. Results and Discussion

3.1. Mechanism

Figure 5 depicts the setup of the solar-powered water purification system. High efficiency polycrystalline solar cells with a 12 Volt, 20W capacity each were used. The water was heated with a 600 W immersion heater. As a backup power source and to store excess power from the solar cells, a 12-volt rechargeable battery was used. Condensation was done through bended copper tubing coil. A storage tank made of stainless steel with 750 ml capacity with heating coil. Raw water is filled into the tank and is heated by heating coil. As the steam passes through the copper coil, it condenses and collects at the other tank which is made of plastic. The plastic tank has capacity of 750 ml. The batteries do not involve in the process at day. However, at night when there is no sun light, the batteries start working to provide energy to vaporize the raw water. The solar powered water purification system was tested under various conditions. Initial tests were conducted to observe the volume of pure water produced at different times of the day as the sun's brightness varies. Figure 6 shows the block diagram of the system.

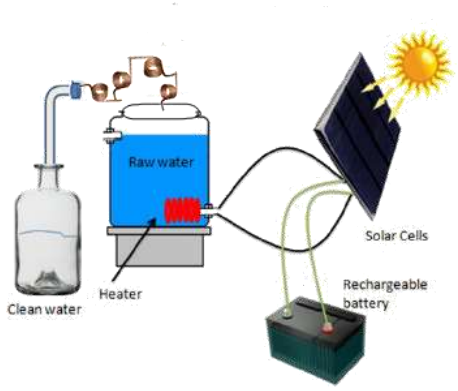


Figure 5. Setup for the desalination system

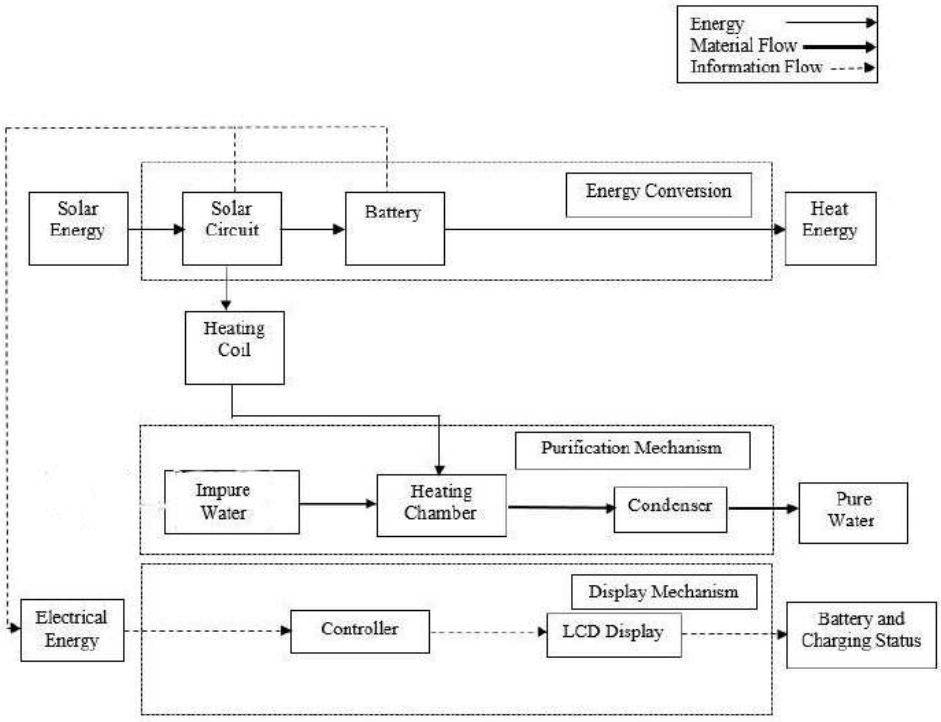


Figure 6. Block diagram of the system

3.2 Energy Calculations

Battery capacity is measured in Amp Hours (AH). It is needed to be converted to Watt Hours by multiplying the AH by the battery voltage (V).

$$\text{Power in battery (watt hours)} = AH \times V, \quad (1)$$

$$\text{Time to charge the battery} = \text{Power in battery (watt hours)} / \text{Power of solar panel (watt)}, \quad (2)$$

$$\text{Total heat input to raise the temperature of water } (Q) = V \times \rho \times Cp \times \Delta T, \quad (3)$$

Where Q is the total heat input (kJ), V is the volume (m^3), ρ is the density (kg/m^3), C_p is the specific heat ($kJ\ kg^{-1}\ K^{-1}$), and ΔT is the temperature rise (K or ^0C)

$$\text{Time needed to rise temperature of the water, t (min)} = (Q \times 1000) / (\text{Power of heating coil} \times 60) \quad (4)$$

3.3 The Final Product

The overall system is composed of the power supply (battery of 12V and 5A and solar panel if 12V and 20W), the solar charger controller, heating mechanism followed by a cooper coil in between two tanks as shown in Figure 7 and Figure 8, and one of the tanks are well-insulated.

The solar panel work as a charger for the batteries. The charging process is controlled by a solar charger controller. The power supply is 12V batteries connected in parallel inside an acrylic case cut by laser cutter and fixed by screws as shown in Figure 9. The batteries have a total capacity of 60 Amp-hour. They are responsible for providing the whole system with the required energy to perform by feeding the solar panel controller as well as the heater for the desalination process to occur. The solar charger controller is responsible for control the timing of the system and when to turn on and off when the batteries are fully charged and connected. Then, the first tank that is integrated with the

heater to desalinate the dirty water is insulated using a duct wrap. Also, it is connected with a copper coil used as a colling mechanism for the evaporating water before entering the second tank where the clean water is tested using TDS, pH, Tds, Ec, temperature sensor.

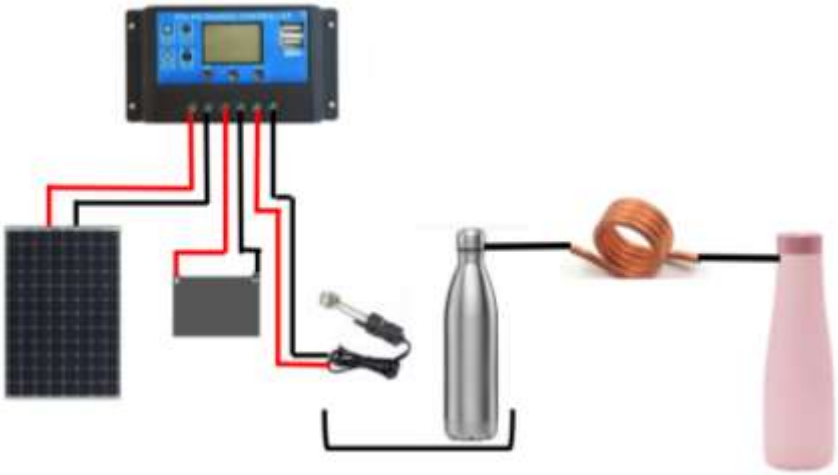


Figure 7. The overall connection of the system

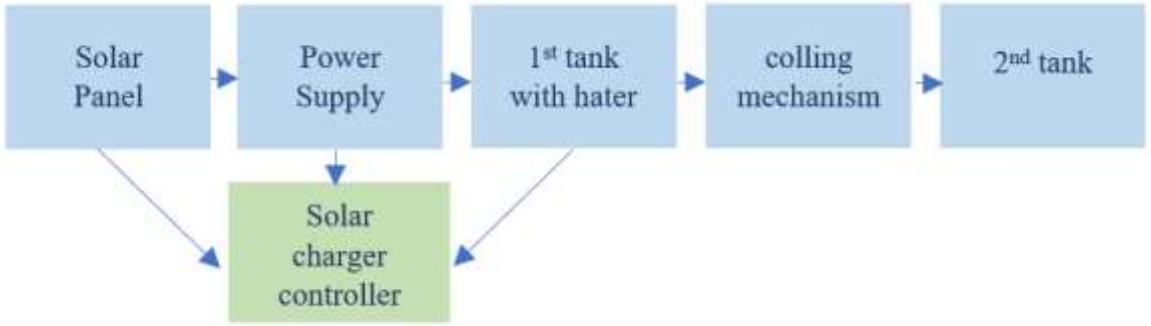


Figure 8. Illustration of the block diagram of the overall connection of the system

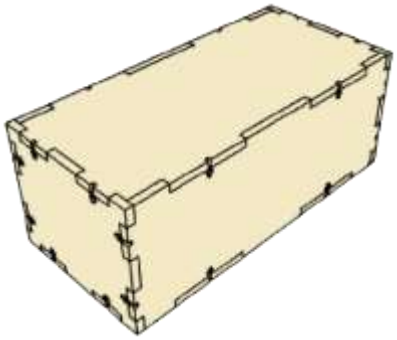


Figure 9. The acrylic box that is cut using the laser cutter.

The implemented system is shown in Figure 10. It tests and gives the following result. The solar panel charges the batteries in around 1 and half hours and the batteries can charge and power the

system at the same time. The water in the 1st tank is boiled and starts to evaporate in 30 minutes. Hence, the distillation process starts and operates for 1 hour. Thus, the system is working for 1 and a half hours when the batteries are fully charged.

Note: the system efficiency is quite low since the heater is AC. The efficiency can be improved in 2 possible scenarios. first, the system uses a DC heater. Second, the system uses an inverter to convert the coming power from direct current (DC) to alternative current (AC).



Figure 10. Picture of the overall implemented system

4. Cost

Total cost of the unit is 166 US$. This price is the cost of the built design that had some time limitations. Without this limitation this unit can be built at a lower price due to the availability of cheaper options overseas. In addition, this unit will cost much less when it is massively produced. Finally, the price can be lowered drastically by choosing other batteries options that can give the same results. The total cost is distributed as follows:

1. Copper wire at 26 US$
2. Battery Controller at 9 US$
3. Two liquid containers at 16 US$
4. 20-Watt foldable solar panel at 48 US$
5. Acrylic Sheets at 32 US$
6. Heater at 8 US$
7. Special Adhesives at 12 US$
8. Insulation Sheets at 8 US$
9. Bolts at 4 US$
10. Wires at 3 US$

5. Conclusions

The portable STD unit proved highly effective in producing the outcomes needed for its expected usage. Wrapping the feed tank with thick insulation greatly improved the process. The first droplets of the product water appeared at the twelfth minute almost half the duration it took without the insulation. It also helped improved the efficiency of the entire process by reducing heat losses. The

final model charged its batteries to the fullest in around 55 minutes. It was able to completely boil the feed in around 50 minutes. Total operation time on a full charge was one hour and fifteen minutes. Thus, the model can boil one and a half the maximum feed capacity. This can be extended to full two times the maximum feed capacity if the solar panel is charging the batteries while operating the process. The total cost of the unit was about 166$. The unit was small enough to be portable. This shows promise for future small scale desalination units to be developed. The target of such future devices being communities where potable water is scarce or the natural supply is of bad quality. Such a device will prove useful as an aid for various humanitarian efforts. Also, this model can be equipped as an emergency device for people who happen to be heading to a location were energy and clean water is not available. In addition, a lot of enhancement can be done to further improve the overall process. The suggested improvements are in the following areas:

1. Batteries: Replacing the battery set with a single battery of the same capacity or larger will make the overall design more compact, reduce energy losses, and reduce costs.
2. Heater: A better more efficient heater is needed that is more suitable for such operations. A lower cost heater would be preferred.
3. Tanks: Better shaped tanks might allow for a more effective insulation. Better shaped tanks would also allow for easier cleaning of any accumulated residue salts at the bottom of the feed tank.
4. Insulation: Using other insulation products like foam insulation might yield better overall results.
5. Condensation: Replacing the typical copper wire with a more complex cooling system might drastically improve the overall process.

Acknowledgment

We would like to express our special thanks of gratitude to “Kayen Solar” for donating some of the components used on this design. Also, this research was funded by the King Faisal University.

References

1. G. N. Tiwari, H. N. Singh, and R. Tripathi, *“*Present status of solar distillation,*”* *Solar energy*, vol. 75, no. 5, pp. 367–373, 2003.
2. I. Al-Hayeka and O. O. Badran, *“*The effect of using different designs of solar stills on water distillation,*”* *Desalination*, vol. 169, no. 2, pp. 121–127, 2004.
3. M. A. Al-Nimr and K. S. Qananba, *“*A solar hybrid system for power generation and water distillation,*”* *Solar Energy*, vol. 171, pp. 92–105, Sep. 2018, doi: 10.1016/j.solener.2018.06.019.
4. T. Arunkumar *et al.*, *“*Effect of parabolic solar energy collectors for water distillation,*”* *Desalination and Water Treatment*, vol. 57, no. 45, pp. 21234–21242, 2016.
5. G. W. Crabtree and N. S. Lewis, *“*Solar energy conversion,*”* *Physics today*, vol. 60, no. 3, pp. 37–42, 2007.
6. M. Forstmeier, W. Feichter, and O. Mayer, *“*Photovoltaic powered water purification ─ challenges and opportunities,*”* *Desalination*, vol. 221, no. 1, pp. 23–28, Mar. 2008, doi: 10.1016/j.desal.2007.04.063.
7. D. Saraceno, *“*Solar powered portable water purifier,*”* US6863827B2, Mar. 08, 2005 Accessed: Aug. 16, 2021. [Online]. Available: https://patents.google.com/patent/US6863827B2/en
8. Wright,A.V.2011.*“*Solar-powered water purification system*”* US20110186529A1,Jan.01,2011 Accessed:Aug.15,2021.[Online].Available:https://patents.google.com/patent/US20110186529A1/en

9. Thomas A. Joseph, III, Charles Christopher Newton, Henry Maurice Wandrie, III, Matthew Carter, "Solar powered water purification system",US10953341B2,Sep.13,2012 Accessed: Aug.15,2021.[Online]. Available: https://patents.google.com/patent/US10953341B2/en
10. M. Jaskolski, L. Schmitz, P. Otter, and Z. Pellegrino, "Solar-powered drinking water purification in the oases of Egypt's Western Desert," *Journal of Photonics for Energy*, vol. 9, p. 043107, Oct. 2019, doi: 10.1117/1.JPE.9.043107.
11. Rockenbaugh, C., Dean, J., Lovullo, D., Lisell, L., Barker, G., Hanckock, E. & Norton, P. 2016. High-performance flat plate solar thermal collector evaluation (No. NREL/TP-7A40-66215). National Renewable Energy Lab. (NREL), Golden, CO (United States).
12. Cdc.gov. 2021. Solar Disinfection | The Safe Water System | CDC. [online] Available at: <https://www.cdc.gov/safewater/solardisinfection.html> [Accessed 16 August 2021].
13. Y. Zhang, M. Sivakumar, S. Yang, K. Enever, and M. Ramezanianpour, "Application of solar energy in water treatment processes: A review," *Faculty of Engineering and Information Sciences - Papers: Part B*, pp. 116–145, Jan. 2018, doi: 10.1016/j.desal.2017.11.020.
14. K. Vinoth Kumar and R. Kasturi Bai, "Performance study on solar still with enhanced condensation," *Desalination*, vol. 230, no. 1, pp. 51–61, Sep. 2008, doi: 10.1016/j.desal.2007.11.015.
15. B. Sommer *et al.*, "SODIS—an emerging water treatment process," *Journal of Water Supply: Research and Technology AQUA*, pp. 127–137, 1997.
16. J. Ghannam, G. M. Ayoub, and A. Acra, "A Profile of the Submarine Springs in Lebanon as a Potential Water Resource," *Water International*, vol. 23, no. 4, pp. 278–286, Dec. 1998, doi: 10.1080/02508069808686783.

Total safety operation management (TSOM) & business continuity management (BCM) of fire, life safety design aspect

Jalal R. Omar *

[1] Mechanical Engineer, Faculty of engineering Hashemite University;
[2] National Fire protection Association (NFPA) Subject Matters Expert (SME), Certification Advisory Group (CAG);

***** *Corresponding author: sjalal.omar.911@gmail.com ; Tel.: +966502081824, +966508581505*

Abstract: The Major Concepts of Fire & Life Safety Aspect meanwhile Embracing "Safety is Everyone's Responsibility" culture will ensure that the highest standards are compiled to protect People and Assets and what is the difference Between Codes & Standards, Furthermore, shows the Goals of Plan & Design Review and best practices of Fire Life safety (FLS), Health Safety Environment (HSE) Protection Finally TSOMS, BCMS Target Operating Model within Governance (Peace Time) and Recovery (Crisis Time) in Three tiered structure, Level 1- Strategic for Takes strategic decisions taken support and align to the organization's mission and vision and Project Communication Plan, Project Management Plans and Invoke response and recovery plans as required, during a business disruption and Ensure that Policies & Procedures and plans are developed and fit for purpose including the performance of management reviews. Level2-Tactical for Manage preparation and planning for Inspection, Risk Assessment, Fire & Life Safety Evacuation Plan & Drill, Before, During, After disruptions, and Oversee the execution of response and plans within their respective departments, sectors / business units, and Liaise with the Strategic team on a continual basis to obtain support for seamless implementation and continual improvement. Level 3-Operational for Participate in preparation of business impact analysis, threat scenario analysis and development of response plans, and Execute for Inspection, Risk Assessment, Fire & Life Safety Evacuation Plan & Drill, Response and Recovery Procedures, and Attend training, awareness and exercises. Finally the Conclusions: to Indicate What Should Know If you are an architect, must ensure that the plans and specifications are prepared to satisfy the necessary requirements to pass the approval process, including those requirements in the referenced codes and standards. / If you are a contractor / installer, must ensure that installation is in compliance with all necessary requirements, including referenced codes and standards — which often include manufacturer's installation instructions. / If you are an Authority having jurisdictions (AHJ), must ensure that your plan review process and onsite inspections verify compliance with all aspects of the code, including all referenced codes and standards. / If you are a building owner / facility manager, you must ensure that you follow the inspection, testing, and maintenance (ITM) requirements in the referenced documents to keep your buildings, occupants, and contents safe on an ongoing basis.

Keywords: TSOM; BCM; Fire, Life Safety Design;

Theme 7: General Chemical Engineering

APC Plants Zero Liquid Discharge (ZLD) Case Study

Ala'a Omari

Solar Pond Manager / The Arab Potash Company

APC's projects are set up according to the internationally acceptable procedure for collection and disposal of waste which is implemented through layout the design; most of the liquid process waste from the refineries are returned to the Dead Sea without any adverse effect. Another similar stream of liquid wastes that is saturated in sodium chloride is discharging in a stacking area (salt tailing disposal area) where the sodium chloride is naturally dewatered without entering into the ground water.

Achieving stringent waste potassium chloride brine, reducing process water usage and reducing operating running cost have become one of the most critical considerations in potash production today. Numerous environmental regulations, rigorous permitting processes, and lack of water availability in Jordan, among other factors, as well as, the principal goal of the Arab Potash Company has been to attain the best equipment performance and plant recoveries consistent with environmental compatibility at APC sites and reduce environmental impact as far as possible in accordance with highest international standards because it reduces operating costs and no effluent, or discharge, is left over.

A molecule of brine takes up to 12 months on the trip from the Dead Sea through APC's ponds system and back again after shedding its cargo of minerals. Consequently, APC process employs the most advanced technologies to purify and recycle virtually all of the waste potassium chloride brine and solid and this drive The Arab Potash Company facilities to implement zero liquid discharge (ZLD) systems as a key solution. Another objective of ZLD is to gain potash production rate without any need for extra carnallite raw material.

This paper will highlight on APC methodology and projects of Zero liquid discharge (ZLD) that have been taken:

- Controlling and monitoring process parameters are the main category in decrease potassium chloride stream losses and a key to consistent production by adding new carnallite decomposition tanks, hot leach tanks, installing a new modernized distributed control system and on line instrumentation devices such as K40.
- Collect, treat and recover valuable K^+ ions from plant purge streams by construct carnallite pond (C-4) with an area of 5 km^2. On average the yearly recover KCl product is 0.35 MMTPY.

- Reduce plants losses and improvements in the front-end of the process, plant feed through plants recovery projects that not required carnallite raw material such as carnallite decomposition and carnallite thickener underflow stream dewatering project.
- Better management of the reclaimable process water.

APC has meanwhile continued to undertake improvements at the plants to reduce KCl losses and improve the overall plant performance which will result in an increase of plant recoveries. Recently APC has completed the implementation of the following ZLD projects.

- Recover KCl from the plants tails brine, currently, tails stream from the 3 plants (HLP, CCP1 & CCP2) is pumped to the tailings area to the west of the plants. This stream consists of solid phase (tails solids) and liquid phase (tails brine). The tails solids accumulate in the tailings area, while the brine percolates and flows by gravity to the truce canal through long channels. The brine from the tailings pile collecting point with an average amount of 260 m^3/hr will be rerouted into the settling pond and then to carnallite pond C-4 to recover an approximate of 35,000 TPY KCL.
- Reclaim Grade B Potash and dust by collecting them in separate piles (open yard), and after its physical treatment, grade B potash is dissolved at hot leach tank #5 in the hot leaching plant (HLP). Within its "Dust & Rejected Materials Reclaiming System Project", APC is recycling and utilizing an approximate 10,000 TPY of grade B Potash and maintain a clean environment and good housekeeping.

1. QMS - APC Accreditation

APC management recognizes that Safety, Quality & Environment are crucial for assuring business sustainability, profitability and growth. Therefore, a Quality Assurance system has been established to ensure the establishment, effective implementation and continual performance improvement of an Integrated Safety, Quality & Environment Management System according to the relevant updated local and international standards. Furthermore, APC has developed a long-term strategy that draws a map to the future and raising the company's capabilities in all respects

As a result of management commitment at all levels, the cooperation of all departments through active participation in internal audits and management review processes, and the effectively implemented awareness programs, APC successfully achieved certificates of compliance of the following international and local standards:

1. Occupational Safety and Health Management System Standard –OHSAS -18001 on May-15 -2004, being the second company in Jordan to achieve this certification.
2. Environmental Management System Standard (EMS) -ISO -14001:2004 on May-18 -2005, being the first company in Jordan to achieve this certification.

3. Quality Management System Standard (QMS) - ISO -9001:2000 on June - 07-2001, being one of the pioneers' companies in Jordan to implement this standard.
4. Quality Management System Standard (QMS)- ISO- 9001:2000 on August-05-2004 for our APC Hospital and Clinics.
5. "General requirements for the competence of testing and calibration laboratories" standard-ISO-17025:2005 on September-23-2008, as a result of which our APC laboratory was certified as an accredited laboratory at local and international levels.
6. Jordan Quality Mark on March-18 -2004.
7. Indonesian National Standard (SNI): APC is proud to update regularly its quality management system certificate to the Indonesian National Standard (SNI) as indication to meet requirements and allow potash to be sold anywhere in the Republic of Indonesia.
8. Australian Quarantine & Inspection Service: APC strive to keep AQIS biosecurity certificate to assure potash products are free from organic materials.
9. **Award:** As national; APC won the best Jordanian producer in the chemical Industries sector's award for a period of two years 2017 and 2018.
10. **IFA**, As international; APC is a member in the International Fertilizer Association (IFA) and is certified and comply with IFA requirements of Product stewardship; This program focus on product care and maintaining the Safety, Health, Security and Sustainable Environment requirements during the product life cycle to the end users.

2. Introduction

About APC

The idea of the Potash project was based on the Potash Plant located on the north-western shores of the Dead Sea during the British Mandate. The old plant was destroyed but the idea remained alive and a Pan Arab company was formed in 1956 to implement a project for the production of Potash using the minerals of the Dead Sea.

The site is located 110 kilometers south of Amman and 200 kilometers north of Aqaba. The site is a Solar Evaporation Pond System of a large area and processing plants for the ore.

The investment in the original project, including substantial infrastructure was nearly 480 Million USD. Financing was obtained through loans from international finance institutions and aid agencies as well as Arab development funds. The project began in 1976 with tests and experiments to determine the parameters of various technologies and ideas in a very hostile environment. Construction began in 1979 and was completed in 1982. At the end of construction, about (117) kilometers of seepage proof dykes were built (other dykes built later on). These were more than 8 meters wide at the top and were an engineering challenge to be built on top of a non- stable sea bed. The excavation carried

out during the construction period was of a colossal magnitude, 16 million cubic meters of earth material was displaced.

Potash production began in 1983 and has since progressed with various schemes aimed at optimizing and expanding this production. The initial plant was built to a capacity of 1.2 million tones of product.

This was expanded in the late eighties to handle 1.4 million tones and key modifications were undertaken with the Solar System to enhance the production of the ore accordingly. A second plant based on different technology and of a capacity of 0.4 million tones was built in 1994 and this brought the total production capacity to 1.8 million tones. Then another cold crystallization plant of 0.45 million tones was built in 2010 and this brought the total production capacity to 2.45 million tones. Currently, the plants are accomplished a production of 2.62 million tons of potash, Further expansion is currently under evaluation to bring the total potash capacity to 3.2 MMTP.

The capital of the Arab Potash Company is 83.3 million Jordanian Dinars. It has a concession from the Jordanian Government to exploit, manufacture, and market the mineral resources of the Dead Sea, until 2058.

The Arab Potash Company employs over 2000 personnel and has offices in Amman, Safi and Aqaba. It owns extensive housing and recreational facilities near its plants, and in addition, it provides the surrounding region with assistance in social, medical, economic and vocational development.

3. Background

Potash production involves the separation of the valuable product from largely inert waste materials. These waste materials typically comprise a coarse soluble component, mostly sodium chloride or other salts, and fine grained insoluble clay. Each ton of potash produced generates about 2 tons of waste salt, together with slimes and brine. Traditionally, these wastes have been disposed of either by discharge into waters and or by storage in surface disposal facilities. The disposal of these waste products, particularly the salt and slimes which are discharged on the surface, has recently become an environmental concern. This concern is forcing companies and regulatory authorities to review disposal practices.

The Arab Potash plants is situated in an environmentally sensitive area, well-known for its vegetable farming. In such an area it was recognized that the storage of brine waste on surface would be unacceptable, and the plant was designed around this principle.

Two main waste streams – salt and brine - must be managed as an integral part of the plants system. The total quantity of sodium chloride produced in the plants as solid wastes is around 2.0 million tons per annum, sodium chloride is pumped as a slurry mixture from both plants to a situated 2-3 km from the refineries tails site. Tails area, sufficiently large as to absorb all the solid wastes resulting from one hundred years' production period, constitutes salty soil (inconvenient for flora) that was part of

the Dead Sea ground; the topographical nature of this area assists the flow of the brine from the tails area to the Dead Sea through the truce channel.

In an attempt to reduce the requirement for discharge of waste material into the environment and the necessity of extensive surface disposal facilities, APC had evaluating alternative to recover the waste clarified brine by withdrawing it by channels and to be pumped to surface as a feedstock for the carnallite ponds - a process which recovers the contained potash values in the brine. By designing such system which integrates the mining, processing and disposal of all product streams, and by careful production planning, it has been shown that zero effluent potash mining is possible and points the way for the industry in the future.

4. Potash Production Process Description

The Dead Sea is located in the Dead Sea Rift, which is part of a long fissure in the Earth's surface called the Great Rift Valley. The 3,700 mile (6,000 km) long Great Rift Valley extends from the Taurus Mountains of Turkey to the Zambezi Valley in southern Africa. The Dead Sea lies 426.78 m below sea level, making it the lowest elevation and the lowest body of water in the world.

At the heart of the Ghor El-Safi site are a 112 km^2 solar evaporation ponds system and ore processing plants. The brine from the Dead Sea is pumped at a yearly average rate of 350 million tons into the solar evaporation system by main intake pumping station, where the initial concentration process is undertaken at the salt ponds where NaCl deposits. The remaining brine is pumped into the Carnallite ponds, to precipitate the raw Carnallite.



The precipitated raw Carnallite is the raw material for producing potash is precipitated as mixture of Carnallite ($KCl.MgCl_2.6H_2O$) and NaCl. This bed is harvested as a slurry from beneath the brine and delivered to booster pumps on the dikes and then to the refinery through floating pipes.

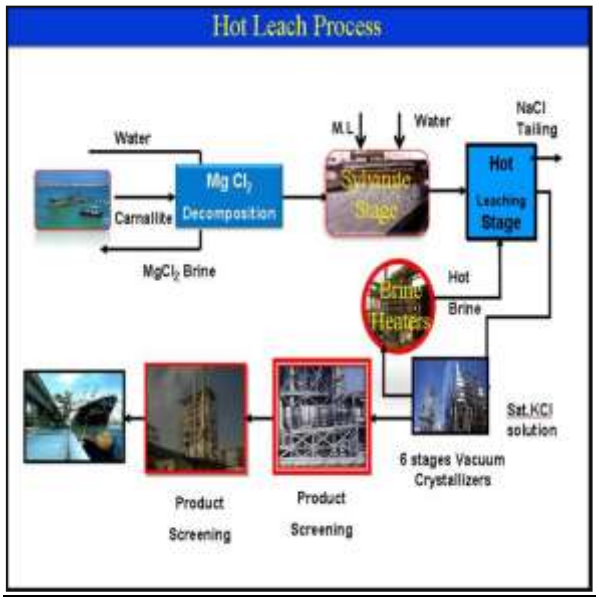


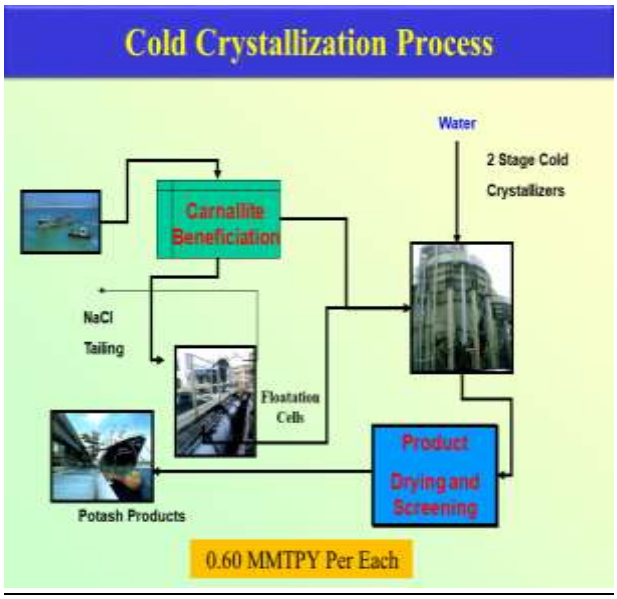
The Raw Carnallite is harvested and pumped to three refineries. The original plant employs hot leach technology to process the Carnallite to extract potash, but the newer facilities employ cold crystallization.



The original plant employs hot leach technology to process the Carnallite to extract potash, but the newer facilities employ cold crystallization.

To ensure a clean environment and to minimize potash losses as dust, APC has installed several de-dusting systems, such as bag filtration units and high-efficiency cyclones.





5. Methodology

A molecule of water takes up to 12 months on the trip from the Dead Sea through APC's ponds system and back again after shedding its cargo of minerals, therefore the running cost is relatively high compared with other potash industries.

Producing an excellent quality of potassium chloride, optimizing process water usage and reducing operating running cost have become one of the most critical considerations in potash production today. Stringent environmental regulations, and lack of water availability in Jordan, among other factors, as well as, the principal goal of the Arab Potash Company has been to attain the best equipments performance and plant recoveries in parallel with environmental compatibility at APC sites

APC employs the most advanced technologies processes to purify and recycle virtually all of the waste potassium chloride brine and solid and this drive The Arab Potash Company facilities to implement zero liquid discharge (ZLD) systems as a key solution.

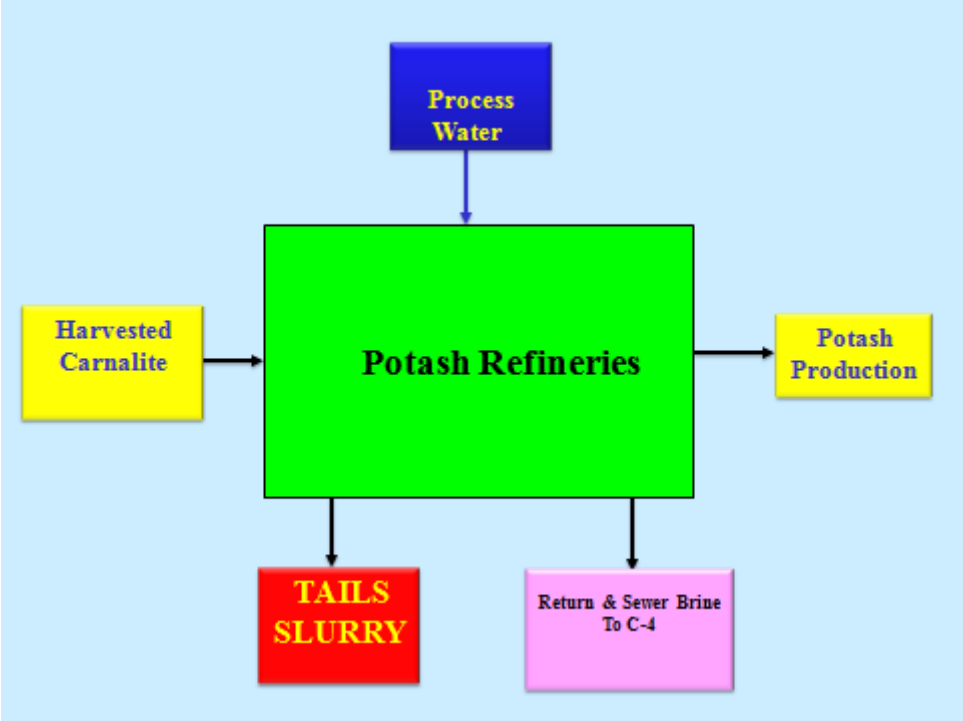
This paper will address the APC methodology and projects to achieve Zero liquid discharge (ZLD) that have been taken: -

- Collect, and recycle the streams to recover valuable K^+ ions from plant purge streams by constructing carnallite pond (C-4) with an area of 5 km^2. On average the yearly recover KCl product is 0.35 MMTPY.
- Controlling and monitoring plants process parameters are the main category in reducing potassium chloride stream losses (brine losses)
- Adding process equipments in the plants and on line control devices to enhance production and reduce losses, this is another key to a consistent production, for instance, new carnallite decomposition tanks, hot leach tanks, new modernized distributed control system and on line instrumentation devices such as K40 have been installed in the plants.
- Reduce plants losses and improvements in the front-end of the process, plant feed through plants recovery projects that not required carnallite raw material such as carnallite decomposition and carnallite thickener underflow stream dewatering project.
- Better manage of the reclaimable process water by collecting the drainage water which contains KCl brine and utilize it in the operating process by a mean of sumps and pumping station from different locations at plants so as to recover KCl and reduce water consumption. In addition, a new reclaiming sump has been constructed in the HLP in order to collect all running water which contains KCl under the screening area and return it back to the HLP water circuit to make use of it in the operational processes instead of losing it in the sewer stream.
- Plants Sewer collection sump: sewer boxes have been constructed at the plants to measure the quantities of the liquid phase coming out of the plant so far the to control the KCl brine losses.
- Using low flow packing / expeller / mechanical seals for all process pumps

APC continue to undertake improvements at the plants to reduce KCl losses and improve the overall plant performance which will result in an increase of plant recoveries. Recently APC has completed running phase one for one of the major ZLD project, **Tails Brine capturing Project:** it's aimed to recover KCl from the plants tails brine, currently, sodium chloride is pumped as a slurry mixture from plants to the refineries tails site. the topographical nature of this area assists the flow of the brine from the tails area to the Dead Sea through the truce channel. An approximate 500 m^3/hr of tails brine stream will be recycled back to the solar ponds system to recover more potash (two phases).

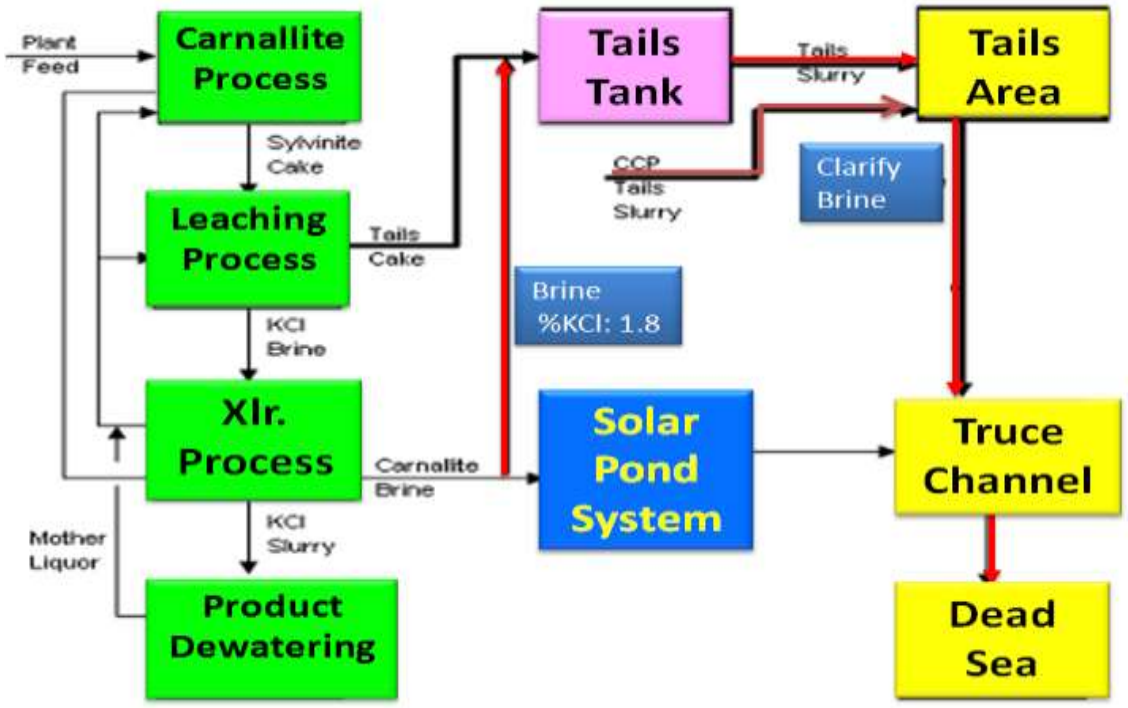
6. Case Study: APC Plants Zero Liquid Discharge (ZLD)

The brine wastes or tailings produced by the potash industry are the main topic of this paper. The waste is composed primarily of sodium chloride. Brine is used for repulping tails waste to the tailings piles. The release of brine to the local environment is the prime environmental problem facing the potash mining industry since some runoff carrier brine can alter containment the adjacent soil area.



Only one solid waste is produced upon potash producing processes, this is being sodium chloride, NaCl. Through the hot leach plant mechanical process, the carnallite solid is separated from the brine. As the brine is highly rich with KCl, a high percentage of this brine is directed back to the carnallite ponds to recover KCl. Small percentage of this brine is reused in the HLP in different processes. The tails cake is one of these uses where the brine is added to the tails cake in the tails repulp tank so as to facilitate the pumping of the tails waste to the ultimate disposal point. The percentage of the brine rich with KCl is lost with the tails as waste have an average of 1.8%. The quantity of the brine depleted for solid tailings is around 500 m^3/hr.

As well, In Cold Crystallization Plants (CCP1 & CCP2), crude carnallite slurry is beneficiated by wet screening to separate the high-grade carnallite, which is fed directly to the Cold Crystallizers. Fine material – screen under size – is treated with flotation reagent to remove NaCl and pumped it to tailing area. The percentage of the brine rich with KCl is lost with the tails as waste have an average of 2.65%.The quantity of brine consumed to dispose CCP1 & CCP2 plants tails are around 200 m^3/hr.

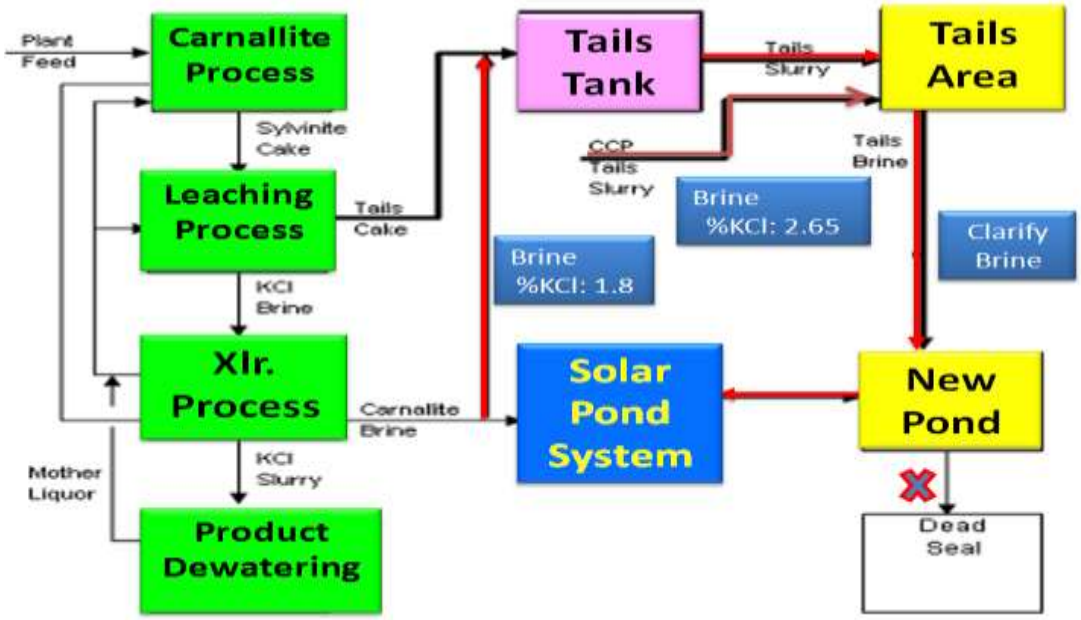


Sodium chloride is pumped as a slurry mixture from both plants to a situated 2-3 km from the refineries tails site, just to the south of the plants. Tails area, sufficiently large as to absorb all the solid wastes resulting from one hundred years' production period, constitutes salty soil (inconvenient for flora) that was part of the Dead Sea ground The topographical nature of this area assists the flow of the brine from the tails area to the Dead Sea through the truce channel.



The principal objective of the project is the utilizing of the rich runoff brine with KCl in the nearby #10 Dike by rerouting it to carnallite ponds. The first step was studying alternatives of recovering lost KCl through the refineries tailing in order to develop a system for tailing disposal.





The investigation works consist of a leaching field for recovering KCl from the tails slurry and disposing the NaCl at the tails end, a pilot filed leaching test had been carried out with the same configuration that would be applied in the actual leaching filed. The main findings of the tailing pilot test had shown staisfactory efficiency; however the system was not checked with higher depth of salt.

KCl Recovery Estimate: -

To estimate the KCl recovery quantities, the following have been assumed: -

- The above brine amounts will be delivered for the carnallite ponds for further deposition.
- The deposited quantities will be 55% of the total KCl delivered to the carnallite ponds.
- Plants recovery is 78%.

Table (1): Overall Estimate Of KCl Losses with Tailing Slurries

	KCl Losses With Tails Solid (TPH)	KCl Losses With Tails Brine (TPH)	KCl Losses With Tails Slurry (TPH)
HLP	5.9	8.0	13.9
CCP1	3.2	3.2	6.4
CCP2	3.2	3.2	6.4
Total	12.3	4.8	26.7
Average Yearly Total (Tons)	HLP: 48,984 CCP1: 26,560 CCP2: 26,560 Total: 102,104	HLP: 66,400 CCP1: 26,560 CCP2: 26,560 Total: 119,520	HLP: 115,384 CCP1: 53,120 CCP2: 53,120 Total: 221,624

Based on the above, the total approximate quantity of sodium chloride produced as solid wastes is around 2.0 million tons per annum, or equivalently one-ton sodium chloride per ton potash produced. The project conserves carnallite thickener over flow streaming to C-4 pond and thus, augments the raw material production in the solar ponds by a quantity equivalent to about **60,000TPY potash**.

Tailing Project Process Description

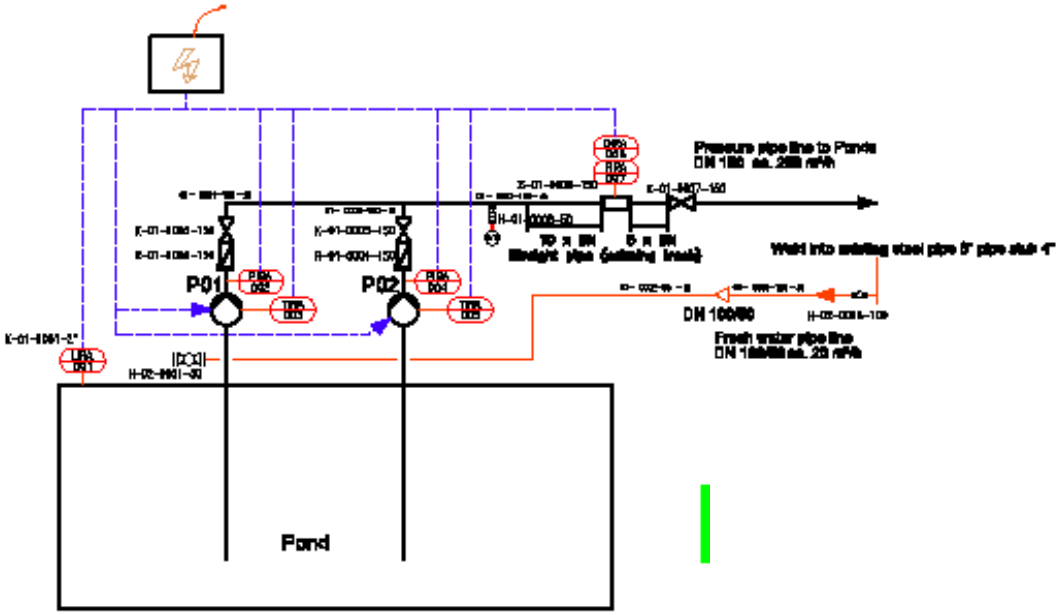
The project commences in construction of Collecting Pool to receive the brine from the existing collecting channels in the area. The existing proposed channels will collect the seepage rich KCl brine and directed it towards pumping station sump pump. The seepage channels will be protected on slopes with loose riprap and with a facility to allow seepage of brine into the channel.



Existing Tails Brine Collecting Trench

In this pond a pump station has been installed as per below P&ID. The pump station consists of vertical sump pumps. One of them is reserve. The pumps and measuring instruments are controlled by the control center via radio.

The brine pipe extends from the pump station to the pond No. C4. In the area around the new tailing pond the brine pipeline is supported on sliders. To run through the dyke 10 a protection tube is used. The material of the brine pipe line and the protection tube is steel. The design of the pipeline embankment side slopes and its foundation.



Tailing Project Components

The project consists of following units:

- Collecting pond.
- Vertical submerged centrifugal pumps.
- Weir flow calculation V-Notch triangular.
- Pipelines and Fittings with a pipe bridge.
- Measurement devices: Flow Meter/ Densitometer, level meter, pressure & temperature measurement.

7. Conclusion & Recommendations

With "Zero liquid discharge" it's really complicated topic in potash industry, there are nearly no potash plants known with zero liquid discharge, especially not when the process depends on raw carnallite material.

However, to achieve zero liquid discharge at potash plants and maximize the possibility of recovering the potassium chloride in liquid phase, APC has carried out the detailed engineering of tails brine capturing project, the proposed system will consist of collecting channels, leaching pond, pumps and piping station.

This system will avail additional 60,000 TPY KCl recovery gained, and based on the commercial net profit of KCl: 50 $/ton, the additional net profit from this project will be 3,000,000 $ per year with a payback period 4 months.

Based on the above figures, the project is feasible and its highly recommended to proceed with the second phase (implementation).

COVID-19 effect on health and safety of workers in the workplace: A case study in Jordan

Heba Alzaben , Ali AlShquar , Ban Baniatta , Ibrahim Alzoubi and Sameer AlTawabini *

Mechanical and Energy Engineering Departments, Al-Hussein Technical University

***** *Corresponding authors: Heba.AlZaben@htu.edu.jo; ali.alshquar@htu.edu.jo, Ban.Baniatta@ htu.edu.jo, ibrahim.alzoubi@htu.edu.jo; sameer.altawabini@htu.edu.jo Tel.: +962 6 580 8787.*

Abstract: The COVID-19 pandemic has made changes in different sectors, including the occupational health and safety sector. This paper presents an overview of the impact of COVID-19 related to health and safety of workers in different workplace environment including office work, industry, construction, and pharmaceutical laboratories in Jordan. In addition, this study presents the general control measures followed by different companies in Jordan to protect the health and safety of the workers and minimize the community spread of the virus, which were suggested by health and safety agencies including the World health organization (WHO), Occupational Safety and Health Administration (OSHA), and Centers of Disease Control and Prevention (CDC). The main control measures include maintaining physical distance of 2 m, conducting COVID screening questions, washing, and sanitizing hands regularly, and wearing masks. The data were obtained from surveys and interviews to understand the impact of COVID-19 on various companies' productivity and performance. Finally, this study compiled a list of recommendations that will help different sectors in Jordan to adopt effective strategies that will improve the health and safety of workers during and after the COVID-19 pandemic.

Keywords: Occupation health and safety; COVID-19 in Jordan; Risk assessment; Physiological hazard; Personal protective equipment; Engineering control measures.

Green Hydrogen (New Vision for Clean Energy)

Raudh Jamal Raheem*

University of technology, Chemical Engineering Department ,Iraq/ Baghdad

* *Corresponding author: raudhjamal@gmail.com*

Abstract: this paper discusses the near future of green Hydrogen starting from its production to the way it will stored and its use in clean energy production . The paper compares the use of hydrogen with the conventional types of fuels that being used nowadays and presents the challenges that faces this technology as well as the safety considerations .the need of a new technology to provide energy is increasing with time , Because of the various processes that people have been used in many aspects like electricity, motor engines , industries . the CO2 emissions increased and it continues increasing With time , Scientists and countries are collaborating to involve green hydrogen in producing clean fuels and storing energy .Depending on this type of hydrogen , scientists are working to produce electricity and heat to households with the same efficiency and power but without harming the environment with pollutants . The hydrogen will be the feedstock, and the only by-product of this process will be the water . It's a new renewable source that will work together with solar and wind energy which expected to be fully used by the year 2050

Keywords: Green Hydrogen ; CO2 emissions ; Decarbonizing ; Clean energy ; Sustainable energy .

1. Introduction

Hydrogen is a non-toxic colourless gas , Even when it's referred to as a green hydrogen. it's the most abundant element in the universe , about 90% of all atoms being hydrogen atoms . Hydrogen has been used in many processes contributing with another components for centuries[1,3] . But Now the world is seeking a new renewable energy source from this element . First use of Hydrogen was to fuel the first internal combustion engine over 200 years ago,And it has been an integral part of the energy industry since the mid-20th century when it takes place in oil refining [1]. These are the gray and blue forms of hydrogen that used in energy. Although these two colours of hydrogen are used in many life applications. They are not clean sources due to CO2 emittance to the atmosphere. To save the environment , the Climate and human health . A new way to use this component is being explored, and so called green hydrogen.

Table 1. The results of using the three different colours of hydrogen.[1]

Colour	**Grey hydrogen**	**Blue hydrogen**	**Green hydrogen**
Production	Split natural gas into CO2 and hydrogen.	Split natural gas into CO2 and H2 Residual gases also in H-vision scope.	Split water into hydrogen by electrolysis powered by wind and sun .
Result	CO2 emitted in the atmosphere	CO2 stored or re-used	No CO2 emitted

2. Materials and Methods

This technology is based on the generation of hydrogen through a chemical process Known as electrolysis . the first demonstration of water electrolysis and fuel cells came to the minds of engineers was in the 1800s .

The process is explained by these four stages[9] :

1. To conduct the electricity ,the water used in the electrolysis must contain salts and minerals.
2. The Two electrodes are immersed in water and connected to a power source and a direct current is applied.
3. The decomposition of hydrogen and oxygen happens when the electrodes attract ions with an opposite charge to them.
4. During the electrolysis process ,an oxidation-reduction reaction occurs due to the effect of the electricity.

Carbon dioxide emissions rates are increasing day by day, and decarbonizing the planet is one of the goals that countries around the world have set and want to achieve by 2050 by reducing CO2 emissions in many methods, including giving rise to green Hydrogen and using it as a sustainable energy source[2] . once we highlight the use of more clean energies , we make better impacts on the environment.

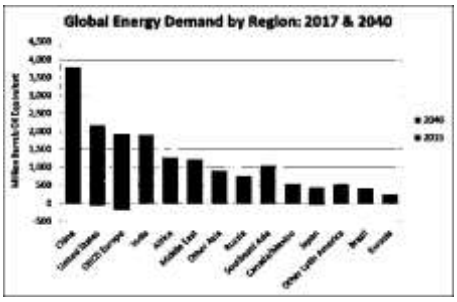


Figure 1. Global energy demand by region2017-2040.[9]

The latest estimate by IEA (International energy agency) which was published at the end of 2019, Predicted that global energy demand will increase by between 25% and 30% by 2040 . And if this happens by an economy which fully depends on coal and oil then it means more CO2 , stronger changes in climate , and more global warming[9] . Since we need more electricity and energy for our way of life , thinking about a cleaner way to obtain energy is the goal .And this method of obtaining green

Hydrogen from electrolysis would save the 830 million tons of CO2 that is emitted when using fossil fuels to produce it .

3. Results and Discussion

3.1 Challenges facing this technology

1. Production cost:The way to produce hydrogen from low-carbon energy is costly at this period , Some possible solutions is to improve the hydrogen production process by high temperature environment which can lowers the production cost of carbon-free hydrogen
2. 2Hydrogen infrastructure: is slow to develop which hinders widespread adoption.
3. Hydrogen supplier: is totally supplied from natural gas and coal nowadays .
4. Countries economies: some cannot handle the cost of renewable energies and continue using the traditional types of fuels.

3.2 Green Hydrogen as energy storage

The most common use of green hydrogen is to use it for electricity production via fuel cells. But there are many scientific challenges.If the hydrogen is produced from renewable , clean energy via electrolysis, there will be an efficiency trouble , the AC-to-AC round-trip efficiency will falls to around 35 percent, and for the efficiency that can be achieved with batteries, it will be far below the 95 percent[7].However Recent studies have found that hydrogen can be used as energy storage for more than 13 hours, while Sun power is available only in the morning , and wind power blows more in springs, hydrogen is the most viable technology for storing energy over lenghthly periods. Therefore, the use of hydrogen will not only help reducing pollutants emissions from the plant , because once it is done , it will help countries economically , this is especially true After the

pandemic[4]. When electricity converted into hydrogen by electrolysis , the hydrogen will stored to be re-electrified any time . Small amounts of hydrogen can be stored in pressurized vessels , solid metal hydrides or nanotubes . While large amounts of hydrogen can be stored in under-ground caverns[11].

3.3 Green Hydrogen safety considerations ? Is it safer than conventional fuels ?

Certainly, no fuel is 100% safe . But green hydrogen has been shown to be safer comparing it to the conventional fuels in many aspects[6].

1. Toxicity: Hydrogen is not toxic, unlike conventional fuels , for example when it comes to its using in vehicles as a hydrogen fuel cells, hydrogen will produces only water, while vehicle that use the other conventional fuels generates harmful air pollution.
2. Lightness : Hydrogen is 14 times lighter than air and 57 times lighter than gasoline vapor. So This means that when hydrogen released, it will rise and disperse rapidly, and will re-ducing the risk of ignition at ground level, in the other-hand propane and gasoline vapor are heavier than air, and more likely to remain at ground level, increasing the risk of fires.
3. Radiant Heat: Hydrogen has a lower radiant heat than gasoline, meaning the air around the flame of hydrogen less hot than gasoline flame. So, the risk of hydrogen secondary fires is lower.
4. Explosive Potential: Hydrogen has a higher oxygen requirement for explosion than fossil fuels. Hydrogen needs oxygen concentrations between 18 and 59 percent to explosive while gasoline can be explosive even when oxygen concentrations between 1 and 3 percent.

3.4 Shift to the hydrogen economy .

Table 2. Comparison made by hyundai to discuss the differences between green hydrogen economy and the current carbon economy[8] .

Type of economy	Carbon economy	Hydrogen economy
Energy paradigm	Fossil fuel (gasoline,coal,gas)	Hydrogen-centered
Energy supply	Concentrated	Distracted
competition	Raw material development	Technology and economy development
How green	Emits greenhouse gas and pollutants like CO2,NOx,Sox,etc.	Eco-friendly , by product = water (H2O)

4. Conclusions

Each sustainable and renewable energy that has been used to produce electricity , has its limiting conditions , Solar energy can Provide us electricity only during daylight, similarly, turbine powered by wind depends on the suitable wind speed , thus, finding a new sustainable- clear energy source which can provide electricity in all conditions is the goal , Green Hydrogen is being used in china as a fuel for some types of vehicles . And it's expected to be used for trains, aircrafts, lorries, buses in the future . While hydrogen is being used in chemical industries to manufacture ammonia and fertilizer , petrochemical industries to produce petroleum products and in the Steel industries , Green hydrogen will takes place to lower the aggressive effects of these industries on the environment . Studies and many projects are now aim to replace the natural gas network with a green Hydrogen network to provide electricity and heat to households without pollutant emissions . Economically , all renewable energies started with and then it started to decrease . And it's not different for Green hydrogen .It's our mission to make our plant healthier and cleaner , Technology could make human lives easier but in the other hand it is harming the environment , Global warming danger is increasing so the time to use renewable-clean energies is started now

References

i. [the future belongs to green hydrogen alone ...],[mergers-alliance]
2. green Hydrogen and the rise of the hydrogen economy],[wood mackenze]
3. [What is green hydrogen? And why should we start using it in 2019?],[Andrew Cun-ningham Managing Director]
4. [Is green hydrogen the sustainable fuel of the future?],[Vanora bennett]
5. [green hydrogen, a guide to policy making],[IRENA]
6. [Hydrogen Safety: Let's Clear the Air],[christian tae]
7. [5 Early Applications for Green Hydrogen],[jason deign]
8. [from the carbon economy to hydrogen economy],[hyundaimotor group]
9. [Green hydrogen: an alternative that reduces emissions and cares for our planet],[Iberdrola]
10. [The Future of Hydrogen],[IEA for the G20, Japan]
11. [Solar integration:solar energy and storage basics],[office of energy efficiency & renewable energy]

Impacts of Non-Pharmaceutical Interventions (NPIs) on the Trends of COVID 19 Pandemic in selected MENA Region Countries

Ziad Al-Ghazawi[1], Nidal M. Hussein [1*] and Zaid Abdelkhaleq [3]

[1] Civil Engineering Department, Jordan University of Science and Technology, PO Box 3030, Irbid, 22110, Jordan.
[2] Civil Engineering Department, University of Petra, Amman – Jordan, ORCID: 0000-0002-4188-7694
[3] Civil Engineering Department, AlHussain Technical University, PO Box 783, Amman, 11831, Jordan,

***** *Corresponding authors: nidal.hussein@uop.edu.jo; alghazawi@just.edu.jo ; Zaid.abdelkhaliq@htu.edu.jo Tel.:00962795931416.*

Abstract: This study covers eleven Middle Eastern and North African (MENA) countries and aimed to analyze the impact of public health and societal measures (hereunder called non-pharmaceutical interventions - NPIs) taken to suppress and/or mitigate the pandemic within these countries at the early stages of its spread. In the absence of a vaccine, we assessed the actual role of these NPIs in reducing transmission of the virus and managing the crisis. NPIs investigated are flight suspensions, restrictions on gatherings, school closures as well as intermittent lockdown. The impact of NPIs on the outbreak dynamics was assessed by the number of cases per million people and the number of deaths per thousand people. Results indicate that dynamics of the outbreak differ from one country to another as NPIs differ in kind, timing, swiftness and adaptation of the public to enforced measures. Although testing is extremely important in detecting infection and reducing the mortality ratio (in terms of deaths per 1000 reported cases) by 45%, the analysis in this study shows that NPIs play a very important role in containing the pandemic and reducing its impact. Slower responses in terms of NPIs implementation resulted in up to 67 % increase in mortality rate (deaths per 1000 reported cases). The outcome of this study can help in dealing similar events in the future.

Keywords: COVID-19, Non-Pharmaceutical Interventions (NPIs), Pandemic Dynamics, MENA Countries.

1. Introduction

During the first few months of 2020, people around the world started to follow the disturbing news coming from China regarding a new human respiratory illness, identified as a novel coronavirus or COVD-19. The illness was first identified in Wuhan City, Hubei Province of China and reported to the WHO China Country Office on 31 December 2019 [1].

The illness rapidly spread to countries around the world. By March 11th, 2020, more than 118,000 cases of COVID-19 were reported in 114 countries which lead to the characterization of COVID-19 as a pandemic by the World Health Organization (WHO) [2]. By the end of April 2020, the total cases had surpassed five million with a death total exceeding 326,000 worldwide [3]. Research suggested a remarkable genomic resemblance of 2019-nCoV to Severe Acute Respiratory Syndrome (SARS) which has a history of a pandemic in 2002 [4,5].

The Public Health Emergency of International Concern (PHEIC) has been established by the World Health Organization (WHO) with strategic objectives for public health to curtail the outbreak's impact on global health and economy.

COVID-19 is identified as highly infectious and can be transmitted through droplets and close contact. The relatively long 14-day incubation period is a serious challenge [6,7]. Controlling the spread of the epidemic and reducing mortality as soon as possible is vitally important. Researchers have been assessing the reported data from infected countries to get a better understanding of the

spread dynamics of this outbreak. The specific mechanism of the virus at early stages of the spread was unknown to a certain extent, and no specific antiviral drugs have been developed [3, 4, 6, 8]. Therefore, it is important to control the source of infection, cut off the route of transmission, and use existing drugs and means to control progress of the disease proactively [5, 9].

Social distancing is an essential measure in counteracting the pandemic and stretching the curve. Strict implementation and timing of preventive and precautionary measures that support such behavior is far more important than announcing them and should be properly contextualized, meaning that social and collective consciousness is indispensable [10, 11]. Hence, it is crucial to monitor the progress of this outbreak and evaluate the effects of preventive and precautionary measures, including the social distancing measures in real-time.

As the COVID-19 pandemic progressed , countries implemented a broad range of responses and measures to slow the spread of the virus, from quarantines to school closures, and more than a third of the planet's population was under some form of restriction [10, 11].

Ferguson et al. (2020) identified two strategies to deal with the pandemic in European countries and the United States, namely: mitigation and suppression. They found that optimal mitigation policies might reduce peak healthcare demand by two-thirds and deaths by half. Suppression, which aims to reverse epidemic growth, reducing case numbers to low levels and maintaining that situation continuously, is more appropriate to countries with fewer resources and less adaptive health systems but requires the layering of more intensive and socially and culturally disruptive measures than mitigation [12].

To avoid a rebound in transmission, these policies need to be maintained until large stocks of vaccine are available to immunize the population – which could be 18 months or more [12, 13]. If intensive NPI packages aimed at suppression are not maintained, their analysis suggests that transmission will rapidly rebound, potentially producing an epidemic comparable in scale to what would have been seen had no interventions been adopted [14 – 16]. Chinazzi et al (2020) suggests that travel restrictions have modest effect on reducing the spreading of COVID-19. They also argue that the main cause for relieving the epidemic is by transmission reduction interventions [17].

Lou et al (2020) analyzed the available data by the Center for Systems Science and Engineering at Johns Hopkins University in the period between February 22nd, 2020 and March.15th,2020 [18]. They concluded that there is a need to analyze data from many countries to proof any hypothesis regarding this pandemic as culture factors may have a large impact on infection rate. Moreover, Ghiasvand shows the results of the curfew that started in Germany as of March 22nd, 2020 which had a crucial impact on slowing down the spread of COVID-19 [19].

The valid measures to slowed down the spread of the pandemic and flattened the curve of cases are non-pharmaceutical such as case isolation, travel restrictions, curfews and social distancing [18 - 24]. According to the Chinese government, lockdown in some areas caused the pandemic to show an increase in the doubling time of COVID-19 cases in these areas while the number of cases increased outside these areas [25]. Therefore, lockdown helped the healthcare sector to buy time by reducing daily number of cases but its effectiveness depends on different social contexts [26]. Generally speaking, the effectiveness of any intervention alone is likely to be limited, and therefore, a set of multiple interventions should be deployed to have an effective impact on transmission and containment of the outbreak.

Most countries in the MENA region had implemented unprecedented non-pharmaceutical interventions (NPIs) including case isolation, schools and universities closures, banning of mass gatherings and/or public events, and wide-scale social distancing including local and national lockdowns.

This paper documents the list of NPIs implemented by selected MENA countries, and investigates the impacts of such measures on the dynamics of COVID19 pandemic in these countries at early stages of the outbreak. The interventions considered (The Parameters) are the number of tests per million people, the date of flight suspension, the date of gathering restrictions and the date of partial or national lockdown. The impacts of these parameters on the dynamics of the pandemic outbreak are documented in terms of the following responses: number of cases per million people, the number of deaths per thousand people and the number of deaths per thousand tests implemented.

Other factors at country level are also important such as level of preparedness, vulnerability, governance status, flexibility and responsiveness of the national governmental health sectors as well as the economic and social characteristics in each country. The study focuses on analyzing the pandemic progression in each of the investigated MENA countries and relates the spread pattern to preventive and precautionary measures (NPIs) implemented by each country.

2. Methods and Procedures

Data from the date first confirmed cases to April 25, 2020, for 11 MENA countries were imported from the Worldometers website [27]. Data collected include: population in million, total number of confirmed COVID-19 cases, total number of tests, number of test per million of population, number of cases per million of population, total number of deaths, number of deaths per million of population, and date of first confirmed case of COVID-19.

The number of reported deaths per million, number of reported deaths per thousand tests and the number of deaths per thousand cases were calculated. Figure 1 shows the progress of pandemic in each of the investigated MENA country. Table 1, 2 and 3 give a summary of collected data on three occasions: April 10, 2020, April 21, 2020 and April 25, 2020

Data on implementation and timing of preventive and precautionary measures in response to COVID-19 pandemic in the investigated countries that support social distancing behavior was also collected. Table 4 gives a summary of collected data on these preventive and precautionary measures (NPI: Non Pharmaceutical Interventions) as well as the date of the first confirmed cases in each of the investigated country.

The first case in the selected countries was identified and reported on February 15th, 2020, in UAE, Egypt and Algeria, followed by the detection of cases in other countries later. However, the number of confirmed cases of COVID-19 started to increase in the subsequent days.

To organize our analysis into useful insights that can be of benefit for other countries in the region and in the southern hemisphere, we organize the NPIs and measures taken collectively called as parameters versus the output indicators or impacts of such measures on the progression of the pandemic, namely the number of deaths per million, the number of deaths per reported positive cases of infection (Table 5).

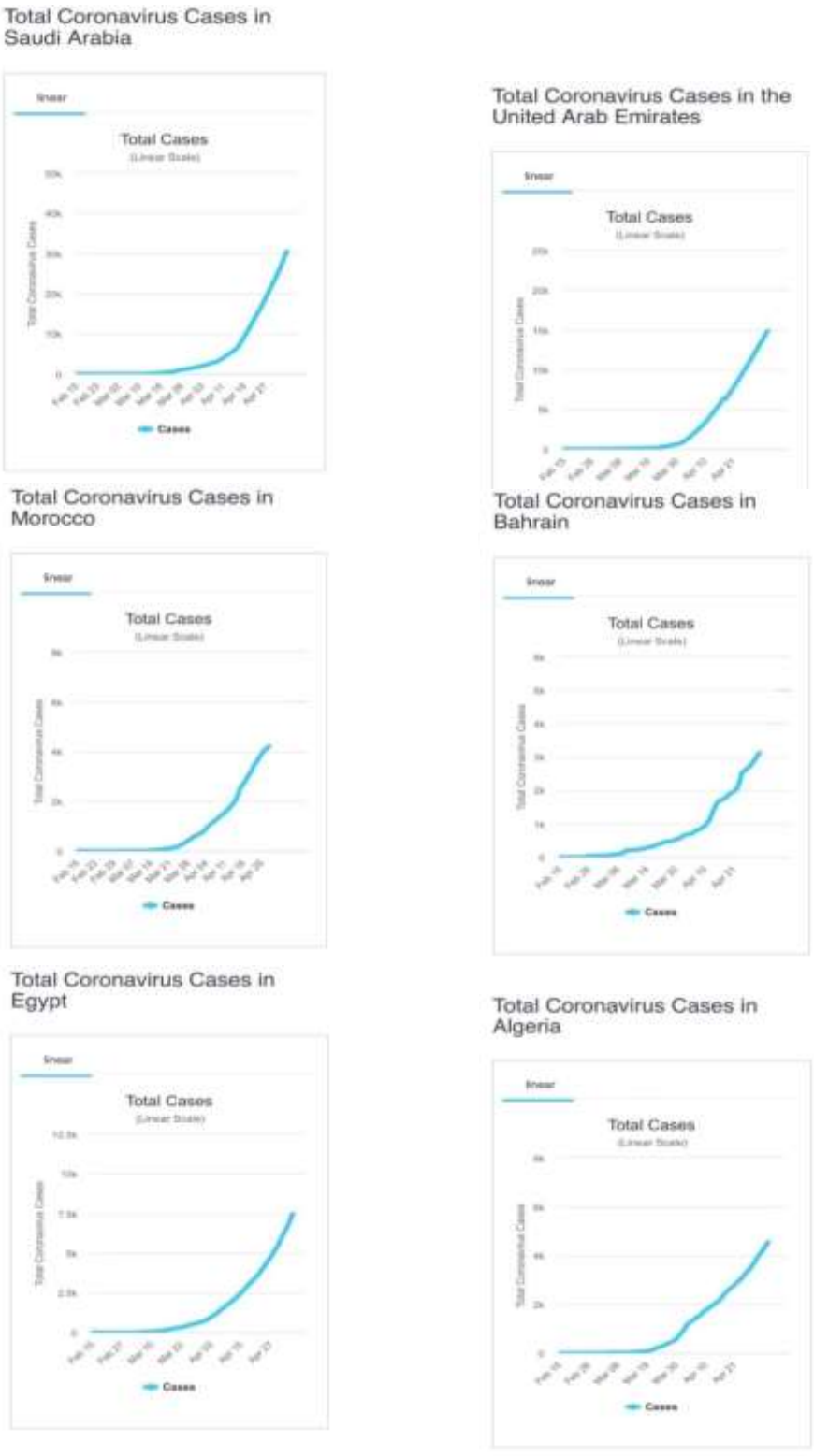


Figure 1: Progression of COVID 19 cases in selected MENA countries



Figure 2: Progression of COVID 19 cases in selected MENA countries (Cont'd)

Table 1: Pandemic variables for selected MENA countries as of April 10, 2020

As of Apr 10 2020									
Country	Population in M	Total Number of Confirmed Cases	Total Number of Tests	Number of Test per M	Number of Cases per M	Total Number of Deaths	Number of Deaths per M	Number of Deaths per Thousand Tests	Number of Deaths per Thousand Cases
Qatar	2.881	2,512	45339	15737	872	6	2.08	0.132	2.389
UAE	9.890	3360	593095	59967	340	16	1.62	0.027	4.762
Bahrain	1.702	998	57681	33899	587	6	3.53	0.104	6.012
KSA	34.814	3,651	115585	3320	105	47	1.35	0.407	12.873
Jordan	10.203	372	17000	1666	36	7	0.69	0.412	18.817
Lebanon	6.285	619	13530	1982	91	20	3.18	1.478	32.310
Tunisia	11.819	671	10087	853	57	25	2.12	2.478	37.258
Iraq	40.222	1279	32158	800	32	70	1.74	2.177	54.730
Morocco	36.911	1448	7239	196	39	107	2.90	14.781	73.895
Egypt	102.334	1,794	25000	244	18	135	1.32	5.400	75.251
Algeria	43.851	1761	3359	77	40	256	5.84	76.213	145.372

Table 2: Pandemic variables for selected MENA countries as of April 21, 2020

As of Apr 21 2020									
Country	Population in M	Total Number of Confirmed Cases	Number of Tests	Number of Tests per M	Number of Cases per M	Number of Deaths	Number of Deaths per M	Number of Deaths per Thousand Tests	Number of Deaths per Thousand Cases
Qatar	2.881	6,533	66725	23160	2268	9	3.12	0.135	1.378
UAE	9.890	7755	790000	79875	784	46	4.65	0.058	5.932
Bahrain	1.702	1973	94380	55466	1160	7	4.11	0.074	3.548
KSA	34.814	11,631	180000*	5170	334	109	3.13	0.606	9.372
Jordan	10.203	428	33000	3234	42	7	0.69	0.212	16.355
Lebanon	6.285	677	21764	3189	99	21	3.34	0.965	31.019
Tunisia	11.819	901	18165	1537	76	38	3.22	2.092	42.175
Iraq	40.222	1602	60837	1513	40	83	2.06	1.364	51.810
Morocco	36.911	3209	18100	490	87	145	3.93	8.011	45.185
Egypt	102.334	3,490	55000	537	34	264	2.58	4.800	75.645
Algeria	43.851	2811	6500	148	64	392	8.94	60.308	139.452

* The total number of tests in Saudi Arabia as of April 22nd, 2020

Table 3: Pandemic variables for selected MENA countries as of April 25, 2020

As of Apr 25 2020									
Country	Population in M	Total Number of Confirmed Cases	Number of Tests	Number of Tests per M	Number of Cases per M	Number of Deaths	Number of Deaths per M	Number of Deaths per Thousand Tests	Number of Deaths per Thousand Cases
Qatar	2.881	9,358	79705	27665	3248	10	3.47	0.125	1.069
UAE	9.890	9813	1E+06	103365	992	71	7.18	0.069	7.235
Bahrain	1.702	2588	110379	64869	1521	8	4.70	0.072	3.091
KSA	34.814	16,299	200000	5745	468	136	3.91	0.680	8.344
Jordan	10.203	444	63737	6247	44	7	0.69	0.110	15.766
Lebanon	6.285	704	26467	3878	103	24	3.82	0.907	34.091
Tunisia	11.819	939	20408	1727	79	38	3.22	1.862	40.469
Iraq	40.222	1763	68224	1696	44	86	2.14	1.261	48.780
Morocco	36.911	3897	25443	689	106	159	4.31	6.249	40.801
Egypt	102.334	4,319	90000	879	42	307	3.00	3.411	71.081
Algeria	43.851	3256	6500	148	74	419	9.56	64.462	128.686

Table 4: Non-Pharmaceutical Interventions (NPIs) taken and date of action in selected MENA countries

Country	Date of first confirmed case (s)	Date of flight suspension	Days to flight suspension	Business / Public Gathering Restrictions	Days to Business / Public Gathering Restrictions	Date of first Nationwide partial curfew	Days to first Nationwide partial curfew	Number of cases on the partial Curfew day
Qatar	Feb 29 2020	Mar 17th, 2020	17	Mar 16th, 2020	16	N/A	N/A	N/A
UAE	Feb 15 2020	Mar 24th, 2020	38	Mar 25th, 2020	39	March 26th, 2020	40	333
Bahrain	Feb 24 2020	N/A	N/A	March 19th, 2020	24	March 24th, 2020	29	392
KSA	March 2 2020	Mar 15th, 2020	13	March 25th, 2020	23	March 23rd, 2020	21	562
Jordan	March 2 2020	Mar 17th, 2020	15	March 17th, 2020	15	Mar 21st, 2020	19	100
Lebanon	Feb 21 2020	Mar 18,2020	26	Mar 18,2020	26	March 26th, 2020	34	368
Tunisia	March 2 2020	Mar 17th, 2020	15	March 17th, 2020	15	March 17th, 2020	15	27
Iraq	Feb 21 2020	Mar 17th, 2020	25	March 9th, 2020	17	March 22nd, 2020	20	233
Morocco	March 2 2020	Mar 15th, 2020	13	March 16th, 2020	14	March 19th, 2020	17	63
Egypt	Feb 15 2020	Mar 19th, 2020	33	March 22nd, 2020	36	March 25th, 2020	39	456
Algeria	Feb 25 2020	Mar 17th, 2020	21	March 10th, 2020	14	N/A	N/a	N/a

Table 5: Listing of NPI parameters taken and response/indicator of outbreak mitigation potential

#	**Response indicator**	**Acronym**	**NPIs Parameter**	**Acronym**
1	Total number of cases	TNCs	Total number of tests	TNTs
2	Cases per million	CPM	Tests per million	TPM
3	Total number of deaths	TND	Days to flight suspension since the first reported case	DFS
4	Deaths per million	DPM	Days to business / public gathering restriction since the first reported case	DBP
5	Deaths per thousand tests	DPKT	Days to nationwide curfew since the first reported case	DNC
6	Deaths per thousand cases	DPKC		

3. Results and Discussion

Amid collecting and processing numerical data of the casualties, specialists in diverse fields are probing and looking beyond the numbers. First and foremost, the publicized numbers are indices of the health system's efficiency in detecting, locating and suppressing the spread of the disease. In this regard, detecting the infections is essential to containing the spread and determining its pattern. The low confirmed cases are popularly welcome, but professionally a cause for unease. The reported positive cases are cases a country managed to detect simple and pure. The devil is in the undetected cases wandering and spreading the virus. Figure 2 presents number of tests per million of population versus number of reported cases per thousand in the selected MENA countries as of April 25, 2020.

Figure 2 suggests that the four GCC gulf countries, namely: KSA, UAE, Qatar and Bahrain have significantly higher counts of cases per million people than the rest of countries in this study. Kuwait and Oman were the two GCC gulf countries that were not considered in this study due to the unavailability of data on number of test performed by each county. This coincides with the fact that these Gulf countries conducted higher number of tests per million people. Figure 3 presents number of tests per million versus the reported number of deaths per 100 thousand cases for the investigated countries as of April 25th, 2020. Algeria, Morocco and Egypt are high in Deaths per million while the three countries were lowest in tests per million and also lowest in cases per million. This might indicate they had many undetected and consequently unreported cases. Figure 4 & 5 displays the relation between mortality rates in terms of (deaths per thousand reported cases) compared to time delay in enacting suspension of flights and curfew.

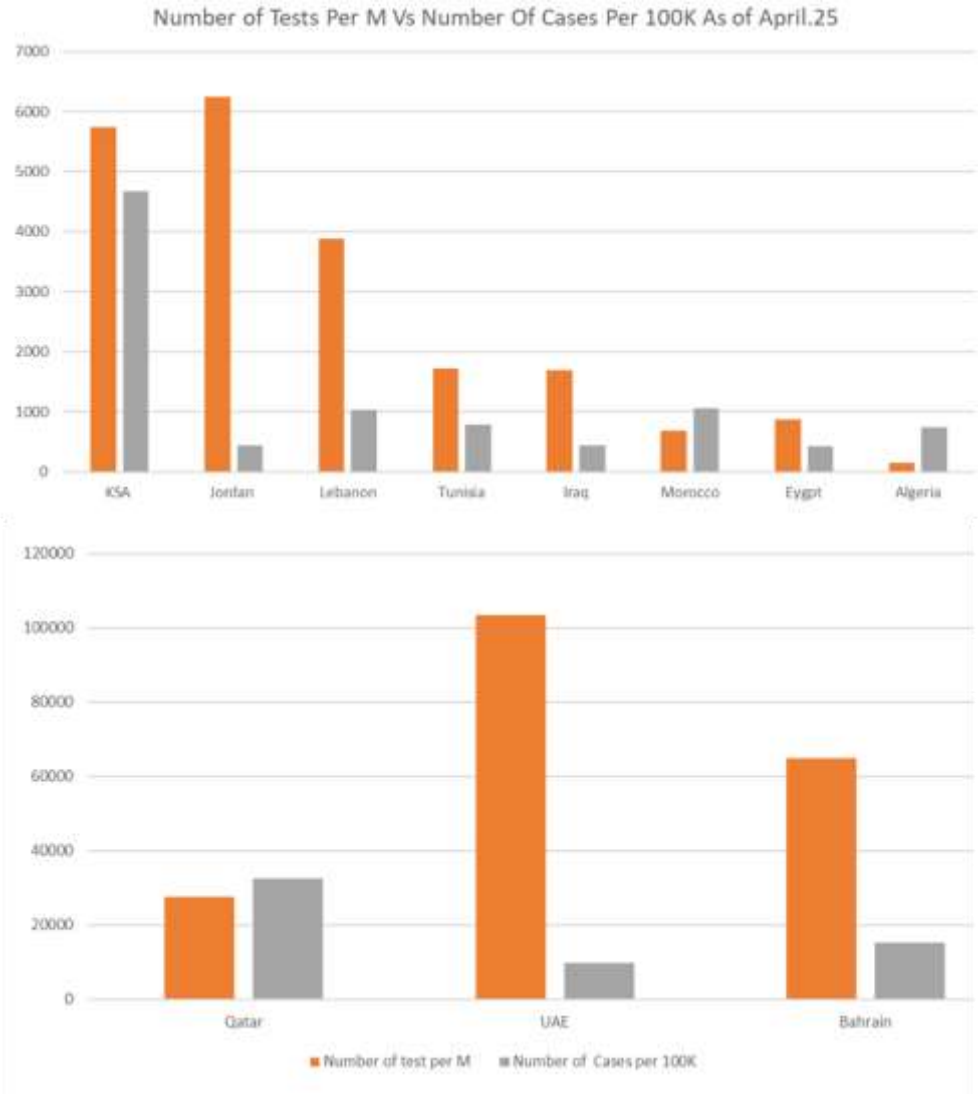


Figure 2: Number of tests per million versus number of reported cases per thousand in 11 MENA countries as of April 25, 2020

For the case of Iraq and Tunisia, figure 6, the two countries performed a comparable number of tests per million of population as of April 25th, 2020. But Iraq was slower in restricting mobility, internally and externally. It took Iraq 5, 2, and 10 more days (since first reported case) to their first nationwide curfew, Business / Public Gathering Restrictions, and flight suspension respectively, resulting in 23% increase in deaths per 1000 reported cases in Iraq as of Apr. 25th, 2020.

Same trend was noticed for the case of Egypt and Morocco, figure 7. The two countries performed a comparable number of tests per million of population as of April 25th, 2020, but Egypt was slower in restricting mobility, internally and externally. It took Egypt almost double the time to their first nationwide curfew (38 vs. 17 days since first reported case) and more than double the time to their first Business / Public Gathering Restrictions (36 vs. 14 days since first reported case). Egypt was also slower in their flight suspension. It took Egypt nearly triple the time (33 vs. 13 days since the first reported case). Consequently, 67.4 % increase in deaths per 1000 reported cases as of April 25th, 2020 was noticed in Egypt compared to Morocco.

Tunisia and Morocco, figure 8, reported their first cases at the same date. They responded similarly in terms of a nationwide curfew, Business / Public Gathering Restrictions, and flight

suspension. But Tunisia was more active in conducting tests per million of population. As of April 10th, 2020, Tunisia has conducted more than four times more tests per million of population (853 vs. 196 test per million) as of April 10th, 2020 when compared to Morocco. Tunisia reported 46 % more cases per million of population, but the mortality ratio in Morocco was almost double. Morocco reported 98.3 % increase in deaths per 1000 reported cases than Tunisia as of April 10th, 2020. Later, Morocco intensified their testing programs, and reduced the gap with Tunisia (1727 vs. 689 tests per million of population) as of April 25th, 2020. As a result, Morocco was able to reduce the mortality ratio in terms of deaths per 1000 reported cases by 45%, from 73.9 to 40.8 cases of deaths per 1000 reported cases of infection.

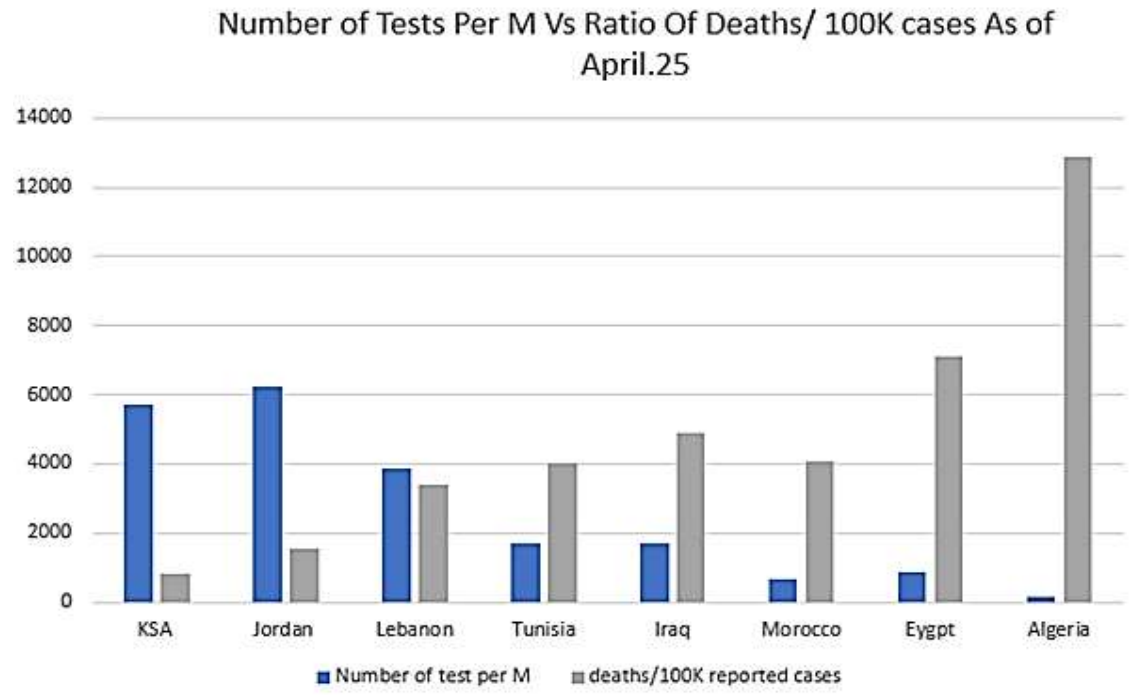


Figure 3: Number of tests per million versus the reported number of deaths per 100 thousand cases for the investigated countries

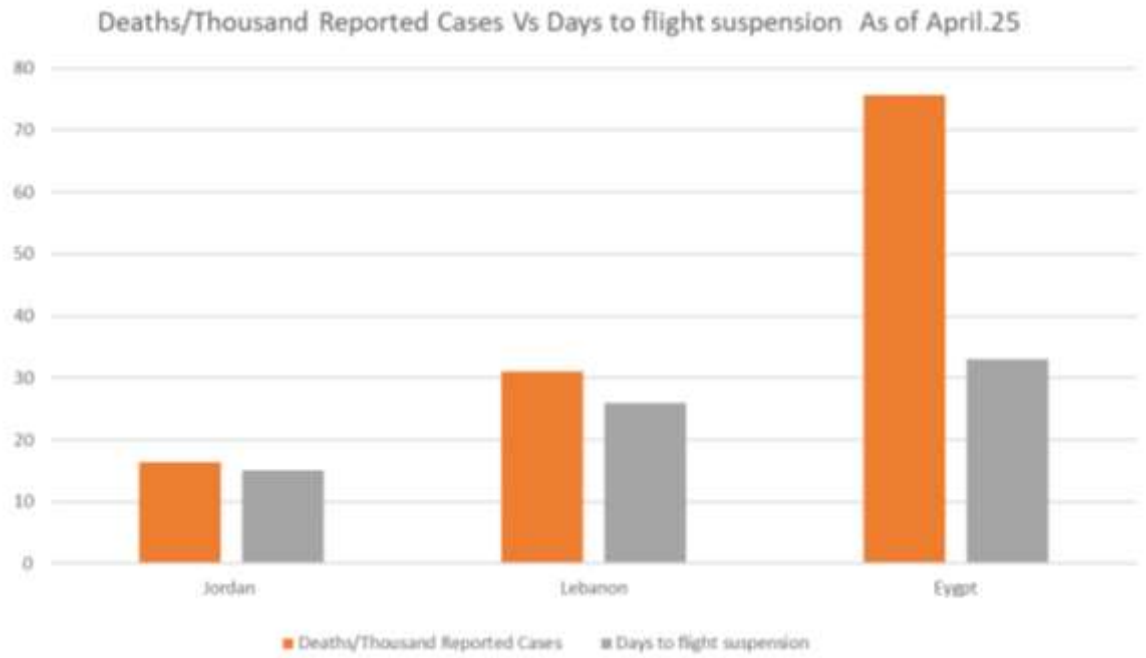


Figure 4: Deaths per thousand reported cases compared to time delay in enacting suspension of flights

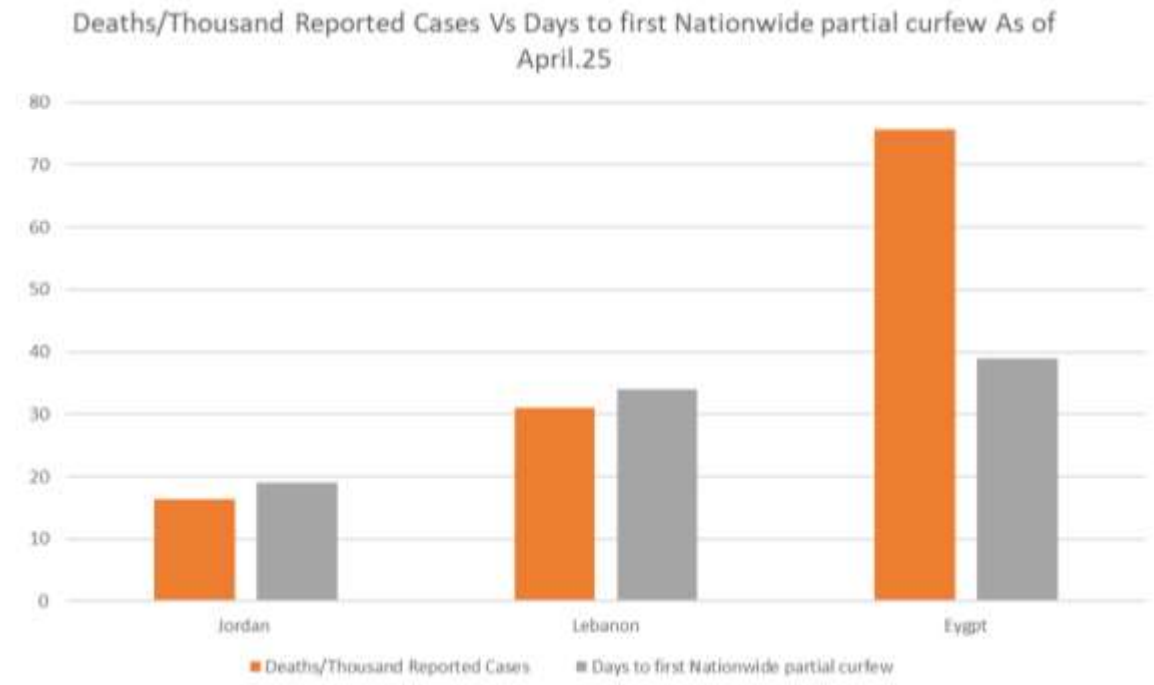


Figure 5: Deaths per thousand people compared to time delay in enacting curfew

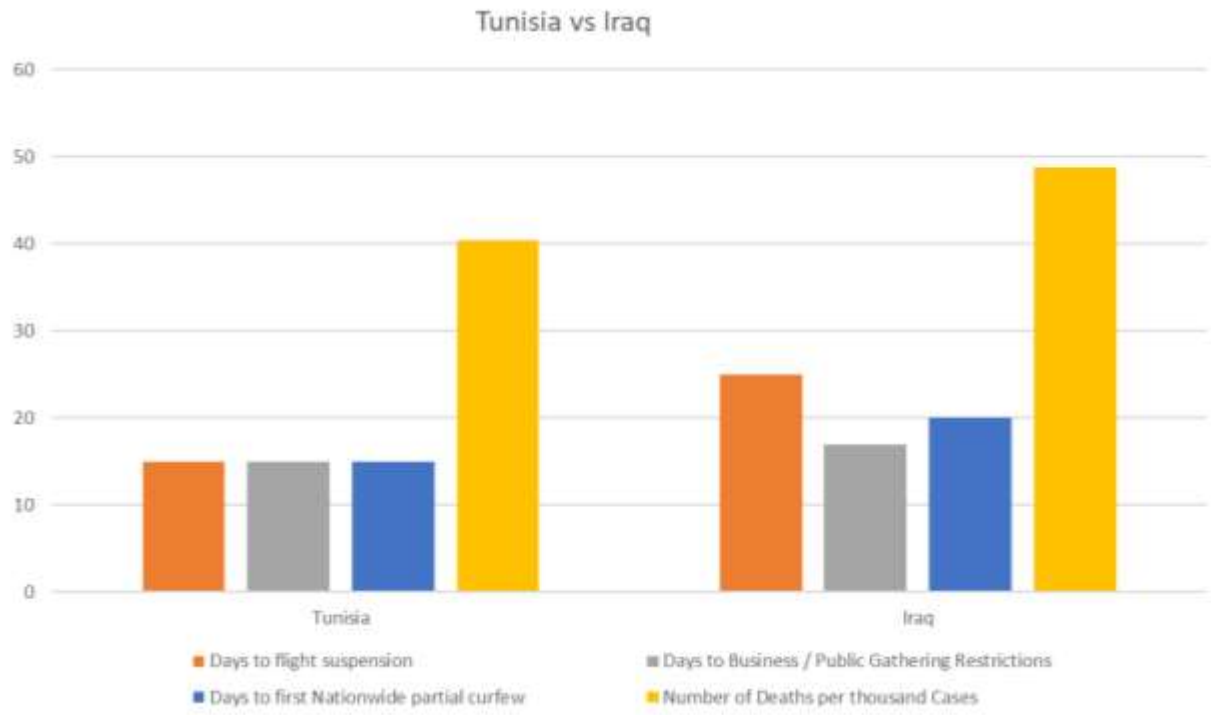


Figure 6: Deaths per thousand reported cases in Tunisia and Iraq as influenced by NPIs as of April 25 th, 2020.

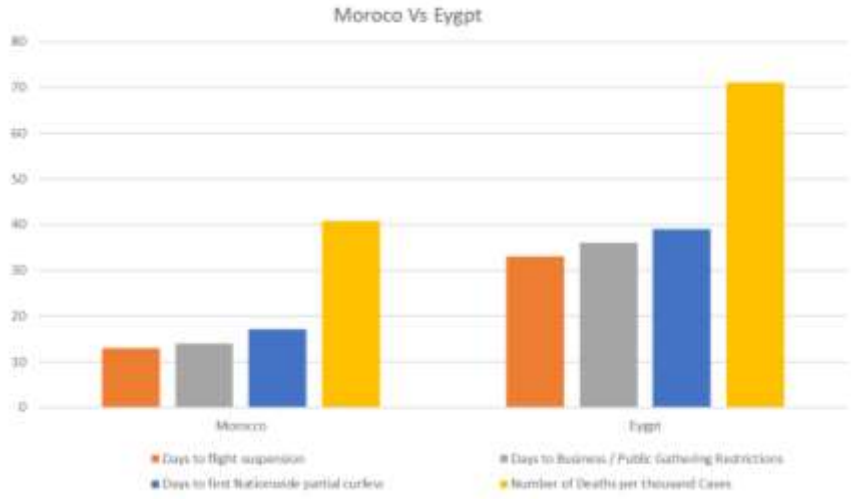


Figure 7: Deaths per thousand reported cases in Egypt and Morocco as influenced by NPIs as of April 25th 2020.

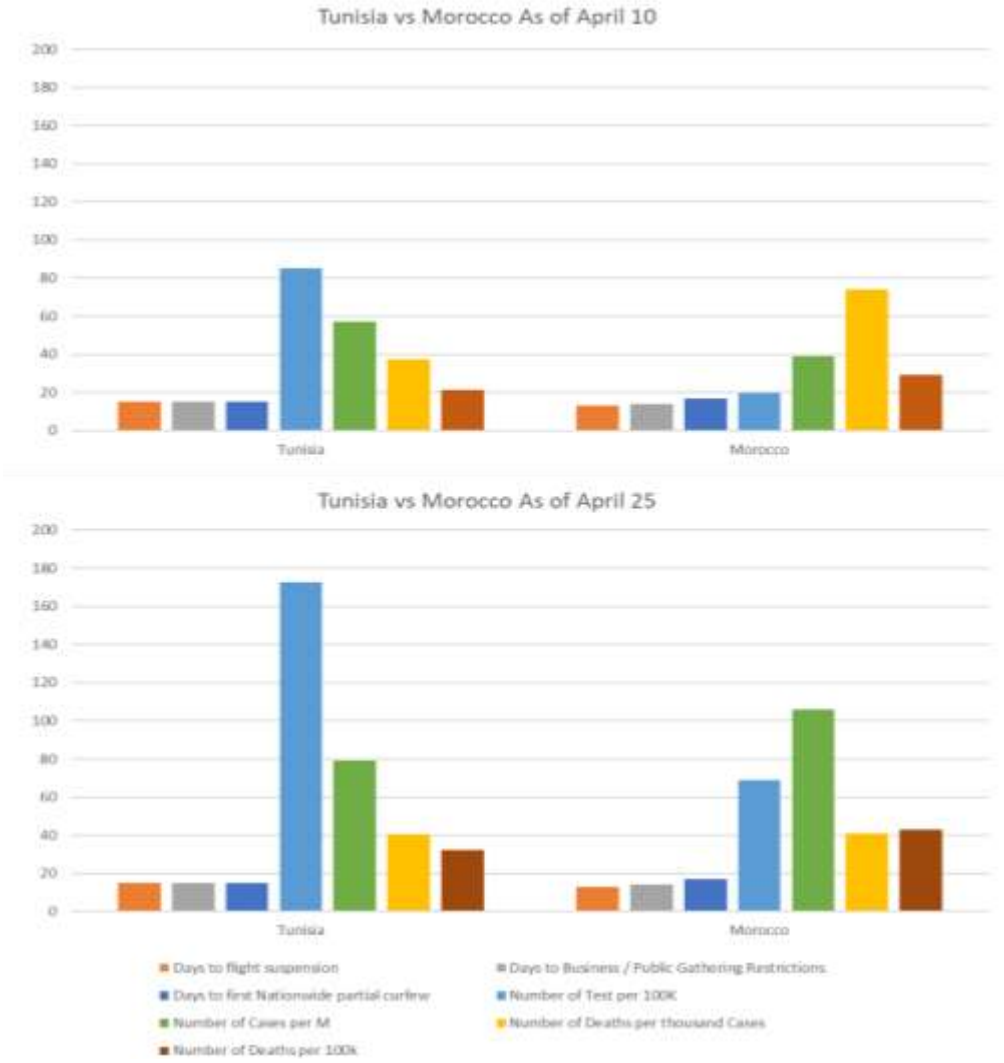


Figure 8: Impact of NPIs taken on dynamics of the outbreak (deaths per 100K and deaths per thousand cases between April 10th and April 25th, 2020 in Tunisia and Morocco

The contradictory statistics in some cases are indicators of desperation and exhaustion permeating the healthcare system that could no longer contain the pandemic. The decreasing confirmed cases are alarming and can translate the low numbers into overstrained medical teams that are incapable of reaching out or detecting all existing cases. This concern stood on another foot yet: the surge in reported deaths. The latter could either be due to late detection or triaging dictated by the influx of new patients.

On the one hand, constant high numbers could be an assuring sign: it is the apex; it may signal that these countries' detection aids have been pushed to their limits. Perhaps, the detection efforts target one hot spot at the cost of less urgent ones.

The Jordanian case represents a rather different model. The speedy reaction and resolute implementation of one of the strictest measures preemptively contributed to containing and slowing down the spread. The country succeeded in slowing the spread at early stages of the pandemic.

The social and economic costs of NPIs on societies of the selected MENA counties have been high and some governments are struggling to keep a balance between suppressing the outbreak and maintaining acceptable levels of economic activities. The results of this study are useful to other countries in the southern hemisphere of similar governance, cultural and political conditions to MENA countries.

4. Conclusions and Recommendations

Based on the analysis in this study, the NPIs namely: testing, flight suspension, public gathering restrictions and curfews were found to be essential in containing the spread of a pandemic outbreak and determine the dynamics of its spread. The number of tests conducted is important to realize the size of the outbreak in each country. For the selected MENA countries in this study, it was generally found that more confirmed COVID 19 cases resulted when a country executed more tests per million people. Fewer number of tests per million resulted in more deaths per thousand reported for the cases in Algeria, Morocco and Egypt, indicating that there might be many undetected and consequently unreported cases. For countries that conducted same number of tests, the delay of other NPI's (curfew, business / public gathering restrictions, and flight suspension), resulted in up to 67 % increase in mortality rate (deaths per 1000 reported cases). Intensifying testing programs resulted in reducing the mortality ratio in terms of deaths per 1000 reported cases by 45%.

References

1. World Health Organization (WHO). (2020 a). Pneumonia of unknown cause—China (https://www.who.int/csr/don/05-january-2020-pneumonia-of-unkown-cause-china, [accessed 25 April 2020].
2. World Health Organization (WHO). (2020 b). WHO Director-General's opening remarks at the media briefing on COVID-19, (Press release). 11 March 2020. Archived from the original on 11 March 2020. [accessed 15 March 2020].
3. Johns-Hopkins Reports, (https://coronavirus.jhu.edu/data/new-cases). [last accessed 21 May 2020].
4. Sanche, S., Lin, Y. T., Xu, C., Romero-Severson, E., Hengartner, N., & Ke, R. (2020). High Contagiousness and Rapid Spread of Severe Acute Respiratory Syndrome Coronavirus 2. Emerging infectious diseases, 26 (7), DOI: 10.3201/eid2607.200282
5. Wu, J. T., Leung, K., & Leung, G. M. (2020). Nowcasting and forecasting the potential domestic and international spread of the 2019-nCoV outbreak originating in Wuhan, China: a modelling study. The Lancet, 395 (10225), 689-697. DOI:https://doi.org/10.1016/S0140-6736(20)30260-9
6. Backer, J. A., Klinkenberg, D., & Wallinga, J. (2020). Incubation period of 2019 novel coronavirus (2019-nCoV) infections among travellers from Wuhan, China, 20–28 January 2020. Eurosurveillance, 25 (5), 2000062. doi: 10.2807/1560-7917.ES.2020.25.5.2000062.
7. Lauer, S. A., Grantz, K. H., Bi, Q., Jones, F. K., Zheng, O., Meredith, H., Azman, A. S., Reich, N. G., & Lessler, J. (2020). The incubation period of 2019-nCoV from publicly reported confirmed cases: estimation and application. Annals of Internal Medicine, 172 (9), 557 - 583. https://doi.org/10.7326/M20-0504
8. Wang, C., Horby, P. W., Hayden, F G., & Gao, G. F. (2020). A novel coronavirus outbreak of global health concern. The Lancet, 395 (10223), 470 – 473. https://doi.org/10.1016/ S0140-6736(20)30185-9.
9. Chen, S., Yang, J., Yang, W., Wang, C., & Bärnighausen, T. (2020). COVID-19 control in China during mass population movements at New Year. The Lancet, 395 (10226), 764-766. DOI:https://doi.org/10.1016/S0140-6736(20)30421-9
10. Pung, R., Chiew, C. J., Young, B. E., Chin, S., Chen, M. I-C., Clapham, H. E., Cook, A. R., Maurer-Stroh, S., Toh, M. P. H. S., Poh, C., Low, M., Lum, J., Koh, V. T. J., Mak, T. M., Cui, L., Lin, R. V. T. P., Heng, D., Leo, Y.-S., Lye, D. C., & Lee, V. J. M. (2020). Investigation of three clusters of COVID-19 in Singapore: implications for surveillance and response measures. The Lancet, 395 (10229), 1039 - 1046. DOI:https://doi.org/10.1016/S0140-6736(20)30528-6
11. Bastola, A., Sah, R., Rodriguez-Morales, A. J., Lal, B. K., Jha, R., Ojha, H. C., Shrestha, B., Chu, D. K. W., Poon, L. M. L., Costello, A., Morita, K., & Pandey, B. D. (2020). The first

2019 novel coronavirus case in Nepal. The Lancet Infectious Diseases, 20 (3), 279-280. DOI:https://doi.org/10.1016/S1473-3099(20)30067-0

12. Ferguson, N. M., Laydon, D., Nedjati-Gilani, G., Imai, N., Ainslie, K., Baguelin, M., Bhatia, S., Boonyasiri, A., Cucunubá, Z., Cuomo-Dannenburg, G., Dighe, A., Dorigatti, I., Fu, H., Gaythorpe, K., Green, W., Hamlet, A., Hinsley, W., Okell, L. C., Van Elsland, S., Thompson, H., Verity, R., Volz, E., Wang, H., Wang, Y., Walker, P. G.T., Walters, C., Winskill, P., Whittaker, C., Donnelly, C. A., Riley, S., Ghani, A. C. (2020). "Report 9: Impact of non-pharmaceutical interventions (NPIs) to reduce COVID19 mortality and healthcare demand. Imperial College London. DOI: https://doi.org/10.25561/77482.
13. Tian, H., Liu, Y., Li, Y., Wu, C-H., Chen, B., Kraemer, M. U. G., Li, B., Jun, C., Xu, B., Yang, Q., Wang, B., Yang, P., Cui, Y., Song, Y., Zheng, P., Wang, Q., Bjornstad, O. N., Yang, R., Grenfell, B. T., Pybus, O. G., & Dye, C. (2020). An investigation of transmission control measures during the first 50 days of the COVID-19 epidemic in China. Science, 368 (6491), 638-642. DOI: 10.1126/science.abb6105
14. Phan, L. T., Nguyen, T. V., Luong, Q. C., Nguyen, T. V., Nguyen, H. T., Le, H. Q., Nguyen, T. T., Cao, T. M., & Pham, Q. D.. (2020). Importation and human-to-human transmission of a novel coronavirus in Vietnam. The New England Journal of Medicine, 382 (9), 872-874. DOI: 10.1056/NEJMc2001272
15. Prem, K., Liu, Y., Russell, T. W., Kucharski, A. J., Eggo, R. M., Davies, N., Jit, M., & Klepac, P. (2020). The effect of control strategies to reduce social mixing on outcomes of the COVID-19 epidemic in Wuhan, China: a modelling study. The Lancet Public Health, 5 (5), 261 - 270. DOI:https://doi.org/10.1016/S2468-2667(20)30073-6.
16. Wilder-Smith, A. & Freedman, D. O. (2020). Isolation, quarantine, social distancing and community containment: pivotal role for old-style public health measures in the novel coronavirus (2019-nCoV) outbreak. Journal of travel medicine, 27 (2), 1-4. https://doi.org/10.1093/jtm/taaa020
17. Chinazzi, M., Davis, J. T., Ajelli, M., Gioannini, C., Litvinova, M., Merler, S., Piontti, A. P. Y., Mu, K., Rossi, L., Sun, K., Viboud, C., Xiong, X., Yu, H., Halloran, M. E., Longini Jr., I. M., & Vespignani, A. (2020). The effect of travel restrictions on the spread of the 2019 novel coronavirus (COVID-19) outbreak. Science 368 (6489), 395-400. DOI: 10.1126/science.aba9757
18. Lau, H., Khosrawipour, V., Kocbach, P., Mikolajczyk, A., Schubert, J., Bania, J., & Khosrawipour, T. (2020). The positive impact of lockdown in Wuhan on containing the COVID-19 outbreak in China. Journal of Travel Medicine, 27 (3), 1-7. https://doi.org/10.1093/jtm/taaa037
19. Ghiasvand, S. Predicting the Prevalence of COVID-19 Pandemic in Germany. (published online March 13th, 2020) (preprint). DOI: 10.13140/RG.2.2.12200.32006
20. Cowling, B. J., Ali, S. T., Ng, T. W., Tsang, T. K., Li, J. C., Fong, M. W., Liao, Q., Kwan, M. Y., Lee, S. L., Chiu,S. S. Wu, J. T., & Wu, P. (2020). Impact assessment of non-pharmaceutical interventions against coronavirus disease 2019 and influenza in Hong Kong: an observational study. The Lancet Public Health, 5 (5), 279 - 288. https://doi.org/10.1016/S2468-2667(20)30090-6.
21. Fanelli, D. & Piazza, F. (2020). Analysis and forecast of COVID-19 spreading in China, Italy and France. Chaos, Solitons & Fractals, 134 (109761), 1-5. https://doi.org/10.1016/j.chaos.2020.109761.
22. Ngonghala, C. N., Iboi, E., Eikenberry, S., Scotch, M., MacIntyre, C. R., Bonds, M. H., & Gumel, A. B. (2020). Mathematical assessment of the impact of non-pharmaceutical interventions on curtailing the 2019 novel Coronavirus. Mathematical Biosciences, 325 (108364). https://doi.org/10.1016/j.mbs.2020.108364.
23. [dataset] Gandhi, K. R. R., Murthy, K.V. R., Prasada Rao, S. S., & Casella, F. Non-Pharmaceutical Interventions (NPIs) to reduce COVID-19 mortality. KAGGLE - COVID-19

Open Research Dataset Challenge (CORD-19). (https://www.kaggle.com/allen-institute-for-ai/CORD-19-research-challenge/tasks?taskId=587) (2020).

24. Lai, S., Ruktanonchai, N. W., Zhou, L., Prosper, O., Luo, W., Floyd, J. R., Wesolowski, A., Santillana, M., Zhang, C., Du, X., Yu, H. & Tatem, A. J. (2020). Effect of non-pharmaceutical interventions for containing the COVID-19 outbreak: an observational and modelling study. medRxiv (published online March 13th, 2020) (preprint). https://doi.org/10.1101/2020.03.03.20029843
25. Zitoun, O. A. (2020). COVID-19 Pandemic: Other Perspective. Saudi Arabia. International Journal of Medical Students, 8 (1), 64-65. DOI 10.5195/ijms.2020.50
26. Barry, M., Ghonem, L., Alsharidi, A., Awadh, A., Al-Shahrani, F., & Naif, H. A. (2020). Coronavirus Disease 2019 (COVID-19) Pandemic in the Kingdom of Saudi Arabia: Mitigation Measures and Hospitals Preparedness. J Nat Sci Med, 1-11. DOI: 10.4103/JNSM.JNSM_29_20
27. WORLDOMETERS, COVID-19 CORONAVIRUS PANDEMIC Updates (Live) (https://www.worldometers.info/coronavirus/#countries) [last accessed 3 May 2020].

Institutional Performance Development in the Water Sector of Jordan

Mohammed Al-Waqfi [1,*] and Noor El-Ali Al-Waqfi [2]

[1] Fire and Safety Engineering Department, Prince Al-Hussein Bin Abdullah II Academy of Civil Protection;
[2] Finance and Banking Department, Yarmouk University;
***** *Corresponding author: m_alwaqfi@hotmail.ca; Tel.: 962 772 833587.*

Abstract: This study investigates the impact of the establishment of state-owned companies on the quality and sustainability of water services provision in Jordan. The performance of Miyahuna, the largest water company, was investigated. Its performance was assessed by using the 10 KPIs adopted by the Program Management Unit for the monitoring of the performance of the established companies. The assessment consisted of two parts; performance of the year 2017 compared to 2016 and the long-term performance from 2007-2017 was assessed. It was found that the performance of Miyahune improved in fields of quality of services (complaints and water consumption per capita), cost recovery, water quality, human resources. Regarding water loss reduction, Miyahuna did well in the first five years then the NRW indicator unfavorably started to rise. To conclude, the establishment of water companies by WAJ proved to be a viable option to enhance the sustainability of water services provision. Improved institutional performance (financially and operationally) of the water sector may be considered as the main driver for achieving sustainable water and wastewater services.

Keywords: Institutional performance, key performance indicators, performance indicators, performance development

1. Introduction

The Jordanian Water Sector is a governmental one. It is overseen by the Ministry of Water and Irrigation (MWI) and two authorities; the Water Authority of Jordan (WAJ) (the bulk water owner and the service provider by law) and the Jordan Valley Authority (JVA) (the supplier of irrigation water). According to WAJ Law no. 18 of 1988, article 28(a), WAJ was authorized to establish water companies and delegate water and wastewater services to the found entities through assignment agreements (AAs) [1-3]. Therefore, WAJ created three water companies that assumed wastewater services.

The established companies are Jordan Water Company Miyahuna (2007) in the Greater Amman area, Aqaba water company (2004) in Aqaba, and Yarmouk water company (2010) in the northern region; Jerash, Ajloun, Mafraq, and Irbid governorates.

The water service levels provided by the Water Administrations of WAJ before 2004 progressively declined. This underperformance has been attributed to the lack of expertise and using governmental business practices rather than applying the commercial principles. Therefore, in an attempt to improve water services, O&M water companies were established. These companies are administratively and financially independent. [1-3]

To monitor the implementation of the AAs with water companies, the Ministry of Water and Irrigation (MWI) established an entity, which directly reports to the minister; that is called Program Management Unit (PMU). The AAs have a set of quantitative indicators that are used in monitoring and assessing performance. These indicators were taken from the International Water Association (IWA) indicators list. The set (in the assignment agreements) is composed of two groups; Key Performance Indicators (KPIs) and lower-level indicators [1-3].

Generally, by developing SMART Key Performance Indicators (KPIs), businesses can establish measures that provide a consistent method for tracking the achievement of organization goals and

targets. SMART means Specific, Measurable, Achievable, Relevant, and Timely. The selection and the development of indicators should always consider the availability of data and collection feasibility. The IWA developed several lists of quantitative performance indicators relevant for gauging water and wastewater services. These indicators are the most commonly applied worldwide for monitoring water utility performance. They are also used at the management-level, and potentially for metric benchmarking practices. Stretching [4] underlined the need for monitoring the performance of water utilities using quantitative indicators. The monitoring system reveals what to improve, where to allocate money and people, the need to compare and benchmark with good performers and learn from good and bad. One of the potential users of the IWA indicators list is the water companies. Furthermore, performance indicators (PIs) may provide a quantitively-based management tool, highlight strengths and weaknesses, encourage benchmarking among utilities, and provides a sound technical basis for auditing [5].

Alegre et al. [6] emphasized that the International Water Association (IWA) performance indicators system is just general guidelines. It is up to each undertaking to define the importance and applicability of every indicator for the organization. They recommended that a subset must be selected as per the utility's needs and objectives. So, the interpretation of an undertaking's performance should consider the context information. Lately, Berg [7] reported that Key Performance Indicators (KPIs) are a widely accepted tool for assessing water utility operations in developing countries and designing the required regulatory and managerial incentives to improve performance. KPIs and operation performance indicators (KPIs) can be more understandable and more comprehensive than benchmarking.

Several studies have investigated the institutional performance of water service providers. Some of these studies indicated that private water utilities performed better than governmental agencies, driven by commercial practices, the economy of scales, and ownership [8-10]. As revealed by several workers, the size positively impacted water utility efficiency. The larger the size is, the more efficient the utility is [11, 12]. The ownership may also directly affect the efficiency of water utilities. Duygun & Zambell [12] investigated the efficiency of many Italian water utilities over the period 2008-2011. The studied parameters mainly included financial indicators; cost of services, wages, materials cost, other costs, and the generated revenue. Also, the effect of size and geographic location was examined. The results showed that the private utilities, which were monitored by a public entity, achieved higher efficiencies. Further, the size and structure have positively influenced the utility efficiency. Therefore, the introduction of performance measures for water service providers is becoming a very vital tool to institutionalize professional accountability and gauge costs, technical serviceability, financial sufficiency, etc., within the water utilities.

A study of the intent of merging water service providers in Palestine into legally and financially independent utilities was carried out. The determined efficiency (i.e., the ratio of the output to a given input) revealed a significant difference in the performance of the newly structured utilities. Multivariate analysis showed significant improvements in water consumption, which positively impacted the average price, and the non-revenue water depending on utility structure. Regarding ownership, the water utilities performed better than municipalities when examining working ratio, gross profit, and collection efficiency [13]. Recently, Mishra [14] has assessed the institutional performance using the indicators functionality index, institutional setup, staff productivity index, the operator capacity (Water Supply Users Committee), and employees.

The current study aims at evaluating the impact of establishing state-owned water companies on the quality of water services and sustainability of service provision, financially and operationally. The case of the Jordan Water Company (Miyahuna) is going to be studied. Miyahara is an O&M company 100% owned by WAJ. Its creation came in response to the growing challenges in the water sector and to improve the provision of water services to the City of Amman.

2. Method

Miyahuna has been selected as a case study due to the increasingly growing water demand in Amman area, geographical expansion and commercial development. Besides, Miyahuna serves about 4 million inhabitants (approximately 800,000 subscribers).

The variables required for the calculation of the 10 KPIs for the years 2007-2017 were obtained from Miyahuna. No KPIs for the years 2018-2020 were calculated, due to the institutional reform taking place in the water sector, which has paused the collection of data and hence the calculation of the pertaining PIs. These Indicators are the most important ones. They are used to gauge the utility adherence to the strategic goals of MWI of improved and sustainable water services and those of the utility. KPIs values give the various stakeholders (e.g., the public, the decision-makers in MWI/WAJ, the board of directors, and the top management of the company, etc.) an overview of the standing of the utility. The 10 KPIs, which cover the different performance categories, are as follows,

- water consumption per capita,
- Microbiological water quality,
- Water losses per water service connection,
- Non-revenue water by volume,
- Collection ratio,
- Operating cost coverage ratio (water and sewerage),
- Subscribers receiving continuous supply,
- Non-billing (service) complaints,
- Billing complaints,
- Total employees per 1000 subscribers.

The assessment methodology is two folds. The performance of Miyahuna for the year 2017 is compared to its performance in 2016 (i.e., cycle to cycle). The performance of 2007 to 2017 is also assessed to predict the long-term performance of the company. This may help in planning and the evolution of a national benchmarking system. It may also lay the grounds for a fair comparison and sharing of improvement efforts and related effects among utilities nationwide and internationally, based on the fact that quite several indicators were adopted unmodified from the IWA recommendations.

3. Results and Discussion

Table 1 shows the performance of Miyahuna using the 10 (KPIs).

3.1. Cycle to cycle performance assessment

3.1.1. Water Consumption per Capita (WRc02)

It measures the amount of water delivered (and sold) to domestic consumers. This KPI signifies whether the population supplied receives enough water for its needs; drinking, cooking, cleaning, etc. Table 1 shows that there has been a slight improvement in the domestic water sales as indicated by the increase in the daily water consumption per capita from 72.75 L in 2016 to 73.37 L in 2017. For the year 2017, the water consumption becomes about 59 L/cap/d in case the Non-Jordanian consumers accounted. Despite that, the water consumption per capita is still within the WHO guidelines for the daily consumption per person.

3.1.2. Microbiological Water Quality Compliance (QS17)

This indicator measures the Percentage of microbiological tests that comply with the Jordanian Drinking Water Standards. Table 1 shows that the water provided to customers shows full microbiological compliance.

3.1.3. Water Loss per Service Connection (Op22)

It measures the volume of water lost (both physical and apparent) per water service connection. It reflects the technical conditions of the service connections for distribution systems of a density of 20 or more service connections per km. As shown in Table1, the water loss per service connection (Op22) indicator has significantly improved (-2.86%) in 2017 compared to 2016, probably, due to the increase in the number of service connections as well as the very significant improvements achieved in the operational indicators; the service connection repair rate and the speed of repair. This result may indicate that the serviceability of the water network is good. The vital operational indicator, the meters replacement, has declined for the same assessed cycle but is still acceptable.

3.1.4. Non-Revenue Water by Volume (Fi36)

The non-revenue water (NRW) is the difference between the system input and the billed authorized consumption. It is expressed as a percentage of the system input volume. Furthermore, it is a financial indicator that measures water losses, both physical and apparent. It may also indicate the technical conditions of the network, including the water meters. As shown in Table 1, the NRW by volume has insignificantly improved (-0.24%) in 2017 compared to 2016. Eliminating the effect of exported water raises the NRW to about **46%** in both years. The high NRW may indicate a decline in the technical efficiency of the distribution network.

3.1.5. Collection Ratio (Fic01)

It measures the proportion of billings that are converted into cash receipts (i.e., it measures the cash flow). The collection reported for 2017 has significantly improved (+2.93%) compared to 2016 and recorded a value of about 98% (see Table 1). Maintaining high collection ratios is of prime importance since this provides the company with the necessary cash to sustain its day-to-day services.

Table 1. Miyahuna annual and long-term performance

Indicator	Definition	Unit	Category	Period		Variance %	Assessment	
				2017	2016		2017	Long-term
WRc02	Water consumption per capita	L/cap/d	Water resource	73.37	72.75	+0.85	Positive	P
QS17	Microbiological water quality compliance	%	Water quality	99.83	99.89	Full compliance		
Op22	Water loss per water service connection	l/Sc/d	Water loss	1270.97	1,308.4	-2.86	Positive	P/N
Fi36*	Non-revenue water by volume	% of system input	Financial / Water loss	37.38	37.47	-0.24	Insignificant	P/N
Fic01	Collection ratio	%	Financial	97.85	95.06	+2.93	Positive	N
Fic03	Operating cost coverage ratio (water and sewerage)	%	Financial	112.90	110.00	+2.63	Positive	P
QSc01	Subscribers receiving continuous supply	%	Service quality	1.50	1.49	+0.67	Insignificant	N
QS22	Non-billing (Service) complaints	% of no. of subs.	Service quality	28.03	23.29	+20.35	Negative	P
QS27	Billing complaints	% of no. of subs.	Service quality	1.82	2.08	-12.50	Positive	N
PEc01	Total employees per 1000 water subscribers	Nr/1000 subs.	Human resource	2.22	2.26	-1.77	Positive	P

3.1.6. Operating Cost (water and sewerage) Coverage Ratio (Fic03)

It is the ratio of water and wastewater revenues to the total water and wastewater services operating costs for the same period. This indicator measures the financial sustainability of the utility. This ratio is usually considered by the financial agencies and donors for funding eligibility. Table 1 shows that Miyahuna was able to cover its operating costs in 2017. The coverage ratio recorded a value of 112%, which is higher than the preceding year by two percent.

3.1.7. Subscribers Receiving Continuous Supply (QSc01)

This indicator measures the number of subscribers receiving continuous supply as a percentage of the total number of active subscribers. It indicates the continuity of supply. Table 1 shows that this indicator has almost remained unaltered in 2017 compared to 2016. This indicator may lose its significance under the intermittent water supply conditions.

3.1.8. Non-Billing (Service) Complaints (QS22)

This indicator expresses the number of non-billing complaints as a percentage of the total number of the registered subscribers. It includes complaints related to pressure, water continuity, water quality, interruptions, etc. It also reflects customer satisfaction with the services provided. Table 1 shows that this indicator has increased by 20% in 2017 compared to 2016, which may signify increasing customer dissatisfaction with services provided. Examining the nature of the filed complaints reveals that the no water complaints have increased from 62,204 in 2016 to 91,244 in 2017.

3.1.9. Billing Complaints (QS27)

It computes the billing complaints as a percentage of the total registered subscribers. It measures customer satisfaction regarding the billing activity. As shown in Table 1, the billing complaints have decreased considerably (-12.50%) in 2017 compared to 2016, hence, indicating growing customer satisfaction in this respect.

3.1.10. Total Employees per 1000 Water Subscribers (PEc01)

It is the total number of staff employed by the utility (regardless of their function or status) per 1000 water subscribers. It measures the manning level at the utility. The indicator PEc01 has significantly decreased (-1.77%), hence, reflecting sincere efforts exerted by the company's management to reduce overmanning (see Table 1).

3.2. Long-term performance assessment

3.2.1. Water Consumption per Capita (WRc02)

Figure 1 shows a plot of the water consumption per capita from 2006 (Management Contract, LEMA) to 2017. On the whole, it reveals a positive performance trend with time. Also, for all assessed years, the water consumption per capita has been higher than its corresponding value in 2006. Before 2011, the improvements may be due to both reductions in water losses and a lesser extent to water availability. While since 2013, the improvement can be, mainly, attributed to the increase in water resource use per capita.

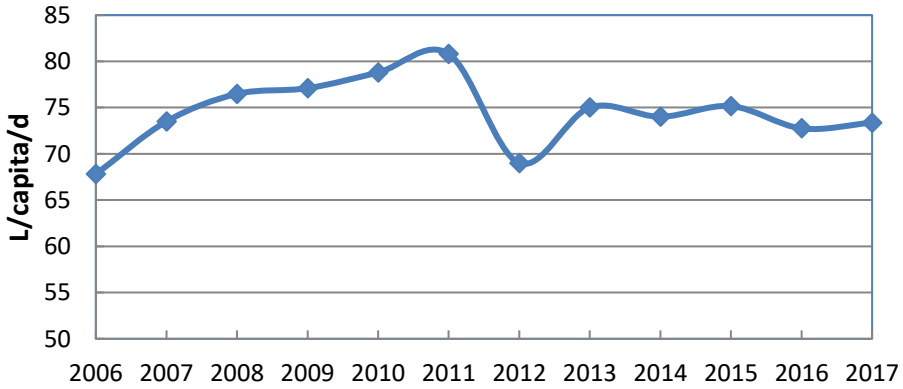


Figure 1. Water consumption per capita

3.2.2. Microbiological Water Quality Compliance (QS17)

As illustrated by Figure 2, the long-term evaluation of the quality of water supplied to customers shows full microbiological compliance with the applicable Jordanian standards.

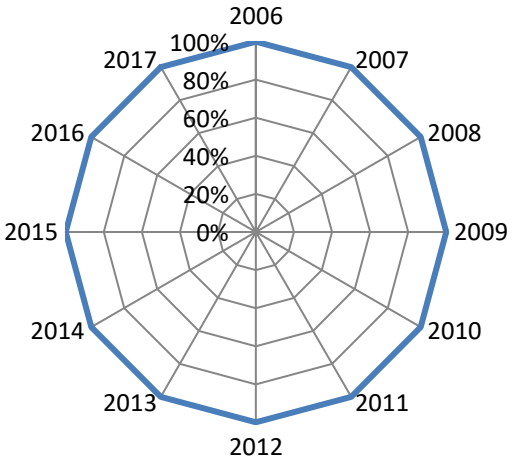


Figure 2. Microbiological compliance

3.2.3. Water Loss per Service Connection (Op22)

Figure 3 shows that the water loss per service connection continually decreased from 2006 to 2011. Since then, it has significantly and constantly increased. This result may indicate that the network technical conditions are, lately, worsening with time and hence more efforts should be exerted in maintenance and repair.

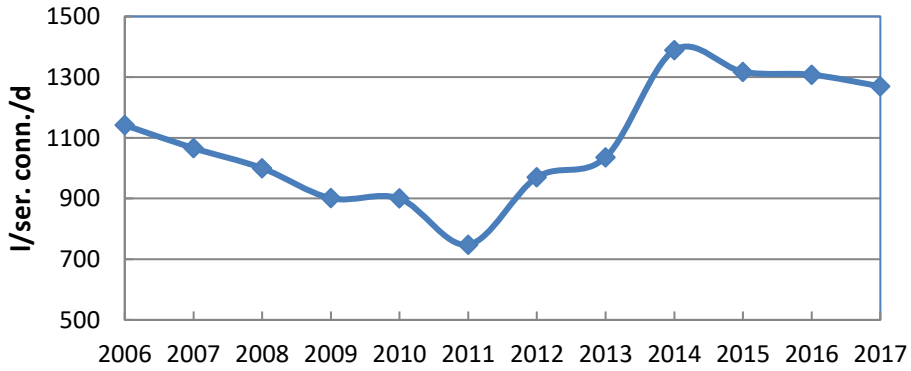


Figure 3. Water loss per service connection

3.2.4. Non-Revenue Water by Volume (Fi36)

As shown in Figure 4, similar to the water loss per service connection, the NRW shows a decreasing trend with time until 2011 then has exhibited almost constant rise ever since.

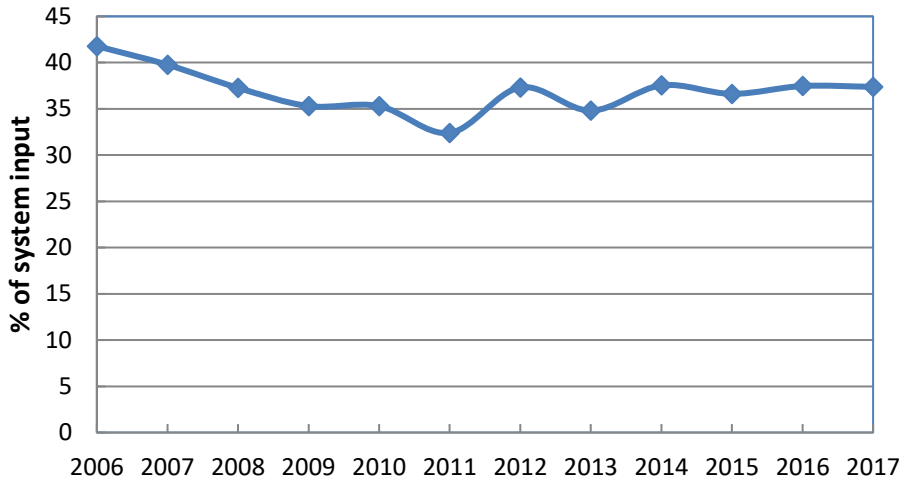


Figure 4. Non-revenue water by volume

3.2.5. Collection Ratio (Fic01)

Figure 5 shows the variation of the collection ratio with time. It demonstrates that the collection continually improved until 2010, followed by a wide variance in the ratios recorded; a result may indicate an unsteadiness in efforts exerted towards this vital activity. In most years, the achieved collection ratios were less than 100%. This long-term negative performance may have led to the increasing accounts receivable with time.

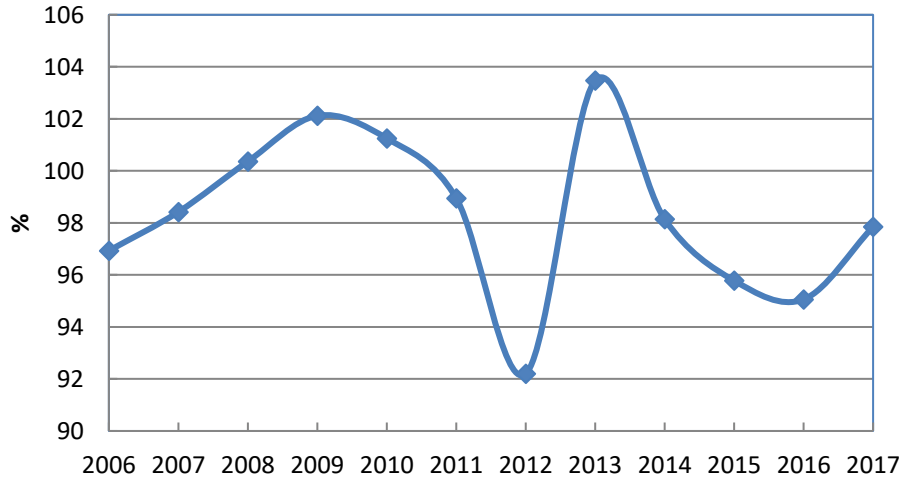


Figure 5. Collection ratio

3.2.6. Operating Cost (water and sewerage) Coverage Ratio (Fic03)

Figure 6 shows that Miyahuna covered the operating costs in all years except 2008 and 2014. Since 2011, the cost recovery ratio has declined at a high rate due to continual rises in operating costs, especially electricity, the main input to the water and wastewater services industry. Maintaining high coverage ratios may help the company financing its investment projects since this ratio is usually considered by the financing agencies for eligibility for funding.

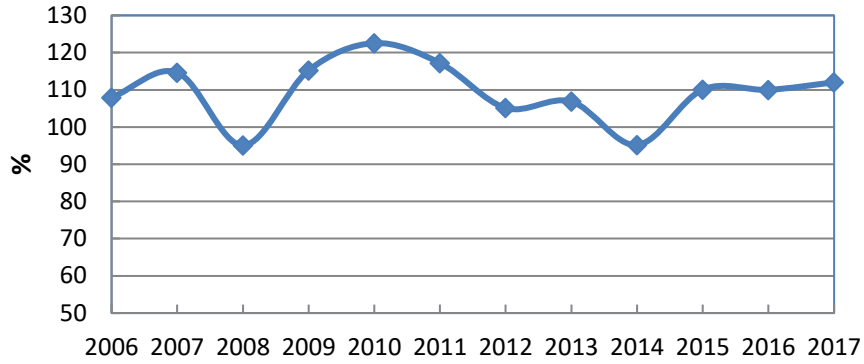


Figure 6. Operating cost coverage ratio

3.2.7. Subscribers Receiving Continuous Supply (QSc01)

As shown in the figure below, the percentage of subscribers receiving continuous supply significantly declined since 2006, except in years 2013, 2014, and 2016 due to Disi water arrival.

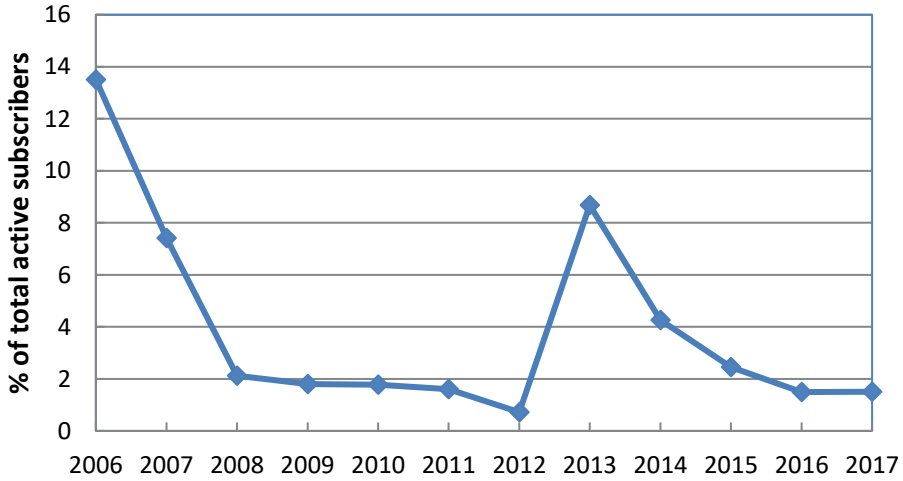


Figure 7. Subscribers recieving continuous supply

3.2.8. Non-Billing (Service) Complaints (QS22)

As shown in Figure 8, the long-term evaluation reveals that the service complaints exhibited a decreasing trend with time and at a higher decreasing rate in the last four years due to the completion of the Disi water project, which has become operational in the second half of 2013.

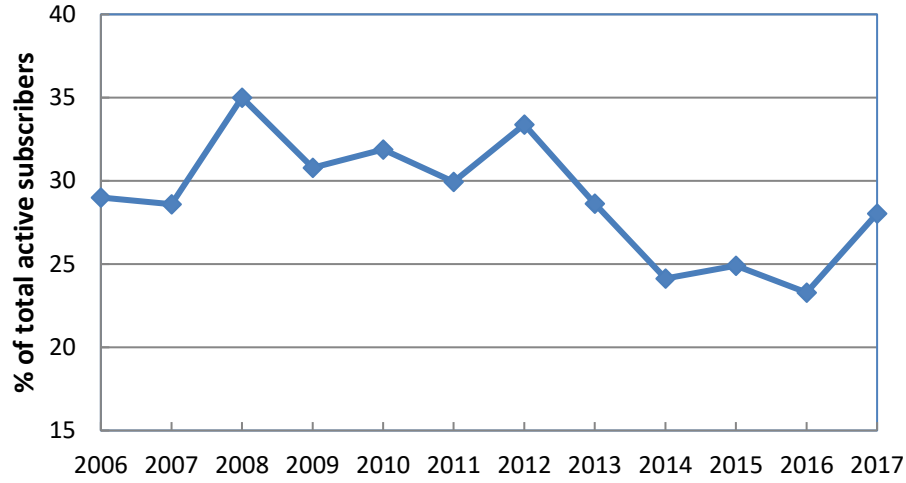


Figure 8. Sevice complaints

3.2.9. Billing Complaints (QS27)

The annual billing complaints show an increasing trend since 2006 as shown in the figure below.

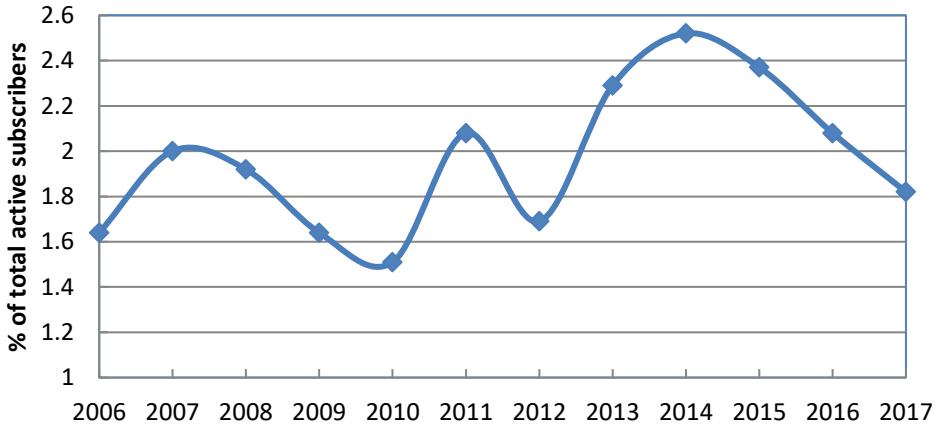


Figure 9. Billing complaints

.

3.2.10. Total Employees per 1000 Water Subscribers (PEc01)

As exhibited by Figure 10, the long-term evaluation may signify a firm commitment of the company management to reduce overmanning at the utility as indicated by the decreasing trend in the number of employees per 1000 subscribers, especially in the last three years.

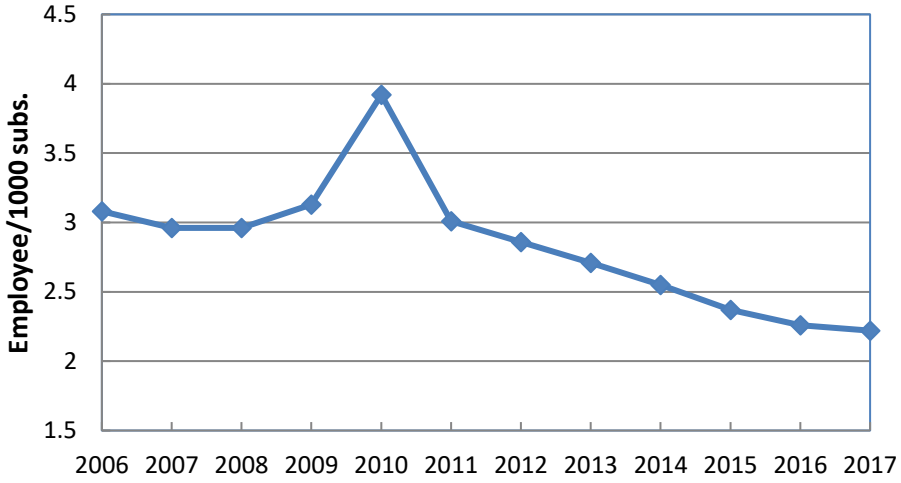


Figure 10. Total employees per 1000 water subscribers

4. Conclusions

Miyahuna performed well on most KPIs in 2017 compared to 2016. Also, Miyahuna's long-term performance has improved in most of the aspects as indicated by water consumption per capita and non-billing (service) complaints, total employees per 1000 Water Subscribers, operating cost (water and sewerage) coverage ratio. Regarding water loss reduction, Miyahuna did well in the first five years then the NRW indicator unfavorably started to rise. Moreover, the creation of a state-owned company has improved the water quality and water services provision in Amman Area.

To reduce water losses, Miyahuna should develop a plan to improve the network efficiency with clear targets and milestones monitored by the PMU. Performance reports should be available to the public to enhance the governance, performance, and reliability of the company.

Lastly, the creation of state-owned water companies may provide a viable option to promote the institutional performance of the water sector of Jordan if the companies are given entire legal, administrative and financial dependence.

References

1. WAJ and Miyahuna,. Assignments Agreement, 2007, Amman.
2. WAJ and Aqaba Water Company, Assignments Agreement, 2004, Amman.
3. WAJ and Yarmouk Water Company, Assignments Agreement, 2011, Amman.
4. Stretching, S., 2011. SMART criteria. Organ. Complete Daily. Work Act. 28.
5. Alegre, H., Performance Indicators for Water Supply Services. IWA Publishing, 2006.
6. Alegre, H., Hirner, W., Baptista, J.M., Parena, R., Highlights of the IWA system of performance indicators for water supply services, in: Beitrag Zum Workshop „Views and Experience Gained Through Implementing IWA Performance Indicators Project “, Im Rahmen Des 3rd World Water Congress in Melbourne, 2002.
7. Brugmann, J., 1997. Is there a method in our measurement? The use of indicators in local sustainable development planning. Local Environ. 2, 59–72.
8. Abrate et al., (2016). Efficiency in the Consolidation of the Italian Water Sector. Water Resour Manage. Springer Science+Business Media Dordrecht 2016. DOI: 10.1007/s11269-016-1376-9
9. Andrea et al., (2015). The Effects of Operational and Environmental Variables on Efficiency of Danish Water and Wastewater Utilities. Water 2015, ISSN 2073-4441 www.mdpi.com/journal/water.7, 3263-3282; DOI: 10.3390/w7073263

10. Marta et al., (2016). Ownership and Performance in Water Services Revisited: Does Private Management Really Outperform Public? Water Resour Manage. Springer Science+Business Media Dordrecht 2016. DOI: 10.1007/s11269-016-1495-3
11. Peda, P., Grossi, G. and Liik, M. (2013) Do Ownership and Size Affect the Performance of Water Utilities? Evidence from Estonian Municipalities. Journal of Management & Governance, 17, 237-259.
12. Pazzi, Ausina, Duygun & Zambell. (2016). The Cost Efficiency of Water Utilities: When Does Public Ownership Matter? Article in Local Government Studies. August 2016. DOI: 10.1080/03003930.2016.1207630
13. Murrar, A., Sadaqa, A., Rabayah K., Samhan, S., Tamimi, A., Sabbah, W. and Barghothi, I. The Efficiency and Institutional Performance of the Palestinian Water Service Providers. American Journal of Environmental and Resource Economics, 2017, 2(4): 162-174
14. Mirsha, A. K. Institutional Performance Assessment of Water Supply System. Saudi J Bus Manag Stud., 2019, DOI: 10.36348/sjbms.2019.v04i09.002

واقع المخاطر المهددة للأمن والسلامة في بيئة قطاع غزة

The reality of threats to security and safety in environment of Gaza Strip

د. محمد محمد عبد ربه المغير

Dr. Mohammed M. A. Al-Mougher

أستاذ مساعد برنامج ماجستير إدارة الأزمات والكوارث-أستاذ مساعد كلية الهندسة جامعة فلسطين

Assistant Professor- Master Program of Crisis and Disaster Management- Assistant Professor-Faculty of Engineering, Palestine University

مدير إدارة الأمن والسلامة (الدفاع المدني) -عضو اللجنة الوطنية للسلامة والصحة المهنية، عضو اللجنة الرئيسية للأمن والسلامة.

Director of Safety and Security management (Civil Defense) - Member of National Committee for Occupational Safety and Health, Member of Main Committee for Safety and Security.

ملخص : هدفت الدراسة إلى تحليل واقع الأمن والسلامة والمخاطر المهددة لبيئة قطاع غزة، مما ينعكس على تراجع مؤشرات الاستقرار الاقتصادي والتنموي. لتحقيق الأهداف اتبع الباحث المنهج الوصفي الذي يصف حالة الأمن والسلامة العامة، والمنهج التحليلي لتحليل المخاطر التى تهدد قطاع غزة، بالاعتماد على تحليل التقارير والسياسات الوطنية في مجال السلامة العامة، ومحاضر الاجتماعات للجان الحكومية ذات العلاقة بالأمن والسلامة، والملاحظة المباشرة للعديد من المخاطر، والتحليل الكيميائي. توصلت الدراسة إلى واقع الأمن والسلامة صعب جدًا على الصعيد القانوني والاجرائي والتنظيمي وأن مؤشرات الموارد البشرية المؤهلة للأمن والسلامة ضعيف جدًا مقارنة بما ورد في الوصف الوظيفي للأمن والسلامة، وأن الاحتلال يشكل تهديد واضح للأمن والسلامة ساهم في عشوائية التخطيط والتحكيم بمسارات التنمية المستقبلية، وضعف المكاتب الفنية والهندسية المؤهلة للقيام بمهام الأمن والسلامة العامة، وأن الاحتلال يمنع وصول المعدات الخاصة بالفحوصات الفنية. أوصت الدراسة بدعم الأمن والسلامة في المحافظات بخريجي دبلوم السلامة و(3) لكل محافظة، وتوفير توفير مهندس ميكانيكي عدد (2)، و(3) مختصين في الكيمياء لإدارة قسم المواد الخطرة. وتوفير طاقم مختص في فحص المصاعد، وتقديم برامج تدريبية تعالج الفجوات، وإعادة هيكلة الأمن والسلامة، وتحديث وتطوير اللوائح الحالية للتناغم مع الأنظمة المحدثة.

The study aimed to analyze the reality of safety and security or risks threatening in the environment of the Gaza Strip, which is reflected in decline indicators of economic and development stability. To achieve the goals, the researcher followed the descriptive approach that describes the state of security and public safety, and analytical approach to analyze the risks which threaten the Gaza Strip, relying on the analysis of national reports and policies in the field of public safety, the reports of meetings for government committees related to security and safety, direct observation of many risks, and chemical analysis .The study concluded that the reality of security and safety is very difficult at the legal, procedural and organizational levels which indicators of qualified human resources for security and safety are very weak compared with what was stated in the job description for safety and security, the occupation constitutes a clear threat to security and safety that contributed to random planning and arbitration for future development paths, and the weakness of technical offices and engineering qualified to carry out security and public safety tasks, also the occupation prevents the arrival of equipment for technical examinations. The study recommended supporting security and safety in the governorates with safety diploma graduates and (3) for each governorate, a providing a mechanical engineer number (2) and (3) specialists in chemistry to manage the Department of Hazardous Materials. Providing a specialized team to inspect elevators, providing training programs that address gaps, restructuring security and safety, updating and developing the current regulations to harmonize with updated systems.

الكلمات المفتاحية: المخاطر; المهددات ; الأمن والسلامة ;قطاع غزة

Keywords: Risk ; Threats ; Safety and Security ; Gaza Strip.

1. The general framework research study

1.1 Introduction

Countries are interested in formulating a strong system for security and public safety in order to achieve continuity in sustainable national development to reduce risks which threaten internal environment of the state, especially in the field of safety and security in industrial, commercial and economic fields, also dealing with facilities that pose a threat to societies. Societies have incurred many losses. As a result of threats societal security, which can turn into disasters with long-term damages. (Al-Shibi, 1993)

The approach of managing risks expected to occur in the Gaza Strip represented a clear work policy by government institutions after tragic incident which occurred in the Nusseirat area, which caused lives of (28) citizens working in crafts and industries in an area crowded with trade activities, accordingly that the reality was diagnosed to study effects of risks Therefore, the Council of Ministers in the sector worked to direct national policies towards paying attention to quality of safety also prevention in dangerous establishments and trades, moreover to reduce human and material losses due to its direct impact on the lives of workers and increase production.

The Gaza Strip has witnessed many factors affecting on development paths, including industrial, economic and development fields, and there have been relief interventions to support the development sectors without developing those activities for programs that contribute sustainability and risk reduction, especially in the field of training for workers in public, private, community and civil sectors in the field of safety and risk prevention. National institutions have worked to enhance preventive activities through many government institutions that are directly related to limiting further damage in national sectors. (El-Mougher and Mahfuth, 2021)

National institutions are adopting various methods to manage changing situation in the Gaza Strip as a result of effects resulting from suffocating siege on the Strip, also destruction of occupation's components in industrial and economic resilience in the repeated military attacks on the Strip, the resulting residues of dangerous chemicals that threaten environmental stability in the Gaza Strip and effect on natural resources, furthermore government agencies have sought to bypass the radical changes brought about by the Israeli destruction mechanism on the development sectors; Including the industrial sectors that have an impact on economic development; Which helps in developing government ideas and policies to face industrial development risks, and building capabilities which can contribute to risk management systems. (Al-Saud, Al-Ashqar, and Al-Mougher, 2021)

1.2 The problem of the study:

government and meeting reports indicate reality of safety and security also Gaza Strip suffers from a number threats to the environment of the Gaza Strip, moreover Gaza Strip is almost devoid of academic specialists in security and safety engineering, firefighting engineering, rescue engineering or risk management engineering; also through nature of the researcher's work in the field of safety and security, it is noted that reality requires more controls and procedures that can reduce risks and threats moreover update local regulations, laws and legislation; Through the analysis of government reports, it is clear that there is a lack of some procedural evidence for its application, including guide for classifying establishments and crafts according to levels of risk. The researcher believes that there are several indicators which help to reduce the research gap, which are :

1. There are many elements of advance planning to reduce risks in the industrial and economic sectors.
2. Civil Defense's need to modernize vehicles and accident response equipment.
3. Introduce regulations, laws, and legislation that address existing problems.

4. The emergence an exceptional reality due to political, security and economic changes which caused by the occupation.
5. Lack of experts in chemical engineering at Gaza Strip.

Therefore, the research problem can be crystallized in following main question: "What is reality of safety and security also risks threatening at Gaza Strip"?

1.3 Objectives of the study:

The aim of study describe the reality of threats to safety and security in the environment at Gaza Strip in order to reach treatments that are in line with the exceptional reality experienced by the Palestinian society، and to analyze the risks that threaten the security and public safety system in Gaza Strip. Improving the levels of inspection on hazardous facilities and trades in light of the existing threats.

1.4 Importance of the study:

1.4.1 Scientific importance:

The safety and security or risks which threatening the environment of Gaza Strip are considered and analyzed in line with economic، administrative and political variables of the Gaza Strip، and taking into account the exceptional developmental reality and planning under unstable conditions to build on a scientific study on which government decision-making is based.

1.4.2 Applied importance:

Striving to provide a matrix to assess the risks and threats to security and safety in the Gaza Strip that can be the ground that can be updated by the competent governmental committees, and benefit from it in scientific studies related to dangerous facilities and trades, and improve legislative systems to enhance the public safety system; This will be reflected in the development of economic development in a way that enhances the protection of the economic cycle in the Gaza Strip.

1.5 Study methodology:

The study adopted the descriptive approach that describes the reality of security and safety in the Gaza Strip and the government agencies concerned with it, and the analytical approach that analyzes the risks threatening the environment of the Gaza Strip and their impacts, based on the analysis of reports issued by the competent government agencies, and chemical analysis for one of the most important letters Dangerous according to classification of risks Enterprises and Crafts Committee in the Gaza Strip, and the approach of policies, standards and indicators that affect risk control in accordance with international standards.

1.6 Limitations of Study:

1.6.1 Spatial boundaries:

The spatial boundaries extend to Gaza Strip, which has an area of 365 km2, which various activities vary despite high population and urban density in it.

1.6.2 Objective limits:

The study was limited to dealing with safety and security, threats to public safety, dangerous installations and trades in the Gaza Strip.

1.6.3 Temporal limits:

The study was limited to the time period for its preparation from March 2021 AD until the date of the ninth engineering conference.

2. literature review

The Gaza Strip suffers from the academic weakness of the safety and security engineering disciplines, similar to the surrounding countries where this specialization is available due to its importance. The Palestinian government in the Strip tried to compensate for this deficiency by qualifying a group of engineers in this field through training courses held by the General Directorate of Civil Defense. There is still a gap in this specialization due to its reflection on the usual daily life of the Palestinian society and the nature of the risks that threaten the environment of the Gaza Strip.

2.1 Previous Studies:

2.1.1 A study (Al-Saud, Al-Ashqar, and Al-Mougher, 2021), entitled:

Risk Management in Chemical Industrial Plants in Gaza Strip-Case Study: Detergent Factories Sector

The study aimed to analyze the current reality of chemical industry facilities and the extent of compliance with laws and standards which related to occupational safety and health. To achieve the goals, the researchers followed descriptive and analytical approach, through the interview as a tool. The study found that there are major violations in the detergent factories, and the lack of application of safety standards, especially in unlicensed factories. The researchers recommended following up and monitoring these factories, which are classified as dangerous facilities, but without imposing more taxes for what they suffer as a result of the siege imposed on the Gaza Strip.

2.1.2 A study (Abu Sharekh, Al-Mougher, and Al-Ashqar, 2019) entitled:

Analysis Reality of Hazardous Materials Management at Gaza Strip for the Point of View the Workers in Occupational Safety and Health- Case Study Pharmaceutical

The study aimed to analyze the reality of the management of hazardous pharmaceuticals from the point view of workers in occupational safety and health, by using the descriptive analytical method through interviews and a questionnaire. The study found that there is knowledge of the world about occupational safety and health in the field of laws and legislation to a small degree, storage a medium degree, pharmaceutical manufacturing a large degree. The study recommended the development of communication mechanisms for accidents, and the provision of a code that helps workers in occupational safety to deal with the management of dangerous pharmaceutical materials.

2.1.3 A study (El-Sayed, 2019), entitled: Safety and Security Systems in Buildings

The study aimed to identify the risks that threaten the safety of the building and study the factors affecting on building. The study used the descriptive analytical method through a questionnaire to collect data. The study concluded that choosing the site of the building as the first threat to , and that the most safety and security risks facing buildings are slips, followed by falls, fires, obstacles to use and operation, and partial and total demolition. The study concluded to ensure the application of safety and security systems during construction, knowledge of modern construction methods, and adoption of modern and advanced systems for safety and security.

2.1.4 A study (Al-Mughayer, 2018), entitled: Risk Assessment and Risk Indicators in Industrial Institutions in the Gaza Strip

The study aimed to reach a set of indicators and applied models for risk management in industrial establishments at Gaza Strip. The study found the weakness of national indicators which used in the assessment, their failure to meet risk management procedures, and the absence of a reference guide for assessing and analyzing risks arising in the work environment. The risks can be controlled if they are understood, and thus the priorities for combating risks and minimizing their effects. The study recommended activating scientific research in protecting against risks and limiting their effects that

institutions work to estimate an annual position on risks in industrial facilities, and follow preventive, exploratory, remedial and corrective measures to reach a safe and fair environment that contributes to staving off risks from the work environment.

Commenting on previous studies:

The researcher believes that previous studies were concerned with risk management, safety and security in educational facilities, chemical industries, or the pharmaceutical sector. Threats to security and safety in the Gaza Strip, which is considered the most region characterized by security, political and economic instability, and the current study will be characterized by using chemical analysis of mobile risks threatening safety and security in the Gaza Strip.

2.2 Study terms:

- Threat: the declared and undeclared, intentional and unintended activities, events and programs that work to destabilize security and stability and pose a clear danger that has consequences and damages to security and community peace; This results in halting development paths and halting life activities in the area exposed to dangers, and requires interventions from various parties within the state and may extend outside it. (Al-Azawwi, 2020)
- Risk: It is about threats and expected events that threaten the security and stability of society, peace and security, halting the life cycle of institutions, working to regress indicators of implementing strategic goals, exposing people and their surrounding environment to material and human damage and losses, and threatening natural resources and the environment with all its components. (Directorate of Policies and Studies, 2016) that is, the threats that work to stop the course of life in its normal or usual way.
- Risks: are the actions and damages that contribute to threatening the business sustainability of projects, programs or development plans and result in negative and positive effects by seizing opportunities. The scope of the geographical risk varies according to the nature of the risk and the components of the impact on the surrounding environment. (Al-ramlawi, El-Mougher, and Al-Agha, 2021(
- Risk management: It is the ability of countries, institutions, organizations or companies to understand all risks in all their dimensions, and to reduce the vulnerability of people to damage, property and the work environment through instructions, instructions, laws and regulations that regulate their management; By planning their management and assessing the expected impact of risks, the process takes place in several planned steps by strengthening risk management, starting from the establishment of industrial facilities, until reaching their operation and determining the possibility of recurring all expected risks. (United Nations, 2015(
- safety and Security: defined by the Palestinian Civil Defense Law as "a set of engineering, organizational and educational methods aimed at protecting human and property" (General Directorate of Civil Defense, 1998). The researcher believes that it is a set of systems, procedures, and measures necessary to provide protection for individuals and private and public properties, reduce danger, prevent disasters or reduce their occurrence, i.e. take engineering measures from means of alarm, risk monitoring and control systems, forecasting expected damage, means of fire protection and methods of manual control. mechanical and electronic.

2.3 The current safety and security situation at Gaza Strip:

The safety and security system in the Gaza Strip developed after the arrival of the Palestinian National Authority at the end of the year 1994 AD, as this was accompanied by the building of a national system through the system of laws and legislation. The Palestinian Authority has been pursuing economic and industrial growth in order to achieve development paths that develop human life.

The impact of Israeli occupation in the Palestinian territories on national development projects and directing activities projects in a way that reduces development opportunities and leads to the depletion of resources, the deterioration of the economic structure, and the decline in security and public safety indicators. The repeated targeting of facilities, buildings and natural resources has contributed to fundamental changes in the destruction of the public safety system; The occupation contributed to bulldozing of industrial and commercial areas, the intensive bombing of economic, industrial and commercial development projects, roads and energy, and the depletion of natural resources and targeting with rockets. (Esposito, 2009(

In 2006, the indicators of Israeli targeting of economic facilities increased and the pace of the siege increased and prevented the supply of equipment and devices that would reduce the gap for the development of safety and prevention equipment, and as a result, energy resources, roads, and the economic, commercial and industrial infrastructure were directly targeted. The Israeli occupation also targeted all elements of steadfastness and all supplies Human life (Barghouth, 2013), which the Palestinian people still suffer from, and society has increased the rates of danger in establishments, crafts and industries as a result of the strict Israeli siege, which caused the spread of risks related to threatening the industrial and economic environment and crafts as a result of the inability to modernize equipment and develop and improve the sector industrial.

From the foregoing, it appears that the level of challenges facing safety and security system at Gaza Strip are as follows:

- The Israeli military operations, in which the direct targeting of industrial, economic and commercial development sectors appears in a large way, and this was evident in the targeting of agricultural materials stores in the North Governorate.
- The Israeli blockade imposed on the Gaza Strip.
- The link between project financing and external agendas from international organizations and institutions.
- Weak interest in safety and security system on the part of the Palestinian Authority. This was evident in the weakness of the legislative system, the decline in support for development projects for safety and prevention, and the conflict of regulations with regulations.
- The lack of real guidance on security and safety priorities, due to the lack of clarity in development paths and the increasing pressure in urban expansion on other land uses.
- The great pressure on the Civil Defense in light of the weak operating budgets, and this has affected the deterioration of the firefighting and rescue vehicles, the decline in their performance indicators, and the increase in operating expenses on their maintenance.
- The lack of clear indicators to identify and assess the risks arising from dangerous installations and trades.

Methodology and study tools

To achieve the objectives of study, the researcher followed methodology which depend on analyzing the reality of legal system and human resources specialized in safety and prevention in the public sector and threats of safety and security, by relying on the reports of Main Committee for safety and security which formed by the decision of Council of Ministers, and through direct observation.
The reality of the administrative organization for safety and security:

The administrative authorities regulating security, safety and prevention in the Gaza Strip vary. Based on the analysis of the report for the Committee to Study Regulations and Procedures for safety and security, formed by the Council of Ministers, the researcher concluded that the departments concerned on safety and prevention are following:

- The Ministry of Interior and National Security, through the following departments:
  - The General Directorate of Civil Defense - safety and security Department: It is the authority authorized to issue permits of inspect installations and crafts with regard.
  - Palestinian Police - Department of General Investigations through the Supply Investigations: This is done by following up on food and economic safety and consumer protection, investigating and providing information about violators of safety and security, administrative violations and bypassing regulations in the event of crises and disasters, which submitted to stockholders.
- Ministry of Labor - General Administration of Inspection and Labor Protection: It is concerned on the management occupational safety and health, protection of workers and their rights, insurance and rehabilitation in the field protecting themselves from work risks according to the nature of the risks threatening them.
- Ministry of Public Health – Department of Occupational Health: The department concerned on health safety conditions inside the home, crafts and industries, and is concerned with periodic inspection of address.
- Ministry of National Economy: There are many departments and sections in the ministry that are directly related to safety of society and the provision of technical conditions and specifications for industrial, commercial and economic establishments that enhance the safety of society. The most important of these departments is the Palestinian Standards Organization headed by the Minister of National Economy, the General Administration of Industries, the General Administration of Inspection Consumer Protection, Industrial Cities Authority.
- Environmental Quality Authority: It is governmental agency authorized to inspect and follow up safety and pollution environmental also relationship of establishments to level of environmental damage. There are many specialized drug and drug departments available.

  There are also many other committees that are concerned with security, safety and risk reduction and that work to coordinate efforts, including temporary technical committees and permanent technical committees, which are:
- The National Committee for Occupational Safety and Health: It is a committee headed by the Ministry of Labor concerned with occupational safety and health moreover drawing up its general policies. It has technical committees in the governorates working on educating the community about the risks affecting the work environment and the mechanisms to reduce them. It was formed by a decision of the Minister of Labor in the year 2017. Representation of the public and private sectors, trade unions, industry and academic institutions.
- The Main Committee for Safety and Security, which was formed by the Council of Ministers after the Nuseirat incident, headed by the Ministry of Interior and

membership of Ministry of Labor and Local Government, the General Administration of Petroleum and the Ministry of Economy. This committee is concerned on developing regulations and legislation which related to security and public safety, furthermore enhancing coordination between government agencies on controlling the state of public safety and reducing conflict between regulations and laws, and organizing the computerization of security and public safety procedures in the field of inspection , licensing and integration of operations in a manner that reduces violations and bypassing regulations and legislation in this regard. To inspect industrial establishments, bakeries, gas and gas stations, kitchens, restaurants, fuel stores, domestic gas distributors and other various establishments.

There are also many meetings, meetings and workshops held by Civil Defense and Main Committee for Safety and Security in partnership with the Public Prosecution, the Ministry of Economy, the Ministry of Local Government, the Ministry of Labor, and other executive government agencies for improving regulations and legislation in line with the reality of safety and security also with conditions it is going through. Sector.

The reality of legislative and legal system:

There are many laws and regulations related to safety and security in the Palestinian territories, all of which are based on the amended Palestinian Constitution No. (3) of 2003 AD. The following are the most important laws and regulations:

- **Amended Basic Law No. (3) of 2003:**

Article 25 states that work is a right for every citizen, a duty and an honor, and National Authority seeks to provide it to everyone who is capable of it. Labor relations are organized in a way that ensures justice for all and provides workers with care, security, health and social care. Trade union organization is a right regulated by law. The right to strike is exercised within the limits of the law.

- **Law No. (3) of 1998 regarding civil defense**

Emergency planning and the development of preparedness is based on the Civil Defense Law No. (3) of 1998, which stipulates the formation of the Supreme Council of Civil Defense, which specializes in planning to face disaster risks and crises and developing existing plans in the following articles: (2), (5), (6), (12), (14), (16), (26.(

Articles No. (16 to 21) of the Civil Defense Law relate to the inspection of special requirements for fire prevention, while Resolution No. (19) of 2000, in which civil defense crews were granted the status of judicial police for industrial security inspectors in civil defense. See Appendix No. (1) explaining the safety and fire prevention regulations approved by Resolution No. (27) for the year 2000 AD.

- **Palestinian Labor Law No. 7 of 2000**

Articles (90-91-92) of Chapter Four, Chapter Five, related to occupational safety and health, Articles (107 to 115) of Chapter Eight, related to labor inspection, and Articles (116 to 130) of Chapter Nine, related to work injuries and occupational diseases, and Article (34).) From Chapter One, Chapter Three, related to the obligation of occupational safety and health rules at work, of the Labor Law, to organize the work system for occupational safety and health in a holistic manner. See Appendix No. (2) that explains the secondary legislation issued under the Palestinian Labor Law No. (7) of 2000 AD.

- **Public Health Law No. (20) of 2004**

Articles (31 to 35) of Chapter Five relating on occupational health regulate relationship between the Ministry of Health and the rest of the ministry related to occupational safety and health, and the organization of the work of health inspectors in monitoring the occupational environment and health of workers and the extent of compliance with the conditions of occupational safety and health

- **Standards and Metrology Law No. (6) of 2000**

Paragraph (1) of Article 4 of the law stipulates preparation and approval of Palestinian specifications and standards for goods, materials, services and others, their review, amendment, replacement and publication, with exception of human and veterinary medicines, baits and serums. And paragraph (6) of the same article on accrediting examination and testing laboratories and qualified calibration laboratories specialized in conducting examinations, analyzes and tests on goods and materials for the purposes of applying specifications and standards.

- **Consumer Protection Law No. (12) of 2005**

Clause (1) of Article 2, provides for the protection and guarantee of consumer rights to ensure that he is not exposed to any health risks, injustice or economic losses.

- **Law No. (7) of 1999 regarding the environment**

Article (20) of Chapter Two, Chapter Two, states: "The owner of the facility shall provide the necessary means of protection for workers and neighbors of facility in implementation of the conditions of occupational safety and health against any leakage or emission of any pollutants inside or outside the workplace. Article (27) of Chapter Two also stipulates "The level of radioactivity or concentrations of radioactive materials emitted by the facility or any other activity may not exceed the permissible limits determined by the competent authorities." For more, see Appendix No. (3) of the Environmental Quality Authority's instructions for the year 2003 AD.

- **Decree-Law No. (10) of 2011 regarding the Industrial Law**

Article No. (23) sets out the powers granted to judicial control officers for the purposes of inspecting industrial facilities, and paragraph (3-4) of the article shows the verification of licensing conditions, industrial security, health and public safety, and the extent of compliance with the necessary environmental conditions in accordance with the provisions of the relevant laws.

- **Executive Instructions for Cabinet Resolution No. (1) of 2009 regarding the system of local authority employees**

Articles (67 to 79) refer to the regulation of work injuries and occupational diseases.

There is also a large set of regulations issued by the Central Committee for Buildings and Urban Planning, the most important of which are:

- Gas station licensing system.
- Gas distribution stations licensing system.
- Wedding and event halls system
- Fuel storage system.
- Public and commercial buildings system.
- The system of crafts and industries.
- Industrial establishments system.
- Commercial premises system.
- Tourist establishments system.
- Gas Distributors System.

The reality of human resources working at safety and security:

Many technical and engineering disciplines work at safety and security, as the disciplines must focus on chemical engineering, industrial engineering, mechanical engineering, architecture, security and safety engineering, fire and rescue engineering, and risk management engineering. Of them, (9) engineering sciences did not have a specialty in safety and security engineering, mechanical engineering, chemical engineering, or risk management engineering, and there were an architect (1), an electrical (1), an industrial (1), (6) civil engineer, the rest of the resources Humanity (5) holds

a high school diploma, (3) an intermediate diploma, (7) an industrial and craft technician diploma, (6) administrative sciences, (2) law, (8) social and educational sciences, and (1) computer.

The General Directorate of Civil Defense has held several training courses for non-engineering specializations in safety and prevention regulations that explain Law No. (3) of (1998 AD), a course in inspection assets, a course in the management of hazardous materials, a course in judicial police, and a course in the management of war disasters. , hazardous materials disasters, risk management, and other various administrative courses that can perform tasks with minimal inspections and licensing of hazardous facilities and trades.

The researcher worked on analyzing the organizational structure and job description guide for the Safety and Security Department in the Civil Defense and it appeared that there is a shortage in the various human resources of up to (60) employees in different engineering disciplines, security and public safety technicians, analytical chemistry specialists, elevator technicians, and law.

واقع المخاطر والمهددات المتوقعة:

The reality of expected risks and threats:

The executive regulations issued by Resolution No. (27) for the year (2000 AD) refer, for example, the list of safety conditions, fire prevention, means of protection, and specifications of extinguishing and warning devices that must be available in fuel transport stations and vehicles. Article No. 22 states**: "It is not permissible to permit the establishment of any A station or its expansion before the license applicant submits a technical study prepared by one of the technical offices specialized in safety work and approved by the General Directorate of Civil Defense. months to another year by order of the Director General, according to what the Civil Defense determines and the nature of the work to be carried out to complete the requirements and instructions contained in this regulation. Because of the danger it poses, the Director General of Civil Defense may refuse to issue a permit for that".**

Where this article has been repeated in all civil defense regulations, and here the technical study is intended for analytical studies, including risk analysis and management. external.

First: the expected internal risks

- fires
- bangs
- Interactions of chemicals and the dissemination of toxic gases such as chlorine gas.
- Chemical leakage of hazardous materials stored in buildings and facilities.
- Deliberate sabotage in vital areas.
- Dissemination of infectious diseases and epidemics.

Second: scenarios for expected risks:

The researcher worked on using the chemical package analysis program issued by the US Environmental Protection Agency on the simulation scenario of a moving gas tank explosion in front of densely populated areas, which poses a clear threat to the population.

- Scenario of a moving tanker accident in front of Al-Shati camp:

A simulation was carried out using chemical packages programs for the scenario of a moving gas tank explosion in Al-Rasheed Street in the Shati area. The outputs of the analysis are as follows:

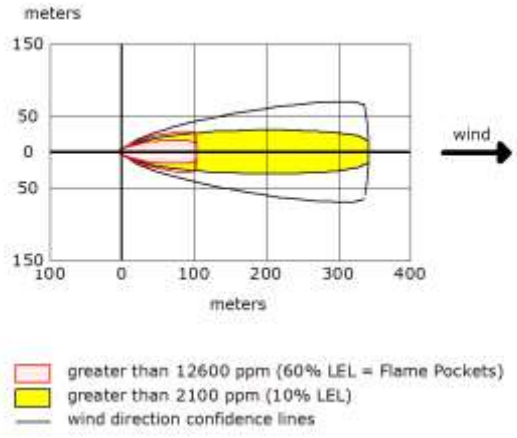


Figure 2. Effect on ignition in the beach area

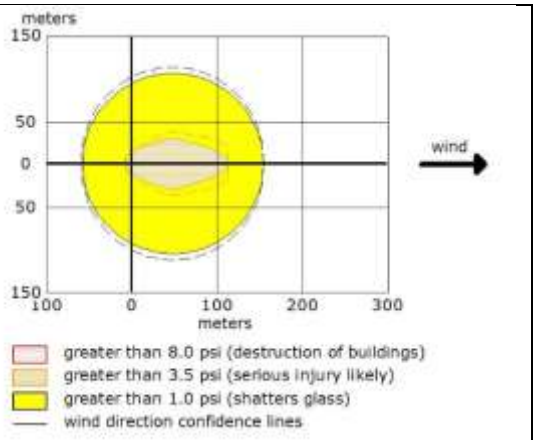


Figure 1. Effect on explosion in the beach area

Figure (1) shows that: the red and orange regions combined together at 79 m towards the southeast; As this area has fatal human losses and very high damage to assets and property, while the yellow area, which is characterized by toxic gases and fumes, is estimated at 111 m and has slight material damage and weak human injuries.

Figure (2) indicates that: the risks of ignition reached the red and orange area, in which the flame mass is formed, 105 m towards the southeast, in which human and material losses are high, and it is the most overcrowded area, which portends heavy losses, while the yellow area is spread in which toxic gases and fumes are spread, 342 m.

- Al-Shuja'iya Scenario:

A simulation was carried out on the chemical packages programs for the expected risks from the leakage of a moving gas tank with a capacity of 30 tons in the Al-Bastat market area in Al-Shujaiya, and the outputs were as follows:

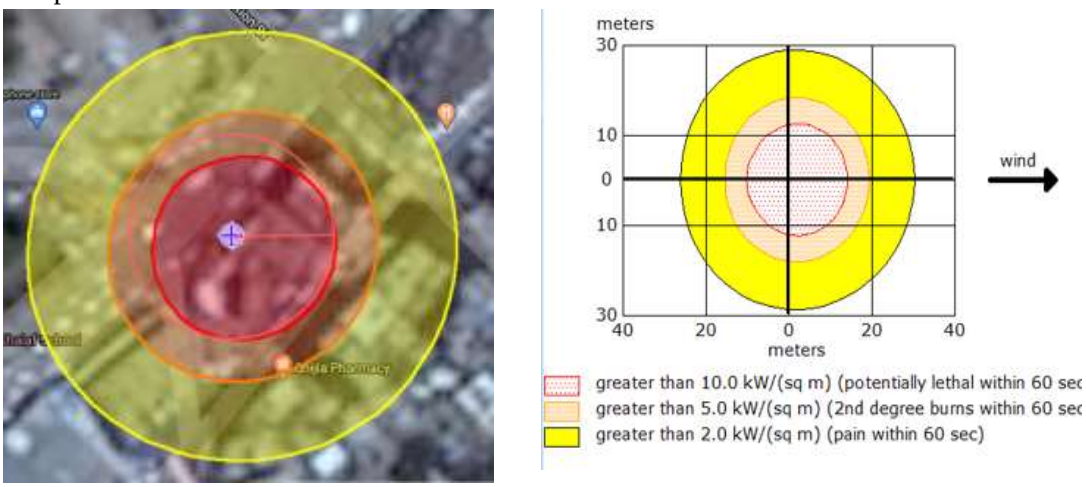


Figure 3. geographical impact of the gas leak in the Shujaiya area

It is clear from Figure No. (3) that: The diameter of the red circle in the scenario is 13.6 m towards the southeast, as it appears that it is burning the entire Shujaiya market. It is expected that all of the red zone will melt, and the orange circle will be 19.3 m, in which thermal radiation spreads and the rate of rise in it Injuries and material losses, and the yellow circle with a radius of 29.9 m towards the southeast, in which toxic gases and fumes spread. The data indicate that the rate of combustion of the amount of gas reaches 6 minutes, according to what is stated in Figure (4.(

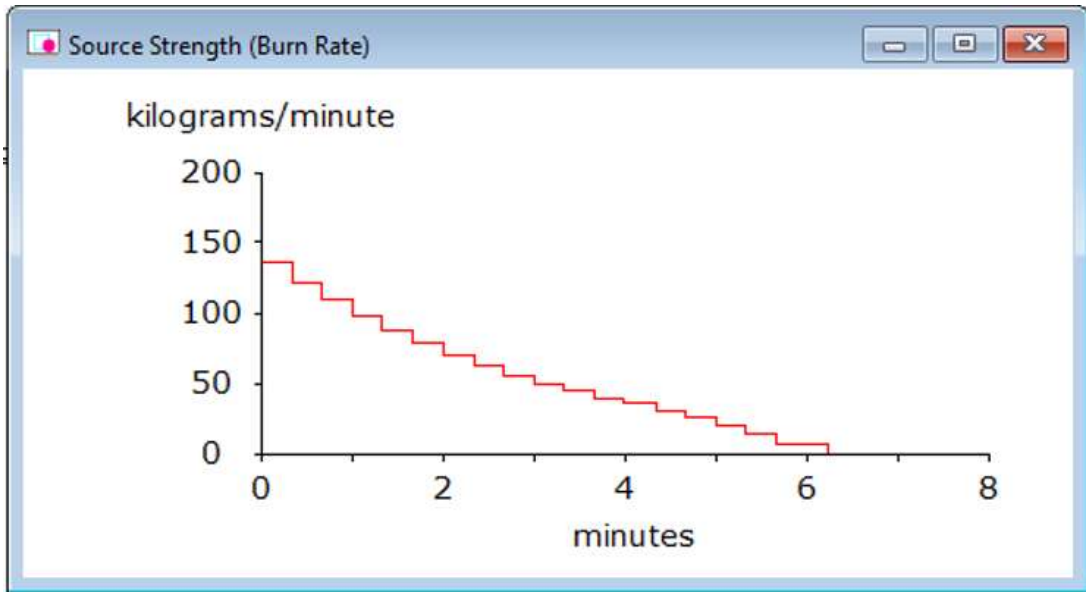


Figure 4. The rate of combustion of the gas substance

Sources of threats to safety and security:

Based on the researcher's cumulative experiences in risk management and planning, the researcher has prepared a matrix to analyze risks and show the impact, threat and probability of their occurrence in order to reach procedures to control the effectiveness of risk reduction and protection of community human resources.

The researcher relied on the analysis of the minutes of the meetings of the Main Committee for Security and Safety, the field survey reports of the Dangerous Facilities Licensing Committee for a number of (389) facilities, the reports of the technical committees emanating from the Central Committee for Buildings and Urban Planning, and the final report of the Committee to Study Regulations and Legislation for Security and Safety. Explains the matrix of threats to security and safety in the Gaza Strip.

threatened	**Risks**	**expected action**	Impact	likelihood	**level**	**control measures**
Occupation	Deliberate targeting of facilities	The high rate of human losses, including deaths and injuries. Losses of assets and property, and environmental pollution in the spread of dangerous substances that threaten public health in the long run	4	5	20	That international organizations in neutralizing the industrial, commercial and economic sector bear direct targeting and protection in accordance with the rules and protocols of international humanitarian law. Accelerate the reduction of the increase in environmental pollution and the safe disposal of hazardous waste.
	Banning the supply of safety equipment	High accident rates, which is reflected in human injuries and partial work stoppage.	3	4	12	Opening the supply routes for safety and personal protection equipment from the Egyptian side, and working to maintain the existing equipment periodically, taking into account the extension of its lifespan.
	Prohibition of modernization of equipment for installations of gas stations and tanks	High accident rates, and the possibility of explosion or ignition	3	5	15	Working on opening new routes for the supply of gas tanks and extensions and updating them in accordance with local and international specifications and standards.
	Preventing entry of maintenance equipment to dangerous facilities and trades	Work accidents, fires, poisoning accidents, and dangerous chemical reactions	3	3	9	Working on the medical maintenance of equipment in partnership with industrial associations, in coordination with the Egyptian side.

	Targeting energy sources	Fires in the facilities as a result of the tendency to use traditional means of energy, generators, and others	4	4	16	Working on the use of renewable energy means and reducing the use of generators, candles and other traditional means.
	Exploitation of water resources	Poor implementation of development plans and low water access to firefighting networks, and consequently high rates of human and material losses, and an increase in the time to control accidents	4	2	8	Enhancing the sustainability of water sources, treating gray water, promoting seawater desalination projects, re-examining the depletion of water from the community and rationalizing water consumption, by enhancing the water quota, and providing the underground reservoir with rainwater.
Interference and conflict between regulations and laws	Introduce regulations and legislation	The construction of many exceptionally dangerous buildings, crafts and installations to bypass the age of regulations.	3	2	6	Work on the inventory of regulations and laws and the dates of their issuance, and update the rules and regulations every 5 years in a way that contributes to national development in a legal manner consistent with reality.
	The interference of the regulators of legislation	Weak implementation of safety and security procedures, and conflicting technical procedures by the supervisory authorities for security and safety	3	3	9	Determining the matrix of powers through government committees, according to the tasks contained in the regulations and laws, following up their implementation by the supervisory authorities, forming joint inspection committees, preparing a manual of security and safety procedures that define the role of each competent authority, and the hierarchical procedures in technical follow-up.
	Conflict of laws and regulations	The inability to issue permits for dangerous establishments and trades, and the delay in citizens' interests in completing transactions in accordance with the rules.	3	2	6	Identify and clarify conflicts, whether technical or legal, and work to resolve them through holding technical committees to study the conflict and its effects on the reality of dangerous facilities and the level of risk spread and expansion, and prepare a

						manual of technical and administrative procedures to complete the transactions of citizens.
	Licensing businesses and crafts in violation of the law	The difficulty of applying safety and prevention measures, especially urban safety, which takes into account reducing the transmission of heat radiation, which transfers fire from one building to another.	2	5	10	Taking strict legal measures to prevent the formation of a reality that violates the regulations that contributes to overcoming the crises that can be caused by violating the regulations, and working to put financial fines higher than the value of reforming them in order to be a strong deterrent to prevent the recurrence of a reality that poses a threat to the urban safety system.
Random planning and organizing	Interference with land use	The spread of environmental pollution associated with the types of use that threaten urban stability, the spread of noise, the spread of insects and rodents, the spread of building density that threatens natural ventilation and lighting, and the decline in the balance in land uses	3	5	15	The spread of urban slums in which uses are mixed, including dangerous crafts, and consequently the high rate of danger and impact on the life of the community residing in the slums, working to prevent adhesion in buildings and setting controls for ventilation and natural lighting of buildings, setting operating hours for handicrafts and traditional crafts in buildings and facilities, and working to develop a vision National balance in land use until 2030
	Construction of residential buildings next to dangerous installations	Damage to the life of the population and the possibility of human and material losses in assets, properties and residential buildings, and the spread of toxic gases that threaten the security and stability of society.	4	4	16	Setting safety distances between facilities and dangerous trades based on risk analysis for those facilities, taking into account the strict safety procedures on the facilities and setting mechanisms to prevent damage to the surrounding residential buildings based on technical studies based on effective risk control and loss reduction.
	Mixing of commercial, industrial and craft activities	The spread of environmental pollution, noise and human congestion, impeding the	2	3	6	Working to separate the organization of crafts, industries and commercial occupations in order to achieve speed of movement and reduce traffic

		arrival of response crews in the event of a danger threatening the industrial, commercial or craft area, the spread of solid and hazardous waste among the movement of citizens visiting the commercial area				congestion. Re-designing the commercial, economic and military multi-use areas, which contributes to freedom of movement, wide vertical and horizontal corridors, and the opening of traffic paths for emergency vehicles that prevents them from being occupied by any obstacles, whether stalls or other vehicles.
	Traffic congestion at intersections and popular markets	It is difficult for civil defense and ambulance crews to reach the areas surrounding the popular markets	2	2	4	Updating traffic at responding agencies, identifying alternative traffic paths in case of high traffic density, and enhancing safety measures that enhance the initial response
	Construction of buildings and crafts without regulatory approval	The spread of random crafts, and the emergence of a reality that is difficult to modify, which threatens societal stability, the inability to commit to land uses	2	5	10	Establishing deterrent legal controls and procedures for violators, removing all crafts and establishments that cannot be corrected, and strengthening local authorities and various government agencies' follow-up on new construction.
Weak technical procedures for dangerous crafts	Random spread of domestic gas filling points in residential areas	Gas leakage in residential areas, which constitutes a huge step on the lives of residents, and the possibility of fire accidents and explosion of gas cylinders, and previous accidents have occurred.	4	5	20	Taking legal deterrent measures for the owners of random points, confiscating all tools and means that threaten community security, such as filling and unloading cylinders and gas discharging destinations, and closing the shops that work to empty gas from large cylinders to small
	Absence of accredited laboratories to examine fuel and gas tanks and extensions	Damage to tanks and the end of their lifespan without controls that contribute to their protection, accidents of leakage on the roads, the	3	2	6	Opening joint cooperation paths with the brothers in the Arab Republic of Egypt to establish testing laboratories for tanks and containers for transporting hazardous materials, working on periodic inspection according to the currently available capabilities,

		possibility of explosion and ignition accidents of materials, and the occurrence of economic and human losses				opening the door to competition for companies in the private sector to work on supplying testing and measuring devices.
	Lack of safety regulation regulation in elevators.	The inability to inspect and license elevators, the diligence of the inspection crews, the prevalence of accidents related to falls from height or accidents of imprisoning citizens in elevators	3	3	9	Working on preparing a regulation for security and safety in elevators in partnership with the Federation of Engineering Industries and mechanical engineering departments in local universities. Periodic inspection of facilities and requirements for operation and maintenance in elevators, and work on elevator maintenance periodically by specialists and accredited companies.
	The lack of clear standards in the building system for stairs and stairs for escape and emergency	The occurrence of victims during the evacuation of citizens in cases of crises and disasters, the accumulation of citizens on the stairs, and the difficulty of the civil defense dealing with expected accidents in high buildings.	4	3	12	Coordination between the Ministry of Local Government, the General Directorate of Civil Defense and architecture experts by setting clear standards procedures for the number of building occupants, the number of residential units on the floor, and the floor space of buildings that require escape stairs and other stairs that assist in vertical movement and movement.
	Randomly creating popular markets threatens the safety of users	It is difficult for civil defense, health and ambulance crews to reach dangerous places, which is reflected in high human or material losses and an increase in response time	2	2	4	Opening emergency traffic paths of no less than 4 meters, regulating the electricity networks distributed in the markets to reduce the risks of electricity, using fire-resistant barriers for no less than two hours, limiting random storage operations inside popular markets and satisfying daily needs.
	Warehouses for the sale and storage of detergents and reactive materials	The leakage of chemicals dangerous to citizens, and the possibility of chemical reactions between the	4	2	8	Establishing a regulation on chemical safety in warehouses for storing hazardous materials, and setting standards for urban safety in terms of the distance between the warehouse, laboratories,

	that produce dangerous chemical gases	materials causing ignition and explosion accidents, which raises the rate of human and material losses.				factory, and residential buildings, which contribute to preventing the transmission of infection from fires, the effects of explosions, or the leakage of hazardous materials.
	Laxity in the application of prevention and safety measures by the owners of establishments	High accident rates in industrial, commercial and economic establishments; This negatively affects the lives of citizens and economic security	4	4	16	The need to work on approving the list of penalties and penalties for Civil Defense Law No. (3) of 1998 AD, granting the executive authorities the status of temporary closure of facilities until safety procedures are completed, and sequencing the application of penalties for facilities that do not comply with public safety.
	The use of extinguishing materials in violation of Palestinian specifications and standards by companies	The failure of the automatic operation of the devices during accidents, which is reflected on the lives of citizens and society, and increases the economic losses of the facilities at risk	4	1	4	Establishing a laboratory for testing firefighting materials, activating specifications and standards for importing firefighting materials and public safety equipment, investing in security, safety and firefighting equipment, which enhances competition, which is reflected in the quality of products, closing companies that violate specifications.
strategic risk	Weak experience of security and safety specialists	Inability to take technical measures that contribute to addressing existing risks, and developing procedures to correct violations that were formed as a result of violating regulations and laws	3	2	6	Working on opening new paths to create specializations related to security and safety, a diploma in security and safety engineering or a master's in security and safety engineering, and sending a group of engineers and workers in security and safety for training and transferring expertise from abroad to civil defense.
	Weak capacity of engineering offices to take technical measures	Failure to complete engineering plans according to what is stated in local regulations, rules and legislation, and the difficulty of implementing ideal	2	2	4	Rehabilitation of engineering offices in terms of the measures to be taken to reduce the risks threatening safety and security, and work on preparing graduation projects related to public safety and security for the training course participants that touch the reality and

		procedures for security and safety				are in line with the possibilities available in the Gaza Strip.
	Some engineering offices adopted the investor's view against the system	Violation of safety and security procedures, non-compliance with rules and regulations, the emergence of a reality that violates safety, delays in the transactions and interests of citizens.	4	3	12	Working on the impartiality of engineering offices and non-interference in the procedures of dangerous facilities, following the technical instructions issued by the competent authorities in the field of safety and prevention, strengthening cooperation between the Safety and Security Department and the Engineers Association.
	Moral assassination of security and safety workers	Their psychological state threatens their continued work and reform of the public safety system	3	5	15	Holding accountable anyone who works to defame or offend security and safety workers, enhance psychological support for inspectors, and enhance measures to protect them from those with economic influence in government agencies, and strengthen oversight over owners of companies that promote rumors.
	Security and safety is a threat to economic security and an obstacle to development	Disrupting safety and security procedures and procrastinating transactions and procedures for dangerous establishments and trades under the pretext of studying files and studying their effects	3	4	12	Strengthening the unity of common understanding between the authorities concerned with safety and security and the economic security committees, obligating all companies to security and safety, and working to develop the idea of safety and security that supports sustainable economic development.

From the previous table it is clear that:

The occupation and its practices constitute the most prominent threat to safety and security at Gaza Strip through many risks that result in human losses, followed by the weakness of technical procedures for dangerous trades, which result in a series of accidents threatening development stability, then random planning and organization, followed by interventions and conflict between regulations and laws to end with risks The strategy is arranged in order of threat sources, impact levels, and probability.

The researcher believes that the threats and their sources in the Gaza Strip vary and form different effects with relative weights according to the nature of the geographical impact of the threat, and the economic impact associated with material, economic, human and social losses and the consequent circles of influence and the constant threat to the remnants of accidents resulting from it, as happened in the occupation targeting the Khudair warehouse for agricultural materials, which It resulted in a hazardous waste that requires a great risk to the Palestinian environment, amounting to approximately 300 tons of pesticide residues.

3. Discuss the results:

The security and safety system suffers from inconsistencies in regulations, laws and legislations between urban safety determined by Central Committee for Buildings and Urban Planning on the one hand, and the executive regulations interpreting the Civil Defense Law No. (3) of 1998 AD, in accordance with Resolution No. (27) of 2000 AD, which threatens private stability Public safety in terms of safety distances between the dimensions of the regulatory setback, which works to prevent the transfer of heat radiation or reduce the effects of expected accidents in dangerous facilities and trades.

The occupation exercises major problems related to preventing modernization of equipment and tools for safety and prevention, including tanks for transporting fuel, gas and other dangerous materials and their extensions, as tanks and extensions violate many of the conditions for their technical examination, and tanks are considered the first and greatest threat to security and safety at Gaza Strip. The researcher believes that the tanks should be dealt with according to the following scenarios.

- **The first scenario:** destroying all tanks and turning them into tanks that do not pose a threat to the life and health of the population and society.

Advantages of this scenario:

- Implementation of security and public safety standards at Gaza Strip.
- Commitment with international, local specifications and standards in accordance with manufacturing conditions of tanks.
- These tanks can be used for other uses, thus reducing the loss rate to a minimum.

Providing new tanks with a lifespan of at least 3 years, provided that the tank was manufactured in 2017.

Scenario disadvantages:

- The high financial cost of the scenario, as the hydrocarbons, oil, gas and petrochemicals sector suffers from stifling economic crises due to the embargo and its consequences.
- It may contribute to collapse of some companies as a result of their weak financial capacity.

- **Second scenario:** Classification of tanks into two parts**:**

- The first classification is tanks that have not been modified by welds or have been subjected to beating or change in the external shape, and official examinations are

conducted for them by the Metallurgical Industries Department of the General Administration of Industries, which supervises the examination of gas cylinders of all sizes.

- The second category is tanks that have been modified and welded also must be disposed of and not run on gas and can be used in fuel.

Scenario advantages:

- Take advantage of reservoirs in a way that can reduce losses for companies in light of deteriorating economic situation.
- The lowest economic cost for companies.
- Gradual change of tanks operations in line with companies, which contributes to enhancing public safety requirements.

Scenario disadvantages:

- The presence of expired tanks according to tank manufacturers.
- The occurrence of some financial loss on the owners of the stations in disposing of the tanks treated in a wrong way and need to be changed.

Mechanisms for handling hazardous materials tanks

- Follow safety and prevention measures in all stages assigned to dealing with tanks.
- That the Department of Metallurgical Industries at the Ministry of National Economy be assigned to develop an examination protocol for fixed and mobile tanks and tanks.
- That the examinations of tanks be carried out through the private sector and that it bears responsibility for this matter and under the direct supervision of the General Administration of Industries at the Ministry of National Economy
- Speeding up the issuance of a final decision to deal with the tanks according to the variables specific to each tank.
- Preparing a certificate for each tank and a number for each tank.

From the above, the researcher believes that the safety and security threats are very high due to the planning and organizational instability of the situation of the Gaza Strip and the urban expansion of the population due to the scarcity of land and the economic variables related to the price, price and value of land, the construction cost of projects, and the negative effects resulting from the coarse force used by the occupation in its siege of the Gaza Strip.

4. Conclusions

- The reality of safety and security is very difficult at the legal, procedural and organizational levels, and the indicators of qualified human resources for safety and security are very weak compared to what is stated in the job description for safety and security.
- The need for the Gaza Strip to work on providing an academic specialization for safety and security.
- Occupation constitutes a clear threat to safety and security that begins with the randomness of planning and arbitration of development and future planning tracks, and its relationship to the components of the public safety system.
- The occupation threatens economic development and commercial establishments, which poses a clear threat to the safety of society and preventive measures.
- The safety and security system suffers from a weakness in the technical and engineering offices qualified to carry out tasks of public safety and security, and that the technical examinations are mostly carried out visually because the occupation prevents the arrival of equipment for the technical examinations.

- Fixed and mobile gas tanks pose a major threat to the safety and security system, and their accidents have occurred in previous periods of time.

5. Recommendations

- Supporting safety and security in the governorates with the graduates of the Occupational Safety and Health Diploma, number (3) for each governorate, and providing a mechanical engineer number (2), and (3) specialists in chemistry to manage the Department of Hazardous Materials.
- Providing a crew specialized in examining elevators. This team undertakes the periodic inspection of elevators in the facilities to manage the elevators section.
- Providing training programs that address existing gaps in partnership with local and Arab engineering unions, universities and academies.
- Restructuring public safety and security also strengthening the organizational structure. Sections and departments that simulate the sections available in the departments of safety and prevention in the surrounding countries.
- Update and develop the current regulations to be in harmony with the updated regulations.
- Strengthening the methodology of prior analysis of risks and future prediction of accidents through computerized programs.
- Assigning specialized technical offices to prepare risk analysis studies for high-risk facilities. And linking the outputs of risk analysis reports to the various security and sovereign authorities to take decisions related to sabotage operations.
- Redistribution of urban communities in a way that contributes to reduce the expected and affecting risks on the environment at Gaza Strip.

المراجع:

1. Ahmed H .Al-ramlawi ،Mohammed M .El-Mougher و،Mohammad R. Al-Agha .(2021) . *The Role of Al-Shifa Medical Complex Administration in Evacuation & Sheltering Planning* .Belgrade: International Journal of Disaster Risk Management, 2(2), 19-36.
2. Mohammed M. El-Mougher و،Kamal Mahfuth .(2021) .*Indicators of Risk Assessment and Management in Infrastructure Projects in Palestine* .Serbia: International Journal of Disaster Risk Management, Volume 3 Number1.
3. United Nations .(2015) .*Sendai Framework for Disaster Risk Reduction 2015-2030* . Sendai, Japan,: the Third UN World Conference in Sendai, Japan, on March 18, 2015- United Nations Office for Disaster Risk Reduction.
4. Ahmed Al-Shaibi. (1993). Safety between concept and application. Jeddah, Saudi Arabia: Al Falah Press for Publishing and Distribution.
5. Raad Qassem Al-Azzawi. (2020). Confirmed Global Threats - A Situation Assessment for the year 2020. Berlin: Journal of Strategic Studies for Disasters and Opportunity Management, Vol. 2, No. 4.
6. Sheba Al-Fateh Mr. (2019). Safety and Security systems on buildings. Sudan: an unpublished master's thesis, Sudan University of Science and Technology.
7. Sabah Ahmed Abu Sharekh, Mohammad Mohammad al-Mougher, and Nizam Mahmoud al-Ashqar. (2019). Analysis of the reality of hazardous materials management in the Gaza Strip from the point of view of workers in occupational safety and health - a case study of the pharmaceutical sector. Algeria: Journal of the Development of Social Sciences Vol. 12, No. (2), Ziane Achour University of Djelfa.
8. Ghada Barghouth. (2013). Evaluation of infrastructure projects funded by international organizations at Gaza Strip from point of view of partners during the period (2008-2012). Gaza: an unpublished master's thesis of the Islamic University.

9. Mohammed Mohammed Al-Mougher. (2018). Indicators of risk assessment and management in industrial establishments at Gaza Strip. Gaza: Journal of Engineering Sciences and Information Technology, Arab Journal of Science and Research Publication.
10. Directorate of Policies and Studies. (2016). Ministry of Agriculture risk management strategy 2016-2019. Amman: Ministry of Agriculture, Hashemite Kingdom of Jordan.
11. General Directorate of Civil Defense. (1998). Law No. (3) of 1998 AD. Gaza: Office of Fatwa and Palestinian Legislation.
12. Mona Al-Saud, Nizam Al-Ashqar, and Muhammad Al-Mughir. (2021). Risk Management in Chemical Industrial Facilities at Gaza Strip "Case Study: Detergent Factories Sector". Berlin: Journal of Political Science and Law, Arab Democratic Center, Volume (5), Issue (27.(
13. Michel Esposito. (2009). A year after the Gaza war, the Israeli military operations against Gaza, 2000-2008 AD. Beirut - Lebanon: Institute for Palestine Studies, Council for Palestine Studies, Volume Twenty, Issue 80-81.

The expected effects of each risk (risk effect:(

)Risk Impact Levels(				
)Very Low(	)Low(	)Medium(	)High Impact(	)Gross Impact(
1	2	3	4	5
Very low impact and does not require planning.	Low impact, does not require specific plans and can be bypassed	Medium effect and taken into account during preparation of plans.	High impact and you need to analyze the situation and build plans.	The impact is grave and requires urgent measures and plans to confront it.

Hazard Analysis Form

)Risk Matrix(					
Very High 5	5	10	15	20	25
High 4	4	8	12	16	20
Medium 3	3	6	9	12	15
Low 2	2	4	6	8	10
Very Low 1	1	2	3	4	5
	very little (1)	Little (2)	Possible (3)	Mostly (4)	Certain (5)
	likelihood				

Risk value coefficient

(Very Low)	(Low)	(Medium)	(High)	(Very High)
2-1	4-3	8-5	15-9	25-16

Interpretation of Risk Level

)Interpretation of Risk Level(				
)Very Low(	(Low)	)Medium(	)High	Very High
1	2	3	4	5
hardly ever	Frequency is low and does not affect on workflow	Moderate repetition and obstruction of some parts at work	Repetition greatly and the level of repetition affects at work	They are very repetitive and their level of repetition hampers work

Development of New Electrode for Phosphoric Acid Fuel Cell

Mohammad Ali Freij *

Al-Hussein Bin Talal University
Corresponding author: mohammadfrayj@yahoo.com

Abstract: Fuel cells are important future sources of electrical power as they could contribute to the reduction of the amount of petroleum imported by Jordan. The objectives of this study are to develop a new electrode for phosphoric acid fuel cell (PAFC), to optimize the performance of the PAFC at different operating conditions, electrode fuel cell at different conditions to operates, and to evaluate and characterize the PAFC. The graphite-Pt catalyst was characterized using physical methods such as scanning electron microscopy (SEM), X-ray powder diffraction (XRD) as well as electrochemical methods, such as cyclic voltammetry (CV). Differential pulse amperometry and voltammetry Membrane electrode assemblies (MEAs) were fabricated for phosphoric acid membrane fuel cell (PAMFC) of 25 cm2 active area. The results show that the constant cell voltage is useful in maintaining the quantities of platinum on the electrodes as a catalyst for the cell during its work when it increases the efficiency and durability of its operation. The surface area of electrodes refers to the amount of charge exchanged during the hydrogen desorption, and should be proportional to the platinum active area. Also, to reach the maximum value of current, the fuel cell operate under normal conditions must have a constant voltage with appropriate areas of the electrodes are sufficient and suitable for cell size; thus, less internal resistance of the fuel cell system. On the other hand, the increased cell operating temperature helps to improve the system performance, reduce the life time and stability of the fuel cell.

CO_2 Capture by Kaolinite based geopolymer

Mohammad Al-Harahsheh [1], Sabreen Mheidata* and Kamel Al-zboon [2]

[1] Chemical Engineering Department, Faculty of Engineering, Jordan University of Science and Technology, Irbid 3030, Jordan

[2] Al-Huson University College, Al-Balqa' Applied University, Jordan

Abstract: Carbon dioxide emissions have increased in the recent years; they must be reduced. One of the emerging methods used to capture CO_2 is the use of geopolymers. This work investigates the synthesis of a geopolymer from kaolin suitable for CO_2 adsorption. Several parameters were studied to achieve the best geopolymer characteristics for CO_2 adsorption; these include the kaolin calcination temperature (400,450, 500,550, 600, and 650 ˚C), the concentration of NaOH (8, 10, 12, and 14 M), drying (aging) temperature of the geopolymer (105 and 80 ˚C), drying time of the geopolymer (20 and 48 hrs). Solid samples were analyzed by X-Ray diffraction and Fourier transform infrared analysis techniques. For selected samples, thermogravimetric analysis and brunauer–Emmett–Teller analyses were also performed. Also, kaolin was analyzed by X-ray fluorescence analysis technique. The XRD analysis of kaolin, the main precursor of the geopolymer, revealed that it contains kaolinite, quartz, and muscovite as the main crystalline phases. XRF of raw kaolin shows that it contains Si, Al, and Fe as major elements, while the minor elements were Mg, Ti, K, P, and S. The XRD analysis shows that the geopolymer contains quartz and hydroxy sodalite. TGA analysis also shows that the geopolymer loses water and CO2 from the structure in the temperature range between 105 to 120 ℃. FTIR analysis of raw kaolin shows that the main bond in kaolin is Al-OH at wavenumber about 911.35 cm^{-1}, while for the geopolymer it shows that the main functional group in geopolymer is OH, which has two bands: above 3000 bending vibration and in the range 1400-1500 for stretching vibration. It also has an Si-O-T bond at 969 cm^{-1}. The results show that the best calcination temperature was found to be 500 ˚C. The adsorption capacity of geopolymers was found to increase with the increase of NaOH concentration up to 12 M. Then, the adsorption capacity of geopolymer dropped due to the formation of Na_2CO_3 at 14 M. Additionally, synthesis of geopolymer requires drying temperature equal to 80 ˚C. Besides, the drying time of geopolymer is preferably to be performed for 20 hrs. The best geopolymers achieved an adsorption capacity of about 3.67 mmol/ g; it was prepared at the following conditions: calcination temperature of 500 ˚C, 12 M of NaOH, drying time of 20, drying temperature of 80 ˚C, contact time = 3 hr, pressure =10 bar and adsorption temperature = 20 ˚C. The mechanism of adsorption of CO2 on hydroxy sodalite includes physical adsorption that occurs by entering CO2 inside the pores of hydroxy sodalite and formation a physical bond (hydrogen and Vanderwall bonds). Chemical adsorption also occurs between CO2 and O-H group inside hydroxy sodalite, which forms Na_2CO_3 and $NaHCO_3$.

Theme 8: Heat and Mass Transfer in Chemical Processes

A Review on Dissolution Behaviour of Multi-Component Dnapls

Praveengouda Patil [1], Gautham Jeppu [2] and C. R Girish[2,*]

Manipal Institute of Technology, Manipal Academy of Higher Education, (M.A.H.E)
Corresponding author: girishcrtd@gmail.com; Tel.: +91-8197185488

Abstract: Dense non-aqueous phase liquids (DNAPLs) are considered priority pollutants in groundwater. Due to the slow dissolution and toxicity in low concentrations, the DNAPLs pollute groundwater and soil in many parts of the world. The impact of accidental release of the pollutant could be seen disturbing the balance of human health and the environment. So, there is a need to study the overall process of the dissolution behavior of accidentally released DNAPLs to find a suitable remediation technique. To date, significant investigations have been confined to single component dissolution in lab scale, onsite, and successfully correlating the mass transfer rate with velocity and NAPL saturation. However, limited experimental studies have been carried out to understand the dissolution behavior of multi-component NAPL. There are no review papers on the dissolution of multi-component NAPLs. The purpose of this paper is to summarise various analytical, mathematical models and experimental studies of multi-component NAPL dissolution carried out in saturated, homogeneous/heterogeneous porous media. The paper also discusses various methods used for the enhanced dissolution of organic pollutants.

Keywords: DNAPL; multi-component dissolution; groundwater; models.

1. Introduction

Contamination of underground water resources by non-aqueous organic liquids spills or leaks is of serious concern for the environment since the component compounds constitute a long-term health hazard for human beings. Non-aqueous phase liquids (NAPL's) do not mix thoroughly with water[1]. Long-term groundwater contamination can occur when a water-immiscible NAPL liquid penetrates the subsurface, contaminating the soil and water. Such situations are caused by underground storage tanks (USTs), landfills, and surface spills. The spilled pollutant infiltrates into the saturated zone through the vadose zone. Two types of NAPLs are primarily found in contaminated sites: Dense and Light non-aquoes phase liquids. DNAPL are denser than water, such as chlorinated solvents, whereas LNAPL is those that are lighter, such as petroleum products[2] refer to table 1. These immiscible liquids entering groundwater may form pools (near saturation) at the aquifer's bottom or in low-permeability regions (DNAPL pools), or they may float at the water table (LNAPL pools). Groundwater pollution will occur in the presence of pools due to NAPL dissolving in the water flowing above or below the pool[3]. In this article, the assumptions and studies carried out to understand the dissolution of NAPL, enahncement of dissolution of organic pollutnats are discussed.

Several early studies for NAPL dissolution in the subsurface made a simplifying assumption of a steady source at a constant equilibrium strength [4](Water and Petroleum working group. [5] derived one of the first empirical mass transfer correlations for dispersed oil globules in typical porous media based on experimental data from [6] [5] also studied the mass transfer of petroleum hydrocarbons from an oil lens on top of the water's surface. [7]used a compartmental approach to model the partitioning of TCE into the soil, air, water, suspended solids, biota, and sediments. Most of the first NAPL dissolution models were adapted from chemical engineering literature to dissolve idealized

spheres and cylinders in packed bed columns to understand dissolution. These studies dealt with mass transfer during flow around spheres and cylinders (Raanz and Marshall, 1952; [8]. Several chemical engineering researchers proposed correlations between heat transfer coefficient (Nu) and its similar mass transfer coefficient (Sh) and Peclet number (Pe). [9]provide a summary of early (before the 1950s) mass transfer correlations in chemical engineering. [10][11][12] first derived one of the first widely used correlations for equilibrium NAPL dissolution using dimensional analysis and experimental data to choose the model. [13] modeled NAPL dissolution as isolated spheres that shrink with dissolution. [14,15] derived widely used correlations for transient dissolution, which used NAPL saturation as a surrogate for the surface area since it was hard to measure the surface area experimentally.

Table 1. Solubility of major NAPL found in groundwater

Sl.No	Compound	Solubility @ 25ºC (mg/L)	Density @ 20ºC (g/cc)	Ref.
1.	Benzene	1640	0.877	[16]
2.	Dichloromethane	19800	1.330	[17]
3.	Tetrachloroethene	149	1.62	
4.	Chlorobenzene	500	1.11	[18]
5.	Toluene	520	1.62	[2]
6.	1,1,1-Trichloroethane	1554	1.34	[19]
7.	Trichloroethylene	1099	1.463	[20]
8.	Perchloroethylene	200	1.623	[21]
9.	Ethylbenzene	184	.86	[22]
10	p-Xylene	171.1	0.89	
11	1,2,4-Trimethylbenzene	65.4	.87	
12	1,3,5-Trimethylbenzene	48.2	.87	
13	Styrene	300	0.909	[23]
14	o-Xylene	180	0.88	
15	3-Ethyltoluene	40	0.9	
16	1,2,3-Trimethylbenzene	60	0.9	
17	Indene	20	0.997	
18	2-Methylindene	20		
19	Naphthalene	30	1.14	

2. Single Component Dissolution Studies

2.1 Equilibrium Vs non-equilibrium dissolution

Several contrasting reports have been published discussing whether equilibrium is achieved during DNAPL dissolution. [14] reported that small lengths of NAPL (few cm) were enough to reach equilibrium. The time required to reach equilibrium is around 15 mins. Several studies have suggested that equilibrium conditions always existed in columns [12,24]. However, later studies have found that non-equilibrium conditions could exist for a short contact time [5], [7-8]. They also theoretically showed non-equilibrium conditions could be found for short contact time, large NAPL blobs, and high velocity. They also proved this experimentally in short columns at high velocity. Several other studies also reported non-equilibrium dissolution at high velocities. At low rates typical of

groundwater (~10 m/ year), equilibrium can be expected. However, dilution could cause apparent non-equilibrium. [25] found that non-equilibrium conditions existed in a two-dimensional tank dissolution experiment. [26] Suggested that much of the evident non-equilibrium could be explained using models that account for heterogeneity. Though non-equilibrium is possible at high velocities, most groundwater conditions could have equilibrium dissolution, and apparent non-equilibrium could be due to subsequent three-dimensional dilutions and mixing. Dissolution of NAPLs can be a steady-state or transient dissolution. When the concentration of dissolved NAPL reaches a constant value, it is called steady-state dissolution; when the concentration of dissolved NAPL changes, it is called transient dissolution. Usually, dissolution is steady-state for residually saturated NAPL until a critical NAPL saturation (or surface area) is reached. The concentration of NAPL reduces continuously and may exhibit long tailing. The transition from steady-state dissolution to transient dissolution has not been explored and can play an essential role in remediation modeling.

2.2 Surface area estimation

The surface area of the NAPL-water interface is an essential parameter that is hard to estimate. [27] proposed using sodium dodecylbenzene sulfonate as an interfacial tracer to measure NAPL-water interfacial area in column experiments. This technique was later extended for residual saturation, vadose zone, and multiple component NAPLs [15-17]. The limitation of this method is that it is not accurate, involves many assumptions, and provides an approximate interfacial area. Comparative use of synchrotron X-ray microtomography and interfacial partitioning tracer tests and showed that the values obtained from tracer tests were significantly larger was also demonstrated [28]. They suggested that this could be due to the inability of the microtomography techniques to determine surface micro-heterogeneity.

2.3 Analytical dissolution models

Method to solve advection-dispersion equation with dissolution primarily involves Laplace or Fourier transformation. One of the first analytical solutions for DNAPL dissolution in one-dimensional groundwater flow was given by [31]. The solutions to three-dimensional are complicated for use. [32] developed an analytical solution for three-dimensional NAPL dissolution using Green's function method. Several others used the greens method to account for the dissolution of NAPLs. [33] developed an analytical solution for NAPL dissolution using the mass superposition technique.

2.4 Dissolution of DNAPLs with Degradation byproducts

The daughter products of degraded halogenated NAPLs can repartition back into the NAPL phase. They can also influence the dissolution of the parent NAPL[34]. The effect of daughter products on the dissolution of NAPLs could be significant but is understudied. The formation of daughter products by microbial degradation can enhance the rate of dissolution of NAPL. The formation of daughter products can deplete the aqueous-phase concentration of the parent NAPL and increase the concentration gradient for dissolution [35]. For example, [36] found that the formation of daughter products by microbial degradation can enhance the dissolution of PCE by a factor of 16 times. [35] found that the formation of daughter products by biodegradation increased the PCE removal rate by approx. 14 times.

Dissolution of single component NAPLs has been studied widely by [5,7] and [9-10]. However, fewer studies exist for the dissolution of multi-component NAPLs. [2,37–39] studied the dissolution characteristics of a NAPL mixture containing MTBE, BTEX, 1, 2, 4 trimethyl benzene, and octane.

They found that MTBE dissolved in an ideal manner (i.e., followed Raoult's law), whereas other NAPLs (BTEX, 12, 4 trimethyl benzene and octane) dissolved non-ideally to some extent[40].

The effect of repartitioning of hydrocarbons during the dissolution of NAPLs was studied[41]. They also investigated the interaction of DCM (dichloromethane) and TCE in-series during dissolution. They found that the upstream DCM can repartition into the downstream TCE (Trichloroethane) and thereby delay the dissolution of TCE. The DCM plume gets retarded due to its repartitioning into the downstream TCE NAPL [41]. Ignoring repartitioning of daughter products into NAPLs could cause significant errors in laboratory and field predictions. Researchers suggest that up to 60% of the product mass could be repartitioned into NAPLs even at a modest NAPL saturation of 2% [42].

The daughter products can also repartition themselves back into the NAPL phase and influence the dissolution of the parent compound. There have been limited studies on the effect of repartitioning of daughter products on the dissolution of NAPLs. [42] quantified the dissolution and partitioning of DCE (Dichloroethane) and VC (Vinyl chloride) between NAPL and water in batch experiments. They found that the partitioning could be approximately described by Raoult's law analogy (RLA). [43] studied partitioning of DCE into PCE in column experiments. They modeled kinetic mass transfer during multi-component DNAPL dissolution using correlations developed in previous studies by Imhoff and Powers for single component dissolution [5],[9]. However, the model does not consider the change in the constitution of NAPL during dissolution and assumes a constant NAPL constitution during dissolution. Several other studies have focused more on the biological aspects of daughter product formation and not on the physical dissolution and repartitioning [44–46]. The influence of daughter products on the dissolution of NAPLs is a new area that needs further study. A comprehensive model has not been proposed and tested using experimental data.

3. Multi-component Dissolution

3.1 Model and Case Studies

Several studies are carried out in batch and column mode to understand the dissolution of single and multi-component systems[47–49]. Most of the new studies have developed 2D and 3D models and equations correlating Sherwood number, mass transfer coefficient, Reynolds number, the moment of inertia as seen in table 1 and table 2. A study on the dissolution of mixtures of synthetic hydrocarbons, crude oils, diesel oil, and synthetic chlorobenzene for extra water to oil (also NAPL) ratios showed that some constituents of mixture with more excellent solubility depleted at a faster rate and the one with lesser solubility were at a slightly slower pace [24]. In all the cases, it was evident that benzene showed more significant depletion as compared to toluene. Only in synthetically prepared mixtures was it feasible to predict the varying consumption of water theoretically. The study also suggests that dissolution kinetics and equilibria of sparingly soluble chemicals in NAPLs behave according to well-established physical-chemical principles and are thus basically predictable. Impact of surfactants on the dissolution and adsorption behavior of chlorophenols. It was found that there was an increase in dissolution rate with increased surfactant dose. The adsorption of chlorophenols onto clayey adsorbent in the presence of surfactant decreased, attributed to hydrophobic interaction [50]. Several studies carried out dissolution experiments in saturated porous media. Some showed complete dissolution on flushing with 290 pore volumes. For similar NAPL residuals at contaminated sites, equilibrium between pore water and residual NAPL is achieved over a short spatial scale [14]. It can be observed from the literature that various case studies on multi-component dissolution in

saturated media considering ideal/non-ideal conditions are done. Some have performed these studies on multi-component droplets in fractured porous media, as seen in Table 2.

3.2 Enhanced Solubility

It can be found in the literature where enhancement of DNAPL solubility is done by cosolvent flushing, using surfactants, cyclodextrin [28], microbial enhancement [51] and few studies by sound waves are also found [33-34] refer to table 3. Because of the poor solubility of many NAPLs and their comparatively strong capillary forces in the aquifer, traditional remediation techniques like pump and treat are unsuccessful in natural field circumstances [35-36]. New technologies such as in situ cosolvent flushing, steam flooding, air sparging, and soil vapor extraction have been developed in response to the demand for alternate NAPL remediation approaches [36-37]. In situ flushing of cosolvent as a remediation technique involves the injection of cosolvents into the contaminant source zone to enhance the dissolution of the NAPL and reduce its interfacial tension to render it more mobile. Low molecular weight alcohols, such as ethanol, 1-propanol, and 2-propanol, are widely used as cosolvents because they are highly soluble and water-miscible, leading to improved solubilization and mobilization of chlorinated solvents trapped in the subsurface [37-38]. It is critical to choose the right flushing agent before starting the remediation procedure because the removal behavior of each pollutant varies substantially depending on the flushing agent used [15]. Several other studies have demonstrated the efficacy of in situ cosolvent flushing as a technique for improved NAPL removal from the subsurface to design these remediation technologies [39-42] effectively.

Table 2. Multi-component dissolution case studies (With model)

Sl. No	NAPL	Model	Experimental Conditions	Equations developed	Findings/Inference/Significance
	Organic Pollutant	Phenomenological model	Velocity, DNAPL saturation (constant), interfacial area, porous media	$Sh' = 12.Re^{0.75}.\theta_n^{0.6}.S^{0.5}$	This study found that mass transfer rate coefficient and aqueous phase velocity were directly proportional. The study also shows no relation between grain size and as a parameter as a surrogate measure of NAPL distribution.
	Tetrachloroethylene	MISER (Michigan soil-vapor extraction remediation) model	2 D, 3 phase model, Intermediate and strong wettability condition.	Mass exchanged per unit time per unit volume between the NAPL and aqueous phases $E_{ow} = \frac{-\partial(\varepsilon S_o \rho_o)}{\partial t} = k_{ow}(\alpha A_{ow}^t + \beta A_{ow}^e)(C_e - C)$	In this study, the dissolution behavior of NAPL depends on two parameters: the wettability of soil and NAPL's spatial distribution. Shorter dissolution times tended to occur when NAPL distributes over more significant regions, and this is because of increased access to flowing water.
	Trichloroethene Tetrachloroethene 1,1,1-trichloroethane	Diffusion model	2D model, ternary NAPL, Pore-scale, and intermediate scale.	The dissolution flux is integrated over the spherical blob surface (also account for mass loss and NAPL body shrinkage) is given by $\frac{\partial M_i}{\partial t} = k_f \cdot A_i \cdot \left(c_i^* - c_i^\infty\right)$	For a non-ideal mixture, the time of dissolution reduced up to 15% compared to the ideal case. Non-ideal mix increased effective solubilities of each component of the ternary mixture resulting in more significant mass loss whereas the ideal combination did not show considerable mass loss and their dissolution time remained almost.
	Hydrofluoroether (HFE-1700)	2D tank reconstructed aquifer	DNAPL saturation, hydraulic condition	Relationship between Sherwood number and Raynolds no. $S_h = \alpha * Re^{\beta 1} * S_m^{\beta 2} * Re^{\beta 2} * (P/A)^{\beta 3} * I_y^{\beta 4}$	In this study, the model can be used to find essential parameters of NAPL dissolution rates over a broad spectrum of NAPL saturation. It is because the variables are related to geometry and the rate of water flow. The proposed correlation can be used for

Sl. No	NAPL	Model	Experimental Conditions	Equations developed	Findings/Inference/Significance
					an initial assessment of non-aqueous phase liquid (NAPL) dissolution rates over a wide range of saturation (residual and non-residual) conditions and different aqueous phase velocities within the NAPL source zone.
	Trichloroethylene	Empirical model	Non-destructive visualization technology	Equations to compare the mass transfer process for 2D and 3D model is given below. 2D micromodel: $S_h = 1.98Re^{0.79}$ 3D packed bed: $S_h = 11.06Re^{0.56}$	In this study, the NAPL saturation reduced from 24.5% to 9.5% in 10h. After 10h of a continuous water flow, most blobs disappeared, as seen in the 2D image due to dissolution. MTC was higher for the packed bed system than micromodel due to the inherent pore structure.
	Tetrachloroethylene	Conceptual model (Linear driving force model)	Fractional wettability, porous media	$S_h = 1.15*Re^{0.654}*Sc^{0.486}$	In this study, for a given NAPL saturation, the calibrated model can predict more extended periods of higher effluent concentrations. It was followed by reduction in concentraion and tailing. It also accounts for the relationship between dissolution behavior and mean grain size. Simulation data of the new modified model are better than the earlier used model.

E_{ow}: aqueous phases, k_{ow}: film mass transfer coefficient, $A^1_{ow:}$ NAPL-water interfacial area per unit volume of porous media, C: NAPL-water interfacial area per unit volume of porous media, C_e: equilibrium solubility concentration, α and β: parameter to account for fraction interfacial area, M_i: mass of component i, A_t: external surface area of the sphere, $c_i^* - c_i^\infty$: concentration gradient, Sh: Sherwood Number, P/A and I_y: dimensionless parameter, α: dispersivity, R_e: Reynold's no.

Table2. Multi-component dissolution case studies (Without model/using existing model)

l. No	NAPL type	Model Type/method	Experimental Conditions/ Expressions/Assumptions	Findings/Inference/Significance	
	Methyl tertiary butyl ether Benzene, Toluene, Ethylbenzene, Xylene	1D laboratory model	Batch and Column Studies	In this study, the observed NAPL dissolution followed equilibrium dissolution behavior over a concentration range of four essentially- to five orders of magnitude. It was also found that the requirement of pore volume increased 3 times to reduce the MTBE concentration to less than 100µL.	3
	Benzene Trichloroethylene Chloropropane Toluene	2D dimensional FEM (Extended Multiphase flow model)	Assumption: Local chemical equilibrium Gas pressure gradient: Negligible	The mass transfer rate and fluid density updating have the most negligible impact during highly transient non-aqueous liquid phase migration periods. It becomes essential for long-term simulations as cumulative dissolution to the water phase and volatilization to the gas phase account for more significant proportions of the total mass.	6
	Ethyl Acetate/Butyl Acetate Butyl Acetate/Amyl Acetate	Two-chamber micropipette-based method	Mass flux individual component, $\frac{dm_i}{dt} = A_{interface} D_i (c_i - c_s)\left\{\frac{1}{R} + \frac{1}{\sqrt{\pi D_i t}}\right\}$ Assumption: Approximation of reduced surface area and homogeneous mixing (ideal).	This modified model can predict the dissolution of microdroplets accurately for the ethyl acetate/butyl acetate and butyl acetate/amyl acetate systems given the solubility and diffusion coefficients of each of the pure components in water as well as the initial droplet radius	6

l. No	NAPL type	Model Type/method	Experimental Conditions/ Expressions/Assumptions	Findings/Inference/Significance	
	1, 3, 5-trifluorobenzene	Laboratory scale: Sherwood Gilland model	$Sh'_{SG} = \frac{K_L^{SG} \cdot d_m^2}{D^*} = (b_R \cdot Re^c) \cdot (b_S \cdot S_N^d)$	In this study, the validity of earlier Sherwood Gilland models was found at the lab scale using dissolution data was performed. The development of empirical models that connect lumped mass transfer rates to velocities and organic saturations has been a significant focus of research into NAPL depletion. The relative behavior of the five models is demonstrated to be dependent on system and source zone features. Through theoretical analysis, comparing Sherwood–Gilland type models to a process-based, thermodynamic dissolution model, it is shown that the coefficients of the Sherwood–Gilland models can be related to measurable soil properties.	6
	Trichloroethylene	Residual/dead-end pool dissolution	Entrapped residual blobs (gravity fingering), Pooling in a dead-end fracture.	Model to simulate dissolution of the residual blobs under different water flushing velocities. The simulated relationship between the Sherwood number Sh and Peclet number Pe could be well fitted with a simple power-law function (Sh = 1.43Pe0.43). The findings also suggest that a power-law function of Pe and the remaining mass percentage may be successfully matched to the Sh. The discovered dimensionless group connections relating to mass transport characteristics at individual fractures can be employed in dissolution prediction modeling.	6
	BTEX, Trimethyl benzene (Isomers)	Multi-component dissolution model	fresh, weathered, and synthetic gasoline	The effect of weathering on the degraded gasoline resulted in the loss of lighter aliphatics, and it showed a trend towards the ideal dissolution of the BTX aromatics. Results showed that the volatilization of 50% of the unleaded 91 decreased the molar fraction of benzene by 17%, while the other BTEX and TMB compounds increased by 95%. These trends are mainly due to the higher partial pressures of benzene and aliphatics from the nC4 to nC6 range.	6
	Creosote	Multi-component coupled dissolution with phase transport	Fractured environment. Spatially homogeneous source	In this paper, an advanced model using the analytical solution Laguerre series was studied. Different components of NAPL show varied dissolution, and transport and the developed in this study accounts for both processes. The approach is most applicable to screening-level calculations.	7

Sl. No	NAPL type	Model Type/method	Experimental Conditions/ Expressions/Assumptions	Findings/Inference/Significance	
	Tetrachloroethylene	Steady-state dissolution	Ambient Groundwater condition	Results from dissolution experiments revealed a positive, statistically significant correlation between K_L and DNAPL-water interfacial area and between KL and DNAPL saturation, analogous to porous media experiments	
	Tetrachloroethylene	Non-ideal mixture dissolution	Batch Lab-scale experiment	The aim was to provide insight into the primary reasons for non-ideal behavior during the dissolution of gasoline-type spills to more comprehensive and accurate models of petroleum NAPL dissolution.	
	Trichloroethene	1D heterogeneous-source model	Column Study	The results indicate that the model adequately simulated the presence of multiple organic-liquid zones in porous media with different configurations and hydraulic accessibilities, which accounts for the non-ideal dissolution behavior observed. The calibrated mass transfer terms for each source type were consistent with those obtained for systems that contained only one of either source type.	
	Trichloroethylene Perchloroethylene	Analytical model in subsurface media	Column Study	Initially added amount of NAPL was 11% for TCE and 4% for PCE. Residual saturation in the column mode was 5% and 2.5% for TCE and PCE, respectively. A substantial difference between initial and residual amounts is observed due to pooling, and the experimental data was in line with modified simulation.	
	Phenanthrene Naphthalene, phenanthrene, 2,3-benzofuran, phenol, m-cresol, 1-naphthol and phenoxathiin.	CSTR model	Single compound Multicompound	Raoult's law assumption did not hold good for a multi-component system. A numerical model with a variable activity coefficient was developed (By following the mass balance equation and Raoult's law. The actual and predicted profiles of solutes in the aqueous phase were quite similar. The numerical model provided here is a valuable tool for measuring activity coefficients in complicated organic mixtures.	

l. No	NAPL type	Model Type/method	Experimental Conditions/ Expressions/Assumptions	Findings/Inference/Significance	
	Industrial Creosote	Physical and Mathematical model	Generator column, contact time, groundwater velocity	Most components of creosote attained equilibrium after the 60th hour. Few elements reached equilibrium in a shorter duration following Raoult's law. From the data, it can be concluded that, due to the higher value of the water/oil ratio, water flushing cannot be recommended as a remedial measure	7
	Tetrachloroethene Trichloroethene	Simulation analysis	Coupling of dissolution, sorption and biodegradation	In this study, 3 distinct reactions, namely dissolution, partition, and degradation of DNAPL transport, are modeled using a mathematical tool. This developed framework is valuable for understanding the combined effects of 3 reactive transport mechanisms in the subsurface water system.	7
	Methyl tert-butyl ether	1 D model	Column Study Groundwater velocity, MTBE saturation Grain size of media	Dissolution increased with higher velocity and reduced with greater initial MTBE.Smaller the grain size higher the dissolution rate. In the presence of trichloroethylene, while in the presence of p-xylene, the dissolution is prolonged.	7

Table 4. Enhanced dissolution of single and multi-component NAPL

Sl No.	NAPL Type	Chemical or method used	Experimental Conditions/Parameters/ Expressions/Assumptions	Findings/Inference/Significance
1.	Benzene and Tetrachloroethylene Tetrachloroethylene and Dichloromethane Dichloromethane and toluene	Three binary mixtures	Natural Remobilization	For a binary mixture of NAPL, Benzene/PCE at a ratio of 25:75, it was found that there is a change in density which leads to natural remobilization. For PCE/DCM, there was no natural remobilization as their densities had not much difference. But in the case of DCM/toluene, density was decreased, which reduced the tendency of downward displacement. Sites with DNAPL pools containing a mix of components of sufficiently different densities and relative solubilities, natural remobilization may be an active mechanism, with implications for site evaluation and remediation the ultimate transformation from a DNAPL to an LNAPL may induce upward displacement
2.	TCE, 1,1,2-TCA PCE	Acoustics waves	Multicomponent NAPL Gangalia, Column Study	In this study, enhancement in dissolution was found directly proportional to the frequency of the acoustic wave. Further, the study also demonstrates that the NAPL mixture with less solubility had a more significant enhancement in the presence of square waves instead of sinusoidal or triangular sound waves.
3.	Perchloroethylene	Acoustic enhancement and mobilization	Frequency 75Hz Pore water velocity	The dissolution concentrations collected in the presence of acoustic waves/slow waves are consistently more significant than those in the absence of waves due to the 180-degree oscillation of fluid within the pore space. Also, the study demonstrates that oscillatory pore water velocity is inversely proportional to frequencies.
4.	P-xylene	Tween-80	FEM MODFLOW	The steady-state concentrations are still lesser than the aqueous (equilibrium) solubility which indicates rate-limited mass transfer.
5.	Chlorinated Organic Compounds	Chemical & thermal enhancement	2D tank experiment, Permeability Flow rates	Measured volumes of DNAPL recovered, and the displacement of the DNAPL-water interface (radius and height of the cone of depression) are consistent with the modeling results. Furthermore, chemical enhancement results in a significant increase in the recovery rates of DNAPL. This study shows that it is possible to accurately determine water and DNAPL saturations by image interpretation during pumping tests in a 2D tank in the laboratory. For field-scale applications, the two-phase flow model allows determining remediation yields and the volumes of the cone of depression according to the different operating.

Sl No.	NAPL Type	Chemical or method used	Experimental Conditions/Parameters/ Expressions/Assumptions	Findings/Inference/Significance
6.	Tetrachloroethene, Trichloroethene	Anaerobic mixed culture	Batch and Column study, Methanogens and Homoacetogens.	DNAPL dissolution rate was significantly enhanced when directly coupled with biological dehalogenation.
7.	Perchloroethylene	Glass Micromodel	Cosolvent: Ethanol/Water Airflow rate	Co-solvent/Air flooding with a higher airflow rate resulted in higher PCE removal, attributed to improved distribution of cosolvent in the pore network. Also, the reduction was more significant with a higher cosolvent/water ratio.
8.	Trichloroethene	Dissolution via partition	Batch reactor (Biotic and Abiotic) T =20^{0}C Dechlorination bacteria	Dechlorination of TCE was observed at the interface of TCE-NAPL that demonstrated no previous TCE biodegradation, suggesting that microbes may help develop a source-zone bioremediation system. In conclusion, dechlorinating mixed culture could enhance dissolution in NAPL that may be useful in applying source zone bioremediation.
9.	Tetrachloroethene	Dissolution and dechlorination		Microbially enhanced dissolution and reductive dechlorination of PCE by a mixed culture: Model validation and sensitivity analysis
10.	DNAPL LNAPL	Cyclodextrin	The influence of an enhanced-solubility agent on the equilibrium aqueous concentration (CAi) of a multi-component NAPL can be represented as $C_i^A = C^{sat} \cdot X^N \cdot \gamma^N \cdot \left(\gamma_i^{cyc}/\gamma_i^A\right) \cdot E_i$ The macroscopic expression for the NAPL mass dissolution rate in this $\rho_n \frac{\partial \eta}{\partial t} = -k_f a(C^* - C)$ model is written as:	The contaminant elution curves exhibit an initial maximum concentration coincident with the arrival of the maximum cyclodextrin concentration, followed by a gradual decline to a somewhat constant value for most contaminants. The dissolution phenomena discussed here may contribute to understanding the dissolution behavior of organic pollutants in solutions of other enhanced-solubility agents, such as surfactants or cosolvents.

Sl No.	NAPL Type	Chemical or method used	Experimental Conditions/Parameters/ Expressions/Assumptions	Findings/Inference/Significance
11.	o-xylene, o-dichlorobenzene	Ethoxylated alcohol/ Witconol SN90	The macroscopic expression for the NAPL mass dissolution rate in this model can be is written as $\rho_n \frac{\partial \eta}{\partial t} = -k_l \cdot (C^* - C)$	The surfactant removed the maximum chemical from the soil for the first 10 PV (90%). However, removal efficiency followed a steady path for the next 20 PV.
12.	Naphthalene	Dissolution with degradation model	A coupled dissolution-degradation model describes the concurrent processes of mass transfer and biodegradation in mixed batch systems. $\frac{dC_{(t)}}{dt} = k_l \cdot a\left[C_{eq(t)} - C_{(t)}\right] - k_{bio} \cdot C_{(t)}$	The work reported here demonstrates the influence of naphthalene mass transfer from coal tar on the microbial degradation of naphthalene. The equilibrium aqueous naphthalene concentration and the mass transfer rate coefficient affect the aqueous naphthalene concentration and the biodegradation rate for the NAPL systems.
13.	Aromatic hydrocarbons	Dissolution and microbial degradation	Density and viscosity	In this investigation, it was found that the main component found in the Pintsch gas tar was phenanthrene. Some MAH (monocyclic aromatic hydrocarbons), to name styrene, di and triethyl benzene etc., were also reported at the contaminated tar site. Also, a significant quantity of metabolites related to indene was found, which can be attributed to degradation due to microbes.
14.	Tetrachloroethene	Dissolution with dechlorination	Zero-valent iron nanoparticle	Zero-valent iron nanoparticles (NZVI) could not cause DNAPL dissolution/ mass-depletion rate for a concentration of 10 g/L. The rate of reaction was found inversely proportional to longevity. With the increase in particle rate of reaction, there was an increase in dechlorination rate and hence a reduction in pollutant concentration.
15.	Ethyl Acetate, Butyl Acetate	UNIQUAC: Dissolution with growth (multi-component system)	Local thermodynamic equilibrium, linearization	The two theories' predictions are similar when the solutions are close to ideal, or there is a significant difference in the solubilities, or diffusivities, of the drop constituents in the host liquid, unless initially, the drop consists mainly of the more soluble component. When the solubilities and diffusivities are close, the differences can be substantial for any drop composition.

4. Summary

In this review article, background of NAPL, different types of dissolution in single and multi-component pollutants, a section about partition of DNAPL into daughter products is discussed. Also, tables 2-4 are tabulated to understand various mathematical, analytical models for single and multi-component dissolution, transport, degradation, partition, and recent advances in multi-component modeling (laboratory simulations). As shown by many studies cited in this review paper, substantial progress has been achieved in developing different models (numerical, phenomenological, and experimental) for the single-component system. Further studies are required in the laboratory scale to understand the dissolution kinetics of the binary and ternary component system.

5. Conclusion and future scope

Though the dissolution of NAPLs has been studied widely, there are many areas we need more study. A fundamental method to estimate the NAPL surface area has not emerged. Further study is required in NAPL source zone detection, modeling heterogeneity, etc. A model that can model the change from steady-state dissolution to transient dissolution is yet to be developed. Novel techniques for improving dissolution and natural remobilization can be discovered. The effect of NAPL architecture and heterogeneities on the dissolution must be further investigated.

References

[1] A.A. Keller, M.J. Blunt, P. V Roberts, Behavior of Nonaqueous Phase Liquids in Fractured Porous Media under Two-Phase Flow Conditions, Transp. Porous Media. (2000) 189–203.

[2] S. Lesage, S. Brown, Observation of the dissolution of NAPL mixtures, J. Contam. Hydrol. 15 (1994) 57–71. https://doi.org/10.1016/0169-7722(94)90010-8.

[3] K.Y. Lee, C. V Chrysikopoulos, Dissolution of a multi-component DNAPL pool in an experimental aquifer, J. Hazard. Mater. 128 (2006) 218–226. https://doi.org/10.1016/j.jhazmat.2005.08.005.

[4] J.W. Mercer, R.M. Cohen, A review of immiscible fluids in the subsurface: Properties, models, characterization and remediation, J. Contam. Hydrol. 6 (1990) 107–163. https://doi.org/10.1016/0169-7722(90)90043-G.

[5] D.I. Siegel, H.O. Pfannkuch, Silicate dissolution influence on Filson Creek chemistry, northeastern Minnesota, Geol. Soc. Am. Bull. 95 (1984) 1446. https://doi.org/10.1130/0016-7606(1984)95<1446:SDIOFC>2.0.CO;2.

[6] D.M. Ward, O. Trass, A.I. Johnson, Mass transfer from fluid and solid spheres at low Reynolds numbers: Part II, Can. J. Chem. Eng. 40 (1962) 164–168. https://doi.org/10.1002/cjce.5450400409.

[7] Y. Cohen, P.A. Ryan, Multimedia modeling of environmental transport: trichloroethylene test case, Environ. Sci. Technol. 19 (1985) 412–417. https://doi.org/10.1021/es00135a004.

[8] R. Dobry, R.K. Finn, Mass Transfer to a Cylinder at Low Reynolds Numbers, Ind. Eng. Chem. 48 (1956) 1540–1543. https://doi.org/10.1021/ie51400a044.

[9] F.H. Garner, R.D. Suckling, Mass transfer from a soluble solid sphere, AIChE J. 4 (1958) 114–124. https://doi.org/10.1002/aic.690040120.

[10] W.J. Powers, Susan E. Abriola, Linda M. Weber, An Experimental Investigation of Nonaqueous Phase Liquid Dissolution in Saturated Subsurface Systems : Steady State Mass Transfer Rates, Water Resour. Res. 28 (1992) 2691–2705.

[11] P.T. Imhoff, M.W. Farthing, C.T. Miller, Modeling NAPL dissolution fingering with upscaled mass transfer rate coefficients, Adv. Water Resour. 26 (2003) 1097–1111. https://doi.org/10.1016/S0309-1708(03)00091-5.

[12] A.S. Miller, Cass T. Mcneill, Poirier. Mayer, Dissolution of Trapped Nonaqueous Phase Liquids' Mass Transfer Characterstics, Water Resour. Res. 25 (1990) 2783–2796.

https://doi.org/https://doi.org/10.1029/WR026i011p02783.

[13] J.T. Geller, J.R. Hunt, Mass transfer from nonaqueous phase organic liquids in water-saturated porous media, Water Resour. Res. 29 (1993) 833–845. https://doi.org/10.1029/92WR02581.

[14] P.T. Imhoff, P.R. Jaffé, G.F. Pinder, An experimental study of complete dissolution of a nonaqueous phase liquid in saturated porous media, Water Resour. Res. 30 (1994) 307–320. https://doi.org/10.1029/93WR02675.

[15] S.E. Powers, L.M. Abriola, W.J. Weber, An experimental investigation of nonaqueous phase liquid dissolution in saturated subsurface systems: Transient mass transfer rates, Water Resour. Res. 30 (1994) 321–332. https://doi.org/10.1029/93WR02923.

[16] J.W. Roy, J.E. Smith, R.W. Gillham, Natural remobilization of multi-component DNAPL pools due to dissolution, J. Contam. Hydrol. 59 (2002) 163–186. https://doi.org/10.1016/S0169-7722(02)00056-6.

[17] J.W. Roy, J.E. Smith, R.W. Gillham, Laboratory evidence of natural remobilization of multi-component DNAPL pools due to dissolution, J. Contam. Hydrol. 74 (2004) 145–161. https://doi.org/10.1016/j.jconhyd.2004.02.009.

[18] R.G. McLaren, E.A. Sudicky, Y.J. Park, W.A. Illman, Numerical simulation of DNAPL emissions and remediation in a fractured dolomitic aquifer, J. Contam. Hydrol. 136–137 (2012) 56–71. https://doi.org/10.1016/j.jconhyd.2012.05.002.

[19] P.P. Brahma, T.C. Harmon, The effect of multi-component diffusion on NAPL dissolution from spherical ternary mixtures, J. Contam. Hydrol. 67 (2003) 43–60. https://doi.org/10.1016/S0169-7722(03)00087-1.

[20] Y.C. Lee, T.S. Kwon, J.S. Yang, J.W. Yang, Remediation of groundwater contaminated with DNAPLs by biodegradable oil emulsion, J. Hazard. Mater. 140 (2007) 340–345. https://doi.org/10.1016/j.jhazmat.2006.09.036.

[21] M.O. Rivett, R.M. Allen-King, A controlled field experiment on groundwater contamination by a multi-component DNAPL: Dissolved-plume retardation, J. Contam. Hydrol. 66 (2003) 117–146. https://doi.org/10.1016/S0169-7722(03)00006-8.

[22] M. Vasudevan, C.D. Johnston, T.P. Bastow, G. Lekmine, J.L. Rayner, I.M. Nambi, G. Suresh Kumar, R. Ravi Krishna, G.B. Davis, Effect of compositional heterogeneity on dissolution of non-ideal LNAPL mixtures, J. Contam. Hydrol. 194 (2016) 10–16. https://doi.org/10.1016/j.jconhyd.2016.09.006.

[23] J.A. Van Leeuwen, N. Hartog, J. Gerritse, C. Gallacher, R. Helmus, O. Brock, J.R. Parsons, S.M. Hassanizadeh, The dissolution and microbial degradation of mobile aromatic hydrocarbons from a Pintsch gas tar DNAPL source zone, Sci. Total Environ. 722 (2020) 137797. https://doi.org/10.1016/j.scitotenv.2020.137797.

[24] A.M. and S.F. Donald Mackay , Wan Ying Shiu, Dissolution of non-aqueous phase liquids in groundwater, J. Contam. Hydrol. 8 (1991) 23–42.

[25] S.E. Powers, I.M. Nambi, G.W. Curry, Non-aqueous phase liquid dissolution in heterogeneous systems: Mechanisms and a local equilibrium modeling approach, Water Resour. Res. 34 (1998) 3293–3302. https://doi.org/10.1029/98WR02471.

[26] J.H. Soerens, Thomas S. Sabatini, David A. Harwell, Effects of flow bypassing and nonuniform NAPL distribution on the mass transfer characteristics of NAPL dissolution, 34 (1981) 63–65.

[27] K.P. Saripalli, H. Kim, P.S.C. Rao, M.D. Annable, Measurement of specific fluid-fluid interfacial areas of immiscible fluids in poreus media, Environ. Sci. Technol. 31 (1997) 932–936. https://doi.org/10.1021/es960652g.

[28] K.C. Carroll, M.L. Brusseau, Dissolution, cyclodextrin-enhanced solubilization, and mass removal of an ideal multi-component organic liquid, J. Contam. Hydrol. 106 (2009) 62–72. https://doi.org/10.1016/j.jconhyd.2009.01.002.

[29] M.K. Mahal, A. Murao, G.R. Johnson, A.E. Russo, M.L. Brusseau, Non-ideal behavior during

complete dissolution of organic immiscible liquid: 2. Ideal porous media, Water. Air. Soil Pollut. 213 (2010) 191–197. https://doi.org/10.1007/s11270-010-0377-1.

[30] J.E. Mccray, M.L. Brusseau, Cyclodextrin-enhanced in situ flushing of multiple-component immiscible organic liquid contamination at the field scale: Analysis of dissolution behavior, Environ. Sci. Technol. 33 (1999) 89–95. https://doi.org/10.1021/es980117b.

[31] F.J. Leij, T.H. Skaggs, M.T. Van Genuchten, Analytical Solutions for Solute Transport in Three-Dimensional Semi-infinite Porous Media, Water Resour. Res. 27 (1991) 2719–2733. https://doi.org/10.1029/91WR01912.

[32] F.J. Leij, E. Priesack, M.G. Schaap, Solute transport modeled with Green's functions with application to persistent solute sources, J. Contam. Hydrol. 41 (2000) 155–173. https://doi.org/10.1016/S0169-7722(99)00062-5.

[33] T.C. Sale, D.B. McWhorter, Steady state mass transfer from single-component dense nonaqueous phase liquids in uniform flow fields, Water Resour. Res. 37 (2001) 393–404. https://doi.org/10.1029/2000WR900236.

[34] F.H. Chapelle, L.J. Kauffman, M.A. Widdowson, Modeling long-term trends of chlorinated ethene contamination at a public supply well, J. Am. Water Resour. Assoc. 51 (2015) 1–13. https://doi.org/10.1111/jawr.12230.

[35] C.S. Carr, S. Garg, J.B. Hughes, Effect of dechlorinating bacteria on the longevity and composition of PCE-containing nonaqueous phase liquids under equilibrium dissolution conditions, Environ. Sci. Technol. 34 (2000) 1088–1094. https://doi.org/10.1021/es990989t.

[36] N. Cope, J.B. Hughes, Biologically-enhanced removal of PCE from NAPL source zones, Environ. Sci. Technol. 35 (2001) 2014–2021. https://doi.org/10.1021/es0017357.

[37] S. Feenstra, Dissolution of an Emplaced Source of DNAPL in a Natural Aquifer Setting, Environ. Sci. Technol. 39 (2005) 447–455.

[38] S. Garg, W.G. Rixey, The dissolution of benzene, toluene, m-xylene and naphthalene from a residually trapped non-aqueous phase liquid under mass transfer limited conditions, J. Contam. Hydrol. 36 (1999) 313–331. https://doi.org/10.1016/S0169-7722(98)00149-1.

[39] W.G. Rixey, S. Joshi, Dissolution of MTBE from a residually trapped gasoline source. A summary of research results, API Soil Groundw. Res. Bull. (2000).

[40] A.E. Russo, M.K. Mahal, M.L. Brusseau, Nonideal behavior during complete dissolution of organic immiscible liquid, J. Hazard. Mater. 172 (2009) 208–213. https://doi.org/10.1016/j.jhazmat.2009.06.160.

[41] C. Serralde, M.O. Rivett, J.W. Molson, Interaction of multiple in-series DNAPL residual source zones: Implications for dissolution, repartitioning and DNAPL mobilization at contaminated industrial sites, IAHS-AISH Publ. (2008) 388–395.

[42] C.A. Ramsburg, C.E. Thornton, J.A. Christ, Degradation product partitioning in source zones containing chlorinated ethene dense non-aqueous-phase liquid, Environ. Sci. Technol. 44 (2010) 9105–9111. https://doi.org/10.1021/es102536f.

[43] C.A. Ramsburg, J.A. Christ, S.R. Douglas, A. Boroumand, Analytical modeling of degradation product partitioning kinetics in source zones containing entrapped DNAPL, Water Resour. Res. 47 (2011) 1–14. https://doi.org/10.1029/2010WR009958.

[44] K.C. Glover, J. Munakata-Marr, T.H. Illangasekare, Biologically enhanced mass transfer of tetrachloroethene from DNAPL in source zones: Experimental evaluation and influence of pool morphology, Environ. Sci. Technol. 41 (2007) 1384–1389. https://doi.org/10.1021/es060922n.

[45] P.L. Morrill, B.E. Sleep, D.J. Seepersad, M.L. McMaster, E.D. Hood, C. LeBron, D.W. Major, E.A. Edwards, B. Sherwood Lollar, Variations in expression of carbon isotope fractionation of chlorinated ethenes during biologically enhanced PCE dissolution close to a source zone, J. Contam. Hydrol. 110 (2009) 60–71. https://doi.org/10.1016/j.jconhyd.2009.08.006.

[46] Y. Yang, P.L. McCarty, Comparison between donor substrates for biologically enhanced

tetrachloroethene DNAPL dissolution, Environ. Sci. Technol. 36 (2002) 3400–3404. https://doi.org/10.1021/es011408e.

[47] Z. Gong, K. Alef, B.M. Wilke, P. Li, Dissolution and removal of PAHs from a contaminated soil using sunflower oil, Chemosphere. 58 (2005) 291–298. https://doi.org/10.1016/j.chemosphere.2004.07.035.

[48] M.G. Mahmoodlu, E.M. Pontedeiro, J.S. Pérez Guerrero, A. Raoof, S. Majid Hassanizadeh, M.T. van Genuchten, Dissolution kinetics of volatile organic compound vapors in water: An integrated experimental and computational study, J. Contam. Hydrol. 196 (2017) 43–51. https://doi.org/10.1016/j.jconhyd.2016.12.004.

[49] B. Agaoglu, T. Scheytt, N.K. Copty, Laboratory-scale experiments and numerical modeling of cosolvent flushing of multi-component NAPLs in saturated porous media, J. Contam. Hydrol. 140–141 (2012) 80–94. https://doi.org/10.1016/j.jconhyd.2012.07.005.

[50] J.C. Liu, P.S. Chang, Solubility and adsorption behaviors of chlorophenols in the presence of surfactant, Water Sci. Technol. 35 (1997) 123–130. https://doi.org/10.1016/S0273-1223(97)00122-4.

[51] C.A. Ramsburg, J.A. Christ, S.R. Douglas, A. Boroumand, Analytical modeling of degradation product partitioning kinetics in source zones containing entrapped DNAPL, Water Resour. Res. 47 (2011). https://doi.org/10.1029/2010WR009958.

[52] C. V Chrysikopoulos, E.T. Vogler, Acoustically enhanced multi-component NAPL ganglia dissolution in water saturated packed columns, Environ. Sci. Technol. 38 (2004) 2940–2945. https://doi.org/10.1021/es034665n.

[53] C. V Chrysikopoulos, E.T. Vogler, Acoustically enhanced ganglia dissolution and mobilization in a monolayer of glass beads, Transp. Porous Media. 64 (2006) 103–121. https://doi.org/10.1007/s11242-005-1525-8.

[54] R. Martel, A. Hébert, R. Lefebvre, P. Gélinas, U. Gabriel, Displacement and sweep efficiencies in a DNAPL recovery test using micellar and polymer solutions injected in a five-spot pattern, J. Contam. Hydrol. 75 (2004) 1–29. https://doi.org/10.1016/j.jconhyd.2004.03.007.

[55] S. Saenton, T.H. Illangasekare, K. Soga, T.A. Saba, Effects of source zone heterogeneity on surfactant-enhanced NAPL dissolution and resulting remediation end-points, J. Contam. Hydrol. 59 (2002) 27–44. https://doi.org/10.1016/S0169-7722(02)00074-8.

[56] M. Oostrom, J.H. Dane, T.W. Wietsma, A Review of Multidimensional, Multifluid Intermediate-Scale Experiments: Nonaqueous Phase Liquid Dissolution and Enhanced Remediation, Vadose Zo. J. 5 (2006) 570–598. https://doi.org/10.2136/vzj2005.0125.

[57] Z. Yang, A. Niemi, F. Fagerlund, T. Illangasekare, Effects of single-fracture aperture statistics on entrapment, dissolution and source depletion behavior of dense non-aqueous phase liquids, J. Contam. Hydrol. 133 (2012) 1–16. https://doi.org/10.1016/j.jconhyd.2012.03.002.

[58] G.R. Tick, J.R. Harvell, D. Murgulet, Intermediate-Scale Investigation of Enhanced-Solubilization Agents on the Dissolution and Removal of a Multi-component Dense Nonaqueous Phase Liquid (DNAPL) Source, Water. Air. Soil Pollut. 226 (2015). https://doi.org/10.1007/s11270-015-2636-7.

[59] D. Aydin-sarikurt, G.P. Karatzas, Experimental Investigation and Numerical Modeling of Enhanced DNAPL Solubilization in Saturated Porous Media, Water, Air, Soil Pollut. (2016) 1–16. https://doi.org/10.1007/s11270-016-3136-0.

[60] A.J. Kaye, J. Cho, N.B. Basu, X. Chen, M.D. Annable, J.W. Jawitz, Laboratory investigation of flux reduction from dense non-aqueous phase liquid (DNAPL) partial source zone remediation by enhanced dissolution, J. Contam. Hydrol. 102 (2008) 17–28. https://doi.org/10.1016/j.jconhyd.2008.01.006.

[61] S.A. Bradford, K.M. Rathfelder, J. Lang, L.M. Abriola, G.E. Brown, Entrapment and dissolution of DNAPLs in heterogeneous porous media, J. Contam. Hydrol. 67 (2003) 133–157. https://doi.org/10.1016/S0169-7722(03)00071-8.

[62] A. Luciano, G. Mancini, V. Torretta, P. Viotti, An empirical model for the evaluation of the dissolution rate from a DNAPL-contaminated area, Environ. Sci. Pollut. Res. 25 (2018) 33992–34004. https://doi.org/10.1007/s11356-018-3193-6.

[63] Y. Hu, A. Patmonoaji, H. Xu, K. Kaito, S. Matsushita, T. Suekane, Pore-scale investigation on nonaqueous phase liquid dissolution and mass transfer in 2D and 3D porous media, Int. J. Heat Mass Transf. 169 (2021) 120901. https://doi.org/10.1016/j.ijheatmasstransfer.2021.120901.

[64] S.A. Bradford, L.M. Abriola, Dissolution of residual tetrachloroethylene in fractional wettability porous media: Incorporation of interfacial area estimates, Water Resour. Res. 37 (2001) 1183–1195. https://doi.org/10.1029/2000WR900374.

[65] J.J. Kaluarachchi, J.C. Parker, Modeling Multicomponent Organic Chemical Transport In Three-Fluid-Phase Porous Media, J. Contam. Hydrol. 5 (1990) 349–374.

[66] J.T. Su, D. Needham, Mass transfer in the dissolution of a multi-component liquid droplet in an immiscible liquid environment., Langmuir. 29 (2013) 13339–45. https://doi.org/10.1021/la402533j.

[67] A. Kokkinaki, D.M. O'Carroll, C.J. Werth, B.E. Sleep, An evaluation of Sherwood-Gilland models for NAPL dissolution and their relationship to soil properties., J. Contam. Hydrol. 155 (2013) 87–98. https://doi.org/10.1016/j.jconhyd.2013.09.007.

[68] Z. Yang, A. Niemi, F. Fagerlund, T. Illangasekare, R.L. Detwiler, Dissolution of dense non-aqueous phase liquids in vertical fractures: Effect of finger residuals and dead-end pools, J. Contam. Hydrol. 149 (2013) 88–99. https://doi.org/10.1016/j.jconhyd.2013.03.006.

[69] G. Lekmine, T.P. Bastow, C.D. Johnston, G.B. Davis, Dissolution of multi-component LNAPL gasolines: The effects of weathering and composition, J. Contam. Hydrol. 160 (2014) 1–11. https://doi.org/10.1016/j.jconhyd.2014.02.003.

[70] S.K. Hansen, B.H. Kueper, A new model for coupled multi-component NAPL dissolution and aqueous-phase transport, with application to creosote dissolution in discrete fractures, Water Resour. Res. 50 (2014) 58–70. https://doi.org/10.1002/2013WR013773.

[71] K.E. Christensen, P.W. Altman, C. Schaefer, J.E. McCray, Steady State DNAPL Dissolution in Three-Dimensional Fractured Sandstone Network Experiments, J. Environ. Eng. 141 (2015) 4014047. https://doi.org/10.1061/(asce)ee.1943-7870.0000871.

[72] Z. Guo, A.E. Russo, E.L. DiFilippo, Z. Zhang, C. Zheng, M.L. Brusseau, Mathematical modeling of organic liquid dissolution in heterogeneous source zones, J. Contam. Hydrol. 235 (2020) 103716. https://doi.org/10.1016/j.jconhyd.2020.103716.

[73] M.T. Gönüllü, Modelling dissolution of an organic mixture in the subsurface, Water Res. 30 (1996) 649–653. https://doi.org/10.1016/0043-1354(95)00193-X.

[74] L. Liu, U. Maier, P. Grathwohl, S.B. Haderlein, Contaminant Mass Transfer from NAPLs to Water Studied in a Continuously Stirred Flow-Through Reactor, J. Environ. Eng. 138 (2012) 826–832. https://doi.org/10.1061/(asce)ee.1943-7870.0000528.

[75] M.W. Priddle, K.T.B. MacQuarrie, Dissolution of creosote in groundwater: an experimental and modeling investigation, J. Contam. Hydrol. 15 (1994) 27–56. https://doi.org/10.1016/0169-7722(94)90009-4.

[76] T.P. Clement, T.R. Gautam, K.K. Lee, M.J. Truex, G.B. Davis, Modeling of DNAPL-dissolution, rate-limited sorption and biodegradation reactions in groundwater systems, Bioremediat. J. 8 (2004) 47–64. https://doi.org/10.1080/10889860490453177.

[77] H. Li, L. Zhao, X. Gao, X. Li, Experimental investigation of methyl tert-butyl ether dissolution in saturated porous media, Chinese J. Chem. Eng. 23 (2015) 1685–1690. https://doi.org/10.1016/j.cjche.2015.08.022.

[78] S. Colombano, H. Davarzani, E.D. van Hullebusch, D. Huguenot, D. Guyonnet, J. Deparis, F. Lion, I. Ignatiadis, Comparison of thermal and chemical enhanced recovery of DNAPL in saturated porous media: 2D tank pumping experiments and two-phase flow modelling, Sci. Total Environ. 760 (2021) 143958. https://doi.org/10.1016/j.scitotenv.2020.143958.

[79] Y. Yang, P.L. Mccarty, Biologically Enhanced Dissolution of Tetrachloroethene DNAPL, Environ. Sci. Technol. 34 (2000) 2979–2984.

[80] S.W. Jeong, A.L. Wood, T.R. Lee, Enhanced removal of DNAPL trapped in porous media using simultaneous injection of cosolvent with air: Influencing factors and removal mechanisms, J. Hazard. Mater. 101 (2003) 109–122. https://doi.org/10.1016/S0304-3894(02)00313-8.

[81] S. Lee, Enhanced dissolution of TCE in NAPL by TCE-degrading bacteria in wetland soils, J. Hazard. Mater. 145 (2007) 17–22. https://doi.org/10.1016/j.jhazmat.2006.10.073.

[82] M. Chen, L.M. Abriola, B.K. Amos, E.J. Suchomel, K.D. Pennell, F.E. Löffler, J.A. Christ, Microbially enhanced dissolution and reductive dechlorination of PCE by a mixed culture: Model validation and sensitivity analysis, J. Contam. Hydrol. 151 (2013) 117–130. https://doi.org/10.1016/j.jconhyd.2013.05.005.

[83] J. Fortin, W.A. Jury, M.A. Anderson, Enhanced removal of trapped non-aqueous phase liquids from saturated soil using surfactant solutions, J. Contam. Hydrol. 24 (1997) 247–267. https://doi.org/10.1016/S0169-7722(96)00013-7.

[84] Y. Arcand, J. Hawari, S.R. Guiot, Solubility of pentachlorophenol in aqueous solutions: The pH effect, Water Res. 29 (1995) 131–136. https://doi.org/10.1016/0043-1354(94)E0104-E.

[85] F. Fagerlund, T.H. Illangasekare, T. Phenrat, H.J. Kim, G. V Lowry, PCE dissolution and simultaneous dechlorination by nanoscale zero-valent iron particles in a DNAPL source zone, J. Contam. Hydrol. 131 (2012) 9–28. https://doi.org/10.1016/j.jconhyd.2011.08.011.

[86] S. Chu, A. Prosperetti, Dissolution and growth of a multi-component drop in an immiscible liquid, J. Fluid Mech. 798 (2016) 787–811. https://doi.org/10.1017/jfm.2016.310.

Evaluation of Mechanical and Thermal Properties of Carrageenan/Hydroxypropyl Methyl Cellulose Hard Capsule

Nur Amalina Ramli[1], Fatmawati Adam[1,2]*, Khairatun Najwa Mohd Amin[1], Adibi Rahiman Md. Nor[3] and Michael E. Reis[4]

[1] Faculty of Chemical & Process Engineering Technology, Universiti Malaysia Pahang, Gambang, Pahang, Malaysia;
[2] Centre of Excellence for Advanced Research in Fluid Flow (CARIFF), Universiti Malaysia Pahang, Gambang, Pahang, Malaysia;
[3] International Institute of Public Policy and Management, University of Malaya, Kuala Lumpur, Malaysia;
[4] School of Physics & Astronomy, University of Leeds, Leeds, United Kingdom
***** *Corresponding author: fatmawati@ump.edu.my; Tel.: +6095492824*

Abstract: The inherent source of gelatin used for commercial hard capsules causes a surging demand on vegetarian capsules. In this work, carrageenan is utilized in preparing hard capsules to meet consumer preferences. Hydroxypropyl methylcellulose (HPMC) was incorporated as a reinforcing agent to improve the low mechanical properties of hard capsules made of carrageenan. HPMC concentration was manipulated from 0.2 w/v% to 1.0 w/v% in the carrageenan matrix. Increasing concentration of HPMC exerts significant effects on the tensile strength and elongation at break, with an improvement of 59.1% and 46.9%, respectively, at the optimized HPMC concentration of 0.8 w/v%. The loop strength of the capsule is also increased by 56.4% with decreasing moisture content. A downfield movement around 3.20 ppm of the carrageenan proton to 3.33 ppm in 1H-NMR spectrum suggests the formation of intermolecular hydrogen bonding between carrageenan and HPMC, which correlates to the results of FTIR and zeta potential. SEM images of the film depict good miscibility between the composite materials. The glass transition of the film is increased from 37.8°C to 65.3°C, showing an upgrade in thermal stability. The film possesses a major mass loss with an activation energy of 64.7 kJ/mol with an increment of 43.4% compared to the control carrageenan. These findings support the conclusion that HPMC enhanced the mechanical properties and thermal stability of the carrageenan film, and the comprehensive analysis of the molecular interaction and decomposition kinetics subsequently may expand the application fields of the carrageenan-HPMC hard capsule as an alternative to gelatin in the future.

Keywords: activation energy; carrageenan; hydroxypropylmethyl cellulose; mechanical strength; thermal stability

1. Introduction

Hard capsules are predominantly employed dosage form for oral administration of active ingredients due to their simplicity and ease of manufacture.[1] At present, gelatin is the most widely applied material and remains appealing to hard capsule manufacturers because it is soluble in biological fluids at body temperature, able to undergo thermal gelation, and forms a strong, flexible and homogeneous film.[2] Despite these advantages offered by gelatin, its inherent source from animals has given rise to a huge concern towards consumers' preference based on the vegetarian dietary requirement. Commercial gelatin is commonly extracted from mammals, mainly porcine and bovine.[3] It is the primary goal of the pharmaceutical industry to satisfy the therapeutic needs of consumers. Considering the awareness of this issue, great attempts are being conducted to search for an alternative capsule shell material, preferably of plant origin, and able to present comparable properties and performance to gelatin.

Carrageenan, a marine-derived polysaccharide exhibits potential as a film-forming material attributed to its superior gelling and high viscosity properties.[4–6] Carrageenan offers value-added properties in food and pharmaceutical products as a thickener, stabilizer, coagulant, and emulsifier which assured its surging market demand.[7,8] Considering these key attributes, carrageenan can be a promising option as an alternative to gelatin. In contempt of that, since natural biodegradable polymer usually possesses certain unfavourable physicochemical properties, carrageenan-based hard capsule exhibits low mechanical strength which restricts its applicability and feasibility in production.[6,9] A multitude of chemical modifications have been studied in order to modulate the mechanical properties of carrageenan in preparing hard capsules. In our recent study, the incorporation of 2.0 wt.% carboxymethyl cellulose (CMC) substantially increased the viscosity of carrageenan biocomposite up to 50% and the tensile strength of the film up to 37%.[10] In a separate study, the inclusion of 1.6 wt.% CNC resulted in an increment of tensile strength by 58% compared to film without CNC.[11] The effect of physical crosslinking with the inclusion of 3 wt.% isovanillin in the carrageenan/cellulose nanocrystals composite was also proven to improve the tensile strength up to 49%.[12] A thorough study on the mixing time in preparing hard capsule was conducted to optimize its mechanical properties.[9] Another approach of blending carrageenan with Arabic gum was also investigated and the capsule strength at a mass ratio of 67 wt.% carrageenan was reported to be enhanced due to their compatibility to produce homogeneous and viscous biocomposite solution [13]. In terms of thermal stability, blends of higher concentrations of carrageenan with Arabic gum and polyethylene glycol induced higher activation energy (E_a) on the decomposition of the composite film.[14] In the development of a film-based product, the most important characteristic is its ability to withstand mechanical damage and exhibit an appropriate level of flexibility for ease of handling and processing.[15]

The formulations of hard capsule are modified to improve their mechanical and thermal properties, which has been the target of recent works, with the composite matrix being the most promising and widely explored. Hydroxypropylmethyl cellulose (HPMC), an excipient function as a reinforcing agent, is introduced in the formulation of hard capsule to deal with the brittleness of carrageenan film. HPMC is a recurrent hydrophilic polymer of choice over other cellulosics due to its excellent thickening, film-forming, swelling, and miscibility.[8,16] The capsules made up of HPMC are less brittle and can exhibit higher tensile strength even with lower moisture content compared to gelatin.[16] HPMC can form a hydrogel at high temperature as opposed to the gelation upon-cooling property of carrageenan.[17] The gelation capacity of HPMC decreases at low temperatures. This is one of the issues to develop HPMC hard capsules, where the adjustment of the pin temperature is needed. The pins used must be maintained at higher temperatures to prevent the liquefaction of the films formed on the pins.[2] In this case, when HPMC is mixed with carrageenan, metal pins can be dipped in a warm biocomposite solution at room temperature, which is similar to those used for gelatin. Therefore, no special manufacturing apparatus and procedures are needed and the existed manufacturing apparatus for immersion and moulding of traditional gelatin capsules can be used without modification.

Even though there are numerous studies available on plant-based capsule shell materials, it is still important to develop a composite matrix with improved characteristics to be comparable to gelatin. Moreover, there are limited reports that exist on the use of HPMC as a reinforcing agent in preparing carrageenan composite film and hard capsule.[8] There is further scope to improve this system and to provide an understanding of the molecular interaction mechanism and decomposition E_a related to the mechanical and thermal properties of the hard capsule. The stability of particles in the carrageenan matrix through zeta potential analysis is also a significant study to prevent the formation of aggregation. This work aims to evaluate the mechanical properties of Carra-HPMC composite film and to study its thermal characteristics by calculating the decomposition E_a. Blend of carrageenan and HPMC to form composite for hard capsule through hydrogen bonding networking is hypothesized to be able to increase the mechanical and thermal properties by formation of intermolecular interaction.

2. Materials and Methods

2.1. Materials

Refined carrageenan was purchased from CV Simpul Agro Globalindo, Indonesia (molecular weight ranges from 930 to 1010 g/mol with 31.5% carbon, 5.97% hydrogen, 0% nitrogen, and 6.28% sulphur.[12] Hydroxypropylmethyl cellulose (average molecular weight of 86 kDa), 4-methoxybenzyl alcohol (98%) (anise), and calcium alginic acid (alg) were obtained from Sigma-Aldrich (USA). Polyethylene glycol (PEG) as a plasticizer was purchased from Merck (Germany). All chemicals used are of analytical grade.

2.2. Preparation of film and hard capsule

Table 1 summarizes the formulation which was used to prepare Carra-HPMC composite film. The solution of refined carrageenan (3.0 g) mixed with 0.2 w/v% to 1.0 w/v% of HPMC was prepared in 150 mL of deionized water at 60°C. Formulation without the addition of HPMC was used as a control. The same amount of anise, polyethylene glycol (PEG), and calcium alginic acid was then added to each sample as a crosslinker, plasticizer, and toughening agent, respectively. After 3 hours of mixing, approximately 20 mL of the solution was poured into a stainless-steel tray and left overnight at room temperature to form a film. Meanwhile, the other portion of the solution was dipped using stainless-steel mold capsule pins size "1" to prepare hard capsules. The dried resulting film and hard capsules were then employed for characterization and analysis.

Table 1. Formulation of Carra-HPMC composite films and hard capsules.

Samples	Carrageenan (w/v%)	HPMC (w/v%)
Control	2.0	0
Carra-HPMC 0.2	2.0	0.2
Carra-HPMC 0.4	2.0	0.4
Carra-HPMC 0.6	2.0	0.6
Carra-HPMC 0.8	2.0	0.8
Carra-HPMC 1.0	2.0	1.0

2.3. Zeta potential measurement

The zeta potential of Carra-HPMC biocomposite was measured using a DelsaMax Pro zeta potential analyzer (Beckman Coulter, UK), utilizing the phase analysis light scattering (PALS) technique. The sample was diluted with deionized water to a final concentration of 0.1 v/v%. The Bi-PALS software provided an average of electrophoretic mobility and measured the zeta-potential using the Smoluchowski model.

2.4. ^{1}H-NMR spectroscopy analysis

The 500 MHz of ^{1}H NMR spectra were recorded using an NMR spectrometer (Bruker Ultra Shield Plus, Germany) which operated at room temperature. Samples were prepared in DMSO-d_6 and tetramethylsilane (TMS) as the internal standard. The chemical shifts were measured with respect to the remaining proton resonance of DMSO-d_6 (2.50 ppm).

2.5. FTIR spectroscopy analysis

FTIR spectra of the film were measured by ATR-FTIR spectrometer (Perkin Elmer, USA) within the range of 400 to 4000 cm^{-1}. A total of 16 scans were acquired at 0.15 s/scan and with a spectral resolution of 8 cm^{-1}. The spectra were analyzed using OMNIC software.

2.6. Viscosity measurement

The viscosity of carrageenan biocomposite was measured using a rotational rheometer (Rheo3000, USA) equipped with LCT 25 4000010 geometry. Approximately 15 mL of the biocomposite solution was filled in the measuring block. The measurement was programmed at a speed of 300 revolutions per minute, with 100 MPoints at a pre-heated temperature of 40°C.

2.7. Mechanical properties analysis

The tensile strength and elongation at break of 2 cm × 6 cm Carra-HPMC film strips were measured using a texture analyzer (CT3, USA) equipped with a 5 kN load cell. The trigger force was applied at a crosshead speed of 30 mm/min to a maximum distance of 15 mm. A hard capsule loop test was also conducted using the same texture analyzer (CT3, USA). The target value of 5.0 mm and the speed of 0.50 mm/s were predetermined. The maximum force (N) used to tear the hard capsule before rupture was recorded as an indication of the loop strength of the hard capsules.

2.8. Moisture content analysis

The moisture content of the film was determined using a moisture analyzer (MS70, A&D, Japan). The moisture content was calculated in mass on completion of the heating regime compared to the initial mass of 0.1 g of the sample. The measurement would stop once the sample attained a constant value of moisture content.

2.9. Disintegration test

Following United States Pharmacopeia (USP), a disintegration test was performed using a disintegration tester (Distek 3100, Germany), in which capsules were placed in the tubes and then immersed in 600 mL of distilled water at 37 ± 2°C. For ease of observation, the capsules were filled with lactose as a placebo. The disintegration time of the capsules was measured as the time (min) required for the lactose to initially diffuse from the capsules into the medium.

2.10.Morphological analysis

The morphology of Carra-HPMC film surface was observed using the scanning electron microscope (S26000-N Hitachi, Japan). The sample was sputter-coated with a platinum film to prevent any charging up to the surface by the electron beam. The film was observed under 3000× magnification.

2.11.Thermal stability analysis

The glass transition, melting and crystallization temperature was determined from the thermograms recorded by differential scanning calorimeter (DSC) (Polyma214, Germany). Approximately 3 mg of the sample was heated at 10°C/min from 30°C to 400°C in a nitrogen atmosphere. Thermographic profiles of carrageenan films were analyzed using a thermogravimetric analyzer (TGA) (STA7200 Hitachi, Japan). Approximately 3 mg of the film was heated in the airflow from 30°C to 700°C at 10°C/min. Mass loss and differential thermal analysis profiles were also reported.

2.12.Kinetic analysis by Broido's model

The E_a for the major stage of decomposition was calculated following the Arrhenius kinetic theory based on the results of DSC and TGA. E_a is the minimum energy required to break the bond between molecules in the structure of the material during thermal degradation.[14] At first, in thermogravimetric measurement, the degree of conversion was calculated using Equation (1) as follows:

$$y = \frac{wt - w\infty}{wo - w\infty}, \quad (1)$$

where y is the degree of conversion, w_t is the weight at any time in gram, w_o is the initial weight and w_∞ is the weight of residue. Based on the degree of conversion, a graph was drawn by plotting ln [ln (1/y)] *vs* 1000/T, where the value of E_a was provided from the slope of the graph [18,19] as in Equation (2) by the following:

$$\ln [\ln \left(\frac{1}{y}\right)] = -\left(\frac{Ea}{RT}\right) + \ln A, \quad (2)$$

where R is the universal gas constant ($R = 8.314\ J \cdot mol^{-1} \cdot K^{-1}$), E_a is the activation energy (kJ/mol), T is the temperature recorded in thermogram (K), and A is the pre-exponential factor (min^{-1}). The entropy of activation (ΔS), enthalpy of activation (ΔH), and Gibbs free energy change (ΔG) were also calculated based on the activation energy.

2.13.Statistical analysis

All measurements were presented as the mean ± standard deviation of the results from at least three independent experiments. The one-way analysis of variance (ANOVA) was performed to calculate the confidence level of p-value, where $p<0.05$ was regarded as statistically significant. The testing null analysis (H_o) and alternative analysis (H_i) were assigned for viscosity, tensile strength, elongation at break, capsule loop strength, moisture content, and disintegration time for Carra-HPMC at different concentration of HPMC.

3. Results and Discussion

3.1 Zeta potential of biocomposite

The zeta potential values of carrageenan, HPMC, and other materials in the biocomposite are all in negative values (Figure 1a). The zeta potential of carrageenan has the highest negative value which is -54.0 mV. It is similar to the result found by Ellis et al.[20] and it reflects the negatively charged ester sulphate groups of carrageenan, while HPMC is -3.94 mV which is slightly negative as reported by Nemazifard et al.[21] The reduction in net negative charges of carrageenan biocomposite added with the increasing amount of HPMC can be linked to the interaction between both materials (Figure 1b). It can be speculated that the helix structure of carrageenan is surrounded by HPMC and prompts the reduction of zeta potential of the composite. Nonetheless, it is considered to have a high value of zeta potential ≥30 mV indicating a physically stable dispersion due to the predominance of electrostatic repulsion over Van der Walls forces [22,23].

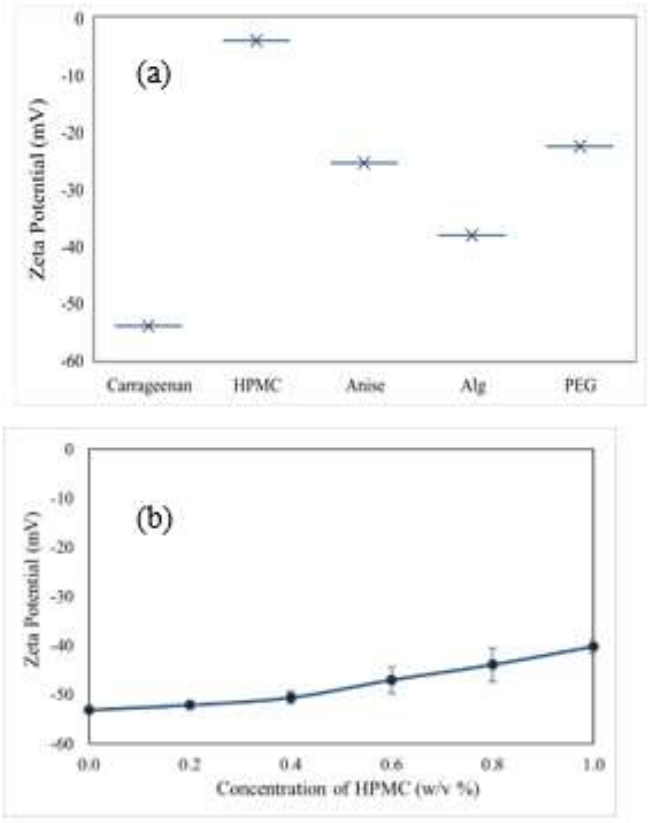


Figure 1. (a) Zeta potential for each material in biocomposite and (b) the effect of HPMC concentration on the zeta potential of biocomposite.

Abbreviations: HPMC, hydroxypropylmethyl cellulose; alg, alginic acid; PEG, polyethylene glycol.

3.2 ^{1}H-NMR spectroscopy of biocomposite

^{1}H-NMR was conducted to acquire molecular-level insight through the changes of the ^{1}H spectrum of Carra-HPMC biocomposite compared to the raw HPMC to identify preferential intermolecular interactions that occur. In the raw HPMC spectrum, the polymer repeating unit protons exhibited resolved signals at 2.41-3.64 ppm (H-1-8, H-10) (Figure 2a). These multiple peaks assign to the methyl protons adjacent to the oxygen moieties of ether linkages (O-CH_3), inner methylene (O-CH_2) and methine protons (-CH-O), and HPMC backbones of anhydroglucose unit [24]. Another single signal that appeared at 1.02 ppm (H-9) is associated with the methyl protons in the hydroxypropyl moieties of HPMC (3H, CH-CH_3). Signal assignment observed of HPMC appears at lower chemical shift but corresponds to the one reported by Lu et al.[25] (2.75-4.75 and 1.05 ppm) and Amin et al.[26] (2.89-5.10 and 1.13 ppm). Different sources of sample and different sample treatment prior to analysis might be the reasons of this variation.

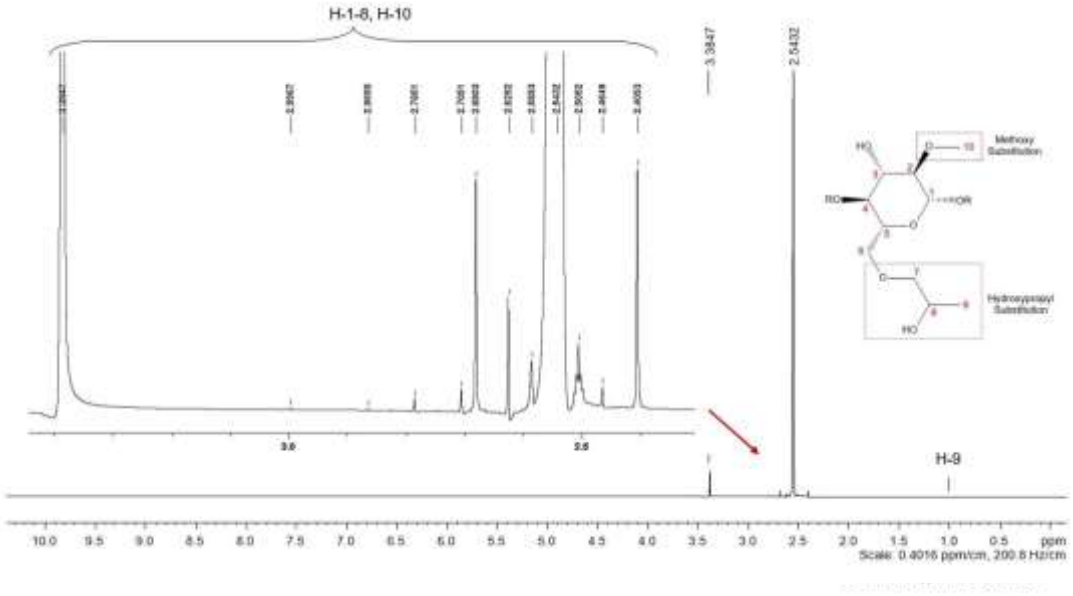


Figure 2. (b) ^{1}H NMR spectrum of biocomposite.

Table 2. ^{1}H NMR results of biocomposite in comparison with HPMC.

Samples	Integration of peak at 3.2-3.4 ppm	Number of protons at 2.35-2.99 ppm	Integration of peak at 1.0-1.3 ppm
HPMC	3.385	23.572	1.020
Carra-HPMC	3.335, 3.338, 3.353,3.376, 3.377, 3.385	25.617	1.232

By examining the change in proton shifts, NMR analysis can be utilized to detect whether the different elements are interacting. In general, hydrogen bond formation causes shifts to a higher frequency (higher ppm) owing to deshielding. As the peak shifts to the left and becomes further downfield, the electronegativity increases. The chemical shift improved the conjugate molecule's shielding effect, bringing the hydrogen closer to the electronegative atom. The peak that corresponds to the proton at 3-linked β-d-galactopyranose (G)-2 (O-2H) of carrageenan spectrum around 3.2 ppm [27] has a slight downfield movement to 3.33 after incorporation of HPMC, which is thought to be caused by the formation of intermolecular hydrogen bonds between carrageenan and the HPMC molecule. This indicates the molecular distribution of HPMC surrounds the helix structure of carrageenan as mentioned in zeta potential analysis. There are also additional minor peaks detected at around 3.35-3.38 contributed by the interaction between these two materials (Figure 2b). A change in the integration values of the area between 2.35-2.99 is observed in Table 2, which shows an increasing number of protons detected bounded to Carra-HPMC biocomposite compared to the raw materials. Peaks at this range depict upfield chemical shifts to lower frequency after being introduced in carrageenan matrix attributed to the hydrophobic interaction between highly methylated glucose zones of HPMC.[28] This type of interaction occurs during the gelation of HPMC which increases the viscosity of the biocomposite for reinforcement. Meanwhile, chemical shifts of HPMC at 1.0-1.3 ppm deshielded to a higher frequency, which prescribed that hydrogen bond interaction with carrageenan could also occur at H9 (methyl protons of the hydroxypropyl group).

Figure 3 depicts a film-forming mechanism based on the proposed hydrogen bonding interaction between carrageenan and HPMC corresponding to the NMR results. The molecules of carrageenan and HPMC are initially dispersed randomly in the solution. Carrageenan interacted with HPMC via intermolecular hydrogen bonding, and both molecules' three-dimensional network structures are entangled and formed inter-phases. Cross-linking and gelation are also caused by the intermolecular interactions of the hydrophobic groups of the HPMC chains. The formation of carrageenan-HPMC biocomposite provides a synergistic effect on enhancing the mechanical properties that are attributed to interpenetration between the two polysaccharides. To verify the hypothesis, the mechanical properties of Carra-HPMC biocomposite film and hard capsule are examined and its subsequent improvement on thermal properties is investigated.

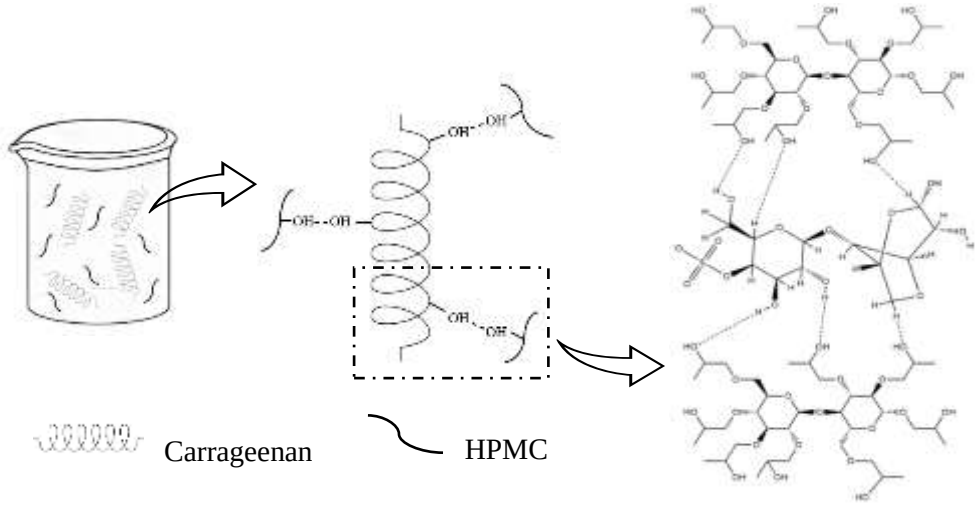


Figure 3. Schematic representation of the proposed hydrogen bonding interaction between carrageenan and HPMC.

3.3 FTIR spectroscopy of film

Figure 4a depicts the spectra of carrageenan and HPMC as the raw materials together with the spectrum of Carra-HPMC composite film. Carrageenan prompts its characteristic peaks at 1223 cm^{-1} and at 1034 cm^{-1} which indicate the -SO sulphate esters and the glycosidic linkage (-CO) of carrageenan, respectively. The characteristic peak of 3,6-anhydro-D-galactose appears at 921 cm^{-1} while the peak at 841 cm^{-1} is attributed to C-O-SO_4 on D-galactose-4-sulphate. The spectrum of carrageenan is comparable with the findings presented in the literature.[8,12,29] The expanded band centres around 3443 cm^{-1} and the peak at 2900 cm^{-1} refer to the -OH and -CH stretching vibrations, respectively, which are also detected in the spectra of HPMC and Carra-HPMC film. An increase in the peak intensity of the hydroxyl band of Carra-HPMC film is owing to the increase in the amount of -OH bond, implying hydrogen bonding formed between carrageenan and HPMC. For the spectrum of HPMC, the band at 1638 cm^{-1} is associated with the C=O group while the absorption peak at 1453 cm^{-1} refers to the -CH scissoring. These correspond to the results found by Liu et al.[17] and Bodini et al.[30] for HPMC-based films. Meanwhile, the characteristic peaks of cellulose C-O-C in HPMC are detected around the same region as reported by Pacheco-Quito et al.[31] and Suksaeree et al.[32], which are at 1060 cm^{-1} and 958 cm^{-1}. Carra-HPMC film presents similar spectra with identical functional groups of raw carrageenan and HPMC. There are no new adsorption peaks that emerged in Carra-HPMC film spectrum, implying there is no new chemical bond formation in the biocomposite. This suggests that a biocomposite system is formed with separated phases.

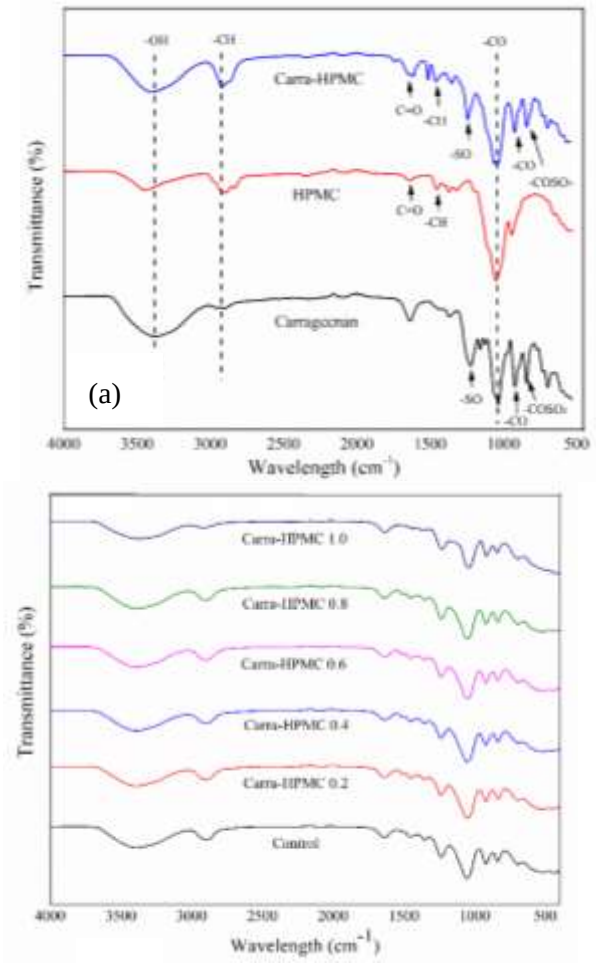


Figure 4. FTIR spectra of (A) carrageenan, HPMC, and Carra-HPMC and (B) film at different HPMC concentration.

FTIR spectra of all prepared films with different HPMC concentrations are reported in Figure 4b for a thorough understanding of the created hydrogen bonding between the molecules. It is expected that intermolecular hydrogen bonding would exist between the hydroxyl groups of carrageenan and HPMC.[8] The regions of hydroxyl groups situated at 3700-3200 cm^{-1} are focused on determining the shifted peak and its intensity. As the HPMC concentration increases from 0.2 to 0.8 w/v%, the hydroxyl band moves from 3394 cm^{-1} to a lower wavenumber of 3382 cm^{-1} with increasing intensity, suggesting that a greater intermolecular hydrogen bond was formed between the materials.[33] This interaction corresponds to the NMR results as discussed in the previous section. The improved hydrogen bonding interaction will lead to an increment in film strength.[9] At HPMC concentration of 1.0 w/v%, however, the intensity of the hydroxyl bond peak is becoming lower compared to 0.8 w/v% due to weaker hydrogen bonding created, which might be due to the aggregation of HPMC which is in excess. This observation would relate to the lower mechanical properties depicted from the composite film prepared at this concentration.

3.4 Viscosity of biocomposite and mechanical properties of film and hard capsule

The presence of HPMC causes the viscosity to increase significantly ($p<0.05$) from 172.1 mPa·s to its highest point achieved at 0.8 w/v% with 616.5 mPa·s (Figure 5a). The higher concentration of

HPMC in the formulation retards the flow of the biocomposite, resulting in higher viscosity.[34,35] The viscosity provides an insight into the behavior and intermolecular interaction between the composite chains and gives an indication of its mechanical performance. The direct correlation between viscosity and the mechanical strength is displayed in the same figure where the results depict a similar profile with the same optimum point at Carra-HPMC0.8. The higher viscosity of biocomposite leads to a higher tensile strength.[36] It is notable that Carra-HPMC0.8 achieved the highest strength of 51.2 MPa. Great difference ($p<0.05$) in tensile strength related to the incorporation of HPMC is observed when the strength was optimized up to 59.1% compared to film without HPMC. Carra-HPMC0.8 film could endure higher applied pressure up to 47.3% and displays a higher resistance to mechanical stress compared to the control film with 14.5% ($p<0.05$) (Figure 5b). The high viscosity of HPMC gives rise to the breaking point and exhibits flexibility of the film, thereby implies a greater resistance to break under tension. More effective resistance against external load could be due to the compactness of the blending polymer, where HPMC fills the voids in restructuring the carrageenan film.[37] The capsule loop strength is also significantly enhanced by 56.4% ($p<0.05$) to a maximum of 37.4 N at the same concentration before falling to 27.8 N at 1.0 w/v%. The viscosifying effect of HPMC enforces the physical structure of the film and serving as a reinforcing agent. In capsule manufacturing, forming harder and stronger capsules translates into lesser defects and lower rejection rates during capsule filling.

Despite that, a higher concentration of Carra-HPMC1.0 expecting of agglomeration and has disturbed the intermolecular interaction between carrageenan and HPMC, thus reduced the viscosity of the biocomposite.[38] At this point, the increase of HPMC concentration is most likely not resulted in higher tensile strength because the maximum ability of the film to restrain the applied load is reached. Instead, the tensile strength is decreased abruptly after incorporating a higher concentration of HPMC. It has overridden the reinforcement effect of the carrageenan film. Moreover, there might be an insufficient amount of plasticizer in the matrix that inhibits the flexibility and continuity of the matrix chain.[39]

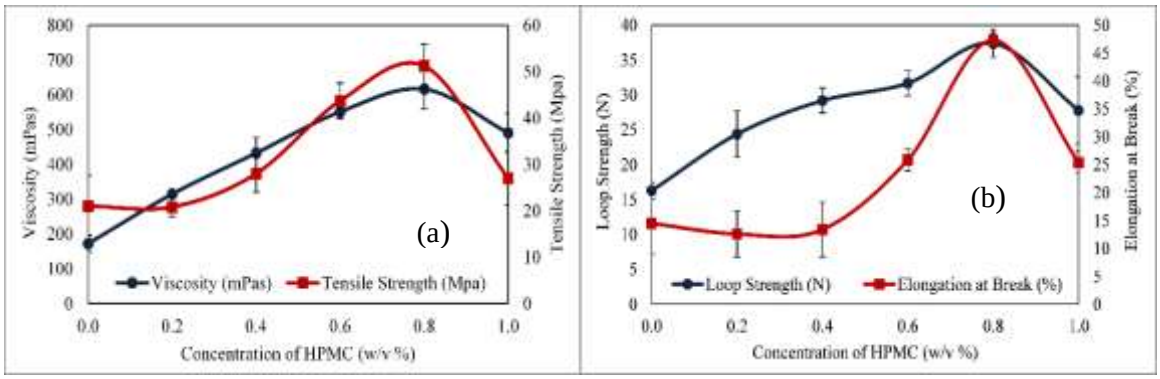


Figure 5. Effect of HPMC concentration on the (a) viscosity and tensile strength, and (b) elongation at break of film and its hard capsule loop strength.

3.5 Moisture content of film and disintegration time of hard capsule

Control film without incorporation of HPMC has the highest moisture content with 23.2% (Table 3). This is due to the fact that carrageenan is composed of sulphate groups which impart higher hydrophilicity, thereby affecting the moisture content presents in the film.[40] Increasing concentration of HPMC in the film matrix greatly decreases ($p<0.05$) the affinity of film to adsorb more water. When water adsorption of the films is low, it enhances the tensile strength of the film and reduces its brittleness.[41] The moisture content of Carra-HPMC0.8 is 14.6% and it displays the

optimum mechanical strength among others. This value is comparable to that of commercial gelatin capsules (13%) even it is greater than commercial HPMC capsules (4.5%).[42] Carra-HPMC1.0 shows the lowest moisture content; however, its decreased mechanical properties give drawbacks in forming capsules.

The disintegration test determines whether the hard capsule will rupture or expand in a liquid medium, particularly water in this test, to fulfill its function as a drug delivery medium. The control hard capsule disintegrates after 10.6 min while increased disintegration time is reported as the concentration of HPMC is increased. High molecular weight and viscosity of HPMC together with the gel promoter of carrageenan cause a delay in the initial burst of the capsule in aqueous medium. Fu et al.[43] emphasized that higher viscosity and molecular weight of the polymer tend to dissolve slower because of greater entanglement and higher gel viscosity. This explains the increasing disintegration time of Carra-HPMC capsules with increasing concentration of HPMC.

Carra-HPMC0.8, the best concentration of HPMC based on mechanical properties, takes 18.7 min to dissolve, exhibiting a longer disintegration time than the control capsule, with $p<0.05$ indicating a significant difference between capsules of all formulations. In a recent study, carrageenan hard capsule crosslinked with maltodextrin was reported to disintegrate in 18 min, while gelatin and HPMC capsules were within 15 min and 30 min, respectively. [44,45] The time frame of 30 min satisfying the USP criteria for dietary supplement formulations.[2,45] Delayed *in vivo* disintegration of HPMC capsules, however, does not give a negative effect *in vivo*.[2] Thus, HPMC capsules can be comparable to gelatin capsules.

Table 3. Effect of HPMC concentration on the moisture content of film and disintegration time of hard capsule.

Samples	Moisture content (%)	Disintegration time (min)
Control	23.2 ± 2.8	10.6 ± 2.1
Carra-HPMC 0.2	21.4 ± 2.1	12.8 ± 1.0
Carra-HPMC 0.4	16.0 ± 2.4	14.7 ± 1.7
Carra-HPMC 0.6	17.1 ± 3.0	17.1 ± 1.6
Carra-HPMC 0.8	14.6 ± 1.2	18.7 ± 1.8
Carra-HPMC 1.0	12.9 ± 1.9	23.6 ± 2.2

3.6 Physical appearance and surface morphology of film

Visually, the transparency and gloss of composite films and hard capsules are retained until the addition of 0.8 w/v% of HPMC (Figure 6). The uniform matrix without any separation of the phase depicts the compatibility between the materials due to uniform mixing.[12] This shows good miscibility between carrageenan and HPMC. Excess addition of HPMC (1.0 w/v%) in the formulation results in a heterogenous film with increased thickness and less opacity. SEM image of Carra-HPMC1.0 shows that macromolecules are visible at the film surface, possibly due to the deformation forces acting during the polymer chain aggregation during solvent evaporation.[46] This result explains the translucent film exhibited at this concentration. Non-uniformity of polymer matrix due to excess inclusion of HPMC intensifies the film brittleness, thereby leading to poor mechanical properties. The non-uniform dispersion may also be attributed to the poor mixing of Carra-HPMC1.0 composite because of the highly viscous effect of HPMC.

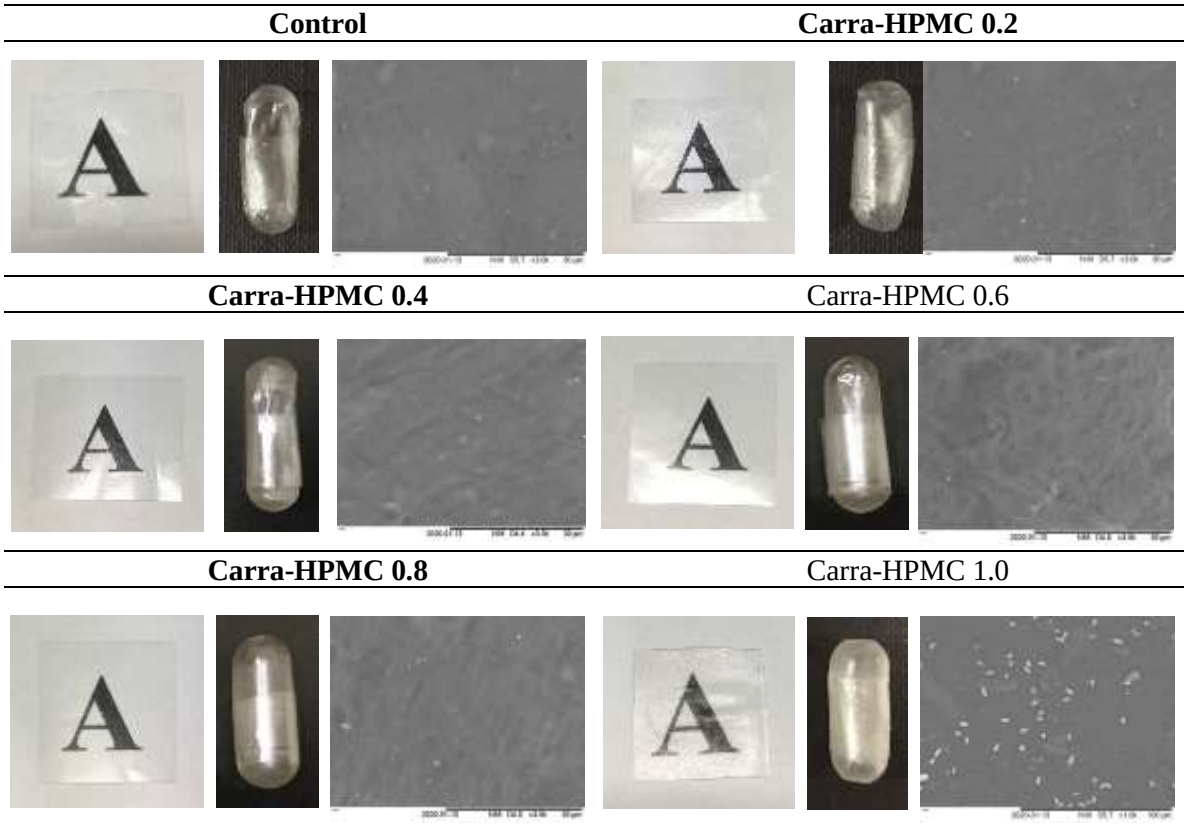


Figure 6. Images of films and capsules, and their surface morphology at different HPMC concentration.

3.7 Thermal analysis of film

The thermal properties attributed to the composite materials are scrutinized since they could affect their applicability to be marketed in the form of hard capsules. A significant drawback of biopolymers is their poor thermal stability compared to synthetic polymers. Carra-HPMC0.8 film presents optimum mechanical strength in terms of tensile strength, elongation at break, and capsule loop strength. Therefore, a thermal stability study was conducted using DSC and TGA for Carra-HPMC at this concentration.

3.7.1. DSC analysis

The heating profiles for Carra-HPMC at all concentration are illustrated in Figure 7 together with pure carrageenan and HPMC. Glass transition temperature (T_g) of every film is investigated since it is a rescindable transition in amorphous or in some cases semi-crystalline constituents from a stiff glassy state to a rubbery state.[47] The film changes from elastic to brittle due to changes in chain mobility. In Table 4, the T_g of carrageenan film is 40.3°C. This value is lower compared to the previously reported T_g of carrageenan which ranging from 50°C to 70°C.[48,49] Probably, the differences in preparation method and heating rate may affect the T_g values. The control film of carrageenan possesses a lower T_g (37.8°C) because of the presence of plasticizers which leads to the formation of hydrogen bonds with polymeric chains and increases the free volume in the structure, thus facilitates mobility of carrageenan chains at lower temperatures.[50] Meanwhile, T_g of HPMC film is recorded at 143.4°C. The previously reported T_g is slightly higher in the range of 150°C to 180°C.[15,51]. Another apparent endothermic peak is observed at 358.8°C due to HPMC thermal decomposition.

Notably, T_g of the carrageenan film is shifted by 42.1% from 37.8°C to 65.3°C after the inclusion of HPMC, indicating a structure modification in the matrix (Table 4). It could be ascribed to the mobility restriction imposed by HPMC added in the carrageenan matrix, thereby reducing the free volume in the film structure.[51] Similarly, this observation of elevated peak was also reported by Barik et al. [52] in the study of shellac-HPMC composite. Generally, a composite film with higher T_g values is desirable due to physical stability for processing and handling qualities. The elevated temperature can also be seen at melting temperature (T_m) of Carra-HPMC composite film when it is shifted by 36.4% from 66.8°C to 105.0°C. Results show that the addition of HPMC increases the enthalpy of melting transition by 50.5% from 151.5 J/g to 306.2 J/g, which represents higher energy required to break the bond between molecules in the matrix.[53] The hydrogen bonding interaction formed between the hydroxyl groups of carrageenan and HPMC has been discussed in FTIR analysis leads to the increment in enthalpy, and subsequently stabilized the composite film.

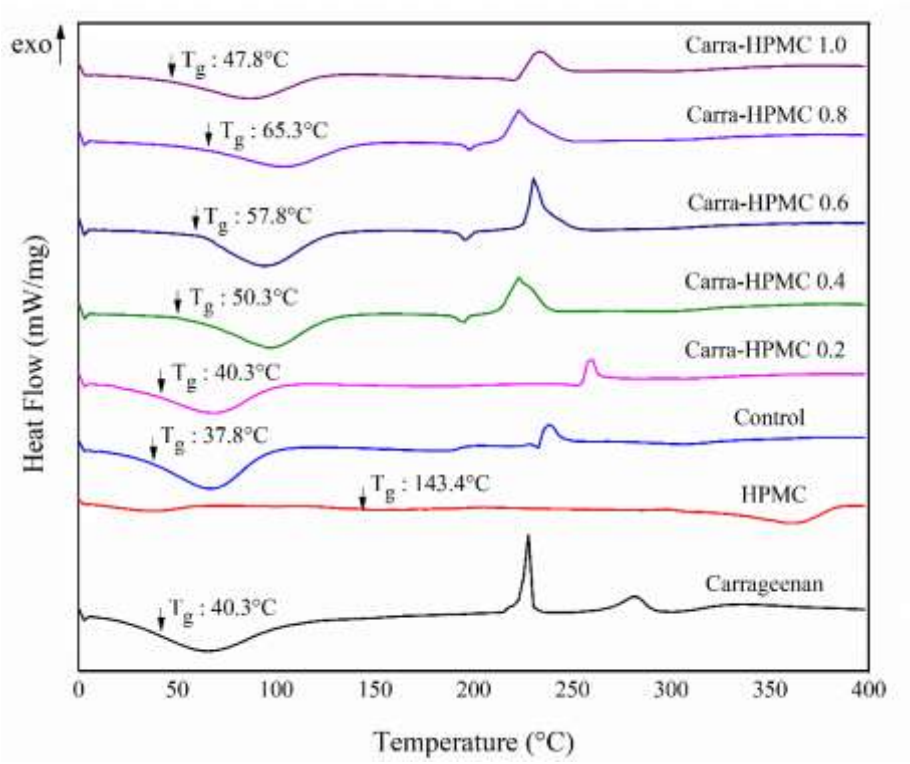


Figure 7. DSC thermograms of carrageenan, HPMC, and films at different HPMC concentration

Table 4. Transition temperatures and enthalpies of carrageenan, HPMC, and films at different HPMC concentration.

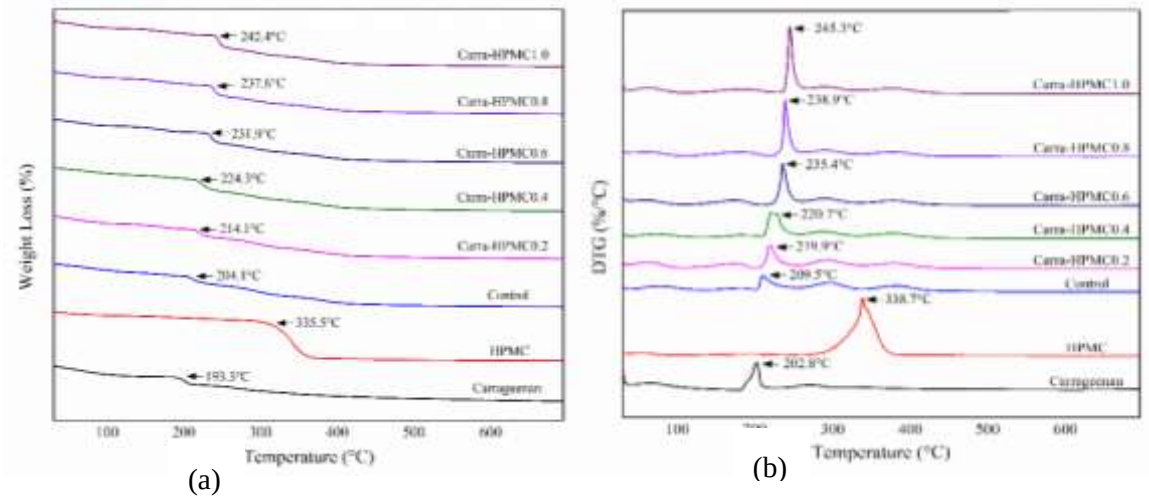
Samples	T_g (°C)	T_m (°C)	ΔH_m (J/g)	T_c (°C)	ΔH_c (J/g)
Carrageenan	40.3	65.3	229.8	227.8	71.6
HPMC	143.4	358.8	179.3	-	-
Control	37.8	66.8	151.5	238.0	79.8
Carra-HPMC 0.2	40.3	74.1	189.2	258.7	49.2
Carra-HPMC 0.4	50.3	96.5	238.8	222.0	152.5
Carra-HPMC 0.6	57.8	95.4	323.7	231.3	183.7
Carra-HPMC 0.8	65.3	105.0	306.2	222.7	137.1
Carra-HPMC 1.0	47.8	86.9	191.5	232.6	72.85

Abbreviations: T_g, glass transition; T_m, melting temperature; ΔH_m, melting enthalpy, T_c, crystallization temperature; ΔH_c, crystallization enthalpy.

3.7.2. TGA analysis

TGA thermograms generally present three stages of thermal effect on the polysaccharide sample during thermal analyses.[54] The first stage is the degradation of volatile components, such as moisture which could be perceived at a temperature of lower than 100°C for all film samples (Figure 8a). The gradual weight loss of less than 30% at this stage indicates that the films start to melt, and free water is removed when heated from ambient temperature to 100°C.[15] The second stage is the volatilization of the plasticizers which occurs between 170°C to 225°C. This approaches to the third stage between 240°C and 275°C, which depicts the decomposition of the carrageenan polymer chain and the crosslinker as reported by Adam et al.[12] Meanwhile, HPMC thermograms show only two stages of weight losses which are around 70°C ascribed for the evaporation of loosely bound moisture and the actual decomposition of HPMC at 335.5°C with 75.3% of weight loss similar to the observation reported by Dharmalingam and Anandalakshmi.[55] It displays a sharp decline in weight due to its degradation followed by a plateau, suggesting no further change in weight.

Derivative thermogravimetry (DTG) curves are also plotted to reflect the peak at which temperature with the maximum weight loss during thermal decomposition (Figure 8b). The major decomposition stage for the control film is increased from 202.8°C to 209.5°C compared to the pure carrageenan film due to a stronger bonding between carrageenan with crosslinker and plasticizer which were included in the matrix. The inclusion of HPMC considerably delays the mass loss during the thermal decomposition, suggesting that HPMC improves the thermal stability of Carra-HPMC film. When compared to the control, the onset temperature of Carra-HPMC0.8 films is shifted to 238.9°C with a 12.3% delay. Higher degradation temperature reflects better film thermal stability. This is attributed to the intermolecular interaction between carrageenan and HPMC in the matrix proven in NMR analysis which also corresponded positively to its higher mechanical properties. The summary of the degradation behavior of different films is tabulated in Table 5 which is extracted from TGA data. Such results indicate that the existence of HPMC retards the egress of water and plasticizer from the film matrix and further supports the notion that HPMC thermally stabilizes carrageenan as the base material to some degree. This positive effect on thermal properties due to the inclusion of cellulose was also claimed in the study on the reinforcement of carrageenan film conducted by Sedayu et al.[54]



(a) (b)

Figure 8. TGA (a) and DTG (b) thermograms of carrageenan, HPMC and films at different HPMC concentration.

Table 5. Thermal degradation behavior of films by TGA analysis.

Samples	Step	Temperature range (°C)	Weight loss at step end (%)	Temperature at maximum degradation rate (°C)	Residues at 700°C (%)
Carrageenan	1	30-200	26.7	202.8	34.3
	2	200-700	39.0		
HPMC	1	30-200	11.0	353.4	9.6
	2	200-700	79.4		
Control	1	30-200	23.2	209.5	21.6
	2	200-700	55.3		
Carra-HPMC 0.2	1	30-200	23.8	219.9	21.6
	2	200-700	54.0		
Carra-HPMC 0.4	1	30-200	20.4	220.7	20.7
	2	200-700	58.9		
Carra-HPMC 0.6	1	30-200	24.1	235.4	19.9
	2	200-700	56.0		
Carra-HPMC 0.8	1	30-200	23.1	238.9	22.5
	2	200-700	54.4		
Carra-HPMC 1.0	1	30-200	22.9	245.3	17.2
	2	200-700	59.9		

3.8 Kinetic analysis by Broido's model

Thermal properties of different films are compared by kinetic analysis of their E_a following Broido's mathematical model. TGA has been recognized to be an effective and reliable tool to study the kinetics and to explicate the thermal stability of materials.[56] Kinetic analysis by Broido's model allows the calculation of E_a from only one TGA curve in contrast to the other kinetic models where they use three or more TGA analyses with different heating ramps. Overall, from all DSC, TGA, and DTG curves, the major decomposition for all films occurred between 200°C to 400°C. Therefore, the E_a is calculated from one major peak at this temperature range. Figure 9 graphically presents Broido's model applied to the thermal degradation of different films.

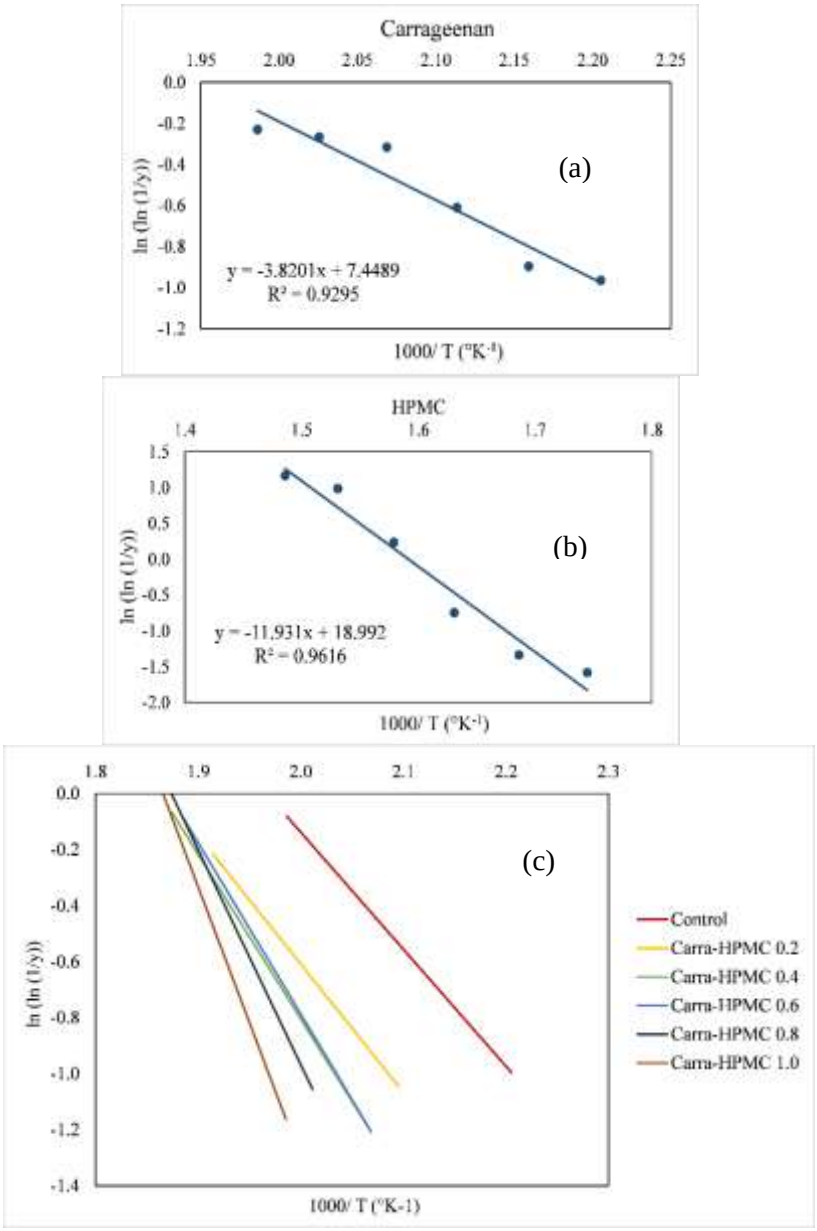


Figure 9. Graphical representation of Broido's plots for degradation of: (a) carrageenan; (c) HPMC; and (c) films at different HPMC concentration.

By using logarithmic non-linear regression, all data present a good fit of Broido's model to describe the thermal degradation with high values of determination coefficient (R^2> 0.8997). The changes of E_a value would occur due to the modification of polysaccharides formulation. As in Table 6, HPMC possesses higher thermal stability since its E_a is higher with 99.2 kJ/mol compared to E_a of carrageenan (31.8 kJ/mol). It is notable that the E_a of Carra-HPMC film is lower than HPMC itself due to the presence of sulphate group of carrageenan as been examined by Jamaludin et al.[57]. The measured E_a of carrageenan is around the similar range (11.0-31.4 kJ/mol) as reported by Valenta et al.,[58] which depends on the heating rate of TGA analysis. The E_a value of HPMC is in agreement with the value (104 kJ/mol) determined by Zaccaron et al.[59] The E_a calculated at the major decomposition peak of Carra-HPMC0.8 thermogram is even higher up to 64.7 kJ/mol with an increment of 43.4%, confirming the positive effect of HPMC on the thermal stability of carrageenan film. The sample with the highest E_a indicates the highest resistance of its molecular structure to

temperature.[58] This effect could be linked to the good dispersion of HPMC in the carrageenan matrix and to the intermolecular interaction between carrageenan and HPMC which increases the E_a and slowed down the film decomposition due to the improved heat distribution within Carra-HPMC film. Based on the E_a values, the thermal stability of the film is in the order of HPMC>Carra-HPMC>control>carrageenan. This sequence corresponds to the previous results proven by DSC and TGA and proven the positive inclusion of HPMC as the thickening and reinforcing agent in the formulation.

Table 6. Kinetic and thermodynamic parameters of thermal degradation by Broido's model.

Samples	E_a (kJ/mol)	A	R^2	ΔS (J/K·mol)	ΔH (kJ/mol)	ΔG (kJ/mol)
Carrageenan	31.8	1.7×10^3	0.9295	-186.9	-3925.3	8.5×10^4
HPMC	99.2	1.8×10^8	0.9565	-93.2	-5109.9	5.3×10^4
Control	36.6	2.7×10^3	0.8997	-183.3	-3976.1	8.5×10^4
Carra-HPMC 0.2	37.7	4.7×10^3	0.9565	-178.7	-4061.5	8.4×10^4
Carra-HPMC 0.4	43.7	1.7×10^4	0.9103	-168.1	-4062.2	7.9×10^4
Carra-HPMC 0.6	54.9	2.5×10^5	0.9504	-146.1	-4173.2	7.0×10^4
Carra-HPMC 0.8	64.7	2.2×10^6	0.9504	-127.9	-4192.5	6.1×10^4
Carra-HPMC 1.0	85.8	2.5×10^8	0.9416	-88.7	-4224.6	4.2×10^4

Abbreviations: E_a, activation energy; A, pre-exponential factor; R^2, coefficient of determination; ΔS, entropy; ΔH, enthalpy; ΔG, Gibbs free energy.

In the thermal degradation process, change of enthalpy (ΔH) is the energy that reflects absorbed or released heat, where the higher values indicate low reactivity, while lower values show high reactivity.[18] The enthalpy changes of all films reported in the table are in negative value which demonstrated an exothermic nature of reaction (ΔH>0, exothermic). These results reflect the exothermic process indicated through the crystallization peak of the films in previous DSC analysis. Meanwhile, the change of entropy (ΔS) relates to the disorder degree of a system.[60] The values of ΔS show that the disorder degree of films through bond dissociations are lower than the initial. The negative values indicate a quite ordered structure of the synthesized complex (ΔS<0, ordered). A lower entropy change indicates a system that is close to its thermodynamic equilibrium and less reactive.[56] On the other hand, Gibbs energy represents the degree of system stability, whereby a change in state occurs spontaneously or not.[56,60] The positive values of ΔG reveals that the thermal degradation of all films is a non-spontaneous process (ΔG>0, endergonic) and difficult to be carried out at the end of the process, subsequently increased the thermal stability of the film.[18]

4. Conclusions

Introducing HPMC in the carrageenan matrix plays a vital role that significantly influenced the mechanical and thermal behaviour of the film. Carra-HPMC0.8 film has demonstrated comparable yet promising mechanical properties in terms of tensile strength, elongation at break, and capsule loop strength, confirming the positive effect of HPMC on the carrageenan film. Tg of Carra-HPMC0.8 film is improved to 65.3°C from 37.8°C of the control film. The apparent Ea of carrageenan film calculated by Broido's model is found to increase by 33.3% from 36.6 to 54.9 kJ/mol. These

remarkable results prove the higher thermal stability of Carra-HPMC0.8 compared to the control without HPMC, which are attributed to the intermolecular interactions between carrageenan and HPMC, being supported by 1H NMR and FTIR analyses. Plant-based materials introduced in this study, which are carrageenan and HPMC offer a better commercial prospect to a wider consumers preference. This distinct advantage over gelatin is a key driver for the development of Carra-HPMC hard capsule on a larger scale. However, the processing steps of preparing these capsules from carrageenan and HPMC need to be improved and modifications should be done to ensure the establishment of hard capsules with higher-level quality and to be comparable to gelatin.

Funding: This research was funded by the Ministry of Higher Education (Fundamental Research Grant Scheme FRGS/1/2019/TK05/UMP/02/2) and Postgraduate Research Scheme (PGRS2003131).

References

1. Augsburger, L.L.; Hoag, S.W. Advances in capsule formulation development and technology. *Pharm. Dos. Forms* **2017**, 1–14.
2. Majee, S.B.; Avlani, D.; Biswas, G.R. Hpmc as capsule shell material: physicochemical, pharmaceutical and biopharmaceutical properties. *Int. J. Pharm. Pharm. Sci.* **2017**, *9*, 1.
3. Hassan, N.; Ahmad, T.; Zain, N.M. Chemical and chemometric methods for halal authentication of gelatin: an overview. *J. Food Sci.* **2018**, *83*, 2903–2911.
4. Adam F.; Hamdan M.A.; Abu Bakar S.H. Carrageenan: A novel and future biopolymer. In *Industrial Applications of Biopolymers and their Environmental Impact*, 1st ed.; Maamun, A.A., Chen, J. Y., Eds.; CRC Press: Boca Raton, Florida **2020**; pp. 225–240.
5. Yadav, M.; Chiu, F. Cellulose nanocrystals reinforced κ-carrageenan based uv resistant transparent bionanocomposite films for sustainable packaging applications. *Carbohydr. Polym.* **2019**, *211*,181.
6. Khalil, H.P.S.A.; Tye, Y.Y.; Saurabh, C.K.; Leh, C.P.; Lai, T.K.; Chong, E.W.N.; Fazita, M.R.N.; Hafiidz, J.M.; Banerjee, A.; Syakir, M.I. Biodegradable polymer films from seaweed polysaccharides : A review on cellulose as a reinforcement material. *Express Polym. Lett.* **2017**, *11*, 244–265.
7. Bagal-Kestwal, D.R.; Pan, M. H.; Chiang, B.H. Properties and applications of gelatin, pectin, and carrageenan gels. *Bio Monomers Green Polym. Compos. Mater.* **2019**, 117–140.
8. Sun, G.; Liang, T.; Tan, W.; Wang, L. Rheological behaviors and physical properties of plasticized hydrogel films developed from κ-carrageenan incorporating hydroxypropyl methylcellulose. *Food Hydrocoll.* **2018**, *85*, 61–68.
9. Hamdan, M.A.; Adam, F.; Mohd Amin, K.N. Investigation of mixing time on carrageenan-cellulose nanocrystals (cnc) hard capsule for drug delivery carrier. *Int. J. Innov. Sci. Technol.* **2018**, *3*.
10. Hamdan, M.A.; Ramli, N.A.; Othman, N.A.; Mohd Amin, K.N.; Adam, F. Characterization and property investigation of microcrystalline cellulose (mcc) and carboxymethyl cellulose (cmc) filler on the carrageenan-based biocomposite film. In *Mater. Today Proc.*, International Conference of Chemical Engineering & Industrial Biotechnology, Kuala Lumpur, Malaysia, 9-11th September 2020; Abdul Rasid, R., Setiabudi, H.D., Eds.; Elsevier Ltd: United Kingdom. **2021**; pp 56-62.
11. Hamdan, M.A.; Najwa, K.; Amin, M.; Hassan, Z.; Jose, R. Tuning mechanical properties of seaweeds for hard capsules : A step forward for a sustainable drug delivery medium. *Food Hydrocoll. for Health* **2021**, 1–39.
12. Adam, F.; Hamdan, M.A.; Hana, S.; Bakar, A.; Yusoff, M.; Jose, R. Molecular recognition of isovanillin crosslinked carrageenan biocomposite for drug delivery application for drug delivery application. *Chem. Eng. Commun.* **2020**, *208*, 741.
13. Adam, F.; Jamaludin, J.; Abu Bakar, S.H.; Abdul Rasid, R.; Hassan, Z. Evaluation of hard capsule application from seaweed: gum arabic-kappa carrageenan biocomposite films. *Cogent Eng.* **2020**, *7*.
14. Jamaludin, J.; Adam, F.; Rasid, R.A.; Hassan, Z. Thermal studies on arabic gum - carrageenan polysaccharides film. *Chem. Eng. Res. Bull.* **2017**, *19*, 80.

15. Owusu-Ware, S.K.; Boateng, J.S.; Chowdhry, B.Z.; Antonijevic, M.D. Glassy state molecular mobility and its relationship to the physico-mechanical properties of plasticized hydroxypropyl methylcellulose (HPMC) films. *Int. J. Pharm.* **2019**, *1*, 100033.
16. Faulhammer, E.; Kovalcik, A.; Wahl, V.; Markl, D.; Stelzer, F.; Lawrence, S.; Khinast, J.G.; Paudel, A. Multi-methodological investigation of the variability of the microstructure of hpmc hard capsules. *Int. J. Pharm.* **2016**, *511*, 840–854.
17. Liu, X.; Ji, Z.; Peng, W.; Chen, M.; Yu, L.; Zhu, F. Chemical mapping analysis of compatibility in gelatin and hydroxypropyl methylcellulose blend films. *Food Hydrocoll.* **2020**, *104*, 105734.
18. Khalil, M.; Alqahtany, F.Z. Comparative studies of the synthesis and physical characterization of ZNO nanoparticles using nerium oleander flower extract and chemical methods. *J. Inorg. Organomet. Polym. Mater.* **2020**, *30*, 3750–3760.
19. Cecci, R. R. R.; Passos, A.A.; Albino, N.R.V; Vicente, D.S; Duarte, A.S.D.; Tavares, M.I.B. Effect of graphene nanoplatelets presence on the thermal and mechanical properties of polypropylene fibers produced by melt spinning. *J. Mater. Sci. Eng. B* **2020**, *10*.
20. Ellis, A.L.; Mills, T.B.; Norton, I.T.; Norton-Welch, A.B. The hydrophobic modification of kappa carrageenan microgel particles for the stabilisation of foams. *J. Colloid Interface Sci.* **2019**, *538*, 165–173.
21. Nemazifard, M.; Kavoosi, G.; Marzban, Z.; Ezedi, N. Physical, mechanical, water binding, and antioxidant properties of cellulose dispersions and cellulose film incorporated with pomegranate seed extract. *Int. J. Food Prop.* **2017**, *20*, 1501–1514.
22. Ramli, N.A.; Ali, N.; Hamzah, S.; Yatim, N.I. Physicochemical characteristics of liposome encapsulation of stingless bees' propolis. *Heliyon*, **2021**, *7*, e06649.
23. Othman, N.A.; Adam, F.; Mat Yasin, N.H. Reinforced bioplastic film at different microcrystalline cellulose concentration. In *Mater. Today Proc.*, 11th Malaysian Technical Universities Conference on Engineering & Technology, Pahang, Malaysia, 19-22nd November 2019; Wan Azmi, W.A., Mahmud, J., Rahman, M., Eds.; Elsevier Ltd, United Kingdom. **2020**; pp 77–82.
24. Wang, J.; Caceres, M.; Li, S.; Deratani, A. Synthesis and self-assembly of amphiphilic block copolymers from biobased hydroxypropyl methyl cellulose and poly(l-lactide). *Macromol. Chem. Phys.* **2017**, *218*, 1–10.
25. Lu, A.; Petit, E.; Jelonek, K.; Orchel, A.; Kasperczyk, J.; Wang, Y.; Su, F.; Li, S. Self-assembled micelles prepared from bio-based hydroxypropyl methyl cellulose and polylactide amphiphilic block copolymers for anti-tumor drug release. *Int. J. Biol. Macromol.* **2020**, *154*, 39–47.
26. Amin, M.; Hussain, M.A.; Aqsa, S.; Bukhari, B.; Sher, M.; Shafiq, Z. Green synthesis and isoconversional thermal analysis of hpmc acetate: A potent matrix for drug delivery. *Cellul. Chem. Technol.* **2017**, *51*, 245–252.
27. Youssouf, L.; Lallemand, L.; Giraud, P.; Soulé, F.; Bhaw-Luximon, A.; Meilhac, O.; D'Hellencourt, C.L.; Jhurry, D.; Couprie, J. Ultrasound-assisted extraction and structural characterization by NMR of alginates and carrageenans from seaweeds. *Carbohydr. Polym.* **2017**, *166*, 55–63.
28. Nasatto, P.L.; Pignon, F.; Silveira, J.L.M.; Duarte, M.E.R.; Noseda, M.D.; Rinaudo, M. Methylcellulose, a cellulose derivative with original physical properties and extended applications. *Polym.* **2015**, *7*, 777–803.
29. Ili Balqis, A.M.; Nor Khaizura, M.A.R.; Russly, A.R.; Nur Hanani, Z.A. Effects of plasticizers on the physicochemical properties of kappa-carrageenan films extracted from eucheuma cottonii. *Int. J. Biol. Macromol.* **2017**, *103*, 721–732.
30. Bodini, R.B.; Guimarães, J. das G.L.; Monaco-Lourenço, C.A.; Aparecida de Carvalho, R. Effect of starch and hydroxypropyl methylcellulose polymers on the properties of orally disintegrating films. *J. Drug Deliv. Sci. Technol.* **2019**, *51*, 403–410.
31. [31] Pacheco-Quito, E.M.; Ruiz-Caro, R.; Rubio, J.; Tamayo, A.; Veiga, M.D. Carrageenan-based acyclovir mucoadhesive vaginal tablets for prevention of genital herpes. *Mar. Drugs* **2020**, *18*.
32. [32] Suksaeree, J.; Nawathong, N.; Anakkawee, R.; Pichayakorn, W. Formulation of polyherbal patches based on polyvinyl alcohol and hydroxypropylmethyl cellulose: Characterization and in vitro evaluation. *AAPS PharmSciTech*, **2017**, *18*, 2427–2436.

33. Chi, W.; Cao, L.; Sun, G.; Meng, F.; Zhang, C.; Li, J. Developing a highly pH-sensitive k - carrageenan-based intelligent fi lm incorporating grape skin powder via a cleaner process. *J. Clean. Prod.* **2020**, *244*, 118862.
34. Aydogdu, A.; Sumnu, G.; Sahin, S. A novel electrospun hydroxypropyl methylcellulose/polyethylene oxide blend nanofibers: Morphology and physicochemical properties. *Carbohydr. Polym.* **2018**, *181*, 234–246.
35. Oh, C.M.; Wan, P.; Heng, S.; Chan, L.W. A study on the impact of hydroxypropyl methylcellulose on the viscosity of PEG melt suspensions using surface plots and principal component analysis. *AAPS PharmSciTech* **2015**, *16*, 466–477.
36. Hiremath, P.; Nuguru, K.; Agrahari, V. Material attributes and their impact on wet granulation process performance. In *Handbook of Pharmaceutical Wet Granulation*, 1st ed; Narang, A.S., Badawy, S.I.F., Eds.; Academic Press: Massachusetts, United States, **2019**; pp 263-315.
37. Abral, H.; Basri, A.; Muhammad, F.; Fernando, Y.; Hafizulhaq, F.; Mahardika, M.; Sugiarti, E.; Sapuan, S.M.; Ilyas, R.A.; Stephane, I. A simple method for improving the properties of the sago starch films prepared by using ultrasonication treatment. *Food Hydrocoll.* **2019**, *93*, 276–283.
38. Kargarzadeh, H.; Mariano, M.; Huang, J.; Lin, N.; Ahmad, I.; Dufresne, A.; Thomas, S. Recent developments on nanocellulose reinforced polymer nanocomposites: A review. *Polymer* **2017**, *132*, 368–393.
39. Munthoub, D.I.; Rahman, W.A.W.A. Tensile and Water Absorption Properties of biodegradable composites derived from cassava skin/poly vinyl alcohol with glycerol as plasticizer. *Sains Malaysiana* **2011**, *40*, 713–718.
40. Nur Hanani, Z.A.; Aelma Husna, A.B. Effect of different types and concentrations of emulsifier on the characteristics of kappa-carrageenan films. *Int. J. Biol. Macromol.* **2018**, *114*, 710–716.
41. Jones, A.; Zeller, M.; Sharma, S. Thermal, mechanical, and moisture absorption properties of egg white protein bioplastics with natural rubber and glycerol. *Prog. Biomater.* **2013**, *2*, 12.
42. Smith, A.M.; Grover, L.; Perrie, Y. Polymer film formulations for the preparation of enteric pharmaceutical capsules. *J. Pharm. Pharmacol.* **2010**, *62*.
43. Fu, M.; Blechar, J.; Sauer, A.; Al-Gousous, J.; Langguth, P. In vitro evaluation of enteric-coated HPMC capsules-Effect of formulation factors on product performance. *Pharmaceutics* **2020**, *12*, 1–17.
44. Fauzi, M.A.R.D.; Pudjiastuti, P.; Hendradi, E.; Widodo, R.T.; Amin, M.C.I.M. Characterization, disintegration, and dissolution analyses of carrageenan-based hard-shell capsules cross-linked with maltodextrin as a potential alternative drug delivery system. *Int. J. Polym. Sci.* **2020**, *2020*.
45. Glube, N.; Moos, L. Von; Duchateau, G. Results in pharma sciences capsule shell material impacts the in vitro disintegration and dissolution behaviour of a green tea extract. *Elsevier* **2013**, *3*, 1–6.
46. Sánchez-González, L.; Vargas, M.; González-Martínez, C.; Chiralt, A.; Cháfer, M. Characterization of edible films based on hydroxypropylmethylcellulose and tea tree essential oil. *Food Hydrocoll.* **2009**, *23*, 2102–2109.
47. Shojaei, M.; Eshaghi, M.; Nateghi, L. Characterization of hydroxypropyl methyl cellulose–whey protein concentrate bionanocomposite films reinforced by chitosan nanoparticles. *J. Food Process. Preserv.* **2019**, *43*, 1–12.
48. Liu, J.; Wang, H.; Wang, P.; Guo, M.; Jiang, S.; Li, X.; Jiang, S. Films based on κ-carrageenan
49. Liew, J.W.Y.; Loh, K.S.; Ahmad, A.; Lim, K.L.; Wan Daud, W.R. Synthesis and characterization of modified κ-carrageenan for enhanced proton conductivity as polymer electrolyte membrane. *PLoS One* **2017**, *12*, 1–15.
50. Shoaib, M.H.; Yousuf, R.I.; Ahmed, F.R.; Ali, F.R.; Qazi, F.; Ahmed, K.; Zafar, F. Polymer coatings for pharmaceutical applications. *Polym. Coatings* **2020**, 275–317.
51. Aydogdu, A.; Sumnu, G.; Sahin, S. A Novel Electrospun hydroxypropyl methylcellulose / polyethylene oxide blend nano fibers : Morphology and physicochemical properties. *Carbohydr. Polym.* **2018**, *181*, 234–246.

52. Barik, A.; Patnaik, T.; Parhi, P.; Swain, S.K.; Dey, R.K. Synthesis and characterization of new shellac–hydroxypropylmethylcellulose composite for pharmaceutical applications. *Polym. Bull.* **2017**, *74*, 3467–3485.
53. Joshi, S.C. Sol-gel behavior of hydroxypropyl methylcellulose (hpmc) in ionic media including drug release. *Material* **2011**, 1861–1905.
54. Sedayu, B.B.; Cran, M.J. Reinforcement of refined and semi-refined carrageenan film with nanocellulose. *Polymers* **2020**, *12*,1145.
55. Dharmalingam, K.; Anandalakshmi, R. Fabrication, characterization and drug loading efficiency of citric acid crosslinked nacmc-hpmc hydrogel films for wound healing drug delivery applications. *Int. J. Biol. Macromol.* **2019**, *134*, 815–829.
56. Ozsin, G. Application of master-plots kinetic method to non-isothermal cellulose pyrolysis and thermodynamic analysis of the pyrolysis process.*BSEU J. Sci.* **2020**, *7*, 313–328.
57. Jamaludin, J.; Adam, F.; Rasid, R.A.; Hassan, Z. Thermal studies on polysaccharides film arabic gum carrageenan. *Chem. Eng. Res. Bull.* **2017**, *19*, 80–86.
58. Valenta, T.; Lapčíková, B.; Lapčík, L. Determination of kinetic and thermodynamic parameters of food hydrocolloids/water interactions by means of thermal analysis and viscometry. *Colloids Surfaces A Physicochem. Eng. Asp.* **2018**, *555*, 270–279.
59. Zaccaron, M.; Oliveira, R.V.B.; Guiotoku, M.; Pires, A.T.N.; Soldi, V. Blends of hydroxypropyl methylcellulose and poly (1-vinylpyrrolidone-co-vinyl acetate): Miscibility and thermal stability **2005**, *90*, 21–27.
60. Çanakçı, D. Synthesis, spectroscopic, thermodynamics and kinetics analysis study of novel polymers containing various azo chromophore. *Sci. Rep.* **2020**, *10*.

Experimental Investigation on The Performance of Phase Change Material (PCM) Incorporated with Solar Water Heating System

Ali Musmar, Obada Dwekat, Taha Karaki and Abdelrahim Abusafa*

Chemical Engineering Department, An- Najah National University. Nablus, Palestine.
Corresponding author: abusafa@najah.edu.

Abstract: This study aims at investigating the thermal energy storage behavior of a solar water heater (SWH) incorporated with solid paraffin as a phase change material (PCM). The proposed PCM container is a novel one and has not been used before up to the author's knowledge. As Latent heat thermal energy storage is known to be one of the most efficient methods to store thermal energy, it is necessary to investigate more efficient, practical, and low-volume storage systems. In this study, the solar water heater was simulated using a 30 Liter cylindrical tank. The PCM is incorporated within the tank in a new innovative method. The solar energy was simulated using variable power heating resistance corresponding to the solar radiation profile in Palestine. The temperature distribution inside the tank and for the inlet and outlet water was measured and recorded using thermocouples connected to a data logger. The performance of the system was observed during the heat charging and discharging process while the heated water flowrate varied between 0.2 and 0.3 L/minute. All the PCM is totally melted during the heating process as an indicator of good heat transfer associated with the proposed configuration. The results show that the hot water supply time increased by 42% more than the conventional system. Also, the system with PCM stores 3139 joules of energy more than the conventional one, which is enough to supply 24.2 liters of hot water.

Keywords: Thermal Energy storage, solar water heaters, Phase change material, Solar water heaters, Phase change material, and Paraffin wax.

1. Introduction

The continuous increase in the level of greenhouse emissions and fuel prices are the key driving forces behind multiple attempts to effectively rely on alternative sources of renewable energy. Storing solar energy has currently become an essential need due to the depletion of fossil fuels and global warming [1].

Thermal energy storage (TES) is used to store thermal energy through heating or cooling. Latent heat storage (LHS) system is one of the effective ways of storing energy in large quantities due to its chemical stability, high energy storage density, and low price. Phase change material (PCM) in the domestic solar water system demonstrates a reliable behavior in storing thermal energy and can be reused at peak periods [2].

Thermal energy is stored and released with changes in the material's phase. The most common phase change to exploit is the solid-liquid transition. As shown in Figure 1, when the PCM is heated initially it behaves like sensible heat energy storage, and the temperature of the material is increased However, once the transition temperature is reached the material will continue to absorb heat at a constant temperature while it changes state. To retrieve the energy the PCM can be changed back from the liquid to the solid phase and the energy stored as latent heat is released [3]

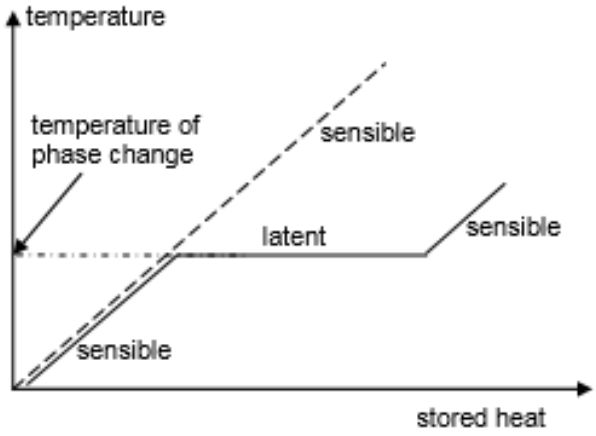


Figure 1 Latent heat storage for solid-liquid phase change *[3]*.

The geographic nature of Palestine plays a significant role in using solar energy. A 3000-sunshine hour per year drives to utilize solar water heaters, therefore 65% of the current water heating energy consumed in Palestine is through solar energy [4].

The average solar irradiation in Palestine is 5.4 kWh/m^2.day. In some areas, the maximum irradiation reaches 8.5 kWh/m^2.day in June while the minimum goes down in December to reach 2.8 kWh/m2 [5].

Unfortunately, the usage of solar water heaters has declined significantly due to the large population growth and the consequent rise of residential buildings in narrow areas. The percentage of households using solar heaters decreased from 75% in 2006 to 66% in 2011 [6], which lead to investigate the performance of using PCM in solar water heaters to increase the efficiency and encouraging people to utilize this combined system

The daily hot water consumption for solar water heaters is an important parameter for determining the necessary sensible heat. Figure 2 illustrates the daily hot water demand for domestic use. The real consumption starts at 7:00 am and finished at midnight; there is no consumption during nighttime from 1:00 am to 6:00 am [7].

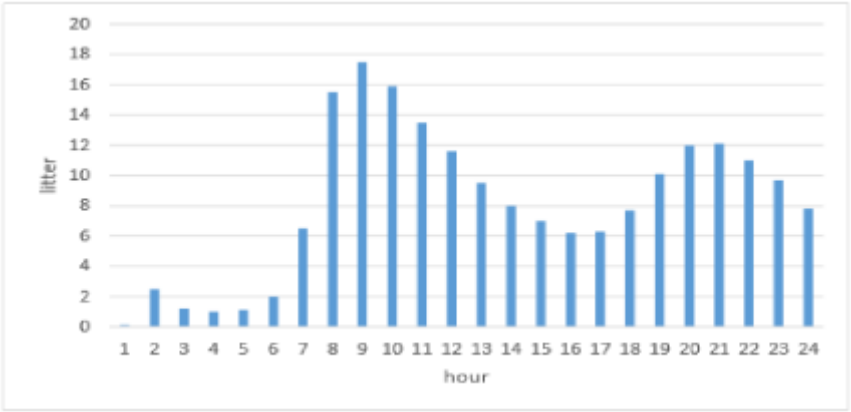


Figure 2. Daily hot water demand for domestic use [7].

2. Literature review

Phase change materials (PCM) absorb or release a large amount of latent heat during the process of transforming physical properties (i.e., the phase transition process). Consequently, PCM has been introduced into solar water heaters to store excess thermal energy and reuse it during peak hours or at evening periods.

Researchers have been conducting and testing PCMs' behavior in different configurations for a long time. Fazilati et al. [8] investigated experimentally the effects of using (PCM) as a storage medium on the performance of a solar water heater. Energy storage density enhanced up to 39%. Also, it was observed that using PCM in the tank improves the time of hot water supply at a specified temperature by 25%. L Mongibello et al. [9]designed a well-developed system for hot water storage system including a macro-encapsulated phase change material (PCM). A 3 litters aluminum bottle was filled with bio-based PCM without any additives, Test carried with, with a constant water mass flow rate through the serpentine of 0.2 kg/s, and with an increment of the water temperature at the serpentine inflow section of 5°C/ (30 min), Two cases were tested in this work, water with PCM and water alone. And the results show that not all the PCM has undergone melting. Additionally, Bhagyalakshmi et al. [10] showed that the effects of using Paraffin and Palmitic acid and the eutectic mixture in a cylinder shell type heat exchanger. A constant water mass flow rate through the tank of 0.2 kg/s. At the end of the period, the water temperature reached 85°C with an initial water temperature of 30°C and results show that not all the PCM was melt. Results show that the eutectic PCM can store energy for a longer period than the base materials. Akgu¨n, et al. [11] investigated the time required for charging and discharging paraffin wax as a PCM medium. They used shell and tube configuration, where the hot water was in the tubes and PCM was placed in the shell side. Nallusamy et al. [12] have investigated experimentally the sensible and latent heat storage systems by using 264 HDPE Capsules paraffin as PCM inserted in a 43 L water tank at 50%volume. Results show that increasing inlet temperature of hot water from 66 to 70°C. decreased charging time from 220 to 160 minute. Kailiang Huang et al. [13] have discussed the enhancement of charging and discharging time for paraffin, inserting a high thermal conductivity material into the liquid PCM considerably. Three tests were performed. Microstructure observation shows that the float stones were immersed by PCM, and it can be assumed it's a mixture of uniformity. Finally, it was found that as the diameter of the container decreased, the time of melting decreased, as the surrounding temperature of the container increased, and the time of melting decreased too. As a final point, the third time of paraffin melting can be reduced by using float stones.

3. Methodology

3.1 Methodology and Experimental Setup:

The main purpose of this work is to enhance the performance of domestic solar water heating systems without design complexity or high costs. Commercial hydrocarbon paraffin wax is used as a phase change material due to its low price, availability, compatibility, melting point of approx. 55 *°C* and its relatively high latent heat. Table (1) shows paraffin physical properties *[8]*

Table 1 Paraffin wax physical properties *[8]*

Melting temperature (°C)	**55**
Latent heat of fusion (kJ/kg])	190
Solid density (kg/m^3)	910
Liquid density (kg/m^3)	790
Thermal conductivity (W/m. °C)	0.21
Solid specific heat (kJ/kg. °C)	2
Liquid specific heat (kJ/kg. °C)	2.15

As shown in Figure 3, a hot water storage tank was used to achieve an experimental study that simulates the real solar heating system. The tank is incorporated with the PCM in a suitable innovative configuration. A variable power electrical heater tank was used to simulate the variable solar energy gained by regular solar collectors. Thermocouples and data loggers were used to measure and record the temperatures of water and PCM at different positions along with the storage tank.

PCM storage tank contains 26 vertical holes of 2 cm diameter distributed regularly around a 5.5 cm diameter central open pipe. The PCM is charged around the tubes while the tubes are open on both sides to allow the water natural flow. This configuration was chosen to give enough heat transfer area and a high heat transfer rate at the same time. Such configuration is believed to overcome the low thermal conductivity of the paraffin wax. This has, to the best of the authors' knowledge, such configuration was not studied before.



Figure 3 photo of the pilot system of the study

Galvanized steel was used as the construction material of the outer storage tank. Galvanized steel is known for its high strength, corrosion resistance, and low cost. Furthermore, Stainless-steel was found to be the preferable choice for the construction of the PCM storage pipes. The details of other materials used are given in Table 2

Table 2 Description of construction material used in the pilot system

Components	Material	Dimensions (mm)
Storage Cylinder	Galvanized steel	250*750
PCM storage	Stainless Steel	230*400
Heater tank	Galvanized steel	150*350
Insulation	Polyurethane	100

The location of the thermocouples (Type K) inside the tank and PCM are shown in Figure 4. The thermocouples are also used to measure inlet and outlet water temperatures.

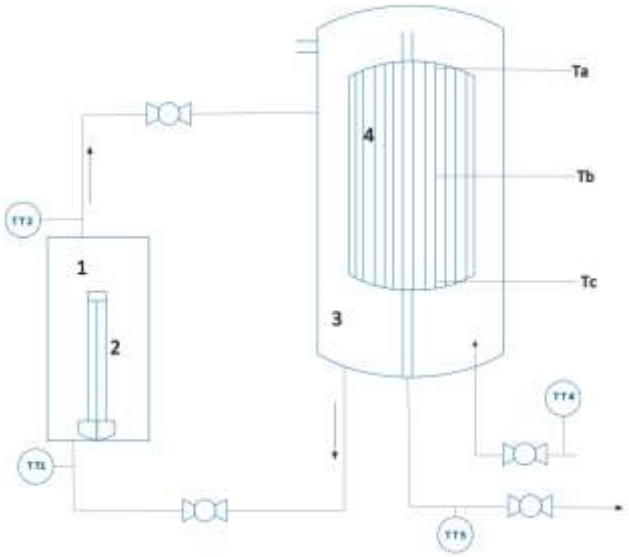


Figure 4 Schematic of experimental setup, (1) Heater tank, (2) 2 Electric heater, (3) Hot water storage tank, (4) PCM storage, (TT1) Thermocouple at water inlet to the heating tank), (TT2) Thermocouple at water outlet from heating tank. (TT4) Thermocouple at water inlet to the storage tank and (TT5) thermocouple at the water outlet from the storage tank. Ta, Tb, and Tc are thermocouples located inside the PCM ((Ta: 5cm, Tb: 28cm, and Tc: 55 cm from tank top)

Several experiments have been conducted to test the system performance under different heating rates and water flowrates. The heating rate input by the electrical heater was varied between 700 and 900W. These values are corresponding to a typical solar heating flat plate. On the other hand, the water flowrate was varied between 0.25 - 0.3 (L/min) which is like domestic hot water demand. The experiments were categorized as charging and discharging modes energy-wise, continuous, and batch Waterflow-wise.

3.2 Charging mode

The charging mode tests were performed by heating the water inside the tank using the auxiliary electrical heating tank. during the charging period, the heater is turned on at a constant heating rate until

all the PCM is melted. The charging mode was also categorized to batch and continuous waterflow-wise.

Batchwise means there is no water flow in or out of the storage tank. this test simulates the state of standby mode where no water is consumed. The continuous mode was used to simulate the instantaneous heating and water consumption. The system was also tested under conventional conditions where no PCM is used.

3.3 Discharging mode

This mode is designed to simulate the night condition where there is no heating but there is hot water consumption. of course, this mode is in succession to the charging mode.

3.4 Temperature profiles inside the tank

Stratification inside the tank is a natural phenomenon due to the dependency of water density on temperature. Thus, the thermocouples inside that tank were located at different levels (see Figure 4) and observed to assure the steady-state conditions if necessary.

3.5 Cumulatively stored energy calculations

To see the effect of adding the PCM, the cumulative energy was calculated for both conventional and PCM incorporated system for both modes. For this purpose, the flowing equations were used to calculate the stored energy.

$$Ki = m \times cp \times (Tout - Tin) \times ti \quad (1)$$

Where:

Ki: Cumulative energy (Joule)

M: Water flowrate (L/min)

Cp: Water heat capacity assumed (4.18 J/kg. ℃)

T_{out}: Water outlet temperature from the storage tank (℃)

T_{in}: Water inlet temperature (℃)

ti: Time interval for reading T_{out} (5 min in this study), Tin was kept constant.

$$En = K_i + K_{i+1} \quad (2)$$

$$\Delta E = En - En' \quad (3)$$

En: Cumulative Energy in combined heat system (joule)

En': Cumulative Energy in conventional System (joule)

Stored energy and water supply time were the main parameters that were used to verify the system's superiority.

4. Results and discussion

4.1 Charging mode

4.1.1 PCM temperature in Batch-wise and continuous stages:

Figure 5 represents the PCM temperature vs. time during heating the system incorporated with PCM. The heating process was performed at both 700 and 900 W heating rates at the batch-wise process. Obviously, at both heating rates, the PCM starts melting at 53 °C while the PCM temperature starts to increase abruptly after 200 minutes of heating. These findings are consistent with the regular melting behavior of such materials. Similar behavior with a slower temperature increasing rate was observed when a continuous system was used. As clearly can be seen from Figure 6., for batch mode 320 and 240 min were needed to melt the PCM at 700 and 900 W, respectively. on the other hand, for the continuous process at water flowrate of 0.27 L/min, 510 and 410 min were the time need to totally melt the PCM at 700 and 900 W, respectively.

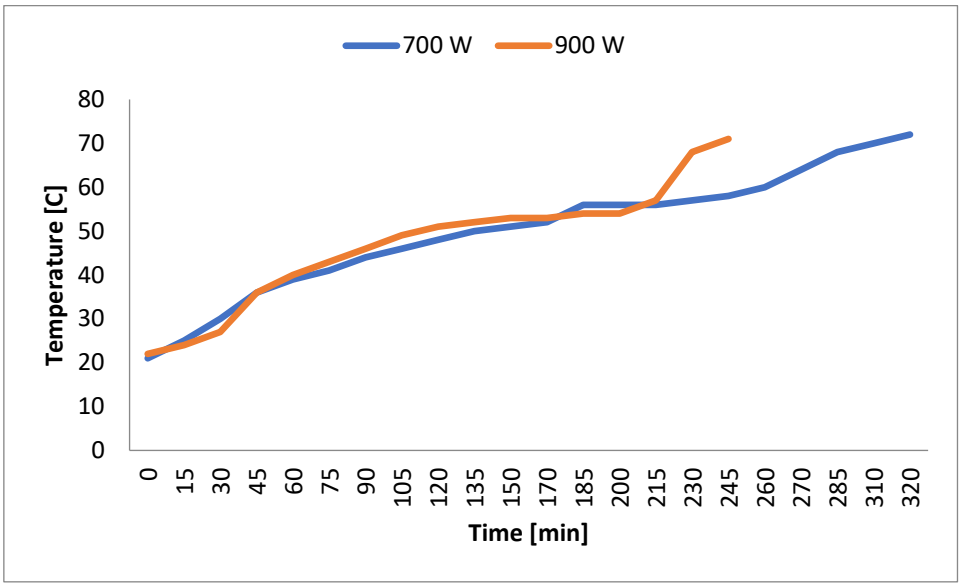


Figure 5 PCM temperature during charging in the batch-wise stage

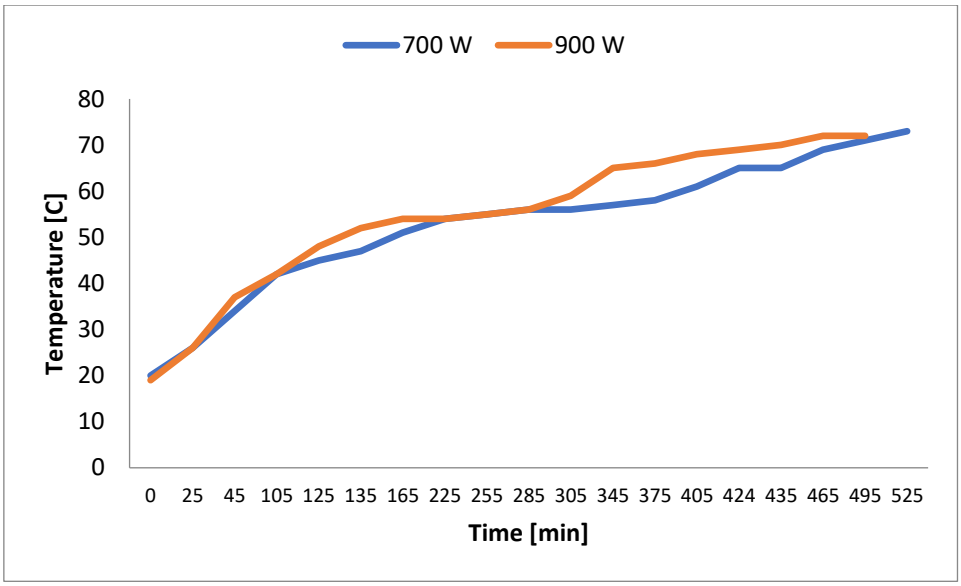


Figure 6 PCM temperature during charging in the continuous stage

4.1.2 Water temperature during batch-wise stage:

In a conventional solar water heater, the hot water is drained out from the top layer of the tank that has the highest temperature. Thus, to test the performance of these systems, it is necessary to measure the top tank temperature during experimental work. Figures 7 and 8 represent the top tank temperature for batch-wise systems. As in figure 7, the top temperature of the system with PCM took more time than the conventional system due to the larger energy stored within the PCM. This is a rational fact that using PCM will help in reducing the volume of the storage tank without compromising the stored energy. To have a penetrative view, some numerical data are presented in Table 3 to compare between PCM incorporated and conventional systems at two heating rates.

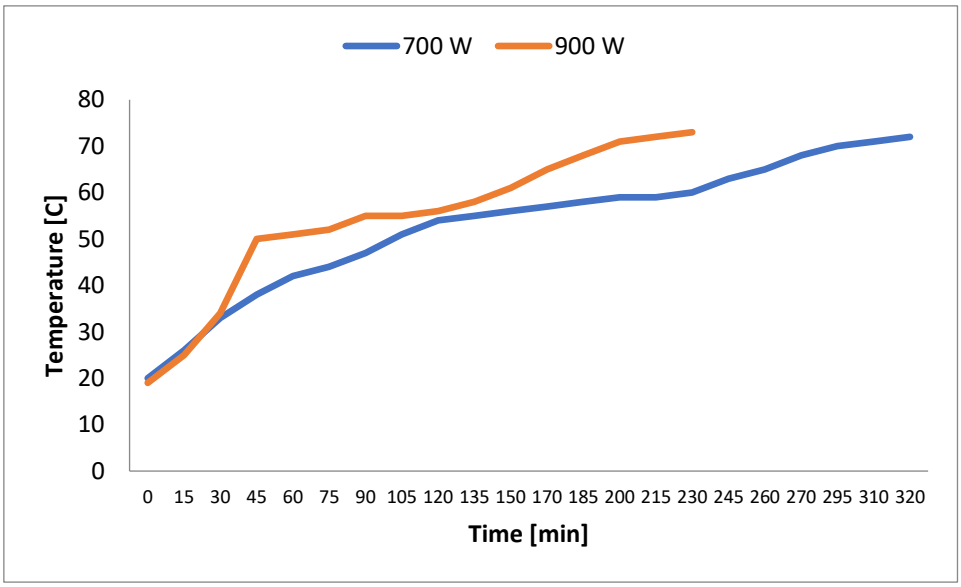


Figure 7 Water temperature during charging in the batch-wise system with PCM

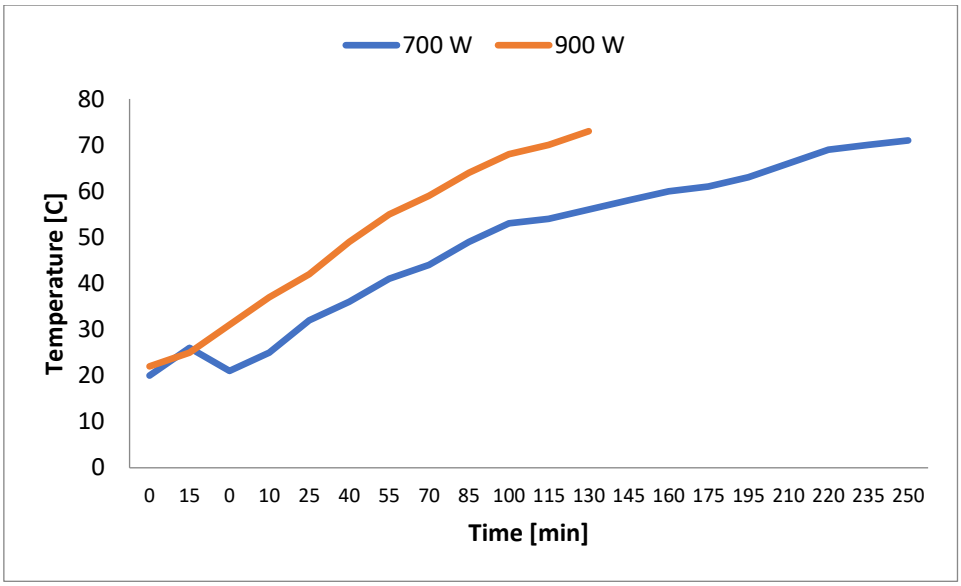


Figure 8 Water temperature during charging in Batchwise stage (conventional)

Table 3 Detailed numerical data for Figure 7 and 8

System type	Power input (W)	T_{in} (℃)	T_{out} (℃)	Heating time (min)
Conventional	700	20	72	250
	900	19	73	160
With PCM	700	20	72	320
	900	19	73	230

4.1.3 Water outlet temperature during continuous stage:

The continuous phase is the process that mimics the real-life use of the solar water heater. During this process, the heater is turned on while the water is allowed to flow in and out of the storage tank figure 9 shows the smoothness of the water temperate of the effluent water due to the existence of the PCM. A moderate temperature is observed at both heating rates. A longer time was observed to get temperatures higher than needed. The process shows the role of PCM in storing excess energy that can be used late in the nighttime. Contradict, the convention system shows a rapid increase in temperature in a shorter time indicating the less energy stored as a sensible one as in Figure 10.

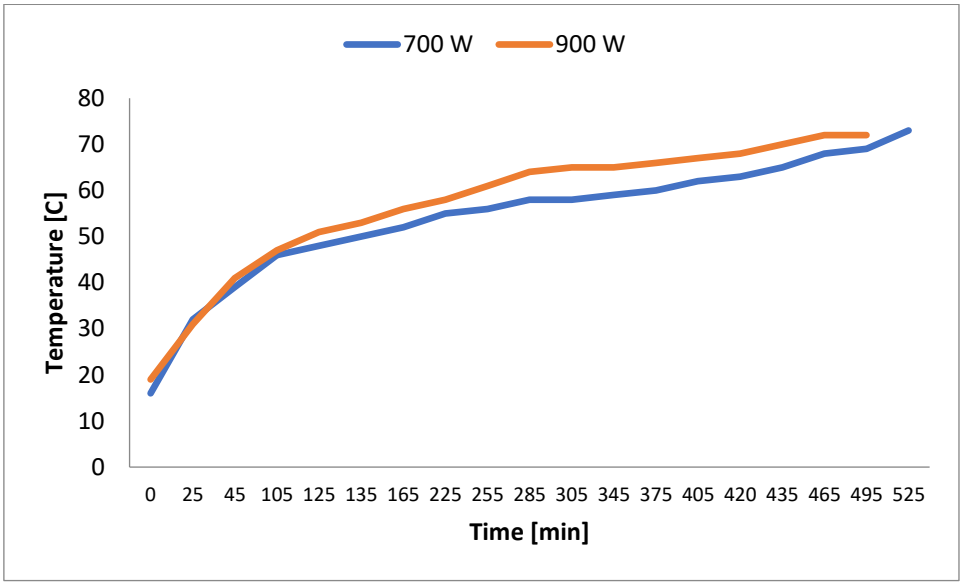


Figure 9 effluent Water temperature during charging of PCM incorporated tank

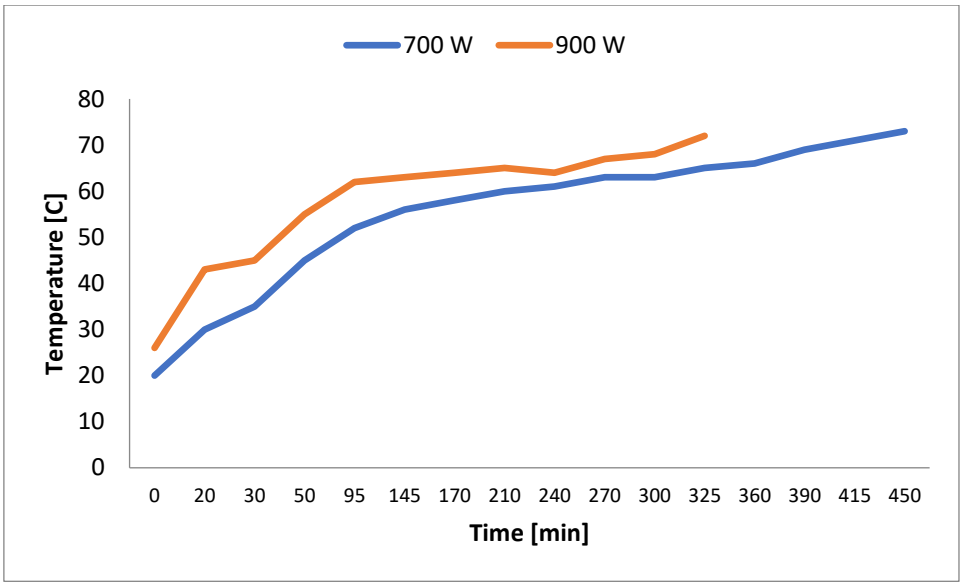


Figure 10 Water outlet temperature during charging in continuous stage (conventional)

4.2 Discharging process:

The discharging process is the real process that asses the performance of the used system, this stage is exactly what happens after sundown. To have a more understandable look, one should compare the conventional system and the PCM system after charging both systems to a certain temperature. During discharging, water flow continuously into the system at a rate of 0.27 (L/min), with a temperature of 20°C. The effluent temperature is recorded for both systems as in Figure 11. Clearly can be noticed the rapid depletion of the energy stored in the conventional system where the system is exhausted to 40 °C in 210 min, while the PCM system continued to give usable hot water 90 min more. By ease calculation, the PCM system gives a %42 longer time than the conventional system at the same conditions.

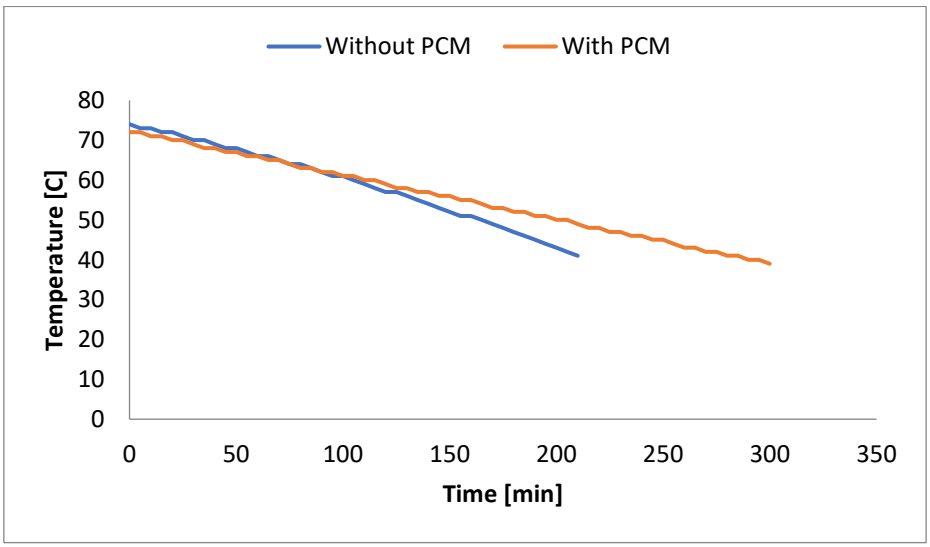


Figure 11 effluent Water Temperature during discharging stage for conventional (without PCM) system and PCM system.

4.2.1 Temperature profiles along the Storage tank:

During the continuous process, cold water is fed from the bottom of the tank and hot water is drawn out from the tank top to reserve the natural buoyancy phenomenon. Measuring the temperature at different layers in the tank could give constructive information regarding the heat transfer rate inside the system. Figure 12 shows the temperatures at three different levels inside the PCM tank (see Figure 4). The thermocouple Tc is located exactly below the PCM container and measures the water temperature there. It is noticeable that this layer of water losses temperature rapidly since the system below this point possess only sensible heat. At the same time, the water temperature approximates the tank top temperature at point b. The thermocouple b measures the temperature in the water layer at the middle of the PCM container. This is clear evidence of a sufficient heat transfer rate between the PCM and water in the vicinity.

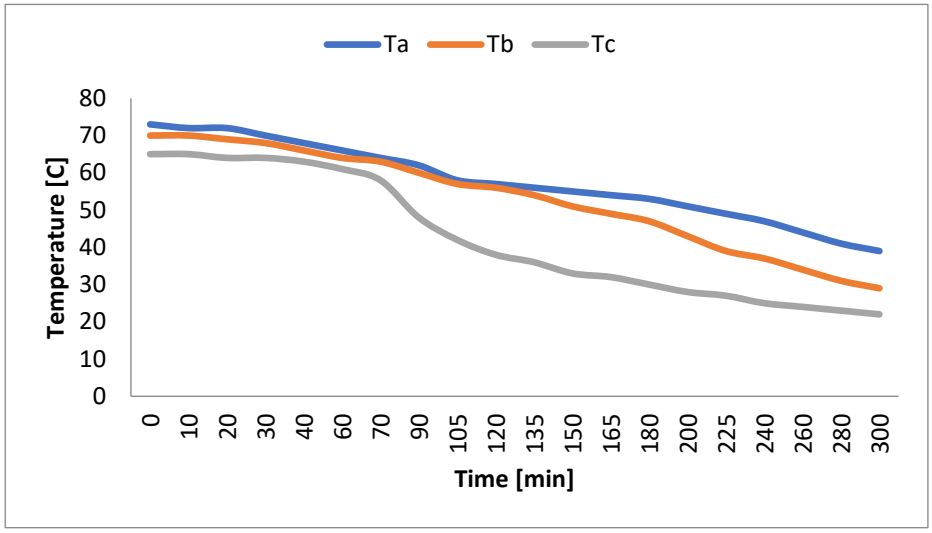


Figure 12 Temperature distribution along the tank at discharging period with PCM

4.2.2 Effect of flowrate on effluent water temperature for PCM system

Doubtless, the flow rate of water in the tank affects the rate of heat transfer from the PCM to the vicinity water. Higher water flow rates mean less retention time and nonsufficient time for transferring heat to the water. Figure 13 gives a good comparison between water temperature at different water flowrates. The higher the water flow rate the rapid depletion of stored energy consequently the water temperature. At 0.45 (L/min) water flow rate, it took 155 minutes for the effluent water temperature to decrease from 74 to 39 ℃. on the other hand, 300 minutes was the time needed for water temperature to drop from 74 to 39 ℃, at water flowrate of 0.27 L/min. it can be concluded that water flowrate plays a very important role in the performance of such systems and should be studied carefully.

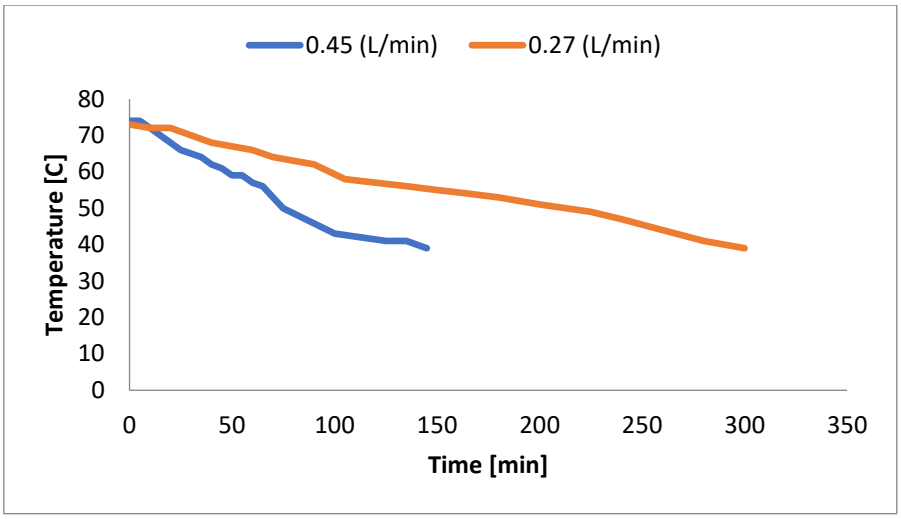


Figure 13 Effect of water flowrate on water temperature for PCM tank.

4.3 Cumulatively stored energy

To have a better insight into the performance of PCM systems, it is preferable to calculate the stored energy and compare it with the conventional one. Such a comparison will be good enough for engineers to design the required storage tank and to determine the optimum ratio of the PCM. To do that, the cumulative energy stored in the two mentioned systems is plotted in Figure 14 by measuring the water inlet and outlet temperature till the effluent water temperature dropped to 40 ^{o}C. Using the aforementioned equations, it was found that the system containing the PCM shows higher stored energy of 3139 J more than a conventional system. This energy is enough to give 90 min of usable hot water at the same water flow rate. also, this excess energy is sufficient to heat 24.2 L of water to 40°C.

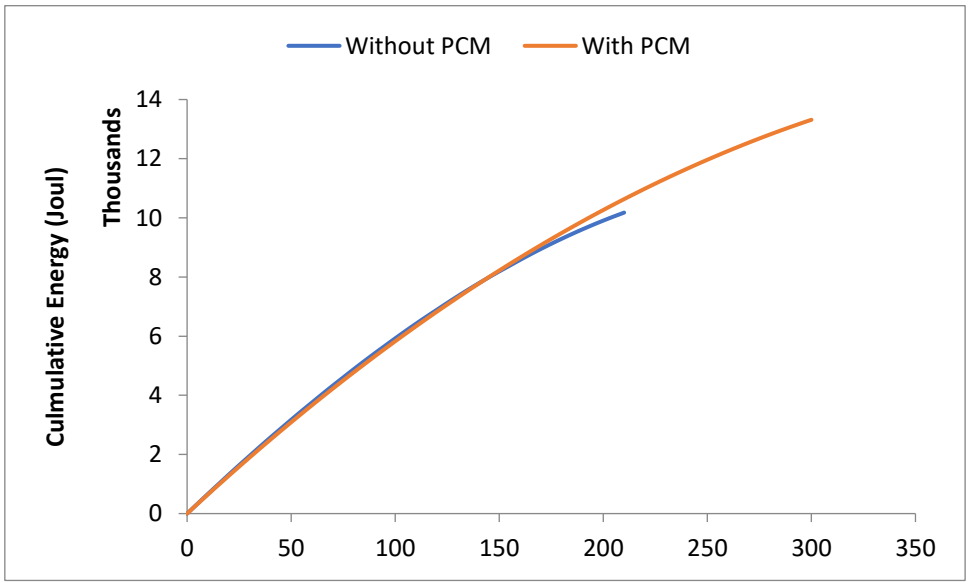


Figure 14 comparison between the conventional and PCM system regarding the stored energy.

5. Conclusion

This study aims at designing, constructing, and testing a solar water storage tank incorporated with a PCM container. The container design is novel and is used for the first time up to author knowledge. The experimental work was done by varying the power input and water flow rate. Moreover. the system was run under batch-wise and continuous modes through the charging process. The proposed model of hot water storage tank incorporated with PCM shows superiority to the conventional one under all studied conditions. The proposed configuration has enough heat transfer area and more stored energy. Heat transfer deficiency was noticed only at a very high-water flowrate. The used system gave more hot water at night mode at the desired water temperature. The extra stored energy was enough to give continuously hot water for 90 min more than the conventional system at the standard demand water flowrate.

Water temperature profiles along the storage tank have also been studied. The obtained data from the temperature profile along the tank grave more clear information about the heat transfer rate inside the system. It showed that the water has enough retention time to get the desired temperature before the water reaches the top of the tank.

Acknowledgement

The authors gratefully acknowledge the financial support of the Palestinian council for innovation and excellence, and the Palestinian incubator for energy.

References

[1] "Climate Change - driving force," [Online]. Available: https://ec.europa.eu/eurostat/statistics-explained/index.php/Climate_change_-_driving_forces. [Accessed 9 January 2021].

[2] L.F. Cabeza, I. Martorell, L. Miró, A.I. Fernández, C. Barreneche, "Introduction to thermal energy storage (TES) systems," in *Advances in Thermal Energy Storage Systems*, L. F. Cabeza, Ed., Woodhead Publishing, 2015, pp. 1-28.

[3] E. Barbour, "Energy Storage Sense," 2013. [Online]. Available: http://energystoragesense.com/thermal-energy-storage/. [Accessed 4 october 2020].

[4] Adel Juaidi, Francisco G. Montoya, Imad H. Ibrik, Francisco Manzano-Agugliaro, "An overview of renewable energy potential in Palestine," *ELSEVIER,* vol. 65, pp. 943-960, 2016.

[5] A. R. Isam Ghanem, "Pre Master Plan Solar Energy Production in Palestine," Palestinain Enviromental NGOs Network, Palestine, 2016.

[6] W. Agency, "Solar Water System in palestine," 22 March 2014. [Online]. Available: http://info.wafa.ps/. [Accessed 25 September 2018].

[7] M. A. Arrah, "Efficiency Improvement of Solar," An-Najah National University, Nablus, 2017.

[8] Mohammad Ali Fazilati, Ali Akbar Alemrajabi, "Phase change material for enhancing solar water heater, an experimental approach," *Energy Conversion and Management,* vol. 71, no. 138-145, 2013.

[9] M. A. N. B. M. D. S. G. G. a. N. R. L Mongibello, "Experimental test of a hot water storage system including a macro-encapsulated phase change material (PCM)," in *34th UIT Heat Transfer Conference 2016*, Italy, 2016.

[10] K. R. K. S. K. S. S. R. Pasam Bhagyalakshmi, "EXPERIMENTAL STUDY ON SOLAR ENERGY STORAGE IN PHASE CHANGE MATERIALS USING CYLINDRICAL SHELL TYPE HEAT EXCHANGER," *ARPN Journal of Engineering and Applied Sciences,* vol. 13, 2018.

[11] O. A. K. K. Mithat Akgün, "Experimental study on melting/solidification characteristics of a paraffin as PCM," *Energy Conversion and Management,* vol. 48, no. 2, pp. 669-678, 2007.

[12] S. S. R. V. N. Nallusamy, "Experimental investigation on a combined sensible and latent heat storage system integrated with constant/varying (solar) heat sources," *Renewable Energy,* vol. 32, no. 7, pp. 1206-1227, India.

[13] L. D. F. G. J. M. Z. Y. L. X. J. B. Huang K, "Macro-Encapsulated PCM Cylinder Module Based on Paraffin and Float Stones," *Materials,* vol. 9, no. 5, p. 361, 2016.

Experimental Study of Hydrodynamic Behavior with Mono-particles of Glass Beads in Three Phase Fluidized Bed Reactor-Part I

Omar S. Mahdy *, Amer A. Abdulrahman and Jamal M. Ali

Department of Chemical Engineering, University of Technology, 52 Alsinaa St., P.O. Box 35010, Baghdad, Iraq.

***** *Corresponding author: omarsabaah@yahoo.com; Tel.: +9647710582008.*

Abstract: In the present study the hydrodynamics parameters of the fluidized bed were analyzed. The study undergoes the co-current gas-liquid-solid three-phase fluidized bed, utilized the liquid as the continuous phase, gas as the discontinuous phase and glass beads with diameter of (0.003, 0.004, 0.005 and 0.006) m with density of 2500 kg/m^3 were used as solid phase. Pressure drop, bed expansion, minimum fluidization velocity and individual phase hold-up had been investigated as hydrodynamic parameters. Response surface methodology with central composite design was used to determine the effect of two variables (superficial liquid and gas velocity) on the response (pressure drop, gas holdup and bed expansion). The experiments were carried in a Perspex cylindrical column with diameter of 0.0115 m and 1.7 m height occupied with liquid distribution plate to support the bed. Five pressure sensors transducers were fitted on fluidizing column with specific spaces to estimate the pressure drop throughout the bed. All experiments were completed under liquid superficial velocities varied 0.013-0.08 cm/s with respect to air superficial velocity ranging 0-0.17 cm/s for each size of glass beads. It was recorded that; the liquid superficial velocity and the diameter of the beads have an effect on the pressure drop. It's varied with the liquid velocity before fluidization, then it's effect almost disappear and pressure drop become constant when fluidization occurs. The size of solid beads has great influence on the minimum fluidization velocity, as the bed of smaller beads diameter required low minimum fluidization velocity value and it became greater when the diameter of beads increased. The expansion ratio linked to the liquid and gas superficial velocities in direct relationship, while this relation becomes in invers proportional with respect to the bead's diameter. As the gas velocity increased, the gas holdup increased and decreased with increasing in liquid velocity, while the holdup of liquid followed the opposite pattern. The experimental results and those predicted by the response surface models were in good agreement, indicating that the proposed models are applicable.

Keywords: Three-phase fluidization; Hydrodynamics; pressure drop; Holdups; Response surface methodology.

1. Introduction

Fluidization phenomenon is a process happened when solid particles are behaved like fluids that make the solid particles suspended in fluid media. The fluid-solid contact techniques utilized to suspend the solid particles [1]. The drag force produced on the solid particles as a result of fluid-liquid and/or gas- flow of in opposite direction to gravitational force is essential aspects to develop the fluidization phenomenon. The large and significant contact between the fluid and solid particles generated in this phenomenon provides important advantages for wide range of scientific and industrial applications [2]. Due to its industrial relevance, three-phase fluidization has been the focus of fundamental research for the last four decades. Many industrial processes have been successfully applied to three-phase fluidized beds, such as the H-oil process for residual oil hydro-desulfurization and hydrogenation, the H-coal process for coal liquefaction, the Fischer-Tropsch process, and the bio-oxidation process for waste water treatment. In several industries, the three-phase fluidized bed is desired because of easy construction and design, high rates of mass transfer as a result of good mixing [3-6]. The fluidized beds'

efficient scale-up, design, and development depend primarily on the accurate system behavior prediction and features such as gas holdup. Many researchers have made valuable contributions over the years to the holdup of gas in fluidized beds [7-14]. For the effective operation of gas-liquid-solid fluidized beds, accurate prediction of a minimum liquid fluidization condition is important particularly when the properties of particles or liquids are concerned [15]. Many researches have been published in three phases on the minimum velocity of fluidized beds [15-20]. Several minimum fluidization velocity studies in three-phase fluidized beds are applied to air-water glass bead systems whose particle density is 2 to 3 times greater than that of the liquid [21].

Most researches deal with the characteristics of phase holdup, as well as the bed expansion. Researchers have been particularly interested in the bed's contraction behavior, bubble and wake characteristics, and the distribution of flow regimes in the bed (Begovich & Watson) utilized three phase (gas-liquid- solid) fluidized beds with two columns of diameter 7.62 and 15.2 cm, in order to determine the minimum fluidization velocity as a function of liquid viscosity, particles density and size [4]. (Brien et. al.) investigated the minimum liquid fluidized velocity for three phase fluidized bed with low density solid particles estimated dependent on the bed pressure gradient and local conductivity [18]. (Ramish et.al.) By taking advantage of the recorded data from 209 experiment was conducted with co-current three-phase fluidized reactor, an empirical correlation, with a wide range of variables and with various gas hold up fractional, was suggested to estimate the minimum fluidization velocity in two and three phases [7]. (Abdul Rahman et. al.) by using wide range of particle sizes, investigated the solid properties and solid loading of both single and binary mixtures on the gas holdup and the dynamics of bubbles in fluidized bed column of diameter 15 cm [22]. (Sulaymon, et. al.) investigated the hydrodynamic specification of non-Newtonian, three-phase fluidized beds. Such as, the velocity of raise bubbles, minimum fluidization velocity, gas- holdup, and the superficial gas velocity. The experimental work was performed in QVF glass column with inner diameter of 10.6 cm and 200 cm height. Dimensionless groups correlation with and independent parameters with correlation coefficient is 0.9929was suggested to estimate the gas holdup [16]. (Pare) discovered that as gas velocity increases, the bed pressure drop and minimum fluidization velocity decreases. The bed expansion ratio rises as the liquid's values rise, while it falls as dp and the initial static bed height rises [11]. (Li, et. al.) The fluidization parameters of two (gas-solid) and three phase(gas-liquid-solid) for nonfluidized beds (MFBs) were experimentally studied based on the evaluation of visual observations and pressure drop in the bed [15]. (Kumar, et. al.) The liquid phase consisted of an electrolyte from the ferriferous redox system. As fluidizing solids, glass balls of various diameters were used, with nitrogen as the gas phase. Measured bed height was used to calculate bed porosity. Data on pressure drop was used to compute gas holdup. The sum of gas and solid hold up was subtracted from unity to obtain liquid hold up [23]. Visually or from the estimated pressure drop gradient, the expanded bed height can be determined [24]. The researchers employed statistical experimental design methodologies. The experimental design technique is a highly valuable tool for understanding the interaction among the factors and building statistical models, and it specifies the condition under which the process parameters have been optimized [25]. Response Surface Methodology (RSM) is the most appropriate among the various design methodologies. Even in the presence of complicated interactions, RSM will be used to analyze the relative effect of several affecting variables. RSM is used to determine the system's optimal operating conditions or to define a section that fits the operation condition [26]. As well to analyzing the effects of the independent variables on response, in addition, the experimental methodology develops a mathematical model which describes the process. The gas holdup value is determined by the interaction of many parameters, including the superficial gas velocity, the physical properties of the liquid phase (such as viscosity, density, and surface tension), the column cross section, particle diameters, and particle densities [22].

For three phase system the relationship between phase holdups is represented by the following expressions [27]:

$$\varepsilon_S + \varepsilon_L + \varepsilon_g = 1 \quad \text{.....1}$$

The average holdup of solids can be measured using:

$$\varepsilon_S = M_S / \rho_S \; A_C \; H_e \quad \text{.....} \quad 2$$

While, A_c is the cross-sectional area of the column; H_e is the expanded bed height; M_s, is the solid mass of the column. In the absence of frictional pressure drop, the static pressure gradient is expressed as:

$$\Delta P/H_e = g\ (\rho_g\ \varepsilon_g\ +\ \rho_L\ \varepsilon_L\ +\ \rho_S\ \varepsilon_S\ )\ \ \ldots\ldots\ldots\ldots\ldots\ldots 3$$

Equations (1) to (3) could be used for the calculation of individual holdups in equations (2) and (3), the bed height is determined visually.

2. Experimental Work

The experimental study was carried out to the hydrodynamics and the interaction between different phases of liquid, gas, solid. In addition, the effect of the superficial liquid velocity, superficial gas velocity and solid- particles diameter on the minimum fluidizing velocity, pressure drop, bed expansion and individual phase hold up in fluidized bed column. All experiments were completed in three phase fluidization bed unit as shown in figure (1). Different size of uniform shape of glass beads with diameters ranging (0.003, 0.004, 0.005 and 0.006) m and density of 2500 kg/m^3 utilized to represent the solid bed systems, while water as liquid phase and air as gas phase. Table 1, listed the scale of the experiments in present study.

The fluidized column designed and formed from two main parts, first: the test section and the second: the distributor of the gas-liquid that also used to support the glass beads. A vertical cylindrical Perspex column with an inner diameter of 0.115 m and a height of 1.7 m is represented the main component of the test unit, that in which the fluidization process occurs. Table 2 listed the mean part of test unit.

Table 1: Experimental data set in the present study.

Materials	**d_p (m)**	**p_p (kg/m^3)**	**Initial static bed height (m)**
Properties of bed materials			
Glass beads	0.003	2500	0.12
Glass beads	0.004	2500	0.121
Glass beads	0.005	2500	0.123
Glass beads	0.006	2500	0.126
Properties of Medium Fluidizing			
Materials	**p (kg/m^3)**	**μ(pa.s)**	**superficial velocity(m/s)**
Air at 30 ˚C	1.187	0.0000181	0.0-0.10
Water at 30 ˚C	997.15	0.000891	0.0-0.17

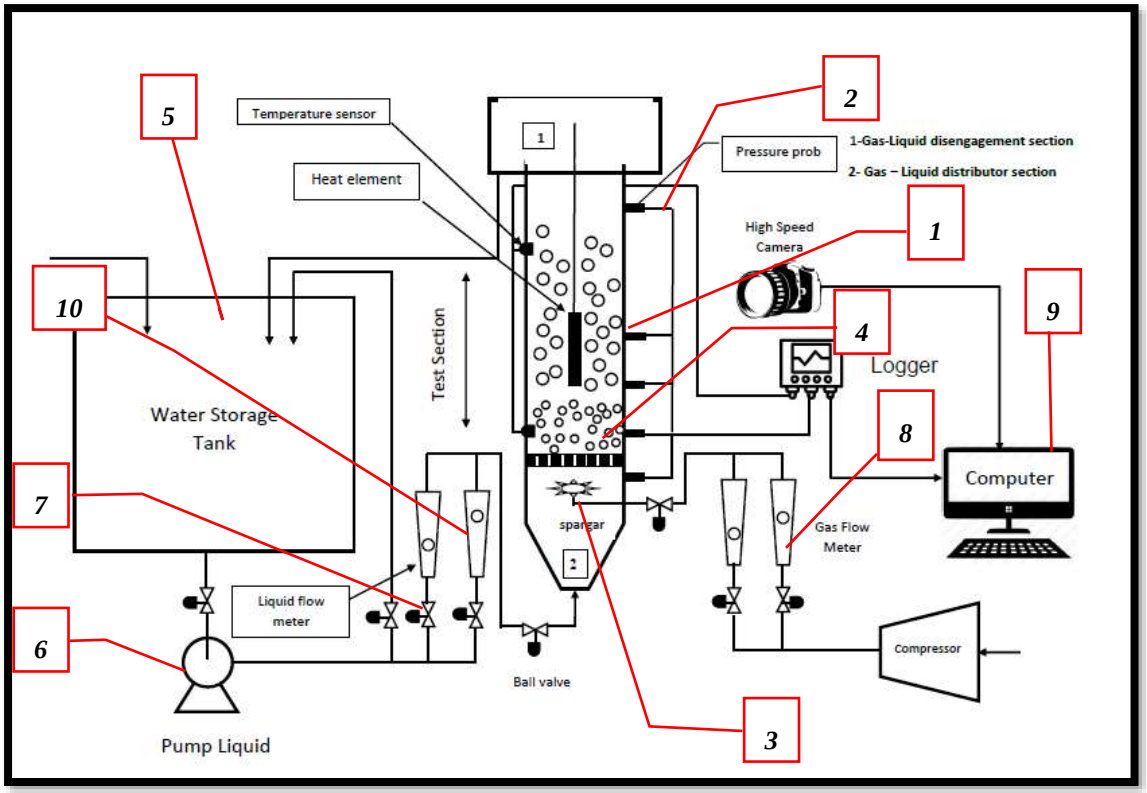


Fig.1: Schematic diagram of the experimental unit

Table 2: Mean part of test unit.

Item No.	Description
1	Fluidized column diameter 0.115m
2	Pressure transducer
3	Air sparger
4	Glass beads bed diameter (0.003, 0.004 ,0.005, and 0.006) m
5	Tank of liquid (water) capacity 0.1 m^3
6	Water pump
7	Liquid flow control valve
8	Gas flow meter
9	Laptop for data record
10	Liquid Flow meters

The distributor made of Perspex sheet of 0.004 m thickness is fixed at first lower quarter of column. The distributor plate was directly designed from the theory of orifices (Kunii) [28]. It designed in order to join the two parts of the test section, further more to support the beads of the bed. The plate was drilled with a (274 holes) of diameter equal to (2 mm) to provide the warranty of the uniform distribution of the liquid-gas mixture flow through all the bed. The liquid distributor's shape and dimensions are highlighted in figure 2 and listed in table 3.

Table 3: Properties of liquid Distributor

Distributor	Holes Dia. (mm)	No. of Holes	Free Surface area (%)
Perforated Perspex	2	274	8.3

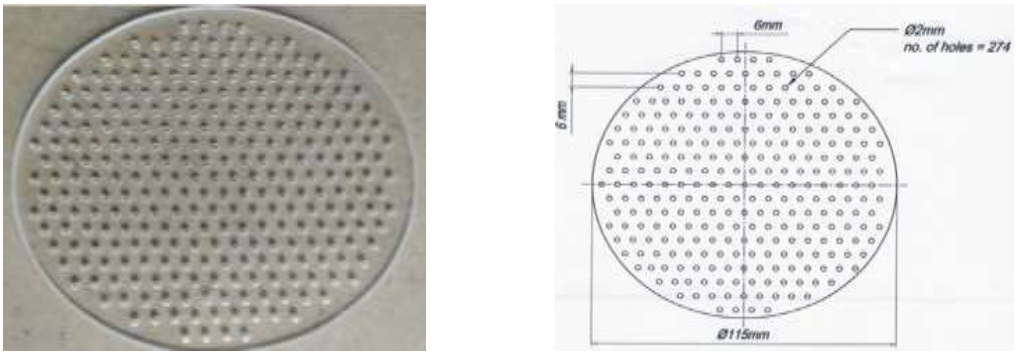
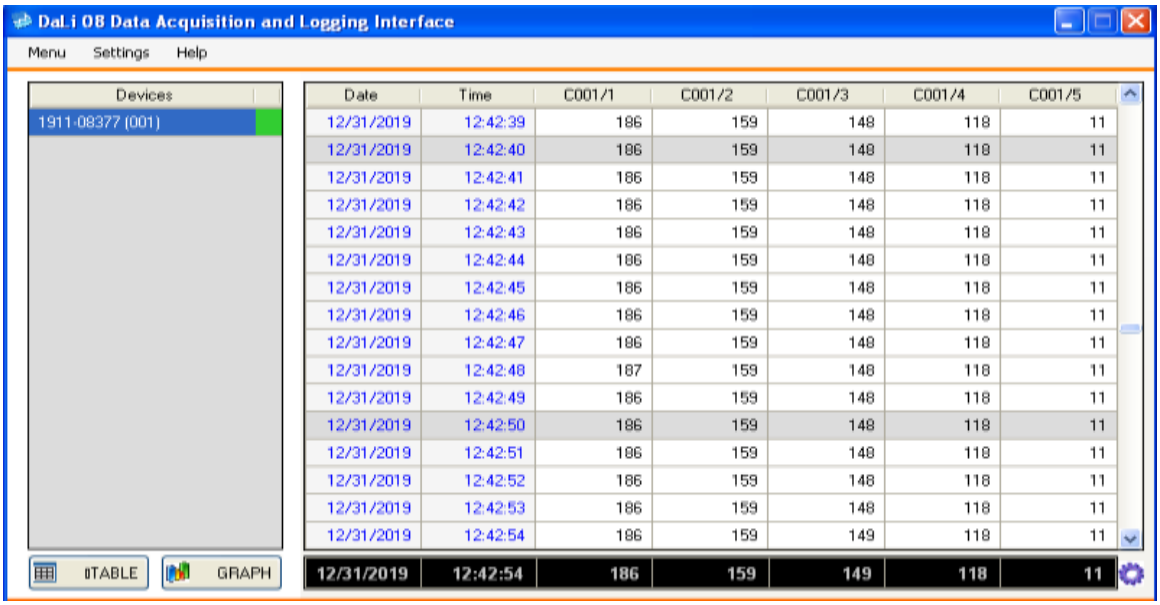


Fig.2: Liquid distributor plate.

The water pumped into the test column through pipe fitted in the lower part of the column by water pump with capacity of 0.0015 m^3/sec and maximum head reach to (30 m), which the pump connected to water tank with capacity of 0.1 m^3. The water flow rate accurately controlled and measured by utilizing needle valve rotameters fitted on the feed and bypass lines. The same technique used to provide the desired air flow rate introduced into the test column through the sparger. The sparger fixed just below the distributor plate to generate uniform bubbles distribution in the most cross section area of the column by 20 holes with diameter of 0.002 m equally arranged around the sparger. The liquid and gas mixture passed through the perforated grid and the beads of the bed. The pressure drop in the bed was measured using five Keller model PA 21Y/4 differential pressure transducer in the current analysis fitted at a certain interval up the column wall, every pressure data recorded by laptop. A pressure transducer is a novel device that converts pressure into an analog electrical signal. Ordeal model UDL 100 data loggers were used to convert the analog signals to numeric value. UDL 100 (Universal Design License) Model devices translate numerous analog signals used in industrial environments into digital values that can then be sent to a computer. These devices are set up on the computer and then used DALi 08 software, which allows for computer configuration and storing of device values as show in figure3.



Date	Time	C001/1	C001/2	C001/3	C001/4	C001/5
12/31/2019	12:42:39	186	159	148	118	11
12/31/2019	12:42:40	186	159	148	118	11
12/31/2019	12:42:41	186	159	148	118	11
12/31/2019	12:42:42	186	159	148	118	11
12/31/2019	12:42:43	186	159	148	118	11
12/31/2019	12:42:44	186	159	148	118	11
12/31/2019	12:42:45	186	159	148	118	11
12/31/2019	12:42:46	186	159	148	118	11
12/31/2019	12:42:47	186	159	148	118	11
12/31/2019	12:42:48	187	159	148	118	11
12/31/2019	12:42:49	186	159	148	118	11
12/31/2019	12:42:50	186	159	148	118	11
12/31/2019	12:42:51	186	159	148	118	11
12/31/2019	12:42:52	186	159	148	118	11
12/31/2019	12:42:53	186	159	148	118	11
12/31/2019	12:42:54	186	159	149	118	11
12/31/2019	**12:42:54**	**186**	**159**	**149**	**118**	**11**

Fig.3: Recorded data with DALi 08.

The regression analysis of experimental data to calculate statistical parameters, the experimental study was conducted utilizing Response Surface Methodology (RSM) based on central composite design model (CCD). As a result, RMS was carried out using MINITAB version 18.

3. Results and Discussion

3.1. Pressure drop and minimum fluidization velocity

In order to evaluate the influence of the fluids flow rate on the pressure drop, four packed bed of diameter (3, 4, 5, and 6) mm of glass beads are used.

For two phases (water-solid), The pressure drop at bed has been observed exhibit with two behaviors: first before the fluidization process, essentially influence with superficial water velocity, bed pressure drops increased with the increase in superficial water velocity. The second: after the fluidization of bed, pressure drop commences stability without being influenced by an increase of the superficial water velocity. This refer to the change of fluid moving resistance, when fluid is moved through the glass beads bed, beads remain intact as a static bed, and thus more pressure is lost in allowing the bed particles to fluidize. As bed is fluidized, the pressure drop becomes constant because the resistance for the fluid (liquid) decreases significantly. For three phases (liquid-gas-solid) the pressure drop maintains the same pattern of behavior. It has been discovered that as the superficial air velocity increases, the bed pressure drop decreases. This is owing to that the gas hold-up increased as the superficial air velocity increase, thus decreases the density of the bed material as figure 4 shows the bed pressure drop variation respect to superficial water velocity for different superficial air velocities. The effect of increase of superficial air velocity led to decrease the minimum fluidization velocity V_{Lmf}.

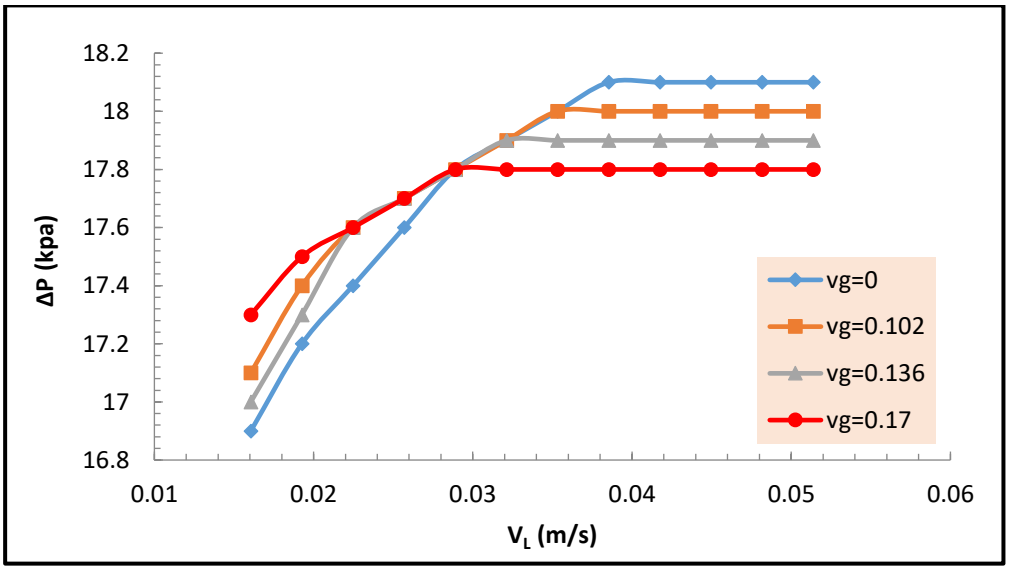


Fig.4: Effect of superficial velocity of water on pressure at different values of superficial velocity of air and d_P =3 mm.

Figures (5, 6 and 7) show the effect of water superficial velocity and air superficial velocity on pressure drop at different diameters of bed beads (0.004, 0.005 and 0.006) m. The pressure drop increase as the diameter of glass beads increased, this is due to the fact that the pressure drop required to counterbalance the weight of the bed particles increases as the diameter of the beads increases. Thus, the minimum fluidization velocity increased as the particles diameter increased.

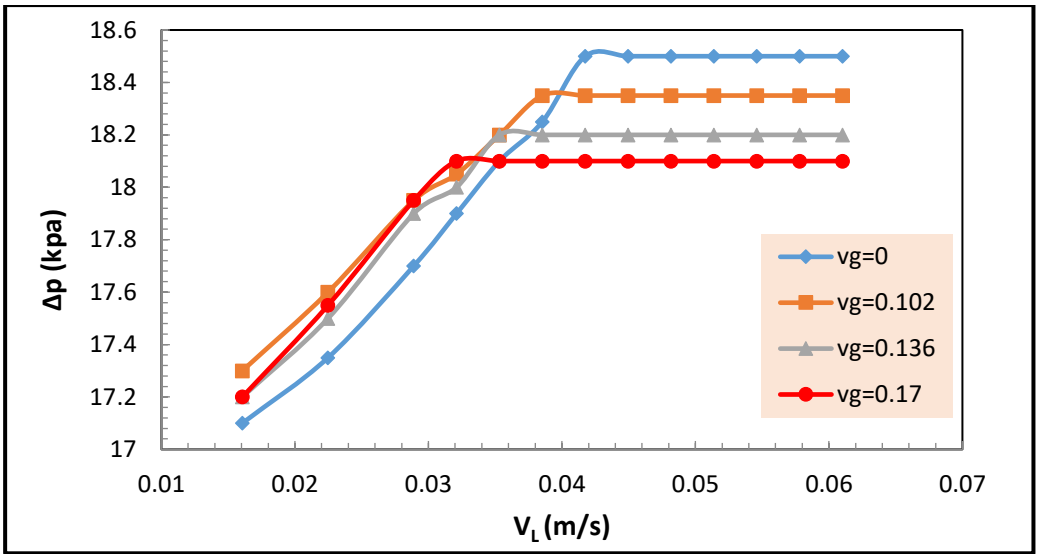


Fig.5: Effect of superficial velocity of water on pressure at different values of superficial velocity of air and d_P =4 mm.

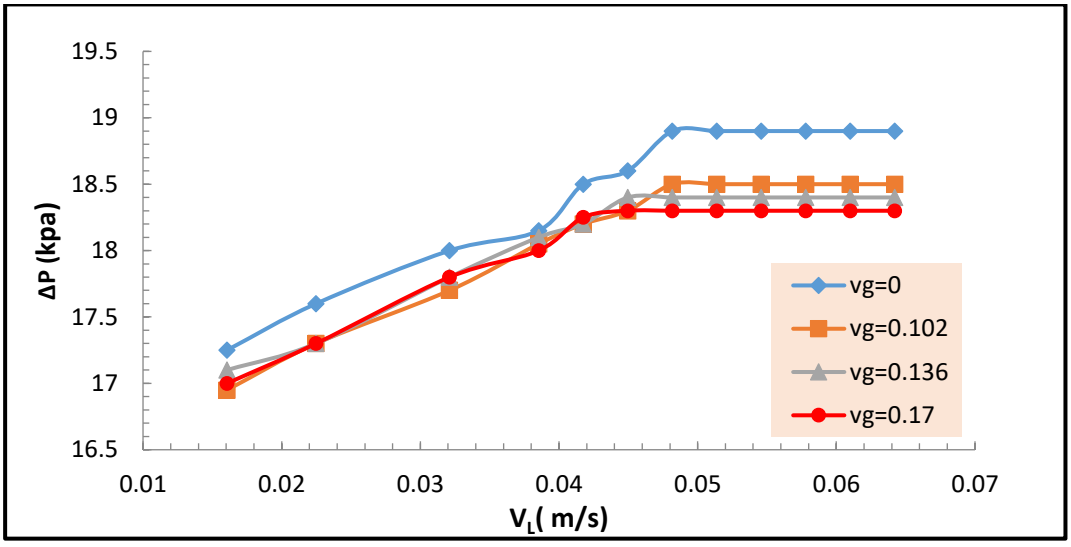


Fig.6: Effect of superficial velocity of water on pressure at different values of superficial velocity of air and d_P =5 mm.

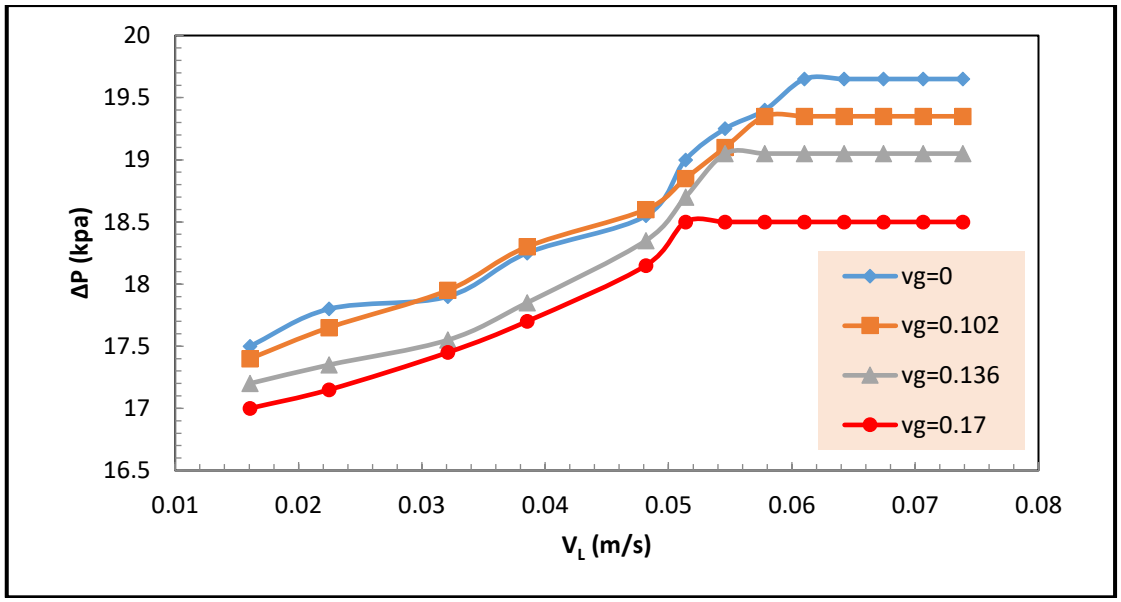


Fig.7: Effect of superficial velocity of water on pressure at different values of superficial velocity of air and d_P =6 mm.

The superficial Air velocity has fundamental effect on the minimum fluidization velocity. Figure (8) illustrates that with increasing superficial air velocity leads to a reduction in the minimum fluidization velocity. Because of this, the statement that rise in superficial air velocity tend to increase the gas hold-up lead in turn reductions the density of the bed material, therefore, the decreases in the bed density lead to a decrease in the amount of fluidization velocity. Thus, the good understandings of this statement give a reasonable reflection on the diameters of the bed glass beads.

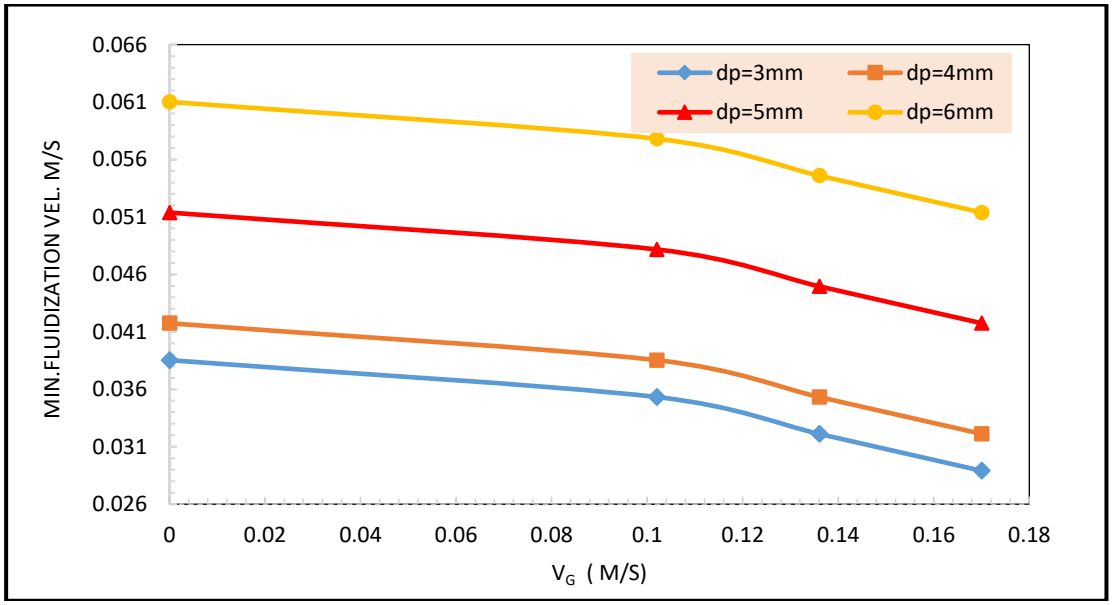


Fig.8: Effect of air velocity on water minimum fluidization velocity at different particle diameter.

3.1.1. Bed expansion

Figure 9 illustrated the effect of water superficial velocity on the ratio of bed expansion at different values of air superficial velocity. For a certain diameter of glass bead equal to 3mm, and according to

the variation of superficial air velocity with the minimum fluidization velocity. It is logical explain that, the bed expansion ratio increases in the increase of superficial air velocity. This is due to the fact that the minimum fluidization velocity decreases with the increase in superficial air velocity.

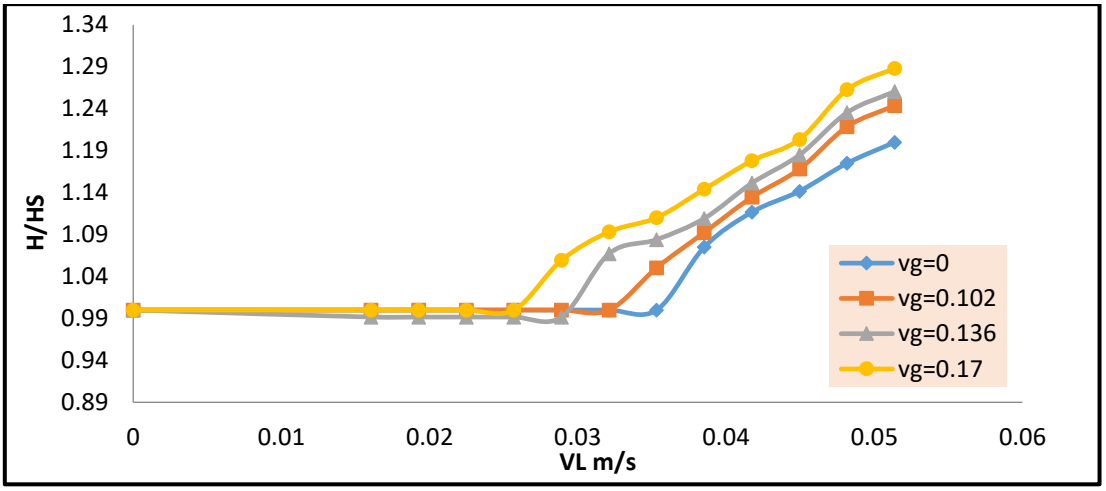


Fig.9: Effect of water superficial velocity on the ratio of bed expansion at different values of air superficial velocity and d_p = 3 mm.

Figure 10 shows the effect of water velocity on the ratio of bed expansion with respect to the diameter of particles for two phase flow (liquid-solid). The bed still stationary as water velocity increased till reach to the minimum fluidization velocity. A cording to the statement the minimum fluidization velocity increase in the increase of particle diameter, therefore the bed expansion ratio increases as the liquid velocity increased for a certain particle diameter. While for greater particles diameter the bed expansion ratio decreased. This is due to the particles with great diameter have great specific weight.

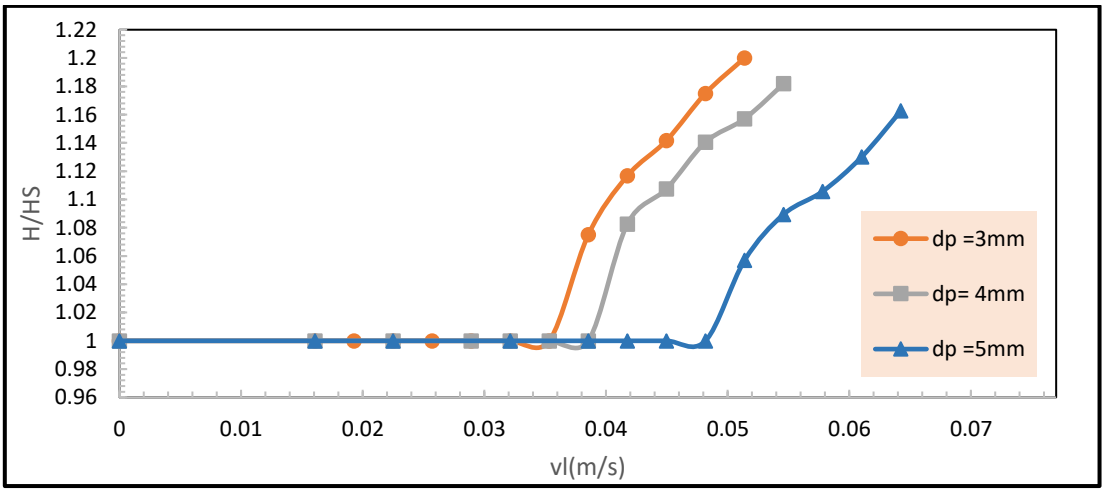


Fig.10: Effect of water velocity on the ratio of bed expansion at different particle diameters and V_g=0 m/s.

3.1.2. Gas-liquid holdup

The variation in fraction gas holdup and superficial liquid velocity for various fixed superficial gas velocity values is represented in Figure 11. The figure shows that as the liquid velocity increases, the gas holdup decreases. This is due to the fact that the bubbles are quickly driven by the liquid at higher liquid velocity. Since the residence time of bubbles decreases as liquid velocity increases, therefore the gas holdup is decreases.

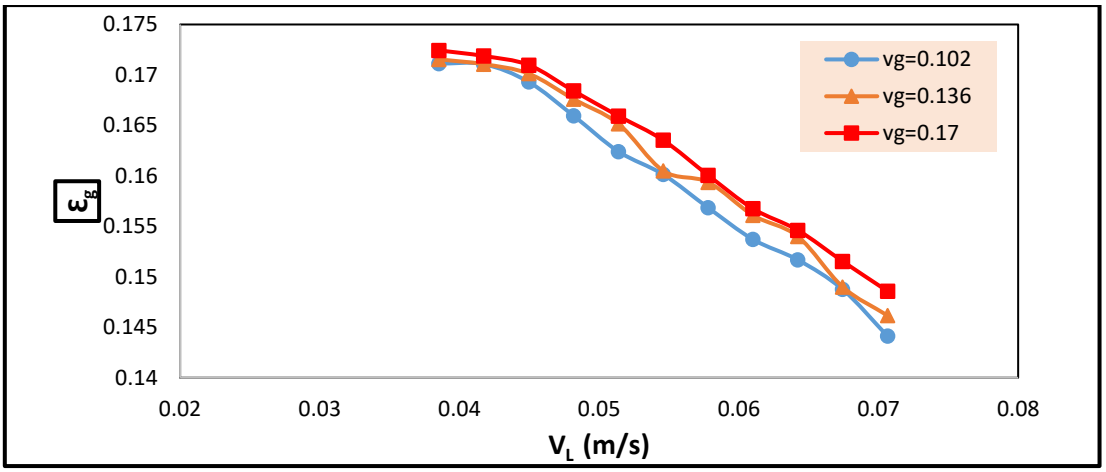


Fig.11: Effect of water superficial velocity on gas holdup with respect to the air superficial velocity at d_p = 5 mm.

Figure 12 shows the effects of gas velocity on the gas holdup. Since the volume of gas pumped into the riser increases, thus led to increase the superficial gas velocity that in turn increasing the gas holdup. Figures 13 and 14 show how liquid holdup varies with liquid velocity at various fixed gas velocities and with gas velocity at various fixed liquid velocities. The liquid holdup increases rapidly as the liquid velocity increases, while the liquid holdup decreases as the gas velocity increases at constant liquid velocity.

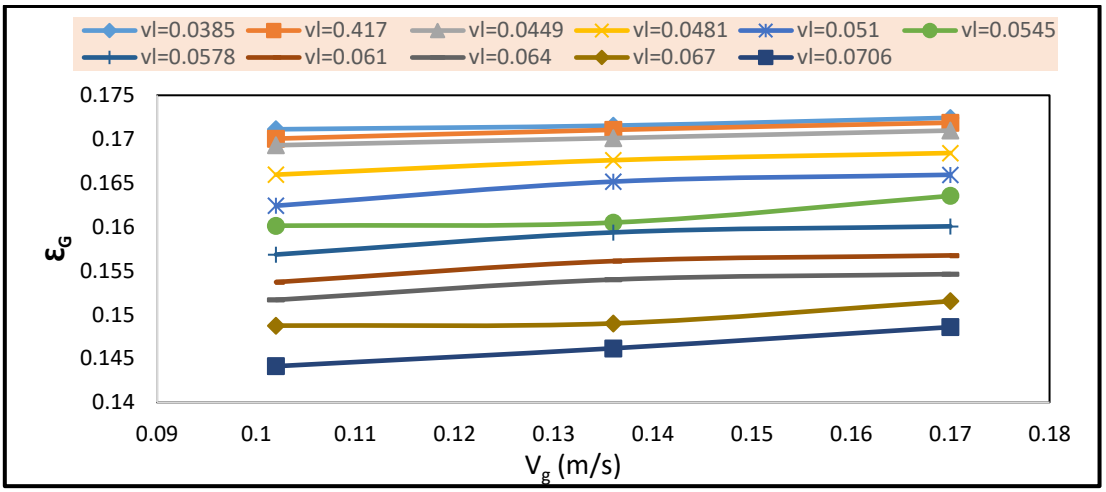


Fig.12: Gas hold-up variation with respect to gas velocity and various liquid velocities at bed diameter of 5 mm.

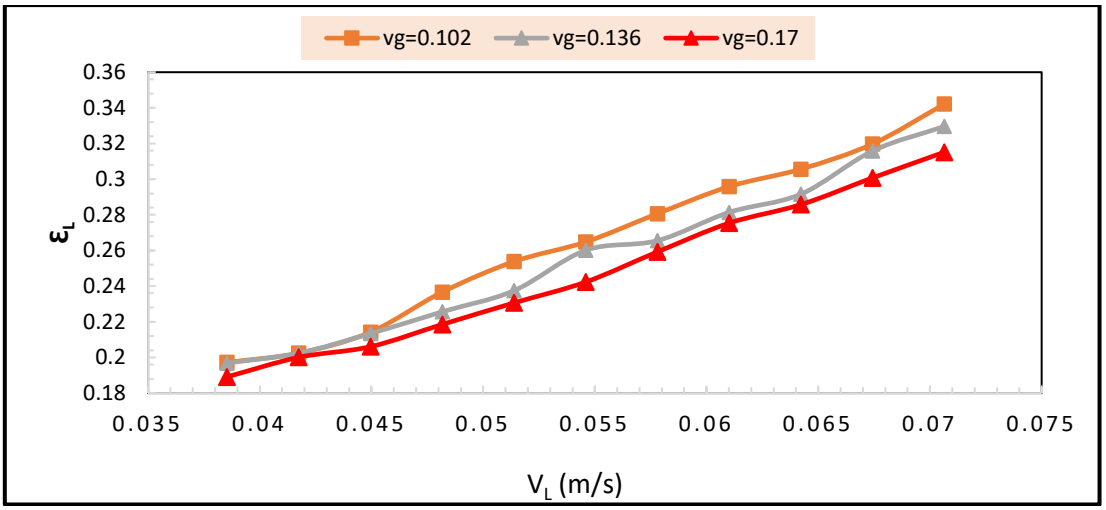


Fig.13: Effect of water velocity on liquid holdup at different air velocity for dp = 5 mm.

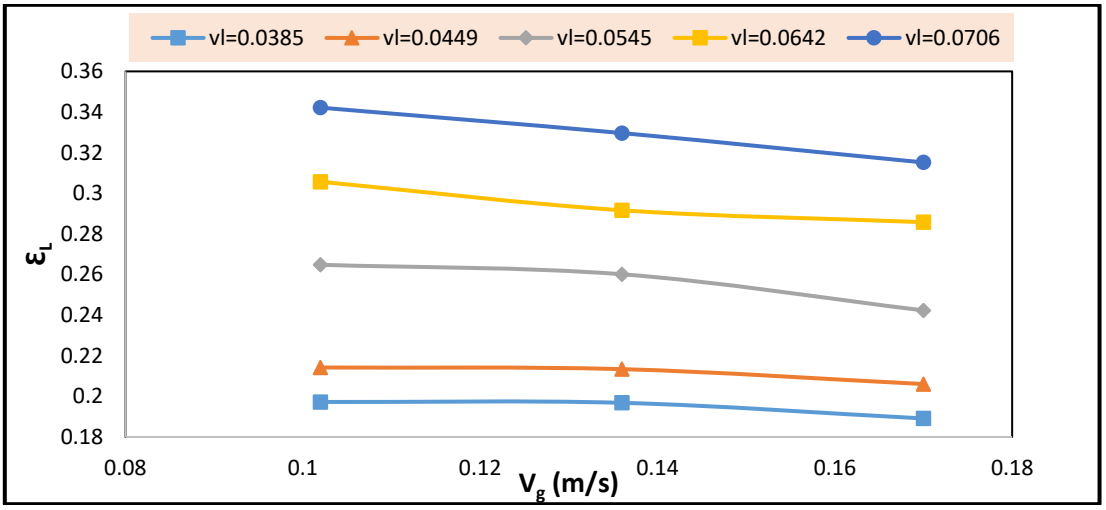


Fig.14: Effect of air velocity on liquid holdup at different liquid velocity and dp = 5 mm.

3.2. Statistical analysis and modelling by response surface models

RSM based on CCD model is an experimental statistical modeling approach that uses data from the experimental design to solve multivariable equations simultaneously. The superficial liquid velocity, m/s (X_1) and superficial gas velocity, m/s (X_2) process parameters (independent variables) were specified for optimization. All of the possible interactions of parameters (X_1 and X_2) and their effects on the response were fit into a polynomial regression equation (the yield) as given by Eq.4[26].

$$Y = \beta_0 + \sum_{i=1}^{n} \beta_i X_i + \sum_{i=1}^{n} \beta_{ii} X_i^{\,2} - \sum_{i=1}^{n} \sum_{j=i+1}^{n} \beta_{ij} X_i X_{ij} + \epsilon \qquad \ldots 4$$

Where Y is response, β_0 represents the constant coefficient, β_i represents the linear coefficients, β_{ii} represents the interaction coefficients, and β_{ij}represents the quadratic coefficients. The random error is denoted by the symbol ϵ. The number of factors studied is denoted by the symbol n.

3.2.1. Effect of variables

2-dimention contour plots were used to understand the model graphically. The 2D contour plots help to describe the effect of independent variables on the response. The type of interaction between the independent variables is represented by the 2D contour plots. The absence of interaction between

the variables is shown by a circular or parallel plane shape, whereas the presence of interaction between the variables is indicated by an elliptical or curved shape [29-30].

3.2.2. Effect of superficial liquid/gas velocity on pressure drop

The interaction effect of the liquid/gas velocity on pressure drop at constant particle size is shown in Figure (15). The curved form of the contour plots indicates that there is an interaction between liquid and gas velocity, as can be observed. The pressure appears to be dropping at highest value in the overlapping period of V_L from 0.04-0.07 and V_g from 0.0 to 0.1 (m/s) and then decrease with increase gas velocity.

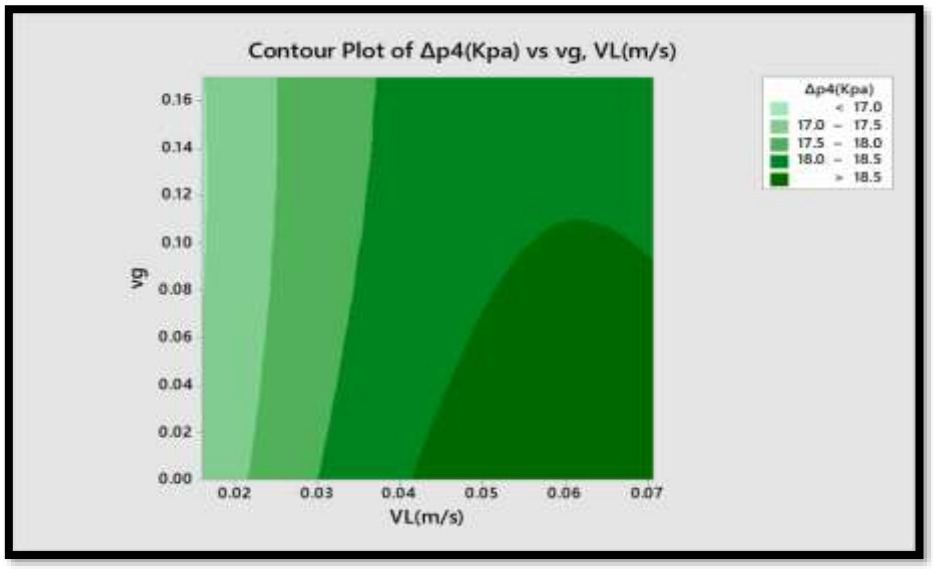


Fig.15: 2D counter plot of the effect of superficial liquid and gas velocity on pressure drop at particle size 5mm.

When water moves through the glass beads bed, the beads remain intact as a static bed, and so more pressure is lost in enabling the bed particles to fluidize. However, as air velocity grows, the bed pressure drops decreases. This is because the gas hold-up increased as the air velocity increased, lowering the bed's density. As shown in Equation (5), the response bed pressure drop was fitted to modified second-order regression models. All effects (first, second order, and interaction) were derived from a quadratic model.

$$\Delta p(Kpa) = 15.7579 + 96.82\ V_L - 1.531\ V_g - 736.9\ V_L^2 + 9.37\ V_g^2 - 54.7\ V_L * V_g \quad \ldots 5$$

The predicted values were reasonably close to the experimental data, indicating that the predicted model had acceptable prediction accuracy and generalizability. The model's fitness and adequacy were shown by higher multiple regression coefficient values, as shown in table 4.

Table 4: Results RSM for pressure drop of central composite design (CCD).

parameter	value
R^2	97.81%
Adjusted-R^2	97.59%
Predicted-R^2	97.11%
Std. Dev.	0.502

3.2.2. Effect of superficial liquid/gas velocity on pressure drop

Figure 16 shows the RSM analysis results and the influence of operational variables such as air flow and liquid flow rate on gas holdup as contour lines. The highest gas holdup value is found as 0.11 - 0.17 m/s and 0.04 m/s gas and liquid velocity, respectively, as shown in Fig.16. The increase in the gas holdup is caused by a reduction in the liquid flow rate and an increase in the gas flow rate, as seen in this figure.

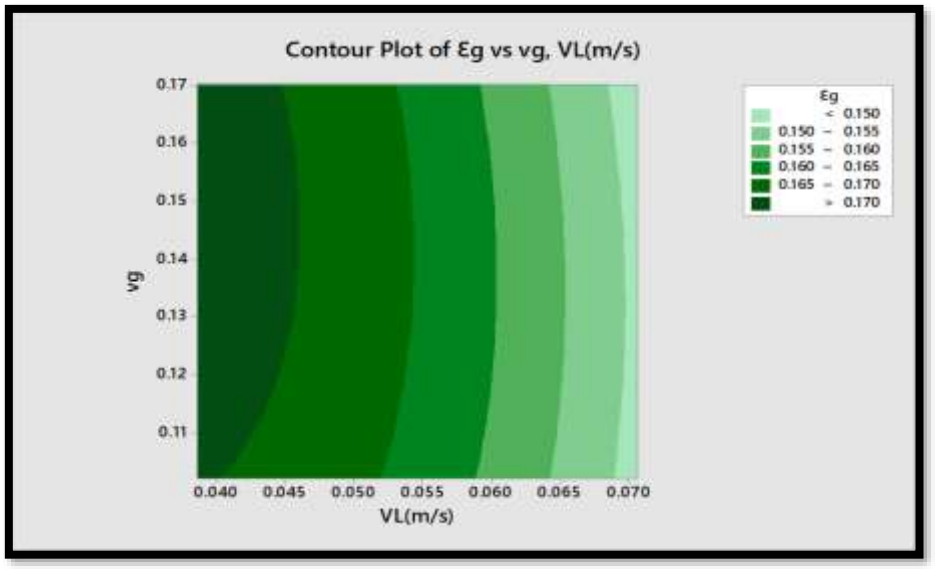


Fig.16: 2D counter plot of the effect of superficial liquid and gas velocity on gas holdup at particle size 5mm.

This is due to an increase in the volume of gas pushed into the column, which has resulted in an increase in the superficial gas velocity, which has resulted in an increase in gas holdup. Table 5 shows a suitable level of adaptability (goodness-of-fit).

Table 5: Results RSM for gas holdup of central composite design (CCD).

parameter	Value
R^2	97.44%
Adjusted-R^2	96.96%
Predicted-R^2	95.55%
Std. Dev.	0.00788

Moreover, the reduced model is obtained from Table 5 is as follows:

$$Ɛ_g = 0.1279 + 1.167\ V_L + 0.361\ V_g - 16.00\ V_L^2 - 1.063\ V_g^2 - 1.150\ V_L * V_g \quad \ldots 6$$

3.2.3. Effect of superficial liquid/gas velocity on bed expansion

The response surface plots with contours for bed expansion was plotted and is shown in Fig. 17. It displays how operating variables such as superficial gas and liquid velocity have an effect on the bed expansion. The maximum percentage bed expansion can be achieved by Superficial liquid and gas velocity as greater than 0.065 m/s and 0.0 m/s.

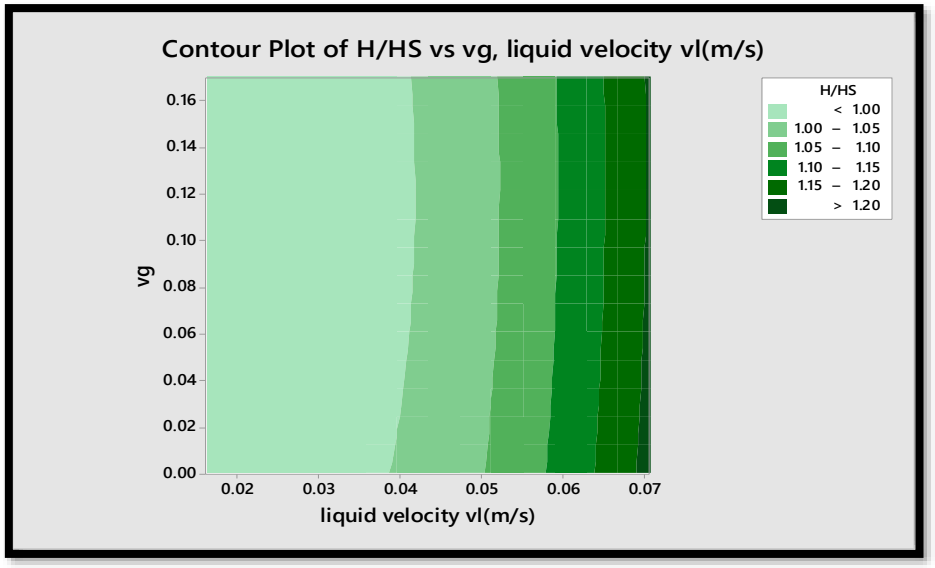


Fig. 17. 2D Contour plot of the bed expansion, H/H_s as function of V_L and V_g at particle size 5mm.

RMS values for bed expansion are shown in Table.6. The R^2 and adjusted R^2 were calculated to see if the model's fitness was enough. The R^2 values were determined as shown in table.6, indicating that 99% of the experimental data was compatible.

Table 6: Results RSM for bed expansion of central composite design (CCD).

parameter	Value
R^2	97.70%
Adjusted-R^2	97.47%
Predicted-R^2	97.12%
Std. Dev.	0.0747

For predicting bed expansion, second order polynomial models were created using multiple regression analysis of the experimental data. The empirical results from CCD were used to fit the second-order equation. The resulting equation for factors is shown below.

$$H/H_S = 1.0765 - 6.779\ V_L - 0.140\ V_g + 124.31\ V_L^2 + 0.709\ V_g^2 - 0.71\ V_L{*}V_g \quad \ldots 7$$

4. Conclusions

The effect of gas velocity, liquid velocity, and particle size on pressure drop, minimum fluidization velocity, bed expansion, gas holdup and liquid holdup in three phase fluidized bed has been studied extensively with detailed experimental investigations. The pressure drop across the bed increases as the liquid velocity increases at a constant gas velocity before reach the minimum fluidization velocity, then the pressure drop is almost unaffected by the increase in water velocity and remains stable after fluidization phenomena. The particles size has great effect on the pressure drop and minimum liquid fluidized velocity, as it increased the pressure drop increases, and the minimum liquid fluidization velocity (V_{lmf}) increases, therefore gas holed up decreased. The expansion ratio related with direct relationship with liquid and gas velocity, while inversely contributed with particle size. The gas holds up have a direct linear form with gas velocity. At a constant gas velocity, the gas holdup decreases as the liquid velocity increases. Increases in liquid velocity resulted in an increase in liquid holdup, while increases in gas velocity resulted in a decrease in liquid holdup. The response surface method was used

to find information about regression analysis and variable optimization. To correlate the two variables to the response, a model was developed. The effect of process factors on pressure drops, gas hold up, and bed expansion can be described using a 2D response surface plot. The experimental values obtained agree satisfactorily with the model predicted value, according to the results of the process optimization.

Acknowledgments: I am deeply grateful to my friends Dr. Abbas J. Sultan for his effort, advice, help and encouragement throughout the research period. I would like to express my thanks to Assist. Prof. Maher A. Abdulrahman for his kind and valuable help in providing the required software programs. I would like also to express my thanks to the staff of Department of Chemical Engineering Department, University of Technology, Baghdad, Iraq. for their cooperation and assistance. Special Thanks go to anyone who were supported, encouraged and helped me.

References

1. Dimpi Sinha, Ravi Baliyan, Akash Rana, Rekha Israni "Hydrodynamics of Three Phase Fluidized Bed Using Low Density Particles", IJARIIE, Issue - 6, Vol. 2, No. 2, pp.236-244 2016 2016.
2. Katsuhiko Muroyama, Liang-Shih Fan, "*Fundamentals of Gas- Liqu id -Solid Fluidization*," Vol. 31, No. 1, 1985.
3. H. M. Jena, B. K. Sahoo, G. K. Roy, and B. C. Meikap, "*Characterization of Hydrodynamic Properties of A Gas – Liquid – Solid Three-Phase Fluidized Bed With Regular Shape Spherical Glass Bead Particles*," Vol. 145, pp. 50–56, 2008, doi: 10.1016/j.cej.2008.03.002.
4. J. M. Begovich, J. S. Watson, "*Hydrodynamic Characteristics of Three- Phase Fliuidized Beds*," Cambridge University Press,1978.
5. S. Venkatachalam, K. Kandasamy, and S. Kandasamy, "*Correlation for Prediction of Minimum Fluidization Velocity and Riser Liquid Holdup in Three-Phase External Loop Air Lift Fluidized Bed Reactor*", International Journal of Chemical Reactor engineering, Vol. 8, Article, A123, 2010, doi: 10.2202/1542-6580.2337.
6. H. M. Jena, G. K. Roy, and B. C. Meikap, "*Gas Holdup in A Three-Phase Fluidized Bed With Cylindrical Particles*", National Conference on Frontiers in Chemical Engineering, 2007.
7. K. Ramesh and T. Murugesan, "*Minimum Fluidization Velocity and Gas Holdup in Gas–Liquid–Solid Fluidized Bed Reactors*", jornal of Chimecal technology and Biotechnology, Vol. 77, pp. 129–136, 2002, doi: 10.1002/jctb.533.
8. H. M. Jena, "*Hydrodynamics of Gas-Liquid-Solid Fluidized and Semi-Fluidized Beds Hara*," Thesis Submitt. to Natl. Inst. Technol. Rourkela, 2009.
9. A. Knesebeck and R. Guardani " *Estimation of Particle Concentration Profiles in A Three-Phase Fluidized Bed From Experimental Data and Using The Wake Model*" Brazilian Journal of Chemical Engineering, Vol. 21, No.1, PP 47-57, 2004
10. Satish J. Parulekar, Yatish T. Shah, "*Steady State Behavior of Gas-Liquid-Solid Fluidized Bed Reactors*.," The Chemical Engineering Journal, Vol. 20, pp.21-33, 1980.
11. Aakanksha Pare, "*Hydrodynamics of Three Phase Fluidized Bed Using Low Density Particles* Department of Chemical Engineering National Institute of Technology Rourkela Bed Using Low Density Particles, 2013.
12. Fangfang Tao, Shanglei Ning, Bo Zhang, Haibo Jin, and Guangxiang He, "*Simulation Study on Gas Holdup of Large and Small Bubbles in a High Pressure Gas–Liquid Bubble Column*," MDPI Process, Vol. 7, No. 594, 2019.
13. M. Safoniuk, J. R Grace, L. Hackman and C. A. McKnight "*Gas Hold-Up in a Three-Phase Fluidized Bed"*, AIChE Journal, Vol. 48, No. 7, pp. 1581-1587, 2002.
14. J. Schweitzer, J. Bayle, and T. Gauthier, "*Local gas hold-up measurements in fuidized bed and slurry bubble column*", Chemical Engineering Science, Vol.56, pp. 1103–1110, 2001.
15. Yanjun Li, Mingyan Liu, Xiangnan Li, "*Minimum Fluidization Velocity in Gas-Liquid-Solid*

Minifluidized Beds," AIChE J., Vol. 62, No. 6, pp. 1940–1957, 2016, doi: 10.1002/aic.

16. Abbas H. Sulaymon, Thamer J. Mohammed Ali H. Jawad, "*Hydrodynamic Characteristics of Three-Phase Non- Newtonian Liquid-Gas-Solid Fluidized Beds*," Emirates Journal For Engineering Research, Vol. 15, No. 1, pp. 41–49, 2010.
17. Velmurugan SIVASUBRAMANIAN, "*Minimum Fluidization Velocity in a Three Phase Inverse Fluidized Bed Reactor with Newtonian and Non-Newtonian Fluids*," Journal of Chemical Engineering of Japan, Vol. 37, No. 12, pp. 1436–1444, 2004.
18. L. A. Briens, C. L. Briens, A. Margaritis, and J. Hay, "*Minimum Liquid Fluidization Velocity In Gas-Liquid-Solid Fluidized Beds of Low-Density Particles*," Vol. 52, No. 97, 1997.
19. F. Larachi, I. Iliuta, O. Rival, and B. P. A. Grandjean, "*Prediction of minimum fluidization velocity in three-phase fluidized-bed reactors*," Ind. Eng. Chem. Res., vol. 39, no. 2, pp. 563–572, 2000, doi: 10.1021/ie990435z.)
20. Dandan Zhou, Shuangshi Dong, Heli Wang, Hsiaotao T. Bi, "*Minimum fluidization velocity of a three-phase conical fluidized bed in comparison to a cylindrical fluidized bed*," Ind. Eng. Chem. Res., vol. 48, no. 1, pp. 27–36, 2009, doi: 10.1021/ie8001974.
21. D. Lee, A. Macchi, N. Epstein, and J. R. Grace, "*Transition Velocities and Phase Holdups at n Gas-Liquid-Solid Systems Minimum Fluidization* i," Can. J. Chem. Eng., vol. 79, no. August, 2001.
22. Amer A. Abdul Rahman, Mohammed F. Abed & Adiba A. Mahmod, "*Hydrodynamic Characteristics of a Gas-Liquid–Solid Fluidized Bed Containing a Binary Mixture of Particles,*" Eng. & Tech. Journal, Vol. 27, No. 12, 2009.
23. P Rohini Kumar, K V Ramesh, P Venkateswarlu, "*Phase Holdups in A Three- Phase Fluidized Bed in the Presence of Coaxially Placed String of Spheres Internal*," IOP Conference Series: Materials Science and Engineering, Vol. 225, No. 012210, 2017, doi:10.1088/1757-899X/225/1/012210.
24. P. Dargar and A. Macchi, "*Effect of Surface-Active Agents on The Phase Holdups of Three-Phase Fluidized Beds*", Chemical Engineering and Processeing, Vol. 45, pp. 764–772, 2006, doi: 10.1016/j.cep.2006.03.004.
25. M. Alam, S. Muyibi and J.Toramae, *"Statistical optimization of adsorption processes for removal of 2,4-dichlorophenol by activated carbon derived from oil palm empty fruit bunches"*, J Environ Sci 19:674–677,(2007) , doi:10.1016/S1001-0742(07)60113-2.
26. D.Das, S. Behera • B. Meikap "*Removal of CO 2 in a multistage fluidized bed reactor by amine impregnated activated carbon : optimization using response surface methodology*," International Journal of Coal Science & Technology, Vol. 06, No. 03, 2019, doi. 10.1007/s40789-019-0261-6.
27. T. J. Mohammed, Abbas H. Sulaymon and Amer A. Abdul-Rahmun "*Hydrodynamic Characteristic of Three-Phase (Liquid-Liquid-Solid) Fluidized Beds*," Journal of Chemical Engineering and Process Technology, Vol. 05, No. 02, 2014, doi: 10.4172/2157-7048.1000188.
28. Andreas Acrivos, James E. Bailey, Manfred Morari, E. Bruce Nauman, E. Bruce Nauman, Robert K. Prud'homme, "*Fluidization Engineering"* 2nd Edition, Butterworth-Heinemann, Boston, MA ., 1991.
29. K. Anupam, S. Dutta,C. Bhattacharjee, and S. Datta, "*Adsorptive removal of chromium (VI) from aqueous solution over powdered activated carbon: Optimisation through response surface methodology*". Chemical Engineering Journal, 173(1), 135-143.,2011, doi: 10.1016/j.cej.2011.07.049.
30. Z. Noorimotlagh, R. Soltani, , A.Khataee,S. Shahriyar, anaH. Nourmoradi, . "*Adsorption of a textile dye in aqueous phase using mesoporous activated carbon prepared from Iranian milk vetch*". Journal of the Taiwan Institute of Chemical Engineers,45(4), 1783-1791, 2014, doi: 10.1016/j.jtice.2014.02.017

Heat Exchange in the Processes of Welding of Rails and Hardening of Railway Wheels

Alexey Lykov , Vladimir Saranchin *

Moscow State University of Land Use Planning.
***** *Corresponding authors: alykov49@mail.ru ; saranchin@yandex.ru ; Tel: +7-985-9240126, +7-916-215-6981*

Abstract. The technological processes determining the operating efficiency of a wheel-rail system are presented in this paper. Thermal conditions during the aluminothermal rail-welding process such as metal pre-heating, temperature of the liquid metal filled into the mould cavity on the weld, and rail metal temperature were analyzed. The computed and experimental values of the weld dimensional parameters were compared. The plasma-hardening process of the steel surface was computed. The temperature and its rate on the surface and in the bulk of the material were determined. The thickness of the hardened layer and the structure of the metal, which were formed under different modes of plasma treatment, were determined. Computations and experimental data were compared under various hardening regimes.

Keywords: rails, aluminothermic welding, thermal conditions, welded seam-welded rail system, hardening

1. Introduction

The aluminothermic welding technique for rails and railway turnouts and the plasma hardening process for locomotive wheel ridges were studied.

The aluminothermic welding technique is now widely used by various industries. Its most common use lies in welding rails and especially railway turnouts because contact welding of such turnouts is rather difficult. Aluminothermic welding is widely used on railway networks in Russia and worldwide. The weld-joint quality depends on such factors as the technological process parameters, composition of aluminothermic reaction mix (aluminothermites), and quality of crucibles and moulds. Therefore, improvements to this process address both the welding equipment quality [1,2] and the welding technique [3].

Plasma hardening of locomotive wheel ridges is used to increase their service life and has been used on the Russian railway network since the late 1990s. Plasma hardening of steel consists of intense heating of the surface to temperatures above that of the austenitic transformation of wheel steel #2 and subsequent heat dissipation into the bulk of the material. As a result, metal structures with increased hardness are formed in the surface layer and, accordingly, are subject to less wear, which leads to an increase in the weld lifetime.

2. Alumothermal Rails Welding

The basic parameters that affect the structure, physical and mechanical characteristics and operational parameters of the weld and the near-weld zone (NWZ) are thermal conditions (temperature, cooling rate) occurring during melting, crystallization and cooling of the weld-rail system.

The preliminary heating mode of the welded ends of the rails (intensity, duration, temperature) is the determining factor of the welding process. Under unfavorable technological conditions, including thermal ones, dendritic structures can form in the weld (Fig. 1) and have negative effects

on the physical and mechanical characteristics. This may lead to non-compliance with their specifications.

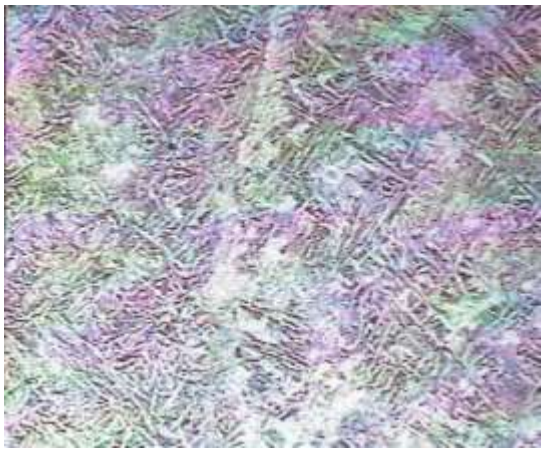


Figure 1: Weld metal structure (×200)

Theoretical computations play an important role due to the complexity of experimental studies of thermal conditions in the weld-NWZ system. The purpose of this work is to compute the process of aluminothermic welding of rails taking into account the melting of the rail metal with subsequent crystallization of the metal in the weld-NWZ system and the cooling process.

2.1 Computation of the thermal conditions in the process of aluminothermic welding of railway rails

The influences of the temperature of the metal poured into the weld and the degree of preliminary heating of the ends of the welded rails were computationally analyzed. The rail-welding process included the following stages: heating the ends of the rails, filling the weld with metal at temperature T_0, which was higher than the melting point T_P = 1536 ^{0}C, melting of the ends of the rails, crystallization of the weld, and cooling of the seam-NWZ system.

Preliminary results for the influence of the technological parameters on the thermal conditions were obtained by considering the welding process in a one-dimensional formulation [T (x, t), where x is the coordinate and t is the duration]. At the same time, exact solutions of the thermal conductivity problem are used to compute the temperature T(x, t) in the melt and the rail material. The equation of the melt front motion was solved numerically [4]. It should be noted that this method for computing thermal conditions can be used to compute other technological processes, for example, surfacing. The metal poured into the weld had an initial temperature of T_0. The problem was considered to be axially symmetric, i.e. the axis of symmetry (x = 0) was equidistant from the ends of the rails by 12.0 mm (the gap between the rails was 24 mm). For this reason, ideal thermal insulation was provided at the coordinate x = 0, i.e., $\partial T/\partial x = 0$. Preheating of the rail ends was simulated by an initial temperature distribution in the rail of $T(x,0) = T_m \bullet e^{-kx}$ (T_m is the melting point of the metal, 1536^{0}C). The coefficient k determines the degree of preheating of the rail (before pouring the metal into the weld). After crystallization of the melt in the weld (metal temperature less than 1536 ^{0}C), the thermal conditions were computed using the dependences of the cooling of the half-space on the initial temperature distribution obtained in the process of crystallization of the weld-NWZ system.

The zone of thermal influence was defined as the distance from the axis of symmetry at which the temperature in the rail reached the austenitic transformation temperature (720 ^{0}C for steel with a carbon content of 0.8 %) minus half of the weld thickness. The temperature distribution in the rail at preheating intensity K = 11.5 (corresponding to heating the ends of the rails to the melting point for 500 seconds before welding) and K = 35.9 is shown in Fig. 2.

The temperatures in the melt and in the rail as functions of the time coordinate of the melting-crystallization process (for K = 11.5) at the initial temperature of the metal poured into the weld equal to 2300 ^{0}C are shown in Fig. 3.

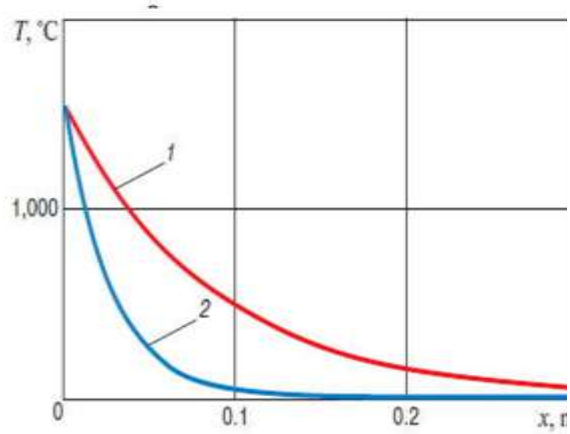


Figure 2: Initial in-rail temperature distributions under various heating rate values: 1- k = 11.5; 2 - k = 35.9

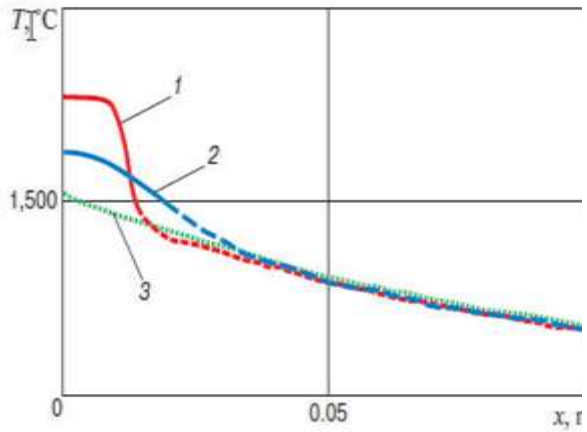


Figure 3: In-melt (solid lines) and in-rail (dash lines) temperature at various points of time as measured from the process start (T0=2,300 °C, k = 11.5): 1 – 0.2 s; 2 – 10 s; 3 – 58 s

The time dependence of the melting-front movement for these parameters is shown in Fig. 4, from which it can be seen that the end of the rail is melted to a depth of 6 mm and the crystallization process ends after 58 s.

Temperature distributions in the weld and the rail after crystallization of the melt for different times are shown in Fig. 5.

The range of thermal influence is 62 mm (80 – 12 – 6 = 62 mm, Fig. 6, curve 3). With these technological parameters, the cooling rate in the temperature range 300-800°C is 0.02-0.35 K/s (Fig. 6).

Increasing the initial metal temperature T_0 to 2800^0C increases the crystallization time to 142 s (Fig. 7) while the range of thermal influence increases slightly (up to 67 mm) and practically does not change the cooling rate for the above temperature range.

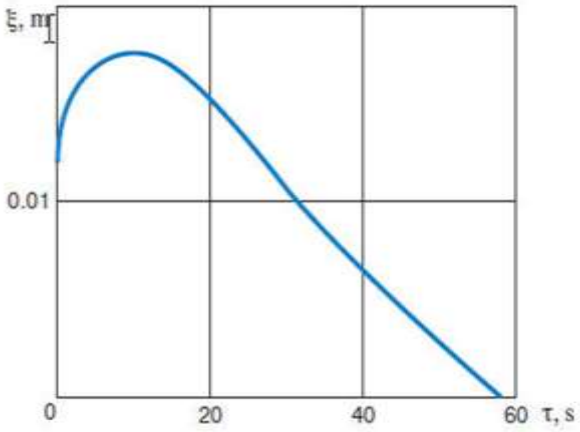


Figure 4. Movement of the melting front depending on time (T_0=2300^0S, K=11.5).

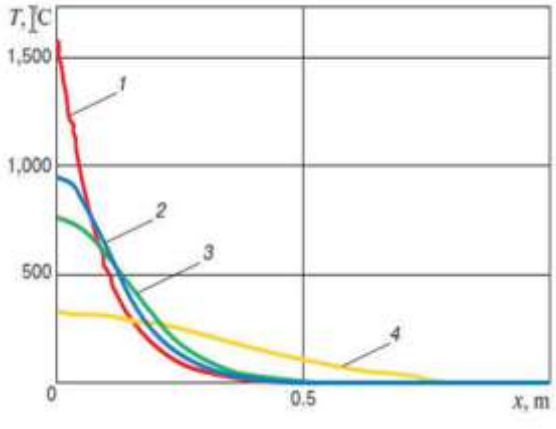


Figure 5. Temperature distribution in the weld and the rail (after solidification of the melt) at various times (T_0=2300^0S, K=11,5): 1-0; 2-5,8; 3-13,3; 4-125 min.

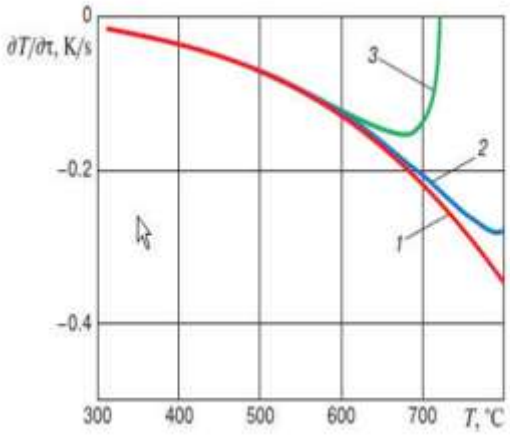


Figure 6. The cooling rate of the metal in the weld and rail (after solidification of the melt) depending on the temperature at various distance from the axis of symmetry (T_0=2300^{0}C, K=11,5): 1-1,0; 2- 60; 3-80mm

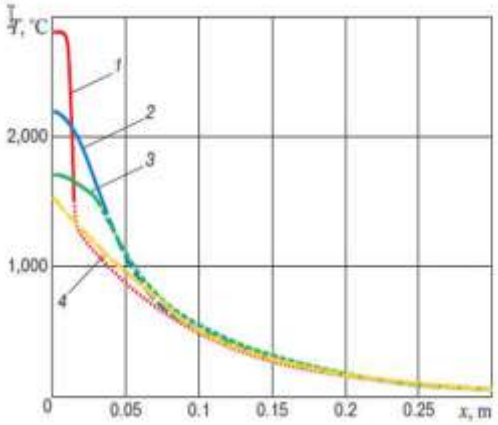


Figure 7. Temperature in the melt (solid lines) and rail (discontinuous lines) at various times from the beginning of the process (T_0=2800^{0}C, K=11,5): 1-0,2; 2-30; 3-60; 4-142 s.

If the degree of preliminary heating of the rail (K = 35.9) at the temperature of molten metal 2800 ^{0}C decreases, the range of thermal influence decreases to 14 mm (30 – 12 – 4 mm, Fig. 8, curve 4). Cooling rates (after crystallization of the melt) increase by almost an order of magnitude and are 0.2-2.0 K/s (Fig. 8), which should positively affect the structure of the metal in the weld and in the rail with a corresponding increase in the hardness of the metal and, accordingly, resistance to wear.

For preliminary heating of a rail (K = 35.9) and a low temperature of the metal poured into the weld (T_0 = 2300 ^{0}C), reflow of rail end does not occur (there is no welding process).

2.2 Experimental results

Temperatures and cooling rates of the melt and metal during aluminothermic welding are extremely difficult to measure by contact methods due to the high temperatures (>2500^{0}C). In this regard, computational methods for the study of non-stationary temperature fields in the weld and NWZ have practical importance. The correctness of the computed data was evaluated by comparison with the experimental results, namely: the width of the weld and the range of thermal influence.

Aluminothermic welding technologies were tested in the Complex Office "Welding" of JSC VNIIZhTA for compliance to specifications of TU 0921-127-01124323-2005. The measured dimensional characteristics were: width of the rail weld (by "Snaga" technology) was for a head of rails of 70 mm, a neck of 40 mm, a bottom base of 55 mm. Dimensional characteristics of the weld (by "Electrothermit" technology, Germany) were 77, 40, and 52 mm, respectively. This weld width in the head was due to the presence of an additional mass of metal and slag over the rail head during the process of crystallization of the weld-rail system. The ranges of thermal influence (from weld borders) were 36-41 mm ("Snaga"), and 17-18 mm ("Electrothermit").

Figure 9 shows the dimensional characteristics of the weld obtained in our studies conducted in conjunction with the CO "Welding" JSC VNIIZhTA technology and equipment of the company "Snaga". It can be seen from Fig. 9 that the width of the weld in the bottom of the rail is approximately 44 mm; the heat affected range, 28 mm.

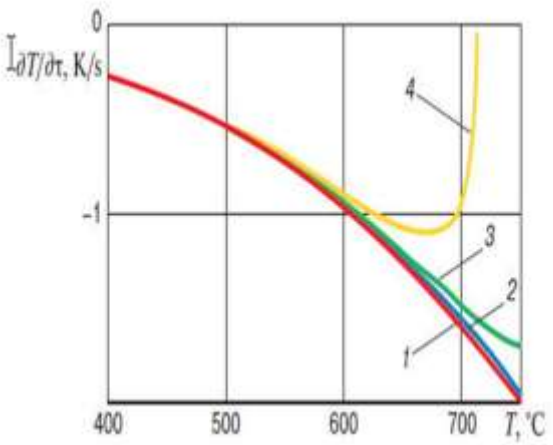


Figure 8. The rate of cooling of the metal in the weld and rail (after solidification of the melt) depending on the temperature at a different distance from the axis of symmetry (T_0=2800^{0}C, K=35,9): 1-1,0; 2- 20; 3-25; 4-30 mm.

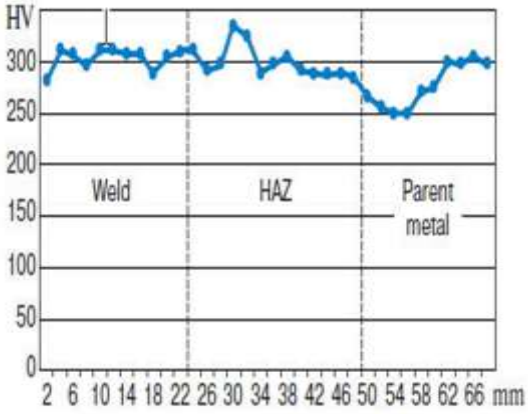


Figure 9. Hardness and dimensional characteristics of the weld and the heat affected zone (HAZ)

Figure 10 shows the computed values of the reflow depth of the rail end and the range of thermal influence depending on the metal temperature T_0 with a significant preheating of the rails before welding (K=11.5). In this case, the width of the weld for T_0 = 2400^{0}C is 44 mm [(10 + 12) x 2 mm], which is in satisfactory agreement with the values for the neck and bottom of the rails obtained during welding under real conditions.

The computed range of thermal influence for T_0 = 2400ºC is about 60 mm (Fig. 10), which is 19 mm larger than the range of thermal influence obtained by welding technology company "Snaga". This discrepancy between computed and experimental values of the thermal influence range is due to heat exchange of the rail with the environment.

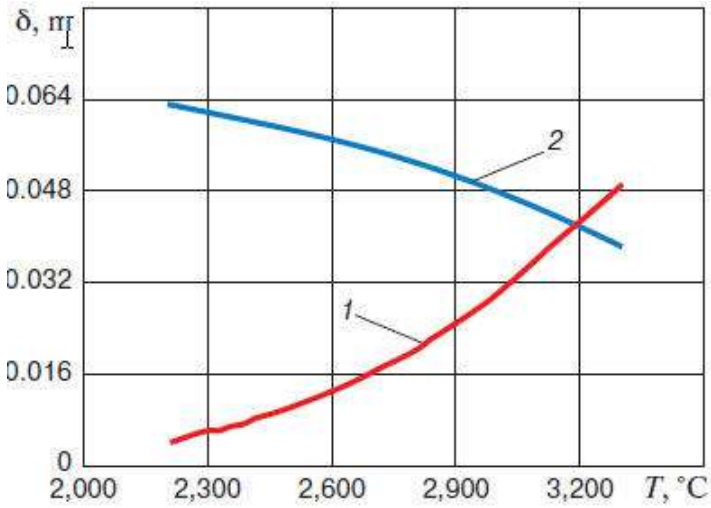


Figure 10. The depth of melting of the rail end (1) and the heat affected zone (2) depending on the melt temperature T_0 (K=11.5)

Taking into account the assumptions made in computations of the aluminothermic welding process, the agreement of the real and computed characteristics of the weld-NWZ system can be considered satisfactory.

3. Plasma Hardening of Railway Wheel Ridges

The hardening of the ridges of railway wheels occurs because of a modifications in the structure of the surface layer of the metal. The structure of the metal changes due to phase transformations during intensive heating by a plasma source and subsequent cooling of the surface layer. The heat exchange of the surface with a plasma heating source and the intensity of heat removal to the metal bulk determine the nature of phase transformations in the hardened layer and, accordingly, the structure of the metal.

The technology of plasma hardening of steel consists in intensive heating of the surface to temperatures above the temperature of austenitic transformation of wheel steel 2 and subsequent heat removal into the bulk of the material. In consequence, metal structures with increased hardness are formed in the surface layer. They accordingly, subject to less wear. This leads to an increase in the service life of the railway wheel (locomotive wheel brace).

The hardening process was computed as a one-dimensional distribution of heat from the plasma source in the material. The equation for heating and cooling of steel under the influence of a single heat pulse of rectangular shape using dimensionless variables has the form:

$$\frac{T}{T_n} = \sqrt{V}e^{-\frac{U^2}{V}} - \sqrt{V-1}e^{-\frac{U^2}{V-1}} + \sqrt{\pi}U\left(erf\frac{U}{\sqrt{V}} - erf\frac{U}{\sqrt{V-1}}\right), \quad (1)$$

Where

$U = \frac{1}{\sqrt{\pi}}Ki, \quad V = \frac{4}{\pi}Ki^2F_0$. Ki - Kirpichev criterion, Fo- Fourier number, T- temperature, Tm- steel melting point (1500^0C) [5].

When sequential heat pulses of different intensity are used, it is appropriate to compute the surface heating and cooling under various boundary conditions, which are realized by plasma heating of the plasma generator with a real space-time distribution of specific heat flux on the treated surface, including radiation and convection heat losses, as well as in the form of discontinuous functions that simulate intense heat after exposure to the plasma followed by surface cooling with water jets [4]. Figure 11 shows values of specific heat flux as functions of the exposure time including heat dissipation and surface heating by convection and radiation, which do not have a significant impact on temperature conditions in the material mass because they are 3-5% of the total heat flux when exposed to a plasma heating source

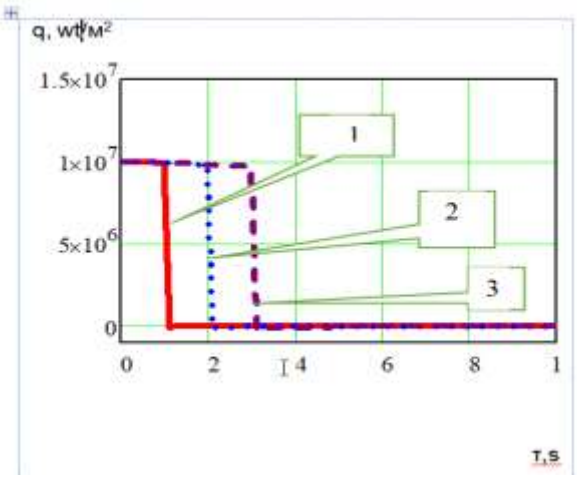


Figure 11. Specific heat fluxes depending on time 1-1s, 2-2s, 3-3s. q=1.0*10^7 W/m^2

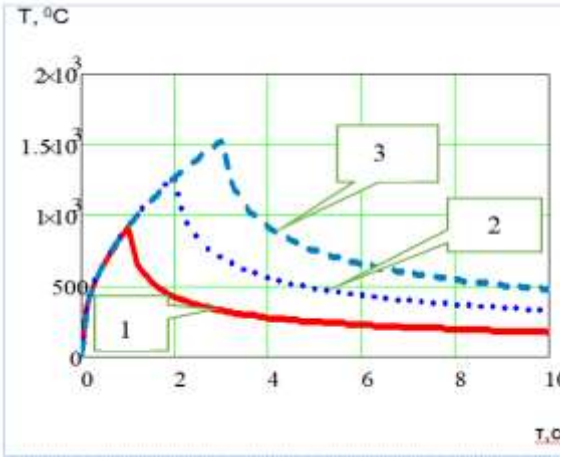


Figure 12. The surface temperature of steel depending on the time of exposure to heat flow. 1-1s, 2-2s, 3-3s, q=1.0*10^7 W/m^2

When implementing the hardening process, the surface is heated to a temperature close to the melting point of steel (1500^{0}C). This temperature is achieved during thermal action for 3 s when specific heat flux q = 1.0*10^7 W/m^2, (Fig. 12).

It can be seen from Fig.13 that the penetration depth of the isotherm at the beginning of the austenitic transformation of wheel steel 2 (750^{0}C) is 3.5 mm, so the thickness of the hardened layer should be approximately the same. At the same time, the cooling rate of the steel surface reaches more than 1500 K/s (Fig. 14).

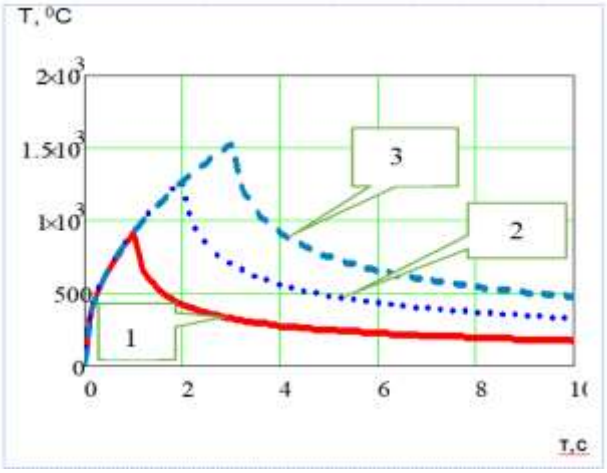


Figure 13. Temperature changes over time at different depths from the surface.1- 0,0; 2-1,0; 3-4,5 mm. τ0=3s, q=1.0*10^7 W/m^2

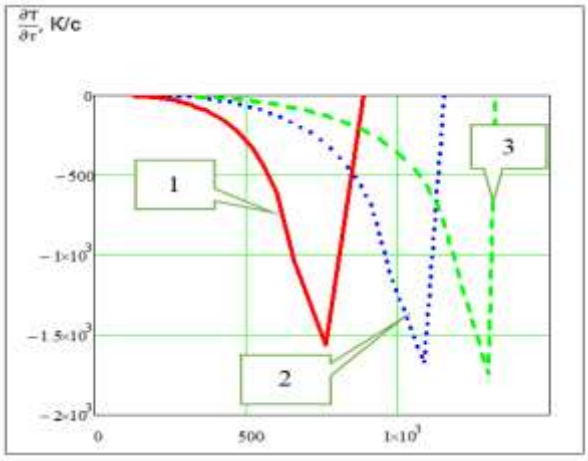


Figure 14. The cooling rate of the surface depending on its temperature at different times of exposure to heat flow: 1-1s, 2-2s, 3-3s. q=1,0*107 W/m^2

The surface temperature on the non-isothermal cooling diagram of wheel steel 2 is shown in Figs. 15 and 16. The temperature change over time is given for different specific heat fluxes and times of exposure to a single heat pulse of rectangular shape of various durations that are conditioned upon reaching the surface melting temperature.

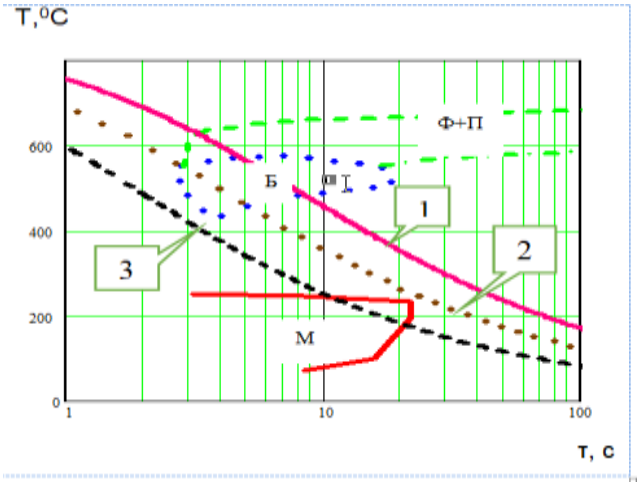


Figure 15. Cooling of the steel surface during hardening by different specific heat flows at different times of its action: 1-q=0,6*10^7 W/m2, T$_0$=7s ; 2 - q=1,0*10^7 W/m2, T$_0$=3s ; 3-q=2,0*10^7 W/m2, T$_0$=1s.m-martensite, b-bainite, f+p-ferrite +perlite

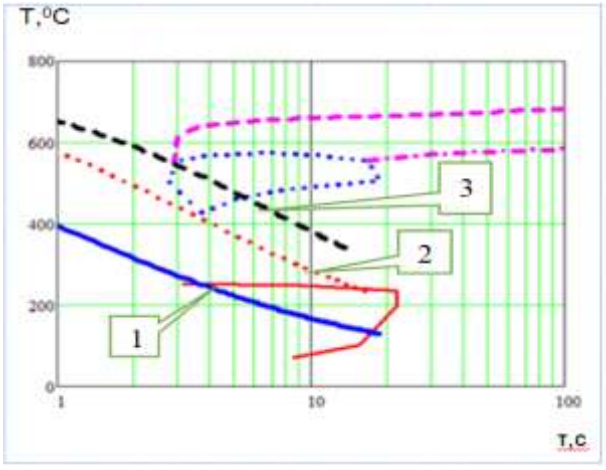


Figure 16. Cooling of steel surface during hardening with different times of thermal action:1- T$_0$-1s; 2- T$_0$-2s; , 3-T$_0$-3s. q=1,0*10^7 Wt/m^2.

The hardening is carried out at q = $1.0*10^7$ W/m^2 and various exposure times and, consequently, motions of the plasma generator relative to the treatment surface. Curves 2 in Fig. 15 and 3 in Fig. 16 (calculated according to a program [4] taking into account heat losses from radiation and convection) practically coincide. The depth of austenitic transformation of steel (the thickness of the hardened layer is: 0.5, 2.5, 3.5 mm, respectively, for τ_0-1 s, 2 s and 3 s (Fig. 16). For q = $2.0*10^7$ W/m^2 and exposure time τ_0 = 1 s, 100% martensite should be formed on the surface (Fig. 15). For softer surface-hardening modes, highly disperse structures of perlite in the form of bainite, troostite, and sorbite are formed. At values of heat flux q = $0,6*10^7$ W/m^2 and τ_0 = 7 s, the hardening process does not occur.

Figure 17 presents experimental data for hardening by a direct-acting electric arc (higher intensity heat fluxes are realized) and by an electric arc controlled remotely by magnetic fields (softer thermal effect, but more extended in the direction of the plasma generator relative to the treatment surface). When hardening with a direct electric arc occurs, the thickness of the hardened layer is 1.5 mm (Fig. 17a), and the surface structure is represented by 100% martensite (Fig. 17 c). Hardening by remote electric arc of about 4 mm (Fig. 17 b) gives a mixed structure consisting of martensite and a more plastic troostite component (Fig. 17 d).

It was shown [6] that the presence of 100% martensite leads to high stresses in the hardened layer - basic metal system, including circumferential stresses, the maximum values of which (1320 MPa) are close to the tensile strength for wheel steel 2. This leads in practice to the formation of cracks in the bandage during operation with unpredictable results. Confirmation of the above is the formation of cracks in the bands of locomotive wheels during hardening by various technologies for high hardness to obtain the appropriate structures in the layer on various Railways of the Russian Federation. At the same time, during the operation of locomotive wheels hardened by an electric arc at enterprises of the Far Eastern railway (JSC "Russian Railways") to a moderate hardness of 450-650 HV (without 100% martensite on the surface), no cracks were observed for many years of operation.

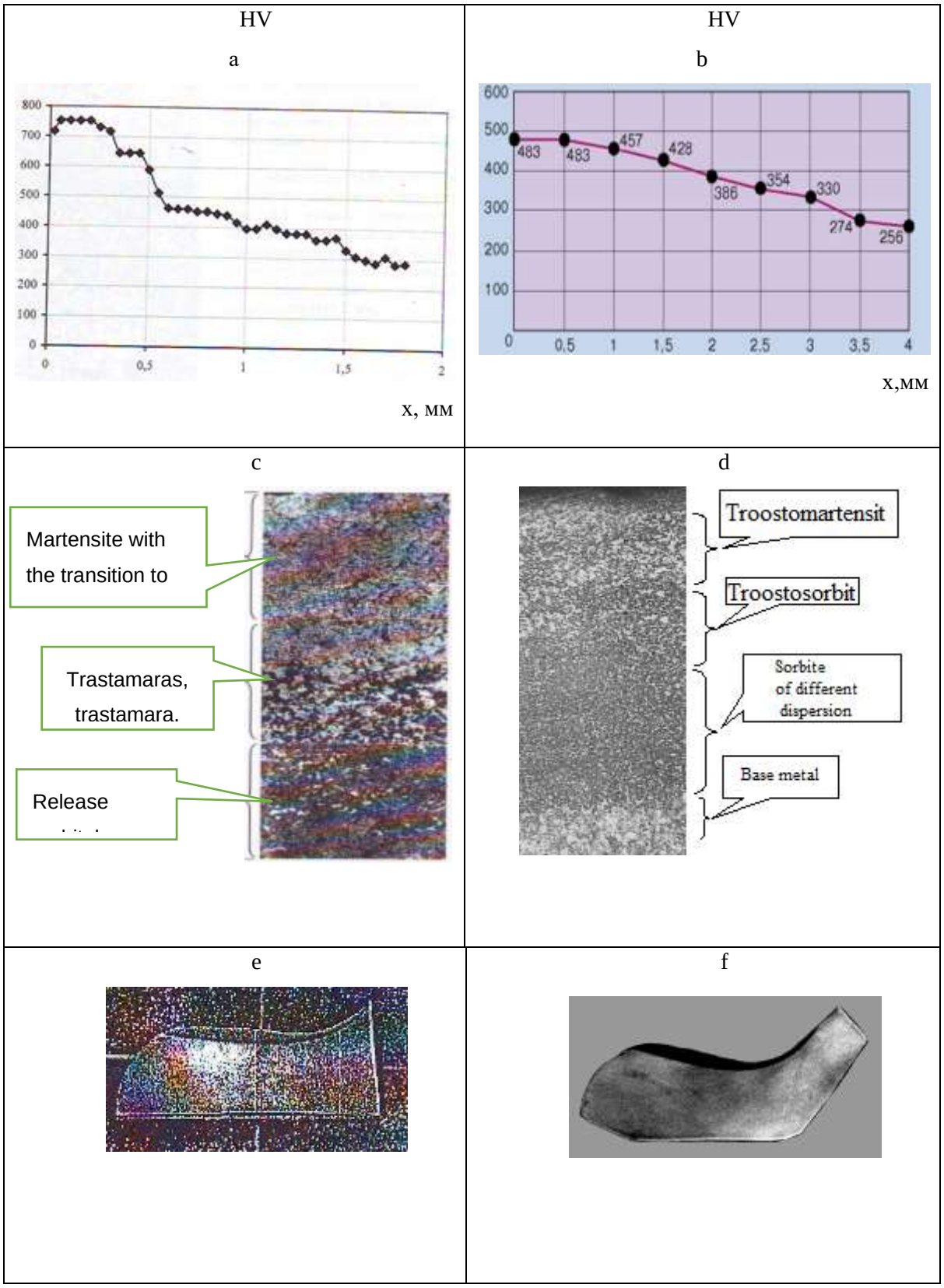


Figure 17. Properties of the hardened layer at different hardening modes. Microhardness (a) and hardness (b) of the hardened layer depending on its depth. Microstructure of the hardened layer at different depths (c) and (d). Microstructure of the hardened layer (e) and (f). Hardening by an electric arc of direct action - a, c, e. Hardening by an electric arc- b, d, f.

4. Conclusions

1. Theoretical analysis of thermal conditions in the weld and near-weld zone during aluminothermic welding of rails showed a satisfactory correspondence of the computed and experimental values of the dimensional characteristics of the weld and near-weld zone.
2. The process of aluminothermic welding conducted with decreased preheating of rails before welding and increased heating of the molten metal poured into the mold in order to improve the structure of the metal and, accordingly, the strength and operating characteristics of the weld, can be applied in practice when welding rails.
3. Thermal conditions in the ridge of the locomotive wheel during plasma hardening were computed.
4. The plasma-heating parameters were shown to influence the dimensional characteristics of the hardened layer and its structure, which correlated satisfactorily with experimental data that ensure safe operation of locomotive wheels.

References

1. Ing M. E., Mur D. T., Flejkherti D. Independent crucible and igniter to welding apparatus. RF Patent № 2302325 of July 10, 2007. IPC B23K23/00.
2. Janichko Sh., Greshova M. Liteynaya forma dlya alyuminotermitnoy svarki rel'sov [Casting mold for aluminithermic welding of rails]. RF Patent № 2116875 of August 10, 1998. IPC B23K23/00.
3. Karabanov V. I., Ivakin N. I., Aleshin A. I., Toritsyn I. V., Gvozdev I. E. Sposob alyuminotermitnoy svarki rel'sov [Method for aluminothermic welding of railway road rails]. RF Patent № 2163184 of February 20, 2001. IPC B23K23/00.
4. A. M. Lykov, The Program for the Calculation of Thermal Processes of Modification of the Surface of Materials. Certificate of State Registration of Computer Programs. № 2018617509 from 25.06.2018.
5. A. M. Lykov, N. N. Naumenko, Plasma modification of the material surface (Ark, Minsk, 2012).

Hot air drying of celery: Drying kinetics, pretreatment effect and color changes

Cansin Kurt, Ilknur Kucuk* and İbrahim Doymaz

Department of Chemical Engineering, Yildiz Technical University, 34210 Esenler, Istanbul, Turkey
*****Corresponding author: kucuk@yildiz.edu.tr; Tel.:+90 212 383 4761.*

Abstract: In this study, celeries were dried in convection dryer at a temperature range of 55-75°C with a constant air velocity of 2 m/s. To determine pretreatment effect celeries were treated %1 citric acid solution. Drying process continued until sample moisture fell down to 0.10 kg water/kg dry matter. It was observed that pretreatment did not significantly affect the drying time while drying time decreased with increased temperature. The experimental results illustrated the absence of constant-rate drying period and drying took place in the falling-rate period. Eight well-known mathematical models were used to predict drying kinetics by nonlinear analysis of regression. The models were compared using statistical criteria based on, coefficient of determination, reduced chi-square and root mean square error values. Midilli and Kucuk model best fitted the experimental data for the whole range of temperatures. The moisture diffusivity coefficient at each temperature was determined by Fick's second law of diffusion and the diffusion coefficient values of celery were between 1.701 × 10-10 and 3.317 × 10-10 m2/s and 1.753 × 10-10 and 3.797 × 10-10 m2/s for the pretreated celery samples. The dependence of effective diffusivity coefficient on temperature was expressed by an Arrhenius type equation. Activation energy values were calculated as 31.66 and 32.70 kJ/mol for untreated and pretreated samples, respectively. It was determined that L * (brightness), a * (redness) and b * (yellowness) values closest to the color values of fresh celery belonged to the pretreated sample dried at 55 ° C.

Keywords: Drying; effective diffusivity; celery; pretreatments.

1. Introduction

Celery (Apium gravelens L.) is a low-calorie vegetable with a high water content and contains appreciable amounts of natural bioactive components essential oil and flavonoids and also is an excellent source of vitamin K, molybdenum, folate, potassium, dietary fiber, manganese, and pantothenic acid [1,2].

Drying is one of the oldest methods of food preservation. It is used to extend the self-life of vegetables and to reduce the mass transportation. It also reduces the weight and bulk of foods which cuts down on transport and storage costs.The drying process is intended to remove water from foodstuff to prevent microbial spoilage and chemical alterations, thus prolonging shelf-life while realizing space and weight savings. The low water activity of the products prevents growth of microorganisms, enzymatic reactions, and other deteriorative reactions [3]. Hot-air drying is the most widely used method for preservation of food in processing industry. The applied drying conditions and pretreatments highly influence the resulting physical, chemical, microbial, functional and organoleptic properties of the agricultural products. Sodium and potassium hydroxide, sodium bicarbonate, potassium metabisulfate, potassium carbonate, methyl and ethyl ester emulsions, ascorbic and citric acids are common and commercially used materials for pretreatment. [4,5].

Many mathematical models have proposed to describe the drying process, of them drying models have been widely in use. These models can be categorized as theoretical, semi-theoretical, and empirical. A large number of studies have been conducted to investigate the drying kinetics, determine the water diffusivity and assess the influence of drying conditions on the drying process of different agricultural products [3,6]. So far, there a little information available about modelling, effective diffusivity and activation energy of drying of celery roots in cube form and there is no information available about drying of celery cubes with pretreated with citric acid solution. The aims of this research

were to (1) investigate the effect of temperature and pretreatment on drying and colour characteristics, (2) to select the best mathematical model to describe the drying curves, and (3) compute effective moisture diffusivity and activation energy of celery.

2. Materials and Methods

2.1 Preparation of samples

Good quality fresh celery (Apium gravelens L.) were purchased from a local market in Istanbul, Turkey. Fresh celery were washed and cut into cube form with e 6±0,5 mm in thickness The initial moisture content of celery was determined by using an oven at 105°C for 24 h. Triplicate samples were used for the determination of moisture content and the average values were reported as 9.43 kg water/kg dry matter (d.b.). Prior to drying of samples were pretreated by the following pretreatment methods: (1) no pretreatment (Control) and (2) soaking in 1% citric acid solution (CA).

2.2 Drying Experiments

The drying of celery was investigated in experimental drying cabinet (APV&PASILAC Limited of Carlisle, UK) and the cabinet dryer was described by Doymaz [R]. The dryer was started about 30 min before drying experiments to achieve steady-state conditions before each drying run. Then, the samples weighing about 30±0.5 g was spread on the tray. The drying experiments were conducted at 55, 65 and 75°C air temperatures and constant air velocity of 2±0.1 m/s. Mass changes of celery were recorded every 15 minute by a digital balance (Mettler-Toledo AG, Switzerland) during drying. Drying was stopped when the moisture content of samples were 0.10±0.02 kg water/kg dry matter (d.b.). Then, the dried samples were packed into polyethylene bags, which were then heat-sealed and stored in incubators at ambient temperature. The experiments were replicated three times and the average of the moisture ratio at each value was used for drawing the drying curves.

2.3 Mathematical Modelling and Data Analysis

Eight semi-theoretical models were selected to describe the drying kinetics of the celery samples (Table 1). The moisture content (M) and moisture ratio (MR) of celery cubes were calculated using the following Equations :

$$M = \frac{W - W_d}{W} \quad (1)$$

$$MR = \frac{M_t - M_e}{M_0 - M_e} \quad (2)$$

where M is the moisture content (kg water/kg dry matter), W is the weight of sample (kg), W_d is the dry matter content of sample (kg), and t is the drying time (min). M_e and M_t are equilibrium moisture content and moisture content at t (kg water/kg dry matter), respectively. As the M_e is very small compared to M_0 and M_t values, the Me can be neglected and MR can be expressed as M_t / M_0 [9].

Table 1. Mathematical models for fitting to the drying of celery

Model name	Model	Reference
Wang&Singh	$MR = 1 + at + bt^2$	**[6]**
Lewis	$MR = \exp(-kt)$	**[7]**
Henderson and Pabis	$MR = a\exp(-kt)$	**[8]**
Logarithmic	$MR = a\exp(-kt) + c$	**[9]**
Page	$MR = a\exp(-kt^n)$	**[10]**
Midilli and Kucuk	$MR = a\exp(-kt^n) + bt$	**[11]**
Vega-Lemus	$MR = (a + bt)^2$	**[12]**
Vega-Galvez	$MR = \exp(n + kt)$	**[12]**

Experimental data were analyzed using the Statistica 8.0.550 (StatSoft Inc., USA) software package. The parameters of the models were estimated using a non-linear regression procedure based on the Levenberg-Marquardt algorithm. The fitting quality of the experimental data to all models was evaluated using the coefficient of determination (R^2), reduced chi-square (χ^2) and root mean square error (RMSE). The R^2, χ^2 and RMSE were calculated from the following formulas:

$$R^2 = 1 - \frac{\sum_{i=1}^{N}\left(MR_{pre,i} - MR_{\exp,i}\right)^2}{\sum_{i=1}^{N}\left(\overline{MR}_{pre} - MR_{\exp,i}\right)^2} \quad (3)$$

$$\chi^2 = \frac{\sum_{i=1}^{N}\left(MR_{\exp,i} - MR_{pre,i}\right)^2}{N - z} \quad (4)$$

$$RMSE = \left[\frac{1}{N}\sum_{i=1}^{N}(MR_{pre,i} - MR_{\exp,i})^2\right]^{1/2} \quad (5)$$

where $MR_{exp,i}$ and $MR_{pre,i}$ are the experimental and predicted dimensionless moisture ratios, respectively; N is the number of observations; z is the number of constants. A higher R^2 value and lower χ^2 and RMSE values indicate a better fit [13].

2.4 Determination of Effective Moisture Diffusivity

The values of effective moisture diffusivity (D_{eff}) of dried celery are determined by using the Fick's second law of diffusion equation:

$$\frac{\partial M}{\partial t} = D_{eff}\nabla^2 M \quad (6)$$

The analytical solution of Fick's second law (Eq. 6) unsteady state diffusion in a spherical coordinates with the assumptions of moisture migration being by diffusion, negligible shrinkage, constant effective diffusivity and temperature during the drying process is given as follows [14] :

$$MR = \frac{6}{\pi^2}\sum_{n=1}^{\infty}\frac{1}{n^2}exp\left(-n^2\pi^2\frac{D_{eff}\,t}{r^2}\right) \tag{7}$$

For long drying periods, Eq. (7) can be further simplified to only the first term of the series. Thus, Eq. (7) is written in a logarithmic form as follows:

$$ln(MR) = ln\left(\frac{6}{\pi^2}\right) - \left(\frac{\pi^2 D_{eff}\,t}{r^2}\right) \tag{8}$$

The effective moisture diffusivity is obtained by plotting the experimental drying data in terms of ln (*MR*) versus time (min). From Eq. (8), a plot of *ln MR* versus *time* gives a straight line with a slope of (*K*), in which:

$$K = \frac{\pi^2 D_{eff}}{r^2} \tag{9}$$

2.5 Computation of Activation Energy

The dependence of the effective diffusivity on temperature is generally described by the Arrhenius equation:

$$D_{eff} = D_0\,exp\left(-\frac{E_a}{R(T+273.15)}\right) \tag{10}$$

where D_0 is the pre-exponential factor of Arrhenius equation (m^2/s), E_a is the activation energy (kJ/mol), R is the universal gas constant (kJ/(mol.K)), and T is temperature (°C).

2.6 Colour Analysis

The colour values of the fresh and dried samples, at between 50 and 80°C, were evaluated using a hand-held tristimulus colorimeter (Chroma Meter-CR-400). Colour was determined by CIELab method, where L is whiteness or brightness, a is redness/ greenness, and b is yellowness/blueness coordinates. For the colour determinations, four measurements were done, and the corresponding average and standard deviation were calculated for each set of celery, fresh and dried at each drying temperature.

3. Results and Discussion

3.1 Analysis of drying curves

Figure 1. presents variations in the moisture content as a function of drying time at 55, 65 and 75°C. It is clear that the moisture content decreases continuously with drying time. The pretreatment does not significant affected the drying time. The celery dipped in pretreatment solutions before the drying process was found to have a close drying time to the control ones. The drying times required for reducing the moisture content of pretreated samples were 210, 195 and 135 min. Corresponding values for the control samples were 210, 195 and 150 min at same temperatures, respectively. It was observed that the pretreatment did not significant affect the total drying time, but the total drying time decreased

with the increase in drying temperature. It can be seen from figure1 D that the drying rate increases with the increase in temperature, but the pretreatment with citric acid solution does not have a significant effect on the drying period for all three different drying temperatures. A similar result was found in the studies conducted by Heybeli at. all [15], in the trial of drying celery with infrared dryer, steaming for two minutes and boiling in boiling water were applied as a pretreatment, and it was seen that these pretreatments had no effect on drying speed and time.

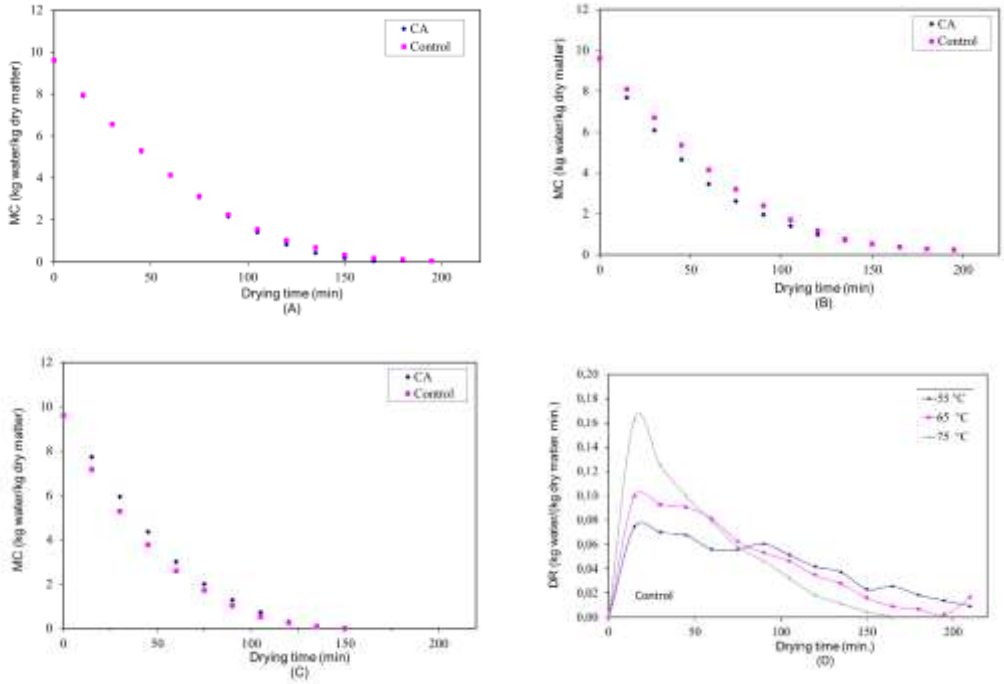


Figure 1. Effect of pre-treatments on moisture contents of celery, (A) 55°C, (B) 65°C and (C) 75°C and (D) drying rate versus drying time of celery for control sample

3.2 Evaluation of models

The moisture content data obtained from the drying experiments were fitted eight drying models presented in Table 1. The best model selected is based on the highest R^2 and the lowest χ^2 and RMSE values. Results of the statistical computing are shown in Table 2. The R^2 values for all models were above 0.98. Among the drying models tested, Wang ve Singh model obtained the R^2 values as 0.9872 and the lowest $\chi 2$ values as 0.002146 and RMSE values as 0.112962 describe best model for 55 °C. The closest values to these values are Midilli et al. found to be included in the model. For 65 and 75 °C, the most revealing model is Midilli et al. and the R^2 values are 0.9995 and 0.9998,χ^2 values are 0.000055 and 0.000024 and RMSE values are 0.019765-0.010345 for 65°C and 75 °C, respectively.

Table 2. Statistical parameters of models for different temperatures

T (°C)	*Model*	R^2	χ^2	*RMSE*
55	Lewis	0.9976	0.000262	0.044078
	Henderson and Pabis	0.9978	0.000263	0.044229
	Logarithmic	0.0993	0.000093	0.020364
	Page	0.09996	0.000043	0.014832
	Midilli and Kucuk	0.09997	0.000040	0.012221
	Wang&Singh	0.09827	0.002146	0.0112962
	Vega-Lemus	0.9875	0.001543	0.100661
	Vega-Galvez	0.9878	0.000263	0.044229
65	Lewis	0.9915	0.001274	0.065284
	Henderson and Pabis	0.9920	0.001490	0.069382
	Logarithmic	0.9963	0.000903	0.044298
	Page	0.9997	0.000038	0.009645
	Midilli and Kucuk	0.9998	0.000073	0.009920
	Wang&Singh	0.9955	0.000831	0.060479
	Vega-Lemus	0.9957	0.000792	0.049894
	Vega-Galvez	0.9920	0.001490	0.069379
75	Lewis	0.9970	0.000558	0.027740
	Henderson and Pabis	0.9970	0.000830	0.029457
	Logarithmic	0.9997	0.000145	0.010448
	Page	0.9986	0.000384	0.021432
	Midilli and Kucuk	1.0000	6.21×10^{-33}	6.59×10^{-17}
	Wang&Singh	0.9948	0.001450	0.043248
	Vega-Lemus	0.9934	0.001863	0.056004
	Vega-Galvez	0.9970	0.000830	0.029458

3.3. Effective moisture diffusivity and Activation Energy

By plotting ln(*MR*) against drying time and using the slope methods the effective moisture diffusivity of the samples was calculated under different drying conditions. The values of effective moisture diffusivity (D_{eff}) were calculated using Eq. (10) and are shown in Figure 3(A). The D_{eff} values of celery in the drying at 55-75°C varied between 1.701×10^{-10} and 3.317×10^{-10} m^2/s for pretreated samples , 1.753×10^{-10} and 3.797×10^{-10} for control samples. It can be seen that D_{eff} values increased with increasing air temperature. Drying at 75°C has the highest value of D_{eff} and the lowest value was obtained for 55°C. The values of D_{eff} from this study lie within in general range 10^{-12} to 10^{-8} m^2/s for drying of food materials [16]. The obtained moisture diffusivity values for celery slices agree well with the values reported in the literature [16].

A plot of ln (D_{eff}) as a function of 1 / (T+273.15) is produced a straight line with a slope equal to ($-E_a/R$), so E_a can be easily estimated (Figure 3.(B)). Equation 11 and 12 show the effect of temperature on D_{eff} of the samples with following coefficients :

$$D_{eff} = 2.732 \times 10^{-5} \exp\left(-\frac{3933}{(T+273.15)}\right) \quad (R^2 = 0.9744) \quad \text{(pretreated with CA)} \qquad (11)$$

$$D_{eff} = 1.8737 \times 10^{-5} \exp\left(-\frac{3809.1}{(T+273.15)}\right) \quad (R^2 = 0.9911) \qquad \text{(control)} \qquad (12)$$

The value of activation energy were found as 32.70 kJ/mol and 31.66 kJ/mol for pretreated and control samples. The values of activation energy lie within the general range of 12.7-110 kJ/mol for food materials[17]. The activation energy values recorded in the present study to reasonable agreement with the activation energy recorded for drying of various vegetables in the literature [17].

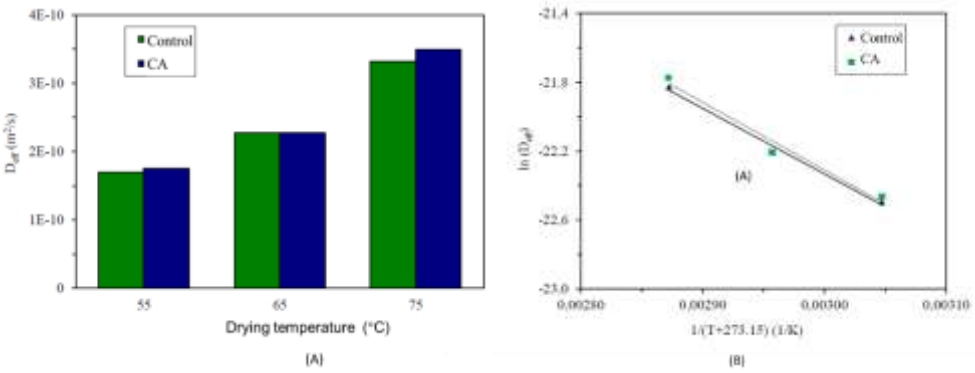


Figure 3. Variation of effective moisture diffusivity with air temperatures (A) and Arrhenius-type relationship between effective diffusivity and reciprocal absolute temperature (B)

3.4 Colour parameters

Colour is an important parameter related to the quality of the product, being an important criteria to consumers of dried fruits and vegetables. The average values for the colour parameters of fresh celery were as follows: L: 86.50, a: -2.05, and b: 11.33. values of dried celery samples varies as follows : L : 70.75-65.05, a: -0.80-1.71 and b:15.1-20.16.

The colour parameters of dried samples are presented in Table 3. It can be seen that the entire dried celery had lower values of *L* than the fresh samples. The L values which show whiteness of product. The decrease in L values might be caused by browning reactions [18]. It was determined that the colour parameters of the pretreated samples were closer to the fresh samples compared to the control samples for all temperatures. It was observed that the closest colour to fresh celery samples were in celery dried at 55 ℃ by soaking in citric acid.

Table 3. Colour parameters of dried celery

	L		A		b	
	Control	CA	Control	CA	Control	CA
55 °C	68.83	70.75	-0.456	-0.806	15.6	15.11
65 °C	68.05	65.39	-0.196	0.675	19.62	15.83
75 °C	65.05	65.52	1.715	0.815	20.16	19.03

4. Conclusions

Drying characteristics of celery were investigated in a cabinet dryer at various temperatures of 55, 65 and 75°C and constant air velocity of 2 m/s. Air temperature was important factor in drying of celery. High drying temperature resulted in a shorter drying time. Also, pretreated and control samples have very similar drying characteristic. To explain the drying kinetics of celery, eight drying models were applied and fitted to the experimental data. According to the results of statistical analysis, the experimental data were well predicted by Wang ve Singh for 55 °C and Midilli and Kucuk model for 65 °Cand 75 °C. The values of effective diffusivity of the pretreated and control samples were in the

range 1.701×10^{-10} m^2/s to 3.797×10^{-10} m^2/s. The activation energy values found to be between 32.70 and 31.66 kJ/mol.

References

1. Illes J.D. Blood Pressure Change After Celery Juice Ingestion in a Hypertensive Elderly Male.Journal of Chiropractic Medicine 2021, 00-00. Article in press.
2. Xu, C.; Liu, D.; Guo, C.; Wu, Y. Effect of cooling rate and super-chilling temperature on ice crystal characteristic, cell structure, and physicochemical quality of super-chilled fresh-cut celery. International Journal of Refrigeration 2020, 113, 249–255.
3. Jin, X.; Oliviero, T.; Van Der Sman, R.G.M.; Verkerk, R.; Dekker, M.; Van Boxtel, A.J.B. Impact of different drying trajectories on degradation of nutritional compounds in broccoli (Brassica oleracea var. italica). LWT – Food Science and Technology 2014, 59, 189-195.
4. Kingsly, R.P; Goyal, R.K; Manikantan,M.R.; Ilyas, S.M. Effects of pretreatments and drying air temperature on drying behaviour of peach slice. International Journal of Food Science and Technology 2007, 42, 65-69.
5. Adiletta, G.; Russo, P.; Senadeera, W.; Di Matteo, M. Drying characteristics and quality of grape under physical pretreatment. J. Food Engineering 2016, 172, 9-18.
6. Deng, L.Z.; Yang, X.H.; Mujumdar, A.S.; Zhao, J.H; Wang, D.; Zhang, Q.; Wang, J.;. Gao,Z.J; Xiao, H.W. Evolution and modeling of colour changes of red pepper (Capsicum annuum L.) during hot air drying. Drying Technology 2018, 36, 893-907.
7. El-Beltagy, A.; Gamea, G.R.; Essa, A.H.A. Solar Drying Characteristics of Strawberry. Journal of Food Engineering 2007, 78, 456–464.
8. Erbay, Z.; Icier, F. Thin-layer Drying Behaviours of Olive Leaves (Olea Europaea L.). Journal of Food Process Engineering 2010, 33, 287-308.
9. Afolabi, T.J.; Tunde-Akintunde, T.Y.; Adeyanju, J.A.; Mathematical Modeling of Drying Kinetics of Untreated and Pretreated Cocoyam Slices. Journal of Food Science and Technology 2015, 52, 2731-2740.
10. Falade, K.O.; Ogunwolu, O.S; Modeling of Drying Patterns of Fresh and Osmotically Pretreated Cooking Banana and Plantain Slices. Journal of Food Processing and Preservation 2014, 38, 373-388.
11. Midilli, A.; Kucuk, H. Mathematical Modeling of Thin Layer Drying of Pistachio by Using Solar Energy. Energy Conversion and Management 2003, 44, 1111-1122.
12. Vega-Galvez, A.; Scala, K.D.; Rodrguez, K.; Lemus-Mondaca, R.; Miranda, M.; Lopez, J.; Perez-Won, M. Effect of Air-drying Temperature on Physico-Chemical Properties, Antioxidant Capacity, Colour and Total Phenolic Content of Red Pepper. Food Chemistry 2009, 117, 647-653
13. Marianni, V.C; Perussello, C.A.; Cancelier, A., Lopes; T.J. and Silva, A. Hot-air Drying Characteristics of Soybeans and Influence of Temperature and Velocity on Kinetic Parameters. Journal of Food Process Engineering 2015, 37, 619–627.
14. Crank, J.; The Mathematics of Diffusion, Oxford University Press, London,1975.
15. Heybeli, N., Ertekin, C., Dikici, G., Infrared Kurutucu ile Kerevizin Kurutulması, Tralleis Elektronik Dergisi 2013, 1:16-25.
16. Wei, X.; Fan, K.; He,J.; Yan, F. Characterization of Thin Layer Hot Air Drying of Celery Root. Advance Journal of Food Science and Technology 2015, 9, 412-421.
17. Zogzas, N.P., Maroulis, Z.B., Marinos-kouris, D., 1996. Moisture Diffusivity Data Compilation in Foodstuffs. Drying Technology 14 (10), 2225-2253.
18. Torki-Harchegani, M.; Sadeghi, M.; Ghanbarian, D.; Moheb, A. Dehydration Characteristics of Whole Lemons in a Convective Hot Air Dryer. Iranian Journal of Chemistry and Chemical Engineering 2016, 35, 65-73.
19. Ju, H.Y., El-Mashad, H.M., Fang, X.M., Pan, Z., Xiao, H. ., Liu, Y. H., & Gao, Z.J. Drying characteristics and modeling of yam slices under different relative humidity conditions. Drying Technology 2016, 34(3), 296–306.

Performance Evaluation of Triple Concentric Tube Heat Exchanger Using [EMIM][BF_4] Ionic Liquid and MWCNT/[EMIM][BF_4]

Huda Majid Hasen [1,*] and Prof. Dr. Basma A. Abdulmajeed [2]

[1] Department of Chemistry, College of Science, University of Thi-Qar, Thi-Qar, Iraq;
[2] Chemical Engineering Department, College of Engineering, University of Baghdad, Baghdad, Iraq
* *Corresponding author E-mail Huda.maged0907@coeng.uobaghdad.edu.iq*

Abstract: A triple, concentric tube heat exchanger (TCTHE) made of high conductivity copper tube was designed in this study. The designed TCTHE consisted of three tubes of diameter 34.925 mm, 22.25 mm, and 9.525 mm, and the tubes' thicknesses were 1.27 mm, 1.143 mm, and 0.762 mm, respectively. The length of the outer, middle, and inner tubes was about 670 mm. The TCTHE performance was experimented with using the hydrophilic ionic liquid (IL) and its ionanofluid (INF) of 0.5%MWCNT/[EMIM][BF_4] as cooling medium and oil forty stock as hot fluid. The cooling medium flows at a flow rate range of 20-55 l/hr and a temperature of about 25-27 ^oC. Oil of forty stock flows at a constant flow rate of 20 l/hr and three temperatures of 50, 60, and 70 ^oC in countercurrent flow. The heat transfer was studied by measuring the Nusselt number, friction factor, pressure drop, and overall heat transfer coefficient of the cold fluid. The results showed that Nusselt number and the overall heat transfer coefficient of both the cooling fluid [EMIM][BF_4] IL and INF increased with flow rate and Reynolds number for the inner tube and the outer annular TCTHE. On the other hand, the friction factor of both the cooling fluid [EMIM][BF_4] IL and INF decreased with flow rate and Reynolds number for the inner and outer annular of TCTHE. The pressure drop of IL and INF increased linearly with the flow rate. In addition, the pressure drop in the inner tube for the INF increased by 95% or doubled compared with that of the IL. The overall heat transfer coefficient of both the cooling fluid [EMIM][BF_4] IL and INF increased with the inlet temperature of the hot fluid (the oil).

Keywords: triple concentric heat exchanger ; ionic fluids ; ionanofluid ; MWCNTs ; [EMIM][BF_4].

1.Introduction

1.1. Ionic liquid

To increase the lifetime and the efficiency of a heat exchanger and reduce the corrosion, erosion, and explosion problems, a new heat transfer fluid HTF must be used instead of the traditional HTFs such as water and ethylene glycol, especially in the high-temperature operation up to 200 °C.

ILs are pure salt composed of two non-symmetrical parts, organic cation, and organic or inorganic anion; for that reason, these salts have a low melting point of about 25-100 ^oC. Figure 1 shows common cations and anions of ionic liquid [1], [2].

Many researchers studied the possibility and the efficiency of using ILs as HTF for different applications, especially imidazolium type of ILs, because of their popularity, versatility [3], and

miscibility with organic and inorganic compounds [4]. in 2009 Castro et al. studied for the first time the thermophysical properties enhancement of imidazolium and pyrrolidinium ILs [5].

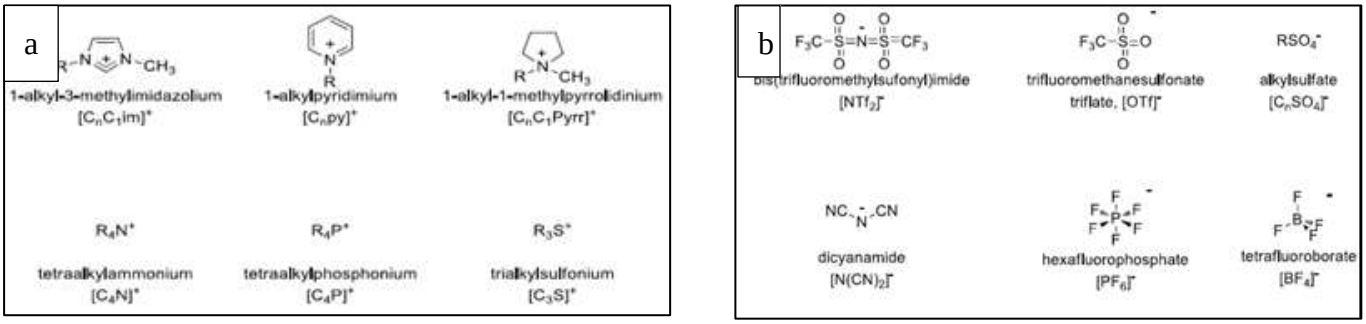


Figure 1. (a) Cations and (b) Anions used in ionic liquid preparation [1]

Ionic liquids have many advantages that make them an excellent candidate to use as HTFs in HE, especially their thermal stability, low saturated vapor pressure under normal conditions, non-volatility, high flash point, and environmentally friendly.

Using ionic liquids as HTFs for cooling purposes in a heat exchanger in chemical and solar power plants depends mainly on the desired thermophysical properties values, especially the heat capacity, thermal conductivity, density, viscosity, the required thermal stability and vapor pressures.

Furthermore, HE's suitable design greatly affects the efficiency of the cooling or heating process required for different applications.

1.2. NFs and INFs in Heat Exchanger Applications

In the last decade, many authors studied the possibility of replacing conventional HTFs in the heat exchangers with the newly invented nanofluids (NFs) and ionic liquids (ILs) of different nanoparticles NPs. For examples:

Kumar et al. studied the heat transfer variations, and the pressure drop of water flow in a double pipe heat exchanger (DPHE) by measuring Nusselt number, using activated carbon (AC)/solar glycol (SG) based NFs. The results show that the average convective HTC (CHTC) of 0.6% of AC/ SG NF was improved by 71% at 0.04 kg/sec [6].

Chavda et al. presented two researches of NFs prepared of different volume fractions of Al_2O_3 in water and investigated their effect on the friction factor [7]. Furthermore, they investigated these NFs in DPHE for co-current and counter current flow and found that the HTC increased with increasing Al_2O_3 [8].

Laminar flow of NFs is experimented by Sudarmdji, by measuring the pressure drop and the friction factor of the Al_2O_3in water NFs [9]. The same NFs were used by Wen and Ding. They measured the Nusselt number during flowing through a copper tube, recording an increase in the Nusselt number by 47% for a 1.6% volume fraction of Al_2O_3 [10].

Ezzat and Hasan studied the thermal behavior of γ- Al_2O_3/distilled water NF as a cooling medium in an annulus channel under forced convection at steady state conditions. The result showed an improvement in the heat transfer coefficient ratio of the NF to that of pure water of about (1.2 - 4.7%) [11].

Jaafer et al, studied NFs prepared by dispersing Al_2O_3 of 30 nm diameter nanoparticle in water between (0.3- 2) % volume fraction and experimented them in countercurrent turbulent flow through the horizontal shell and tube heat exchanger. They found that the HTC viscosity and friction factor increased with increasing volume fraction of Al_2O_3 [12].

Zamzamian et al. prepared two types of NFs by dispersing Al_2O_3 and CuO in ethylene glycole in different concentrations and experimented with them in a DPHE. They found that using NFs of (2-50) % increased the HTC [13].

K.Logesh et al. prepared NFs with different concentrations of MWCNTs in isopropyl alcohol and investigated their thermophysical properties during flowing in laminar flow through a heat exchanger. The result showed an improvement of the HTC and Nusselt number with increasing the MWCNTs concentration [14].

Nasirzadehroshenin. F. et al. investigated the heat transfer performance of carbon nanotube (CNT)/water NF flowing in turbulent regime through a horizontal tube of constant wall temperature. The result showed that the HTC was improved in these NF comparing with water [15].

Basma and Noor prepared NFs of Al_2O_3 in water. Then used these NFs for cooling in countercurrent flow in shell and DCTHE. The results showed that Nusselt number and overall HTC increased with increasing NFs concentrations [16].

Perumal et al. gave a review on the use of NFs in a concentric tube heat exchanger (CTHE) with the thermophysical properties of NFs, including thermal conductivity, viscosity, density, and specific heat. Furthermore, studying the heat transfer performances of CTHE using these NFs [17].

In two separate papers [18] and [19], the researchers prepared ionic fluids of 1-Butyl-3-methylimidazolium chloride [Bmim][Cl] / distilled water in different concentrations and tested them in shell and tube heat exchanger. The results showed that these INFs exhibit superior thermophysical properties comparing with their base fluids. As a result, they could be a very promising HTF, especially in shell and tube heat exchangers.

Palanisamy and Kumar prepared NFs of MWCNT/water in a three-volume concentration of 0.1%, 0.3%, and 0.5%. They experimented these NFs in a cone helically coiled tube heat exchanger. The 0.5% MWCNT/water improved the overall HTC by 52% comparing with water. On the other hand, the 0.1%, 0.3%, and 0.5% MWCNT/water reached HTC enhancement of about 14%, 30%, and 41% respectively and Nusselt numbers improvement of 28%, 52%, and 68% respectively with no significant deposit of MWCNTs in the coiled cone tube inner surfaces even after several experimental tests. [20].

M. Meikandan et al. selected several ionic liquids [BMIM] [BF_4], [BMIM] [PF_6], and [HMIM] [BF_4] to be used as HTFs in tubular heat exchanger designed for solar application in laminar flow. Furthermore, investigated the heat transfer of this system using CFD analysis [21].

1.3. TCTHE design

TCTHE was developed to enhance the heat transfer between the hot and cooling medium by increasing the heat transfer area using the additional cooling liquid passage. TCTHE looks like a double concentric tube heat exchanger with an intermediate tube between them. This means increasing the contact area between the hot and the cold mediums. This, in turn, will improve the heat transfer and increase the HE efficiency.

Many reviews are published on TCTHE, including[17], [22] and [23] to display the research development of TCTHE.

Zuritz made simulations on TCTHE. These simulations show that creating an annular region within the inner pipe improves the overall heat transfer efficiency and reduces the heat exchanger length by almost 25 %. Furthermore, they derived a simple approximate equation for the total heat transfer rate in terms of logarithmic mean temperature difference for well-insulated heat exchangers and tested it with the analytical equations [24].

Saeid and Seetharamu studied the thermal performance of TCTHE presenting an experimental study for different flow arrangements for insulated and non-insulated heat exchangers using the finite element method [25].

Quadir et al. studied experimentally TCTHE for different flow arrangements for insulated and non-insulated conditions of a heat exchanger [26], [27].

Hossain et al designed and fabricated TCTHE made of copper tubes. The experimental results found that the overall HTC increased with the mass flow rate for hot and cold water. In addition, the overall HTC of TCTHE showed better performance comparing with the equivalent DCTHE. Furthermore, the length of the TCTHE reduced by 65.17% comparing with DCTHE for the same heat transfer area and the same heat transfer rate [28].

Meikandan et al. selected several ionic liquids [BMIM][BF_4], [BMIM][PF_6] and [HMIM] [BF_4] to use as HTFs in tubular heat exchanger designed for solar application in laminar flow. Furthermore, investigated the heat transfer of this system using CFD analysis [21].

1.4. Objective

The objective of this study is to design TCTHE, then study the heat transfer efficiency by using [EMIM][BF_4] and its INF of 0.5% MWCNT/[EMIM][BF_4] as cooling fluid against forty stock oil as hot fluid. First, a comparison between the performance of the two cooling fluids depending on different parameters such as the flow rates of the cooling fluid and inlet temperature of the hot fluid, and Reynolds number, then study the effect of these parameters on Nusselt number, pressure drop, friction factor, and overall heat transfer parameters. In this process, countercurrent flow is used.

2. Materials and Methods

2.1. Materials.

2.1.1. The hot medium:

Three liters of oil (forty stock) were used as the heating fluid. Table 1 represents the physical properties of the oil (forty stock). These properties were obtained from Al-Doraa Refinery, Laboratory Research of Oil). The hot fluid flow through the inner annular of the TCTHE.

Table 1. The physical properties of the oil (forty stock)

No.	Specification	The values
1	Specific gravity @60/60 oF	0.86
2	Kinematic viscosity @ 40 oC, C.st	16.47
3	Kinematic viscosity @100 oC, C.st	3.64
4	Viscosity index	104
5	COC flash point, oC	182
6	Pour point, oC	-12
7	Colour, ASTM-D1500, @ 25 oC	0.5
8	Water content %vol.	NiL

2.1.1. The cold medium

The molten salt [EMIM][BF4] and the INF 0.5% MWCNTs/[EMIM][BF4] was used as cooling fluid. The two fluids' thermophysical properties have been measured experimentally and shown in table (2). The cold fluid passed through the inner tube and outer annulus tube of the TCTHE.

Table 2. The thermophysical properties of the IL and the INF [29]

	[EMIM][BF4]				0.5% MWCNT/[EMIM][BF4] INF			
T, ºC	**ρ, kg/ m3**	**μ, kg/m.sec**	**K, w/m.k**	**Cp, kJ/kg.k**	**ρ, kg/ m3**	**μ, kg/m.sec**	**K, w/m.k**	**Cp, kJ/kg.k**
20	1.283	0.033866	0.18	1.548	1.2855	0.06042	0.182	1.558
30	1.274	0.026749	0.181	1.565	1.277	0.04929	0.184	1.575
40	1.267	0.018807	0.182	1.582	1.27	0.03572	0.185	1.593
50	1.259	0.014133	0.184	1.6	1.261	0.03144	0.186	1.611

2.2. Ionanofluids Preparation

Ionanofluids are prepared using the two-steps method. The suitable amount of multi-walled carbone nanotubes was dispersed in about three litters of (1-ethyl-3-methyl imidazolium tetrafluoroborate in 0.5% weight percent depending on the equation:

$$\text{nanoparticles weight percent in ionanofluid} = \frac{\text{weight of nanoparticles}}{\text{weight of nanoparticles} + \text{weight of ionicliquid}} * 100\% \quad \text{.....(1)}$$

This was followed by the dispersing process, which includes two steps:

A magnetic stirrer was used for 10 min at room temperature, followed by 10 minutes homogenizer. Although this step is necessary to get rid of aggregation of the particles after the preparation and during the long time storage, it is not enough for good dispersion of the nanoparticles in ionic liquid. So the next step is necessary to homogenize the prepared ionanofluids

Sonication of the mixture using an ultrasonic probe homogenizer for 20 minutes.

2.3 TCTHE design

The metal used for the TCTHE tubes is copper (suitable for cooling and heating) since copper has a high thermal conductivity of about 385 W/m.ºC and low cost compared with other metals such as brass and aluminum. Figure (2) shows the 2D front side and top view of the designed TCTHE system in addition to the supporting equipment in the heat exchanger system such as the power supply, the pump, the volumetric flow rate sensor, the fin and tube HE, and the cooling fluid mixer. TCTHE system consists of two stainless steel tanks, one for the hot fluid medium (oil forty stock) and the other for the cold fluid medium (IL or INF), each of them have 4-liter capacity. Each of these tanks is supplied with a temperature sensor to detect the temperature of the fluid inside the tank. The output of each tank is supplied with a valve to close when not in use. TCTHE tubes are put horizontally above the tanks of about 40 cm so that two pumps are used to pump the fluid to the TCTHE tubes. A volumetric flow rate controller is used to detect and control the flow. After leaving the TCTHE the cold fluid medium passes through a fin and tube heat exchanger supplied with an air cooler to decrease the fluid temperature. There is a mixer Inside the cold fluid medium. In the case

of using NF or INF as a cooling fluid, it is necessary to mix the fluid and prevent nanoparticles from aggregating and sedimentation inside the tank and then block the system tubes.

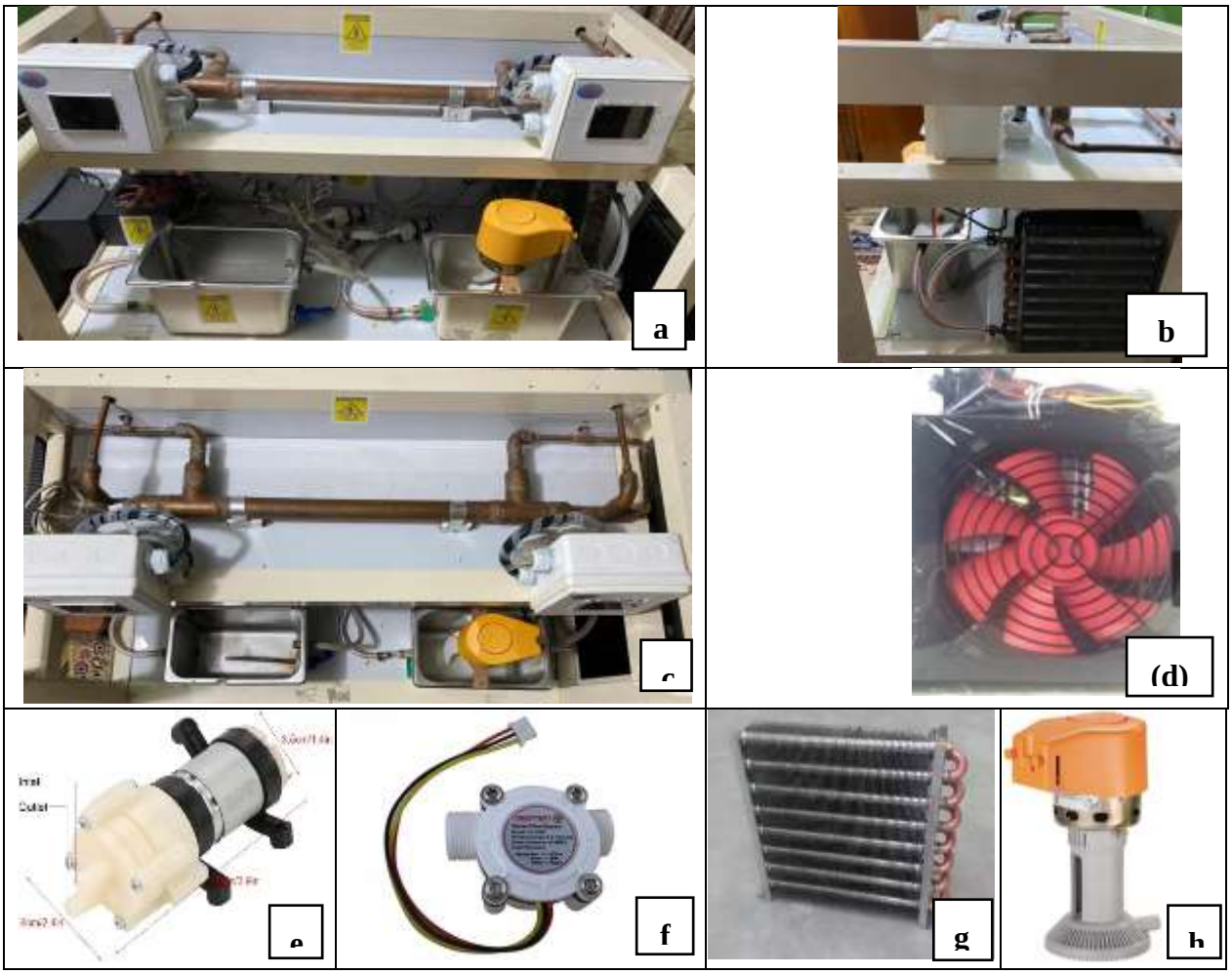


Figure 2. Shows (a) the front, (b) the side, and (c) the top view (d) the power supply, (e) the pump, (f) the flow sensor, (g) the fin and tube HE, and (h) the cooling fluid mixer of the TCTHE

On the other hand, a heater inside the hot fluid tank can heat the fluid to the desired temperature. The flow direction of the cold fluid medium still the same (unchanged). The flow arrangement could be changed to countercurrent or co-current by changing the flow direction of the hot fluid medium automatically using the program or manually.

TCTHE system is supplied with two screens to display the flow rate, the inlet and the outlet temperature of the TCTHE, and the tank temperature of the cold and hot fluids.

TCTHE consists of three tubes: outer, inner, and intermediate tube. The TCTHE tubes have outside, inside diameters and thickness, as shown in table 3.

Table 3. Outside, inside diameters, and thickness of TCTHE tubes.

	tube1	**tube2**	**tube3**
Inside diameter, mm	8.001	19.964	32.385

Outside diameter, mm	9.525	22.25	34.925
Tube thickness, mm	0.762	1.143	1.27

In this research, countercurrent flow is used. The cold fluid (IL) and (INF) flow in the inner tube and the outer annular tube in the same direction. On the other hand, the hot medium (the oil) flows in the opposite direction. The heat exchanger has an effective length of (67) cm.

2.4. TCTHE calculations

TCTHE parameters could be calculated using the equation in Table 4.

Table 4. TCTHE equations.

	Cooling fluid (IL or INF) in the inner tube	**Hot fluid (Oil forty stock) for inner annular**	**Cooling fluid (IL or INF) for outer annular**
The mean bulk temperature	$T_{b1} = \frac{T_{c1i}+T_{c2e}}{2}$ (2)	$T_{bw} = \frac{T_{Hi}+T_{He}}{2}$ (3)	$T_{b3} = \frac{T_{c2i}+T_{c2e}}{2}$ (4)
The linear velocity	$v_{c1} = \frac{V_{c1}*4}{\pi*d_{in2}^2}$ (5)	$v_H = \frac{V_H*4}{\pi*(d_{in2}^2-d_{out1}^2)}$(6)	$v_{c2} = \frac{V_{c2}*4}{\pi*(d_{in3}^2-d_{out2}^2)}$…(7)
The hydraulic diameter	$d_{h1} = d_{i1}$	$d_{h2} = d_{i2} - d_{o1}$	$d_{h3} = d_{i3} - d_{o2}$
Reynolds number	$Re_{c1}=\frac{\rho_{c1}V_{c1}d_{h1}}{\mu_{c1}}$ (8)	$Re_H=\frac{\rho_H V_H d_{h2}}{\mu_H}$ (9)	$Re_{c2}=\frac{\rho_{c2}V_{c2}d_{h3}}{\mu_{c2}}$ (10)
Nusselt number for laminar flow condition (Re< 2300)	$Nu_c = Re^{0.5} * Pr^{1/3} * (\frac{Pr}{pr_w})^{0.25}$ (11)		
The convective heat transfers co-efficient	$h_{c1} = \frac{Nu_{c1}*k_{c1}}{d_{h1}}$ (12)	$h_H = \frac{Nu_H*k_H}{d_{h2}}$ (13)	$h_{c2} = \frac{Nu_{c2}*k_{c2}}{d_{h3}}$ (14)
Heat Transfer Rates	$Q_{c1} = m_{c1}*C_{Pc1}*(T_{c1e} - T_{c1i})$ …..(15)	$Q_H = m_H*C_{PH}*(T_{Hi} - T_{He})$ ….(16)	$Q_{c2} = m_{c2}*C_{Pc2}*(T_{c2e} - T_{c2i})$ … (17)
the frictional pressure loss	$\Delta P1C1 = \frac{f\ l\ \rho {v_{c1}}^2}{d_{h1}\ 2}$ …(18) f =64/Re_{c1} for laminar regime	$\Delta P1H = \frac{f\ l\ \rho {v_H}^2}{d_{h2}\ 2}$ (19) f =64/Re_H for laminar regime	$\Delta P1C2 = \frac{f\ l\ \rho {v_{c2}}^2}{d_{h3}\ 2}$ ...(20) f =64/Re_{c2} for laminar regime
the entrance and exit pressure losses	$\Delta P2=\frac{\rho * {v_{c1}}^2}{2}$ (21)	$\Delta P2=\frac{\rho * {V_H}^2}{2}$ (22)	$\Delta P2=\frac{\rho * {V_{c2}}^2}{2}$ (23)

Total pressure drop:	$\Delta P=\Delta P1+\Delta P2$ (24)	$\Delta P=\Delta P1+\Delta P2$ (25)	$\Delta P=\Delta P1+\Delta P2$ (26)
Overall heat transfer co-efficient for inner annular space	$\frac{1}{U_{o1}}=\frac{d_{o1}}{d_{i1}*h_{c1}}+\frac{d_{o1}*\ln\left(\frac{d_{o1}}{d_{i1}}\right)}{2*k_{copper}}+\frac{1}{h_H}$ (27)		
Overall heat transfer co-efficient for outer annular space	$\frac{1}{U_{i2}}=\frac{d_{i2}}{d_{o2}h_{c2}}+\frac{d_{i2}\ln\left(\frac{d_{o2}}{d_{i2}}\right)}{2k_{copper}}+\frac{1}{h_H}$ (28)		

3. Results and discussion

3.1. The effect of IL and its INF on Nusselt Number

Figures 3 and 4 show that the Nusselt number of the cooling fluid in the inner tube of the TCTHE (C1) was increased linearly with the flow rate of both the IL and the 0.5% MWCNT/[EMIM][BF4] INF. This is resulting from increasing the cooling fluid velocity. Generally, the INF appeared a high Nusselt number comparing with the IL. However, the Nusselt number of INF shows an improvement of about 5% comparing with IL. That could be due to enhancing the thermophysical properties and increasing the Brownian motion of the MWCNT nanoparticles of the INF. On the other hand, the Nusselt number increased slightly with the inlet oil temperature increasing from 50 to 67 ºC.

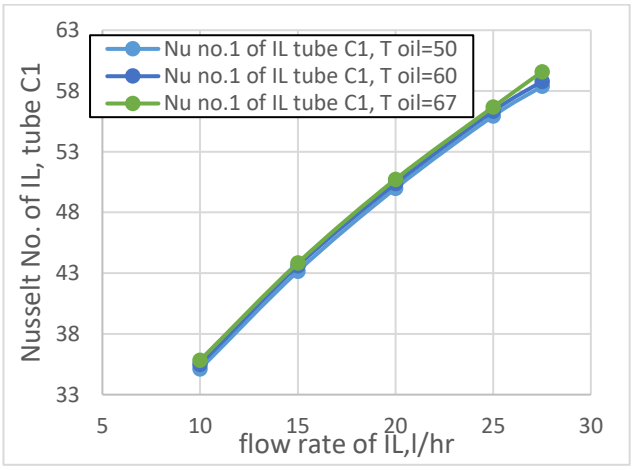


Figure 3. Nusselt number of IL against flow rate at a constant flow rate of oil 20 l/hr and different temperature (50-67 oC) for the inner tube of TCTHE.

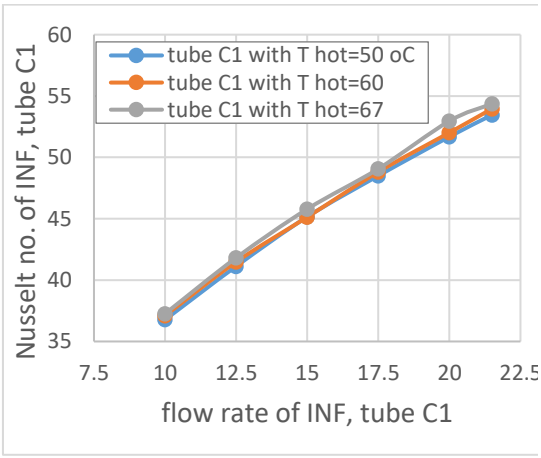


Figure 4. Nusselt number against flow rate of INF at a constant flow rate of oil 20 l/hr and different temperature (50-67 oC) for the inner tube of TCTHE.

Note: C1 and C2 refer to the inner tube and the outer annular of the TCTHE

The same behaviour occurred for Nusselt number of the outer annular C2 of the TCTHE as shown in figures 5 and 6 with little enhancement of Nusselt no. because of decreasing the values of Renolds no. in the outer annular C2 comparing with the inner tube C1.

As shown in figures 7, 8, 9, and 10 of Nusselt no. against Reynolds no, the values of Reynolds no. decreased from 19-58 in C1 to 3-8 in C2 for the IL and from 11-23 in C1 to C2 1.6-3.4 for the INF. The decrease in the Reynolds no. means an increase in the laminar flow behavior and so no effect of MWCNT on improving the cooling process.

3.2. The effect of IL and its INF on Friction Factor

Figures 11 and 12 show clearly that the friction factor was decreased with volumetric flow rate increasing for both the IL and its 0.5% MWCNT/[EMIM][BF4] INF, but it is slightly reduced with increasing the oil inlet temperature. That's resulting from increasing the velocity of the cooling fluid. Generally, the friction factor of INF increased by 75% comparing with that of IL. That could be due to an increase in Reynold's number of IL comparing with that of INF. In addition to increasing the viscosity of INF comparing with that of IL.

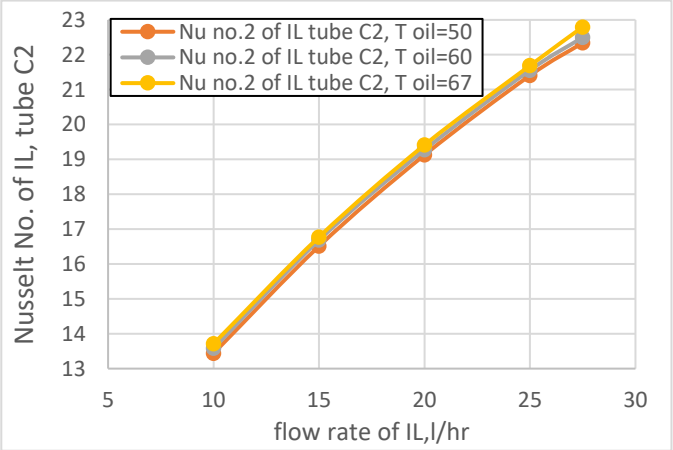


Figure 5. Nusselt number against flow rate of IL at a constant flow rate of oil 20 l/hr and different temperature (50-67 oC) for outer annular of TCTHE.

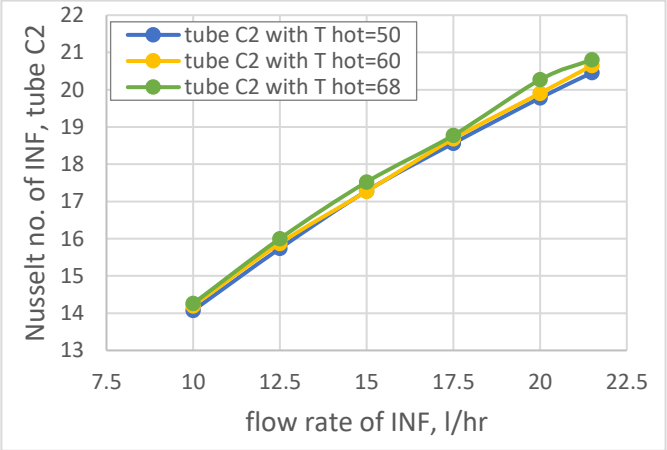


Figure 6. Nusselt number against flow rate of INF at constant flow rate of oil 20 l/hr and different temperature (50-68 oC) for outer annular of TCTHE.

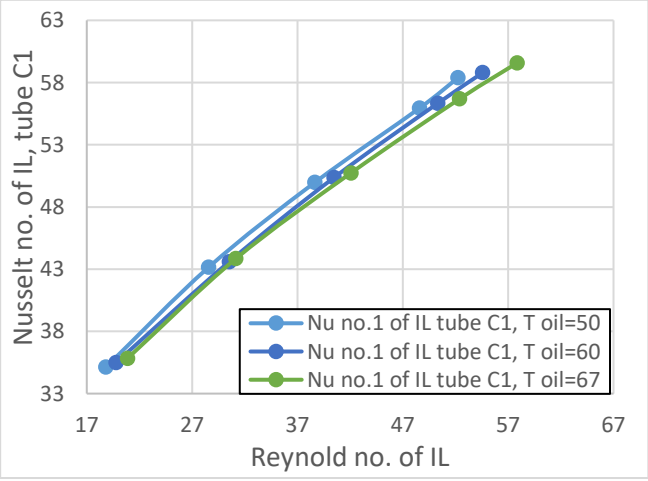


Figure 7. Nusselt number against Reynold number of IL at a constant flow rate of oil 20 l/hr and different temperature (50-67 oC) for the inner tube of TCTHE.

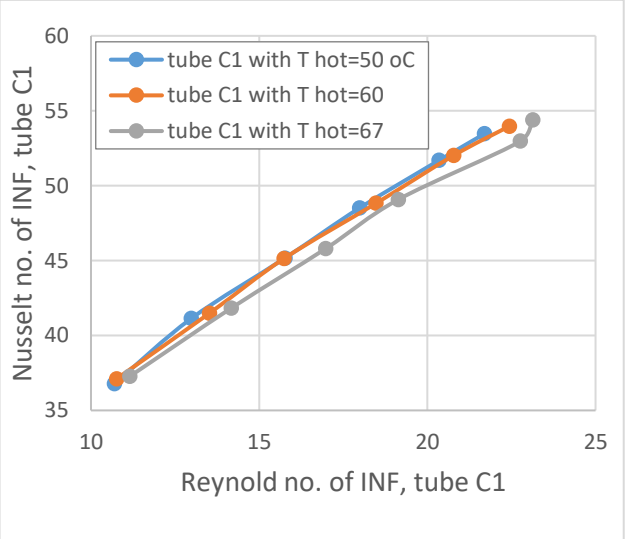


Figure 8. Nusselt number against Reynold number of INF at a constant flow rate of oil 20 l/hr and different temperature (50-67 oC) for the inner tube of TCTHE

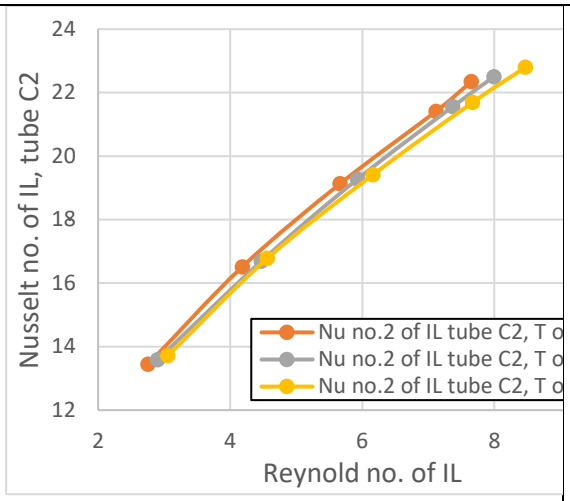


Figure 9. Nusselt number against Reynold number of IL at a constant flow rate of oil 20 l/hr and different temperature (50-67 oC) for outer annular of TCTHE.

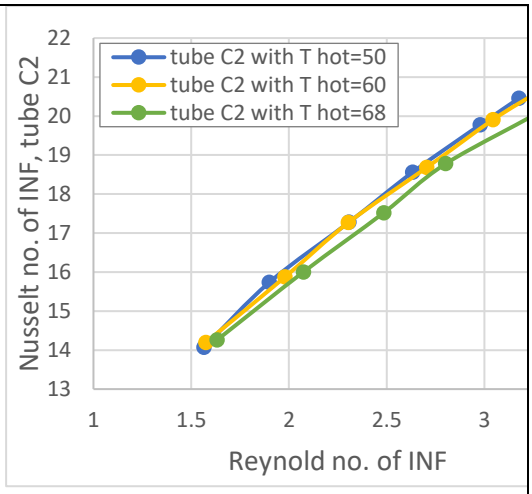


Figure 10. Nusselt number against Reynold number of INF at a constant flow rate of oil 20 l/hr and different temperature (50-68 oC) for outer annular of TCTHE.

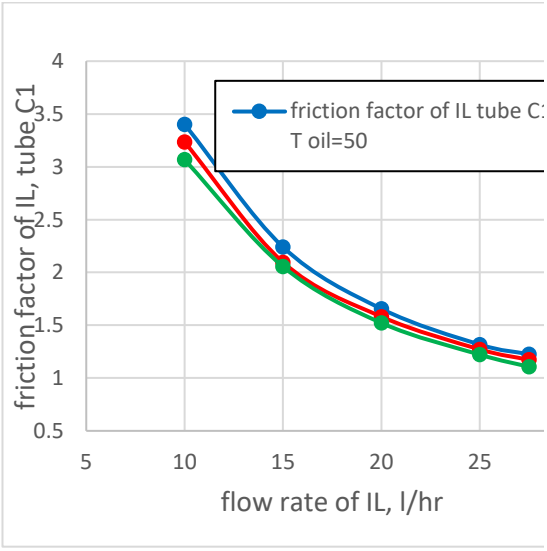


Figure 11. Friction factor against flow rate of IL at a constant flow rate of oil 20 l/hr and different temperature (50-67 oC) for the inner tube of TCTHE.

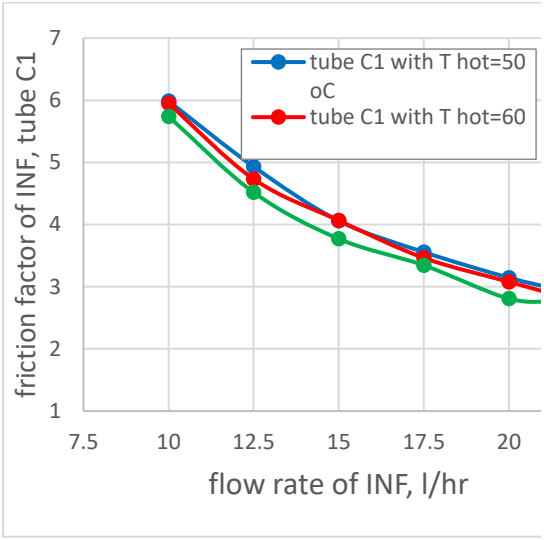


Figure 12. Friction factor against flow rate of INF at a constant flow rate of oil 20 l/hr and different temperature (50-67 oC) for the inner tube of TCTHE.

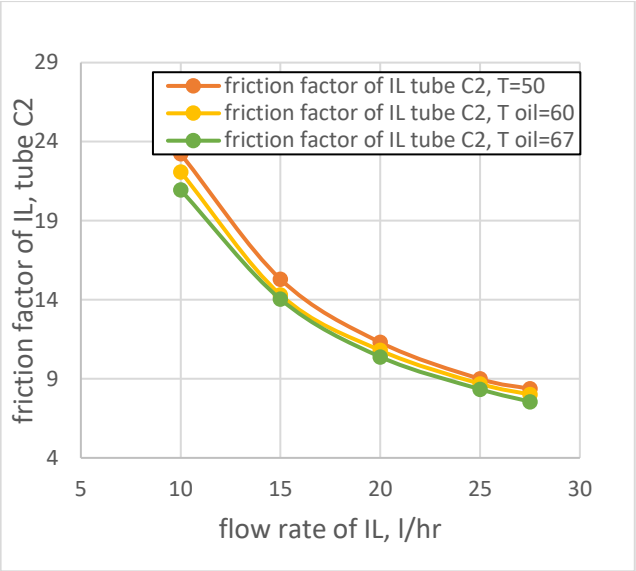


Figure 13. Friction factor against flow rate of IL at a constant flow rate of oil 20 l/hr and different temperature (50-67 oC) for outer annular of TCTHE.

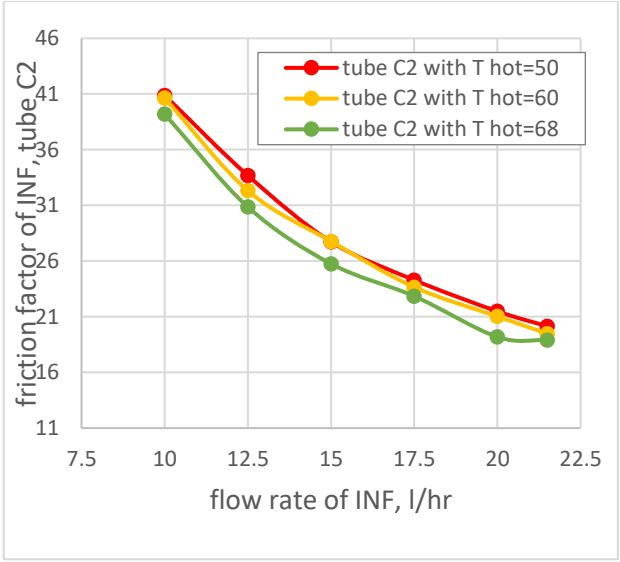


Figure 14. Friction factor against flow rate of INF at a constant flow rate of oil 20 l/hr and different temperature (50-68 ºC) for outer annular of TCTHE.

When comparing the friction factor values of the inner tube C1 in figures 15 and 16 with the outer annular C2 in figures 17 and 18 of both the IL and the 0.5% MWCNT/[EMIM][BF4] INF, it's found that the lower friction factor values were for the inner tube since C1 has the higher values of Reynold's number comparing with C2, as shown in figures 15 and 16 for friction factor values of C1 and 17, 18 for friction factor values of C2.

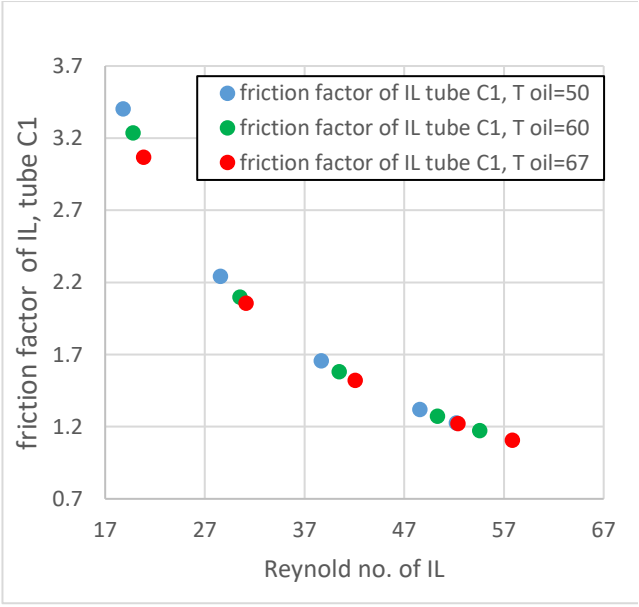


Figure 15. Friction factor against Reynold number of IL at a constant flow rate of oil 20 l/hr and different temperature (50-67 oC) for the inner tube of TCTHE.

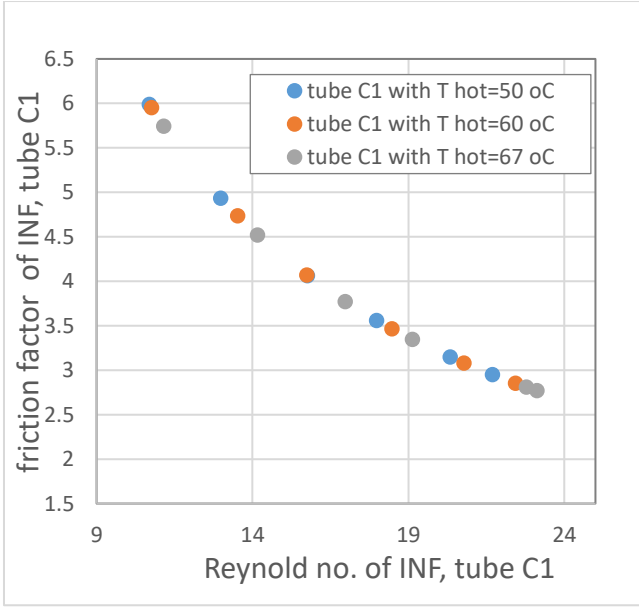


Figure 16. Friction factor against Reynold number of INF at a constant flow rate of oil 20 l/hr and different temperature (50-70 oC) for the inner tube of TCTHE.

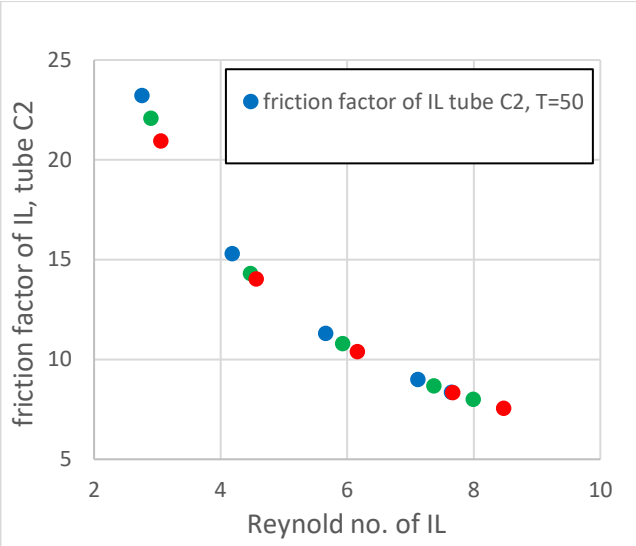


Figure 17. Friction factor against Reynold number of IL at a constant flow rate of oil 20 l/hr and different temperature (50-67 oC) for outer annular of TCTHE.

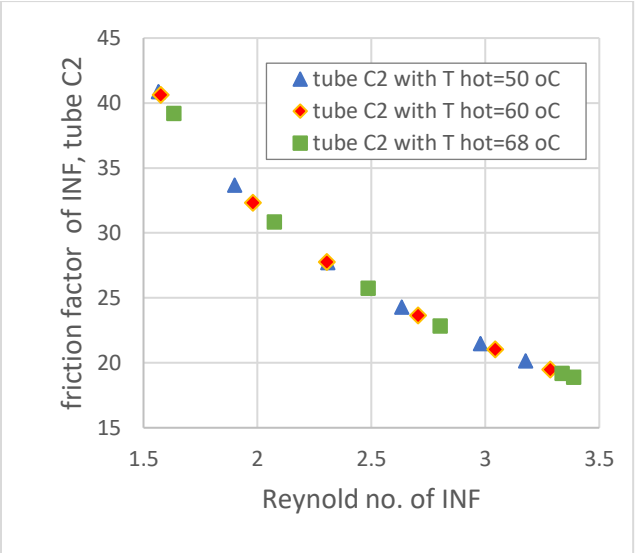


Figure 18. Friction factor against Reynold number of INF at a constant flow rate of oil 20 l/hr and different temperature (50-70 oC) for outer annular of TCTHE.

3.3. The effect of IL and its INF on Pressure Drop

Figures 19 and 20 show that the pressure drop of IL and 0.5% MWCNT/[EMIM][BF_4] INF increased linearly with flow rate. In addition, the pressure drop for the INF in C1 was larger than that of the IL in C1of, about 95% or doubled. That is because it increases the density of the INF comparing with the IL as a result of MWCNT existences. The same behaviour occurred for C2, but the values of pressure drop in C1 more than ten times the values for C2 for both IL and INF. That could be due to an increase in the velocity of the fluid inside C1 compared with C2. And pressure drop depending on the velocity as shown in the equations (18) & (21) of pressure drop.

Figures 23, 24, and 25, 26 show that the pressure drop of IL and 0.5% MWCNT/[EMIM][BF_4] INF for C1 increased compared to the pressure drop of IL and INF of C2, with Reynold number increasing. This agrees with [30]

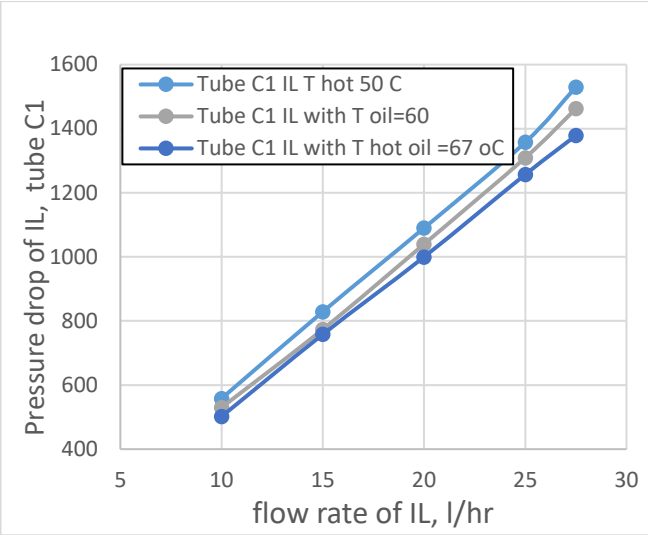


Figure 19. Pressure drop against flow rate of IL at a constant flow rate of oil 20 l/hr and different temperatures (50-67 oC) for the inner tube of TCTHE.

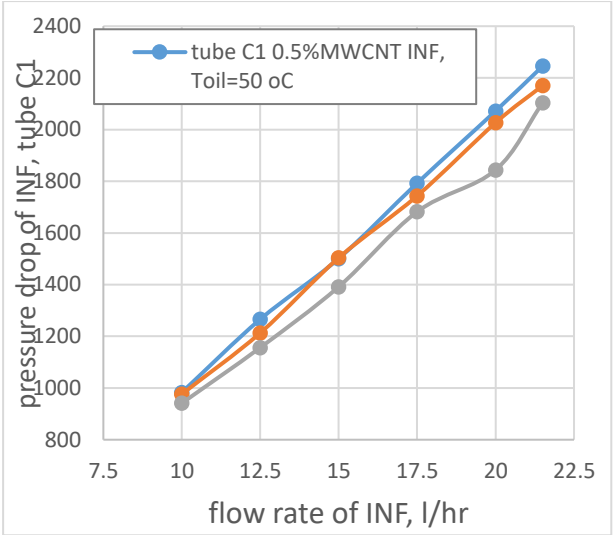


Figure 20. Pressure drop against flow rate of INF at a constant flow rate of oil 20 l/hr and different temperatures (50-67 oC) for the inner tube of TCTHE.

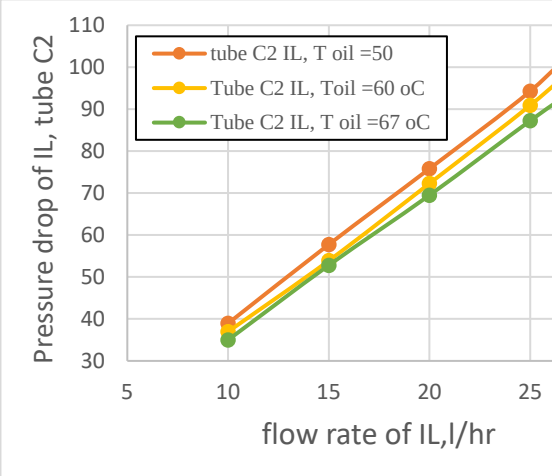


Figure 21. Pressure drop against flow rate of IL at a constant flow rate of oil 20 l/hr and different temperature (50-67 oC) for outer annular of TCTHE.

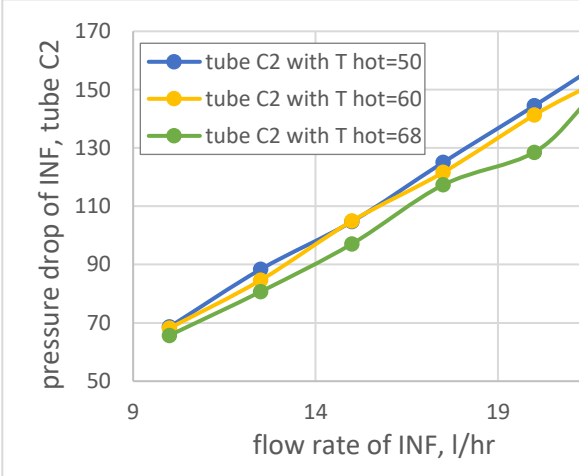


Figure 22. Pressure drop against flow rate of INF at a constant flow rate of oil 20 l/hr and different temperature (50-67 oC) for outer annular of TCTHE.

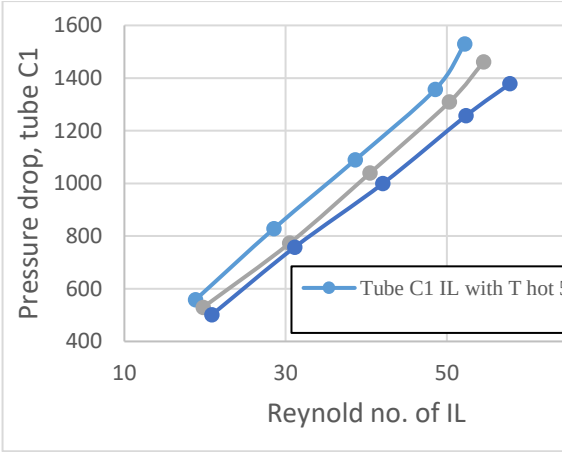


Figure 23. Pressure drop against Reynold number of IL at a constant flow rate of oil 20 l/hr and different temperature (50-67 oC) for the inner tube of TCTHE.

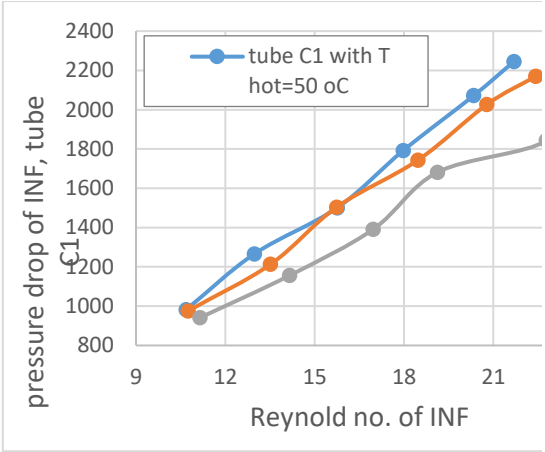


Figure 24. Pressure drop against Reynold number of INF at a constant flow rate of oil 20 l/hr and different temperature (50-67 oC) for the inner tube of TCTHE.

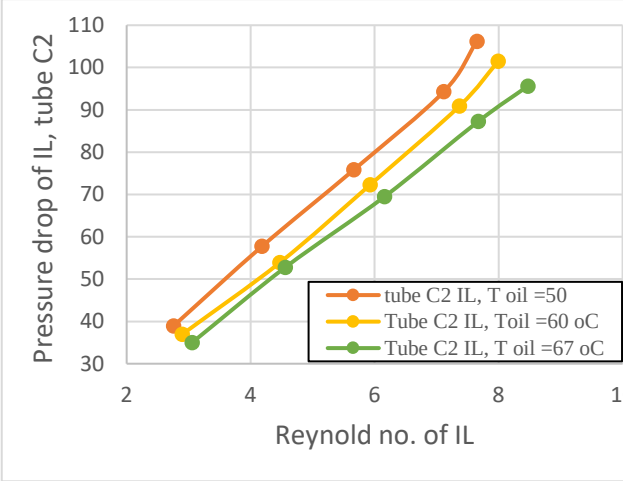


Figure 25. Pressure drop against Reynold number of IL at a constant flow rate of oil 20 l/hr and different temperature (50-70 oC) for outer annular of TCTHE.

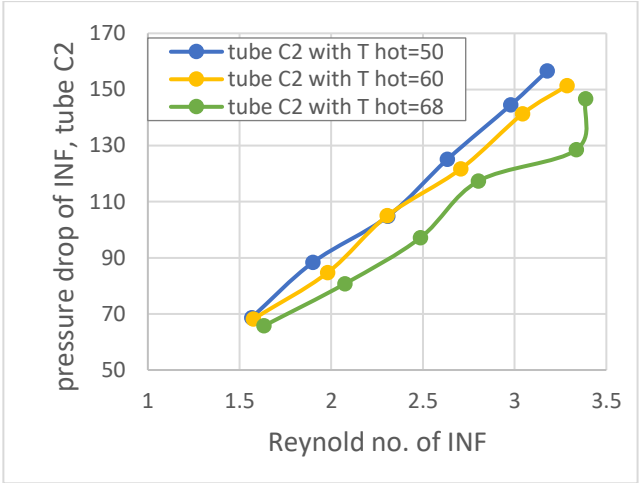


Figure 26. Pressure drop against Reynold number of INF at a constant flow rate of oil 20 l/hr and different temperature (50-70 oC) for outer annular of TCTHE.

3.4. The Overall Heat Transfer Coefficient of IL and its INF

Figures 27 and 28 show that IL's overall heat transfer coefficient and 0.5% MWCNT/[EMIM][BF4] INF increased dramatically with flow rate. The overall heat transfer coefficient of INF improved by 3% compared with that of IL because of the enhancement of the thermophysical properties of the INF by adding MWCNT, especially the thermal conductivity and the specific heat capacity.

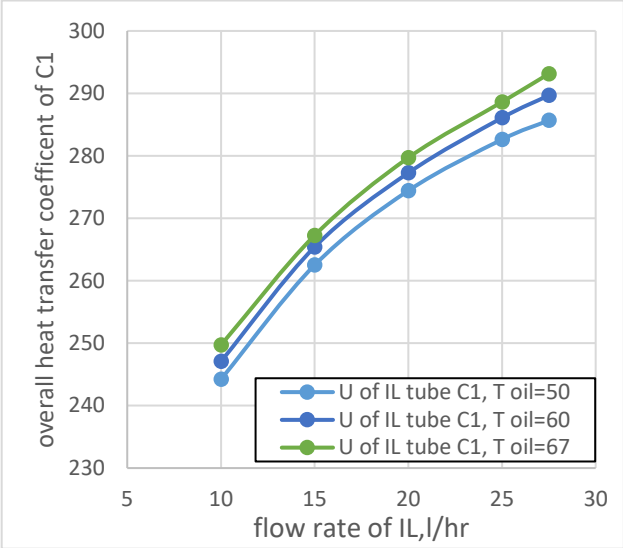


Figure 27. Overall Heat Transfer Coefficient against flow rate of IL at a constant flow rate of oil 20 l/hr and different temperature (50-70 oC) for the inner tube of TCTHE.

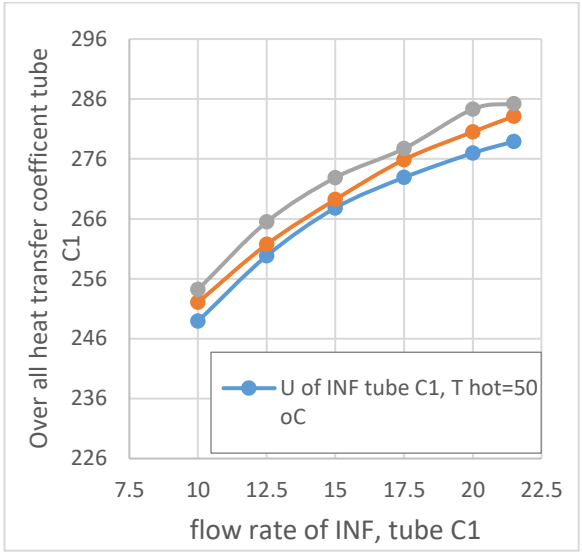


Figure 28. Overall Heat Transfer Coefficient against flow rate of 0.5% MWCNT/[EMIM][BF4] INF at a constant flow rate of oil 20 l/hr and different temperature (50-70 oC) for the inner tube of TCTHE.

Comparing the overall heat transfer coefficient of IL and INF in C1 in figures 27 and 28 with that of C2 in figures 29 and 30, the result shows that the overall heat transfer coefficient for IL and INF in C1 was greater than that in C2 by 50%.

Figures 31 and 32 show that the overall heat transfer coefficient of IL and 0.5% MWCNT/[EMIM][BF4] INF of the inner tube of TCTHE increased with flow rate reaching maximum values of 293, 285 at 27.5l/hr, 21.5 l/hr, respectively for both IL and INF. In addition, the overall heat transfer coefficient increased with temperature for both IL and INF. But the overall heat transfer coefficient for INF enhanced slightly comparing with that of INF for the same flow rate.

It is observed that the same above behavior is shown in figure 33 and 34 for the overall heat transfer coefficient of IL and 0.5% MWCNT/[EMIM][BF4] INF for outer annular of TCTHE with increasing the overall heat transfer coefficient of C1 by 40-50% compared with that of C2.

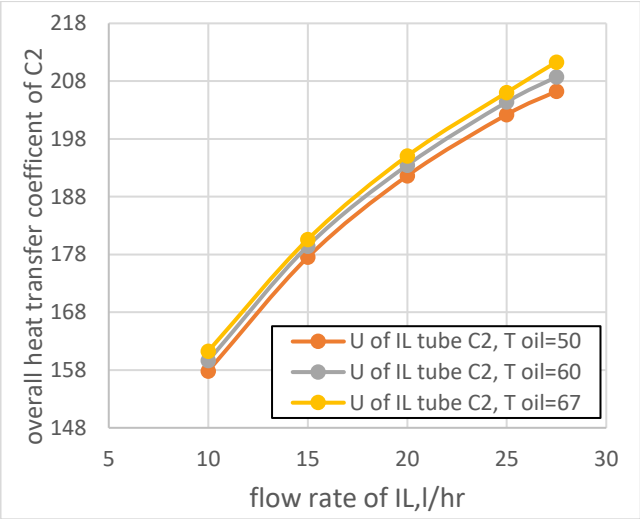


Figure 29. Overall Heat Transfer Coefficient against flow rate of IL at a constant flow rate of oil 20 l/hr and different temperature (50-70 oC) for outer annular of TCTHE.

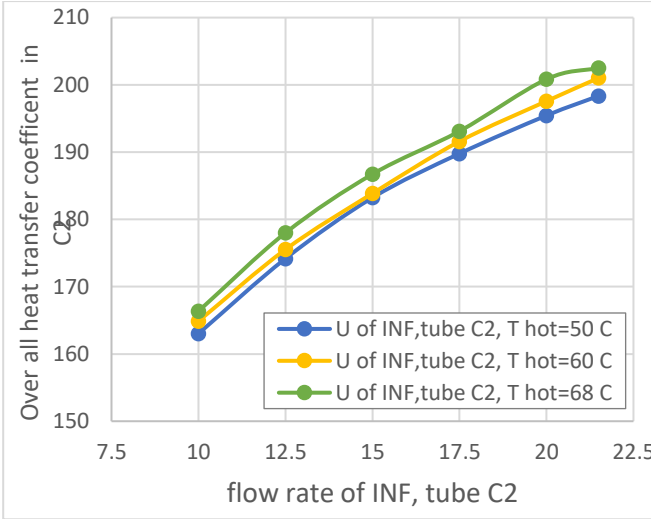


Figure 30. Overall Heat Transfer Coefficient against flow rate of INF at a constant flow rate of oil 20 l/hr and different temperature (50-70 oC) for outer annular of TCTHE.

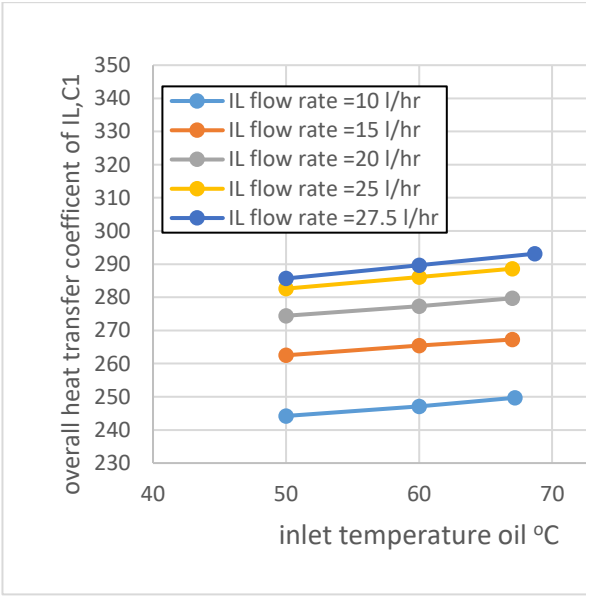


Figure 31. Overall Heat Transfer Coefficient against inlet oil temperature at different flow rate of IL and constant oil flow rate 20 l/hr for inner tube of TCTHE.

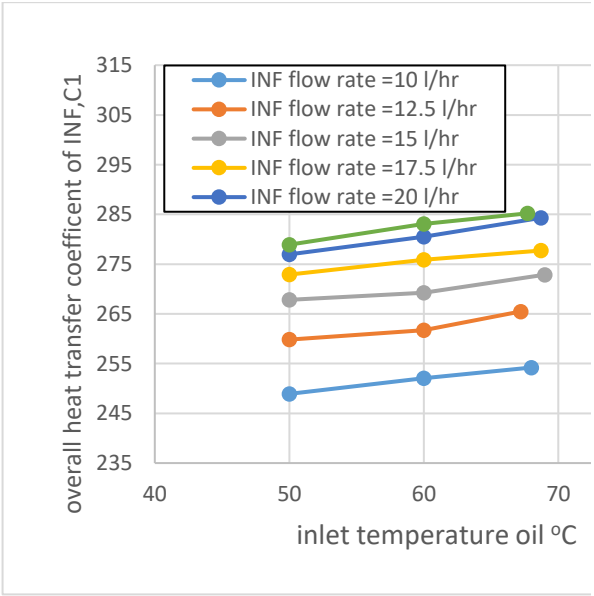


Figure 32. Overall Heat Transfer Coefficient against inlet oil temperature at different flow rate of INF and constant oil flow rate 20 l/hr for inner tube of TCTHE.

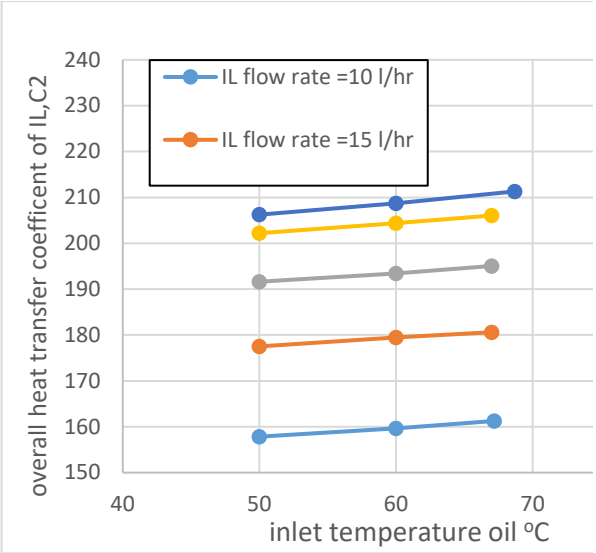


Figure 33. Overall Heat Transfer Coefficient against inlet oil temperature at a different flow rate of IL and constant oil flow rate 20 l/hr for outer annular of TCTHE.

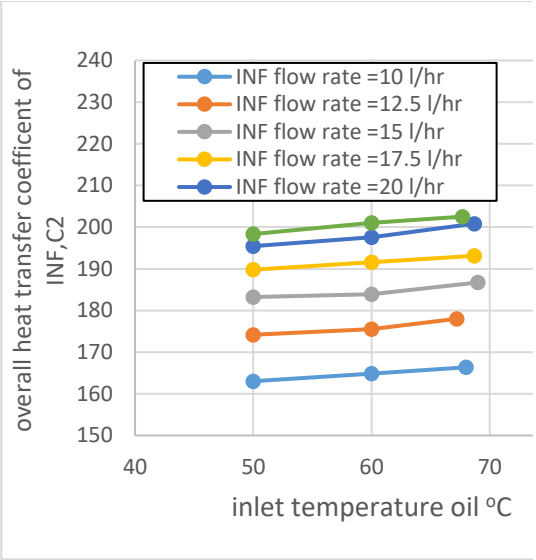


Figure 34. Overall Heat Transfer Coefficient against inlet oil temperature at a different flow rate of INF and constant oil flow rate 20 l/hr for outer annular of TCTHE.

4. Conclusions

In the present study, TCTHE designed and experimented using oil forty stock as hot fluid and [EMIM][BF_4] IL and 0.5% MWCNT/[EMIM][BF_4] INF separately as the cooling fluid. A countercurrent flow pattern is used in all the experiments. Different flow rates (20-55 l/hr) and Reynolds number are used for the cooling fluid with constant flow rate (20 l/hr) and different inlet temperatures of (50-67 °C) of the hot fluid.

In summary, the results indicated that:

Nusselt number and overall heat transfer coefficient of both the cooling fluid [EMIM][BF_4] IL and 0.5% MWCNT/[EMIM][BF4] INF increased with flow rate and Reynolds number for the inner and outer annular of TCTHE.

The friction factor of both the cooling fluid [EMIM][BF_4] IL and 0.5% MWCNT/[EMIM][BF_4] INF decreased with flow rate and Reynolds number for the inner and outer annular of TCTHE.

The pressure drop of IL and 0.5% MWCNT/[EMIM][BF_4] INF increased linearly with the flow rate. In addition, the pressure drop in the inner tube for the INF increased by 95% or doubled comparing with that of the IL.

The overall heat transfer coefficient of both the cooling fluid [EMIM][BF_4] IL and 0.5% MWCNT/[EMIM][BF_4] INF increased with the inlet temperature of the hot fluid (the oil).

The result shows clearly that using [EMIM][BF_4] as cooling fluid gave a good result but using 0.5% MWCNT/[EMIM][BF_4] INF instead of [EMIM][BF_4] have improved the heat transfer rate by increasing the Nusselt number and the overall heat transfer coefficient values of INF comparing with that of IL.

References

1. Welton T. Ionic liquids: a brief history. *Biophys Rev*. 2018;10(3):691-706.
2. Santos D, Santos M, Franceschi E, Dariva C, Barison A, Mattedi S. Experimental Density of Ionic Liquids and Thermodynamic Modeling with Group Contribution Equation of State Based on the Lattice Fluid Theory. *J Chem Eng Data*. 2016;61(1):348-353.
3. Shukla M, Saha S. A Comparative Study of Piperidinium and Imidazolium Based Ionic Liquids: Thermal, Spectroscopic and Theoretical Studies. In: *Ionic Liquids - New Aspects for the Future*. ; 2013:1-25.
4. Zhang S, Sun N, He X, Lu X, Zhang X p. Physical properties of ionic liquids: database and evaluation. *J Phys Chem Ref data*. 2006;35(4):1475-1517.
5. Nieto de Castro C, Lourenço MJ V, Ribeiro APC, Langa E, Vieira SIC. Thermal properties of ionic liquids and IoNanoFluids of imidazolium and pyrrolidinium liquids. *J Chem Eng Data*. 2010;55(2):653-661.
6. Poongavanam GK, Kumar B, Duraisamy S, Panchabikesan K, Ramalingam V. Heat transfer and pressure drop performance of solar glycol / activated carbon based nano fluids in shot peened double pipe heat exchanger. *Renew Energy*. 2019;140:580-591.
7. Chavda NK, Jani JP, Patel AK, Zala KP, Nimbark NG. Effect of Nanofluid on Friction Factor of Pipe and Pipe Fittings: Part I-Effect of Aluminum Oxide Nanofluid. *Int J Curr Eng Technol*. 2014;4(6):4069-4074.
8. Chavda N. Effect of nanofluid on heat transfer characteristics of double pipe heat exchanger: part-II: effect of copper oxide nanofluid. *Int J Res Eng Technol*. 2015;4(4):688-697.
9. Sudarmadji S. A new correlation for pressure drop in the cooling process of Al2O3-water nanofluid in pipes. *FME Trans*. 2015;43(1):40-46.
10. Wen D, Ding Y. Experimental investigation into convective heat transfer of nanofluids at the entrance region under laminar flow conditions. *Int J Heat Mass Transf*. 2004;47(24):5181-5188.
11. Ezzat AW, Hasan IM. Investigation of Alumina Nano Fluid Thermal Conductivity. *Int J Comput Appl*. 2014;102(11):15-23.
12. Albadr J, Tayal S, Khasaal MT. Heat transfer through heat exchanger using Al2O3 nanofluid at different concentrations. *Case Stud Therm Eng*. 2013;1(1):38-44.
13. Zamzamian SA, Nasseri Oskouie S, Doosthoseini A, Joneidi Jafari A, Pazouki M. Experimental investigation of forced convective heat transfer coefficient in nanofluids of Al2O3/EG and CuO/EG in a double pipe and plate heat exchangers under turbulent flow. *Exp Therm Fluid Sci*. 2011;35(3):495-502.
14. Logesh K, Baskar S, Siddarth BY, Sherwin KA, Naresh P. Multi-walled carbon nanotube mixed with isopropyl alcohol Nano fluid for heat transfer applications. *Mater Today Proc*. 2019;18:4690-4694.
15. Nasirzadehroshenin F, Sadeghzadeh M, Khadang A, et al. Modeling of heat transfer performance of carbon nanotube nanofluid in a tube with fixed wall temperature by using ANN – GA. *Eur Phys J Plus*. 2020;123.
16. Majeed NS, Abdulmajeed BA. Study and analysis of concentric shell and double tube heat exchanger using γ-Al2O3 nanofluid. *J Eng*. 2017;23(9):50-62.
17. Pillai P, Mohan R, Sasidharan S, Venkatesh K. Study On Concentric Tube Heat Exchanger With Different Nano Fluids For Enhancing The Heat Transfer : A Review. *Imp J Interdiscip Res*. 2017;3(9):682-688.
18. Shirgire N., Bhansali S., Bhagat A., Padgelwar A., Ghawade P. Influence of Ionic Fluid in Counter flow in Shell and Tube Heat Exchanger. *Int J Eng Trends Technol*. 2014;13(2):55-58.

19. Jikar PC, Bondre A, Pati A, Korpe S. Heat Transfer Enhancement in Shell and Tube Heat Exchanger by using Ionic fluid (BMIMCL). *Int J Mech Prod Eng*. 2018;6(2):11-14.
20. Palanisamy K, Kumar PCM. Experimental investigation on convective heat transfer and pressure drop of cone helically coiled tube heat exchanger using carbon nanotubes/water nanofluids. *Heliyon*. 2019;5(May):e01705.
21. Meikandan M, Kumar PG, Sundarraj M, Yogaraj D. Numerical analysis on heat transfer characteristics of ionic liquids in a tubular heat exchanger. *Int J Ambient Energy*. 2020;41(8):911-917.
22. Pancholi M, Virani B. A BASIC REVIEW ON TRIPLE CONCENTRIC TUBE HEAT EXCHANGER. *Int J Adv Technol Eng Sci*. 2017;5(1):350-354.
23. Sagar J, Prasad I, Deepak M. Review on triple tube heat exchanger with dimple on internal tube & internal threaded middle tube using CFD and Experimental analysis for heat transfer. *J INFORMATION, Knowl Res Mech Eng*. 2017;4(2):796-798.
24. Zuritz CA. ON THE DESIGN OF TRIPLE CONCENTRIC-TUBE HEAT EXCHANGERS. *J Food Process Eng*. 1990;12(2):113-130.
25. Saeid NH, Seetharamu KN. Finite element analysis for co-current and counter-current parallel flow three-fluid heat exchanger. *Int J Numer Methods Heat Fluid Flow*. 2006;16(3):324-337.
26. Quadir GA, Jarallah SS, Ahmed NJS, Badruddin IA. Experimental investigation of the performance of a triple concentric pipe heat exchanger. *Int J Heat Mass Transf*. 2013;62:562-566.
27. Quadir GA, Badruddin IA, Ahmed NJS. Numerical investigation of the performance of a triple concentric pipe heat exchanger. *Int J Heat Mass Transf*. 2014;75:165-172.
28. Hossain M, Uddin M, Hossen M, Afroz H. Experimental Analysis of a Triple Concentric Tube Heat Exchanger. *Int J Mod Stud Mech Eng*. 2017;3(3):1-10.
29. Hasen HM, Abdulmajeed BA. Thermophysical properties of [EMIM][BF4] and [HMIM][PF6] imidazolium ionic liquids with MWCNTs. In: *IOP Conference Series: Materials Science and Engineering PAPER*. London; 2020.
30. Pirhayati M, Akhavan-Behabadi MA, Khayat M. Pressure drop of CuO-base oil nanofluid flow inside an inclined tube. *Int J Adv Eng Technol*. 2012;5(1):122.

Polymeric Heat Exchangers in Seawater Desalination – Impact of Surface Characteristics and Process Conditions on Cleanability

Hendrik Kiepfer[1], Patrik Sobolciak[2], Igor Krupa[2] and Hans-Jörg Bart[1,*]

[1] Laboratory of Reaction and Fluid Process Engineering, TU Kaiserslautern, 67663 Kaiserslautern, Germany
[2] Center for Advanced Materials, Qatar University, P. O. BOX 2713, Doha, Qatar
***** *Corresponding author: bart@mv.uni-kl.de*

Abstract: The suitability of polymers and polymer composites as materials for thermal seawater desalination is verified. For this purpose, fouling tests are carried out with the high-performance polymer polyether ether ketone (PEEK) and polyethylene/graphite composites. In addition, the thermal conductivities and overall heat transfer coefficients of the polymer composites are measured and compared with stainless steel and the pure polymer. The composites in particular are characterized by a very low fouling susceptibility. In addition, it was found that plasma treatment of the composites leads to a slight increase in fouling susceptibility, but also to a significant improvement in the initial heat transfer rate. As a result, plasma-treated polymer composites achieve heat transfer rates equivalent to 93 % of stainless steel when fouling processes are considered. Pure PEEK shows very good results regarding cleanability. In contrast to stainless steel, it has been found that the fouling layer is brittle and only weakly adherent to the pure PEEK polymer film. A cleaning in place thus seems to be feasible with simple methods, since even an increase of the flow velocity in the screening experiments leads to a removal of the fouling layer. Due to their poorer mechanical properties, the polymer composites, on the other hand, have to be cleaned with acid, which resulted in a restoration of the initial heat transfer rates.

Keywords: Polymer heat exchanger; Polymer composites; Seawater desalination; Crystallization fouling; cleaning in place

1. Introduction

Population and economic growth, increasing urbanization and industrialization, and limited natural drinking water resources are causing serious drinking water deficits in many regions of the world [1]. Increased use of desalinated seawater is therefore essential to ensure an acceptable water supply. This is also shown by the development of the last years and decades. Since the middle of the last century, desalination of brackish and seawater has gained immense importance [2]. In 2013, there were more than 17,000 active desalination plants, providing about 80 × 106 m³ of water per day for 300 million people [2]. In 2015, the production capacity increased to nearly 97.5 × 106 m³ of water per day [3]. In addition, the supply of desalinated water is predicted to increase to 192 × 106 m³ of water per day in 2050 [4].

In this context, the application of energy-efficient processes, such as multi-effect distillation (MED), the most energy-efficient thermal desalination process, and the reduction in both capital and operating costs is of particular interest. Due to the partly very high salinities of seawater, however, corrosion and fouling (the undesired deposition of particles, precipitates or scales on heat transfer surfaces [5]) occur more frequently in such plants. To prevent corrosion as effectively as possible and due to their high thermal conductivities, high-alloy stainless steels, titanium alloys or aluminum brass are usually used as materials for seawater desalination [6,7]. However, these corrosion-resistant materials are associated with high costs and to tackle the fouling issues regular cleaning processes and the use of anti-scaling chemicals are required. Hence, permanent research is being conducted into materials that offer both low costs and a low fouling tendency.

A promising class of materials, especially with regard to MED, since low temperatures < 90 °C are present, are polymers. In addition to their corrosion resistance, they are characterized in particular

by a low fouling propensity compared to metallic materials. However, their low thermal conductivity (< 0.5 W/mK [8]) and usually poor mechanical stability prevent them from being used without further effort. One possibility to compensate the low thermal conductivity is the production of very thin polymer films, which leads to a reduction of the thermal resistance in the wall. With this approach, other authors were already capable of realizing very high heat transfer rates with 25 µm thick polymer films [9]. With the use of spacers and the high-performance polymer PEEK, it was also possible to achieve sufficient mechanical stability. Another approach, which in addition to mechanical stability also increases thermal conductivity, is to fill the polymers with a highly conductive filler like hexaboron nitride or graphite particles that can increase the thermal conductivity to a value of up to 20 W/mK. [10].

Both, PEEK as a material for heat exchangers, as well as particle enhanced materials have been studied extensively [11,12]. However, there are few experimental studies on their susceptibility to fouling [13], especially with regard to the real but, as already pointed out, extremely important test system of seawater. The objective of this study is to classify both materials or groups of materials in the state of the art with regard to seawater fouling. The focus is primarily on composites of polyethylene and graphite particles, as these stand out due to their great potential in terms of thermal conductivity as well as the moderate cost of the feedstock materials.

2. Materials and Methods

2.1 Materials and Preparation

The polymer films investigated in this study were pure semi-crystalline PEEK (LITE TK) and PEEK filled with 30% talcum (LITE TKT), which were purchased from Lipp Terler GmbH (Gaflenz, Austria). More detailed information on the materials investigated can be found in Table .

Table 1. Properties of the investigated heat transfer materials

Heat transfer material	**Composition**	**Thickness / µm**	**Thermal conductivity / W/mK**
PEEK	Polyether ether ketone, semi- crystalline	25	0.25
PEEK-Talc	Polyether ether ketone with up to 30 % talcum as filler, semi- crystalline	35	0.43
LLDPE	Linear low-density polyethylene	1500	0.33
LLDPE-EG	Linear low-density polyethylene, 60 wt. % expanded graphite	1500	3.1
SS 1.4301	Austenitic chromium-nickel steel	25	15
SS 1.4571	Austenitic chromium-nickel-molybdenum steel	1500	15

The polymer composites studied were manufactured, provided and plasma treated by the Center for Advanced Materials at Qatar University. Linear low-density polyethylene (LLDPE, Q3802, Q-Chem, Qatar) and a mixture of three different expanded graphite (EG) grades (GFG 600, 300, 5 microns in ratio 80:10:10; SGL Carbon, Germany) were used for the composite preparation. LLDPE was mixed with EG using a Brabender Instrument (Plastograph EX, Brabender) at 180 °C for 10 minutes. Subsequently, the blends were hot pressed (Carver, Wabash, IN, USA) at a pressure of 3 tons at 160 °C for 3 min.

Prior to the plasma treatment, the LLDPE and LLDPE/EG films were washed by acetone, to eliminate any grease residues or possible contaminations from the production process that might affect the surface properties and were air-dried for 20 min at room temperature. The low temperature plasma treatment was carried out using radiofrequency (RF) and corona plasma system. The vacuum pressure

system generating RF plasma was Venus75-HF (Plasma Etch Inc., Carson, USA). During the plasma treatment, the ions and electrons in this system were generated by the means of RF power supply operating at a typical frequency of 13.56 MHz. The treatment time was 60 s at 80 W of nominal power. The distance between the plasma generating electrodes and film surface was 1 mm to ensure homogeneous plasma discharge.

2.2 Surface characterization

The measurement of thermal diffusivity and through-plane thermal conductivity was conducted by ISOMET 2114. This can examine the thermal properties with a surface probe using a modified transient pulse method in a short time. Once the composite was in thermal equilibrium with the environment, a heat flux was generated by applying a thermal pulse to determine the thermal properties of the specimen. The probe was placed in the center of the specimen and each surface was tested three times. A round specimen with a diameter of 7 cm and a thickness of 1 cm was used.

For the evaluation and analysis of the results of the fouling experiments, the energetic and topographic surface properties of the investigated materials, in particular the surface free energy and the roughness, are utilized. A confocal microscope (μsurf Explorer, Nanofocus AG) is used to generate 3D surface profiles from which various roughness parameters can be extracted and quantified according to EN ISO 25178. The mean arithmetic surface roughness is used as a representative for the topographic characterizations. The surface free energies are determined according to the OWRK method [14,15] based on the measurement of static contact angles. Therefore, contact angle measurements with at least two liquids with known polar and disperse fractions of surface tension are necessary. To improve the accuracy of the results, static contact angle measurements were performed with four reference liquids (deionized water, ethylene glycol, DMSO, diiodomethane) using an OCA 15 EC setup (Dataphysics). The corresponding disperse and polar fractions of the surface tension were taken from the literature [16].

2.3 Experimental set-up

The measurements of the overall heat transfer rates of the composites and the fouling experiments were carried out in the screening apparatus schematically shown in

Figure . For a detailed description of the system components, reference is made to an previous publication [17]. The facility consists of two test sections, one designed for testing polymer films (4) and the other for testing polymer sheets (5).

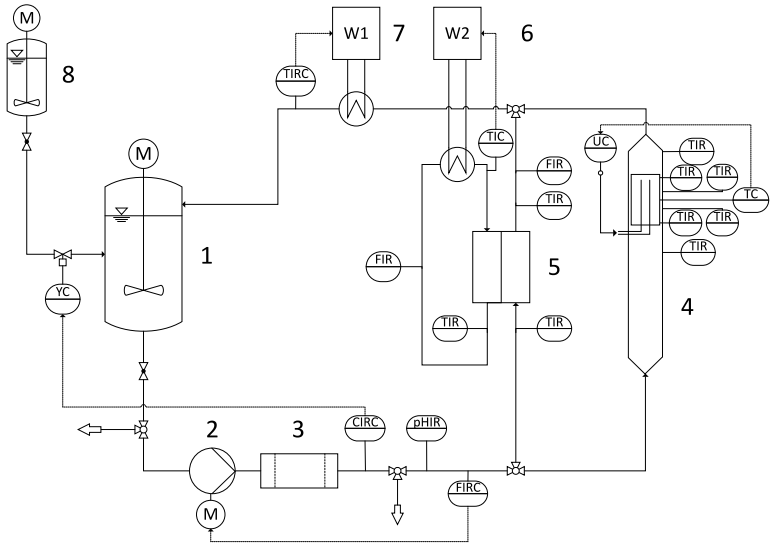


Figure 1. Process flowchart of the experimental set-up. (1) Storage tank. (2) Pump. (3) Filter. (4) Electrically heated flow channel. (5) Heat exchanger test cell. (6) Thermostat for heating circuit. (7) Thermostat for bulk temperature control. (8) pH dosing tank.

The electrically heated test section (4) which provides a heat transfer surface of 128 cm², consists of a rectangular channel made of poly (methyl methacrylate) (PMMA) with a removable block made of copper on which the specimens are attached. Two heating cartridges (Maxiwatt; 230 V; 1000 W) integrated in the copper block serve as heat sources. To ensure nearly adiabatic conditions, the heating block is insulated by a polyoxymethylene (POM) shell. Two temperature sensors (Pt100 1/3 DIN) in the copper block and three in the fluid flowing over the copper block are used for data acquisition. The power of the heating cartridges is controlled in order to maintain a constant temperature in the copper block and thus on its surface. The overall heat transfer coefficient is thus given by equation 1:

$$U = \frac{\dot{Q}}{A(T_{\mathrm{W}} - T_{\mathrm{B}})} \tag{1}$$

The test section for the investigation of plate material (5) corresponds to a plate heat exchanger with a heat transfer surface of 144 cm². The material to be tested separates the cold fluid (water or artificial seawater) from the hot fluid (hot water). The heating side of the test section is manufactured of POM and is additionally insulated to guarantee adiabatic conditions. The solution side is made of PMMA for reasons of visibility. Temperature sensors were placed in the flow directly at the inlet and outlet of the test section, where the temperature distribution and flow profile are homogeneous. The volume flow rates of the fluids entering the heat exchanger, as well as their temperature, are controlled for constant test conditions. All relevant temperatures and volume flows are recorded transiently to guarantee an accurate energy balance. Using the energy balance for the calculation of the heat transfer rate $\dot{Q}$, the overall heat transfer coefficients U are calculated according to equation 2:

$$U = \frac{\dot{Q}}{A\Delta T_{\mathrm{lm}}} \tag{1}$$

As a result of crystallization fouling, the heat transfer rate changes with increasing test duration, providing a transient overall heat transfer coefficient U_{f}. The resulting fouling resistance R_{f} is then calculated according to equation 2 referring to the initial overall heat transfer coefficient U_0 of the clean surface:

$$R_{\mathrm{f}} = \frac{1}{U_{\mathrm{f}}} - \frac{1}{U_0} \tag{3}$$

Before each experiment, the samples under investigation were cleaned with isopropanol and deionized water and the screening apparatus was rinsed with deionized water several times to ensure that there were no foreign ions left in the system. 50 kg of artificial seawater was prepared according to Kester et al. [18] with analytical-grade salts (p.a., purity > 99,5 %), where gravimetric salts were added initially before each experiment and volumetric salts were added after steady state was reached. By using a high amount of seawater compared to the heat transferring surface (and the masses deposited as a result) and a pH control, the experimental conditions are kept almost constant over the entire duration of the experiments. The pH control provides a constant value of 8.0, which corresponds to the value of seawater, thus maintaining the initial carbonate equilibrium. With regard to the heat transfer measurements, the measured values were recorded for 15 minutes after reaching a steady state. The bias uncertainties in the overall heat transfer coefficients were determined by calculating the 95 % confidence intervals according to equation 4, which are composed of the measurement uncertainties of the recorded temperatures ($T_{h,in}$, $T_{h,out}$, $T_{c,in}$, $T_{c,out}$) and the mass flow of the cold fluid.

$$B_U = \sqrt{\left[\sum_T \left(\frac{\partial U}{\partial T} B_T\right)^2 + \left(\frac{\partial U}{\partial \dot{m}_{\mathrm{c}}} B_{\dot{m}_{\mathrm{c}}}\right)^2\right]} \tag{4}$$

The heat transfer measurements were performed for several operating conditions. These are listed next to the test conditions of the fouling studies in Table . The test duration of the fouling experiments was adapted till reaching an asymptotic fouling resistance.

Table 2. Operating parameters of the heat transfer and fouling measurements.

	Heat transfer composites	**Fouling composites**	**Fouling PEEK**
Reynolds number hot fluid	5840, 6600	4050	-
Reynolds number cold fluid	300, 450, 920, 2700	600	6810, 9085
Inlet temperature hot fluid / °C	70, 80	80	-
Inlet temperature cold fluid / °C	25	40	-
Surface temperature / °C			75
Salinity in g/kg	-	45, 70	45

3. Results and Discussion

3.1 Heat Transfer and Scaling

Particularly for the polymer composites, which have a thermal conductivity of only approx. 20 % of that of stainless steel and, due to their mechanical properties, the thickness cannot be reduced arbitrarily, the determination of the heat transfer coefficients under the subsequent conditions of use is decisive. However, in order to cover a wide operating range, the overall heat transfer coefficients of all test conditions (see Table) were averaged for each sample and compared with stainless steel of the same thickness. The results are shown in Figure 1 for the LLDPE-EG composites and the corresponding pure polymers.

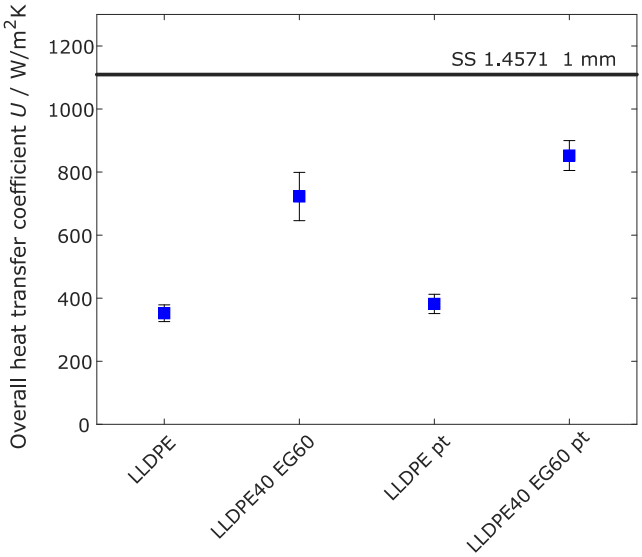


Figure 4. Averaged overall heat transfer coefficients of the investigated polymer composites and the corresponding pure polymers.

The plasma treatment of the polymers provides a significant increase in the overall heat transfer coefficient (U) by about 10 %, consequently, the plasma treatment is expected to increase the heat transfer coefficient (α). The plasma-treated composite sample achieves an overall heat transfer coefficient equal to 75% of the stainless steel value on average. However, this value is strongly dependent on the degree of turbulence of the flows. The more turbulent the flows become, the greater the differences in performance between the composites and stainless steel. The measurements with the unloaded polymers show that the heat transfer rate with the composite is up to three times higher than that of the unloaded polymer, depending on the Reynolds number. Even though both the thermal

conductivities and the heat transfer rates of the composites have been significantly increased compared to the pure polymer, the polymer composites still have values compared to stainless steel. Nevertheless, polymer heat exchangers can have significant advantages over metallic ones, not only due to a much cheaper prize per kg, but also in the performance in fouling-prone environments [16]. Whether the latter also applies to the real test system of artificial seawater is discussed below using the examples of the polymer composites already mentioned and PEEK.

3.1.1 Polyether ether ketone films

The results shown in this subsection are part of a previously published study [19] and are reviewed here to provide a clearer overall context. The detailed discussion of the results can be found in the reference literature. Figure 3 shows the curve of the measured fouling resistance over time for the polymer films compared to stainless steel as a result of crystallization fouling under fully developed turbulent flow conditions. It was found that with pure PEEK as the heat transferring surface, both a smaller asymptotic fouling resistance is formed and a longer induction phase (represented by the negative part of the curve) is obtained compared to the reference materials. Hence, the asymptotic fouling resistance of PEEK corresponds to 19×10^{-5} (m²K)/W, whereas the value obtained for stainless steel reaches 26×10^{5} (m²K)/W after 72 hours (tendency further increasing).

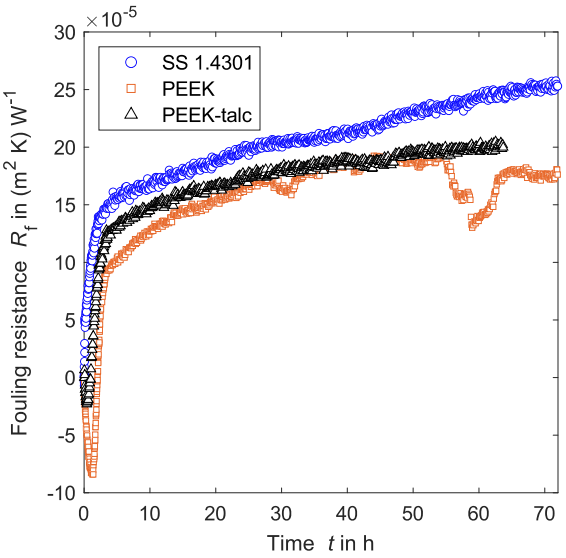


Figure 5. Thermal fouling resistance due to crystallization fouling of artificial seawater on the investigated polymeric heat transfer films and stainless steel [19]. SA = 45 g/kg; T_S = 75 °C; T_B = 30 °C; Re = 6810.

Differences in the topographical and energetic properties of the individual materials can be taken as an explanation for the results shown. Therefore, the mean arithmetic roughnesses and the surface free energies of the materials and salts used are shown in Table . However, a differentiated view usually proves difficult due to conflicting effects. Consequently, an assessment based on the two parameters shown is not sufficient for a comprehensive view, but may serve as a first point of reference.

Table 3. Surface properties of the investigated materials.

Material	γ_s / **mNm**	θ_{H_2O} / °	S_a / **µm**
SS 1.4301	32.38	83.71	0.13
PEEK	40.57	77.19	0.06
PEEK-talc	43.55	82.75	0.59
SS 1.4571	32.78	98.9	0.15
LLDPE-EG	30.24	91.0	0.68
LLDPE-EG after cleaning	33.68	78.9	-
LLDPE-EG-pt	35.53	86.7	0.52
LLDPE-EG-pt after cleaning	36.70	73.6	-
$CaCO_3$ [20]	57.05	-	-
$CaSO_4$ [21]	47.88	-	-

Both the kinetics of crystal formation (and thus the amount of deposits) and the duration of the induction period depend on the interfacial energy differences between crystal and surface. Thereby, smaller differences are related to a greater susceptibility to fouling [13]. Based on the respective salt concentrations in the artificial seawater and the saturation concentrations of the fouling-relevant components [22,23], it can be assumed that in the fouling investigations carried out, mainly deposits of $CaCO_3$ and $CaSO_4$ occur.

Consequently, one would expect PEEK to have a higher fouling susceptibility than stainless steel because of the minor interfacial energy differences. This seems to be confirmed at first, as can be seen from the steep slope of the fouling resistance curve in the first hours of the experiment. However, the curve then flattens out sharply and drops occur in the fouling curve (t = 55 h), which correspond to a detaching of fouling coatings. This positive characteristic was attributed to the extremely low roughness of PEEK compared to the reference materials (see Table).

3.1.2 Polyethylene/graphite composite plates

The process parameters for the evaluation of the polyethylene/graphite composites were set close to the initial conditions in the MED. The inlet temperature of the artificial seawater was 40 °C with a Reynolds number of 600 and the salinity chosen is 45 g/kg, as this corresponds to a high salt concentration of seawater. Once again, the composites are compared with stainless steel (1.4571). As shown in Figure (a), the polymer composites, in particular the untreated sample, have a significantly reduced fouling propensity compared to stainless steel. This is reflected in slower kinetics, the lower asymptotic fouling resistances and a longer induction phase.

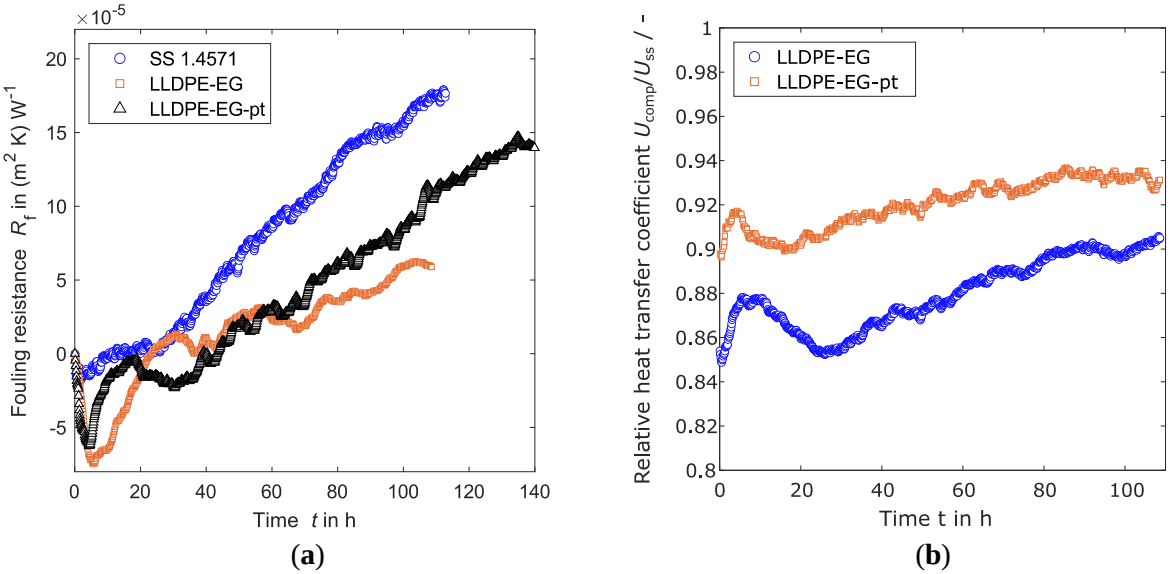


Figure 4. (**a**) Thermal fouling resistance due to crystallization fouling of artificial seawater on the investigated polymer composite plates and stainless steel. *SA* = 45 g/kg; $T_{hot,in}$ = 80 °C; $T_{sol,in}$ = 40 °C; Re_{sol} = 600; Re_{hot} = 4050.; (**b**) Overall heat transfer coefficients of the investigated polymer composites in the fouling experiments relative to stainless steel.

The stainless steel sample already changes to a curve with positive fouling resistance after 15 hours, whereas for the polymers this occurred not before 40 hours. Particularly remarkable is the high negative fouling resistance that appears after the first few hours for the polymer samples. This effect can be explained by the increase of local turbulence and thus of the heat transfer coefficient due to nucleating crystals [24]. Moreover, for the stainless steel sample this positive effect is almost not pronounced. The same trends were already evident in Figure 3. Instead of homogeneous crystal layers, initially larger crystals appear to form on the polymers. On the one hand, these cause additional thermal resistance, but on the other hand, they also reduce the thermal resistance in the circulating fluid, which leads to a net improvement in heat transfer [25]. The direct comparison between the treated and untreated polymer composite sample shows that there is a clear difference in fouling susceptibility for the test system used. Although both samples show similar induction phases, lower asymptotic fouling resistance and slower kinetics are seen for the untreated sample, which could also be proven by means of the deposit masses (see Table). For better comparability between the polymer composites and stainless steel, the fouling curves are plotted in Figure (b) in the form of relative overall heat transfer coefficients. These correspond to the ratio between the U-values of the polymer composites and stainless steel. It can be found that the plasma-treated sample already at the beginning corresponds to an overall heat transfer coefficient, which is 5 % higher than the value of the untreated sample. This difference in performance cannot be compensated by a slightly lower fouling susceptibility of the untreated sample. As the experiment duration increases and the fouling process progresses, the performance difference to stainless steel is reduced continuously. After 110 h, the overall heat transfer coefficient for the plasma-treated sample is equal to a value corresponding to 93% of the value of stainless steel, whereas the untreated sample only reaches a value of 90 %. A high surface roughness generally leads to a shorter induction phase due to faster nucleation processes. Since the topographical properties of the composites are less favorable than those of stainless steel in terms of fouling, the reason must lie in the energetic surface properties. However, no clear trend can be identified here either. As expected, the untreated polymer has the lowest fouling susceptibility, but the treated composite should be the most susceptible to fouling due to its high surface free energy. Hence, larger crystals are likely to form on the polymeric surfaces. As already mentioned the presence of particles, large with respect to the original roughness of the unfouled surface, reduces the resistance to heat transfer through the fluid film at the fluid-deposit interface [25].

In contrast, the fouling experiments with a salinity of 70 g/kg, which corresponds to the brine concentration in the MED, confirm the theory that more alike surface free energy differences between surface and crystal lead to higher fouling susceptibilities. The results are displayed in Figure .

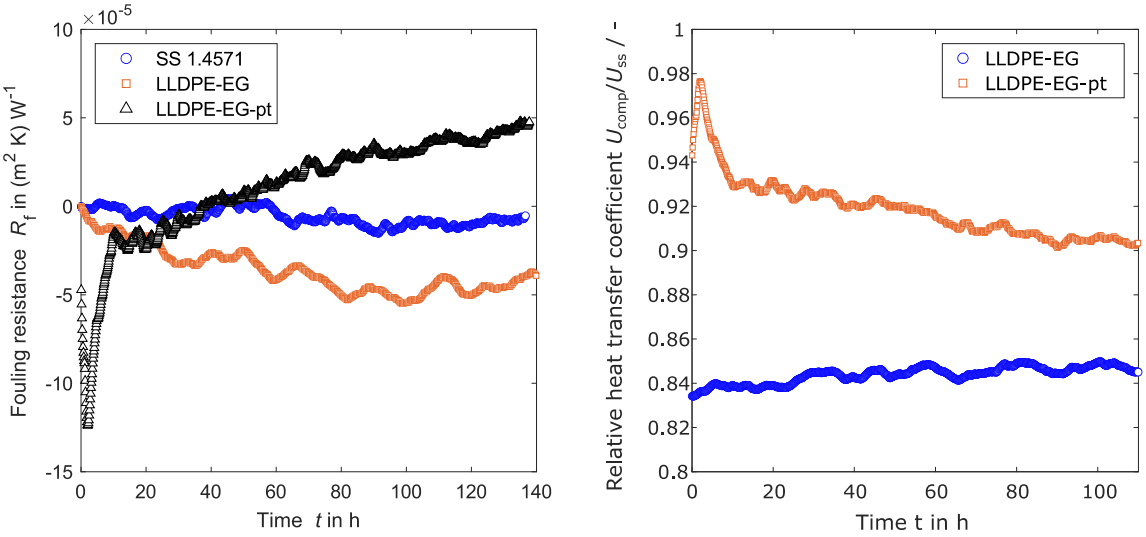


Figure 5. (**a**) Thermal fouling resistance due to crystallization fouling of artificial seawater on the investigated polymer composite plates and stainless steel. *SA* = 70 g/kg; $T_{hot,in}$ = 80 °C; $T_{sol,in}$ = 40 °C; Re_{sol} = 600; Re_{hot} = 4050.; (**b**) Overall heat transfer coefficients of the investigated polymer composites in the fouling experiments relative to stainless steel.

According to Figure (a), the plasma-treated sample reaches the highest asymptotic fouling resistance, the untreated sample the lowest. Of particular interest is the fact that for the higher salinity all materials show lower fouling susceptibilities, stainless steel and the untreated polymer even none at all. As a result, the performance differences between polymer composite and stainless steel change only slightly over the test period compared to the initial value. One explanation for this is found in the complexity of the underlying multicomponent electrolyte system. Thus, different ion concentrations can affect the solubility of e.g. $CaCO_3$ and $CaSO_4$. For example, the presence of $CaCl_2$ increases the solubility of $CaSO_4$ [26], whereas NaCl decreases the solubility of $CaSO_4$ [27]. In particular, the high NaCl concentration at an artificial seawater salinity of 70 g/kg could inhibit $CaSO_4$ depositions. In addition, Chen et al. [28] showed that a high concentration of Mg^{2+}, which is the most abundant ion in seawater along with Na^+ and Cl^-, inhibits the formation of $CaCO_3$ deposits.

Despite the higher fouling susceptibility of the plasma-treated sample, it should again be highlighted that it delivers significantly higher overall heat transfer coefficients, which remain at about 5% even after reaching the asymptotic fouling resistance.

Another result that can be drawn from the present results is whether there is any undesired aging of the plasma treatment. Therefore contact angle measurements were carried out before and after the fouling experiments (see Table). The long contact time with the test system significantly improves the wettability of the samples, which is a major advantage, especially with regard to the MED. Thus, the contact angle of the untreated sample with water could be reduced by 12.1 °. In this respect, plasma treatment does not really seem necessary. This effect of improved wettability, however, is equally significant for the plasma-treated sample. The contact angle with water was reduced by 13.1 ° for this sample. If the contact angle measurements are used as a basis, the effect of the plasma treatment thus tends to be amplified. However, whether the resulting increased surface energies lead to an increase in fouling susceptibility needs to be investigated in long-term experiments.

3.2 Cleaning-In-Place

3.2.1 Polyether ether ketone films

The most outstanding property of PEEK was found to be its excellent cleanability, which is already visible in Figure 5 in the form of a drop in fouling resistance (t = 55 h). That this was not an isolated phenomenon and is confirmed by Figure , which shows the development of the fouling resistance over time for PEEK in relation to the Reynolds number.

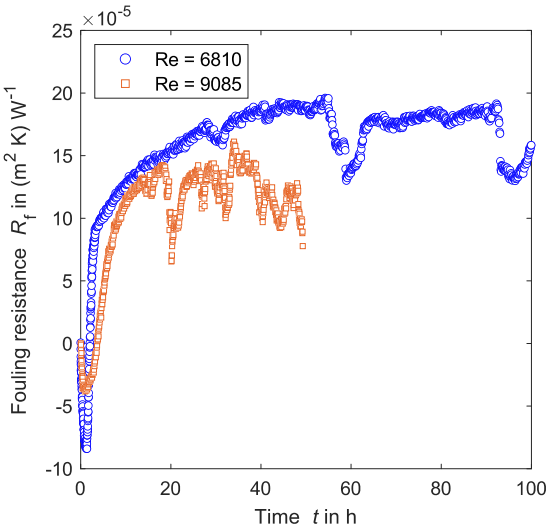


Figure 6. Influence of the Reynolds number on the thermal fouling resistance of PEEK [19]. *SA* = 45 g/kg; T_S = 75 °C; T_B = 30 °C.

With the higher volume flow, and consequently the higher Reynolds number, there are constant drops in the fouling curve, which correspond to the classic sawtooth curve in which the deposit detaches again when a critical layer thickness is reached at the heat transfer surface [29]. It is precisely the low adhesion of the coatings to PEEK, which has already been experimentally demonstrated by Dreiser for $CaSO_4$ precipitates [30], that is attributed to the low roughness of the PEEK films.

3.2.2 Polyethylene/graphite composite plates

After the fouling tests with a salinity of 45 g/kg shown above, the samples were exposed to different cleaning procedures in place. Initially, an attempt was made to remove the coatings by strong shear forces in the form of a surge flow. Therefore, the Reynolds number was increased to approx. 4200 for 1 min. The result was a removal of about 20% of the deposits. Hence, higher shear forces are required, which, however, cannot be realized in the apparatus used due to the low pressure stability of the materials. As a consequence, an acid cleaning procedure with diluted hydrochloric acid was tested. For this purpose, the pH of the cleaning solution (deionized water) was reduced to 2 and the sample was rinsed for 40 minutes under the same conditions as in the fouling experiments ($T_{sol,in}$ = 40 °C; Re_{sol} = 600). The impact on the deposit mass is quantitatively recorded for both composite samples in Table . It is apparent that in the case of the untreated sample, the bulk of the deposits could be removed. However, only 40% of the residues could be removed from the plasma-treated sample using this procedure. The observation, that not all salts dissolved at the present pH value of 2, suggests the presence of sulfate deposits. These dissolve more poorly than carbonates at low pH values. According to the results of the cleaning, sulfates are increasingly deposited on the plasma-treated sample.

Table 4. Fouling quantity before and after acid cleaning process.

Material	$m_{deposit}$ / g/m²
LLDPE	70.42
LLDPE *after cleaning*	19.38
LLDPE-pt	100.42
LLDPE-pt *after cleaning*	62.43

For a complete cleaning of the samples, longer cleaning procedures or lower pH values (e.g. 1-1.5) are necessary. Nevertheless, Figure 5 shows that the cleaning process has a sufficient effect on the overall heat transfer coefficient. For the untreated composite, the initial U-value of 425 W/(m²K) can thus be restored or exceeded in place. Consequently, the selected cleaning-in-place procedure is perfectly adequate for the untreated polymer in terms of the subsequent resulting heat transfer rate.

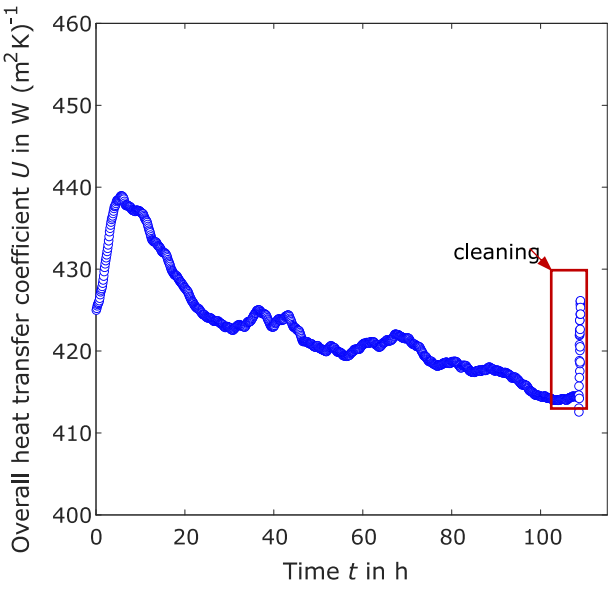


Figure 7. Visualization of the cleaning process of LLDPE-EG by means of the overall heat transfer coefficient. $t_{cleaning}$ = 40 min; $pH_{cleaning}$ = 2.

4. Conclusions

The production of LLDPE filled with 60% EG provided a sharp increase in thermal conductivity compared to pure LLDPE. The materials obtained in this way are conceivable for use in MED. PEEK, on the other hand, must be manufactured in extremely thin films to compete with conventional materials.

Whereas PEEK is characterized by its excellent cleanability in place, the polymer composites stand out due to their very cost-effective raw materials and better handling. Since, in the fouling experiments shown here, the already achieved heat transfer rates correspond to over 90% of the value of stainless steel, which gives a clear cost advantage in using these materials. For an in-place cleaning of the composites, acidic cleaning methods must be used, which proved to be the most effective in removing the fouling deposit as the initial heat transfer could be restored. Plasma treatment of the materials also leads to a further increase in heat transfer and is therefore advisable.

Properly designed, both high-performance polymers such as PEEK and polymer composites consisting of polyethylene and graphite represent an interesting alternative material for MED compared to conventional materials.

Funding: This work was made possible by NPRP grant No.: NPRP10-0205-170349 from the Qatar National Research Fund (A Member of the Qatar Foundation). The statements made herein are solely the responsibility of the authors.

Nomenclature

A	Heat transfer surface area (m^2)
B	Bias uncertainty
$\dot{m}$	Mass flow rate (kg/s)
$\dot{Q}$	Heat flow (W)
R_f	Thermal fouling resistance (m^2 K W^{-1})
Re	Reynolds number
S_a	Mean arithmetic surface roughness (µm)
SA	Salinity (g/kg)
t	Time (s)
T	Absolute temperature (K)
U	Overall heat transfer coefficient (W m^{-2} K^{-1})

Special characters

γ	Surface free energy (mN/m)
θ	Contact angle (°)
λ	Thermal conductivity (W m^{-1} K^{-1})
ΔT_{lm}	Mean logarithmic temperature difference (K)

Subscript/Superscript

0	Initial value
B	Bulk
c	Cold
f	Fouled surface
L	Liquid (solution)
S	Surface
sol	Solution
W	Wall

Abbreviations

EG	Expanded graphite
LLDPE	Linear low-density polyethylene
MED	Multi-effect-distillation
PEEK	Polyether ether ketone
PMMA	Poly(methyl methacrylate)
POM	Polyoxymethylene
PT	Plasma treated
RF	Radiofrequency
SS	Stainless steel

References

1. Trieb, F.; Müller-Steinhagen, H. Concentrating solar power for seawater desalination in the Middle East and North Africa. *Desalination* **2008**, *220*, 165–183, doi:10.1016/j.desal.2007.01.030.
2. Nriagu, J.; Darroudi, F.; Shomar, B. Health effects of desalinated water: Role of electrolyte disturbance in cancer development. *Environ. Res.* **2016**, *150*, 191–204, doi:10.1016/j.envres.2016.05.038.
3. He, W.; Wang, J. Feasibility study of energy storage by concentrating/desalinating water: Concentrated Water Energy Storage. *Applied Energy* **2017**, *185*, 872–884, doi:10.1016/j.apenergy.2016.10.077.

4. Frank, H.; Rahav, E.; Bar-Zeev, E. Short-term effects of SWRO desalination brine on benthic heterotrophic microbial communities. *Desalination* **2017**, *417*, 52–59, doi:10.1016/j.desal.2017.04.031.
5. Lestina, T. Heat Exchangers Fouling, Cleaning, and Maintenance. *Handbook of Thermal Science and Engineering*; Springer International Publishing: Cham, 2018; pp 1609–1641, ISBN 978-3-319-26694-7.
6. Wang, C.P.; Wang, H.Z.; Ruan, G.L.; Wang, S.H.; Xiao, Y.X.; Jiang, L.D. Applications and prospects of titanium and its alloys in seawater desalination industry. *IOP Conf. Ser.: Mater. Sci. Eng.* **2019**, *688*, 33036, doi:10.1088/1757-899X/688/3/033036.
7. Olsson, J.; Snis, M. Duplex — A new generation of stainless steels for desalination plants. *Desalination* **2007**, *205*, 104–113, doi:10.1016/j.desal.2006.02.051.
8. T'Joen, C.; Park, Y.; Wang, Q.; Sommers, A.; Han, X.; Jacobi, A. A review on polymer heat exchangers for HVAC&R applications. *International Journal of Refrigeration* **2009**, *32*, 763–779, doi:10.1016/j.ijrefrig.2008.11.008.
9. Christmann, J.B.; Krätz, L.J.; Bart, H.-J. Falling film evaporation with polymeric heat transfer surfaces. *Desalination* **2013**, *308*, 56–62, doi:10.1016/j.desal.2011.05.027.
10. Breuer, O.; Sundararaj, U. Big returns from small fibers: A review of polymer/carbon nanotube composites. *Polym Compos* **2004**, *25*, 630–645, doi:10.1002/pc.20058.
11. Glade, H.; Moses, D.; Orth, T. Polymer Composite Heat Exchangers. In *Innovative Heat Exchangers*; Bart, H.-J., Scholl, S., Eds.; Springer International Publishing: Cham, 2018; pp 53–116, ISBN 978-3-319-71639-8.
12. Bart, H.-J.; Dreiser, C.; Laaber, D. Polymer Film Heat Exchangers. In *Innovative Heat Exchangers*; Bart, H.-J., Scholl, S., Eds.; Springer International Publishing: Cham, 2018; pp 1–52, ISBN 978-3-319-71639-8.
13. Dreiser, C.; Krätz, L.J.; Bart, H.-J. Kinetics and Quantity of Crystallization Fouling on Polymer Surfaces: Impact of Surface Characteristics and Process Conditions. *Heat Transfer Engineering* **2015**, *36*, 715–720, doi:10.1080/01457632.2015.954954.
14. Kaelble, D.H. Dispersion-Polar Surface Tension Properties of Organic Solids. *The Journal of Adhesion* **1970**, *2*, 66–81, doi:10.1080/0021846708544582.
15. Owens, D.K.; Wendt, R.C. Estimation of the surface free energy of polymers. *J. Appl. Polym. Sci.* **1969**, *13*, 1741–1747, doi:10.1002/app.1969.070130815.
16. David, R.; Spelt, J.; Zhang, J.; Kwok, D. Contact Angles and Solid Surface Tensions. In *Applied surface thermodynamics*, 2. ed.; Neumann, A.W., David, R., Zuo, Y., Eds.; CRC/Taylor & Francis: Boca Raton, Fla., 2011, ISBN 9780849396878.
17. Ataki, A.; Kiepfer, H.; Bart, H.-J. Investigations on crystallization fouling on PEEK films used as heat transfer surfaces: experimental results. *Heat Mass Transfer* **2020**, *56*, 1443–1452, doi:10.1007/s00231-019-02769-w.
18. Kester, D.R.; Duedall, I.W.; Connors, D.N.; Pytkowicz, R.M. Preparation of Artificial Seawater. *Limnol. Oceanogr.* **1967**, *12*, 176–179, doi:10.4319/lo.1967.12.1.0176.

19. Kiepfer, H.; Omar, W.; Schröder, T.; Bart, H.-J. Polymer Film Heat Transfer Surfaces in Seawater Desalination: Fouling Layer Formation and Technology. *Chem. Eng. Technol.* **2020**, *43*, 1205–1213, doi:10.1002/ceat.201900492.
20. Calhoun, A.; Chiang, E. Determination of the surface energetics of surface modified calcium carbonate using inverse gas chromatography. *J Vinyl Addit Technol* **2006**, *12*, 174–182, doi:10.1002/vnl.20084.
21. Förster, M.; Augustin, W.; Bohnet, M. Influence of the adhesion force crystal/heat exchanger surface on fouling mitigation. *Chemical Engineering and Processing: Process Intensification* **1999**, *38*, 449–461, doi:10.1016/S0255-2701(99)00042-2.
22. Plummer, L.; Busenberg, E. The solubilities of calcite, aragonite and vaterite in CO2-H2O solutions between 0 and 90°C, and an evaluation of the aqueous model for the system CaCO3-CO2-H2O. *Geochimica et Cosmochimica Acta* **1982**, *46*, 1011–1040, doi:10.1016/0016-7037(82)90056-4.
23. Wang, W.; Zeng, D.; Chen, Q.; Yin, X. Experimental determination and modeling of gypsum and insoluble anhydrite solubility in the system CaSO4–H2SO4–H2O. *Chemical Engineering Science* **2013**, *101*, 120–129, doi:10.1016/j.ces.2013.06.023.
24. Albert, F.; Augustin, W.; Scholl, S. Enhancement of Heat Transfer in Crystallization Fouling. In . Heat Exchanger Fouling and Cleaning VIII, Schladming, Austria, 14-19 June; Müller-Steinhagen, H., Malayeri, M.R., Watkinson, A.P., Eds., 2009.
25. Crittenden, B.D.; Alderman, N.J. Negative fouling resistances: The effect of surface roughness. *Chemical Engineering Science* **1988**, *43*, 829–838, doi:10.1016/0009-2509(88)80078-2.
26. Li, Z.; Demopoulos, G.P. Solubility of CaSO 4 Phases in Aqueous HCl + CaCl 2 Solutions from 283 K to 353 K. *J. Chem. Eng. Data* **2005**, *50*, 1971–1982, doi:10.1021/je050217e.
27. Blounot, C.W.; Dickson, F.W. The solubility of anhydrite (CaSO4) in NaCl-H2O from 100 to 450°C and 1 to 1000 bars. *Geochimica et Cosmochimica Acta* **1969**, *33*, 227–245, doi:10.1016/0016-7037(69)90140-9.
28. Chen, T.; Neville, A.; Yuan, M. Influence of Mg2+ on CaCO3 formation - bulk precipitation and surface deposition. *Chemical Engineering Science* **2006**, *61*, 5318–5327, doi:10.1016/j.ces.2006.04.007.
29. Müller-Steinhagen, H. C4 Verminderung der Ablagerungsbildung in Wärmeübertragern. *VDI-Wärmeatlas*; Springer Berlin Heidelberg: Berlin, Heidelberg, 2013; pp 91–122, ISBN 978-3-642-19980-6.
30. Dreiser, C. Falling liquid film enhancement, fouling mitigation and conceptual design of polymer heat exchangers. Ph.D. Thesis; TU Kaiserslautern, Kaiserslautern, 2016.

Review of Multicomponent Adsorption and Isotherms for Multicomponent Adsorption

Amrutha [1,*], Balakrishna Prabhu [2] Girish C R [2,] and Gautham Jeppu [*]

[1] Ms. Amrutha ,Ph.D. Research Scholar, Department of Chemical Engineering, Manipal Institute of Technology, Manipal, Udupi, Karnataka, PIN: 576104, India

[2] Associate Professor Department of Chemical Engineering, Manipal Institute of Technology, Manipal, Udupi, Karnataka, PIN: 576104, India

**Corresponding authors: amruthaachar8@gmail.com; gautham.jeppu@gmail.com Tel.: +91-9590935226; +91-8762213942*

Abstract: Water purification often is carried out using adsorption using adsorbents such as activated carbon. The common pollutants in water are heavy metals, non-metal, chemical waste, volatile organic matter, etc. Adsorption is one of the best methods to remove these compounds, which are toxic to human health. Adsorption depends on the interaction between the adsorbent and the adsorbate, the effect of temperature, pH, and concentration of adsorbents. While considering the equilibrium data, the isotherm models are essential to know the interaction mechanism of adsorbate and the adsorbent. The process of adsorption occurs, forming physical and chemical bonds between the adsorbate and the adsorbent. Predominant studies focused on single adsorbate systems. There are many isotherm models for single-component adsorption, but multicomponent adsorption modeling is less common. A few research papers have carried out studies for multicomponent adsorption (MCA), where several adsorbates (such as arsenic, chromium, lead, fluoride) have simultaneously adsorbed. Interdependency of multicomponent adsorption can be predicted from the simulation using multicomponent isotherm models such as the extended Langmuir isotherm model. This paper summarizes available multicomponent isotherm models and analyses several case studies. Optimum analysis of linear and non-linear regression has reduced the error function to give the best fit of multicomponent adsorption models.

Keywords: Multicomponent adsorption; Isotherm; Langmuir isotherm; Freundlich isotherm

Testing and Commissioning of a Cold Inflow Free Chimney Dryer

Hooi Kim Phang [1,*], Sivakumar Kumaresan [1], Chi Ming Chu [1] and Md. Mizanur Rahman [2]

[1] Chemical Engineering Programme, Faculty of Engineering, Universiti Malaysia Sabah.

[2] Department of Mechatronics Engineering, World University of Bangladesh.

***** *Corresponding author: phang83@gmail.com; Tel.: +60 128824088.*

Abstract: A physical model of chimney dryer has been constructed and tested indoors using an electrical heating system to study the cold inflow phenomenon. Computational Fluid Dynamics (CFD) was first implemented as a design tool to demonstrate the adverse cold inflow in a conceptual model. The conceptual model that proposed for testing and commissioning was a chimney dryer with a low height-to-gap ratio. This design originated from prior work with a pilot scale greenhouse dryer or tunnel dryer for seaweed drying. CFD was first simulated to predict the distribution of air velocity and temperature profiles inside the drying chamber with and without cold inflow into chimney dryer. The optimization of computation grid on the grid convergence errors was carried out for the severest cold inflow case without wire mesh fitting followed by wire mesh fitting. Commissioning of the test facility showed that the wide chimney gap had caused severely adverse cold inflow that could not be mitigated by employing wire mesh fitting where heat gain to heat supply ratio was as high as 0.397. There is discrepancy between CFD results and experimental results for air temperature, a high height-to-gap ratio chimney is proposed for further experimental investigation to verify the validity of the experimental methods and experimental data for low height-to-gap ratio chimney dryer.

Keywords: Cold inflow; Heat transfer; Chimney, Natural convection, Dryer

1. Introduction

Drying is a simultaneous heat and mass transfer process. The energy sources for the drying operation of a dryer are either renewable energy or fossil fuels. The seaweed processing industry in Malaysia initiated by the Department of Fisheries (DOF) has planned to set up a solar seaweed dryer for post harvesting process. A modified chimney with a low height-to-gap ratio incorporated into a natural convection dryer was initially proposed to DOF in Malaysia because of 90% improvement on air velocity efficiency if compared to conventional chimney [1]. The challenge encountered by the DOF was the case hardening [2] issue during the drying process where temperature was high with insufficient ventilation in a natural convection solar dryer. Case hardening is a moisture removal process where the moisture content is trapped within where the formation of hard surface that caused by shrinkage and deformation of plant-based materials most probably under high temperature and low ventilation rate. The hard surface inhibits the bound water of seaweed transferrings to the surface and therefore affects the final quality of dried seaweed. A one-tenth scale physical model of the proposed solar dryer was designed and constructed at Universiti Malaysia Sabah for testing and commissioning [3-4]. CFD was employed and served as a design tool to predict air movement within a chimney dryer. A modified chimney of low height-to-gap ratio did not show the expected experimental results as simulated in CFD briefly where there were many simplifications and assumptions [5]. The complex transport phenomena of seaweed drying were not understood sufficiently, the drying process was modelled empirically [3-4, 6-8] without taking into account the

shrinkage and deformation of seaweed as well as the physical features of the dryer. A semi-theoretical or semi-empirical model to describe the drying behaviour is important for modelling and scaling up. Mathematically modelling the chimney dryer can predict the drying air characteristics on various products under conditions with and without cold inflow.

The chimney effect on the air velocity efficiency as well as the ventilation rate with and without cold inflow were first investigated using CFD under no-load conditions using a conceptual model. It will later be validated using experimental set up with a real physical model.

1.1 *Cold Inflow Phenomenon*

Cold inflow is a common problem in natural convection cooling towers. The unstable ambient air flow sinks into chimney creates an unfavourable downdraft due to the density difference between the hot air inside the tower and cool air around the tower. Cold inflow, also known as reverse flow, affects the chimney thermal performance. Jörg and Scorer [9] predicted the cold inflow by filling the hot air into an insulated glass tube whereas Chu [10] used smoke generator to trace cold inflow in a duct. Sparrow [11] reported cold inflow in an open-ended vertical channel for natural convection. The downdraft was observed from the ambient to the top of heated vertical channel. Fisher & Torrance [12] quantified the cold inflow effect at the chimney exit on the overall heat transfer. The overall heat transfer decreased 4% for the natural convection chimney. The cold inflow phenomenon was also significantly been shown based on temperature distribution inside the cooling tower [13]. A wire mesh was applied by Chu [10] to prevent cold inflow into chimney to ensure correct measurement of temperature for heat balance. 90% improvement on air velocity efficiency was reported by preventing cold inflow into chimney by proper set up [1]. A numerical investigation about cold inflow into vertical channel for natural convection using finite volume method by Andreozzi et al. [14] The cold inflow effects on buoyancy induced air flow in a solar chimney for ventilation applications was also investigated numerically by Khanal and Lei [15]. Chen et al. [16] reported that the prediction method of air flow rate in the literature overpredicted the air flow rate for the geometry chimney in their experimental work for vertical chimney with large gap-to-height ratios. Jing et al. [17] and Hou et al. [18] further investigated on the cold inflow into chimney with the gap-to-height ratio of 0.5 and 0.4 respectively. The experimental studies fixed the height and width of chimney and focused on manipulating the gap or length of the chimney to study the distribution of temperature and velocity of air and airflow rate into chimney. All the research works about the cold inflow effect were carried out either in experiments or theoretical and/or numerical studies, focused on cooling towers and solar chimneys. The drying behaviour and air movement of chimney dryer have not been related to the cold inflow effect. This paper presents the air temperature and velocity distribution inside the chimney dryer that is predicted by employing CFD. The testing and commissioning of the cold inflow free chimney dryer will be further validated by using experimental set up and data measurement of inlet air velocity and temperature points at various locations.

2. Experimental Procedure

2.1 Computational Fluid Dynamics (CFD)

CFD software, Phoenics 2019 v1.1 64 bit was employed as a design tool to simulate the air movement to predict the distribution of air velocity and temperature inside the chimney dryer with and without cold inflow. The application of wire mesh onto the chimney was the method used to mitigate the cold inflow into the chimney drying system. The Phoenics code that applied is based on the finite volume method that developed by Pantakar and Spalding (1972). CFD solves set of differential equations numerically based on the conversation of mass, momentum and energy using

Reynolds Average Navier-Stokes equations (RANS) in turbulent form. The turbulent flow was simulated using Chen-Kim (1987) $k\varepsilon$ model that has been succesfully used in the simulation to demonstrate cold inflow [19]. The CFD solutions for parametric studies as listed in Table 3.1 were simulated under steady state mode and 2 dimensional or 3-dimensional.

Table 1. Parametric study of CFD simulation

Parameters	Range of Parameters
Heat flux	200-1000 W
Height of chimney	0.1524-1.0668 m
Gap of chimney	0.6096 m
Width of chimney	0.3429 m

The computational geometry used a Cartesian coordinate system for air movement prediction inside chimney dryer. The boundary conditons were set up in the compuational domain. At the inlet, a fixed mass flow rate opening whereas at the outlet, a fixed pressure opening where mass is allowed to leave the solution domain with a non-resistance boundary conditions without a wire mesh fitting at ambient temperarutre. However, a resistance boundary conditions was imposed on the solution domain where mass is allowed to leave the wire mesh fitting. The ambient temperature was set to 30°C. The computational diagram and optimised grid mesh of chminey dryer for CFD simulation is illustarted in Figure 1.

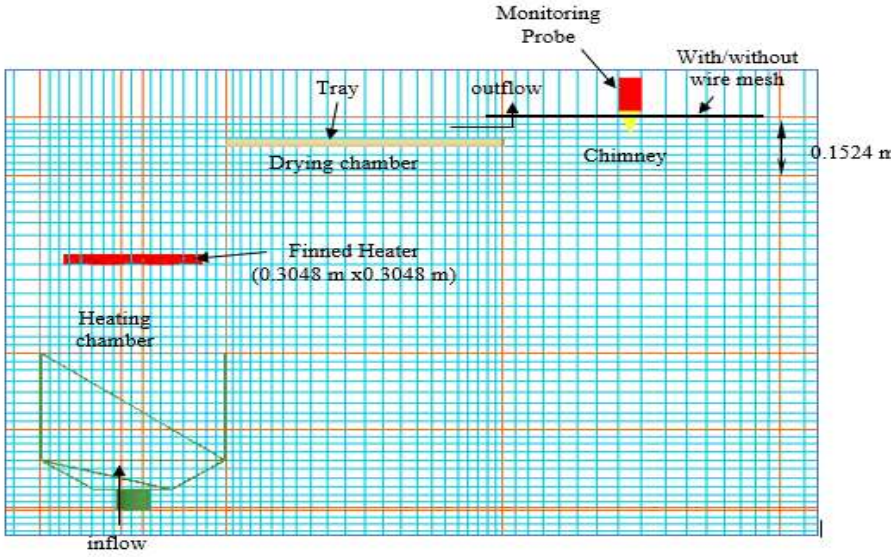


Figure 1. Computational domain and optimized mesh grid of chimney dryer

The CFD simulaton was first simulated with automated number of domain cells with the worst cold inflow scenario. The optimisation of grid mesh size was then carried out to validate the CFD solutions under steady state simulation. The validation of discretization was focused on the severest case of cold inflow where small height-to-gap ratio of chimney (0.1524 m of height, 0.3429 m of width and 0.6096 m of length) and highest turbulent flow under 1000 W of heat flux. After the optimisation of grid convergence errors, the simulated data such as air temeprature, velocity, air flow rate, and heat flux were extracted by using user defined function in the CFD software at the inlet and outlet of chimney.

2.2 Natural Convection Chimney Dryer

A chimney dryer with a low height-to-gap ratio was constructed and tested in laboratory by using an electrical heating system to study the effect of modified chimney on the cold inflow prevention without load to validate the simulation results from CFD. Figure 2 shows the schematic view of the experimental set up of chimney dryer in term of top view and front view. The chimney dryer consists of heating chamber, drying chamber, and chimney. It was made from 12 mm thick plywood, 0.8 mm aluminium sheet as inner layer and Formica sheet as outer layer as insulator to prevent heat loss. The design of chimney dryer was out of radiative heat effect in the system.

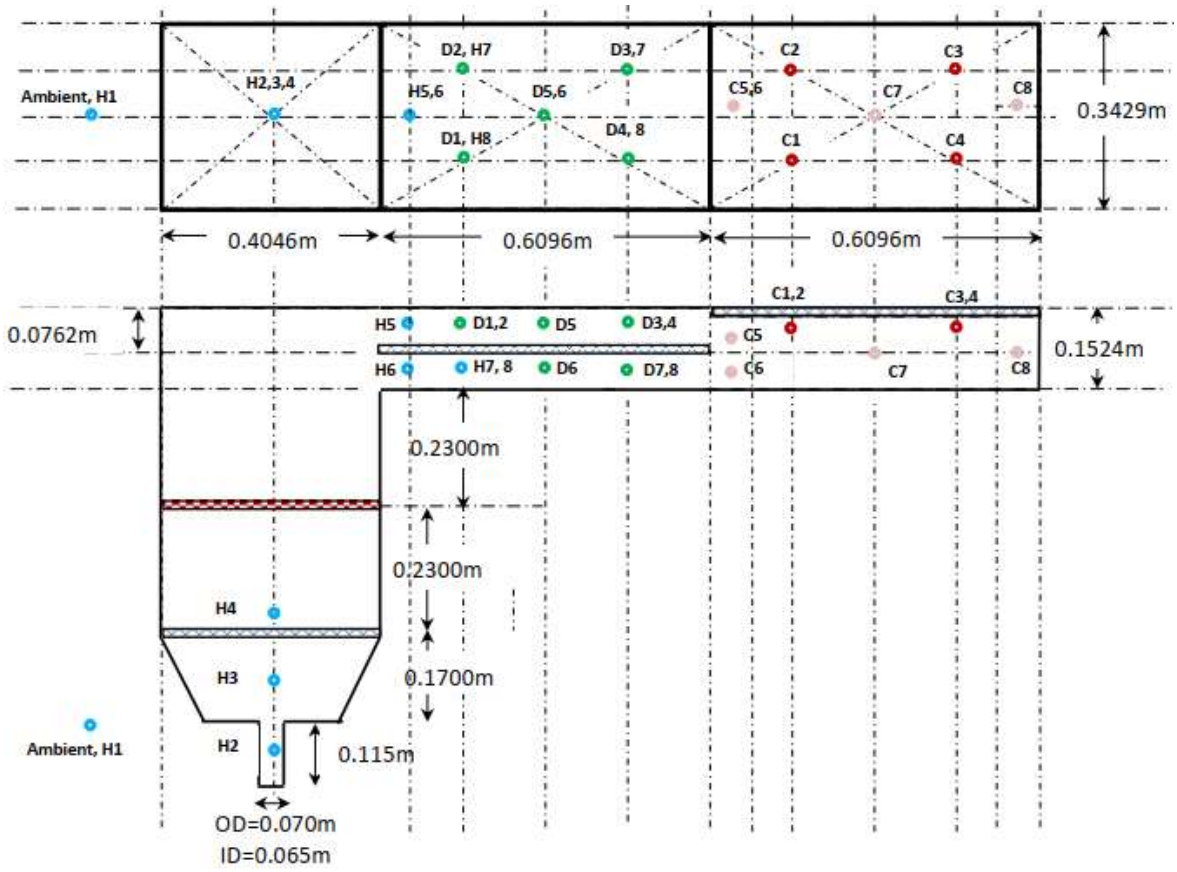


Figure 2. Experimental set up of natural convection chimney dryer

The chimney dryer was heated up in heating chamber. The heater was connected to AC (alternating current) with a variable voltage transformer (0-240 V) for simulating a desirable power output or heat flux in the system. A digital clamp meter (Kyoritsu, KEW SNAP 2017) was applied to measure the output of current and voltage after regulated a constant voltage. K-type wire thermocouples connected with dataloggers (Cole Parmer Data Acquisition Module) were calibrated and used for temperature measurements at different locations in heating chamber, drying chamber, and chimney. All the temperature sampling points were logged every minute. A vane anemometer (CENTER 330) was attached at the inlet of heating chamber to measure the inlet air velocity into the chimney drying system at steady state.

Experiments were performed with chimney height of 0.1524 and 1.0668 m respectively. The length was 0.6096 m and the width was 0.3049 m as fixed geometry of chimney. The experiment started from ambient temperature and the heater was set at 200, and 1000 W respectively with and without wire mesh fitting for the specific height of chimney. The temperatures were taken for mass and energy balance analysis was the average value of the last 5 minutes at the steady state.

3. Data Analysis

The operating parameters of data collection were chimney height, wire mesh fitting, and average ambient air temperature from surroundings. The dependent parameters were average inlet air velocity of anemometer and air temperature at different locations points inside chimney dryer.

The system is assumed top operate adiabatically with proper insulation and completely sealed. The heat supplied is estimated by converting electrical power is expressed as below:

$$\dot{Q}_{supplied} = IV \quad (1)$$

where $\dot{Q}_{supplied}$ is electrical power that measured (W), I is electrical current that measured from the heating system (Ampere) and V is voltage that regulated to the heating system (Voltage). A simplifying assumption was made the electrical energy was fully converted into heat energy with 100% efficiency. The heat balance of the system is calculated by comparing the heat gain in the system and heat supplied to the system.

$$\dot{Q}_{gain} = \dot{m}C_p\Delta T \quad (2)$$

The air flow rate prediction is expressed by equation 3.

$$\dot{m} = \rho A v \quad (3)$$

where ρ is the air density at ambient temperature (kg/m^3), A is the inlet cross sectional area of anemometer (m^2) and v is the measured velocity of anemometer at steady state (m/s). Although there would be heat loss in the conduction, convection, and radiation, the value would be minimal if compared with the effect that caused by cold inflow [1, 10].

4. Results and Discussion

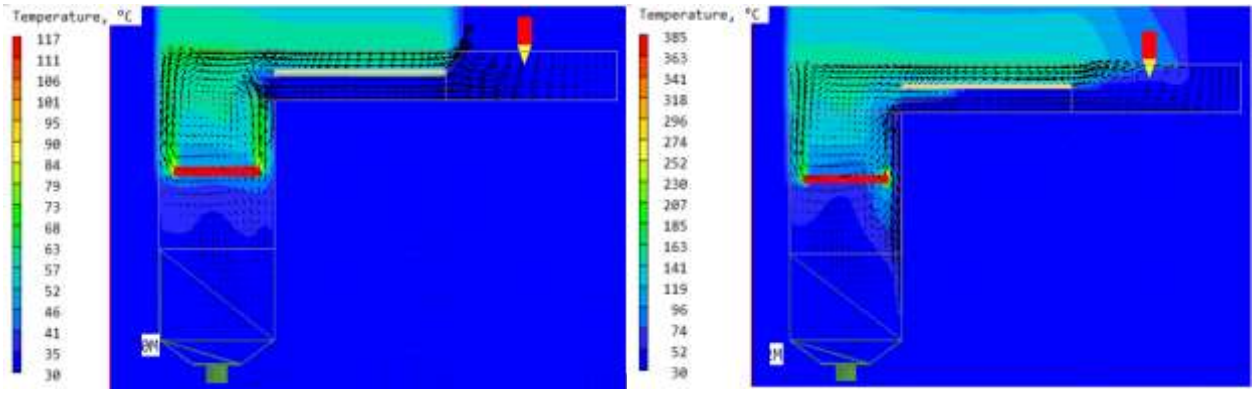
CFD is a design tool that used to demonstrate cold inflow into chimney dryer. The CFD solution was first validated by optimizing the mesh grid size on the convergence errors on the air temperature and velocity distribution inside chimney dryer. The mesh grid optimization was validated on severest cold inflow case and then followed by cold inflow free into chimney dryer. In this study, the grid convergence error less than 10% for severest cold inflow phenomenon was acceptable and it will be further verified on experimental data. The convergence error of low height-to-gap ratio (0.1524 m height, 0.3429 m width, 0.6096 m gap) and high height-to-gap ratio (1.0668 m height, 0.3429 m width, 0.6096 m gap) chimney dryer without wire mesh fitting is presented in Table 2.

Table 2. Convergence error of velocity and temperature at chimney outlet under optimized mesh grid

$\dot{Q}_{supplied}$	Chimney Height	Wire Mesh	Convergence Error, %			
W	m	Yes /No	x-axis velocity (u), m/s	Y-axis velocity (v), m/s	Z-axis velocity (w), m/s	Temperature, °C
200	0.1524	No	4.41E-01	5.19E-01	5.02E+00	3.28E-02
		Yes	1.92E-01	2.12E-01	1.23E+00	3.92E-02
	1.0668	No	4.64E+00	5.23E+00	7.94E+00	9.38E-03
		Yes	9.12E-02	8.60E-02	5.31E-01	1.20E-02
1000	0.1524	No	2.62E-01	2.86E-01	3.02E+00	2.36E-02
		Yes	2.22E-01	3.13E-01	1.36E+00	1.39E-01
	1.0668	No	2.84E-01	3.15E-01	6.50E+00	2.68E-02
		Yes	3.01E-01	3.54E-01	1.10E+00	3.52E-01

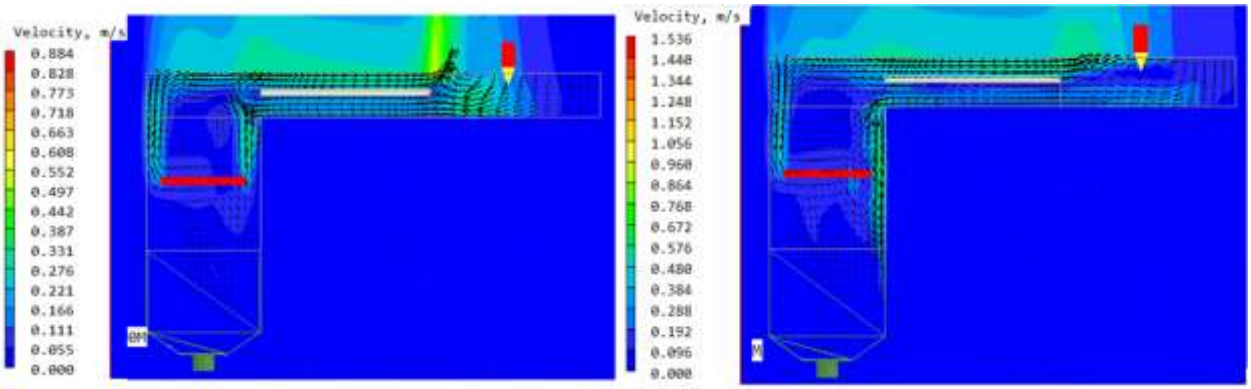
The high error of grid convergence was due to the maldistribution of air temperature and velocity caused by the big chimney gap. There are studies also reported that air temperature and velocity distribution was highly non-uniform with large gap for vertical chimney experimentally [12, 15-16] and numerically [4, 13, 14, 18, 19].

The CFD was also used to predict the air movement inside the chimney dryer and identify the discharge rate of heat flux. The buoyancy flow inside the chimney dryer increased with high uniform heat flux as well as with wire mesh fitting. The air temperature and velocity evenly distributed when wire mesh was fitted onto the chimney. The contour plot of velocity and temperature able to highlight the difference between cold inflow and without cold inflow. It is determined that the cold inflow was more severe on chimney dryer at low height-to-gap ratio without wire mesh fitting than wire mesh fitting onto chimney under uniform heat flux of 1000 W. CFD contour plot of temperature and velocity as well as air movement profiles were illustrated in Figure 3 and Figure 4.



(**a**) (**b**)

Figure 3. Air temperature profile of chimney dryer: (**a**) with cold inflow, (**b**) without cold inflow under heat flux of 1000 W



(**a**) (**b**)

Figure 4. Air velocity profile of chimney dryer: (**a**) with cold inflow, (**b**) without cold inflow under heat flux of 1000 W

The CFD contour shows that the wire mesh plays an important role to resist the cold inflow from the surrounding flows into the system and resulted uniform heat flux and air flow inside the chimney dryer. A phenomena has also been reported by Kumaresan et al. [5] and Chu et al. [19] numerically. These similar results imply that the enhancement of thermal energy and air velocity with the implementation of wire mesh through prevention of cold inflow into the chimney. In this study, commissioning of the chimney dryer is intended to prove the effectiveness of wire mesh on the mitigation of cold inflow experimentally. However, the adverse cold inflow was very severe at low height-to-gap ratio chimney as well as in the extended height of chimney. The cold inflow could not be mitigated by extending the height of chimney based on experimental data. The air velocity could not be measured inside the chimney during experiment. However, the cold inflow could be observed in contour plot of air velocity as shown in Figure 5.

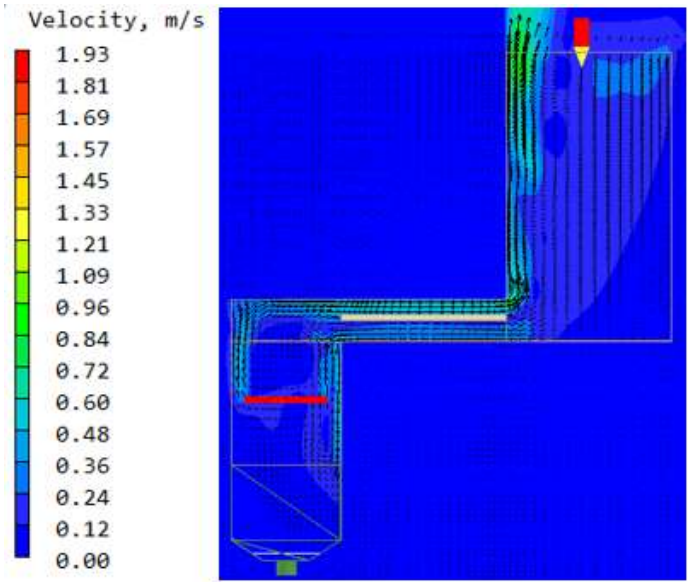


Figure 5. Cold inflow inside wide chimney gap with an extension height of 1.0668 m

The testing and commissioning served as an essential process to ensure the experimental procedures are valid and reliable though it may be different from the CFD simulated results through proper set up and consistency trend of experimental data. There are some simplifying assumptions were made during CFD simulation such as ideal gas behaviour, no pressure loss, and no heat loss. The quantification of heat balance is the key to ensure the validity of this study. The energy balance has been demonstrated and reported area averaged temperature at the chimney outlet shall be considered in the case of cold inflow instead of the Favre averaging method to avoid discrepancy in between cold inflow and without cold inflow [19]. The outlet chimney temperature used for the heat gain calculation was the average temperature of C1 to C4. The heat gain was calculated based on inlet velocity, ambient temperature, and average outlet temperature of chimney using equation 2 and equation 3. The heat supplied from the heating system into the chimney dryer and the heat gain that calculated from the temperature data numerically and experimentally is reported in Table 3.

Table 3. Heat supplied and heat gain that calculated numerically and experimentally

Chimney height, m	Wire Mesh	Heat supplied, W		Heat gain, W	
		CFD	Experiment	CFD	Experiment
1.0668	Yes	200	202	126	29
	No			31	5
	Yes	1000	1004	776	235
	No			-26	30

The 1.0668 m height was the maximum possible chimney height inside the research laboratory. Therefore, further investigation on commissioning is required to validate the scenario with and without cold inflow using small gap chimney under a chimney height of 1.0668 m. The wide gap of chimney might be the issue that caused the quantification of heat supply and heat gain did not comply the mass and energy conversation laws. The cold inflow issue shall be enhanced by reducing the gap of chimney with the achievable maximum height of chimney on the commissioning with experimental data before can justify the effectiveness of wire mesh on cold inflow prevention for low height-to-gap ratio chimney dryer.

5. Conclusions

The cold inflow phenomenon at the wide opening chimney outlet as well as low height-to-gap ratio chimney dryer was unable to be mitigated by utilizing wire mesh fitting. An extended height of chimney or small gap-to-height with and without cold inflow phenomena was proposed to further verify the validity of the low height-to-gap experimental data. The further verification on the commissioning can be confidently applied to explain the effect of wire mesh on the effectiveness of cold inflow prevention as well as thermal performance.

References

1. Chu, C., Rahman, M.M., Kumaresan, S. Effect of cold inflow on chimney height of natural draft cooling towers. *Nuclear Engineering and Design* 2012, Volume 249, 125-131.
2. Gulati, T., Datta, A.K. Mechanistic understanding of case-hardening and texture development during drying of food materials. *Journal of Food Engineering* 2015, Volume 166, pp. 119-138.

3. Rahman, M.M., Phang, H.K., Chu, C.M., Kumaresan, S., Yasir, S.M. A cold-inflow free solar chimney dryer for seaweed drying in Sabah, Malaysia. Proceedings of the International Conference on Industrial Engineering and Operations Management, Bandung, Indonesia, 2018. pp. 3062-3070.
4. Phang, H., Chu, C., Kumaresan, S., Rahman, M.M., Yasir, S.M. Preliminary of study of seaweed drying under a shade and in a natural draft solar dryer. *International Journal of Science and Engineering* 2015, Volume 8(1), pp. 10-14.
5. Kumaresan, S., Rahman, M.M., Chu, M., Phang, H.K. A chimney of low height to diameter ratio for solar crops dryer. In Developments in *Sustainbale Chemical and Bioprocess Technology*, Pogaku, R., Bono, A., Chu, C. Springer New York Heidelberg Dordrecht London, 2013, pp. 145-150.
6. Ali, M.K.M., Fudholi, A., Muthuvalu, M.S., Sulaiman, J., Yasir, S.M. Implications of drying temperature and humidity on the drying kinetics of seaweed. AIP Conference Proceedings, Kedah, Malaysia, 2017, Volume 1905, Article number 050004.
7. Fudholi, A., Othman, M.Y., Ruslan, M.H., Yahya, M., Zaharim, A., Sopian, K. Design and testing of solar dryer for drying kinetics of seaweed in Malaysia. Proceedings of the 4th WSEAS international conference on energy and development-environment-biomedicine, 2011, pp. 119-124.
8. Ali, M.K.M., Ruslan, M., Muthuvalu, M.S., Wong, J., Sulaiman, J., Yasir, S.M. Mathematical modelling for the drying method and smoothing drying rate using cubic spline for seaweed Kappaphycus Striatum variety Durian in a solar dryer. AIP Conference Proceedings, Kuala Lumpur, Malaysia, 2013, Volume 1602, pp. 113-120.
9. Jörg, O. and Scorer, R.S. An experimental study of cold inflow into chimneys. *Atmospheric Environment*, Pergamon Press 1967, Volume 1, pp. 645-654.
10. Chu, C.M. Studies of the plumes above air-cooled heat exchangers operating under natural convection. Ph.D Thesis, Chemical Engineering Department, Birminghan University, Edgbaston, United Kingdon, 1986.
11. Sparrow, E.M., Chrysler, G.M., Azevedo, L.F. Observed flow reversals and measured-predicted Nusselt numbers for natural convection in a one-sided heated vertical channel. *Journal of Heat Transfer* 1984, Volume 106, pp. 325-332.
12. Fisher, T.S., and Torrance, K.E. Experiments on chimney-enhanced free convection. *Journal of Heat Transfer* 1999, Volume 121, pp. 603-607.
13. Li, X., Gurgenci, H., Guan, Z., Sun, Y. Experimental study of cold inflow effect on a small natural draft dry cooling tower. *Applied Thermal Engineering* 2018, Volume 128, pp. 762-771.
14. Andreozzi, A., Buonomo, B., and Manca, O. Numerical investigation of transient natural convection in a vertical channel-chimney system symmetrically heated at uniform heat flux. *International Heat ana Mass Journal* 2012, Volume 55, pp. 6077-6089.
15. Khanal, R. and Lei, C. Flow reversal effects on buoyancy induced air flow in solar chimney. *Solar Energy* 2012, Volume 86, pp. 2738-2794.
16. Chen, Z.D., Bandopadhaya, P., Halldorsson, J., Byrjalsen, C., Heiselberg, P., Li, Y. An experimental investigation of a solar chimney model with uniform wall heat flux. *Building and Environment* 2003, Volume 38, pp. 893-906.
17. Jing, H., Chen, Z.D., Li, A. Experimental study of the prediction of the ventilation flow rate through solar chimney with large gap-to-height ratios. *Building and Environment* 2015, Volume 89, pp. 150-159.
18. Hou, Y., Li, H., Li, A. Experimental and theoretical study of solar chimneys in building with a uniform wall heat flux. *Solar Energy* 2019, Volume 193, pp. 244-252.
19. Chu, C., Rahman, M.M., Kumaresan, S. Improved thermal energy discharge rate from a temperature-controlled heating source in a natural draft chimney. *Applied Thermal Engineering* 2016, Volume 98, pp. 991-1002.

20. Nguyen, Y.Q., Wells, J.C. A numerical study on induced flow rate and thermal efficiency of a solar chimney with horizontal absorber surface for ventilation for buildings. *Journal of Building Engineering* 2020, Volume 28, 101050.

Environmentally Safe Microwave Heating of Non-Polar Materials

Vladimir Saranchin, Alexey Lykov *

[1] Moscow State University of Land Use Planning,;
***** *Corresponding authors: saranchin@yandex.ru,; alykov49@mail.ru, +7-985-9240126 ;+7-916-215-6981*

Abstract: The paper presents results for the theoretical basis of heat transfer and experimental studies of the processes of a microwave method of heating uranium hexafluoride for its safe evaporation from containers, including defective and low- and medium-temperature heating of oil fractions. The processes are environmentally safe due to the fact that heat generation occurs in the bulk of the heated medium and is easily controlled. The proposed method is based on uranium hexafluoride evaporation at the expense of heat energy transferred from substances absorbing microwave energy. These substances are located on the surface of solid uranium hexafluoride. These substances play a role in microwave energy – to – heat energy conversion. This technique avoids damage from deterioration of a hermetic container due to local overheating because the microwave energy is reflected by the metal container walls and the wall temperature is no more than that of the gas released. No overheated container walls are a characteristic property of the microwave technique with resulting safety and suitability for evaporation of damaged containers. The above advantages allow the emergency and environmental pollution risk to be reduced at the expense of no overheated container walls and reduction of removal time. Oil and oil fractions are also non-polar liquids and therefore are poorly heated by the energy of the microwave field. Materials that absorb microwave energy, for example, ferrite ceramics, are distributed in the bulk of the heated liquid and have the necessary total surface for effective heat transfer to the liquid. With this method of heating, the maximum temperature difference allowed by the properties of the liquid can be used. The paper considers the heat exchange of microwave – heat-absorbing material and heat-absorbing material - non-polar liquid. For the evacuation of uranium hexafluoride, experimental studies were conducted for the selection of absorbing materials. Also, this process was implemented on a laboratory installation and showed high efficiency.

Keywords: microwave energy, heat-absorbing agent, heat transfer; non-polar materials

1. Introduction

Currently, large amounts of depleted uranium hexafluoride, which are a by-product of uranium enrichment, have accumulated in the world. Containers with depleted uranium hexafluoride are stored for a long time in open areas and are subject to corrosion. After the evacuation and conversion of depleted uranium hexafluoride, depleted metallic uranium can be used in various industries and, first of all, for the manufacture of metal (uranium-steel) containers and heavy concrete for radioactive waste storage [2,3].

Currently, uranium hexafluoride is evacuated from containers by heating with an outer source supporting a pressure in the container sufficient for UF_6 sublimation. During the process of outer heating, the temperature of the container walls can exceed the melting point of UF_6. The density of UF_6 decreases upon melting by ~1.4 times (from 5.06 g/см^3 up to less than 3.63 g/см^3), which can result in hydraulic shocks even during sublimation/evaporation from the solid phase with local

overheating, for example, with heating of a container bottom. The relevant characteristics, from the point of view of process safety, for UF_6 evaporation are: the duration of evaporation from a container, lag of UF_6 consumption control, and calorific intensity of the container walls. These characteristics are particularly significant for the process of depleted UF_6 (DUF_6) evaporation from long-term storage containers. Obvious and latent defects are possible in such containers. Therefore, for safety, the evaporations are conducted at very low rates. The main reason for the poor efficiency is the poor heat transfer from the walls of the container to solid DUF_6. In a rather short period (some hours), a gap appears between the wall of the container and solid DUF_6, which increases with time. The pressure in a container during sublimation is supported at a low level that does not provide a high rate of evaporation. The unexpected failure of "ex-melting" pieces of solid DUF_6 is possible during evaporation that is fraught with accidents and excursions of the technological mode. It is necessary to add to the above as a deficiency, the low efficiency of heating installations of UF_6 containers, as heating through a wall is accompanied with large heat losses to the environment due to heat radiation.

An analysis of all factors demonstrates that external heating of containers during UF_6 evaporation does not guarantee the safety of a process and, as a matter of fact, reaches a limiting output. The temperature rise of a container wall by induction heating can reduce the draining cycle by up to 5 days, although at the same power input, according to thermodynamic calculations, the draining cycle can be reduced by up to one day. It is possible to reach such productivity and to secure the process safety during evaporation of DUF_6 from long-term storage containers, even defective ones, only by using an internal heat source in a container.

This is possible if a microwave electromagnetic field is used as the energy carrier. The optimal version is direct heating of solid DUF_6 by microwave energy without heat transfer through a wall. However, according to literature data on UF_6 electrophysical properties, it does not absorb electromagnetic field energy in the microwave range to conduct evaporation or sublimation processes.

Therefore, this process can be realized by placing a material that absorbs microwave energy on the UF_6 surface or to imbue the UF_6 with an applicable liquid so that the heating of solid UF_6 will be ensured at the expense of its direct contact with the heated substance.

An analysis of UF_6 electromagnetic properties allows the following conclusions to be made:

1. Direct heating of solid and liquid UF_6 by microwave energy is most likely ineffective or unfeasible owing to the low values of both dielectric and magnetic permeabilities and loss factors.
2. Indirect heating of solid UF_6 is made possible by locating solids on its surface or by impregnating it with liquids which absorb microwave energy well.

To realize the proposed method, materials capable of heating with microwave energy and inert in uranium hexafluoride must be chosen. According to these limitations, tablets of uranium and iron oxides (ferrites) from solid substances, i.e., heat-absorbing agents, and series of liquid ethane halocarbons of the marks 112, 113, 122A can be recommended for the tests.

Uranium oxides (UO_2 and U_3O_8) are most preferred, since in conglomerate form they have a high thermal capacity and a high density ≈10 g/cm^3 (approximately twice that of UF_6), that should reduce the effect of a «gas cushion» upon contact of the heated tablets with subliming UF_6. Being good dielectrics, ferrites, i.e., sintered iron oxides (with special additions), have high magnetic susceptibility and magnetic permeability. This makes it possible to heat them effectively with the magnetic component of a microwave field. The magnetic properties of ferrites, including in the microwave range, are well known but investigations on their application as heat-absorbing agents have not been carried out. Liquid heat-absorbing agents, i.e., halocarbons 112, 113, and 122A, give steady solutions with UF_6 up to 100^{0}C and permeate well the solid UF_6. The solution properties are close to theoretical, which simplifies subsequent separation of the halocarbon from UF_6, if necessary,

and recycles it for reuse. Isomers of halocarbon molecules can have dipole moments. It is possible that UF_6 solutions in halocarbons can have particular dielectric properties contributing to their heating in a microwave field. There are no data in the literature about such research and they must be obtained experimentally.

The heat exchange process in this system is complex and can be divided into heating by the microwave field of heat absorbing agents and their heat exchange with the material (DUF_6).

The heating process of materials with a given heat capacity c and density ρ by microwave energy with intensity **E** is described by the heat transfer equation:

$$\rho c \frac{\partial T}{\partial t} = \mathbf{0.5}\varepsilon_0 \varepsilon'' \omega \left\langle \mathbf{E}^2 \right\rangle \tag{1}$$

When materials are subjected briefly to a microwave field, differential equation (1) can be replaced by the finite difference one:

$$\Delta T = \frac{\mathbf{0.5}\varepsilon_0 \varepsilon'' \omega \left\langle \mathbf{E}^2 \right\rangle}{\rho c V} \Delta t \tag{2}$$

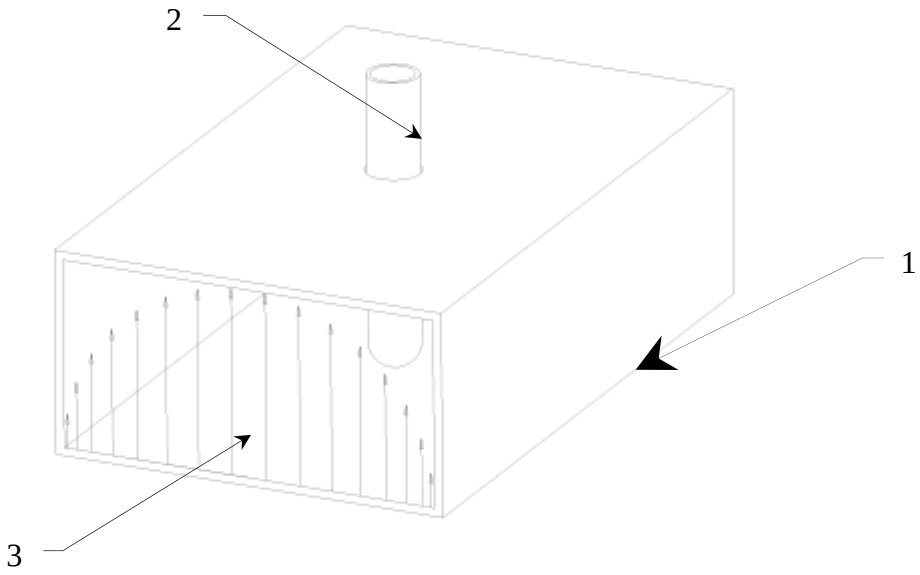
1. If the interaction zone of the microwave field and the tested material is organized so that the average intensity E-squared for the period will be given, the dielectric losses ε'' of the material can be calculated from equation (2). The relative orientation of the electric component of the microwave field and the tube with the studied heat-absorbing agent is shown in Fig. 1.
2. For microwave energy acting on the tube with the sample (with a given volume, density and specific heat) (as measured with a wattmeter or calorimetric method) and the given electric field intensity E during a fixed time Δt, the dielectric losses are calculated from equation (2):

$$\varepsilon'' = \frac{c\rho V}{0.5\varepsilon_0 \omega \frac{E_m^{\ 2}}{2}} \cdot \frac{\Delta T}{\Delta t} \tag{3}$$

The following equation determines the amplitude of the electric field intensity of a traveling wave of type H_{10} at the middle of a broad wall of the waveguide with channel dimensions **a** and **b**:

$$E_m = 2\sqrt{\frac{W}{a \cdot b}} \cdot \sqrt[-4]{\frac{1-\left(\frac{\lambda_0}{2a}\right)^2}{\frac{\varepsilon_0 \varepsilon}{\mu_0 \mu}}} \tag{4}$$

where: ***W*** is the power passing on the waveguide without a dielectric; λ_0, the wavelength in free space (it is 12.2 cm for frequency 2450 MHz); and ε и μ, the relative dielectric and magnetic permittivities of the medium.



1. Section of rectangular single-mode waveguide;
2. Quartz tube with heated material;
3. Electric field pattern for mode H_{10};

Fig.1 Scheme of working unit of laboratory bench

The energy absorbed by the sample is determined by energy balance:

$$P_{abs} = P_0 - P_{refl} - P_{pass}; \quad (5)$$

where: P_0, is the microwave energy traveling on the sample;
P_{pass}, microwave energy passed out of the sample and absorbed by the matched load;
P_{refl}, microwave energy reflected by the sample.

The field distribution of a traveling electromagnetic wave in the waveguide is determined by solving uniform wave equations that may be derived from a system of fundamental Maxwell's equations.

Dielectric losses in the material (studied sample) or the energy dissipated by the dielectric is determined by equation:

$$P_{diss} = 0{,}5\varepsilon_0\varepsilon''\omega E^2 \cdot V; \quad (6)$$

The intensity is determined by the ratio:

$$E^2 = \frac{4P_0}{ab} \cdot \frac{120\pi}{\sqrt{1-\left(\frac{\lambda_0}{2a}\right)^2}}; \quad (7)$$

The formula for calculation of the dielectric losses factor is derived from (6) and (7):

$$\varepsilon'' = \frac{P_{abs}}{0.5 \cdot \varepsilon_0\omega} \cdot \frac{a \cdot b\sqrt{1-\left(\frac{\lambda_0}{2a}\right)^2}}{4P_0 \cdot 120\pi} \cdot \frac{4}{V} \quad (8)$$

It must be emphasized that calculations based on such measurements can give dielectric loss factors with significant errors. However, this accuracy is sufficient for comparison and substantiated determination of a heat-absorbing agent. The required orientation of the microwave field electric intensity and the tube with the studied materials is arranged in the working unit where the conditions are appropriate for measuring the temperature of samples and the indirect electric component of the microwave field intensity (by passing power measurement).

Thermograms of halocarbon heating were obtained in the range from 20 to 95^0 C and tan δ was determined as well. It was found that the general shape of the temperature dependence of the absorption coefficient of water and its value agree well with the ones represented in literature [4]. The results were used to apply a correction for the calibration characteristics of power meters that did not take into account heat losses to the environment during the experiments.

Figure 2 presents a typical heating diagram for mixtures of halocarbons with uranium hexafluoride and distilled water for comparison.

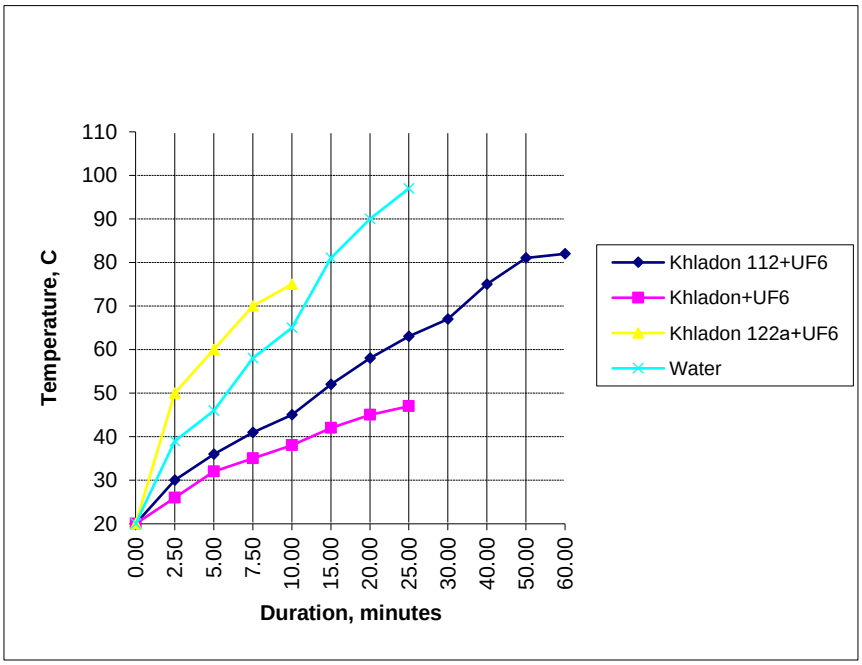


Fig. 2 Typical heating diagram

The short-circuit method was used to evaluate the dielectric properties of the most promising heat-absorbing agents (UO_2 and U_3O_8). The measuring procedure and calculation of dielectric characteristics are discussed in detail in the literature.

Figures 3 and 4 present the dielectric properties of the heat-absorbing agents (UO_2 и U_3O_8). It was found that the dielectric properties of the uranium oxides varied within large limits.

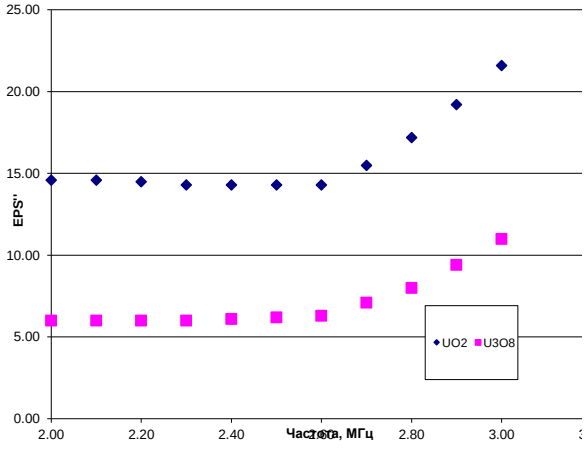


Fig.3 Dielectric permeability and frequency dependence

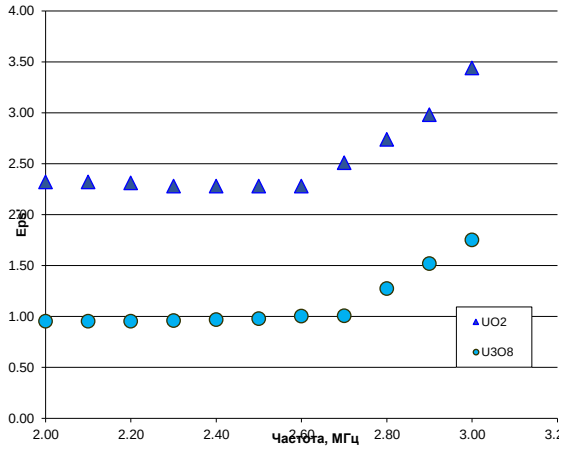


Fig.4 Loss factors and frequency dependence

The heat-exchange efficiency between a heat absorbing agent and a solid can be evaluated as follows. The electrophysical properties of the solid UF_6 - heat absorbing agent mixtures determine the penetration depth of the microwave field and the heat release. The technological process of UF_6 evaporation from containers includes loading a heat-absorbing agent into a container and irradiation with microwave energy. Heat release occurs in the heat-absorbing agents which are distributed in a certain surface layer of the solid uranium hexafluoride.

A heat-balance equation is used to determine the total microwave energy for uranium hexafluoride sublimation:

$$wVdt = L_{UF_6} Gdt + c_p \rho_{uh} V_{uh} \Delta T dt + c_{p\,haa} \rho_{haa} V_{haa} \Delta T dt \qquad (9)$$

here: w is the absorbed microwave energy, wt/cm^3; ρ, density of the heat-absorbing agent, g/cm^3; c_{haa}, the specific heat capacity of the heat-absorbing agent, J/g · ºC; L_{uh}, the specific sublimation heat of uranium hexafluoride, J/g; c_p, the specific heat capacity of gaseous uranium hexafluoride, J/g · ºC; V, the volume in which the microwave energy is absorbed, cm^3; V_{uh}. the amount of evaporated uranium hexafluoride, cm^3; and V_{haa}, the amount of heat-absorbing agent loaded on solid uranium hexafluoride, cm^3.

The absorbed microwave energy per unit volume is written:

$$w = 0.5\varepsilon_0 \varepsilon'' \omega E^2 \qquad (10)$$

Total absorbed energy:

$$W_{micr} = wV \qquad (11)$$

The absorbing volume V is equal to the product of solid uranium hexafluoride surface area S in the container and the penetration depth h of the microwave field into the uranium hexafluoride and the heat-absorbing agent mixture:

$$W_{micr} = wSh \qquad (12)$$

The quantity S is determined by the cross-section surface of the container where the uranium hexafluoride stored and the penetration depth, by the electrophysical properties of uranium hexafluoride and the heat-absorbing agent mixture. A series of formulas may be applied to compute the dielectric characteristics of the two-component mixture. The following dependence is applied for determination of the penetration depth of microwave energy into the mixture of uranium hexafluoride and heat-absorbing agent

$$h = \frac{\lambda_0}{\pi\sqrt{\varepsilon'}\,\frac{\varepsilon''}{\varepsilon'}} = \frac{\lambda_0\sqrt{\varepsilon'}}{\pi\varepsilon''} \tag{13}$$

where ε' and ε'' are given values for the mixture; wavelength λ_0, in free space.
The experimental dependence of the penetration depth of microwave energy into a mixture of uranium hexafluoride and uranium dioxide pellets and the volume fraction of pellets is shown in Fig.5.

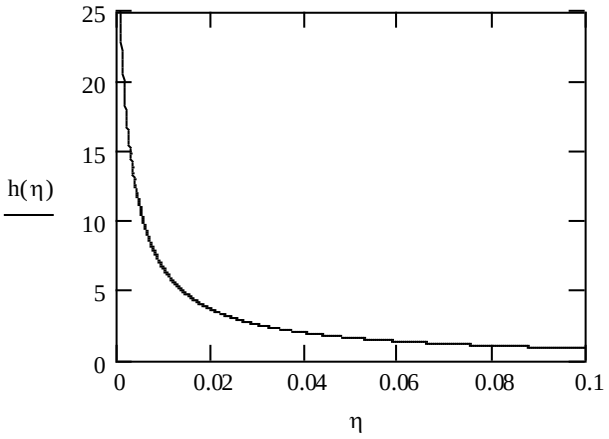


Fig.5 Dependence of penetration depth of microwave into mixture and volume fraction of pellets

An experimental test of the environmentally safe technology was conducted as follows. Depleted uranium hexafluoride (8-9 kg) was charged into an evaporative container. Then a heat-absorbing agent (about 600 g) was located on the surface of the solid uranium hexafluoride. The experimental study was conducted under various conditions of microwave energy supply. After the experiments, the containers were weighed to determine the average rate of evaporation.

During process the following parameters were controlled:

- Temperature before the metal-ceramic filter
- Temperature of the evaporation container bottom
- Temperature in the gas outlet from the container
- Temperature over the heat-absorbing agent
- Pressure before the flow-rate disk
- Pressure before the metal-ceramic filter
- Pressure behind the flow-rate disk

The controlled parameters to decrease the supplied energy or to switch-off the generator were:

- temperature of the heat-absorbing agent above 100^0C;
- equilibrium pressure of UF_6 in the container greater than the vapor pressure at given temperature;
- pressure increase in the receiving container breaking the critical gas flow-rate through the disk;
- alert conditions: vacuum violation, microwave escape, etc.

Below is a diagram of the demonstration installation for testing the microwave heating technology for DUF_6 evacuation from the container

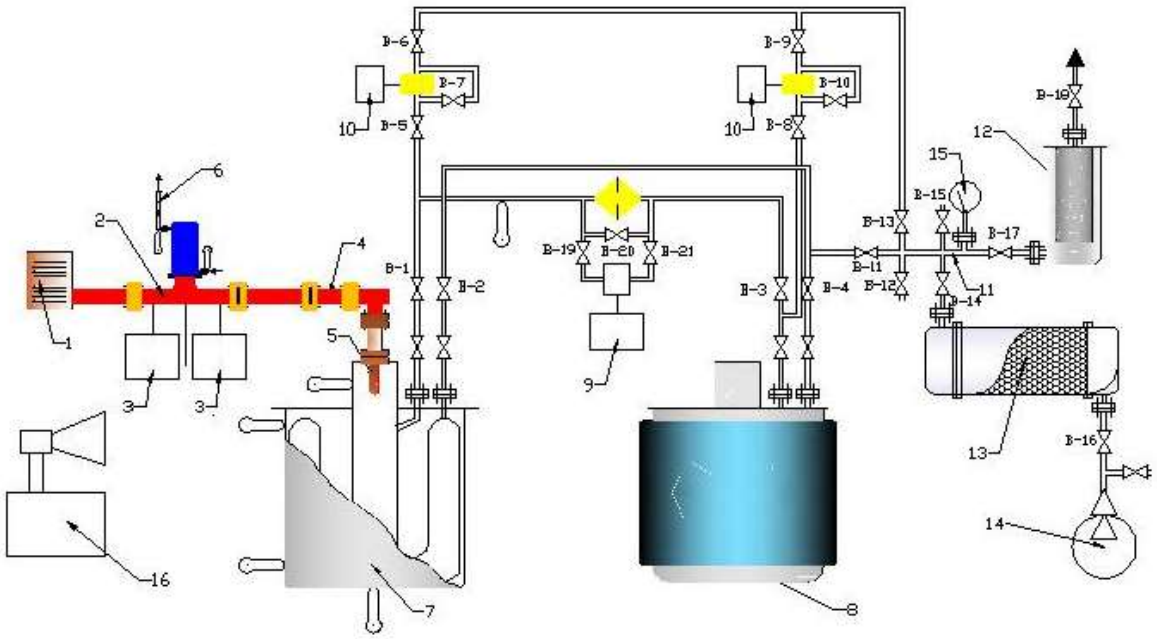


Fig.6 Diagram of the demonstration installation 1. Microwave generator; 2. Ferrite circulator; 3. Wattmeters of absorbed power; 4. Coaxial waveguide junction; 5. Antenna; 6. Rotameter; 7. Evaporation container; 8. Receiving container; 9. Flowmeter UF_6; 10. Differential pressure gages; 11. Vacuum rake; 12. Metal-ceramic filter; 13. Absorption column; 14. Vacuum pump; 15. Vacuum meter; 16. Device for microwave radiation measurement

Figures 7 and 8 show results of experiments where the microwave energy was supplied in continuous mode. Figure 7 shows the dependence of the pressure in the evaporation container during depleted uranium hexafluoride sublimation. This value is proportional to the sublimation rate. Figure 8 shows diagrams of temperatures at control points.

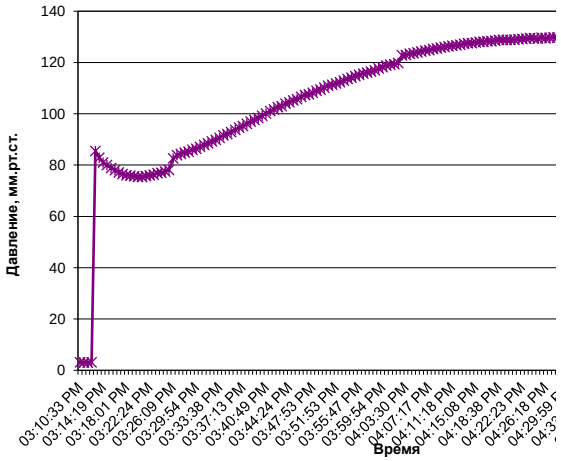


Fig.7 Dependence of pressure in container during depleted uranium hexafluoride sublimation vs. duration

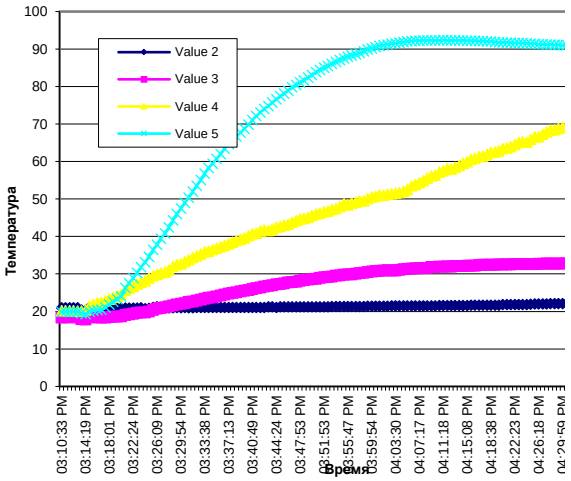


Fig.8 Temperature dependence at monitoring points: 2 – temperature before metal-ceramic filter, 3 - temperature of evaporation container bottom, 4 - temperature in gas outlet from container, 5 - temperature over heat-absorbing agent

The conducted experiments found:

- the feasibility of evaporating uranium hexafluoride from containers using microwave energy;
- a microwave method for depleted uranium hexafluoride sublimation that is a safe technique maintaining «cold" walls and a given pressure in the container and flow rate of gas;
- a proposed technique that allows damage by deterioration of the hermetic container due to the local overheating to be avoided;
- an easily controlled process;
- a technique that is applicable to any kind of container;
- the ability to control temperatures and conditions of container walls;
- a method recommended for pilot and industrial tests. It is easy to realize and there is a technical basis for its application.

When heating materials are liquids, for example, low- and medium-temperature heating of oil fractions and similar flows by microwave energy at technological installations of oil refining, oil and coke chemistry and other industries, it is advisable to use ferrites (thermal conductivity, 3.5 wt/m·K; specific heat, 0.7 kj/kg·K; density, 3-5 kg/m^3; specific resistance, 10^7 ohm·cm) as heat-absorbing agents. The process of microwave heating of ferrites is similar to the above. Currently, the aforementioned liquid flows are heated by fire tube heat exchangers. Combustion products in such heat exchangers are released into the atmosphere and pollute the environment. A low efficiency conductive heat-exchange process is carried out through the outside surface of pipe-heated furnace gases. Microwave heating avoids this problem because heat is released in the bulk of material and sharply increases heat exchange. The heat exchange of a mix of liquid and ferrites can be considered heat exchange in a fluidized bed.

Funding: This research was funded by "International Science and Technology Center"**,** grant number №2285, https://www.istc.int

Acknowledgments: Leading engineers A. N. Evdokimov and V. I. Dushechkin. have made a great contribution to the implementation of the project (experimental studies, design, manufacture, and commissioning of installations). We thank Dr. Dennis W. Wester, Pacific Northwest National Laboratory, for collaboration on ISTC project #2285.

References

1. ISTC Project #2285, Final Technical Report , 2005, 30p.
2. Gotovchikov V.T, Forsberg C.W. Saranchin V.K**.** Use of an induction cold crucible melter to manufacture depleted uranium dioxide (DUO_2) particles for use in spent nuclear fuel casks, The 10th International Conference on Environmental Remediation and Radioactive Waste management, ICEM'05September 4 – 8, 2005, Glasgow, Scotland
3. Gotovchikov V.T, Forsberg C.W. Saranchin V.K Melted and Granulated Depleted Uranium Dioxide for Use in Containers for Spent Nuclear Fuel, 2006 International High-Level Radioactive Waste Management Conference, Las Vegas, Nevada
4. H. Püschner. Heating with microwaves, Fundamentals, components and circuit technique, 1966, 311p

Theme 9: Nanotechnology Application in Chemical Engineering

An Iron Rotating Disk for the Elimination of Hexavalent Chromium Ion from Industrial Wastewaters; Putting it to Work

Mohammed S. El-Ali Al-Waqfi [1], Zakaria Al-Qodah [2]

[1] Technical Monitoring & Auditing Manager, Ministry of Water & Irrigation, Amman-Jordan

[2] Chem. Eng. Depart., Faculty of Eng. Technol., Al-Balqa Applied University, P.O. Box 15008, Marka, Amman 11134, Jordan

*****Corresponding author: m.alwaqfi@hotmail.ca; Tel.: 962 772 833587.*

Abstract: This paper aims at predicting the optimum operational limits for the utilization of an iron rotating disk for the reduction of Cr(VI) ions to settleable trivalent chromium. The kinetics of the reduction of hexavalent chromium using an iron rotating disk were, therefore, investigated under different experimental conditions, including contact time, rotation rate, ion initial concentration and disk surface area. All experiments were conducted at room temperature and initial pH of 1.5. It was found that the reduction of Cr(VI) to Cr(III) can be well-modeled by first order reaction kinetics with deviation tendency at low rotation speeds. The first order kinetics were also well-fitted at varying initial concentrations of Cr(VI). Plotting the reaction rate constant versus the square root of the rotation speed has revealed almost a constant positive slope (i.e., mass transfer controlled) which starts to decrease at higher angular velocities until it almost becomes independent of the rotation speed (i.e., reaction kinetics controlled) as the flow transits to a turbulent state. Accordingly, the achievement of high removal efficiencies in a reasonable contact time requires operating the rotating disk under optimal conditions of Cr(VI) initial concentration, rotation speed and disk area that assure diffusion controlled reduction reaction.

Keywords: industrial wastewater ; hexavalent chromium ; iron rotating disk ; reduction.

1. Introduction

Hexavalent chromium-containing compounds can be toxic to humans and animals as well as to the biological life. Cr(VI) can enter human body by inhalation, ingestion or absorption through the skin. It is usually present as a dissolved ion in aqueous solutions and can therefore be easily mobilized through marine and land environments. On the other hand, Cr(III) is comparatively less soluble and can simply be precipitated as hydroxide [Richard and Bourg, 1991].

Cr(VI) is commonly found in wastewaters originated from a wide range of industries such as, metal finishing, tannery, corrosion inhibitors, stainless steel, inks, dyes, etc. Aiming at protecting drinking water resources as well as water bodies from pollution with Cr(VI), the related standards and norms, worldwide, are becoming more stringent; setting the maximum permissible concentrations of total chromium (mainly Cr(VI) plus Cr(III)) at 0.05 ppm for drinking water, 0.10 ppm for treated effluents released to water bodies and environment, and 3 ppm for wastewater discharged to sewer systems.

The elimination of Cr(VI) from industrial effluents is usually achieved via its reduction to Cr(III) by using meta bisulfites and ferrous ions followed by precipitation of chromium hydroxide. In case of concentrated Cr(VI) wastewaters, recovery of hexavalent chromium through evaporation has proved technically and economically to be a feasible removal practice [Beukes et al., 1999; Sedlak

D. L. and Chan P. G., 1997; Patterson J.W., 1985]. Other treatment technologies include ion exchange, adsorption and electro dialysis [Huang and Bowers, 1979; Patterson J.W., 1985].

In recent years, there has been a growing interest in the reduction of hexavalent chromium encountered in wastewaters by iron metal (i.e., zero valent). Cr(VI) ions can be reduced to the trivalent chromium, mainly, by reacting with iron metal as well as its aqueous ferrous ions (Eary and Ray, 1988; Buerge and Hug, 1997a; Shamra et al., 2008; Abdo and Sedahmed, 1998; Demirbas et al., 2004; El-Shazly et al., 2005; Junyapoon and Weerapong, 2006; Ahmed et al., 2015). Several forms of the iron metal have been employed as reductants such as metal wool, chips, shots, etc., which can be contained in packed columns, rotating chambers or tumble barrels.

The current article aims at the identification of the optimum process conditions controlling and determining the removal efficiency of hexavalent chromium by using a rotating iron disk through examining the reduction kinetics. The use of rotating disk commonly enhances multi-phase contact by virtue of the generated streamlines, which may increase mass transfer of the reacting species (Levich, 1962; Al Taweel et al., 2003). The use of an iron rotating disk also hinders covering the metal surface with reaction products and settleable materials while other forms of iron are more susceptible to become shielded with such products, thus, adversely affecting the reduction rate. Several workers have reported the formation of magnetite (Fe_3O_4), green rust ($Fe_4Fe_2(OH)_{12}SO_4.H_2O$), goethite (FeOOH) and ferric hydroxide (Fe(OH)3) on the metal surface [Mackenzie et al., 1999; Scherer et al., 1998; Pratt et al., 1997; Lee et al., 2003; Ponder et al., 2000; Kendelewicz et al., 2000; Gilmore et al., 1998; Buerge and Hug, 1999 b]. In addition, the use of a rotating disk offers an easily controllable and accessible surface area; an important parameter for scale up and design purposes.

In a previous study, Al-Waqfi1 and Telfah (2018) investigated the reduction of Cr(VI) to Cr(III) in an acidic aqueous medium using a batch treatment process that utilizes an iron rotating disc as the reducucing metal. The studied the removal of the Cr(VI) under various operating coditions including rotation rate, residence time, ion initial concentration and the initial pH. They reported that Cr(VI) was completely removed in a retention time of 15 min,pH of 1.5 and initial concentration of 100 ppm. In addition, they found that Cr(VI) removal become independent of the rotation speeds above 600 rpm and retention time of 15 min. Accordingly, this study, the kinetics of Cr(VI) removal in iron the rotating disc process will be investigated at different operating conditions.

2. Materials and Method

A dichromate solution was taken from a dichromate dip tank and used as a stock solution from which several samples of hexavalent chromium solution were prepared. The experimental set up used for the removal of Cr^{6+},is shown in Fig. 1.

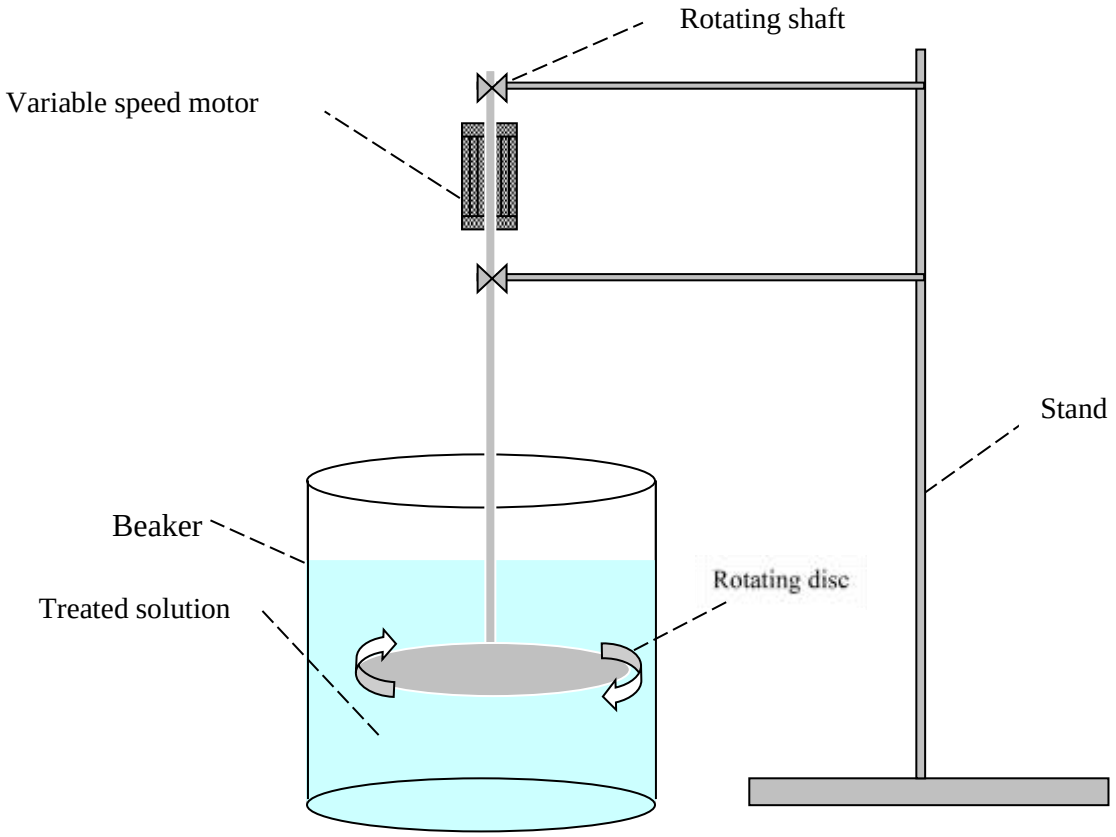


Figure 1. Schematic diagram of the experimental setup

As shown in Fig. 1, the apparatus consists of a rotating disk, its rotation rate is controlled via a variable speed motor, immersed in a 2000 ml beaker containing Cr^{6+} solution. The rotating shaft is made of stainless steel to prevent its interference in the reduction process. Several batch experiments on the sample solution were conducted at varying conditions (rotation speed, initial concentration and disk radius) at solution starting pH 1.5 and room temperature. The initial pH of the samples was adjusted by using either 1 N NaOH or 1 N H_2SO_4. The treated samples were then filtered through a 0.45 µm membrane filter and their pH was modified to 8.5; the optimum value for maximum trivalent chromium precipitation as hydroxide, which could then be easily filtered. The filtrate was then examined to determine the concentration of the residual Cr(VI), in accordance with the Standard Methods for the Examination of Water and Wastewater, 22nd edition, using a HACH Direct Reading Spectrophotometer (model DR2000). All reagents used in the research were of AR grade (HACH, USA). A microprocessor pH meter (model pH3000.WTW) was used for pH measurement.

3. Results and Discussion

In the current research, Cr^{6+} is reduced to Cr^{3+} through the oxidation-reduction reaction between the dichromate ion and the iron metal as illustrated by Equation (1)

$$Cr_2O_7^{2-} + 3Fe + 14H^+ \rightarrow 2Cr^{3+} + 3Fe^{2+} + 7H_2O \quad (1)$$

Then, the produced ferrous ions react with the dichromate ions as per Equation (2)

$$Cr_2O_7^{2-} + 6Fe^{2+} + 14H^+ \rightarrow 2Cr^{3+} + 6Fe^{3+} + 7H_2O \quad (2)$$

Since the reduction process is heterogeneous (i.e., solid-aqueous phases) in nature, the first reaction takes place at the surface of the rotating disk, which necessitates the diffusion of dichromate ions from the bulk of solution to the surface by virtue of the streamlines created by the disk movement while the produced ferrous and Cr^{3+} ions are diffused away to solution bulk where the dichromate ions are further reduced by ferrous ions according to Equation (2).

Since the concentrations of the reactants Fe^0, Fe^{2+} and hydrogen ion are essentially constant compared to the dichromate concentration. The reduction rate

of Cr(VI) can, therefore, be expressed as follows:

$$\frac{d(Cr(VI))}{dt} = -K\left[Cr^{6+}\right] \tag{3}$$

Where K is the rate constant

$$\text{Or} \qquad \frac{dC}{dt} = -K\,C \tag{4}$$

where C is the concentration of Cr(VI) at time t and C_0 is the initial Cr(VI) concentration. Integrating above equation gives

$$-\ln\frac{C}{C_0} = Kt \tag{5}$$

With C_0 is the initial Cr(VI) concentration.

Eq. 5 is then plotted at different rotation rates and 100 ppm as an initial concentration of Cr(VI) in order to test for first order kinetics as shown in Fig. 5:.

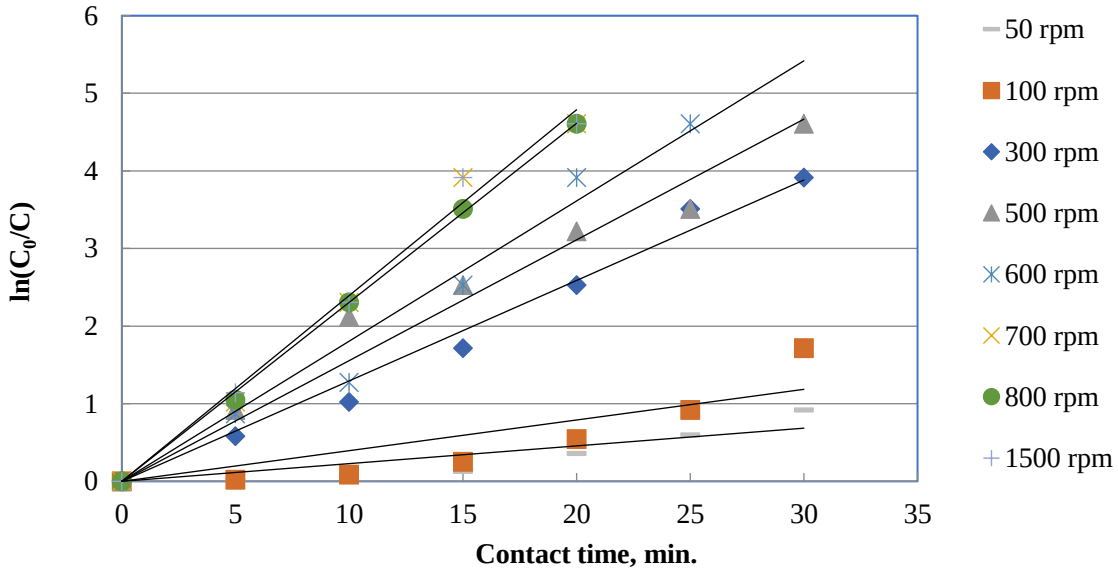


Figure 2. Reduction kinetics (C_0 = 100 ppm, pH 1.5, Radius 4.75 cm)

As can be seen from Fig.2, $\ln(C_0/C)$ linearly varies with time at all investigated rotation rates, hence, indicating that the reduction of Cr(VI) to Cr(III) can be well-modeled by first order reaction kinetics except with noticeable nonconformities at low speeds (e.g., 50 and 100 rpm). This result is consistent with the findings of Junyapoon and Weerapong (2006) and El-Shazly et al. (2005).

The results of data fitting to first order kinetics at the studied rotation rates are displayed in Table 1. The observed deviations from first order kinetics (linearity) at low rotation rates may be attributed

to changes in iron surface reactivity due to the increased tendency of passivation as well as the formation of precipitates on metal's surface, which unfavorably affects the reduction rate. Several workers have identified the secondary products magnetite (Fe_3O4), green rust ($Fe_4Fe_2(OH)_{12}SO_4.H_2O$), goethite (FeOOH) and ferric hydroxide ($Fe(OH)_3$) on the surface of other forms of iron metal used for the reduction of Cr(VI) [Mackenzie et al., 1999; Scherer et al., 1998; Pratt et al., 1997; Lee et al., 2003; Ponder et al., 2000; Kendelewicz et al., 2000; Gilmore et al., 1998; Buerge and Hug, 1999].

Table 1. First order kinetics fitting results

Rotation rate, rpm	***Re***	**R^2**	***K*, s^{-1}**
50	13,203	0.7894	0.023
100	26,432	0.7497	0.04
300	79,320	0.9842	0.129
500	132,183	0.9750	0.156
600	158,537	0.9744	0.181
700	185,115	0.98882	0.239
800	211,560	0.9990	0.231
1500	396,676	0.9898	0.239

According to Levich (1962) a disk rotating, with Reynolds numbers less than 100,000, creates laminar flow conditions, under which the solute diffusional rate constant from the solution bulk to the metal's surface can be correlated by the following equation

$$k = 0.62 D^{2/3} \nu^{-1/6} \omega^{1/2} \qquad (6)$$

D: Diffusion coefficient of solute, v: kinematic viscosity of fluid, ω: angular velocity.

Assuming that the angular velocity is the only variable, the controlling mechanism of Cr(VI) reduction can, therefore, be examined by plotting the reaction rate constant versus the square root of the rotation speed. As shown in Fig.(3) under laminar flow conditions at lower rotation speeds, almost a constant positive slope is observed (part A) that starts to decrease as the angular velocity increases until it becomes almost independent of the rotation speed (part B) as the flow transits to a turbulent state. Part A may, therefore, indicate that the reduction of Cr(VI) is diffusion (i.e., mass transfer) controlled while in part B at higher velocities the reaction kinetics turn out to be the rate determining step. Similar results were revealed by Gould (1982) who reported that the rate constant was augmented as the mixing rate increased reaching a maximum value after which it became independent of mixing.

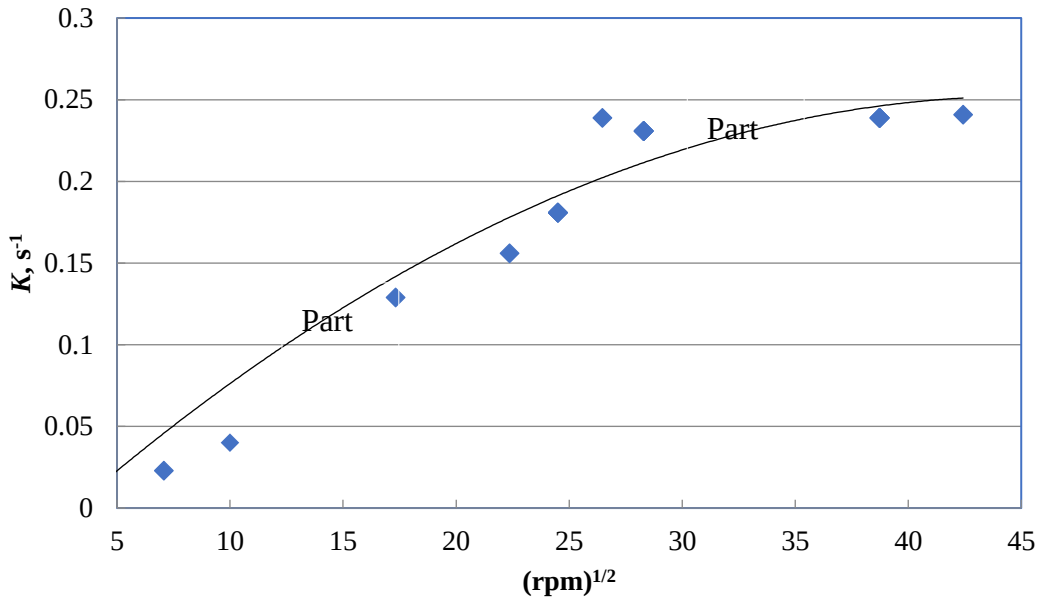


Figure 3. Variation of reaction rate constant with rotation speed

As shown in Fig.4., the achieved treatment efficiencies suggest that the required time for complete reduction of Cr(VI) becomes independent of rotation speeds of 500 rpm and above. As observed earlier, as the rotation speed increases the relative mass transfer controlling effects are expected to diminish in favor of the reaction kinetics, which tend to become the dominant rate-determining step.

To investigate the effect of initial Cr(VI) concentration on the removal of hexavalent chromium, Equation 5 is plotted at different initial Cr(VI) concentrations as illustrated in Fig.5. As can be seen, $\ln(C_0/C)$ linearly varies with contact time at all investigated concentrations, hence, indicating that the reduction of Cr(VI) to Cr(III) fits well first order reaction kinetics with relatively poor fit at low initial concentrations.

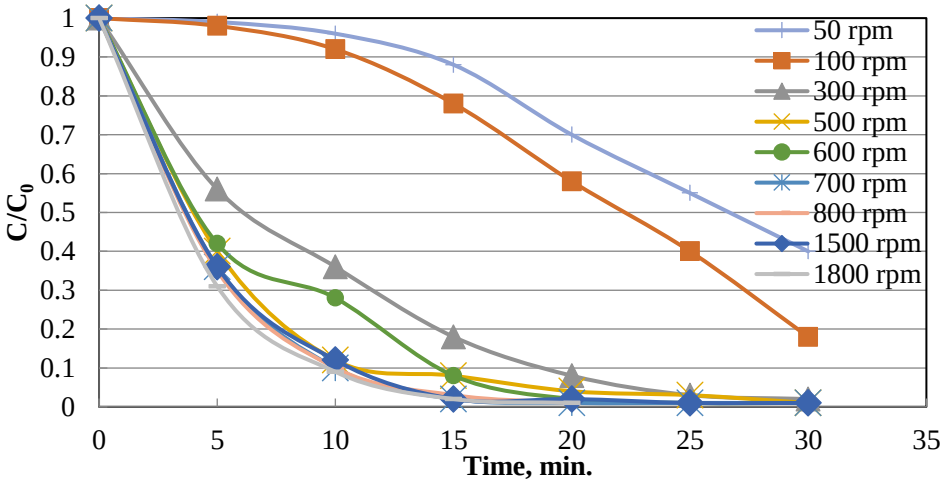


Figure 4. Effect of Elapsed Time on the Removal C_0 =100 ppm, pH 1.5, Radius 4.75 cm.

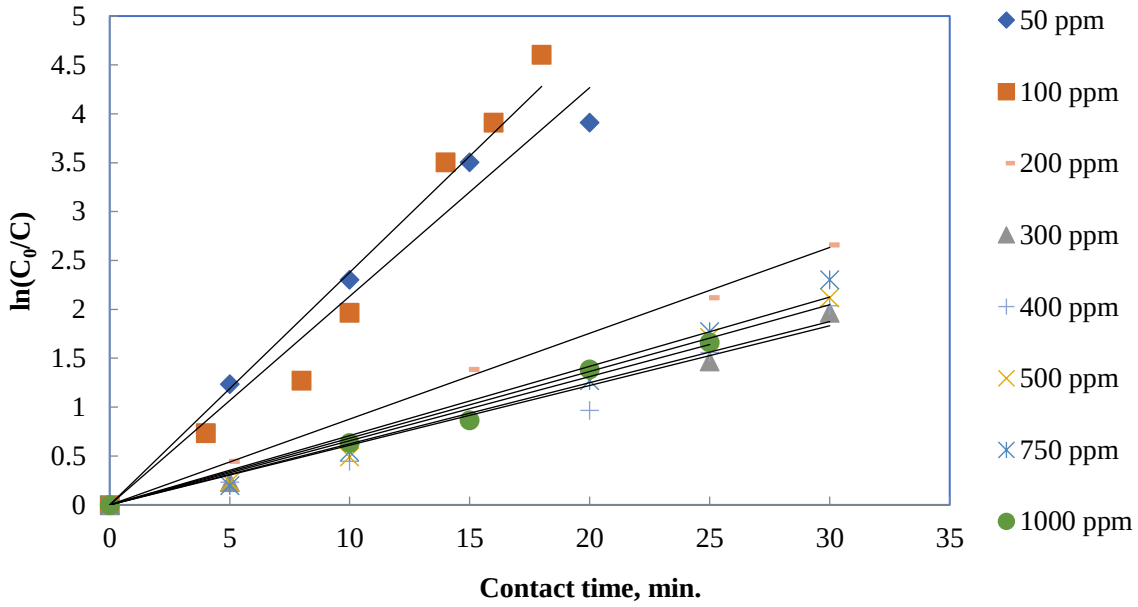


Figure 5. Reduction kinetics (pH 1.5, 600 rpm, Radius 4.75 cm)

Moreover, Fig.6 reveals that the rate constant is dependent on initial concentration at low values; it dramatically decreases with increasing concentration until 300 ppm, after which it becomes almost constant.

It can therefore be concluded that at low concentrations the reduction of Cr(VI) is diffusion controlled while it becomes dominated by reaction kinetics as concentration increases. Therefore, as exhibited in Fig.(7), the required reaction time for the complete elimination of hexavalent chromium at first gradually increases with increasing initial Cr(VI) concentration up to 300 ppm, above which it drastically rises with no significant removals achieved. At low concentrations, less Cr(VI) is available compared to the number of reactive iron sites; a situation encourages maintaining iron reactivity and hence leading to more removal of Cr(VI).

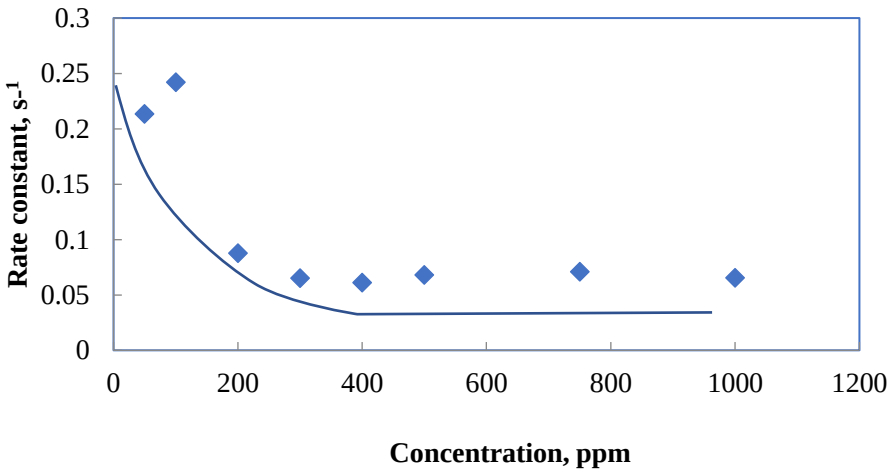


Figure 6.Variation of rate constant with Cr(VI) initial concentration (pH 1.5, 600 rpm, radius 4.75 cm)

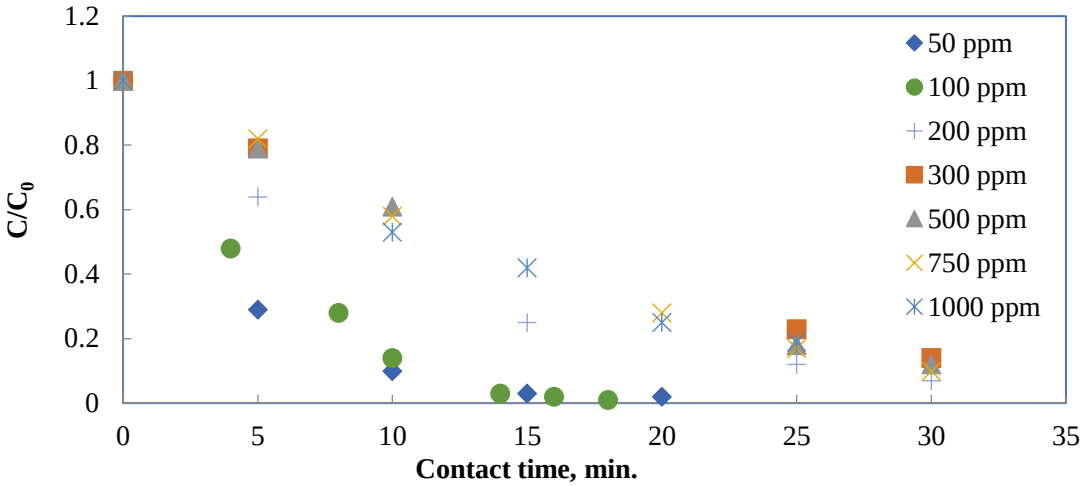


Figure 7. Reduction of Cr(VI) by iron metal at different initial concentration (pH 1.5, 600 rpm, radius 4.75 cm).

The above conclusion is further verified by investigating Cr(VI) reduction using rotating disks of different radii. The results of the conducted experiments are displayed in Fig.(8). It is clear that the required time for the complete removal of Cr(VI) is strongly dependent on the disk area at low radii; the time required for complete reduction decreases as the radius of the rotating disk increases. At higher radii more reactive sites will be available for maintaining the reaction and thus resulting in removal enhancements. Similar results were observed by Huang et al. (2008) who studied the reduction of Cr(VI) using Micro and Nano scales of zero valent iron . However, at certain initial concentration, further enlargement of the disk area may not result in a significant reduction in the time required for complete removal as some of the available reactive sites will be redundant as their number may far exceed the need by the reaction.

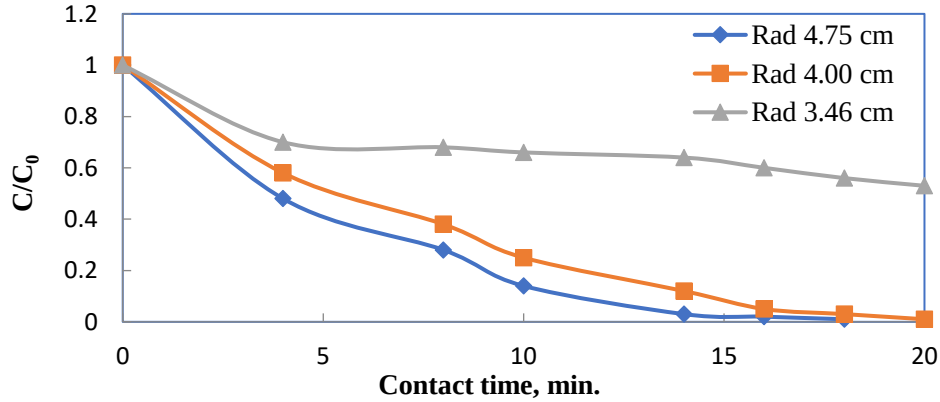


Figure 8. Reduction of Cr(VI) by iron rotating disk of different surface areas (C_0=100 ppm, pH 1.5, 600 rpm.

4. Conclusions

- An iron rotating disk may offer a practical and viable replacement to other forms of iron metal (e.g., wool, chips, shots, etc., packed in columns or contained in tumble barrels) used for the reduction of Cr(VI) ions encountered in industrial wastewaters especially for small industrial firms.
- The achievement of high removal efficiencies of Cr(VI) requires operating the rotating disk under circumstances that assure a diffusion controlled reduction reaction. Such conditions include,

- At a given concentration, to maximize removal efficiency while keeping minimal operating costs, it is advised to operate the rotating disk within the transitional flow regime at about 600 rpm of Re nos. 130,000 to 150,000, under which the reaction is, essentially, diffusion controlled with a relatively high rate constant. Increasing the rotation rate necessarily means additional energy consumption with no significant enhancement to the reduction efficiency of Cr(VI) (i.e., the reaction becomes kinetics controlled).
- At the optimum rotation speed (i.e., 600 rpm), complete removals of Cr(VI) can be achieved for concentrations less than 300 ppm. As Cr(VI) initial concentration increases, the reaction kinetics become more controlling; a situation should be avoided from an operational point of view.
- Large disk area doesn't necessarily mean shorter time for complete Cr(VI) removal. At a given concentration, there should be a tradeoff between the disk surface area and the time required to achieve complete reduction of Cr(VI).

- The above stated conclusions may constitute the parameters of prime importance for scale up and design purposes of a feasible treatment unit.

References

1. Abdo M. S. and Sedahmed G. H., (1998). "A New Technique for Removing Hexavalent Chromium from Wastewater and Energy Generation via Galvanic Reduction with Scrap Iron, Energy Convers. Mgmt., 39: 943-951.
2. Ahmed, A. M., El Batouti, M., Darweesh A. M., and Said, S. M., (2015). "The Reduction of Hexavalent Chromium by Ferrous Ions to Trivalent Chromium in Presence of Organic Acid Additives", Asian Journal of Chemistry. 27 (11), 3998-4006.
3. Alowitz M. J. and Scherer M. M., (2002). "Kinetics of Nitrate, Nitrite, and Cr(VI) Reduction by Iron Metal", Environ. Sci. and Technol., 36, 299–306.
4. Al Taweel, A.M., El-Ali, M., Azizi F., Liekens B., Odedra, D., Uppal, A., and Gomaa, H.G.. (2003) "In-Line Processing for Intensifying Multi-Phase Contacting Operations" proceedings of the 5th Inter. Conf. Process Intensification, Oct., pp. 59-73, Maastricht, The Netherlands.
5. Beukes, J. P., Pienaar J. J., Lachman N. G., and Giesekke E. W., 1999. The Reduction of Hexavalent Chromium by Sulphite in wastewater, Water SA 25: 363-370.
6. Buerge I. J. and Hug S. J., (1997). "Kinetics and pH Dependence of Chromium(VI) Reduction by Iron(II)", Environ. Sci. Technol., 31, 1426-1432.
7. Buerge I. J. and Hug S. J., (1999). "Influence of Mineral Surfaces on Chromium Reduction by Iron(II)", Environ. Sci. Technol., 33(23), 4285-4291.
8. Demirbas E., Kobya M., Senturk E. and Ozkan T., (2004). "Adsorption Kinetics for the Removal of Chromium(VI) from Aqueous Solutions on the Activated Carbons Prepared from Agricultural Wastes", Water SA 30 (4), 533-539.
9. Eary L. E. and Rai D., (1988). "Kinetics of Chromium(III) Oxidation to Chromium(VI) by Reaction with Manganese dioxide", Environ. Sci. Technol., 21, 1187-1193.
10. El-Shazly A. H., Mubarak A. A., and Konsowa A. H., (2005). "Hexavalent Chromium Reduction Using a Fixed Bed of Scrap Bearing Iron Spheres", Desalination, 185, 307-316.

11. Gilmore T. J., Holdren G. R., and Kaplan D. I., (1998). "Groundwater Well with Reactive Filter Pack", U.S. Patent 5,803,174, U.S. Patent Office, Washington, D.C.
12. Gould J. P., (1982). "The Kinetics of Hexavalent Chromium Reduction by Metallic Iron", Water Res., 16, 871-877.
13. Huang, C. P. and Bowers, A. R. (1979). "The Development of an Activated Carbon Process for the Treatment of Chromium VI-Containing Plating Wastwater", In. 2nd Conf. on Advanced Pollution Control for the Metal Finishing Industry, EPA-6018-79-014, Cincinati, OH, pp. 114-122.
14. Huang Y., Chen T., Huang J. and Chen Y., (2008). "Effects of Size and Surface Area of Iron on Reduction of Hexavalent Chromium", Journal of University of Science and Technology, Beijing, 30, 53-57.
15. Junyapoon S. and Weerapong S., (2006). "Removal of Hexavalent Chromium from Aqueous Solutions by Scrap Fillings", KMITL Sci. Tech. J., 6 (1), 1-12.
16. Kendelewicz T., Liu P., Doyle C. S. and Brown G. E., (2000). "Spectroscopic Study of the Reaction of Aqueous Cr(VI) with Fe_3O_4(III) Surfaces", Surface Sci., 469, 144-163.
17. Lee T., Lim H., Lee Y. and Park J. W., (2003). "Use of Waste Iron Metal for Removal of Cr (VI) from Water", Chemosphere, 53, 479-485.
18. Levich V. G., (1962). Physiochemical Hydrodynamics, 2nd Ed., Prentice Hall, New Jersey, U.S.A.
19. Mackenzie P. D., Horney D. P. and Sivavec T. M., (1999). "Mineral Precipitation and Porosity Losses in Granular Iron Columns", J. Hazard. Mater., 68, 1-17.
20. Patterson J.W., (1985). Industrial Wastewater Treatment Technology, 2nd Edition, Butterworth, Boston, USA.
21. Ponder S. M., Darab J. G. and Mallouk T. E., (2000). "Remediation of Cr(VI) and Pb(II) Aqueous Solutions Using Supported Nanoscale Iron", Environ. Sci. Technol., 34(12), 2564-2569.
22. Pratt A. R., Blowes D. W. and Ptacek C. J., (1997). "Products of Chromate Reduction on Proposed Remediation Materials", Environ. Sci. Technol., 31, 2492-2498.
23. Richard F. C., and M Bourg A. C., (1991). "Aqueous Geochemistry: A Review", Water Res., 25(7), 807-816.
24. Scherer M. M., Balko B. A. and Tratnyek P. G., (1998). "The Role of Oxides in Reduction Reactions at the Metal-Water Interface, Mineral water interfacial reactions: kinetics and mechanisms", ACS Symposium Series 715, Sparks D. and Grundl T. (Eds.), American Chemical Society, Washington, D.C., pp. 301-322.
25. Sedlak D. L. and Chan P. G., (1997). "Reduction of Hexavalent Chromium by Ferrous Iron", Geochim, Cosmochim., Acta 61, 2185-2192.
26. Shamra Y. C., Singh B., Agrawal A. and Weng C. H., (2008). "Chromium Removal of Chromium by Riverbed Sand from Water and Wastewater: Effect of Important Parameters", J. Hazard. Mater., 151, 789-793.

Carbon nano-dots from natural resources as optical sensors for iron ions/Fe^{3+}: a review

Aseel Yaseen, Marah Daraghmah *, Tamara Hanani and Shadi Sawalha

Chemical Engineering Department, Faculty of Engineering, An-Najah National University, Nablus, Palestine.

**Corresponding author: marahdaraghmah@gmail.com , tel: +970595857633*

Abstract: Carbon nanodots (CDs) are a new category of carbon nanomaterials with sizes under 10 nm, displaying a range of fascinating properties. Broadly speaking, they can be described as small, surface functionalized carbonaceous nanoparticles characterized by an intense and tunable fluorescence, a marked sensitivity to the environment and a range of interesting photochemical properties. CDs are currently the subject of very intense research, motivated by their possible applications in many fields, including bio-imaging, nano-sensing and photo-catalysis. Also, CDs have really been synthesized from a large variety of precursors, natural resources and some waste materials. There are many methods for the synthesis of CDs for example Arc Discharge, Laser ablation, Chemical Oxidation and Hydrothermal Synthesis. Hydrothermal Synthesis method was the most commonly used in the synthesis of CDs. Since the setup is simple and with high Quantum Yield, the result particle is almost uniform in size. In this work, we searched for the different natural resources of CDs and identify their synthesis methods, properties and some of their applications, 69 natural sources of CDs were found. We found nearly 21 natural resources of CDs for sensing iron ions Fe^{3+}, that has a great importance in monitoring iron levels in the water, whose excess may cause many diseases.

Keywords: carbon nanodots; fluorescence ; synthesis methods; hydrothermal ; natural resources ; bio-imaging ; sensing.

1. Introduction

Issues regarding global energy and environment have driven the development of new materials and techniques in order to minimize financial and environmental costs [1]. The speedy development of nanomaterials has now not solely resulted in numerous benefits to many science and engineering fields, however has moreover brought some new issues. Among these troubles is that the synthesis of nanomaterials commonly requires high energy consumption and use of toxic chemical reagents, which no longer solely increases production prices, however is the opposite of the core standards of sustainable development. Therefore, it is critical to make use of environmental-friendly and renewable raw resources to handle the challenges confronted via the use of the sustainable manufacturing of nanomaterials without the use of poisonous chemicals [2][3]. Carbon nanodots (CDs) are a new category of carbon nanomaterials with sizes under 10 nm [4] They first received throughout the purification of single walled carbon nanotubes via preparative electrophoresis in 2004 [5]. CDs have step by step grow to be a rising celebrity in the nano carbon family, due to their benign, plentiful and cheaper nature [4]. Carbon is oftentimes a black material, and until these days was generally viewed to have low solubility in water and vulnerable fluorescence [6]. The most important purpose why such tiny CDs have currently attracted vast interest is due to the fact of their strong fluorescence, for which they are referred to as fluorescent carbon [7].

Over the last decade, a broad range of techniques have been proposed for the preparation of CDs [8]. Synthesis methods for CDs are based on cutting larger carbon materials (top-down) or fusing smaller (bottom-up) precursor molecules [9].

Top-down approach refers to breaking down larger carbon structures via chemical oxidation, arc discharge, laser ablation and extraction [10]. However, drawbacks of this approach includes the requirement of expensive materials, harsh reaction conditions, and long reaction time [8]. On the other hand, the bottom-up approach refers to the conversion of smaller carbon structure (polymerization and carbonization by chemical reaction) into CDs of the desired size. This bottom-up approach is consisting of combustion routes, microwave pyrolysis, hydrothermal synthesis and electrochemical methods to synthesize CDs [11].

CDs have really been synthesized from a large variety of precursors, mostly man-made, such as graphite [12], fullerene [13], or natural resources such as orange juice [14], coffee grounds [15], egg white [16], banana [17]. In addition, some waste materials have also been well used for the synthesis of CDs for instance, paper pieces [18], which not only reduces CDs production costs but also abates environmental pollution. CDs have become a hot topic of numerous scientific studies since their discovery due to their obvious advantages over conventional semiconductor quantum dots whose notable toxicity and environmental hazards[19]. Compared to florescent organic dyes and genetically engineered fluorescent proteins, CDs excel themselves with significant advantages like high PL quantum yield, photo-stability, resistance to metabolic degradation and so on, which endows the huge potential of carbon dots based bio-applications [20]. CDs have many physical and chemical properties such as Components and structure [21] , Dispersibility [22], Cytotoxicity [23] and Optical Properties [21] for example Absorbance [24] and Fluorescence [4]. Dual functional fluorescence Nano sensors have many potential applications in biology and medicine such as Optronics [25], Bio-imaging [26], Photocatalysis [21] and Sensing [27]. Where monitoring temperature with higher precision at localized small length scales or in a Nano cavity is a necessity in various applications. As well as the detection of biologically interesting metal ions using low-cost and sensitive approach is of great importance in bio analysis [28], A wide variety of biological/chemical sensors were developed based on the fluorescence properties and surface functional groups of CDs, such as the detection of $Hg^{2+,}$ Cu^{2+}, Fe^{3+}, Ag^{1+},Cd^{2+}, etc. [29].Iron homeostasis problems are one of the utmost everyday diseases of people and cowl an expansive range of diseases with a number of signs and symptoms, starting from anemia to excesses of iron, liver and kidney diseases, diabetes Mellitus, cardiovascular sickness and very probably to neurodegenerative disorders [28].

The most frequent oxidation states of iron are Fe^{3+} and Fe^{2+} vigorously altering to one another, which makes it challenging detecting Fe^{3+} or Fe^{2+} ions only. However, considering an easy, precise, and field-appropriate detection method for total iron (Fe^{3+} and/or Fe^{2+} ions) probing is via a ways from super significance for the analysis of iron elaborating in medical diagnosis, environmental monitoring of water nice and other quality control examinations [23-25]. The most ordinary method for the detection of iron ions consists of voltammetry, electron paramagnetic resonance, spectrophotometry, atomic absorption spectrometry, inductively coupled plasma-atomic emission spectroscopy and inductively coupled plasma mass spectrometry. The cited techniques favor elaborate instrumentation, tedious sample preparation, lengthy procedures, and professional personnel that restricts their hobbies contrast and are inapplicable for most laboratories [21-26]. Among all detection methods, fluorescence spectrometry has obtained a whole lot undertaking and is a dominant optical approach for trace assessment of excellent sized biological samples due to the fact of its immoderate sensitivity, simple operation, being reproducible and speedy implementation [28].

In this work, we searched for the different natural resources of CDs and identify their synthesis methods, properties and some of their applications where the applications of CDs had been based on the principle that the interactions between analytes and CDs either limit the fluorescence by quenching. The focus in this review was on the sensing of iron ions Fe^{3+} that come from natural resources. we have identified limit of detection (LOD) for Iron and their sensing range, the applications of CDs had been based on the principle that the interactions between analytes and CDs either limit the fluorescence by quenching mechanism or increase fluorescence by suppressing the quenching effect.

2. Sensing

Two distinct techniques were produced through CD-based nanosensors: the nanosensors were essentially pure" CDs, as-synthesized or passivated by unique target groups; and (ii) the practical sensing medium was a nano-composite that was fabricated by pairing CDs with other nano- or micro-materials. Differently prepared CDs can be used, also in a biological setting, to detect different metal cations such as Hg^{2+}, Cu^{2+}, Fe^{3+} or small molecules or macromolecules in solution [27]. Usually, as CDs are immersed in a solution with a particular analyte, their luminescence is quenched (decreases), allowing high sensitivity and also high selectivity analytes to be detected, as obtained by correctly designing the functional groups of the surface, reacting only with a certain form of metal cation. The sensitivity to detection can be very high and the minimum detectable ion concentration can be as low as femtomolar [34]. The fundamental causes of quenching, however are widely studied and can include multiple fundamental interactions, such as a shift of charge from the dot to the ions, which hinders radiative recombination [35], or an energy transfer from the dots to the acceptor, quenching the CD emission and increasing the latter's emission [36][37].

Table 1 summarizes some of the natural resources of CDs with their synthesis method and application in bioimaging or sensing.

Table 1.Natural Resources of CDs and their applications.

Source	Method	Size (nm)	QY (%)	Application	Ref.
Winter melon	Hydrothermal	4.5-5.2	7.51	Bio-	[38]
Onion	Hydrothermal	9	28	Bio-	[39]
Coriander	Hydrothermal	1.5-2.98	6.48	Detecting	[40]
Pomegranate	Hydrothermal	2.5-6.5	7.6	Bio-	[41]
Bagasse	Hydrothermal	2.94	4.7	Bio-	[42]
Grass	Hydrothermal	3-5	2.5-6.2	Solar cells	[43]
Flaxseed	Hydrothermal	4-8	14.2	Biosensors	[44]
Fish scale	Hydrothermal	4-9	9	Detecting	[45]
Peach gum	Hydrothermal	2-5	28.46	Detecting	[46]
Black tea	Hydrothermal	4.6		Detecting	[47]
Prawn shell	Hydrothermal	6	54	Drug	[48]
Oatmeal	Hydrothermal	20-40	37.4	Bio-	[49]
Shiitake	Hydrothermal	2-6	5.5	Bio-	[50]
Lentil	Hydrothermal	5	10	Detecting	[51]
Egg white	Hydrothermal	2.1	64	Detecting	[16]
Sweet pepper	Hydrothermal	2-7	19.3	Detecting	[52]
Yam	Hydrothermal	2.7	9.3	Detecting	[53]
Carrot	Hydrothermal	3~8	5.16	Bio-	[54]
Cucumber	Hydrothermal	>10	3.25	Detecting	[55]
Durian	Hydrothermal	2-6	79	Bio-	[56]
Prunus avium	Hydrothermal	7	13	Bio-	[57]
Citrus pectin	Hydrothermal	2.7	1.1	Bio-	[58]
Dragon fruit	Hydrothermal	2.5		Bio-	[59]
Gelatin	Hydrothermal	1.7	31.6	Bio-	[60]
Bamboo	Hydrothermal	2-6	7.1	Detecting	[61]
Waste paper	Hydrothermal	3-7	10.8		[62]
Aloe	Hydrothermal	5	10.37	Detecting	[63]
Kitchen waste	Hydrothermal	50		Drug	[64]
Lignin	Hydrothermal	2-6	21	Bio-	[65]
Starch	Hydrothermal	2.25-3.5	21.7	Bio-	[66]
Corn flour	Hydrothermal	2-6	7.7	Bio-	[67]
coriander	Hydrothermal	2.98	6.48	Detection	[68]
Humic acid	Hydrothermal	4	5.2	Bio-	[37]
Beef meat	Hydrothermal		40	Cell	[69]
Red pepper	Hydrothermal		19.3		[69]
Rose heart	Hydrothermal		13.6	Fe^{3+}	[69]
Paper ash	Hydrothermal		6	Bio-	[69]
Coffee bean	Hydrothermal	1-5		Bio imaging	[69]
Wheat straw	Hydrothermal		9.2	Labeling	[69]
Pumpkin	Hydrothermal		9.42	PH sensing	[69]
Chitosan	Hydrothermal		13	Nitro	[70]
Egg shell	Microwave	5	14	Biosensor	[7]
Goose feathers	Microwave	21.5	17.1	Detecting	[71]
Coconut water	Microwave	1-6	54	Detecting	[72]
Lotus	Microwave	18.7	19	Hg2+	[73]

.	Rose	Microwave	4-6	13.45	Detecting	[74]
.	Silk worm	Microwave	19	46	Bio-	[70]
.	Serum	Microwave	2.4-5	14	Detecting	[75]
.	Eutrophic	Microwave	8	13	Bio-	[76]
.	Natural	Microwave	2-3		Bio-	[77]
.	Peach gum	Microwave		28.46	Au^{3+},Fe^{3+}	[78]
.	Starch	Microwave			Imagined	[69]
.	Fingernail	Microwave		42.8	Sunset	[69]
.	Flour	Microwave	1-4	5.4	Sensing	[79]
.	Crab shell	Microwave				[69]
.	Silkworm	Microwave	13-26	46	Cell	[69]
.	Feathers	Microwave		17.1		[69]
.	Lotus root	Microwave		23	Hg^{2+}	[70]
.	Activated	Chemical	4.5	12.6	Bio-	[80]
.	Candle soot	Chemical	1			[81]
.	Rice husk	Pyrolysis	3-6	15	Bio-	[82]
.	Lychee seed	Pyrolysis	1.12	10.6	Bio-	[37]
.	Lychee	Pyrolysis	1.4		Bio-	[83]
.	Eggs	Pyrolysis	2.15	5.96	Bio-	[9]
.	Urine	Pyrolysis	20.6	14	Detecting	[84]
.	Peanut shell	Pyrolysis	0.4-2.4	9.91	Bio-	[85]
.	Peanut skin	Pyrolysis	10-40	7		[86]
.	Olive solid	Pyrolysis	10	10	Detecting	[87]
.	Wool	Pyrolysis	10	22.5	Cell	[88]

We note in this table, the different natural sources of carbon nano-dots with different synthesis methods , where the hydrothermal method is the most common method, and the parameters of each differ, such as size and QY%, and their applications such as bio-imaging and detecting Fe3+.

3. Iron Sensing

Over latest decade, there has been widespread pastime for the detection of heavy and transition metallic ions using fluorescent chemo sensors due to the fact fluorometric technique is tremendously sensitive. So an Important application of surface functionalization is oriented towards sensing, detection of heavy metals or transition ions [89], amongst these metal ions is the iron, Ferric ion (Fe^{3+}) is one amongst the most essential metallic ion which is abundantly reachable in the environment. These ions play significant role in retaining many biological processes. Where Total physique iron in adult males and ladies is usually about 50 and 34–42 mg/kg of physique weight, respectively [90]. Any change in the optimum stage of ferric ions may also disturb cell method stability and can lead to numerous ailments like Alzheimer's disease, Parkinson's disease, heart failure, inflammation, hemochromatosis etc. [91][92]. Hence sensitive and selective detection of Fe^{3+} ions are of extensive value in biological purposes [93]. And it also has great importance for monitoring its levels in water basins according to the guideline limit of Fe^{3+} concentration (5.36 μM) proposed by World Health Organization (WHO), iron in water can be determined by atomic absorption spectrometry (detection limit 1 μg/L) or by colorimetric methods (detection limit 5 μg/L), these methods are costly and time consuming, therefore, developing a sensor based on CDs which are extracted from natural resources is a necessity and a point of researchers interest [90].

Several researches have reported the use of CDs as sensing probes of $Fe^{3+,}$ almost of the researchers followed the quenching phenomena of carbon dots upon addition of ferric ions as shown in **Figure 1**, and the quenching percentage could be corresponded to the concentrations of added ions. The most important of sensor performance parameters are the sensing range which defines the range in which a signal allows quantification of the concentration of an analyte (linear range), sensitivity which is the slope of linear range, and limit of detection (LOD) is defined the minimal detectable value, where low LOD usually implies a rather high sensitivity.

Table 2 summarizes some of the natural resources of CDs Detecting Fe^{3+} Sensing with their synthesis method and applications.

Table 2. Natural Resources of CDs Detecting Fe^{3+} Sensing.

	Sourc	**Method**	**Size**	**QY**	**Application**	**Sensin**	**LO**	**Ref.**
	Corian	Hydrothe	1.5-	6.4	Detecting Fe^{3+}	0-6	0.4	[40]
	Garlic	Hydrothe	10.7	17.	Bio-imaging			[96]
	Papay	Hydrothe	3.4	18.	Detecting Fe^{3+}	1-8	0.29	[97]
	Potato	Hydrothe	0.2-	6.1	Detecting Fe^{3+}			[98]
	Black	Hydrothe	4.6		Detecting Fe^{3+}	0.25-		[47]
	Egg	Hydrothe	2.1	64	Detecting Fe^{3+}	50-250	-	[16]
	Sweet	Hydrothe	2.5-	8.6	Bio-imaging	1-100	0.32	[95]
	Papay	Hydrothe	3	7	Bio-imaging			[99]
	Prunus	Hydrothe	7	13	Bio-imaging	0-100	0.96	[57]
.	Cocoo	Hydrothe	70	38	Bio imaging	0-6	0.4	[100]
.	Honey	Hydrothe	2	19.	Detecting Fe^{3+}			[101]
.	Onion	Hydrothe	9	28	Detecting Fe^{3+}	0-20	0.31	[39]
.	corian	Hydrothe	2.98	6.4	Detection Fe^{3+}	0-6	0.4	[68]
.	Jinhua	Hydrothe		50.	Detection			[102]
.	Rose	Hydrothe		13.	Fe^{3+} Detection			[69]
.	Entero	Hydrothe	2.75 _	8	Detecting Fe^{3+}	1-370	0.5	[103]
.	Goose	Microwa	21.5	17.	Detecting Fe^{3+}	2-7	196	[71]
.	Peach	Microwa		28.	Au^{3+},Fe^{3+}			[78]
.	Chick	Microwa	2.2-	6-8	Detecting Fe^{3+}			[69]
.	Konja	Pyrolysis	3.37	22	Detecting Fe^{3+}	0-5	-	[92]
.	Olive	Pyrolysis	10	10	Detecting Fe^{3+}	0-50	1	[87]

We note in this table, different natural sources of CDs detecting Fe3+ Sensing with their synthesis method, applications and parameters such as size, QY%, sensing range and LOD.

4. Conclusion

The main reason of these that these tiny CDs have attracted considerable attention at the moment is that they have a strong fluorescence renamed fluorescent carbon. Due the superior properties of CDs, they are used in many applications and field such as biomedical, optronics, Photocatalysis and sensing. Great improvement has been achieved in the synthesis, properties and applications of CDs. Several methods for preparing CDs have been published, which can be generally classified into "Top-down" and "Bottom-up" methods that can be adjusted during preparation or post-treatment. Most recent researches on CDs have focused on their fluorescence characteristics and photocatalytic properties. This review summarizes the primary synthesis method, physical and chemical properties, application and Fe3+ sensing. In this review we came up with 69 natural resources to extract CDs for different applications. 21 resources of them are for Fe3+ detection. As a result, the most commonly used in the synthesis of CDs is hydrothermal methods. The applications of CDs had been based on the principle that the interactions between analytes and CDs either limit the fluorescence by quenching, or increase fluorescence by suppressing the quenching effect

Reference

1. P. A. Julien, C. Mottillo, and T. Friščić, "Metal-organic frameworks meet scalable and sustainable synthesis," *Green Chem.*, vol. 19, no. 12, pp. 2729–2747, 2017, doi: 10.1039/c7gc01078h.
2. S. Sangam *et al.*, "Sustainable synthesis of single crystalline sulphur-doped graphene quantum dots for bioimaging and beyond," *Green Chem.*, vol. 20, no. 18, pp. 4245–4259, 2018, doi: 10.1039/c8gc01638k.
3. C. Rajasekhar and S. Kanchi, "Green nanomaterials for clean environment," *Handb. Ecomater.*, vol. 1, pp. 63–79, 2019, doi: 10.1007/978-3-319-68255-6_73.
4. S. N. Baker and G. A. Baker, "Luminescent Carbon Nanodots : Emergent Nanolights Angewandte," pp. 6726–6744, 2010, doi: 10.1002/anie.200906623.
5. A. Jaiswal, S. Sankar Ghosh, and A. Chattopadhyay, "One step synthesis of C-dots by microwave mediated caramelization of poly(ethylene glycol)," *Chem. Commun.*, vol. 48, no. 3, pp. 407–409, 2012, doi: 10.1039/c1cc15988g.
6. Y. Wu, X. Liu, Q. Wu, J. Yi, and G. Zhang, "Carbon Nanodots-Based Fluorescent Turn-On Sensor Array for Biothiols," 2017, doi: 10.1021/acs.analchem.7b00956.
7. Q. Wang, X. Liu, L. Zhang, and Y. Lv, "Microwave-assisted synthesis of carbon nanodots through an eggshell membrane and their fluorescent application," *Analyst*, vol. 137, no. 22, pp. 5392–5397, 2012, doi: 10.1039/c2an36059d.
8. Y. Wang and A. Hu, "Carbon quantum dots: Synthesis, properties and applications," *J. Mater. Chem. C*, vol. 2, no. 34, pp. 6921–6939, 2014, doi: 10.1039/c4tc00988f.
9. W. Meng, X. Bai, B. Wang, Z. Liu, S. Lu, and B. Yang, "Biomass-Derived Carbon Dots and Their Applications," *Energy Environ. Mater.*, vol. 2, no. 3, pp. 172–192, 2019, doi: 10.1002/eem2.12038.
10. S. Y. Lim, W. Shen, and Z. Gao, "Carbon quantum dots and their applications," *Chem. Soc. Rev.*, vol. 44, no. 1, pp. 362–381, 2015, doi: 10.1039/c4cs00269e.
11. A. Sharma and J. Das, "Small molecules derived carbon dots: Synthesis and applications in sensing, catalysis, imaging, and biomedicine," *J. Nanobiotechnology*, vol. 17, no. 1, pp. 1–24, 2019, doi: 10.1186/s12951-019-0525-8.
12. Q. Wang, H. Zheng, Y. Long, L. Zhang, M. Gao, and W. Bai, "Microwave-hydrothermal synthesis of fluorescent carbon dots from graphite oxide," *Carbon N. Y.*, vol. 49, no. 9, pp. 3134–3140, 2011, doi: 10.1016/j.carbon.2011.03.041.
13. J. Lan, C. Liu, M. Gao, and C. Huang, "An efficient solid-state synthesis of fluorescent surface carboxylated carbon dots derived from C60 as a label-free probe for iron ions in living cells," *Talanta*, vol. 144, pp. 93–97, 2015, doi: 10.1016/j.talanta.2015.05.071.
14. S. Sahu, B. Behera, T. K. Maiti, and S. Mohapatra, "Simple one-step synthesis of highly luminescent carbon dots from orange juice: Application as excellent bio-imaging agents," *Chem. Commun.*, vol. 48, no. 70, pp. 8835–8837, 2012, doi: 10.1039/c2cc33796g.
15. H. Xu, L. Xie, and M. Hakkarainen, "Coffee-Ground-Derived Quantum Dots for Aqueous Processable Nanoporous Graphene Membranes," *ACS Sustain. Chem. Eng.*, vol. 5, no. 6, pp. 5360–5367, 2017, doi: 10.1021/acssuschemeng.7b00663.
16. Z. Zhang, W. Sun, and P. Wu, "Highly Photoluminescent Carbon Dots Derived from Egg White: Facile and Green Synthesis, Photoluminescence Properties, and Multiple Applications," *ACS Sustain. Chem. Eng.*, vol. 3, no. 7, pp. 1412–1418, 2015, doi: 10.1021/acssuschemeng.5b00156.
17. B. De and N. Karak, "A green and facile approach for the synthesis of water soluble fluorescent carbon dots from banana juice," *RSC Adv.*, vol. 3, no. 22, pp. 8286–8290, 2013, doi: 10.1039/c3ra00088e.

18. Y. Jeong, K. Moon, S. Jeong, W. G. Koh, and K. Lee, "Converting Waste Papers to Fluorescent Carbon Dots in the Recycling Process without Loss of Ionic Liquids and Bioimaging Applications," *ACS Sustain. Chem. Eng.*, vol. 6, no. 4, pp. 4510–4515, 2018, doi: 10.1021/acssuschemeng.8b00353.
19. Y. P. Sun *et al.*, "Quantum-sized carbon dots for bright and colorful photoluminescence," *J. Am. Chem. Soc.*, vol. 128, no. 24, pp. 7756–7757, 2006, doi: 10.1021/ja062677d.
20. S. T. Yang *et al.*, "Carbon dots as nontoxic and high-performance fluorescence imaging agents," *J. Phys. Chem. C*, vol. 113, no. 42, pp. 18110–18114, 2009, doi: 10.1021/jp9085969.
21. X. Zhang *et al.*, "Review of natural productderived carbon dots: from natural products to functional materials," *ChemSusChem*, vol. 11, no. 1, pp. 11–24, 2018, doi: 10.1002/cssc.201701847.
22. D. Kong, F. Yan, Y. Luo, Q. Ye, S. Zhou, and L. Chen, "Amphiphilic carbon dots for sensitive detection, intracellular imaging of Al3+," *Anal. Chim. Acta*, vol. 953, pp. 63–70, 2017, doi: 10.1016/j.aca.2016.11.049.
23. R. Ye *et al.*, "Bandgap Engineering of Coal-Derived Graphene Quantum Dots," 2015, doi: 10.1021/acsami.5b01419.
24. X. Wang, Y. Feng, P. Dong, and J. Huang, "A Mini Review on Carbon Quantum Dots: Preparation, Properties, and Electrocatalytic Application," *Front. Chem.*, vol. 7, no. October, pp. 1–9, 2019, doi: 10.3389/fchem.2019.00671.
25. I. Mihalache *et al.*, "Charge and energy transfer interplay in hybrid sensitized solar cells mediated by graphene quantum dots," *Electrochim. Acta*, vol. 153, pp. 306–315, 2015, doi: 10.1016/j.electacta.2014.11.200.
26. J. Wang and J. Qiu, "A review of carbon dots in biological applications," *J. Mater. Sci.*, vol. 51, no. 10, pp. 4728–4738, 2016, doi: 10.1007/s10853-016-9797-7.
27. A. Sciortino, A. Cannizzo, and F. Messina, "Carbon Nanodots : A Review — From the Current Understanding of the Fundamental Photophysics to," 2018, doi: 10.3390/c4040067.
28. L. J. Mohammed and K. M. Omer, "Dual functional highly luminescence B, N Co-doped carbon nanodots as nanothermometer and Fe3+/Fe2+ sensor," *Sci. Rep.*, vol. 10, no. 1, pp. 1–12, 2020, doi: 10.1038/s41598-020-59958-5.
29. M. Tuerhong, Y. XU, and X. B. YIN, "Review on Carbon Dots and Their Applications," *Chinese J. Anal. Chem.*, vol. 45, no. 1, pp. 139–150, 2017, doi: 10.1016/S1872-2040(16)60990-8.
30. E. Hasegawa *et al.*, "Benzimidazolium Naphthoxide Betaine Is a Visible Light Promoted Organic Photoredox Catalyst," *J. Org. Chem.*, vol. 83, no. 7, pp. 3921–3927, 2018, doi: 10.1021/acs.joc.8b00282.
31. C. Li *et al.*, "Red fluorescent carbon dots with phenylboronic acid tags for quick detection of Fe(III) in PC12 cells," *J. Colloid Interface Sci.*, vol. 526, pp. 487–496, 2018, doi: 10.1016/j.jcis.2018.05.017.
32. S. He, S. Qi, Z. Sun, G. Zhu, K. Zhang, and W. Chen, "Si, N-codoped carbon dots: preparation and application in iron overload diagnosis," *J. Mater. Sci.*, vol. 54, no. 5, pp. 4297–4305, 2019, doi: 10.1007/s10853-018-3150-2.
33. S. Bian *et al.*, "One-pot synthesis of sulfur-doped graphene quantum dots as a novel fluorescent probe for highly selective and sensitive detection of lead(II)," *RSC Adv.*, vol. 6, no. 74, pp. 69977–69983, 2016, doi: 10.1039/c6ra10836a.
34. R. Liu *et al.*, "Ultra-sensitive and selective Hg2+ detection based on fluorescent carbon dots," *Mater. Res. Bull.*, vol. 48, no. 7, pp. 2529–2534, 2013, doi: 10.1016/j.materresbull.2013.03.015.
35. C. Liu *et al.*, "Photoinduced Electron Transfer Mediated by Coordination between Carboxyl on

Carbon Nanodots and Cu2+ Quenching Photoluminescence," *J. Phys. Chem. C*, vol. 122, no. 6, pp. 3662–3668, 2018, doi: 10.1021/acs.jpcc.7b12681.

36. S. Hu, Q. Zhao, Q. Chang, J. Yang, and J. Liu, "Enhanced performance of Fe3+detection via fluorescence resonance energy transfer between carbon quantum dots and Rhodamine B," *RSC Adv.*, vol. 4, no. 77, pp. 41069–41075, 2014, doi: 10.1039/c4ra06371f.
37. F. Paquin, J. Rivnay, A. Salleo, N. Stingelin, and C. Silva, "Multi-phase semicrystalline microstructures drive exciton dissociation in neat plastic semiconductors," *J. Mater. Chem. C*, vol. 3, pp. 10715–10722, 2015, doi: 10.1039/b000000x.
38. X. Feng *et al.*, "RSC Advances Easy synthesis of photoluminescent N-doped carbon dots from winter melon for bio-imaging †," *RSC Adv.*, vol. 5, pp. 31250–31254, 2015, doi: 10.1039/C5RA02271A.
39. R. Bandi, B. R. Gangapuram, R. Dadigala, R. Eslavath, S. S. Singh, and V. Guttena, "Facile and green synthesis of fluorescent carbon dots from onion waste and their potential applications as sensor and multicolour imaging agents," *RSC Adv.*, vol. 6, no. 34, pp. 28633–28639, 2016, doi: 10.1039/c6ra01669c.
40. A. Manuscript, "www.rsc.org/analyst," 2015, doi: 10.1039/C5AN00454C.
41. B. S. B. Kasibabu, S. L. D'souza, S. Jha, R. K. Singhal, H. Basu, and S. K. Kailasa, "One-step synthesis of fluorescent carbon dots for imaging bacterial and fungal cells," *Anal. Methods*, vol. 7, no. 6, pp. 2373–2378, 2015, doi: 10.1039/c4ay02737j.
42. F. Du *et al.*, "Economical and green synthesis of bagasse-derived fluorescent carbon dots for biomedical applications," *Nanotechnology*, vol. 25, no. 31, 2014, doi: 10.1088/0957-4484/25/31/315702.
43. S. Liu *et al.*, "Hydrothermal treatment of grass: A low-cost, green route to nitrogen-doped, carbon-rich, photoluminescent polymer nanodots as an effective fluorescent sensing platform for label-free detection of Cu(II) ions," *Adv. Mater.*, vol. 24, no. 15, pp. 2037–2041, 2012, doi: 10.1002/adma.201200164.
44. Y. Song *et al.*, "Highly photoluminescent carbon dots derived from linseed and their applications in cellular imaging and sensing," *J. Mater. Chem. B*, vol. 6, no. 19, pp. 3181–3187, 2018, doi: 10.1039/c8tb00116b.
45. Y. Zhang, Z. Gao, X. Yang, J. Chang, Z. Liu, and K. Jiang, "Fish-scale-derived carbon dots as efficient fluorescent nanoprobes for detection of ferric ions," *RSC Adv.*, vol. 9, no. 2, pp. 940–949, 2019, doi: 10.1039/C8RA09471C.
46. J. Liao, Z. Cheng, and L. Zhou, "Nitrogen-Doping Enhanced Fluorescent Carbon Dots: Green Synthesis and Their Applications for Bioimaging and Label-Free Detection of Au3+ Ions," *ACS Sustain. Chem. Eng.*, vol. 4, no. 6, pp. 3053–3061, 2016, doi: 10.1021/acssuschemeng.6b00018.
47. P. Song *et al.*, "A multianalyte fluorescent carbon dots sensing system constructed based on specific recognition of Fe(III) ions," *RSC Adv.*, vol. 7, no. 46, pp. 28637–28646, 2017, doi: 10.1039/c7ra04122e.
48. G. Gedda, C. Y. Lee, Y. C. Lin, and H. F. Wu, "Green synthesis of carbon dots from prawn shells for highly selective and sensitive detection of copper ions," *Sensors Actuators, B Chem.*, vol. 224, pp. 396–403, 2016, doi: 10.1016/j.snb.2015.09.065.
49. C. Yu, T. Xuan, Y. Chen, Z. Zhao, Z. Sun, and H. Li, "A facile, green synthesis of highly fluorescent carbon nanoparticles from oatmeal for cell imaging," *J. Mater. Chem. C*, vol. 3, no. 37, pp. 9514–9518, 2015, doi: 10.1039/c5tc02057c.
50. W. J. Wang, J. M. Xia, J. Feng, M. Q. He, M. L. Chen, and J. H. Wang, "Green preparation of carbon dots for intracellular pH sensing and multicolor live cell imaging," *J. Mater. Chem. B*, vol. 4, no. 44, pp. 7130–7137, 2016, doi: 10.1039/c6tb02071b.

51. M. Amjadi, T. Hallaj, and M. A. Mayan, "Green synthesis of nitrogen-doped carbon dots from lentil and its application for colorimetric determination of thioridazine hydrochloride," *RSC Adv.*, vol. 6, no. 106, pp. 104467–104473, 2016, doi: 10.1039/c6ra22899b.
52. B. Yin *et al.*, "Green synthesis of carbon dots with down- and up-conversion fluorescent properties for sensitive detection of hypochlorite with a dual-readout assay," *Analyst*, vol. 138, no. 21, pp. 6551–6557, 2013, doi: 10.1039/c3an01003a.
53. Z. Li, Y. Ni, and S. Kokot, "A new fluorescent nitrogen-doped carbon dot system modified by the fluorophore-labeled ssDNA for the analysis of 6-mercaptopurine and Hg (II)," *Biosens. Bioelectron.*, vol. 74, no. Ii, pp. 91–97, 2015, doi: 10.1016/j.bios.2015.06.014.
54. Y. Liu *et al.*, "Green synthesis of fluorescent carbon dots from carrot juice for in vitro cellular imaging," *Carbon Lett.*, vol. 21, no. 1, pp. 61–67, 2017, doi: 10.5714/CL.2017.21.061.
55. C. Wang, D. Sun, K. Zhuo, H. Zhang, and J. Wang, "Simple and green synthesis of nitrogen-, sulfur-, and phosphorus-co-doped carbon dots with tunable luminescence properties and sensing application," *RSC Adv.*, vol. 4, no. 96, pp. 54060–54065, 2014, doi: 10.1039/c4ra10885j.
56. G. Wang *et al.*, "Facile and Highly Effective Synthesis of Controllable Lattice Sulfur-Doped Graphene Quantum Dots via Hydrothermal Treatment of Durian," *ACS Appl. Mater. Interfaces*, vol. 10, no. 6, pp. 5750–5759, 2018, doi: 10.1021/acsami.7b16002.
57. T. N. J. I. Edison, R. Atchudan, J. J. Shim, S. Kalimuthu, B. C. Ahn, and Y. R. Lee, "Turn-off fluorescence sensor for the detection of ferric ion in water using green synthesized N-doped carbon dots and its bio-imaging," *J. Photochem. Photobiol. B Biol.*, vol. 158, pp. 235–242, 2016, doi: 10.1016/j.jphotobiol.2016.03.010.
58. X. J. Zhao, W. L. Zhang, and Z. Q. Zhou, "Sodium hydroxide-mediated hydrogel of citrus pectin for preparation of fluorescent carbon dots for bioimaging," *Colloids Surfaces B Biointerfaces*, vol. 123, pp. 493–497, 2014, doi: 10.1016/j.colsurfb.2014.09.048.
59. V. Arul, T. N. J. I. Edison, Y. R. Lee, and M. G. Sethuraman, *Biological and catalytic applications of green synthesized fluorescent N-doped carbon dots using Hylocereus undatus*, vol. 168. Elsevier B.V, 2017.
60. Q. Liang, W. Ma, Y. Shi, Z. Li, and X. Yang, "Easy synthesis of highly fluorescent carbon quantum dots from gelatin and their luminescent properties and applications," *Carbon N. Y.*, vol. 60, pp. 421–428, 2013, doi: 10.1016/j.carbon.2013.04.055.
61. Y. Liu, Y. Zhao, and Y. Zhang, "One-step green synthesized fluorescent carbon nanodots from bamboo leaves for copper(II) ion detection," *Sensors Actuators, B Chem.*, vol. 196, pp. 647–652, 2014, doi: 10.1016/j.snb.2014.02.053.
62. J. Wei *et al.*, "Simple one-step synthesis of water-soluble fluorescent carbon dots from waste paper," *New J. Chem.*, vol. 38, no. 3, pp. 906–909, 2014, doi: 10.1039/c3nj01325a.
63. H. Xu, X. Yang, G. Li, C. Zhao, and X. Liao, "Green Synthesis of Fluorescent Carbon Dots for Selective Detection of Tartrazine in Food Samples," *J. Agric. Food Chem.*, vol. 63, no. 30, pp. 6707–6714, 2015, doi: 10.1021/acs.jafc.5b02319.
64. J. Xu, T. Lai, Z. Feng, X. Weng, and C. Huang, "Formation of fluorescent carbon nanodots from kitchen wastes and their application for detection of Fe3+," *Luminescence*, vol. 30, no. 4, pp. 420–424, 2015, doi: 10.1002/bio.2754.
65. Z. Ding, F. Li, J. Wen, X. Wang, and R. Sun, "Gram-scale synthesis of single-crystalline graphene quantum dots derived from lignin biomass," *Green Chem.*, vol. 20, no. 6, pp. 1383–1390, 2018, doi: 10.1039/c7gc03218h.
66. Z. Yan, Z. Zhang, and J. Chen, "Biomass-based carbon dots: Synthesis and application in imatinib determination," *Sensors Actuators, B Chem.*, vol. 225, pp. 469–473, 2016, doi: 10.1016/j.snb.2015.10.107.

67. J. Wei *et al.*, "Dual functional carbon dots derived from cornflour via a simple one-pot hydrothermal route," *Mater. Lett.*, vol. 123, pp. 107–111, 2014, doi: 10.1016/j.matlet.2014.02.090.
68. W. Chen *et al.*, "Synthesis of graphene quantum dots from natural polymer starch for cell imaging," *Green Chem.*, vol. 20, no. 19, pp. 4438–4442, 2018, doi: 10.1039/c8gc02106f.
69. V. Sharma, P. Tiwari, and S. M. Mobin, "Sustainable carbon-dots: Recent advances in green carbon dots for sensing and bioimaging," *J. Mater. Chem. B*, vol. 5, no. 45, pp. 8904–8924, 2017, doi: 10.1039/c7tb02484c.
70. M. L. Liu, B. Bin Chen, C. M. Li, and C. Z. Huang, "Carbon dots prepared for fluorescence and chemiluminescence sensing," *Sci. China Chem.*, vol. 62, no. 8, pp. 968–981, 2019, doi: 10.1007/s11426-019-9449-y.
71. R. Liu *et al.*, "A facile microwave-hydrothermal approach towards highly photoluminescent carbon dots from goose feathers," *RSC Adv.*, vol. 5, no. 6, pp. 4428–4433, 2015, doi: 10.1039/c4ra12077a.
72. S. L. YE *et al.*, "Preparation of Carbon Dots and Their Application in Food Analysis as Signal Probe," *Chinese J. Anal. Chem.*, vol. 45, no. 10, pp. 1571–1581, 2017, doi: 10.1016/S1872-2040(17)61045-4.
73. D. Gu, S. Shang, Q. Yu, and J. Shen, "Green synthesis of nitrogen-doped carbon dots from lotus root for Hg(II) ions detection and cell imaging," *Appl. Surf. Sci.*, vol. 390, no. Ii, pp. 38–42, 2016, doi: 10.1016/j.apsusc.2016.08.012.
74. S. Wang, Y. Wang, K. Yang, Y. Zhong, X. Yang, and Z. Chen, "Synthesis of Carbon Dots Originated from Hydroxypropylmethyl Cellulose for Sensing Ciprofloxacin," *Anal. Sci.*, vol. 33, no. 10, pp. 1129–1134, 2017, doi: 10.2116/analsci.33.1129.
75. X. Liu, T. Li, Y. Hou, Q. Wu, J. Yi, and G. Zhang, "Microwave synthesis of carbon dots with multi-response using denatured proteins as carbon source," *RSC Adv.*, vol. 6, no. 14, pp. 11711–11718, 2016, doi: 10.1039/c5ra23081k.
76. V. Ramanan, S. K. Thiyagarajan, K. Raji, R. Suresh, R. Sekar, and P. Ramamurthy, "Outright green synthesis of fluorescent carbon dots from eutrophic algal blooms for in vitro imaging," *ACS Sustain. Chem. Eng.*, vol. 4, no. 9, pp. 4724–4731, 2016, doi: 10.1021/acssuschemeng.6b00935.
77. M. Si *et al.*, "Synchronous and rapid preparation of lignin nanoparticles and carbon quantum dots from natural lignocellulose," *Green Chem.*, vol. 20, no. 15, pp. 3414–3419, 2018, doi: 10.1039/c8gc00744f.
78. W. Liu *et al.*, "Analysis of factors associated with disease outcomes in hospitalized patients with 2019 novel coronavirus disease," *Chin. Med. J. (Engl).*, vol. 133, no. 9, pp. 1032–1038, 2020, doi: 10.1097/CM9.0000000000000775.
79. J. Y. Dong *et al.*, "Effect of probiotic fermented milk on blood pressure: A meta-analysis of randomised controlled trials," *Br. J. Nutr.*, vol. 110, no. 7, pp. 1188–1194, 2013, doi: 10.1017/S0007114513001712.
80. Z. A. Qiao *et al.*, "Commercially activated carbon as the source for producing multicolor photoluminescent carbon dots by chemical oxidation," *Chem. Commun.*, vol. 46, no. 46, pp. 8812–8814, 2010, doi: 10.1039/c0cc02724c.
81. Y. Xu *et al.*, "Nitrogen-doped carbon dots: A facile and general preparation method, photoluminescence investigation, and imaging applications," *Chem. - A Eur. J.*, vol. 19, no. 7, pp. 2276–2283, 2013, doi: 10.1002/chem.201203641.
82. Z. Wang *et al.*, "Large-Scale and Controllable Synthesis of Graphene Quantum Dots from Rice Husk Biomass: A Comprehensive Utilization Strategy," *ACS Appl. Mater. Interfaces*, vol. 8, no.

2, pp. 1434–1439, 2016, doi: 10.1021/acsami.5b10660.
83. A. Manuscript, "10.1039@C2Cy20635H," no. 207890, 2011.
84. J. B. Essner, R. N. McCay, C. J. Smith, S. M. Cobb, C. H. Laber, and G. A. Baker, "A switchable peroxidase mimic derived from the reversible co-assembly of cytochrome c and carbon dots," *J. Mater. Chem. B*, vol. 4, no. 12, pp. 2163–2170, 2016, doi: 10.1039/c6tb00052e.
85. M. Xue, Z. Zhan, M. Zou, L. Zhang, and S. Zhao, "Green synthesis of stable and biocompatible fluorescent carbon dots from peanut shells for multicolor living cell imaging," *New J. Chem.*, vol. 40, no. 2, pp. 1698–1703, 2016, doi: 10.1039/c5nj02181b.
86. M. Saxena, S. Maity, and S. Sarkar, "Carbon nanoparticles in 'biochar' boost wheat (Triticum aestivum) plant growth," *RSC Adv.*, vol. 4, no. 75, pp. 39948–39954, 2014, doi: 10.1039/c4ra06535b.
87. H. Liu, T. Ye, and C. Mao, "Fluorescent carbon nanoparticles derived from candle soot," *Angew. Chemie - Int. Ed.*, vol. 46, no. 34, pp. 6473–6475, 2007, doi: 10.1002/anie.200701271.
88. L. Shi *et al.*, "Green-fluorescent nitrogen-doped carbon nanodots for biological imaging and paper-based sensing," *Anal. Methods*, vol. 9, no. 14, pp. 2197–2204, 2017, doi: 10.1039/c7ay00163k.
89. D. W. M. Arrigan, "Tutorial review. Voltammetric determination of trace metals and organics after accumulation at modified electrodes," *Analyst*, vol. 119, no. 9, pp. 1953–1966, 1994, doi: 10.1039/AN9941901953.
90. World Health Organization, "Iron in drinking-water. WHO Guidelines for drinking-water quality," *Who/Sde/Wsh/03.04/08*, vol. 2, p. 4, 2003.
91. X. Yang, Y. Zhuo, S. Zhu, Y. Luo, Y. Feng, and Y. Dou, "Novel and green synthesis of high-fluorescent carbon dots originated from honey for sensing and imaging," *Biosens. Bioelectron.*, vol. 60, pp. 292–298, 2014, doi: 10.1016/j.bios.2014.04.046.
92. X. Teng *et al.*, "Green synthesis of nitrogen-doped carbon dots from konjac flour with 'off-on' fluorescence by Fe3+ and l-lysine for bioimaging," *J. Mater. Chem. B*, vol. 2, no. 29, pp. 4631–4639, 2014, doi: 10.1039/c4tb00368c.
93. S. Sailaja Prasannakumaran Nair, N. Kottam, and P. K. S G, "Green Synthesized Luminescent Carbon Nanodots for the Sensing Application of Fe3+ Ions," *J. Fluoresc.*, vol. 30, no. 2, pp. 357–363, 2020, doi: 10.1007/s10895-020-02505-2.
94. S. Sawalha, A. Silvestri, A. Criado, S. Bettini, M. Prato, and L. Valli, "Tailoring the sensing abilities of carbon nanodots obtained from olive solid wastes," *Carbon N. Y.*, vol. 167, pp. 696–708, 2020, doi: 10.1016/j.carbon.2020.06.011.
95. J. Shen, S. Shang, X. Chen, D. Wang, and Y. Cai, "Facile synthesis of fluorescence carbon dots from sweet potato for Fe3 + sensing and cell imaging," *Mater. Sci. Eng. C*, vol. 76, pp. 856–864, 2017, doi: 10.1016/j.msec.2017.03.178.
96. S. Zhao *et al.*, "Green Synthesis of Bifunctional Fluorescent Carbon Dots from Garlic for Cellular Imaging and Free Radical Scavenging," *ACS Appl. Mater. Interfaces*, vol. 7, no. 31, pp. 17054–17060, 2015, doi: 10.1021/acsami.5b03228.
97. N. Wang, Y. Wang, T. Guo, T. Yang, M. Chen, and J. Wang, "Green preparation of carbon dots with papaya as carbon source for effective fluorescent sensing of Iron (III) and Escherichia coli," *Biosens. Bioelectron.*, vol. 85, pp. 68–75, 2016, doi: 10.1016/j.bios.2016.04.089.
98. J. Xu, Y. Zhou, S. Liu, M. Dong, and C. Huang, "Low-cost synthesis of carbon nanodots from natural products used as a fluorescent probe for the detection of ferrum(iii) ions in lake water," *Anal. Methods*, vol. 6, no. 7, pp. 2086–2090, 2014, doi: 10.1039/c3ay41715h.
99. B. S. B. Kasibabu, S. L. D'Souza, S. Jha, and S. K. Kailasa, "Imaging of Bacterial and Fungal Cells Using Fluorescent Carbon Dots Prepared from Carica papaya Juice," *J. Fluoresc.*, vol. 25,

no. 4, pp. 803–810, 2015, doi: 10.1007/s10895-015-1595-0.

100. W. Li *et al.*, "Plant leaf-derived fluorescent carbon dots for sensing, patterni," *Angew. Chemie - Int. Ed.*, vol. 52, no. 31, pp. 8151–8155, 2013, doi: 10.1002/anie.201303927.
101. A. Ve, D. Dergisi, S. Dinc, and M. Kara, "Synthesis and Applications of Carbon Dots from Food and Natural Products: A Mini-Review Gıda ve Doğal Ürünlerden Karbon Noktaların Sentezi ve Uygulamaları: Derleme," *J. Apitherapy Nature/Apiterapi ve Doğa Derg.*, vol. 1, no. 1, pp. 33–37, 2018, [Online]. Available: www.dergipark.gov.tr/jan.
102. C. J. Reckmeier, J. Schneider, A. S. Susha, and A. L. Rogach, "Luminescent colloidal carbon dots: optical properties and effects of doping [Invited]," *Opt. Express*, vol. 24, no. 2, p. A312, 2016, doi: 10.1364/oe.24.00a312.
103. Y. Xu, D. Li, M. Liu, F. Niu, J. Liu, and E. Wang, "Enhanced-quantum yield sulfur/nitrogen co-doped fluorescent carbon nanodots produced from biomass Enteromorpha prolifera: Synthesis, posttreatment, applications and mechanism study," *Sci. Rep.*, vol. 7, no. 1, pp. 1–12, 2017, doi: 10.1038/s41598-017-04754-x.

CO2 capture by graphene-based nanocomposites: effects of oxygen and nitrogen contents

Ali M. Alkadhem [1] and Sagheer A. Onaizi [1, 2,*]

[1] Department of Chemical Engineering, King Fahd University of Petroleum and Minerals, Dhahran 31216, Saudi Arabia

[2] Interdisciplinary Research Center for Hydrogen and Energy Storage, King Fahd University of Petroleum and Minerals, Dhahran 31261, Saudi Arabia

**Corresponding author: onaizi@kfupm.edu.sa*

Abstract: In the past few decades, a considerable research work on graphene-based nano-composites has been carried out because of their excellent properties such as thermal stability, mechanical strength, and good conductivity. Thus, the work presented herein aims to functionalize graphene oxide (GO) with different amines (i.e., effect of nitrogen content) and employ it for CO_2 capture. Additionally, the effect of oxygen content on CO_2 capture was investigated via the reduction of GO with different inorganic reducing agents (i.e., zinc powder and aluminum foil). The results showed that the unmodified GO can adsorb 45 mg CO_2/g at ambient conditions (i.e., 1 atm and 30 ºC). However, the decrease in the oxygen content upon the reduction of GO resulted in more than 3-fold decrease in CO_2 capture (i.e., the CO_2 adsorption capacity of rGO is about 13.1 mg/g). The functionalization of GO with 3-aminopropyl-triethoxysilane (APTS) and diethylenetriamine (DETA) resulted in an enhanced CO_2 adsorption while its functionalization with polytheylenimine (PEI) and hexamethylenetetramine (hexamine) provided a negative effect. Additionally, the alteration of amine/GO ratio in the composite revealed that the optimum mass ratio is 1:1 (in the synthesis solution), which provided a CO2 capture capacity (at ambient conditions) of 63 mg/g. Above and below this ratio, the adsorption of CO_2 on the APTS-functionalized GO decreased. The synthesized graphene-based nanocomposites were characterized using BET surface area, X-ray diffraction (XRD), scanning electron microscopy with energy dispersive X-ray spectroscopy (SEM-EDX), and Fourier transform infrared spectroscopy (FTIR).

Keywords: graphite oxide; carbon dioxide; CO_2 capture; amine; adsorption; reduced graphene oxide.

1. Introduction

The concentration of CO_2 in the atmosphere is increasing since the beginning of the industrial era [1]. CO_2 is considered as the most significantly produced gas among the greenhouse gases due to the current human activities and the continuous use of fossil sources [2-4]. Additionally CO_2 emission is one of the main drivers of the abnormal climate change [2, 5]. As a result, the atmospheric temperature of the world is anticipated to still increase to an extra 1.5 °C throughout the twenty-first century with the current massive CO_2 emission [2, 6]. For those reasons, the CO_2 concentration has to be reduced to satisfy the ecological guideline and to meet the global need for CO_2 reduction. In the effort to control the massive amount of the produced CO_2, a number of developed technologies have been utilized including, chemical and physical solvent absorption processes by using amine solution [2, 3, 7-9], cryogenic processes [10], adsorption processes [11, 12], membrane and biological separation technics [13, 14]. Because of the fewer energy requirements and simple regeneration steps, adsorption is the most preferred approach among those different technologies [15].

Over the last two decades, significant research work was aimed to develop novel adsorbents for removing carbon dioxide including microporous and mesoporous silica [16, 17], carbon-based adsorbents [18, 19], metal oxides [20, 21] and metal-organic frameworks MOFs [22, 23]. During the

last decades, Graphene has appealed considerable attention among the scientific research and has implanted in a wide range of technological applications such as energy storage (super-capacitors) [24] and adsorbents material including water purification [25], gas sensing, [26] and selective chemical aqueous adsorption [27].

In general, Graphene is a new founded material that appealed research attention due to the fabulous physical and mechanical properties of the graphene surface. Typically, graphene is stable and exhibits excellent electronic and mechanical features [28]. Nevertheless, the analog oxidized form of graphene (graphite oxide) equivalently has obtained great research appreciation as well since it has been produced in 1855 by Brodie. This extraordinary attention is attributed to the abundance of oxygen functionalities such as carbonyl (C=O), alkoxy (C–O–C) and hydroxyl (OH) groups, which permit a relaxed manipulation and configuration [29]. Three commonly approaches for the preparation of graphite oxides have been reported in the literature, Brodie method, Staudenmaier's (ST) and method Hummers' (HU) method [30, 31]. In addition to the interest that given to GO, reduced graphite oxide (rGO) as well takes a roll in research attention. Overall, rGO has several preparation approaches; the first approach is chemical reduction [32, 33] which includes hydrothermal [34], Solvothermal [35, 36] and electrochemical reduction [37, 38]. The second approach is a thermal reduction that includes thermal annealing [39-41], microwave, and photo reduction [42]. In general, Graphene oxide's reduction methods are conducted using oxygen functional groups removal. Apart from the applications stated of Graphene-based Nano-composites, the main goals of this study are to highlight the significance of graphene derivative's (GO & rGO) as based adsorbent for carbon dioxide.

In this study, graphite oxide was synthesized using graphite as the starting material. The produced graphite oxide was converted to reduced GO by chemical reduction means using two reducing inorganic reducing agents (Zn powder and Al foil). Both GO, and rGO were functionalized with APTS to enhance the CO_2 adsorption capacity. Additionally, GO was modified other amines (i.e., PEI, DETA, and hexamine). The effect of APTS/GO mass ratio on the CO2 uptake capacity was also investigated.

2. Materials and methods

2.1 Chemicals and materials

The required chemicals are Graphite powder, H_2SO_4, $NaNO_3$, H_2O_2 (30%), $KMnO_4$, 37%HCl, 3-aminopropyl-triethoxysilane (APTS), Diethylenetriamine (DETA), Hexamethylenetetramine (Hexamine), polyethylenimine (PEI), Zn powder, Al foil, NaOH pallets, and deionized water. All the chemicals are lab-grade purchased from Sigma-Aldrich.

2.2 Synthesis of graphene oxide (GO)

The synthesis of graphene oxide (GO) achieved by the oxidization of graphite powder using the procedure of modified Hummer's method [43]. In concise, first of all, 2.007 g of graphite powder blended with 1.0002 g of potassium nitrate. Afterward, 46 ml of concentrated sulphuric acid 98% was poured over the blend, and the obtained mixture was kept under constant stirring in an ice bath for one hour. Then, 6.007g of $KMnO_4$ was added slowly in small quantity to the mixture while maintaining the temperature below 20°C to avoid overheating and outburst. After that, the mixture temperature was kept at 35 °C under continuous stirring for four hours, and then 92 ml of water was added gradually followed by stirring at 98 °C for 15 minutes. After that, the suspension was treated with 2ml of 30% H_2O_2 solution in 280ml of deionized to assure the complete reaction with $KMnO_4$. Then, the mixture was stirred at room temperature overnight. For refinement, the mixture is centrifuged at 4500 rpm for 7 minutes and washed with 10% HCl two times and then washed with deionized water three times to eliminate the residual metal ions and acid. Finally, the precipitate was dried at 60 °C for two days, then GO obtained as a powder.

2.3 Synthesis of amine-modified graphite oxides

In brief, One gram of the synthesized GO was first dispersed in 600 ml of water solution. Then, one gram of amine molecule was added to the dispersed GO. In this study, GO was functionalized by APTS, DETA, PEI, and hexamine separately in different batch. For APTS-GO with variants APTS/GO mass ratios, different APTS quantities were added to GO dispersion in different batch to attain various APTS/GO ratios. Then, the mixture was stirred for 5 minutes, followed by bath sonication in ultrasonicator for one hour. After that, the mixture was refluxed for 45 h at 80 °C with continuous stirring. After the end of solvent-assisted amine modification; the sample was rinsed three times with deionized water and obtained using a centrifuge at 4500 rpm for 5 minutes [44]. The past was left in the dry oven at 60 °C overnight. Those, the modified GO samples were coded as APTS-GO, PEI-GO, DETA-GO, and Hexamine-GO following the attached amine compound.

2.4 chemical reduction using Zn/HCl

First, the synthesized GO was dissolved in water with a concentration of 1mg/ml. Then, it was stirred for 5 minutes at RT, followed by sonication for 10 minutes. After that, the PH of the mixture was adapted to 2 by a small addition of 37% HCl. Then, the Zn powder was added to the mixture in a ratio of 2:1 to the GO. After that, the mixture was immediately sonicated for another 20 minutes. Then, an additional amount of 37% HCl was added around 20 ml for every 1g of Zn to ensure the dissolving of the excessive Zn powder and stirred for an extra 5 minutes [45]. Finally, the resulting rGO was collected with centrifugation and washed with deionized water three times. Then, it was dried at 60 °C overnight, and the obtained adsorbent was coded as rGO-1.

2.5 Chemical reduction using Al / HCl (1N)

In concise, one gram of the synthesized GO was diluted first with 918.3ml deionized water. Then, the solution is sonicated for 10 minutes to obtain a homogenous mixture. After that, 81.7 ml of 37% HCl was added to the GO dispersions to get 1 mol /l HCl concentration mixture. Then, the mixture was left for an additional 10 min of mixing and sonication to get a proper homogenization .followed by the addition of 3 g, Al foil for every 1 g of GO solution with 1mg/ml dilution. The reduction was completed by continuous stirring for two hours [46]. rGO recovered by centrifugation, and the paste was washed with 0.1N HCl and water several times. Finally, the paste was dried at 60 °C overnight and coded as rGO-2.

2.6 Chemical reduction using (Al foil & Zn)/ NaOH (1N)

In this experiment, the synthesized GO was diluted with deionized water up to 1.0 mg /ml. Then, the solution was sonicated for 10 min to obtain a homogenous mixture. After that, 40 g of NaOH ballets were added gradually to the graphene oxide dispersions until 1N NaOH achieved. Then, an additional 10 min of mixing and sonication was applied for dispersing the formed aggregate .followed by the addition of 2 g of Zn powder & Al foil for every 1 g GO solution with 1mg/ml dilution. The reduction was completed by continuous stirring for one hour. rGO obtained with centrifugation and washed with 0.1N HCl and water several times. Finally, the paste was dried at 60 °C overnight and named as rGO-3.

2.7 Sample characterization

The surface area BET (Brunauer−Emmett− Teller) of Graphene derivative-based adsorbents & modified GO were measured using nitrogen adsorption isotherms at 77 K using an ASAP 2020 system (Micromeritics Instruments, Inc.). The morphologies structures of prepared adsorbents were studied using scanning electron microscopy (SEM). The adsorbents crystal structures were studied using XRD pattern by Shimadzu XRD-6000 X-ray diffractometer with Curadiation 40 kV and 30 mA. The

elemental analysis was carried out using Energy-dispersive X-ray spectroscopy (EDX) equipped with SEM. Functional groups were identified using Fourier Transform Infrared (FTIR) spectra and recorded at room temperature on range 400 to 4000 cm^{-1} by NICOLET 6700 spectrometer from Thermo Scientific using KBr pellets.

2.8 Evaluation of CO2 adsorption capacity

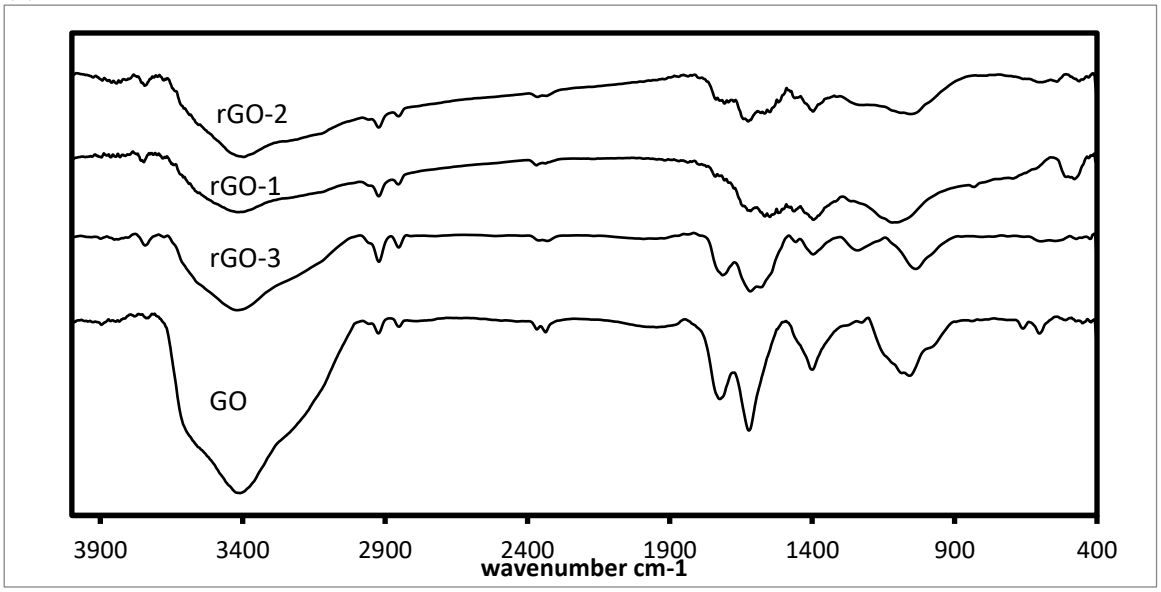
The measurement of CO_2 uptakes capacity for the synthesized samples was carried out by using a TA Q600 SDT. Roughly, 10 mg of the sample was weighted by TGA using alumina oxide pan. After that, the sample was outgassed at 100°C under the flow of pure N_2 gas at 100 mL/min for 30 minutes. Then, the temperature equilibrated to 30 °C. As a final point, the gas was switched to pure carbon dioxide (99.9%) with a flow rate of 100 ml/min for 90 minutes to compute the uptake capacity of the synthesized sample.

3. Result and discussion

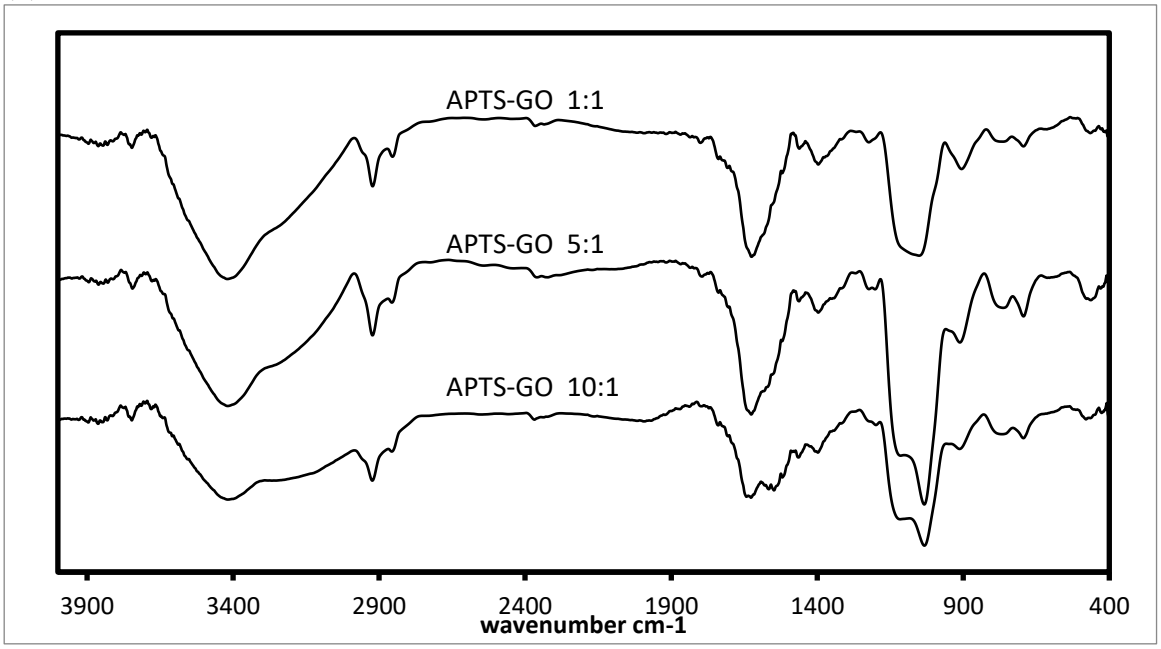
3.1 Characterization of samples

Fig. 1 shows the FTIR spectra mode of the synthesized samples in the range of 400 to 4000 cm^{-1} wavenumber. Accordingly, Fig. 1(a) presents the FTIR spectra manner of graphite oxide and the reduced graphite oxides. Both GO, and rGOs have the same FTIR pattern, but the peaks band intensity of the functional group which identified in GO has weakened or disappeared in rGOs samples. The Wide-ranging Peak centered at 3400 cm^{-1} stand for O–H stretching vibration while the minor peaks at 2920 and 2850 cm^{-1} are corresponding to C–H bending vibration [30, 47, 48]. The band peak at 1750 cm^{-1} stand for –C=O stretching vibration of the carboxyl group and the band at 1615 cm^{-1} could refer to the skeletal vibrations of un-oxidized sp^2 hybridized carbons from the graphitic structure [30, 45, 47, 48]. The peak at 1400 cm^{-1} corresponds to C–OH stretching vibrations of carboxyl group while the band at 1220 $cm^{-1}$is corresponding to C–O–C stretching vibration. The bands at 1040 and 970 cm^{-1} stand for to C–O stretching of epoxide groups [30, 48]. Fig. 1(b) depicts the FTIR spectra of APTS-GO prepared at variants APTS / GO ratio. After APTS grafting, the peaks at 3395 and 694 cm^{-1} is attributed to the N–H stretching vibration and the peaks at 2920 − 2850 cm^{-1}, which were related to the bending vibration of CH_2 now is associated with the CH_2 bending vibration of the APTS chain molecules[49, 50]. The peak at 1750 cm^{-1} has reduced or disappear that corresponding to -C=O stretching vibration while the intensity of the peak at 1615 cm^{-1} has increased which might be attributed to the presence of C–N groups at 1615 cm^{-1}. The vibrational band at 1050 cm^{-1} can be assigned to Si–O stretching vibration [50, 51]. Fig. 1(c) displays the FTIR spectra of GO, DETA-GO, APTES-GO, and PEI-GO. Concerning PEI functionalization, the new peak at 3200 cm^{-1} is corresponding to vNH stretching vibration. The peaks at 2920 and 2850 cm^{-1} are attributed to symmetric and asymmetric C-H stretching in PEI, respectively[49]. The bands at 1600 and 1450 cm^{-1} are assigned to NH bending [49, 52, 53]. The DETA-GO demonstrates new band at 1200 cm^{-1} which attributed to CN stretch.

(a)


rGO-2
rGO-1
rGO-3
GO
3900
3400
2900
2400
1900
1400
900
400
wavenumber cm-1

(b)


APTS-GO 1:1
APTS-GO 5:1
APTS-GO 10:1
3900
3400
2900
2400
1900
1400
900
400
wavenumber cm-1

(C)

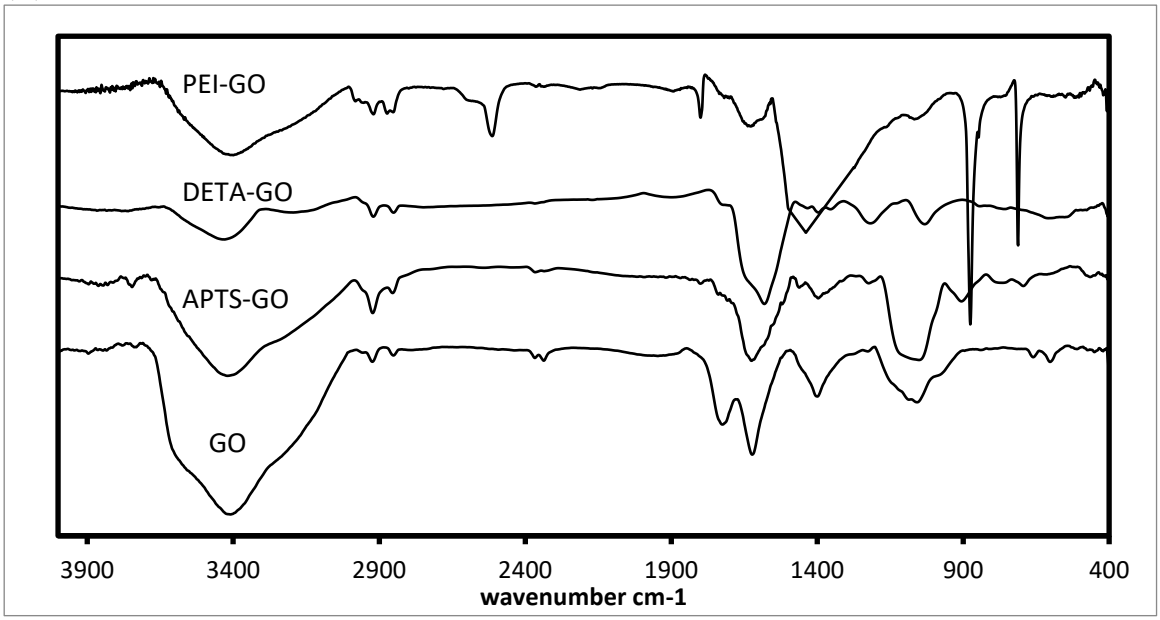


Fig. 1. (a) FTIR patterns of GO, rGO-1, rGO-2 and rGO-3, (B) FTIR patterns of APTS-GO for variants ratio of APTS/GO, (C) FTIR patterns of GO and amine factionalized GO.

The XRD patterns of GO, rGO-1, APTS-GO, and APTS-rGO-1 are presented in Fig. 2. According to the reported result in the litterateur, The pristine graphite exhibits a very intense and narrow sharp peak around 26°, which corresponding to the standard graphite spacing about 0.34 nm [54, 55]. Concerning the obtained result of graphite oxide, a sharp diffraction peak appeared around 10°. This typical shifting of the sharp peak toward a lower peak angle is assigned to the attachment of a large amount of oxygen-containing groups to the carbon atoms such as hydroxyl, epoxy, and carboxyl groups that give rise to expand the interlayer distance between graphite layers [26, 56]. Moreover, a small diffraction peak of about 43° is attributed to a short-range order in stacked graphene layers [57]. In the case of reduced graphite oxide, a sharp peak around 10° has disappeared. As a result, the narrow graphite peak around 26° has restored around 23.5° as a broad and less intense peak. This result indicates that the interlayer distance has decreased after GO reduction, and some of the oxygen functional group was removed [36, 55, 56, 58]. APTS-GO and APTS-rGO obtained less intense diffraction peak around 5.7° and 14.9°, respectively. These results indicate that after amine modification of GO, and rGO, they exhibited a further expanding in d-spacing, which could be regarded as amine molecules intercalation among the layers [49, 59].

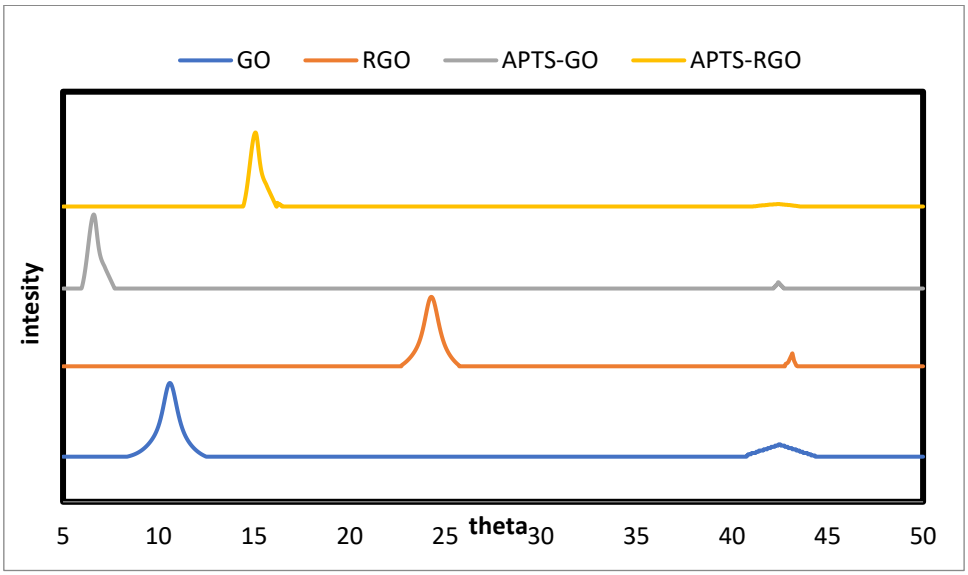


Fig. 2. XRD pattern of GO, rGO, APTS-GO and APTS-rGO

Table 1 presents the textural properties of the synthesized GO, rGO-1, APTS-GO, and APTS-rGO-1. The N_2-physisorption measurement at 77 K was applied to determine the surface textural properties of produced adsorbents, including surface area, pore size, and pore volume. According to the IUPAC standard, Nano-porous particles could be well-ordered into three classifications: macroporous (diameter > 50 nm), mesoporous (2 nm < diameter < 50 nm) and microporous (diameter < 2 nm) [48]. As a result, all of the samples fall in microporous order according to the measured pore size of prepared samples. Thus, microporous pores could have a positive impact of high selectivity towards CO_2 molecules of 0.33 nm of kinetic radius as previously reported [60, 61]. However, the synthesized GO using hummer modified method has obtained equivalence textural properties to the reported value in literature with 53.75 m^2/g surface area, 0.023 cm^3/g pore volume, and 1.745 nm pore size [53, 62]. On the other hand, the prepared rGO-1 has achieved a minimal surface area and pore volume that can be attributed to the influence of reducing agents and experiments condition [63, 64]. After amine modification of GO and rGO-1 surface, the surface area, pore-volume, and pore size have further reduced as a result of amine attachment to the GO and rGO-1 structure.

Table 1: textural properties of GO, rGO-1, APTS-GO and APTS-rGO-1

Samples	Surface area (BET) (m^2/g)	Pore volume (cm^3/g)	Pore size (nm)
GO	53.750	0.023	1.745
rGO-1	5.367	0.002	1.499
APTS-GO	29.094	0.012	1.612
APTS-rGO-1	8.595	0.003	1.429

The surface microscopic and morphology of the selected samples was investigated using the scanning electron microscopic. Fig. 3 displays the SEM image of GO, rGO, APTS-GO, and APTS-

rGO. As shown in Fig. 3(a), GO shows lamellar morphology that composed of flakes and folded graphitic sheets due to oxidization with concentrated acid and dispersive forces of the formed surface groups [49, 65]. rGO as well demonstrates the crumpled and wrinkled structure of randomly aggregated sheets. The wrinkled and folded sheet reflects the extent of reduction in which the more crumpled structure the highest achieved reduction degree [46]. After amine modification of GO and rGO, as shown in Fig. 3(c) and (d), the adsorbent still pertains the same morphology of crumpled and randomly aggregated sheets but with higher dense and less flexible solid structure due to amine grafting on the surface. Also, the surface area and pore volume have further reduced as a result of chemical functionalization, which is in good agreement with BET surface area analysis.

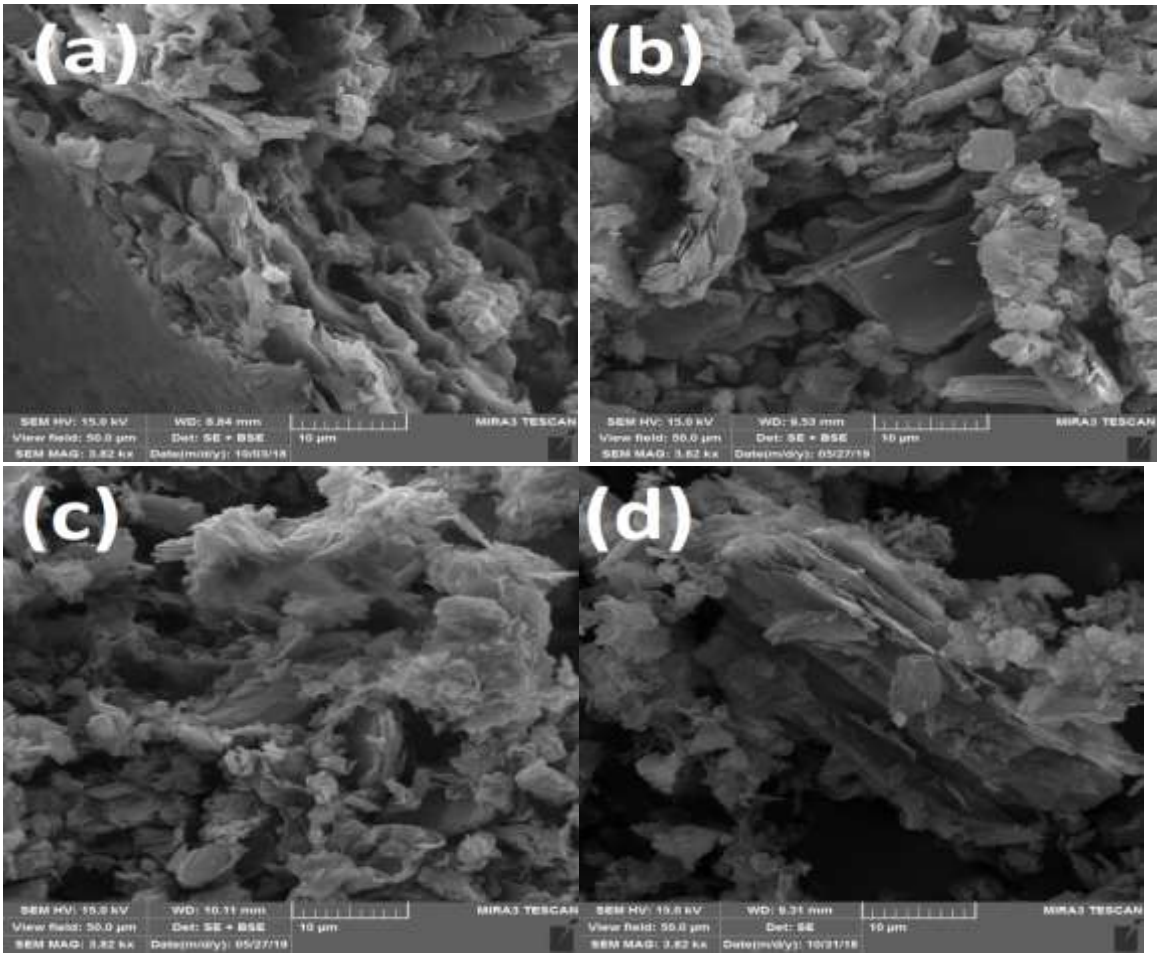


Fig. 3. SEM images of (a) GO, (b) rGO-1, (c) APTS-GO, and (d) APTS-rGO-1.

Table 2 summarizes the elemental composition (C, O, and N) of GO, rGO-1, rGO-2, rGO-3, APTS-GO, DETA-GO, and PEI- GO. As illustrated in Table 2, GO has the highest oxygen content as a result of containing a large number of oxygen functional groups on the surface. After the chemical reduction, carbon content has increased while oxygen has reduced due to the removal of some oxygen functional groups. Concerning the shown result in Table 2, rGO-1 that obtained by Zn/HCl reduction of GO has reached a greater extent of reduction. Regarding the amine-modified GO, including APTS-GO, PEI-GO, and DETA-GO, the existing of nitrogen content has confirmed the successful functionalization of amine. It should be notified that PEI-GO contains higher nitrogen content comparing to DETA-GO and APTS-GO.

Table: 2 Elemental compositions of the synthesized samples.

Samples	C % w/w	O % w/w	N % w/w
GO	57.87	42.13	_
rGO-1	89.4	10.6	_
rGO-2	88.2	11.8	_
rGO-3	85.4	14.6	_
APTS-GO	49.9	39.98	10.12
APTS-rGO-1	86.1	8.3	5.6
DETA-GO	51.51	35.99	12.5
PEI-GO	55.11	26.51	18.38

3.2 The CO_2 adsorption capacity of the synthesized samples

Studying of CO_2 adsorption capacity for the recently founded materials is one of the most reliable parameters to examine the material suitability for CO_2 removal. In the current study, TGA was used to evaluate the CO_2 adsorption extent of all the synthesized adsorbents under 100 ml/min flow of CO_2 for 90 minutes. The experiments conducted at the ambient condition of 30 °C and atmospheric pressure, as shown in Fig. (4-7). The abscissa axis indicates the interval time of CO_2 adsorption, and the ordinate presents the adsorption capacity. However, the evaluation of CO_2 uptake capacity of graphene derivatives based adsorbent has started by comparing the adsorption capacity of GO and rGO-1, as shown in Fig. 4. As a result, the GO has higher adsorption than rGO-1 did with a capacity of 45 mg/g. The considerable difference in adsorption capacity of GO and rGO-1 can be attributed to the existence of oxygen functional groups such as carboxyls and hydroxyls on GO surface that play a part to increase CO_2 adsorption [66, 67]. As well, the higher surface area of GO compared to rGO-1 has also significant influence toward CO_2 capture enhancement. To assess the impact of increasing the basicity of adsorbent surface on CO_2 adsorption, a mass ratio of 1:1 of APTS was grafting over the GO and rGO surfaces. Fig. 5 exhibited the uptake capacity of APTS-GO and APTS-rGO-1. As a result, APTS-GO and APTS-rGO-1 had a significant increase in CO_2 capture up to 63.29 mg/g and 20.62 mg/g, respectively. In this sense, the reason of higher CO_2 adsorption on APTS modified GO, and rGO-1 is not attributed to surface area while it is regarded to the higher affinity of CO_2 to react with amine groups (acid & base interaction) and yields carbamates than the quadrupole-dipole interaction with oxygen functional groups on GO and rGO-1 [68]. According to the obtained result, GO would be more suitable based adsorbent for CO_2 capture. Thus, GO was further considered as a base adsorbent to investigate the influence of different kind of amines on enhancing CO_2 removal.

Fig. 6 compares the adsorption capacity of GO and variants type of amines modified GO, including APTS-GO, DETA-GO, PEI GO, and Hexamine-GO with a mass ratio of 1:1. As a result, both APTS-GO and DETA-GO had shown improvement in CO_2 capture comparing to GO with a capacity of 63.29 mg/g for APTS-GO which is in good agreement with the reported result in literature [49, 65] and DETA-GO has 56.64 mg/g which is higher than the earlier conducted work [69].

On the other hand, both PEI-GO and Hexamine-GO had less uptake capacity of CO_2 in contrast to unmodified GO with a capacity of 17.95 mg/g and 28.99 mg/g respectively. The positive impact of APTS and DETA grafting in increasing GO adsorption capacity and the reverse effect of PEI and

Hexamine impregnation, it can be well explained to the less loss of oxygen functional groups after APTS and DETA modification [49]. Thus, the addition of PEI and hexamine did not compensate for the vast lost in an oxygen functional group, which cause a higher reduction in GO surface that results in less adsorption as observed in APTS-rGO-1. Moreover, the long chain of PEI and high molecular weight of both PEI and Hexamine could restrict the pathway of CO_2 and reduce the adsorption capacity [70]. As APTS-GO was the highest adsorbent capacity among the synthesized amine-modified GO adsorbents, it was further examined to identify the optimum APTS/GO mass ratio of the produced APTS-GO which can have higher adsorption capacity of CO_2.

Fig. 7 shows the adsorption capacity of variants APTS-GO adsorbents prepared by different solution mass ratio including 0.5:1, 1:1, 5:1, 10:1 and 15:1 APTS/GO mass ratio. As a result, only APST-GO with 1:1 and 5:1 mass ratio had better enhancement on CO_2 capture. Thus, the higher mass ratio can restrict the CO_2 pathway as well the GO would be much reduced. For the low mass ratio of APTS/GO, which is 0.5:1 in this study, it seems to be not adequate to compensate for the loss of oxygen functional groups on the GO surface. Therefore, the optimum mass ratio with the highest adsorption capacity has to be a value between 1 and 5.

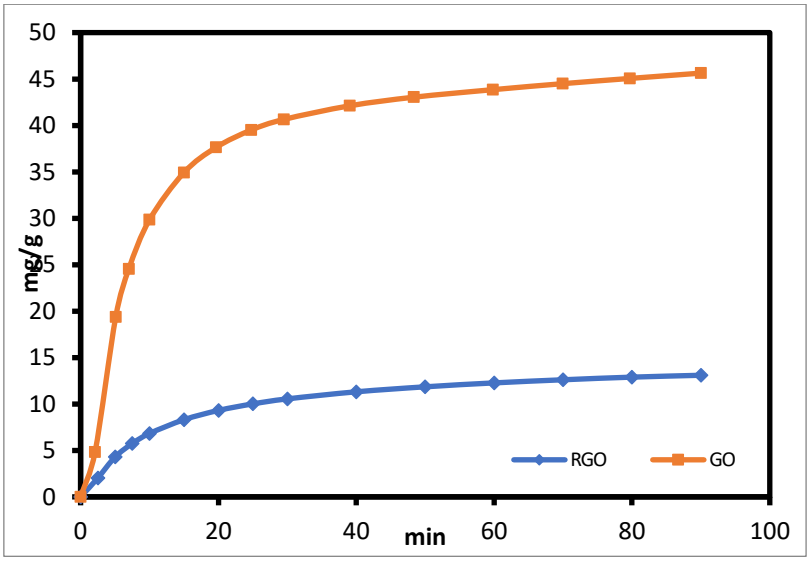


Fig. 4. CO_2 adsorption of graphite oxide and reduced graphite oxide at 30 °C under atmospheric pressure**.**

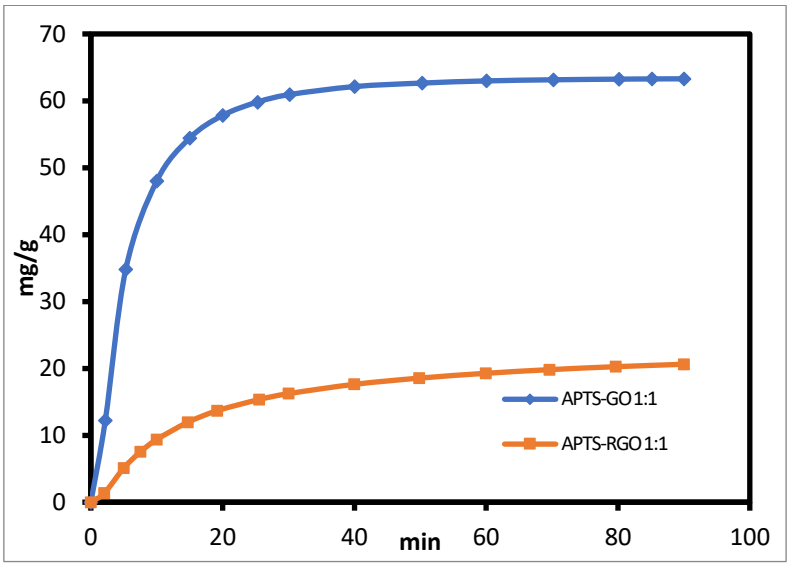


Fig. 5. CO_2 adsorption of APTS-modified graphite oxide and APTS -modified reduced graphite oxide (1:1 amine/ GO ratio) at 30 °C under atmospheric pressure**.**

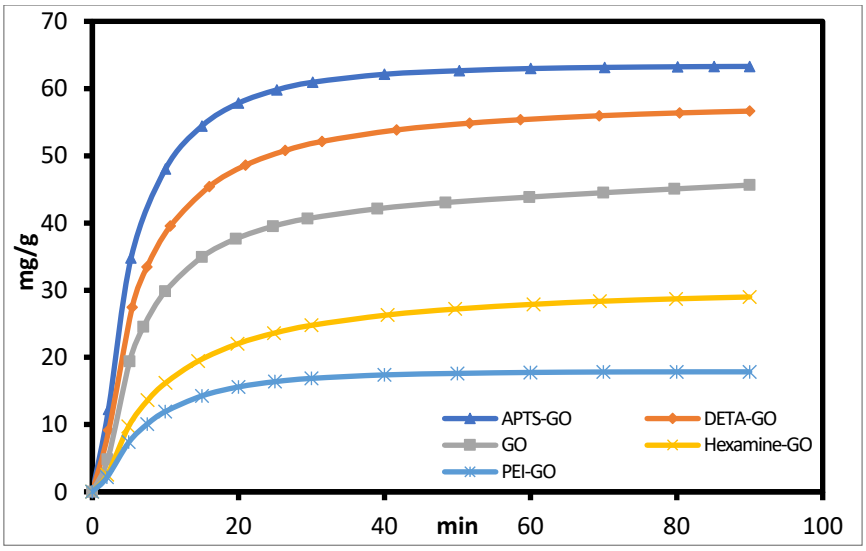


Fig. 6. CO_2 adsorption of graphite oxide, APTS-modified graphite oxide, DETA-modified graphite oxide, Hexamine-modified graphite oxide and PEI-modified graphite oxide at 30 °C under atmospheric pressure.

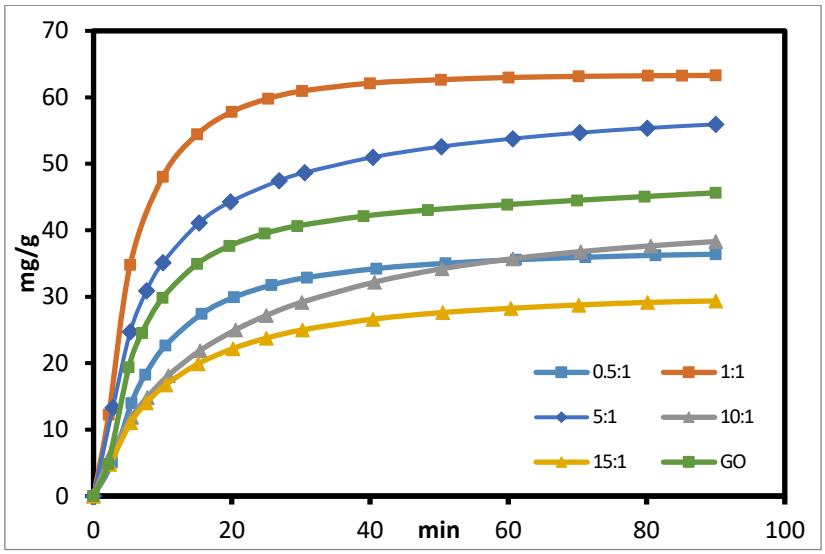


Fig. 7. CO2 adsorption at 30 °C and 1 bar for GO and APTS modified graphite oxide of variants amine/GO ratio.

4. Conclusion

This work was aimed to highlight the efficient utilization of graphene derivatives Nano-composites as base adsorbent of CO_2 capture at ambient operating condition of 30°C and atmospheric pressure. First of all, Graphite oxide was typically produced using hummer modified method through the graphite oxidization by $KMnO_4$ in strong acid. Three reduced graphite oxides were consecutively produced by chemical reduction using Zn powder and Al foil as reducing agent, respectively. As a result, the Zn powder reducing agent shows the highest reduction degree for GO in acidic media. However, the evaluation of GO and rGO capacity for CO_2 capture and the abundance of oxygen functional group on GO surface have shown the suitability of GO as based adsorbent for CO_2 removal. The influence of the basicity and amine modification for the GO surface on the CO_2 uptake capacity was investigated in detail. Four types of amine, including APTS, DETA, PEI, and hexamine with the same mass ratio of amine/GO, were employed separately to modified GO. Among these four synthesized adsorbents, only APTS-GO and DETA-GO have shown an excellent enhancement in the CO_2 uptake capacity comparing to the unmodified GO with a capacity of 63 mg/g and 56 mg/g respectively. Moreover, the effect of APTS dissolved quantities in the APTS/GO solution was studied in detail to identify the optimum APTS/GO mass ratio. Results indicate that the optimum ratio has to be in the range of 1to 5.

Acknowledgment: This work was supported by the Deanship of Research Oversight and Coordination (DROC) at King Fahd University of Petroleum and Minerals (KFUPM) in the terms of Internal Research Grant # DF191027.

References

1. T.-L. Chew, A.L. Ahmad, S. Bhatia, Ordered mesoporous silica (OMS) as an adsorbent and membrane for separation of carbon dioxide (CO2), Advances in Colloid and Interface Science, 153 (2010) 43-57.
2. C.H. Yu, C.H. Huang, C.S. Tan, A Review of CO2 Capture by Absorption and Adsorption, Aerosol and Air Quality Research, 12 (2012) 745-769.

3. A.A. Olajire, CO2 capture and separation technologies for end-of-pipe applications energy 35 (2010) 2610-2628.
4. R. Strube, G. Pellegrini, G. Manfrida, The environmental impact of post-combustion CO2 capture with MEA, with aqueous ammonia, and with an aqueous ammonia-ethanol mixture for a coal-fired power plant, Energy, 36 (2011) 3763-3770.
5. P. Luis, Use of monoethanolamine (MEA) for CO2 capture in a global scenario: Consequences and alternatives, Desalination, 380 (2016) 93-99.
6. G. Gómez-Pozuelo, E.S. Sanz-Pérez, A. Arencibia, P. Pizarro, R. Sanz, D.P. Serrano, CO2 adsorption on amine-functionalized clays, Microporous and Mesoporous Materials, 282 (2019) 38-47.
7. P.J.G. Huttenhuis, N.J. Agrawal, J.A. Hogendoorn, G.F. Versteeg, Gas solubility of H2S and CO2 in aqueous solutions of N-methyldiethanolamine, Journal of Petroleum Science and Engineering, 55 (2007) 122-134.
8. H. Zare Aliabad, S. Mirzaei, Removal of CO2 and H2S using Aqueous Alkanolamine Solusions, World Academy of Science, Engineering and Technology, 3 (2009) 50-59.
9. E.B. Rinker, S.S. Ashour, O.C. Sandall, Absorption of carbon dioxide into aqueous blends of diethanolamine and methyldiethanolamine, Industrial & engineering chemistry research, 39 (2000) 4346-4356.
10. K. Maqsood, A. Mullick, A. Ali, K. Kargupta, S. Ganguly, Cryogenic carbon dioxide separation from natural gas: A review based on conventional and novel emerging technologies, Reviews in Chemical Engineering, 30 (2014) 453-477
11. H. Bamdad, K. Hawboldt, S. MacQuarrie, A review on common adsorbents for acid gases removal: Focus on biochar, Renewable and Sustainable Energy Reviews, 81 (2018) 1705-1720.
12. F.D. Lamari, P. Langlois, M. Dicko, C. Chile, C. Chilev, I. Pentchev, CARBON DIOXIDE CAPTURE BY ADSORPTION, Journal of Chemical Technology and Metallurgy, 51 (2016) 609-626.
13. G. George, N. Bhoria, S. AlHallaq, A. Abdala, V. Mittal, Polymer membranes for acid gas removal from natural gas, Separation and Purification Technology, 158 (2016) 333-356.
14. B. Belaissaoui, E. Favre, Membrane Separation Processes for Post-Combustion Carbon Dioxide Capture: State of the Art and Critical Overview, Oil Gas Sci. Technol. – Rev. IFP Energies nouvelles, 69 (2014) 1005-1020.
15. S. Choi, J.H. Drese, C.W. Jones, Adsorbent Materials for Carbon Dioxide Capture from Large Anthropogenic Point Sources, ChemSusChem, 2 (2009) 796-854.
16. X. Liu, J. Li, L. Zhou, D. Huang, Y. Zhou, Adsorption of CO2, CH4 and N2 on ordered mesoporous silica molecular sieve, Chemical Physics Letters, 415 (2005) 198-201.
17. S.-H. Liu, Y.-C. Lin, Y.-C. Chien, H.-R. Hyu, Adsorption of CO2 from Flue Gas Streams by a Highly Efficient and Stable Aminosilica Adsorbent, Journal of the Air & Waste Management Association, 61 (2011) 226-233.
18. M.M. Maroto-Valer, Z. Tang, Y. Zhang, CO2 capture by activated and impregnated anthracites, Fuel Processing Technology, 86 (2005) 1487-1502.
19. M.C. Castrillon, K.O. Moura, C.A. Alves, M. Bastos-Neto, D.C.S. Azevedo, J. Hofmann, J. Möllmer, W.-D. Einicke, R. Gläser, CO2 and H2S Removal from CH4-Rich Streams by Adsorption on Activated Carbons Modified with K2CO3, NaOH, or Fe2O3, Energy & Fuels, 30 (2016) 9596-9604.
20. L. Li, X. Wen, X. Fu, F. Wang, N. Zhao, F. Xiao, W. Wei, Y. Sun, MgO/Al2O3 Sorbent for CO2 Capture, Energy & Fuels, 24 (2010) 5773-5780.
21. A. Hakim, T.S. Marliza, N.M. Abu Tahari, R.W.N. Wan Isahak, R.M. Yusop, W.M. Mohamed Hisham, A.M. Yarmo, Studies on CO2 Adsorption and Desorption Properties from Various

Types of Iron Oxides (FeO, Fe2O3, and Fe3O4), Industrial & Engineering Chemistry Research, 55 (2016) 7888-7897.
22. T. Remy, S.A. Peter, S. Van der Perre, P. Valvekens, D.E. De Vos, G.V. Baron, J.F.M. Denayer, Selective Dynamic CO2 Separations on Mg-MOF-74 at Low Pressures: A Detailed Comparison with 13X, The Journal of Physical Chemistry C, 117 (2013) 9301-9310.
23. S. Couck, J.F.M. Denayer, G.V. Baron, T. Rémy, J. Gascon, F. Kapteijn, An Amine-Functionalized MIL-53 Metal−Organic Framework with Large Separation Power for CO2 and CH4, Journal of the American Chemical Society, 131 (2009) 6326-6327.
24. B. Wang, J. Park, C. Wang, H. Ahn, G. Wang, Mn3O4 nanoparticles embedded into graphene nanosheets: Preparation, characterization, and electrochemical properties for supercapacitors, Electrochimica Acta, 55 (2010) 6812-6817.
25. T.S. Sreeprasad, S.M. Maliyekkal, K.P. Lisha, T. Pradeep, Reduced graphene oxide–metal/metal oxide composites: Facile synthesis and application in water purification, Journal of Hazardous Materials, 186 (2011) 921-931.
26. C. Wang, J. Zhu, S. Liang, H. Bi, Q. Han, X. Liu, X. Wang, Reduced graphene oxide decorated with CuO–ZnO hetero-junctions: towards high selective gas-sensing property to acetone, Journal of Materials Chemistry A, 2 (2014) 18635-18643.
27. N. Li, M. Zheng, X. Chang, G. Ji, H. Lu, L. Xue, L. Pan, J. Cao, Preparation of magnetic CoFe2O4-functionalized graphene sheets via a facile hydrothermal method and their adsorption properties, Journal of Solid State Chemistry, 184 (2011) 953-958.
28. A.K. Geim, K.S. Novoselov, The rise of graphene, Nature Materials, 6 (2007) 183.
29. J.G.S. Moo, B. Khezri, R.D. Webster, M. Pumera, Graphene Oxides Prepared by Hummers', Hofmann's, and Staudenmaier's Methods: Dramatic Influences on Heavy-Metal-Ion Adsorption, ChemPhysChem, 15 (2014) 2922-2929.
30. F. Pendolino, N. Armata, Synthesis, Characterization and Models of Graphene Oxide, in: F. Pendolino, N. Armata (Eds.) Graphene Oxide in Environmental Remediation Process, Springer International Publishing, Cham, 2017, pp. 5-21.
31. B.C. Brodie, F.R. S., XIII. On the atomic weight of graphite, Phil. Trans. R. Soc. Lond., 19 (1859) 249-259.
32. S. Stankovich, D.A. Dikin, R.D. Piner, K.A. Kohlhaas, A. Kleinhammes, Y. Jia, Y. Wu, S.T. Nguyen, R.S. Ruoff, Synthesis of graphene-based nanosheets via chemical reduction of exfoliated graphite oxide, Carbon, 45 (2007) 1558-1565.
33. H.-J. Shin, K.K. Kim, A. Benayad, S.-M. Yoon, H.K. Park, I.-S. Jung, M.H. Jin, H.-K. Jeong, J.M. Kim, J.-Y. Choi, Y.H. Lee, Efficient Reduction of Graphite Oxide by Sodium Borohydride and Its Effect on Electrical Conductance, Advanced Functional Materials, 19 (2009) 1987-1992.
34. J.-L. Shi, W.-C. Du, Y.-X. Yin, Y.-G. Guo, L.-J. Wan, Hydrothermal reduction of three-dimensional graphene oxide for binder-free flexible supercapacitors, Journal of Materials Chemistry A, 2 (2014) 10830-10834.
35. X. Zhang, X. Sun, Y. Chen, D. Zhang, Y. Ma, One-step solvothermal synthesis of graphene/Mn3O4 nanocomposites and their electrochemical properties for supercapacitors, Materials Letters, 68 (2012) 336-339.
36. S. Dubin, S. Gilje, K. Wang, V.C. Tung, K. Cha, A.S. Hall, J. Farrar, R. Varshneya, Y. Yang, R.B. Kaner, A One-Step, Solvothermal Reduction Method for Producing Reduced Graphene Oxide Dispersions in Organic Solvents, ACS Nano, 4 (2010) 3845-3852.
37. S.J. An, Y. Zhu, S.H. Lee, M.D. Stoller, T. Emilsson, S. Park, A. Velamakanni, J. An, R.S. Ruoff, Thin Film Fabrication and Simultaneous Anodic Reduction of Deposited Graphene Oxide Platelets by Electrophoretic Deposition, The Journal of Physical Chemistry Letters, 1 (2010) 1259-1263.

38. Z. Wang, X. Zhou, J. Zhang, F. Boey, H. Zhang, Direct Electrochemical Reduction of Single-Layer Graphene Oxide and Subsequent Functionalization with Glucose Oxidase, The Journal of Physical Chemistry C, 113 (2009) 14071-14075.
39. H.C. Schniepp, J.-L. Li, M.J. McAllister, H. Sai, M. Herrera-Alonso, D.H. Adamson, R.K. Prud'homme, R. Car, D.A. Saville, I.A. Aksay, Functionalized Single Graphene Sheets Derived from Splitting Graphite Oxide, The Journal of Physical Chemistry B, 110 (2006) 8535-8539.
40. Z.-S. Wu, W. Ren, L. Gao, J. Zhao, Z. Chen, B. Liu, D. Tang, B. Yu, C. Jiang, H.-M. Cheng, Synthesis of Graphene Sheets with High Electrical Conductivity and Good Thermal Stability by Hydrogen Arc Discharge Exfoliation, ACS Nano, 3 (2009) 411-417.
41. X. Wang, L. Zhi, K. Müllen, Transparent, Conductive Graphene Electrodes for Dye-Sensitized Solar Cells, Nano Letters, 8 (2008) 323-327.
42. Y. Zhu, S. Murali, M.D. Stoller, A. Velamakanni, R.D. Piner, R.S. Ruoff, Microwave assisted exfoliation and reduction of graphite oxide for ultracapacitors, Carbon, 48 (2010) 2118-2122.
43. L. Shahriary, A. Athawale, Graphene oxide synthesized by using modified Hummers approach, Renew. Energy Environ. Eng., 2 (2014) 58-63.
44. S.M. Hong, K.B. Lee, Solvent-assisted amine modification of graphite oxide for CO2 adsorption, RSC Advances, 4 (2014) 56707-56712.
45. X. Mei, J. Ouyang, Ultrasonication-assisted ultrafast reduction of graphene oxide by zinc powder at room temperature, Carbon, 49 (2011) 5389-5397.
46. V.H. Pham, H.D. Pham, T.T. Dang, S.H. Hur, E.J. Kim, B.S. Kong, S. Kim, J.S. Chung, Chemical reduction of an aqueous suspension of graphene oxide by nascent hydrogen, Journal of Materials Chemistry, 22 (2012) 10530-10536.
47. Rattana, S. Chaiyakun, N. Witit-anun, N. Nuntawong, P. Chindaudom, S. Oaew, C. Kedkeaw, P. Limsuwan, Preparation and characterization of graphene oxide nanosheets, Procedia Engineering, 32 (2012) 759-764.
48. Y. Liu, B. Sajjadi, W.-Y. Chen, R. Chatterjee, Ultrasound-assisted amine functionalized graphene oxide for enhanced CO2 adsorption, Fuel, 247 (2019) 10-18.
49. J. Pokhrel, N. Bhoria, S. Anastasiou, T. Tsoufis, D. Gournis, G. Romanos, G.N. Karanikolos, CO2 adsorption behavior of amine-functionalized ZIF-8, graphene oxide, and ZIF-8/graphene oxide composites under dry and wet conditions, Microporous and Mesoporous Materials, 267 (2018) 53-67.
50. S. Yan, Y. Yang, L. Song, X. Qi, Y. Xue, B. Fan, Influence of 3-aminopropyltriethoxysilane-graphite oxide composite on thermal stability and mechanical property of polyethersulfone, High Performance Polymers, 29 (2016) 960-975.
51. Y. Matsuo, Y. Nishino, T. Fukutsuka, Y. Sugie, Introduction of amino groups into the interlayer space of graphite oxide using 3-aminopropylethoxysilanes, Carbon, 45 (2007) 1384-1390.
52. A. Huang, B. Feng, Facile synthesis of PEI-GO@ZIF-8 hybrid material for CO2 capture, International Journal of Hydrogen Energy, 43 (2018) 2224-2231.
53. G.-J. Shin, K. Rhee, S.-J. Park, Improvement of CO2 capture by graphite oxide in presence of polyethylenimine, International Journal of Hydrogen Energy, 41 (2016) 14351-14359.
54. Q. Huang, H.J. Sun, T.J. Peng, The Influence of Temperature and Oxidation Time on the Preparation of Graphite Oxide, Advanced Materials Research, 366 (2012) 291-295.
55. P. Liu, Y. Huang, L. Wang, A facile synthesis of reduced graphene oxide with Zn powder under acidic condition, Materials Letters, 91 (2013) 125-128.
56. Z. Fan, K. Wang, T. Wei, J. Yan, L. Song, B. Shao, An environmentally friendly and efficient route for the reduction of graphene oxide by aluminum powder, Carbon, 48 (2010) 1686-1689.
57. L. Stobinski, B. Lesiak, A. Malolepszy, M. Mazurkiewicz, B. Mierzwa, J. Zemek, P. Jiricek, I. Bieloshapka, Graphene oxide and reduced graphene oxide studied by the XRD, TEM and

electron spectroscopy methods, Journal of Electron Spectroscopy and Related Phenomena, 195 (2014) 145-154.
58. M. Khan, A.H. Al-Marri, M. Khan, M.R. Shaik, N. Mohri, S.F. Adil, M. Kuniyil, H.Z. Alkhathlan, A. Al-Warthan, W. Tremel, M.N. Tahir, M.R.H. Siddiqui, Green Approach for the Effective Reduction of Graphene Oxide Using Salvadora persica L. Root (Miswak) Extract, Nanoscale Research Letters, 10 (2015) 281-290.
59. S.-M. Hong, S.H. Kim, K.B. Lee, Adsorption of Carbon Dioxide on 3-Aminopropyl-Triethoxysilane Modified Graphite Oxide, Energy & Fuels, 27 (2013) 3358-3363.
60. J. Li, B. Michalkiewicz, J. Min, C. Ma, X. Chen, J. Gong, E. Mijowska, T. Tang, Selective preparation of biomass-derived porous carbon with controllable pore sizes toward highly efficient CO2 capture, Chemical Engineering Journal, 360 (2019) 250-259.
61. J. Serafin, U. Narkiewicz, A.W. Morawski, R.J. Wróbel, B. Michalkiewicz, Highly microporous activated carbons from biomass for CO2 capture and effective micropores at different conditions, Journal of CO2 Utilization, 18 (2017) 73-79.
62. Y. Zhang, Y. Chi, C. Zhao, Y. Liu, Y. Zhao, L. Jiang, Y. Song, CO2 Adsorption Behavior of Graphite Oxide Modified with Tetraethylenepentamine, Journal of Chemical & Engineering Data, 63 (2018) 202-207.
63. T. Strachowski, M. Woluntarski, M. Djas, K. Kowiorski, Z. Wiliński, M. Baran, J. Jagiełło, M. Winkowska, L. Lipińska, the influence of reducing agents on the reduced graphene oxide specific surface area determined on the basis of nitrogen adsorption isotherm, Electronic Materials, 45 (2017) 2-4.
64. W. Hooch Antink, Y. Choi, K.-d. Seong, J.M. Kim, Y. Piao, Recent Progress in Porous Graphene and Reduced Graphene Oxide-Based Nanomaterials for Electrochemical Energy Storage Devices, Advanced Materials Interfaces, 5 (2018) 1-19.
65. S.-M. Hong, S.H. Kim, a.K.B. Lee, Adsorption of Carbon Dioxide on 3-Aminopropyl-Triethoxysilane Modified Graphite Oxide, energy & fuels, 27 (2013) 3358-3363.
66. S. Furmaniak, P. Kowalczyk, A.P. Terzyk, P.A. Gauden, P.J.F. Harris, Synergetic effect of carbon nanopore size and surface oxidation on CO2 capture from CO2/CH4 mixtures, Journal of Colloid and Interface Science, 397 (2013) 144-153.
67. Y. Liu, J. Wilcox, Effects of Surface Heterogeneity on the Adsorption of CO2 in Microporous Carbons, Environmental Science & Technology, 46 (2012) 1940-1947.
68. J.H. Lee, H.J. Lee, J.W. Choi, Unveiling anomalous CO2-to-N2 selectivity of graphene oxide, Physical Chemistry Chemical Physics, 19 (2017) 22743-22748.
69. Y. Zhao, H. Ding, Q. Zhong, Preparation and characterization of aminated graphite oxide for CO2 capture, Applied Surface Science, 258 (2012) 4301-4307.
70. Z. Liu, D. Pudasainee, Q. Liu, R. Gupta, Post-combustion CO2 capture using polyethyleneimine impregnated mesoporous cellular foams, Separation and Purification Technology, 156 (2015) 259-268.

Co-catalyzed with MIL-47 (V) metal organic framework and carbon nanotubes for an enhanced Mgh_2 hydrogen sorption performance

Atikah Kadri [1,*], Jia Yi [2] and Yao XiangDong [2,]

[1] School of Chemical Engineering, College of Engineering, Universiti Teknologi MARA, 40450 Shah Alam, Selangor, Malaysia;
[2] Queensland Micro and Nanotechnology Centre, Griffith University, 170 Kessels Road, Brisbane, 4111, Queensland, Australia;
***** *Corresponding author: atikahkadri@uitm.edu.my; Tel.: +60104609616.*

Abstract: The potential of Metal Organic Framework (MOF) and carbon nanotubes (CNTs) as catalyst in magnesium hydride storage system was investigated by combining MIL-47 (V) with CNTs in MgH2 prepared by high energy ball milling technique. The composites exhibited a significantly low temperature for both hydrogen absorption and desorption where the best hydrogen absorption rate of 4.3 wt% and released of 4.0 wt% of hydrogen within 10 minutes at 100 ºC and 280 ºC respectively. The desorption thermodynamics properties were also investigated, and the composites show a reduction in enthalpy and entropy due to the synergistic effect of both MIK-47(V) and CNTs. The absorption and desorption cyclic stability of the composites demonstrated an excellent reversibility of 6 wt% of hydrogen absorbed and released after 6 cycles. These results confirm that co-catalyzing MOF and CNTs can be an excellent candidate as a hydrogen storage catalyst in magnesium-based nanocomposites.

Keywords: hydrogen storage; magnesium hydride; metal organic framework; carbon nanotube

1. Introduction

The development of a safe, efficient, and economical hydrogen storage system is still a challenge in practical mobile application. Storing hydrogen in metal hydride particularly in magnesium hydride (MgH2) is one of the promising modes of storage due to high gravimetric (7.6 wt% of hydrogen) and volumetric (110 kg/m3) densities on top of its excellent reversibility as well as low in cost. However, the major drawback in practical application of such material is due to its sluggish hydrogenation/dehydrogenation kinetics as well as high operational temperature. This is attributed to the fact that there is a very strong ionic bonding between magnesium and hydrogen thus requires a bulk MgH2 decomposition enthalpy of about 75 kJ/mol H2, which corresponds to a desorption temperature of 300°C at 1 bar [1].

Numerous of research efforts have been reported in the literature to improve MgH2 hydrogen storage properties, amongst the strategies are by reducing MgH2 particle size [2, 3] and adding catalytic additives which serve as active sites [4, 5]. A wide range of transition metals [6], oxides [7-10] and metal halides [11-13] have been demonstrated to be effective for enhancing the de/hydrogenation kinetics when ball milled with Mg to form nanocomposites. On the other hand, the unique characteristics of combining carbon materials in hydrogen storage material have drawn interest amongst research groups and this topic was recently reviewed in detail [14, 15]. Amirkhiz et al. [16] have studied the performance of 1 hour co-milling MgH2 with unpurified CNTs containing 10% metallic nanoparticles. The researchers found that at longer co-milling time, the CNTs were completely destroyed, and the enhancement was largely lost. The positive traits of single-walled carbon nanotubes (CNTs) in a MgH2 system are said not to alter the microstructure but rather act as a surface dispersant and/or 'hydrogen pump' in the composites [17]. An investigation in combining TiFe and CNTs discovered that the main role of TiFe is to promote the hydrogen dissociation/combination, whereas the presence of CNTs preserve the reversibility property of the composite by avoiding the Mg/MgH2 particles from aggregating [18]. In our previous work [19] we

reported the synergistic effect of combining partially destroyed CNTs and vanadium-based catalyst which enhanced the hydrogen sorption performance.

Recent substantial progress has been made in utilizing metal-organic frameworks (MOFs) as hydrogen storage material via physisorption [20-23]. Owing to the hybrid architecture, it is anticipated to create large pore volume and surface area to promote the capture and/or regeneration of hydrogen. Furthermore, MOFs possess a large density of active sites in which the constitutional metal node has free or exchangeable coordination positions and the high porosity draw a large potential for MOFs in solid catalysts application [24-26]. The use of MOFs as an additive in the MgH2 system is motivated by the fact that the unique structure of the MOFs which contains metals - particularly transition metals, which are known in providing catalytic effect in a MgH2 based storage systems. To the best of our knowledge, no studies devoted to the sorption properties of MgH2 have tackled the use of MOFs as additives. In the present work, the effects of MOFs of Vanadium (MIL-47(V)) and CNTs on sorption performance in MgH2 are systematically investigated, and the results show that enhanced kinetics and high capacity are both achieved in Mg-based nanocomposites at low temperatures. A plausible synergetic effect of MIL-47(V) and CNTs on the de/hydrogenenation on MgH2 will be presented and discussed.

2. Materials and Methods

2.1. Synthesis of MIL-47(V)

The preparation of MIL-47(V) was based on a literature procedure [27]. Typically, a mixture of vanadium (III) chloride (VCl3, Sigma Aldrich, 97%), terephthalic acid (TPA, C6H4-1,4-(CO2H)2; Sigma Aldrich, 98%) and deionised water with a molar ratio of 1:0.25:100 is heated in teflon-lined steel autoclave at 200 oC for four days. The resulting solid was washed with water, N,N-dimethylformamide (DMF) and acetone followed by drying under vacuum at 115oC for one hour to remove all moisture that may present. The final light yellow powder was kept in an argon-filled glove box (MBraun) to protect against moisture.

2.2. Synthesis of MgH2 based nanosomposites

The MgH2 composites were prepared by pre-milling MgH2 (hydrogen storage grade - purchased from Sigma-Aldrich) in a sealed vial of high energy SPEX 8000 vibration ball mill under argon atmosphere for 2 hours. The synthesized MIL-47(V) and/or CNTs (prepared and purified in our laboratory) were then introduced to the pre-milled MgH2 and the composites were subjected to an additional 2 hours milling time. The amount of the additives introduced to MgH2 was kept at 5 wt% each and 40:1, ball to powder ratio was used in all samples preparation. Samples are noted as the followings: pre-milled MgH2 + MIL-47(V) (denoted as M2Vf2), pre-milled MgH2 + CNTs (denoted as M2cnt2) and pre-milled MgH2 + MIL-47(V) + CNTs (denoted as M2Vfcnt2). For comparison purposes, MgH2 powder was milled in a similar total milling time of 4 hours and is denoted as M4. All sample handling was performed in an argon-filled glove box in which the water and oxygen level were kept below 1 ppm.

2.3 Characterization

The microstructure of the samples was characterized by X-ray diffraction (XRD, Rigaku) with Co Kα radiation at scanning rate of 2°/min. The N2 adsorption was performed at 77 K using TriStar II 3020. The morphology and composition of the samples were further analyzed by employing a transmission electron microscope (TEM, FEI F20) equipped with energy dispersive X-ray spectrometry (EDXs). The samples were prepared by dipping a TEM substrate (consisting of a holey carbon film on a copper grid) in pre-sonicated octane sample mixture. The XPS data was acquired using a Kratos Axis ULTRA X-ray photoelectron spectrometer incorporating a 165 mm hemispherical electron energy analyzer. The incident radiation was monochromatic Al Kα X-rays (1486.6 eV) at 225 W (15 kV, 15 mA) and at 45° to the sample surface. Photoelectron data was

collected at take off angle of θ = 90°. Survey (wide) scans were taken at analyzer pass energy of 160 eV and since the amount of vanadium in the composite is so little, the multiplex narrow scans of V 2p, O 1s and C 1s are taken at a pass energy of 80 eV with at least 6 sweeps. Survey scans were carried out over 1200 – 0 eV binding energy range with 1.0 eV steps and a dwell time of 100ms. In the meantime the narrow scans were run with 0.1eV steps and 250 ms dwell time. Base pressure in the analysis chamber was 1.0 x 10-9 torr and during sample analysis 1.0 x 10-8 torr.

All hydrogenation measurements of the milled powders were evaluated using an automated Sieverts apparatus (Suzuki Shokan PCT H2 Absorption Rig). The absorption and desorption tests were performed under an initial pressure of 2.0 MPa and 1 KPa respectively at various temperatures following a complete dehydrogenation and hydrogenation cycle. Non-isothermal hydrogen desorption of the samples was investigated by temperature program control desorption with mass spectrometry (TPD-MS), which is attached with a quartz reactor in a tube furnace. The temperature was raised from room temperature to 500 °C at the rate of 5 °C/min, with Ar as carrier gas at a rate of 50 mL/min.

3. Results and Discussion

3.1. Characterization of prepared MIL-47(V)

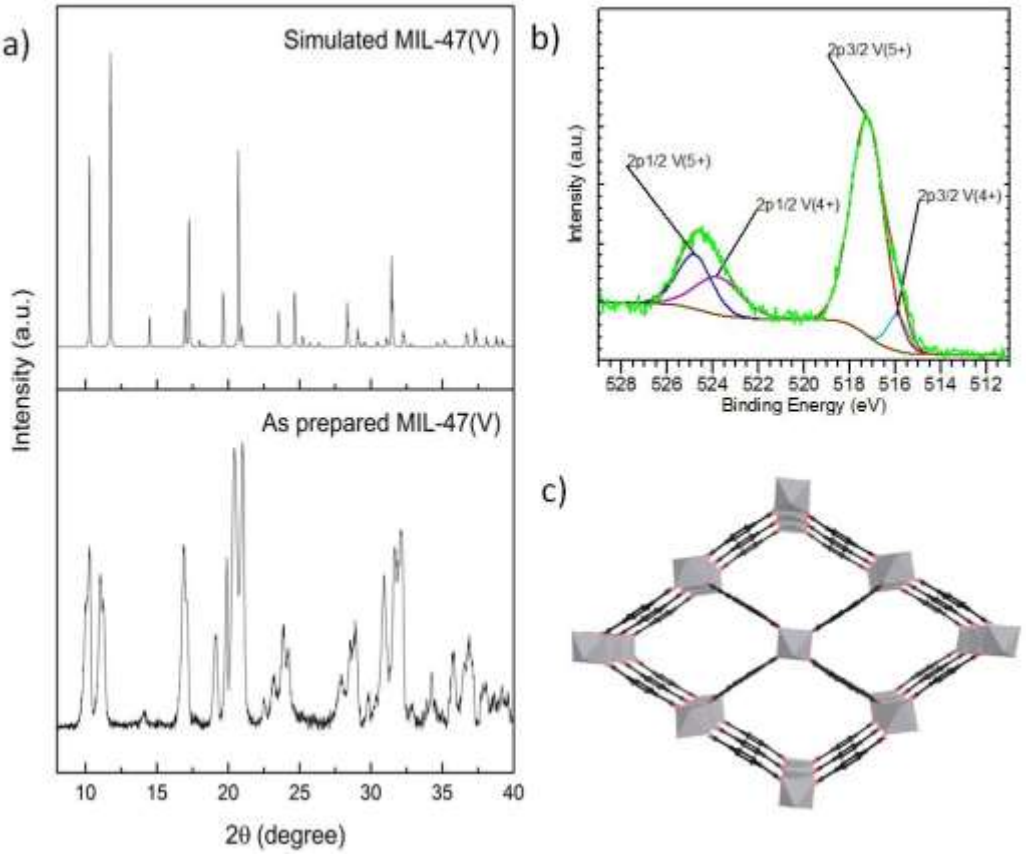


Figure 1. Images for MIL-47(V) of a) XRD pattern of simulated and as-prepared, b) Narrow scan XPS spectra of V2p, c) Typical 3D scheme: Grey = vanadium, Black = carbon and Red = oxygen while hydrogen has been omitted for clarity.

Figure 1 show the structure characterization of the as-synthesized MIL-47(V). Comparison of the sample XRD patterns to the pattern simulated from the published MIL-47(V) [29] structure data indicates that the product is pure-phase MIL-47(V) material (Figure 1a)). The surface chemical

composition and valence states of the as synthesized MIL-47(V) were identified by XPS. As shown in Figure 1b), the V2p spectrum exhibits a 3/2-1/2 spin orbit doublet of two oxidation states. One doublet at binding energy of 515.2(V2p3/2) and 523.7 eV (V2p1/2) corresponds to VO2 (V4+), whereas the other doublet at higher binding energies of 517.2 (V2p3/2) and 524.7 eV (V2p1/2) corresponds to V2O5 (V5+) [28, 29]. It is noteworthy that there is no 0 state present in the sample and a typical 3-dimension scheme of MIL-47(V) is shown in Figure 1c).

3.2. Characterization of MgH2 based nanocomposites

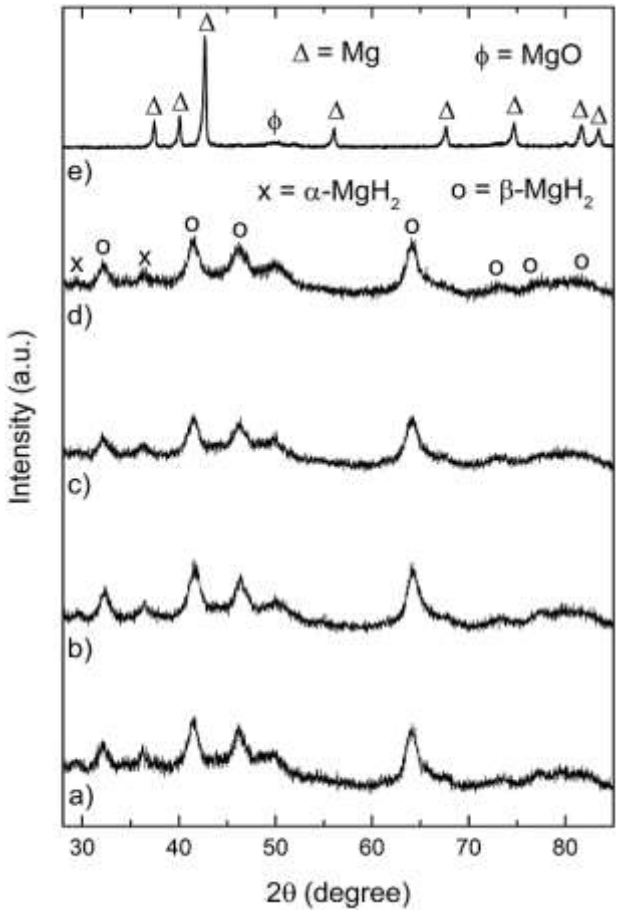


Figure 2. XRD profile for as-milled a) M4, b) M2cnt2, c) M2Vf2, d) M2Vfcnt2 and dehydrogenated e) M2Vfcnt2.

Figure 2 shows the XRD patterns of all the MgH2 composites in as milled and M2Vfcnt2 at dehydrogenated states. In the case of the as-milled sample, the most intense Bragg peaks are identified as tetragonal β-MgH2 (PDF 12-0697), and a meta-stable orthorhombic phase γ-MgH2 (PDF 35-1184) also can be observed, which has been previously reported to form upon milling MgH2 [30, 31]. In the dehydrogenated sample, the most observed peaks are from Mg (PDF 41-1443) and small peak of MgO (PDF 45-0946) was detected in all samples, which is likely due to the slight oxygen contamination during the XRD measurement. It is also noteworthy that there is no peak that indicates formation of new phase as a result of reaction between MgH2 and CNTs and/or MIL-47(V) being observed. It is also observed that no peak of CNTs as well as MIL-47(V) can be observed in all as-milled composites, indicating both CNTs and MIL-47(V) are well incorporated or dispersed in the prepared MgH2 based composites. Several reports have been published on the effect of ball milling on CNTs which also demonstrate the planar structure is severely damaged during long period of milling [32-34]. Nevertheless the tubular structure may be retained by applying shorter milling time [16, 32]. After 4 hours milling, all the as-milled MgH2 composites showed a broaden diffraction

peaks and the effects observed are resulting from plastic deformation, re-crystallization, fracturing and cold welding of material [35]. The grain size of host MgH2 in all as-milled samples were estimated to be about 10 nm from the modified Scherrer equation thus suggested that the additives does not affect the diffraction patterns in any appreciable way.

To further investigate the microstructure and composition of as-milled M2Vfcnt2 nanocomposite, the TEM bright field mode combining with energy dispersive X-ray spectrometry (EDXs) were employed. As shown in Figure 3a), the observed grain sizes of MgH2 are in the range of less than 10 nm that agrees well with the XRD estimation. Several authors demonstrated that reducing the grain size of Mg to the nanoscale range decreased the hydrogen desorption temperature [8, 36]. Thus excellent sorption properties are expected from the prepared samples. Moreover, the EDXs element analyses are performed on the same sample to observe the dispersion of MIL-47(V) in the synthesized composites and are shown in Figure 3b), which shows vanadium element existing in different selected spots in the M2Vfcnt2 matrix, suggesting that the MIL-47(V) segments are well distributed in the as-synthesized M2Vfcnt2 composite after ball milling.

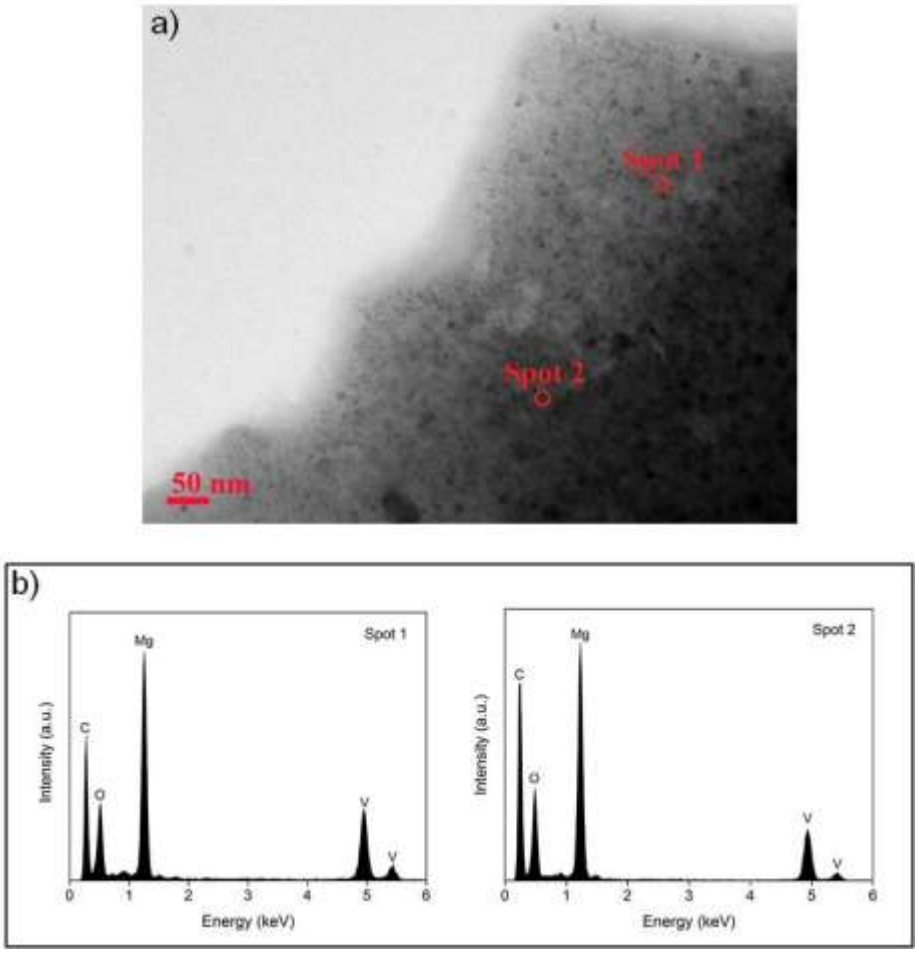


Figure 3. Images for M2Vfcnt2 of a) TEM dark field and b) EDX element analysis correspond to spots on a).

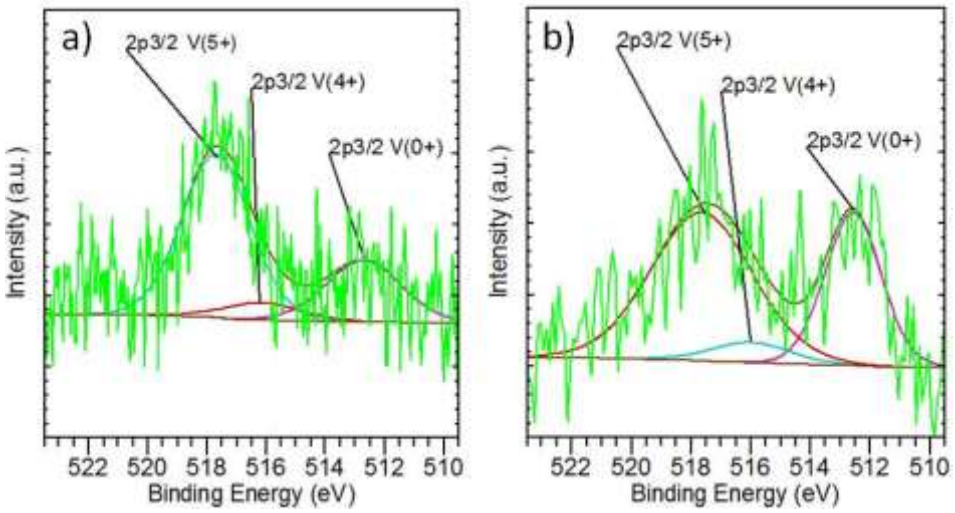


Figure 4. Narrow scans XPS spectra of V2p of a) as-milled and b) re-hydrogenated M2Vfcnt2.

The XPS V2p spectrum of 3/2 spin orbital of as-milled MgH2 composite (M2Vfcnt2) shows that there are three peaks at 517.5, 516.1 and 512.6 eV correspond to V2O5 (V5+), VO2(V4+) and V (V0+), respectively (Figure 4a)). The reduction of vanadium oxide may be ascribed to the effect of high milling energy impact on MgH2 during the milling process, which also allows the ball milling-induced vanadium metal species in MIL-47(V) being distributed amongst MgH2 matrix to contact with MgH2 crystallites intimately. The existence of vanadium metal is even obvious in re-hydrogenated sample as shown in Figure 4b). Further reduction of the oxide of vanadium takes place when the composite is subjected under hydrogen atmosphere during re-hydrogenation process. Since there is no new phase observed after the milling, we speculate that the well-distributed metal species, which are intimately in contact with the partially destroyed CNTs enhanced the hydrogen sorption performance of the composites.

3.3. Absorption

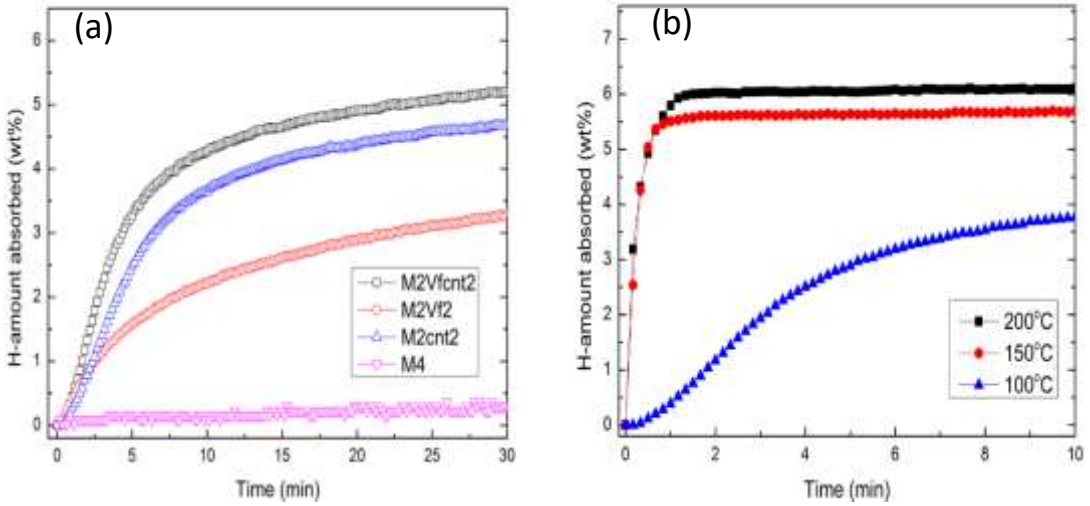


Figure 5. Hydrogen absorption (a) at 100 °C based on Mg of M2Vfcnt2, M2Vf2, M2cnt2 & M4, respectively and (b) at 200, 150 & 100 °C, respectively based on composite of M2Vfcnt2.

The operating temperature of the hydrogen storage material determines the practicality in mobile applications. Figure 5a) shows the comparison of absorption kinetics at 100 °C of M2Vfcnt2, M2Vf2,

M2cnt2 and M4, respectively. As can be noted that the combination of MIL-47(V) and CNTs exhibits the best hydrogen absorption property with 4.3 wt% absorbed in 10 minutes compared to 3.7 wt% and 2.2 wt% in M2cnt2 and M2Vf2 respectively, indicating the coupling MIL-47(V) and CNTs has a synergistic effect to promote hydrogen absorption at such a low temperature (100 °C).

To further investigate this synergistic effect, the hydrogen absorption rate of M2Vfcnt2 sample was studied at different temperatures of 200 and 150 °C. As shown in Figure 5b), the composite absorbed 6.0 wt% of hydrogen within only two minutes at 200 °C. Even at a lower temperature of 150 °C, the composite still can absorb 5.6 wt% of hydrogen within the same time limit. This superior low temperature absorption performance is very significant for practical applications. To the best of our knowledge, this is the best absorption kinetics of CNTs with metal catalysts systems at 100 °C. The synergistic effect of both MIL-47(V) and CNTs can be ascribed to the function of each additive in promoting fast hydrogen sorption. Based on the above results (XRD and TEM-EDXs), vanadium species are well-dispersed in the composites thus creating active sites for nucleation and a growth centre of the magnesium hydride phase as proposed by Pang et al [37]. Moreover, short milling time creates defects to CNTs and these defects promote CNTs interaction with the dissociated hydrogen while retaining the nanotube structure provide channels for improved diffusion of hydrogen in the magnesium matrix to form hydrides.

3.4. Desorption

Temperature programmed desorption with mass spectrometry (TPD-MS) spectra of hydrogen from the prepared samples are shown in Figure 6. All samples display a single desorption peak with M4 exhibiting the highest peak at 368 °C. Desorption peak temperature shows a drop of about 50 °C when MIL-47(V) or CNTs was introduced in the composites individually. More interestingly, the peak temperature shows further reduction of 87 °C when both MIL-47(V) and CNTs are introduced in the composites as shown in M2Vfcnt2 pattern. This suggests that the combining MIL-47(V) and CNTs further enhanced hydrogen release of the composite. With respect to the onset temperature, M2Vfcnt2 displays the lowest of 183 °C compared to 310, 207 and 240 °C for M4, M2cnt2 and M2Vf2 respectively, implying that synergistic effect of both MIL-47(V) and CNTs promotes lower temperature hydrogen released. A broader peak was observed for M2Vf2 suggesting that the different vanadium species in the composites has different catalytic effects.

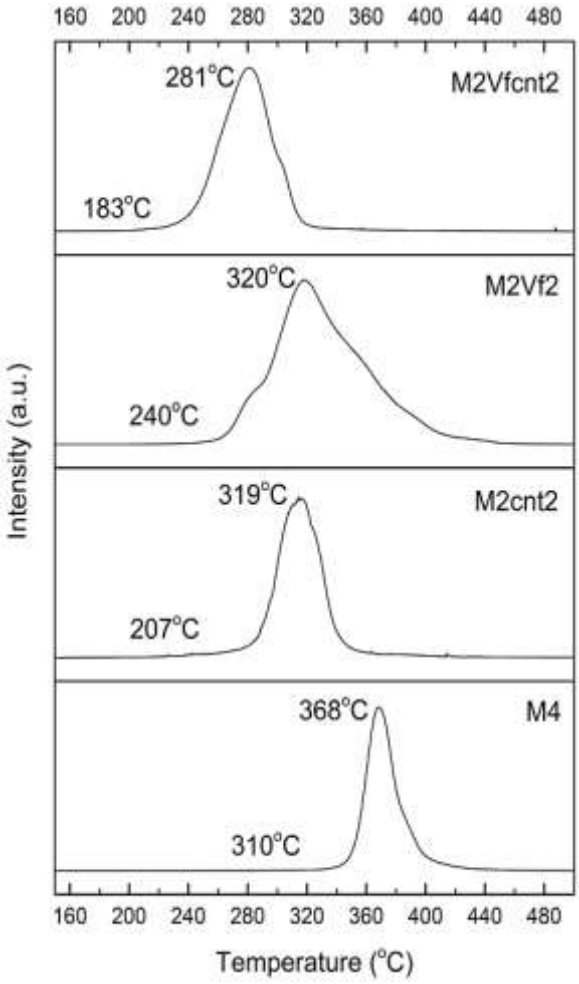


Figure 6. TPD-MS profiles of M4, M2cnt2, M2Vf2 and M2Vfcnt2.

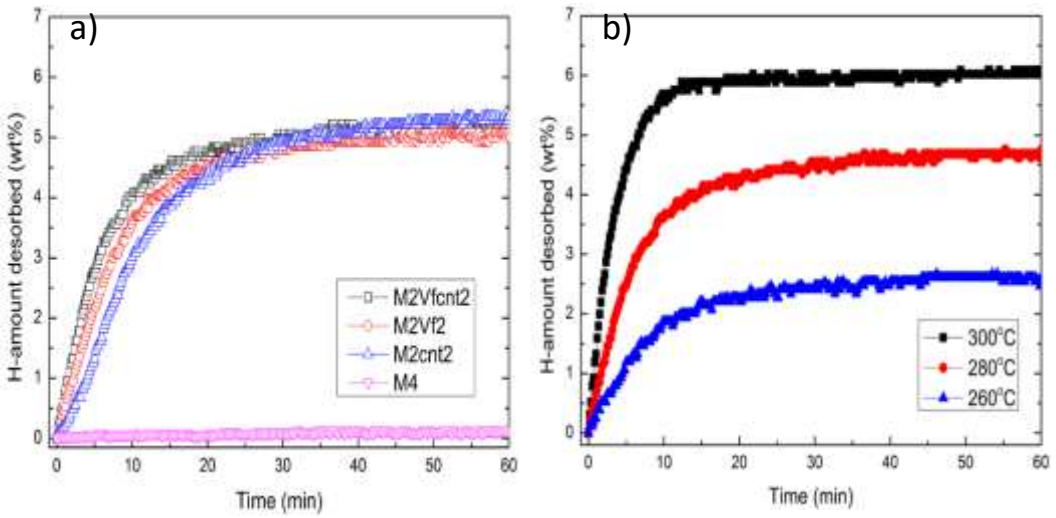


Figure 7. Hydrogen desorption a) at 280 °C based on Mg of M2Vfcnt2, M2Vf2, M2cnt2 & M4, respectively and b) at 300, 280 and 260 °C, respectively based on composite of M2Vfcnt2

To further investigate the desorption kinetics, dehydrogenation rate measurement were characterized for all samples at 280 °C. Composites with additives show an improved rate of

desorption compared to non-catalyzed MgH2 (M4) as shown in Figure 7a). In 10 minutes M2Vfcnt released 4.0 wt% of hydrogen, while M2Vf2 and M2cnt2 only desorbed 3.5 and 2.9 wt% of hydrogen respectively. This trend is in accordance to the observation from TPD suggesting that both MIL-47(V) and CNTs are responsible for the enhanced desorption kinetics. The advantage of employing MOF (specifically MIL-47(V) in this study) into the system is benefited by highly dispersed metal catalytic sites with large specific surface area and porosity due to self-assembled microporous structure by the coordination of metal cations/clusters with organic linkers. Moreover, combining with the effect of high-energy ball milling, the distribution of the metal species in this case vanadium will be further enhanced as shown in the previous section. With more vanadium species being well distributed it will provide more intimate contacting interfaces between the catalysts and MgH2 thus making available more active sites.

According to Isobe et al. [38] during dehydrogenation process, hydrogen atoms diffuse from MgH2 phase through Mg phase before recombining to form hydrogen molecules at the interface between Mg and catalyst. From our previous work [19, 39] we found out that the role of CNTs is to provide fast diffusion channel for hydrogen in the Mg/MgH2 matrix. The same function is also observed here thus it is acceptable that coupling both additives will boost up the kinetic further as manifested in rate of desorption of M2Vfcnt2. Furthermore, the composites display reasonably good kinetics even at lower temperature. As shown in Figure 7b), the composites desorb 4.5 wt% of hydrogen within 30 minutes at 280 °C and 2.5 wt% of hydrogen at 260 °C, respectively.

The desorption thermodynamic properties were investigated according to a similar technique adopted from Paskevicius et al. [40], where desorption equilibrium pressure is measured at a very long collection time (≥ 18 hours) to ensure true Mg-H equilibrium was reached. The inset in Figure 8 shows the equilibrium desorption pressure curves of M2Vfcnt2 at 300, 280 and 260 °C, respectively. Since the equilibrium pressure measured for samples are relatively low (less than 100 KPa) it is acceptable to assume that fugacity is equal to pressure thus van't Hoff plot was constructed (Figure 8).

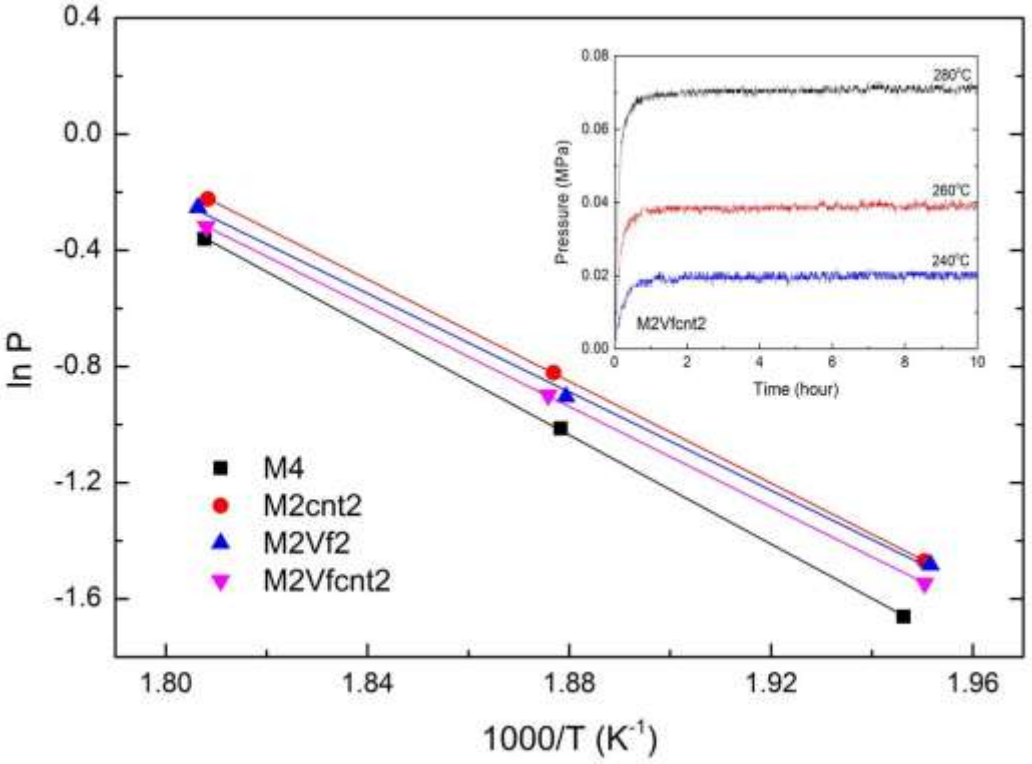


Figure 8. van't Hoff plot for desorption of M4, M2cnt2, M2Vf2 and M2Vfcnt2, respectively. Inset: Kinetics desorption plots of M2Vfcnt2 showing that hydrogen desorption equilibrium was reached at all temperatures.

Table 1. Thermodynamic properties of MgH2 composites.

Sample	Desorption enthalpy (ΔH, kJ/mol H_2)	Desorption entropy (ΔS, J/mol H_2·K)
M4	77.41 ± 2.08	136.86 ± 3.49
M2cnt2	72.75 ± 1.16	129.71 ± 2.16
M2Vf2	72.84 ± 1.41	129.37 ± 2.58
M2Vfcnt2	71.34 ± 1.58	126.38 ± 2.91

The decomposition thermodynamic properties were extracted from the plot and tabulated in Table 1. All samples with additives show a drop in enthalpy (ΔH) and entropy (ΔS) as compared to M4. Each of the additives of CNTs and MIL-47(V) show a similar effect towards thermodynamic stability, having a decomposition enthalpy (ΔH) of 72.75 ± 1.16 and 72.84 ± 1.41 kJ/mol H2 respectively and entropy (ΔS) of 129.71 ± 2.16 and 129.37± 2.58 J/mol H2·K respectively. Further reductions in the thermodynamic properties are observed when both CNTs and MIL-47(V) are introduced to the system. Displaying ΔH and ΔS of 71.34 ± 1.58 kJ/mol H2 and 126.38 ± 2.91 J/mol H2·K suggests that the synergistic effect of coupling both CNTs and MIL-47(V) enables hydrogen release at lower temperature which agrees well with the observation in the TPD-MS analysis (Figure 6).

3.5. Cycling stability

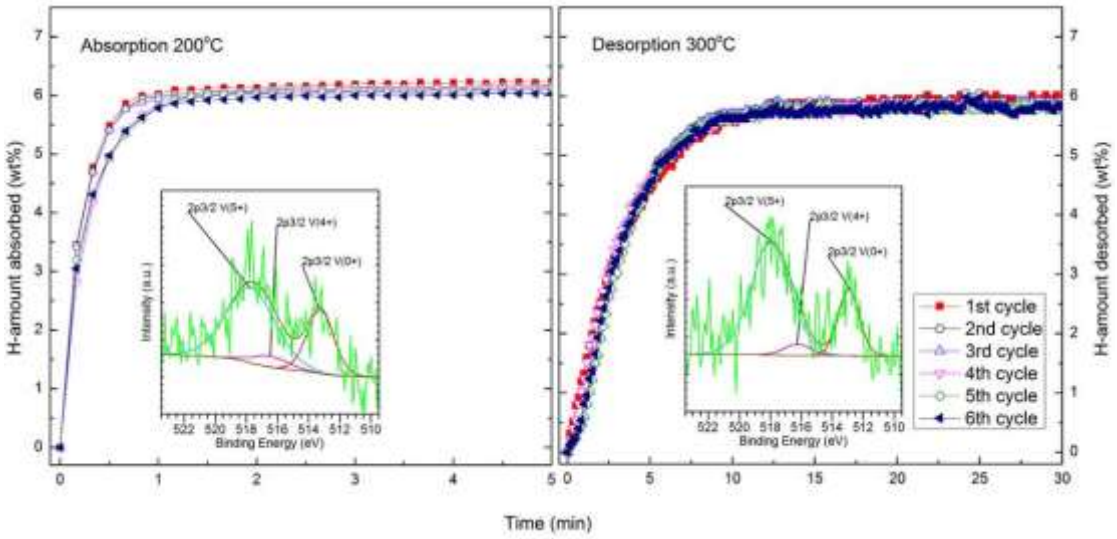


Figure 9. Cycling stability of M2Vfcnt2 at absorption and desorption of 200 and 300 °C respectively. Inserts: Narrow scans XPS spectra of V2p of sample after 5th cycle of absorption and after 6th cycle of desorption respectively.

Figure 9 illustrates the cycling stability for 6 absorption-desorption cycles of M2Vfcnt2, with respective inserts of XPS spectra showing that both vanadium species (MOF structure) still exist even after 6 cycles, suggesting that the access to the MIL-47(V) catalyst is retained even after few dehydriding-hydriding cycles. It is reported that Mg or MgH_2 coarsening is observed during absorption-desorption cycles which contributes to deterioration of sorption properties [41, 42]. However in this work, partially destroyed CNTs which are in close contact with the active sites provides diffusion channels and enables access to Mg or MgH_2 surfaces for hydrogenation and dehydrogenation. An excellent reversibility was demonstrated in M2Vfcnt2 with about 6 wt% of hydrogen absorbed and released after 6 cycles.

4. Conclusions

In conclusion, the synergistic effect of the combination of both MIL-47(V) with CNTs exhibited a significantly low temperature reduction of both hydrogen absorption and desorption. The composite exhibits the best hydrogen absorption rate of 4.3 wt% and released 4.0 wt% of hydrogen within 10 minutes at 100 °C and 280 °C respectively. These results confirm that MOFs can be an excellent candidate as a hydrogen storage catalyst in magnesium-based nanocomposites due to following merits: (1) its high thermal stability preventing catalyst destruction during de/hydrogenation cycling at high temperature, (2) relatively large surface area to increase the Mg-MOFs catalytic interface and (3) uniform microporous structure which is of benefit for hydrogen diffusion in the Mg-MOFs composite matrix. Additionally, CNTs served as hydrogen diffusion channel further enhance the storage properties.

Funding: This research received no external funding.

Acknowledgments: The authors wish to thank the Australian Research Council (ARC), the University of Queensland, Australia and the Universiti Teknologi MARA, Malaysia for the financial support in carrying out this work.

References

1. Stampfer J.F., Holley C.E.,Suttle J.F. The Magnesium Hydrogen System. *Journal of the American*

Chemical Society, 1960, 82(14): 3504-3508
2. Rahmalina D., Rahman R. A., Suwandi A., Ismail. The recent development on MgH2 system by 16 wt% nickel addition and particle size reduction through ball milling: A noticeable hydrogen capacity up to 5 wt% at low temperature and pressure. *International Journal of Hydrogen Energy*, 2020, 45(53): 29046 - 29058
3. Ma Z., Panda S., Zhang Q., Sun F., Khan D., Ding W., Zou J. Improving hydrogen sorption performances of MgH2 through nanoconfinement in a mesoporous CoS nano-boxes scaffold. *Chemical Engineering Journal*, 2021, 406(0), 126790
4. Galey B., Auroux A., Sabo-Etienne S., Dhaher S., Grellier M., Postole G. Improved hydrogen storage properties of Mg/MgH2 thanks to the addition of nickel hydride complex precursors. *International Journal of Hydrogen Energy*, 2019, 44(54): 28848-288625.
5. Peng D., Ding Z., Fu Y., Wang Y. Bi J.,Li Y., Han S. Enhanced H2 sorption performance of magnesium hydride with hard-carbon-sphere-wrapped nickel. *Royal Society of Chemistry*, 2018, 8: 28787 - 28796
6. Paul D.R.,Sharma R., Sharma A., Panchal P., Singh A., Chaudhary S., Nehra S.P. Structural properties of Mg - x wt% Co (x = 0, 5, 10 & 20) nanocomposites for hydrogen storage applications. *Materials Today: Proceedings*, 2021, 42(4): 1713-1717
7. Zhang Y., Zhang W., Wei X., Yuan Z., Gao J., Guo S., Ren H. Catalytic effects of TiO2 on hydrogen storage thermodynamics and kinetics of the as-milled Mg-based alloy. *Materials Characterization*, 2021, 176(0), 111118
8. Zhang M., Xiao X., Mao J., Lan Z., Huang X.,Lu Y. Luo B., Liu M., Chen M., Chen L. Synergistic catalysis in monodispersed transition metal oxide nanoparticles anchored on amorphous carbon for excellent low-temperature dehydrogenation of magnesium hydride. *Materials Today Energy*, 2019, 12(0): 146-154
9. Kumar S., Kojima Y., Dey G.K. Morphological effects of Nb2O5 on Mg–MgH2 system for thermal energy storage application. *International Journal of Hydrogen Energy*, 2018, 43(2): 809 - 816
10. Khandelwal A., Agresti F., Capurso G., Lo Russo S., Maddalena A., Gialanella S.,Principi G. Pellets of MgH(2)-based composites as practical material for solid state hydrogen storage. *International Journal of Hydrogen Energy*, 2010, 35(8): 3565-3571
11. Sulaiman N.N., Ismail M. Effects of TiF3 addition on the hydrogen storage properties of 4MgH2 + Cd composite. *International Journal of Hydrogen Energy*, 2019, 44(58): 30574 - 30582
12. Wang K., Wu G., Cao H., Li H., Zhao X. Improved reversible dehydrogenation properties of MgH2 by the synergetic effects of graphene oxide-based porous carbon and TiCl3. *International Journal of Hydrogen Energy*, 2018, 43(15): 7440 - 7446 13
13. Zhu L., Liao Y., Zhong Y., Cui J., Wang D., Wang K. Improved reversible dehydrogenation performance of MgH2 by the synergistic effects of porous boron nitride and NbF5. *Journal of Energy Storage*, 2020, 29(0), 101418
14. Rather S.U. Preparation, characterization and hydrogen storage studies of carbon nanotubes and their composites: A review. *International Journal of Hydrogen Energy*, 2020, 45(7): 4653-4672
15. Ze S., Xiong L.,Michael N.F., Nianhua Y., Jiankun X., Shichuan S., Liuting Z. Enhancing Hydrogen Storage Properties of MgH2 by Transition Metals and Carbon Materials: A Brief Review. *Frontiers in Chemistry*, 2020, 8(0), 552
16. Amirkhiz B.S., Danaie M.,Mitlin D. The influence of SWCNT-metallic nanoparticle mixtures on the desorption properties of milled MgH2 powders. *Nanotechnology*, 2009, 20(20)
17. Babak Shalchi A., Mohsen D.,David M. The influence of SWCNT–metallic nanoparticle mixtures on the desorption properties of milled MgH 2 powders. *Nanotechnology*, 2009, 20(20): 204016
18. Lu X., Zhang L., Yu Z., He J., Zheng J., Wu F., Chen L. Achieving superior hydrogen storage properties of MgH2 by the effect of TiFe and carbon nanotubes. *Chemical Engineering Journal*, 2021, 44(0), 130101219.
19. Kadri A., Jia Y., Chen Z., Yao X.D..Catalytically enhanced hydrogen sorption in Mg-MgH2 by coupling vanadium-based catalyst and carbon nanotubes. *Materials*, 2015, 8(6): 3491-3507
20. Ahmed A., Seth S., Purewal J., Antek G., Wong-Foy, Veenstra M., Matzger A.J., Siegel D.J..

Exceptional hydrogen storage achieved by screening nearly half a million metal-organic frameworks. *Nature Communications*, 2019, 10: 1568

21. Akash G., Miroslav A., Devina R. P., Ekta P., Luthra J.R., Anshu S. Metal-Organic Framework MOF-76(Nd): Synthesis, Characterization, and Study of Hydrogen Storage and Humidity Sensing. *Frontiers in Energy Research*, 2021, 8(0), 604735
22. Kassaoui M.E., Lakhal M., Benyoussef A., Kenz A. E. Loulidi M. Enhancement of hydrogen storage properties of metal-organic framework-5 by substitution (Zn, Cd and Mg) and decoration (Li, Be and Na). *International Journal of Hydrogen Energy*, 2021, 46(52): 26426-26436
23. Bambalaza S. E., Langmi H.W., Mokaya R., Musyoka N.M., Khotseng E. Co-pelletization of a zirconium-based metal-organic framework (UiO-66) with polymer nanofibers for improved useable capacity in hydrogen storage. *International Journal of Hydrogen Energy*, 2020, 46(12): 8607-8620
24. Kumari A., Kaushal S., Singh P.P. Bimetallic metal organic frameworks heterogeneous catalysts: Design, construction, and applications. *Materials Today Energy*, 2021, 20(0), 100667
25. Feng X., Wang K., Zhou M., Li F., Liu J., Zhao M., Zhao L., Song X., Zhang P., Gao L. Metal organic framework derived Ni/CeO2 catalyst with highly dispersed ultra-fine Ni nanoparticles: Impregnation synthesis and the application in CO2 methanation. *Ceramics International*, 2021, 47(9): 12366-12374
26. Cheng H., Ning L., Liao S., Li W., Tang S., Li J., Chen H., Liu X., Shao L. Nickel−alkyne−functionalized metal−organic frameworks: An efficient and reusable catalyst. *Applied Catalysis A: General*, 2021, 623(0), 118216
27. Barthelet K., Marrot J., Riou D.,Ferey G. A breathing hybrid organic-inorganic solid with very large pores and high magnetic characteristics. *Angewandte Chemie-International Edition*, 2001, 41(2): 281-+
28. Biesinger M.C., Lau L.W.M., Gerson A.R.,Smart R.S.C. Resolving surface chemical states in XPS analysis of first row transition metals, oxides and hydroxides: Sc, Ti, V, Cu and Zn. *Applied Surface Science*, 2010, 257(3): 887-898
29. Silversmit G., Depla D., Poelman H., Marin G.B.,De Gryse R. Determination of the V2p XPS binding energies for different vanadium oxidation states (V5+ to V0+). *Journal of Electron Spectroscopy and Related Phenomena*, 2004, 135(2-3): 167-175
30. Yoo Y., Tuck M., Kondakindi R., Seo C.-Y., Dehouche Z.,Belkacemi K. Enhanced hydrogen reaction kinetics of nanostructured Mg-based composites with nanoparticle metal catalysts dispersed on supports. *Journal of Alloys and Compounds*, 2007, 446–447(0): 84-89
31. Floriona R., Deledda S., Hauback B.C., Leiva D.R., Botta W.J. Iron and niobium based additives in magnesium hydride: Microstructure and hydrogen storage properties. *International Journal of Hydrogen Energy*, 2017, 42(10): 6810-6819
32. Pierard N., Fonseca A., Colomer J.F., Bossuot C., Benoit J.M., Van Tendeloo G., Pirard J.P.,Nagy J.B. Ball milling effect on the structure of single-wall carbon nanotubes. *Carbon*, 2004, 42(8–9): 1691-1697
33. Darsono N., Yoon D.H.,Kim J.Y. Milling and dispersion of multi-walled carbon nanotubes in texanol. *Applied Surface Science*, 2008, 254(11): 3412-3419
34. Lee J.H., Rhee K.Y.,Park S.J. Effects of cryomilling on the structures and hydrogen storage characteristics of multi-walled carbon nanotubes. *International Journal of Hydrogen Energy*, 2010, 35(15): 7850-7857
35. Aguey-Zinsou K.F., Ares Fernandez J.R., Klassen T.,Bormann R. Effect of Nb2O5 on MgH2 properties during mechanical milling. *International Journal of Hydrogen Energy*, 2007, 32(13): 2400-2407
36. Li J., Li B., Shao H., Li W., Lin H. Catalysis and Downsizing in Mg-Based Hydrogen Storage Materials. *Catalysts*, 2018, 8(2): 8937.
37. Pang Y., Wang Y., Yang J., Zheng S. Engineering dual-functional VB2 nanoparticles in MgH2 for highly efficient hydrogen storage. *Composites Communications*, 2021, 26(0), 100781
38. Isobe S., Ono A., Yao H., Wang Y.M., Hashimoto N.,Ohnuki S. Study on reaction mechanism of dehydrogenation of magnesium hydride by in situ transmission electron microscopy. *Applied Physics Letters*, 2010, 96(22)

39. Yao X.D., Wu C.Z., Du A.J., Zou J., Zhu Z.H., Wang P., Cheng H.M., Smith S.,Lu G.Q. Metallic and carbon nanotube-catalyzed coupling of hydrogenation in magnesium. *Journal of the American Chemical Society*, 2007, 129(50): 15650-15654
40. Paskevicius M., Sheppard D.A.,Buckley C.E. Thermodynamic Changes in Mechanochemically Synthesized Magnesium Hydride Nanoparticles. *Journal of the American Chemical Society*, 2010, 132(14): 5077-5083
41. Cuevas F., Korablov D.,Latroche M. Synthesis, structural and hydrogenation properties of Mg-rich MgH2-TiH2 nanocomposites prepared by reactive ball milling under hydrogen gas. *Physical Chemistry Chemical Physics*, 2012, 14(3): 1200-1211
42. Amirkhiz B.S., Zahiri B., Kalisvaart P.,Mitlin D. Synergy of elemental Fe and Ti promoting low temperature hydrogen sorption cycling of magnesium. *International Journal of Hydrogen Energy*, 2011, 36(11): 6711-6722

Evaluation of corrosion and scaling in Khoms Power Plant

Abdulhamid. Elwaer *, Abdulroaf Shahein *, Giuma Elhamile

Planning, Studies & Development department, General Electricity Company of Libya

**Corresponding authors: a_elwaer2010@yahoo.com; abmshaheen2000@gmail.com ; Tel.: 00218 926186275 ; 00218 912206385 ; 00218 927017237.*

Abstract: The General Electricity Company of Libya (GECOL) is the unique, state-owned electricity utility in the country; it is vertically-integrated and responsible for the generation, transmission and distribution of electricity nationwide. Presently, GECOL supplies a variety of consumers over different voltage levels, including the residential, commercial, industrial, public utilities, street lighting and agricultural sectors through the country. This required the expansion of the power plants as well as the transmission and distribution networks which are, currently, extending from east to west and deep into the desert for thousands of kilometers. The objective of this paper is to study the scale formation and corrosion in waters used in Khoms steam turbine power plant and desalination plant . This paper explains the prediction of calcium carbonate ($CaCO_3$) scale by using Stiff & Davis (S&DSI) Index and Skillman Index (S) is used to predict calcium sulfate ($CaSO_4$) scale.

Keywords: Corrosion, Scaling ,Stiff & Davis (S&DSI) Index, Skillman Index (S). Inhibitors

Fairdeal's Introduces Innovative Waste Management Solutions Based on Nano Engineering

Fairdeal Marine Services, one of the first maritime businesses in the Middle East Gulf, solely dedicated to the protection of the marine environment, is expanding to catch up with stricter Environmental rules.

FAIRDEAL Research & Development team is constantly exploring new technologies to improve the eco-friendly material collection and handling operations, announces the construction of the first treatment plant of oily sludge and of sludge arising from:

- Oil industry
- Metal industry
- Food Industry
- Flue gas treatment systems.

A first such facility will be set up in UAE within 2021. It should be stressed that this plant is able to treat waste and sludge deriving from the industries. The plant design is based on an integrated environmental and economic waste management process, creating a modern facility with low footprint requirements which will be ready to respond to future environmental challenges.

The new patented method leaves post-treatment waste in a state that is not environmentally hazardous. Such waste can, therefore, be disposed of safely and cheaply.

Fairdeal claims no comparable facility using its nanotechnology-based method exists. The pioneering waste management technology applies to an increasing number of new sectors, providing comprehensive environmental solutions to companies with a high pollutant load deriving from their activities

FAIRDEAL envisage the installation of more plants using this technology in the Gulf region, addressing the recognized environmental problems of the region and the need to install state of the art infrastructure to support Green Environment.

GACS (Geochemical Active Clay Sediment) is a process which:

- is friendly to the environment
- can be applied to a wide range of environmental projects
- is based upon the usage of geopolymer materials with high absorption ability,
- relies on the principles of nanomechanics, achieving treatment of the pollutant load at nanoscale level. Pollutant load is captured on the crystal structure of the geopolymer materials

Optimization of the Templated Synthesis of Lithium Iron Phosphate Nanowires

Jeh Hua Beh [1], , Teck Hock Lim [2], Jau Choy Lai [1]*, Jiun Hor Low [3], Kian Hong Gan [1], Kok Yeow You [4], Kar Lun Chong [1]

[1] School of Chemical and Energy Engineering, Faculty of Engineering, Universiti Teknologi Malaysia Skudai 81310 Johor, Malaysia.;
[2] Department of Physical Science, Faculty of Applied Science, Tunku Abdul Rahman University College, Jalan Genting Kelang, Setapak; Kuala Lumpur, 53300 Kuala Lumpur, Malaysia.;
[3] School of Computer Science and Engineering, Faculty of Innovation and Technology, Taylor's University, Lakeside Campus, No.1, Jalan Taylor's, 47500 Subang Jaya, Selangor, Malaysia.;
[4] School of Electrical Engineering, Faculty of Engineering, Universiti Teknologi Malaysia, Skudai, 81310 Johor, Malaysia.;
***** *Corresponding author: jclai@utm.my; Tel.: +607-5535536*

Abstract: This paper reports the synthesis of highly crystalline lithium iron phosphate ($LiFePO_4$) nanowires via templated synthesis i.e. coating and sintering the precursors on the surface of an aerogel template prepared from sago pith cellulose nanofibrils (SPCNF) extracted from sago pith waste (SPW), an agricultural waste. The effects of SPCNF aerogel quantity (X_q), sintering duration (X_t) and sintering temperature (X_T) on the quality of the nanowires were studied and elucidated. Specifically, SPCNF (diameter 15-30 nm) aerogel was coated with $LiFePO_4$ via two consecutive steps: (i) prepare a uniform solution containing Li^+, Fe^{2+} and PO_4^{3-} in 1:1:1 molar ratio with assistance of heat; (ii) direct coating on aerogel with the solution followed by calcinations/sintering. The final product, LiFePO4 nanowires had diameters between 15-30 nm and were characterized via Field Emission-Scanning Electron Microscopy (FE-SEM), Powder X-Ray Diffraction (PXRD) and Transmission Electron Microscopy (TEM). Effects of X_q, X_t and X_T on the nanowire morphology and coating quality were studied and the inter-correlations between the three parameters were computed using JMP, a software used for design of experiment (DOE). Results showed that all the three parameters are significant and can be co-related to the quality of LiFePO4 nanowires with the following correlation: $Y = 5.662 + 7.23875X_q + 7.23875X_t + 5.60125X_T + 7.23875X_qX_t + 5.60125X_qX_T + 5.60125\ X_tX_T + 5.60125\ X_qX_tX_T$. The simple method developed in this study is significant in that it could lead to cost-effective, scalable production of functional $LiFePO_4$ nanowires, after future refinement of the method to remove minute impurities.

Keywords: Cellulose nanofibril, aerogel, sago pith waste, lithium iron phosphate nanowire, full factorial design

1. Introduction

Lately, lithium ion-based batteries have been developed as high energy power source appliances for electrical based vehicles [1] and lithium iron phosphate ($LiFePO_4$) has been a potential candidate for cathode compound because of its environmental friendliness, low toxicity, affordable price and excellent thermal stability [2]. Moreover, $LiFePO_4$ possesses a smaller density and greater theoretical capacity comparing to other lithium ion-based oxide compounds [3]. In terms of physical form, it is well known that $LiFePO_4$ nanowires has a better conductivity comparing to its spherical counterpart, due to its longer mean free path [4]. However, to date, $LiFePO_4$ is only available commercially in spherical nanoparticle form owing to its synthesis method is easier to be industrialized for mass production [5,6]. Moreover, the existing $LiFePO_4$ nanowires synthesis methods suffer from problems like high energy consumption and complicated chemical purification process due to the formation of iron phosphide impurities [7]. Therefore, a simple and scalable method for synthesizing LiFePO4 nanowires is needed in order to meet this need and, templated synthesis seems to be a potential solution.

In templated synthesis, a pre-existing nanostructured template is utilized so that nanomaterials which hold a well-defined shape, size and configuration can be obtained [8]. To dates, researchers from different parts of the world utilized different materials such as polycarbonate filter [9], amylose [10] and block copolymer [11] as template for synthesizing $LiFePO_4$ nanowires. In this study, $LiFePO_4$ nanowires was synthesized via templated synthesis by coating the $LiFePO_4$ precursors onto the surface of sago pith cellulose nanofibril (SPCNF) aerogel. The template used, SPCNF aerogel was extracted from sago pith waste (SPW), a fibrous, water polluting agricultural waste from sago starch manufacturing industry [12]. In our earlier studies, the SPCNF aerogel was characterized in terms of morphological and thermal properties; the aerogel also performed excellently in methylene blue adsorption [13]. The abundant hydroxyl groups exist in the SPCNF aerogel make it readily open to chemical reactions or physical interactions e.g. hydrogen bonds [14]. Furthermore, its porous structure remains intact even after going through calcination, making it an excellent choice for the template. The templated synthesis of $LiFePO_4$ nanowires was also optimized via 2^3 full factorial design method. Significance of each synthesis parameter and their interactions were determined, a model describing the relationships between the synthesis parameters and the conductivity of the nanowire was also generated and validated.

2. Materials and Methods

2.1. Materials

Detailed information regarding SPW, SPCNF extraction and SPCNF aerogel formation are available in our earlier publication [13] and thus will not be explained here. Lithium hydroxide monohydrate ($LiOH.H_2O$), 85% ortho-phosphoric acid (H_3PO_4), iron (II) chloride tetrahydrate ($FeCl_2.4H_2O$) and ethylene glycol ($C_2H_6O_2$) were purchased from Sigma-Aldrich and used directly without further purification.

2.2. Synthesis of $LiFePO_4$ Precursors

630 mg of $LiOH.H_2O$ was added into a 100 mL round bottom flask together with a mixture of solvent, namely ethylene glycol/water (15 mL EG /3 mL H_2O or at the ratio of 5:1) at 70°C to form a solution. Next, H_3PO_4 was added into the solution together with 12 mL of ethylene glycol/water (5:1) solvent. After that, 0.99 g of $FeCl_2.4H_2O$ was added into the mixture with 15 ml of ethylene glycol/water (5:1) solvent. The mixture was then sealed and stirred for 30 minutes at 70°C until a homogenous solution was obtained.

2.3. Templated Synthesis of $LiFePO_4$ Nanowires

$LiFePO_4$ nanowires were synthesized via a two-stage process namely coating and calcination. At the stage of coating, a pre-determined amount of SPCNF aerogel was placed into a beaker and stirred slowly by using a small magnetic stirrer at the speed of 125 rpm. $LiFePO_4$ precursor solution was then dropped slowly onto the SPCNF aerogel in the beaker at room temperature. The magnetic stirrer was used in order to ensure that the precursors were coated well onto the aerogel. The dropping stopped when the added precursor solution was not able to be absorbed by the aerogel anymore. At the calcination stage, the coated aerogel was placed inside a gas furnace at 260 °C with nitrogen gas flowed slowly for 3 hours. It was then sintered at a higher temperature, 500°C for another 3 hours. After the heating, it was cooled down to room temperature and a black powder sample, $LiFePO_4$ nanowires was obtained.

2.4. Characterization of the Synthesized $LiFePO_4$ Nanowires

Powder X-ray diffraction (PXRD) was used for the phase identification of the $LiFePO_4$ nanowires. XRD diffractograms were obtained by using a Rigaku Smartlab Multipurpose X-ray diffractometer with Ni-filtered Cu-Kα radiation (λ= 1.5406A) at 45 kV and 200 mA. Scattered radiation was detected in the range of 2Θ =10°- 100° at the scanning rate of 1°/min. Morphologies of the nanowires were characterized using a Hitachi SU8020 Field Emission Scanning Electron

Microscope at 5 kV with magnification of 100,000 times. Besides, Field Emission Scanning Microscope/Energy Dispersive X-ray Analysis (FE-SEM/EDX) and EDX mapping were also done to analyse the elemental composition of the nanowires. Lattice structure in the nanowires was analysed via a JEOL JEM-2100 Transmission Electron Microscope (TEM) at 200 kV, corresponding to an electron wavelength of 2.5 pm. Besides, Transmission Electron Microscope/Energy Dispersive X-ray Analysis (TEM/EDX) was also done to analyse the elemental composition of the nanowires at high count rates.

2.5. $LiFePO_4$ Nanowires Quality Optimization via Design of Experiment

DoE was utilized to identify the significance of the three synthesis parameters namely, SPCNF aerogel quantity, X_q, sintering temperature, X_T and sintering duration, X_t and their relationships with the nanowire quality. The range of each parameter was determined based on preliminary experiments. JMP 13 statistical software was used to optimize the nanowire quality through 2^3 full-factorial design. As shown in Table 1, parameter levels (upper and lower limits) were chosen to cover the range of practical interest values and these values were normalized from -1 to 1. Eleven samples were synthesized based on the conditions listed in Table 2.

Table 1: Parameter levels of the experimental design

Parameters	**Levels**		
	-1 (minimum)	**0 (average)**	**+1 (maximum)**
Quantity of SPCNF Aerogel (g), X_q	0.02	0.04	0.06
Sintering Temperature (°C), X_T	300	400	500
Sintering Duration (min), X_t	60	120	180

Table 2: Formulation table

Samples	**Quantity of SPCNF Aerogel (g), X_q**	**Sintering Temperature (°C), X_T**	**Sintering Duration (min), X_t**
L1	+1	+1	+1
L2	-1	-1	-1
L3	-1	+1	+1
L4	+1	-1	+1
L5	+1	+1	-1
L6	-1	-1	+1
L7	-1	+1	-1
L8	+1	-1	-1

With the help of Image J software, FE-SEM micrographs of the samples were used to quantify the nanowire quality. A mathematical model which best describes the experimental data was then developed by using a statistical software, namely JMP 13. Finally, the mathematical model which was developed to represent the quality of the $LiFePO_4$ nanowires was validated through the comparison between their predicted and experimental values.

3. Results and Discussion

3.1. Characterization of the Synthesized $LiFePO_4$ Nanowires

Figure 1(a)(i) apparently shows that after the 3-hour calcination at 500°C under N_2 flow, the control namely, SPCNF aerogel without precursor coating was carbonised into carbon fibre aerogel. At high temperature, the fibrous frameworks of SPCNF aerogel underwent an obvious shrinkage during carbonization because of the removal of non-carbon elements and carbon-containing compounds [15]. EDX results presented in Figure 1(a)(ii) indicates that after carbonization, SPCNF aerogel was transformed into 1D carbon fibre with the presence of small amount of other elements impurities such as sodium, Na (1.3 wt.%), chloride, Cl (1.4 wt.%) and oxygen, O (8.9 wt.%) which were the residues from the chemical treatment of sago pith waste (SPW) during the SPCNF extraction process. The 1D carbon fiber facilitates easy access of reaction to the inner surface of it, and this nanopore size of 1D carbon fibre effectively increased the surface area for active site dispersion. Therefore, there is a high chance for the deposition of $LiFePO_4$ particles onto the surface of carbon fibre aerogel (serve as template) which eventually helped for the growth of nanowires.

Figure 1(b) shows the FE-SEM micrograph and EDX spectrum of $LiFePO_4$ nanowires. It is clearly shown that the $LiFePO_4$ nanowires consisted of iron, Fe (49.6 wt.%), oxygen, O (36.5 wt.%) and phosphorus, P (13.9 wt.%) with diameters between 15-30 nm. On the other hand, TEM images and the EDX analysis presented in Figures 2(e), 2(f) and 2(g), respectively confirm that the surface of the carbonized SPCNF fibre (termed as carbon fiber) was covered with $LiFePO_4$ (Fe: 49.1 wt. %, O: 24.3 wt. %, P: 4.5 wt. %, C: 2.0 wt. %) and its lattice spacing was between 0.46-0.48 nm. This result is similar to the results reported by [16] for coaxial-type of $LiFePO_4$ nanowires.

This section may be divided by subheadings. It should provide a concise and precise description of the experimental results, their interpretation as well as the experimental conclusions that can be drawn.

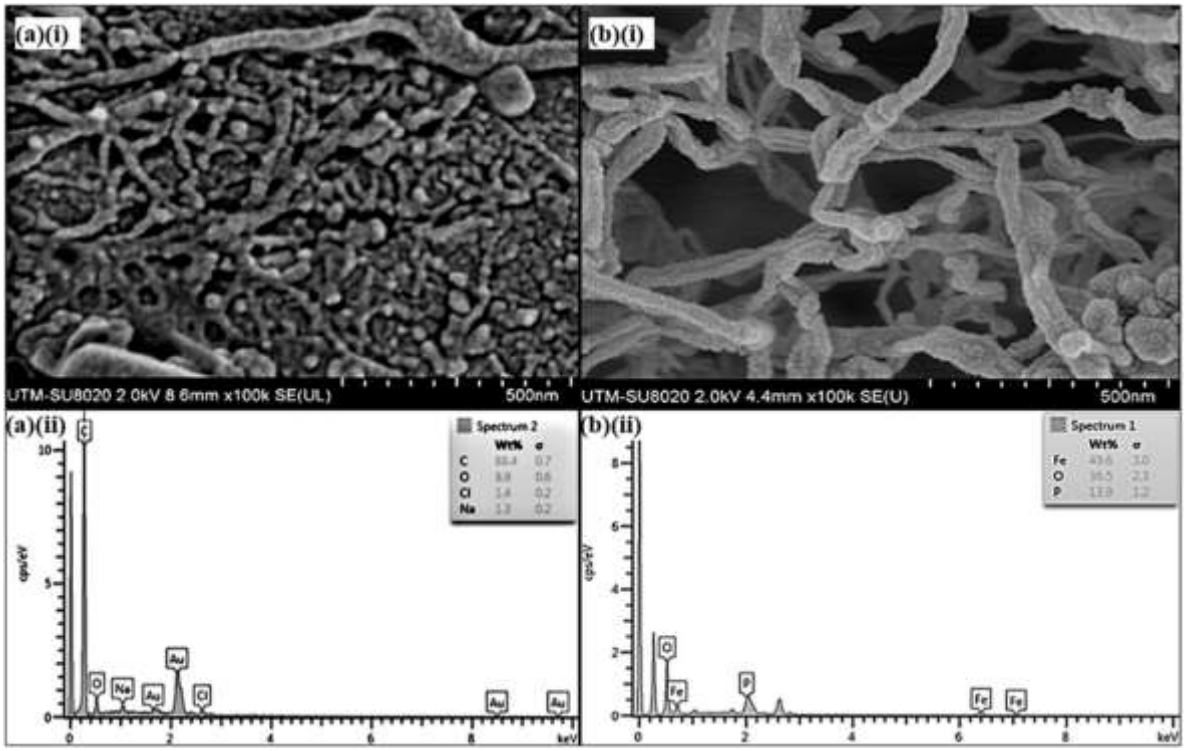


Figure 1: FE-SEM micrograph and EDX spectrum of (a) thermally annealed SPCNF aerogel without $LiFePO_4$ coating (as a control). Au signals arisen from the coating process (for FE-SEM sample preparation) to reduce charging effect (b) $LiFePO_4$ nanowires.

The synthesized $LiFePO_4$ nanowires was further characterized and verified by using XRD. Figure 2(a) shows the XRD diffractogram of the nanowires. During the peak matching, as can be seen in Figure 2(b), majority of the diffraction peaks of the synthesized $LiFePO_4$ nanowires matched well with that of lithium iron phosphate (V), $LiFe(PO_4)$ [ICDD (PDF-2 Release 2015 RDB) 01-082-9758)] but slightly different in terms of peaks intensity and position due to the fact that the growth of $LiFePO_4$ nanowires were not in a random orientated distribution [10]. The sharp main peaks in the patterns shows that the synthesized $LiFePO_4$ nanowires were in highly crystalline structure. However, there were also some impurity phases present in the sample. Peaks for iron oxides [Fe_3O_4 (Fe^{2+}/Fe^{3+})] was present in the diffractogram [Figure 2(c)], probably due to the excess amount of iron, Fe which was present in the product of the synthesized $LiFePO_4$ nanowires [17,18]. Besides, lithium phosphate (Li_3PO_4) phase was also detected, as exhibited in Figure 2(d), probably due to the carbothermal reduction of $LiFePO_4$ in the nitrogen environment [19]. As a conclusion, based on the characterization results, crystalline $LiFePO_4$ nanowires with diameters in the range of 15-30 nm were formed successfully at sintering temperature of 500°C for 3 hours under nitrogen gas flow.

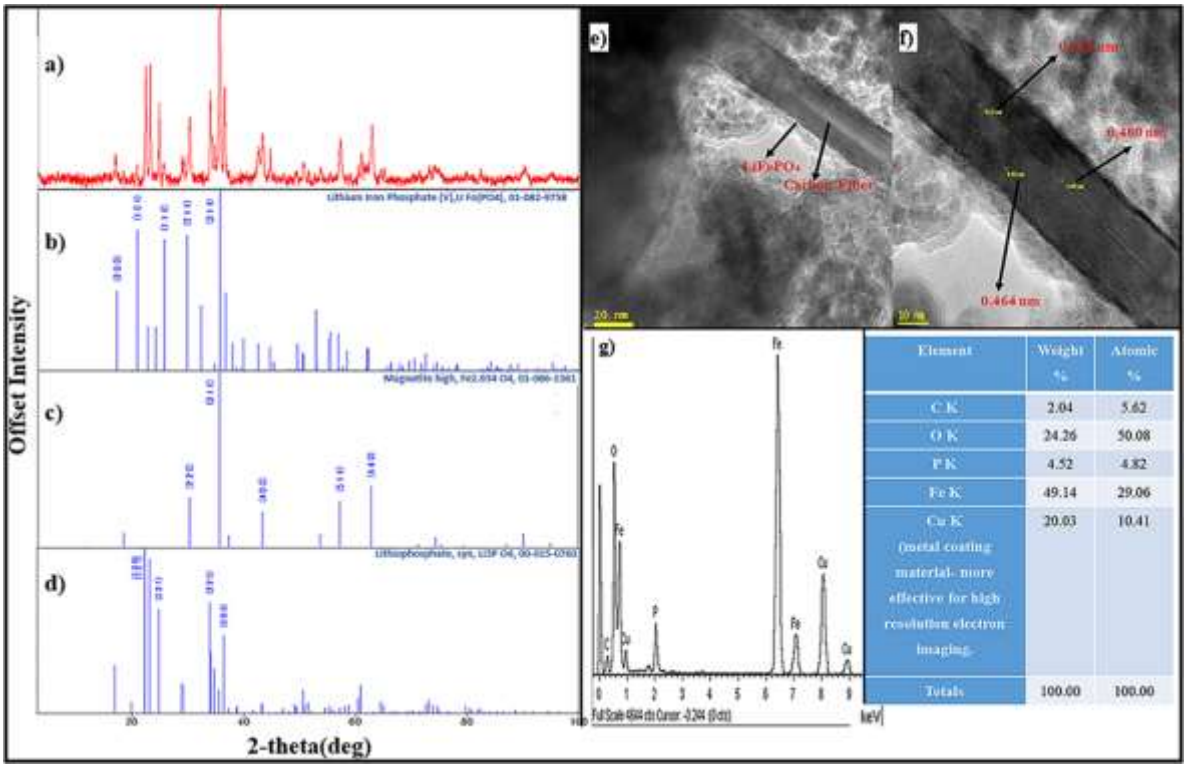


Figure 2: (a) XRD diffractogram of the $LiFePO_4$ nanowire matched with (b) standard $LiFePO_4$ (c) standard Li_3PO_4 and (d) standard Fe_3O_4. TEM images show (e) $LiFePO_4$ coated the carbonized SPCNF (f) the lattice spacing of 0.46-0.48 nm. (g) EDX analysis results.

3.2. Modelling and Simulation for the Quality of $LiFePO_4$ Nanowires

Effects of the three synthesis parameters namely, quantity of SPCNF aerogel (X_q), sintering temperature (X_T) and sintering time (X_t) on the quality of $LiFePO_4$ nanowires produced was quantitatively evaluated via a 2^3 full-factorial design using JMP13 software. For this reason, the $LiFePO_4$ synthesis process was carried out at different combination of X_q, X_t and X_T conditions, as shown in Table 3. The final indicator, quality of $LiFePO_4$ nanowires (measured in %), were defined based on three criteria namely, yield, smoothness and aspect ratio. The three criteria were quantified based on the analyses of FE-SEM micrographs of the products.

Table 3: Experimental results for the $LiFePO_4$ nanowires quality (%)

No. Sample	Pattern			Yield of $LiFePO_4$ Nanowires (%)	Smoothness of $LiFePO_4$ Nanowires	Aspect Ratio of $LiFePO_4$ Nanowires (> 20, rate as 1 < 20 rate as 0.5)	Quality of $LiFePO_4$ Nanowires (%)
	X_q	X_T	X_t				
1	+1	+1	-1	26.20	0.5	0.5	**6.55**
2	+1	-1	+1	0	0	0	0
3	+1	-1	-1	0	0	0	0
4	+1	+1	+1	64.20	0.8	1.0	**51.36**
5	-1	-1	-1	0	0	0	0
6	-1	+1	+1	0	0	0	0
7	-1	+1	-1	0	0	0	0
8	-1	-1	+1	0	0	0	0
9	0	0	0	0	0	0	0
10	0	0	0	8.35	0.5	0.5	**2.09**

Figure 3 shows the FE-SEM images of the nanowire at different mode of smoothness. Each of the smoothness mode was given a rate value for example, 1.0, 0.8 and 0.5 referred to very smooth, smooth and rough, respectively. Meanwhile, 0 referred to no formation of $LiFePO_4$ nanowires. On the other hand, the yield of $LiFePO_4$ nanowires (%) were obtained via measuring the total area covered by the nanowires in the FE-SEM micrographs taken at five different locations using Image J software. Determination of the yield of Sample No. 4 is shown in Figure 4. Lastly, the aspect ratio of the nanowires was calculated by dividing the length of one nanowire with its diameter.

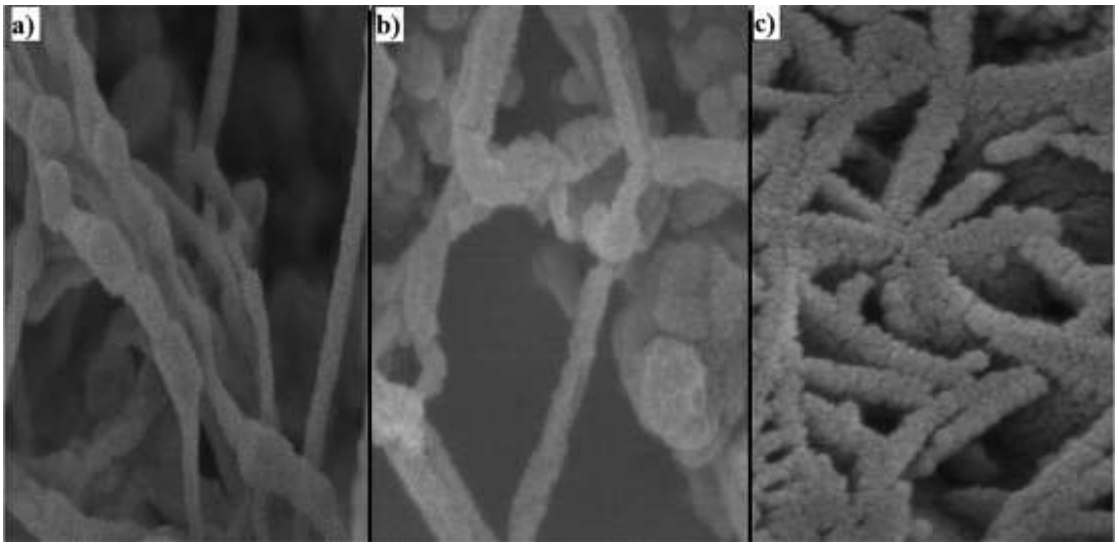
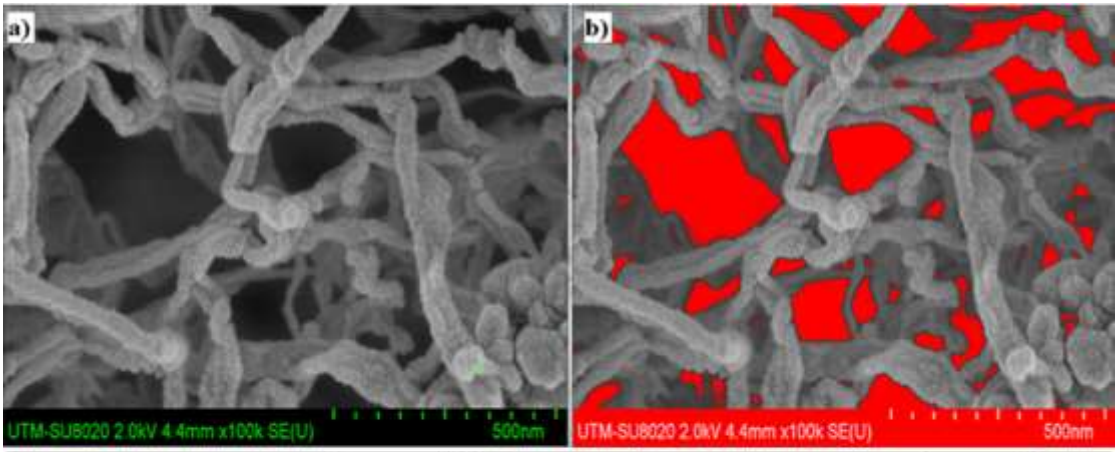


Figure 3: FE-SEM images of $LiFePO_4$ nanowires at different smoothness mode (a) very smooth (b) smooth (c) rough.



FE-SEM Micrographs	Area of FE-SEM Micrographs, y	Area without $LiFePO_4$ Nanowires, x	Area of $LiFePO_4$ Nanowires, (y-x)
1	1111094	366937.7	744156.3
2	1115936	747260.5	368675.5
3	1108046	262468.3	845577.7
4	1110660	269096.3	841563.7
5	1109827	342897.6	766929.4
Total	5555563	1988660.4	3566902.6
Yield of $LiFePO_4$ nanowires (%)			[(y-x)/y]x100% =64.20

Figure 4: Determination of the nanowire yield of Sample No. 4 using Image J software (a) Original FE-SEM micrograph (b) Area without $LiFePO_4$ nanowires are filled with red colour

By analysing the findings with the statistical software (JMP 13), a full model equation (Equation 1) was developed to study the interaction among the synthesis parameters (X_q, X_T and X_t) as well as their effects on the quality of the $LiFePO_4$ nanowires synthesized in the process.

Quality of $LiFePO_4$ nanowires (%) $= 5.662 + 7.23875X_q + 7.23875X_t + + 5.60125X_T + 7.23875X_qX_t + 5.60125X_qX_T + 5.60125\ X_tX_T + 5.60125\ X_qX_tX_T,$ (1)

The coefficient of determination (R^2) and the adjusted coefficient of determination (adj. R^2) of the developed model equation are tabulated in Table 4. Based on the coefficient of determination (R^2), the model equation can simulate 96.74 % of the variability observed in the response variable (quality of $LiFePO_4$ nanowires). The R^2 (96.74 %) is also considered closed with the adj. R^2 (89.14 %), which mean that the developed model equation has goodness of fit between the experimental values and predicted values. In addition, the P-value of lack of fit of the model equation (0.0212) is also less than 0.05. This shows that the developed model equation is significant and sufficient to represent the experimental value for the quality of $LiFePO_4$ nanowires synthesized in this process.

Table 4: Summary of fit of the developed model equation

Summary of Fit	
Coefficient of determination, R^2	0.9674
Adjusted coefficient of determination, Adj. R^2	0.8914
P-value of Lack of Fit	0.0212
Root Mean Square Error	5.0380
Mean of Response	5.6618

Based on the developed model equation (1), the coefficient of SPCNF aerogel quantity, X_q (7.23875) and sintering time, X_t (7.23875) revealed that their effects are almost 1.3 folds relative to the sintering temperature, X_T (5.60125). Moreover, both synthesis parameters exerted a positive effect on the quality of $LiFePO_4$ nanowires. On the other hand, the numerical coefficient value (7.23875) of the interaction between the quantity of SPCNF aerogel (X_q) and sintering time (X_t) shows that their combination should also be taken into consideration during the $LiFePO_4$ nanowires synthesis process, since it is the highest among the interaction of the synthesis parameters. In a nutshell, all the three parameters i.e. quantity of SPCNF aerogel (X_q), sintering temperature (X_T) and sintering time (X_t) play important roles in determining the quality of the $LiFePO_4$ nanowires produced in the process.

3.3. Validating of the Model Equation

With the aim to further validate the developed model equation, the synthesis conditions to produce the $LiFePO_4$ nanowires with the quality of 20%, 35% and 50% based on the use of 0.06 g of SPCNF aerogel were identified through the graphical method. Based on the developed model equation, the relevant synthesis conditions were identified by overlaying the contour plot of the quality of $LiFePO_4$ nanowires as a function of the sintering temperature (X_T) and sintering time (X_t). The predicted synthesis conditions are tabulated in Table 5.

To validate the predicted synthesis conditions, $LiFePO_4$ nanowires were synthesized based on the predicted synthesis condition and their quality was then computed and tabulated in Table 5 for comparison. Comparison shows that the quality of $LiFePO_4$ nanowires synthesized based on the predicted conditions are close to the expected quality values. Therefore, this validation test further confirmed the consistency and accuracy of the developed model equation to predict the quality of $LiFePO_4$ nanowires since there is only a deviation of ~5 % between the predicted and experimental values.

Table 5: Comparison between the predicted and experimental values of the $LiFePO_4$ nanowires quality

Sample No.	Quantity of SPCNF Aerogel (g), X_q	Sintering Time (min), X_t	Sintering Temperature (°C), X_T	Predicted Values for $LiFePO_4$ Nanowires Quality (%)	Experimental Values for $LiFePO_4$ Nanowires Quality (%)	Deviation (%)
1	0.06	136	423	20	14.68	5.32
2	0.06	163	460	35	29.60	5.40
3	0.06	180	500	49.78	45.14	4.64

Figure 5 shows the morphologies of $LiFePO_4$ nanowires synthesized at different sintering temperature (423, 460 and 500°C) and sintering time (136, 163 and 180 min). Nonetheless, the nanowires in Figure 5 are slightly different compared to the nanowires in Figure 1 in terms of their morphologies. Most probably this was due to the fact that SPCNF aerogel synthesized at different batches was used throughout this study. Morphology of the SPCNF aerogel was different due to the concentration of its own suspension. According to previous studies by other researchers, CNF aerogel with the suspension concentration below 0.2 wt.% will self-aggregate into 3D web-like structure [20]. However, when the concentration of CNF aerogel exceeds or equal to 0.5 wt.%, the insufficient space for the long SPCNF fibres dispersion caused the fibers to tightly cross-link with one another and eventually formed a 2D-sheet-like structure [20]. Consequently, this concentration factor affected the length of the $LiFePO_4$ nanowires synthesized, and their morphologies. It is therefore strongly recommend that the CNF suspension to be controlled at below 0.2 wt % in order to obtain aerogels which will lead to the ideal morphology.

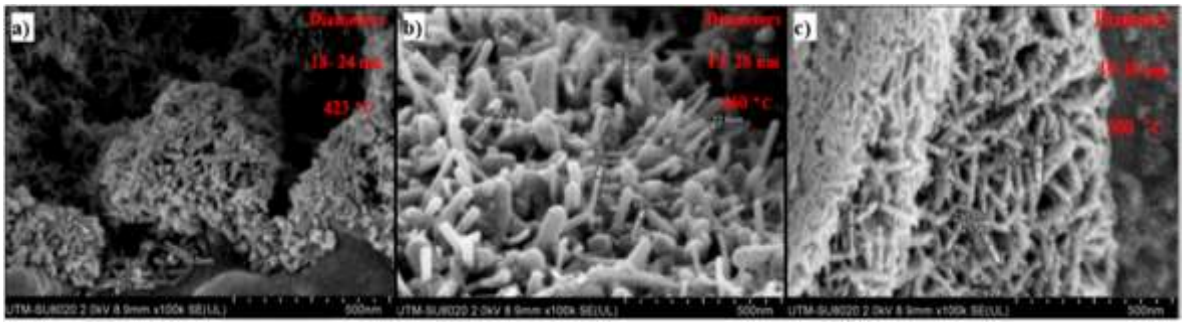


Figure 5: FE-SEM micrographs of $LiFePO_4$ nanowires synthesized at (a) 423°C for 136 min (b) 460 °C for 163 min and (c) 500°C for 180 min.

Figure 6 shows the XRD diffractograms of the $LiFePO_4$ nanowires synthesized at different sintering temperatures (423, 460 and 500°C) and sintering times (136, 163 and 180 min). Comparison of the XRD patterns shows that all the samples were in the same phase patterns and matched with lithium iron phosphate (V), $LiFe(PO_4)$ but slightly different in terms of the peaks intensity and position. The XRD peak widths became less broadened with increasing the sintering temperature from 423 to 500°C. This phenomenon is attributed to the larger mean crystallite size of $LiFePO_4$ nanowires which induced the nanostructure of $LiFePO_4$ nanowires were favourable to grain growth [21]. Besides, there is also a low intensity of carbon diffraction peak due to either its amorphous structure

or low content in the $LiFePO_4$ nanowires. However, its existence does not affect the structure of $LiFePO_4$ nanowires [17].

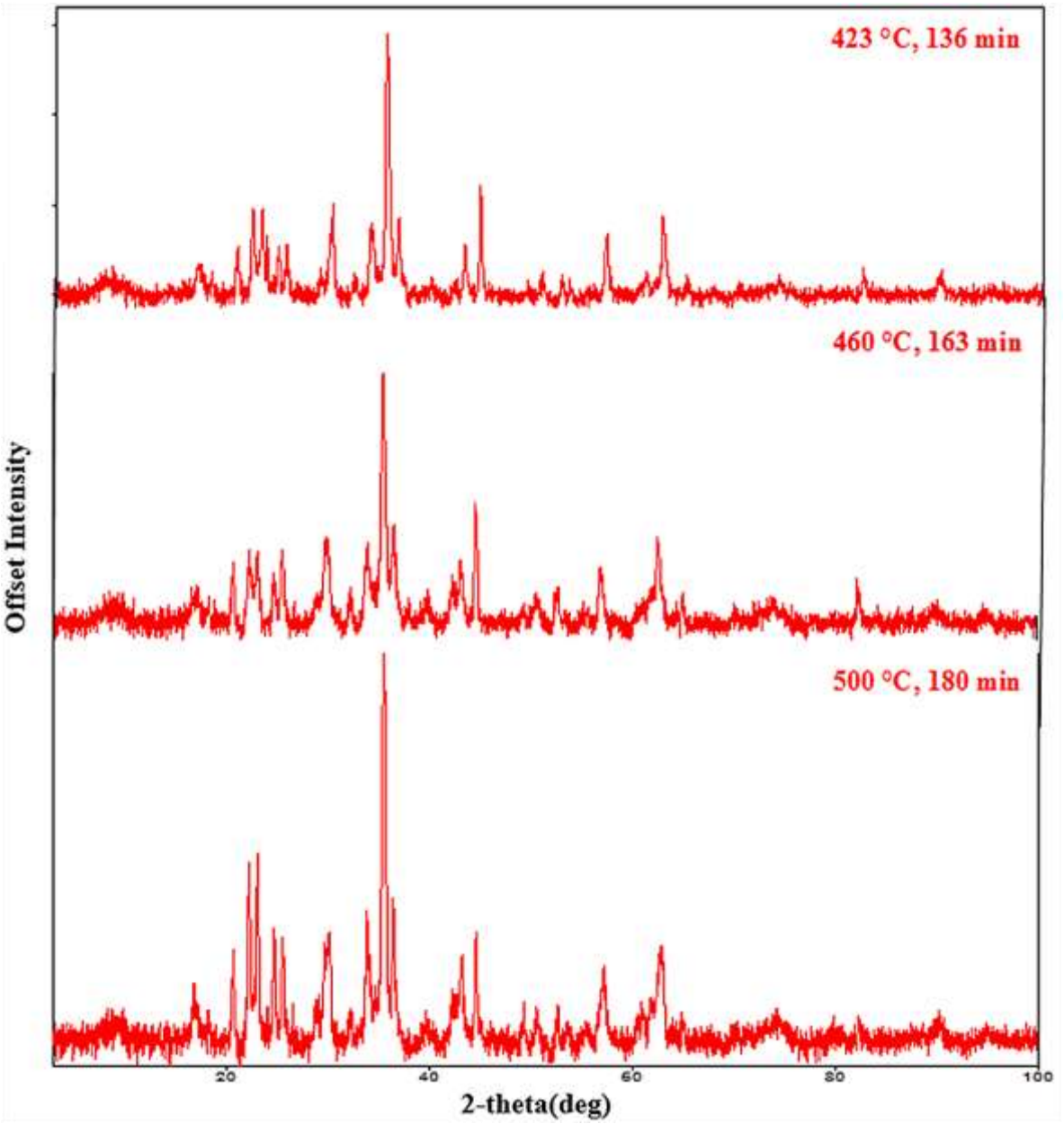


Figure 6: Comparison of the XRD patterns of the $LiFePO_4$ nanowires synthesized under the specified conditions.

4. Conclusions

In this study, $LiFePO_4$ nanowires with diameter of 15-30 nm were successfully synthesized by using SPCNF aerogel as the template. Based on the analysis, the synthesis parameters namely, quantity of SPCNF aerogel (X_q), sintering temperature (X_T) and sintering time (X_t), should be properly controlled throughout the synthesis process since they have an intimate relationship with the quality of $LiFePO_4$ nanowires synthesized in the process. A model equation was developed to represent and simulate the quality of the $LiFePO_4$ nanowires synthesized at different combinations of synthesis parameters. The validation test further confirmed the accuracy of the developed model equation, whereby the discrepancy between the predicted and experimental value for the quality of $LiFePO_4$ nanowires is about 5%.

Funding: The authors wish to express their gratitude to Malaysia Ministry of Higher Education (MOHE), Universiti Teknologi Malaysia (UTM) and Universiti Tun Hussein Onn Malaysia (UTHM) for the funding through Fundamental Research Grant Scheme (Grant Number 4F827) and Collaborative Research Grant (CRG) UTM-National grant scheme (Grant Number 4B421).

References

1. Zhang, Y.; Wang, Y.; Zhang, H.; Li, Y.; Zhang, Z.; Zhang, W. Recycling spent lithium-ion battery as adsorbents to remove aqueous heavy metals: Adsorption kinetics, isotherms, and regeneration assessment. *Resources, Conservation and Recycling* **2020**, 156, 104688.
2. Neef, C.; Wadepohl, H.; Meyer, H.P.; Klingeler, R. High-pressure optical floating-zone growth of Li (Mn, Fe) PO4 single crystals. *Journal of Crystal Growth* **2017**, 462, 50-59.
3. Costa, C. M.; Lizundia, E.; Lanceros-Méndez, S. Polymers for advanced lithium-ion batteries: State of the art and future needs on polymers for the different battery components. *Progress in Energy and Combustion Science* **2020**, 79, 100846.
4. Zhu, B.Q.; Li, X.H.; Wang, Z.X.; Guo, H.J.; Novel synthesis of $LiFePO_4$ by aqueous precipitation and carbothermal reduction. Materials Chemistry and Physics **2006**, 98, 373-376.
5. Park, J.C.; Kim, J.; Kwon, H.; Song, H.; Gram-Scale. Synthesis of Cu2O Nanocubes and Subsequent Oxidation to CuO Hollow Nanostructures for Lithium-Ion Battery Anode Materials. *Advanced Materials* **2009**, 21, 803-807.
6. Kanagaraj, A.B.; Chaturvedi, P.; Alkindi, T.S.; Susantyoko, R.A.; An, B.H.; Patole, S.P.; Choi, D.S. Mechanical, thermal and electrical properties of LiFePO4/MWCNTs composite electrodes. *Materials Letters* **2018**, 230, 57-60.
7. Banitaba, S.N. Application of electrospun fibers for the fabrication of high performance all-solid-state fibrous batteries. *In Nanosensors and Nanodevices for Smart Multifunctional Textiles*, Ehrmann, A., Nguyen, T.A., Nguyen Tri, P.; Eds; Elsevier: Amsterdam, The Netherlands, 2021; pp. 229-244
8. Liu, Y.; Goebl, J.; Yin, Y. Templated synthesis of nanostructured materials. *Chemical Society Reviews* **2013**, 42, 2610-2653.
9. Sides, C.R.; Croce, F.; Young, V.Y.; Martin, C.R.; and Scrosati, B. A high-rate, nanocomposite LiFePO4/carbon cathode. *Electrochemical and Solid-State Letters* **2005**, 8(9), 484–487.
10. Bai, N.; Xiang, K.; Zhou, W.; Lu, H.; Zhao, X.; Chen, H. LiFePO4/carbon nanowires with 3D nano-network structure as potential high performance cathode for lithium ion batteries. *Electrochimica Acta* **2016**, 191, 23–28.
11. Fischer M.G.; Hua X.; Wilts B.D.; Martínez E.C.; Steiner U. Polymer-Templated LiFePO4/C Nanonetworks as High-Performance Cathode Materials for Lithium-Ion Batteries. *ACS Applied Materials & Interfaces* **2018**, 10, 1646-1653.
12. Lai J.C.; Wan Abdul Rahman W.A.; Toh W.Y. Mechanical, Thermal and Water Absorption Properties of Plasticised Sago Pith Waste. *Fibers and Polymers* **2014**, 15, 971-978.
13. Beh J.H.; Lim T.H.; Lew J.H.; Lai J.C. Cellulose Nanofibril-based Aerogel Derived from Sago Pith Waste and Its Application on Methylene Blue Removal. *International Journal of Biological Macromolecules* **2020**, 160, 836-845.
14. Wang, J.; Tavakoli, J.; and Tang, Y.; Bacterial cellulose production, properties and applications with different culture methods – A review. *Carbohydrate Polymers* **2019**. 219, 63–76.
15. Meng, Y.J.; Timothy, M.Y.; Liu, P.Z.; Cristian, I.C.; Huang, B.; Wang, S.Q. Ultralight Carbon Aerogel from Nanocellulose as A Highly Selective Oil Absorption Material, *Cellulose* **2014**, 22, 435-477.
16. Sun, X.; Li, J.; Shi, C.; Wang, Z.; Liu, E.; He, C.; Du, X.; Zhao, N. Enhanced Electrochemical Performance of LiFePO4 Cathode with In-Situ Chemical Vapor Deposition Synthesized Carbon Nanotubes as Conductor. *J. Power Sources* **2012**, 220, 264-268.

17. Hong, S.A.; Kim, S.J.; Kim, J.; Lee, B.G.; Chung, K.Y.; Lee, Y.W. Carbon Coating on Lithium Iron Phosphate (LiFePO4): Comparison between Continuous Supercritical Hydrothermal Method and Solid-State Method. *J. Chem. Eng* **2012**, 198-199, 318-326.
18. Wang, B.; Liu, A.; Abdulla, W.A.; Wang, D.; Zhao, X.S. Desired Crystal Oriented LiFePO4 Nanoplatelets In-Situ Anchored on A Grapheme Cross Linked Conductive Network for Fast Lithium Storage. *Nanoscale* **2015**, 7, 8819–8828.
19. Rho, Y.H.; Nazar, L.F.; Perry, L.; Ryan, D. Surface Chemistry ofLiFePO4 Studied by Mossbauer and X-Ray Photoelectron Spectroscopy and Its Effect on Electrochemical Properties. *J. Electrochem. Soc.* **2007**, 154, A283–A289.
20. Chen, W.; Li, Q.; Wang, Y.; Yi, X.; Zeng, J.; Yu, H.; Liu, Y.; Li, J. Comparative Study of Aerogels Obtained From Differently Prepared Nanocellulose Fibers. *ChemSus Chem* **2014**, 7, 154-161.
21. Hosono, E.; Wang, Y.; Kida, N.; Enomoto, M.; Kojima, N.; Okubo, M.; Matsuda, H.; Saito, Y.; Kudo, T.; Honma, I.; Zhou, H. Synthesis of TriaxialLiFePO4 Nanowire with a VGCF Core Column and a Carbon Shell through the Electrospinning Method. *ACS Appl Mater Interfaces* **2010**, 2(1), 212-218.

Sulphonated MIL-101(Cr): Microwave Responsive Catalyst for Fructose Dehydration into Platform Chemicals

Noor Aljammal [1,3,*], Jeroen Lauwaert [2], Francis Verpoort [1,4], Philippe M. Heynderickx [1], Joris W. Thybaut [3]

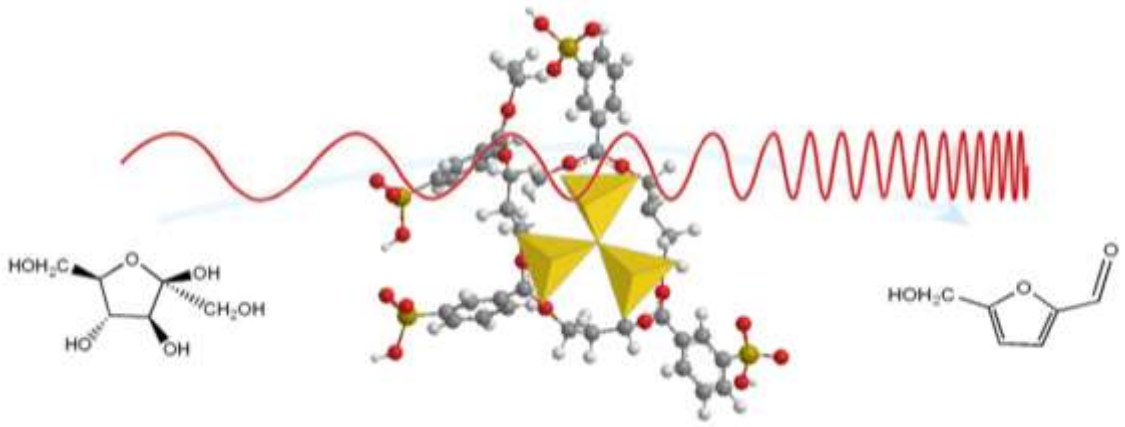
[1] Department of Green Chemistry and Technology, Faculty of Bioscience Engineering, Ghent University, Ghent, Belgium

[2] Industrial Catalysis and Adsorption Technology (INCAT), Department of Materials, Textiles and Chemical Engineering, Faculty of Engineering and Architecture, Ghent University, Ghent, Belgium

[3] Laboratory for Chemical Technology, Faculty of Engineering and Architecture, Ghent University, Ghent, Belgium

[4] Department of Organometallics, Catalysis and Ordered Materials, State Key Laboratory of Advanced Technology for Materials Synthesis and Processing; Center for Chemical and Material Engineering, Wuhan University of Technology, Wuhan, Chin

**Corresponding author: nour.aljammal@ugent.be, +32496749492*



Although being used progressively in the research and biomass transformation, the intrinsic nature of microwave irradiation (MW) effects on chemical reactions remains unclear. Herein, fructose dehydration over a Brønsted acid sulphonated MOF, MIL-101-SO_3H, was studied in one-pot microwave transformation. Set of reaction conditions were examined under different temperatures, times, and several catalysts to substrate ratio to evaluate the potential of MIL-101(Cr)-SO_3H as a microwave-responsive catalyst towards sugar conversion into 5-HMF. DMSO-acetone reaction media resulted in a 95% yield of 5-HMF for 99% conversion at 160 ◦C after 10 minutes reaction time. While, at the same conditions, conventional heating resulted in 13.23% fructose conversion and no 5-HMF yield. Thus, it was proven that there is a special effect of microwave and the catalyst activity, as MIL-101-SO_3H consists of a polar sulfo-group. This polar species rotates fast in the microwave field, increasing catalysts' reactivity and significantly reducing the total reaction time.

This paper also attempts to tackle the deviation of reactions performed in MW reactor and CH heating using a kinetic approach. There is at least an element of doubt about whether the Arrhenius parameters obtained from the reaction performed in MW are actual or apparent. Thus, in the present case, the argument for their being apparent is solid. However, under the conditions studied, the reaction was found to be of first-order in fructose dehydration into 5-HMF. Furthermore, it was

demonstrated that a 10-fold rate coefficient enhancement was observed using the microwave over convective heating. Therefore, the changes in Ea of fructose dehydration between MW and CH must be at least partly compensated by changes in the pre-exponential factor and or effective temperature.

Keywords: 5-HMF; MOF; Microwave; Fructose; platform chemicals

Synthesis of Ag Nanoparticles Loaded NanoTiO_2 Catalyst Using Mechanical Ball Milling for Phenol Photodegradation

Mohammad Ashraf Ali*, Ahmed Abutaleb, Mohd Imran, Ali Nasser Salhaby, Abdo Zalaei Faranti, Saeed Mohammed Ali

Department of Chemical Engineering, College of Engineering, Jazan University, Jazan 41524, Saudi Arabia

**Corresponding author: maali8000@gmail.com, Mobile: 966-507961837*

Abstract: The nanoTiO_2 loaded with Ag nanoparticles (Ag/nanoTiO_2) was prepared by the mechanical ball milling method and used for the photocatalytic degradation of phenol in an aqueous solution. The Ag/nanoTiO_2 catalyst was characterized by X-Ray Diffraction (XRD) and UV-Visible spectrophotometer. The bandgap analysis for the Ag/nanoTiO_2 catalyst was performed by the Tauc plot method. The bandgap of pure TiO_2 generally ranges from 3.2 eV-3.4 eV, but after loading with Ag, it was found to have 2.6 eV. The presence of Ag and nanoTiO_2 were identified by their peaks in the XRD spectrum. The photodecomposition of phenol was carried out using pure nanoTiO_2 and Ag/nanoTiO_2 under sunlight, ultraviolet light, and visible white light using different amounts of catalyst and phenol concentration. The visible white light provided highest phenol degradation among the three irradiation sources. The loading of Ag on nanoTiO_2 improved the phenol degradation rate and offered higher phenol degradation as compared to nanoTiO_2. A maximum of 94% degradation was recorded in 120 minutes for 10 mg of Ag/nanoTiO_2 catalyst and 10 ppm concentration of phenol at pH 8 under the visible white light source. The phenol photodegradation reaction with Ag/nanoTiO_2 catalyst was found to follow zero-order kinetics.

Keywords: Photocatalytic degradation, phenol, nanostructured materials, nanoTiO_2, Ag/nanoTiO_2, zero-order kinetics, UV-Vis monitoring

1. Introduction

The refining and petrochemical industry uses large quantities of water and produces subsequently large volumes of wastewaters containing several organic compounds. The effluents contain organic and inorganic chemical species that hurt human health and the environment. Organic compounds present in these wastewaters are not readily biodegradable because of the complexity of their chemical structures. Concentrations of these pollutants in the effluents should be controlled to respect environmental customs and legislation on water quality, which have become more stringent in recent years. Treatment of effluents is a major challenge, especially for developing countries. Management of these wastewaters requires specific treatment techniques such as activated carbon adsorption, membrane processes, coagulation-flocculation, reverse osmosis, chemical oxidation, and reduction. The advanced oxidation processes (AOPs) show specific advantages over conventional treatments because they can eliminate non-biodegradable organic components and avoid the need for residual sludge disposal. AOPs based on the generation of very reactive and oxidizing free radicals, especially hydroxyl radicals, have been used with increasing interest due to their high oxidant power. There is a growing interest in the use of semiconductors as photosensitizers for the complete oxidative mineralization of pollutants by oxygen [1], pointing out its potential prominent role in wastewater purification. Many different semiconducting materials are readily available but only a few are suitable for sensitizing the photomineralization of a wide range of organic pollutants. The metal oxides such as TiO_2, ZnO, Fe_2O_3, CdS, SnO_2, and ZnS are some of the semiconducting photocatalysts, among which TiO_2 is one of the most suitable semiconducting materials in different media [2-7] and it is capable of decomposing a wide range of organic and inorganic pollutants and toxic materials [2,4]. The main polymorphs of TiO_2, rutile, and anatase, are commonly used in photocatalysis, with anatase showing a higher photocatalytic activity [5-7]. The higher activity Anatase is usually attributed to its larger specific surface area. Though TiO_2 is superior to other semiconductors for many practical uses, the following two types of defects limit its photocatalytic activity [8,9]:(i) Because of its high

bandgap (3.2 eV), TiO_2 is active only under UV light (λ <380 nm) which is only 4-5% of the overall solar spectrum. This restricts the use of sunlight or visible light. (ii) The high rate of electron-hole recombination in TiO_2 particles results in low photo quantum efficiency. To overcome these limitations of TiO_2, several strategies have been proposed among which, doping of selective metal ions into TiO_2 is significant [10-12]. The advantage behind doping the metal ions into TiO_2 is the temporary trapping of the photogenerated charge carriers by the dopant and the inhibition of their recombination during migration from inside the material to the surface [10]. Many researchers have used transition metal ions, alkaline metals, Zn^{+2}, Fe^{+3}, Ag, Au, Pd, Pt, Li, and Rb [10-20] to improve the photocatalytic activity of TiO_2. The properties and photocatalytic activity of a photocatalyst are greatly influenced by the preparation methods. Previous workers have developed numerous techniques for fine TiO_2 powders preparation which include vapor decomposition, hydrolysis, hydrothermal treatment, hydrolysis, oxidation, hydrothermal oxidation, mechanical alloying, co-precipitation impregnation, and sol-gel method. Organic pollutants including phenol are persistent pollutant materials that are difficult to decompose by microbiological treatment processes. Their oxidation through photocatalysis is an alternative way to prevent contamination of the environment. Phenol is used in many industries such as oil refineries and petrochemical plants. Phenol is a contaminant to the environment and difficult to remove. It has short and long-term adverse effects for humans and animals. The preparation of inexpensive nanocatalyst with high efficacy in the degradation of phenol presents in wastewater under light irradiation at ambient conditions is needed. This project focused on finding the right catalyst for phenol photocatalytic degradation with higher performance. The objective of this study was to prepare and use a titania-based metal-modified catalyst for photocatalytic degradation of phenol present in wastewater using photocatalysts under visible light irradiation. In this study, a titania-based catalyst doped with silver was prepared and used for the photocatalytic degradation of phenol. The main factors, which govern photocatalytic efficiency were investigated. These factors include the concentration of catalyst, initial concentration of phenol, and irradiation time.

2. Experimental

2.1 Materials

The materials and chemicals used in this study were nano titanium dioxide P25 (nanoTiO2) from Degussa, silver nitrate 99% pure, pure phenol 99% pure, sodium hydroxide 98% pure, and H_2SO_4 95% concentrated, from Fluka, deionized water, and potable water. The wavelength of UV lamp was 100 to 380 nm while 390 nm to 700 nm for white visible light.

2.2 Experimental Procedures

2.2.1 Ag/nanoTiO_2 Photocatalyst Synthesis

The nanoTiO_2 was used as received. The Ag loaded nanoTiO_2 photocatalyst was prepared by mixing equimolar amounts of silver nitrate and nanoTiO_2 and subjected to electromechanical treatment in a ball mill. The milling procedure was as follows: The ball mill machine was programmed for 15 min operation followed by 15 min stop to avoid overheating of the ball mill. This operation continued for seven days to ensure the solid-state reaction between silver nitrate and nanoTiO_2. The resultant solid was then removed from the ball mill and calcined in a furnace in the presence of air at 500 °C for 3 hours in a furnace to remove nitrates. The heating rate was 5 °C /min. The resultant calcined Ag/nanoTiO_2 was grinded to a fine powder and used in the photocatalytic phenol degradation experiments (**Figure 1**). Degradation tests were carried out in two photocatalytic reactors equipped with UV light and white visible light, and under sunlight under different operational conditions of irradiation time, amount of catalyst, and initial concentration of phenol in water.

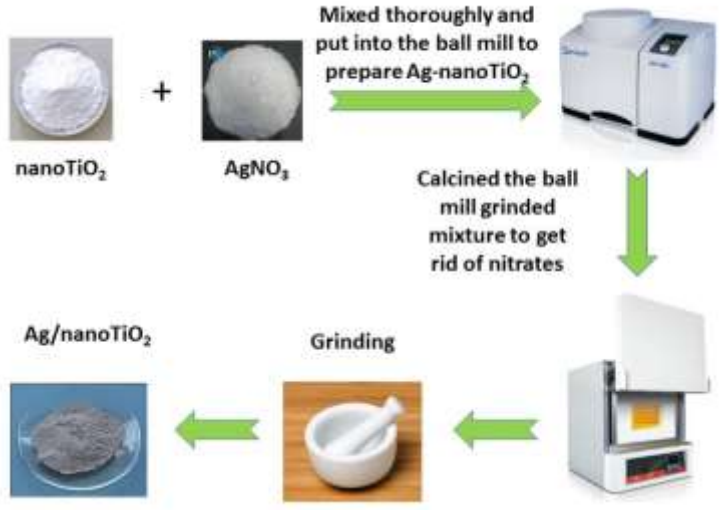


Figure 1. Schematic showing the preparation of Ag/nanoTiO$_2$ photocatalyst using mechanical ball milling method

2.3. Photocatalytic Study

One hundred (100) mL of the aqueous solution of phenol, with a known concentration, was introduced in a special glass air-light bottle with a known amount of Ag/nanoTiO$_2$ catalyst, and the bottle was sealed. The mixture was stirred for 20 min in the dark to reach adsorption equilibrium on the solid surface of the catalyst. The mixture was then irradiated in the two photoreactors based on UV and white visible light radiation. The idea of the photoreactor fabricated for this study using visible white light was adopted from AizatArif et al. 2019 [**6**]. A sample (5ml) was withdrawn from the glass bottle at a predetermined time interval, resealed the bottle, and again subjected to irradiation. The withdrawn samples were centrifuged with a speed of 2000 rpm for 30 min to allow all the catalyst nanoparticles to separate from the solution. In parallel, samples were also exposed to sunlight and periodic sampling was done to extract the samples at a fixed time interval. The temperature of the irradiated mixture in sunlight, UV light and white visible light was between 30-35 °C. The exposed samples were centrifuged at 2000 rpm speed for 30 minutes to remove the catalysts. The absorbance of the clear catalyst-free solution was then measured using a UV/Visible spectrophotometer set at 270nm. The parameters studied were performed using different types of light sources such as UV light, sunlight and white light, amount of catalyst (10, 20, 30 mg), and concentration of phenol solution (10, 50, 100 ppm). The absorbance data was recorded to determine the concentration of unreacted phenol in the sample (C_t) and percent degradation was calculated. The plots of percent degradation with irradiation time were developed. Then the phenol concentration data vs irradiation time was plotted and correlated to determine the slope, which represented the rate constants of the reaction.

2.4 Catalyst Characterization

The phase of Ag/nanoTiO$_2$ catalyst was examined using X-ray diffraction technique (XRD) with D8 AαS Advance X-ray diffractometer using Cu Kα radiation (λ = 1.54156Å). UV-Vis diffuse reflectance/absorbance spectroscopy of the Ag/nanoTiO$_2$ was done using VARIAN, Cary 5000 UV-VIS-NIR double beam spectrophotometer.

3. Results and discussion

3.1 Catalyst Characterization

3.1.1 XRD analysis

Figure 2a represents the XRD analysis of Ag/nanoTiO$_2$ which represents the dual-phase. The mixed-phase contains peaks at 2 theta value of 24, 25.3, 29.9, 34.4, 37.8, 48.5, and 68.9 which is

corresponding to the (101), (110),(121), (103), (004), (200) and (301) crystal planes respectively. This is confirmed from the JCPDS card no. 01-075-2550. These values confirmed the presence of Ag and three different TiO_2 crystal structures. The XRD techniques also show some major peaks of the FCC crystal phase which were observed at 2 theta value of 38.5, 44.4, 64.4, and 77.5 which is corresponding to the (111), (200), (220), and (311) respectively [21, 22].

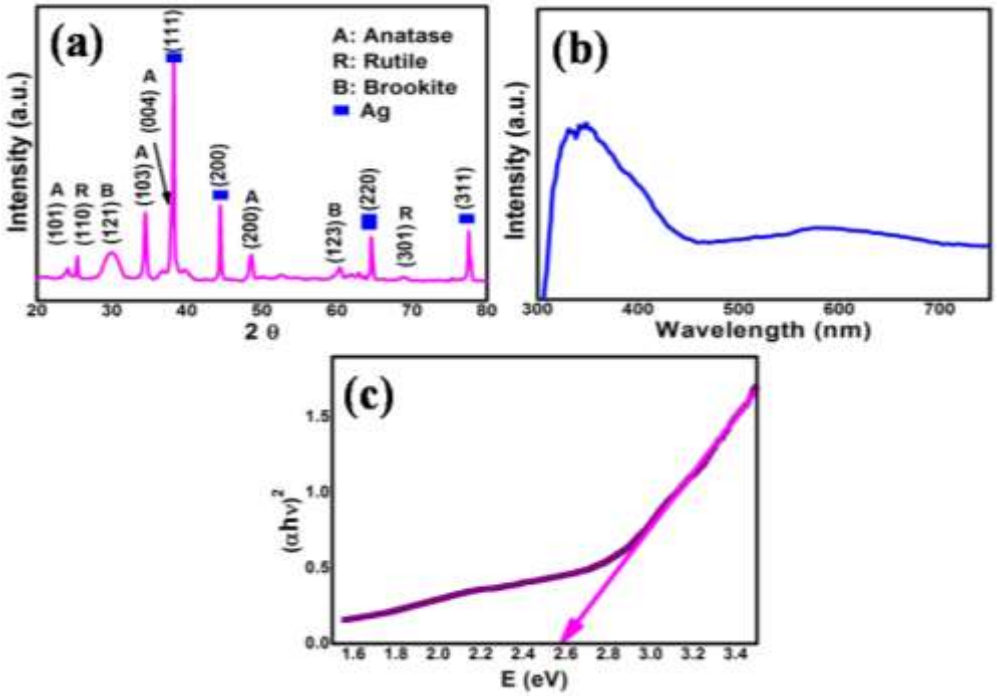


Fig. 2(a) XRD analysis, (b) UV-Visible spectra, and (c) Tauc plot for Ag/nanoTiO_2.

3.1.2 UV-Visible Spectroscopy

The UV-Visible spectra of Ag/nanoTiO_2 is shown in Fig. 2c. The analysis shows that there is the absorption of light is in the UV-visible range. Further, it can be explained that absorption in this range is due to the loading of Ag on nanoTiO_2 which also led to a decrease in the bandgap of nanoTiO_2.

3.1.3 Tauc Plot (Band Gap Calculation)

The indirect bandgap data were calculated from UV-Visible analysis represented in Fig.2d. The indirect bandgap of Ag/nanoTiO_2 was calculated by approximately 2.6 eV. The calculated band gap is comparatively lower than the pure titania as observed from the literature. Due to the presence of silver in the lattice of the titania, it was observed that the redshift moved towards a more visible region. The introduction of silver ions in titania derives intermediate electronic states from the strong coupling between silver and titania orbitals [25]. Hence mixing and interaction of Ag with pure nanoTiO_2 led to a lowering of the bandgap which may promote photodegradation study under visible light.

3.2 Photodegradation of phenol

The parameters studied were the amount of catalyst (10-30 mg), the concentration of phenol (10-100 ppm) in the reacting mixture, and the type of light source (UV light, sunlight, white light). The two catalysts were compared and found that Ag/nanoTiO_2 performed better than pure nanoTiO_2 catalyst and it was shown by the %degradation of phenol with irradiation time using the two catalysts. Percent Photocatalytic degradation =100 x $[(C_0 - C_t) / C_0]$, Where C_0 is the initial concentration of phenol before light irradiation, and C_t is the concentration of phenol after irradiation at time t.

3.2.1 Effect of light source Type

The effect of the light source type was evaluated on phenol degradation and has been graphically presented in **Figure 3a.** It was observed that the concentration of phenol was less using sunlight compared to visible light (400-watt) and in 300 minutes of irradiation, phenol degradation was 30.7% using sunlight as compared to 40.5% using visible light. The use of ultraviolet light (19 watt) was not very effective due to its low power, and it was expected that a higher percentage of phenol degradation may be achieved using high power ultraviolet light. The rate constant (k) was obtained from the plot of Ct vs. irradiation time.

3.2.2 Effect of amount of catalyst (nanoTiO2)

The effect of the amount of nanoTiO_2 catalyst on phenol degradation was observed under 400-watt power visible white light irradiation at pH 8 of the solution. The pH of 8 was found optimum for phenol degradation efficiency. The data is presented graphically in **Figure 3b.** It was observed that the % degradation of phenol (100ppm) was 31.5% using 30 mg of TiO_2 for 300 minutes compared to 10 mg of TiO_2, where the % degradation was only 10.7%. The rate constant (k) was obtained from the plot of Ct vs. irradiation time.

3.2.3 Effect of amount of catalyst (Ag(0)/nanoTiO2).

The effect of the amount of catalyst (Ag/nanoTiO_2) on phenol degradation was observed under 400-watt power visible white light irradiation at optimized pH 8 of the solution. The data is presented graphically in **Figure 3c.** It was observed that the concentration of phenol decreased using 30 mg of Ag/nanoTiO_2 for 300 minutes and % degradation was 88.7% comparing to the 10 mg of Ag/nanoTiO_2, where the maximum percent degradation was approximately 40.5%. Rate constants (k) were obtained from a plot of Ct vs. irradiation time for various amounts of catalyst.

3.2.4 Effect of phenol concentration

The effect of phenol concentration on photocatalyst activity was examined and was reported graphically presented in **Figure 3d**. It was observed that the percent degradation of phenol was high at low initial phenol concentrations (10 ppm) as compared to higher initial phenol concentrations (50 ppm and 100 ppm). The rate constant (k) was obtained from the Ct plotted against the irradiation time for variable phenol concentration used in the experiment.

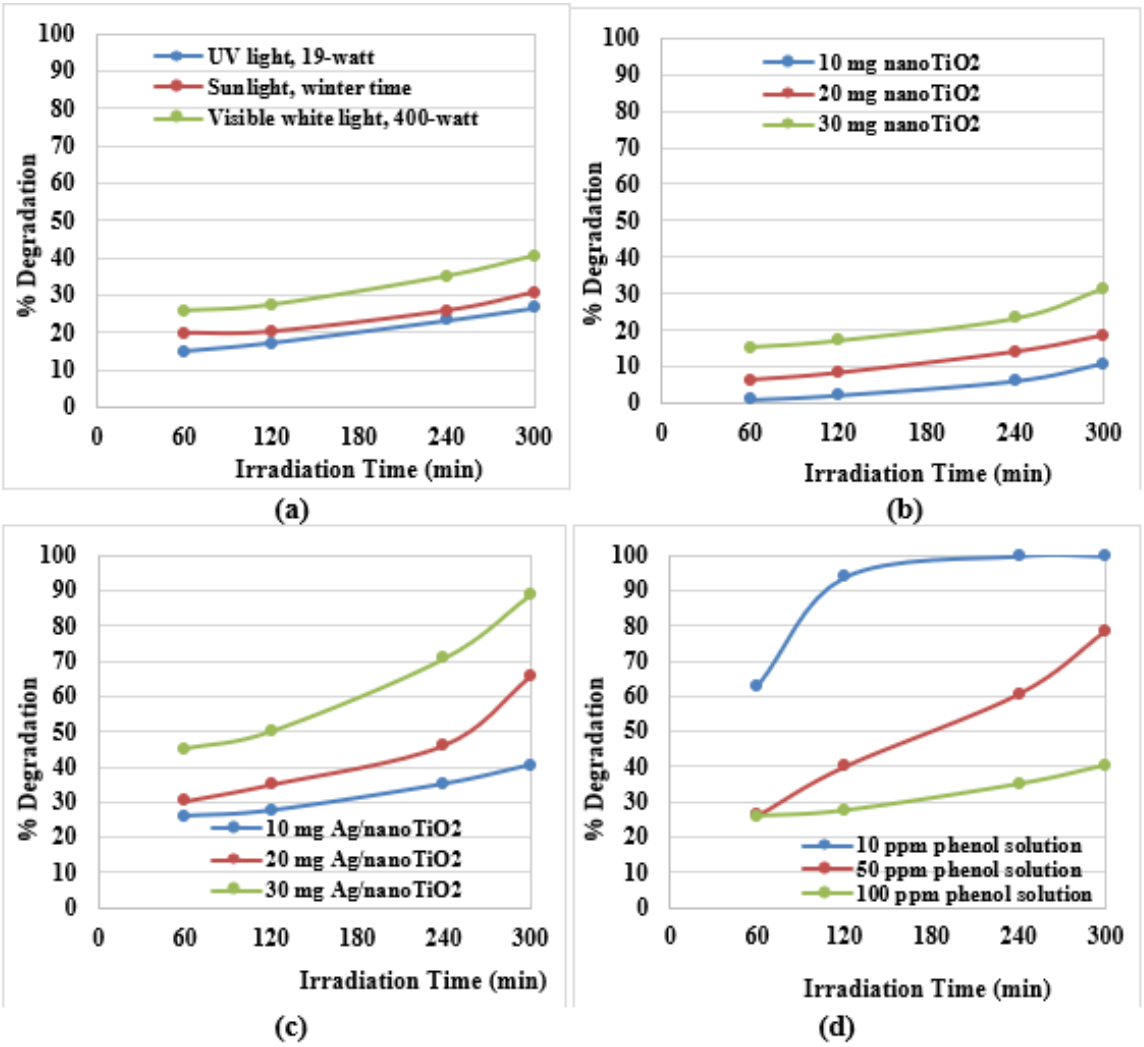


Fig. 3 Phenol degradation of 100 ml solution vs. irradiation time for (**a**) 100 ppm phenol solution using 10 mg Ag/nanoTiO_2 catalyst under different irradiation sources, (**b**) 100 ppm phenol solution using visible white light 400-watt at different amount of nanoTiO_2 catalyst, (**c**) 100 ppm phenol solution using visible white light 400-watt with different amount of Ag/nanoTiO_2 catalyst, (**d**) 10 mg Ag/nanoTiO_2 catalyst under visible white light 400-watt with different phenol concentration.

The photocatalytic degradation rate was deduced from the plot of the concentration of phenol as a function of irradiation time.

- Phenol concentration at time t (C_t) as a function of irradiation time (t). (*to check if the reaction followed zero order*).
- Natural log of phenol concentration at time t (Ln C_t) as a function of irradiation time (t). (*to check if the reaction followed 1st order*).
- Reciprocal of phenol concentration at time t (1/ C_t) as a function of irradiation time (t). (*to check if the reaction followed 2nd order*)

Through examining the plots and the correlation coefficient R^2, it was observed that the plot of phenol concentration at time t (Ct) as a function of time of irradiation (t) showed a straight-line relationship and the value of correlation coefficient was also indicative that the data obtained during photocatalytic degradation of phenol was best fitted for zero-order reaction kinetics (**Figure 4**). For a zero-order, rate of reaction = k and k = - slope of the plot of Ct vs t.

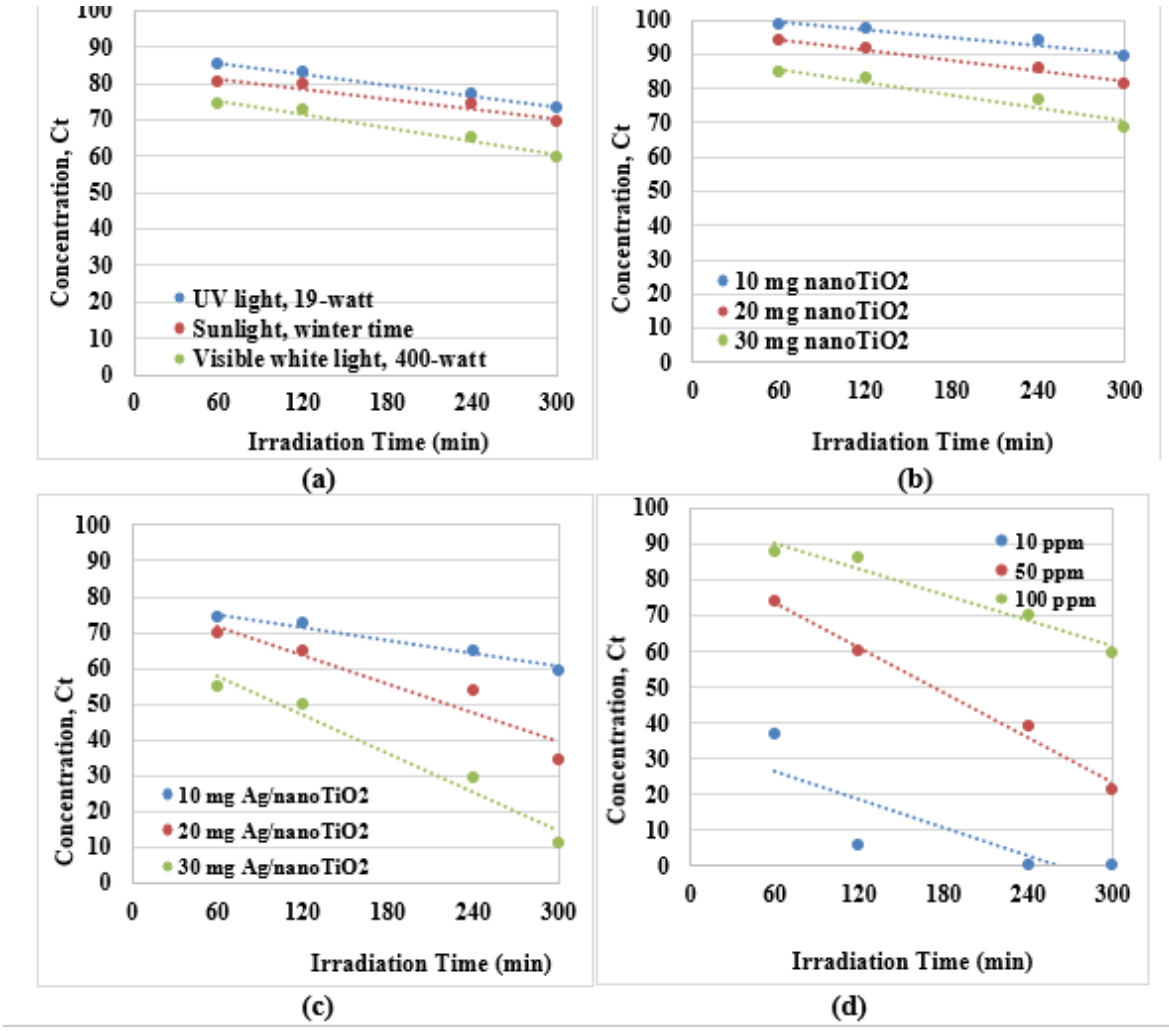


Figure 4. Plot of concentration (Ct) vs. irradiation time for (**a**) 100 ppm phenol solution using 10 mg Ag/nanoTiO_2 catalyst under different irradiation sources, (**b**) 100 ppm phenol solution using visible white light 400-watt at different amount of nanoTiO_2 catalyst, (**c**) 100 ppm phenol solution using visible white light 400-watt with different amount of Ag/nanoTiO_2 catalyst, (**d**) 10 mg Ag/nanoTiO_2 catalyst under visible white light 400-watt with different phenol concentrations.

A summary of the results of the kinetic study is shown in **Table 1** for all the reaction variables studied showing the rate constants values obtained with their correlation coefficients. The two catalysts were compared and found that Ag/nanoTiO_2 performed better than pure nanoTiO_2 catalyst. The positive effect of loaded metal in zero oxidation state has been demonstrated in 2019 by Dong and coworkers who synthesized Ni(0) NPs implanted Ni_xAl_yO supported catalyst which exhibited high phenol hydrogenation performance due to the better dispersion of the active Ni(0) species, as well as strong interaction between Ni(0) NPs and the support [**26**]. A comparison of the results obtained in this study was made with the reported literature values and is shown in **Table 2**. The degradation results of this study were found better than the literature values obtained for N-doped titania and Cu-N-doped titania catalysts.

Table 1 Summary of the rate constants and correlation coefficients obtained for zero-order kinetics.

Parameter	R^2	Rate Constant (k) mg. L^{-1}. min^{-1}
Type of irradiation source using 10 mg Ag/nanoTiO_2, 100 ppm phenol solution		
• UV light, 19 watt	0.9964	0.0495
• Sunlight	0.9367	0.0457
• visible white light, 400 watt	0.9738	0.0613
mg nanoTiO_2 catalyst, 100 ppm phenol solution		
• 10	0.9391	0.0383
• 20	0.9821	0.0515
• 30	0.9242	0.0642
mg Ag/nanoTiO_2 catalyst, 100 ppm phenol solution		
• 10	0.9738	0.0613
• 20	0.9035	0.1385
• 30	0.9638	0.1793
Initial phenol concentration (ppm) in water using 10 mg Ag/nanoTiO_2		
• 10	0.6789	0.1213
• 50	0.9894	0.0880
• 100	0.9651	0.0613

Table 2 Comparison of photocatalysis results of this study with those reported in the literature. The value of TOF was calculated as mg phenol converted per mg of catalyst (TOF = mg phenol degraded/mg catalyst)

No.	Photocatalyst	Time (min)	Phenol Conc.	Irradiation light	% Degradation, (TOF)	Reference
1.	Ag/nanoTiO_2, 10mg	120/300	100 ml of 10 ppm aq. sol., pH 8 (1mg)	visible white light (400 watts)	94/100, (0.094/0.100)	This study
2.	Ag/nanoTiO_2, 10mg	120/300	100 ml of 50 ppm aq. sol., pH 8 (5mg)	visible white light (400 watts)	40/79, (0.200/0.400)	This study
3.	Ag/nanoTiO_2, 10mg	120/300	100 ml of 100 ppm aq. sol., pH 8 (10mg)	visible white light (400 watts)	28/41, (0.280/0.410)	This study
4.	Ag/nanoTiO_2, 20mg	120/300	100 ml of 100 ppm aq. sol., pH 8 (10mg)	visible white light (400 watts)	35/66, (0.175/0.330)	This study
5.	Ag/nanoTiO_2, 30mg	120/300	100 ml of 100 ppm aq. sol., pH 8 (10mg)	visible white light (400 watts)	50/89, (0.167/0.296)	This study
6.	N-TiO_2 2.5mg	120	40 ml of 50 ppm sol. (2mg)	visible light	5.7, (0.0456)	[1]
7.	N-TiO_2 2.5mg	120	40 ml of 50 ppm sol. (2mg)	UV light	5.7, (0.0456)	[1]
8.	Cu-N-TiO_2 2.5mg	120	40 ml of 50 ppm sol. (2mg)	visible light	5.0, (0.0400)	[1]

The recycling of the catalyst was checked 5 times and the data obtained showed a slight decrease in the performance of the catalyst. It was observed that the absorbance decreases, demonstrating the degradation of phenol, with increasing irradiation time that produced an enhanced photocatalytic reaction. The photocatalytic reaction pathway was believed to involve the reaction of phenol with the

generated OH• radicals, resulting in the decomposition of phenol into H_2O and CO_2. It was noted that the degradation rate of phenol was reduced with increasing initial phenol concentration, indicating that the photonic efficiency decreases rapidly with an increasing initial concentration of phenol. Several researchers have reported this behaviour earlier in their studies [**27-29**]. The Proposed mechanism of photocatalytic mineralization of phenol by Ag-nanoTiO_2 catalyst is shown in **Figure 5**.

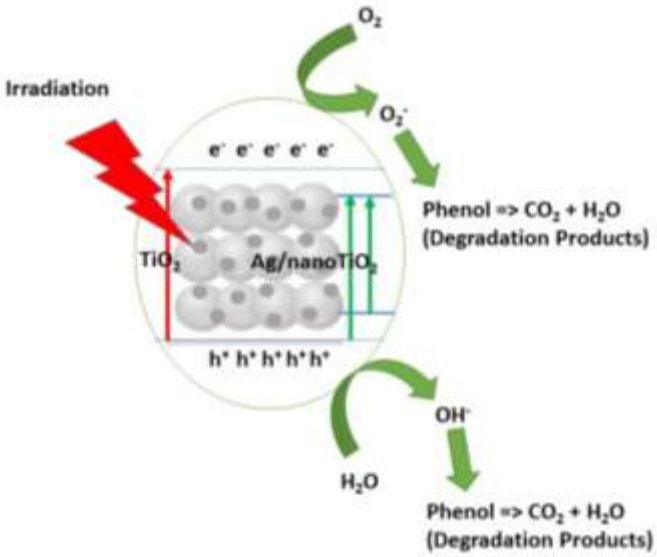


Figure 5. Proposed mechanism of photocatalytic mineralization of phenol by Ag/nanoTiO_2 catalyst.

4. Conclusions

The Ag nanoparticles loading on nanoTiO_2 (Ag/nanoTiO_2) achieved through the mechanical ball milling method showed a significant increase for phenol photodegradation compared to pure nanoTiO_2. This improved efficiency was the result of the Ag loading on nanoTiO_2 which reduced the bandgap of pure TiO_2 (3.2 eV) to 2.6 eV. The highest photodegradation rate of phenol was achieved using 30 mg of Ag/nanoTiO_2, using a 400-watt white visible light, for 300 minutes, at pH 8 of the solution. The pH of 8 was found optimum for phenol degradation efficiency. Complete mineralization of phenol was achieved using 10 mg Ag/nanoTiO_2 catalyst with 100 ml of 10 ppm of phenol solution under visible white light 400-watt with different phenol concentrations. Kinetic studies of photocatalytic degradation revealed that the degradation of phenol in water followed zero-order reaction kinetics using Ag/nanoTiO_2 and nanoTiO_2 catalysts. The phenol degradation results of this study using Ag/nanoTiO_2 were found improved as compared to the values for N-doped titania catalysts reported in the literature.

Acknowledgments: The authors wish to acknowledge the support provided by the Jazan University under the 9th future scientist program (Project No. FS10-081).

References

1. Marjorie G. S. Photocatalytic decomposition of phenol under visible and UV light utilizing titanium dioxide based catalysts, *Honour's Theses*, University of New Hampshire, **2017**.
2. Sin, J-C.; Lim, C-A.; Lam, S-M.; Mohamed, A.R.; Zeng, H. Facile synthesis of novel ZnO/Nd-doped BiOBr composites with boosted visible light photocatalytic degradation of phenol, *Materials Letters*, **2019**, 248:20–23.
3. Marissa, C-L.; Wudneh, A.S.; Jerald, A.L.; Saravanan, R.S. Photocatalytic degradation of phenol and phenol derivatives using a nano-TiO_2 catalyst: integrating quantitative and qualitative factors using response surface methodology, *water*, **2014**, 9-19.
4. Feryal, A.; Nur, O.A. Photocatalytic degradation of phenol, *Environmental Monitoring and Assessment*, **2003**, 83(3):295–302.

5. Li, G.; Xuanxuan, H.; Kailai, Z.; Yuanyuan, Z.; Qiang, Z.; Danjun, W.; Feng, F. In-situ construction of 2D/2D $ZnIn_2S_4$/BiOCl heterostructure with enhanced photocatalytic activity for N_2 fixation and phenol degradation, *Catalysts*, **2019**, 9:729.
6. Aizat A.; Farhana A.; Nazri M.S.; Muhammad S.S.; Nursyazwani Y.; Juhana J.; Wan N.; Wan S.; Norhaniza Y.; Ahmad F.I.; Photocatalytic degradation of phenol by $LaFeO_3$ nanocrystalline synthesized by gel combustion method via citric acid route, *Springer Nature Applied Sciences*, **2019**, 1:91.
7. Shahmoradi, B.; Farahani, F.; Kohzadi, S.; Maleki, A.; Pordel, M.A.; Zandsalimi, Y.; Gong, Y.; Yang, J.; McKay, G.; Lee, S-M.; Yang, J-K. Application of cadmium-doped ZnO for the solar photocatalytic degradation of phenol, *Water Science and Technology*, **2019**, 79 (2): 375–385.
8. Junbo C.; Qiaoling Z.; Youzhi L.; Yanting S.; Zhao Q. Preparation of Fe_3O_4/ TiO_2 magnetic photocatalyst for photocatalytic degradation of phenol, *Journal of Materials Science:Materials in Electronics*, **2018**, 29:8258–8266.
9. Pardeep S.; Sonu P.R.; Anita S.; Pooja S.; Pankaj T.; Shilpi A.; Vinod K.G. Enhanced photocatalytic activity and stability of AgBr/BiOBr/graphene heterojunction for phenol degradation under visible light, *Journal of Saudi Chemical Society*, **2019**, 23:586–599.
10. Hayrie, M.; Hatta, M.; Lintang, H.O.; Lee, S.L.; Yuliati, L. Synthesis of highly active crystalline carbon nitride prepared in various salt melts for photocatalytic degradation of phenol, *Turk J Chem*, **2019**, 43:63–72.
11. Barakat M.A.; Al-Hutailah R.I.; Qayyum E.; Rashid J.; Kuhn J.N. Pt nanoparticles/TiO_2 for photocatalytic degradation of phenols in wastewater, *Environmental Technology*, **2014**, 35(2):137-144.
12. Linsebigler A.; Lu G.; Yates J. Photocatalysis on TiO_2 surfaces: principles, mechanisms, and selected results", *Chemical Reviews*, **1995,** 95:735-758.
13. Okamoto K.; Yamamoto Y.; Tanaka H.; Tanaka M.; Itaya A. Heterogeneous photocatalytic decomposition of phenol over TiO_2 powder, *Bulletin of the Chemical Society of Japan*, **1985**, 58:2015-2022.
14. Dewidar, H.; Nosier, S.A.; El-Shazly, A.H. Photocatalytic degradation of phenol solution using zinc oxide/UV. *J. Chem. Health Saf.* **2018**, 25:2–11.
15. Chiou, C.H.; Juang, R.S. Photocatalytic degradation of phenol in aqueous solutions by Pr-doped TiO_2, nanoparticles. *J. Hazard. Mater.* **2007**, 149:1–7.
16. Al-Hamdi, A.M.; Sillanpää, M.; Dutta, J. Photocatalytic degradation of phenol in aqueous solution by rare earth-doped SnO_2 nanoparticles. *J. Mater. Sci.* **2014**, 49:5151–5159.
17. Sánchez-Rodríguez, D.; Medrano, M.G.M.; Remita, H.; Escobar-Barrios, V. Photocatalytic properties of BiOCl-TiO_2 composites for phenol photodegradation. *J. Environ. Chem. Eng.* **2018**, 6:1601–1612.
18. Li, Q.B.; Zhao, X.; Yang, J.; Jia, C.J.; Jin, Z.; Fan, W.L. Exploring the Effects of nanocrystal facet orientations in g-C3N4/BiOCl heterostructures on photocatalytic performance. *Nanoscale* **2015**, 7:18971–18983.
19. Cai, L. Enhanced visible light photocatalytic activity of BiOCl by compositing with g-C3N4. *Mater. Res. Innov.* **2015**, 19:392–396.
20. Liu, H.; Jin, Z.T.; Xu, Z.Z.; Zhang, Z.; Ao, D. Fabrication of ZnIn2S4-G-C3N4 sheet-on-sheet nanocompositesfor efficient visible-light photocatalytic H2 evolution and degradation of organic pollutants. *RSC Adv.* **2015**, 5:97951–97961.
21. Wu, Wan-Yu, Chun-Fa Hsu, Menq-Jion Wu, Chao-Nan Chen, and Jung-Jie Huang. "Ag–TiO2 composite photoelectrode for dye-sensitized solar cell." *Applied Physics A* **2017**, 123(5):357.
22. Alsharaeh, E.H.T.; Bora, A.S.; Faheem A.; Bharath G.; Ghoniem, M.G.; Abu-Salah, K.M.; Dutta, J. Sol-gel-assisted microwave-derived synthesis of anatase Ag/TiO_2/GO nanohybrids toward efficient visible light phenol degradation. *Catalysts* **2017**, 7(5):133.
23. Chalastara, K.; Fuqiang G.; Samir E.; George, P.D. Tunable composition aqueous-synthesized mixed-phase TiO_2 nanocrystals for photo-assisted water decontamination: comparison of anatase, brookite and rutile photocatalysts." *Catalysts* **2020**, 10(4):407.
24. Ahamed, M.; Khan, M.A.M.; Akhtar, M.J.; Alhadlaq, H.A.; Alshamsan, Aws. "Ag-doping regulates the cytotoxicity of TiO_2 nanoparticles via oxidative stress in human cancer cells." *Scientific Reports* **2017**, 7(1):1-14.
25. Hamrouni, A.; Hanen A.; Ali R.; Leonardo, P.; Riccardo, C.; Francesco, P. Enhanced solar light photocatalytic activity of Ag doped TiO_2–Ag_3PO_4 composites. *Nanomaterials* **2020**, 10(4):795.

26. Dong, J.; Wen, X.; Zhu, T.; Qin, J.; Wu, Z.; Chen, L.; Bai, G. Hierarchically nanostructured bimetallic NiCo/MgxNiyO catalyst with enhanced activity for phenol hydrogenation. *Molecular Catalysis*, 485, **2020**, 110846. https://doi.org/10.1016/j.mcat.2020.110846.
27. Chakhtouna, H., Benzeid, H., Zari, N. et al. Recent progress on Ag/TiO2 photocatalysts: photocatalytic and bactericidal behaviors. Environ Sci Pollut Res (2021). https://doi.org/10.1007/s11356-021-14996-y
28. Pant, B.; Saud, P.S.; Park, M.; Park, S-J.; Kim, H-Y. General one-pot strategy to prepare Ag–TiO2 decorated reduced graphene oxide nanocomposites for chemical and biological disinfectant, *Journal of Alloys and Compounds*, 671, **2016**, 51-59.
29. Karagoz, S.; Kiremitler, N.B.; Sakir, M.; Salem, S.; Onses, M.S.; Sahmetlioglu, E.; Ceylan, A.; Yilmaz, E. Synthesis of Ag and TiO2 modified polycaprolactone electrospun nanofibers (PCL/TiO2-Ag NFs) as a multifunctional material for SERS, photocatalysis and antibacterial applications, *Ecotoxicology and Environmental Safety*, 188, 2020, 109856, https://doi.org/10.1016/j.ecoenv.2019.109856.

Tools of Material Engineering for Designing Membrane Materials with Desire Features

Samer Al-Gharabli [1],* and Joanna Kujawa [2,*]

[1] Pharmaceutical and Chemical Engineering Department, German Jordanian University, Amman 11180, Jordan;

[2] Faculty of Chemistry, Nicolaus Copernicus University in Toruń, 7 Gagarina Street, 87-100 Toruń, Poland.

***** *Corresponding authors: samer.gharabli@gju.edu.jo;. joanna.kujawa@umk.pl; Tel. +48-56-611-43-15 ; +962-6-429-4404*

Abstract: Highly efficient, hybrid separation materials for water purification were generated following a bioinspired system available in nature. The desert beetle (*Stenocara gracilipes*) was the inspiration for the formation of separation materials. Applying the hydrophobic poly(vinylidene fluoride) (PVDF) material as the substrate, the membrane was first activated and then functionalized with silane-based linkers, and the covalent anchoring of chitosan was successfully performed. The obtained surface architecture was a copy of the desert beetle's armor possessing a hydrophobic matrix with hydrophilic domains. The modification was done to adjust easily wettability, roughness, and chemistry of the materials as well as adhesive properties. The membrane morphology and surface chemistry were studied by applying a series of analytical techniques. As a result of chitosan anchoring, substantial improvement in transport and separation was reported. Pristine PVDF was characterized by a water flux of 5.28 kg m^{-2} h^{-1} and an activation energy of 48.16 kJ mol^{-1}. The water flux and activation energy for a hybrid membrane with chitosan were equal to 15.55 kg m^{-2} h^{-1} and 33.98 kJ mol^{-1}, respectively. The hybrid materials possessed enhanced stability and water resistance that were maintained after 10 cycles of membrane distillation tests.

Keywords: PVDF, surface architecture, roughness and chemistry modulation, biomimicry

1. Introduction

During recent years, water scarcity has been one of the most considerable global crises that greatly menaces the existence of organisms, including even human beings in some arid and undeveloped countries [1, 2]. Luckily, nature and natural selection, have developed a variety of biomimetic inspirations [3-6]. One of the very interesting examples is a desert beetle (*Stenocara gracilipes*) possessing an extraordinary engineered armor allowing him to survive harsh conditions on the desert. Namely, the outside layer of the armor consists of waxy, hydrophobic layer with hydrophobic joints by which the water can be collected. By inspiration and adaptation of such solution to membrane science with the help of material engineering the highly effective membranes were generated. Nano and micro architecture of the membrane was design by biomimicry of the mentioned surface. Specifically, hydrophobic surface and membrane matrix was equipped with hydrophobic joints allowing to significantly boost transport and separation. PVDF was selected as a polymeric matrix, and chitosan played the role of hydrophilic joints. All the fancy structure was generated by chemical grafting generating highly stable materials, solving the problem of chitosan leakage.

2. Materials and Methods

Poly(vinylidene fluoride) (PVDF) membranes with the nominal pore size of 0.22 μm were purchased from Merck Millipore (Germany). Methyl acetate (MeAc), methanol (MeOH), dimethylformamide (DMF), dichloromethane (DCM), toluene, hydrogen peroxide (H2O2) 30%, 3-isocyanatopropyldimethylchlorosilane (M-Cl), N,N-diisopropylethylamine (DIPEA), were bought from ABCR Chemicals (Germany). Chitosan (deacetylation 75%, low molecular weight - mol weight

50-190 kDa) was supplied by Sigma-Aldrich (Germany). And sodium chloride (NaCl) was purchased from Avantor Performance Materials (Poland). Aqueous solutions were prepared based using deionized water 15MΩ·cm (Elix, Millipore).

The following advanced analytical methods were selected to characterized the generated materials: ATR-FTIR (Bruker Vertex 80v.); SEM (Quantax 200 with an XFlash 4010 detector, Bruker AXS machine, Czech Republic). Pore size (Coulter Porometer II, Coulter Electronics Ltd., UK). AFM (Veeco, Digital Instrument, England). Goniometer (Attention Theta from Biolin Scientific, Gothenburg, Sweden).

3. Results and Discussion

3.1. Bioinspired materials formation

The design of the materials has been accomplished in the following way presented in Figure. 1.I A-F. The accomplishment of the hybrid bio-mimicked membranes begun from the activation process. During this step, the materials rich in hydroxyl groups were formed. The high efficiency of the reaction has been confirmed by ATR-FTIR technique. The gained spectra revealed the formation of hydroxyl groups (OH) owing to the presence of a wide band for hydroxyl groups (OH) at 3333 cm^{-1} (Figure 1.II A1-B2). Furthermore, new bands were observed at 3320, 2972, 2931, and 2876 cm^{-1} on the spectrum of hydroxylated support (P-OH). The bands were associated with the activation process and with proving the fluorine reduction in the PVDF matrix, followed by the substitution of -CF with -CH. Samples rich in hydroxyl groups were subsequently used during the grafting process with isocyanate-terminated organosilanes, i.e. 3-isocyanatopropyldimethylchlorosilane (M-Cl) (Figure 1. I). The reaction took place between these groups and the hydroxyl ones available on the membrane surface leaving the isocyanate group free for further modification. An essential was to observe intensive peak at 2274 cm^{-1} ensuring that isocyanate groups were not used and available for further modification. In the second step of modification, the CNO group was the most important element, generating a connection with chitosan molecules.

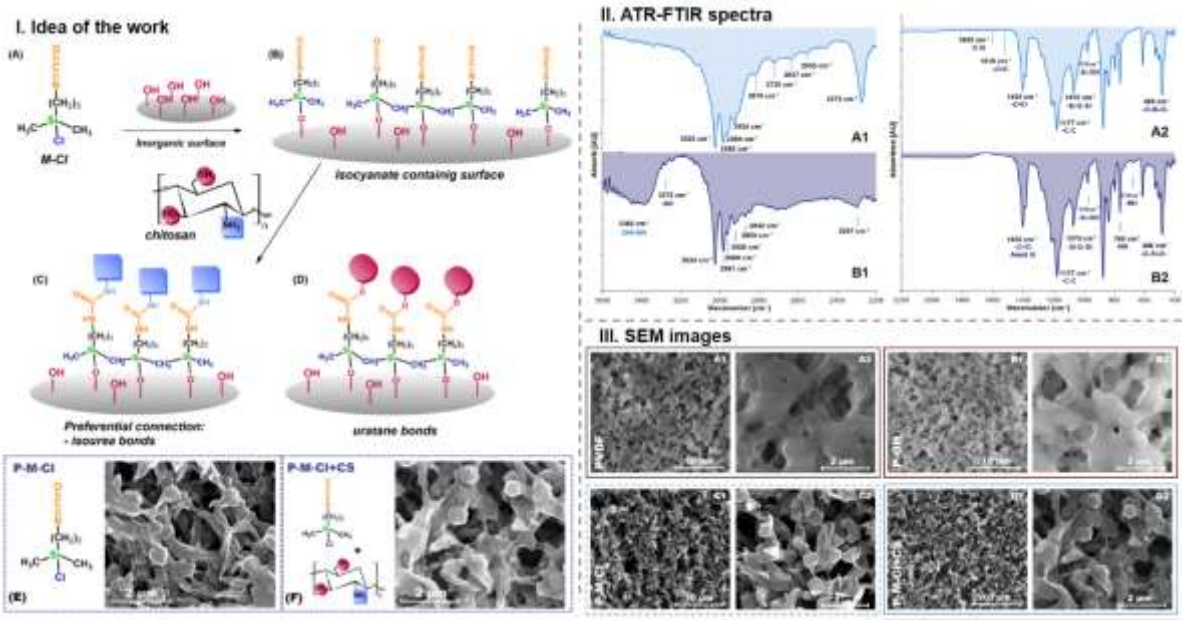


Figure 1. I – idea of the work – Example with M-Cl modifier (A). Effect of material silanization (B). Hybrid materials – connection of chitosan by amine group (preferential connection) (C) and by hydroxyl groups (D). SEM images of the generated materials (E, F). II – ATR-FTIR spectra – A1, A, silanized material; B1, B2, material with chitosan. III – SEM images – A1, A2 – pristine, B1,B2 – activated material, C1,C1 – silanized, D1,D2 – with chitosan.

Microscopic study and porosity tests shed light on the morphological changes of the developed materials. After the first step of the membrane treatment, a blister-like structure was observed (Figure 1. III. A1, A2, B1, B2). That observation was in good accordance with the previous results of PVDF treatment with piranha reagent.[7] The activation process also influenced the membrane roughness and pore size of the material. An increase of roughness from 85 nm to 110 nm was noticed. However, the average pore size of the activated materials grew by 4%. Membranes modified with silanes possessed meaningfully different features then activated and pristine one. The presence or lack of catalysis had a significant impact. Less visible changes were found for materials silanized with M-Cl, in the overall volume morphology (Figure 1.III C1, C2). It was linked to the structure of the modifier and the small amount of reactive group (1 chlorine group).

As a result of hybrid material formation, an alteration in membrane morphology was noticed. The general trend exhibits the increase of material roughness in the range of 5% to 24%, depending on the modifier. This variety in the roughness changes is an important outcome for the tuning of the material properties depending on the material application. Furthermore, wing to the introduction of the chitosan to the hybrids, the visible flakes on the SEM images and a slight diminution of the pore size was noticed in the range of 12% - 25%.

3.2. Wettability assessment

The material wettability is an essential factor in the evaluation of material utility as well as resistance to fouling and damaging the surface. In defining the wettability, the level of hydrophobicity or hydrophilicity must be measured. Membrane wetting can take place by the accumulation and adsorption of an amphiphilic particle, lipids, proteins, or fat on the membrane surface.[8] The attraction between these molecules and the membrane decreases the surface tension of liquid at the membrane surface, which in turn diminishes the wetting pressure directly related to the critical surface tension.[9-11] If the wetting pressure is smaller than the gradient of operating pressure, the liquid can enter the membrane pores. Membrane wetting upsurges the resistance of mass transfer of membrane owing to the diffusivity in the liquid phase is smaller than the vapor phase. The critical situation is that when the membrane is completely wetted-out, water molecules would not diffuse in vapor form anymore.

Moreover, it should be pointed out that material features *e.g.*, chemistry, phase composition, and roughness, possessed a significant influence on the final hydrophilicity/hydrophobicity of the material, principally on PVDF-base samples.[12-14]

In our work, a very effective method inspired by a nature has been developed. The two-steps procedure made it possible to tune both contact angle and roughness in an easy way. Firstly, the activation process with piranha reagent produces the highly reactive, hydroxyl-rich surface with high contact angle (PVDF: 119.4 ± 1.1°; P-OH: 135.9° ± 1.2°) and improved roughness angle (PVDF: 110 nm; P-OH: 85 nm) (Figure 2). In this particular case, the high level of hydrophobicity was associated with the roughness from one side and from the other one with the chemistry, *i.e.* phase composition of the sample. The first step of modification with silane-based modifiers gave materials with higher roughness. However, the level of hydrophobicity was smaller than for the activated one (Figure 2). The most interesting part of the obtained wettability features was observed for the hybrid materials after the chemical attachment of the chitosan particles. During the hybrid formation, a material with a contact angle equal to 164.8° ± 0.8° and roughness of 260 nm was generated. The data are in accordance with the Cassie−Baxter's wetting model,[15, 16] foreseeing that for a heterogeneous hydrophobic surface, a nonwetting liquid may not enter into surface cavities, resulting in the generation of air pockets, leading to a composite solid−liquid−air interface where surface roughness rises with the hydrophobicity. The mentioned behavior was proved by the linear relation between these two factors for all modified samples.

The resistance of wettability was also assessed by the critical surface tension, which defines the limit of surface wettability. All of the liquids possessing a value of surface tension lower than the critical surface tension of the material will wet the surface. This is crucial from the application point of view in order to produce the material with the possible low value of γ_{cr} to cover the broad range of

the liquids that might have contact with the membrane without the risk of the wetting just limiting the separation across the material. In Figure 8B the correlation between the level of hydrophobicity and γ_{cr} is presented. The slightly higher value of the critical surface tension of the silanized materials was related to the presence of -NCO groups and different chemistry, in comparison to pristine and activated PVDF materials. However, the substantial reduction of critical surface tension values for the hybrid materials (P-M-Cl +CS) was owing to the chitosan molecules and their character. Even though chitosan with hydrophilic character was attached, the value of γ_{cr} was diminished (Figure 2). This outcome verified that chitosan-like islands structures were produced. Additionally, it is shown that more influential for SFE and γ_{cr} is surface chemistry than its morphology.[17]

The overall SFE changed in the following way: 29.52 ± 0.88 mN m^{-1}, 23.35 ± 0.70 mN m^{-1}, for the PVDF and P-OH. Then a slight improvement was observed as an effect of the silanization process, 28.43 ± 0.50 mN m^{-1} (P-M-Cl). Finally, the hybrids possessed the value of total SFE equal to 20.51 ± 0.65 mN m^{-1} (P-M-Cl+CS). The polar part of the SFE was in the range of 9 and 25% of total SFE, depending on the sample. However, the small impact of polar interaction ensures these materials' suitability to the membrane distillation process.

The differences in wettability of material were also observed in the LEP values. For the non-modified material, *i.e.* PVDF, the value of LEP was equal to 146.6 kPa that is comparable to the literature data [18]. Nevertheless, the activated and hybrid materials were characterized by LEP higher than the pristine sample. P-OH was characterized by 227.5 kPa, but the silanized membranes possessed LEP on the following level 164.4 kPa and 187.3 kPa. The upsurge of the liquid entry pressure for modified and hybrid materials referred to neat PVDF need to be connected to smaller value of the maximum pore size. This phenomenon is favors higher LEP [17-19]. The obtained results confirmed that developed method allows to generate more water-resistant membranes.

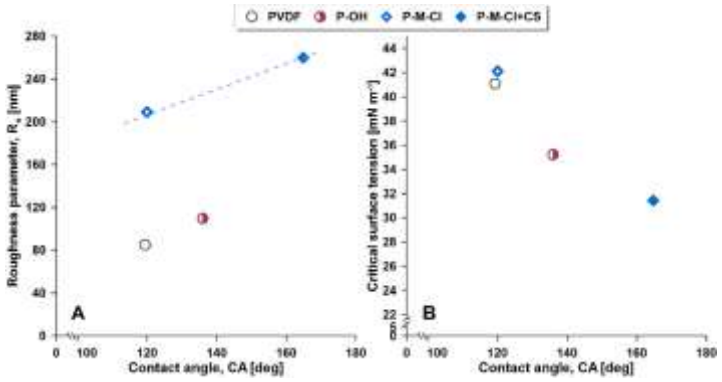


Figure 2. The relation between contact angle and roughness parameters (A) and critical surface tension (B).

3.3 Transport features

Based on the collected results from the systematic material study, it was verified that fabricated separation membranes are appropriate for MD process. The generated membranes fulfilled all the requirements of materials for MD, *i.e.* the materials are porous, hydrophobic, and no wetting behavior was revealed. In the first step of membrane application, transport features, *i.e.* water transport across the membrane was determined. To do so, 3 different driving forces were used to evaluate the (E_a) (Eq. 1).[17, 20]

$$J = J_0 \, exp\left(-\frac{E_a}{RT_f}\right) \, [kg \, h^{-1} m^{-2}] \qquad (1)$$

where J_0 is the pre-exponential factor (*i.e.* the flux of permeate at infinite temperature), E_a – apparent activation energy for flux of permeate, R – gas constant, T_f – temperature of feed solution.

It needs to be stressed that activation energy is a complex factor.[20-23]. Taking into account the E_a, a surge of the activation energy for transport of water from 48.16 kJ mol^{-1} (PVDF) to 53.41 kJ mol^{-1} (P-OH) was observed after material activation. It can be explained by the production of a stronger hydrophobic barrier (Figure 2), creating the water transport limited. Subsequently, owing to the silanization process (47.55 kJ mol^{-1}) as well as hybrids containing chitosan materials (41.43 kJ mol^{-1}), a substantial reduction of activation energy was noticed (Figure 3). It was particularly interesting to observe the influence of the presence of catalysts on that physicochemical factor, *i.e.* E_a. Furthermore, the observed lower values of E_a for the hybrid materials was associated with the chitosan attachment and production of stable hydrophilic layer on the membrane. The determined values of E_a for all membranes were in good agreement with the data from other PVDF modified membranes.[7, 17]

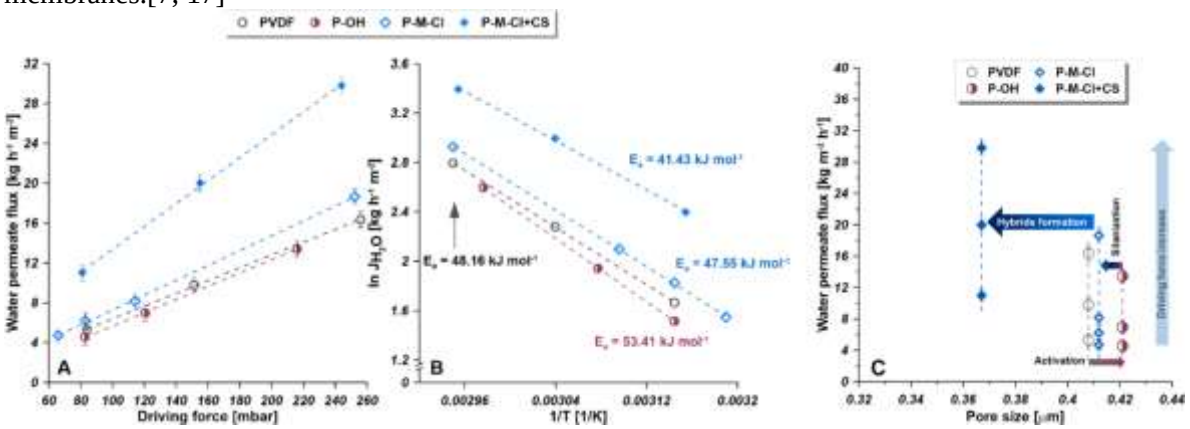


Figure 3. A –permeate flux of water in the function of driving force, B - E_a for water transport across the membranes, C - The relation between transport properties and pore size after activation, silanization, and hybrid formation.

The hydroxylated membrane (P-OH), owing to its character (Figure 3) was less permeable than a pristine one (Figure 3). It was related not only to the hydrophobicity level but also to the roughness and pore size of the materials (Figure 3). The improvement in the transport properties for the silanized materials in comparison with activated ones was in the range of 16-39% for the P-M-Cl, depending on the driving force. However, substantial differences have been noticed after the introduction of chitosan particles. In this situation, the enhancement was 221-286% for the P-M-Cl+CS. Such improvement was possible to obtain only owing to the chitosan presence and their chemistry, making the final material much more permeable for vapors of solvent, *i.e.* water. For all investigated samples, a linear correlation between driving force and the water flux was observed (Figure 2). Additionally, all the created membranes have been characterized by outstanding stability during the MD process. The lack of flux reduction verified that no wetting occurred in the course of AGMD.

3.4. Separation properties

After the detailed characterization of transport of water across the generated materials, the desalination process was performed. In Figure 4 the comparison of permeate fluxes when pure water (Figure 4 A) and salty water (Figure 4 B) were used as a feed solution for various driving forces has been presented. The concentration of salty water was selected as similar to seawater.[24] The observed lower value of the permeate flux for the salty water as a feed is related to the fact that only vapors of solvents can be transported through the hydrophobic pores of the membrane in the membrane distillation process. In the previous sections of the work, it was presented that these conditions are fulfilled. Namely, all membranes were porous and hydrophobic. The diminution of transport features for the NaCl solution is controlled by the Raoult's law [25, 26].The transport of solvent vapors in MD is relative to the difference of water vapor pressure between the feed and the

permeate. For that reason, the increase of transport properties with the increase of driving force was observed, independent of the used feed (Figure 4). Generally, the lower value of the permeate flux was noticed for the activated membrane that was related to its chemistry. Furthermore, an interesting observation was found for the modified membranes. A gradual increase of the transport features was noticed after the first step of modification, *i.e.* silanization process. Subsequently, more significant improvement has been observed after hybrids formation, a hydrophobic surface possessing hydrophilic islands. The permeate flux was enhanced from 3.60 ± 0.11 kg m^{-2} h^{-1} for P-OH membrane to 11.18 ± 0.17 kg m^{-2} h^{-1} for P-M-Cl +CS when 0.5M NaCl was used as a feed (Figure 4). To evaluate the membrane stability, all membranes were tested in runs of ca 50 h (Figure 12A), with pure water and 0.5M NaCl aqueous solutions. The data for the selected driving force was presented in Figure 11. Moreover, the salt rejection coefficient (R_{NaCl}) was monitored (Figure 12B). For all membranes, the values of R_{NaCl} were close to unity, ensuring no leakage in the course of AGMD. Furthermore, the stability of the membranes was proven by unchanged values of the flux in long-time measurements (Figure 12). The slightly reduced value of R_{NaCl} for the activated membrane (P-OH) might be associated with small alterations in material properties (CA, RMS, and critical surface tension).

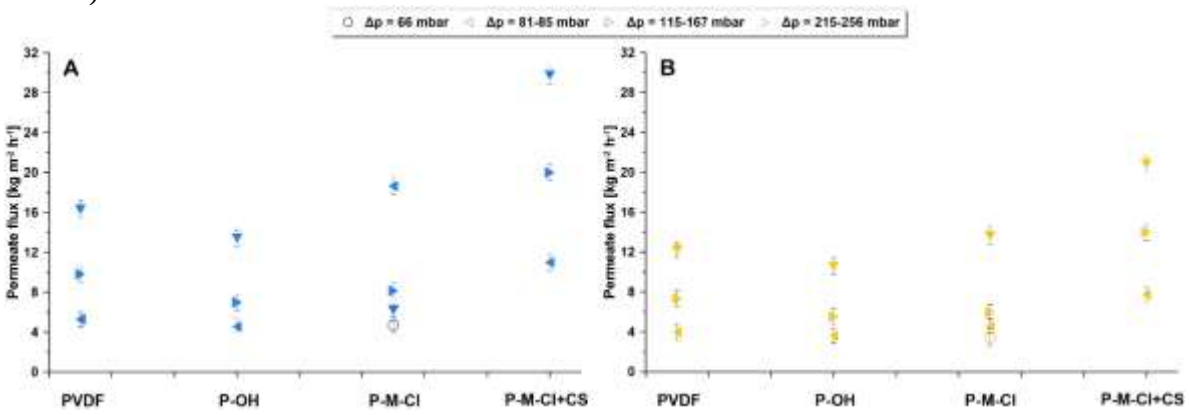


Figure 4. Transport properties – A – feed: water, B – feed: 0.5M NaCl across the investigated membranes under different driving forces.

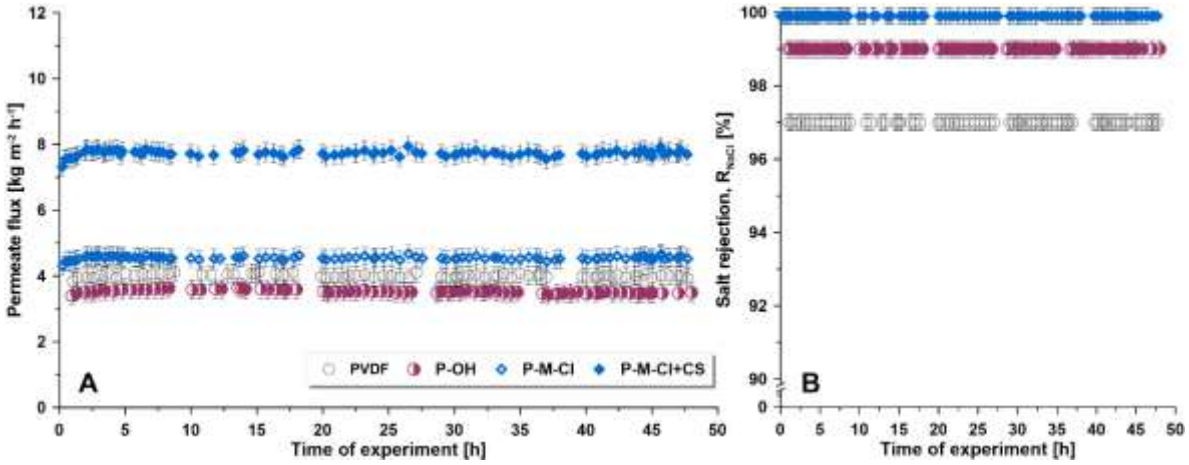


Figure 5. Membranes stability, the evolution of permeate flux (A) and salt rejection (B) during long-term desalination process (driving force 81-85 mbar).

The obtained data demonstrated the high effectiveness of the generated materials possessing very good permeability and salt rejection. Based on the literature survey, it can be concluded that the

developed method of hybrid membrane formation having a hydrophobic matrix with hydrophilic islands makes it possible to prepare promising separation materials.

The hybrid materials with chemically anchored chitosan might have important implications for other water treatment processes *e.g.* for the removal of volatile organic compounds or filtration process. Moreover, owing to the dual nature, *i.e.* combining hydrophobic and hydrophilic feature, the material can be applied for the separation of water-oil mixtures.

3.5. Stability of biomimicked membranes

In the final step, the membrane stability and utility in the desalination process was determined during 10 cycles of membrane distillation processes. Each run lasted for *ca* 40-45h. During the experiments, permeate flux, salt rejection coefficient, and value of contact angle for pristine PVDF and hybrid P-M-Cl+CS were monitored (Figure 6). All membranes were characterized by a very good stability. However, the diminution of flux and contact angle of about 35% and 14%, respectively was observed for the PVDF membrane. The hybrid materials containing chitosan were much more stable with the reduction of permeate flux on the level of 8% for P-M-Cl+CS sample. The contact angle change for the hybrid materials was about 7% and 10%. Furthermore, there was no influence of the long-term utilization of the membrane on the salt rejection coefficient.

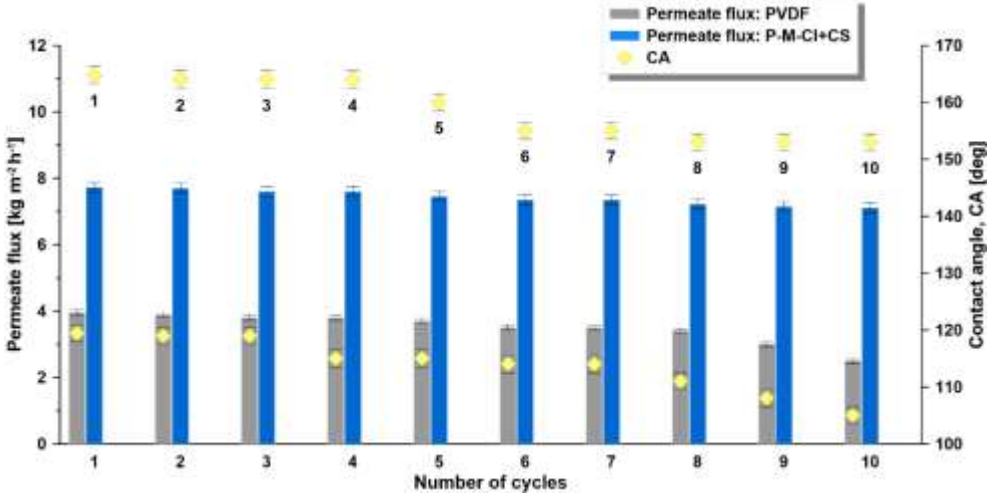


Figure 6. Membrane stability during the desalination processes.

4. Conclusions

The efficient method of modifying fluoropolymer membranes by the formation of hybrid hydrophobic/hydrophilic materials was presented. In the developed method, the engineering of the desert beetle's armor possessing a hydrophobic surface with hydrophilic islands were was bio-mimicked. To form hydrophilic domains, biowaste, a natural polymer, chitosan was used and covalently attached *via* silanes linkers to the membrane. The presence of chitosan significantly improved membrane stability and effectiveness in the course of the desalination process. The substantial enhancement of water transport across the membranes was related to the introduction of hydrophilic chitosan, promoting transport. The high efficacy of the process was verified by the set of advanced techniques giving the holistic image of functionalized materials. FTIR-ATR, FTIR-ATR confirmed that the functionalization of chitosan took place *via* its amine and hydroxyl groups and terminal isocyanate groups from the modifier attached to the PVDF membrane. Application of the linker's molecules with highly reactive chlorine moieties allowed made it possible to generate a highly organized surface. The hydrophobicity level of the hybrid materials rose from 119.4° for pristine PVDF to 164.8° for P-M-Cl+CS, respectively. Water flux increased from 5.28 kg m^{-2} h^{-1} to 11.00 kg m^{-2} h^{-1} for membrane with chitosan and membrane with chitosan modified, respectively.

Funding: Author Joanna Kujawa received funding from National Science Centre (2017/26/D/ST4/00752 - Sonata 13), Poland.

References

1. C. Xu, R. Feng, F. Song, X.-L. Wang, Y.-Z. Wang, Desert Beetle-Inspired Superhydrophilic/Superhydrophobic Patterned Cellulose Film with Efficient Water Collection and Antibacterial Performance, ACS Sustain. Chem. Eng., 6 (2018) 14679-14684.
2. H. Zhu, R. Duan, X. Wang, J. Yang, J. Wang, Y. Huang, F. Xia, Prewetting dichloromethane induced aqueous solution adhered on Cassie superhydrophobic substrates to fabricate efficient fog-harvesting materials inspired by Namib Desert beetles and mussels, Nanoscale, 10 (2018) 13045-13054.
3. W. Chen, Z. Guo, Hierarchical fibers for water collection inspired by spider silk, Nanoscale, 11 (2019) 15448-15463.
4. H. Liu, W.-Y. Xie, F. Song, X.-L. Wang, Y.-Z. Wang, Constructing hierarchically hydrophilic/superhydrophobic ZIF-8 pattern on soy protein towards a biomimetic efficient water harvesting material, Chem. Eng. J., 369 (2019) 1040-1048.
5. J. Feng, L. Zhong, Z. Guo, Sprayed hieratical biomimetic superhydrophilic-superhydrophobic surface for efficient fog harvesting, Chem. Eng. J., 388 (2020) 124283.
6. X. Li, Y. Yang, L. Liu, Y. Chen, M. Chu, H. Sun, W. Shan, Y. Chen, 3D-Printed Cactus-Inspired Spine Structures for Highly Efficient Water Collection, Adv. Mater. Interfaces, 7 (2020) 1901752.
7. S. Al-Gharabli, W. Kujawski, Z.A. El-Rub, E.M. Hamad, J. Kujawa, Enhancing membrane performance in removal of hazardous VOCs from water by modified fluorinated PVDF porous material, J. Membr. Sci., 556 (2018) 214-226.
8. A. Chanachai, K. Meksup, R. Jiraratananon, Coating of hydrophobic hollow fiber PVDF membrane with chitosan for protection against wetting and flavor loss in osmotic distillation process, Sep. Purif. Technol., 72 (2010) 217-224.
9. H.W. Fox, W.A. Zisman, The spreading of liquids on low energy surfaces. I. polytetrafluoroethylene, J. Colloid Sci., 5 (1950) 514-531.
10. Y. Kano, S. Akiyama, Critical surface tension of poly(vinylidene fluoride-co-hexafluoroacetone) by the contact angle method, Polymer, 33 (1992) 1690-1695.
11. K.-Y. Law, H. Zhao, Determination of Solid Surface Tension by Contact Angle, in: Surface Wetting: Characterization, Contact Angle, and Fundamentals, Springer International Publishing, Cham, 2016, pp. 135-148.
12. S. Al-Gharabli, W. Kujawski, H.A. Arafat, J. Kujawa, Tunable separation via chemical functionalization of polyvinylidenefluoride membranes using piranha reagent, J. Membr. Sci., 541 (2017) 567-579.
13. M. Fortunato, D. Cavallini, G. De Bellis, F. Marra, A. Tamburrano, F. Sarto, M.S. Sarto, Phase Inversion in PVDF Films with Enhanced Piezoresponse Through Spin-Coating and Quenching, Polymers, 11 (2019) 1096.
14. L. Ruan, X. Yao, Y. Chang, L. Zhou, G. Qin, X. Zhang, Properties and Applications of the β Phase Poly(vinylidene fluoride), Polymers, 10 (2018) 228.
15. Y. Kwon, S. Choi, N. Anantharaju, J. Lee, M.V. Panchagnula, N.A. Patankar, Is the Cassie−Baxter Formula Relevant?, Langmuir, 26 (2010) 17528-17531.
16. H.Y. Erbil, C.E. Cansoy, Range of Applicability of the Wenzel and Cassie−Baxter Equations for Superhydrophobic Surfaces†, Langmuir, 25 (2009) 14135-14145.
17. S. Al-Gharabli, B. Al-Omari, W. Kujawski, J. Kujawa, Biomimetic hybrid membranes with covalently anchored chitosan – Material design, transport and separation, Desalination, 491 (2020) 114550.
18. F. Abdulla AlMarzooqi, M. Roil Bilad, H. Ali Arafat, Improving Liquid Entry Pressure of Polyvinylidene Fluoride (PVDF) Membranes by Exploiting the Role of Fabrication Parameters in Vapor-Induced Phase Separation VIPS and Non-Solvent-Induced Phase Separation (NIPS) Processes, Appl. Sci., 7 (2017) 181.

19. M. Rezaei, D.M. Warsinger, J.H. Lienhard V, M.C. Duke, T. Matsuura, W.M. Samhaber, Wetting phenomena in membrane distillation: Mechanisms, reversal, and prevention, Water Res., 139 (2018) 329-352.
20. J. Kujawa, W. Kujawski, Driving force and activation energy in air-gap membrane distillation process, Chem. Pap., 69 (2015) 1438-1444.
21. B. Baranowski, Non-equilibrium thermodynamics as applied to membrane transport, J. Membr. Sci., 57 (1991) 119-159.
22. H. Eyring, The Activated Complex in Chemical Reactions, J. Chem. Phys., 3 (1935) 107-115.
23. M.P. Godino, V.M. Barragán, M.A. Izquierdo, J.P.G. Villaluenga, B. Seoane, C. Ruiz-Bauzá, Study of the activation energy for transport of water and methanol through a Nafion membrane, Chem. Eng. J., 152 (2009) 20-25.
24. J. Kujawa, S. Cerneaux, S. Koter, W. Kujawski, Highly Efficient Hydrophobic Titania Ceramic Membranes for Water Desalination, ACS Appl. Mater. Interfaces, 6 (2014) 14223-14230.
25. A.A. Kiss, O.M. Kattan Readi, An industrial perspective on membrane distillation processes, J. Chem. Technol. Biotechnol., 93 (2018) 2047-2055.
26. R.W. Schofield, A.G. Fane, C.J.D. Fell, R. Macoun, Factors affecting flux in membrane distillation, Desalination, 77 (1990) 279-294.

Ultimate eradication of the ciprofloxacin antibiotic from the ecosystem by nanohybrid go/o-cnts

Ahmad Rafiq Muosa Mohammad *

Jordan university of science and technology
*****Corresponding author: ahmadrafiq.altamary@gmail.com*

Abstract: Eradication of pharmaceutical drugs from the global ecosystem has received remarkable attention due to the extensive horrible consequences on the human immunological system and the high rate of human deaths. The urgent need for drug eradication became the dominant priority for many research institutions worldwide due to the sharp increase of antimicrobial resistance (AMR) in the human body, which inhibits drug effectiveness and leads ultimately to death. Nanohybrid GO/O-CNTs was fabricated from graphene oxide (GO) cross-linked via calcium ions (Ca_2+) with oxidized carbon nanotubes (O-CNTs) to eradicate the well-known ciprofloxacin antibiotic drug from aqueous solutions. The ciprofloxacin drug is medically prescribed in millions of medical prescriptions every year and typically exists in domestic and wastewaters. Characterization of the nanohybrid GO/O-CNTs was carried out through spectroscopic (Fourier Transform Infrared (FTIR) and X-ray diffraction (XRD)), thermal (Thermogravimetric analysis (TGA) and derivative thermogravimetry (DTG)), and microscopic (scanning electron microscopy (SEM)) techniques. Optimum parameters for the drug eradication process from aqueous solutions were verified and selected as follows: contact time = 4 h, pH = 6.0, temperature = 290 K, %CaCl2 = 0.5%, GO/O-CNT ratio = 4:1, and adsorbent mass = 1.0 mg. The equilibrium data were fitted to different adsorption isotherms, and the Langmuir isotherm provided the best fit to our data. Dynamic studies demonstrated a pseudo-second-order removal process for the ciprofloxacin drug, and thermodynamic parameters confirmed exothermic drug adsorption (−27.07 kJ/mol) as well as a physisorption process. For the sake of fighting against the generated AMR, our working strategy demonstrated a removal efficiency of 99.2% of the ciprofloxacin drug and drug uptake as high as 512 mg/g.

Theme 10: Potentials and Challenges of Local Industrial

A review on the size reduction technology using mechanochemistry approach

Mohammad Alrbaihat. Ph.D *

Teacher Training Institute, Emirates School Establishment, Dubai, 3962, United Arab Emirates
**Corresponding author: moh.irbeihat83@hotmail.com*

Abstract: Size reduction is one of the most widely used unit operations in the chemical and allied industries. Comminution is the process of exposing materials to stress through collisions and reducing the size of bigger solid units into smaller unit masses. Stress and other impacts are transmitted to the larger unit via the mechanochemical process. Mills and crushers are two of the most used production technologies. The concept of mechanochemical reactions is not new; scientists have been using it for a long time. Even though many various size reduction techniques are available, the knowledge of the qualities of the material to be prepared is the most important factor. As a smart material, size reduction provides benefits like as enhanced surface area and the creation of unique slow/control nutrients (drugs, fertilizers...etc).

Keywords: Size reduction; mechanochemistry; crusher; mills.

1. Introduction

Recently, the increasing number of applications of mechanochemistry to synthesis of chemicals and preparation of nano and fine materials has driven a novel, rapid surge of interest. Therefore, the study of mechanically activated transformations is, presently, one of the most rapidly growing subjects in organic and materials chemistry. Yet, a lot of threatening issues discourage endeavors to shift technology from the laboratory domain to industry one.

Particle size is one of the most important factors influencing the powder process, as it affects mixing, stream, and compaction qualities. Reducing particle size is critical for increasing surface territory and flow properties. Larger estimated particles have problems with dissolvability since they need more time to dissolve. In some rare circumstances, particles are not soluble in any liquids. Particles must be dissolved in a suspension with the same particle size as the dissolving particles in such circumstances. The significance of particle size in absorption is that when particle size decreases, the surface area of these particles increases, resulting in enhanced absorption. (Mulla et al., 2016)

2. Mechanochemistry

First definition of mechanochemistry was suggested by Ostwald in the late 19th century, originated from industrial phenomenology. In other words, from mineral processing and the related practices of combination and grinding, he studied chemical reactions from an energetic point of view (Ostwald, W., 1887). Heinicke, (1984), formulated a featured definition which has become accepted by the scientific community. He stated that mechanochemistry is a branch of chemistry which is concerned with chemical and physicochemical transformations of substances in all states of accumulation produced by the effect of mechanical energy (Heinicke, 1984).

Other definition from the IUPAC Compendium of Chemical nomenclature states that mechanochemistry is a chemical reaction that is induced by the direct adsorption of mechanical

energy (McNaught, and Wilkinson, 1997). Tribochemistry, or impact chemistry, came from different origins but deals with similar subjects, and nowadays both expressions are unified as mechanochemistry (Masuda, *et al*,2006).
In 1974, Juhasz emphasized that processes influenced by mechanical activation can be divided into primary and secondary processes. The primary processes include the increase in internal and surface energies, increase of surface area and decrease of coherent energy of solids which all generally increase the reactivity of the mineral. The secondary processes such as aggregation, adsorption and crystallization take place spontaneously in activated systems during or after grinding has been completed (Juhasz, 1974).

Mechanochemistry has been practiced for over a century, but the core question is which processes are the subject of mechanochemistry is still debated. Moreover, as new areas of science and technology discover the possibilities offered by mechanical treatment, the views on mechanochemistry shift to accommodate new systems and phenomena. (L. Takacs, 2014)

Milling Types

The multi-stage character of mechanical activation (MA) requires high-energy mills with different working regimes (compression, shear, impact). The principles of the most frequently applied mills are shown in Fig. 1.

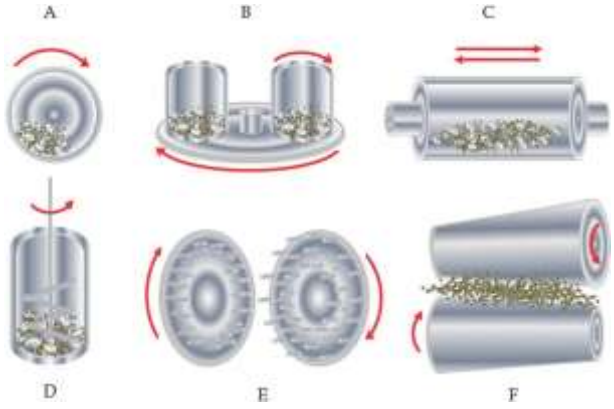


Fig. 1. Types of mills applied on mechanochemistry; A – ball mill, B – planetary mill, C – vibratory mill, D – stirring ball mill (attritor), E – pin mill, F – rolling mill (modified from Boldyrev, 1986).

There are several variables which influence the milling process, e.g., type of the mill, material of milling media, ball to powder ratio, filling extent of the milling chamber, milling atmosphere, milling speed, milling time, etc.

The purpose of an ideal device for a mechanochemical synthesis (MCS) is to insert the maximum amount of energy into the treated solid to enable the accumulation of the input energy. This energy is responsible for the occurrence of defects, which greatly affect chemical reactivity.

The most significant advancement for material science in recent years has been the increased use of mechanical activation, mainly in organic synthesis. Low-energy mechanical mixing/milling is used to enable solvent-free reactions and prepare co-crystals, whereas high-energy milling is used

to break primary bonds. Mechanophores are signaling molecules that are embedded into materials (Al Bazedi et al 2021)

In powder metallurgy and mineral processing, the mechanical force of the ball milling (BM) technique is historically used to mix granular matter, reduce particle size, refine microstructure, and increase chemical reactivity (AlShamaileh et al, 2017., Baláž et al, 2013., Sopicka-Lizer, 2010., Delogu and Mulas, 2010., and Suryanarayana, 2001). The unit operation is based on the transfer of mechanical energy to powders that occurs inside the reactor of a ball mill during collisions between milling instruments. In the volumes of powder mixture caught either between colliding balls or between a ball and the reactor wall, processes on the mesoscopic and microscopic dimensions occur impulsively. Cold-welding and fracture, as well as physical and chemical reactions, can emerge from the mechanical deformation of powder particles. (AlShamaileh et al, 2017., Baláž et al, 2013., Sopicka-Lizer, 2010., Delogu and Mulas, 2010., and Suryanarayana, 2001)

During high-energy milling, the size of crystals decreases to some critical value. Further energy supply to these crystals of limiting size causes further deformation of crystals, energy accumulation in the volume or at the surface of crystals, and subsequently amorphization. The particle size reduction is in many cases complicated by particle size enlargement, where smaller particles are put together to form larger entities in which the original particles can still be identified. This phenomenon, called equilibrium state of milling, was experienced with solids, and is closely related to the effects of aggregation and agglomeration (Baláž et al, 2013).

Size reduction is the process of reducing bigger solid unit masses into smaller or finer particles utilizing various techniques such as jaw crushers, gyratory crushers, roll crushers, hammer mills, and ball mills (Kumar et al, 2019). The attrition and impact principles are mostly applied here.

Size reduction, also called as comminution, diminution, or pulverization, is accomplished primarily by two methods: precipitation and mechanical. Precipitation entails dissolve in a suitable solvent, while the mechanical phase entails submission to mechanical forces via grinding machines. The former is mostly utilized to make bulk pharmaceuticals, inorganic raw materials, and compounds such as magnesium and calcium carbonate (Kumar et al, 2020 and Abouzeid AZ, 1994).

Several factors influence size decrease. Moisture content, hardness, stickiness, toughness, slipperiness, abrasiveness, and other physical qualities are among them. Other material parameters, including as the product's coarse and bulk density, material structure, flow, form, and size, all have an impact on size reduction (Bishop, D. 1934., Patel et al, 2008 and Kumar et al, 2020)

The primary goal of particle size reduction is to maximize particle surface area. Other benefits of size reduction include improved and uniform mixing of powders due to the particles' limited size range, quicker absorption, reduced sedimentation, improved physical appearance, and higher stability in the case of emulsions (Rudd DF, 1973 and Kumar et al, 2020).

Mechanisms of Size Reduction

The mechanisms have shown that a variety of pressures are required to acquire a larger education.

The most typical method of size reduction is as follows: [Table 1] (Kumar et al, 2020 and Abouzeid AZ, 1994).

Table 1: Size reduction mechanisms and their approximate particle size

Methods	Examples	Approximate size of particle ((μm)
Attrition	Colloidal mill and Roller mill	1-50
Impact and attrition	Ball mill and Fluid energy mill	1-2000
Impact	Hammer mill and Disintegrator	50-8000
Compression	Roller mill and Pestle-Mortar	50-10,000
Cutting	Scissors, Cutter mill and Shears	100-80,000

Parts of Size Reduction Equipment in General

Hopper, milling chamber, and Discharge chute are the three basic components of a size reduction apparatus. (Figure 2) (Kumar et al, 2020., Subramanyam, 2004., Sushant S and Archana K, 2013).

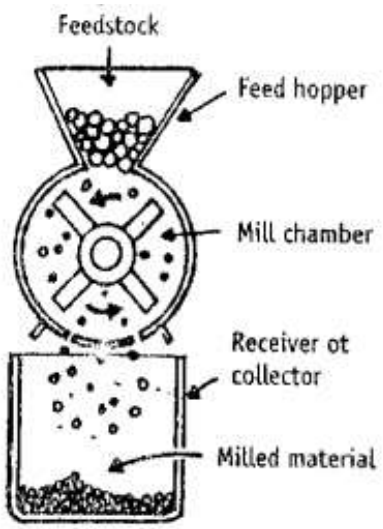


Figure 2: General Parts of Size Reduction Equipment (Three basic Components)

Types of Size Reduction Methods

Grinding, compression, and impact forces are examples of unit activities used in size reduction. Compression, impact, and attrition forces are among the forces involved.
During size reduction, the material is put under stress, and the resulting internal strains cause the material to deform or shatter. The hardness of the material, its structure, the amount of heat generated in the material, and its susceptibility to crack are all factors that influence the degree of deformation. Harder materials also need more energy to fracture. The sort of impact required for size reduction is determined on the nature of the materials. Softer materials, for example, require shearing forces, while fibrous materials require a mix of shearing forces and impact (Boldyrev, 1986 and Kumar et al, 2020).

Some of the common mechanical size reduction methods are listed as follows:

Equipment for cutting: Extensively used in food industry for cutting of vegetable or meat products. A bowl chopper is a common example.

Equipment for milling: These include both grinders and crushers. Grinders make use of impact and shear forces for size reduction. Examples include hammer mills, roller mills and hammer mills. Crushers can be commonly seen in usage in sugar cane industry where, sugar cane is subjected to compression forces.

Equipment for homogenization: In homogenization, two immiscible liquids are combined into an emulsion thereby dispersing the particles. During this the liquid is forced through a narrow nozzle resulting in shear, impact, turbulence, and compressive forces acting on the particles in the liquid.

Equipment for size reduction:

1. Ball mill

The ball mill is made up of a zirconia, steel hollow cylindrical rotating shell coated with porcelain or high carbon steel plate. The shell can be filled with steel balls or stones up to half of its volume. The balls are uniform in weight but vary in size depending on the amount of feed used. The size reduction is caused by the balls grinding against the substance to be comminuted. The size of the ball, the speed of rotation of the shell, and the feed rate all influence the particle size and form of the material to be comminuted. (AlShamaileh, et al, 2017)

When the shell is turned, centrifugal forces inside the shell propel the ball along the mill wall, where it is dropped owing to gravitational force when it reaches a certain height.
This ensures that the material is ground. Due to the controlled environment in a ball mill, the fine grinding of a wide range of materials and the grinding of dangerous substances are some of the additional advantages of ball mills.



Fig. 3. Planetary ball mill (Pulverisette-7, Fritsch, Germany

Hammer mill

A fast-moving hammer is coupled to a high-speed rotor in a cylindrical case in a hammer mill. On a horizontal shaft are installed hammers with up to four digits. It works based on a collision between the hammer and the particles to be reduced in size. The materials are introduced into the hammer mill through the top of the metal casing and are directly exposed to the hammer during operation, resulting in size reduction. The particles are then gathered at the receiver after passing through a screen at the bottom. The feed rate, screen size, and rotor speed are all important aspects in size reduction. A hammer mill is usually turned at a speed of 2500-5000 rpm (Lynch, A. and Rowland, C. 2005).

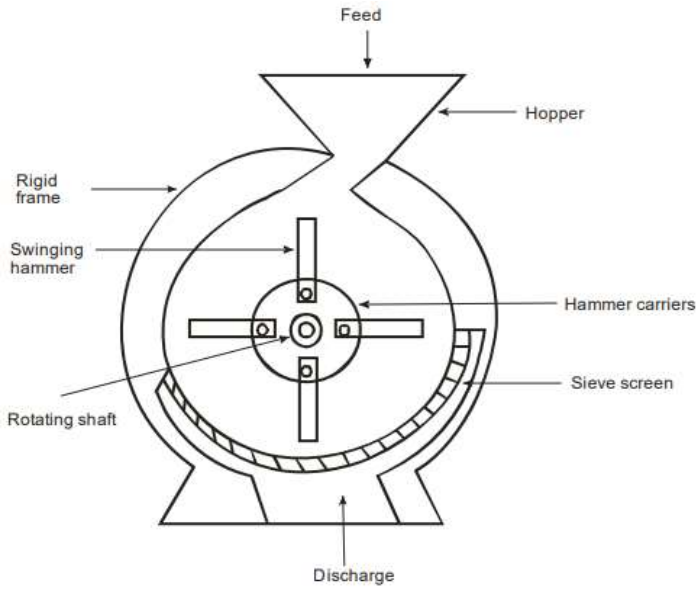


Fig. 4. A Conventional Hammer Mill (Lynch, A. and Rowland, C. (2005).

1. *Jaw crushers*

The jaw crusher is V-shaped, with one moveable jaw and the other fixed, forming a 10-20° angle between them. The materials for size reduction are introduced between the two jaws at the top, and the moveable jaw applies compressive force. The jaw's size is reduced from top to bottom, with larger lumps in the higher half breaking and plunging into the lower, narrower portion below. At the next stroke, the cracked fragments are further decreased. The jaw crusher is normally run at 300 times per minute (Kumar et al, 2020).

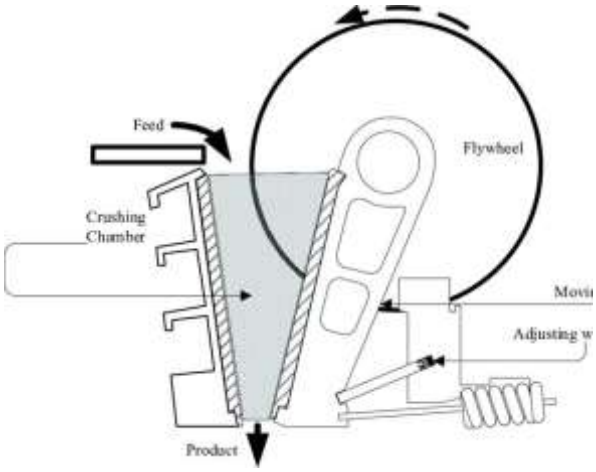


Fig. 5. V-shaped jaw crusher. (Kumar *et al*, 2020)

2. *Gyratory crusher*

The solid materials are fed between circular jaws. The solid materials are introduced into a V–shaped notch between the metal casing and the head. Size reduction happens in this V-section where the materials are caught up and the comminuted particles pass out from the bottom. The speed of operation varies from 100 to 450 gyrations per minute. The gyratory crusher has added advantages like lower energy consumption and reduced maintenance compared to jaw crusher (J.F. Richardson, et al, 2002).

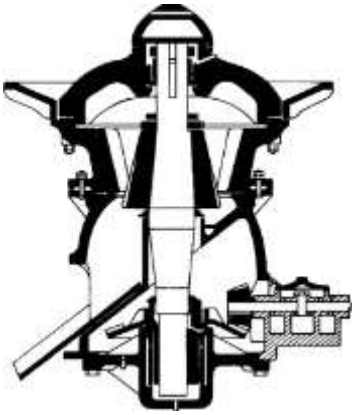


Fig. 4. Gyratory crusher. (J.F. Richardson, et al, 2002)

3. *Roll crushers*

Roller crushers are made up of two equal-sized and smoothened rolls that rotate at the same speed, one clockwise and the other anti-clockwise. The two rollers are appropriately hefty, rotating on horizontal axes that are parallel. Depending on the use, the rolls can also be jagged. The key factor influencing the extent of size reduction is the coefficient of friction between the substance to be size decreased and the surface of the roller. In a roll crusher, larger particles can be accommodated since size reduction is impacted by impact, shear, and compression - all of which act in concert (Ashok Gupta, Denis Yan, 2016).

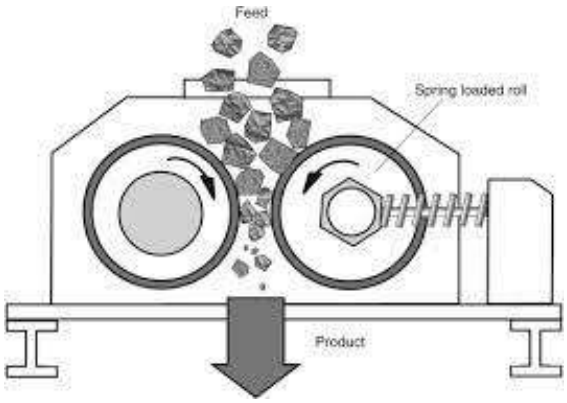


Fig. 5. Model of Roll crushers (Ashok Gupta, Denis Yan, 2016)

Advantages and applications of mechanochemical processing

The fundamentals features of mechanochemical processing include combustion reactions, formation of amorphous phases, phases of novel crystalline synthesis, mineral and waste processing, metals refining, ultrafine powder production, production of a fine dispersion of second-phase particles, extension of solubility limits, refinement of the matrix microstructure and nanoparticle formulation, the possibility of alloying difficult-to-alloy elements, and extensibility (McCormick and Froes, 1998). Several of the most important applications/advantages of mechanochemistry in different fields of minerals and materials treatment are summarized below (Lin and Nadiv, 1979; Gutman, 1998):

- Regeneration of drilling mud, and production of drill-hole cementation mixtures.
- Increase of fertilizer efficiency.
- Production of special concretes for building.
- Simplifying the production of cement when milling the reactants by depressing the furnace temperature and reaction time.
- Grinding of clinker for improvement of compressive strength and reduction of the tuning time of concrete.
- Improving parameters of moreover processing of product; increasing efficiency of reaction by changing the properties of the mixture.
- Creating a high-quality industrial material through processing some secondary materials (which could not be used in classic technological systems).
- Preparation of useful materials from initial sources that cannot be processed by other methods (e.g. converting appetites of low quality to fertilizer of approximately the same efficiency as superphosphates).
- Implementing certain high temperature reactions with acceptable rates at normal pressure.
- To integrate two or more technological processes (e.g., mixing, simultaneous refining and activation in the production of filled polymers during mechanical activation).
- To manufacture a new product of high quality or with novel properties by mechanical processing of initial or intermediate products, which cannot be obtained by other methods. (Boldyrev and Tkacova, 2000; Lin and Nadiv, 1979 and Gutman, 1998).

3. Conclusion

Mechanochemistry has made significant progress during the last ten years, it is one of plethora types for size reduction instrument. The mechanochemical process of size reduction is major for diverse industries like chemical, pharmaceutical, agricultural, etc. Currently an abundance of size reduction equipment with varying capacity and sizes are available. They could handle a wide variety of raw material. The nature of feed to be processed is also as critical as the choice of size reduction equipment. Overall, size reduction helps in achieving uniform mixing, homogeneity, and ideal flow of the materials.

References

1. Abouzeid AZ. Processing of fine particles in mineral beneficiation. Part1. Powder Handling and Processing 1994; 6: 35-48.

A. Kumar *et al* /International Journal of ChemTech Research, 2020,13(1): 48-54. DOI= http://dx.doi.org/10.20902/IJCTR.2019.130106.

2. Ashok Gupta, Denis Yan, 2016) Mineral Processing Design and Operations (Second Edition), Ashok Gupta, Denis Yan , Chapter 6 - Roll Crushers, Elsevier, 2016, Pages 169-188, ISBN 9780444635891
3. Baláž, P.; Achimovičová, M.; Baláž, M.; Billik, P.; Cherkezova- Zheleva, Z.; Criado, J. M.; Delogu, F.; Dutková, E.; Gaffet, E.; Gotor Martinéz, F. J.; Kumar, R.; Mitov, I.; Rojac, T.; Senna, M.; Streletskii, A.; Wieczorek-Ciurowa, K. Hallmarks of mechanochemistry: from nanoparticles to technology. Chem. Soc. Rev. 2013, 42, 7571−7637. (DOI: 10.1039/c3cs35468g).
4. Bala´zˇ. P, Mechanochemistry in Nanoscience and Minerals Engineering, Springer-Verlag, Berlin Heidelberg, 2008.
5. Boldyrev, V.V. (1986) Mechanochemistry of inorganic solids. Proceedings of Indian National Science Academy 52, 400–417.
6. Boldyrev VV and Tkacova K., (2000), Mechanochemistry of Solids: Past, Present, and Prospects. Journal of Materials Synthesis and Processing ;8(3-4):121-32.
7. Dana L. Bishop. A sedimentation method for the determination of the particle size of finely divided material. Part of Bureau of Standards Journal of Research; 1934; 12: 173-183.
8. Delogu, F., Mulas, G., Eds. Experimental and Theoretical Studies in Modern Mechanochemistry; Transworld Research Network, Kerala, India, 2010.
9. Ehab AlShamaileh, Mohammad R. Al-rbaihat , Aiman Eid Al-Rawajfeh, Mechanochemical Synthesis of Slow-Release Fertilizers: A Review (2017), The Open Agriculture Journal, 12, 11-19.
10. Ghada A. Al Bazedi, Aiman Eid Al-Rawajfeh, Mona A. Abdel-Fatah, Mohammad R. Alrbaihat, Ehab AlShamaileh, Handbook of Greener Synthesis of Nanomaterials and Compounds, 1st Edition, (2021), ISBN: 978-0-12-821938-6.
11. Gutman E M. (1998), Mechanochemistry of Materials. Cambridge: Cambridge International Science Publishing.
12. Heinicke, G., (1984), Tribochemistry, Academie-Verlag, Berlin.
13. Jameel Ahmed S Mulla, Shraddha C Hajare, Rajendra C Doijad. Particle Size and it's Importance in Industrial Pharmacy: A Review. Indian Journal of Novel Drug Delivery 2016; 8(4):191-198.
14. Juhasz A.Z., (1974), Mechanochemical activation of silicate minerals by dry fine grinding. Aufbereitungs-Technik, 10, 558-562.
15. Lin IJ and Nadiv S. (1979), Review of the Phase-Transformation and Synthesis of Inorganic Solids Obtained by Mechanical Treatment (Mechanochemical Reactions). Materials Science and Engineering, 39(2):193-209.
16. Lynch, A. and Rowland, C. (2005), "The History of Grinding". Society of Mining, Metallurgy and Exploration, SME 2005, pp115- 125.
17. McCormick P, Froes F. (1998), The Fundamentals of Mechanochemical Processing. JOM Journal

of the Minerals, Metals and Materials Society; 50(11):61-5.
18. McNaught, A.D. and Wilkinson, A. (1997), IUPAC, Compendium of Chemical Terminology, (The "gold Book"), Blackwell Scientific publications, Oxford, 2nd edit, 1997.
19. Ostwald, W., (1887), Lehrbuch der AllgemeinenChemie, Auflage, Band, Leipzig.
20. Price M.Size reduction.In:OthmerK,editor.Encyclopedia of chemical technology. NewYork: John Wiley and Sons; 1999:836-8.
21. Rakesh P Patel, Ashok H Baria, Nikunjana A Patel. An overview of size reduction technologies in the field of pharmaceutical manufacturing. Asain Journal of Pharmaceutics 2008; (October – December): 216-220.
22. Richardson. J.F and J.R. Backhurst, in Chemical Engineering (Fifth Edition), Volume 2, 2002
23. Rudd DF, Powers GJ, Siirola JJ. Process synthesis. Englewood Cliffs, N.J.: Prentice-Hall; 1973:205-208,
24. Sopicka-Lizer, M., Ed. High-Energy Ball Milling. Mechanochemical Processing of Nanopowders; Woodhead Publishing: Cambridge, UK, 2010.
25. Suryanarayana, C. Mechanical alloying and milling. Prog. Mater. Sci. 2001, 46, 1−184.
26. Takacs L, (2014), What Is Unique About Mechanochemical Reactions, ACTA PHYSICA POLONICA A, Vol. 126, No. 4.

Sequential Extraction of Rare Earth Elements from Phosphogypsum

Ahlam Waleed Hunaihen

Al-Hussain Bin Talal University - Jordan
Corresponding author: ahlamhunaihen@gmail.com

1. Introduction

1.1 Background

Phosphogypsum (PG) is a waste by-product from the processing of phosphate rock in plants producing phosphoric acid and phosphate fertilizers, such as superphosphate. The wet chemical phosphoric acid treatment process, or 'wet process', in which phosphate ore is digested with sulfuric acid, is widely used to produce phosphoric acid and calcium sulfate, mainly in dihydrate form (CaSO4 · 2H2O):

$$3CaF_2+10H_2SO_4+20H_2O\rightarrow 6H_3PO_4+10CaSO_4\cdot 2H_2O+2HF. \qquad (1)$$

Heavy metals and REE naturally present in the phosphate rock may be distributed or redistributed in phosphoric acid or physphogypsum. (1)

REE is the collective name for 17 chemically similar metallic elements, usually divided into the light REE (LREE) and the heavy REE (HREE). It is used in mature markets (such as catalysts, glassmaking, metallurgy), also in battery alloys, ceramics. Some REE elements have high economic feasibility, and 1g of it can be worth more than gold.(5)

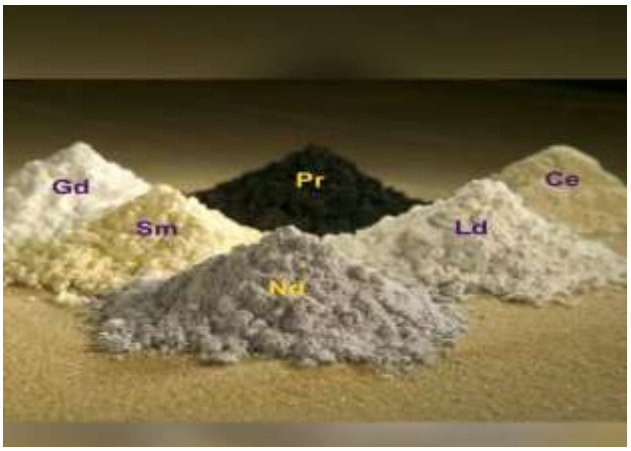


Figure (1.1). Rare Earth Elements

Jordan has huge reserves of phosphate deposits, the main deposits existed in the southern region of the country. The production rate of PG verses marketable P2O5 as acid in the world is high as much as 5 tons of PG are produced for each ton of P2O5; in Jordan the rate is around 5.0 – 5.3 ton of PG per ton of P2O5 produced depending on the phosphate rock composition. This means a huge amount of PG will accumulate at the fertilizer plant in Aqaba. In general, the phosphate industry in Jordan has generated over 40 million tons of this waste material. Production continues at the rate of 3 million tons per year. (2)

The objective of this work was to document the level of rare earth elements in phosphogypsum, in order to better understand the potential pollution problems that may pose hazards for public and environmental health associated with Jordan phosphogypsum.(2)

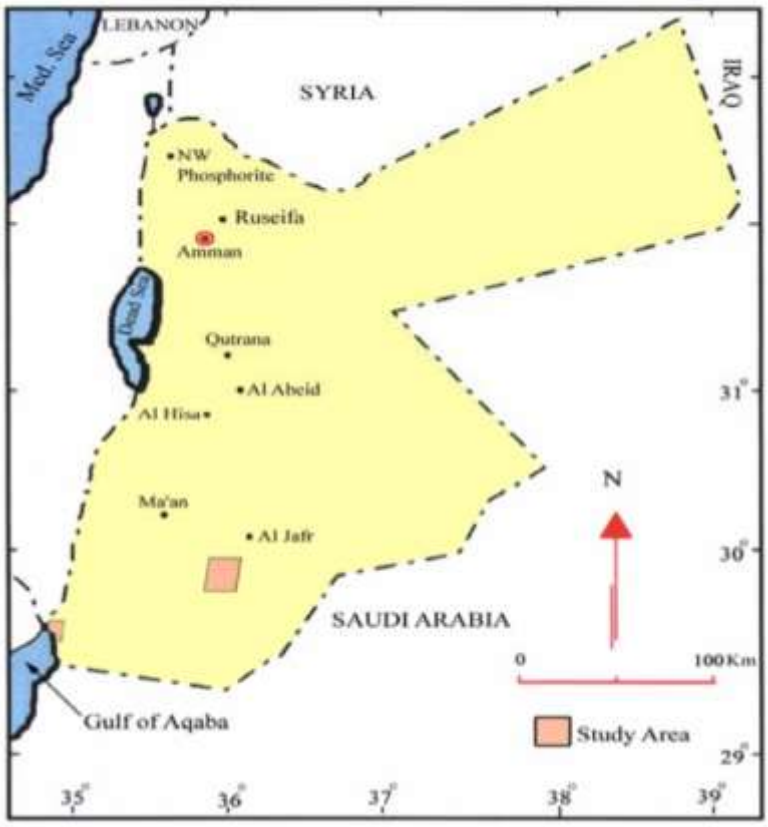


Figure (1.2). Location map of the study area. The Aqaba site is indicated by the shaded rectangle at the lead Gulf of Aqaba. The Eshidiya is indicated by the shaded rectangle southeast of Ma'an.

1.2 The statement of problem

Phosphogypsum is contaminated by chemical and radioactive materials and, therefore, in the world is mostly dumped in stockpiled in controlled areas and only about 15% is recycled, it contains, next to naturally occurring radionuclides, some trace elements such as arsenic, lead, cadmium, chromium, fluoride, zinc, antimony, copper (U.S. Environmental Protection Agency, 1990), which may be leached. (3)

The problem of contaminated phosphogypsum has already become an international ecological problem. For example, a huge amount of phospho-gypsum has accumulated in Florida (more than 1 billion (!) tons), in Europe (where the contaminated phosphogypsum is discharged into the River Rhine close to the North Sea), in Canada, Morocco, Togo, India, China, Korea, Palestine, Jordan, Syria, Russia, and other parts of the world. (3)

The main problem is the slightly elevated radioactivity of phosphogypsum, which is due to the high activity concentration of ^{226}Ra, while the remaining impurities can be extracted relatively easily, but traditional technologies of purification of phosphogypsum from radium are not effective, because of the similarity of chemical properties of radium sulfate and calcium sulfate salts.(3)

1.3 Research questions

Which step of extraction have the highest percentage of rare earth element? In other words, What is the portion of the phosphogypsum that have the largest amount of rare earth elements?

1.4 Scope & limitation

The processes in this project need hard work and long time, also a very high accuracy, because it is sequential, so every step depends on the previous one, therefore we had to be sure that every single step has being done accurately to have the correct results.

1.5 Layout

Next chapter is the literature review and it is a brief table that showed the aims and results for past research which were talked about the phosphogypsum processes for extraction rare earth elements, radionuclides, some trace and toxic elements, and recycle it to use in construction as a gypsum.

After that third chapter "Methods & techniques" talked about the procedure of this project in detailed paragraphs in addition to explain all calculation steps needed to extract the rare earth elements. Finally, chapter four "Result & discussion" talked about the material balance, including diagrams, tables, curves that illustrate the results of this project.

2. Literature Review

1. In this study, a water-soluble phase extraction step was added as an initial step, in addition to the five extractions defined by Tessier et al. (1979). The reagents used for the six extractions are designed to indicate the relative amounts of uranium and some of the trace metals in the following fractions: (1) water-soluble; (2) exchangeable; (3) carbonate; (4) Mn-iron oxide; (5) organic matter; and (6) residual. The method of extraction is dependent on the grade, size, location, and geology of the deposit and is based on maximizing ore recovery within economic constraints. A total of eight representative samples were considered for sequential extraction analysis. The extracts from the different steps were analyzed using ICP-MS for U and other trace metals. The extraction sequences and leaching agents that were used are given in the proceeding paragraphs

   The extraction and recovery of REE from phosphate using px-107 and chelok polymers done by Joseph P.L , with Jack Mustaco in Florida , 2015 the outcomes was that the extraction and recovery yield was between 80%for gadolinium and 8% for praseodymium , between 70% for terbium and 56% for scandium and 31% for praseodymium from waste clay the result of this study was the process may be an efficient means of recovering REE from phosphate mining waste products. And that treatment of phosphogypsum stack water and leachate with poly salt may effectively reduce metal contamination of both surface and groundwater.

2. Recovery of rare earth elements from phosphogypsum done by V.N. rychkov , E.V.Kirillov , S.V.Kirillov ,V.S.Semenishchev , G.M.Bunkov ,M.S.Batalov ,D.V. Smyshlyaev , A.S. Malyshev in Russia ,2018 it describe a technology for complex treatment of phosphgypsume in addition it was shown that the productsc after phosphogypsume treatment can be successfully used instead of natural gypsum as an addition for cements in the production of building materials the result that the REE leaching from the phosphogypsume from 15 to 17% to ore than 70%

3. Leaching f some lanthanides from phosphogypsum fertilizers by mineral acids done by Z.H. Ismail , E.M. Abu Elgoud , F.Abdel Hai , Ibraheem.O.Ali , M.S.Gasser and H.F. Aly in Egypt , 2015 the acides used H2SO4 , HCL and HNO3The result of highest leaching efficiency was obtained using 3.0M HNO3 andmixing time 3 hr at room tempreture the total lanthanides content in the PGF , was found to be about 480 mg/kg after three cycle of leaching and leached out lanthanides from PGF was more than 66%

4. Rare earth and phosphourus leaching from a flotation tailings of florida phosphate rock done by Haijun Liang , Patrick Zhang , Zhen Jin and David W. Depaoli in China , 2018 the result indicated that REEs has similar trends f leaching efficiency to those phosphorus ,REE and phosphours leaching efficiencies reached relatively high values of approximately 61% and 91% respectively analyses indicated that the phosphate ions in the leaching solution tended to combine with REE phosphates which precipitated into PG but other large amount of anions such as sulfate ions and fluoride ions took effect of steric hindrance to prevent the phosphate ions from combining with REE cations .

5. Extraction of Rare Earth Elements from Phosphogypsum (Fertilizer production By -Product) done by Mugdah Walawalkar in Toronto , 2016 the result show that the leaching efficiency is controlled by the soulability limit of PG in the outcome the leaching efficiency using nitric and hydrochloric acids are higher than the sulfuric acid

6. Pilot-scale recovery of rare earths and scandium from phosphogypsum and uranium leachates done by Maxim Mashkovtsev , Maxim Botalov , Denis Smyshlyaev , Risto Parjarre , petteri Kangas , Viadimir Rychov and Pertti Koukkari in Russia, 2016, the experimental work combines solvent extraction with advance ion exchange methodology in apilot facility capable of treating 5 m3 solution per hour . The outcomes of this search cerium carbonate , lanthanum oxide and concentration of heavy metals Finally apurified 99% concentrate of scandium oxide as well as 99% rare earth concentrate are received

7. Partitioning of radionuclides and trace elements in phosphogypsum and its source materials based on sequential extraction methods done by A.J.G Santos , B.P. Mazzilli , D.I.T Favaro , P.S.C Silva in Brazil , 2005 . Among these impurities , radionuclides from U238 and TH232 decay series are of most concern due to their radioxicity other elements such as rare earth element (REE) and Ba are also enriched in the phosphogypsum the sequential extraction results show that most of the radium and lead are located in the (iron oxide) fraction and the only 13 – 18% of these radiounclides are distributed in the most labile fraction . Th ,REE and Ba where found predominantly in the residual phase

8. Recovery of Rare Earths from Wet – Process Phosphoric Acid , the Solvay experience done by Alain Rollat in France , 2016 ,

9. Recovery of rare earth from wet- process phosphoric acid done by Liangshi Wang , Zhiqi long ,Xiaowei Hung , ying Yu , Dali Cui ,Guocheng Zhang in China 2009 ,the result indicate that lower tempreture , higher concentration f phosphoric acid and large liquid solid ratio are benifical to RE enrichment in the phosphoric acid . the RE leach recovery about 75%under optimize condition.

10. Leaching of rare earth elements from egyption western desert phosphate rocks using HCL done by M.Abd Elmottaleb , M.F Cheira , Gamal A.H Ghouda lement leach from phosphate rock using hydrochloric acid the kinetic of leaching process was studied as afunction of tempreture , the result showed that the reaction rate of leaching is controlled by inner diffusion .

11. Extraction of rare earth elememts from upgraded phosphate flotation tailings done by S.Al-Thyabat , P.Zhang attention has mostly focused on the extraction of REEs from phosphogypsume which contain 70 percent of the REEs with only limited work conducted on REEs extraction from sand tailings and slime even through they account for 16 percent and 15 percent respectively of REEs mined with phosphate matrix , the separation with flotation while flotation was conducted in D-12 flotation cell . 20 percent of REE recovery and 368.2 micro gram/gram REEs with 63.5 percent REE recovery
12. Reprocessing of phosphgypsum for recovery of REE done by Jason Yang in Barcelona , 2017 , the method used is wet-process where during it the REE are enriched in the PG with only 20-30% REE in the phosphoric acid leaching

13. Phosphoric acid extraction and rare earth recovery from appatites of the Brazilian phosphate ores done by Fernando Pereira and Essaid Bilal in France 2010 ,in the hydrochloric treatment acidification of conc HCL the results rate of CaO and P2O5 (around 80%) for REE after the adition of a sodium salt to the to the chlorophosphite te precipitate gotten reval that more than 80% constitutes a valorization source of the proposed process

14. Assessment of bacterial (acidic)-leaching of rare earth elements from phosphate ore done by S.Hussien , P. Patra , P. Samasundration and H. Elshali in florida 2018 , the methods for extraction rare earth elemants from law grade phosphate ores .In shake flak studies the leaching rate relied mostly on the bacterial activity -acid , producing ability of the bacteria , bacterial activity reduce according to the F ions can cout a processes challenge in the chemical leaching methods

15. The extraction of REE from hydrate phosphate precipitates of apatite processing done by M.O Androvop , A.S. Buynovskiy , V.I Sachkov , A.VAnufrivew, A.N.Maseov ,O.B Stepanova , R.A Nefedov , I.N.Mazof , A.V Vakov in Russia 2015 , oreliminary purification of nitric solution of REE from impurities of titanium , aluminum , iron , uranium and thorium . Technical decision were suggested for the separation of REE in groups without the use of salting – out agent

16. Method for extraction rare earth elements from phosphogypsume in united states 2010 , recovering rare earth elements in particular from phosphogypsum using sulfuric acid – nitric acid mixture solution at 3-2-1-2 ratio with concentration of 1-3% by weight , The claimed method allows both to increase the recovery rate of rare earth elements and reduce by half the time at the process accomplished at lower concentrations and with smaller volumes of a acidic reagent

17. Centerifugal extraction rare earths from wet process phosphoric acid Wang Liangshi , Yu Ying , Liu Ying and Long Zhiqi in China 2010 , Recovery of RE from wet- process phosphoric acid WPA is the results indicate that higher rotational speed that the phase contact time for efficiently exctracting RE and that for iron are of great difference which provides an effective method for separation factor b is enhanced from .07 to 17.6

18. Phosphogypsumtechnology with extraction of valuable components done by A.V Valkov , V.A. Andreev , A.V Aufrevia , S.A Benzurkova , Y.N. Makaseev and N.V.Demianenko in Russia 2014 the result at studies aimed at implementing the steps to obtain envieronmentally friendly waste from the production of fertilizerThe research described herein is focused on the latter half of the process. It was demonstrated that calcium sulfide could be converted to ammonium bisulfide (NH4SH), and that ammonium bisulfide could be oxidized by air in the presence of a catalyst, to elemental sulfur, which was adsorbed on the catalyst. Two methods for recovering sulfur from the catalyst were developed: (1) thermal treatment to volatilize sulfur, and (2) leaching the sulfur from the catalyst with liquid anhydrous ammonia. Over 90 pct of the sulfur adsorbed on activated carbon (the catalyst) was recovered by both methods. Based upon the encouraging laboratory investigations, a hydrometallurgical scheme was proposed for the overall conversion of calcium sulfide to elemental sulfur.

19. Speciation of Heavy Metals by Modified BCR Sequential Extraction in Soils Contaminated by Phosphogypsum in Sfax, Tunisia Ahmed Wali1, Gilles Colinet2, Mohamed Ksibi 2014 , its determined the concentrations of trace metals (Zn, Pb, Cu, Cr, Co, Ni, Mn, and Fe) in soil using the sequential extraction method recommended by Community Bureau of Reference (BCR) and analysed chemical properties, such as the pH, cation exchange capacity, total organic carbon, electrical conductivity, and calcium carbonate. Our results revealed higher concentrations of trace metals in topsoil samples (0–20 cm) than in subsoil samples (20–40 cm and 40–60 cm) for most metals at four sites. Zn in the topsoil was mostly associated with the non-resistant fraction at all sites. Approximately 60% more Pb was bound to the non-residual, exchangeable and reducible fractions at all sites, and soil depths. Cr, Cu, Ni and Fe were mainly in the residual fraction, whereas Mn was largely present in the non-resistant fraction. The global contamination factor of trace metals decreased with soil depth. The mobility and bioavailability were greatest for Zn, followed by Cu and Pb.

20. The recovery of sulphur from waste gypsumryneth Nkhangweleni Nengovhela in Pretoria2016 , shows the effect of various reaction parameters on the CaS yield during the thermal conversion of gypsum to CaS. Effect of time. Experiment 1 (Table 6.1) showed that good conversion yields (> 96%) were achieved at a reaction time of 20 min. At a reaction time of 5 min, the yield was only 45% Effect of different gypsum compounds. that 91% of gypsum was converted to CaS when pure gypsum was used. The lower conversion percentages (76% and 81%) obtained when Anglo gypsum and Foskor gypsum were reduced to CaS can be ascribed to the impurities contained in the two gypsum compounds

21. EXTRACTION AND SEPARATION OF HEAVY RARE EARTH(III) WITH EXTRACTION RESIN CONTAINING DI(2,4,4-TRIMETHYL PENTYL) PHOSPHINIC ACID (CYANEX 272) done by Zhonghuai Wang , Genxiang Ma & Deqian Li in china 2000 its presents the results ofthe adsorption ofheavy rare earth ions (Ho(III), Er(III), Tm(III), Yb(III), Lu(III) and Y(III» from hydrochloric acid solutions at 0.2 mollL ionic strength and 50°C by the extraction resin containing di (2,4,4trimethyl pentyl) phosphinic acid (Cyanex 272) and the chromatographic separation of (Er(III), Tm(lII) and Yb(lII». Technological separation products, with purity and yield ofTm203 >99.97%, >80%; Erz03 >99.9%, >94% and Yb203 >99.8%, >80% respectively, have been obtained from a feed having the composition Tm203 60%, Er203 10%, and Yb2033%, the others 27%.

22. PRODUCTION OF SULFUR FROM GYPSUM AS AN INDUSTRIAL BY-PRODUCT in France 2001 done by S. HILIGSMANN *, S. DESWAEF , X. TAILLIEU , M. CRINE . N. MILANDE and PH. THONART The selection of SRB strains from natural samples provided one ASRB strain purify from rabbit manure and 4 LSRB strains purified from bovine manure, soil, Seine estuary (France) and water from pond. All 5 strains were studied in 2.5 L bioreactorsThe important DOC concentration in the first stage output is constituted primarily (16 g/L) of acetic acid, which was poorly oxidized. These results show the benefit of working with two stages, reducing organic carbon concentration in effluent and also increasing gypsum reduction yield.

23. Rare Earths Extraction, Separation, and Recovery from Phosphoric Acid Media in korea 2016 done by Bontha Ramachandra Reddya and Jyothi Rajesh KumarbRare earths (REs) recovery and processing becomes most important all over the globe due to their versatile applications in modern life. The present general article discusses REs extraction and possible separation and recovery methods from phosphoric acid media. Leaching studies are discussed followed by two extraction techniques: solvent extraction and solid–liquid extraction. Various extractants such as TOPS 99 (or) D2EHPA, Cyanex 272, PC 88A were tested for REs extraction and separation. Three resins, Tulsion T-PAR, CH-96, and CH-93, as well as impregnated TOPS 99 were utilized for solid–liquid extraction studies.

24. Solid-Liquid Extraction of Terbium from Phosphoric Acid Medium using Bifunctional Phosphinic Acid Resin, Tulsion CH-96in India 2009 In the wide range of phosphoric acid concentration 0.01–7.8M the percent extraction of terbium decreases from 98.9% at 0.01M to 16.0% at 1M due to an ion-exchange mechanism and increases to 36% at 7.8M due to a coordination mechanism. The percent extraction increases with an increase in weight of the resin from 2.7% at 0.05g to 80.7% at 1.2g. Under the studied experimental conditions, the loading of Tulsion CH-96 for terbium was determined to be 3.52mg per gram of resin. The percent extraction of terbium increases with the increase in temperature, indicating the endothermic nature of the extraction process. Screening of various eluants suggested 1M (NH4)2CO3 as the best with an efficiency of 99.8%. The extraction behavior of commonly associated metals with terbium such as yttrium, holmium, erbium, dysprosium, ytterbium, and lutetium has been studied as a function of phosphoric acid concentration to determine the separation factors and possible separation.

25. Uranium and Rare Earth Recovery from Phosphate Fertilizer Industry by solvent Extraction in the Rumania-Europe 2009Uranium extraction from the phosphoric acid by acidic organophosphorus esters is discussed in detail. The industrial flowsheets are described. Details are presented for the single cycle extraction process devel- oped in Romania. Cost estimates are given which show the superiority of the single cycle process and its capability to produce uranium at a competitive price, while also producing rare earths as a by-product. Process flowsheet with stream data is also given for treatment of the solution obtained by nitric acid attack of the phosphate rock. Analysis of the uranium green cake (UF,) and the rare earth concentrate is given.

26. RECOVERY OF SULPHUR FROM WASTE GYPSUM in South Africa 2001 done by N.R. MBHELE1*, W. VAN DER MERWE1, J.P. MAREE2 and D. THERON3 The aim of this project was to evaluate a process for converting waste gypsum into sulphur. The process evaluated consists of the following stages: reduction of gypsum to calcium sulphide; stripping

of the sulphide with CO2 gas and the production of sulphur. Thermal reduction study showed that gypsum can be reduced to CaS with activated carbon in a tube furnace operating at 1100 ºC. The CaS yield was 96%. The CaS formed was slurried in water. The reaction of gaseous CO2 with the CaS slurry leads to the stripping of sulphide to form H2S gas and the precipitation of CaCO3. The H2S generated was then reacted with SO2 in the PIPco processes to form elemental sulphur. Sulphur with the purity between 95% and 99% was recovered from waste gypsum in this study.

27. RECOVERY OF RARE EARTH ELEMENTS FROM PHOSPHOGYPSUM (REE–PG) in china done by LUT: Prof. Tuomo Sainio (consortium leader), Dr. Sami Virolainen, Dr. Markku Laatikainen, Dr. Katri Laatikainen. Research professor Jason Yang, Mr. Tero Korhonen, Ms. Neea Heino Pertti Koukkari, Dr. Malin Bomberg, Mr. Jarno Mäkinen Dr. Volha Yahorava, Dr. Volha Bazko, Dr. Christoph Pawlik, Dr. Michelle van RooyenExtensive testwork programs on REE recovery from PG at GTK and VTT in Finland and at MINTEK in South Africa have shown that the PG is highly variable, both in terms of physical properties and REE recovery, which prevents the industry from successfully treating the PG dumps. The REEíPG project extends REE processing beyond state-of-the-art by means of detailed investigation of the fundamental phenomena in the beneficiation, extraction and separation of REE. Understanding the cause of varying responses of PG samples to a certain process will lead to identification of a new methodology to unlock REE accumulated in waste. Biological pretreatment and sulphate reducing bacteria (SRB) precipitation are investigated to provide an efficient, affordable and environmentally friendly concentration of REE in PG. An optimized Resin-in-Leach (RIL) process will provide a viable methodology for REE recovery from low grade sources. Finally, utilizing novel ion exchange materials, aqueous feed and/or eluent modification and novel process configurations will enhance the RIL recovery process, improve REE separation and improve the economics of the process in general.

28. Purification of phosphogypsum from 226Ra and heavy metals for its further utilization in construction in Palstine2016 DONE BY Konstantin Kovler1, Boris Dashevsky1 and David S. Kosson The known purification approaches have failed to produce a breakthrough in the industry, and have remained confined to the laboratory, largely due to cost considerations. In the patent literature 226Ra is removed during recrystallization of the gypsum • in nitric acid • in sulfuric acid with an addition of Ba-ions

29. LEACHING AND BIODEGRADATION OF RARE EARTH-BEARING PHOSPHOGYPSUM in London 2003 done byMoulay Lahcen SBAI , the result show that 70% SCE was achieved within 43 min residence time (flow rate = 3.2 ml/min), which in fact, was more than double of that achieved with a 100 cm height bed (within the same residence time). Besides, the maximum sulphide production achieved was 34 x 10'6 moles min'1 or 11.8 millimoles hr*1 per litre of reactor volume for a flow rate of 3.2 ml/min. This was higher than any value ever achieved on a continuous basis. In fact, the highest sulphide yield achieved by Cork and co-workers [1, 6-8, 10] (who are the most active research team known in this field), was 2.75 millimoles hr'1 per litre of reactor volume.

30. Extraction of Rare Earth Elements from Phosphogypsum (Fertilizer Production By-product) in Toronto 2016 done by Mugdha Walawalkar the main by-product of fertilizer production contains some REEs, so it can be used as a secondary source. The current research focuses on: a thorough characterization analysis; acid leaching process; kinetics of the leaching process;

recycling of consumed acid and effect of microwave pre-treatment on the REEs leaching. The results show that the leaching efficiency is controlled by the solubility limit of PG. Systematic leaching experiments using three acids under various operating conditions were performed. The results indicate the best operating conditions are 1.5 M, 80°C, solid-to-liquid ratio of 1/8 and 20 min residence time, but the leaching efficiency using nitric and hydrochloric acids are higher than the sulphuric acid. Furthermore, it was found that microwave pre-treatment improves the leaching efficiency of REEs.

3. Method and Techniques

3.1 Samples Collection

We collect samples of phosphogypsum from Aqaba Phosphate Mines Company - Industrial Complex and¸ so we took 10 kg from each company.

3.2 Samples Preparation

Firstly we dry the samples of phosphogypsum for a week¸ the we grinded 2 kg from each sample by ball mill at 390 rpm . After that we sift the samples through 75 µm¸ we put it in the oven at 70 C^{o} for 4 hr to take 1300 g from each sample .



Figure (3.1). Ball Mil

3.3 Procedures

3.3.1 Sequential Chemical Extraction

● Step 1: Water-Soluble Form

Milli-Q water was used as an extracting agent. In a 100 ml centrifuge tube, 1.0 g of dry sample, previously ground (10<100 m grain size) and homogenized, was added followed by 50 ml of Milli-Q water (pH 6.7-6.9). The sample mixture was then shaken for 16 h at 20 C assuring that the solid always remained in suspension. The liquid phase was then separated by centrifugation at 7000 rpm for five minutes. The extract was decanted and filtered through 0.45 m membrane. The residue was washed by adding 20 ml of Milli-Q water, shaken/agitated for 15 minutes, and centrifuged at 7000 rpm for five minutes. The snperatant was decanted and discarded, taking care not to discard any of the solid residues. The "cake" that formed as a result of centrifugation was disaggregated by hand shaking prior to the next step. (6)



Figure (3.2). Shaker



Figure (3.3). Centrifuge

● Step 2: Exchangeable Form

The residue from step 1 was reacted with 8 ml of 1 M MgCl2 solution (pH 7). The sample was shaken for 1 h at 20 Cº, assuring that the solid always remained in suspension. The liquid phase was separated by centrifugation at 7000 rpm for five minutes. The extract was decanted and filtered through a 0.45 μm membrane, and then saved for analysis by ICP-MS. The residue was washed by adding 20 ml of Milli-Q water, shaken/agitated for 15 minutes, and centrifuged at 7000 rpm for five minutes. The supernatant was decanted and discarded, taking care not to discard any of the solid residues. (6)



Figure (3.4). filtering through a 0.45 μm membrane

● Step 3: Carbonate Form

The residue from step 2 was leached using 8 ml of 1 M NaOAc, adjusted to pH 5 with HOAc.

The extract was shaken for 5 h at 20 Cº, and then the liquid phase was separated by centrifugation at 7000 rpm for five minutes. The extract was decanted and filtered through a 0.45 μm membrane, and then saved for analysis using ICP-MS. The residue was washed by adding 20 ml of Milli-Q water, shaken/agitated for 15 minutes, and centrifuged at 7000 rpm for five minutes. The supernatant was decanted and discarded, taking care not to discard any of the solid residues. (6)



Figure (3.5). NaOAc adjusted to pH 5 with HOAc

● Step 4: Iron and Manganese Oxides Form

The residue from step 3 was extracted with 20 ml of 0.04 M NH2OH.HCl solution in 25% (v/v) HOAc. The sample was shaken for 6 h in a water bath at 96 ± 3 Cº, assuring that the solid always remained in suspension. The liquid phase was separated by centrifugation at 7000 rpm for five minutes. The extract was decanted and filtered through a 0.45 μm membrane, and then saved for analysis by ICP-MS. The residue was washed by adding 20 ml of Milli-Q water, shaken/agitated for 15 minutes, and centrifuged at 7000 rpm for five minutes. The supernatant was decanted and discarded, taking care not to discard any of the solid residues. (6)

● Step 5: Organic Form

The residue from step 4 was treated with 3 ml 0.02 M HNO3 and 5 ml of 30% H2O2 solution, (adjusted to pH 2 with HNO3), and the mixture is shaken for 2 h in a water bath at 85 ± 2 Cº. The sample was then centrifuged for five minutes at 7000 rpm and the supernatant decanted and filtered in a 0.45 μm membrane, and then saved for analysis by ICP-MS. The residue was washed by adding 20 ml of Milli-Q water, shaken/agitated for 15 minutes, and centrifuged at 7000 rpm for five minutes. The supernatant was decanted and discarded, taking care not to discard any of the solid residues. (6)

● Step 6: Residual Form

The residual material of the previous step was digested with a mixture of 3 ml concentrated HCl and 9 ml concentrated HNO3 , the mixture was poured into Teflon beakers, and the beakers were put on a hotplate to evaporate. The temperature of the hotplate started at 65 Cº and eventually increased to 140 Cº until less than 5 ml solution was remaining. The supernatant was decanted and filtered through a 0.45 μm membrane, and then saved for analysis by ICP-MS. (6)



Figure (3.6). Hotplates

3.3.2 Total Extraction (Full digestion)

Extractions were peformed on 12 composite sample, This method has been developed by Paul Briggs at the U.S. Geological survey (USGS). Twenty mg of composite sample were put in Teflon beakers, with 3 ml HCl, 2ml HNO3, 1 ml HClO4 and 2 ml HF added to each beaker. Samples were dried on a hotplate ovwrnight. 1 ml HClO4 was then added and allowed to dry. The dried sample were removed form hotplate and cooled, 1% HNO3 was added to each beaker. The solutions were analyzed for U and trace elements by ICP-MS at the Savannah River Ecology Laboratory, Aiken, SC. (6)

3.4 Chemical Analysis ICP-MS

Mineral composition was carried out by X-Ray Diffraction (**XRD**) in Al-Hussien bin Talal university .

Chemical composition of major elements was carried out by X-Ray Fluorescence (**XRF**) in Al-Hussien Bin Talal University .

Chemical composition of rare earth elements was carried out by Inductively Coupled Plasma Mass Spectrometry (**ICP-MS**) in Jordan Atomic Energy Commission .

3.4.1 ICP-MS

Table (3.1). Analytical conditions of ICP-MS analysis (6)

Mass Resolution	
^{7}Li	0.75 amu @ 10%
^{89}Y	0.70 amu @ 10%
^{205}Tl	0.80 amu @ 10%
Mass Axis	
^{7}Li	6.95
^{89}Y	88.95
^{205}Tl	204.95
Sensitivity	
^{7}Li	11.4 Mcps/ppm
^{89}Y	27.3 Mcps/ppm
^{205}Tl	19.0 Mcps/ppm
Stability (20 mins)	
^{7}Li	1.18%
^{89}Y	0.38%
^{205}Tl	0.60%
Stability (2hrs)	
^{7}Li	1.35%
^{89}Y	1.27%
^{205}Tl	2.70%
Doubly Charged Species	
$^{70}Ce/^{140}Ce$	1.01%
Oxide Species	
$^{70}Ce/^{140}Ce$	0.46%
Random Background	
Mass 5	2 cps
Detection Limits	
Be	1.2 ppt
In	0.2 ppt
Bi	0.1 ppt
Element	Detection Limits (ppt)
U^{4+}	1
As^{5+}	28
Cd^{2+}	9
Cr^{2+}	13
Cu^{2+}	9
Ni^{2+}	16
Pb^{2+}	17
Zn^{2+}	11
V^{5+}	6

3.4.2 SEM

The scanning electron microscope (SEM) uses a focused beam of high-energy electrons to generate a variety of signals at the surface of solid specimens. The signals that derive from electron-sample interactions reveal information about the sample including external morphology (texture), chemical composition, and crystalline structure and orientation of materials making up the sample. In most applications, data are collected over a selected area of the surface of the sample, and a 2-dimensional image is generated that displays spatial variations in these properties. Areas ranging from approximately 1 cm to 5 microns in width can be imaged in a scanning mode using conventional SEM techniques (magnification ranging from 20X to approximately 30,000X, spatial resolution of 50 to 100 nm). The SEM is also capable of performing analyses of selected point locations on the sample; this approach is especially useful in qualitatively or semi-quantitatively determining chemical compositions (using EDS), crystalline structure, and crystal orientations (using EBSD). The design and function of the SEM is very similar to the EPMA and considerable overlap in capabilities exists between the two instruments.(7)



Figure (3.7). A typical SEM instrument, showing the electron column, sample chamber, EDS detector, electronics console, and visual display monitors. (7)

Fundamental Principles of Scanning Electron Microscopy (SEM) :

Accelerated electrons in an SEM carry significant amounts of kinetic energy, and this energy is dissipated as a variety of signals produced by electron-sample interactions when the incident electrons are decelerated in the solid sample. These signals include secondary electrons (that produce SEM images), backscattered electrons (BSE), diffracted backscattered electrons (EBSD that are used to determine crystal structures and orientations of minerals), photons (characteristic X-rays that are used for elemental analysis and continuum X-rays), visible light (cathodoluminescence--CL), and heat. Secondary electrons and backscattered electrons are commonly used for imaging samples: secondary electrons are most valuable for showing morphology and topography on samples and backscattered electrons are most valuable for illustrating contrasts in composition in multiphase samples (i.e. for rapid phase discrimination). X-ray generation is produced by inelastic collisions of the incident electrons with electrons in discrete ortitals (shells) of atoms in the sample. As the excited electrons return to lower energy states, they yield X-rays that are of a fixed wavelength (that is related to the difference in energy levels of electrons in different shells for a given element). Thus, characteristic X-rays are produced for each element in a mineral that is "excited" by the electron beam. SEM analysis is considered to be "non-destructive"; that is, x-rays generated by electron interactions do not lead to volume loss of the sample, so it is possible to analyze the same materials repeatedly. (7)

Essential components of all SEMs include the following:

- Electron Source ("Gun")
- Electron Lenses
- Sample Stage
- Detectors for all signals of interest
- Display / Data output devices
- Infrastructure Requirements:
  - Power Supply

- Vacuum System
- Cooling system
- Vibration-free floor
- Room free of ambient magnetic and electric fields

SEMs always have at least one detector (usually a secondary electron detector), and most have additional detectors. The specific capabilities of a particular instrument are critically dependent on which detectors it accommodates. (7)

4. Result and Discussion

4.1 Mineral composition of PG

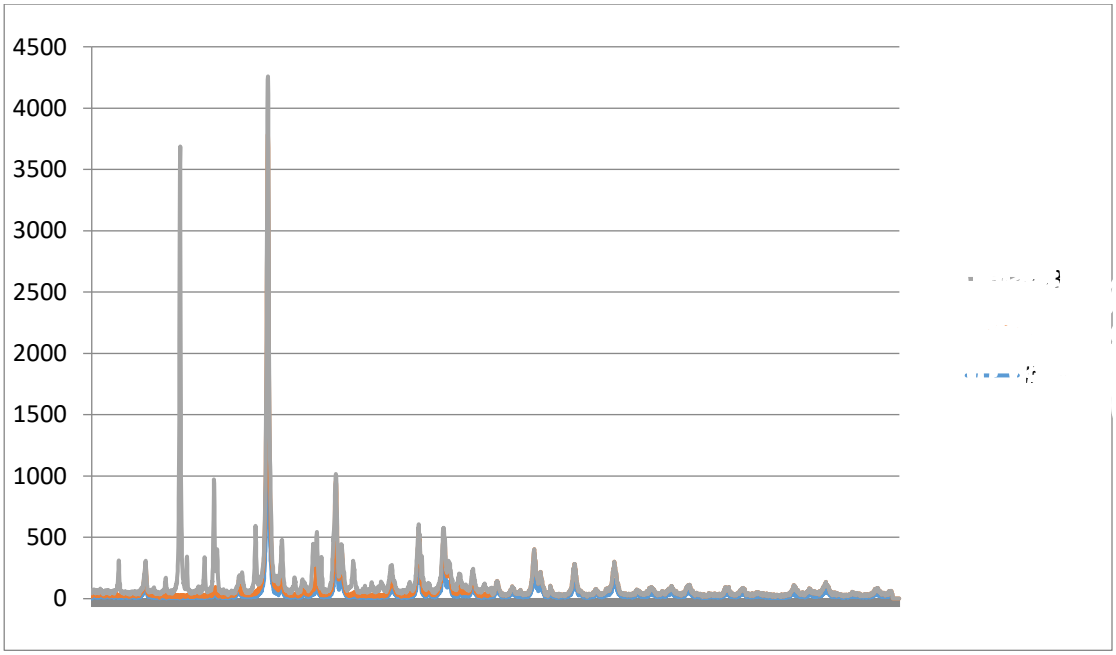


Figure (4.1). XRD curve

This figure show XRD patterns of phosphate rock sample from Al-aqaba, the major mineral finding CaSo4 (gypsum), CaCo3 (calcites), SiO2 (quartz).

4.2 Scan electrometer (SEM)

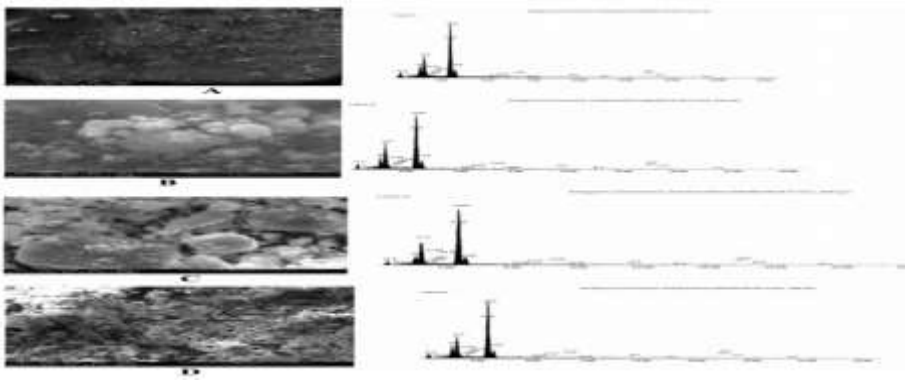


Figure (4.2). SEM shows texture of PG

SEM photographs of phosphate rock: (A) overview of mineral phases; (B) coarse-grained agglomerate crystal of Franco lite and fined-grained agglomerate laced with small bright grains of quartz, calcite, and clay compounds;(C)rounded to subrounded crystal of franco lite and fine-grained agglomerate laced with small bright grains of quartz, calcite, and clay compounds; (D) agglomerate crystal of Franco lite, coarse-grained and fine-grained laced with small bright grains of quartz, calcite, and clay compounds .

4.3.1 Chemical composition of major oxides

Table (4.1). major concentration of SO_3 and CaO in al aqaba and al Eshedia samples

Analyzed	**AQ1**	**AQ2**	**AQ3**	**ESH 1**	**ESH 2**	**ESH 3**
SO_3	55.20%	55.81%	55.42%	53.92%	54.10%	54.20%
CaO	40.75%	40.20%	40.58%	41.13%	40.50%	40.00%
SiO_2	3.36%	3.36%	3.32%	3.59%	3.40%	3.70%
Fe_2O_3	0.29%	0.29%	0.29%	0.12%	0.15%	0.11%
P_2O_5	0.12%	0.14%	0.21%	1.04%	1.70%	1.40%
K_2O	0.04%	0.05%	0.04%	0.09%	0.07%	0.12%
Cr_2O_3	0.02%	0.02%	0.02%	0.01%	0.02%	0.01%
CuO	0.01%	0.01%	0.01%	0.01%	0.01%	0.01%
ZnO	0.01%	0.01%	0.01%	0.01%	0.01%	0.01%
NiO	0.01%	0.01%	0.01%	0.01%	0.01%	0.01%

4.3.2 Chemical composition of REE

Table (4.2). show the concentration of rare earth element in (ppm) of Aqaba samples

	Full digestion	Step 1 (Soluble)	Step 2 (exchangeable)	Step 3 (Carbonate)	step 4 (Iron & Manganese)	step 5 (Organic)	Step 6 (Residual)
Yb	0.06	0.01	0.01	0.01	0.01	0.01	0.01
Y	1.57	0.09	0.10	0.34	0.16	0.24	0.18
Tm	0.06	0.01	0.01	0.01	0.01	0.01	0.01
Tb	0.06	0.01	0.01	0.01	0.01	0.01	0.01
Sm	0.15	0.01	0.01	0.06	0.01	0.03	0.03
Pr	0.15	0.01	0.01	0.06	0.01	0.03	0.03
Nd	0.63	0.01	0.03	0.32	0.02	0.09	0.11
Lu	0.06	0.01	0.01	0.01	0.01	0.01	0.01
La	0.93	0.04	0.11	0.31	0.05	0.15	0.18

Ho	0.07	0.01	0.01	0.01	0.01	0.01	0.02
Gd	0.16	0.01	0.01	0.08	0.01	0.03	0.02
Eu	0.07	0.01	0.01	0.02	0.01	0.01	0.01
Er	0.07	0.01	0.01	0.02	0.01	0.01	0.01
Dy	0.12	0.01	0.01	0.04	0.01	0.03	0.02
Ce	1.89	0.12	0.47	0.34	0.12	0.37	0.28

Table (4.3). show the concentration of REE in (ppm) of the Al-Eshedia samples

	Full digestion	Step 1 (solubl e)	Step 2 (exchangeabl e)	Step 3 (Carbonat e)	Step 4 (Iron & Manganes e)	step 5 (Organi c)	Step 6 (Residua l)
Yb	0.07	0.01	0.01	0.01	0.01	0.01	0.02
Y	1.84	0.07	0.11	0.30	0.24	0.19	0.51
Tm	0.06	0.01	0.01	0.01	0.01	0.01	0.01
Tb	0.06	0.01	0.01	0.01	0.01	0.01	0.01
Sm	0.06	0.01	0.01	0.01	0.01	0.01	0.01
Pr	0.09	0.01	0.01	0.01	0.01	0.01	0.04
Nd	0.23	0.01	0.01	0.05	0.01	0.02	0.13
Lu	0.06	0.01	0.01	0.01	0.01	0.01	0.01
La	1.06	0.05	0.07	0.08	0.03	0.06	0.22
Ho	0.06	0.01	0.01	0.01	0.01	0.01	0.01
Gd	0.10	0.01	0.01	0.02	0.01	0.01	0.04
Eu	0.06	0.01	0.01	0.01	0.01	0.01	0.01
Er	0.10	0.01	0.01	0.02	0.01	0.01	0.04
Dy	0.09	0.01	0.01	0.01	0.01	0.01	0.04
Ce	2.74	0.28	0.39	0.07	0.12	0.25	0.23

This tables present the amount of REE in ppm, and to know the percentage of each element in all fractions, we had the following tables:

Table (4.4). show the percentage of REE in each step for the Aqaba samples

	Full digestion	Step 1 (Soluble)	Step 2 (exchangeable)	Step 3 (Carbonate)	step 4 (Iron & Manganese)	step 5 (Organic)	Step 6 (Residual)
Yb	100%	16.7%	16.7%	16.7%	16.7%	16.7%	16.7%
Y	100%	5.7%	6.3%	21.6%	10.2%	15.3%	11.5%
Tm	100%	16.7%	16.7%	16.7%	16.7%	16.7%	16.7%
Tb	100%	16.7%	16.7%	16.7%	16.7%	16.7%	16.7%
Sm	100%	6.6%	6.6.%	40%	6.6%	20%	20%
Pr	100%	6.6%	6.6%	40%	6.6%	20%	20%
Nd	100%	1.6%	4.7%	50.8%	3.2%	14.3%	17.4%
Lu	100%	16.7%	16.7%	16.7%	16.7%	16.7%	16.7%
La	100%	4.3%	11.8%	33.4%	5.3%	16.1%	19.3%
Ho	100%	14.3%	14.3%	14.3%	14.3%	14.3%	28.6%
Gd	100%	6.25%	6.25%	50%	6.25%	18.7%	12.5%
Eu	100%	14.3%	14.3%	28.6%	14.3%	14.3%	14.3%
Er	100%	14.3%	14.3%	28.6%	14.3%	14.3%	14.3%
Dy	100%	8.3%	8.3%	33.3%	8.3%	25%	16.7%
Ce	100%	6.3%	24.8%	18%	6.3%	19.5%	14.8%

Table (4.5). show the percentage of REE in each step for Eshedia samples

	Full digestion	Step 1 (soluble)	Step 2 (exchangeable)	Step 3 (Carbonate)	step 4 (Iron & Manganese)	step 5 (Organic)	Step 6 (Residual)
Yb	100%	14.3%	14.3%	14.3%	14.3%	14.3%	28.6%
Y	100%	3.8%	6.0%	16.3%	13%	10.3%	27.7%
Tm	100%	16.7%	16.7%	16.7%	16.7%	16.7%	16.7%
Tb	100%	16.7%	16.7%	16.7%	16.7%	16.7%	16.7%
Sm	100%	16.7%	16.7%	16.7%	16.7%	16.7%	16.7%
Pr	100%	11.1%	11.1%	11.1%	11.1%	11.1%	44.4%

Nd	100%	4.3%	4.3%	21.7%	4.3%	8.7%	56.5%
Lu	100%	16.7%	16.7%	16.7%	16.7%	16.7%	16.7%
La	100%	4.7%	6.6%	7.5%	2.8%	5.6%	20.7%
Ho	100%	16.7%	16.7%	16.7%	16.7%	16.7%	16.7%
Gd	100%	10%	10%	20%	10%	10%	40%
Eu	100%	16.7%	16.7%	16.7%	16.7%	16.7%	16.7%
Er	100%	10%	10%	20%	10%	10%	40%
Dy	100%	11.1%	11.1%	11.1%	11.1%	11.1%	44.4%
Ce	100%	10.2%	14.2%	2.5%	4.4%	9.12%	8.4%

1. Cerium (Ce): cerium is iron – gray in color silvery when in a pure form , and about as soft and ductile as tin .It oxidize in air at room temperature to form CeO_2 The concentration of Ce in two samples AL Aqaba and Eshidiya investigated was 2,74 ppm , 1.89 ppm, respectively (Tables 4.2 – 4.3). As can be-seen by the data given in Table 4.2 and 4.3, all the two samples did not contain water-soluble Ce above the detection limit (2.8 ppm) or percent 10.2 % in Eshidya sample . The highest amount of Ce from all samples was clearly extracted in the "exchangeable "extraction steps (28.4%) from ALAqaba ,(14.2%) from Eshidyia and "water soluble " (6.3%) from AL Aqaba and (10.2) From Eshidiya samples , followed by the "organic " (19.5%) (9.12%) and "residual "(14.8%) ,(8.4%) Aqaba and Eshidyia samples respectively (Figure).

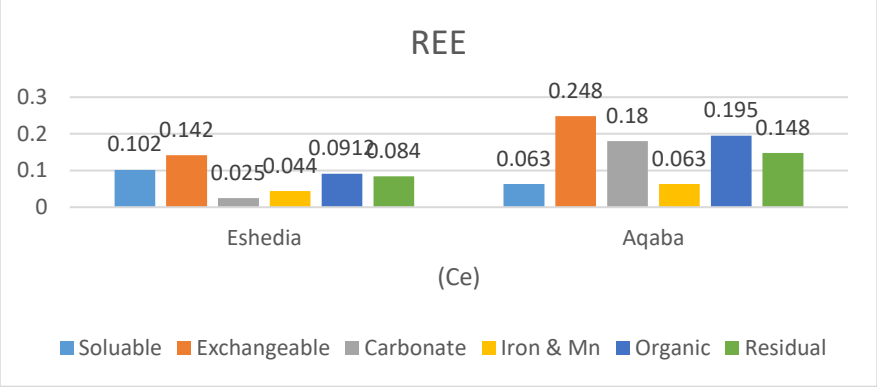


Figure (4.3). Show the distribution of Ce between fractions

The percentage of Ce extracted in the residue (using all five extraction steps) from the Al-Aqaba and Eshidiya samples was significantly (24%) where the Ce can be found in AL-Aqaba samples in a higher concentration than Eshidiya samples . On the other hand, significantly higher proportions of Ce were extracted in the "exchangeable" bound form sequential extraction step" from the Al-Aqaba and Eshidiyia samples (~24%).

2. Yttrium (Y): The concentration of Y in Aqaba and Eshidiya samples investigated was 1.57 ppm ,1.84 respectively (Table4.2 -4.3).As can be seen by the data given inTable4.2 and Table 4.3 , two samples did not contain water-soluble Y above the detection limit (3.05 ppm). The highest amounts

of Y from all samples were clearly extracted in the "residue" (11.5 %) and (27.7%) respectively as shown in Figure () and "carbonate " extraction steps (21.6%) ,(6.3%) Aqaba and Eshidiya samples , followed by the "organic" extraction step in Aqaba sample in percent (15.3%) and in (Fe&Mg Oxides) extraction step in Eshidiya sample (Figure).

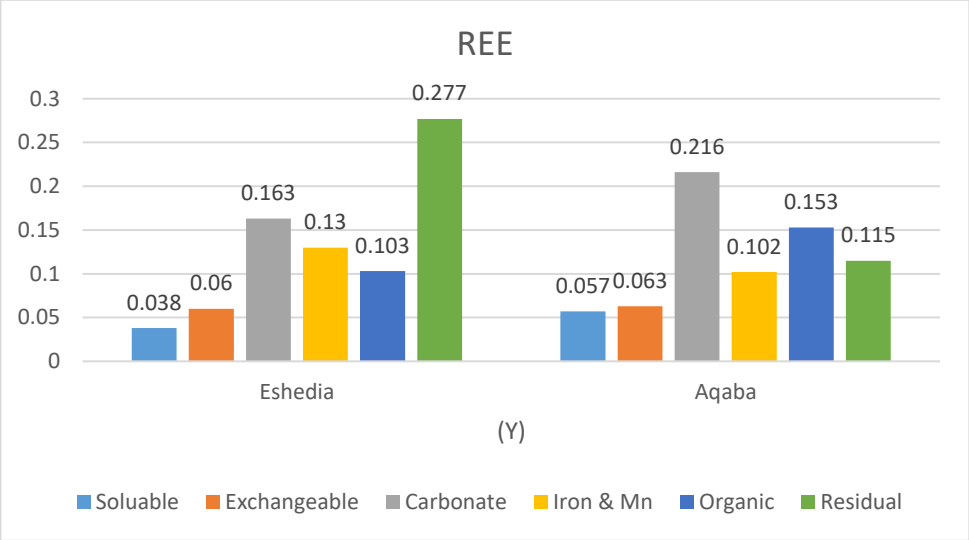


Figure (4.4). Show the distribution of Y between fractions

The percentage of Y extracted in the residue (using all extraction steps) from the Al-Aqaba and Al-Eshidiya samples was significantly lower (39%)

3. Lanthanum (La): The concentration of La in two samples investigated was .93 ppm and 1.06 ppm respectively (Tables 4.2 & 4.3). As can be seen by the data given in Tables , AL-Aqaba and Eshidiya samples did not contain water-soluble La above the detection limit (.05 ppm), which mean its contain very low levels of water-soluble La . The highest amounts of La from AL-Aqaba samples were clearly extracted in the "carbonate" (33.4%) and "residue " extraction steps (19.3%), followed by the "organic" (16.1%) and "exchangeable "(11.8%) where in Eshidiya samples its clearly extracted in the "residual" (20.7%) and "carbonate " (7.5%) followed by the "exchangeable " (6.6%) and "organic" (5.6 %) as showen in (Figure).

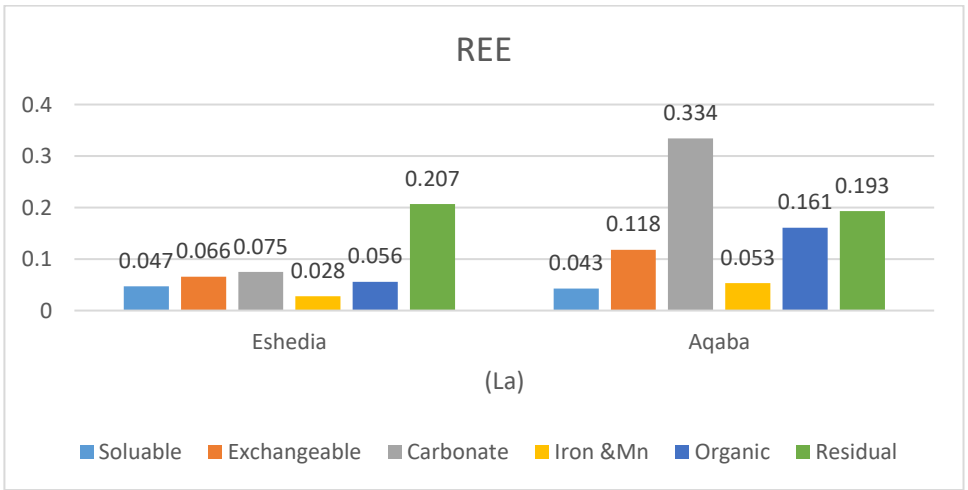


Figure (4.5). Show the distribution of La between fractions

The percentage of La extracted in the residue (using all extraction steps) from the Al-Aqaba (20%) was approximately similar to the amount extracted from the Eshidiya samples (19%). Moreover, significant portions of La were extracted in exchangeable bound form all samples (<19%)—a form that can easily be transferred into the environment.

4. Neodymium (Nd) : The concentration of Nd in the two samples investigated was .23 ppm and 6.3 ppm respectively (Table). As can be seen by the data given in Table , all samples did contain water-soluble Nd (>6%), indicating the Nd is tightly bound in the clay matrix .The highest amounts of Nd from AL-Aqaba samples were clearly extracted in the "carbonate" (50.8%) extraction steps, followed by the "residual" (17.4%) and "organic" (14.3%) extraction step (Figure)

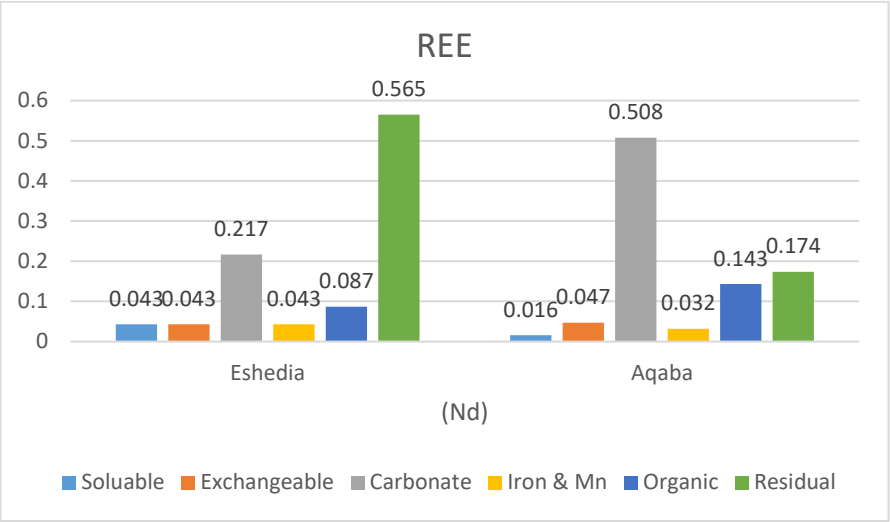


Figure (4.6). Show the distribution of Nd between fractions

where in Eshidiya samples the highest amount of Nd were clearly extracted in the "residual "(56.5%)followed by "carbonate " (21.7%) and "organic"(8.7%) . The percentage of Nd extracted in the residue (using all extraction steps) from the Eshidyia sample was relatively higher(56.5%) than the amount extracted from AL-Aqaba samples (17.4%). The percentage of Nd extracted in exchangeable form (using all extraction steps) from the Al-Aqaba samples was approximately(4.4) similar to the amount extracted from the Eshidiya samples (4.3)% . This form can easily be transferred into the environment.

5. Gadolinium (Gd) : The concentration of Gd in the two samples investigated was .1 ppm and .16 ppm respectively (Table). As can be seen by the data given in Table , all samples did contain water-soluble Gd (<6%) .The highest amounts of Gd from AL-Aqaba samples were clearly extracted in the "carbonate" (50%) extraction steps, followed by the "Organic" (18.7%) and "residual" (12.5%) extraction step (Figure)

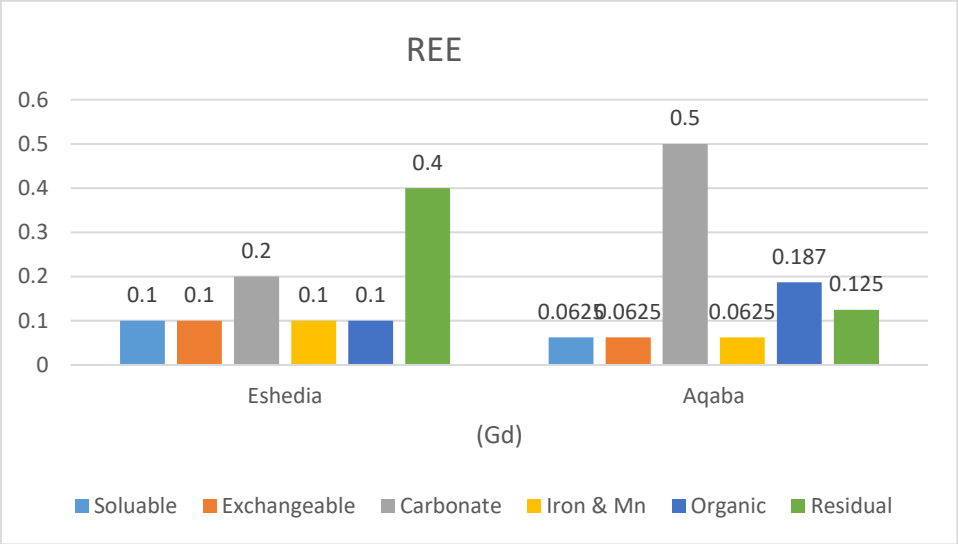


Figure (4.7). Show the distribution of Gd between fractions

where in Eshidiya samples the highest amount of Gd were clearly extracted in the "residual "(40%)followed by "carbonate " (20%) . The percentage of Gd extracted in the residue (using all extraction steps) from the Eshidyia sample was relatively higher(40%) than the amount extracted from AL-Aqaba samples (12.5%). The percentage of Gd extracted in exchangeable form (using all extraction steps) from the Al-Aqaba samples was approximately(6.5%) similar to the amount extracted from the Eshidiya samples (10%) . This form can easily be transferred into the environment.

6. Samarium (Sm): The concentration of Sm in the two samples investigated was .15 ppm and .06 ppm respectively (Table). As can be seen by the data given in Table , all samples did contain water-soluble Sm (<24%) .The highest amounts of Sm from AL-Aqaba samples were clearly extracted in the "carbonate" (40%) extraction steps, followed by the "Organic" (20%) and "residual" (20%) extraction step (Figure) where in Eshidiya samples had approximately the same amount of Sm were extracted in all extraction steps in (16.7%) . The percentage of Sm extracted in the residue (using all extraction steps) from the Eshidyia sample was relatively lower (16.7%) than the amount extracted from AL-Aqaba samples (20%). The percentage of Sm extracted in exchangeable form (using all extraction steps) from the Al-Aqaba samples was approximately(6.6%) lower than the amount extracted from the Eshidiya samples (16.7%) . This form can easily be transferred into the environment.

5. Conclusion

A modified six-step sequential extraction procedure was used to fractionate cerium and some rare earth elements (Y, Yb , Tm , Tb ,Sm , Pr , Nd , Lu , La , Ho , Gd , Eu , Er and Dy) in phosphate rock samples from various locations in Jordan. The method used enabled the different forms of these metals present in the samples investigated to be distinguished. The mean value of Cerium measured in the Al-Aqaba , and Eshidiya samples was 1.89 ppm and 2.47 ppm respectively.

The highest amounts of Y, Yb , Tm , Tb ,Sm , Pr , Nd , Lu , La , Ho , Gd , Eu , Er and Dy from all two samples were clearly extracted in the "residue" step. Ce was the onlyElement studied where the highest amount extracted was not found in the residue step—the highest amounts of Ce were found in the "exchangeable " step. The percentage of Ce and Y extracted(using all five

extraction steps)from the Al-Aqaba samples was relatively similar (90% and 71%, respectively) to the amount extracted from the two Eshidiya samples (81% and 77%, respectively). Considering that the exchangeable form is regarded as a sensitive indicator of mobility and bioavailability, this form can release its metal load by lowering the pH and is more mobile than the other forms. The apparent mobility of Ce, Tm, Tb , Yb , Lu, Eu , Er , Ho ,La , Dy , Sm, Pr , Nd, Y and Gd (using percent of exchangeable step) from the Al-Aqaba samples was as follows: Ce (24.8%) >Tm, Tb , Lu , Yb (16.7%)> Er, Eu, Ho (14.3%) > La (11.8%) > Dy (8.3%) > Sm, Pr (6.6%) >Y (6.3%) >Gd (6.25%) > Nd(4.7%) . The mobility of Tm, Tb, Sm, Lu, Ho, Eu, Yb,Ce , Pr , Dy , Er Gd , La , Y and Nd (using percentage) from Eshidiya samples followed the order: Tm , Tb, Sm , Lu , Ho , Eu (16.7%)>Yb (14.3%)> Ce (14.2%)>Pr , Dy (11.1%) > Er,Gd > (10%) > La (6.6%) >Y (6.0) > Nd (4.3 %)

References

1. HEAVY METAL ASSESSMENT OF PHOSPHOGYPSUM WASTE STOCKPILE MATERIAL FROM JORDAN1 “Al-Hwaiti, M.1, V. Carney, J. F. Ranville, and P. E. Ross”.
2. Selectivty Assessments of a Sequential Extraction Procedure for Potential Trace Metals’ Mobility and Bioavailability in Phosphate Rocks from Jordan Phosphate Mines “MOHAMMAD AL-HWAITI,1 JAMES TARDIO,2 HAILEY REYNOLDS,2 AND SURESH BHARGAVA2”.
3. https://www.sciencedirect.com/topics/engineering/phosphogypsum.
4. Bioavailability and mobility of trace metals in phosphogypsum from Aqaba and Eshidiya, Jordan.” Al-Hwaiti, M., Ross, P., Ranville, J., 2010. Chemie der Erde Geoch. 70, 283–291”.
5. https://geology.com/articles/rare-earth-elements/.
6. Selectivty Assessments of a Sequential Extraction Procedure for Potential Trace Metals’ Mobility and Bioavailability in Phosphate Rocks from Jordan Phosphate Mines
   MOHAMMAD AL-HWAITI,1 JAMES TARDIO,2 HAILEY REYNOLDS,2 AND SURESH BHARGAVA2

7.https://serc.carleton.edu/research_education/geochemsheets/techniques/SEM.html?fbclid=IwAR1Fa8ScrAos9fE111-UAh0C78yUmd42GZ0MUgbTV_pftE-awzWalq8r9TE

Theme 11: Chemical Engineering and the Dead Sea

Dead sea brine water chemical and physical stratification features influenced by the continuous drop in sea level

Tayel El-Hasan [1]*, Nizar Abu-Jaber [2], Amjad Al-Tarawneh [3], Khaled Abu Samhadaneh [3] Jamal Amera [4], Emad Talafhah [4], Alaa Omari [4], Hashem Al-Zubi [5].

[1] Department of Chemistry; Faculty of Science; Mutah University, 61710; Mutah - Jordan.
[2] Department of Civil & Environmental Engineering, German Jordanian University – Jordan
Prince Faisal Center; Mutah University, 61710, Mutah – Jordan.
[4] Arab Potash Company, Al-Safi - Jordan
[5] Geology Directorate, MEMR, Amman - Jordan
** Correspondent author: tayel@mutah.edu.jo ; Tel: +962-79-9915463*

Abstract: Four locations from the northern part of the Dead Sea (DS) were investigated to unravel the spatial and vertical changes for brine water physicochemical characteristics and stratification. 130 samples were collected at 5m depth interval, during October 2017. The thermocline was recognized separated the hot upper layer from the colder lower brine water. Its sharpness reflects the approach of overturning because weather becomes colder as summer is ending. Stratification of DS brine water body is obvious at deeper profiles than shallower ones. There are high salinity layers that correlated positively with high EC and density. Particularly; stratification was clear at the profile located opposite to Wadi El-Mujeib, where the upper layer has lower Na^+, K^+, Ca^{++} and Mg^{++} content due to floating of less dense fresh water flowing into DS above higher dense DS brine. This indicates the influence of freshwater mixing on DS brine. The surface brine water showed higher SO_4^{--}, Cl^- and Na^+ and Mg^{++} than lower brine water, which is rich in K^+. This might be due to the decrease in temperature downward and higher evaporation at surface water. Moreover, SO_4^{--} and Cl^- are increasing from middle DS towards shallow waters due to shore sediments incrimination. Salt budget trend of surface DS brine water from 2008 to 2017 shows continuous Na^+ decreasing trend (rate -0.11 g/kg/year). Meanwhile, there is an enrichment in Ca^{++}, Mg^{++}, K^+ and Cl^-. The ratio [(MgCl2+CaCl2)/KCl] were found to decrease from 15.32 to 14.09 from 2008 and 2017 respectively, with annual changing rate -0.14%.

Keywords: Dead sea; brine water; stratification; freshwater mixing; evaporation; salt budget

1. Introduction

The Dead Sea (DS) is a terminal lake which lies at the lowest point of the Jordan Valley Rift. It represents the latest iteration of water bodies that occupied since the Eocene (28 million years), when the rift was first initiated. The DS consists of two sub-basins, with the northern one comprising 76% of the total area, and having a maximum depth of 360 m. The southern subbasin comprises remaining area and back when the sea level was high level it was only l0 m deep. Today, the southern subbasin is above the natural water level, and it is artificially filled by pumping DS water from the northern basin and used as an evaporation pond for potash extraction (Charrach 2019). The subbasins are separated by the Lisan Peninsula, and the total length of the sea is 67 km, and the width ranges from 12 to 17 km, the total surface areas is about 1000 km^2. Due to drying of the southern basin, it is now only 610 km^2 (TAHAL 2011). DS is the lowest point on earth at -432.38 m below Sea level, (APC

2007), and the saltiest bodies of water on earth. Its salinity reaches 340 g/kg, compared with oceans 35 g/kg, (Al-Nawayseh 2003). Prior to the present DS, the Pleistocene lake at the site is known as

Lake Lisan, which was much more extensive and less saline than the Holocene DS, with a high level reaching 182 meters below sea level (Bowman 1971), compared with the current level of 430 meters below sea level (mbsl) and the historic level of 390 mbsl. Records of the real time monitoring station at the Jetty corner of the Arab Potash Company (APC), show that the rate of water decline is 1.11 m/year over a 9-year period (2008 -2017). The Holocene saw the replacement of Lake Lisan with the DS, which evolved with limnological and geochemical characteristics (Stein et al. 1997).

In more recent times, the DS has been rapidly shrinking as the Jordan River and other headwater sources have been diverted to other uses in the adjacent countries. This diversion caused hydrological imbalances, leading among other things to the aforementioned drop of the sea level as well as the 1979 overturn of its historic pycnocline (Steinhorn 1985). Prior to that, the pycnocline had dropped from a depth of 80 meters in 1975 to 180 meters in 1978. The loss of the pycnoline is attributed to the loss of the major freshwater input into the Dead Sea (i.e. the Jordan River), which dropped from about 1300 million cubic meters per year (MCM/a) to only 60 MCM/a (Al-Weshah 2000). Residual surface flow from all sources after human intervention is now estimated to be from 200 to 335 MCM/a (Greenbaum et al. 2006; Linsky et al. 2005).

When calculating the modern hydrological balance, it has been estimated that about 340-460 MCM/a of groundwater is leaking into the Dead Sea to compensate the difference between the and measured losses seen in the inflows and the observed losses seen in the drop in the water level (Salameh and El-Naser 1999; Oroud 2011). Deep aquifers adjacent to the Dead Sea are under artesian pressure (Abu-Jaber and Wafa, 1996), and the deep aquifer system on the Jordanian plateau actually has been shown to discharge into the Dead Sea (Abu-Jaber and El-Naser 2016). Akawai et al. (2008), had estimated the submarine groundwater discharge to reach up to 200 MCM/a. Thus, while the historical limnology of the Dead Sea has been disrupted, heterogeneity in the water density is to be expected due to the remaining input, both from surface and groundwater. Recently, (Munwes et al. 2020) developed a system based on measure the velocity and density of the ascending submarine groundwater of the spring along the Dead Sea shore.

Investigations into the heterogeneity of water density and chemistry can inform as to the location and volume of freshwater seeping into the DS. Additionally, it can also inform as to the nature of saltwater leakage chemistry, location and volume as well, which can give insight into the evolution of DS water, as will be discussed later. Thus far, use of remote sensing for exploring such heterogeneity can be useful at a larger scale (Oroud 2019), but is less helpful on smaller scales. Herein, we explore spatial and depth profiles of water characteristics at selected sites in the southern part of the northern basin of the DS. The investigation will include temperature, density, and salinity. Besides, the chemical analysis of major, minor and trace element; besides the mineral phases dominating each layer at different water column depth. This study aimed to determine the amount of stratification in water column, and the physical and chemical properties for each level. It also is intended to investigate the horizontal distribution of the physical and chemical properties in the eastern part of Dead Sea. Including the proposed site for Red Sea-Dead Sea conveyer input. Besides determining the elemental enrichment for each layer, and the salt budget trend. These results will be used to draw larger conclusions on the current heterogeneities in the water and their hydrological and geochemical implications.

1.1 Climate and Geology and study area settings

The study area is confined to the northern part of Ds (Fig. 1). The climate in the DS area is hot and dry in the summer, with mean temperatures of about 33 ºC. In winter, the temperature is pleasant, with an average temperature of 16.8 ºC. The rainfall according to the Arab Potash Company (APC) long term records from their Ghor Assafi weather station from 1976 – 2005 was 75 mm/year. The maximum temperature is 40.6 ºC in July, while the minimum temperature is 10.8 ºC in January. The average relative humidity ranges from 40.6% to 44.3% in summer and from 59% to 63.3% in winter season (Al-Nawayseh 2003). Water evaporation is relatively low because the water dissolved salts lower the vapor pressure over the sea surface (Oumeish 1996). It is usually to have less evaporation of saline water than fresh water, because dissolved salts lower free energy of water molecules (Salhotra et al. 1985). Based on the average annual temperature in the last decade which was 26 ºC, and the difference in activity coefficient ($\Delta\beta$) which is -0.11, and taken the long historical value of about 1500-1600 mm/year, then the most likely estimated value for present rate of evaporation is 1200-1250 mm/a.

The geology of the investigated area is controlled by the Jordan Rift Valley, which is a continuation of the East African Rift valley and Red Sea, which began during the Eocene-Oligocene (Powell 1988). The stratigraphy of the exposed rock units in the study area and its surrounding areas include both pre-and post-drift sediments and rocks (Al-Nawyseh 2003). The boundary fault to the east of the DS exposes an uplifted sequence of about 1400 m (starting at -400 m to about 1000 m asl). The sequence begins with the Lower Cambrian Um Ishrin sandstone, Lower Cretaceous Kurnub sandstone, then overlain by the Upper Cretaceous carbonaceous and Eocene rocks (Ajlun & Belqa groups). The Belqa group includes the Um Ghudran formation, Al-Hisa Phosphorite well as the Um Rejam Chert limestone (Mohammed 1988). Some of the later sequences are down faulted and present in the vicinity of the study area. Syn and post rift deposits include recent fluvial fan sediments related to the major drainage systems and the Lisan Marl of Pleistocene age at the shore. Volcanic alkali basaltic flows of Pleistocene age that is found at the upper Wadi Hidan (Mohammed 1988) as well as the area south of Wadi El-Mujib which has some small basaltic flows as well. Tar and oil impregnated sand are present within the Um Ishrin sandstone and the Lisan formation. Moreover, sulfur is found as thin seams within the upper Cretaceous Belqa group, particularly within Um Ghudran formation (Mohammed 1988). El-Hasan et al. (2008) indicated that the chemical and mineralogical characteristics dry deposition on the Eastern highlands facing the Dead Sea are highly influenced by the Dead Sea.

1.2 Geochemical evolution of the DS

The chemistry of the DS has long been a source of interest. It is notable that the second ever chemical analysis of water was published in 1778, and was subsequently followed up by a number of newer analyses in the early 19th Century (Nissenbaum 1970). One of the earliest observations made following these analyses was the differences between DS water and both regular sea water and the water of the Jordan River.

Bentor (1961) first explored this issue in depth. A number of observations require explanation, such as the notably low Na:K, Na:Ca and Na:Mg ratios in the cation concentrations. In addition, the very low CO_3:Cl and SO_4:Cl ratios. Also notable is the high Br: Cl ratio. Mass balance calculations of solutes entering with the Jordan River water could not explain these chemical characteristics, and the ratios were not consistent with normal sea water either. Bentor (1961) concluded that saline springs present in the southern DS were the only plausible explanation for these discrepancies. Abu-

Jaber (1998) conducted thermodynamic modeling of various assumed water mixes from waters in the area along with evaporation to arrive at a similar conclusion.

The source and age of the salts is disputable. Katz and Starinsky (2009) suggest that the waters started out as sea water going through multiple iterations of geochemical evolution. In contrast, (Hardie 1990) suggests that the source of similar calcium chloride rich waters is of deep crustal sources. Katz at al. (1977) suggest that the DS water is residual water from the Pleistocene Lisan Lake, whereas others believe that the DS is a Holocene lake that filled in a desiccated post-

Pleistocene lake (Bentor 1961; Abu-Jaber 1998; Charrach 2019). Evidence of leakage of deep subsurface brines could help to resolve some of these questions

.

2. Materials and methods

2.1 Sampling and field work

Brine water samples were collected from four locations as shown in (Fig. 2) and (Table 1). The sampling took place at 5m interval depths using special collecting device starting from top to bottom. The collected samples were analyzed *in situ* for pH and temperature, the rest were preserved for other analyses. Temperature profile from the surface down to the maximum depth was performed using the CTD and temperature logger (CTD 19 plusV2). Besides, that a horizontal traverse line connecting D1 and D4 were sampled, the length is approximately 18 km, from 1m depth along the traverse, total of 27 samples were collected (Table 1) and (Fig. 2). The sampling location (D2) is a shallow profile, it was chosen because it is most likely to be the proposed location for the Red Sea water feeding point. Therefore, it will serve as a reference to the current condition prior of introducing the Red Sea – Dead Sea Conveyer. The brine water samples were obtained vertically from different brine depths using appropriate device such as Niskin Bottles. All oceanographic equipment necessary for the proposed survey in the DS is fitted for the Boston Whaler (Al-Baheth Boat) (6 m * 2 m). The Boston Whaler was equipped with a winch, an electrical generator, a Global Positioning System (GPS), a depth finder of the Echo scan series. The wire that is connected with the winch can be casted up to 300 m. These four locations had been chosen in order to have a comprehensive view about the Dead Sea brine water body. The sampling has been executed during the 1st week of October 2017, thus marking the end of summer. Each sample brought 5L each time.

Table 1. The coordination and depth of the four sampling profile and surface samples

Location	East	North	Depth (m)	No. samples
D1	35.456674	31.336563	**10**	**3**
D2	35.522891	31.352345	**25**	**6**
D3	35.541075	31.480365	**220**	**45**
D4	35.492155	31.501584	**250**	**51**
Surface			**1**	**27**

2.2 Analytical procedures

Temperature, salinity and density profiles were measured using a Conductivity, Temperature and Depth meter CTD (SBE 19pluseV2 SEACAT PROFILER) that can reach up to 1000 m. Profile of DS brine water temperature and pressure were measured *in situ* using a Conductivity, Temperature and Depth meter ((CTD 19plusV2) with initial accuracy and resolution of ± 0.005 and 0.0001 for temperature; and 0.1%, 0.002% for pressure, respectively. The CTD was setup using a Sea Term Software. The data was retrieved using SBE Data Processing software and converted to ASCII format. The analysis and drawing of the results was performed using Excel and Statview software. Brine water samples were collected using Niskin Bottles (5 Liter) and refilled in special bottles to be conserved for laboratories analyses.

2.3 Salinity and Electrical conductivity measurement procedures

The salinity was determined by titration based on the principle that silver ions and chloride ions form an insoluble white precipitate AgCl. Silver ions and chromate ions form a somewhat more soluble red-orange precipitate $AgCrO_4$. Thus, when a solution containing silver ions was continuously added to a solution chloride is removed from solution and then silver chromate will begin to precipitate. Reagents needed for this titration is prepared freshly and these reagents are:

1. Silver Nitrate ($AgNO_3$).
2. Potassium Chromate (K_2CrO_4).
3. Copenhagen standard water or a working laboratory standard, which can be prepared by taking a known weight of NaCl and the salinity of this reagent, can be measured as follow:

Standard salinity = 1.069 × exact weight in grams of NaCl dissolved.

1. Standardizing the $AgNO_3$ solution was done by titration against the standard seawater. First, fill the burette with $AgNO_3$ solution. Then take 10ml of the seawater standard and place it in an Erlenmeyer flask, add 10 drops of K_2CrO_4 to the flask, and then titrate it with $AgNO_3$ until the endpoint (Red-Orange color).
2. Titrate 10ml of unknown sample in the same manner as in step 1. The calculation:

Unknown salinity (psu) = (ml required to titrate unknown sample / ml required to titrate standard seawater) × Standard salinity 35.01

All samples for the DS brine water were diluted 10 times.

Other portable devices were used for salinity and conductivity for double check after ten times dilution for all samples. WTW Cond 3210 was used for salinity with Range of 0-70 ppt, Resolution of 0.1 ppt and accuracy of ± 0.1-5. OAKTON Con6 device was used for Electrical Conductivity with rang of 0-200 mS, Resolution of 0.1mS and accuracy ± 1%.

2.4 Density

Brine water density was calculated based on the data of temperature, salinity and pressure using the equation of state of seawater [UNESCO 1991].

2.5 TDS and TSS

The value of total dissolved solids (TDS) and the total suspended solids (TSS) was measured according to the standard method 2540C (Standard Method for the Examination of water and wastewater, 22nd edition, 2012). TDS for each sample was determined as the mass of dissolved solid normalized to the volume of water filtered. TSS for each sample was determined as the mass of suspended solid normalized to the volume of water filtered.

2.6 Cations and Hardness

Na^+ and K^+ were measured following the standard methods 3500-Na B and 3500-K B, respectively (Standard Method for the Examination of water and wastewater, 22nd edition, 2012). Using the flame photometry method (Flame photometry ATS 200MKI, Advanced Technical Service - ATS, USA) and following the operating instructions of manufacturer recommendations.

Mg^{++} and Ca^{++} contents in brine water samples were analyzed using ICP-OES machine model (iCAP 6300 radial, Thermo Scientific Corporation), at the Jordan Atomic Energy Commission (JAEC) labs.1150 W plasma power; with 15L/min plasma gas flow rate; and Maximum integration time of Low wavelength range15 seconds. Custom ICP standards (Plasma Emission Standard) traceable to National Institute of Standards and Technology Reference Materials from AccuStandard®, USA. The Hardness were calculated based on the following equation mentioned in [http://keisan.casio.com/exec/system/1350974216]

$$\text{Water hardness (mg/L)} = \text{Ca(mg/L)}\times 2.497 \; + \; \text{Mg(mg/L)}\times 4.118$$

The water hardness is using the American degree equivalent to mg/L.

2.7 Anions

The water samples were analyzed for Br^-, Cl^- and SO_4^{-2} following the standard method 4110B (Standard Method for the Examination of water and wastewater, 22ND edition, 2012). Using an Ion Chromatography Analyzer (IC) (761 compact IC, Metrohm AG, Ionenstrasse, Herisau, Switzerland). Br^- measurement was not available for most of the samples, because in IC analysis the higher Cl^- concentrations caused overlapping with Br^- peak, thus it is being not recognized.

2.8 pH, and Dissolved oxygen (DO)

The pH and DO were measured according to the standard methods; 4500-H^+ B, 4500-O A, and 2510B, respectively [Standard Method for the Examination of water and wastewater, 22nd edition, 2012]. Using the portable electrode meters (pH meter WTW 315i, O_2 meter INO LAB OXi Level 2).

3. Results and Discussion

3.1 Physical parameters

The temperature of lower and upper brine water layers ranges from 24.6 – 32.9 C°. There are a definite two layers regarding the temperature; upper warm layer and lower cold layer. The time of sampling was during the 1st week of October 2017 that mark the end of summer period. Therefore, it was reflected in the hot upper layer to the depth up to 35 m, then a very sharp thermocline was developed from depth 25m to 35m, where the above layer about 25 m thick temperature is above 31C° and below thermocline dropped suddenly to less than 25 C°; as shown in (Fig. 3). The effect of season marked the stratification that will last until the end of November when surface water-cools and overturn in water column happen. The sharpness of the thermocline indicates that overturn would take place soon.

The density ranged from 1.212 to 1.249 g/cm^3 there are somewhat general trend of increasing density toward the bottom and as salinity increases. The density variation became clearer in deeper profiles (D3 & D4), where upper layer marked lower density values and the deep layer showed higher density values increasing toward the bottom. At the location D3 there is an obvious two density anomalies (at 90-125m; 180-220 m) separated with low-density layer. D4 showed similar trend but with slightly lower values (Fig. 3).

The salinity of DS brine water samples rages from 341-385 PSU with average 360 PSU. Previous analyses (2008) found it 339.3 PSU [Khlaifat et al. 2010]; and in (2015) 350 PSU [2015 MSS unpublished report]. While in this study, it shows continuous increase up to 360 PSU. This might be attributed to the continuous drop in DS level and DS area shrinkage that increases its salinity in rapid rate. At profile D3, there are clear 2-layers of high salinity with average 372 and 370 PSU respectively downward as shown in (Fig. 3). These two layers correlated well with previously mentioned density pattern of profile D3.

The pH has shown stratification feature as the upper 10 m have pH=6.13, while it increases to pH=6.18 downward, and continued increasing up to 6.22 at bottom brine water (Fig. 3). The increase in pH marked an increase in alkaline elements; particularly (Mg^{++} and Ca^{+}) at D4 profile content toward the bottom brine water EC ranges 468.6 mS to 521.6 mS with an average 490.6 mS. Generally, it increases downward. The EC pattern in the four profiles shown almost the similar pattern of salinity (Fig. 3), because EC is reflecting the salt content in the measured samples. The patterns of EC, density, salinity and TDS showing the sharp drop at 130-135 m in profile D3. This might be due to intrusion of thin layer of fresh water into the DS from the coastal aquifers. This phenomenon is well known and was calculated to reach 1100 m^3 /year (Salamah and El-Naser, 2000). Usually the porosity of coastal aquifers is about 2.94% and therefore, freshwater may inter DS from its sides or from below. This flushing of groundwater into DS is due to the continuous drop of the level of DS itself.

It is obvious that TDS at shallower brine water is higher than at deeper brine water (Fig. 3). Meanwhile, TSS has nearly opposite pattern. This means that samples with higher TDS have low TSS and vice versa. It can be explained as a function of solubility and it seems that temperature have role in increasing the solubility of upper brine water layer, thus raises the TDS content.

3.2 Chemical parameters

3.2.1 Cations

The average Na^{+} concentration for each sampling location are D1=1.83wt%; D2=1.84wt%; D3=2.27wt% and D4= 2.36wt%, and the overall average = 2.08wt%. In deeper profile, Na^{+} is higher than shallower profiles, as example at D3 the Na^{+} average 2.27wt% and it increasing downward and have two peaks fit well with density and salinity patterns (Fig. 4). Na^{++} showed clear stratification features as at profile D3, there are a sharp increase in Na^{+} concentration after depth 70 m, which fit well with K^{+} pattern too. Besides, at profile D4 the average of Na^{+} is 2.36wt% and it shows steady decreasing trend; and it has 2-rich Na^{+} layers at depth 35m Na^{+}=2.58wt %, and at 140m Na^{+}= 2.65 wt %.

The average K^{+} concentrations for each sampling location are D1=0.69 wt%; D2=0.68 wt%; D3=0.78 wt% and D4=0.80 wt%, and the overall average = 0.78 wt%. K^{+} pattern with depth is almost similar to that of Na^{+} as they are increasing toward the bottom brine water. Moreover, there is no sharp increase in K^{+} thus showed less stratification features comparing with Na^{+}. At deep profile D3 it is obviously more rich in K^{+}; this K^{+} anomaly exist from depths165-190 m with maximum value of K^{+}=0.9wt%, after that it deceases downward. In addition, there is a sharp increase after depth 70m similar to Na^{+}. At the D4 profile K-rich layers exist at depths 30m with K^{+}=0.87 wt% and at 140m, with K^{+}= 0.91wt%, there is high fluctuation with slightly decreasing trend downward (Fig. 4).

The average Ca^{++} concentrations for each sampling location are D1=1.55wt%; D2=1.54wt%; D3=1.75 wt% and D4= 1.81 wt%, and the overall average = 1.76 wt%. As shown in (Fig. 4); only D2 profile showed lower Ca^{++} concentrations in the upper water layer, while D1 at intake point shows relatively elevated concentrations. For deeper profiles (e.g. D3 and D4) has similar fluctuating trend

downward and they are sometimes at depth less than 150m shows opposite patterns, as D4 shows two successive peaks and D3 shows two successive low concentration layers. Those peaks and lows are not correlated with salinity or density patterns of the D3 and D4 profiles.

The average Mg^{++} concentrations for each sampling location are D1=3.45 wt%; D2=3.36 wt%; D3=3.85 wt% and D4= 3.93 wt%, and the overall average = 3.84 wt%. On the contrary of Ca^{++}pattern, D2 upper brine water layer has the highest Mg^{++} concentrations (Fig. 4). Other profiles are slightly decreasing with fluctuating manner. At depths, less than 155 m there are two peaks for both D3 and D4 profiles, but they are not at the same depths. These peaks are not coinciding with Ca^{++} peaks mentioned previously and shown in (Fig. 4). accordingly, the higher $Ca^{++}$and Mg^{++} concentrations was reflected on the unusual higher hardness values as shown in (Fig. 4).

3.2.2 Anions

The average Cl^- concentrations for each sampling location are D1=21.06 wt%; D2=20.86wt%; D3=21.41wt% and D4= 22.63wt%, and the overall average = 21.49wt%. These values are comparable to recent published report (TAHAL 2011). Chloride shows relatively low concentration in upper brine water layer at all studied profiles. And it is increasing toward the bottom. Deeper profiles D3 & D4 have much high Cl^- especially at bottom brine water layers (Fig. 4).

The average SO_4^{--} concentrations for each sampling location are D1=184 ppm; D2=166 ppm; D3=337 ppm and D4= 263 ppm, and the overall average = 230 ppm. Sulfate shows some stratification features as at D3 is the highest concentration at the upper brine water than bottom water; it has three SO_4^{--}-rich layers at upper, middle and lower water profile (Fig. 4). At the other deeper profile D4 it shows one SO_4-rich layer from depth 45-105m (average 298 ppm) just after SO_4^{--} depleted layer above with an average = 126 ppm, downward it continues steady fluctuation toward the bottom.

3.3 Surface brine water characteristics

In order to understand the variation in DS brine water, it is important to recognize the orientation of surface samples; it starts from the middle of DS (i.e. D4) towards the shallow shores (i.e. D1), number of samples are 27 with 700 m spatial interval. The main feature is the enrichment of SO_4^{--} concentrations, which reached up to 1100 ppm, and it showed a clear increasing trend from deep DS towards the shallow shores (Fig. 5). This was accompanied with increasing in Cl^- and decreasing in TDS and TSS as shown in (Fig. 5). The other parameters such as pH, T, EC, salinity and density remain constant all over the horizontal traverse line (D1 to D4) as shown in (Fig. 5).

By comparing surface brine water samples with the average deep brine water of the profiles D3 & D4 (number of samples is 96), the values are summarized in (Table 2). Beside its higher temperature the surface brine water has higher TDS, Na, Ca, Cl and SO_4 content and higher K to lesser extent. Meanwhile, Mg is increasing in the deep brine water. This agreed with the higher TDS values of surface brine water. The average salinity of surface brine water is 360 PSU; which is almost same salinity as deep brine water. Also, density and EC showed no big differences as shown in (Fig. 6).

3.4 Comparison with last surveys.

As reported in (Khalifat et al. 2010) the DS level was 422 m under sea level, and now as recorded by the real-time monitoring station located at the Jetty corner (DS brine intake point) is 432 under sea level. This means 10m drop in 9 years period given a rate of drop about 1.11 m/year. This dramatic drop cause loss of large quantities of water, and DS area shrinkage consequently causing

allot of changes in DS brine water physical and chemistry parameters. This was clear from the average salinity values, which was 342 PSU on 2008, meanwhile it is now 362 PSU and density becomes 1.23 g/cm^3.

Table 2. Table showing the average values of physical and chemical parameters for surface and deep brine water.

Parameters	Surface	Deep
T (ºC)	32.31	25.6
pH	6.14	6.195
EC (mS)	491.6	491
Density (g/cm$^{3)}$	1.23	1.231
Salinity (PSU)	360.1	359.55
TDS (g/l)	481.5	394.5
TSS (g/l)	11.76	16.92
Mg (wt%)	4.0	4.185
Ca (wt%)	1.87	1.52
Na (wt%)	2.38	2.315
K (wt%)	0.81	0.79
Cl (wt%)	225.5	220.2
SO_4 (wt%)	785	284.5

3.5 Stratification features within DS brine water body.

Temperature is decreasing downward with a sharp thermocline indicate the presence of thin stratification in DS brine. Upper hot thin layer with average temperature around 32 C°; the thickness this layer increases towards deeper brine water body at (e.g. D3 & D4). In addition, lower thick layer with average temperature around 24C° (Fig. 3). The stratified feature was obvious at D3 profile were good correlation between density and salinity, were there are distinct 2-layers of high density separated by low-density layer. This pattern was fitted with similar patterns of salinity, which confirms that higher density was due to sudden increase in salinity components. Moreover, this was evidenced by similar patterns of EC, TDS and to less extent Mg, Na and SO_4 too. The stratification was very clear in D3 profile, were salinity, density EC and TDS showed the clear variations as shown in (Fig. 3). There are your distinct layers:

1. Depleted layer from depths 35-45 low salinity, density EC and TDS.
2. Enriched layer from depth 95-125m high values of salinity, density EC and TDS.
3. Depleted layer from depths 130-135 m; low salinity, density EC and TDS values
4. Enriched layer from depths 185-220 m; high salinity, density EC and TDS.

Regarding the chemistry: depths from 0-65 m there is depletion in Na, K Mg, Ca and Hardness (Fig. 4). Then after depth 65 m, it increasing gradually toward the bottom. It fit to some extent to the layer of depleted EC, density, TDS and salinity as shown in (Fig. 3). At the deeper profile D4 there is no stratification but rather steady fluctuation with relative 2-high peaks at depths 30-35 m and at 190m for K, Na, Ca and Mg. Cl show such stratification as Cl has lower concentrations in the upper and increased steadily downward.

SO_4 show lower concentrations in the upper 0-40 m, then it sharply increased 45 – 100m; it deceased toward the bottom, there is some similarity with TDS profile. At D3 profile, SO_4 behavior

is opposite to that at D4 where it shows lower fluctuation from top to bottom. From these profiles we can conclude that the stratification in physical and chemical parameters exist clearly at deep profiles affected by fresh water mixing (i.e. D3). When we go deep inside the DS then stratification became

less clear (i.e. D4). The explanation for lower Na, K, Ca and Mg in the upper brine water layer at D3 is due to fresh water flow inside DS from Wadi El-Mujeib, then it floats in upper layer due to its lower density, thus causing the dilution of these elements in the upper layer, therefore it looks as stratified layer.

3.6 Effect terrestrial factors (i.e. mixing with fresh water):

The effect of fresh water mixing with brine water was clearest at profile D3. At this profile there is a very strange pattern and it has the highest of SO_4 among all profiles. This particular location, which is in front of the mouth of Wadi El-Mujieb that is the largest fresh water attributed to the DS. The upper layer of this profile has low concentrations of cations, which can be due to mixing with fresh water inflowing from the eastern side that might cause dilution of concentrations of such cations and anions. The introduction of fresh water would add additional terrestrial origin elements into the DS. The effect of surface fresh water entering the DS is restricted to the upper layer as their low densities cause them to float above the dense lower brine water. The lower brine water shows higher concentration toward the bottom which is correlated with high density and salinity. Moreover, the surface brine water showed a trending of SO_4 and Cl towards the shallow shores, which might indicate the influence of terrestrial components in DS surface brine water.

3.7 Salt budget

The calculated major salts compared with their values based on the average salt contents from 1978- 2008 (Khalifat et al. 2010) are shown in. (Table 3). This study represents the brine water chemistry after 9 years, and it shows that all cations and anions in brine water are increasing except Na is decreasing. The order of concentration is $Cl^{-}>Mg^{++}>Na^{+}>Ca^{++}>K^{+}$ which is the same order mentioned in (Khalifat et al. 2010). There is a noticeable increase in Mg^{++}, Ca^{++}, K^{+} and Cl^{-} concentrations during the last 9 years, while Na is decreasing with rate -0.11 g/kg per year. The largest increasing rate was in $MgCl_2$ about 0.14 g/kg/year. Accordingly, the [$(Mg+Ca)Cl_2$ / KCl] ratio was decreasing from 15.33 to 14.09 between the years 2008, and 2017 respectively. Beside the noticeable increase in $MgCl_2$ and $CaCl_2$, there is also an increase in KCl in surface brine water (Table 3).

Table 3. Concentrations Mg^{++}, Na^{+}, Ca^{++}, K^{+} and Cl^{-} in the surface brine water and their salts compared with average values for brine water from (1987-2008) Data.

Cations and Anions	Average (1987-2008) (g/kg) (Khalifat 2010)	This study; 2017 (g/kg)	Salts	Average (1987-2008) (g/kg) (Khalifat 2010)	This study; 2017 g/kg	Salts Rate change g/kg/year
Mg^{++}	37.67	40.0	$MgCl_2$	14.77	16.0	0.14
Na^{+}	27.62	23.78	NaCl	7.02	6.05	-0.11
Ca^{++}	14.22	18.7	$CaCl_2$	3.94	5.17	1.04
K^{+}	6.39	8.1	KCl	1.22	1.54	0.04
Cl^{-}	183.6	225.5	$(Mg+Ca)Cl_2/K$	15.33	14.09	-0.14

4. Conclusions

Dead Sea brine water was investigated for stratification. Two shallow and two deep locations were studied during October 2017. Thermocline was recognized as sharp separated the hot upper layer from the colder lower brine water. This sharpness reflects the approach of overturning because weather become colder in November. Slight pH increasing towards bottom water was observed. Stratification of DS brine water body is clearer at deeper profiles than shallow ones. As there are clear high salinity layers or intrusions that is correlated positively with high EC and density too. Clear stratification was clear at the profile in front of Wadi El-Mujeib (i.e. D3), where a layer of low Na, K, Ca and Mg content due to the floating of the less dense fresh water inflow into DS above the highly dense DS brine water causing dilution of this layer. The surface brine water showed high concentrations of Na, Ca, SO_4, Cl and K to less extent than lower brine water which is rich in and Mg. This might be due to the decrease in temperature downward and the higher evaporation effect at surface water. There is an increasing trend of SO_4 and Cl from deep brine water towards the shallow shores. The effect fresh water mixing was clear at profile D3, were higher averages of Mg, Na, Ca and SO_4 were recorded. Salt budget trend of surface brine water of DS from 2008 until now (2017) shows continuous Na decreasing trend and enrichment of Ca, Mg and Cl. The ratio [(MgCl2+CaCl2)/KCl] were found to decrease from 15.32 to 14.09 from 2008 and 2017 respectively, with changing rate -0.14 per year

Funding Information: This work was executed through generous scientific support from APC (contract No. 201702286).

Acknowledgment:

The authors are deeply thankful to Arab Potash Company and Mutah University administration for their encouragement and support.

References

1. Abdel-Fattah A N (1997) Mineralogical, geochemical, healing Characterization and origin of the Dead Sea Clay Deposits, M. Sc. Thesis, University of Jordan. P 140.
2. Abdel-Fattah, AN and Schultz-Makuch D (2004) Dead Sea black mud: Medical geochemistry of a traditional therapeutic agent. AGU, Abstract book.

3. Abdel-Samie S G, ES-Shahat MF, Al-Nawayseh K M (2004) Mineralization Sources of Surface and Subsurface Water at the Southeastern Edges of Dead Sea Basin in Jordan. Isotope and Rad. Res. 36: 167-186
4. Abed A (1985) Geology of the Dead Sea, Dar Al Argam, Amman, Jordan. PP 232
5. Abu-Jaber N, (1998) A new look at the chemical and hydrological evolution of the Dead Sea. Geochimica et Cosmochimica Acta, 62(9):1471–1479
6. Abu-Jaber N, El-Naser H (2016) Geology and hydrochemistry of the deep sandstone aquifers of Jordan. Environmental Earth Sciences, 75(10):875:1-13, DOI 10.1007/s12665-016-5680-8
7. Abu-Jaber N, Wafa NA (1996) Hydrochemistry of aquifers in the southern Dead Sea area, southern Jordan. Environmental Geology, 28(4):213-222
8. Akawwi E, Al-Zouabi A, Kakish M, Koehn F, Sauter M (2008) Using thermal infrared imagery (tir) for illustrating the submarine groundwater discharge into the eastern shoreline of the Dead Sea-Jordan. American Journal Environmental Sciences, 4:693–700
9. Al-Nawayseh K 2003 Evaluation of Surface and Groundwater Sources in Southern Ghore-Jordan, Ph.D. Thesis, Ain Shams University.
10. Al-Weshah RA (2000) The water balance of the Dead Sea: an integrated approach. Hydrological processes, 14(1):145-154
11. APC. (2007) Site measurements (end of April).
12. Bentor YK (1961) Some geochemical aspects of the Dead Sea and the question of its age. Geochimica et Cosmochimica Acta, 25(4):239-260
13. Bowman D (1971) Geomorphology of the shore terraces of the late Pleistocene Lisan lake (Israel). Palaeogeography, Palaeoclimatology, Palaeoecology, 9(3):183-209
14. Charrach J (2019) Investigations into the Holocene geology of the Dead Sea basin. Carbonates and Evaporates, 34(4):1415-1442
15. El-Hasan T, Abu-Jaber, N (2019) Geochemistry, mineralogy and origin of the shallow seawater surface sediments from the Northern part of the Dead Sea, Jordan. Carbonates and Evaporates. 34:975-985
16. El-Hasan T, Momani K, Al-Nawayseh ., Al-Nawayseh K (2008) The influence of Dead Sea on the chemistry and mineralogy characteristics of the dry deposition fallen over the eastern highlands, central Jordan. Environmental Geology 54(1):103-110
17. Epstein JA, Feis, EM, Zmora J, Marcus Y (1981) Extraction of Lithhium from the Dead Sea. Hydrometallurgy 6:269-275
18. Es-Shahat MF, Al-Nawayseh KM, Jiries AG, Al-Nasir FM (2003) Pesticides and Heavy Metal Distribution in Southern Dead Sea Basin. Bull, Environ. Contam. Toxicology. 71: 1230-1238
19. Gervreili L, Lanski N, Yari-Gazit N, Oren A (2002) the impact of the proposed "peace conduit" on the Dead Sea. Evaluation of current knowledge on Dead Sea – seawater mixing. The geological Survey of Israel, Report GSI/23/2002. pp. 24
20. Greenbaum N, Ben-Zvi A, Haviv I, Enzel Y (2006) The hydrology and paleohydrology of the Dead Sea tributaries. Special Papers-Geological Society Of Americ*a*, *401*, p.63
21. Hardie LA, (1990) The roles of rifting and hydrothermal $CaCl_2$ brines in the origin of potash evaporites; an hypothesis. American Journal of Science, 290(1):43-106
22. Katz A, Starinsky A (2009) Geochemical history of the Dead Sea. Aquatic Geochemistry, 15(1-2):159-194
23. Katz A, Kolodny Y, Nissenbaum A (1977) The geochemical evolution of the Pleistocene Lake Lisan-Dead sea system. Geochimica et Cosmochimica Acta, 41(11):1609-1626
24. Khlaifat A, Hogan M, Pillips G, Nawayseh K, Amira J, Talafeha E, (2009) Long term monitoring of the Dead Sea level and brine physico-chemical parameters from 1987 – 2008. Journal of Marine Systems. 81:207-212

25. Lensky N G, Dvorkin Y, Lyakhovsky V, Gertman I, Gavrieli I, (2005) Water, salt, and energy balances of the Dead Sea. Water Resources Research 41(12):1-13
26. Mohammed BK (1988) Ar Rabba geological survey report, sheet 3152 IV. NRA,
27. Momani K, El-Hasan T, Auaydeh S, Al-Nawayseh K (2009) Jordan. Heavy Metal Distribution and Speciation in the Dead Sea Black Mud, Jordan. Journal of Earth and Environmental Sciences (JJEES) 2(1):50-59.
28. Munwes Y, Geyer S, Katoshevski D, Ionescu D, Licha L, Lot t,C, Laronne J, Sieber C (2019) Discharge estimation of submarine springs in the Dead Sea based on velocity or density measurements in proximity to the water surface. Hydrological Processes. First published:11 October 2019; https://doi.org/10.1002/hyp.13598.
29. Neev A, Emery KO (1967) The Dead Sea Depositional Processes and Environments of Evaporates. Geological Survey of Israel Bulletin. 41:1-6
30. Nissebaum A, (1969) Studies in the geochemistry of the Jordan River-Dead Sea system, Unpublished Ph.D. Thesis (In English), UCLA.
31. Nissenbaum A, (1970) Chemical analyses of Dead Sea and Jordan River water, 1778–1830. Israel Journal of Chemistry, 8(3):281-287
32. Oroud IM (2011) Evaporation estimates from the Dead Sea and their implications on its water balance. Theoretical and applied climatology, 106(3-4):523-530
33. Oroud IM (2019) The annual surface temperature patterns across the Dead Sea as retrieved from thermal images. Arabian Journal of Geosciences, 12(22):695-707
34. Oumeish Y (1996) Climatotherapy at the Dead Sea in Jordan. Clinics in Dermatology. 14:659- 664
35. Powell, J.H. (1988): The geology of Karak area, Map sheet No. 3152 II. Nat. Res. Auth. Unpublished Report. Bull. Amman. No. 8, 172 pp
36. Salameh E, Al-Naser H (1999) Does the actual drop in Dead Sea level reflect the development of water sources within its drainage basin?. Acta hydrochimica et hydrobiologica, 27(1):5-11
37. Stein M, Starinsky A, Katz A, Goldstein SL, Machlus M, Schramm A (1997) Strontium isotopic, chemical, and sedimentological evidence for the evolution of Lake Lisan and the Dead Sea. Geochimica et Cosmochimica Acta, 61(18):3975-3992
38. Steinhorn I, (1985) The disappearance of the long term meromictic stratification of the Dead Sea. Limnology and Oceanography, 30(3):451-472
39. TAHAL (2011) Red Sea – Dead Sea water conveyance study program; Dead Sea study. Final report. IL/201280-R11-218. pp. 372
40. UNESCO (1991) UNESCO technical papers in marine science 62: Salinity and density of seawater; tables for high salinities (42-50). The UNESCO press, Paris, France. PP89.
41. (http://keisan.casio.com/exec/system/1350974216)

Figure and Table captions

Table 1 The coordination and depth of the four sampling profile and surface samples

Table 2 Table showing the average values of physical and chemical parameters for surface and deep brine water.

Table 3 Concentrations Mg++, Na+, Ca++, K+ and Cl- in the surface brine water and their salts compared with average values for brine water from (1987-2008) Data.

Fig. 1 Location map for the study area.

Fig. 2 Sampling sites at (D1: APC intake pumps); (D2: East coast, beside Eastern Lisan location); (D3: in the middle of northern lake opposite to Wadi El-Mujeib) and (D4: at middle of Dead Sea near the border).

Fig. 3 Vertical profile for the physical parameters of brine water at the four studied sampling sites.

Fig. 4 Vertical profile for the cations and anions of Brine water at the four studied sampling sites.

Fig. 5 Plots showing the physical and chemical parameters of surface brine water along traverse D1-D4.

Fig. 6 Histogram showing the average values of chemical and physical parameters for surface and deep brine water.

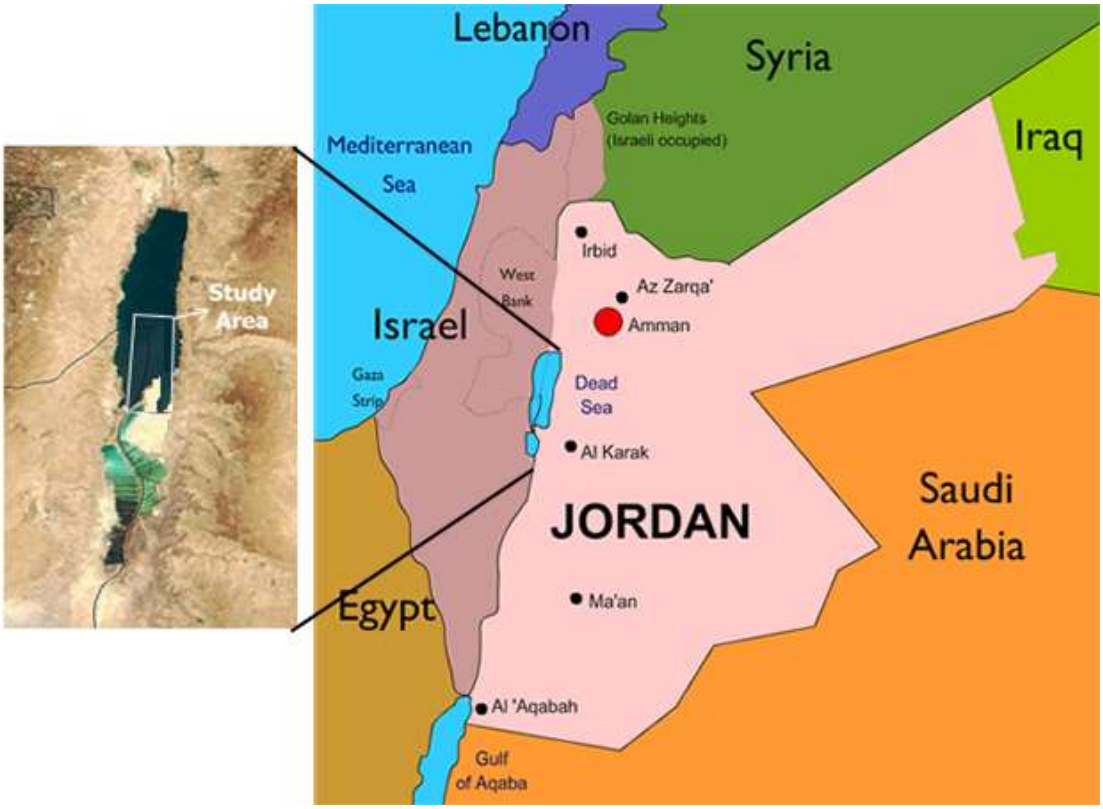


Fig. 1 Location map for the study area

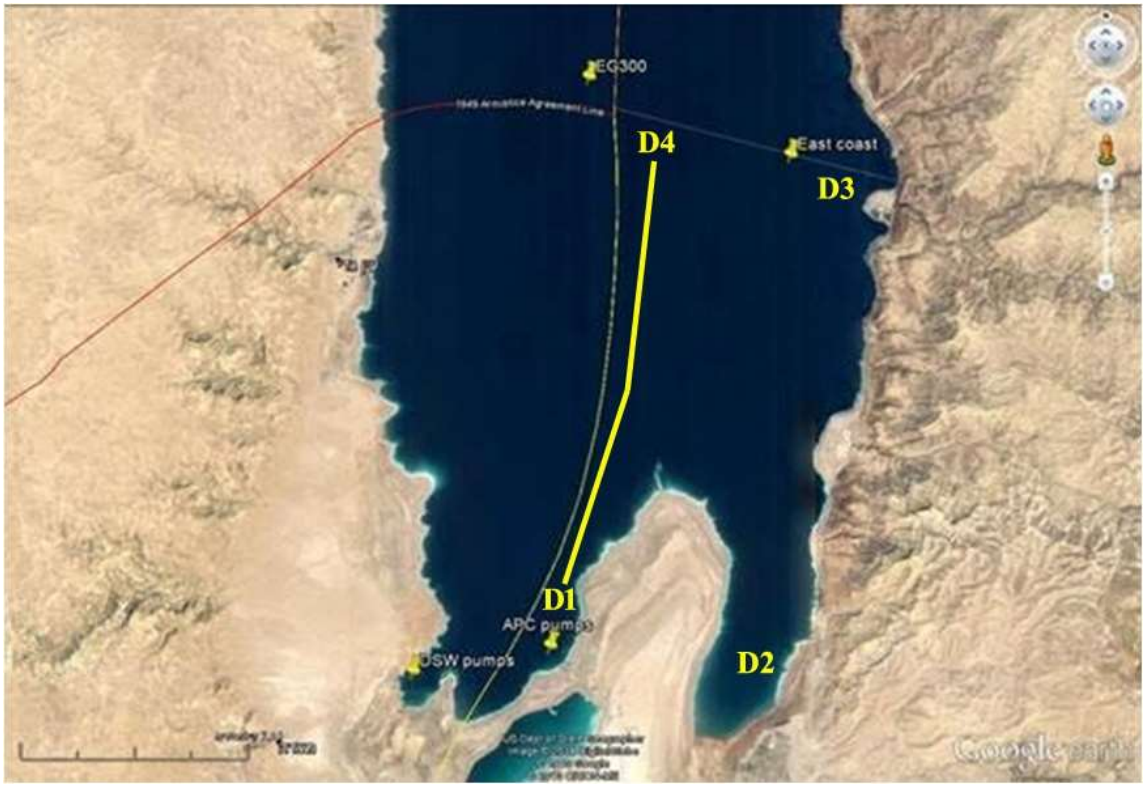
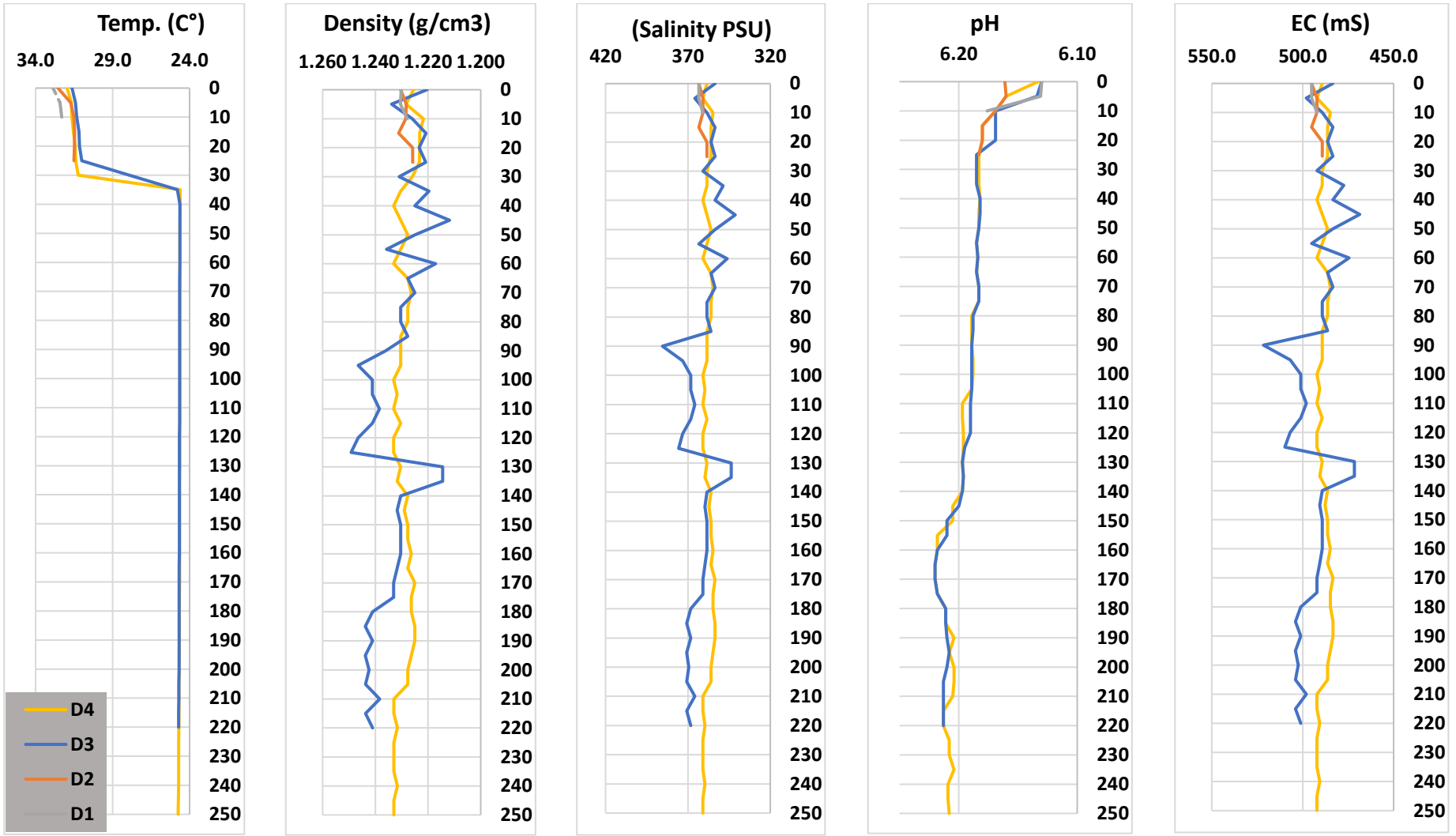


Fig. 2 Sampling sites at (D1: APC intake pumps); (D2: East coast, beside Eastern Lisan location); (D3: in the middle of northern lake opposite to Wadi El-Mujeib) and (D4: at middle of Dead Sea near the border).


Temp. (C°)
34.0
29.0
24.0
Density (g/cm3)
1.260 1.240 1.220 1.200
(Salinity PSU)
420
370
320
pH
6.20
6.10
EC (mS)
550.0
500.0
450.0
0 10 20 30 40 50 60 70 80 90 100 110 120 130 140 150 160 170 180 190 200 210 220 230 240 250
D4
D3
D2
D1

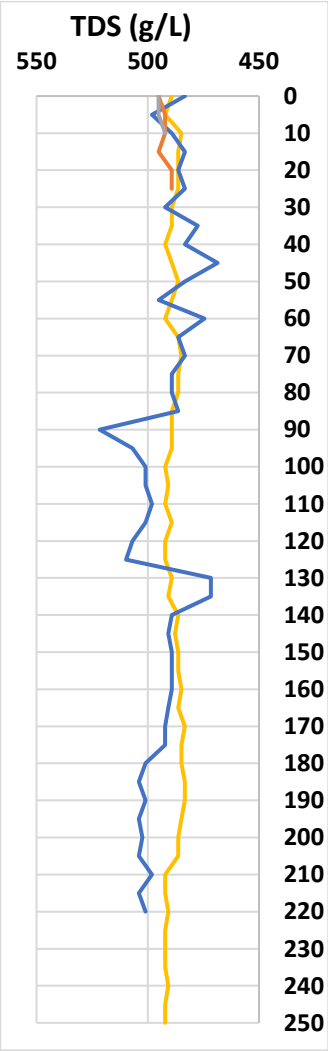
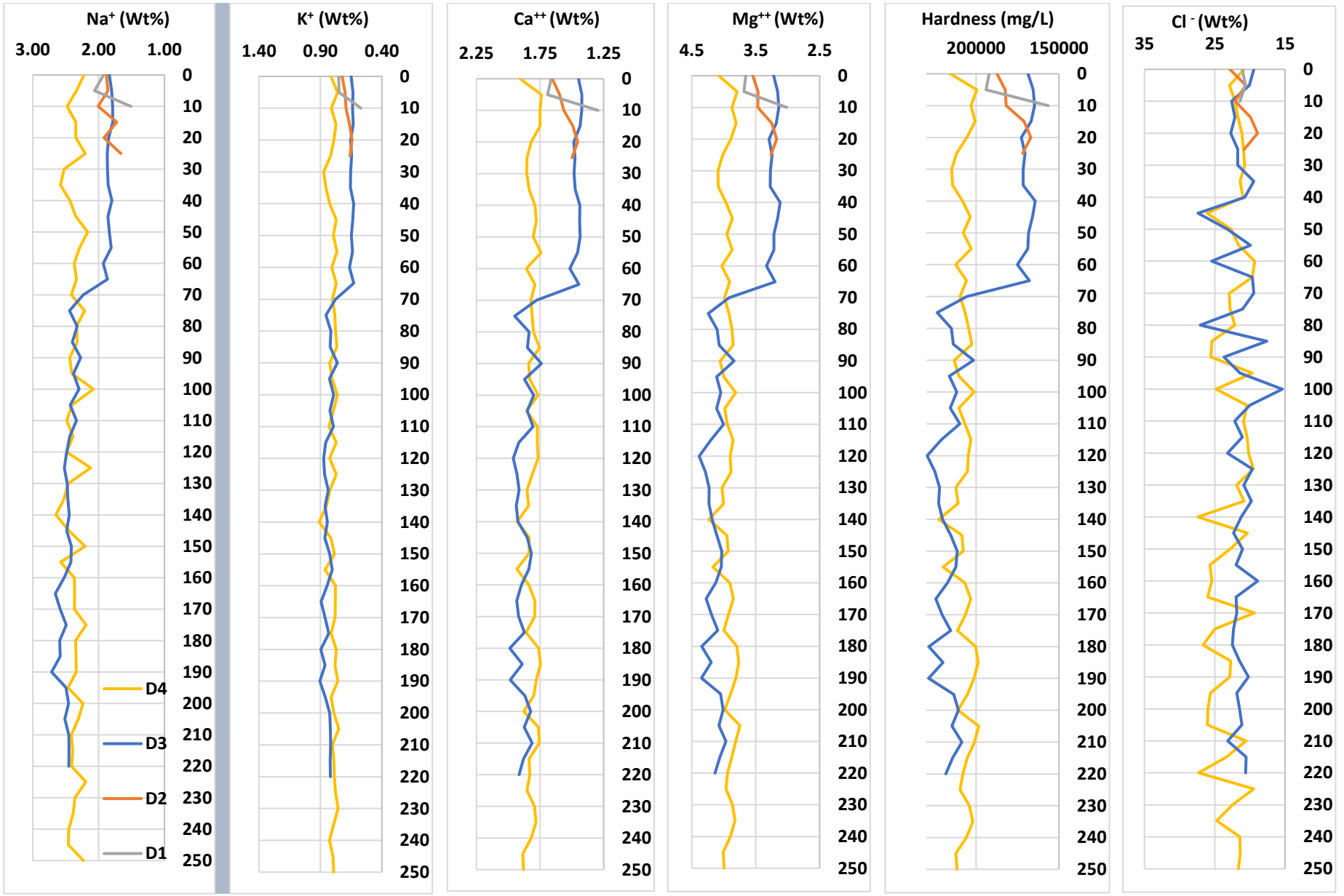


Fig. 3 Vertical profile for the physical parameters of brine water at the four studied sampling sites.


Na+ (Wt%)
3.00
2.00
1.00
K+ (Wt%)
1.40
0.90
0.40
Ca++ (Wt%)
2.25
1.75
1.25
Mg++ (Wt%)
4.5
3.5
2.5
Hardness (mg/L)
200000
150000
Cl - (Wt%)
35
25
15
0
10
20
30
40
50
60
70
80
90
100
110
120
130
140
150
160
170
180
190
200
210
220
230
240
250
D4
D3
D2
D1

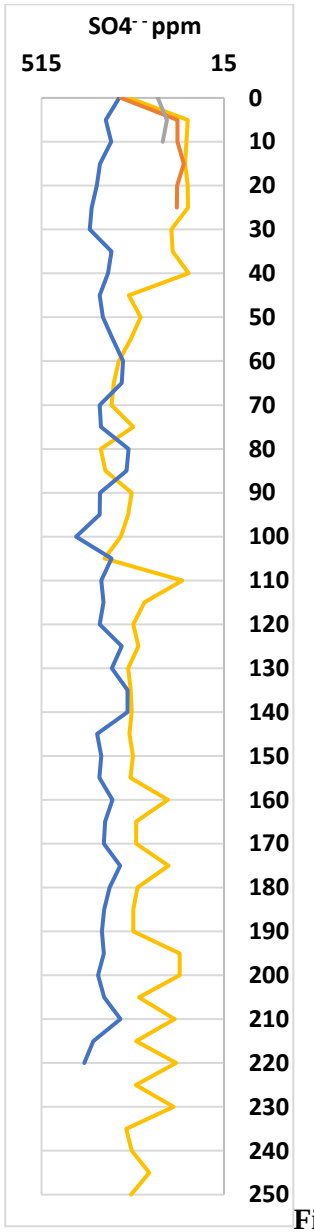
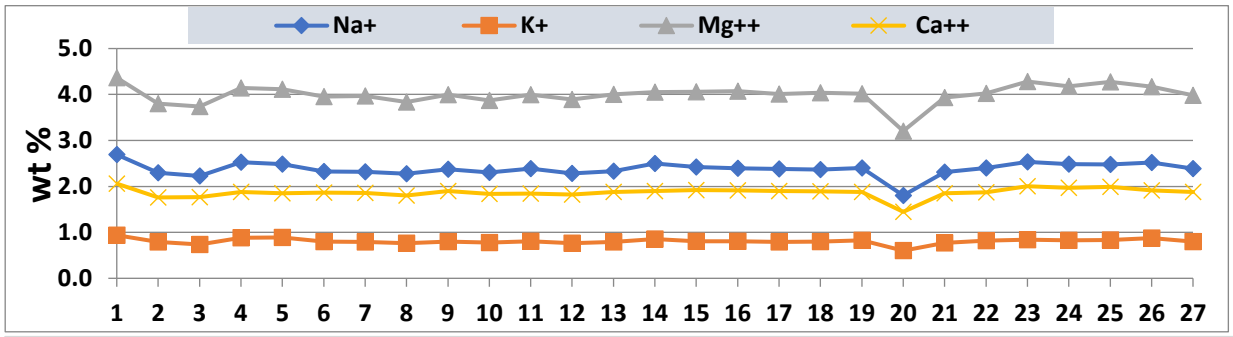
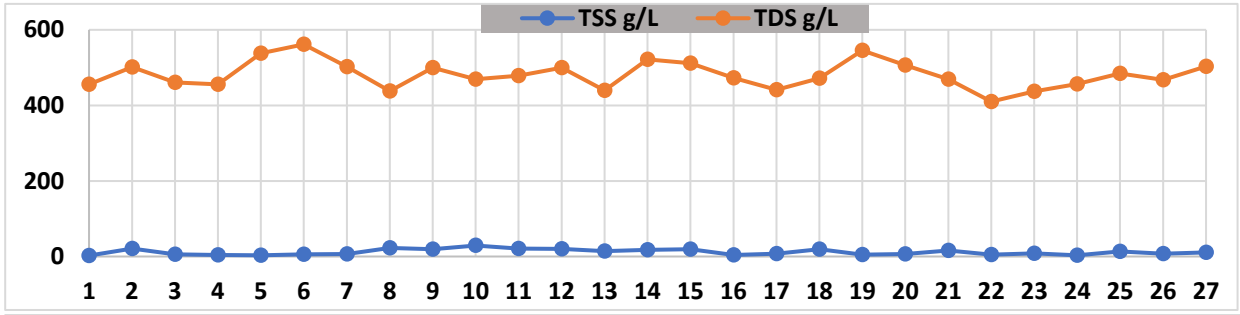
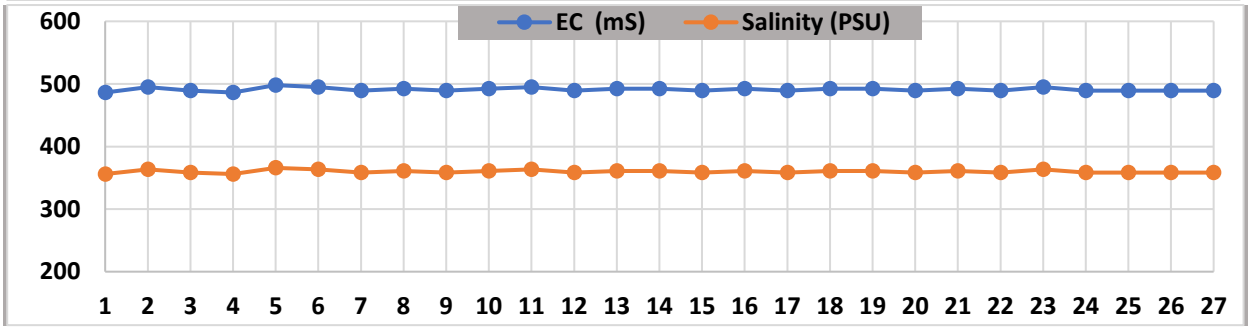


Fig. 4 Vertical profile for the cations and anions of Brine water at the four studied sampling sites.


Na+
K+
Mg++
Ca++
wt %
5.0
4.0
3.0
2.0
1.0
0.0
1 2 3 4 5 6 7 8 9 10 11 12 13 14 15 16 17 18 19 20 21 22 23 24 25 26 27


TSS g/L
TDS g/L
600
400
200
0
1 2 3 4 5 6 7 8 9 10 11 12 13 14 15 16 17 18 19 20 21 22 23 24 25 26 27


EC (mS)
Salinity (PSU)
600
500
400
300
200
1 2 3 4 5 6 7 8 9 10 11 12 13 14 15 16 17 18 19 20 21 22 23 24 25 26 27

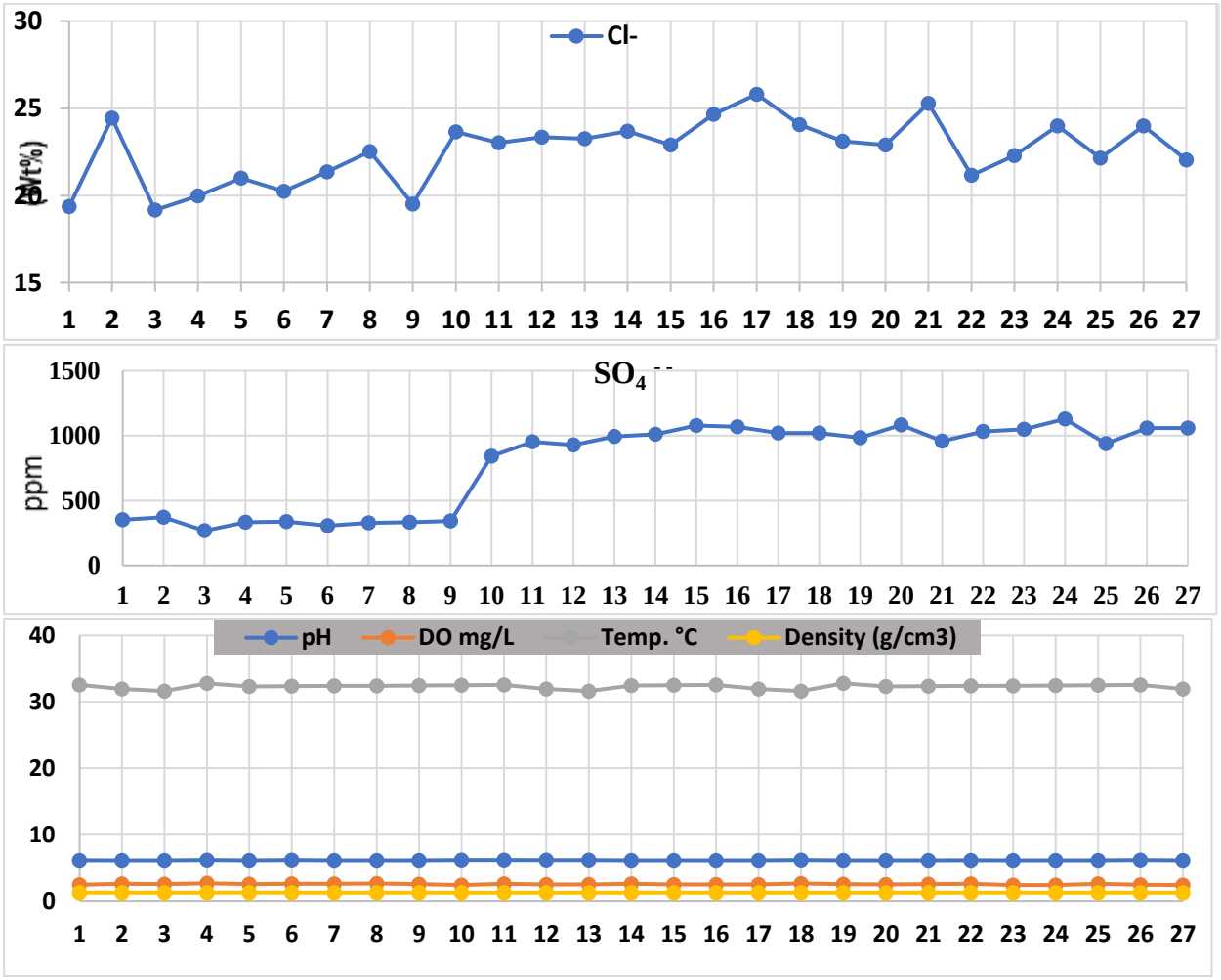


Fig. 5 Plots showing the physical and chemical parameters of surface brine water along traverse D1-D4

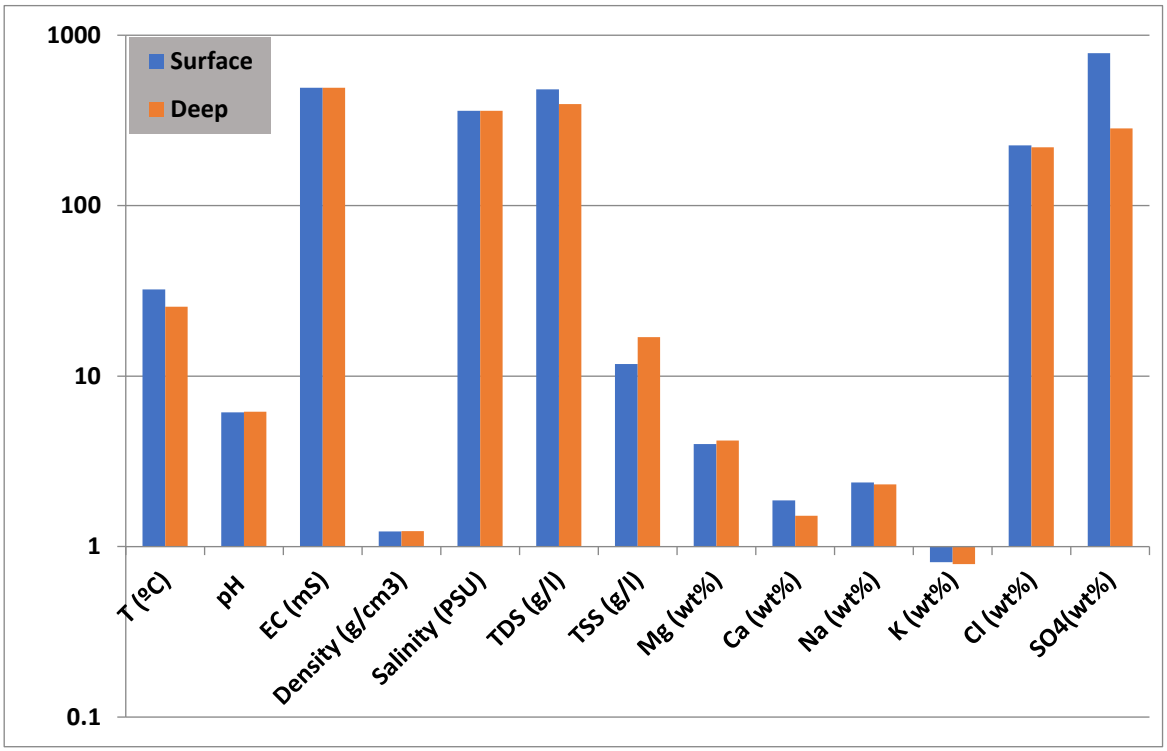


Fig. 6 Histogram showing the average values of chemical and physical parameters for surface and deep brine water.

Selective Recovery of Lithium from Dead Sea End Brines Using UBK10 Ion Exchange Resin

Sewar Aljarrah [1,*], Ahmad Alsabbagh [2], Majdi Almahasneh[1]

[1] Chemical Engineering Department, Jordan University of Science and Technology, P.O. Box 3030, Irbid 22110, Jordan

[2] Nuclear Engineering Department, Jordan University of Science and Technology, P.O. Box 3030, Irbid 22110, Jordan

***** *Corresponding author: saaljarrah18@eng.just.edu.jo ; Tel.: +962775866915*

Abstract: The application of lithium currently extends to diverse industries, including the rechargeable battery and pharmaceutical industries. Lithium enrichment optimization from the Dead Sea evaporation ponds was achieved and lithium concentrations were enriched from 30 − 40 mg/L in the end brine to 1000–1700 mg/kg in the obtained solid precipitate. The obtained precipitate was decomposed by DDW and about 66% of lithium was leached to the water producing an environmental liquor containing an elevated concentration of lithium. Subsequently, selective recovery of lithium was conducted using a successive process of ion exchange method. The ability of the strong acid-type cation exchange resin UBK 10 (Na type) for the removal of lithium from both simulated and environmental lithium-bearing solutions was investigated. The ion exchange mechanism was pH-dependent, and the removal efficiencies were optimum at pH 2. Equilibrium of lithium-ion adsorption was reached after 120 minutes in both solutions at room temperature. Because of the complex matrix comprising components that may compete with lithium adsorption, a greater quantity of adsorbent was required to achieve the equilibrium state for the environmental solution (7 grams) compared to (3.6 grams) for the simulated solution.

Keywords: Lithium, Cation Exchange resin, UBK 10, Dead Sea

1. Introduction

Lithium is known as the 21st century "New Energy Metal". The market need for lithium has grown considerably, especially since the lithium-ion battery has developed rapidly [1]. There are two types of lithium resources: mineral resources; including spodumene (a hard silicate mineral) [2], [3] and petalite ores [4]–[6], and liquid resources; including primarily continental and geothermal brines and secondarily seawater [7]–[9]. The restricted availability of lithium in minerals, together with its elevated extraction expenses has directed the industrial sector toward its liquid state resources, which are estimated to contain more than 85% of the world's recoverable lithium [10]–[12]. The liquid state lithium is predominantly found in salt lakes and subsurface brines. Most of the world's lithium reserves are in brines (21.6 Mt) while Pegmatite ores contain only (3.9 Mt) [13], [14].

1.1. Lithium Extraction from Natural Resources

Due to the industrial rapid expansion of lithium-Ion Batteries (LIBs), global demand for lithium is expected to rise dramatically. Thus, lithium extraction from its natural resources becomes a must. However, not all lithium is alike, and not all lithium is mined and extracted in the same way. The following sections discuss lithium extraction techniques from its various resources.

1.2. Lithium extraction from ore/clay

The important commercial lithium hybrid recovery process from lithium-rich ore/clay consists largely of two steps: mineral beneficiation and mineral metallurgy. For extractive metallurgy, lithium is extracted solely through a method of chemical metallurgy or a mixture of chemical metallurgy and pyrometallurgy. Two different hybrid processes, such as roasting followed by calcination or chlorination, are reported in the literature [15], [16]. Upon lithium ore beneficiation, it is either

calcinated or roasted and then leached to dissolve lithium into the aqueous phase [4]. The leach solution is then filtered and finally, via carbonation, lithium carbonate (Li_2CO_3) is produced [17], [18]. The efficiency of lithium recovery through this method was reported to be above (85%) [15]. Although pyro-metallurgy processes are efficient technological methods of lithium extraction from ores, they are highly expensive and cause environmental pollution [19].

1.3. Lithium Extraction from Salt Lake Brines

For salt lake brines, the story is different. Lithium recovery from salt lake brines does not follow any general scheme, each reported process is specified depending on the brine chemistry and composition [15]. Since the early 1980s, the extraction and use of lithium from salt lake brine have been the primary source for lithium in the industry. Currently, several technologies are available for extracting lithium from brines, such as precipitation, oxidation, adsorption, nano-filtration [6], ion exchange, and solvent extraction [20]–[22]. Despite this, it is still an arduous task to extract lithium from the high (Mg^{2+}/Li^{+}) ratio salt lake brine as they have similar properties with an almost equal ionic radius (0.07 nm) [5], making it hard to distinguish between them [23], [20].
In our previous work [24], lithium enrichment optimization from Dead Sea end brine by chemical precipitation technique was acheived. The optimization process enriched lithium concentrations from 30 − 40 mg/L in the brine to 1000–1700 mg/kg in the obtained solid precipitate and more than 40% of the lithium present in the brine was extracted [24]. In this work, the obtained precipitate was decomposed by DDW and about 66% of lithium was leached to the water producing an environmental liquor containing an elevated concentration of lithium (500-750 mg/L). An ion-exchange method by UBK 10 cation exchange resin was used for selective lithium extraction from both simulated and environmental lithium-bearing solutions. The Batch technique was used to determine the equilibrium data and the optimum adsorption conditions (pH, resin dosage, contact time, and temperature). The results of this study can be further used for lithium extraction from Dead Sea End Brines followed by carbonation ending up with pure lithium carbonate.

2. Materials and Methods

2.1. Materials

The strong acid-type cation exchange resin used in this study was UBK 10 (Na type, Mitsubishi Chemical Co. Ltd.). The cation exchange capacity of the Na type UBK 10 was 2.2 meq/cm^3 and the degree of crosslinking was 10%. Unless otherwise stated, all chemicals were used without further modification. pH adjustments were carried out by using dilute solutions of HCl and NaOH.

2.2. Analysis

The concentrations of Mg, Ca, Li, Na, K, and P in liquid samples were determined by inductively coupled plasma optical emission spectroscopy (ICP-OES) iCap 6300-radial; Thermo scientific. Samples were acid digested and were then diluted with 3% sub-boiled nitric acid (HNO_3 70%) to 15 mL as a last step in the primary chemical preparation before being analyzed in the ICP-OES. BP3001 Professional Benchtop pH-Meter was used for pH measurements

2.3. Equilibrium studies

The batch ion-exchange experiments were performed in a wide variety of conditions including different pH, various resin dosages, contact periods along with various solution temperatures. Effects of each factor were determined keeping other variables constant following one factor at a time strategy of experimentation (OFAT) [25]. In the experiments, 20 mL of both simulated and environmental lithium-bearing solutions containing 500 mg/L of lithium was used. The adsorption study was carried out by varying the pH value (pH 0.1 -6), contact time (30 min to 24 hrs.), and resin dosage (0.1 - 20 g/20 mL solution), and temperature varying (20-60 ºC). pH adjustments were made by using dilute solutions of sodium hydroxide and hydrochloric acid. At the end of contact time, resins were filtered

by 0.45 µm syringe filters and contents of solutions were analyzed by ICP-OES. The percentage removal of lithium from the aqueous solution was calculated according to the following equation [26]:

$$\textbf{\textit{Removal Percentage}}\ (\%) = \frac{(Ci - Cf)}{Ci} * \mathbf{100}, \qquad \text{Eq. (1)}$$

where C_i and C_f are the initial and final lithium concentrations (in mg/L), respectively.

3. Results and Discussion

Adsorption experiment by batch method

3.1. Simulated Lithium bearing solution

3.1.1. Effect of pH

Hydronium ion concentration is a significant parameter affecting the processes of ion exchange. This is somewhat because hydrogen ions themselves are strongly competing adsorbate and the solution pH influences the ionization of surface functional groups [27]. To investigate the effect of pH on the removal percentage of lithium by the UBK 10 resin, 20 ml of 500 mg/L simulated lithium bearing solution was used. Experiments were performed in the pH range (0.1–6), constant resin amount (1.6 g) was added to all reaction bottles, and solutions were kept in contact with the resin for 24 hours at room temperature**.** The effect of pH on lithium removal percentage is shown in *Figure* (a). As can be seen from the figure, the optimal lithium removal percentage occurred at pH =2 that is the original pH of the solution without being adjusted. At higher pH values, lithium removal percentage becomes constant as equilibrium is reached, so, the pH value=2 was chosen as the optimal value and kept constant upon optimizing the remaining factors.

3.1.2. Effect of contact time

To investigate the effect of contact time on the removal percentage of lithium by the UBK 10 resin, 20 ml of 500 mg/L simulated lithium bearing solution was used. Experiments were performed at predetermined optimal value of pH =2, constant resin amount 1.6 g was added to all reaction bottles, and solutions were kept in contact with the resin at room temperature at variable time periods (0-24 hours). *Figure* (b) below shows the dependence of lithium removal percentage with contact time for the simulated solution. The removal percentage increases with time and attains equilibrium in 2 hours with lithium initial concentrations of 500 mg/L. It can be noted that the increase of contact time to 4 hours leads to almost 4% increase in the removal percentage of lithium, so, 2 hours will be considered as the optimal contact time and it will be held constant upon the completion of optimizing other factors.

3.1.3. Effect of resin dosage

It is well known that the resin amount is also one of the important parameters to obtain the quantitative uptake of lithium-ion. The dependence of lithium sorption on resin input amount was studied by varying the amount of UBK 10 (0.1-10 g), while the other parameters such as (pH =2), initial lithium concentration (500 mg/L), room temperature, and 2 hours contact time remained constant. It was apparent that the lithium removal percentage increased sharply with higher resin dosages and a value of 87% was achieved by using 10 g/20 mL resin dosage (*Figure* (C)). This result proved that increasing the amount of adsorbent provides higher removal due to the formation of greater adsorption sites. However, beyond a value of 3.6 g/20mL, the percentage removal of lithium reaches an almost constant value reaching 72%. This may be due to an overlapping of adsorption sites as a result of the over-crowding of adsorbent particles [26]. Therefore, the use of a 3.6 g/20 mL adsorbent dose is justified for economical purposes and will be held constant upon the completion of optimizing other factors.

3.1.4. Effect of contact temperature

Predetermined optimal values of pH, time, and resin dosage were used for analyzing the effect of solution temperature on the lithium removal process. Experiments were performed at pH=2, constant resin amount (3.6 g) was added to all reaction bottles, and solutions were kept in contact with the resin for 2 hours at various temperatures (20-60 ºC). *Figure* (d) below shows the dependence of lithium removal percentage on the temperature of the solution. It can be seen from the figure that the removal percentage of lithium fluctuate with varying temperatures of solution and attains its highest value at room temperature. That's why room temperature will be chosen as the optimal lithium adsorption temperature.

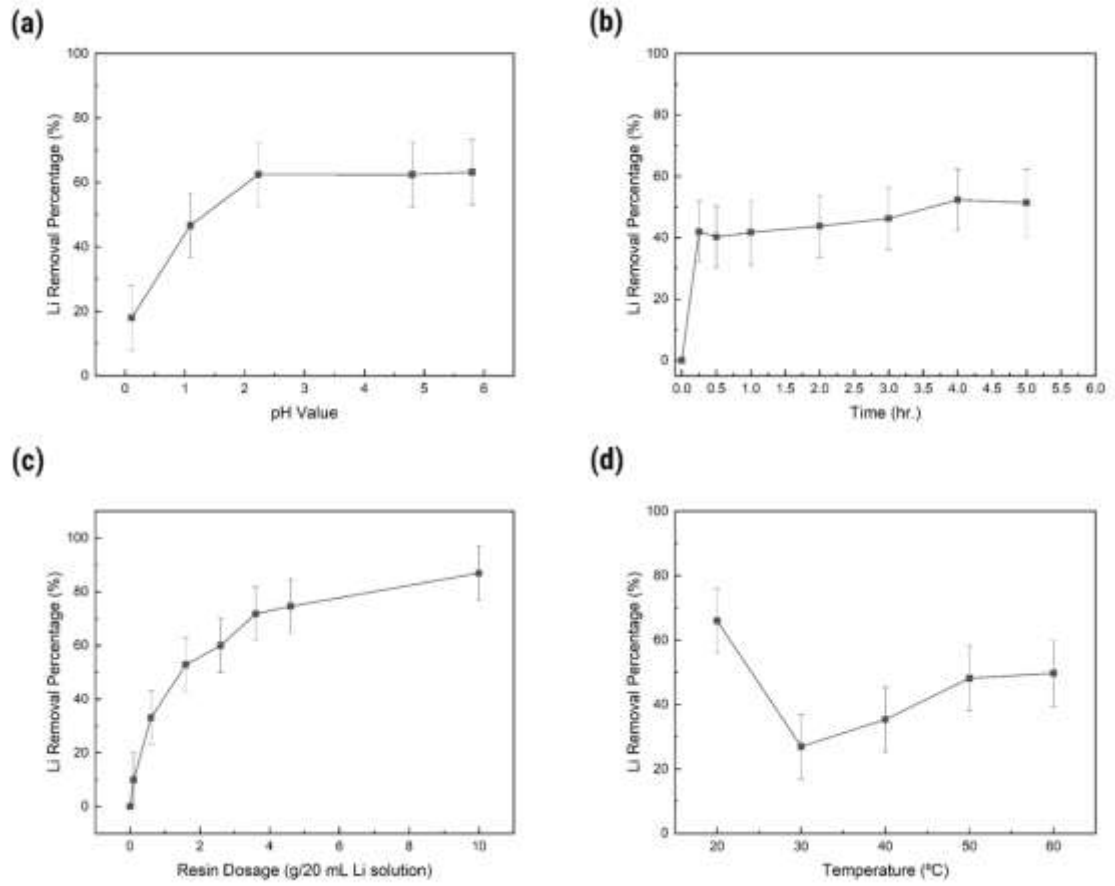


Figure 1: Effect of several factors on lithium removal percentage on simulated lithium bearing solution. pH effects (a), contact time effects (b), resin dosage effects (c), and temperature effects (d), error bars represent the propagated error of the uncertainty (%).

3.2. Environmental lithium bearing solution

3.2.1. Effect of pH

For the environmental lithium bearing solution with 500 mg/L lithium concentration with original pH value =2.2, the raise of pH using NaOH results in a white precipitation occurrence as a result of the presence of the complex matrix including high concentrations of magnesium, calcium, sodium, potassium and phosphorous in the environmental lithium bearing solution. As adsorption is preferred to occur in the absence of precipitation, pH ranges that cause precipitation were avoided and the solution was used without prior adjustment. However, such pH value was found to be the optimal pH

value for the simulated solution and thus, it was held constant upon the completion of the adsorption experiments.

3.2.2. Effect of resin dosage

The effect of resin input quantity on lithium adsorption was investigated by changing the amount of UBK 10 (3-20 g), while other paramerters held constant including pH =2, contact time of 2 hours at room temperature. It was apparent that the lithium removal percentage increased sharply with higher resin dosages and a value of 57% was achieved by using 20 g/20 mL resin dosage **Figure** (a). This result proved that increasing the amount of adsorbent provides higher removal due to the formation of greater adsorption sites. However, it's also notable that 44% of lithium was removed by using 7 grams of the resin/20mL solution and the increase of the dose by almost threefolds (20 grams) increases the removal percentage to 57% only. Therefore, the use of a 7 g/20 mL adsorbent dose is justified for economical purposes and will be held constant upon the completion of optimizing other factors.

3.2.3. Effect of contact time

To investigate the effect of contact time on the removal percentage of lithium by the UBK 10 resin, 20 ml of 500 mg/L environmental lithium bearing solution was used. Experiments were performed at pH =2, constant resin amount (7 g) was added to all reaction bottles, and solutions were kept in contact with the resin for various time intervals (0-24 hours) at room temperature. Results depicted in **Figure** (b) clearly show that the adsorption of lithium onto UBK 10 reached equilibrium in 2 hours. Adsorption first followed linear rising in which instantaneous, fast uptake takes place, and then a stationary or equilibrium state was observed. The fast initial uptake was due to the accumulation of lithium on surfaces of UBK 10 adsorbents which is a rapid step. It was concluded that 2 hours was sufficient for adsorption to attain equilibrium.

3.2.4. Effect of contact temperature

Predetermined optimal values of (pH=2, time= 2 hours, and resin dosage (7 g/20 mL solution) were used for analyzing the effects of solution temperature on the lithium removal process for the environmental lithium-bearing solution. **Figure** (c) below shows the dependence of lithium removal percentage on the temperature of the solution. It can be seen from the figure that the removal percentage of lithium was constant at intermediate temperatures (20-40 ºC) and decreases at higher temperatures (50-60 ºC) and attains its highest value at room temperature. That's why room temperature will be chosen as the optimal lithium adsorption temperature.

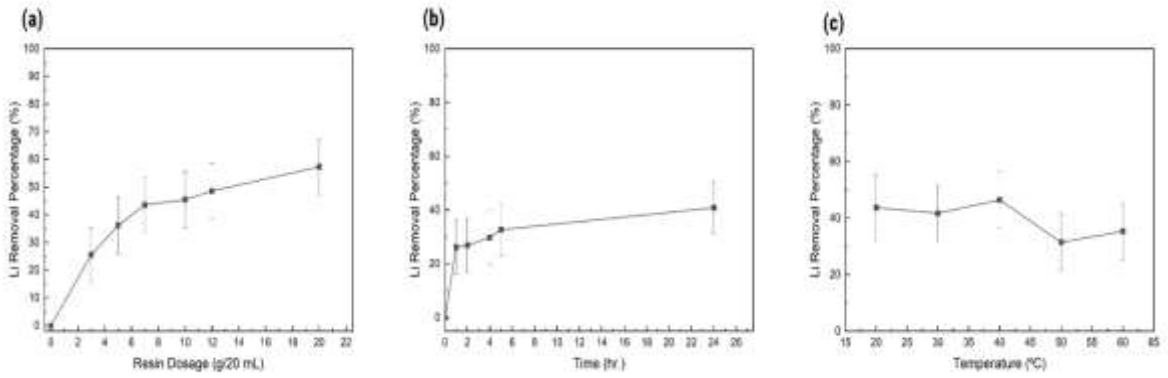


Figure 2: Effect of several factors on lithium removal percentage on environmental lithium bearing solution. Resin dosage effects (a), contact time effects (b), and temperature effects (c), error bars represent the propagated error of the uncertainty (%)

4. Conclusions

This work aimed to investigate the removal of lithium from aqueous lithium-bearing solutions by using UBK 10 cation exchange resin. Optimal removal conditions for lithium from both simulated and environmental lithium-bearing solutions were determined with batch experiments. The ion exchange process was pH-dependent and optimal removal efficiencies was obtained at pH 2. Adsorption of lithium ions reached equilibrium (within 120 min) for both simulated and environmental solutions at room temperature. A higher amount of the adsorbent was needed to reach the equilibrium state for the environmental solution (7 grams) compared to (3.6 grams) for the simulated solution as a result of the complex matrix containing elements that may compete with the adsorption of lithium. The obtained equilibrium conditions will be used for kinetics study and defining the adsorption isotherms for both simulated and environmental lithium-bearing solutions.

Funding: This research was funded by the deanship of research at the Jordan University of Science and Technology [grant number 26-2020].

Acknowledgments: Acknowledgments are due to the chemical laboratories staff at JAEC especially Eng. Faisal Al-dabie, Eng. Islam Alrobbi, Eng. Sawsan Abu Swailem, Eng. Hadeel Alda'ajah, Eng. Karam Dalgamouni, Eng. Salah Bani Hamad and Eng. Kamal Harahsheh for their endless assistance and courage upon the completion of this work.

References

1. X. Liu, M. Zhong, X. Chen, J. Li, L. He, and Z. Zhao, "Enriching lithium and separating lithium to magnesium from sulfate type salt lake brine," *Hydrometallurgy*, vol. 192, p. 105247, 2020, doi: 10.1016/j.hydromet.2020.105247.
2. G. R. Harvianto and S. Kim, "Solvent extraction and stripping of lithium ion from aqueous solution and its application to seawater," 2015, doi: 10.1007/s12598-015-0453-1.
3. M. G. Aylmore *et al.*, "Assessment of a spodumene ore by advanced analytical and mass spectrometry techniques to determine its amenability to processing for the extraction of lithium," *Miner. Eng.*, vol. 119, no. January, pp. 137–148, 2018, doi: 10.1016/j.mineng.2018.01.010.
4. X. Xu *et al.*, "Extraction of lithium with functionalized lithium ion-sieves," *Prog. Mater. Sci.*, vol. 84, pp. 276–313, 2016, doi: 10.1016/j.pmatsci.2016.09.004.
5. R. Chitrakar, Y. Makita, K. Ooi, and A. Sonoda, "Lithium recovery from salt lake brine by H2TiO3," *Dalt. Trans.*, vol. 43, pp. 8933–8939, 2014, doi: 10.1039/c4dt00467a.
6. K. Ooi, A. Sonoda, Y. Makita, R. Chitrakar, and Y. Tasaki-handa, "Recovery of lithium from salt-brine eluates by direct crystallization as lithium sulfate," *Hydrometallurgy*, vol. 174, pp. 123–130, 2017, doi: 10.1016/j.hydromet.2017.10.007.
7. Y. Song and Z. Zhao, "Recovery of lithium from spent lithium-ion batteries using precipitation and electrodialysis techniques," *Sep. Purif. Technol.*, vol. 206, pp. 335–342, 2018, doi: 10.1016/j.seppur.2018.06.022.
8. L. Li., V. G. Deshmane., M. P. Paranthaman*, R. Bhave, B. A. Moyer, and S. Harrison, "Lithium Recovery from Aqueous Resources and Batteries : A Brief Review," *Johnson Matthey Technol. Rev.*, vol. 62, no. 2, pp. 161–176, 2018, doi: 10.1595/205651317X696676.
9. O. Sitando and P. L. Crouse, "Processing of a Zimbabwean petalite to obtain lithium carbonate," *Int. J. Miner. Process.*, vol. 102–103, pp. 45–50, 2012, doi: 10.1016/j.minpro.2011.09.014.
10. X. Liu, M. Zhong, X. Chen, and Z. Zhao, "Hydrometallurgy Separating lithium and magnesium in brine

by aluminum-based materials," *Hydrometallurgy*, vol. 176, no. December 2017, pp. 73–77, 2018, doi: 10.1016/j.hydromet.2018.01.005.

11. Z. Zhao, X. Si, X. Liu, L. He, and X. Liang, "Hydrometallurgy Li extraction from high Mg / Li ratio brine with LiFePO 4 / FePO 4 as electrode materials," vol. 133, pp. 75–83, 2013, doi: 10.1016/j.hydromet.2012.11.013.
12. X. Liu, X. Chen, Z. Zhao, and X. Liang, "Effect of Na + on Li extraction from brine using LiFePO 4 / FePO 4 electrodes," *Hydrometallurgy*, vol. 146, pp. 24–28, 2014, doi: 10.1016/j.hydromet.2014.03.010.
13. S. Virolainen, M. Fallah, V. Miettinen, and A. Laitinen, "Removal of calcium and magnesium from lithium brine concentrate via continuous counter-current solvent extraction," *Hydrometallurgy*, vol. 162, pp. 9–15, 2016, doi: 10.1016/j.hydromet.2016.02.010.
14. A. Çiçek, O. Yilmaz, and Ö. Arar, "Removal of lithium from water by aminomethylphosphonic acid-containing resin," *J. Serbian Chem. Soc.*, vol. 83, no. 9, pp. 1059–1069, 2018, doi: 10.2298/JSC170930020C.
15. Basudev Swain, "Recovery and Recycling of Lithium: A Review," *Sep. Purif. Technol.*, no. August, 2016, doi: 10.1016/j.seppur.2016.08.031.
16. C. F. Davidson, "Recovery of lithium from clay by selective chlorination." U.S. Dept. of the Interior, Bureau of Mines, Pgh. [i.e. Pittsburgh] Pa., pp. ii, 19 p., 1981.
17. P. K. Choubey, M. Kim, R. R. Srivastava, J. Lee, and J. Lee, "Advance review on the exploitation of the prominent energy-storage element : Lithium . Part I : From mineral and brine resources," *Miner. Eng.*, vol. 89, pp. 119–137, 2016, doi: 10.1016/j.mineng.2016.01.010.
18. N. Vieceli, C. A. Nogueira, M. F. C. Pereira, F. O. Durão, C. Guimarães, and F. Margarido, "Optimization of an innovative approach involving mechanical activation and acid digestion for the extraction of lithium from lepidolite," vol. 25, no. 1, pp. 11–19, 2018.
19. T. H. Nguyen and M. S. Lee, "A Review on the Separation of Lithium Ion from Leach Liquors of Primary and Secondary Resources by Solvent Extraction with Commercial Extractants," pp. 1–15, 2018, doi: 10.3390/pr6050055.
20. Q. Bi, Z. Zhang, and C. Z. and Z. Tao, "Study on the recovery of lithium from high Mg 2 þ / Li þ ratio brine by nano fi ltration Qiuyan Bi , Zhiqiang Zhang , Chenying Zhao and Zhenqi Tao," pp. 1690–1695, 2014, doi: 10.2166/wst.2014.426.
21. K. Chung, J. Lee, E. Kim, K. Lee, Y. Kim, and K. Ooi, "Recovery of Lithium from Seawater Using Nano-Manganese Oxide Adsorbents Prepared by Gel Process," vol. 452, pp. 277–280, 2004, doi: 10.4028/www.scientific.net/MSF.449-452.277.
22. A. H. Hamzaoui, H. Hammi, and M. Adel, "Operating Conditions for Lithium Recovery from Natural Brines," vol. 52, no. 12, pp. 1859–1863, 2007, doi: 10.1134/S0036023607120091.
23. Z. Ji, Q. Chen, J. Yuan, J. Liu, Y. Zhao, and W. Feng, "Preliminary study on recovering lithium from high Mg 2 + / Li + ratio brines by electrodialysis," *Sep. Purif. Technol.*, vol. 172, pp. 168–177, 2017, doi: 10.1016/j.seppur.2016.08.006.
24. A. Alsabbagh, S. Aljarrah, and M. Almahasneh, "Lithium enrichment optimization from Dead Sea end brine by chemical precipitation technique," *Miner. Eng.*, vol. 170, no. June, p. 107038, 2021, doi: 10.1016/j.mineng.2021.107038.
25. D. C. Montgomery, *Design and Analysis of Experiments Eighth Edition*, vol. 2. 2012.
26. P. Senthil Kumar, C. Vincent, K. Kirthika, and K. Sathish Kumar, "Kinetics and equilibrium studies of

Pb2+ ion removal from aqueous solutions by use of nano-silversol-coated activated carbon," *Brazilian J. Chem. Eng.*, vol. 27, no. 2, pp. 339–346, 2010, doi: 10.1590/s0104-66322010000200012.

27. B. Alyüz and S. Veli, "Kinetics and equilibrium studies for the removal of nickel and zinc from aqueous solutions by ion exchange resins," *J. Hazard. Mater.*, vol. 167, no. 1–3, pp. 482–488, 2009, doi: 10.1016/j.jhazmat.2009.01.006.

Simple Correlation for Predicting Gypsum Deposition from Brine Solutions

Hosni Ezuber *, Sabri Mrayed and Maeda Altobli

Faculty of Engineering, University of Bahrain, P. O. Box 32038, Bahrain
***** *Corresponding author: halzubair@uob.edu.bh; Tel.: +97317786622.*

Abstract: Calcium sulfate scale occurrence is one of the major problems encountered on heat exchanger surfaces, membrane surfaces of reverse osmosis (RO) plants and oilfield facilities. Scale prevention and treatment are extensively applied for confronting this problem. It is essential for a successful scaling prevention and treatment to be able to identify whether sulfate scale is likely to occur under certain operation conditions.This paper is devoted to predict the solubility product of calcium sulfate (gypsum) in brine solutions, through which the gypsum scaling tendency can be easily obtained. The simple solubility product prediction correlation, presented in the form of a simple mathematical equation, is based on sodium sulfate solubility experimental data available in the literature.The predicted gypsum solubilities from the solubility equation show that the simple method is able to represent gypsum solubility data within the experimental accuracy in the temperature range of 25 to 80oC and the pressure range from 1 to 1,000 bar with NaCl concentration up to 5 M. The method is simple, compact and reliable and can be applied to any environment where gypsum is expected to precipitate.

Keywords: Gypsum, NaCl, solubility product, temperature. Pressure, ionic strength.

1. Introduction

Calcium sulfate can exist in three distinct crystalline phases: gypsum ($CaSO_4$-$2H_2O$), hemihydrate ($CaSO_4$-$0.5H_2O$), and anhydrite ($CaSO_4$). The stability of the crystal structures of these three main phases is highly influenced by temperature. It was postulated that above 120ºC approximately, anhydrite is stable, while Gypsum is the commonly salt that deposited from brines at temperatures less than about 80ºC once its saturation exceeds the solubility limit. Between 80ºC and 120ºC any of the three distinct phases may form [1]. The solubility of gypsum and its precipitation from brines is of practice importance and is influenced by a numeral of parameters including temperature, salinity and to some extent pressure. Many studies have been undertaken on the solubilities of gypsum in natural waters at temperature ranges between 25 and 80oC, and at 1 bar or saturation pressure with NaCl concentration up to 6 M. Solubilities of gypsum in NaCl-H_2O at 25ºC have been investigated by several investigators [2-17]. These data are considerably scattered and outlined in forms of Tables, Figures or in the form of equations. Marshall and Slusher [2] exhibited extensive solubility measurements of calcium sulfate in aqueous NaCl solutions of high ionic strength at temperatures from 0ºC to 110ºC. Marshall et al., [3] presented solubilities at 40ºC and 60ºC and sodium chloride concentration up to 5.37 molal. Carlberge and Mathews [4] reviewed the gypsum solubilities in NaCl brines up to 350 g/L and at temperatures ranges between 0.5ºC and 90ºC. Raju and Atkinson [5] reviewed gypsum solubilities in sodium chloride aqueous solutions and summarized the data sources in a table. They also used fundamental thermodynamic relations to calculate the thermodynamic solubility product of gypsum as a function of temperature. The mean activity coefficient of $CaSO_4$ was calculated by modified Pitzer's equation which include more 12 empirical parameters. There values for K_{sp} are in good agreement with Marshall et al. [3]. Block and waters [6] studied the solubility gypsum at temperatures 25ºC, 40ºC, 55ºC, 70ºC and 85ºC and at salinities up to 4 molal NaCl. They observed that the solubility of gypsum increases with increasing NaCl concentration up to about 3 molal NaCl. After passing this maximum, the solubility decreases at higher concentrations. Bock [7] has studied the solubility of $CaSO_4.2H_2O$ in concentrated aqueous solutions of NaCl (up to about 6 M) at a series of temperatures; 25ºC, 30ºC, 40ºC, and 50ºC. The obtained measured solubilities have shown similar trend to those reported by Block and waters [6]. Blount and Dickson

[8] reviewed gypsum solubilities in sodium chloride aqueous solutions and summarized the data sources in a figure. They also studied the effect of temperature up to 70ºC on the solubilities of gypsum at 2, 4 and 6 M NaCl and 1 bar. Their solubility results are in fair agreement with those obtained by Bock [7], Block and waters [6] as well as with the results of Marshall and Slusher [2] at 2 and 4 M. At 6 M, however, the solubilities of Marshall and Slusher [2] are significantly higher than those of Blount and Dickson [8]. He and Morse [9] studied the solubility of gypsum in relation to ionic strength at 25ºC. They observed that as NaCl is added to a solution of gypsum, an increase in gypsum solubility is observed from 0 to 1 M NaCl. This, however, is followed by decreased in gypsum solubility with NaCl molarties greater than 3. Zhang et al., [10] measured the solubility of gypsum in NaCl aqueous solution at 37oC under atmospheric pressure. The investigated concentration of NaCl solution is 0.0 -5.0 M. Their results showed an increase in gypsum solubility with increasing NaCl concentration in the range of 0.0 to 2.0 M. After passing a maximum, the solubility declines smoothly in the range of higher concentration of NaCl. Glew and Hames [11] determined the solubility of gypsum at 65ºC in aqueous 3 to 6 m NaCl solutions. They observed that gypsum solubility has decreased with NaCl concentration for the salinity range used in their work. The solubility of gypsum in aqueous NaCl solutions up to very high salinities in the pH range of 2.5 to 8.5 at 35oC has been studied by Shukla et al. [12]. They reported that the solubility of gypsum increases with an increase in NaCl solution up to about 2.5 molal and then starts to decrease. Owing to the effect of pH these investigators found a slight increase in the solubility of gypsum with a decrease in the pH of the solution.

In essence, the gypsum solubilities available in the literature concluded that the solubility of gypsum in NaCl solutions is increased with temperature and is greater in highly concentrated brined up to about 3 M before a slight decrease occurs at still higher salt contents [2-16]. The increase in the solubility has been related to bisulfate formation. However, the solubility decrease in concentrated chloride solutions was related to changes in the activity coefficient of the calcium and sulfate ions as well as the activity of water [13].

Earlier gypsum solubility studies in water or chloride containing solutions have not taken effect of pressure in consideration or were restricted to limited pressures. The effect of pressure on gypsum solubility is not as important as temperature change. Nevertheless, to apply to environments common to oilfield operations or reverse osmosis industries, where the system pressure can be higher than 500 bar, the effect of pressure on gypsum solubility must be considered. Blount and Dickson [8] have measured gypsum solubilities in pure water at elevated pressures. They also processed these data to obtain an empirical equation that calculates the effect of pressure on gypsum solubility in pure water as a function of temperature. High pressure gypsum solubility data in the other solutions than pure water were unavailable except a scarce few data. Millero [18] developed a mathematical expression to calculate the effect of pressure on the solubility of sulfate salts. In his model Millero described the pressure dependence of equilibrium constant by the following expression:

$$Ln\frac{K_d(P)}{K_d^o} = \frac{-\Delta\bar{V}^o}{RT}\,P + \frac{-\Delta\bar{K}^o}{2RT}\,P^2 \qquad (1)$$

where: P is applied pressure (bars), R is the gas constant (83.15 cm3 bar K-1 mole-1), T is the absolute temperature (K), $\Delta\bar{\boldsymbol{V}}^{\boldsymbol{o}}$ (cm^3 $mole^{-1}$), and $\Delta\bar{\boldsymbol{K}}^{\boldsymbol{o}}$ (cm^3 K^{-1}) are the differences between the infinite dilution partial molar volumes, and compressibilities, of the products (Ca^{2+} and SO_4^{2-}) and the reactant ($CaSO_4$), respectively .

$$\Delta\bar{V}^o = V_{CaSO_{4(s)}} - V_{Ca^{2+}} - V_{SO_4^{2-}} \qquad (2)$$

$$\Delta\bar{K}^o = K_{CaSO_{4(s)}} - K_{Ca^{2+}} - K_{SO_4^{2-}} \qquad (3)$$

$\bar{V}^o$ and $\bar{K}^o$ are temperature dependent and the changes of these parameters with absolute temperature are in linear fashion. For gypsum the relationship was expressed as [19]:

$$\bar{V}^o = -47.45 + 22.43 \times 10^{-2} T + -22.07 \times 10^{-4} T^2 - 0.748 \times 10^{-6} T^3 \quad (4)$$

$$\bar{K}^o(10^3) = 17.83 - 1.543 \times 10^{-2} T - 16.01 \times 10^{-4} T^2 + 16.84 \times 10^{-6} T^3 \quad (5)$$

Garcia et al. [20] studied the effect of pressure on the solubility product of sulfate scaling minerals ($BaSO_4$, $SrSO_4$, $CaSO_4$) and their mixtures with NaCl. Their proposed equation covers wide range of temperature (up to 300ºC), pressure (up to 1000 bar) and concentrations up to saturation, expressed as:

$$\ln K_d(p) = \ln K_d(0) + \alpha (P - P_0) + \beta (P - P_0)^2 \quad (6)$$

for $CaSO_4$, values of α and β parameters are: 0.1078224×10^{-2} and $-0.3078141 \times 10^{-6}$, respectively.

Solubility of Gypsum, at different pressures (ranges of 1 to 1,500 bar) with respect to impurity of NaCl in the solution have been calculated by Doubra et al [21]. They applied Pitzer's theory to calculate the activity coefficients. Their model results achieved good agreement with the literature data. Li and Duan [22] have developed a thermodynamic equilibrium model for the calculation of gypsum solubility at pressures from 1 to 1000 bar with NaCl concentrations up to the saturation halite. Similar to Doubra et al [21], Li and Duan [22] determined the sulfate related Pitzer parameters in their model.

Solubility of gypsum in brines is usually presented scattered in the form of Tables, graphs or in the form of equations are usually restricted to a particular condition of temperature, or ionic strength. Therefore, unable to predict gypsum solubilities for a wider scope such as temperature, pressure and ionic strength. i.e. does not cover all the changing temperature, pressure and ion composition, as in the case of desalination plants or oilfield industries. Predictions of gypsum solubilities available in the form equations that covers wide range of temperature, pressure and ionic strength are usually requires the calculation of activity coefficient and are commonly developed as a menu-driven software. Thus, the aim of this study is to develop a simple concrete method easy to use and produce fast and reliable predictions for the solubility product of gypsum at wide range of temperature, pressure and ionic strength, and in environments common to desalination plants and oilfield industries.

2. Methodology and Approach

For calcium sulfate (gypsum) in an aqueous solution, the chemical reaction representing the equilibrium between $CaSO_4$ hydrate and its ions is:

$$CaSO_4.2H_2O_{(s)} = Ca^{2+} + SO_4^{2-} + 2H_2O \quad (7)$$

The solubility product (thermodynamic equilibrium constant) takes the form:

$$K_{SP} = (m_{Ca^{2+}} \gamma_{Ca^{2+}})(m_{SO_4^{2-}} \gamma_{SO_4^{2-}})(a_{water})^n = (m_{Ca^{2+}})(m_{SO_4^{2-}}) \gamma^2 \pm (CaSO_4)(a_{water})^n \quad (8)$$

The solubility of calcium sulphate is:

$$[Ca]_{total} = m_{Ca^{2+}} + m_{SO_4^{2-}\,(aq)} \quad (9)$$

Saturation ratio (SR) is the ratio of ion activity product to the solubility product which can be calculated by dividing the composition of the products in real state to that of saturation state.

In actual prediction, it is difficult to obtain activity coefficient because of a variety of coexistence ion in solution, and the free ion solution activity coefficient is close to 1, so it is usually using concentration instead of coefficient [23]. Therefore, the saturation ratio may be defined as:

$$SR = \frac{(C_{Ca^{2+}})(C_{SO_4^{2-}})}{K_{sp}} \quad (10)$$

where ($C_{Ca^{2+}}$) and ($C_{SO_4^{2-}}$) are the measured concentrations of the calcium and sulfate ions in the solution, respectively. SI is a criteria to see if the solution is unsaturated, saturated or supersaturated (SI < 1, SI = 1 and SI > 1, respectively) which is equal to logarithm of SR

K_{sp} is the stoichiometric solubility product constant for CaSO4, defined as

$$K_{sp}^{1/2} = S \times \gamma \quad (11)$$

S is the solubility of $CaSO_4$ in mol/Kg of H_2O and γ is the mean ionic activity coefficient.

In this predictive method the activity coefficient is included in the solubility constant and the resulting conditional solubility product constant Kc (function of temperature, pressure and ionic strength) is used in the predictive equation. Using the term conditional solubility product constant K_c equation "10" can be written as:

$$SR = \frac{(C_{Ca^{2+}})(C_{SO_4^{2-}})}{K_c} \quad (12)$$

At saturation; K_c is given by

$$K_c = S^2 \quad (13)$$

The main objective of this work is to develop a simple and reliable mathematical model to predict the solubility of gypsum in sodium chloride solution at wide range of temperature, pressure and ionic strength. Such a model would a valuable tool for predicting unwanted gypsum precipitation in industrial processes.

In this work, the developed model was actual measured solubility data collected from different sources as a database. The advantage of using numerous measured reliable solubilities is to evade any unreliable measured data might arise from one source of measurement. Obtainable literature experimental data sources including the data of Marshall and Slusher [2], Marshall et al. [3], Block and waters [6], Bock [7] and Blount and Dickson [8] for the entire temperature, and NaCl concentration range, were used to parameterize the model. The effect of pressure on the solubility of gypsum solubility was based on the experimental partial molal volume and compressibility analyzed by Millero [18]. It should be mentioned that prior to the use of experimental data for parameter estimation, the collected data from different sources was imported into a spreadsheet, displayed graphically and visually inspected for consistency. Any inconsistent data (i.e. data systematically diverge significantly from others) was discarded after careful consideration.

The presented model parameter estimation was performed by regressing the experimental solubilities with the regression module of MINITAB® version 16. The best functional form of this derived correlation was found as:

$$Ln\ K_c = A_1 - A_2\ T + A_3\ T^2 + A_4\ P - A_5\ I - A_6\ I^{0.5} + A_7\ I^{0.5}\ T \quad (14)$$

where: I is the ionic strength in (mol/L) = $1/2\ \sum M_i\ z_i^2$ (M_i is the molarity of the ith ion and z_i is the charge of the ith ion). A_1-A_7 are correlation constants. The optimum numerical values of the Ai fitting parameters (conditional constants) with their statistical significant are given in Table 1.

Given a brine of known composition, and a desired temperature and pressure, the value of the Kc is determined using the developed correlation (equation "14"). From the Kc and the water analysis, the scaling potential for $CaSO_4$ is determined from equation (12). A saturation ratio (SR) greater than 1 is expected to form $CaSO_4$ scale. SR less than 1 is predicted not to form $CaSO_4$ scale.

2. 1. Testing and application of the present correlation

Regression data is applied to construct the final equation to guarantee the significance of the predictions anticipated from such a model in yielding compliant and self-consistent outcomes. In

this study the expectedness of the correlation was verified by comparing the model results with the data available in the literature beyond the range of those used for determining the model parameters. The sources of the data used, together with the range of temperatures and pressures, the number of experimental points and the average absolute deviation with respect to equation 14 are given in Tables 2-4. Table 2 summarizes some statistical parameters testifying to the accuracy and tolerable performance of the presented correlation. These parameters included: squared correlation coefficient (R^2) for Ln k_c, As well as median absolute deviation (MAD), mean square error (MSE), root mean square errors (RMSE) and mean absolute percent error (MAPE) for the gypsum solubilities.

Regression plot of solubility product constant obtained from literature against those predicted by the proposed model is given in Figure 1. Critical examination of this diagram showed strong linear relationship with a R^2 value of 0.991, confirming to the constancy and dependability of the proposed model. Deviations of solubility product values predicted by the present correlation from experimental (or predicted) data are presented in Table 2 -3. As indicated in these tables, satisfactory correspondence exists between predicted values and those from literature data. Relative deviation (RD) analysis of as many as 300 individual literature solubility values revealed that about 90% of population of points are below ±10%. Around 6% of the points examined falls between ± 10-15% (RD), around 3% are between ±15-20% and very limited data points show an absolute deviation value beyond 20%.

Figures 2 to 5 show the average deviation with respect to the predicted method and individual reported solubility data at different conditions of temperature, pressure, and NaCl ionic strength. Despite the divergence of the literature solubilities, the presented method compares reasonably well with those obtained in the literature. The deviation of the predicted solubilities from the literature data are mainly caused by the discrepancy among the measured (or estimated) data themselves, as suggested in Figures 2 to 5. As an example, Figure 2 clearly shows that the present method agrees well with the literature in all tested concentration. However, variation in the predicted values of Dourba [21] shows excellent agreement with the presented method at concentrations up to 3 M. Beyond this value Doruba's solubilities shows relatively higher values than those presented in the literature.

The graphs of gypsum solubilities in aqueous NaCl solutions at higher pressures of 41 bar, 500 bar and 1000 bar (25°C) are shown in Figures 4 and 5. The graphs presented in Figure 4 indicate excellent agreement of the predicted solubilities of Dourba et al. [21] with maximum average deviation of about 7% indicating the suitability and reliability of the model under higher pressure and temperature conditions. Fig. 5 shows the effect of NaCl Concentration on the gypsum solubility at 500 bar. Compared with the limited experimental data, we can see that the present method is generally within 3.36% of experimental data (Table. 4).

Tables 2 and 3 present the source of data, used together with the range of temperatures, pressures, NaCl concentration, the number of solubilities points and the average absolute deviation percentage (AAD%) with respect to the present model. Despite the distinct deviation in the literature gypsum solubility data, our predicted values are within a difference of 2.77-10.79% with the literature at temperatures up to 80°C and 1 bar (Table 3). At higher pressures (41-1000 bar), however, the deviation in solubilities with Dourba [21] shows an average MAPE value of 3.76%, 3.35% and 5.62% at 41, 500 and 1000 bar, respectively. In general, the solubility values predicted by the present model corroborate the suitability and applicability of the model and sustains that our predictive method can predict the solubility of gypsum in chloride solutions at temperatures up to 80oC and pressures up to 1000 bar.

The results presented in this section clearly shows that the developed mathematical predictive equation provides close agreement with the literature solubilities for the region of temperature-

pressure and ionic strength common to oilfield environment (I = 0.5-5 m, T = up to 80°C and P = 1-1,000 bar).

2.1. 2. Application in oilfield brines

It should be noted that K_c provided by equation 14 is based on the solubility of gypsum in NaCl solutions. Oilfield brines, however, are complicated solutions and contain, beside Na^+ and Cl^-, other species including Mg^{2+}, Ba^{2+}, Sr^{2+}, and HCO_3^-. The presence of such ions may allow the deposition of other scales e.g. $BaSO_4$, and $SrSO_4$.

Table 5 compares the solubility of $BaSO_4$, $SrSO_4$ and anhydrite $CaSO_4$ in pure water at 25°C (1 atm) [23]. In general, Table 6 shows that the increasing order of sulfate salt solubility is $BaSO_4$ (least soluble) < $SrSO_4$ < $CaSO_4$. The extreme insolubility of $BaSO_4$ make it very likely that barite scaling will occur if both Ba^{2+} and SO_4^{2-} ions were present in solution at appreciated concentrations. Gypsum is the greatest soluble salt and, as a result, the supersaturation of gypsum will depend largely on the concentration of Ba^{2+}, Sr^{2+} and SO_4^{2-} species presented in solution. In general, the precipitation of a less soluble sulfate has a larger effect on effect on the coprecipitation of a more soluble sulfate, such as $BaSO_4$ on $SrSO_4$ or $SrSO_4$ on $CaSO_4$ [24]. It was postulated that if two or all three sulfates ($BaSO_4$, $SrSO_4$, $CaSO_4$) are supersaturated in the same solution, then simultaneous precipitation will occur until solid-liquid equilibrium is reached, which may have expressed as [24]:

$$\underset{m_1-\Delta m_1}{Ba^{2+}} + \underset{x-\Delta m}{SO_4^{2-}} \leftrightarrow \underset{\Delta m_1}{BaSO_{4(s)}} \qquad (13)$$

$$\underset{m_2-\Delta m_2}{Sr^{2+}} + \underset{x-\Delta m}{SO_4^{2-}} \leftrightarrow \underset{\Delta m_2}{SrSO_{4(s)}} \qquad (14)$$

and

$$\underset{m_3-\Delta m_3}{Ca^{2+}} + \underset{x-\Delta m}{SO_4^{2-}} \leftrightarrow \underset{\Delta m_3}{CaSO_{4(s)}} \qquad (15)$$

where m_1, m_2 and m_3 are the initial concentration of Ba^{2+}, Sr^{2+}, Ca^{2+}, respectively, and x is the initial SO_4^{2-} concentration in the solution, Δm_1, Δm_2, Δm_3 are the amounts of precipitation of $BaSO_4$, $SrSO_4$ and $CaSO_4$, respectively. The sulfate supersaturations are related to ksp as outlined in equation 14 (for gypsum). For anhydrite $CaSO_4$, $SrSO_4$ and $BaSO_4$, equations for the calculation of K_c are given in references 25-27. The amounts of precipitation and supersaturation of the sulfates are related to each other's precipitation and cannot be dealt separately [24].

The scaling tendency for mixing of produced water (PW) and supplied water (SW) of Ward County field (Texas, USA) is studied at 73°F and at 415 psi. The chemical composition of both waters is given in Table 5 [28].

The gypsum scaling tendency as a result of commingling of produced water (PW) and supplied water (SW) is given in Table 5. The results indicated that gypsum will form all over the specified ratio between the two waters. The predicted results of our method are in good agreement with the Oddo and Tomson predictions [1], as well as with the Yeboah et al., [28]. Field observation indicated the deposition of gypsum under the specified conditions [28].

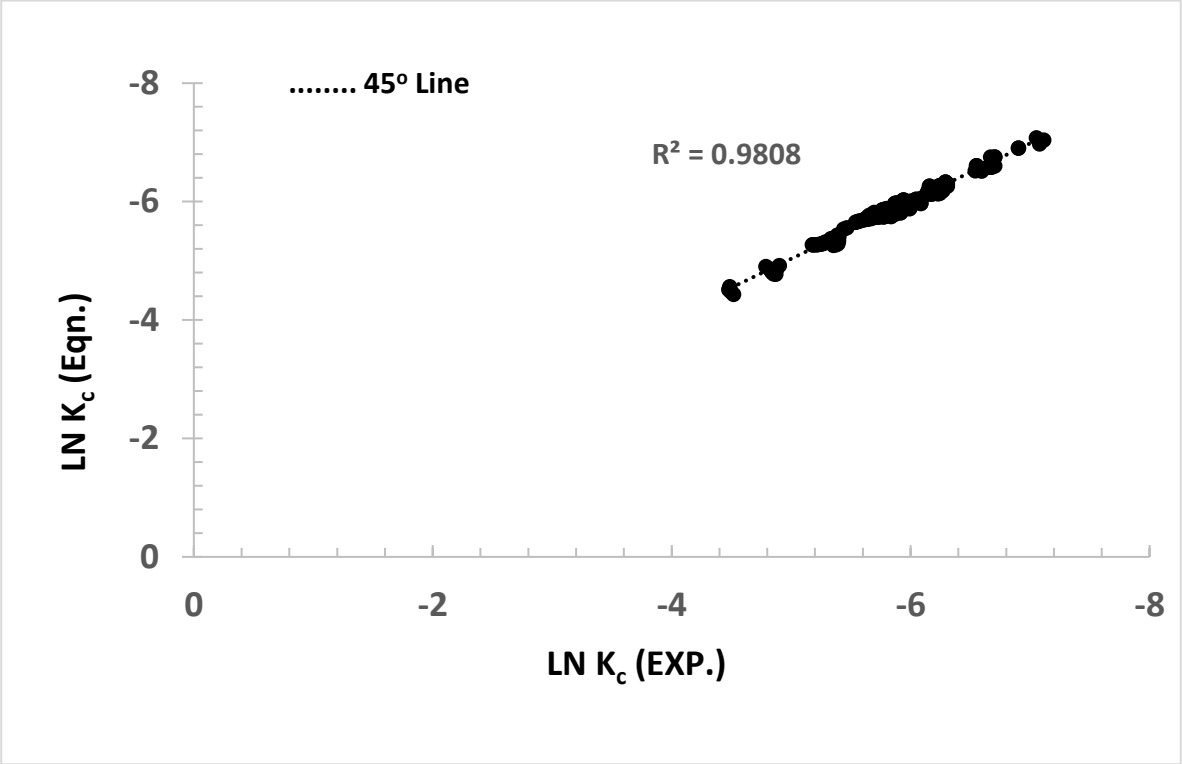


Figure 1 Comparison between solubility product constant obtained from experimental values and model predictions

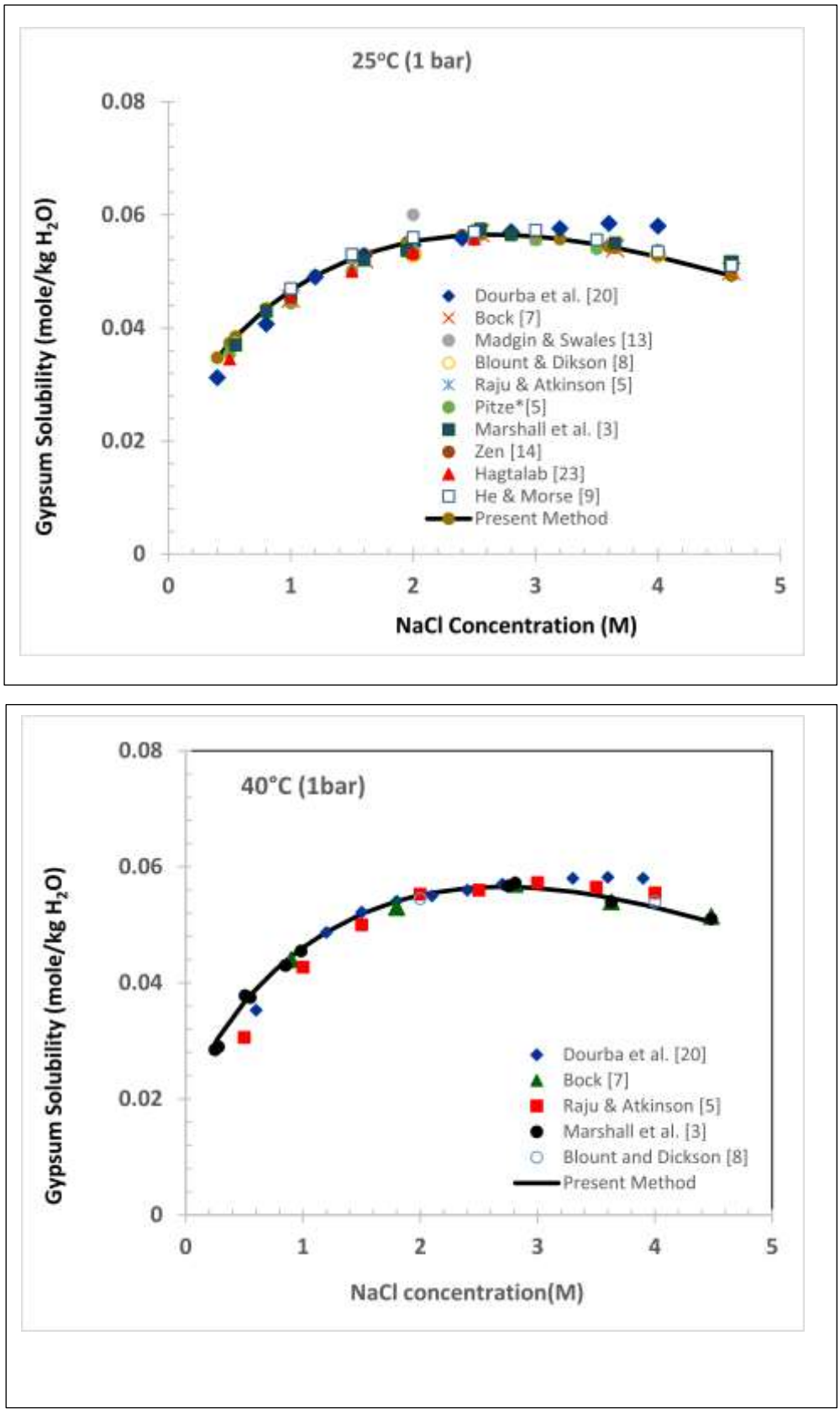
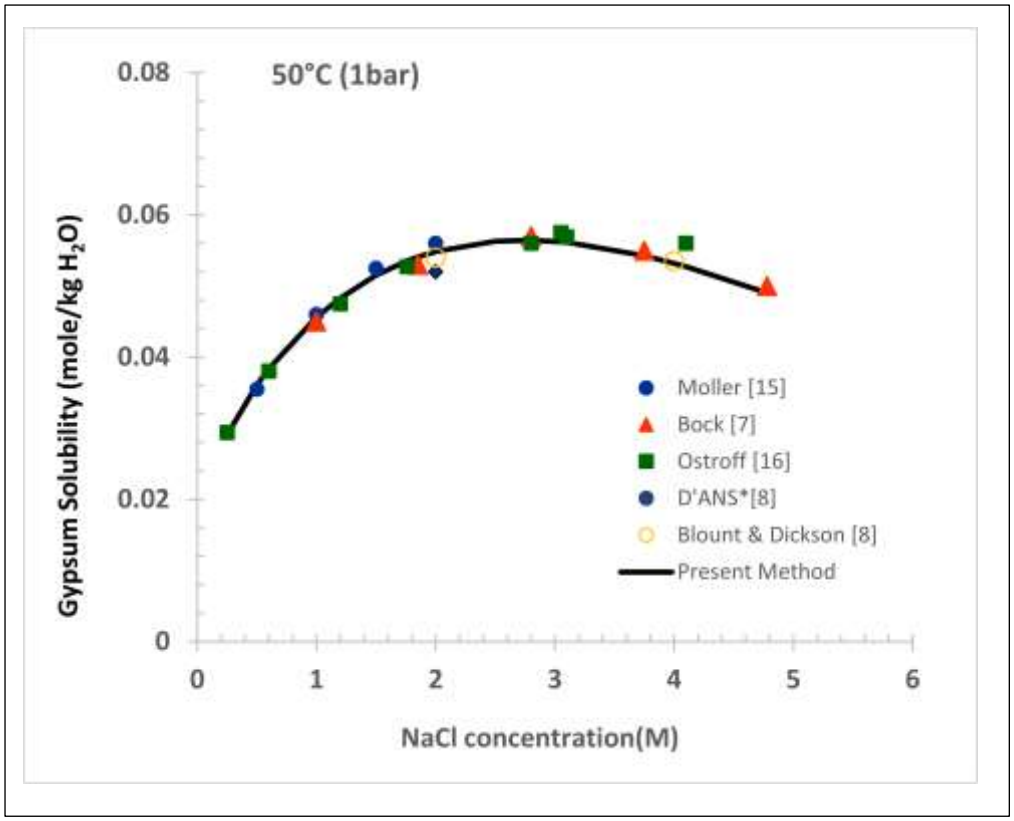


Figure 2 Comparison of predicted gypsum solubility in NaCl solution with experimental results at 25°C and 40°C (1 bar).



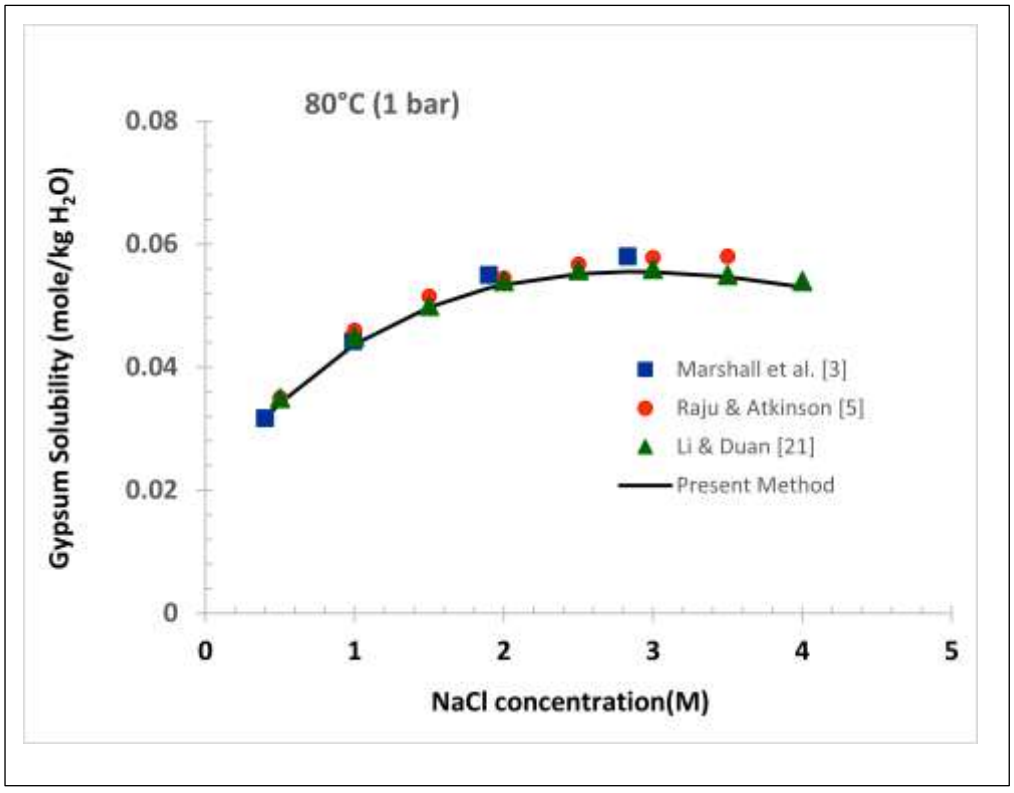


Figure 3 Comparison of predicted gypsum solubility in NaCl solution with experimental results at 50°C and 80°C (1 bar).

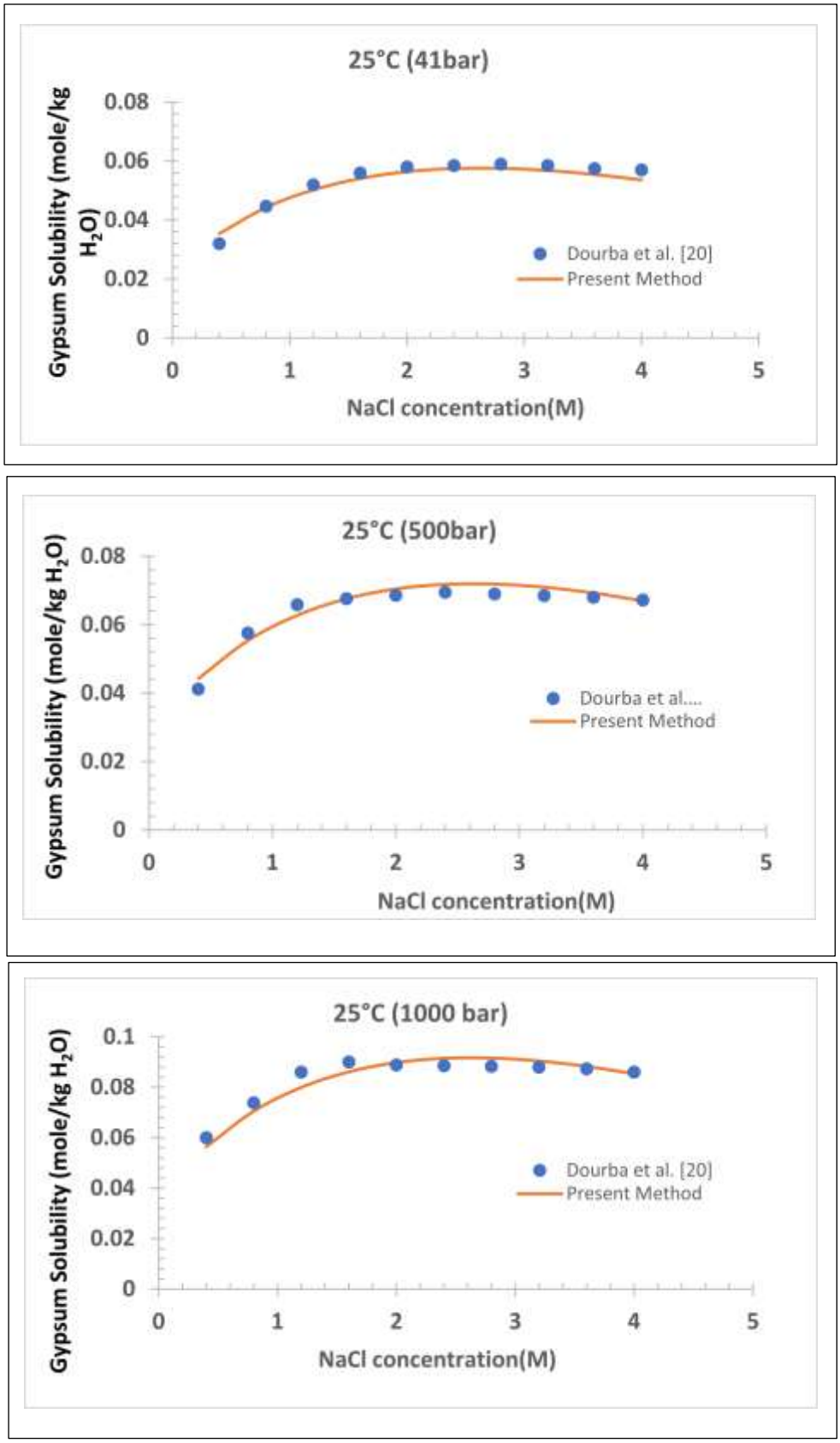


Figure 4 Comparison of predicted gypsum solubility in NaCl solution with experimental results at 41 bar, 500 bar and 1000 bar (25ºC).

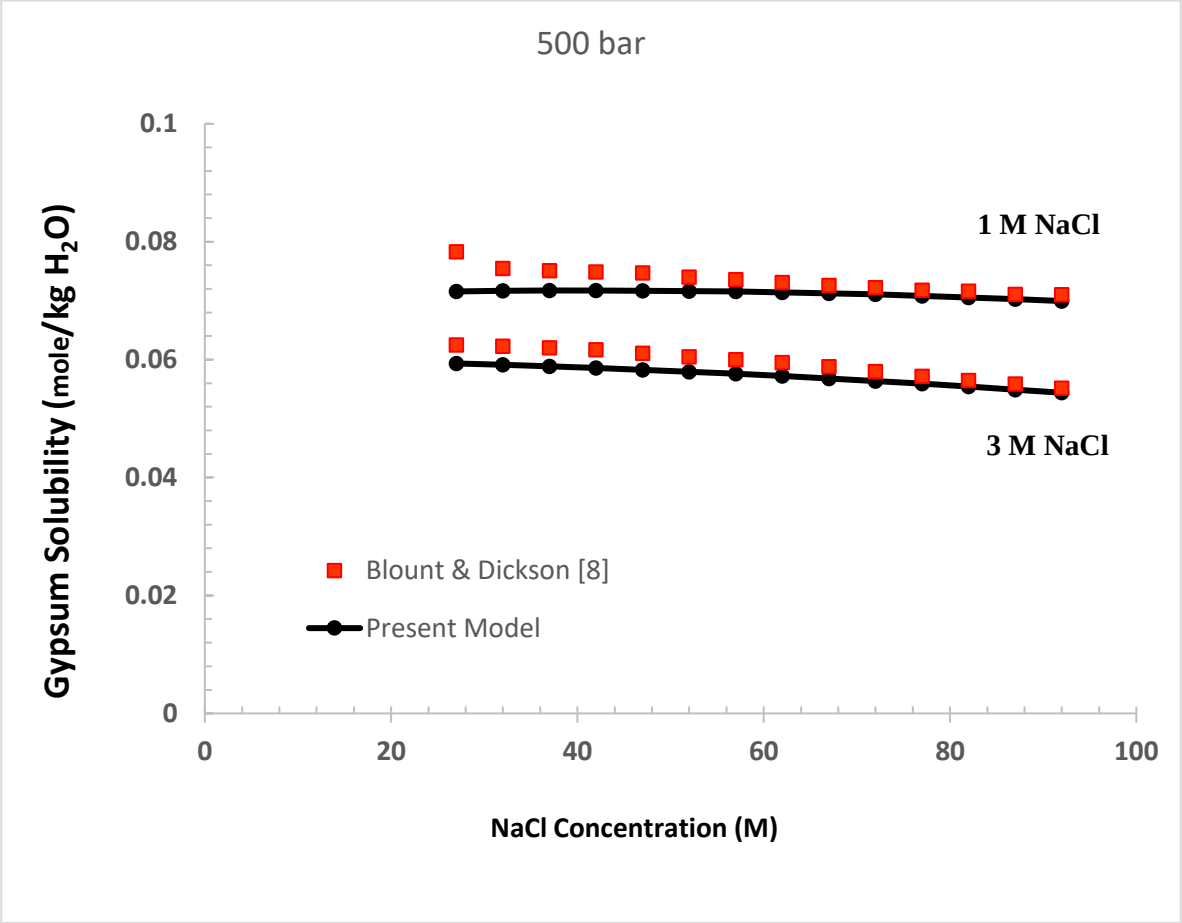


Figure 5 Comparison of predicted anhydrite solubility in NaCl solution with experimental results at 500 bar.

Table 1 Numerical Parameters for equation 11

Parameter	Value	SE Coef	T	P
A_1	- 8.2788	0.1397	-59.25	0.000
A_2	- 0.002983	0.003340	-0.89	0.373
A_3	0.00001978	0.000002646	-0.75	0.455
A_4	0.000969	0.00005720	11.14	0.000
A_5	- 0.997	0.06083	-15.41	0.000
A_6	3.17	0.1626	9.18	0.000
A_7	0.00266	0.0003287	49.37	0.000

S = 0.148892 R-Sq = 98.9% R-Sq(adj) = 98.9%

Table 2 Statistical and regression parameters of the developed model for gypsum solubility prediction.

Statistical Parameter	Value
R^2	0.9812
Median Absolute Deviation *MAD*	1.5E-3
Mean Squared Error *(MSE)*	3.242E-06
Root Mean Squared Error *(RMSE)*	1.8E-3
MAPE	2.63
Number of data	260

Table 3 Average deviation between the predicted model and literature values at different conditions and 1 bar.

	Temperature (°C)	Pressure (bar)	NaCl Concentration (M)	Number of Data	MAPE
Marshall et. al [3]	25-80	1	0.25-4.48	34	2.90
Raju and Atkinson [5]	25-80	1	0.3-4	40	4.79
Pitzer**[5]	25	1	0.5-4	8	3.00
Bock [7]	25-50	1	1.0-4.0	15	7.32
Blount & Dickson [8]	27-92	1	1.0-4.0	34	8.53
D'Ans*[8]	30-50	1	2.0-4.0	3	10.79
He & Morse [9]	25	1	0.5-5	9	3.6
Zhang et al. [10]	37	1	0.5-4.5	9	4.93
Moller [15]	50	1	0.5-4.5	9	5.22
Ostroff [16]	50	1	0.25-4.1	9	2.77
Dourba et.al [20]	25-40	1	0.4-4	22	3.49
Li and Duan [21]	80	1	0.5-4.5	9	5.7
Haghtalab [23]	25-35	1	0.5-3	12	3.95

Table 4 Average deviation between the predicted model and literature values at different conditions and 41, 500 and 1000 bar.

	Temperature (°C)	Pressure (bar)	NaCl Concentration (M)	Number of Data	MAPE
Dourba et al. [20]	25-40	41	0.4-4.0	20	3.76
	25-40	500	0.4-4.0	20	3.35
	25-40	1000	0.4-4.0	20	5.62
Blount and Dickson [8]	27-95	500	1-3	28	3.36

Table 5 Comparative solubilities (in water) at 25°C (1 bar) [22].

Scale	Solubility / *mg/L*
$BaSO_4$	2.3
$SrSO_4$	129
$CaSO_4$ (gypsum)	2080

Table 6 Water chemical analysis and predicted gypsum scaling tendency [25].

mg/L	**Produced Water (PW)**	**Supply Water (SW)**
K^+	-	-
Na^+	85,190	42,800
Ca^{2+}	19,200	1,760
Mg^{2+}	2,544	1,224
Ba^{2+}	-	-
Sr^{2+}	-	-
Cl^-	170,000	65,000
HCO_3^-	439	140
SO_4^{2-}	3,300	10,500
Composition %	3	97
Downhole condition		
Temperature (^oF)	73	
Pressure (Psia)	415	
Predicted scaling tendency		
Yeboah et al. [25] SI	0.2 (Scale)	
Oddo & Tomson [1] SI	0.18 (Scale)	
Present Method SR	2.4 (Scale)	
Field observation	Scale	

SI = Saturation Index.

4. Conclusions

An easy and reliable method useful for gypsum scaling potential at various water compositions, temperature, and pressures covering oilfield conditions is presented. The method is developed to help identifying the potential scaling problems of gypsum associated with formation and/or injection water.

Based on this simple model validated from experimental data, the temperature, pressure and salinity all have significant effects on the solubility of calcium sulfate. The solubility of gypsum decreases as temperature increases and increase as pressure increase. Addition of NaCl to the solution increase gypsum solubility up to about 3 molality of NaCl, adding more NaCl beyond that decreases its solubility.

The reliability of the present method was tested over wide range of temperature, pressure and NaCl concentrations, and the predicted solubility data was in good agreement with sound experimental data

Examples of use of this model were applied to oilfield brines, and the predicted scale results are in excellent agreement with other models and field observation.

The simplicity of the predictive method (only water chemistry, temperature and pressure are required) together with good performance obtained for the systems investigated, make the model useful tool to study gypsum scale formation.

References

1. Oddo, J. E.; Tomson, M. B. Why scale forms in oilfields and methods to predict it. SPE Production & Facilities 1994, 9, 47-54.
2. Marshall, W. L.; Slusher, R. Thermodynamics of calcium sulfate dehydrate in aqueous sodium chloride solutions, 0 to 110ºC, J. Phys. Chem. 1966, 70(12), 4015-4026.
3. Marshall, W. L., Slusher, R.; Ernest V.; Jones, J. Solubility and thermodynamic relationships for CaSO4 in NaCl-H2O Solutions from 40ºC to 200ºC, 0 to 4 molal NaCl. Journal of Chemical and Engineering Data 1964, 9, 187-191.
4. Carlberg, B. L.; Matches, R. P. Solubility of calcium sulfate in brine, SPE paper 4353 presented at the oilfield chemistry symposium of the Society of Petroleum Engineers of AIME, Denver, CO, May 24-25, 1973.
5. Raju, K. U. G.; Atkinson, G. The thermodynamics of scale mineral solubilities. 3. Calcium sulfate in aqueous NaCl, J. Chem. Eng. Data, 1990, 35, 361-367.
6. Block, J.; Waters, O. The $CaSO_4$-Na_2SO_4-NaCl-H_2O System at 25ºC to 100ºC, Journal of Chemical and Engineering Data 1968, 13, 336-344.
7. Bock, E. On the solubility of anhydrous calcium sulphate and of gypsum in concentrated solutions of sodium chloride at 25, 30, 40, and 50ºC. Canadian Journal of Chemistry, 1962, 39, 1746–1751.
8. Blount, C.; Dickson, F. Gypsum-Anhydrite equilibria in systems $CaSO_4$-H_2O and $CaSO_4$-NaCl-H_2O, American Mineralogist 1973, 58, 323-331.
9. HE, S.; Morse, J. W. Prediction of halite, gypsum, and anhydrite solubility in natural brines under subsurface conditions, Computers & Geosciences 1993, 19, 1-22, 1993.
10. Zhang, Y.; Yang, Z.; Guo, D.; Geng, H.; Dong, C. Effect of chloride salts and bicarbonate on solubility of CaSO4 in aqueous solutions at 37oC, Procedia Environmental Sciences 2013, 18, 84 – 91.
11. Glew D. N.; Hames, D. A. Gypsum, sodium pentacalcium sulfate, and hydrite solubilities in concentrated sodium chloride solutions, Can. J. Chem. 1970, 48(23), 3733-3738.
12. Shukla, J.; Mohandas, V. P.; Kumar, A. Effect of pH on the solubility of $CaSO_4.2H_2O$ in aqueous NaCl solutions and physicohemical solution properties at 35oC, J. Chem. Eng. Data 2008, 53(1), 2797-2800.
13. Madgin, W. M.; Swales, D. A. Solubilities in the system $CaSO_4$.NaCI-H_2O at 25ºC and 35ºC, J. Appl. Chem. 1956, 6, 482-487.
14. AN Zen, E. Solubility Measurements in the System $CaSO_4$-NaCl-H_2O at 35°, 50°, and 70°C and one atmosphere Pressure, Journal of Petrology, 1965, 6, Part I, 124-16.
15. Moller, N. The prediction of mineral solubilities in natural waters: A chemical equilibrium model for the Na-Ca-Cl-SO_4-H_2O system, to high temperature and concentration, Geochimica et Cosmochimica Acta, 1988, 52, 821-837.
16. Ostroff, A. G.; Metler, A. V. Solubility of calcium sulfate dehydrate in the system NaCl-MgCl2-H2O from 2 8ºC-70ºC. J Chem Eng. Data 1966,11, 346-350.
17. Millero, F. The effect of pressure on the solubility of minerals in water and sea water. Geochimica et Cosmochimica Acta 1982, 46, 11-22.
18. Atkinson, G.; Mecik, M. The chemistry of scale prediction. J. Petrol Sci. Eng. 1977, 17, 113-121.
19. Garcia, A. V.; Thomsen, K.; Stenby, E. H. Prediction of mineral scale formation in geothermal and oilfield operations using UNIQUAC model, Part I. Sulfate scaling minerals. Geothermics 2005, 34, 61-97.
20. Doubra, P.; Kamran-Pirzaman, A.; Mohamadi, A. H.; Hassanalizadeh, R. Thermodynamic modelling of scale (Calcite, Barite, Anhydrite and Gypsum) deposition from brine, Journal of molecular Liquids 2017, 230, 96-103.
21. Li, J.; Duan, Z. A thermodynamic model for the prediction of phase equilibria and speciation in the H2O-CO2-NaCl-CaCO3-CaSO4 system from 0 to 250ºC, 1 to 1000 bar with NaCl concentrations up

to halite saturation. Geochica et Cosmochimica Acta 2011, 75, 4351-4376
22. Patton, C. C. Applied Water Technology, 2nd ed.; Published by Campbell petroleum series, USA, 1995: pp. 90-101.
23. Haghtalab, A.; Kamali, M. K.; Shahrabadi, A. Prediction mineral scale formation in oil reservoirs during water injection. Fluid Phase Equilibria 2014, 373, 43-54.
24. Yuan, Y.; Todd, A. C. Prediction of Sulfate scaling tendency in oilfield operations. SPE Production Engineering, SPE 18484, 1991, 63-72
25. Ezuber, H. Simple mathematical model for predicting anhydrite calcium sulfate scale deposition in brines. 8th International Conference on Modeling Simulation and Applied Optimization (ICMSAO), Bahrain, 15-17 April, IEEE, 2019.
26. Ezuber, H. Prediction of strontium sulfate scale formation in oilfield environment. Journal of ASTM international, 2007, 4(6), JAI100958.
27. Ezuber, H. Prediction of barium sulfate scale formation in oilfield environment. Journal of ASTM international, 2008, 6(2), JAI102049
28. Yaboah, Y.; Samuah, S.; Saeed, M. Prediction of carbonate and sulfate scales in oilfield, SPE Middle East Oil Technical Conference & Exhibition, Bahrain, 3-6 April, 1993, SPE 25586, pp. 577-586.

Theme 12: Sustainable Environmental Management

Algerian Contaminated Groundwater Treatment by Using Acacia Gum: Organic Pollution Removal

Rania Remmani [1,*], Rachid Makhloufi [1], Malek Meladi [2], Ruiz Canales Antonio [2], Leonardo Piccinetti [3] and Ahmed Boutarfaia [1]

[1] Applied Chemistry Laboratory, University of Biskra, Algeria;

[2] Engineering Department, Miguel Hernández University, Spain;

[3] Europe for Business Ltd, Warrington, United Kingdom;

Corresponding author: rania.remmani@univ-biskra.dz; Tel.:+213656560445.

Abstract: The aim of this study was to investigate the efficiency of organic pollution removal from Illizi groundwater (Algeria) using Acacia gum powder as a bio-adsorbent; The adsorbent was characterized by XRD analysis which show that this prepared adsorbent has no mineral composition, furthermore, the FTIR analysis completely prove the XRD results. Further, the adsorption behavior of produced material was tested by performing batch adsorption tests in contaminated water samples using a ratio of 1:1 (g/L) for 24 hours. groundwater analysis indicated that Acacia gum improved the pH value to neutral and removal a high quantity of organic pollutants; Additionally, the treated water sample has the same excellent class suitable for irrigation applications according to the Wilcox diagram. In consequence, the present study suggests an effective, eco-friendly and economical adsorption process intending to mitigate environmental risk sustainably.

Keywords: acacia gum; FTIR; adsorption; groundwater; organic pollution.

1. Introduction

According to the results of the increase of toxic pollutants on water, there exists a directed major concern toward finding reliable and practical solutions in order to reduce its damaging effects on the environment, furthermore it protects human health and environments . In this context, several technologies such photocatalysis, advanced chemical oxidation, membrane separation technologies, and adsorption process were developed .(1)

Adsorption for water treatment has had a long and productive history from BC, it is a surface phenomenon that is defined as the increase in concentration of a particular component at the surface or interface between two phases. The basic terms shown in fig1; The solid material is referred to as adsorbent, the species that will be adsorbed are named adsorbate. In wastewater treatment, adsorption of organic solutes has been a primary concern in recent years. (2)(3)(4)

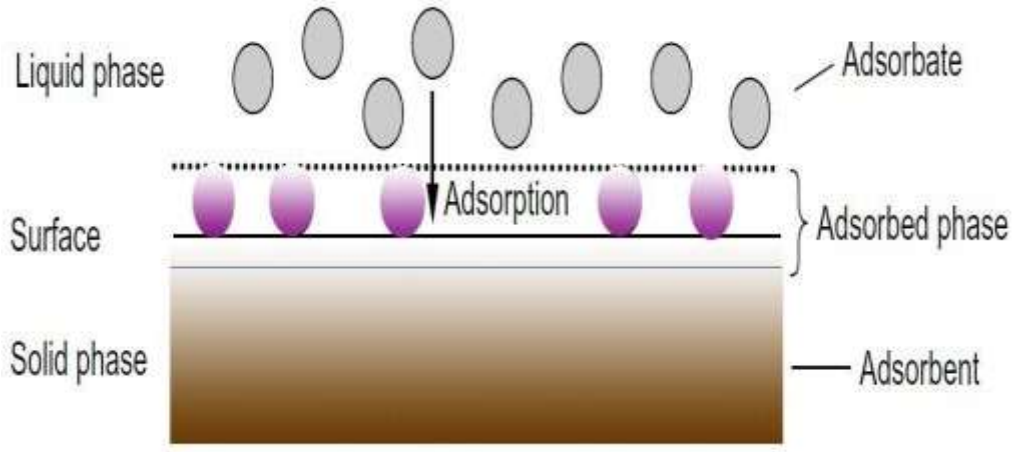


Figure 1. Basic terms of adsorption.(4)

Acacia gum, as a natural adsorbent, is a complex arabinogalactan type polysaccharide which is obtained from the stem and branches of Acacia trees (Fig2); Acacia trees are abundant in central Sudan, central and West Africa, and tropical and semitropical areas of the world; Even though there are more than 1000 species of the genus Acacia gum, only two are significant for commercial purposes: Acacia senegal and Acacia seyal; In modern times, Acacia gum is widely used by industries for its nutritional, pharmaceutical, cosmetic, and surface properties. (2)(5)(6)(7)(8)

The physical properties of Acacia gum may vary depending on the origin and age of trees, the exudation time, and climate. Treatment of Acacia gum after collection such as washing, drying, and bleaching in the sun and storage conditions affected the physical properties of Acacia gum. (5)(9)

Acacia gum improves the antioxidant capacity because it contains several types of amino acid residues such as lysine, tyrosine, and histidine; It affects renal functions through reduction in blood creatinine and urea nitrogen concentrations in diabetic nephropathy patients; It significantly decreased fasting blood glucose levels and glycosylated hemoglobin together with a significant reduction in blood uric acid and total protein concentrations; Acacia gum, as a dietary fiber, helps to reduce body weight and fat deposition. Due to this biological properties of Acacia gum, it may be an efficient agent in water treatment with the adsorption process, although its high water solubility and a relatively low viscosity compared with other gums. (5)

The objective of this work was to show the capacity of Acacia gum powder as naturally efficient adsorbent through organic water pollution removal from Algerian groundwater, Illizi by adsorption phenomena.



Figure 2. Natural Acacia gum on the tree.

2. Materials and methods



Figure 3. Schema of groundwater treatment by acacia gum.

2.1. Acacia gum preparation

The used acacia gum was obtained from a commercial source. Acacia gum powder was prepared by grinding on a porcelain mortar and pestle then sieving by sieve shaker (AS 200, RETSCH, France) to a minimum size < 50 μm, and was dried at 40°C for 5 hours. For Acacia gum powder characterization, XRD and FTIR were used; XRD pattern was obtained by D8 advance diffractometer (Brucker, Germany) with u-K□ radiation (□ = 1.54050 Å) and a scanning speed of

0.004°/S, the analysis of its vibrational spectra was done with Fourier transform infrared spectroscopy using FTIR-Shimadzu 8400s in the range 400-4000 cm-1 as potassium bromide pellet.

2.2. Groundwater treatment

The groundwater samples for this study was from Illizi region, Algeria (DMS coordinates of the place: 26°30'33.965" N 8°28’23.778’’E). This groundwater has been polluted with oil by extraction from local wells.

Groundwater samples for this study were from Illizi region, Algeria (DMS coordinates of the place: 26°30'33.965" N 8°28'23.778"E). This water has been polluted with oil by extraction from local wells. For the adsorption assays, 250 mL maximum capacity leak-proof reaction bottles were used. In each bottle, 100 mL of groundwater and 15 mg of Acacia gum powder were added. The tests were kept in a mechanical shaker for 24 hours at a room temperature of 22°C. After the equilibration period, all the solid materials were filtered.

2.3. Groundwater characterization and suitability for irrigation

The groundwater suitability for irrigation was determined by using the Wilcox Diagram, where the classification of irrigation water is based on different ranges of electrical conductivity (0-800, 800-2000, 2000-3000 and > 3000 micromhos cm-1) and on sodium adsorption-ratio (% Na+) which is defined by the relation shown in Eq.1 , where all the ions are expressed in meq L-1.

$$\%Na=(((Na^{++}K^{+}))/((Ca^{(2+)}+Mg^{(2+)}+Na^{++}K^{+}))*100 \quad \text{Eq.1}$$

Generally, the Wilcox diagram shows the different water classes as Class I " Excellent", Class II " Good", Class III " Eligible", Class IV " poor" and Class V " bad" (Fig4) . Hence, this diagram shows a decreasing water quality trend with an increase in the concentration of sodium percentage and the electrical conductivity. (9)

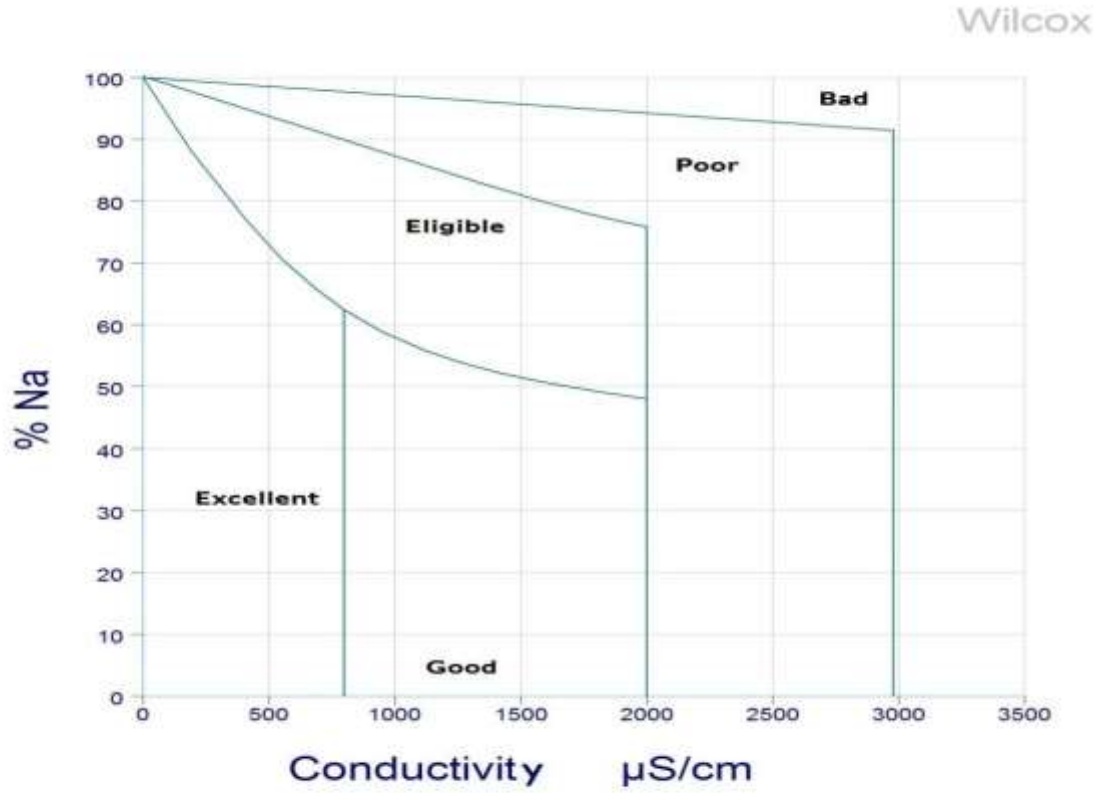


Figure 4. Wilcox Diagram for Conductivity and Sodium percentage.

3. Results and discussion

3.1. Acacia gum characterization

3.1.1. XRD Characterization

The X-ray diffractogram of the used Acacia gum (Fig5) has shown no reflection in all the 2θ scanning due to the amorphous powder that had no mineral composition.

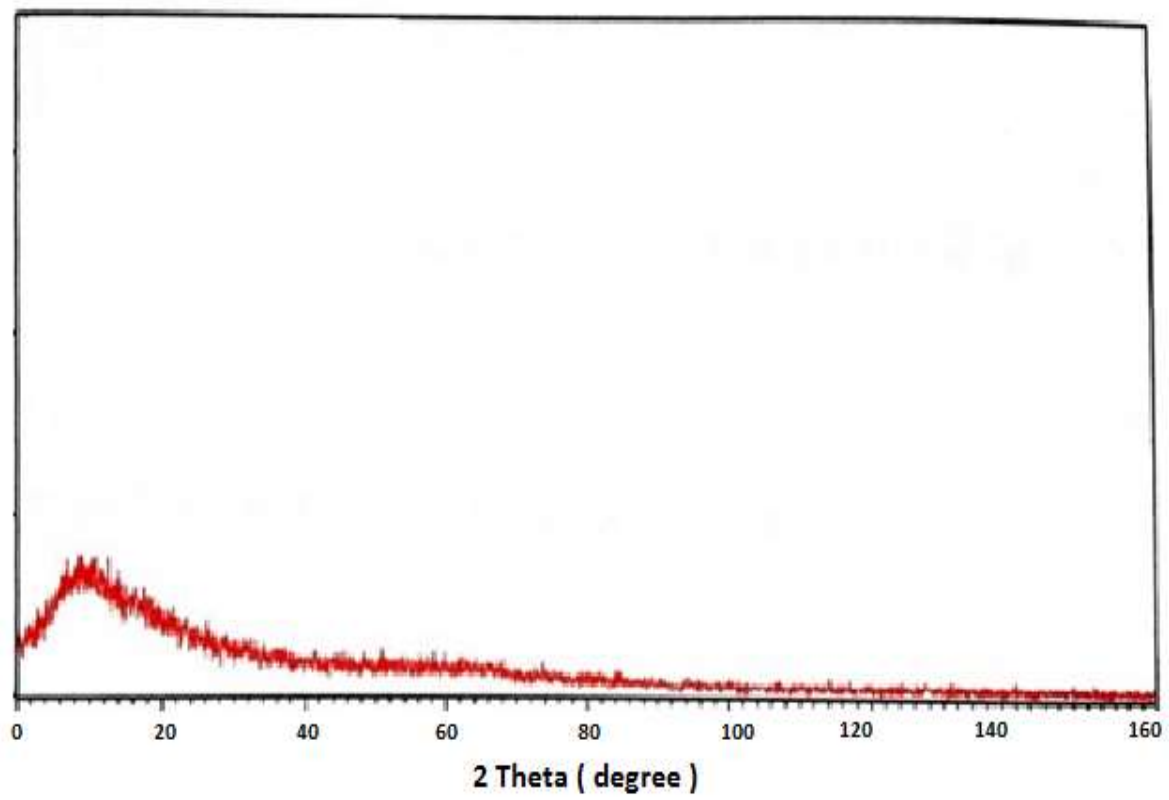


Figure 5. XRD spectrum of Acacia gum.

3.1.2. FTIR Characterization

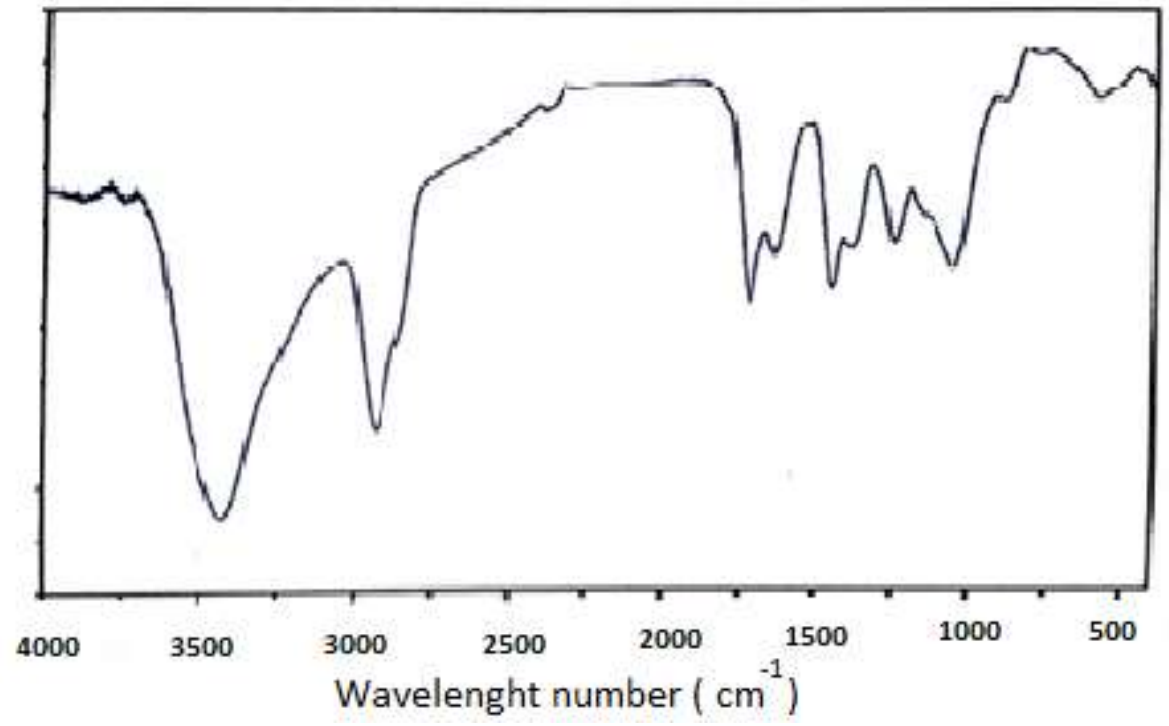


Figure 6. FTIR Spectrum of Acacia gum.

FTIR study of these adsorbent Acacia gum helps in the identification of the bands various forms which are present in the surface of Acacia gum. The broad adsorption at 3500-3600 cm-1 which is correspondent to the free hydroxyl groups (O-H) appears the existence of water. This water refers to the hydratation in the adsorbent Acacia gum. The peak around 2852-2900 cm-1 corresponds to the C-H band of aliphatic -CH2 group. Another peak around 1730-1750 cm-1 corresponds to C=O of aliphatic aldehyde groups. The appearance of symmetric and asymmetric COO^- bands at respectively 1600-1700 cm -1 and 1420-1500 cm-1.

The presence of band at 1080-1220 cm-1 of C-O elongation vibration indicates the possibility of the ester appearance.

3.2. Groundwater Characterization

3.2.1. pH variation

Table 1 shows that before the pollution of the groundwater pH was 7.68 which is a normal value for drinking water. The polluted groundwater pH value was 5.15 that means this water is a polluted water owing to the standard values of pH for drinking water which is always between 6.5 to 9.5, but after the treatment we obtained that Acacia gum improved the pH value (6.70) and the resulted value was normal for drinking water.

Table 1. pH before and after treatment.

Groundwater	Unpolluted	Polluted	Treated
pH	7.68	5.15	6.70

3.2.2. Organic Pollution Variation

The filtration process showed a high capture of adsorbent powder particles and other grain contaminants in the wastewater after the adsorption treatment, yet This physical separation method cannot eliminate all the quantity of Acacia gum, due to the Acacia gum solubility in treated water. For this case of study, a specific method was used to characterize groundwater before and after the treatment; Table 2 and fig7 show that Acacia gum had a high removal efficiency due to the reduction of UV-absorbance of each wavelength related to organic pollution (201; 228 and 260 nm).

Obviously, the experimental results indicate the presence of Carbon-Carbon conjugated bonds of the petroleum molecules structure at the range [200 - 260 nm], these high gaps of UV-absorbance were because of the petroleum removal efficiency by Acacia gum adsorbent.

Table 2. UV-absorbance before and after treatment.

Wavelength (nm)	201	228	260
Polluted Groundwater Absorbance	11	10	3
Treated Groundwater absorbance	0.5	3.2	1.5

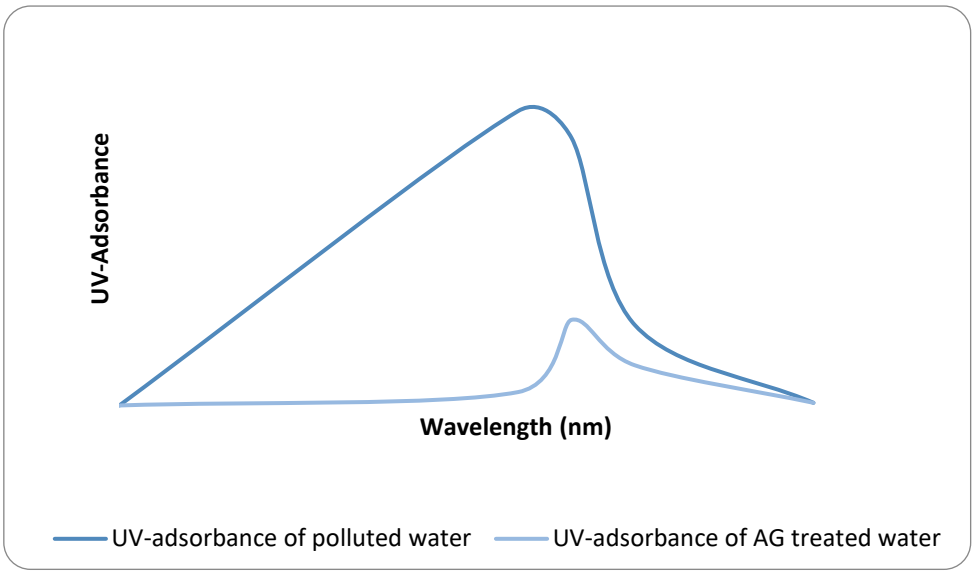


Figure 7. Absorbance of Groundwater before and after treatment.

3.3. Groundwater classes for irrigation

As shown in fig8, the diagram covering the studied samples indicates that these waters present values from 53% to 62% of sodium percentage. Despite the fact that these high sodium percentages are undesirable because of its reduction of water quality, all samples were classed as "Excellent" for irrigation. It can be concluded that organic pollution and the used absorbent didn't change the class of irrigation of the studied groundwater.

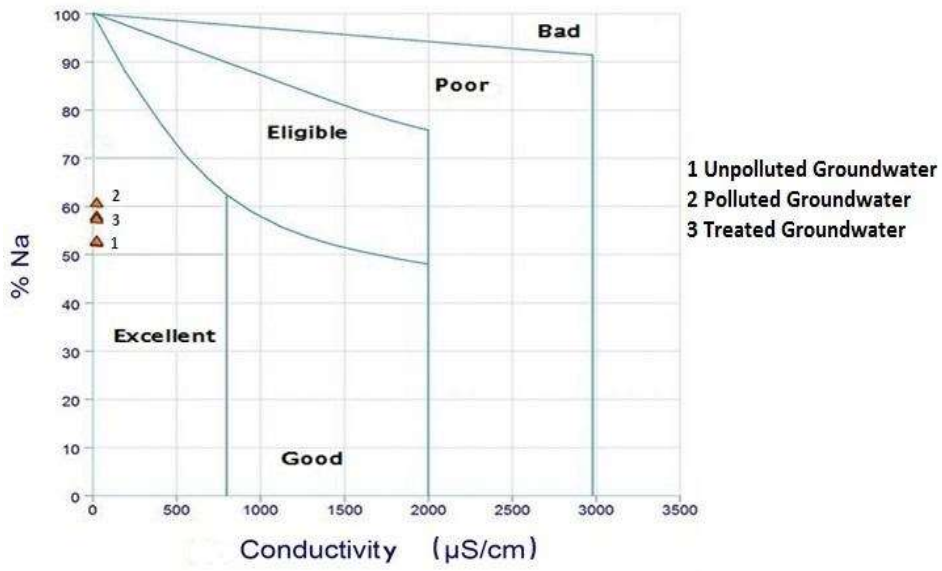


Figure 8. Wilcox diagram showing the suitability of groundwater for irrigation.

4. Conclusions

Acacia gum powder showed a high removal of organic pollution (oil) although acacia gum solubility in water. The organic pollution and the used adsorbent keep the same excellent class for irrigation; the treatment decreased the sodium percentage from 61% to 58% in the same conductivity.

References

1. A review on the adsorption of heavy metals by clay minerals, with special focus on the past decade. UddinMohammadKashif438-462, London , ELSEVIER, 2017, Vol. 308.（1385-8947）.
2. AHMED F. HALBUSZAHRAAH. ATHAB, FALAH H. HUSSEIN ADSORPTION OF DISPERSE BLUE DYE ON IRAQI DATE PALM SEEDS ACTIVATED CARBON. s.l., sadguru publications, 2013.
3. Christian Sanchez Denis Renard, Paul Robert, Christophe Schmitt Structure and rheological properties of acacia gum dispersions. s.l., Food Hydrocolloids ELSEVIER, 2002.
4. Kashif Uddin Authorlinks open overlay panel Mohammad A review on the adsorption of heavy metals by clay minerals, with special focus on the past decade. s.l., ELSEVIER, 2017.
5. Linda Hecini Glossaire de l'eau. s.l., CRSTRA, 2014.
6. PRODUCTION AND CHARACTERIZATION OF GRANULAR ACTIVATED CARBON FROM ACTIVATED SLUDGE. Z. Al-QodahR.Shawabkah01, Brazil, Brazilian Journal of chemical Engineering, 2009, Vol. 26. （0104-6632）.
7. Rashed Mohamed Nageeb Adsorption Technique for the Removal of Organic Pollutants from Water and Wastewater. s.l., IntechOpen, 2012.
8. Samuel D. FaustOsmanM. Aly Adsorption Processes for water treatment. s.l., Butterworths, 1987.
9. Samuel D.Faust Osman M. Aly adsorption processes for water treatment . united states of america , Butterworths, 1987.
10. Suryadi ismadjiFelyciaEdi Soetaredjo, Aning Ayucitra Clay Materials for Environmental remediation . New york , Springer, 2015.
11. WilcoxL.V. Classification and use of irrigation waters . Washington, D.C., US Department of Agriculture Circular 969, 1955. （19620-642240）.
12. WorchEckhard Adsorption Technology in Water Treatment. s.l., DE GRUYTER, 2012.

Application of sentinel 2 to evaluate colored dissolved organic matter algorithms for inland water bodies in Jordan

Nidal M. Hussein [1], Mohammed N. Assaf [2,*] and Sohib S. Abohussein [3]

[1] Department of Civil Engineering, University of Petra, Amman – Jordan, ORCID:0000-0002-4188-7694, 201911339@uopstd.edu.jo;
[2] School of Natural Resources Engineering and Management, German Jordanian University, Amman, Jordan, ORCID: 0000-0002-4003-8690 ;
[3] Department of Civil Engineering, University of Petra, Amman –Jordan,
***** *Corresponding authors: nidal.hussein@uop.edu.jo ; 201911339@uopstd.edu.jo ; m.assaf@gju.edu.jo; Tel.:00962798893942.*

Abstract: The purpose of this article is to investigate the possibility of employing Multispectral Imager's (MSI) on Sentinel 2 to identify the colored dissolved organic matter (CDOM) in inland water. CDOM can be defined as an essential indicator of water quality as it has a key role in biogeochemical processing. This study held in three important Jordanian dams. Mujib, Wadi Al Arab, and lastly King Talal Dam. From these three dams, sixty water samples were taken fairly. The prediction models were validated using the remaining samples after the models were calibrated using forty samples. The predictive models were tested using the remaining samples .The results show that the sentinel 2 blue to green band (B2/B3) has provided the best CDOM retrieval algorithm with an accuracy coefficient of determination R^2= 0.8155, root-mean-squared error RMSE= 1.754 m^{-1}.The study showed that Sentinel 2 data might be used to determine CDOM in a variety of inland water body quality ranges, meaning that remote sensing can be a valuable tool for inland water quality monitoring. This study contains empirical data that can be utilized as a starting point for further research that includes more sites and circumstances.

Keywords: colored dissolved organic matter; remote sensing; Sentinel-2; Jordan dams

1. Introduction

Jordan is a relatively small country with limited natural resources. Jordan is categorized between arid and semi-arid countries [1]. According to recent statistics and reports, Jordan is the 3rd country in the world that suffers from freshwater storage [1-4]. Jordan water demand is around 900 MCM/yr; 75 % of it arises in the Jordan River Basin. Jordan's total dam capacity, including the desert dams, is projected to be 350 MCM. In the north and middle Jordan valleys, seven dams have been built, with a combined storage capacity of 270 MCM. Arab, Ziglab, King Talal, Karameh, Shueib, Kafrein, and Al Wehdah Dams are among them. In addition, three dams have been built in the southern Ghors: Wala, Mujib, and Tanner, with a total live storage of 30 MCM [2].

Jordan Inland water is considered a vital and primary water supply for drinking and irrigation [5]. The rivers, dams, and reservoirs are the most common examples of surface water, and they have significant significance for the environment's most valuable components (VECs). In addition, the dams play an essential role in providing good conditions for species, hydrological, climate-control, carbon-cycle, and nutrient-cycle processes [1].

Inland waters can be broadly described as the principal source of carbon delivery and transfer from ecosystems to aquatic environments [6]. Studies have shown that Inland water releases approximately 1.8 gigatons of Carbon dioxide to the atmosphere and transfer an equal amount of carbon to ocean waters [7]. This flow is higher than previously predicted, with dissolved organic carbon (DOC) from terrestrial ecosystems accounting for more than half of it [8]. As a result, riverine systems (streams and rivers) control a large portion of DOC export from terrestrial to aquatic ecosystems and the geographical and temporal variability of freshwater DOC in drainage watersheds [9]. The principal interaction regions are shallow coastal and estuarine environments to transfer carbon from terrestrial to the aquatic ecosystem.

Colored dissolved organic matter (CDOM) is the optically measurable component of dissolved organic matter in water, which can also be defined as chromophoric dissolved matter [10-14].

The CDOM peak absorption is found in the blue wavelength region and diminishing to around zero in the red region [15]. Several investigations have detected that COD concentrations are highly corrected to CDOM levels in both inland water and costal [16, 17]. Therefore, estimating CDOM absorption through remote sensing techniques will provide a better understanding of carbon cycling.

The term "satellite remote detection techniques" refers to a method for determining geophysical boundaries using electromagnetic radiation reflected or created by the earth [18]. Because of the optical properties of water and the presence of optically dynamic elements, remote sensing offers enormous potential for water-quality monitoring, particularly in Jordan, which has a high number of water-vulnerable bodies.

Water remote detection relies on immediate watercolor perception rather than water tests. It quantifies the relationship between watercolor and ingredients interacting with solar-powered radiation to alter the energy range of reflected radiation from water bodies. Optical water-quality parameters are the term used to describe these elements.

CDOM existing has a significant impact on water column optical properties as it interacts with solar radiation; therefore, the CDOM concentration in the surface water can be determined by remote sensing. Using remote sensing to estimate CDOM can reduce testing costs and provide a spatial and temporal quantification of CDOM, which are the main constraints of traditional field-based water quality measurement [19]. Several multispectral satellites have been used to assess the inland water quality each as Landsat series, Modes, and SPOT XS [20-23]. However, those satellites images had limited by temporal and spatial resolutions. The recently launch Sentinel 2 instrument provide an enhancement in temporal resolution with 5 days' revisit period and better spatial resolution with 10 m and 20 m in wavelength range 490-860 nm [24]. These improved satellite parameters open the door for more investigations of Sentinel-2 potential for estimating inland water quality where few previous studies have used it to developed same works in the lakes [25-28].

The purpose of this research is to assess the utilization of multispectral imaging techniques for monitoring colored dissolved organic materials (CDOM). According to recent studies, a high concentration of CDOM would result in an adverse effect on water purity and quality. Therefore, this research will eventually lead to developing a computational model capable of forecasting CDOM concentrations without the need for in situ measurements and remote monitoring of CDOM concentrations across Jordan's inland water bodies.

2. Materials and Methods

2.1 Study area's

Three Jordanian dams have been chosen for investigation in this study (figure 1). The dams were chosen because of their critical role in Jordan's water sector and the importance of their geographic position, and the variance in CDOM concentration in their water.

The first one is King Talal Dam (KTD), one of the essential projects in the water sector in Jordan. The reason behind that is the size of King Talal Dam and its important role in the Jordanian agricultural sector. According to recent studies, King Talal Dam measures 92 meters in height and 330 meters in width. It has a yearly discharge capacity of 86 million cubic meters and a storage capacity of 75 million cubic meters. This dam is situated in the highlands of Jordan's northern region, on the other side of the Zarqa River. Construction on the dam began in 1971 and was finished in 1972. Building the King Talal dam was an excellent idea for Jordan's agricultural development; it helped increase agricultural production in the Jordan Valley [2]. The water quality of the dam has been significantly affected by the discharge of wastewater plants in the dam's artery [29-31].

Second, Jordan's Wadi Al-Arab Dam (WAD) is located north of Jordan and is considered a vital source of water in this area. This massive dam, which was completed in 1987, was designed to contain 20 million cubic meters of water [32]. The reservoir catchment area is 262 Km^2. This dam's primary goal is to irrigate agriculture in Jordan Valley. Wadi AL- Arab dam water slightly comes from precipitation and the king Abdullah Canal which received water from Wadi Arab and the Yarmouk

River. This dam receives about 400 mm of rain each year, with the majority of the precipitation falling between October to May [33].

Finally, there's the Mujib Dam (MD). The MD is in the Wadi al-Arab, located south of Amman, Jordan's capital city. The dam's capacity is estimated to be around 35 million cubic meters. The dam is a composite dam consisting of a roller compacted concrete (RCC) middle section and a clay core rockfill (CCR) section at both abutments. The construction for this dam started in 1999 and was finished in 2004. The average yearly rainfall at the Mujib Dam is around 70 mm. The water quality in the Al Mujib dam received slightly higher quality than the other Jordanian dam. Therefore, the Mujib dam is mainly used for drinking water and irrigation. In the lower basin, the average temperature is 40°C in summer and 15°C in winter, whereas in the upper basin, the average temperature is 35°C in summer and 10 °C in winter [34].

2.2 Water Sampling and analysis

Ground-based sampling was taken on July 15th, 2019 from KTD, June 30th, 2019 from MD and June 25th, 2019 from WAD. Sixty water samples were taken fairly from these three dams for the purpose of the experiment. Water samples were collected 20 cm below the water's surface and placed in cleaned bottles before being submitted to Petra University lab for analysis. The samples' location was acquired using Global Positioning System (GPS) device. The sampling points' distribution of each dam is shown in figure 1. In the laboratory, CDOM was determined using a spectrophotometer with Mili-Q water as baseline correction [35].

2.3 Sentinel 2 optical sensor and images processing

The Sentinel 2 multispectral instrument (MSI), with 290 km swath width and 12-bit radiometric resolution, has thirteen spectral bands ranging from 430 nm to 2320 nm in the visible (B1-B4), red-edge (B5-B7), near-infrared (B8 and B8a) and shortwave infrared (B9-B12) spectrum region (Table 1). The Sentinel 2 contains two identical satellites, Sentinel-2A and Sentinel-2B, that were launched in 2015 and 2017, respectively. These twin polar-orbiting satellites are running in the sun-synchronous orbit and phased at 180; this provides a high temporal resolution (5 days' revisit time) with two satellites at the equator. Also, the sentinel-2 has relatively high spatial resolutions; three bands with 60 m, six bands with 20 m and four bands with 10 m. Moreover, the MSI sensor improves spectral abilities that comprise beneficial bands for land observations, such as the red-edge bands for water and vegetation studies.

The MSI pictures were taken on the same day as the field sample to avoid any time gap between the in-site measurement and the satellite, which could alter the results. Three data cloud-free images were obtained from the Sentinels Scientific Data Hub (table 2). The Sentinel 2 Level 1-1C (L1C) data contained scaled top of atmosphere reflectance data that resampled to 20 m pixel size using the Sentinel Application Platform (SNAP) version 8.0. Atmospheric conditions significantly affect satellite data and lead to inaccurate using of reflectance data if it is inappropriately corrected. Therefore, the current study was used atmospheric and topographic correction (ATCOR), which perceived as one of the most accurate atmospheric correction methods and is widely used in water applications [36].

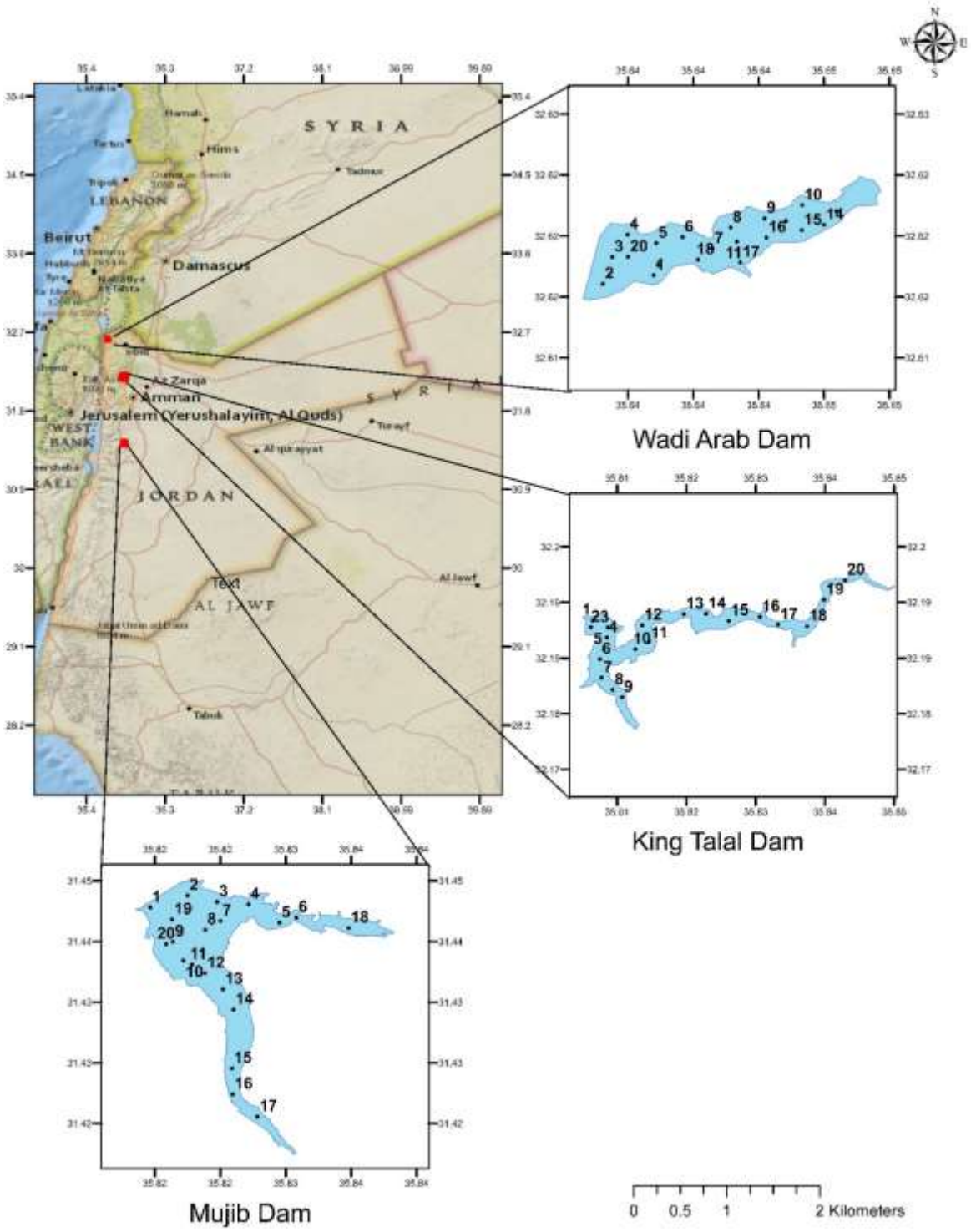


Figure 1: Study areas and sample location points

Table (1): Spectral bands and spatial resolution of Sentinel-2A and Sentinel-2B MSI

Band Number	Spectral Range	Resolution (m)	Bandwidth (nm)	S2A Central wavelength (nm)	S2B Central wavelength (nm)
B1	coastal/aerosol	60	20	442.7	442.2
B2	blue	10	65	492.4	492.1
B3	green	10	35	559.8	559.0
B4	red	10	30	664.6	664.9
B5	VRE	20	15	704.1	703.8
B6	VRE	20	15	740.5	739.1
B7	VRE	20	20	782.8	779.7
B8	NIR	10	115	832.8	832.9
B8a	NIR	20	20	864.7	864.0
B9	WV	60	20	945.1	943.2
B10	cirrus	60	30	1373.5	1376.9
B11	SWIR	20	90	1613.7	1610.4
B12	SWIR	20	180	2202.4	2185.7

Table (2): Sentinel 2 images used in this research

Location	In situ visiting date	Identifier	Sentinel 2 image date	Cloud cover
KTD	2019-07-15	S2B_MSIL1C_20190715T081609_N0208_R121_T36SYA_20190715T120216	2019-07-15	1.4111
Mujeeb	2019-06-30	S2A_MSIL1C_20190630T081611_N0207_R121_T36RYV_20190630T102130	2019-06-30	1.3674
Wadi Al Arab	2019-06-25	S2B_MSIL1C_20190625T081609_N0207_R121_T36SYB_20190625T120443	2019-06-25	0.0018

2.4 Model calibration and validation

To develop the best fit CDOM retrieval model, we tested the linear, exponential, power and logarithmic for a single band and several combinations of two-band ratio models. The 60 samples were randomly divided into 40 samples for calibration and the rest (20 samples) for validation. The coefficient of determination (R^2) was used to evaluate the goodness of fit of the calibrated model. Then, the accuracy of the predicted models was compred using four statistical indicators: coefficient of determination (R^2), root-mean-squared error (RMSE), Mean Absolute Error (MAE), and bias.

$$\text{RMSE}= \sqrt{\frac{1}{N}\sum_{i=1}^{n}[xi^{predicted} - xi^{measured}]^2} \quad (1)$$

$$\text{MAE}=\frac{\sum_{i=1}^{n}|xi^{predicted}-xi^{measured}|}{N} \quad (2)$$

$$\text{Bias}=\frac{\sum_{i=1}^{n}[xi^{predicted}-xi^{measured}]}{N} \quad (3)$$

Where $xi^{predicted}$ and $xi^{measured}$ represent respectively the predicted and measured CDOM concentration, N is the number of samples.

3. Results and Discussion

3.1 Observed CDOM data

The measured CDOM concentrations of samples obtained from the three selected dams and the locations of sampling points are shown in figure (2-4). According to lab data, KTD has the highest average CDOM concentration, which reflected the effect of treated wastewater discharge to the dam and explaining why KTD can only be utilized for agriculture purposes. The Average CDOM concentration reached 12.77 m^{-1}, which is relatively higher than the other two dams. According to the statistics shows in table 3, the WAD came second for an average of 7.32 m^{-1} CDOM concentrations. That means that WAD water is not safe to be used as drinking water for humans or animals. Therefore, for this case, Wadi Al -Arab also can only be utilized for agriculture purposes.

From the statistics table (3), we can readily see that CDOM concentration is slightly low in the MD CDOM concentrate average. The CDOM concentration was only 2.84 m^{-1} on average at the time. Therefore, the MD may be the only one used for safe drinking water between these three dams. In this scenario, the Jordanian government is working hard to ensure that this dam is secure and free of any contaminants that could threaten AL-Mujib dam water quality.

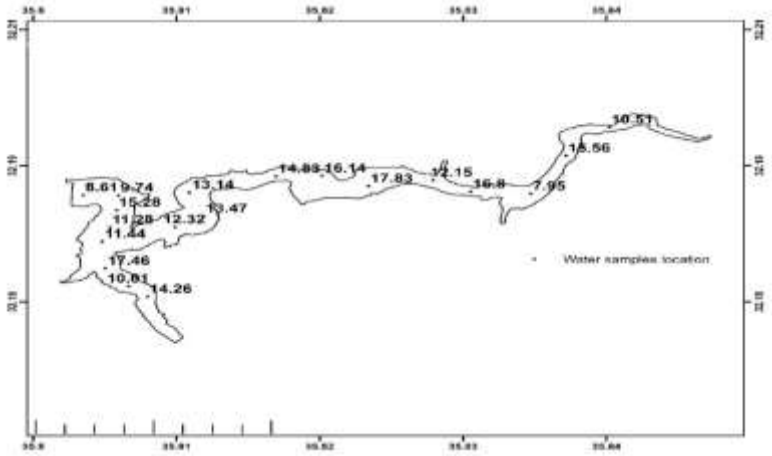


Figure (2): Distribution of king Talal dam sampling locations.

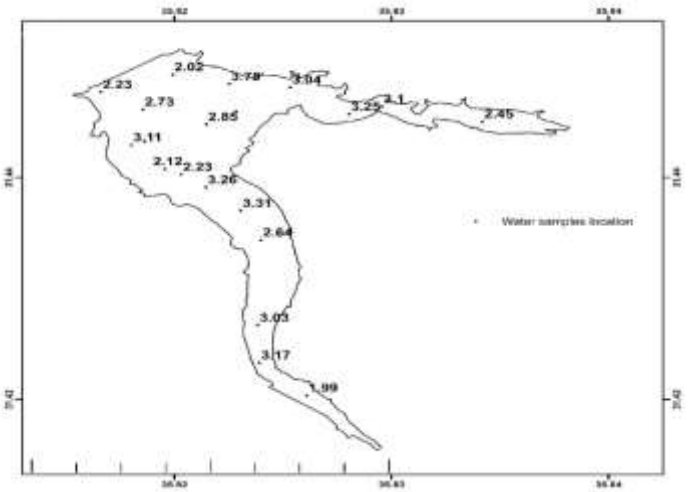


Figure (3): Distribution of Mujib dam sampling locations.

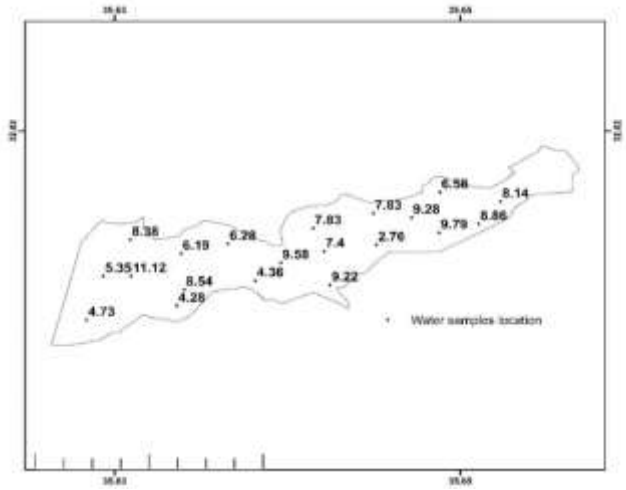


Figure (4): Distribution of Wadi Al-Arab dam sampling locations**.**

Table (3): CDOM descriptive statistics in three dams

	KTD				**MD**				**WAD**			
Statistics	Min	Max	Ave	SD	Min	Max	Ave	SD	Min	Max	Ave	SD
CDOM m^{-1}	7.32	17.83	12.77	3.19	1.99	3.83	2.84	0.54	2.76	11	7.32	2.18

3.2 Colored Dissolved Organic Matter Retrieval model

In this research, 60 water samples were collected between the three dams (King Talal Dam, Mujib Dam, and Wadi Al-Arab Dam) and considered for investigation. The collected data were divided into two sets. The first set contained 40 points and was used for calibration. The second set contained 20 points and was used for validation. The CDOM algorithms applied to the Sentinel 2 spectral band configuration in the literature use ratios and combinations of two and single bands.

3.2.1 Calibration of regression models

The exponential and power relationship was observed in all band combinations between the tested blue and green Sentinel-2 bands and CDOM. This research detected that the relationship between Sentinel-2 reflectance and blue to green bands ratio was preferred to other combinations. Figures 5-7 presented the best-founded calibrated regression between the CDOM and the Sentinel-2 reflectance.

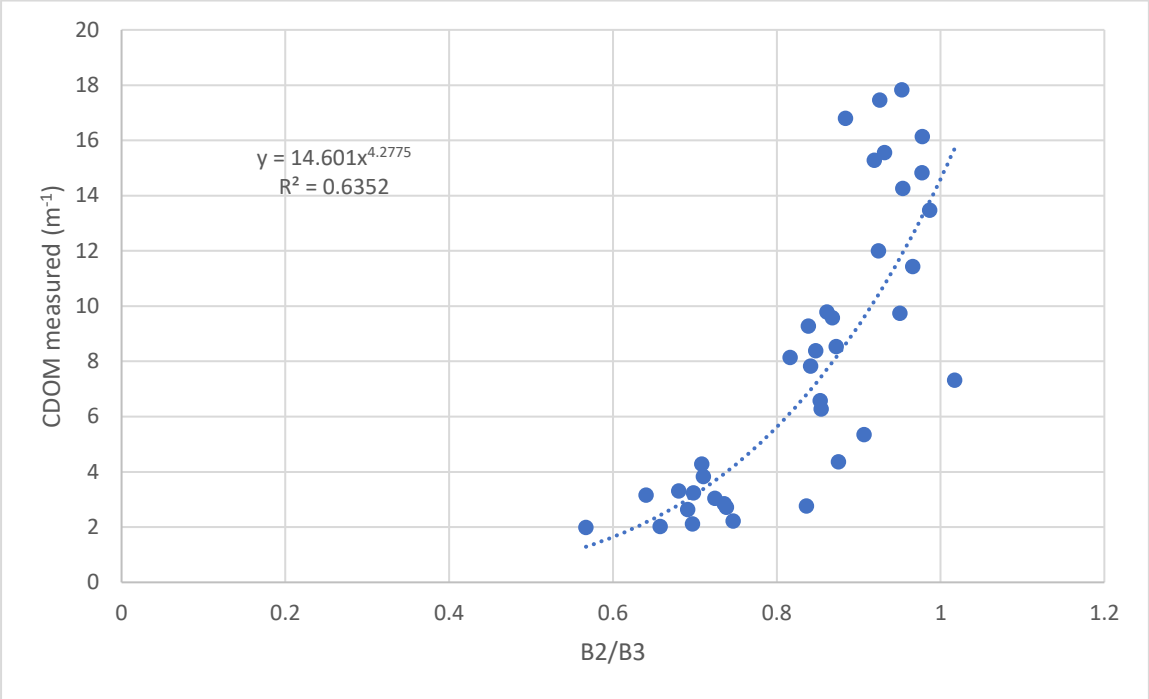


Figure 5: Regression between the Sentinel 2 band index and measured CDOM, using the B2/B3 model

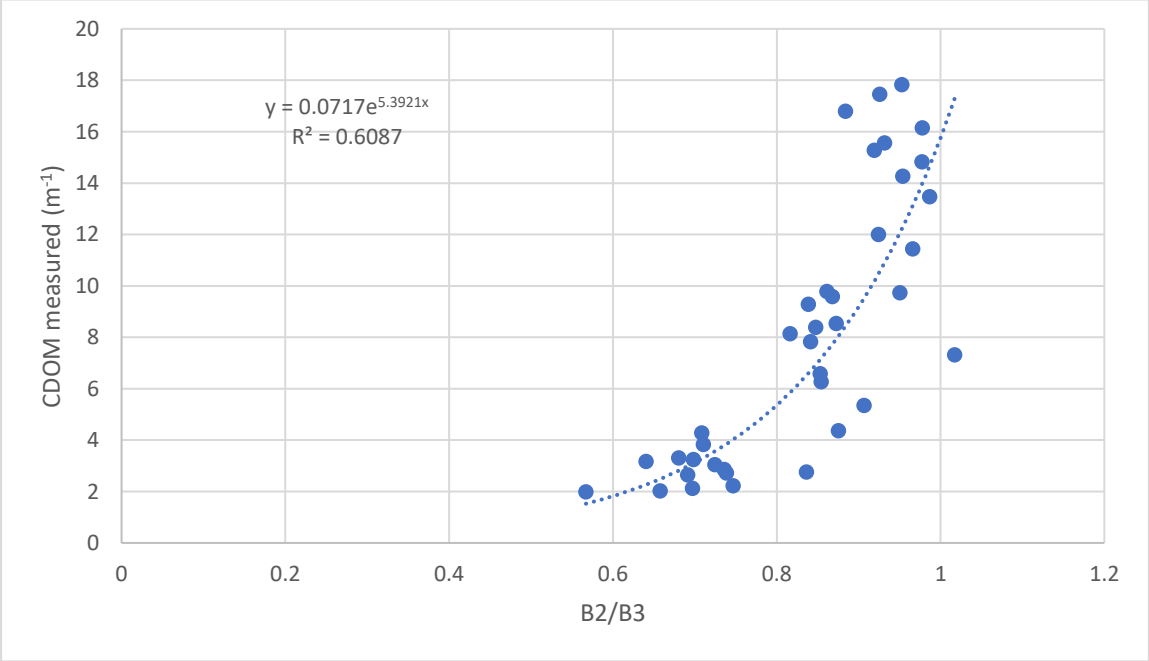


Figure 6: Regression between the Sentinel 2 band index and measured CDOM, using the B2/B3 model

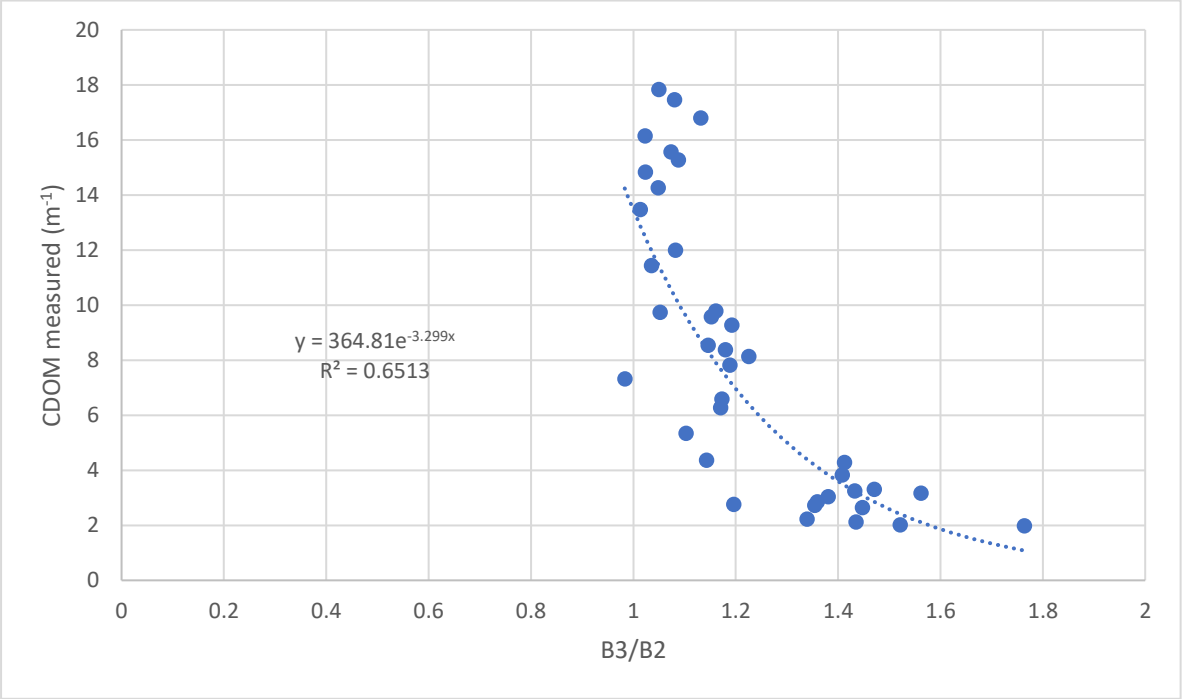


Figure 7: Regression between the Sentinel 2 band index and measured CDOM using the B2/B3 model

3.2.2 validation of regression models

In this study, regression analysis was used to develop the relation between CDOM and Setinal 2 data on the study areas. The calibration results show that three developed models were providing a suitable fitting as shown in Figure 5-7. These models were then validated using a dataset that has never been used for the calibration. The scatter plot of the measured versus predicted is shown in Figure 8-10.

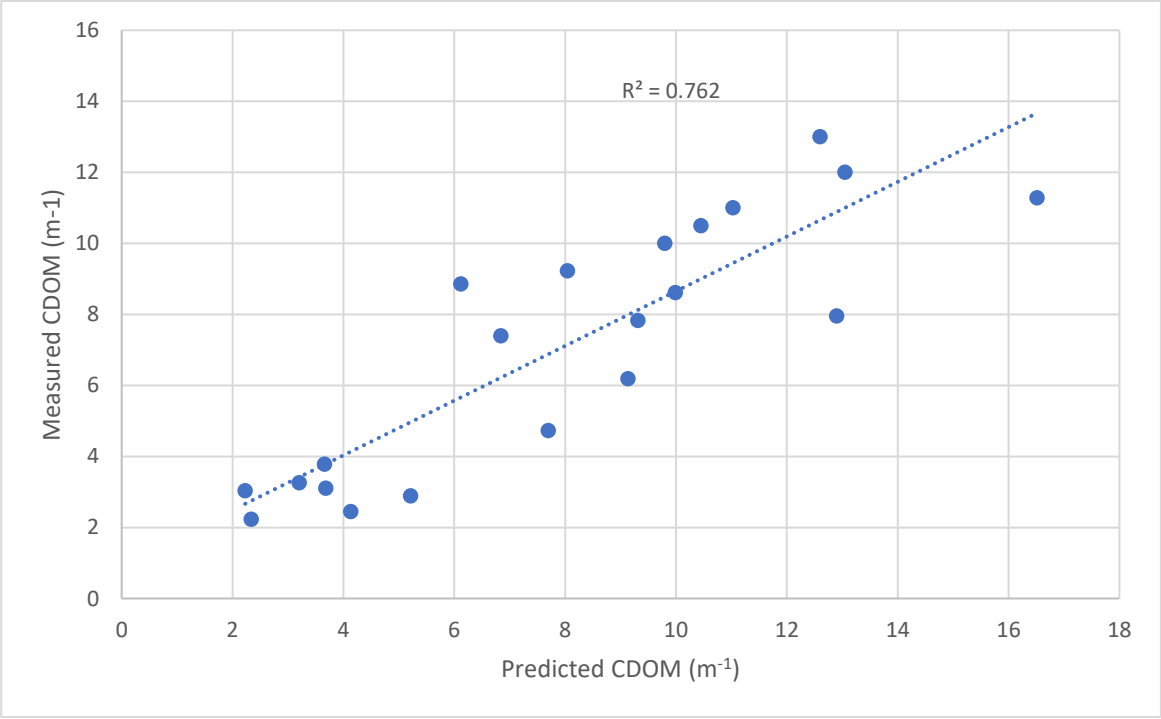


Figure 8: Regression between predicted and measured CDOM using the B2/B3 power model.

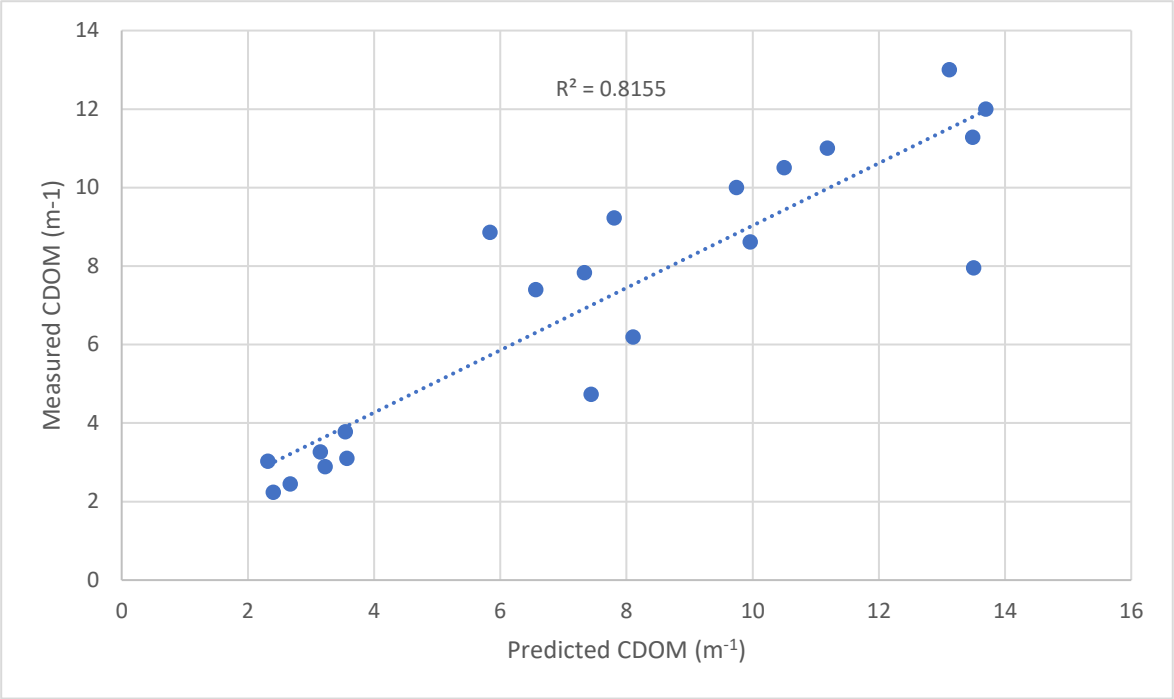


Figure 9: Regression between predicted and measured CDOM using the B2/B3 exponential model.

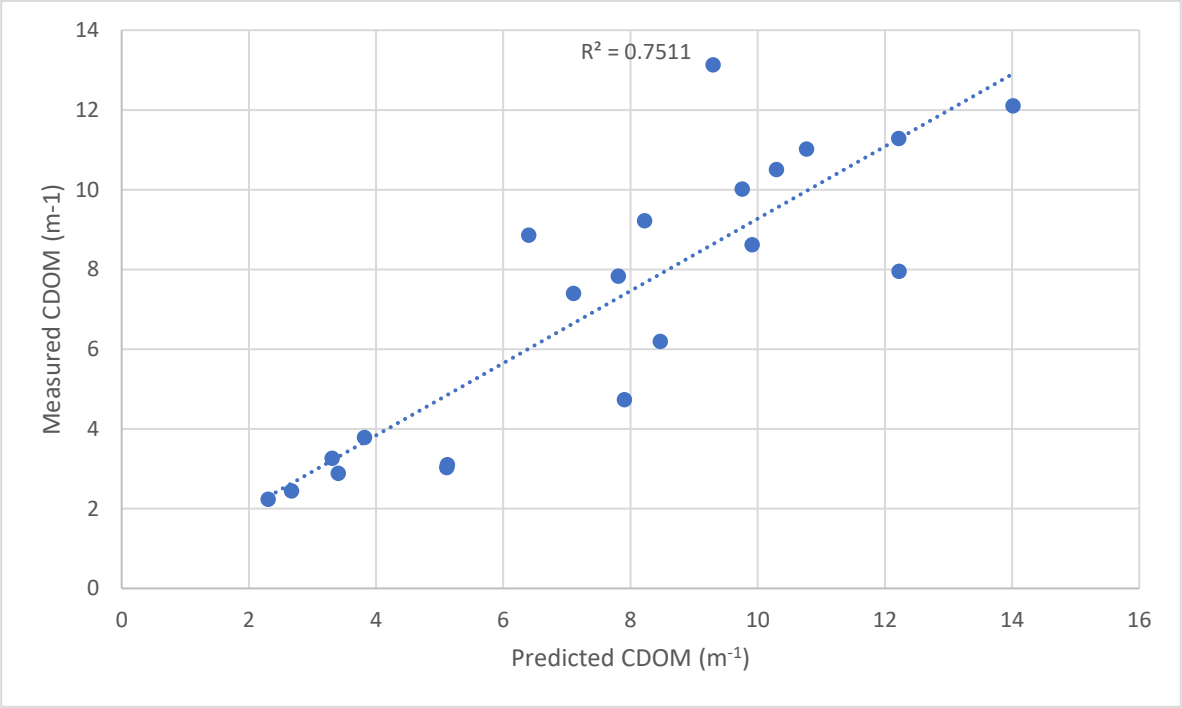


Figure 10: Regression between predicted and measured CDOM using the B2/B3 exponential model.

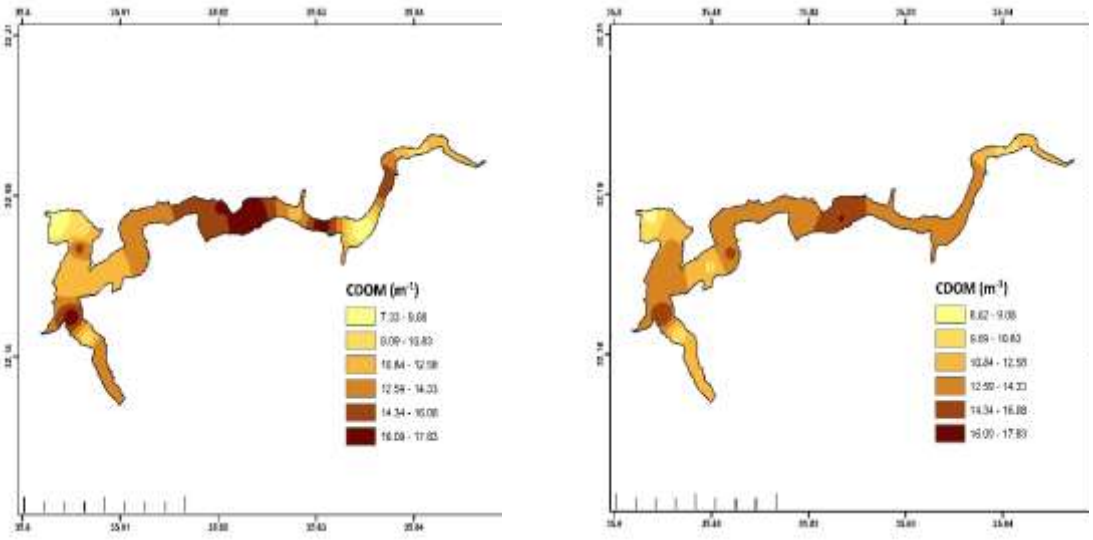
The estimation errors of a blue to green exponential model (B2/B3) were provided the best fitting regression with a RMSE of 1.754 m^{-1}, a MAE of 1.144 m^{-1} and a Bias of -0.469 m^{-1} (Table 4).

Table 4: Validation results of Sentinel 2 CDOM models.

Index	Equation	R^2	RMSE	MAE	Bias
B2/B3	y = 14.601x4.2775	0.762	2.014	1.406	-0.825
B2/B3	y = 0.0717e5.3921x	0.815	1.754	1.144	-0.469
B3/B2	y = 364.81e-3.299x	0.752	1.842	1.295	-0.491

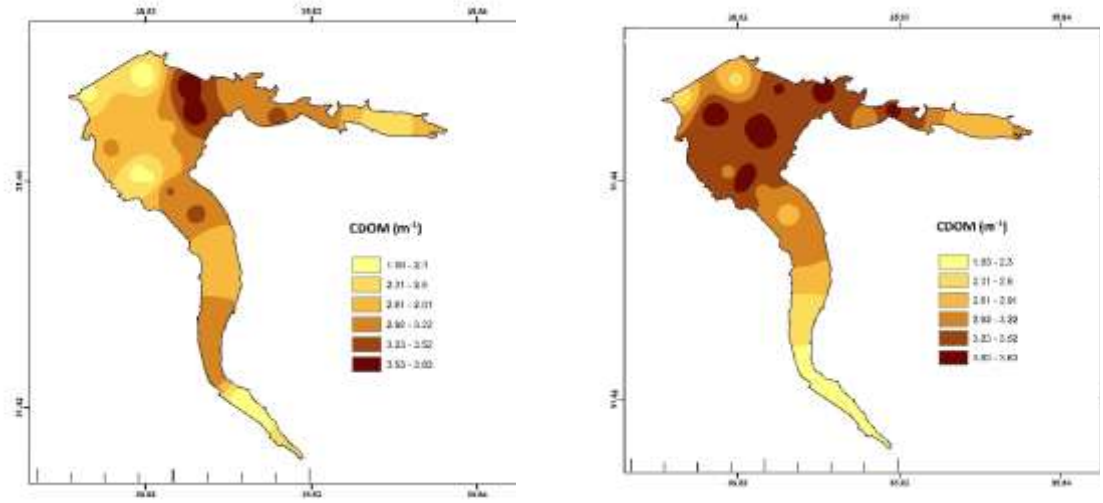
3.3 Mapping CDOM constriction using the Sentinel 2 Retrieval model

The best-fitting model of sentinel-2 (exponential function of B2/B3) was used to produce spatial distribution maps of the CDOM (m^{-1}) inside the three studied dams; KTD (Figure 11), MD (Figure 12) and WAD (Figure 13). The outputs indicate that the Sentinel-2 retrieval model can generate reasonable accurate maps of CDOM in varying concentration levels.



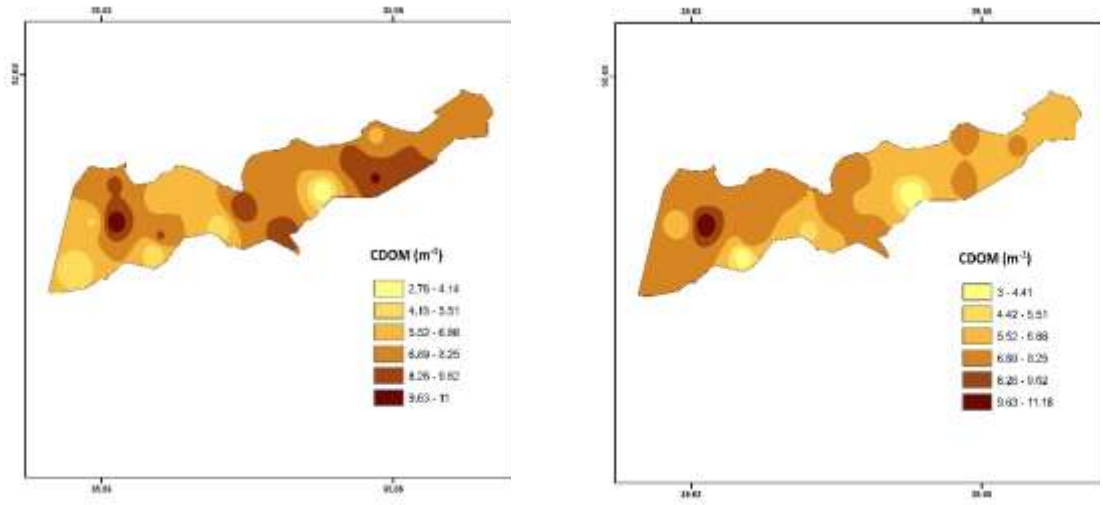
(a) (b)

Figure 11: CDOM distribution on KTD estimated from (a) laboratory analysis and (b) Sentinel-2



(a) (b)

Figure 12: CDOM distribution on MD estimated from (a) laboratory analysis and (b) Sentinel-2



(a) **(b)**

Figure 13: CDOM distribution on WAD estimated from (a) laboratory analysis and (b) Sentinel-2.

4. Conclusions

The applicability and accuracy of using sentinel 2 images to evaluate and monitor CDOM concentration in inland water bodies were evaluated in this investigation. Three diverse Jordanian's dams were picked for CDOM concentration test. Regarding this regard, 60 samples were collected relatively and were measured. According to output results, it appears that three Jordanian dams have different water-quality properties and significant variations in CDOM concentration levels. The statistics results show that CDOM concentration in KTD was the highest between the three dams.

The CDOM concentration in KTD has reached 12.77 m^{-1} on average. However, the MD gets the lowest CDOM concentration, making it the safest dam regarding drinking water. The CDOM concentration of MD was approximately 2.84 m^{-1}on average. Lastly, Wadi Al Arab dam has taken second place as CDOM concentration Level. The average concentration of that dam reached 7.32 m^{-1}.

The empirical model approach was applied to create a CDOM predictive model by testing and examining several bands-based algorithms. A predictive model was developed using about two-thirds of the samples. The created model was used to forecast CDOM concentrations using surface reflectance data for the remaining 20 sampling stations. The validation set's measured CDOM concentrations were compared to the matching anticipated values derived from established models. The exponential of the blue to green ratio model demonstrated the highest capabilities to retrieve CDOM concentration with RMSE of 1.754 m^{-1}, MAE of 1.144 m^{-1} and Bias of -0.469 m^{-1}.

Acknowledgments: authors would like to thank the Deanship of Scientific Research and Graduate Studies at University of Petra (grant no. 3/7/2019).

References

1. Odeh, T.; Mohammad, A. H., Wise Water Resources Management under the Increasing Number of Refugees in the Third Poorest Water Resources Country (Jordan)–A Suggested Future Spatial Plan for Water Resources Investments. International Journal of Sustainable Development and Planning 2020, 15, (2), 235-238.
2. Hadadin, N., Dams in Jordan current and future perspective. Canadian journal of pure applied sciences 2015, 9, (1), 3279-3290.
3. Hammouri, N.; Adamowski, J.; Freiwan, M.; Prasher, S., Climate change impacts on surface water resources in arid and semi-arid regions: a case study in northern Jordan. Acta Geodaetica et Geophysica 2017, 52, (1), 141-156.
4. Odeh, T.; Boulad, N.; Abed, O.; Abu Yahya, A.; Khries, N.; Abu-Jaber, N., The influence of Geology on landscape typology in Jordan: theoretical understanding and planning implications. Land 2017, 6, (3), 51.
5. WATER MANAGEMENT INITIATIVE Review of Water Scarcity Ranking Methodologies; United States Agency for International Development Amma, Jordan, 2017.
6. Tranvik, L. J., Carbon cycling in the Arctic. Science 2014, 345, (6199), 870-870.
7. Battin, T. J.; Luyssaert, S.; Kaplan, L. A.; Aufdenkampe, A. K.; Richter, A.; Tranvik, L. J., The boundless carbon cycle. Nature Geoscience 2009, 2, (9), 598-600.
8. Stedmon, C. A.; Markager, S.; Kaas, H., Optical properties and signatures of chromophoric dissolved organic matter (CDOM) in Danish coastal waters. Estuarine, Coastal Shelf Science 2000, 51, (2), 267-278.
9. Parry, M.; Parry, M. L.; Canziani, O.; Palutikof, J.; Van der Linden, P.; Hanson, C., Climate change 2007-impacts, adaptation and vulnerability: Working group II contribution to the fourth assessment report of the IPCC. Cambridge University Press: 2007; Vol. 4.
10. Kutser, T.; Hedley, J.; Giardino, C.; Roelfsema, C.; Brando, V. E., Remote sensing of shallow waters–A 50 year retrospective and future directions. Remote Sensing of Environment 2020, 240, 111619.
11. Li, J.; Yu, Q.; Tian, Y. Q.; Becker, B. L., Remote sensing estimation of colored dissolved organic matter (CDOM) in optically shallow waters. ISPRS Journal of Photogrammetry Remote Sensing 2017, 128, 98-110.
12. Dvornikov, Y.; Leibman, M.; Heim, B.; Bartsch, A.; Herzschuh, U.; Skorospekhova, T.; Fedorova, I.; Khomutov, A.; Widhalm, B.; Gubarkov, A., Terrestrial CDOM in lakes of Yamal peninsula: connection to lake and lake catchment properties. Remote Sensing 2018, 10, (2), 167.
13. Al-Kharusi, E. S.; Tenenbaum, D. E.; Abdi, A. M.; Kutser, T.; Karlsson, J.; Bergström, A.-K.; Berggren, M., Large-scale retrieval of coloured dissolved organic matter in northern lakes using Sentinel-2 data. Remote Sensing 2020, 12, (1), 157.
14. Liu, D.; Yu, S.; Xiao, Q.; Qi, T.; Duan, H., Satellite estimation of dissolved organic carbon in eutrophic Lake Taihu, China. Remote Sensing of Environment 2021, 264, 112572.
15. Markager, S.; Vincent, W. F., Spectral light attenuation and the absorption of UV and blue light in natural waters. Limnology Oceanography 2000, 45, (3), 642-650.

16. Hestir, E. L.; Brando, V.; Campbell, G.; Dekker, A.; Malthus, T., The relationship between dissolved organic matter absorption and dissolved organic carbon in reservoirs along a temperate to tropical gradient. Remote Sensing of Environment 2015, 156, 395-402.
17. Del Vecchio, R.; Blough, N. V., Spatial and seasonal distribution of chromophoric dissolved organic matter and dissolved organic carbon in the Middle Atlantic Bight. Mar. Chem. 2004, 89, (1-4), 169-187.
18. Pielke Sr, R. A., Mesoscale Modeling and Satellite Simulator. In International Geophysics, Elsevier: 2013; Vol. 98, pp 407-426.
19. Torbick, N.; Hu, F.; Zhang, J.; Qi, J.; Zhang, H.; Becker, B., Mapping chlorophyll-a concentrations in West Lake, China using Landsat 7 ETM+. Journal of Great Lakes Research 2008, 34, (3), 559-565.
20. Womber, Z. R.; Zimale, F. A.; Kebedew, M. G.; Asers, B. W.; DeLuca, N. M.; Guzman, C. D.; Tilahun, S. A.; Zaitchik, B. F., Estimation of Suspended Sediment Concentration from Remote Sensing and In Situ Measurement over Lake Tana, Ethiopia. Advances in Civil Engineering 2021, 2021.
21. He, Y.; Jin, S.; Shang, W., Water quality variability and related factors along the Yangtze River using Landsat-8. Remote Sensing 2021, 13, (12), 2241.
22. Zhu, W.; Huang, L.; Sun, N.; Chen, J.; Pang, S., Landsat 8-observed water quality and its coupled environmental factors for urban scenery lakes: A case study of West Lake. Water Environ. Res 2020, 92, (2), 255-265.
23. Hu, M.; Ma, R.; Cao, Z.; Xiong, J.; Xue, K., Remote Estimation of Trophic State Index for Inland Waters Using Landsat-8 OLI Imagery. Remote Sensing 2021, 13, (10), 1988.
24. Hedley, J.; Roelfsema, C.; Koetz, B.; Phinn, S., Capability of the Sentinel 2 mission for tropical coral reef mapping and coral bleaching detection. Remote Sensing of Environment 2012, 120, 145-155.
25. Hussein, N. M.; Assaf, M. N., Multispectral Remote Sensing Utilization for Monitoring Chlorophyll-a Levels in Inland Water Bodies in Jordan. The Scientific World Journal 2020, 2020.
26. Assaf, M. N. Utilizing Landsat 8 and Sentinel 2 Satellites Images for Water Quality Evaluation in King Tala Dam. German Jordanian University, 2019.
27. Chen, J.; Zhu, W.; Tian, Y. Q.; Yu, Q.; Zheng, Y.; Huang, L., Remote estimation of colored dissolved organic matter and chlorophyll-a in Lake Huron using Sentinel-2 measurements. Journal of Applied Remote Sensing 2017, 11, (3), 036007.
28. Ouma, Y. O.; Noor, K.; Herbert, K., Modelling Reservoir Chlorophyll-a, TSS, and Turbidity Using Sentinel-2A MSI and Landsat-8 OLI Satellite Sensors with Empirical Multivariate Regression. Journal of Sensors 2020, 2020.
29. Hilal, A. H. A.; Alhaija, M. M. A., Nutrients in Water and Sediments of King Talal Dam-Jordan. Jordan Journal of Biological Sciences 2010, 3, (3), 87-100.
30. Abualhaija, M. M.; Shammout, M. a. W.; Mohammad, A.-H.; Hilal, A. H. A., Heavy Metals in water and sediments of King talal Dam the largest Man-Made water Body in Jordan. Water Energy International 2019, 62, (5), 49-62.
31. Al-Taani, A. A.; El-Radaideh, N. M.; Al Khateeb, W. M., Status of water quality in King Talal Reservoir Dam, Jordan. Water Resources 2018, 45, (4), 603-614.
32. Shatnawi, A.; Diabat, A., Siltation of Wadi Al-Arab reservoir using GIS techniques. Jordan Journal of Civil Engineering 2016, 10, (4).
33. Saadoun, I.; Batayneh, E.; Alhandal, A.; Hindieh, M., Physicochemical features of Wadi Al-Arab Dam (reservoir), Jordan. Oceanological Hydrobiological Studies 2010, 39, (4), 189-203.
34. Yusra, A.-h., Landforms Classification of Wadi Al-Mujib Basin in Jordan, based on Topographic Position Index (TPI), and the production of a flood forecasting map. Dirasat, Human Social Sciences 2019, 46, (3).
35. Zhu, W.; Yu, Q.; Tian, Y. Q.; Becker, B. L.; Zheng, T.; Carrick, H. J., An assessment of remote sensing algorithms for colored dissolved organic matter in complex freshwater environments. Remote Sensing of Environment 2014, 140, 766-778.

36. Bilal, M.; Nazeer, M.; Nichol, J. E.; Bleiweiss, M. P.; Qiu, Z.; Jäkel, E.; Campbell, J. R.; Atique, L.; Huang, X.; Lolli, S., A Simplified and Robust Surface Reflectance Estimation Method (SREM) for Use over Diverse Land Surfaces Using Multi-Sensor Data. Remote Sensing 2019, 11, (11), 1344.

Conversion of Oil Palm Empty-Fruit Bunches Waste to Activated-Carbon Using Superheated Steam

N A S Wakari [1], M N F Mustaza [1], H. Yoshida [2], S Izhar [1,*]

[1] Department Chemical and Environmental Engineering, Universiti Putra Malaysia, 43400 UPM Serdang, Malaysia;

[2] Ecology Research Center, Research Organization for the 21st Century, Osaka Prefecture University, 1-1 Gakuen-Cho, Naka-ku, Sakai, Osaka 599-8570,

***** *Corresponding author: shamizhar@upm.edu.my; Tel.:+60-3-97694428.*

Abstract: Activated carbon (AC) from oil palm waste empty fruit bunches (EFB) synthesized via carbonization and activation using superheated steam. The study aims to utilize superheated steam as a medium to convert EFB waste to AC with desired physiochemical properties. A combination of carbonization and activation stages was employed for the process. The physical activation process was performed by purging superheated steam at 3 ml/min using a rotary kiln carbonizer. The carbonization process for each sample was fixed at 400°C for 50 minutes, and the activation temperatures were between 500°C and 800°C for 40 minutes. The 800°C activated EFB showed enhanced proximate value, surface functional group, and surface area properties. The proximate analysis illustrated 1.0% moisture, 8.0% ash content, and 71.6% fixed carbon content. The optimum activation temperature of 800°C gave the maximum BET surface area of 475 m^2g^{-1}. The increased number of carbonyl and hydroxyl functional groups on the surface could enhance the anionic properties of activated carbon to act as an adsorbent for treating cationic contaminants, methylene blue dye, and phenol. This study confirmed that carbonization and activation of EFB-derived AC using superheated steam at 800°C is possible in producing activated carbon.

Keywords: Activated carbon; Empty fruit bunches; carbonization; activation; proximate analysis

1. Introduction

In Malaysia, oil palm plantation is the major crop that contributes to the largest generation of waste. Improper disposal and poor waste management directly affected the natural ecosystems. Oil palm biomass, such as oil palm trunks (OPT), oil palm fronds (OPF), empty fruit bunches (EFB), and palm oil mill effluent (POME), has a lot of potential for being converted into more value-added goods, including biogases, activated carbon, and solid fuel. About one million tons of biomass are generated in Malaysia yearly, including oil palm biomass, timber residue, and municipal solid waste. However, about 43-45% of this palm oil residue is in the form of EFB, shell, and fiber [1]. Therefore, converting biomass into more value-added products can promote sustainability and reduce the disposal problems of biomass waste into the landfill.

Since EFBs have a high carbon density and lignin, they can be an excellent raw material for activated carbon manufacturing. Activated carbon is widely used in industries for various applications such as removing contaminants and environmental purposes such as the recovery of solvents, sewage treatment, gases separation, and dye treatment [2]. However, chemical agents for impregnation and activation in the activated carbon production process involve the use of concentrated acid or alkali. The chemical treatment of EFB requires 75% sulphuric acid to have a highly developed pore [3]. Carbon activation using concentrated 60%-85% potassium hydroxide yields a high surface area of

activated carbon [4]. However, the use of these chemical demand effluent treatment before it can be discharged into the environment. Exposing these chemicals effluent into the environment provided a high risk to both human health and the environment.

EFB can be converted to activated carbon by the carbonization and activation process. Physical activation is a two-step process that involves carbonizing a carbon substance and then activated the resulting bio-char at higher temperatures in the presence of oxidizing gases such as carbon dioxide, steam, or air [3]. Compared with steam activation, activation of bio-char with carbon dioxide and air gives a lower surface area of activated carbon. According to Hashemipour et al. [2], steam activation is a better activating agent in preparing activated carbon from EFB. High pore development is observed after the steam activation process. This is attributable to the smaller particles being able to diffuse and react more quickly within the carbon matrix than air and carbon dioxide. Hence, this study focuses on utilizing EFB as a raw material to produce activated carbon using superheated steam for both carbonization and activation processes.

The effect of using superheated steam for carbonization followed by physical activation needs to study and compare with other researchers using other chemical and gases mediums.

2. Materials and Methods

2.1 Raw material preparation

Raw EFB was collected from a local oil palm plantation. The collected EFB was cut into 4-5 cm size. The EFB was cleaned and dried in the oven for 2 hours at 105°C to avoid damage, fungal growth, remove the excessive moisture content on its surface, and kept in an air-tight bag for further thermal treatment. 50 g of the dried EFB was placed in a reactor made of stainless steel equipped with a steel mesh to prevent the treated EFB from going out during activation**.**

2.2 Rotary kiln and apparatus setup

Figure shows the equipment setup of a rotary kiln carbonizer (Tanaka Tech, Japan) to perform the carbonization and activation process, injecting superheated steam as a medium. The system was equipped with an evaporator, right furnace, body furnace and kiln, a left furnace, and a condenser system from the left. The evaporator vaporizes the distilled water into superheated steam at 300 ºC at a constant flow rate of 3 ml/min generated by a pump. The ribbon heater heated the connector pipeline, connected the cooling system, and left the furnace at 250 ºC to prevent the tar from solidification in the pipeline. The evaporator and the right/left furnaces were set to 200ºC.

The superheated steam flows from the right furnace and into the body furnace that contains the EFB sample. EFB samples were carbonized and activated in the kiln where the volatile matter, tar, and uncondensed gas were released. The decomposition of hemicellulose, cellulose, and lignin has occurred. Then, all the vaporized matter will flow into the left furnace and be quenched to condense the volatile matter and tar extracted from EFB samples. The condensed substances or water-soluble organic tar will be collected in round bottom flask one. At the same time, the uncondensed gases will flow into round bottom flask two and be released to the surrounding.

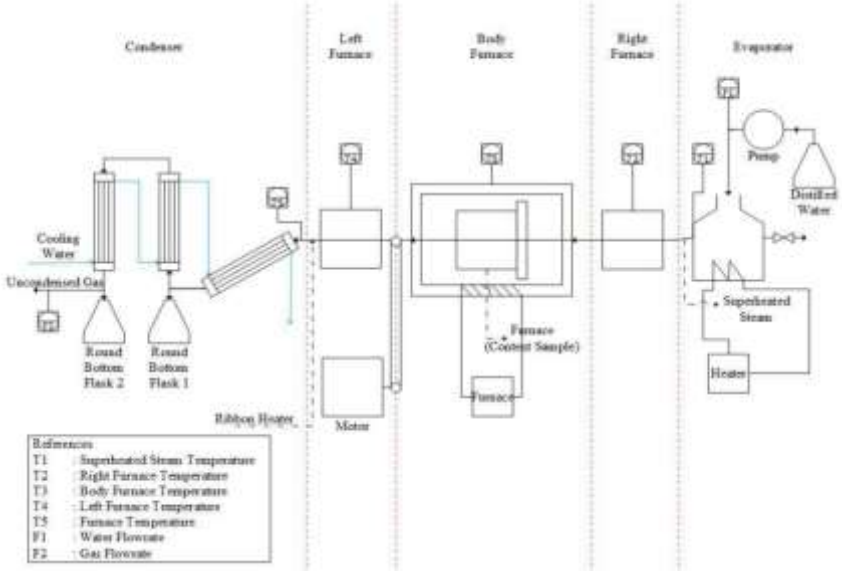


Figure 1 Rotary kiln carbonizer setup arrangement [5]

2.3 Carbonization and activation of EFB using superheated steam

The EFB sample undergoes two steps of the thermal treatment process: carbonization and activation. The medium used for these processes was superheated steam generated from distilled water. The superheated steam was injected at a flow rate of 3 ml/min into the system. The dried EFB sample (50 gram) was carbonized at 400ºC for 50 minutes to develop the initial porosity of biochar. Then, the carbonized biochar was further activated at an elevated temperature at 500ºC, 600 ºC, 700 ºC and 800 ºC for 40 minutes. Figure shows the temperature profile of the carbonization and activation of EFB in the rotary kiln carbonizer. Several phases were included in this activated carbon production. The stage started with drying, torrefaction and carbonization, activation, and finally, cooling steps. After the activated process was completed, the treated EFB was left to cool down at room temperature for 24 hours.

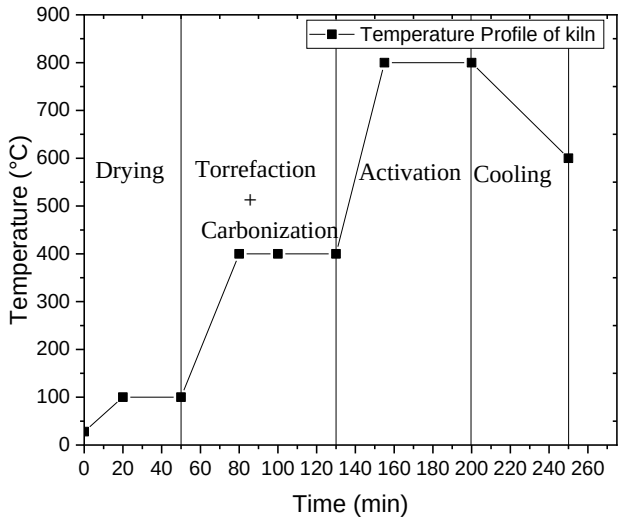


Figure 2 The theoretical temperature profile of the carbonization and activation of the EFB in rotary kiln carbonizer

2.4 Solid characterization

Percentage of mass yield is defined as the percentage of solid remains after the carbonization and activation process. It was calculated using the initial mass of the EFB used and mass after the carbonized and activated raw material. The mass of these samples was measured using a microbalance. The formula used for calculating the percentage mass yield (y_M) is shown in Eq.1

$$y_M = \frac{Mass\ of\ solid\ after\ carbonization\ and\ activation}{Initial\ mass\ of\ solid\ Empty\ Fruit\ Bunches} \times 100 \qquad \text{Eq. 1}$$

Proximate analysis was performed to determine the moisture, volatile substances, ash contents, and fixed carbon contents. The samples were loaded into the crucibles and heated in the muffle furnace **(**Nitto Kagaku, Japan**).** The moisture content of the carbon material is determined using ASTM D2867-17. 1 gram of activated-EFB was put into the crucible, then placed in an oven at 105°C to a constant weight. The difference between the initial and final mass of the carbon represents the moisture content. The moisture content (MC %) was computed using a dry basis as in Eq.2

$$MC\ \% = \frac{Initial\ mass\ of\ sample - Final\ mass\ of\ sample}{Final\ mass\ of\ sample} \qquad \text{Eq. 2}$$

The volatile matter in the sample used ASTM D3175 method. The sample (1 g) was heated at 500°C for 10 minutes. Mass loss due to volatile is measured as the difference in weight before and after heating. The volatile matter (VM%) was calculated using Eq.3

$$VM\ \% = \frac{Mass\ loss\ due\ to\ volatile}{Initial\ dry\ mass\ of\ sample} \times 100 \qquad \text{Eq. 3}$$

The ash content (mineral content) was calculated using ASTM D2866. The sample (1 g) was allowed to rise to 750°C for 90 minutes and allowed to cool in a desiccator to room temperature and reweighed. The ash content was calculated using Eq.4

$$Ash\ \% = \frac{Mass\ of\ residue}{Initial\ mass\ of\ sample} \times 100 \qquad \text{Eq. 4}$$

The fixed carbon content is defined as the percentage difference between the ash content, volatile matter, and moisture content, calculated using Eq.5

$$FC\ \% = 100\% - (\ \%ASH + \%VM + \%MC) \qquad \text{Eq. 5}$$

FTIR was used to observe the type of functional group that exists on the surface of activated carbon. This is important since the functional group on the surface of activated carbon determines the type of adsorbate that can be absorbed and deposited into the surface of the activated carbon. FTIR was analyzed between 650-4000 cm^{-1}.

Surface area and porosity of solid were measured using a BET analyzer (Micromeritics). Porosity characterization involves determining the surface area of the activated carbon, micropores surface area, total pore volume, and pore size distribution through nitrogen adsorption-desorption isotherms. The sample's surface area was evaluated using the BET method over a relative pressure (P/P_O) range of 0.01 to 1.0. The degassing gas used was nitrogen, and the activated carbon was degassed at a temperature of 300°C.

2.5 Liquid characterization

The bio-oil residue from the condensation of steam downstream of the kiln was collected and analyzed using a GC-MS (GC-2010 Shimadzu). The GC column was a Zebron ZB-50 (30 m × 0.25 mm × 0.25 µm) with injection temperature and volume of 300°C and 1 µL, respectively. Chromatography was conducted from 60°C and ramping rate of 8°C/min until 275°C. The resulted mass spectrum allows for the identification of the components using standard reference libraries.

3. Results and Discussion

3.1 Temperature profile of kiln body furnace

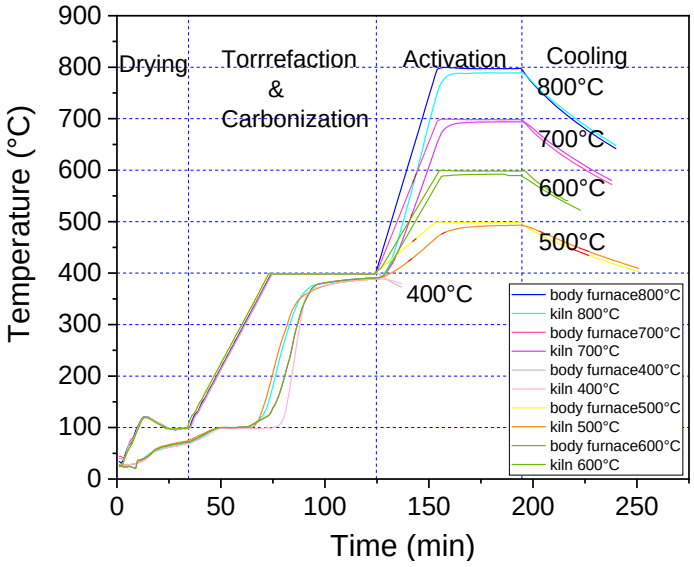


Figure 3 Temperature profiles of EFB during carbonization and activation.

The physical treatment process was carried out using superheated steam with a flow rate of 3 ml/min. The heating rate at the drying phase was 7°C/min. The EFB was carbonized for 50 min at 400°C. During the pre-activation process, the heating rate for each activation temperature from 500°C to 800°C was increased significantly from 3.43°C/min to 13.3°C/min respectively**.** The increased heating rate was due to the increased activation temperature of the body furnace and kiln at a given heating time, which is 30 min. Once the desired activation temperature was achieved, the reaction was allowed to take place for 40 min. The solid product was cooled down for 24 h to room temperature before the activated carbon was retrieved and weighed.

3.2 Solid characterization

3.2.1. Solid appearances and yield

Figure shows the photos of activated carbon produced from the EFB taken using a Digital Microscope with 1600× magnification. The color of the raw EFB changes from yellowish-brown to black after carbonization and activation. The higher the temperature, the severe the heating of the EFB and thus produces darker and brittle activated carbon. The more brittle the activated carbon, the better it is due to the completed combustion of the carbon fibers.

Figure shows the effects of activation temperature on the mass yield of activated carbon produced from EFB. The ratio of activated carbon produced over the mass of initial dry EFB (AC/g EFB) significantly decreased from 0.27 to 0.16 g ACs/g EFB. The mass reduction increased from 400°C to 800°C due to the severe decomposition and degradation of the hemicellulose and cellulose from 73% to 84%, respectively. Increasing temperature from 400°C to 800°C illustrated a significant decrease of the solid yield from 27% to 16%. Increased activation temperature showed a considerable decline in solid yields. This could be attributed to a higher reaction rate between carbon and superheated steam, releasing more volatile components and simultaneously improving textural features and carbon burn-off.



Figure 4 The appearances of superheated steam treated and untreated EFB. Raw EFB (a) and activated carbon produced at (b) 500, (c) 700 and (d) 800°C.

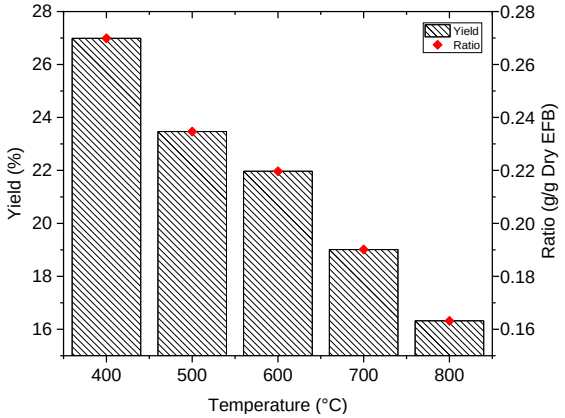


Figure 5 Solid yield produce after the carbonization and activation process

3.2.2. Proximate analysis

The proximate analysis of the EFB was performed to determine their characteristics as precursors for activated carbon. Figure shows the significant decrease of the volatile matter of the activated carbon produced from 31.2% to 19.4% after undergoes the carbonization and activation process using superheated steam. The moisture content of the samples decreased when the activation temperature increased from 500°C to 800°C. The moisture content decreased from 3.4% to 1.0% with increasing temperature. The significant decrease in the moisture is due to the release of water during the thermal treatment of the samples. At the same 800°C, the amount of moisture content of activated carbon produced using superheated steam activation (1.01%) is comparable with that prepared by KOH activation (0.98%) [6]. However, activated carbon from KOH activation showed lower volatile matter (11.44%) than superheated steam activation (19.42%) at 800°C. Watfi et al. [7] reported the purposed of the carbonization phase was to reduce the volatile content of the material and convert the bio-char into higher fixed carbon content. At higher activation temperatures, more volatile materials will be released due to the degradation of components contained in raw materials such as tar, cellulose, hemicellulose, and lignin.

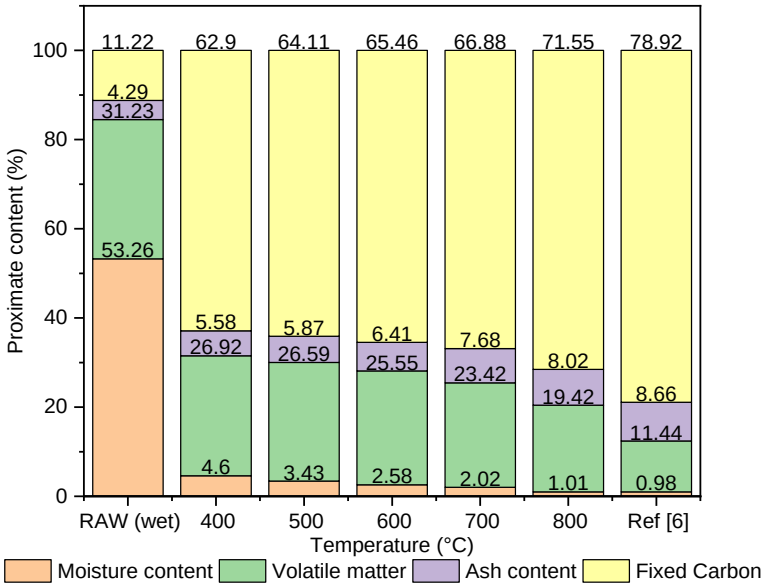


Figure 6 The proximate analysis of the raw EFB and activated carbon produced

The ash content influences the quality of activated carbon produced. The ash content increased from 5.5% to 8.0% from 400°C to 800°C. This is because the increase of activation temperature would increase the carbon-burn-off and inorganic material. Excessive ash can cause pores on activated carbon to clog, reducing the surface area of the activated carbon. Sánchez [8] reported the higher ash content in activated carbon reduces the overall activity of the material and thus, reduces the efficiency of the adsorption process. Other studies by Haridan et al. [9] stated that in solid fuel, the decrease of calorific value is attributed by a large amount of ash content inside the excess sewage sludge. The ash content in activated carbon is generally in the range between 2-10%. Figure 6 shows that fixed carbon content significantly increased from 11.2% to 71.5% when the temperature increased from 400°C to 800°C. Bakhtiar et al. [6] concluded that high fixed carbon content is crucial since it determines stability and resistance to physical, chemical, and biological degradation.

3.2.3. Surface functional groups

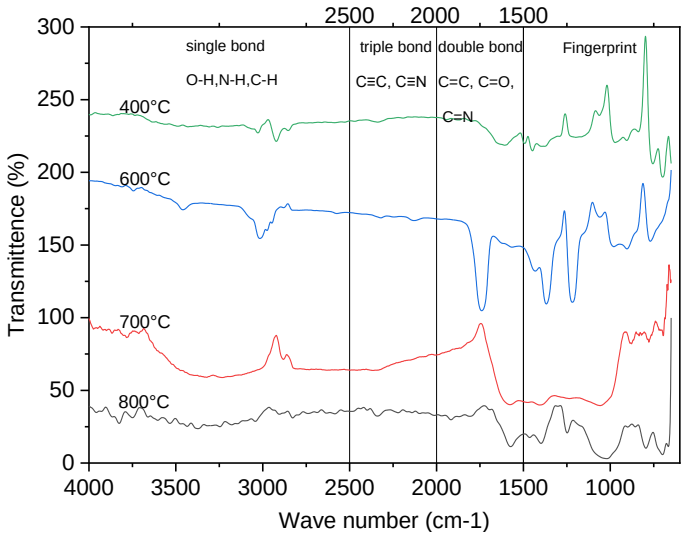


Figure 7 FTIR spectrums of activated carbon treated with superheated steam at from 400°C, 600°C, 700°C to 800°C

The FTIR combine spectrums of the activated carbon samples at carbonized temperature 400°C, and activation temperatures 600°C, 700°C, and 800°C are given in **Figure** . The determination of functional groups makes it easier to classify the type of adsorbates suitable to be treated. There is an increase of oxygen functional group such as carbonyl and hydroxyl presented on the surface of activated carbon when the temperature increased from 400°C, 600°C, 700°C to 800°C**.** The increase was observed especially for the oxygen functional groups such as carboxyl (800-1060 cm^{-1}) and hydroxyl (3534 cm^{-1}) with increasing activation temperature. FTIR showed the stretched and bending of alkene (1608.1, 3016.0 cm^{-1}), alkane (1398.5 cm^{-1}), aromatic (1447.8, 1493.0, 1575.0 cm^{-1}), carbonyl (1368.3, 1431.7, 1916.9 2363.9 cm^{-1}) and a hydroxyl (2881-3500 cm^{-1}) group at the temperature of 400°C, 600°C, 700°C, and 800°C. At temperature 400°C, the surface of activated carbon showed a weak alkene stretch at 3028.45 cm^{-1}. This band was broad at an increasing temperature from 400°C to 600°C.

At higher temperatures, FTIR studies of the surface functional groups revealed that activated carbons had more oxygen functional groups [10]. The activation of EFB at a higher temperature using superheated steam increased the O-H, C-O functional group, making the overall negatively charged surface. The presence of O-H and C-O active groups indicated that the activated carbon tends to be more polar with positive and negative sides. According to Singh et al., [11], the negatively charged surface of activated carbon produced has a greater affinity towards cationic surfaces such as dye methylene blue for adsorption purposes.

3.2.4. BET Surface area

Table shows the surface areas measure by the BET method. Higher activation temperature increased the BET surface area, micropore surface area, and total pore volume using superheated steam. Carbonized biochar-like EFB had the lowest surface area, micropores surface area, micropores volume, and total pore volume, 6.9 m^2g^{-1}, 5.5 m^2g^{-1}, 0.002 $cm^3g^{-1,}$ and 0.004 cm^3g^{-1}, respectively. The low surface area indicated that the superheated steam used could not create enough pores on the surface of EFB.

Activated carbon produced using superheated steam at activation temperatures of 600°C, 700°C, and 800°C illustrated the surface areas of 230.1 m^2g^{-1}, 403.1 $m^2g^{-1,}$ and 475.6 m^2g^{-1}, respectively. The maximum BET surface area was observed when activated at 800°C, whereas the lowest was at 600°C. Total pore volume and micropore surface area increased from 0.004 to 0.296 cm^3g^{-1} and 5.5 m^2g^{-1} to 367.4 m^2g^{-1} when the activation was increased from 600°C to 800°C. The pore size reduced from 1.19 nm to 0.88 nm when the activation temperature was increased to 700°C. However, the pore size increase to 1.33 nm when the activation temperature is 800°C. The increase of pore size, when activated at 800°C, occurred due to the extensive diffusional activity of superheated steam on the EFB surface, which caused the opening of the pore to occur.

This indicated that activating EFB at elevated temperatures is essential to enhance the surface area and microporosity of the biochar produced. The increased porosity and fragmentation of biochar contributed by the release of volatile matter from chemical bond decomposition during carbonization treatment [9]. The data shows that all activated carbon produced was successfully altered from mesoporous originalities to microporous characteristics with almost similar pore diameter within the narrow range from 1.33 nm to 0.8 nm. According to Maulina & Iriansyah [12], the molecular diameter of methylene blue (MB) is about 0.8 to 0.9 nm, which is smaller than the size of the micropores of activated carbon produced at 800°C to allow for the penetration of the particles. Thus, activated carbon produced with superheated steam at an activation temperature of 800°C showed an optimum surface area, high micropores surface area, high micropores volume, and narrowest pore diameter, so this treatment might also be a suitable choice to produce activated carbon. The use of superheated steam as an oxidizing agent can reduce the usage of chemical substances, which can be harmful to the environment and require enormous operation costs.

Table 1 BET surface area, micropores surface area, micropores volume, total pore volume, and pore size of activated carbon under various activation temperatures using superheated steam

Temp (°C)	**Surface area (S_{BET}) (m^2g^{-1})**	**Micropore area (S_{MICRO}) (m^2g^{-1})**	**Micropore vol. (V_{MICRO}) (cm^3g^{-1})**	**Total pore vol. (V_{TOTAL}) (cm^3g^{-1})**	**Pore size (nm)**
400	6.9	5.5	0.002	0.004	1.19
600	230.1	193.6	0.076	0.099	0.86
700	403.2	317.1	0.125	0. 178	0.88
800	475.6	367.4	0.147	0.296	1.33

3.3. Liquid characterization using GC-MS

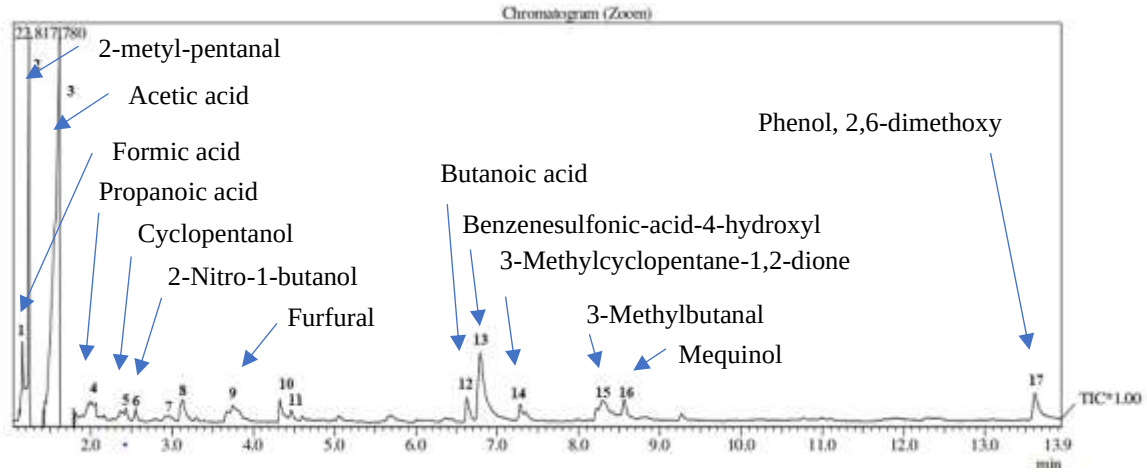


Figure 8 The gas chromatography spectrum of bio-oil was obtained from the thermal treatment process from EFB (400°C), using superheated steam.

Figure shows the spectrum of GC-MS of bio-oil obtained from the thermal treatment process of EFB (400°C) using superheated steam. The retention time (RT) of 13.9 mins was observed to determine the possible byproducts in the liquid product. At RT=1.617 min, the acetic acid spectrum was detected. Mustaza et al. [5] claimed that commercialized bio-char from mangrove wood produced also had acetic acid in their liquid product. Additionally, the torrefaction of mangrove wood using superheated steam at 300°C also produced a high concentration of acetic acid. At 400°C, the bio-oil produced contained more components with oxygen groups such as ketones, alcohol, aldehydes, carboxylic acid, phenols, and esters. Using superheated steam instead of nitrogen gas allowed for the recovery of torrefaction byproducts such as formic acid and acetic acid, which are currently burnt and released into the atmosphere as flue gas. Activation by superheated steam could generate value-added products from waste EFB while making it more environmentally friendly [13].

4. Conclusions

Activated carbon produced at 400°C to high temperature 800°C contributed to the low yield, low moisture and ash content, high fixed carbon content, contains more aliphatic properties, rich with oxygen-containing surface functional groups, and higher surface area. The enhanced properties of activated carbon show that the thermal treatment using superheated steam is possible as an effective oxidizing agent in producing good quality activated carbon. In addition, the residual liquid obtained from the carbonization of EFB at 400°C by condensation of superheated steam contained oxygen-rich compounds such as acetic acid, alcohol, aldehydes, acids, ketones. This showed that activation by superheated steam increased the amount of oxygen group recovered from the biomass. This liquid product can be sold as vinegar to prevent pesticides growth. According to Mustaza et al. [5], the acetic acid liquid product from the torrefaction of mangrove wood is commercialized as anti-pesticides.

Acknowledgments: The funding of this work was obtained under the grant in aid from Universiti Putra Malaysia under the project titled “Carbonization of Excess Sewage Sludge by Using Super-heated Water Vapor to Make Fuel” (Geran Inisiatif Putra IPS 9491400).

References

1. Abdullah, N., & Sulaiman, F. (2013). The Oil Palm Wastes in Malaysia, Biomass Now-Sustainable Growth and Use. Biomass Now - Sustainable Growth and Use, 75–100.
2. Hashemipour, H., Baroutian, S., Jamshidi, E., & Abazari, A. (2009). Experimental study and artificial neural networks simulation of activated carbon synthesis in fluidized bed reactor. International Journal of Chemical Reactor Engineering, 7. https://doi.org/10.2202/1542-6580.1825
3. Ooi, C. H., Ang, C. L., & Yeoh, F. Y. (2013). The properties of activated carbon fiber are derived from direct activation from oil palm empty fruit bunches fiber. Advanced Materials Research, 686, 109–117. https://doi.org/10.4028/www.scientific.net/AMR.686.109
4. Abdul Khalil, H. P. S., Jawaid, M., Firoozian, P., Rashid, U., Islam, A., & Akil, H. M. (2013). Activated carbon from various agricultural wastes by chemical activation with KOH: Preparation and characterization. Journal of Biobased Materials and Bioenergy, 7(6), 708–714. https://doi.org/10.1166/jbmb.2013.1379
5. Mustaza, M. N.F., Mizan, M. N., Yoshida, H., & Izhar, S. (2021). Torrefaction of mangrove wood by introducing superheated steam for biochar production. IOP Conference Series: Earth and Environmental Science, 765(1). https://doi.org/10.1088/1755-1315/765/1/012027
6. Bakhtiar, M. H. A. B. M., Sari, N. B. A., Yaacob, A. Bin, Yunus, M. F. B. M., & Ismail, K. Bin. (2019). Characterization of oil palm Empty Fruit Bunch (EFB) biochar activated with potassium hydroxide under different pyrolysis temperatures. Journal of Engineering Science and Technology, 14(5), 2792–2807.
7. Wafti, N. S. A., Lau, H. L. N., Loh, S. K., Aziz, A. A., Rahman, Z. A., & May, C. Y. (2017). Activated carbon from oil palm biomass as potential adsorbent for palm oil mill effluent treatment. *Journal of Oil Palm Research*, *29*(2), 278–290. https://doi.org/10.21894/jopr.2017.2902.12
8. Javier Sánchez, A. (2011). Characterization of activated carbon produced from coffee residues by chemical and physical activation. KTH Chemical Science and Engineering, March, 66.
9. Haridan, N. A., Yoshida, H., Salleh, M. A. M., & Izhar, S. (2020). Carbonization of excess sewage sludge using superheated water vapor to produce fuel. *IOP Conference Series: Materials Science and Engineering*, *991*(1). https://doi.org/10.1088/1757-899X/991/1/012068
10. Allwar, A. (2018). Preparation and characteristics of highly microporous activated carbon derived from empty fruit bunch of palm oil using KOH activation. Rasayan Journal of Chemistry, 11(1), 280–286. https://doi.org/10.7324/RJC.2018.1112000
11. Singh, S., Sidhu, G. K., & Singh, H. (2019). Removal of methylene blue dye using activated carbon prepared from biowaste(CPLC) precursor. *Indian Chemical Engineer*, *61*(1), 28–39. https://doi.org/10.1080/00194506.2017.1408431
12. Maulina, S., & Iriansyah, M. (2018). Characteristics of activated carbon resulted from pyrolysis of the oil palm fronds powder. IOP Conference Series: Materials Science and Engineering, 309(1). https://doi.org/10.1088/1757-899X/309/1/012072
13. "Fuel and Biochar from Biomass?" Science in Poland, 2019, scienceinpoland.pap.pl/en/news/news%2C33152%2Cfuel-and-biochar-biomass.html.

Dynamic Mechanical Analysis and Morphological Study of Composites of Polyvinyl Chloride - Date Palm Leaf Fiber

Abir Berkouk*, Ahmed Meghezzi , Hamza Chelali

Departement des sciences de la matière, Laboratoire de chimie appliquée, Université Mohamed-Khider de Biskra, Biskra 07000, Algeria.

***** *Corresponding author: abir.berkouk@univ-biskra.dz; Tel.:00213 0669556255.*

Abstract: This scientific work aims to study some properties of composites based on polyvinyl chloride (PVC) containing a natural waste date palm leaf fiber (DPLF) in various proportions, in order to improve the properties of the polymer. For this purpose, have made composite plates containing fiber at rates of 10 % and 30% at weight. In this research, we have carried out a dynamic mechanical analysis (DMA). In addition, we conducted morphological study followed by SEM scanning electron microscopy. This research shows that the DMA study behavior of the PVC / DPLF compositions showed a growth in the glass transition temperature value for the composition containing a 10% and 30% of DPLF fiber rate. The SEM morphology detected cohesion between the polymer and the fiber.

Keywords: date palm leaf fiber, mechanical proprieties, morphology, polyvinyl chloride

Evaluation of the Anti-inflammatory Activity of Polyphenols from Algerian Monovarietal Olive Oil Mill Wastewaters

Zakia Gueboudji [1,2,*], Kenza Kadi [1,2] and Kamel Nagaz [3]

[1] Biotechnology, Water, Environment and Health Laboratory, Abbes Laghrour University of Khenchela, Algeria;
[2] Faculty of Nature and Life Sciences, Abbes Laghrour University of Khenchela, Algeria;
[3] Drylands and Oases Cropping Laboratory, IRA Medenine, Tunisia.
***** *Corresponding author: gueboudji.zakia@gmail.com; Tel.: +213 99 67 58 24.*

Abstract: Olive oil mill wastewater (OMW) is a by-product of the olive oil industry. It is very polluting and causes serious environmental problems but is very loaded with polyphenols, which have antioxidant and anti-inflammatory power. This study aimed to evaluate in vitro the anti-inflammatory potential of the phenolic extract of OMW from two varieties Chemlal and Zlitni, extracted from a modern olive mill located in Khenchela, eastern Algeria. The extraction of the polyphenols was done by the maceration method. The dosage of total polyphenols and flavonoids content was determined by Folin-Ciocalteu and aluminum trichloride methods successively. The anti-inflammatory activity was made by two tests, inhibition of protein denaturation (IPD) and membrane-stabilizing potential (MSP), comparing with sodium diclofenac. The results obtained showed that the phenolic extract of Chemlal was found to exhibit the highest inhibitory effect anti-inflammatory activity (IPD: IC_{50} = 91.27 ± 2.73 µg/mL) and (MSP: IC_{50} = 98.41 ± 1.22 µg/mL) more than sodium diclofenac. The in vitro assays carried out indicate that the phenolic extract of OMW has an important source of natural anti-inflammatory agents, which can be used in the pharmaceutical industry on the one hand, and on the other hand reducing its dangerous impact on the environment.

Keywords: anti-inflammatory; polyphenols; olive oil mill wastewater; olive oil; monovarietal.

1. Introduction

The olive oil industry is particularly significant in Mediterranean nations, which is an important part of their economic activity [1]. The major waste product from the extraction of olive oil in highly contaminated acidic liquid form is olive oil mill wastewater (OMW). It has a strong purple-brown or brown-red to black hue due to the presence of tannins and phenolic compounds with low molecular weight, as well as an olive oil odor. Its composition is varied and complicated, mostly consisting of sugars, lipids, polyalcohol, proteins, polyphenols and organic acids [2,3]. Because the extraction process requires a considerable amount of water, this sector creates a large amount of (OMW), which is high in polyphenols. It has the ability to pollute ecosystems because it is slowly biodegradable [4]. OMW has a more varied content. This variable is influenced by the quality of the olives, their level of maturity, the extraction technique, and other factors as well as the quality of water used during the oil recovery stage [5]. Nowadays, with its huge volume and high concentration of organic compounds, the treatment of OMW is exceedingly challenging. OMW is now industrially valorized in order to recover polyphenols [6,7]. Olives and their derivatives may find application in the biopharmaceutical industry since they are high in phenol compounds [8,7]. Indeed, phenolic compounds exhibit a wide range of biological characteristics, including antioxidant and anti-inflammatory effects [9].

This study aimed to evaluate in vitro the anti-inflammatory potential of the phenolic extract of olive mill wastewater from two varieties Chemlal and Zlitni, extracted from a modern olive mill located in Khenchela, eastern Algeria.

2. Materials and Methods

2.1. Sampling

OMW samples were collected from a modern olive oil mill with a cold extraction system (temperature not exceeding 25 °C) located at Khenchela, eastern of Algeria. It is an oil mill constructed in Italy that was built in 2016. The OMW samples were collected during the harvest season in February 2020. The samples of olive oil mill are from two varieties of olive which were Chemlal and Zlitni. All analyses were carried out in triplicate.

2.2. Polyphenol Extraction Method

It was done by the maceration method after drying the samples of OMW according to the method described by [10].

2.3. Qualitative phytochemical analysis of OMW

Six tests were carried out. To test for alkaloids, use 2 mL of Wagner's reagent to 1 mL of extract (iodine in potassium iodide). The presence of alkaloids is confirmed by the appearance of a reddish-brown precipitate [11]. To test for phenols, dilute 1 mL of extract with 2 mL distilled water and a few drops of 10% $FeCl_3$. The presence of phenols is indicated by the presence of a blue or black color [12]. Test for Saponins: In a test tube, 2 mL of extract and 2 mL of distilled water were combined to determine the presence of saponins. For a few seconds, the mixture was vigorously agitated to see whether any persistent foam formed. Saponins are confirmed by the presence of foam [11]. Test for Flavonoids: they were tested by adding a few drops of 10% ferric chloride solution to roughly 2 mL of extract. The presence of flavonoids is indicated by the development of a green or blue color. To test for steroids, 2 mL chloroform and 0.2 mL concentrated H_2SO_4 were added to 1 mL extract. The presence of steroids is indicated by the development of a red-colored precipitate. Test for tannin, add a few drops of dilute ferric chloride solution to 1 mL of extract. The development of a blue black or greenish black precipitate indicates the presence of tannin [12].

2.4. Quantitative Phytochemical Screening of OMW

2.4.1. Total Phenolic Content (TPC)

The total phenolic content was measured using the Folin–Ciocalteu technique described by [13] with slight modification. The results were given in milligrams of Gallic acid equivalents per milliliter (mg GAE / mL). Triplicate analyses were performed. The total phenolic content (TPC) of extracts was estimated according to the calibration curve prepared from gallic acid ($y = 0.0048 x + 0.0111$, $R^2 = 0.9778$).

2.4.2. Total Flavonoid Content (TFC)

The total flavonoid content was determined using the protocol described by [14] with slight modifications. The findings were measured in milligrams of quercetin equivalents per milliliter (mg QE / mL). Triplicate analyses were performed. The total flavonoid contents (TFC) was calculated following the calibration curve prepared from quercetin ($y = 0.0109 x + 0.0073$, $R^2 = 0.9684$).

2.5. In vitro anti-inflammatory activity

2.5.1. Inhibition of protein denaturation (IPD)

It was estimated using the method described by [14], with slight adjustments. The basic idea is that the phenolic extract of OMW prevents BSA denaturation produced by heat (72 °C). 1 mL of each different extracts was added to 1 mL of 0.2 percent BSA solution made in Tris-HCl pH 6.6, then incubated at 37 °C for 15 minutes, followed by 5 minutes in a 72 °C water bath. After cooling, the turbidity is measured in a cell spectrophotometer at 600 nm (SPECORD 210 plus). Diclofenac sodium standard (injectable form) was produced using the same technique in ultra-pure distilled water from a 500-ppm mother solution, with distilled water serving as a negative control.

2.5.2. Membrane stabilizing potential (MSP)

It was calculated using the method of [15] An equivalent volume of blood was collected from a healthy human volunteer who had not taken any NSAIDs for two weeks before to blood collection and combined with an equal volume of sterile Alsever solution. This blood solution was centrifuged

for 10 minutes at 3000 rpm, the packed cells were separated and rinsed with iso-saline solution, and iso-saline was used to make a 10% (v/v) suspension. 1 mL phosphate-buffered saline, 0.5 mL 10% blood suspension, 0.5 mL phenolic extract of OMW with various concentrations, and 2 mL hypotonic saline represent approximately the dose combination. All test combinations were incubated for 30 minutes at 37 °C before being centrifuged for 20 minutes at 3000 rpm. The hemoglobin concentration was measured using a spectrophotometric measurement at 560 nm after the supernatant was separated. Diclofenac sodium at the final concentration was used as a positive control and distilled water as a negative control. The IC_{50} was measured once again using a graph that indicated inhibition at different concentrations.

2.6. Statistical study

Data obtained were given as (mean ± standard) deviation of three dependent determinations. Significant differences between means of total phenolic and total flavonoids results were evaluated by Student t-test, and p values (< 0.05) were regarded as significant. Results of anti-inflammatory activity were subjected to statistical analysis of variance (ANOVA) using ECXEL STAT (version 2014) package at $p < 0.05$ significant levels.

3. Results and Discussion

3.1. The phytochemical analysis

The results of the phytochemical analysis of OMW are illustrated in Table 1.

The phytochemical analysis of phenolic extract of OMW revealed the presence of alkaloids, phenols, flavonoids, steroids and tannins in the two extracts. While it revealed the absence of saponins in the two extracts.

Table 1. Phytochemical analysis of OMW

Phytochemicals	**Chemlal**	**Zlitni**
Alkaloids	+	+
Phenols	+	+
Saponins	-	-
Flavonoids	+	+
Steroids	+	+
Tannin	+	+

(+) = presence of phytochemicals (-) = absence of phytochemicals

3.2. Total Phenolic and Flavonoids Contents

The results of total phenolic and flavonoid contents are presented in (Figure 1)

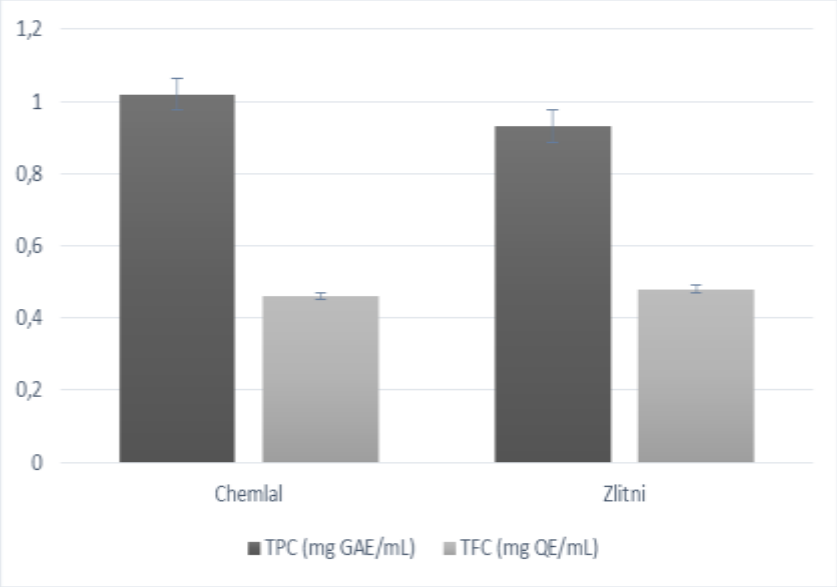


Figure 1. Total phenolic and flavonoid contents of OMW

According to the results obtained in Figure 1, the content of OMW in phenolic contents differs between the extracts of the two varieties. The extracts of Chemlal contain the highest concentration (1.02 ± 0.02 mg GAE / mL) and the low concentration was recorded in the extracts of Zlitni (0.93 ± 0.05 mg GAE / mL). Numerous researchers have determined the level of polyphenols in OMW: value of (950 ± 14.2 µg GAE/ mg of extract) quantified by [7].

The content of flavonoid from OMW of the two varieties was almost similar (0.46 ± 0.07 mg QE / mL for Chemlal and (0.48 ± 0.08 mg QE / mL). The level of flavonoids of OMW was largely determined by many researchers such as [7] who found a value of (80.6 ± 17.27 µg QE/mg of extract).

3.3. Anti-inflammatory activity

The anti-inflammatory activity of OMW extract was determined using protein denaturation and membrane stabilizing potential methods. The results were represented in figure 2.

3.3.1. Inhibition of protein denaturation (IPD)

The investigated phenolic extract of OMW from Chemlal has a thermal denaturation inhibitory efficiency (IC_{50} = 91.27 ± 2.73 µg/mL) that is more than that of the reference anti-inflammatory medication diclofenac sodium (IC_{50} = 92.98 ± 1.31 µg/mL) and higher than Zlitni (97.36 ± 0.5 µg/mL).

The extract has an anti-inflammatory potential as a result of its protein stabilizing action, which has to be validated by additional in vivo testing.

Indeed, a protein's conformation is connected to its secondary and tertiary structure; it is performed by lower energy connections (hydrogen bonds, electrostatic, hydrophobic, and disulfide bridges), making it unstable.

Denaturation is caused by a change in the quaternary, tertiary, and secondary structures without fragmentation of the peptide chain caused by different chemical or physical causes [16,17]. Denaturation of a protein enables the inflammatory response to be triggered by the formation of auto-antigens, which are essential contributors in the development of chronic inflammation [16].

Many flavonoids and related polyphenols have been demonstrated in recent research to contribute considerably to antioxidant and anti-inflammatory properties. The presence of these bioactive chemicals in the OMW extract may explain its anti-inflammatory effect.

As a result, compounds that inhibit protein denaturation might be beneficial in the development of anti-inflammatory drugs [18].

3.3.2. Membrane stabilizing potential (MSP)

According to the findings, the extract significantly stabilized the red blood cell membrane when compared to diclofenac sodium. The extract of Chemlal had a higher inhibitory concentration (IC_{50} = 98.41 ± 1.22 µg/mL) than diclofenac sodium (IC_{50} = 99.78 ± 0.92 µg/mL), whereas Zlitni had a lower power (IC_{50} = 107.2 ± 0.1 µg/mL).

Because the erythrocyte membrane is similar to the lysosomal membrane, stabilization of the red blood cell membrane has been utilized to examine anti-inflammatory effects in vitro [17].

This means that the phenolic extract of OMW can effectively stabilize the lysosomal membrane. The lysosome must be stabilized in order to minimize the inflammatory response by limiting the release of lysosomal components such as bacterial enzymes and protease from active neutrophils.

Nonsteroidal anti-inflammatory drugs, such as diclofenac sodium, act by either inhibiting lysosomal enzymes or stabilizing lysosomal membranes [19].

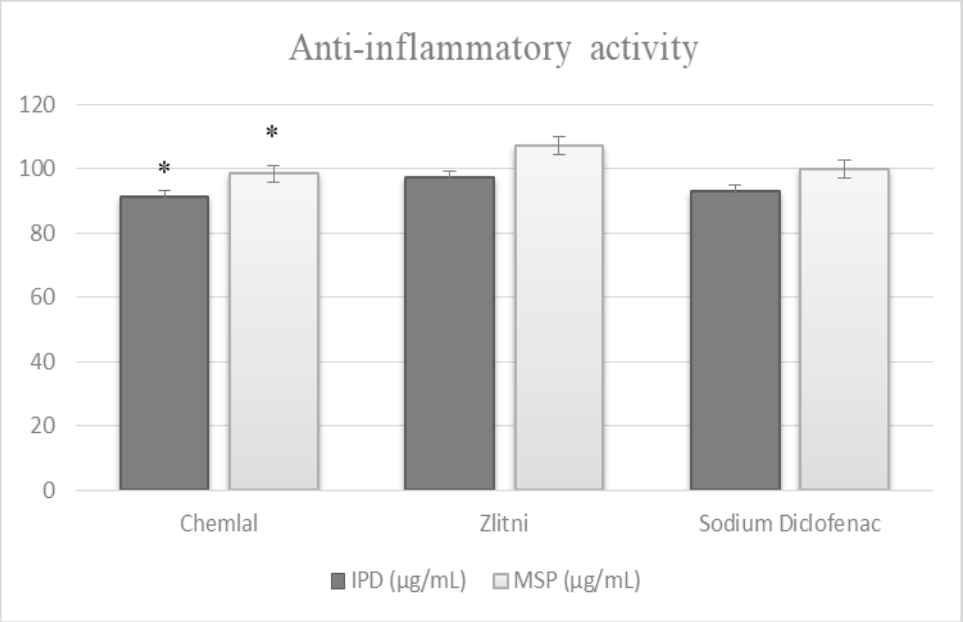


Figure 2. The anti-inflammatory activity of OMW

4. Conclusions

The in vitro assays carried out indicate that the phenolic extract of OMW has an important source of natural anti-inflammatory agents, which can be used in the pharmaceutical industry on the one hand, and on the other hand reducing its dangerous impact on the environment.

Funding: This research received no external funding.

Acknowledgments: The authors thank Drylands and Oases Cropping Laboratory, Institute of Arid Regions, Medenine, Tunisia for their technical assistance and support.

References

1. Esteves, B. M.; Morales-Torres, S.; Maldonado-Hódar, F. J.; Madeira, L. M. Fitting biochars and activated carbons from residues of the olive oil industry as supports of Fe-catalysts for the heterogeneous Fenton-like treatment of simulated olive mill wastewater. *Nanomaterials*, **2020**, *10*(5), 876.

2. Hocaoglu, S.M.; Gursoy, B.H.; Basturk, I.; Talazan, P.; Aydoner, C. Assessment of technology modification for olive oil sector through mass balance: A case study for Turkey. *Journal Cleaner Prod*. **2018**; 188:786–795.
3. Genç, N.; Durna, E.; Cicigün, H.K.K. Response Surface Modeling and Optimization of Microwave-Activated Persulfate Oxidation of Olive Oil Mill Wastewater. *Clean – Soil, Air, Water*, **2020**, 48, 1900198
4. Gueboudji, Z.; Bagues, M.; Kadi, K.; Nagaz, K.; Addad, D. Effect of storage time on the biodegradability of olive oil mill wastewater from the cold extraction of olive oil system. *The EuroBiotech Journal*, **2021b**, 5 (3), 142-154; https://doi/10.2478/ebtj-2021-0023
5. Battista, F.; Mancini, G.; Ruggeri, B.; Fino, D. Selection of the best pretreatment for hydrogen and bioethanol production from olive oil waste products. *Renewable Energy*, **2016**, 88, 401e407.
6. Rahmanian, N.; Jafari, S. M.; Galanakis, C. M. Recovery and removal of phenolic compounds from olive mill wastewater. *Journal of the American Oil Chemists' Society*, **2014**, *91*(1), 1-18.
7. Gueboudji, Z.; Kadi, K.; Nagaz, K. Extraction and Quantification of Polyphenols of Olive Oil Mill Wastewater from the Cold Extraction of Olive Oil in the Region of Khenchela-Algeria. *Genetics And Biodiversity Journal (GABJ)*, 116-122; **2021a**. http://ojs.univ-tlemcen.dz/index.php/GABJ
8. De Leonardis, A.; Macciola, V.; Lembo, G.; Aretini, A.; Nag, A. Studies on oxidative stabilisation of lard by natural antioxidants recovered from olive-oil mill wastewater. Food Chemistry, **2007**, 100(3), 998-1004.
9. Khan, Y.H.; Hadi, S.M.; Mohammad, R.M.; Azmi, A.S. Prooxidant anticancer activity of plant-derived polyphenolic compounds: An underappreciated phenomenon. In Functional Foods in Cancer Prevention and Therapy, 221-236, Academic Press; **2020**. https://doi/10.1016/B978-0-12-816151-7.00012-0
10. Gueboudji, Z.; Kadi, K.; Nagaz, K. Evaluation Of The Anticoagulant Effect Of Phenolic Extracts Of Two Olive Mill By-products: Olive Mill Wastewater And Olive Mill Pomace, European Journal of Science and Technology, 2021c, 28, 826-830; doi:10.31590/ejosat.1005114
11. Inamdar, P.R.I.Y.A.L.; Jelamvazir, D.S.; Patel, D.; Meshram, D. Phytochemical screening and in vitro antifungal activity of Camellia sinensis. *International Journal of Pharmacy and Pharmaceutical Sciences*, **2014**, *6*(5), 148-150.
12. Ganatra, S.H.; Durge, S.P.; Ramteke, A.M. Phytochemical's investigation and TLC analysis of Jasminum multiflorum leaves. *Int J Pharm Sci Res.*, **2013**; 4(3); 1135-1139.
13. Siangu, B. N.; Sauda, S.; John, M. K.; Njue, W. M. Antioxidant activity, total phenolic and flavonoid content of selected Kenyan medicinal plants, sea algae and medicinal wild mushrooms. *African Journal of Pure and Applied Chemistry*, **2019,** 13(3), 43-48. DOI: 10.5897/AJPAC2018.0775
14. Tona, M.; Tareq, A.M.; Sayeed, M.; Mahmud, H.; Jahan, I.; Sakib, S.; Shima, M.; Emran, T.B. Phytochemical screening and in vitro pharmacological activities of methanolic leaves extract of Caryota mitis. *J. Adv. Biotechnol. Exp. Ther*., **2020**, 3, 109.
15. Murugan, R.; Parimelazhagan, T. Comparative evaluation of different extraction methods for antioxidant and anti-inflammatory properties from Osbeckia parvifolia Arn.–an in vitro approach. *J King Saud Univ Sci*, **2014**, 26(4): 267–275.
16. Karthik, K.; Bharath, R.P.; Venu Priya, R.; Sunil Kumar, K.; Ranjith Singh, B.; Rathore. Evaluation of anti-inflammatory activity of canthium parviflorum by in-vitro method. *Indian Journal of Research in Pharmacy and Biotechnology*, **2013**, 2320 – 3471.
17. Marliyah, M.; Ananthi, T. In-vitro anti-inflammatory activity of seed extract of Zea Mays (L.). *Journal of Global Biosciences*, **2015**, 4 (5): 2168-2173.
18. Chatterjee, P.; Chandra, S.; Dey, P.; Bhattacharya, S. Evaluation of anti-inflammatory effects of green tea and black tea: A comparative in vitro study. *Journal of Advanced Pharmaceutical Technology & Research Apr-Jun.*, **2012,** 3: 136-138. https://doi/10.4103/2231-4040.97298
19. Kumari, C.S.; Yasmin, N.; Hussain, M.R.; Babuselvam, M. In vitro anti-inflammatory and anti-arthritic property of Rhizopora mucronata leaves. *Intern J Pharma Scie Res* **2015**, 6, 482-485; 2015.

Groundwater Hydrogeochemical and Quality Appraisal for Agriculture Irrigation in Greenbelt Area, Iraq

Eman Sh. Awad [1,2,*], Noor S. Imran [3], Tamara M. Sabirova [1], Natalia A. Tretyakova [1], Qusay F. Alsalhy [4], Vyacheslav Snegirev [1]

[1] Department of Chemical Technology of Fuel and Industrial Ecology, Institute of Chemical Technology, Ural Federal University named after the first President of Russia B.N. Yeltsin, 620002 Yekaterinburg, Russia;

[2] Environmental Research Center, University of Technology-Iraq, Baghdad 10066, Iraq;

[3] Department of Architecture Engineering, Al Safwa University College, Baghdad, Iraq;

[4] Membrane Technology Research Unit, Department of Chemical Engineering, University of Technology-Iraq, Baghdad 10066, Iraq; 80006@uotechnology.edu.iq;

***** *Corresponding author: ial-samarraii@urfu.ru.*

Abstract: This study highlights the groundwater hydrogeochemical characteristics (hydrochemistry characteristics, evaporation, ion exchange, and salinization) and quality suitability assessment for agriculture irrigation purpose from five wells in the Greenbelt area locates in the northwestern of AL-Najaf Governorate, a southwestern of Iraq. The groundwater suitability for irrigation was assessed based on the irrigation water quality index (IWQI) for thirteen parameters and groundwater quality indices such as electrical conductivity (EC), total dissolved solid (TDS), sodium adsorption ratio (SAR), residual sodium carbonate (RSC), soluble sodium percent (SSP), total hardness (TH), permeability index (PI), potential salinity (PS), Kelley's ratio (KR), and magnesium hazard ratio (MHR). According to irrigation water quality index (IWQI) of the study area, the groundwater in the sampling sites S1 and S2 were unsuitable and unsafe for irrigation, while the others sites were safe and possible used for irrigation. The EC, TDS and PS, MHR for all sites and about 80% of sites with KR were unsuitable for irrigation. However, the SAR, SSP, RSC, PI, and TH for all sites were suitable for irrigation. As a result of this study, it has been determined that groundwater in the study area is unsuitable for agricultural irrigation. For sustainable groundwater exploitation, it is advised that a continuous water quality monitoring program be implemented, as well as the development of suitable management practices.

Keywords: Groundwater; irrigation; SAR; water quality index; irrigation indices; ion exchange.

1. Introduction

Groundwater is a natural resource and a major source of water in urban and sub-urban areas in Africa and Asia which is used for domestic and agricultural purposes that may be due to the low availability and quality of surface water resources (1). The groundwater quality is affected by the natural and anthropogenic activities. Natural factors like geology and geochemical processes can have an impact on groundwater quality. The increase in population, Urbanization and industrialization has led to significant deterioration of groundwater quality, salinization of groundwater and land subsidence, as a result of its frequent contamination with sewage seepage, intrusion of industrial wastewater, and manure for weed growing (2–4).

Hydrogeochemical investigations that control the chemistry of groundwater aid in developing knowledge of hydrochemical systems, this, in turn, can help with the efficient use and sustainable management of groundwater resources by identifying relationships between various hydrogeological parameters (5). Water quality index (WQI) is a practical and comparably simple approach that uses a wide set of water quality data and converts it into a single value to represent overall groundwater quality and suitability for drinking, irrigation, and other uses (6). The chemical ions present in groundwater determine its suitability for different purposes. Water quality assessment is utmost important; especially in areas that depend on groundwater (7).

The hydrogeochemical and quality assessment of groundwater based on the irrigation water quality index (IWQI), various indices were conducted to evaluate the suitability of groundwater for agriculture irrigation purposes in the Green-belt project (northwestern of AL-Najaf Governorate, Iraq). The objectives of this study are (i) to understand the groundwater chemistry, (ii) to assess groundwater quality, and (iii) to determine the suitability of groundwater usage for irrigation purpose.

2. Materials and Methods

2.1. Site Description (location and climate)

Iraqi government established Greenbelt project at 2006 to improve the environment in the area. It is one of the most important projects in Al-Najaf Governorate, which locates southwestern of Iraq about 160 km south of Baghdad (Capital of Iraq). The Greenbelt area locates in the northwestern of AL-Najaf Governorate on the high way between AL-Najaf and Karbala governorates. It have eight wells, three wells were out of service.

AL-Najaf Governorate has a hot desert climate, with long, very hot summers and mild winters. The weather conditions for the study area were mean air temperature (min. 18.3^{o}C and max. 32.1^{o}C), relative humidity (41.8%), wind speed (1.63 m/s), sun shine (8.62 hr/day), evaporation (294.3 mm) and rain (7.78 mm) (8) (9).

2.2. Geo Database

Groundwater samples were collected from five selected wells (Table 1) at Greenbelt area during 2015-2016. Figure 1 illustrating the location of groundwater sampling sites. Table 1 presented the boundaries and information for each well (well depth (WD), static water level (SWL), dynamic water level (DWL), and discharge (D)).

Groundwater samples were preserved in stopper fitted polyethylene bottles, were kept in an ice box during transportation to the laboratory to be analyzed as soon as possible. Conductivity and pH were measured on the sites by using portable measuring devices.

In the laboratory, the groundwater samples were analyzed for thirteen parameters: pH; Electrical Conductivity (EC); Total Dissolved Solid (TDS); Carbonate (CO_3^{2-}); Bicarbonate (HCO_3^{-}); Chloride (Cl^{-}); Calcium (Ca^{2+}), Magnesium (Mg^{2+}); Sodium (Na^{+}); Potassium (K^{+}); Phosphate (PO_4^{2-}); Nitrate

(NO_3^+) and Sulfate (SO_4^{2-}), according to the Standard Method for Examination of Water and Wastewater (10).

Table 1. Coordinates of the groundwater sampling sites by GPS (Garmin navigator).

Well (Site No.)	X- Latitude	Y- Longitude	WD, m	SWL, m	DWL, m	Discharge, L/s
S1	32 9 59.64	44 11 46.02	183	48	45	7
S2	32 9 56.7	44 14 7.08	172	25	48	9
S3	32 9 58.2	44 15 41.28	50	24.9	32.1	6
S4	32 10 22.02	44 16 46.32	50	16	22	7
S5	32 10 46.26	44 17 58.68	50	18	25	9



Figure 1. The sites of groundwater samples at the Greenbelt area northwestern of AL-Najaf Governorate, Iraq.

2.3. Assessment methods

2.3.1 Irrigation water quality index

The water quality index method presents a cumulatively numerical expression specifying a given level of water quality that is extensively utilized around the world because of its ability to properly represent water quality information. It's one of the most useful instruments and crucial parameters for assessing and managing groundwater quality (11) (12). The weighted arithmetic module was used to calculate the irrigation water quality index (IWQI) in this study. This approach gives data on water quality evaluations and it's calculated using the following formula (13):

$$IWQI = \frac{\sum W_i Q_i}{\sum W_i} , \quad (1)$$

Where:

Qi signifies a quality relative value of ith parameters which represents the number of water quality parameters; Wi is a unit weight which measures the importance of a parameter in the calculation of the WQI index; Qi and Wi are calculated by formulas:

$$Q_i = \frac{V_i - V_o}{S_i - V_o} * 100 , \quad (2)$$

$$W_i = \frac{K}{S_i} , \quad (3)$$

Where:

Vi represents the value experimentally obtained from laboratory analysis; V_o represents the ideal value of the water quality parameter, The ideal value of all parameters took as zero excepting pH value counted 7; Si represents the standard guidelines of water quality for agriculture (14); K is a constant which can obtained from $K = 1/\sum(1/S_i)$.

The index equation makes a number between 1 and 100, with 1 being the best and more than 100 indicating the poorest water quality. The classification of the water quality status based on IWQI is illustrated in Table 2.

Table 2. Classification of water quality according IWQI score (15)(16).

Score	<25	26-50	51-75	76-100	>100
IWQI class	Excellent	Good	Poor	Very poor	Unsuitable
Possible usage	Drinking, irrigation and industrial	Drinking, irrigation and industrial	irrigation and industrial	irrigation	Proper treatment required before use.
		SAFE			UNSAFE

2.3.2 Irrigation water quality indices

Groundwater is the main water source for agricultural irrigation activities, so it's important to assess the suitability of groundwater irrigation by using the parameters include physical and chemical characteristics (17). These parameters are used in the irrigation water quality indices such as electrical conductivity (EC), total dissolved solid (TDS), sodium adsorption ratio (SAR), residual sodium carbonate (RSC), soluble sodium percent (SSP), total hardness (TH), permeability index (PI)potential salinity (PS), Kelley's ratio (KR), and magnesium hazard ratio (MHR). Irrigation water quality indices for the groundwater which is used in this study are summarized in Table 3. In calculating these indices, all the concentrations of ions were expressed in milli-equivalent per liter (meq/L).

Table 3. Formula of irrigation water quality indices.

Indices	Formula	Ref.
SAR	$SAR = \frac{Na^+}{\sqrt{\frac{Ca^{2+} + Mg^{2+}}{2}}}$	(18)
SSP	$SSP = \frac{Na^+}{Ca^{2+} + Mg^{2+} + Na^+ + K^+} * 100$	(19)
RSC	$\mathrm{RSC} = (\mathrm{CO_3^{2-}} + \mathrm{HCO_3^-}) - (\mathrm{Ca^{2+}} + \mathrm{Mg^{2+}})$	(20)
PS	$PS = Cl^- + (0.5 * SO_4^{2-})$	(21)
KR	$KR = \frac{Na^+}{Ca^{2+} + Mg^{2+}}$	(22)
MH	$MH = \frac{Mg^{2+}}{Ca^{2+} + Mg^{2+}} * 100$	(23)
TH	$TH = 2.50 * Ca^{2+} + 4.12 * Mg^{2+}$	(23)
PI	$PI = \frac{Na^+ + \sqrt{HCO_3^-}}{(Na^+ + Ca^{2+} + Mg^{2+})} * 100$	(21)

3. Results and Discussion

3.1. Hydrogeochemical processes

3.1.1. Hydrochemistry characteristics

Descriptive statistical analyses of groundwater parameters obtained from field measurements and laboratory analysis were calculated, including the mean, minimum, maximum, and standard deviation with the help of SPSS 28.0 software. The statistical analysis are tabulated in Table 4. Physicochemical parameters are (pH, electrical conductivity (EC), and total dissolved solids (TDS)), major cations (Ca^{2+}, Mg^{2+}, Na^+ and K^+), and anionic concentrations (Cl^-, HCO_3^- , PO_4^{2-}, NO_3^- and SO_4^{2-}). Explanation as follows:

Physicochemical parameters: The pH of the groundwater samples is slightly basic (6.9–8.0) with an average of 7.34, indicating good water quality in terms of pH (24).

The analyzed samples have very high values of EC and range from 4680 to 5960 µS/cm (mean value 5026 µS/cm), exceeding the permissible limits values (EC 3000 µS/cm) of the water quality for agriculture guideline (14), due to the long period of stay of groundwater in the well and no fresh water entering in it. Also the high EC values indicate that there is some form of mixing between freshwater and saline water may have place as proposed by Egbi et al.(25).The TDS vary between 2995-3814

mg/L with mean value 3216 mg/L, exceeding the guideline value of TDS 2000 mg/L (14), indicating that the obtained groundwater samples are extremely salinized.

Cations and anions: The order of abundance of the major cations (in mg/L) show the decreasing order as $Na^+ > Ca^{2+} > Mg^{2+} > K^+$ for groundwater of sampling site S1, $Mg^{2+} > Na^+ > Ca^{2+} > K^+$ for sampling site S2 and $Mg^{2+} > Na^+ > Ca^{2+} > K^+$ for sampling sites S3, S4 and S5. The abundance of the major cations for all sites is presented in Figure 2. The magnesium (Mg^{2+}) is the dominating cation in most of the sample sites varies between 453.78 to 1089 mg/L (mean 669.65 mg/L). Along with Mg^{2+}, both sodium (Na^+) (400-490 mg/L) and calcium (Ca^{2+}) (180.68-471.34 mg/L) contributed in considerable amount for the mineralogical composition of the samples. Potassium (K^+) shows a range (32.8-46 mg/L) with an average 38.65 mg/L.

The order of abundance of the major anions (in mg/L) show the decreasing order as $SO_4^{2-} > Cl^- > HCO_3^- > NO_3^- > PO_4^{2-}$ for the samples of both S1 and S4, $SO_4^{2-} > Cl^- > NO_3^- > HCO_3^- > PO_4^{2-}$ for the samples of both S2 and S3, while for the sampling site S5 as $Cl^- > SO_4^{2-} > NO_3^- > HCO_3^- > PO_4^{2-}$, The abundance of the major anions for all sites is presented in Figure 3. sulfate (SO_4^{2-}) is the dominating anion for the sampling sites S1, S2, and S3, varying in the range of 1040-1940 mg/L while Chloride (Cl^-)is the dominant anion for both sampling sites S4 and S5 with range (969.5- 3278 mg/L) while the other anions were in much negligible concentration.

In terms of major cations and anions, most of the measured parameters of samples satisfy the standard guideline of water quality for agriculture (14) except Mg^{2+} and K^+, which is more than the allowable limit for agriculture irrigation for all sites, while the Cl^- is more than the allowable limit only in sampling sites S4 and S5.

Table 4. Statistical summary of the physicochemical parameters of groundwater samples.

Parameters	Minimum	Maximum	Mean	Std. Deviation
pH	6.9	8.0	7.34±0.2	0.46
EC	4680	5960	5026±238	534.12
TDS	2995	3814	3216.56±153	341.87
Ca^{2+}	180.68	471.34	333.077±48	108.40
Mg^{2+}	453.78	1089.00	669.659±113	252.30
Na^+	400	490	447.6±18	39.89
K^+	32.8	46.0	38.56±2.33	5.21
HCO_3^-	12.20	31.73	22.926±4.13	9.23
Cl^-	969.5	3278.0	1861.3±527	1179.00
PO_4^{2-}	0.01	0.12	0.068±0.02	0.04
NO_3^-	0.000	63.435	40.9504±12.44	27.81
SO_4^{2-}	1040	1940	1512±148	330.33

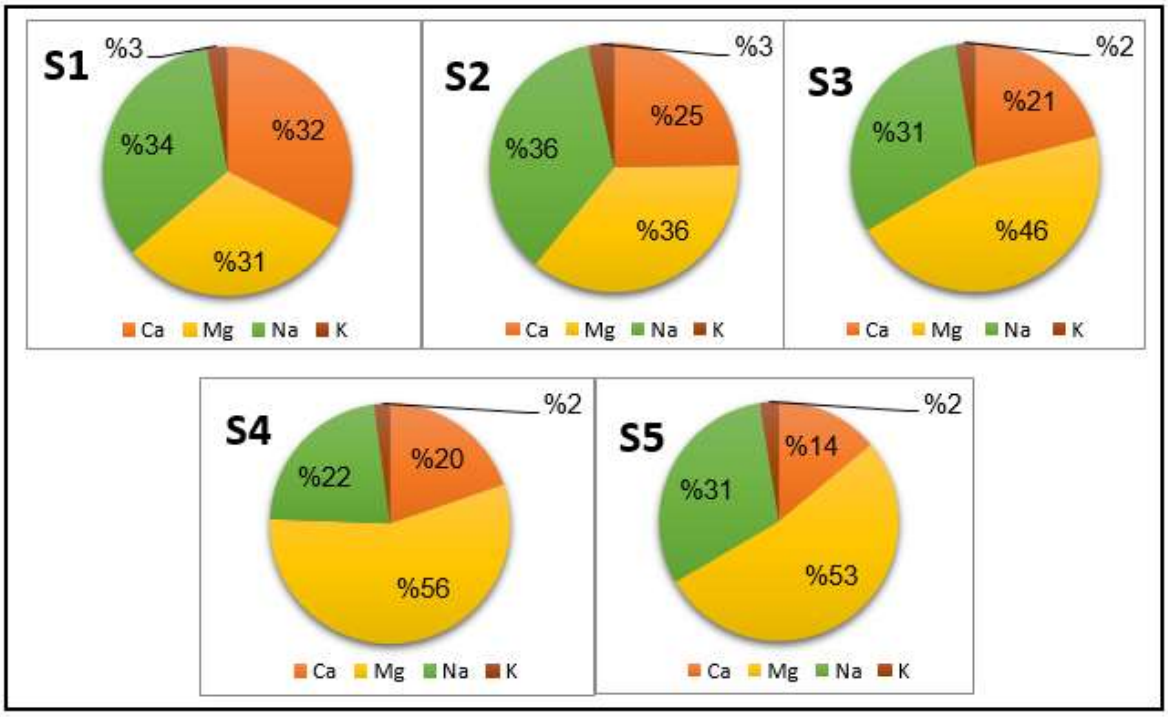


Figure 2. The abundance of the major cations for all sites.

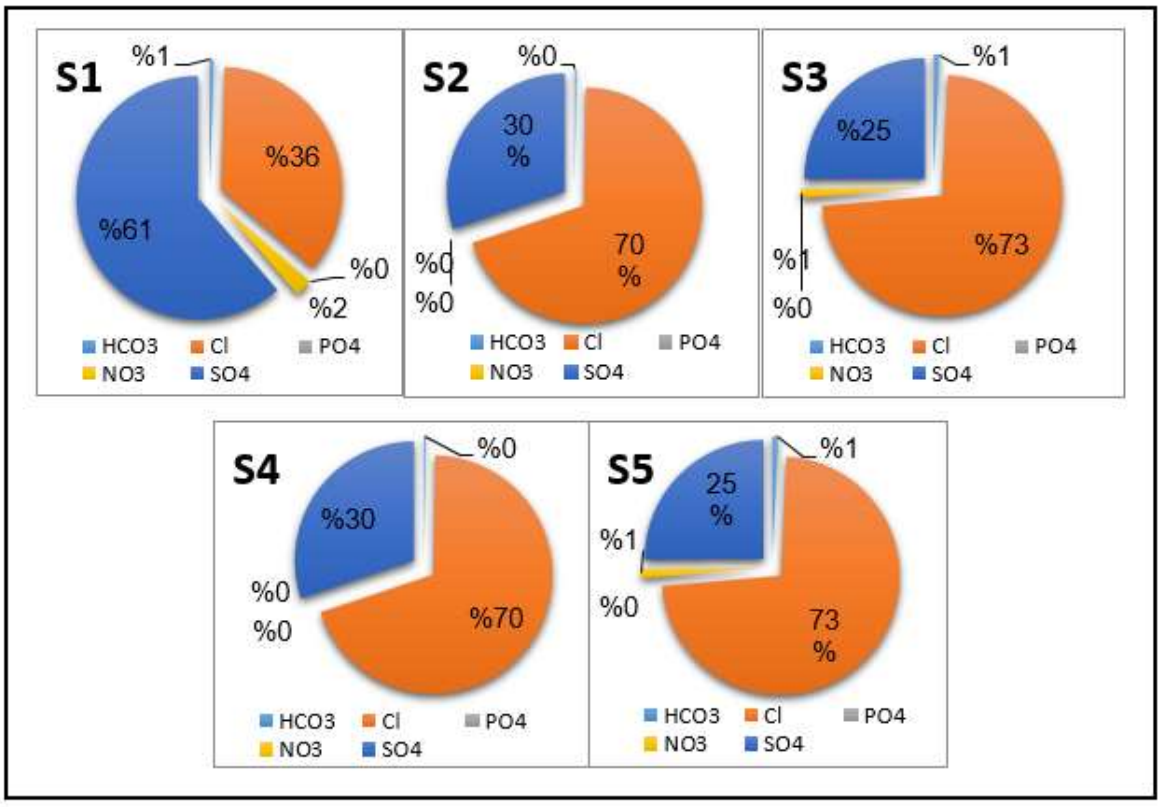


Figure 3. The abundance of the major anions for all sites.

3.1.2. Evaporation

Evaporation is the primary source of changes in groundwater composition. The evaporation's influence depend on the aquifer's temperature and geology (26) (27). It's not only a common phenomenon in groundwater systems, but the Na^+/Cl^- ratio is one of a good indicator of evaporation and is widely utilized to determine it (28). The evaporation is a significant process, as illustrated by the plot of Na^+ versus Cl^- in Figure 4. All samples plot around the freshwater evaporation line in this figure, indicating that evaporation plays an important role in determining the chemical composition of groundwater. The climatic condition increased the evaporation rate, thus, the evaporation contributed to more ions enrichment in the groundwater.

3.1.3. Ion Exchange

Base Exchange Index proposed by Schoeller (29), which is measured by using Chloro-alkaline indices CAI I and CAI II through rock–water interaction. Chloro-alkaline indices used to investigate the ion exchange between the groundwater and the aquifer, which it's occurred in the chemical reaction during the movement and rest state of water. It's calculated by the formulae:

$$CAI\ I = (Cl^- - (Na^+ + K^+))/Cl^- \ , \quad (4)$$

$$CAI\ II = (Cl^- - (Na^+ + K^+))/(SO_4^{2-} + \mathrm{CO_3^{2-}} + \mathrm{HCO_3^-} + NO_3^-) \ , \quad (5)$$

Where, all ions are expressed in meq/L.

The indices CAI I and II may be negative or positive depending on the exchange process between (Na^+ and K^+) from the aquifer material with (Mg^{2+} and Ca^{2+}) in groundwater and vice versa. It would be negative when calcium or magnesium in groundwater exchanges with sodium or potassium in the aquifer material. but when sodium or potassium in groundwater exchanges with calcium or magnesium in aquifer material, the above indices would be positive, indicating reverse ion exchange (29) (30). The indices CAI I and II estimated for samples showed a positive ratio indicating the dominance in this study's groundwater of ion exchange.

The relationship between (Ca^{2+} + Mg^{2+}) and ($SO4^{2-}$ + $HCO3^-$) in reverse ion exchange will be near to 1:1 equiline, indicating minerals dissolution as shown in Figure 5. Also the relationship between (Na^+-Cl^-) and (Ca^{2+}+Mg^{2+}–HCO_3^-–SO_4^{2+}) can be used to identify reverse ion exchange. According to (31), such a relationship will be linear, with a slope of -1. In this study the samples of groundwater were plot in a linear fashion as shown in Figure 5, and the slope was -0.146. As a result, it's clear that reverse ion exchange is one of the key mechanisms governing the chemistry of this region's groundwater.

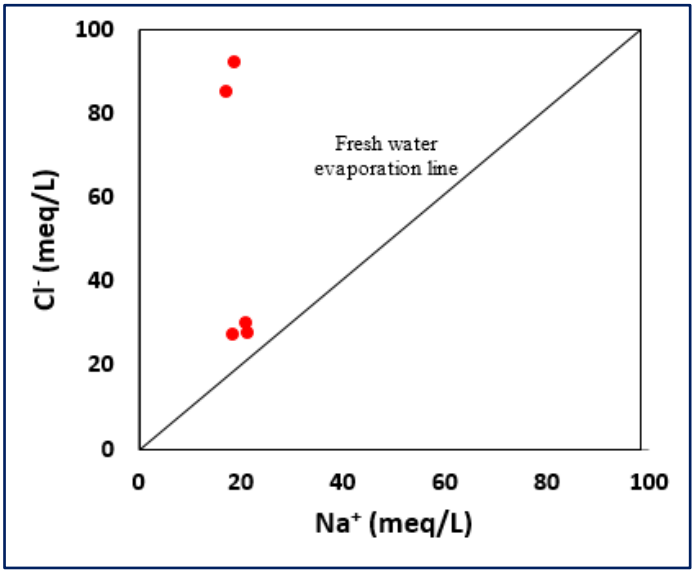


Figure 4. Plot of Na^+ versus Cl^-, indicating evaporation process of the groundwater samples.

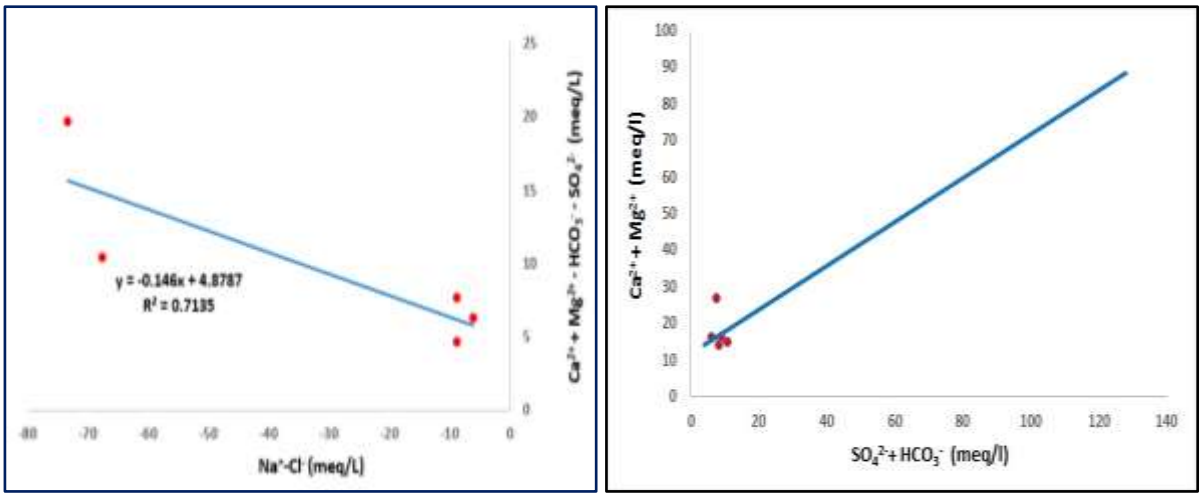


Figure 5. Plot of various ions, indicating reverse ion exchange of the groundwater samples.

3.1.4. Salinization

Revelle index (RI) was used to assess the salinization level of groundwater in the study area. The Revelle Index was calculated using the formula below:

$$RI = Cl^- / (HCO_3^- + CO_3^{2-}) , \quad (6)$$

The ions' concentrations in the equation above are expressed in meq/L.

The groundwater is affected by salinization with RI values > 0.5 (32). The estimated RI values ranged from 51.75 to 461.69 meq/L (Figure 6). All the groundwater samples have RI values more than 0.5 meq/L which indicating they are affected by high salinization. This could be attributed to

geogenic activities in the study area which is caused by anthropogenic inputs like domestic waste, unrestricted activities of agricultural , and septic tank seepage (28).

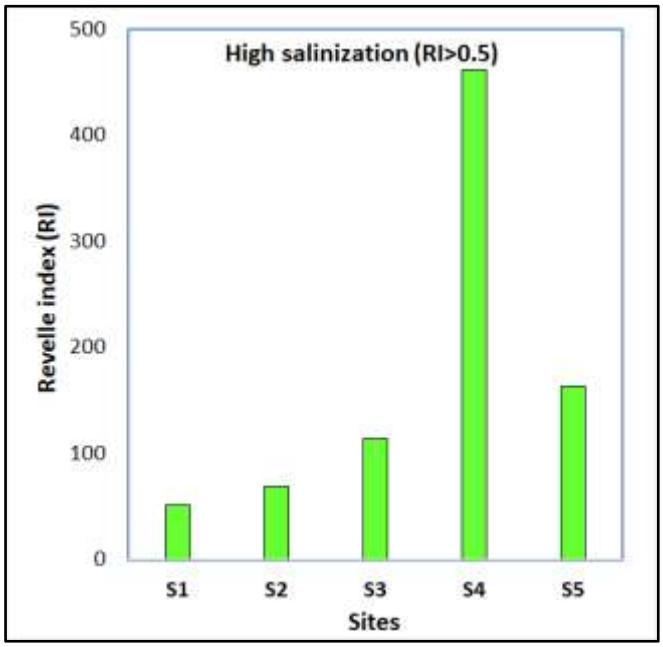


Figure 6. The Revelle index (RI) for the groundwater samples.

3.2. Groundwater quality assessment

In this study, the IWQI was applied for all sites using of standard guideline of water quality for agriculture (14). The first step in 'weighted arithmetic index' method for calculation IWQI include determination of 'unit weight' assigned for each physicochemical parameter which used in the calculation. The highest unit weight 0.840600 is assigned for carbonate (CO_3^{2-}) and 0.042030 for both potassium (K^+) and phosphate-P (PO_4^{2-}-P), indicating the importance of these indicators in water quality assessment and their significant impact on the index. Table 5 shows the standards (permissible values of several parameters) for the groundwater as well as the unit weights assigned to each parameter considered in the calculation of IWQI. The detected values of the selected physicochemical parameters in all the groundwater sites and the WQI values are presented in Table 6.

Average values of IWQIs ranged from 76 to 139. The results of IWQI showed values (139 and 104) in sampling sites S1 and S2,respectively, indicating that the water quality index for irrigation were observed in unsuitable category (>100) and unsafe for irrigation, which resulting from the upper values of physicochemical parameters in groundwater which could cause numerous influences. Thus, public awareness might be raised not to use water of this quality, the highest priority should be given to regular water quality monitoring and appropriate technologies should be employed to make treated water more suitable for irrigation. Also the values were 83 and 97 for sampling sites S3 and S4, they are observed in very poor category (76-100), while the site S5 showed value 76 which indicating poor

category (51-75). All the last three sites are possible usage for irrigation. The summary of IWQI values of the groundwater samples from the five sampling sites are shown in Figure 7.

Table 5. The standard guidelines of water quality for agriculture (14) and unit weights for parameters.

Parameters	**Units**	**Agriculture standard** (14)	**Unit Weights (Wi)**
pH	-	7.25	0.011594
Total dissolved solid (TDS)	mg/l	2000	0.000042
Carbonate (CO_3^{2-})	meq/l	0.1	0.840600
Bicarbonate (HCO_3^-)	meq/l	10	0.008406
Chloride (Cl^-)	meq/l	30	0.002802
Calcium (Ca^{2+})	meq/l	20	0.004203
Magnesium (Mg^{2+})	meq/l	5	0.016812
Sodium (Na^+)	meq/l	40	0.002102
Potassium (K^+)	mg/l	2	0.042030
Phosphate-P ($PO4^{2-}$-P)	mg/l	2	0.042030
Nitrate-N (NO_3^+-N)	mg/l	10	0.008406
Ammonium-N (NH_4^+-N)	mg/l	5	0.016812
Sulfate (SO_4^{2-})	meq/l	20	0.004203
		$\sum W_i$	1.0000

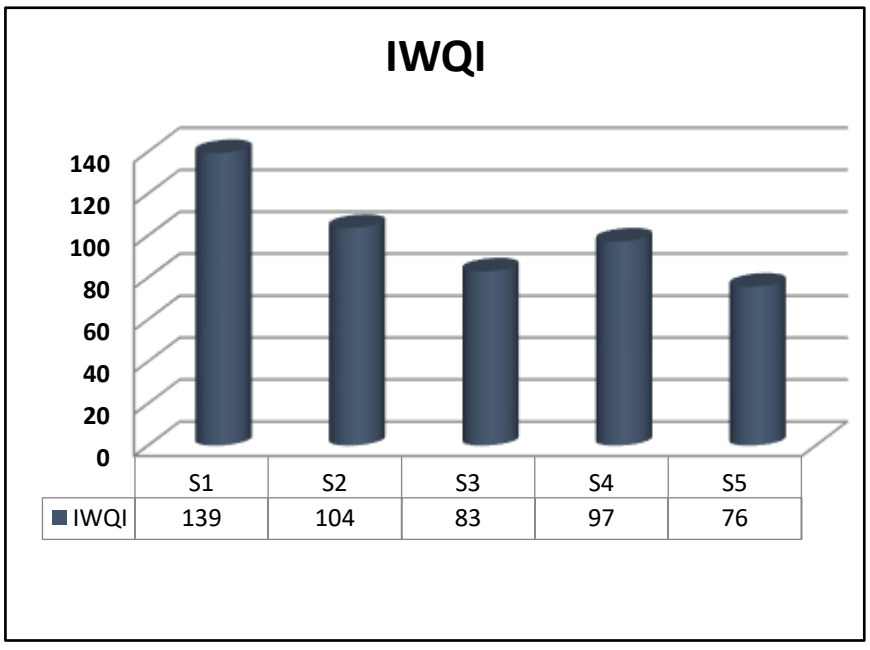


Figure 7. The summary of IWQI values of the groundwater samples.

Table 6. The values of the physicochemical parameters and the WQI values in all the groundwater sites.

Site	Para.	pH	TDS	CO_3^{2-}	HCO_3^-	Cl^-	Ca^{2+}	Mg^{2+}	Na^+	K^+	PO_4^{2-}-P	NO_3^+-N	NH_4^+-N	SO_4^{2-}	WQI
S1	V_i	8.00	3186.20	0.06	0.52	30.00	5.89	9.34	21.22	37.80	0.03	5.60	1.16	12.13	139
	Q_i	400	159.31	60.00	5.20	100.00	29.46	186.7	53.04	1890.0	1.30	56.00	23.30	60.63	
	Q_iW_i	4.64	0.01	50.44	0.04	0.28	0.12	3.14	0.11	79.44	0.05	0.47	0.39	0.25	
S2	V_i	7.20	2994.20	0.00	0.40	27.48	4.24	10.20	21.30	46.00	0.02	14.55	2.07	9.38	103
	Q_i	80.0	149.71	0.00	4.00	91.60	21.21	203.9	53.26	2300.0	1.14	145.45	41.47	46.88	
	Q_iW_i	0.93	0.01	0.00	0.03	0.26	0.09	3.43	0.11	96.67	0.05	1.22	0.70	0.20	
S3	V_i	7.60	3039.00	0.00	0.24	27.31	3.61	12.93	18.48	35.00	0.04	14.30	1.03	10.38	82
	Q_i	240	151.95	0.00	2.39	91.03	18.07	258.5	46.20	1750.0	1.96	143.00	20.50	51.88	
	Q_iW_i	2.78	0.01	0.00	0.02	0.26	0.08	4.35	0.10	73.55	0.08	1.20	0.34	0.22	
S4	V_i	7.00	3813.40	0.00	0.20	92.34	4.81	22.41	18.91	41.20	0.02	0.00	5.41	8.88	97
	Q_i	0.00	190.67	0.00	2.00	307.79	24.06	448.2	47.28	2060.0	0.98	0.00	108.25	44.38	
	Q_iW_i	0.00	0.01	0.00	0.02	0.86	0.10	7.53	0.10	86.58	0.04	0.00	1.82	0.19	
S5	V_i	7.00	3045.40	0.00	0.52	85.03	2.26	14.03	17.39	32.80	0.00	12.00	1.22	6.50	76
	Q_i	0.00	152.27	0.00	5.20	283.43	11.29	280.5	43.48	1640.0	0.16	120.00	24.38	32.50	
	Q_iW_i	0.00	0.01	0.00	0.04	0.79	0.05	4.72	0.09	68.93	0.01	1.01	0.41	0.14	

3.3. Groundwater suitability for irrigation

In the study region, the groundwater suitability for agricultural irrigation is presented through comparing the analytical results of indices with corresponding parameters of irrigation water classifications (Table 7).

Table 7. Suitability classification for agricultural irrigation from groundwater (33) (34) (35).

Indices	Range	Classification	Distribution%
Electrical Conductivity (EC)	<250	Excellent	-
	250-750	Good	-
	750-2000	Doubtful	-
	>2000	Unsuitable	100%
Sodium Adsorption Ratio (SAR)	<10	Excellent	100%
	10-18	Good	-
	18-26	Doubtful	-
	>26	Unsuitable	-
Soluble Sodium Percent (SSP)	<20	Excellent	-
	20-40	Good	-
	40-60	Permissible	80%
	60-80	Doubtful	20%
	>80	Unsuitable	-
Residual Sodium Carbonate (RSC)	<1.25	Good	100%
	1.25-2.5	Doubtful	-
	>2.5	Unsuitable	-
Total Hardness (TH)	<60	Soft	40%
	61-120	Moderately hard	60%
	121-180	Hard	-
	>180	Very hard	-
Permeability Index (PI)	Class I (>75)	Excellent	-
	Class II (25-75)	Good	100%
	Class III (<25)	Poor	-
Potential Salinity (PS)	<3	Suitable	-
	>3	Unsuitable	100%
Kelley's Ratio (KR)	<1	Suitable	20%
	>1	Unsuitable	80%
Magnesium Hazard Ratio (MHR)	<50	Suitable	-
	>50	Unsuitable	100%

The following sections provide an explanation of the observed characteristics:

3.3.1. Salinity Hazard

Salinity is the most essential parameter in establishing the water suitability for irrigation usage. It is usually measured as the electrical conductivity (EC) or the total dissolved solid (TDS) in the water. They are two important interlinked parameters for the water quality in irrigation (33). EC is a measure the degree of water conducts the electricity. It's measure the salinity hazard to crops (36).

The EC values of groundwater samples varied from 4680 to 5960 µS/cm (mean value 5026 µS/cm), while TDS values ranged from 2995 to 3814 mg/L (mean value 3216 mg/L) (Figure 8) indicating sever degree of restriction on using this groundwater in irrigation (Table 8). It is obvious that irrigation with saline water can increase salt concentration in soils, and this might be a problem if the concentration rises to a level that is harm the crop or landscape. As a result, while using groundwater for irrigation, it is needful to keep the salinity under control.

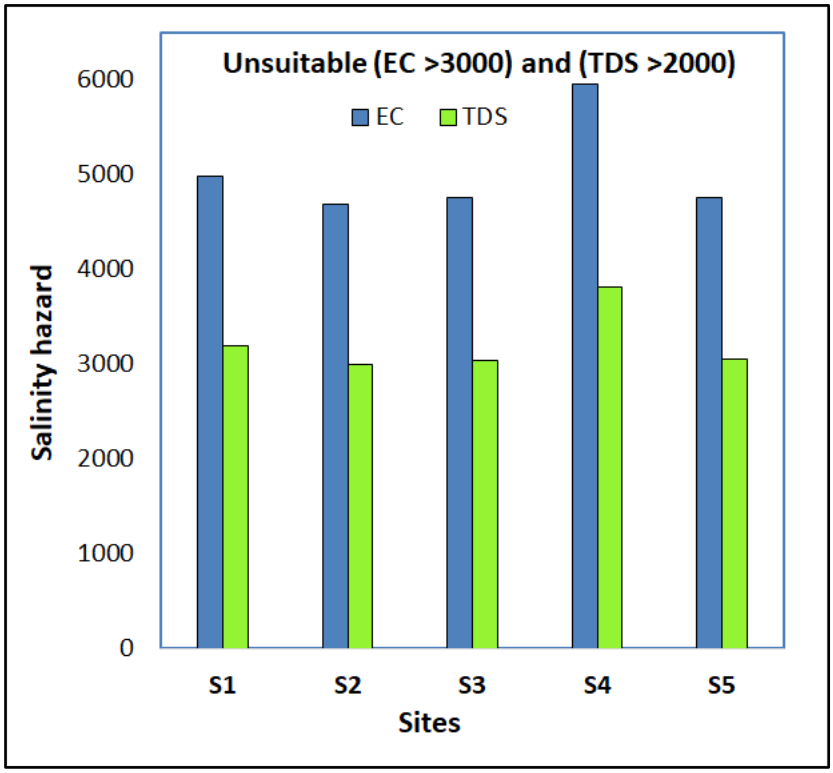


Figure 8. The salinity hazard (EC and TDS) values for the groundwater samples.

3.3.2. Sodium Hazard

Sodium hazard is commonly stated as a sodium adsorption ratio (SAR), which is computed by comparing the proportion of sodium (Na^+) ions to the concentration of calcium (Ca^{2+}) and magnesium (Mg^{2+}) (17). SAR is one of the valuable parameters for evaluating the suitability of groundwater irrigation because it is responsible for the sodium hazard and provides a strong basis for estimating the sodium harm degree in irrigation water, since it was directly concerning with sodium absorption on the soil surface. Also sodium in irrigation water enters the soil and replace the adsorbed calcium and magnesium, which resulting permeability reduction and poor drainage in the soil (37) (38). The SAR values of the samples varies from 5.13 to 7.93 meq/L (Figure 9). All the groundwater samples belonged to the excellent category according to the SAR classification of irrigation water (Table 7), indicating the groundwater can be proper for all type of soil.

In order to assess irrigation water quality more accurately and intuitively in this study, the waters EC was considered together with its SAR, utilizing Table 9 which is based on the combined effect of EC (salinity hazard) and SAR (Sodium hazard). All collected groundwater samples are in the class C4-S1, indicating very high salinity water, and they aren't appropriate for irrigation under normal conditions. Although this sort of water can used for plants with good salt tolerance, but it restricts the suitability for irrigation, especially in soils with limited drainage. (39).

The Soluble Sodium Percentage (SSP) is an important parameter to assess water suitability for irrigation uses. According to the US Department of Agriculture (40), the standard SSP value is between 40%-60% and the SSP classification of irrigation water is presented in Table 7. The SSP values of the collected samples range from 42.32% to 60.89% (Figure 9). All the groundwater samples are placed in the good to permissible zone. However, groundwater sample from station S2 shows a tendency to shift towards permissible to doubtful zone for irrigation purposes. The groundwater in the study area is suitable for irrigation since it doesn't impair soil permeability due to reactions with the soil.

Residual Sodium Carbonate (RSC) was computed to estimate the hazardous influence of carbonate (CO_3^{2-}) and bicarbonate (HCO_3^-) on water quality for agriculture irrigation usage. The excess concentration of CO_3^{2-} and HCO_3^- ions in groundwater over the concentrations of $Ca^{2+} + Mg^{2+}$ ions causes precipitation of Ca^{2+} and Mg^{2+} and influences the unsuitability for irrigation (41). Water having RSC less than 1.25 meq/L (low) are safe and suitable for irrigation purposes whereas marginally suitable up to 2.5 meq/L (medium) and unsuitable for irrigation over 2.5 meq/L (high), recommended by the US Salinity Laboratory (39). The RSC classification of irrigation water is presented in Table 7. The RSC values varied between -27.02 to -14.04 (Figure 9) with an average of -17.55 indicating that all collected samples categorized as safe for irrigation purpose in term of RSC.

3.3.3. Total Hardness (TH)

The water hardness is a result of presence of divalent cations Ca2+ and Mg2+. Water hardness is represented by TH. The dissolution of calcium and magnesium is the primary cause of total hardness. A moderate TH value is beneficial for protecting the plumbing system from corrosion. The acceptable limit of TH is 100 mg/l which providing adequate corrosion control. TH is usually classified (0–60 mg/l) as soft, (60–120 mg/l) as moderately hard, (120–180 mg/l) as hard and (>180 mg/l) as very hard (34) (42). Total hardness varied between 52.62 and 104.35 mg/L (Figure 9) and The TH classification of irrigation water is presented in Table 7. The collected groundwater samples from stations S1 and S2 are grouped in the soft water category, while the rest of them fall under moderately hard water category, showing properness for water supply system (pipes) in irrigation.

3.3.4. Permeability Index (PI)

According to a significant impact of the levels of Na, Ca, Mg, and bicarbonate in irrigation water on soil permeability during long-term use, the permeability index (PI) was utilized in this study to

assess groundwater suitability for irrigation. From the analysis for the samples and calculations, it was found that the values of PI are 60.16, 61.37, 54.17, 41.97and 53.78 meq/L (Figure 9). According to Doneen classification (21) (Table 7), all samples fall under Class II (25<PI<75) which considered that groundwater samples from these sites were not an excellent rating but good (moderately suitable) for long-term agricultural irrigation with little effect on soil property and recommended some cautions when it comes to soil permeability (43) (44).

3.3.5. Potential Salinity (PS)

Potential salinity (PS) is another water quality parameter index. It's chlorides and sulfates dominant index for categorizing water for agriculture irrigation purpose. when PS<3 meq/L indicates that the water is suitable for irrigation (21) (45). The PS values of all collected samples were estimated high values (Table 7); the maximum PS value was 96.04 meq/L and the average PS value was 56.37 meq/L (Figure 9). This is due to the high level of $SO4^{2+}$ and Cl^{-} in the groundwater of the study area. All the samples were classified as unsuitable (PS > 3 meq/L) for agricultural irrigation usage in terms of PS.

3.3.6. Kelley's ratio (KR)

Kelly's Ratio is an important indices used to assess the suitability of groundwater for the irrigation purposes in terms of main cations (Na^{+}, Mg^{2+} and Ca^{2+}). The Kelly Index value 1 indicates that sodium concentration should be almost equal to the sum of calcium and magnesium, resulting in a perfect balance. Waters with a KR less than 1 indicate a sodium deficit and are suitable for irrigation, whereas those with a higher ratio indicate excess sodium and are unsuitable (22).

The KR values varied between 1.48 and 0.69 with an average value of 1.15 (Figure 9), where the groundwater samples showed KR >1 except one sample S4 showed KR<1. Water from sampling station S4 has relatively low sodium ion content more than other samples, which can be used for irrigation purpose while the others samples are unsuitable for irrigation. The KR classification of irrigation water is presented in Table 7.

3.3.7. Magnesium hazard

One of the most significant parameters for irrigation water quality assessment is the magnesium hazardous ration (MHR). The Ca^{2+} and Mg^{2+} are generally in equilibrium in most waterways. The high Mg^{2+} concentration in groundwater would exchange with Na+ in the soil, causing soil alkalization and thereby reduction the crop yield (17) (46). All of the groundwater samples with estimated MHR values as 61.31, 70.62, 78.15, 82.32, and 86.13 for the groundwater samples from stations S1 to S5, respectively (Figure 9), were greater than 50 meq/L, indicating all samples were unsuitable for irrigation purposes (Table 7), could resulting soil magnesium alkalization during long-term irrigation with groundwater.

Table 8. Restriction degree for agriculture irrigation (14).

Parameters	None	Slight to Moderate	Sever
EC, µS/cm	<700	700-3000	>3000
TDS, mg/L	<450	450-2000	>2000

Table 9. Classification of irrigation water for Salinity hazard and Sodium hazard (47).

Salinity hazard class	EC, µS/cm	TDS, mg/L	classes	Characteristics
C1	0-250	< 200	Excellent	Low-salinity water can be used for irrigation on most soil with minimal likelihood that soil salinity will
C2	251-750	200-500	Good	Medium-salinity water can be used for irrigation if a moderate amount of drainage occurs.
C3	751-2250	501-1500	Permissible	High-salinity water is not suitable for use on soil with restricted drainage. Even with adequate drainage,
C4	>2250	1501-3000	Unsuitable	Very high-salinity water is not suitable for irrigation under normal conditions.

Sodium hazard class	SAR meq/L	Irrigation water suitability	Characteristics
S1	0-10	Low	Suitable for all types of soils except for those crops which are highly sensitive to Sodium
S2	10-18	Medium	Suitable for coarse textured or organic soil with good permeability. Relatively unsuitable in fine textured soil
S3	18-26	High	Harmful for almost all types of soils. Requires good drainage, high leaching, and gypsum addition
S4	>26	Very high	Unsuitable for irrigation.

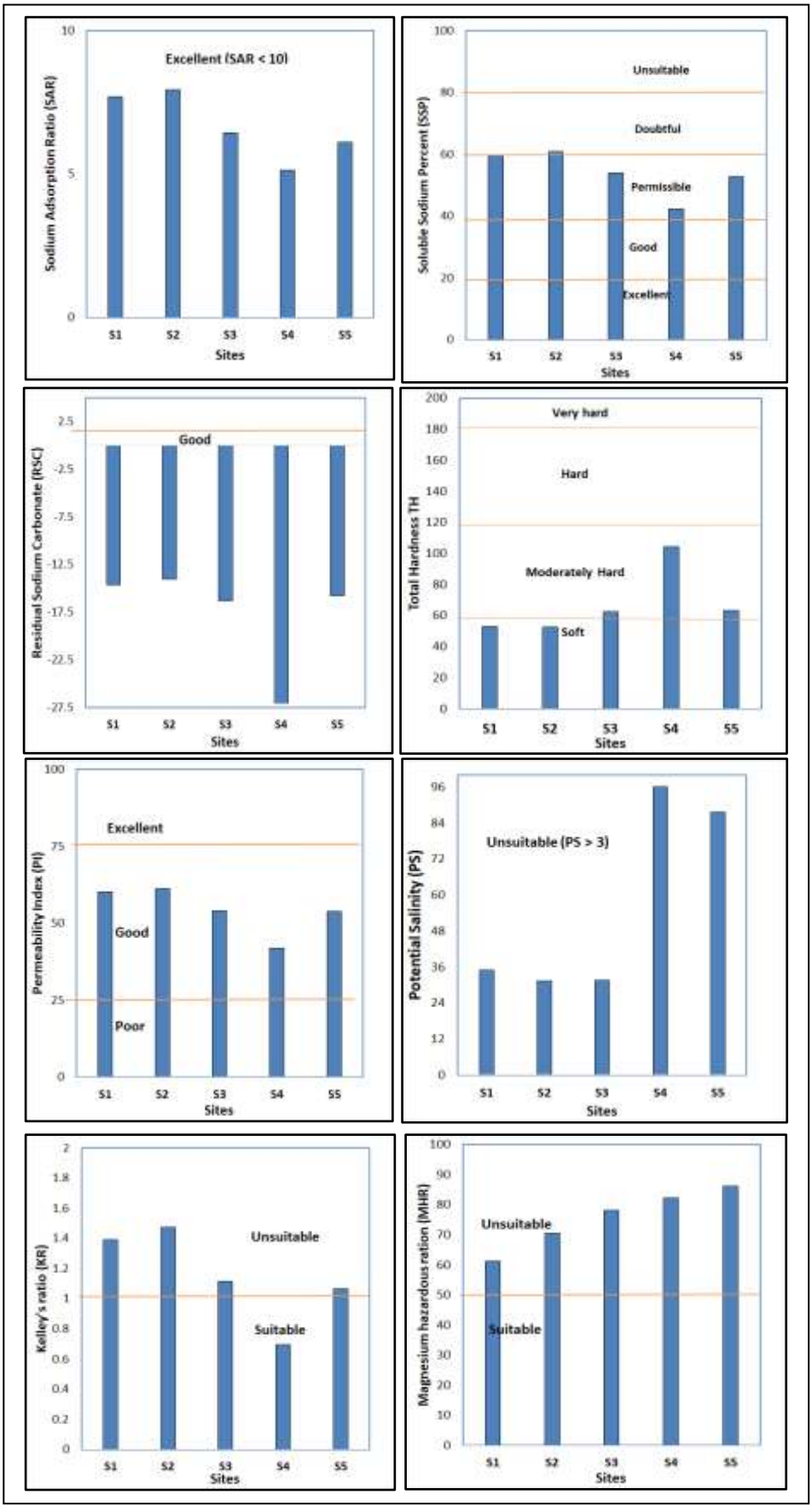


Figure 9. Irrigation quality indices for the groundwater samples.

4. Conclusions

A comprehensive analysis of chemical composition and hydrogeochemical characterri-stics was conducted to determine the suitability of groundwater for agriculture irrigation purposes based on the irrigation water quality index (IWQI), multiple indices, and a multi-aspect assessment. The sequence of the abundance of the major cations was in the order of $Na^+ > Ca^{2+} > Mg^{2+} > K^+$ for groundwater of sampling site S1, $Mg^{2+} > Na^+ > Ca^{2+} > K^+$ for sampling site S2 and $Mg^{2+} > Na^+ > Ca^{2+} > K^+$ for sampling sites S3, S4 and S5. And for the major anions was in the order of $SO_4^{2-} > Cl^- > HCO_3^- > NO_3^- > PO_4^{2-}$ for the samples of both S1 and S4, $SO_4^{2-} > Cl^- > NO_3^- > HCO_3^- > PO_4^{2-}$ for the samples of both S2 and S3, while for the sampling site S5 as $Cl^- > SO_4^{2-} > NO_3^- > HCO_3^- > PO_4^{2-}$. The chemical composition of groundwater was mostly controlled by evaporation and ion exchange, which are the dominant processes in the study area.

By IWQI values, the groundwater samples fall at very poor to unsuitable category in the sites S1 and S2 of the study area, indicating unsafe for irrigation. While the sites S3 and S4 fall at very poor category (76-100), and the S5 fall at poor category (51-75). All the last three sites are safe and possible used for irrigation. The groundwater suitability for irrigation was assessed based on the irrigation quality indices including EC, SAR, SSP, RSC, TH, PI, PS, KR and MHR. The very high values of EC, TDS and PS implied that all of samples belonged to unsuitable strategy. About 80% of samples with KR content fell in the unsuitable category except groundwater from sampling site S4 was suitable for irrigation. The high MHR% values indicated that all groundwater samples were unsuitable for irrigation. However, the samples evaluated based on the index of SAR, SSP, RSC and PI were suitable for irrigation. Also TH of samples fell in the soft to moderately soft category for all groundwater sites. The use of groundwater of the study area as a source of irrigation would impose significant salinity hazard, while the degree of sodium hazards was relatively low, all of the samples fall in C4S1 sector according to the salinity and sodium hazard classification. It is due to the long period of residence of water, minerals' dissolution from the rock structure, and the intrusion of domestic and industrial wastewater.

The findings of this study will be extremely useful for sustainable management of groundwater resources in the study area, as well as allowing planners and policymakers to devise a strategy to address comparable issues in other areas.

References

1. Kawo NS, Karuppannan S. Groundwater quality assessment using water quality index and GIS technique in Modjo River Basin, central Ethiopia. J African Earth Sci. 2018;147:300–11.
2. Adabanija MA, Afolabi OA, Lawal L. The influence of bedrocks on groundwater chemistry in a crystalline basement complex of southwestern Nigeria. Environ Earth Sci. 2020;79(4):1–23.
3. Amiri V, Sohrabi N, Dadgar MA. Evaluation of groundwater chemistry and its suitability for drinking

and agricultural uses in the Lenjanat plain, central Iran. Environ Earth Sci. 2015;74(7):6163–76.

4. El Baba M, Kayastha P, Huysmans M, De Smedt F. Evaluation of the groundwater quality using the water quality index and geostatistical analysis in the Dier al-Balah Governorate, Gaza Strip, Palestine. Water. 2020;12(1):262.
5. Mary IA, Ramkumar T, Venkatramanan S. Application of statistical analysis for the hydrogeochemistry of saline groundwater in Kodiakarai, Tamilnadu, India. J Coast Res. 2012;28(1A):89–98.
6. Patil VBB, Pinto SM, Govindaraju T, Hebbalu VS, Bhat V, Kannanur LN. Multivariate statistics and water quality index (WQI) approach for geochemical assessment of groundwater quality—a case study of Kanavi Halla Sub-Basin, Belagavi, India. Environ Geochem Health. 2020;42(9):2667–84.
7. Brindha K, Neena Vaman K V., Srinivasan K, Sathis Babu M, Elango L. Identification of surface water-groundwater interaction by hydrogeochemical indicators and assessing its suitability for drinking and irrigational purposes in Chennai, Southern India. Appl Water Sci. 2014;4(2):159–74.
8. Salih M. Mohend. Evaluation the Quality of Water Wells in Green-Belt Area North of AL-Najaf Al Ashraf City. University of Technology; 2015.
9. Sataa A-B, Albakeri S, Salih MM. Evaluation The Quality of Wells Water in Greenbelt Area North of AL-Najaf Al Ashraf City. Eng Technol J. 2016;34(14 Part (A) Engineering):2692–704.
10. WEF AA. Standard methods for the examination of waterand wastewater. Am Public Heal Assoc Am Work Assoc Water Environ Fed 21st Ed Washingt DC, USA. 2005;
11. Pei-Yue L, Hui Q, Jian-Hua W. Groundwater quality assessment based on improved water quality index in Pengyang County, Ningxia, Northwest China. E-Journal Chem. 2010;7(SUPPL. 1):209–17.
12. Hameed A, Al-Obaidy MJ. Impact of Medical City and Al-Rasheed Power Plant Effluents on the Water Quality Index Value of Tigris River at Baghdad City. Eng &Tech J. 2016;34(4):28–9.
13. Călmuc VA, Călmuc M, Țopa CM, Timofti M, Iticescu C, Georgescu LP. Various methods for calculating the water quality index. Ann ”Dunarea Jos” Univ Galati Fascicle II, Math Physics, Theor Mech. 2018;41(1):171–8.
14. Ayers RS, Westcot DW. Food, agriculture organization of the United Nations (FAO), water quality for agriculture. Irrig Drainage, Rome, Pap. 1994;29:77042–4.
15. Adebayo TB, Abegunrin TP, Awe GO, Are KS, Guo H, Onofua OE, et al. Geospatial mapping and suitability classification of groundwater quality for agriculture and domestic uses in a Precambrian basement complex. Groundw Sustain Dev [Internet]. 2021;12(September 2020):100497. Available from: https://doi.org/10.1016/j.gsd.2020.100497
16. Bora M, Goswami DC. Water quality assessment in terms of water quality index (WQI): case study of the Kolong River, Assam, India. Appl Water Sci. 2017;7(6):3125–35.
17. Zhao X, Guo H, Wang Y, Wang G, Wang H, Zang X, et al. Groundwater hydrogeochemical characteristics and quality suitability assessment for irrigation and drinking purposes in an agricultural region of the North China plain. Environ Earth Sci [Internet]. 2021;80(4):1–22. Available

from: https://doi.org/10.1007/s12665-021-09432-w

18. Allison LE, Richards LA. Diagnosis and improvement of saline and alkali soils. Soil and Water Conservative Research Branch, Agricultural Research Service …; 1954.
19. Todd DK. Groundwater hydrology (p. 535). New York Jon Wiley Sons Inc. 1980;
20. Eaton FM. Significance of carbonates in irrigation waters. Soil Sci. 1950;69(2):123–34.
21. Doneen LD. Notes on water quality in agriculture. Department of Water Science and Engineering, University of California, Davis; 1964.
22. Kelley WP. Use of saline irrigation water. Soil Sci. 1963;95(6):385–91.
23. Raghunath HM. Groundwater pollution and legislation groundwater 2nd edition. India; 1987.
24. (Programme) G. Water Quality Outlook. GEMS Water; 2006.
25. Egbi CD, Anornu G, Appiah-Adjei EK, Ganyaglo SY, Dampare SB. Evaluation of water quality using hydrochemistry, stable isotopes, and water quality indices in the Lower Volta River Basin of Ghana. Environ Dev Sustain. 2019;21(6):3033–63.
26. Chung SY, Venkatramanan S, Kim TH, Kim DS, Ramkumar T. Influence of hydrogeochemical processes and assessment of suitability for groundwater uses in Busan City, Korea. Environ Dev Sustain [Internet]. 2015;17(3):423–41. Available from: http://dx.doi.org/10.1007/s10668-014-9552-7
27. Mohamed MM, Parimalarenganayaki S, Khan Q, Murad A. Review on the use of environmental isotopes for groundwater recharge and evaporation studies in the GCC countries. Groundw Sustain Dev. 2021;12(January).
28. Sunkari ED, Abu M, Zango MS. Geochemical evolution and tracing of groundwater salinization using different ionic ratios, multivariate statistical and geochemical modeling approaches in a typical semi-arid basin. J Contam Hydrol. 2021;236(August 2020).
29. Schoeller H. Qualitative evaluation of groundwater resources. Methods Tech Groundw Investig Dev UNESCO. 1965;5483.
30. Rajmohan N, Masoud MHZ, Niyazi BAM. Impact of evaporation on groundwater salinity in the arid coastal aquifer, Western Saudi Arabia. Catena. 2021;196(April 2020).
31. Fisher RS, Mullican III WF. Hydrochemical evolution of sodium-sulfate and sodium-chloride groundwater beneath the northern Chihuahuan Desert, Trans-Pecos, Texas, USA. Hydrogeol J. 1997;5(2):4–16.
32. Karunanidhi D, Aravinthasamy P, Deepali M, Subramani T, Sunkari ED. Appraisal of subsurface hydrogeochemical processes in a geologically heterogeneous semi-arid region of south India based on mass transfer and fuzzy comprehensive modeling. Environ Geochem Health [Internet]. 2021;43(2):1009–28. Available from: https://doi.org/10.1007/s10653-020-00676-2
33. Shakir E, Zahraw Z, Al-Obaidy AHMJ. Environmental and health risks associated with reuse of wastewater for irrigation. Egypt J Pet. 2017;26(1):95–102.
34. Rawat KS, Singh SK, Gautam SK. Assessment of groundwater quality for irrigation use: a peninsular

case study. Appl Water Sci. 2018;8(8):1–24.

35. Kaur T, Bhardwaj R, Arora S. Assessment of groundwater quality for drinking and irrigation purposes using hydrochemical studies in Malwa region, southwestern part of Punjab, India. Appl Water Sci. 2017;7(6):3301–16.
36. Shah M, Sircar A, Varsada R, Vaishnani S, Savaliya U, Faldu M, et al. Assessment of geothermal water quality for industrial and irrigation purposes in the Unai geothermal field, Gujarat, India. Groundw Sustain Dev [Internet]. 2019;8(August 2018):59–68. Available from: https://doi.org/10.1016/j.gsd.2018.08.006
37. Hameed A, Jawad M, Obaidy A, Awad ES, Kadhem AJ, Mashhady AA Al. Evaluating Water Quality of Mahrut River, Diyala, Iraq for Irrigation. Eng &TechJournal. 2015;33(33):830–7.
38. Alaya M Ben, Saidi S, Zemni T, Zargouni F. Suitability assessment of deep groundwater for drinking and irrigation use in the Djeffara aquifers (Northern Gabes, south-eastern Tunisia). Environ earth Sci. 2014;71(8):3387–421.
39. Staff USSL. Diagnosis and improvement of saline and alkali soils. Agric Handb. 1954;60:83–100.
40. Wilcox Lv. Classification and use of irrigation waters. US Department of Agriculture; 1955.
41. Keesari T, Ramakumar KL, Chidambaram S, Pethperumal S, Thilagavathi R. Understanding the hydrochemical behavior of groundwater and its suitability for drinking and agricultural purposes in Pondicherry area, South India – A step towards sustainable development. Groundw Sustain Dev. 2016;2–3:143–53.
42. Ahmed FT, Khan AHAN, Khan R, Saha SK, Alam MF, Dafader NC, et al. Characterization of arsenic contaminated groundwater from central Bangladesh: Irrigation feasibility and preliminary health risks assessment. Environ Nanotechnology, Monit Manag [Internet]. 2021;15(January):100433. Available from: https://doi.org/10.1016/j.enmm.2021.100433
43. Adebayo TB, Abegunrin TP, Awe GO, Are KS, Guo H, Onofua OE, et al. Geospatial mapping and suitability classification of groundwater quality for agriculture and domestic uses in a Precambrian basement complex. Groundw Sustain Dev. 2021;12(October 2020).
44. Bhat MA, Wani SA, Singh VK, Sahoo J, Tomar D, Sanswal R. An overview of the assessment of groundwater quality for irrigation. J Agric Sci Food Res. 2018;9(1):9.
45. Avci H, Dokuz UE, Avci AS. Hydrochemistry and groundwater quality in a semiarid calcareous area: an evaluation of major ion chemistry using a stoichiometric approach. Environ Monit Assess. 2018;190(11).
46. Anim-Gyampo M, Anornu GK, Appiah-Adjei EK, Agodzo SK. Quality and health risk assessment of shallow groundwater aquifers within the Atankwidi basin of Ghana. Groundw Sustain Dev. 2019;9:100217.
47. Westcot DW. Quality control of wastewater for irrigated crop production (Water reports-10). Food Agric Organ United Nations, Rome, Italy. 1997;

Lead Ions Removal in Simulated Industrial Wastewater by Using Activated Carbon Produced From Heavy Oil Fly Ash

Faten Hameed kamil [1,*], Waleed Mohammed Abood[2], Zuhair Khudhair[1], Yousra Mohammed[1]

[1] Chemical and Petrochemical Research Center, Corporation of Research and Industrial Development, Ministry of Industry and Minerals, Baghdad, Iraq

[2] Renewable Energy and Environmental Research Center, Corporation of Research and Industrial Development, Ministry of Industry and Minerals, Baghdad, Iraq

***** *Corresponding authors: faten_kamil@yahoo.com ; Tel.: +964-7732405709.*

Abstract: Disposal of industrial waste has become as a significant environmental issue. In this work industrial waste heavy oil fly ash (HOFA) produced from burning heavy oil in power station was investigated to produce activated carbon (AC) as adsorbent from modified HOFA for lead removal. Batch experiments of lead removal were conducted at different adsorbent dose and time contact. Equilibrium isotherm results with good match in with freundlich model with R2=0.971 which shows heterogeneous surface of adsorbent and multilayer of adsorbate on the surface of (AC). Maximum adsorption capacity of 10 mg /g at equilibrium was achieved. Kintic study showed rapid adsorption at first 60 min. with good matching to 2nd order pseudo model with R^2=0.9998 and this equalized to experimental and theoretical adsorption capacity which refers to chemisorption process.

Keywords: Heavy oil fly ash, adsorption isotherm, kinetic rate.

1. Introduction

One of the global important issues are nowadays posing danger to human living is environmental pollution. The heavy metals released from solid and liquid material pollute our environment and pose risk to public health [1]. The concentrations of heavy metals in materials are deemed very low (ppb range to less than 10 ppm), therefore they consider as trace elements. Heavy metals are considered a metallic element that have a high density that are widespread and non-biodegradable [2]. Heavy metals are widely known include chromium, lead, mercury, cadmium, and arsenic), their usage and concentrations in the environment is increasing [3]. Lead is a metal which is widely used in different industrial processes. Lead may stay in the environment for long period and it is very danger for living systems because it is persistency. Lead poses a hazardous element for the ecosystem. The existence of Pb as free radicals causes damage to the living system. Lead exposure is also noted to produce reactive nitrogen species which are found to play a significant role in hypertension incidence [4].

As a method for removing organic and inorganic contaminants from aqueous solution, adsorption technology is considered the best method. The mechanisms of adsorption can be classified according to adsorption nature physically or chemically. Adsorption with physical behave is resulted of Wan der Waales forces. The surface of the adsorbent and the properties of the adsorbed material such as (molecular size and mass and boiling) play as factors which can affect on the capacity of adsorption. Adsorption with chemical behave due to the exchange of electrons between the adsobate molecules and the adsorbent surface [5].In this present study, activated carbon (AC) produced from modified heavy oil fly ash (HOFA) was chosen as the low cost adsorbent.

Finally, the efforts must be made to control pollution resulting from waste disposal by converting these unwanted wastes to usable raw material for various beneficial uses. Therefore, the objectives of this work is : studying the effect of adsorbent mass and contact time on the removal of lead from polluted water and investigating the adsorption using equilibrium isotherm models and the rate of adsorption during kinetic conditions.

2. Materials and Methods

2.1 Preparation of activated carbon

Raw heavy oil fly ash as adsorbent had been collected from electro-static precipitator (ESP) power plant south Baghdad for this experiment. This material is processed to remove impurities through washing and leaching. The chemicals used in washing and leaching process are 28 per cent of nitric acid and 15 per cent of hydrochloric acid. 10 g of heavy oil fly ash was treated with 50 ml of aqueous nitric acid solution at 60 °C for 2 h. The magnetic bar was placed in the solution and stirred continuously at speed of 200 rpm. The filtrate material was washed to remove NO^{3-} ions many times with distilled water till pH of material reach 7. After that, the filtrate material was mixed with 15 per cent of hydrochloric acid at 60 °C for 1 h. Then washing process for filtrate with distilled water several times to remove chloride ions and dried at 100°C for 5 h to get unburned carbon.

Dry unburned carbon was activated by mixing with phosphoric acid at 80 °C for 30 min, and then the material obtained was put in in oven for drying at 100 °C for 5 h. After this process, the carbonization process was applied to the material at 800 with heat rate 5 °C/min with constant nitrogen flow of 5 ml/ min. In carbonization process all organic material is converted into carbon at high temperature and eliminates the volatiles materials from the material. Then the calcined material was mixed with 0.5 N of hydrochloric acid at 80 °C for 30 min. The filtrate material which is activated carbon was washed till the pH reached 7 and then dried at 100 °C for 5 h.

2.2 Adsorption studies experiments

Adsorption studies were achieved by batch technique to get removal of lead and the adsorption capacity of activated carbon produced from HOFA. The stock solution of 1000 mg/l of lead by dissolving of 0.8 g of Pb $(NO_3)_2$ in distilled water 500 ml in acidic condition . Equilibrium experiments were conducted using 25 mg/l lead which was diluted from concentrated solution.

The percentage removal of lead was calculated from equation (1) and the adsorption capacity of adsorbent was calculated by equation (2)[6].

$$\%\, Removal = (Ci - Ce) * 100/Ci \dots\dots\dots\dots\dots\dots\dots\dots\dots 1$$

$$\%\, qe = \frac{Ci - Ce}{m} * V \dots\dots\dots\dots\dots\dots\dots\dots\dots\dots\dots\dots\dots 2$$

Where Ci and Ce are the initial and equilibrium of lead in mg/l before and after adsorption, m is the amount of the adsorbent in g. V is the volume of the sample in ml. The following effects were studied:

- **Adsorbent mass effect**

The activated HOFA dosages were (0.05, 0.1, 0.3, 0.6, 1)g added to 5 samples contain 50 ml of the aqueous solutions of 25 ppm of lead. The contact time was 4 h at temperature 25 °C and agitation speed 250 rpm.

- **Resident time effect**

500 ml of aqueous solution of 25ppm of lead was taken in a 1000 ml beaker and add 2.5g of adsorbent. The sampling were achieved at interval times (5, 10, 15, 30, 60, 120, 180, 240) min with agitation speed 250 rpm using magnetic stirrer.

2.2.1 Adsorption isotherm

Langmuir and Freundlich are well-known of several equilibrium models have been developed to describe adsorption isotherm relationships. Langmuir and Freundlich isotherm formulas were used to analyze the data.

Langmuir isotherm is applied to characterize adsorbent heavy metal sorption. Maximum adsorption potential that corresponds to the monolayer coverage completely on the surface, where the complete saturation of monolayer can is given by the non-linear Langmuir equation [7].

$$\frac{C_e}{q_e} = \frac{1}{kq} + \frac{C_e}{q} \dots\dots\dots\dots\dots\dots\dots\dots\dots\dots\dots\dots\dots\dots\dots\dots 3$$

Where C_e is the equilibrium concentration (mg/l), q_e the amount of metal ion adsorbed (mg/g). q is the amount adsorbed at a complete monolayer (mg/g) and k is the adsorption energy parameter.

Freundlich isotherm is an empirical equation uses isotherms to characterize adsorption equilibrium. Freundlich isotherm is commonly used to describe the adsorption of adsorbate on a wide range of adsorbents. The expressing of the Freundlich equation as shown below [7].

$$q_e = kC_e{}^{1/n} \dots\dots\dots\dots\dots\dots\dots\dots\dots\dots\dots\dots\dots\dots\dots\dots\dots\dots 4$$

the equation of linear form of can be written as

$$logq_e = logk + \frac{1}{n} logC_e \dots\dots\dots\dots\dots\dots\dots\dots\dots\dots\dots\dots\dots 5$$

Where k and n are the constants of freundlich related to the adsorption capacity and the adsorption intensity, respectively. The intercept and the slope of the linear plot of log q_e verses log C_e at given empirical conditions give the values of k and 1/n, respectively.

2.2.2 Adsorption kinetics

The pseudo 1st and 2 nd order equations were applied to modal the kinetics of lead ion adsorption onto Activated HOFA to investigate the mechanism nature of adsorption processes such as mass transfer and chemical reaction.

pseudo-first order (1st)model

1st pseudo kinetic model is introduced by Lagergren [8] as in the following equation:

$$\log(q_e - q_t) = logq_{th} - \frac{k}{2.303} * t \dots\dots\dots\dots\dots\dots\dots\dots\dots\dots 6$$

q_t (mg/g) and q_e (mg/g) is the amount of adsorbed ions s per adsorbent mass at time t (min) and at equilibrium respectively , q_{th} theoretical mass of metal adsorbed ions per mass of adsorbent (mg/g) and k is the rate constant of the pseudo *1st* order adsorption (1/min) at equilibrium .

pseudo second order (2nd)model

The pseudo 2nd order reaction describes the adsorption kinetics [9]. The linearized integral form of the model is

$$\frac{t}{q_t} = \frac{1}{k_2 q_{th}{}^2} + \frac{t}{q_{th}} \dots\dots\dots\dots\dots\dots\dots\dots\dots\dots\dots\dots\dots 7$$

k_2 is the pseudo *2nd* order rate constant of adsorption. .

3. Results and Discussion

- **Adsorbent mass effect**

The adsorbent mass effect on the lead removal was determined using variable quantities of Activated carbon produced from HOFA ranging from (0.05 to 1g) at fixed volume 50 ml with initial dye solution Ci of 100 g/ml. Other parameters kept constant at 25 °C, agitation speed 250 rpm, contact time of 4 h. The results are shown in Figure 1. The maximum adsorption of lead was obtained for adsorbent mass 1 g. The removal of dye increases with the increasing mass of adsorbent due to more available adsorption sites which caused by increased surface area [10]. The results illustrated that the optimum adsorbent mass of Activated HOFA at 1 g , which represents adsorbent value for effective lead removal. Hence, 1 g/ 0.1 liter was chosen as an optimal Activated HOFA mass for others experiments.

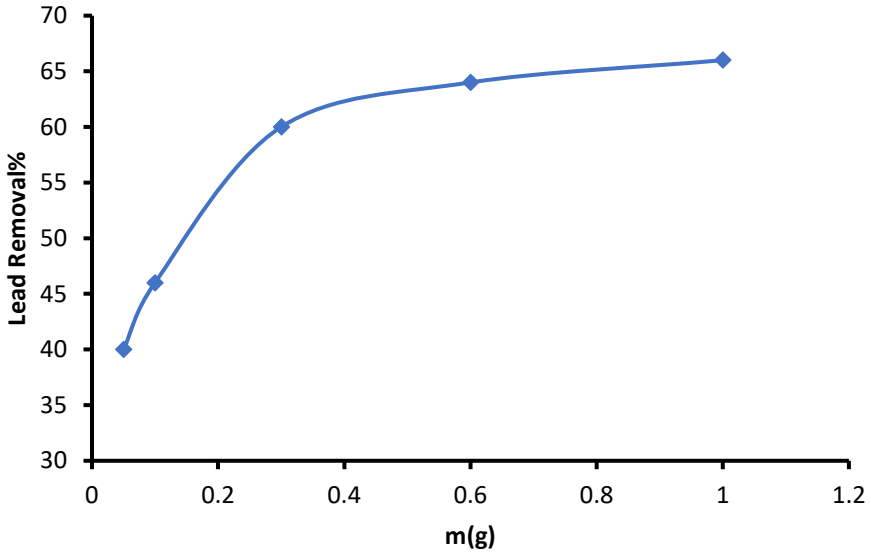


Figure 1. Adsorbent mass effect on Lead removal.

The effect of equilibrium concentration of Activated carbon produced from HOFA is shown in Figure 2. It was observed that the adsorption capacity of Activated HOFA decline at increase adsorbent dosage. The maximum value of adsorption capacity (q_e = 10 mg/g) was achieved with low an adsorbent mass (0.05g ~C_e = 15 mg/ml). In contrast, lowest adsorption capacity (q_e = 0.8 mg/g) decreases as adsorbent mass increase (1g ~ C_e = 8.5 mg/ml). Further increment of adsorbent mass resulted in a decline in adsorption capacity. The similar trend was reported by Che et al. (2012) [11].

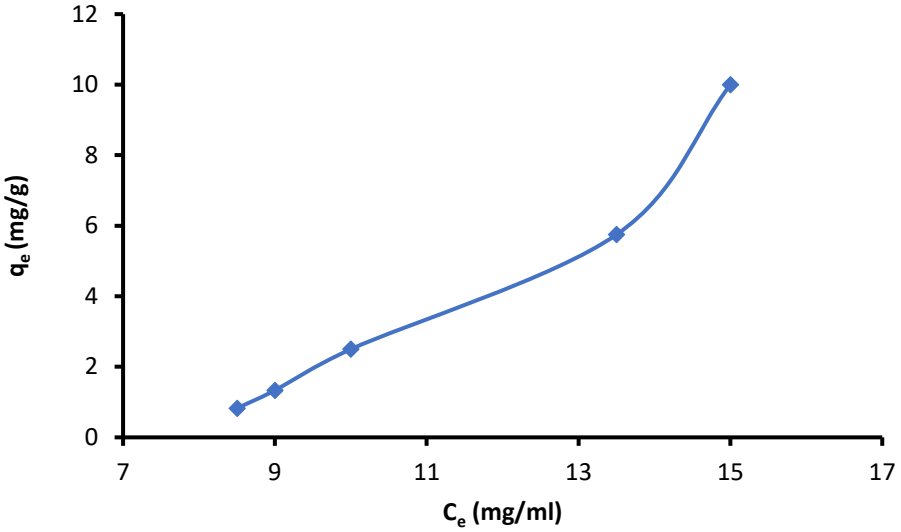
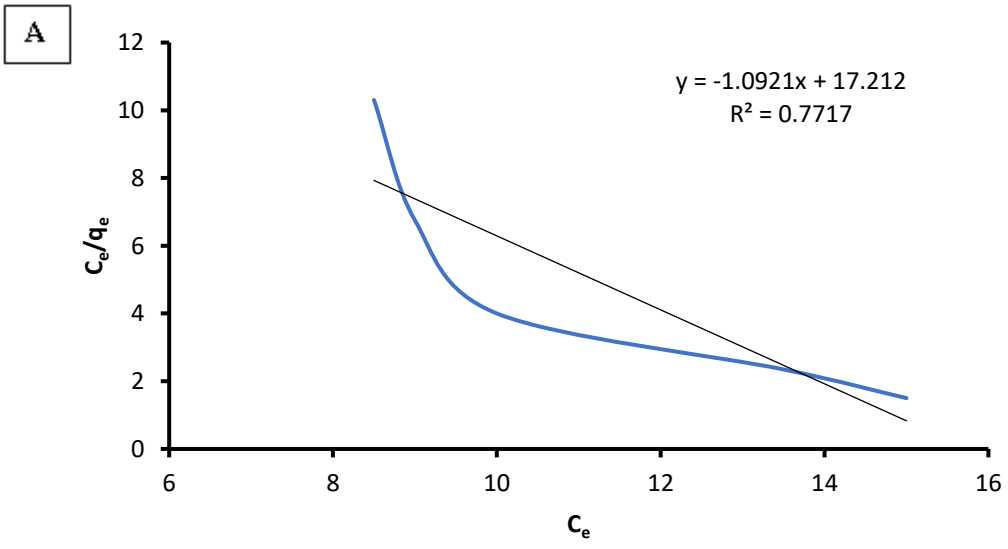


Figure 2. Empirical equilibrium isotherm at different Activated HOFA mass

In order to fitting result of effect of mass by equilibrium isotherm models (Langmuir and Freundlich) were the line plot of C_e vs $\frac{C_e}{q}$ for Langmuir and log q_e vs log C_e of Freundlich to estimate models' constants as shown in Table 1, where experimental results in Figure 3 show more fitting with Freundlich model while invalid with Langmuir model due to negative slop which give unacceptable value. This refers to multilayer adsorption and heterogeneous surface of adsorbent.

Table 1 Values of Langmuir and Freundlich constant for lead adsorption isotherms

Model	Parameters
Langmiur	k_l= - 0.6634
	q_e = - 0.9156
	R^2= 0.7717
Freundlich	k_f = 1.9× 10^{-4}
	1/n = 4
	R^2= 0.971



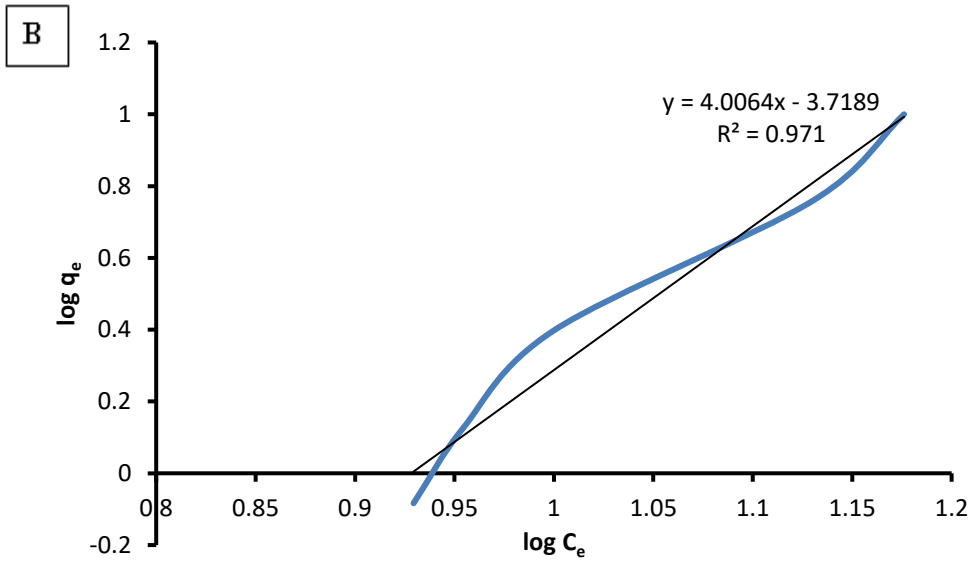


Figure 3. Linearized isotherm for lead adsorption on Activated HOFA (A) Langmuir isotherm (B) Freundlich isotherm

- **Resident time effect**

A 500 ml aqueous solution of 25 ppm concentration with 2.5 g of Pb was agitated for various interaction times (from 5 min to 240 min). Best Pb adsorption was occurred at 60 min. Higher removal rate was observed in the initial stages, and this can be related to the existence of sufficient surface adsorbent area at the initial stages to adsorb lead. When time increases, more ions of lead get adsorbed onto the surface of the Activated carbon. Figure 4 demonstrates removal rate of lead with stirring time. Maximum removal is reached after 1h of stirring.

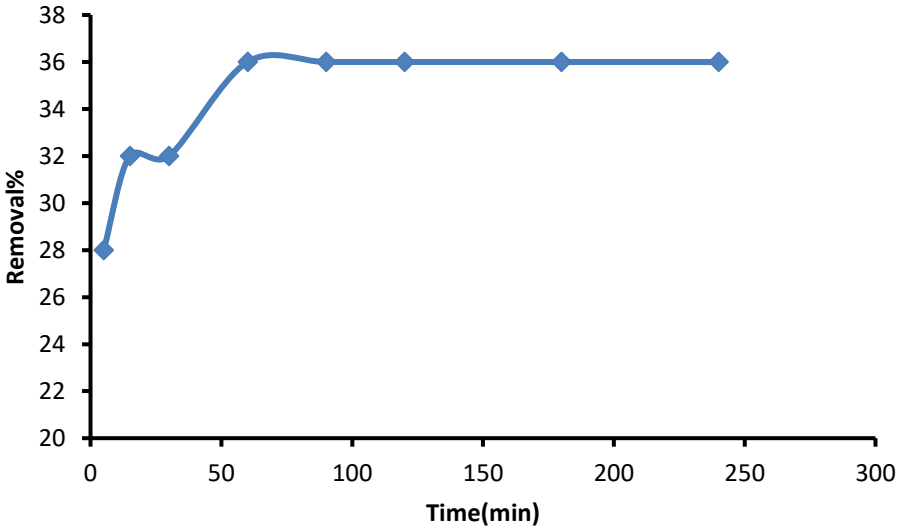


Figure 4. Effect of resident time on lead removal

From the results of the effect of time kinetic study has been achieved with kinetic model pseudo 1st and 2 *nd* order models by linear fitting. From Figures (5& 6) $\log\ (q_e - q_t)$ vs time and $\frac{t}{q_t}$ vs t for pseudo 1*st* and 2 *nd* order models (equations 6 &7, respectively), the results show better fit with

pseudo 2*nd* order than pseudo 1*st* order with R^2=0.9998 as shown in Table 2 and theoretical adsorption capacity q_{th}= 2.27 which approximately equal to the experimental adsorption capacity q_e = 2.25, which is based on the assumption that the limiting step rate is chemi-sorption with valence forces that sharing or exchanging the electrons between Activated HOFA and lead solution [12].

Table 2. Adsorption kinetics parameters of lead on AC

Model	Parameters
Pseudo first order kinetic	k_1 =0.02556 (min^{-1}) q_{th}= 0.975 (mg/g) R^2= 0.6447
Pseudo second order kinetic	k_2= 0.237 (g/(mg min)) q_{th}= 2.27 (mg/g) R^2= 0.9998

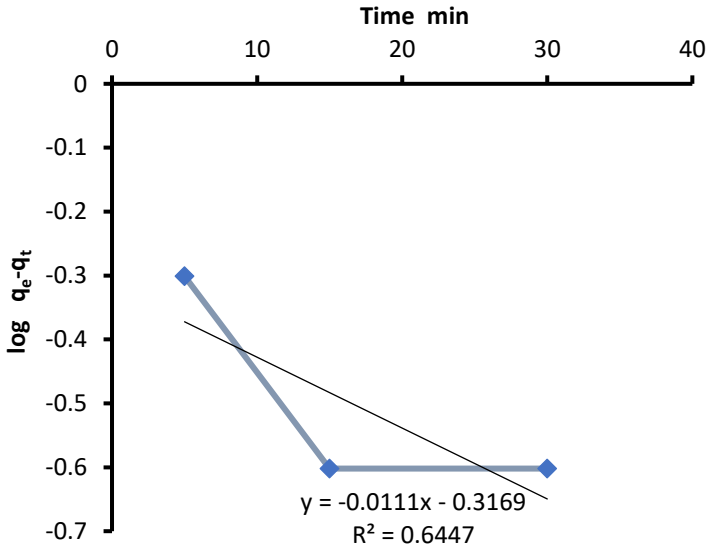


Figure 5. Pseudo first order kinetic curve

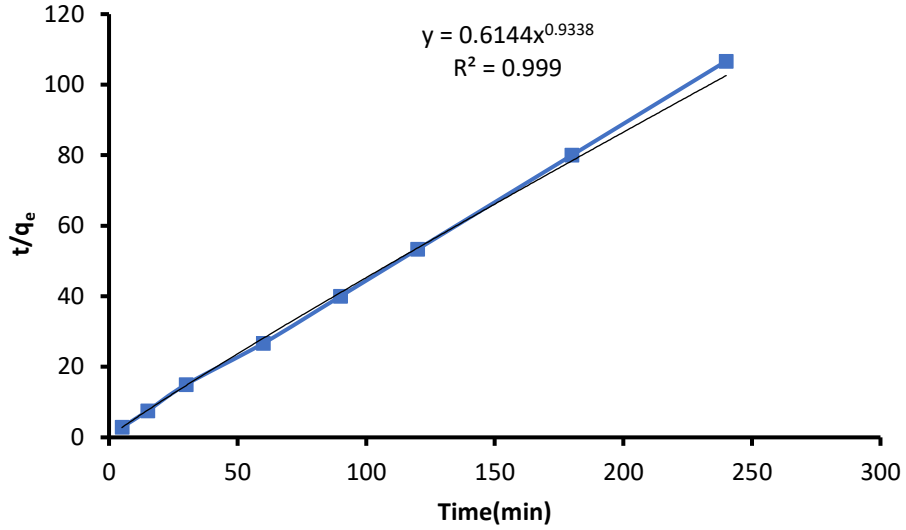


Figure 6. Pseudo second order curve

Conclusion

The acceptability of HOFA as raw material to prepare Activated HOFA as adsorbent for lead ions removing from simulated waste water was investigated in this work. The kinetic study revealed that Pb adsorption obeys the pseudo 2nd order kinetics as chemisorptions of Pb^{+2} ions by activated HOFA with square correlation coefficient R^2 0.9993. Theoretical adsorption capacity 2.27 mg/g while the experimental obtained was 2.25 mg/g and the equilibrium data were in good consistent to Freundlich equilibrium isotherm model as multilayer adsorption on heterogeneous adsorbent's surface.

Reference

1. Padmavathy KS, Madhu G, Haseena PV, A study on effects of pH , adsorbent dosage , time , initial concentration and adsorption isotherm study for the removal of hexavalent chromium (Cr (VI)) from wastewater by magnetite nanoparticles. *Procedia Technol.*(2016), 585–594.
2. Atieh MA, Ji Y, Kochkodan V, Metals in the Environment : Toxic Metals Removal. *Bioinorganic Chemistry and Application* .(2017), 2–4.
3. Alguacil FJ, Alcaraz L , García-Díaz I, López FL, Removal of Pb 2 + in Wastewater via Adsorption onto an Activated Carbon Produced from Winemaking Waste. *Metals* (2018), 8(9), 697.
4. Wu X, S. J. Cobbina SG, Mao G, Xu H, Zhang Z, Yang L, A review of toxicity and mechanisms of individual and mixtures of heavy metals in the environment, *Environmental Science and Pollution Research* .(2016), 23,8244-8259
5. El Qada EN, Allen SJ, Walker GM, Adsorption of Methylene Blue onto activated carbon produced from steam activated bituminous coal : A study of equilibrium adsorption isotherm. *Chemical Engineering Journal*.(2006),124. 103–110.
6. Abdel-Halim SH, Shehata AMA, El-Shahat MF, Removal of lead ions from industrial waste water by different types of natural materials. *Water Research* (2003),37,1678–1683.

7. Foo KY, Hameed BH, Insights into the modeling of adsorption isotherm systems, *Chemical Engineering Journal.* (2010), 156, 2–10.
8. Yadla SV, Sridevi V, Lakshmi MC, Adsorption Performance Of Fly Ash For The Removal Of Lead. *International Journal of Engineering research and technology. (2012),1,* 1–7.
9. Feddal I, Ramdani A, Taleb S, Adsorption capacity of methylene blue , an organic pollutant , by montmorillonite clay. *Desalintion Water Treatment (2014),52,* 2654–2661.
10. Man HC, Chin WH, Zadeh MR, Yusof MR, Adsorption potential of unmodified rice husk for boron removal, *BioREseources. (2012),7* ,3810–3822.
11. Fatiha M, Belkacem B, Adsorption of methylene blue from aqueous solutions using natural clay. *Journal of Materials and Environmental Science*. (2016), 7,285-92.
12. Ong ST, Lee W, Keng PS, Hung YT, HA ST, "Equilibrium studies and kinetics mechanism for the removal of basic and reactive dyes in both single and binary systems using EDTA modified rice husk. *International Journal of Physical Sciences*.(2010),5,582.

Lighting Up the Future New Technologies for Smart Devices

Submitted by the students : Benabdessadok Abdelhadi

Under the supervision of : Dr Bentawila Omar

Algeria Ministry of Higher Education and Scientific Research, University Kasdi Merbah , Ouargla

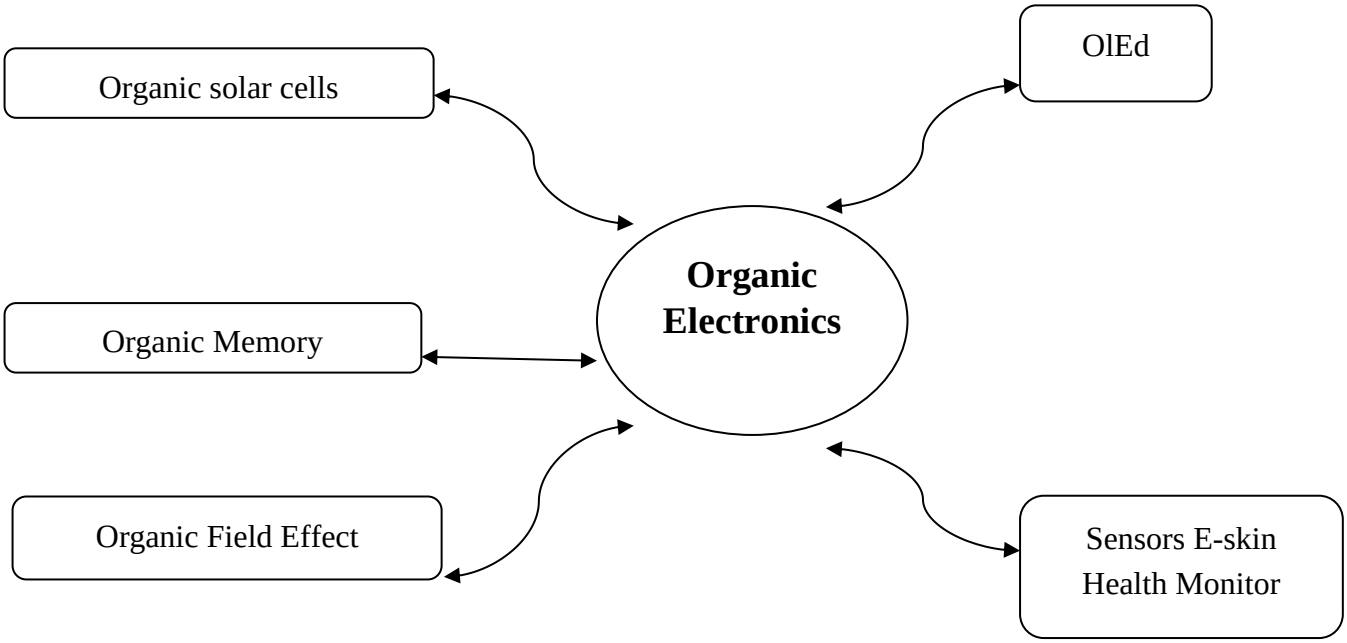
Faculty of Mathematics and Material Sciences, physics department

In the shadow of scientific and technological development in recent centuries, which was the reason for facilitating and serving human life and making it more sophisticated than it was and in pursuit of our scientific duty as researchers and students, where after the good invitation by the organizing team of the 9th Jordan International Conference of Chemical Engineering "JIChEC09" we put in your hands this sporadic research paper with the aim of participating in this distinguished scientific event.

I. Lighting up the future new technologies for smart devices :

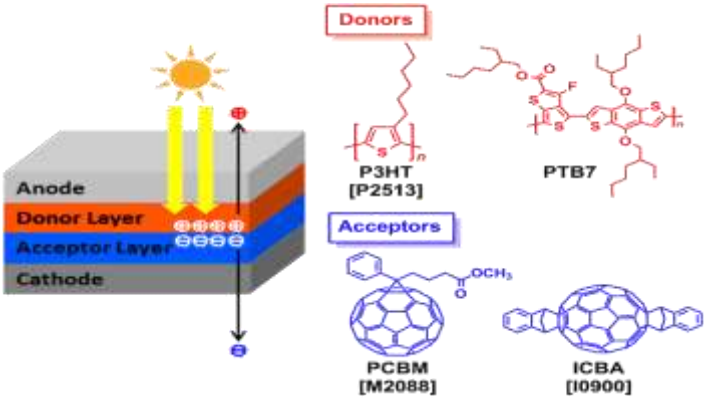
New technologies for innovation Are based on organic electronics organic electrons are organic electronics are a field in materials science related to the design, installation, characterization and application of small organic molecules or polymers that show desired electronic properties such as electrical conductivity and rely in their industry on organic molecules based on modern carbon-based

1. Organic Electrons Applications :



a) Organic Solar cell :

It is a type of photovoltaic cell that uses organic electrons as it deals with organic molecules to absorb light and transfer charges to produce electricity from solar radiation by the photovoltaic effect.

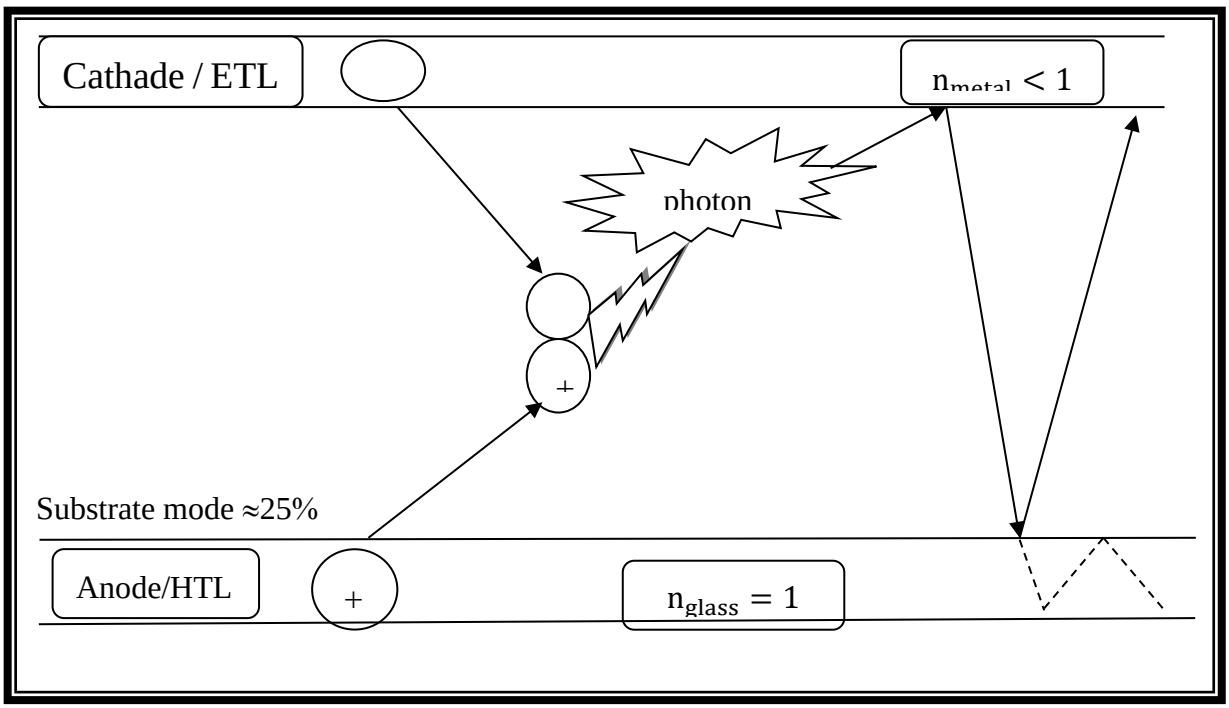


b) OLED :

Light-emitting diode is a semiconductor light source with the potential to release light in different colors

✓ The principle of its work:

- The valve consists of two poles, one negative and the other positive
- The electrical current passing through the valve provokes atoms in semiconductor, and some of their electrons occupy a high energy level in the atom
- These electrons affected by the electric current jump from a high energy level to a low energy level
- Electrons lead the energy difference between the two levels in the form of photon fatton
- This results in a light beam with a frequency and wavelength suitable for the desired light colour



Base:

To determine the color of light in OLED technology, we must choose the type of semiconductor material and the energy level of the two atoms

1. Industrial Scientific Products of Organic Electronics:

a) Smart window :

As these windows change color according to the weather outside, for example, if the weather is sunny, their color turns dark, which prevents sunlight from entering the house, car or vehicles in general.



b) Biocompatible E-Skin:

It was difficult for doctors to find the patient's blood vessels with the aim of taking a sample of his blood or injecting it with medicines, especially in patients with renal failure and people who have excessive obesity, and the medical staff in some third world countries removed the problem from this problem, and thanks to God, a detection device was achieved blood veins easily, and that by exploiting the optoelectronics sciences, as shown in the following figure:



II. Machine Intelligence:

Scientific research in the field of technology has achieved a remarkable development and contributed to making human life more luxurious, by manufacturing devices and machines with design and programming that simulate human mental abilities and patterns of work, so how can these devices mimic human mental abilities and patterns of work?

- The manufacture of these devices is based on two sides, the design side and the programming side

a) Design: It is the design and installation of the device in a manner commensurate with its function, in terms of external appearance and market demand

b) Programming: Programming is a means that enables us to process data, implement it and convert it into business, and it is hosted by a group of languages processed by the machine.

- What are the basics of machine intelligence?

The basics that must be provided for the manufacture of these smart devices is the availability of electronic receivers

- What are electronic receptors?

They are electronic parts that have the ability to sense various external reactions and convert them into electronic signals

- Types of electronic receptors:

1. Sound receptors: Its role is to receive and analyze the sound vibrations issued by it.

✓ This technique has been used in ultrasound analysis in the study of distances Ultrasonic (distance), as well as in the diagnosis of internal diseases ECHO





2. Mechano Receptor:

This technology analyzes the data of direct contacts with surfaces by touch, pressure or intensity .... such as fingerprint identification



3. Light photoreceptors: This technology analyzes the data in the form of light in terms of intensity, color, type and distance.
4. Camera imaging receivers: as this technology analyzes the image and video data and gives it in the form of information to the program, we mention, for example

- ✓ If it is a personal picture profiles can be selected
- ✓ If the data is in the form of a video, the extent of his actions can be determined
- ✓ There are many devices in the medical field that work with this technology, such as this device for optical coherence tomography (OCT).



5. Chemo-receptors: They are receptors that have the ability to sense chemicals, smell, taste, and chemical changes inside liquids, materials, and others, such as quality measuring devices.



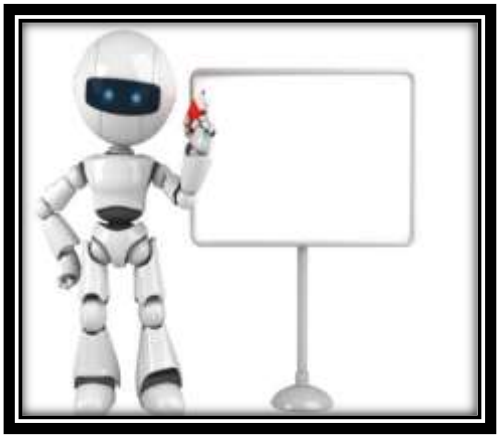
6. Thermo receptors: They are receptors that respond to changes in temperature and that are measured



- Where do we see the application of these technologies in our daily lives?

These technologies have been launched in several areas, including we use them in our daily lives and deal with them, and some of them are still under study, and we mention some of them:

a) Robotics :



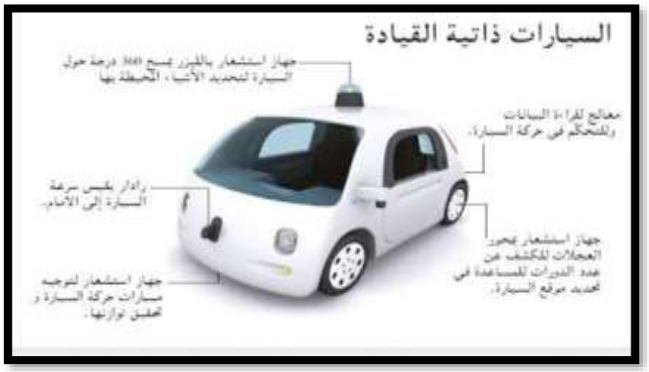
b) Industry: contributing to industrial accuracy and production speed



c) Health

d) Smart cities: still under study

e) Automatic transport



III. Technologies of Energy Solar

Energy is an integral part of our daily life and a basic source in the economy of countries, as it is obtained from several sources, including natural and industrial ones, renewable and non-renewable ones. The sun is a natural renewable source of energy and is characterized by low cost compared to other sources such as fuels. How Can the sun be exploited and made a source of energy?

- We can exploit the sun as a source of electricity production through two technologies: (CSP) and (PV)

- What is the difference between the two technologies (CSP) and (PV)?

a) Concentrated Solar Power technology (CSP) :



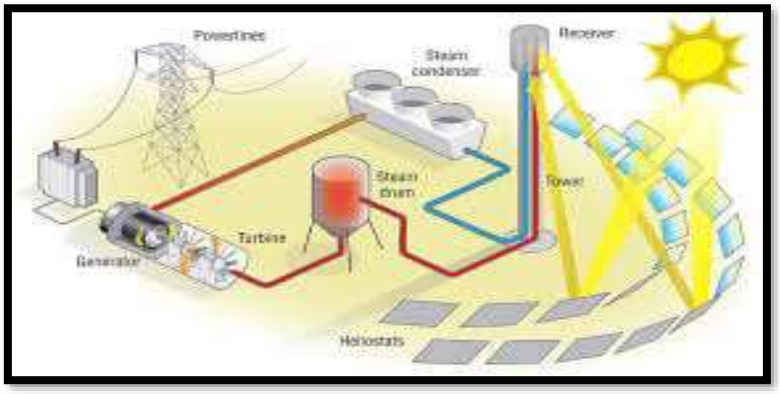
➢ <u>The working principle of CSP technology:</u>

✓ This technology consists of a group of glass in a circular shape around the tower

✓ These glasses track the sun and reflect the solar energy captured at the top of the tower

✓ There are salts at the top of the tower, which leads to raising its temperature between (500-400)°, and the solar energy is fused and stored in these salts as heat.

✓ This heat is used to produce steam, and this steam moves the wheels of a turbin, which produces electricity



- The production canacity of PV is estimated at 0.07$/KWH

b) Photo Voltaic technology (PV):

Photovoltaic technology is based on solar panels, what are solar panels?

✓ Solar panels are cells made of semiconductor materials such as silicon that absorb light from the sun

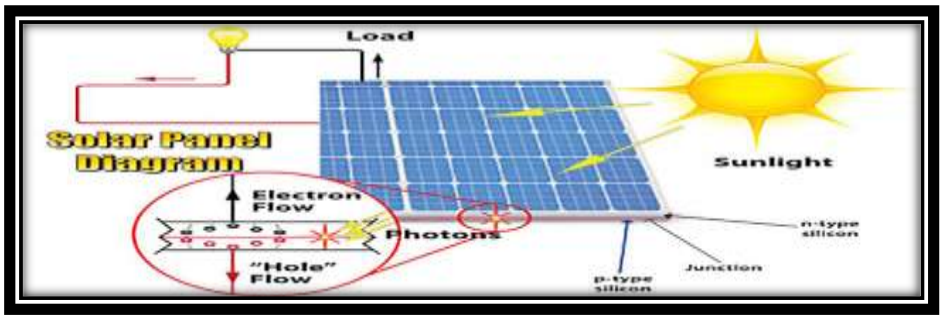


Note:

- Silicon is extracted from sand when ridding it of oxygen and impurities
- White sand is characterized as not containing impurities, while red sand contains iron impurities
- Silicon is naturally very shiny, so in order to take advantage of the photons and prevent them from being reflected outside the cell, an anti-reflection coating is applied

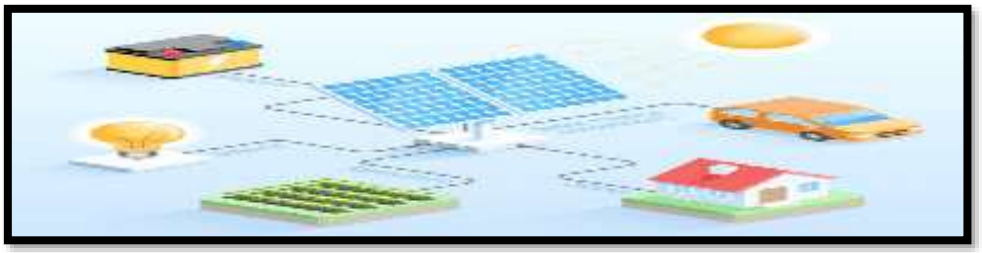
➢ Working Principle (PV):

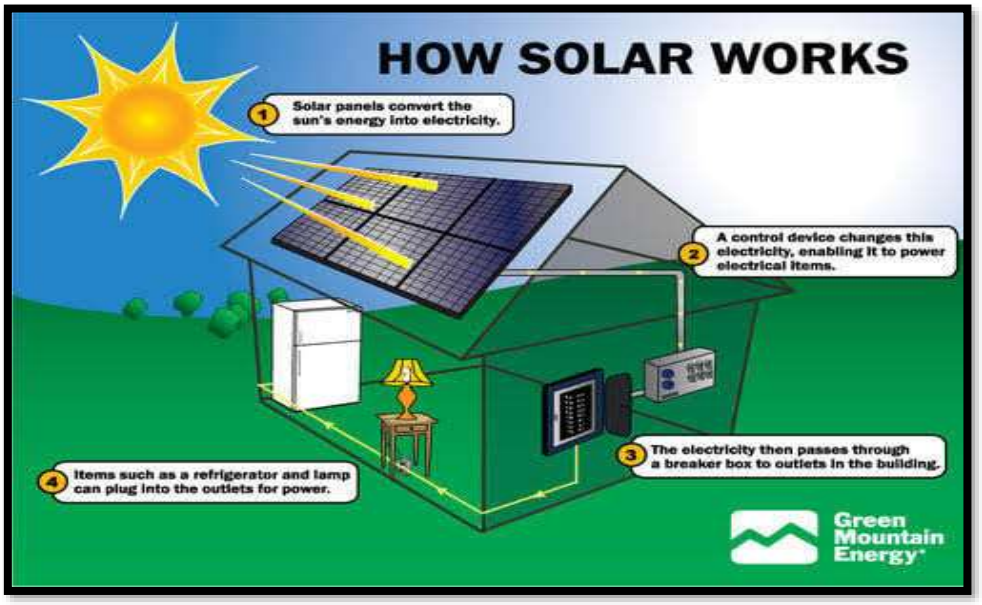
Solar rays contain a group of photons that when absorbed, liberate a group of electrons from atoms, which leads to a difference in voltage (Volt), which results in electricity



- The production canacity of PV is estimated at 0.017$/KWH

➢ We are growing up to use it:





The reviewer

1. A lecture by Dr. Fatima ben Sheikh at the first virtual educational homecamp in Algeria
2. A lecture by Dr. Muhammad ben Ammar Sanousi in the first virtual homecamp educational in Algeria
3. A lecture by Professor Nouar Thabet's in the first virtual educational homecamp in Algeria
4. Atlas of Physics, published by Dar Al-Shark elarabi for printing, publishing and distribution, Beirut, Lebanon

- ✓ Renewable Energies Sources, Page 34-36
- ✓ Light Page 68
- ✓ Reflection of light page 74
- ✓ Refraction of light page 76
- ✓ Electricity Page 92
- ✓ Electric current page 96
- ✓ vector page 100
- ✓ Insulators page 102
- ✓ Electronics page 110 Electronic Components page 112

Nutrients Recovery from Hybrid Adsorbents Through the Application as Slow-Release Fertilizer: A Mini-Review

Nurliyana Nasuha Binti Safie [1,] * and Abu Zahrim Yaser [1]

[1] Chemical Engineering Programme, Faculty of Engineering, Universiti Malaysia Sabah, Malaysia.
***** *Corresponding author: liyanasafie@gmail.com.my; Tel.: +6010 – 9205011*

Abstract: Population demand for food has increased the necessity of continuous supply of fertilizer for crops and plantations. The number of unexploited nutrients in sewage can be reused as fertilizer. Nutrients recovery is feasible through few techniques such as chemical precipitation, distillation, membrane filtration from a high concentration of ammonium ion, NH_4^+. Urine can be a great source for nutrients recovery to be used as fertilizer, however, it has long-term effects such as increasing pH and conductivity. The application of used hybrid encapsulated adsorbents in nutrients recovery is reviewed The recovery efficiency ranges from NO_3^- (38 mg/g - 80.2 mg/g), PO_4^{3-} (48 mg/g – 196 mg/g) and NH_4^+ (0.1mg/g), 73 % and can be used up to 8 cycles. It is shown that the application of adsorbents as slow-release fertilizers (SRFs) has improved the number of leaves and acidity of strawberry fruit though it is a slow process. The application of adsorbents as SRFs after the adsorption is providing an alternative to reuse the valuable adsorbents from being disposed to landfills.

Keywords: hybrid; adsorbents; adsorption-desorption; nutrients; recovery; slow-release-fertilizers

1. Introduction

The necessity to find a new source for nutrients to be utilized as fertilizer has been increasing due to the increase of population and the demand for a steady supply of crops such as paddy, wheat, corn, and palm oil. Based on statistics, for crop production larger than 3 billion tons, about 187 million tons of fertilizer are needed [1]. The application of nutrient-rich fertilizers in agricultural practices has enabled the increase of crop yields with N and P being critical to secure food production [2].

Municipal wastewater is known to have a high volume of nutrients nitrogen (N) and phosphorus (P) that are originated from urine, stools, and washing water [3]. Sewage on average contains 40 mg/L of NH_4^+ contains approximately 15.2 million tons ammonium-N/year that can be recycled into fertilizers [4]. Recovering P from sewage can satisfy 18 % of the world's demand [5]. The potential of sewage to be used as organometal fertilizer are urine (one of the components of sewage) directly use to water the plant that enables reuse of nutrients and organic matter, C-sequestration, and maintenance of soil microbial functions [6-7].

P species in sewage can generally be classified as inorganic phosphorus, polyphosphate, and organic phosphorus. Inorganic P is originated from the combination of P and metals ions such as Fe^{3+}/Fe^{2+}, Al^{3+}, Ca^{2+}, Mn^{2+}, and Mg^{2+}, which are mainly derived from chemical coagulants and raw sewage [8]. P usually combines with Fe^{2+} to form $Fe_3(PO_4)_2$ or crystalline state, vivianite [9]. The species in sewage inorganic P usually in the form of $Ca_3(PO_4)_2$, $Ca_2P_2O_7$, $Mg_3(PO_4)_2$, and hydroxyapatite [10]. The N compounds mainly exist as ammonium nitrogen, (NH_4^+-N) and derive from two sources which are from the influent and return liquid from activated sludge [11]. Normally, a typical influent NH_4^+-N of 30 mg-N/L at a pH of 7 – 8 at 20 ^oC [12].

The nutrients removal process is usually being applied in tertiary treatment, through the adsorption process. The adsorption process can be efficient, cost-effective, and sustainable for N and P removal even at low concentrations [13]. Natural adsorbents namely natural zeolite [14] and biochar [15-16]

have been widely applied and tested to remove N and P. High concentrations of nutrients in the sewage can be recovered by the adsorption process, N and P can be recycled into many useful agricultural purposes by reusing the adsorbents.

According to FAO [17] 200 million tons of fertilizers are needed by 2022 to sustain the population demand. Even though a large number of fertilizers being applied, but not all the nutrients will be absorbed by the plants because of nutrients lost. It is reported that the applied N, P, and potassium (K) as ammonia ($NH_{3)}$, P_2O_5 (phosphate), and K_2O (potassium) are lost by 55 %, 85 %, and 70 % through leaching, photodegradation, chemical hydrolysis and microbial decomposition [18]. Slow released fertilizer or controlled-release fertilizer (SRFs/CRFs) are respectively designed fertilizer that releases active fertilizing nutrients in a controlled delayed manner matched with the sequential needs of plants for nutrients [19].

The advantage of SRFs/CFRs is they provide enhanced nutrient used efficiency and enhanced yields without suffering from nutrient loss [20]. SRFs are not specifically designed to have a certain period to release the nutrients and subject to the changes in soil type and climatic conditions while for CRFs, the pattern, quantity, and time of release can be predicted within the limits for CRFs [20-21].CRFs such as controlled release urea in the polymer-coated urea for maize plantation [22], blended controlled-release fertilizer for wheat plantation [23], and biochar-based SRF for rice paddy fields [24] have enhanced the water-stable aggregates, improved crop N uptake, and increased crops yield.

Application of composite adsorbents as the organic SRFs is desirable as it can improve soil fertility without polluting the ground and surface water as well as cost-effective. Coating such as sulfur (S) and polyethylene was used initially as a coating for SRFs/CRFs but, it has low wettability and adhesion to the coated ore, requires conditioning materials to reinforce its sealing. May react with water that results in acidification of soil [25]. Biopolymer such as alginate [26], chitosan [27], and tapioca starch [28] have been used as an environmentally friendly coating for SRFs/CRFs. It is reported that CRFs/SRFs result in longevity of N release from the final product [28].

This review will compare different types of adsorbents and their respective efficiencies in nutrients recovery. N recovery techniques have been developed in recent years to recover N and P from sewage that can be utilized as fertilizers [29]. Struvite precipitation [30], precipitation, distillation, membrane filtration are few examples of low-energy techniques to recover ammonia from waste streams with a high concentration of NH_4^+-N [29]. The advantages and disadvantages of various nutrients recovery methods using composite materials by adsorption-desorption and their application as SRFs have also been reviewed in this paper.

2. Methods of nutrients recovery

Based on Table 1, nutrients were recovered from urine and synthetic solution on a lab scale. The recovery methods are different based on the source of nutrients. Based on the analysis, the recovery of nutrients will achieve high efficiency of the urine is separated from sewage [31]. However, life cycle assessment studies of urine separation systems also show that storage, transport, and spreading large amounts of urine present serious obstacles to system efficiency [32]. Typical influent of sewage contains ~310 mg/L of P, and urine usually contains slower P depending on the plant configuration and population activity [33].

Separated urine contains a great part of the total nutrients in normal sewage; 80 % of N, 55 % of P, and 60 % of K in just 1.5 % of the volume of the sewage [33-34]. Eco-toilet (collecting separately urine and feces) is an established technique to collect human urine for further use [35]. Direct use of urine as fertilizer has been used on edible crops such as spinach [36], beetroot, carrot, maize, and tomato [37], okra [38] paddy [39] and mainly being practiced in the rural area. A study by Pradhan

et al. [40], has shown that crop yield using urine was almost the same as that of conventional NPK fertilizer. The plant hygienic quality was assured free from microorganisms such as fecal coliforms, enterococci, clostridia, and coliphages.

The drawbacks of using urine directly and repeatedly could increase the pH of the soil by 0.5 and electrical conductivity by 100 µS/cm [41]. This will affect the growth of helpful microbes such as mycorrhiza fungi and reduce the plant root efficiency while absorbing nutrients through the diffusion process [42]. Other than that, the direct application may also increase the possibility of pathogen contaminations and associated diseases which in return will affect humans as consumers [43].

N and P can be recovered as struvite ($MgNH_4PO_4 \cdot 6H_2O$) [30]. The struvite is formed according to the simplified Equation 1.

$$Mg^{2+} + NH_4^+ + PO_4^{3-} + 6H_2O \rightarrow MgNH_4PO_4 \cdot 6H_2O \text{ (solid)} \quad (1)$$

The struvite precipitation process recovers about 99 % of P and only about 10 % of N. The additional stripping technique is required to enhance the recovery of N from urine. But, this method rejects water and only recovers N [44]. Other methods for nutrients recovery from urine such as membrane filtration with reverse osmosis (RO), evaporation, and precipitation of P, and distillation of NH_3 [33]. The separation of P, K, and S using membrane filtration was almost 100 %, while separation of N was dependent on pH [33]. The capacity of flux increased with T and P. In evaporation, all P, K was still in the concentrate, while pH had to be decreased to 4.5 to avoid significant loss of N. In precipitation and distillation, about 90 % of P could be recovered from urine as magnesium ammonium phosphate (MAP) just by adding MgO. For the reject water pH was first increased by aeration to remove CO_2. Ammonium can be distilled from the water phase after precipitation of MAP, without further increase of pH. At least 80 – 90 % of N can be distilled in 5 – 10 % of the total volume.

Recovery of nutrients from urine using evaporation and drying highly depends on the pH. When the pH is lower than 6, recovery of N can reach higher than 70 % [45]. Somehow, the process of pH adjusting will need more cost as acid such as H_2SO_4 needed to reach 4.5 (12 and 13 kg H_2SO_4/m^3 urine respectively). It is estimated that 1 m^3 of urine can produce 95 % of N and almost all other components. Recovery of urine using the precipitation of P can recover up to 90 % of P but it produced about 150 L of sludge, and by increasing the amount of Ca (OH)2/m3 urine does not increase the percentage of P recovery, but by applying filtration or sedimentation with long hydraulic retention time, the yield increases to 95 % and the dry matter content is more than 15 %. pH after the precipitation of urine with MgO was 9.2, and the pH is required to be increased to at least 1- to obtain most of the ammonia in the distillate [45].

The air stripping process is a physicochemical process in which a liquid mixture is contacted with air to remove the volatile components by mass transfer from the liquid to the gas phase. pH 9.3 to 10, the recovery was the highest, but after 10, no significant change was observed. The highest flow rate 14 L min -1 with T = 50 oC has shown a higher rate of NH_3 recovery > 95 %. Based on the economic point of view, unit operating cost for 80 % ammonia recovery, by increasing the airflow rate and temperature could reduce unit operating cost, whereas high pH could induce high unit operating cost due to the increase in chemical input [44].

3. Recovery of nutrients using hybrid adsorbents

By using sewage or synthetic solution where adsorbents such as hybrid chitosan encapsulated magnetic-kaolin beads, zirconium encapsulation chitosan quartenized beads, chitosan-bentonite, EFB, and natural zeolite are summarized in Table 1. The recovery efficiency ranges from NO_3^- (38 mg/g - 80.2 mg/g), PO_4^{3-} (48 mg/g – 196 mg/g) and NH_4^+ (0.1mg/g), 73 %.



Figure 1. Illustration of SRF/CRFs mechanism

Adsorbents can easily be regenerated by using NaOH and HCl [46-47]. Mostly, the nutrients recovery process is affected by pH. The hybrid adsorbent has lower AC at higher pH 7-12, while high AC at pH 3-7 as the surface charge is more positive at lower pH and more negative at pH larger than 7 [46]. It is also reusable for up to 8 cycles [46]. Other than that, by using used natural zeolite as a slow fertilizer, there is improvement in the number of leaves and acidity of strawberry fruit though it is a slow process [48].

Table 1. The efficiency of nutrients recovery methods

Source of nutrients	Recovery methods	Conc. of influent	Efficiency	Advantages	Disadvantages	Refs.
Urine	Air stripping	NH_4^+: 501	pH 10, T: 50 °C, Air flow rate: 4 $L.min^{-1}$: 95 %	High efficiency for NH_3 recovery	Low P recovery > 33 %. requires precipitation process. High cost of operation	[44]
Urine	Evaporation and drying	NH_4^+: 2450 PO_4^{3-} :195	pH 5.5: 86 % N pH 4.5: 95 % N pH < 6: >70 % N 1 m^3 of urine: 50 L concentrate with 95 % of N)	No additional technique is required after the recovery	Depends on pH Requires a high volume of H_2SO_4 to maintain pH.	[45]
Urine	Precipitation of P and distillation of NH_3	NH_4^+: 2450 PO_4^{3-} :195	2.8 kg of Ca $(OH)_2/m^3$: 95 % P and further distillation can get 3 % of N	pH needs to increase to 10 to get more NH_3	Produced sludge Longer hydraulic retention time combined with sedimentation or filtration is required to increase the efficiency	[45]
Synthetic NH_4^+ solution	Struvite precipitation with adsorption Adsorbent: 1) Clinoptilolite	NH_4^+: 1000 mg/L	65 – 80 % of N	The mixture of struvite and natural mineral adsorbent has good nutrient qualities and can be used as a soil conditioner.		[49]

	2) wollastonite					
Synthetic solution	Adsorption – desorption (Hybrid chitosan encapsulated magnetic-kaolin beads)	NO_3^-: 100 PO_4^{3-} :100	NO_3^-: 38 mg/g PO_4^{3-} :48 mg/g Reusable up to 8 cycles	Can be easily regenerated using 0.1 M NaOH	The hybrid adsorbent has lower AC at higher pH 7-12, while high AC at pH 3-7 as the surface charge is more positive at lower pH and more negative at pH larger than 7.	[46]
	Zirconium encapsulated chitosan quartenized beads (Zr@CSQ)	NO_3^-: 100 PO_4^{3-} :100	NO_3^-: 80.2 mg/g PO_4^{3-} :67.7 mg/g	Can be easily regenerated using 0.1 M NaOH	Exothermic process	[50]
	Desorption Chitosan - bentonite	PO_4^{3-} :500	PO_4^{3-}: 196 mg/g		The performance is dependent on the pH	[51]
Synthetic solution	EFB SRF	NH_4^+: 0-4000 mg/L	NH_4^+: 0.1 mg/g	The regeneration was carried out using HCl	The performance is dependent on the pH	[47]
Synthetic solution	SRF	NH_4^+: 1000 mg/L	NH_4^+: 73 %	There is improvement in the number of leaves, fruits acidity	Slow process	[48]

The granules were generally spherically shaped and the addition of anthracite, bentonite, and activated carbon to the alginate formulations led to larger and heavier granules with size and weight is 0.95 mm – 1.73 mm and 2.02 mg/granule respectively [26]. Alginate-anthracite-alginate granules have shown a slower release rate than the technical grade herbicides. 90 % of technical grade chloridazon dissolved in less than 2 h, but it takes at least 48 h to release the same percentage of chloridazon from the alginate-based controlled release formulation [26].

Physical compaction for instance palletization is potentially not a perfect method for CRF fabrication for biochar-based composite or hybrid. This is due to the biochar-based pellets might be loose or fragile [52]. This finding suggests that the addition of cohesive materials such as clays, starch, alginate, and chitosan can strengthen the pellet or hybrid structure if necessary [53-54]. Pellets fabricated from fresh biomass have a limited porous structure, and organic matter parts (lignocellulose) are subject to rapid biodecomposition once incorporated into the soil [52]. In particular, nutrients are released through the nano- to micro-sized channels of biochar, and the released rate depends on chemical retard reactions, for instance, surface complexation, redox reactions, H-bond formation, or electrostatic attractions [52].

The submerged plants can be used as the media for plant growth later. Empty fruit bunch (EFB) can serve as a medium for plant growth [47]. Direct application of NH_4^+ loaded biochar to soils as fertilizers are possible as confirmed by similar research with the growth of water spinach [15].

4. Conclusions

The recovery of nutrients mainly being done on a lab-scale by using urine and synthetic solution. Nutrients recovery from urine is high and chemical precipitation is mainly being used that eventually, it will form struvite that can be used as fertilizer. But, this process dependent on pH, a complex and

energy-intensive process. However, the drawbacks of using urine directly and repeatedly could increase the pH of the soil by 0.5 and electrical conductivity by 100 µS/cm. Other than that, the direct application may also increase the possibility of pathogen contaminations and associated diseases which in return will affect humans as a consumer. Other than desorption, used adsorbents have been applied as soil stabilizers and SRFs. The process can be enhanced and improved for larger-scale applications as this can avoid large wastage of valuable adsorbents after the adsorption.

Funding: This research was funded by UNIVERSITI MALAYSIA SABAH, grant number SDK 0044 – 2018, SPB 0001-2020, and SGI0064 - 2018

Acknowledgments: I would like to thank my supervisor, Assoc. Prof. Abu Zahrim Yaser for the guidance in writing this manuscript.

References

1. Usman, M.; Farooq, M.; Wakeel, A.; Nawaz, A.; Cheema, S.A.; ur Rehman, H.; Ashraf, I.; Sanaullah, M. Nanotechnology in Agriculture: Current Status, Challenges and Future Opportunities. *Sci. Total Environ.* **2020**, *721*, 137778.
2. Cordell, D.; Neset, T.S.S.; Prior, T. The Phosphorus Mass Balance: Identifying "hotspots" in the Food System as a Roadmap to Phosphorus Security. *Curr. Opin. Biotechnol.* 2012, *23*, 839–845.
3. Yaser, A.Z.; Safie, N.N. *Sewage Treatment in Campus for Recycling Purpose: A Review*; 2019; ISBN 9789811372605.
4. Qadir, M.; Drechsel, P.; Jiménez Cisneros, B.; Kim, Y.; Pramanik, A.; Mehta, P.; Olaniyan, O. Global and Regional Potential of Wastewater as a Water, Nutrient and Energy Source. *Nat. Resour. Forum* **2020**, *44*, 40–51, doi:10.1111/1477-8947.12187.
5. Yuan, Z.; Pratt, S.; Batstone, D.J. Phosphorus Recovery from Wastewater through Microbial Processes. *Curr. Opin. Biotechnol.* 2012, *23*, 878–883.
6. Seleiman, M.F.; Santanen, A.; Mäkelä, P.S.A. Recycling Sludge on Cropland as Fertilizer – Advantages and Risks. *Resour. Conserv. Recycl.* 2020, *155*, 104647.
7. Diacono, M.; Montemurro, F. Long-Term Effects of Organic Amendments on Soil Fertility. A Review. *Agron. Sustain. Dev.* 2010, *30*, 401–422.
8. Yu, B.; Luo, J.; Xie, H.; Yang, H.; Chen, S.; Liu, J.; Zhang, R.; Li, Y.Y. Species, Fractions, and Characterization of Phosphorus in Sewage Sludge: A Critical Review from the Perspective of Recovery. *Sci. Total Environ.* 2021, *786*, 147437.
9. Wilfert, P.; Kumar, P.S.; Korving, L.; Witkamp, G.-J.; Van Loosdrecht, M.C.M. The Relevance of Phosphorus and Iron Chemistry to the Recovery of Phosphorus from Wastewater: A Review. *Environ. Sci. Technol.* **2015**, *49*, 9400–9414.
10. Chen, J.; Tang, S.; Yan, F.; Zhang, Z. Efficient Recovery of Phosphorus in Sewage Sludge through Hydroxylapatite Enhancement Formation Aided by Calcium-Based Additives. *Water Res.* **2020**, *171*, 115450, doi:10.1016/j.watres.2019.115450.
11. Liu, Y.; Ngo, H.H.; Guo, W.; Peng, L.; Wang, D.; Ni, B. The Roles of Free Ammonia (FA) in

Biological Wastewater Treatment Processes: A Review. *Environ. Int.* 2019, *123*, 10–19.

12. McCarty, P.L. What Is the Best Biological Process for Nitrogen Removal: When and Why? *Environ. Sci. Technol.* **2018**, *52*, 3835–3841, doi:10.1021/acs.est.7b05832.
13. Mitrogiannis, D.; Psychoyou, M.; Koukouzas, N.; Tsoukalas, N.; Palles, D.; Kamitsos, E.; Pantazidis, A.; Oikonomou, G.; Baziotis, I. Phosphate Recovery from Real Fresh Urine by Ca(OH)2 Treated Natural Zeolite. *Chem. Eng. J.* **2018**, *347*, 618–630, doi:10.1016/j.cej.2018.04.102.
14. Widiastuti, N.; Wu, H.; Ang, H.M.; Zhang, D. Removal of Ammonium from Greywater Using Natural Zeolite. *Desalination* **2011**, *277*, 15–23, doi:10.1016/J.DESAL.2011.03.030.
15. Shang, L.; Xu, H.; Huang, S.; Zhang, Y. Adsorption of Ammonium in Aqueous Solutions by the Modified Biochar and Its Application as an Effective N-Fertilizer. *Water. Air. Soil Pollut.* **2018**, *229*, doi:10.1007/s11270-018-3956-1.
16. Qian, K.; Kumar, A.; Zhang, H.; Bellmer, D.; Huhnke, R. Recent Advances in Utilization of Biochar. *Renew. Sustain. Energy Rev.* **2015**, *42*, 1055–1064, doi:https://doi.org/10.1016/j.rser.2014.10.074.
17. FAO *World Fertilizer Trends and Outlook to 2022*; Rome, Italy, 2019;
18. Tarafder, C.; Daizy, M.; Alam, M.M.; Ali, M.R.; Islam, M.J.; Islam, R.; Ahommed, M.S.; Aly Saad Aly, M.; Khan, M.Z.H. Formulation of a Hybrid Nanofertilizer for Slow and Sustainable Release of Micronutrients. *ACS Omega* **2020**, *5*, 23960–23966, doi:10.1021/acsomega.0c03233.
19. Fertahi, S.; Ilsouk, M.; Zeroual, Y.; Oukarroum, A.; Barakat, A. Recent Trends in Organic Coating Based on Biopolymers and Biomass for Controlled and Slow Release Fertilizers. *J. Control. Release* 2021, *330*, 341–361.
20. Shaviv, A. Advances in Controlled-Release Fertilizers. **2001**.
21. Trenkel, M.E. *Slow-and Controlled-Release and Stabilized Fertilizers: An Option for Enhancing Nutrient Use Efficiency in Agriculture*; IFA, International fertilizer industry association, 2010; ISBN 2952313970.
22. Gao, Y.; Song, X.; Liu, K.; Li, T.; Zheng, W.; Wang, Y.; Liu, Z.; Zhang, M.; Chen, Q.; Li, Z.; et al. Mixture of Controlled-Release and Conventional Urea Fertilizer Application Changed Soil Aggregate Stability, Humic Acid Molecular Composition, and Maize Nitrogen Uptake. *Sci. Total Environ.* **2021**, *789*, 147778, doi:10.1016/j.scitotenv.2021.147778.
23. Li, R.; Gao, Y.; Chen, Q.; Li, Z.; Gao, F.; Meng, Q.; Li, T.; Liu, A.; Wang, Q.; Wu, L.; et al. Blended Controlled-Release Nitrogen Fertilizer with Straw Returning Improved Soil Nitrogen Availability, Soil Microbial Community, and Root Morphology of Wheat. *Soil Tillage Res.* **2021**, *212*, 105045, doi:10.1016/j.still.2021.105045.
24. Dong, D.; Li, J.; Ying, S.; Wu, J.; Han, X.; Teng, Y.; Zhou, M.; Ren, Y.; Jiang, P. Mitigation of Methane Emission in a Rice Paddy Field Amended with Biochar-Based Slow-Release Fertilizer. *Sci. Total Environ.* **2021**, *792*, 148460, doi:10.1016/j.scitotenv.2021.148460.
25. Azeem, B.; Kushaari, K.; Man, Z.B.; Basit, A.; Thanh, T.H. Review on Materials & Methods to Produce Controlled Release Coated Urea Fertilizer. *J. Control. Release* 2014, *181*, 11–21.

26. Flores Céspedes, F.; Villafranca Sánchez, M.; Pérez García, S.; Fernández Pérez, M. Modifying Sorbents in Controlled Release Formulations to Prevent Herbicides Pollution. *Chemosphere* **2007**, *69*, 785–794, doi:10.1016/j.chemosphere.2007.05.005.
27. Safie, N.N.N.; Zahrim, A.Y.Y.; Rajin, M.; Ismail, N.M.M.; Saalah, S.; Anisuzzaman, S.M.M.; Rahayu, A.D.D.; Huslyzam, H.; Jennisha, R.; Calvin, T.T.H.T.H. Adsorption of Ammonium Ion Using Zeolite, Chitosan, Bleached Fibre and Activated Carbon. In Proceedings of the IOP Conference Series: Materials Science and Engineering; IOP Publishing, September 10 2019; Vol. 606, pp. 1–4.
28. Azeem, B.; KuShaari, K.; Naqvi, M.; Keong, L.K.; Almesfer, M.K.; Al-Qodah, Z.; Naqvi, S.R.; Elboughdiri, N. Production and Characterization of Controlled Release Urea Using Biopolymer and Geopolymer as Coating Materials. *Polymers (Basel).* **2020**, *12*, doi:10.3390/polym12020400.
29. Beckinghausen, A.; Odlare, M.; Thorin, E.; Schwede, S. From Removal to Recovery: An Evaluation of Nitrogen Recovery Techniques from Wastewater. *Appl. Energy* **2020**, *263*, 114616, doi:https://doi.org/10.1016/j.apenergy.2020.114616.
30. Morales, N.; Boehler, M.A.; Buettner, S.; Liebi, C.; Siegrist, H. Recovery of N and P from Urine by Struvite Precipitation Followed by Combined Stripping with Digester Sludge Liquid at Full Scale. *Water (Switzerland)* **2013**, *5*, 1262–1278, doi:10.3390/w5031262.
31. Theregowda, R.B.; González-Mejía, A.M.; Ma, X. (Cissy); Garland, J. Nutrient Recovery from Municipal Wastewater for Sustainable Food Production Systems: An Alternative to Traditional Fertilizers. *Environ. Eng. Sci.* **2019**, *36*, 833–842, doi:10.1089/ees.2019.0053.
32. Hilton, S.; Zhou, B.; Keoleian, G.; Daigger, G.; Love, N. *Life-Cycle Analysis of Source Seperated Wastewater Treatment and Urine Derived Fertilizer Production*; 2018;
33. Ek, M.; Bergström, R.; Bjurhem, J.E.; Björlenius, B.; Hellström, D. Concentration of Nutrients from Urine and Reject Water from Anaerobically Digested Sludge. In Proceedings of the Water Science and Technology; IWA Publishing, December 1 2006; Vol. 54, pp. 437–444.
34. McConville, J.R.; Kvarnström, E.; Jönsson, H.; Kärrman, E.; Johansson, M. Source Separation: Challenges & Opportunities for Transition in the Swedish Wastewater Sector. *Resour. Conserv. Recycl.* **2017**, *120*, 144–156, doi:10.1016/j.resconrec.2016.12.004.
35. Pradhan, S.K.; Mikola, A.; Heinonen-Tanski, H.; Vahala, R. Recovery of Nitrogen and Phosphorus from Human Urine Using Membrane and Precipitation Process. *J. Environ. Manage.* **2019**, *247*, 596–602, doi:10.1016/j.jenvman.2019.06.046.
36. Chaggu, E.; Mashauri, D.; Van Buuren, J.; Sanders, W.; Lettinga, G. Excreta Disposal in Dar-Es-Salaam. *Environ. Manage.* **2002**, *30*, 609–620.
37. Mnkeni, P.N.S.; Kutu, F.R.; Muchaonyerwa, P.; Austin, L.M. Evaluation of Human Urine as a Source of Nutrients for Selected Vegetables and Maize under Tunnel House Conditions in the Eastern Cape, South Africa. *Waste Manag. Res.* **2008**, *26*, 132–139, doi:10.1177/0734242X07079179.
38. Akpan-Idiok, A.U.; Udo, I.A.; Braide, E.I. The Use of Human Urine as an Organic Fertilizer in the Production of Okra (Abelmoschus Esculentus) in South Eastern Nigeria. *Resour. Conserv. Recycl.*

2012, *62*, 14–20, doi:10.1016/j.resconrec.2012.02.003.

39. Mackie Jensen, P.K.; Phuc, P.D.; Knudsen, L.G.; Dalsgaard, A.; Konradsen, F. Hygiene versus Fertiliser: The Use of Human Excreta in Agriculture - A Vietnamese Example. *Int. J. Hyg. Environ. Health* **2008**, *211*, 432–439, doi:10.1016/j.ijheh.2007.08.011.
40. Pradhan, S.K.; Nerg, A.M.; Sjöblom, A.; Holopainen, J.K.; Heinonen-Tanski, H. Use of Human Urine Fertilizer in Cultivation of Cabbage (Brassica Oleracea) - Impacts on Chemical, Microbial, and Flavor Quality. *J. Agric. Food Chem.* **2007**, *55*, 8657–8663, doi:10.1021/jf0717891.
41. Sene, M.; Hijikata, N.; Ushijima, K.; Funamizu, N. Application of human urine in agriculture. In *Resource-Oriented Agro-sanitation Systems: Concept, Business Model, and Technology*; Springer Japan, 2018; pp. 213–242 ISBN 9784431568353.
42. Pathy, A.; Ray, J.; Paramasivan, B. Challenges and Opportunities of Nutrient Recovery from Human Urine Using Biochar for Fertilizer Applications. *J. Clean. Prod.* 2021, *304*, 127019.
43. Karak, T.; Bhattacharyya, P. Human Urine as a Source of Alternative Natural Fertilizer in Agriculture: A Flight of Fancy or an Achievable Reality. *Resour. Conserv. Recycl.* 2011, *55*, 400–408.
44. Liu, B.; Giannis, A.; Zhang, J.; Chang, V.W.C.; Wang, J.Y. Air Stripping Process for Ammonia Recovery from Source-Separated Urine: Modeling and Optimization. *J. Chem. Technol. Biotechnol.* **2015**, *90*, 2208–2217, doi:10.1002/jctb.4535.
45. Ek, M.; Bergström, R.; Bjurhem, J.E.; Björlenius, B.; Hellström, D. Concentration of Nutrients from Urine and Reject Water from Anaerobically Digested Sludge. In Proceedings of the Water Science and Technology; 2006; Vol. 54, pp. 437–444.
46. Karthikeyan, P.; Meenakshi, S. Fabrication of Hybrid Chitosan Encapsulated Magnetic-Kaolin Beads for Adsorption of Phosphate and Nitrate Ions from Aqueous Solutions. *Int. J. Biol. Macromol.* **2021**, *168*, 750–759, doi:10.1016/j.ijbiomac.2020.11.132.
47. Zahrim, A.Y.; Ricky, L.N.S.; Hilal, N.; Tamrin, K.F. Ammonia-Nitrogen Recovery from Synthetic Solution Using Agricultural Waste Fibers. *Indian J. Sci. Technol.* **2017**, *10*, 1–5, doi:10.17485/ijst/2017/v10i6/111221.
48. Costamagna, G.; Chiabrando, V.; Fassone, E.; Mania, I.; Gorra, R.; Ginepro, M.; Giacalone, G. Characterization and Use of Absorbent Materials as Slow-Release Fertilizers for Growing Strawberry: Preliminary Results. *Sustain.* **2020**, *12*, 6854, doi:10.3390/SU12176854.
49. Lind, B.B.; Ban, Z.; Bydén, S. Nutrient Recovery from Human Urine by Struvite Crystallization with Ammonia Adsorption on Zeolite and Wollastonite. *Bioresour. Technol.* **2000**, *73*, 169–174, doi:10.1016/S0960-8524(99)90157-8.
50. Banu, H.A.T.; Karthikeyan, P.; Meenakshi, S. Removal of Nitrate and Phosphate Ions from Aqueous Solution Using Zirconium Encapsulated Chitosan Quaternized Beads: Preparation, Characterization and Mechanistic Performance. *Results in Surfaces and Interfaces* **2021**, *3*, 100010, doi:10.1016/j.rsurfi.2021.100010.

51. Piluharto, B.; Suendo, V.; Maulida, I. Composite Beads of Chitosan/Bentonite as a Matrix for Phosphate Fertilizer Controlled-Release. *Asnawati J. Chem. Technol. Metall.* **2017**, *52*, 1027–1031.
52. Nguyen, M.N. Potential Use of Silica-Rich Biochar for the Formulation of Adaptively Controlled Release Fertilizers: A Mini Review. *J. Clean. Prod.* 2021, *307*, 127188.
53. Safie, N.N.; Zahrim, A.. Recovery of Nutrients from Sewage Using Zeolite-Chitosan-Biochar Adsorbent: Current Practices and Perspectives. *J. Water Process Eng.* **2020**, 101845, doi:10.1016/j.jwpe.2020.101845.
54. Calabi-Floody, M.; Medina, J.; Rumpel, C.; Condron, L.M.; Hernandez, M.; Dumont, M.; Mora, M. de la L. Smart Fertilizers as a Strategy for Sustainable Agriculture. In *Advances in Agronomy*; Academic Press Inc., 2018; Vol. 147, pp. 119–157.

Photodegradation of Methylene Blue by Carbon Nanodots Synthesized from Olive Solid Wastes

Dr. Shadi Sawalha *, Hala Azzam , Rasha Bin Ali , Hanan Dweikat , Kayan Anaya

Chemical Engineering Department, An-Najah National University, Nablus, Palestine

**Corresponding author: sh.sawalha@najah.edu , +970599674156*

Abstract: Carbon Nanodots (CNDs) are emerging materials in the nanotechnology field as attractive photocatalysts, owing to their high water-solubility, good chemical and photostability, tunable photoluminescence and photoinduced phenomena.

This study aims to synthesize CNDs from olive solid wastes to be used as photocatalysts for the photodegradation of Methylene blue (M.B). CNDs were synthesized from olive solid waste by pyrolysis at 600 °C converted into carbonized material, followed by a chemical oxidation in the presence of hydrogen peroxide. The as-synthesized CNDs were utilized in this work as photocatalysts for the photodegradation of methylene blue at different conditions, such as; the catalyst concentration (dose), pH of the pollutant solution (M.B), salt content, light source distance, power of irradiation and pollutant concentration (M.B).

The degradation efficiency and rate were studied for all aforementioned factors, finding that the increase the CNDs dose into the M.B solution increases linearly both the efficiency and the rate. On the other hand, the maximum degradation rate was observed at pH = 10.6 with an efficiency of 92% after 120 minutes of irradiation. Moreover, the existence of NaCl salt in the pollutant solution affects adversely the degradation parameters showing a slight decrease in degradation rate, each 2 mg/ml addition decreased the rate with less than 1.2 folds. The potential and the distance of the visible light source from the pollutant cell have an obvious effect on the degradation, increasing the light power from 10 to 50 W, increased the degradation rate 16 times.

Keywords: Olive solid wastes, chemical oxidation, photodegradation, degradation efficiency and rate.

1. Introduction

Carbon Nanodots (CNDs) are small nano-sized carbon nano-materials less than 10 nm, were first synthesized in 2006 from carbon nanotubes (CNTs) during the process of electrophoresis[1], having internal sp^2 and external sp^3 carbon atoms[2]. CNDs surface is rich in hydrophilic functional groups, such as carboxyl, hydroxyl, epoxides, etc. which give them excellent and uniformly dispersion in polar solvents [3]. CNDs exhibit unique chemical and physical properties such as good luminescence, chemical inertness, low toxicity, excellent water solubility and conductivity [4]. They have been used

for various applications, such as sensors, bio-imaging, electrogenerated chemiluminescence, solar to fuel production [5], and photocatalysts for pollutant/dye degradation [6].

CNDs are synthesized through two routes; top-down and bottom-up methods. They include pyrolytic decomposition or carbonization [7], chemical oxidation [8], arc discharge [9], laser etching [10], microwave [11] and hydrothermal or solvothermal methods [12].

CNDs have excellent photoluminescent properties in which they can convert visible light to a shorter wavelength that can extend the wide band-gap of a semiconductor [13]. CNDs are good for trapping and transferring electrons. Therefore, CNDs can be one of the best candidates in the photocatalytic degradation of organic dyes such as Methylene blue (M.B) [14]. Photocatalysis is an energy conversion process of semiconductor materials that can be initiated by light absorption. During photocatalysis, electrons and holes can be generated by light exposure [15]. CNDs can be considered to be good photocatalysts in the degradation of organic dyes owing to their strong visible-light absorption, excellent light-trapping ability, and high efficiency in the separation of photo-generated charge carriers[16].

The photodegradation of the pollutant in the presence of CNDs as photocatalysts is affected by several factors, which can play a role in obtaining the best degradation efficiency and higher rate. The most important factors are; concentration of photocatalyst [17], pH [18], salt concentrations [19], concentrations of pollutant [17], source of light and its location [20].

Synthetic organic dyes are commonly used in various industries, such as in textiles, leather, dyes, foods and cosmetics. They are one of the main water pollutants that can be a major threat to aquatic life [21,22].The most commonly used dye in textile industries is methylene blue, which is used for dyeing and cloth completion processes [14]. However, excessive exposure to methylene blue is harmful to human and aquatic life as it can cause skin allergies, dermatitis, nervous system disorders, and ultimately cardiovascular damages [23,24]. Therefore, it is important to search for economical and environmentally friendly methods to degrade and remove methylene blue and other dyes from pollutant waters.

In this work, CNDs synthesized from olive solid wastes as cheap and abundant precursor will be used as photocatalysts in order to remove organic pollutants such as methylene blue from water. Different factors that may affect the M.B photodegradation process will be studied. These factors are the photocatalyst dose, pH, pollutant concentration, source potential and location in addition to the salt content. Photodegradation efficiency and rate will be the most attractive parameters to be monitored

2. Materials and Methods

Olive solid wastes were obtained from an olive oil extraction plant in Nablus (Palestine). All required chemicals and reagents were purchased form Sigma-Aldrich and used without further purification. Distilled water was used in the synthesis and dialysis of carbon nanodots and also for preparing methylene blue solutions.

Steady state fluorescence spectra in an emission range of 350 to 650 nm and at different excitation wavelengths from 300 to 480 nm were conducted by using Perkin Elmer LS55

Fluorescence spectrophotometer. UV-Vis spectra were recorded on Thermo Scientific™ GENESYS 10S UV-Vis Spectrophotometer from 200 to 800 nm. Transmission Electron microscopy (TEM) analysis was performed by JEOL JEM 1400-Plus microscope operated at an accelerating voltage of 120 kV, equipped with GATAN US1000 CCD Camera. Samples were prepared by drop casting of CDs solution on Lacey carbon film coated copper TEM grids. Fourier transform infrared (FTIR) spectrum was recorded by a PerkinElmer Spectrum One instrument in the ATR (Attenuated Total Reflection) mode and 64 scans were acquired in the range of 4000–800 cm^{-1}. Z-potential measurements were carried out using a Malvern Nano ZS90 Zetasizer.

2.1 Synthesis of Carbon Nanodots (CNDs)

CNDs were synthesized according to the method published previously by the author and other co-workers [25]. Briefly, Olive solid wastes (OSWs) collected from Nablus were purified from impurities and residual oil by means of Soxhlet using hot water as solvent. Purified OSWs were dried and then pyrolyzed at 600°C to obtained a carbon-based material. After cooled down to room temperature a fine powder was prepared by using a pestle and mortar. 0.1 g of the carbon powder was dispersed in 10 ml deionized water contained 150 µl hydrogen peroxide (30 wt.%) and sonicated for 10 minutes. The mixture was then refluxed at 100°C for 90 min. To separate CNDs from large carbon particles, the mixture was centrifuged at 9900 rcf for 20 min., the resulted supernatant was the filtered through 0.2 µm microfilter and then dialyzed against distilled water through a dialysis membrane of 500 – 1000 Da cutoff. Obtained CNDs solution was stored in dark at 4°C for further use.

2.3 Photodegradation of Methylene Blue (M.B)

M.B solution with initial concentration of 35 µM was prepared by dissolving the weighed powder in appropriate volume of deionized water. UV-Vis spectrum scan was performed to M.B solution to find the wavelength of maximum absorption.

Firstly, 500 µl of 0.04 mg/ml CNDs solution were added to 3 ml of previously prepared M.B solution and left in dark for 2 hours to examine if CNDs will interact with M.B and behave as a catalyst.

3 ml of M.B solutions (35µM) in the absence and presence of CNDs were irradiated for 2 hours by visible light source of 50 W. The dose of the photocatalysts (CNDs) was altered by adding 200, 300, 400 and 500 µl of 0.04 mg/ml CNDs solution obtaining final concentrations of CNDs in M.B solution of 2.67, 4, 5.3, and 6.67 mg/L. (separate solutions were prepared). Before light irradiation, all solutions were left for half an hour to obtain an absorption-desorption equilibrium between solution species. The UV-Vis absorption was recorded for each sample at 668 nm (M.B maximum absorption peak) with 10 minutes increment. The same irradiation procedures were carried out for all experiments.

Secondly, the effect of different parameters such as the pH, NaCl, light power/distance and pollutant (M.B) content on photodegradation process was examined at constant CNDs dose (6.67 mg/L). For the pH effect, different M.B solutions with pH of 3.8, 7, and 10.6 were prepared, the pH was adjusted by either drops of NaOH or HCl solutions. The effect of NaCl was followed after adding 6, 12 and 24 mg of salt into 3 ml M.B solution obtaining a final salt concentration of 2, 4, and 8 mg/ml

respectively. Moreover, 10 and 50 W light sources were used and two distances of the light source (5 and 10 cm) form the M.B solution were also tested.

Finally, three pollutant (M.B) concentrations were prepared (35, 23 and 17.5 µM) and mixed with 500 µl of CNDs and then irradiated for 120 minutes to investigate the effect of M.B concentration on photodegradation process.

3. Results and Discussion

3.1 Synthesis and Characterizations of CNDs

Carbon nanodots were synthesized by a combination of bottom-up and top-down routes implementing the pyrolysis of olive solid waste at 600°C followed by extraction and chemical oxidation with H_2O_2 (Figure 1). H_2O_2 acts as a strong oxidizing agent helping in breaking down the carbonaceous particles present in pyrolyzed olive solid wastes, producing CNDs rich of oxygenated groups on their surfaces [26].



Figure 1: Synthesis procedure of CNDs

The morphology of synthesized CNDs was investigated by using the Transmission Electron Microscope (TEM). The TEM micrograph shows well dispersed nanoparticles with good contrast and narrow size dispersion from 1-4 nm with average size of (2.8±0.6 nm). The TEM micrograph and size distribution histograms are illustrated in Figure 2(a).

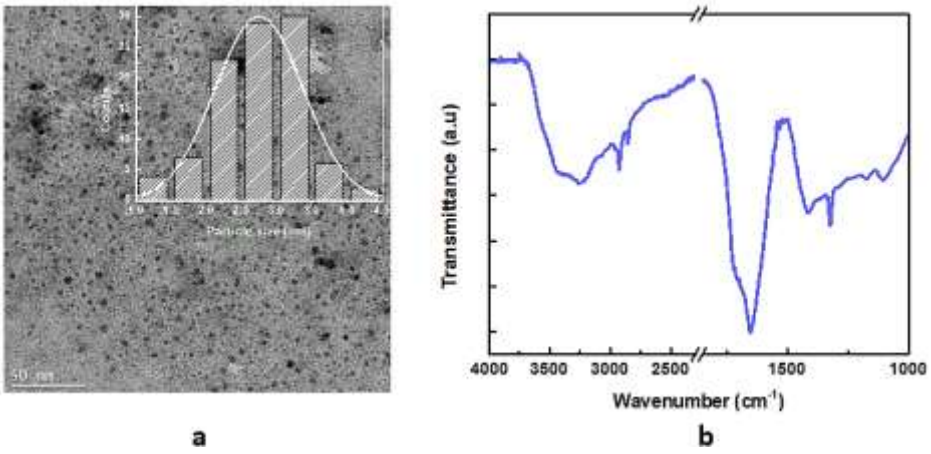


Figure 2: (a) TEM Micrograph, size distribution histogram (the inset). (b) FT-IR spectrum of synthesized CNDs.

The surface functional groups of prepared CNDs were acquired using FT-IR. The FT-IR spectrum in Figure 2(b) shows different peaks at 3424, 3236, 2923/2850, 1656, 1412, 1320, 1116 and 1096 cm^{-1}. These peaks are attributed to –OH, N-H, C-H, C=O (carbonyl), COO- (carboxylate), C-OH (hydroxyl) and C-O-C (epoxide) respectively [27,28]. The presence of oxidized and acidic groups on the surface leads to a strong negative charge of -32 eV (*@10 mM P.B. (pH =7.4))* and -18 eV *@ pH = 3* theses values were attained by ζ-potentials measurements [29-31]. Such negative potential value confers to the excellent solubility of CNDs in water [32].

The optical properties of synthesized CNDs were explored by conducting the UV-Vis absorption and photoluminescence measurements. Usually, the absorption spectrum of CNDs appears in the UV region and the tail extending towards the visible region. UV-visible spectrum of CNDs as in Figure 3(a) shows a strong absorption at 220 – 320 nm which can be related to the π-π^* and n-π^* transition arising from aromatic C=C bonds (sp^2 domain) and C=O groups respectively [31,33].

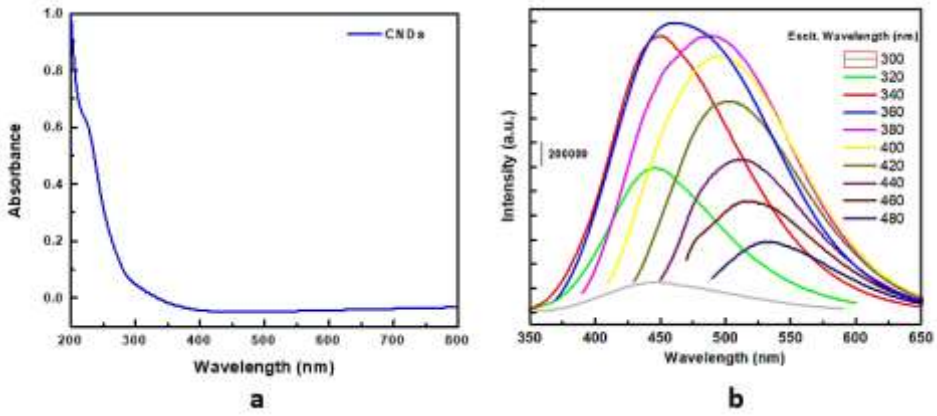


Figure 3: (a) UV-Vis Spectrum of CNDs, (b) Photoluminescence emission at different excitation wavelengths.

Furthermore, detailed photoluminescence (PL) measurement for CNDs (Figure 3(b)) was carried out at different excitation wavelengths. The fluorescence spectra of CNDs show a maximum emission at 460 nm (Ex.360 nm). The emission is excitation dependent, showing peak shifts from 440 to 540 nm while the excitation wavelength changes from 300 to 480 nm, this behavior is a well-known phenomenon of most carbon nanodots [34-36].

3.2 Photodegradation of Methylene Blue

The methylene blue solution showed a maximum UV-Vis absorption at 668 nm. To test whether CNDs will act as catalysts or photocatalysts, equal amounts (500µl) of CNDs (0.04 mg/ml) were spiked into M.B solutions, one of them was left in dark and the other was irradiated for 120 min. Every 10-15 minutes the UV-Vis absorption at 668 nm was recorded as shown in Figure 4(a) and the degradation efficiency was evaluated and plotted versus time (Figure 4(b)).

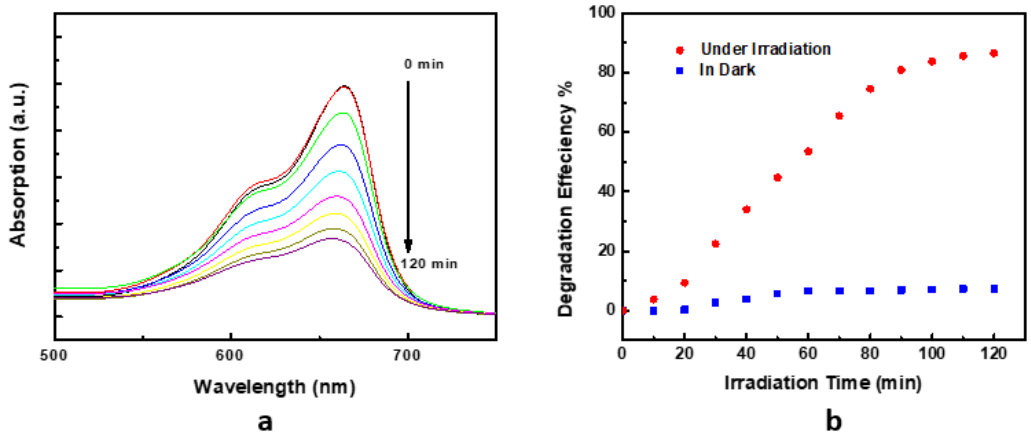


Figure 4: (a) UV-Vis absorption of M.B solution spiked with 500 µl of CNDs and irradiated by 50 W visible light for 120 minutes, (b) The degradation efficiency of M.B under light irradiation and in dark.

It is evident from figure 4(b) that CNDs behave as photocatalysts not as catalysts because they have worked only under irradiation without any significant effect on the concentration of M.B when the mixture remained in dark.

Several factors affect the degradation process (degradation efficiency and rate) of the Methylene blue as follows.

3.2.1 Effect of Dose of Photocatalyst on Degradation of M.B.

The degradation of methylene blue in the presence of different amounts of CNDs was investigated, the concentration of the CNDs (Dose) was changed. 0, 2.67, 4, 5.3, and 6.67 mg/L concentrations of CNDs in M.B solutions were irradiated for 120 minutes, the UV-Vis absorptions were recorded at 668 nm and the degradation efficiency at different time was estimated for each photocatalyst concentration and illustrated in Figure 5(a). As shown in the Figure the degradation efficiency at 120 min is increased from 27.4% in the absence of the photocatalyst up to 86.5% in the presence of CNDs with 6.67 mg/L. It is also obvious in Figure 5(b) the difference in M.B solution color in the presence and absence of CNDs. There was no degradation of the MB dye in the dark because it is a heterocyclic aromatic chemical compound that contains three combined aromatic rings with (C–S), (CN) and (CN = —) functional groups. Due to the complicated carbon-bonding in the MB structure, the adsorption reaction of CNDs and M.B molecules was difficult [20]. While the slow degradation of M.B in the absence of photocatalyst (27.4%) could be ascribed to the to the lone pairs that are located at nitrogen and sulfur atoms in the M.B structure. These are electron-rich regions, which became active once they were irradiated. They exhibited repulsion forces between bond pair electrons, leading to instability, and hence, they attacked the associated water molecules to form a stable bond [37].

The degradation efficiency was calculated according the following equation:

$$Degradation\ Effeciency\ (\%D) = \frac{A_0 - A}{A_0} \times 100\% \qquad (1)$$

Where A_0 the absorbance of M.B at time zero, A absorbance at time = t

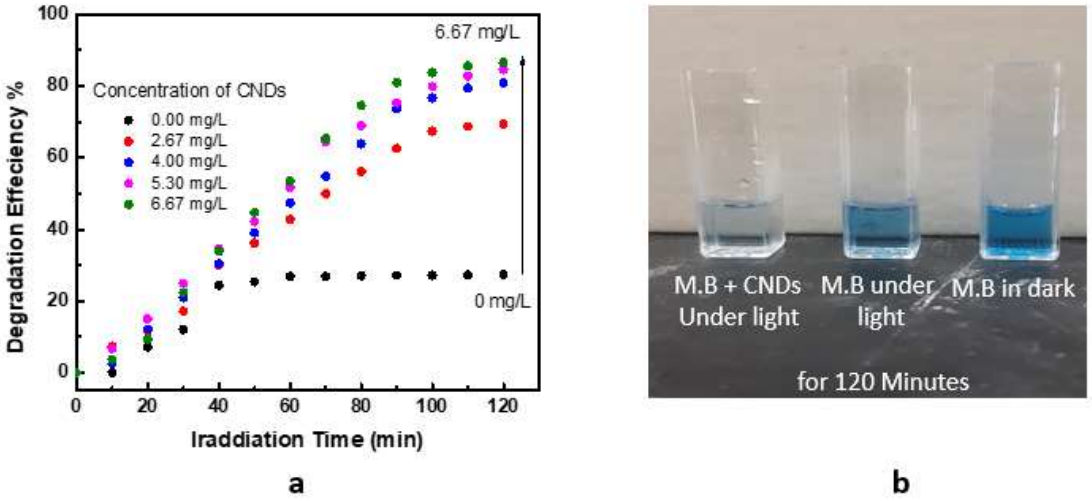


Figure 5: (a) Photodegradation rate of M.B at different concentration of CNDs (dose), (b) Degradation of M.B (color change) in dark and under irradiation in the absence of CNDs and under light irradiation in the presence of CNDs

Another important degradation parameter that should be estimated is the degradation rate. Herein, we have suggested Langmuir–Hinshelwood dynamic model [20], where the degradation kinetics of M.B could be simplified according to the pseudo first-order kinetic as shown in equation (2)

$$\ln\left(\frac{\mathrm{Co}}{\mathrm{C}}\right) = \mathrm{k} \times \mathrm{t} \qquad (2)$$

Where C_0 and C should be the equilibrium concentration of M.B and the concentration of M.B after irradiation time t, respectively. C_0 and C are equivalent to the absorbance of the dyes at time zero (A_0) and the absorbance of the dyes after degradation time t (A), respectively and k represents the dye degradation rate constant.

Therefore, a fitted plot of $ln(A_0/A)$ versus time leads to a straight line with a slope representing the degradation rate as in Figure 6 (a). The degradation rate for all doses (0 to 0.667 mg/L CNDs) was estimated and illustrated in Figure 6 (b)

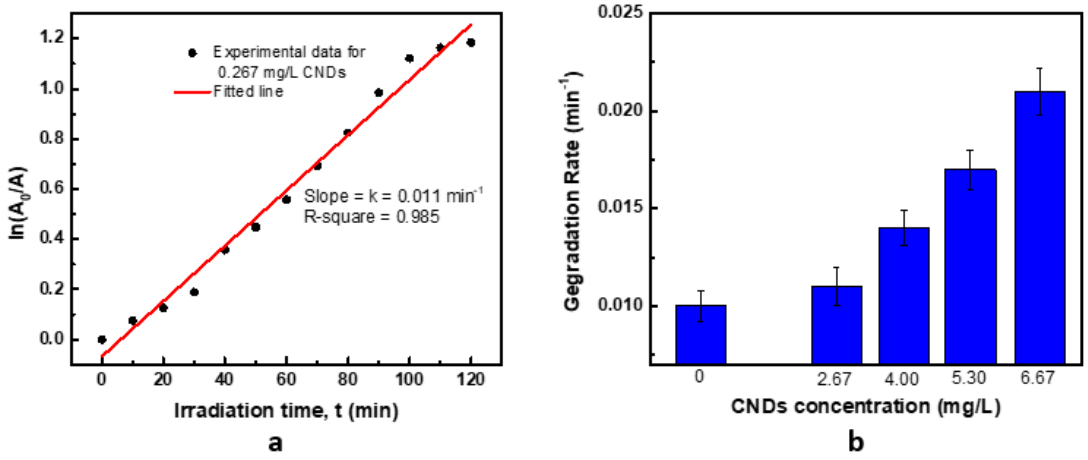


Figure 6: (a) Fitting of Langmuir–Hinshelwood dynamic model at 2.67 mg/L CNDs, (b) Degradation rate of M.B at different concentration of CNDs

Figure 6(b) shows clearly the effect of the photocatalyst dose (CNDs) on the degradation of M.B solution with an increase of about 150% in the degradation rate when the dose concentration increases from 2.67 to 6.67 mg/L. This significant increase could be ascribed to the increase in the active sites (photocatalyst) in the solution and the ability to convert rapidly the M.B into harmless products such as CO_2 and H_2O. Moreover, the degradation mechanism would be explained by Figure 7. When photons of appropriate energy excite CNDs, electrons were excited from the ground state (valence band) to excitation state (conduction band), generating excess electrons (e−) and holes (h+). Due to the rich presence of surface defects on CNDs, some of the excited carriers are trapped, and the recombination of e- and h+ are hindered. As a result, the methylene blue could be oxidized by the h+ directly to cause the degradation [38]. In the meantime, some of the e− could be captured by oxygen dissolved in the solution, forming super oxide radicals, some of the h+ could interact with surface-adsorbed H_2O to form hydroxyl radicals. Reactive oxygen species (ROS) , super oxide [39] and hydroxyl radical [38,40]are known to degrade organic dyes.

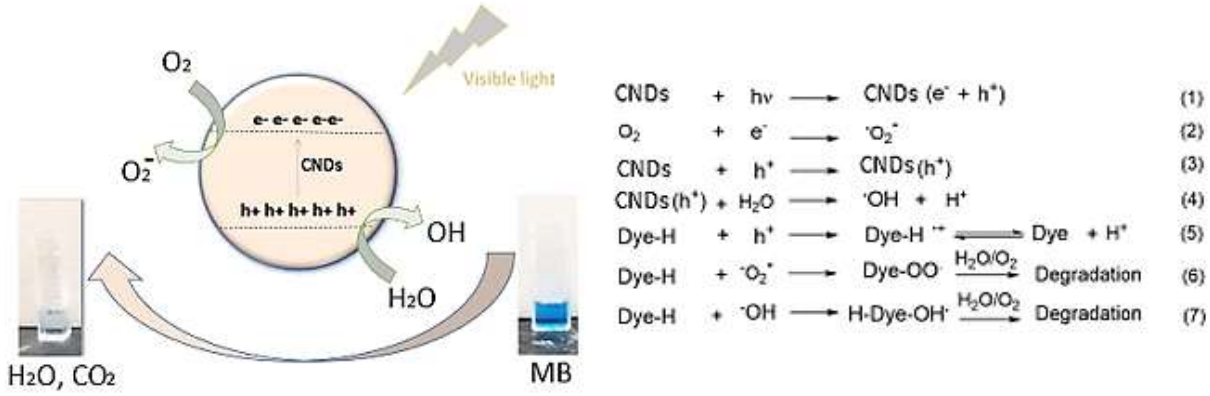


Figure 7: Mechanism of Methylene Blue Degradation

3.2.2 Effect of pH on Degradation of M.B

In general, pH was considered to be a critical role during the photocatalytic process. It impacts the surface charges of photocatalysts, electrostatic interactions between the pollutants and the photocatalysts, the formation of pollutant and the ionization states of M.B [41].

The degradation efficiency and rate of M.B were increased dramatically when the pH of the solution increased from 3.8 to 10.6, the degradation efficiency has been increased from about 64% to 92%, while the rate increased from 0.0012 to 0.061 min^{-1}. See Figure 8 (a) and (b). This could be ascribed to the increase in negativity (anionic) of CNDs, as Zeta-potential decreased from -18 eV at pH=3 (acid condition) to -32 eV on pH =7.4, this change in negativity could be related to increase in hydroxyl surface groups which in their turn act as surface traps causing more hindering of e- and h+ recombination [20].

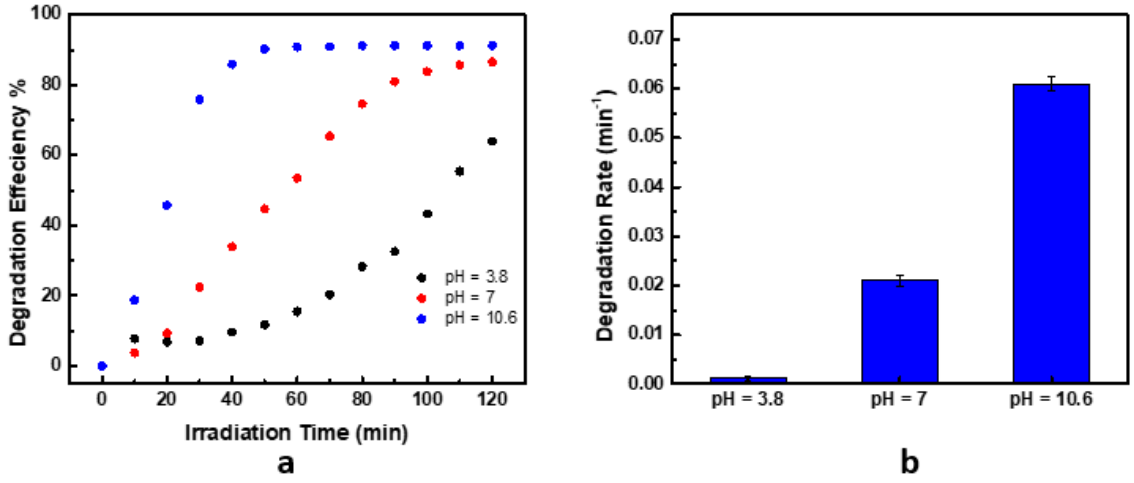


Figure 8: Effect of pH on the degradation of M.B. (a) Degradation efficiency, (b) Degradation rate

3.2.3 Effect of Salt on Photodegradation of M.B

Sodium chloride was added to the pollutant solution (M.B) to explore its influence on the degradation process. Figure 9 displays the degradation rate of M.B under four different concentrations of NaCl salt (0, 2, 4, and 8 mg/ml).

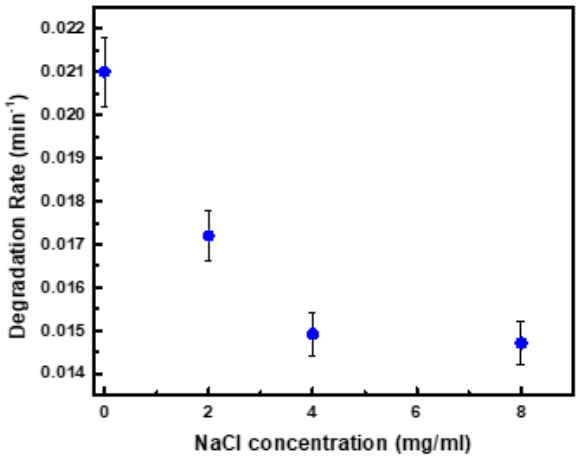


Figure 9: Degradation rate of M.B at different concentrations of NaCl

Figure 9 shows a decrease in degradation rate with increase in NaCl concentration, this could be related to that NaCl salt behaves as a suppressing agent impedes slightly the generation of e- and h+ after excitation from the ground state [19].

3.2.4 Effect of the distance of light source on M.B photodegradation

The distance of the light source from the pollutant was changed from 10 cm to 5 cm, this proximity causes an improvement in degradation efficiency and also a slight increase in degradation rate from 0.02067 to 0.02435 1/min (see Figure 10). The closeness of light results in much more incident photons onto CNDs surface, causing more or fast generation of holes and electrons upon excitation.

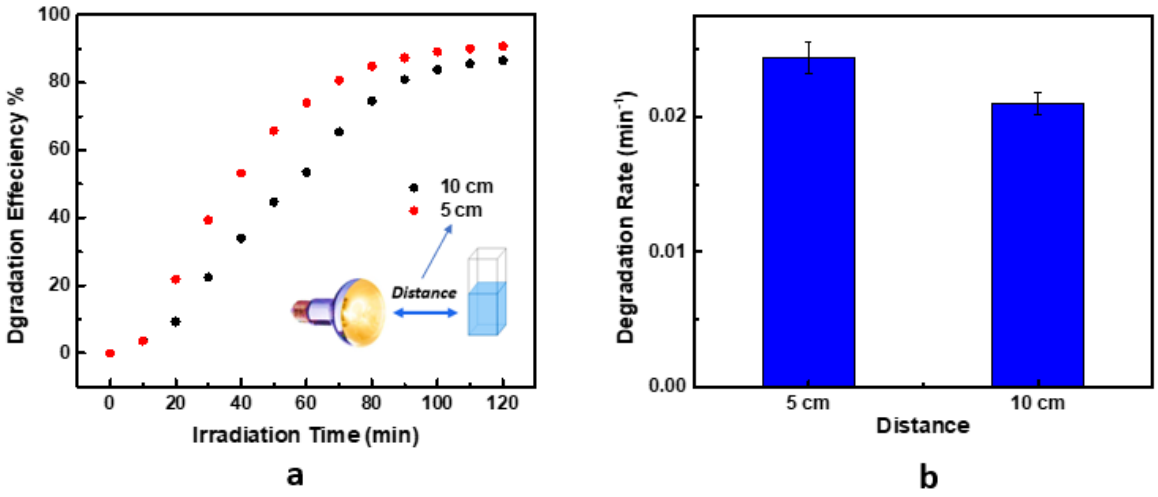


Figure 10: Effect of light source's distance on degradation efficiency and rate of M.B

3.2.5 Effect of the power of light source on M.B photodegradation

Photocatalytic phenomena rely on the energy supplied by light quanta. Electron–hole pairs are generated in the conduction band and valance band of a photocatalytic material when they receive photons with energy equal to or greater than its band gap [42]. Therefore, the light intensity plays a

critical role in photocatalytic dye removal. The visible yellow light with powers 50 and 10 watt were applied. Figure 11 shows the degradation efficiency at both powers. It is obvious that the power of 10 W is not sufficient to cause a significant degradation of M.B. due to very low number of emitted photons which leads to very low degradation efficiency and rate; 16% (@ 120 minutes and 0.0012 min^{-1} respectively.

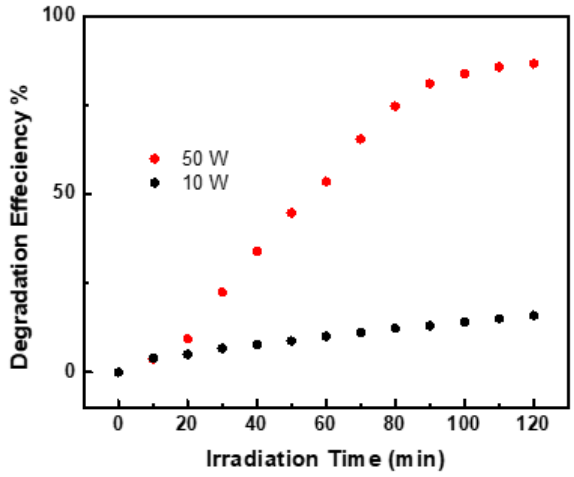


Figure 11: Degradation efficiency of M.B at different light source powers

3.2.6 Effect of the initial concentration of M.B on its biodegradation

Three concentrations of M.B (35, 23.33, 17.5) µM were spiked with same amounts of CNDs and irradiated for 120 minutes. Figure 12 illustrates the degradation efficiency and rate of M.B at these concentrations. The degradation efficiency remains nearly constant while the degradation rate decreased with increasing the concentration. Because photodegradation occurs due to light absorbed by CNDs, therefore, this decrease could be ascribed to that excessive M.B may hamper the reception of light onto the CNDs surface and delay or hinder the activation of the photocatalytic processes [43].

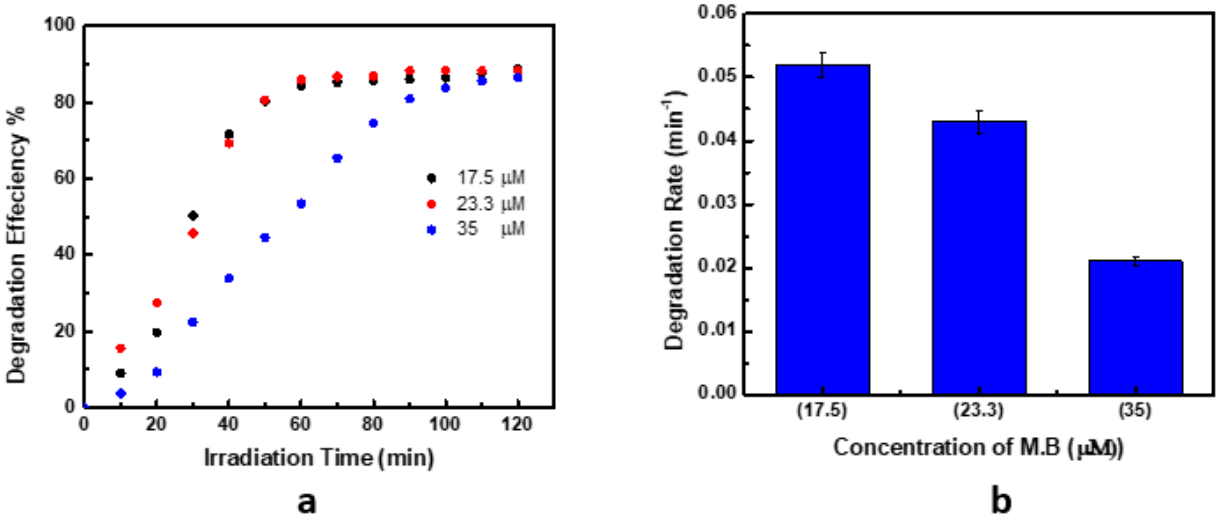


Figure 12: Degradation of different concentrations of M.B: (a) Degradation efficiency, (b) Degradation rate.

It is worthy to point that CNDs prepared in this work are shown to be very promising candidates for dye photodegradation, environment protection, and cleanliness. Synthesized CNDs have been compared with other works in terms of M.B photodegradation efficiency and rate showing excellent results. For instance, a degradation efficiency of 86-92%/120 min and a rate of 0.021 (pH = 7) and 0.061 min^{-1}(pH = 10.6) were obtained for a dose of carbon dots equal to 6.66 mg/L which could be considered attractive and important results of a photocatalyst when they compared to C-dots synthesized from citric acid, there, the photocatalyst resulted in degradation efficiency and rate of 99.9%/170 min and 0.024 min^{-1} respectively with a dose of 750 mg/L CNDs [44].

4. Conclusion

An efficient visible-light photocatalyst CNDs was facilely prepared by combination of bottom-up and top-down routes using pyrolysis and chemical oxidation methods. The synthesized CNDs was fluorescent with about 3 nm size. The photocatalytic activity of these dots was monitored through the degradation of methylene blue dye after irradiation of yellow visible light for 120 minutes. Degradation efficiency and rate were estimated for different conditions, finding that the dose of the photocatalyst (CNDs) in the dye solution had a great effect on both efficiency and rate with maximum efficiency and rate of 87% and 0.021 min^{-1} respectively when a dose of 6.67 mg/L was used. pH of the solution showed a significant enhancement of the photodegradation process, for instance, at pH = 10.6 the degradation rate was the highest value (0.061 min^{-1}) with an efficiency of 92% after 120 minutes. Moreover, it was concluded that an increase in salt content affects adversely the degradation rate and the same results were obtained in the case of increasing the pollutant concentration but with different decrease ratios. Finally, it was found that the power of the source and position with respect to the targeted pollutant have noticeable effect on the degradation process, an increase in degradation rate was obtained for high power and low distances.

Funding: "This research received no external funding"

Acknowledgment: Authors would like to thank prof. Prato's group at CIC biomaGUNE in Sansebastian-Spain and Prof. Valli's group at University of Salento- Italy for their technical help and support in conducting some analytical tests such the transmission electron microscope (TEM).

References

1. Xu X, Ray R, Gu Y *et al.* Electrophoretic Analysis and Purification of Fluorescent Single-Walled Carbon Nanotube Fragments. *Journal of the American Chemical Society*, (2004), 126(40), 12736-12737.
2. Cheng Y, Bai M, Su J *et al.* Synthesis of fluorescent carbon quantum dots from aqua mesophase pitch and their photocatalytic degradation activity of organic dyes. *Journal of Materials Science & Technology*, (2019), 35(8), 1515-1522.
3. Yadav A, Bai L, Yang Y *et al.* Lasing behavior of surface functionalized carbon quantum dot/RhB composites. *Nanoscale*, (2017), 9(16), 5049-5054.
4. Das R, Bandyopadhyay R, Pramanik P. Carbon quantum dots from natural resource: A review. *Materials Today Chemistry*, (2018), 8, 96-109.

5. Namdari P, Negahdari B, Eatemadi A. Synthesis, properties and biomedical applications of carbon-based quantum dots: An updated review. *Biomedicine & Pharmacotherapy*, (2017), 87, 209-222.
6. Di J, Xia J, Ge Y *et al.* Novel visible-light-driven CQDs/Bi2WO6 hybrid materials with enhanced photocatalytic activity toward organic pollutants degradation and mechanism insight. *Applied Catalysis B: Environmental*, (2015), 168-169, 51-61.
7. Zhang X, Jiang M, Niu N *et al.* Natural-Product-Derived Carbon Dots: From Natural Products to Functional Materials. *ChemSusChem*, (2018), 11(1), 11-24.
8. Miao P, Han K, Tang Y, Wang B, Lin T, Cheng W. Recent advances in carbon nanodots: synthesis, properties and biomedical applications. *Nanoscale*, (2015), 7(5), 1586-1595.
9. Dey S, Govindaraj A, Biswas K, Rao CNR. Luminescence properties of boron and nitrogen doped graphene quantum dots prepared from arc-discharge-generated doped graphene samples. *Chemical Physics Letters*, (2014), 595-596, 203-208.
10. Cao L, Wang X, Meziani MJ *et al.* Carbon Dots for Multiphoton Bioimaging. *Journal of the American Chemical Society*, (2007), 129(37), 11318-11319.
11. Li H, Kang Z, Liu Y, Lee S-T. Carbon nanodots: synthesis, properties and applications. *Journal of Materials Chemistry*, (2012), 22(46), 24230-24253.
12. Sahu S, Behera B, Maiti TK, Mohapatra S. Simple one-step synthesis of highly luminescent carbon dots from orange juice: application as excellent bio-imaging agents. *Chemical Communications*, (2012), 48(70), 8835-8837.
13. Rani UA, Ng LY, Ng CY, Mahmoudi E. A review of carbon quantum dots and their applications in wastewater treatment. *Advances in Colloid and Interface Science*, (2020), 278, 102124.
14. Rani UA, Ng LY, Ng CY, Mahmoudi E, Ng Y-S, Mohammad AW. Sustainable production of nitrogen-doped carbon quantum dots for photocatalytic degradation of methylene blue and malachite green. *Journal of Water Process Engineering*, (2021), 40, 101816.
15. Zhou C, Zeng G, Huang D *et al.* Distorted polymeric carbon nitride via carriers transfer bridges with superior photocatalytic activity for organic pollutants oxidation and hydrogen production under visible light. *Journal of Hazardous Materials*, (2020), 386, 121947.
16. Abd Rani U, Ng LY, Ng CY, Mahmoudi E, Ng Y-S, Mohammad AW. Sustainable production of nitrogen-doped carbon quantum dots for photocatalytic degradation of methylene blue and malachite green. *Journal of Water Process Engineering*, (2021), 40, 101816.
17. Lu Q, Zhang Y, Liu S. Graphene quantum dots enhanced photocatalytic activity of zinc porphyrin toward the degradation of methylene blue under visible-light irradiation. *Journal of Materials Chemistry A*, (2015), 3(16), 8552-8558.
18. Wang F, Wu Y, Wang Y *et al.* Construction of novel Z-scheme nitrogen-doped carbon dots/{0 0 1} TiO2 nanosheet photocatalysts for broad-spectrum-driven diclofenac degradation: Mechanism insight, products and effects of natural water matrices. *Chemical Engineering Journal*, (2019), 356, 857-868.
19. Yu H, Huang J, Jiang L *et al.* Enhanced photocatalytic tetracycline degradation using N-CQDs/OV-BiOBr composites: Unraveling the complementary effects between N-CQDs and oxygen vacancy. *Chemical Engineering Journal*, (2020), 402, 126187.

20. Jiang R, Lu G, Yan Z, Wu D, Zhou R, Bao X. Insights into a CQD-SnNb2O6/BiOCl Z-scheme system for the degradation of benzocaine: Influence factors, intermediate toxicity and photocatalytic mechanism. *Chemical Engineering Journal*, (2019), 374, 79-90.
21. Desa AL, Hairom NHH, Ng LY, Ng CY, Ahmad MK, Mohammad AW. Industrial textile wastewater treatment via membrane photocatalytic reactor (MPR) in the presence of ZnO-PEG nanoparticles and tight ultrafiltration. *Journal of Water Process Engineering*, (2019), 31, 100872.
22. Ong CB, Mohammad AW, Ng LY. Integrated adsorption-solar photocatalytic membrane reactor for degradation of hazardous Congo red using Fe-doped ZnO and Fe-doped ZnO/rGO nanocomposites. *Environmental Science and Pollution Research*, (2019), 26(33), 33856-33869.
23. Abdulla NK, Siddiqui SI, Tara N, Hashmi AA, Chaudhry SA. Psidium guajava leave-based magnetic nanocomposite γ-Fe2O3@GL: A green technology for methylene blue removal from water. *Journal of Environmental Chemical Engineering*, (2019), 7(6), 103423.
24. Üner O. Hydrogen storage capacity and methylene blue adsorption performance of activated carbon produced from Arundo donax. *Materials Chemistry and Physics*, (2019), 237, 121858.
25. Sawalha S, Silvestri A, Criado A, Bettini S, Prato M, Valli L. Tailoring the sensing abilities of carbon nanodots obtained from olive solid wastes. *Carbon*, (2020), 167, 696-708.
26. Liu QR, Zhang JJ, He H *et al.* Green Preparation of High Yield Fluorescent Graphene Quantum Dots from Coal-Tar-Pitch by Mild Oxidation. *Nanomaterials-Basel*, (2018), 8(10), 844-854
27. Das P, Bose M, Ganguly S *et al.* Green approach to photoluminescent carbon dots for imaging of gram-negative bacteria Escherichia coli. *Nanotechnology*, (2017), 28(19), 195501-1955014
28. Radhakrishnan K, Panneerselvam P, Marieeswaran M. A green synthetic route for the surface-passivation of carbon dots as an effective multifunctional fluorescent sensor for the recognition and detection of toxic metal ions from aqueous solution. *Anal Methods-Uk*, (2019), 11(4), 490-506.
29. Bandi R, Gangapuram BR, Dadigala R, Eslavath R, Singh SS, Guttena V. Facile and green synthesis of fluorescent carbon dots from onion waste and their potential applications as sensor and multicolour imaging agents. *Rsc Adv*, (2016), 6(34), 28633-28639.
30. Bettini S, Sawalha S, Carbone L, Giancane G, Prato M, Valli L. Carbon nanodot-based heterostructures for improving the charge separation and the photocurrent generation. *Nanoscale*, (2019), 11(15), 7414-7423.
31. Patidar R, Rebary B, Sanghani DA, Bhadu GR, Paul P. Fluorescent carbon nanoparticles obtained from charcoal via green methods and their application for sensing Fe3+ in an aqueous medium. *Luminescence*, (2017), 32(8), 1466-1472.
32. Xue MY, Zhan ZH, Zou MB, Zhang LL, Zhao SL. Green synthesis of stable and biocompatible fluorescent carbon dots from peanut shells for multicolor living cell imaging. *New J Chem*, (2016), 40(2), 1698-1703.
33. Ghosh S, Satapathy SS, Ghosh K, Jauhari S, Panda SK, Si S. Carbon Dots Assisted Synthesis of Gold Nanoparticles and Their Catalytic Activity in 4-Nitrophenol Reduction. *Chemistryselect*, (2019), 4(12), 3416-3422.
34. Zhu SJ, Song YB, Zhao XH, Shao JR, Zhang JH, Yang B. The photoluminescence mechanism in carbon dots (graphene quantum dots, carbon nanodots, and polymer dots): current state and future perspective. *Nano Res*, (2015), 8(2), 355-381.

35. Arcudi F, Dordevic L, Prato M. Synthesis, Separation, and Characterization of Small and Highly Fluorescent Nitrogen-Doped Carbon NanoDots. *Angew Chem Int Edit*, (2016), 55(6), 2107-2112.
36. Sharma A, Gadly T, Gupta A, Ballal A, Ghosh SK, Kumbhakar M. Origin of Excitation Dependent Fluorescence in Carbon Nanodots. *J Phys Chem Lett*, (2016), 7(18), 3695-3702.
37. Ok KM, Ohishi Y, Mitazono Y, Muta H, Kurosaki K, Yamanaka S. Bi-doped lanthanum molybdate: Enhancing the anharmonicity and reducing the thermal conductivity using Bi3+ with lone pair electrons. *Ceramics International*, (2018), 44(13), 15833-15838.
38. Das GS, Shim JP, Bhatnagar A, Tripathi KM, Kim T. Biomass-derived carbon quantum dots for visible-light-induced photocatalysis and label-free detection of Fe (III) and ascorbic acid. *Scientific reports*, (2019), 9(1), 1-9.
39. Zhou Y, Zahran EM, Quiroga BA *et al.* Size-dependent photocatalytic activity of carbon dots with surface-state determined photoluminescence. *Applied Catalysis B: Environmental*, (2019), 248, 157-166.
40. Hu S, Tian R, Dong Y, Yang J, Liu J, Chang Q. Modulation and effects of surface groups on photoluminescence and photocatalytic activity of carbon dots. *Nanoscale*, (2013), 5(23), 11665-11671.
41. Lin X, Liu C, Wang J, Yang S, Shi J, Hong Y. Graphitic carbon nitride quantum dots and nitrogen-doped carbon quantum dots co-decorated with BiVO4 microspheres: A ternary heterostructure photocatalyst for water purification. *Separation and Purification Technology*, (2019), 226, 117-127.
42. Anwer H, Mahmood A, Lee J, Kim K-H, Park J-W, Yip ACK. Photocatalysts for degradation of dyes in industrial effluents: Opportunities and challenges. *Nano Research*, (2019), 12(5), 955-972.
43. Chen J, Shu J, Anqi Z, Juyuan H, Yan Z, Chen J. Synthesis of carbon quantum dots/TiO2 nanocomposite for photo-degradation of Rhodamine B and cefradine. *Diamond and Related Materials*, (2016), 70, 137-144.
44. Peng Z, Zhou Y, Ji C *et al.* Facile Synthesis of "Boron-Doped" Carbon Dots and Their Application in Visible-Light-Driven Photocatalytic Degradation of Organic Dyes. *Nanomaterials (Basel)*, (2020), 10(8), 1560.

Recovery of Glass Fibers from End-of-Life Wind Turbine Fiber Composite Wastes Through Pyrolysis Process

Salman Raza Naqvi [1,*], Imtiaz Ali [2], Wasif Farooq [3]

[1] School of Chemical & Materials Engineering, National University of Sciences & Technology, H-12, Islamabad, Pakistan

[2] Department of Chemical and Materials Engineering, King Abdulaziz University, Rabigh, Saudi Arabia

[3] Department of Chemical Engineering, King Fahd University of Petroleum and Minerals (KFUPM), Dhahran 31261, Saudi Arabia

** Corresponding author: (salman.raza@scme.nust.edu.pk).*

Abstract: It is expected that in 2050 more than 43 million tonnes of wind turbine blades waste which originated from Glass Fiber Reinforced Polymers (GFRP) have to be processed in a circular economy. Pyrolysis is identified as suitable alternative for materials and energy recovery and should be demonstrated comprehensively for composites. This research focuses on finding the mildest possible pyrolysis process conditions to obtain a clean fiber using a batch reactor. The decomposition behavior of powdered GFRP is investigated in both nitrogen and air atmosphere using thermogravimetric analysis (TGA). Optical and SEM pictures are shown to demonstrate the morphology of the recovered fibers. The TGA results showed a decomposition of epoxy above 250 °C and a residual mass of 70%. Pyrolysis test in a N_2 atmosphere in a tunnel oven showed that a minimum pyrolysis temperature of 425 °C is required and that the temperature in an air atmosphere should be at 475 °C for 15 minutes to recover the clean fibers.

Keywords : Recovery; Glass fibers; Epoxy; wind turbine blades; composites; pyrolysis

1. Introduction

Currently, in Europe, waste management & prevention of industrial composite scraps and its re-use for new materials production in a circular economy has gained much attention [1]. Fiber Reinforced Polymers (FRP) are mainly composed out of glass fiber (GFRP) or carbon fiber (CFRP) in combination with a matrix of polyester, phenol resin or epoxy resin [2]. Their properties make FRPs very suitable for usage in a variety of sectors like transportation, construction and energy industry. It is expected that in 2050, there will be a worldwide amount of 43 million tonnes of GFRP waste from wind turbine blades [3]. The least desirable option to handle this waste is landfilling [4]. Therefore, an appropriate way should be found to dispose of the waste in a circular economy.

The three main options; mechanical, chemical or thermal recycling are identified in literature for recycling of fibers [5]. Among others, thermal recycling appeared as promising method to perform the decomposition of the polymer at lower temperatures and maintain the fiber strength [6-8]. In pyrolysis process, firstly, sample is heated in a flow of nitrogen gas. This prevents oxidation and allows non-solid reaction products to be taken away. After this first phase, solid carbon is left on the surface of fibers. This carbon, sometimes called char, is then removed during post-pyrolysis. A heated airflow allows for oxidation of the carbon and removal of gaseous products, leaving clean fibers in the oven.

Naqvi et al. addressed the research gap in the optimized process parameters of both pyrolysis and post-pyrolysis process [9]. Besides, López et al. showed that the strength of glass fibers reduced significantly with the increase of pyrolysis temperature [10]. In view of these challenges, this research aims to find the mildest conditions of thermal treatment that gives clean fibers as a product. In this way the quality of the recovered fibers can be guaranteed the best and on top of that, the least amount of energy is needed to run the process.

In literature it was found that pyrolysis has been tested at temperatures of 500 ^{o}C or higher [11-14]. Others included lower temperatures as well, but they were mainly interested in the composition of pyrolysis products [15, 16] and the kinetics of occurring reactions [17] or mechanical properties of recovered fibers [18, 19].

The pyrolysis temperature is a key parameter for the mechanical strength of the recovered glass fibers. The higher the temperature the higher the loss in mechanical strength. At pyrolysis temperature of 500 °C the reduction in mechanical strength could be 50% [20, 21]. So lower temperature are preferred.

As per author information, there is less work done on the investigation of suitable and mildest temperature and residence time during pyrolysis and post-pyrolysis process. Cunliffe and Williams used 450 °C to burn of char, which was the lowest temperature found, but no variation of temperature was tested [3]. Giorgini et al. concluded that 50 min at 500 ^{o}C or 20 min at 600 ^{o}C was sufficient to achieve clean fibers [6]. This was for large parts of GFRP made of polyester, whereas this research uses lab scale epoxy samples.

The structure of this research paper is illustrated in the *Figure 1*. The effect of temperature and residence time is studied on pyrolysis of GFRP. Once conditions are determined at which pyrolysis is complete, the same is done for post-pyrolysis. Again, temperature and residence time are investigated. The goal is to recover glass fibers with a clean surface, comparable to the surface of a virgin fiber, at the mildest conditions possible.

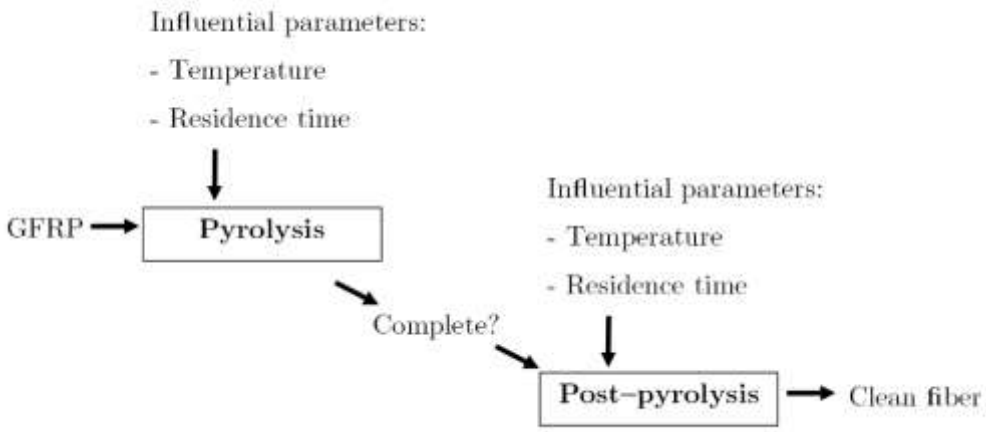


Figure 1: Schematic overview of the structure of the research.

2. Materials and methods

2.1 Sample description

GFRP, originating from the blade of a wind-turbine, a sandwich structure of polymeric foam with panels of fiberglass in a matrix of epoxy, is cut into pieces of 23 by 30 by 150 mm using a diamond cutter. Fig. 4 shows an image of an untreated sample.

2.2 Thermogravimetric analysis

To investigate the decomposition behavior of GFRP in nitrogen and air atmosphere, the thermo-gravimetric analysis (TGA) & differential thermogravimetric (DTG), TA instruments TGA550 is used. The sample is heated from room temperature up to 900 ^{o}C at various heating rates of 5, 10, 20 and 40 ^{o}C min^{-1} to exploit their decomposition behavior in slow pyrolysis regime.

2.3 Pyrolysis setup

In this study, a step batch pyrolysis reactor is used in this study and the schematic diagram is depicted in *Figure 2*. In the diagram, two manual valves are shown used for the connection of nitrogen and oxygen respectively. The furnace with an electric heater that is controlled by a thermostat follows. A fume extractor and a stream for tar come out of the oven. The oven itself is cylindrical with an inner diameter of 40 mm and a length of 600 mm. The outer diameter is 240 mm and includes the heating system and isolation. To investigate the effect of temperature on pyrolysis, the conditions were chosen as presented in the Table 1. In the first series, the temperature is raised from 350 °C to 450 °C by keeping the fixed residence time of 30 min in pyrolysis process. After achieving a desired

mild temperature, 425 °C, the impact of residence time (0, 15 and 30 min) is investigated (second series). For char oxidation, in third series, the pyrolyzed sample at the temperature of 425°C for 30 min is tested at (400, 450, 475 and 500 °) at a residence time of 30 min. The temperature of 475°C at a residence time 30 min is appeared to be the mildest condition to clean the fibers. In the fourth series, the optimum residence time (0, 15 and 30 min) at the temperature of 475 °C is investigated. Through these four series, a suitable mildest pyrolysis and post-pyrolysis operating conditions is achieved. When a residence time is mentioned, it is referred to the isothermal dwell time. Heating up (10 min) and cooling down time (300 min) of the oven are not included in this residence time. Due to the design of the oven, a sample could not be placed after heating, or removed before cooling the oven. The variation of temperature in the oven is ±10 °C. So a residence time of 0 minutes means that the sample is only heated and immediately cooled down again.

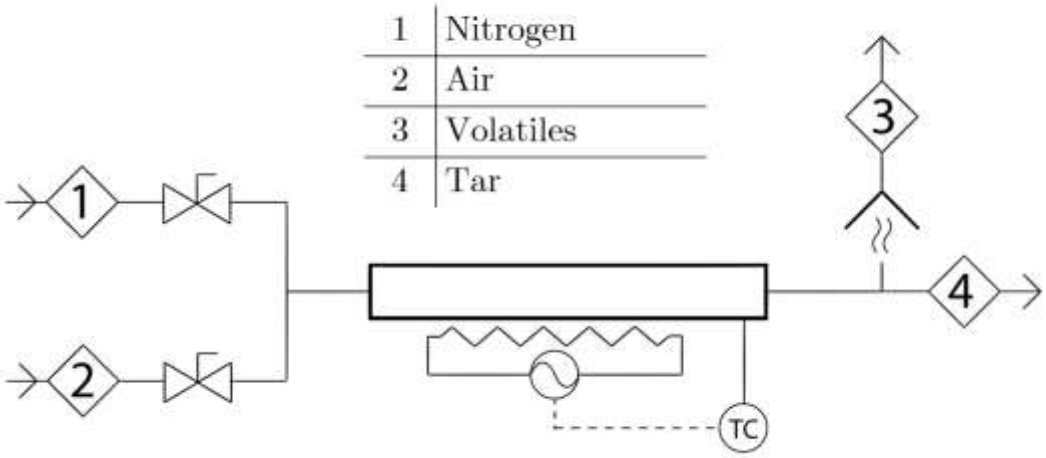


Figure 2: Schematic diagram of the pyrolysis setup.

Table 1: Reaction conditions used to test different effects.

Pyrolysis (N_2)		**Post-pyrolysis (air)**	
Temperature (ºC)	Time (min)	Temperature (ºC)	Time (min)
Effect of temperature on pyrolysis			
350	30	-	-
400	30	-	-
425	30	-	-
450	30	-	-

Effect of residence time on pyrolysis			
425	0	-	-
425	15	-	-
425	30	-	-
Effect of temperature on post-pyrolysis			
425	30	400	30
425	30	450	30
425	30	475	30
425	30	500	30
Effect of residence time on post-pyrolysis			
425	0	475	0
425	0	475	15
425	0	475	30

2.4 Scanning Electron Microscope

The samples that are produced in the oven are processed for morphological analysis in a table top scanning electron microscope (SEM). SEM pictures are made using a NeoScope JCM-5000 with a magnification of 800 times and the accelerate voltage set to 15 kV using a high vacuum.

3. Results and discussion

3.1 Thermo-gravimetric analysis

The thermogravimetric & differential thermogravimetric analysis curves of GFRP in nitrogen (A & C) and air (B & D) atmosphere are depicted in Figure 3. The thermo-gravimetric analysis in nitrogen shows that the thermal decomposition of the polymer starts at 250 ^{o}C and the reduce in mass slows down at 370 ^{o}C (DTG curves). The material hasn't reached its final mass yet, this will only happen at much higher temperature, close to 900 ^{o}C. After that temperature, an amount of about 70% of the initial mass is left. This is expected to be because of the high percentage of inorganic material in GFRP. From the DTG it can be seen that the major mass loss rate is at 320 ^{o}C. Secondary reploymerization reactions among the polymer derived products are responsible for char formation. TG curves of GFRP at various heating rates is compared in Figure 3 (A). For all heating rates, GFRP seems exhibit one main step of decomposition. However, the residual mass obtained at higher heating rates is slightly lower at higher heating rates which suggests competitive reactions.

In comparison of nitrogen atmosphere, TGA & DTG curves of GFRP in air is shown in Figure 3 (B & D). The first phase (dehydration) temperature peak occurred at around 220 °C. The second phase of degradation temperature peak appeared between 260 °C and 395 °C. According to literature the polymer decomposed in the temperature range from 255 °C to 430 °C [17, 19]. The third phase (decomposition of char) occurred at temperature range of 450 – 550 °C. Different compared to nitrogen conditions is the speed at which mass is lost. At 550 °C there is no significant mass loss observed. The total mass loss over the temperature interval 25 – 900 °C is 33 wt.%.

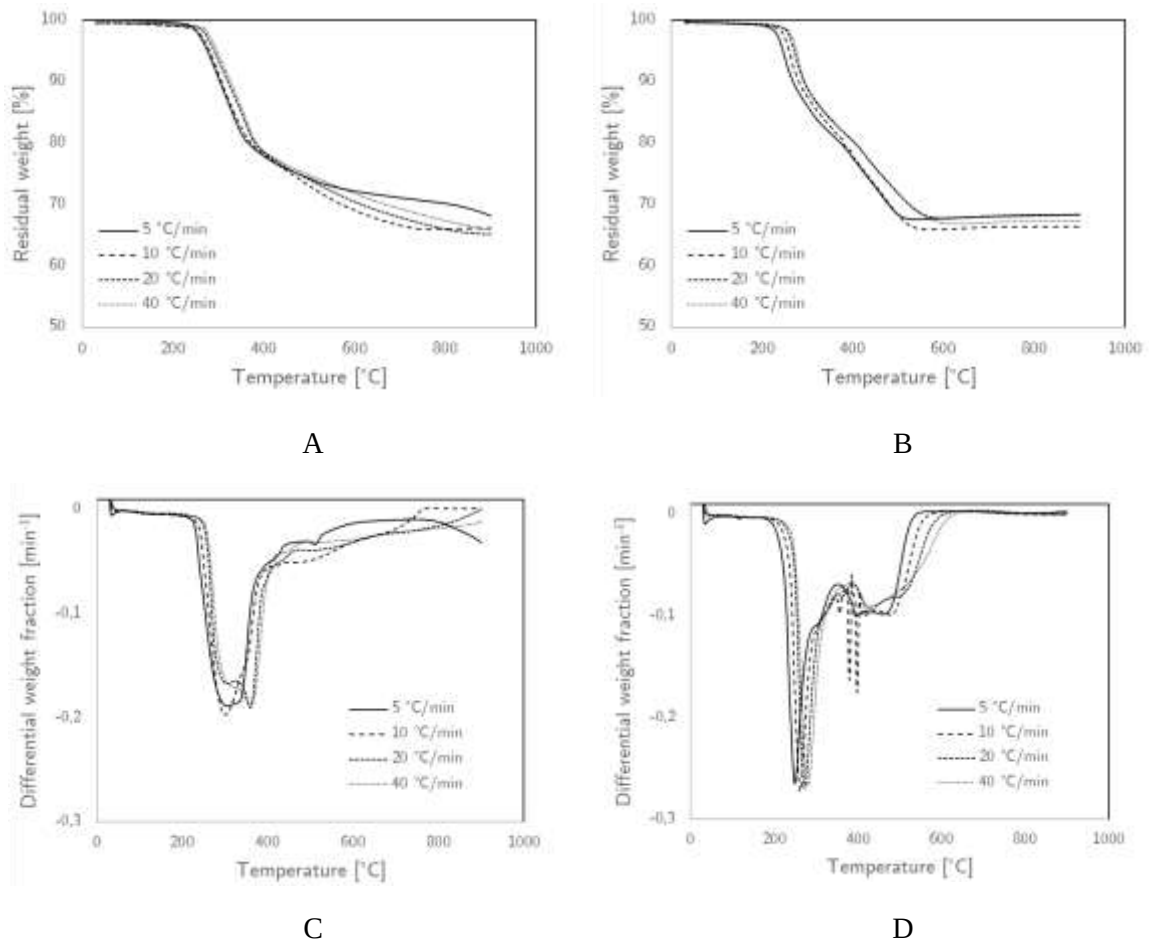


Figure 3: Top: TG curve of GFRP in nitrogen (A) and air (B). Bottom: DTG curve of GFRP in nitrogen (C) and air (D).

3.2 Pyrolysis and post-pyrolysis

During pyrolysis, the products are formed in three phases: gaseous volatiles and condensable, liquid oil and tar and solid char and remaining fibers. For post-pyrolysis process, there is no visible smoke and/or tar production. Given the reduce in weight and color change of samples during this stage of the process, it is expected that invisible gases are created. No analysis is done on the non-solid products, only the remainder of the sample that stayed in the oven is considered. This remainder is mostly a slab of black, stiff glass fiber, and in few cases a bit of the foam still present.

In Figure 4, pictures of the experimental results to the investigation of the effect of temperature and residence time in pyrolysis and post-pyrolysis are presented. Based on a visual inspection, 425 ^{o}C was chosen to be sufficiently clean to be used in post-pyrolysis. There is a significant amount of black residue at 400 ^{o}C, which wasn't present at any higher temperature. With the naked eye, not much difference could be detected between the results to investigate the effect of residence time during pyrolysis. At 450 ^{o}C or below, dark spots remain on the surface of the fiber after post-pyrolysis. This is an indication that not all carbon has been burnt off. A small difference is observed between the sample reacted at 475 ^{o}C and at 500 ^{o}C. Namely that the first had fibers connected in bundles (which could be easily taken apart) whereas the second had unconnected individual fibers. Using this information, 475 ^{o}C is used in the further experiments to investigate the effect of residence time on post-pyrolysis.

Without any isothermal dwell time, 450 ^{o}C is not sufficient to obtain white and clean fibers. On the other hand, at this temperature, residence time of 30 min is also not long enough. The sample is than treated at the temperature of 475 °C by three various residence times. According to visual inspection, the sample at 475 °C for 15 min provide clean fibers.

The results showed a significant impact of pyrolysis and post-pyrolysis operating parameters (temperature and residence time) on recovery of GFRP. The pyrolyzed sample at 425 °C for 0 min (step 1) and post-pyrolysis process at 475 °C for 15 min (step 2) are optimum operating conditions for recovery of GFRP in a batch reactor.

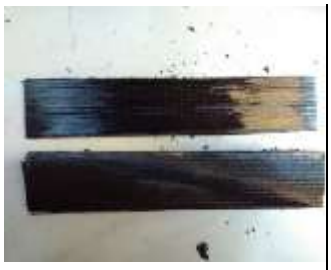
		
Incomplete pyrolysis: P: 350 °C, 30 min	Complete pyrolysis: P: 425 °C, 0 min	Incomplete post-pyrolysis: P: 450 °C, 30 min PP: 400 °C, 30 min
		
Almost complete post-pyrolysis: P: 425 °C, 30 min PP: 450 °C, 30 min	Complete post-pyrolysis: P: 425 °C, 0 min PP: 475 °C, 15 min	Untreated sample

Figure 4: Pictures of sample treated at various pyrolysis conditions.

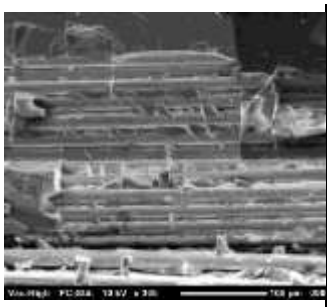
3.3 Scanning Electron Microscope

Figure 5 shows the SEM images of the samples produced at pyrolysis and post-pyrolysis process. The SEM image of virgin glass fiber is also added in the figure (right bottom) to compare the recovered fiber from the experimentation.

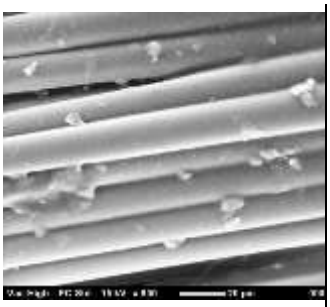
For the effect of temperature on pyrolysis, a clear improvement on the amount of leftover char can be seen. At 350 °C, the sample is not completely decomposed which is clearly visible in Figure 5. The pyrolysis process is completed at 425 and 450 °C and produced char is found on the SEM image. However the pyrolysis temperature of 425 °C for 0 min seems to be mild condition in which polymer is completed decomposed into volatiles and gases and char is produced. The effect of residence time on pyrolysis is not as clear as the effect of temperature. From the SEM picture, no proof can be found that an increase in residence time results in less char.

With the increase of temperature during post-pyrolysis (400 – 500 °C), a significant improvement in surface cleaning is observed through char oxidation. The fiber recovered in second step at 475 °C

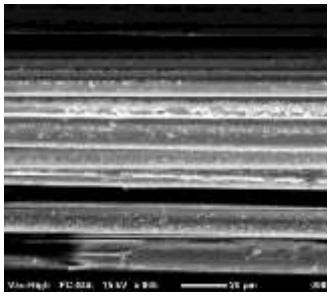
for 15 min provide white, clean and char less. According to these results, it can concluded that temperature and residence time have vital impact on post-pyrolysis process. The mild conditions of the post-pyrolysis are : treatment temperature 475 °C and 15 min.



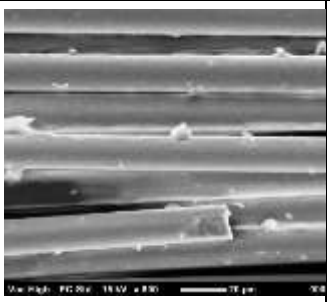
Incomplete pyrolysis:
P: 350 °C, 30 min



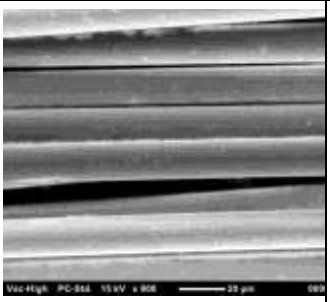
Complete pyrolysis:
P: 425 °C, 0 min



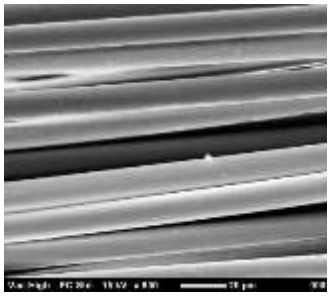
Incomplete post-pyrolysis:
P: 450 °C, 30 min
PP: 400 °C, 30 min



Almost complete post-pyrolysis:
P: 425 °C, 30 min
PP: 450 °C, 30 min



Complete post-pyrolysis:
P: 425 °C, 0 min
PP: 475 °C, 15 min



Virgin fiber

Figure 5: SEM pictures of different stadia of pyrolysis.

4. Conclusions

This study aims to achieve the mildest conditions to pyrolyze GFRP in order to recover clean glass fibers and to keeo the maximum strength of the recovered fibers. TGA analysis shows that the major decomposition temperature of epoxy between 250 °C and 370 °C in nitrogen atmosphere. Using air, the char oxidation is observed in a temperature range of 450 – 550 °C. The pyrolysis experiments showed that a white (clean) fiber is obtained with pyrolysis at 425 °C for 0 min (only heating up and cooling down) and post-pyrolysis at temperatures of at least 475 °C. Residence time has only a secondary influence for pyrolysis. The minimal time needed for post-pyrolysis is 15 min. The SEM pictures support the optical observations. With pyrolysis, an increase in temperature showed a

significant impact leading to a cleaner fiber. Also during post-pyrolysis, the temperature and residence time are key parameters to get clean fibers without residue.

Acknowledgment : This work is funded by Science Based Engineering Program of the University of Twente, Netherlands.

References

1. Bartl, A., *Moving from recycling to waste prevention: A review of barriers and enables.* Waste Management & Research, 2014. **32**(9_suppl): p. 3-18.
2. Senophiyah-Mary, J., R. Loganath, and T. Meenambal, *A novel method for the removal of epoxy coating from waste printed circuit board.* Waste Management & Research. **0**(0): p. 0734242X18782392.
3. Cunliffe, A.M., N. Jones, and P.T. Williams, *Recycling of fibre-reinforced polymeric waste by pyrolysis: thermo-gravimetric and bench-scale investigations.* Journal of Analytical and Applied Pyrolysis, 2003. **70**(2): p. 315-338.
4. Cunliffe, A.M. and P.T. Williams, *Characterisation of products from the recycling of glass fibre reinforced polyester waste by pyrolysis☆.* Fuel, 2003. **82**(18): p. 2223-2230.
5. Awasthi, A.K., et al., *Evaluating waste printed circuit boards recycling: Opportunities and challenges, a mini review.* Waste Management & Research, 2017. **35**(4): p. 346-356.
6. Giorgini, L., et al., *Pyrolysis of fiberglass/polyester composites: Recovery and characterization of obtained products.* FME Transactions, 2016. **44**(4): p. 405-414.
7. Grause, G., et al., *Recovery of glass fibers from glass fiber reinforced plastics by pyrolysis.* Journal of Material Cycles and Waste Management, 2013. **15**(2): p. 122-128.
8. Ma, H., G. Yang, and S. Hao, *Pyrolysis characteristics and recovery of the metallic and nonmetallic materials in wasted printed circuit boards*, in *Advanced Materials Research*. 2012. p. 2107-2111.
9. Naqvi, S.R., et al., *A critical review on recycling of end-of-life carbon fibre/glass fibre reinforced composites waste using pyrolysis towards a circular economy*. Resources, Conservation and Recycling, 2018. **136**: p. 118-129.
10. López, F.A., et al., *Thermolysis of fibreglass polyester composite and reutilisation of the glass fibre residue to obtain a glass–ceramic material.* Journal of Analytical and Applied Pyrolysis, 2012. **93**: p. 104-112.
11. Feih, S., et al., *Mechanical properties of thermally-treated and recycled glass fibres.* Composites Part B: Engineering, 2011. **42**(3): p. 350-358.
12. Meyer, L.O., K. Schulte, and E. Grove-Nielsen, *CFRP-recycling following a pyrolysis route: Process optimization and potentials.* Journal of Composite Materials, 2009. **43**(9): p. 1121-1132.

13. Onwudili, J.A., et al., *Recovery of glass fibre and carbon fibres from reinforced thermosets by batch pyrolysis and investigation of fibre re-using as reinforcement in LDPE matrix.* Composites Part B: Engineering, 2016. **91**: p. 154-161.
14. Palmer, J., et al., *Successful closed-loop recycling of thermoset composites.* Composites Part A: Applied Science and Manufacturing, 2009. **40**(4): p. 490-498.
15. Pickering, S.J., *Recycling technologies for thermoset composite materials-current status.* Composites Part A: Applied Science and Manufacturing, 2006. **37**(8): p. 1206-1215.
16. Quan, C., et al., *Characterization of products recycling from PCB waste pyrolysis.* Journal of Analytical and Applied Pyrolysis, 2010. **89**(1): p. 102-106.
17. Tranchard, P., et al., *Kinetic analysis of the thermal decomposition of a carbon fibre-reinforced epoxy resin laminate.* Journal of Analytical and Applied Pyrolysis, 2017. **126**: p. 14-21.
18. Zheng, Y., et al., *A novel approach to recycling of glass fibers from nonmetal materials of waste printed circuit boards.* Journal of Hazardous Materials, 2009. **170**(2): p. 978-982.
19. Turku, I., et al., *Characterization of plastic blends made from mixed plastics waste of different sources.* Waste Management & Research, 2017. **35**(2): p. 200-206.
20. Job, S., *Recycling glass fibre reinforced composites – history and progress.* Reinforced Plastics, 2013. **57**(5): p. 19-23.
21. Pickering, S.J., et al., *A fluidised-bed process for the recovery of glass fibres from scrap thermoset composites.* Composites Science and Technology, 2000. **60**(4): p. 509-523.

Regeneration of CO_2 Loaded 2-(Diethylamino)ethanol using Organic Solvent and Waste Heat

Shubhashis Adak and Madhusree Kundu*

Department of Chemical Engineering, National Institute of Technology, Rourkela, India
* *Corresponding author:* mkundu@nitrkl.ac.in*; 91-8328829990*.

Abstract: The major problem associated with Carbon capture using chemical absorption is energy intensive regeneration of the loaded solvent. This limitation can also be overcome by using some water soluble organic solvents (acetone/acetaldehyde/dimethoxymethane) having very low dielectric constant compared to water for CO_2 recovery from CO_2 rich alkanolamine (from tertiary alkanolamine or NH_3in specific) solution and applying waste heat for solvent regeneration. 2-(Diethylamino)ethanol (DEAE) was used as a CO_2 absorbent and pure CO_2 was generated by adding organic solvents (acetone/tetrahydrofuran (THF)) in CO_2 loaded DEAE solution. Effect of organic solvent (acetone/THF), proportion of regenerating solvent to the absorbent, absorbent (DEAE) concentration (3/4 mol/L) and temperature (303.15/313.15) K on CO_2 recovery from CO_2 rich solution (loading in mol CO_2/mol DEAE=0.9) were studied. Acetone was found to be more efficient in CO_2 recovery than THF at comparable experimental conditions. Thermodynamically predicted enthalpy due to CO_2 absorption are presented here so that one can estimate the heating requirement in desorption of CO_2fromloaded DEAE solution using steam. Enthalpy was estimated using experimental CO_2 solubility in (1, 2, 3, 4) mol/L aqueous DEAE solutions in the temperature range of (303.15 to 323.15) K and pressure of (0 to 100) kPa.

Keywords: CO_2 capture; DEAE; CO_2 regeneration; Waste heat; Activity coefficient model, Enthalpy prediction.

1. Introduction

Absorption of CO_2 in amine based solvent is a regenerative absorption process, which is enhanced by chemical reaction. For regeneration, the CO_2 loaded solution is fed to the stripping tower and heated at 120°C to regenerate the solvent and this process is associated with high temperature heating thus operating cost of this process is high. In regenerative absorption process most of the energy is utilised for solvent recovery which is major drawbacks of this process. Regeneration energy varies depending upon the solvent formulation and is directly related with enthalpy of CO_2 absorption of that solvent. Hence, to characterize a solvent as a potential CO_2 absorbent, enthalpy of CO_2 absorption of that solvent formulation is a very important parameter. Enthalpy of CO_2 absorption is measured by calorimetric experiment. Many researchers have measured enthalpy of CO_2 absorption for number of solvents like MEA, DEA, and MDEA [1-2]. It is very interesting that, enthalpy of CO_2 absorption can be precisely predicted from thermodynamic model using equilibrium CO_2 solubility data [3]. Since no experimental or predicted enthalpy of CO_2 absorption of aqueous DEAE solution

is available in the open literature, prediction of enthalpy from activity coefficient based model on solubility seems to be a significant contribution.

In regenerative absorption process most of the energy is utilised for solvent recovery which is major drawbacks of this process. Monoethanolamine (MEA) is widely used in industrial purpose because of its high absorption rate and low cost. One of the major disadvantage associated with MEA is it's formation of stable carbamate with CO_2 which demands high regeneration energy [4]. To reduce the heat duty for solvent regeneration of CO_2 loaded MEA solution. Zhang *et al.* (2018) used the composite catalysts, SO_4^{2-}/ZrO2/γ-Al_2O_3 (SZA), with different ZrO_2 and γ-Al_2O_3 mass ratios and they found 36.9 % less heat duty is required compared to catalyst free run [5]. Wang *et al.* (2018) found 31 % less heat duty is required when sulfolane is used as phase splitter with MEA for CO_2 absorption [6]. Limitation of regenerative absorption process can also be overcome by using some water soluble organic solvents (acetone/acetaldehyde/dimethoxymethane) having very low dielectric constant compared to water for CO_2 recovery from CO_2 rich alkanolamine (basically tertiary alkanolamine or NH_3) solution and applying low temperature heat for solvent regeneration (Figure 1) [7]. By this process high purity CO_2, which is a valuable product, can be obtained and for solvent regeneration by distillation, low temperature heat is required because this organic solvents (acetone/acetaldehyde/dimethoxymethane) have very low boiling point. CO_2 and solvent regeneration by this technique is only possible when the CO_2 rich solution contains only bicarbonate and carbonate ions and if carbamate ion is present in the solution then CO_2 can't be regenerated by this technique. Tertiary alkanolamine absorbs CO_2 by formation of bicarbonate and carbonate ion and does not form carbamate ion thus can be used for CO_2 capture and high purity CO_2 and solvent can be regenerated by the aforementioned technique. DEAE has promising CO_2 absorption characteristics compared to MDEA thus has been used in this study for CO_2 capture as single alkanolamine solvent and CO_2 rich DEAE solution was used for the study of CO_2 regeneration by adding organic solvents like acetone/THF [8]. This study was intended to find out the effect of concentration of the absorbing solvent (DEAE), effect of regeneration temperature, and effect of concentration of organic solvent (acetone/THF) on CO_2 regeneration. Regeneration studies were carried using acetone/THF as additive to the CO_2 loaded DEAE solution at 303.15 and 313.15 K.

In view of this, equilibrium CO_2 solubility in (1, 2, 3, 4) mol/L aqueous DEAE solution was correlated efficiently using activity coefficient model with an AAD % of 3.34. Enthalpy of CO_2 solubility in aqueous DEAE solution was predicted from the developed thermodynamic model.

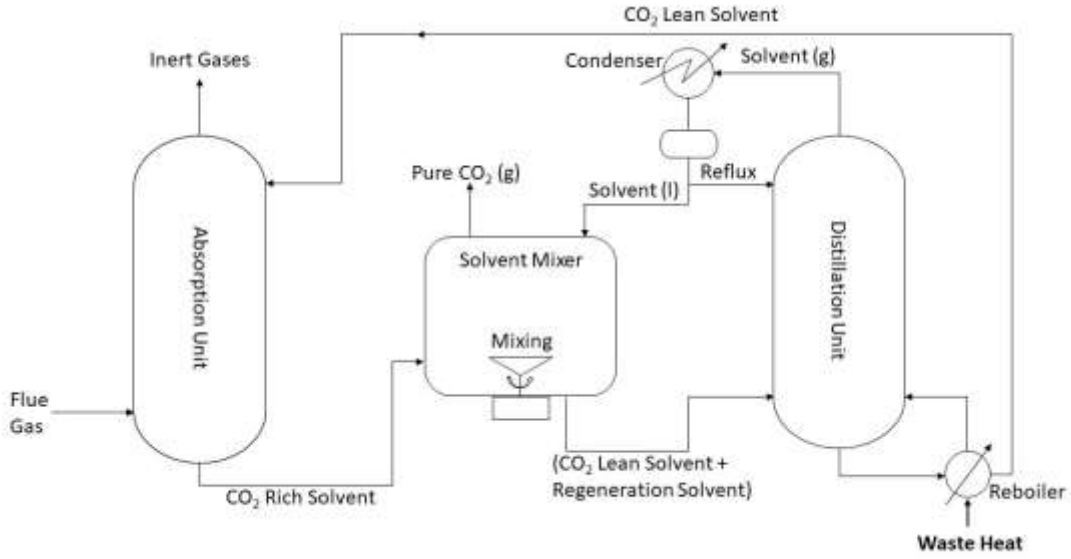


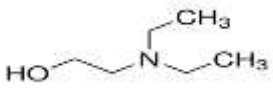
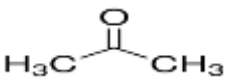
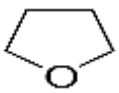
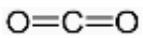
Figure 1: Schematic of CO_2 and solvent regeneration using organic solvent and waste heat

2. Materials and Methods

2.1. Materials

DEAE, Acetone, THF, CO_2 were used for the experimentation. The structure of the compounds, their purity along with their sources is presented in the Table 1. Millipore water having conductivity 1×10^{-7} Ω^{-1} cm^{-1} and surface tension 72 $mN.m^{-1}$ at 298 K was used for solution preparation. Distilled water degassed by boiling followed by cooling to ambient temperature under vacuum was used for making the solutions for CO_2 capture.

Table 1: Chemicals used in this work along with their structure, purity and sources

Compound	Structure	Purity	Supplier
2-(Diethylamino)ethanol (DEAE)		≥ 99 %	Merck
Acetone		≥ 99 %	Fisher Scientific
Tetrahydrofuran (THF)		≥ 99 %	Fisher Scientific
Carbon Dioxide (CO_2)		99.9%	Vadilal Gases Limited

2.1. Vapour-Liquid equilibrium measurement

2.1.1. Experimental set-up

The equilibrium CO_2solubility in different solvent concentrations was measured in a stainless steel made equilibrium vessel. VLE measurements were performed at pressures up to (0.1 to 100) kPa and temperatures (303.1, 313.1 and 323.1) K. The same VLE set-up was utilised for the solubility measurement as well as CO_2 regeneration experiment which was used for our previous work [3].

2.1.2. Experimental method of CO_2 Solubility

Before VLE experimentation, the buffer and the equilibrium vessels were allowed to attain the same temperature as that of the constant temperature water bath (recirculation temperature controller, Polyscience, USA model No: 9712). Both the buffer and the equilibrium vessels were expatriated simultaneously using vacuum pump (HINDVAC). After evacuation, the buffer vessel and equilibrium vessel were disconnected from each other. The handling capacity of the buffer vessel is 1.5 - 2.5 times more than the desired maximum CO_2 partial pressure or total pressure to be attained by the equilibrium vessel. Those vessels are being filled using pure CO_2 gas cylinder. Uncertainty in temperature measurement was ±0.05 K. At a specific temperature, numbers of equilibrium CO_2 solubility in the suggested solutions were made while CO_2partial pressure got varied. 25 ml of freshly prepared amine solution of specific concentration was injected into the equilibrium vessel. Afterwards, the equilibrium vessel went on evacuated for the second time and allowed to live at solution vapour pressure (p_v). The solution vapour pressure was noted. The expected uncertainty in the dispatched solution volume to the equilibrium vessel is estimated to be 0.05 ml. Equilibrium vessel was fed CO_2 gas from the buffer vessel. During the chemical absorption process, the equilibrium vessel was kept disconnected from the buffer vessel. The number of moles of CO_2transferred from the buffer vessel, was estimated using the difference in final and initial pressure of the pressure transducer (Swagelok, model No: PTI-S-NA-100-15AO-B) connected to the buffer vessel ($u(P_1)$ = 0.031 kPa). During absorption, liquid phase present in the equilibrium cell was continuously stirred. Time required to reach equilibrium varies depending upon the used solvents/solvent blends for CO_2 absorption. Time range varies from minutes to hours. As for example, if aqueous PZ solution is used as CO_2 absorbent, then time required is in minutes to reach the equilibrium but if tertiary alkanolamine like MDEA is used as CO_2 absorbent then an hour or so may be required to reach the equilibrium. It is important to mention that, reaching to equilibrium is indicated, when there is no change in CO_2 partial pressure for half an hour in the equilibrium cell during the ongoing absorption of CO_2 by the chosen solvent. The pressure transducer fitted to the equilibrium vessel (Swagelok, model No: PTI-S-NA-50-15AO-B, ($u(P_2)$ = 0.021 kPa) revealed the total vessel pressure (P_t) under which absorption takes place. The equilibrium pressure (P_{CO2}) is the difference of the total equilibrium vessel pressure (P_t) and solution vapour pressure (p_v). The moles of CO_2absorbed by the amine solution was estimated using moles of CO_2 being transferred from the buffer vessel and the moles ofCO_2 present in the vapour space of the equilibrium vessel at a specific equilibrium pressure and temperature. Method adopted for calculation of mole of CO_2 absorbed in the liquid phase as described by Park and Sandall (2001) [9]. CO_2 loading is expressed as moles of CO_2 absorbed per moles of solvent at specific equilibrium CO_2pressure and temperature. Consecutive runs at a specific temperature can be taken by repeating the whole

procedure already stated. The diminishing capacity of the solution necessitates that the successive CO_2 loading values to be taken at increasing CO_2 pressures for a particular temperature.

2.2. Experimental Method of CO_2 Regeneration

Using the VLE setup, CO_2 rich solution (belongs to specific loading) at different DEAE concentrations were prepared by absorbing CO_2 and these CO_2 rich solutions were used as stock solution for regeneration experiments. 5 ml of CO_2 rich stock solution of known CO_2 loading was taken in the equilibrium cell and the temperature of the equilibrium cell was controlled by the water circulator temperature controller. After reaching the desired temperature, specific amount (5/2 ml) of acetone/THF was injected into the equilibrium cell and magnetic stirrer was kept on. During this process equilibrium pressure is rapidly increased due to the release of dissolved CO_2 from CO_2 rich DEAE solution. This pressure increase was recorded in the PC through data acquisition system (National instruments DAQ Card). After 10 minutes of stirring the system pressure reaches equilibrium and no further CO_2 is released. In the next step, the system pressure was decreased quickly to atmospheric pressure by releasing the generated gas by opening an equilibrium cell valve and then valve was closed and again solution was stirred for five minutes. After 5 minutes of stirring system pressure again reached equilibrium and same procedure was repeated again for another 5 minutes. Same experiment was carried out with aqueous unloaded DEAE solutions (CO_2 loading=0) of same concentration at same temperature. From the pressure difference in each step as shown in Figure 2, the amount of CO_2 released was calculated. Total amount of CO_2 released (almost 90 % of the absorbed CO_2) is the sum of the CO_2 released at three successive steps. Maximum amount of CO_2 is generated in the 1st step and it decreases gradually in the successive steps.

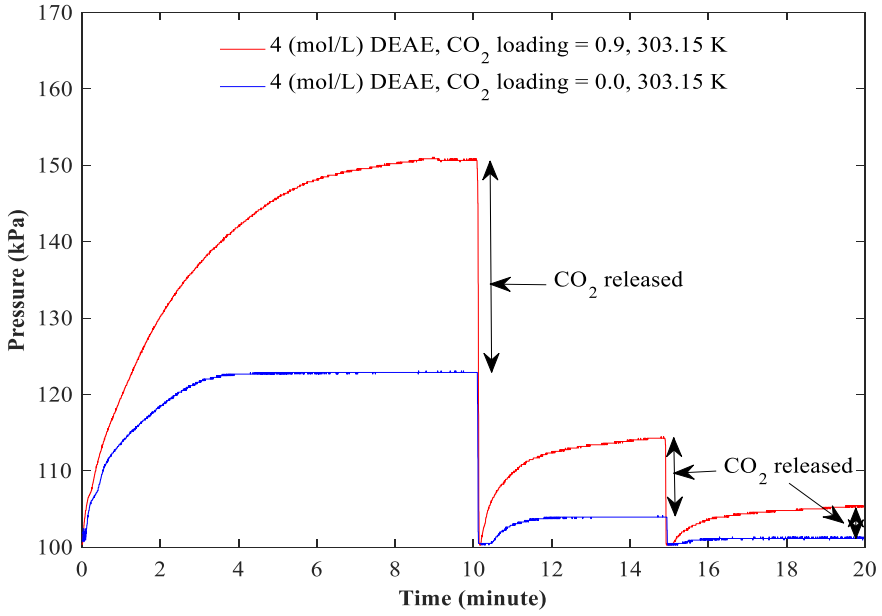


Figure 2: Regeneration of CO_2 from CO_2rich 4 mol/L DEAE solution (loading=0.9) using acetone at 303.15 K

2.3. Thermodynamic model development

2.3.1. Chemical Equilibria

When CO_2 reacts with aqueous solution of DEAE, following sets of reactions may occur in the liquid phase.

Physical solubility of CO_2 in water:

$$CO_2(g) \xleftarrow{H_{CO_2}} CO_2(aq) \quad (1)$$

Dissociation of water:

$$H_2O \xleftarrow{K_1} H^+ + OH^- \quad (2)$$

Formation of bicarbonate:

$$CO_2 + H_2O \xleftarrow{K_2} HCO_3^- + H^+ \quad (3)$$

Dissociation of bicarbonate:

$$HCO_3^- \xleftarrow{K_3} CO_3^{2-} + H^+ \quad (4)$$

Protonation of DEAE:

$$DEAE + H^+ \xleftarrow{K_4} DEAEH^+ \quad (5)$$

The equilibrium constants (K_1-K_4) for these above reactions are expressed as:

$$K_1 = [H^+][OH^-].\gamma_{H^+}\gamma_{OH^-} \quad (6)$$

$$K_2 = \frac{[HCO_3^-][H^+]}{[CO_2]}\frac{\gamma_{HCO3^-}\gamma_{H^+}}{\gamma_{CO_2}} \quad (7)$$

$$K_3 = \frac{[CO_3^{2-}][H^+]}{[HCO_3^-]}\frac{\gamma_{CO_3^{2-}}\gamma_{H^+}}{\gamma_{HCO_3^-}} \quad (8)$$

$$K_4 = \frac{[DEAEH^+]}{[DEAE][H^+]}\frac{\gamma_{DEAEH^+}}{\gamma_{DEAE}\ \gamma_{H^+}} \quad (9)$$

Where [i] and γ_i are the concentration and activity coefficient of the ith species respectively. The temperature dependency of the equilibrium constants as well as Henry's constant are expressed as:

$$K_i / H_{CO_2} = \exp\left(\frac{a_i}{T} + b_i \ln T + c_i T + d_i\right) \quad (10)$$

For the reaction (1 to 5), all the parameters (a_i to d_i) have been taken from literature and presented in Table 2 [3, 10].

Table 2: Parameters used for the estimation of equilibrium constant of reaction (2 to 5) and Henry's constant.

Parameter	a_i	b_i	c_i	d_i	Source
K_1	-13445.9	-22.4773	0	140.932	[10]
K_2	-12092.1	-36.7816	0	235.482	[10]
K_3	-12431.7	-35.4819	0	220.067	[10]
$1/K_4$	-2.4569	15.7336	0	-112.3998	[3]
H_{CO2}	-6789.04	-11.4519	-0.010454	94.4914	[10]

In addition to the above equations, the following set of conditions must also be satisfied.
Charge balance:

$$H^+ + DEAEH^+ = OH^- + HCO_3^- + 2CO_3^{2-} \quad (11)$$

CO_2 balance:

$$\alpha[DEAE]_t = HCO_3^- + CO_3^{2-} + CO_2 \quad (12)$$

DEAE balance:

$$[DEAE]_t = DEAE + DEAEH^+ \quad (13)$$

Where α is the CO_2 loading.
The concentration of CO_2in the liquid phase can be estimated by Henry's law:

$$\phi_{CO_2} P_{CO_2} = \gamma_{CO_2} H_{CO_2} [CO_2] \quad (14)$$

P_{CO2} is partial pressure of CO_2, φ_{CO2} is the fugacity coefficient of gas phase, H_{CO2} is the Henry's constant. In this study, gas phase non-ideality was not considered.
For single aqueous DEAE solutions, set of nonlinear equations 6-9 and 11-14 were solved simultaneously to find out a 4th order nonlinear equation (equation 15) in terms of H^+ ion concentration present in the liquid phase considering liquid phase activity coefficient equals to 1.

$$A_1 * H^{+4} + A_2 * H^{+3} + A_3 * H^{+2} + A_4 * H^+ + A_5 = 0 \quad (15)$$

Where, $A_1 = 1$

$$A_2 = M + 1/K_4$$

$$A_3 = -K_2 * CO_2 - K_1$$

$$A_4 = -K_2 * CO_2 / K_4 - 2 * K_2 * K_3 * CO_2 - K_1 / K_4$$

$$A_5 = -2 * K_2 * K_3 * CO_2 / K_4$$

CO_2 loading (α = mole of CO_2 absorbed/mole of amine) is expressed as:

$$\alpha = ((K_2 * CO_2 / H^+) + (K_2 * K_3 * CO_2 / H^{+2}) + CO_2) / M$$
$$M = DEAE \tag{16}$$

The activity coefficient of all the molecular and ionic species present in the liquid phase were calculated using modified Debye-Huckel theory for the electrolytic solution [11].

$$\ln \gamma_i = -\frac{AZ_i^2\sqrt{I}}{1+B\sqrt{I}} + 2\sum_j \beta_{ij} m_j \tag{17}$$

A is temperature dependent Debye-Huckel constant and B is taken as 1.2 [12]. m_j and $Z_i$are concentration and electrical charge of the ith species. I is the ionic strength of the solution and is calculated as:

$$I = \frac{1}{2}\sum_j m_j Z_j^2 \tag{18}$$

β_{ij} is binary interaction parameter between different molecular and ionic species present in the liquid phase.

A large number of interactions are possible between the species present in solution but some interactions have negligible effect on activity coefficient. Species having high concentration have larger influence on activity coefficient than species present in very low concentration. Also interaction between species of same ionic charge was neglected.

In this study, total 17 binary interaction parameters were considered for (DEAE+CO_2+H_2O) system, to develop activity coefficient models. Interaction parameters were obtained through regression of the experimental CO_2 solubility data. Since the model considered was activity based one, various interaction parameters responsible for liquid phase non-ideality, hence, their contributions in liquid phase CO_2 loading were estimated by minimizing an objective function (equation 2.38) proposed as difference/error between experimental and model-predicted CO_2 loading using fmincon (constrained non-linear minimization) optimization technique under MATLAB platform (optimization toolbox).

$$F = (1/N)\sum_{i=1}^{N}\left[\left|\frac{(\alpha_{i,exp} - \alpha_{i,cal})}{\alpha_{i,exp}}\right|\right] * 100 \tag{19}$$

Where N is the total number of measurements taken during experiment, $\alpha_{i,exp}$is the experimental CO_2 loading and $\alpha_{i,cal}$ is the calculated CO_2 loading. Algorithm flowchart for simulation has been presented in Figure 3.

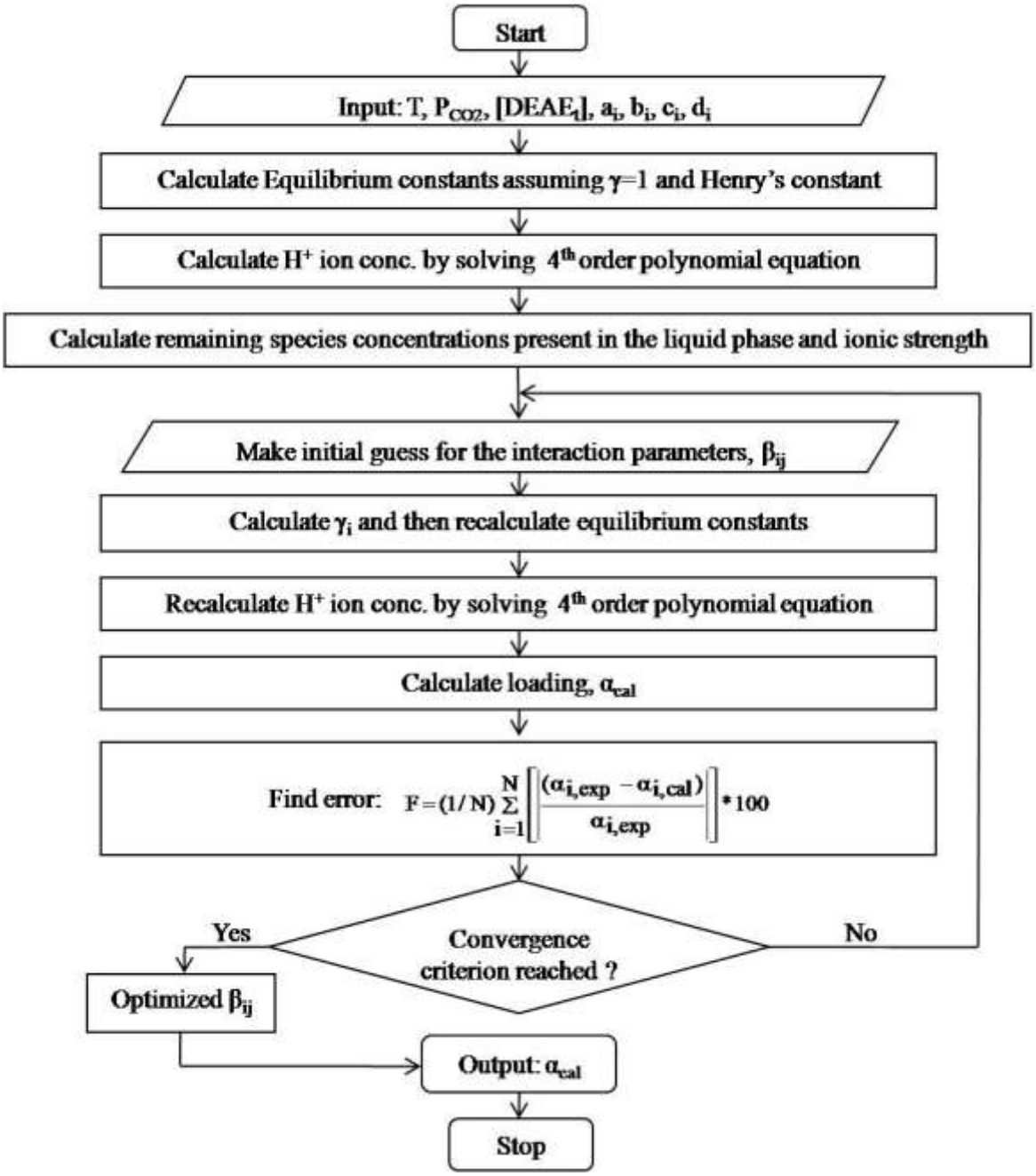


Figure 3: Flow chart for the activity coefficient model solution

2.3.2. Enthalpy Prediction from CO_2 Solubility Data

When any chemical reactions occur, some amount of energy is either absorbed or released. When CO_2 reacts with aqueous DEAE, number of reactions occurs. All the reactions are associated with some energy change. The overall energy change due to absorption of CO_2 into amine blend at thermodynamic equilibrium is called enthalpy of CO_2 absorption. Information about enthalpy due to CO_2 absorption is very important because it is related with heat duty necessary to regenerate solvent using thermal energy.

Enthalpy of CO_2 absorption can be predicted using interaction parameters obtained from regression of equilibrium CO_2 solubility data. Overall enthalpy is the sum of enthalpy associated with every single reaction (chemical and physical). Enthalpy of reaction, Q_i (kJ) for every single reaction can be calculated from the following equation [13].

$$Q_i = \varepsilon_i \left(\Delta H_i^{\,0} + \sum_j \nu_{j,i} H_j^{\,E} \right) \tag{20}$$

ΔH_i^0 (kJ/mole) is the standard reaction enthalpy, H_j^E (kJ/mole) is the partial excess molar enthalpy of species, $\nu_{j,i}$ is the stoichiometric coefficient of different reactants and products of reaction i and ε_i is the extent of reaction.

Standard enthalpy of reaction, ΔH_i^0 and partial excess molar enthalpy, H_j^E can be calculated using van't Hoff equation 21 and equation 22 respectively.

$$\Delta H_i^{\,0} = RT^2 \left(\frac{\partial \ln K_i}{\partial T} \right)_p \tag{21}$$

$$H_j^{\,E} = -RT^2 \left(\frac{\partial \ln \gamma_j}{\partial T} \right) \tag{22}$$

Enthalpy of absorption due to physical dissolution of CO_2, ΔH_{phy} (kJ/ mol of CO_2) was calculated using equation 23.

$$\Delta H_{phy} = -RT^2 \left(\frac{\partial \ln H_{CO_2}}{\partial T} \right) + RT^2 \left(\frac{\partial \ln \gamma_{CO_2}}{\partial T} \right) \tag{23}$$

Overall enthalpy of solution, ΔH_{sol} (kJ/ mol of CO_2) due to CO_2 absorption in the amine solution was calculated using equation 24.

$$\Delta H_{sol} = \Delta H_{phy} + \frac{1}{n_{CO_2}} \sum_i Q_i \tag{24}$$

n_{CO2} is the mole of CO_2 absorbed at equilibrium.

3. Results and Discussion

3.1. VLE of [DEAE+CO_2+H_2O] System

Systematic VLE of [DEAE+CO_2+H_2O] system was measured in a wide concentration range of (1, 2, 3, 4) mol/L, temperature of (303.15, 313.15, 323.15) K and pressure range of (0 to 100) kPa. CO_2 solubility data have been presented in Table S1. Experimentally obtained CO_2 solubility data at 313.15 K have been compared with data available in literature and is presented in Figure 4 [14-15]. Experimental solubility data obtained from our study and data obtained by Monteiro *et al.*(2013) have similar trend but data obtained by Luo *et al.* (2016) have unusual trend in some cases [14-15].

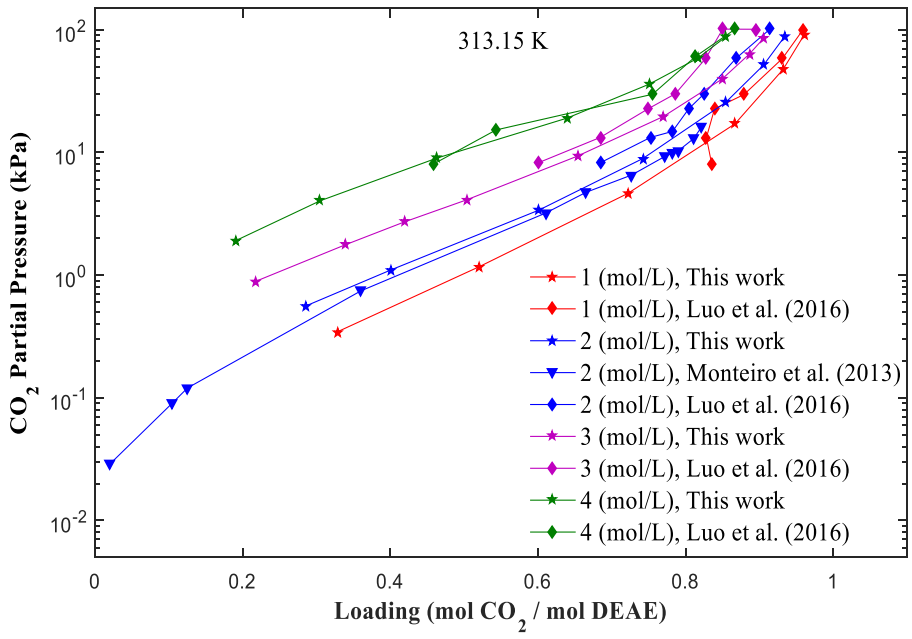


Figure 4: Comparison of CO_2 solubility data of (1, 2, 3,4) mol/L DEAE solution at 313.15 K with literature data.

Experimental CO_2 solubility data of (DEAE+CO_2+H_2O) system were correlated using thermodynamic model. All the experimental CO_2 solubility data (86 data) were correlated using thermodynamically sound activity coefficient model. Experimental and model predicted data are in excellent agreement with AAD % of 3.34, which are shown in Figure 5 and Figure 6. Interaction parameters obtained by regressing the experimental data from the thermodynamic model have been presented in Table S2.

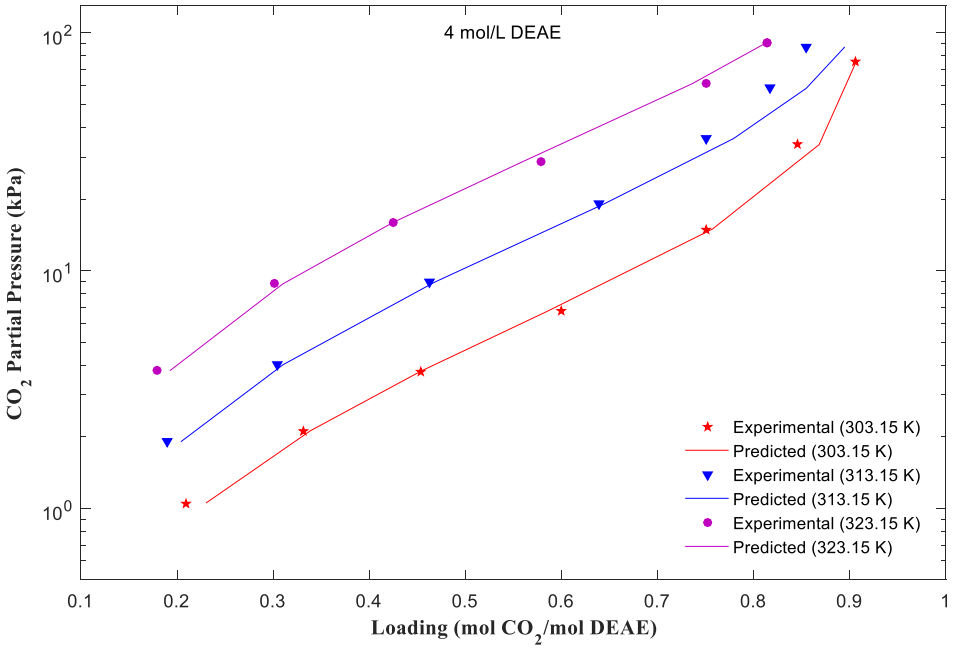


Figure 5: Experimental and model predicted CO_2 solubility in 4 mol/L DEAE solution at 303.15, 313.15 and 323.15 K

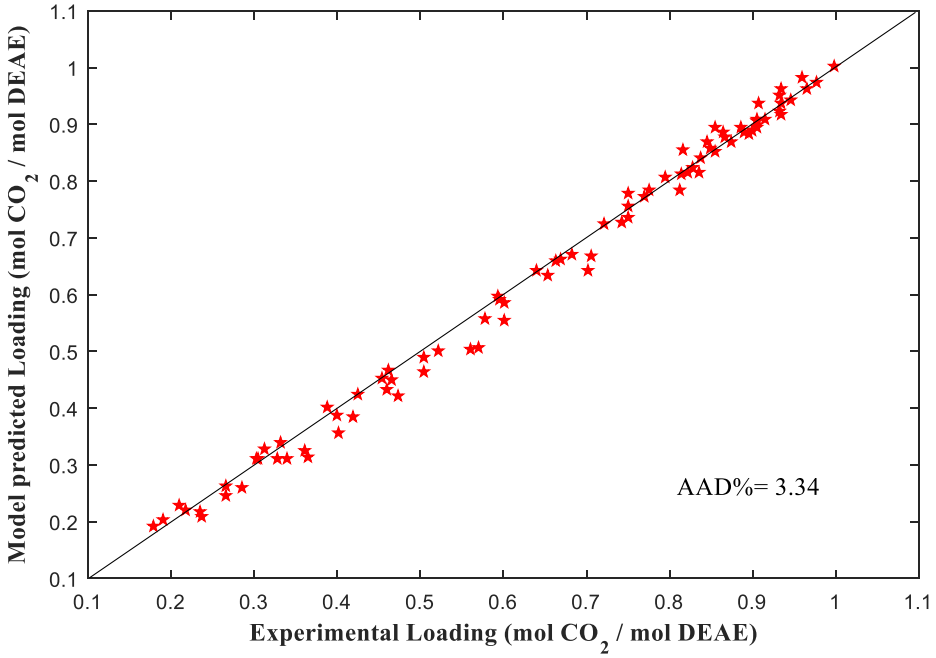


Figure 6: Parity plot of experimental and model predicted CO_2 loading in (DEAE+CO_2+H_2O) system.

3.2. Enthalpy of [DEAE+ CO_2+H_2O] System

Enthalpy of CO_2 absorption of (DEAE+CO_2+H_2O) system have been calculated using equations 20-24, set of reactions 1-5 and interaction parameters obtained by regression of the equilibrium solubility data at different temperatures and DEAE concentrations. Enthalpy of solution for (DEAE+CO_2+H_2O) system is the sum of enthalpy of reaction 1-5 and the enthalpy due to physical absorption of CO_2 in the amine solution. Enthalpy of solution as well as enthalpy of individual reactions is presented in the Figure 7. From the Figure 7, it is seen that enthalpy of absorption due to protonation reaction of DEAE contributes maximum in overall enthalpy (ΔH_{sol}). Enthalpy due to physical absorption (ΔH_{phy}) of CO_2 in the aqueous DEAE solution has significant contribution in overall enthalpy than enthalpy (ΔH_{rxn2} and ΔH_{rxn3}) of reactions 2 and 3 respectively. Bicarbonate formation reaction and bicarbonate dissociation reaction both are endothermic in nature and have little influence on overall enthalpy.

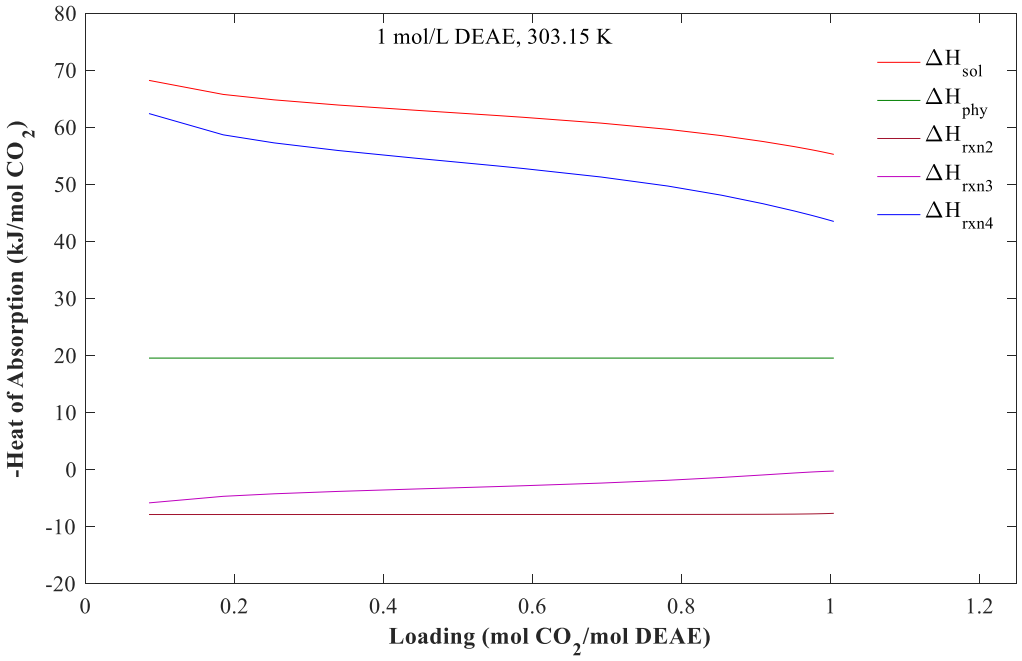


Figure 7: Heat of absorption (kJ/mol CO_2) in aqueous 1 mol/L DEAE solution at 303.15 K.

3.3. CO_2 Regeneration using Organic Solvents

For CO_2 regeneration experiments, two CO_2 rich solutions (loading=0.9) of 3 and 4 mol/L aqueous DEAE were prepared by absorbing CO_2 with aqueous DEAE solution at 303.15 K in stainless steel equilibrium cell. These solutions were used as stock solution for CO_2 regeneration experiments. Acetone and THF were used as organic solvents for CO_2 regeneration. When acetone/THF is added to the CO_2 rich DEAE solution, the polarity of the solution decreases because this organic solvents (acetone, THF) have very low dielectric constant (acetone: 20.7, THF: 7.58) compared to water

(dielectric constant=80.1) and pure CO_2 is released due to weakening of hydration shells surrounding the solvated ions.

The effect of organic solvent (acetone/THF) were studied on CO_2 recovery from 4 mol/L CO_2 rich (loading=0.9) DEAE solution at 303.15 K and CO_2 release profile are presented in Figure 2 and Figure 8. For acetone, 72.85 % and for THF, 38.31 % of CO_2 were recovered from the CO_2 rich DEAE solution at same experimental condition. Due to enhance ability of CO_2 recovery of acetone than THF, acetone was used as organic solvent for CO_2 recovery for rest of the experiments.

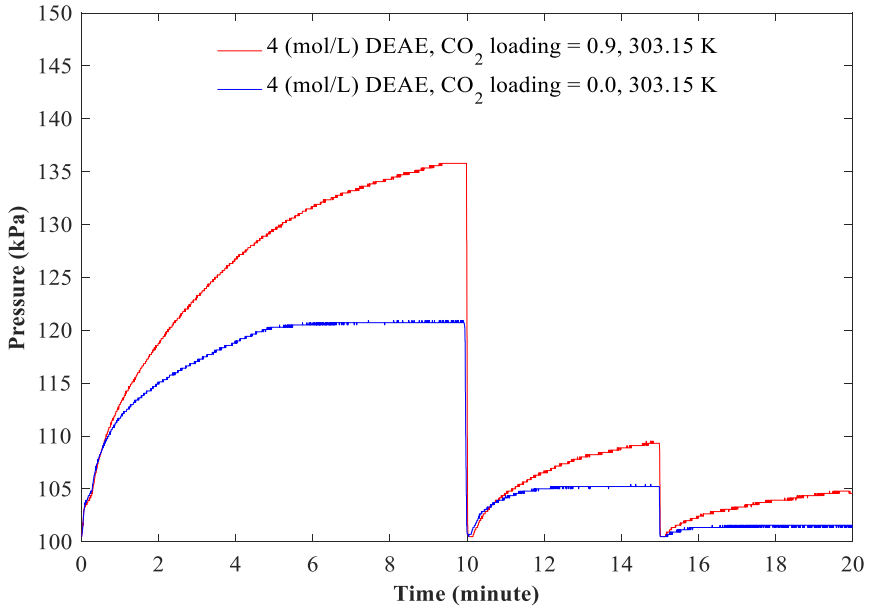


Figure 8: Regeneration of CO_2 from CO_2 rich 4 mol/L DEAE solution (loading=0.9) using THF at 303.15 K

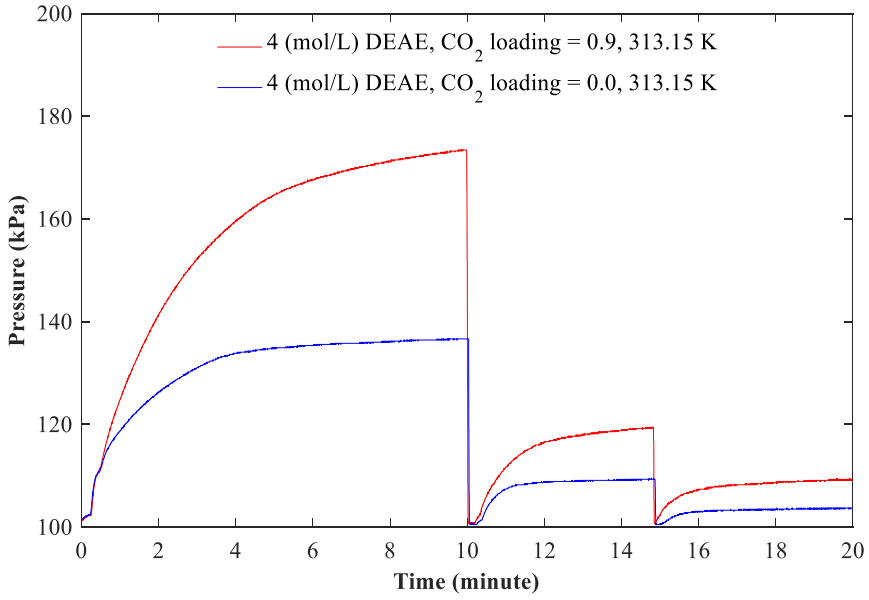


Figure 9: Regeneration of CO_2 from CO_2 rich 4 mol/L DEAE solution (loading=0.9) using 5 ml acetone at 313.15 K

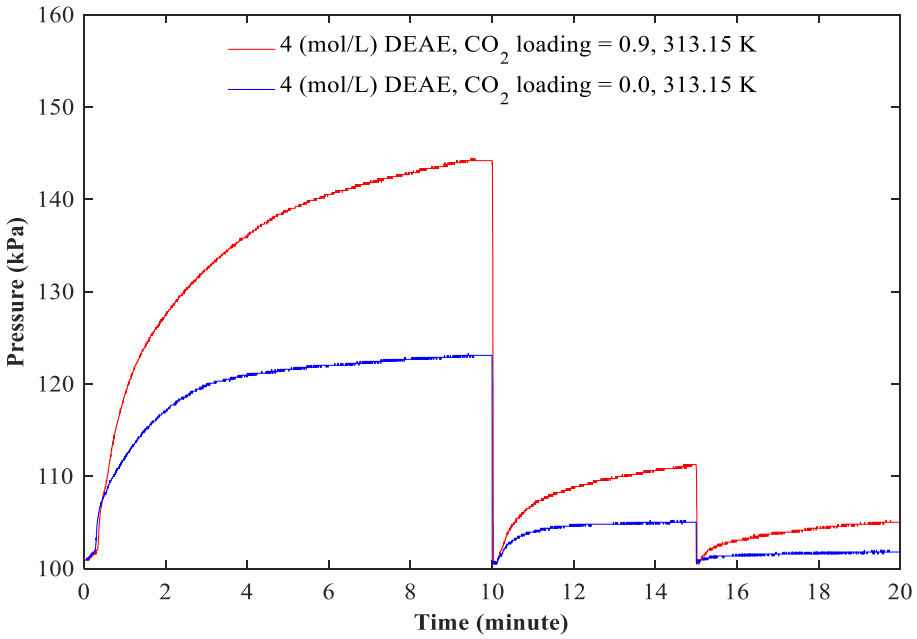


Figure 10: Regeneration of CO_2 from 5 ml CO_2 rich 4 mol/L DEAE solution (loading=0.9) using 2 ml acetone at 313.15 K

To optimize the amount of solvent (acetone) required for CO_2 recovery from 5 ml of 4 mol/L DEAE solution (CO_2 rich) at 313.15 K, 2/5 ml of acetone was added to the CO_2 rich solution. Experimentally obtained results are shown in Figure 9 and Figure 10. For 5 ml of acetone, 88 % CO_2

was recovered and for 2 ml of acetone only 57 % CO_2 was recovered. So for enhanced CO_2 recovery 5 ml of acetone was used for rest of the experimentation.

To study the effect of temperature, CO_2 was regenerated from 4 mol/L CO_2 rich (loading=0.9) DEAE solution using acetone at 303.15 and 313.15 K and CO_2 release profile are presented in Figure 2 and Figure 9. 88 % and 72.85 % of CO_2 were recovered at 313.15 and 303.15 K respectively. So at higher temperature more CO_2 is released. Same trend was observed in case of 3 mol/L CO_2 rich (loading=0.9) DEAE solution at 303.15 and 313.15 K and experimental results have been presented in Figure 11 and Figure 12. 84.58 % and 68.69 % of CO_2 was recovered at 313.15 and 303.15 K respectively. All the experimental results of CO_2 recovery are presented in bar plot; 'Figure 13' to compare the effect of organic solvents (acetone/THF), temperature and concentration of DEAE solution on CO_2 recovery. From the Figure 13 it is evident that acetone is more effective than THF on CO_2 recovery, higher temperature and higher DEAE concentration have enhance effect on CO_2 recovery.

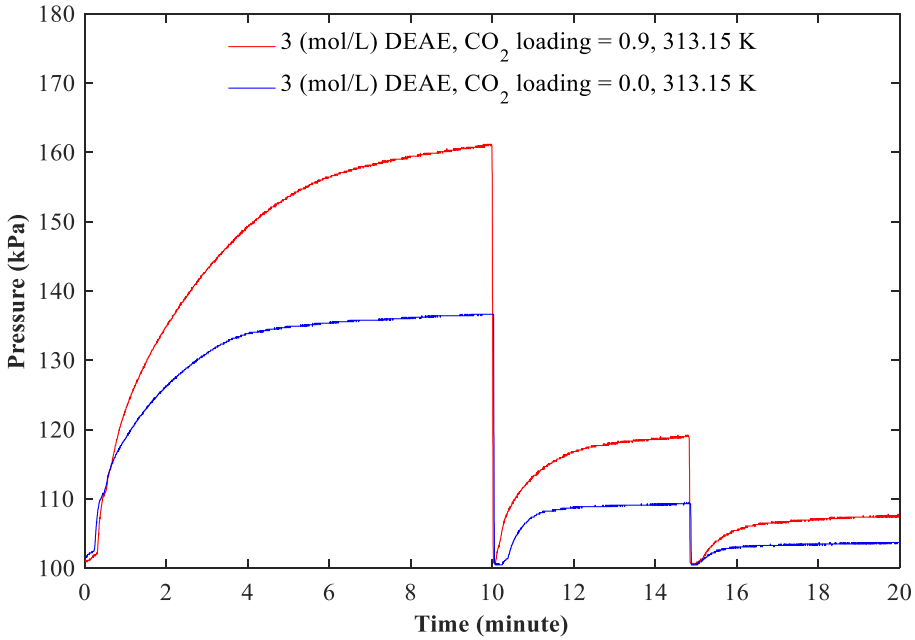


Figure 11: Regeneration of CO_2 from CO_2 rich 3 mol/L DEAE solution (loading=0.9) using acetone at 313.15 K

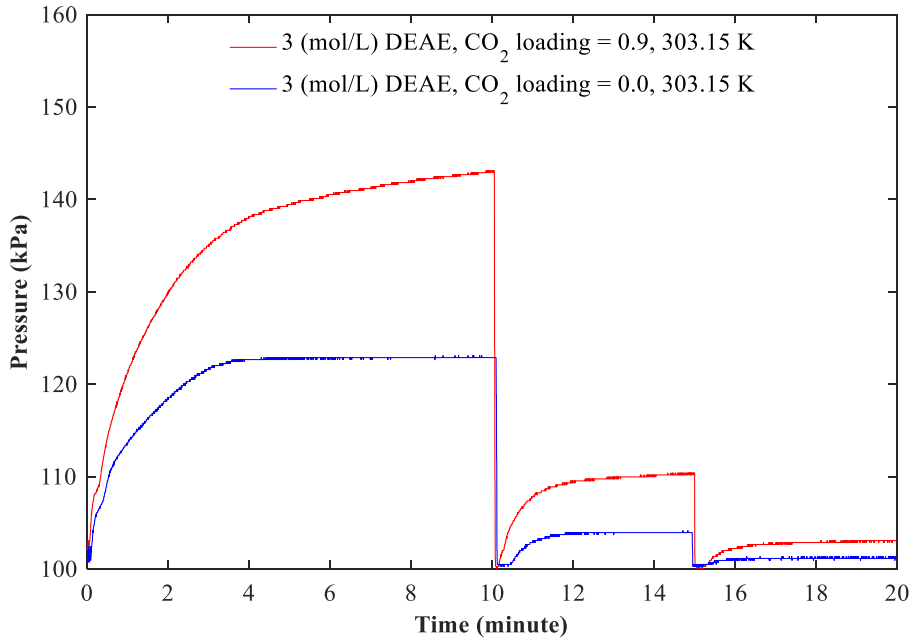


Figure 12: Regeneration of CO_2 from CO_2 rich 3 mol/L DEAE solution (loading=0.9) using acetone at 303.15 K

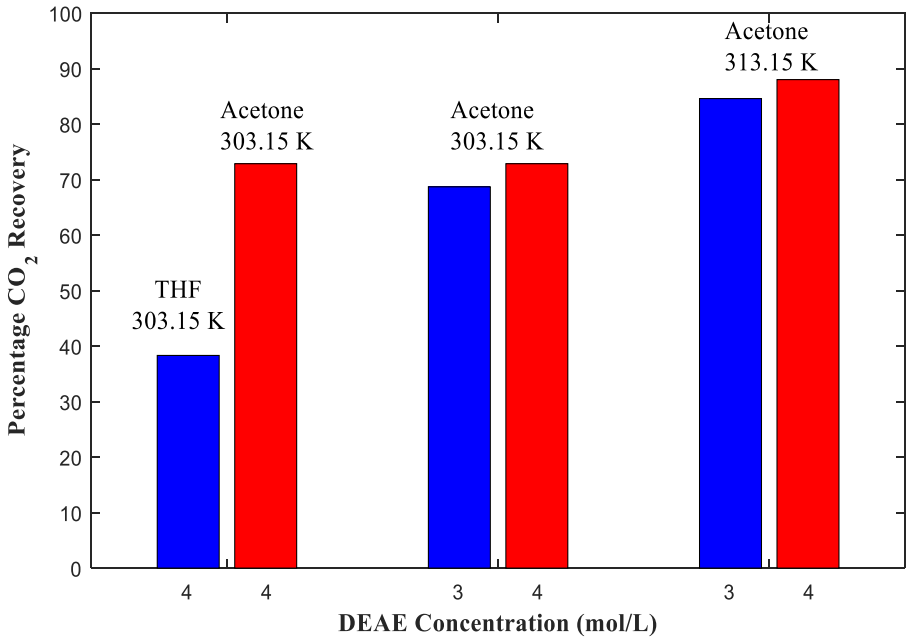


Figure 13: Regeneration of CO_2 from CO_2 rich DEAE solution (loading=0.9) using Acetone/THF at 303.15 K and 313.15 K

4. Conclusions

In this article, CO_2 absorption as well as an unconventional technique of solvent regeneration has been presented. Equilibrium CO_2 solubility in (1, 2, 3, 4) mol/L aqueous DEAE solution was measured in the temperature range of (303.15 to 323.15) K and pressure of (0 to 100) kPa. Experimental solubility data was correlated efficiently using activity coefficient model with an AAD % of 3.34. Enthalpy of CO_2 absorption in aqueous DEAE solution has been predicted from the developed thermodynamic model using experimental CO_2 solubility data. For solvent CO_2 regeneration, a water soluble organic solvent like acetone/THF was explored. Effect of organic solvent (acetone/THF), temperature (303.15/313.15 K) and DEAE concentration (3/4 mol/L) on CO_2 recovery from CO_2 rich DEAE solution were studied. From this study it is seen that up to 88 % of CO_2 can be regenerated from 5 ml of CO_2 rich DEAE (4 mol/L) solution by adding equal volume (5 ml) of acetone at 313.15 K in only 20 minutes of stirring. Also it is seen that, acetone is more effective than THF on CO_2 recovery, higher temperature and higher DEAE concentration have enhance effect on CO_2 recovery. This CO_2 capture technique may be useful where low temperature heat (waste heat) is available and remains unused.

Acknowledgments:

The authors duly acknowledge the research fund provided by the Institute to pursue the research.

References

1. Arcis. H.; Rodier. L.; Ballerat-Busserolles. K. and Coxam. J.Y. Enthalpy of solution of CO_2 in aqueous solutions of methyldiethanolamine at T= 322.5 K and pressure up to 5 MPa. *The Journal of Chemical Thermodynamics* 2008, *40*(6), pp.1022-1029.
2. Carson. J.K.; Marsh. K.N. and Mather. A.E. Enthalpy of solution of carbon dioxide in (water+ monoethanolamine, or diethanolamine, orN-methyldiethanolamine) and (water+ monoethanolamine+ N-methyldiethanolamine) atT= 298.15 K. *The Journal of Chemical Thermodynamics* 2000, *32*(9), pp.1285-1296.
3. Adak. S. and Kundu. M. CO_2 capture using aqueous 1-(2-Hydroxyethyl) piperidine and its blends with piperazine: Solubility and enthalpy. *Fluid Phase Equilibria* 2020, p.112463.
4. Kohl. A.L. and Nielsen. R. *Gas purification*. Elsevier 1997.
5. Zhang. X.; Hong. J.; Liu. H.; Luo. X.; Olson. W.; Tontiwachwuthikul. P. and Liang. Z. $SO4\ 2-/ZrO_2$ supported on γ-Al_2O_3 as a catalyst for CO_2 desorption from CO_2-loaded monoethanolamine solutions. *AIChE Journal* 2018, 64(11), pp.3988-4000.
6. Wang. L.; Zhang. Y.; Wang. R.; Li. Q.; Zhang. S.; Li. M.; Liu. J. and Chen. B. Advanced Monoethanolamine Absorption Using Sulfolane as a Phase Splitter for CO_2 Capture. *Environmental Science & Technology* 2018, 52(24), pp.14556-14563.
7. Novek. E.; Shaulsky. E.; Fishman. Z.; Pfefferle. L. and Elimelech. M. Low-Temperature Carbon Capture Using Aqueous Ammonia and Organic Solvents. *Environmental Science & Technology Letters* 2016, 3(8), pp.291-296.

8. Adak. S. and Kundu. M. Vapor–Liquid Equilibrium and Physicochemical Properties of Novel Aqueous Blends of (2-Diethylaminoethanol + Piperazine) for CO_2 Appropriation. *Journal of Chemical & Engineering Data* 2017, 62(7), pp.1937-1947.
9. Park. M. and Sandall. O. Solubility of Carbon Dioxide and Nitrous Oxide in 50 mass% Methyldiethanolamine. *Journal of Chemical & Engineering Data* 2001, 46(1), pp.166-168.
10. Edwards. T.; Maurer. G.; Newman. J. and Prausnitz. J. Vapor-liquid equilibria in multicomponent aqueous solutions of volatile weak electrolytes. *AIChE Journal*1978, 24(6), pp.966-976.
11. Guggenheim. E. and Stokes. R. Activity coefficients of 2 : 1 and 1 : 2 electrolytes in aqueous solution from isopiestic data. *Transactions of the Faraday Society*1958, 54, p.1646-1649.
12. Pitzer. K.S. and Silvester. L.F. Thermodynamics of electrolytes. VI. Weak electrolytes including H 3 PO 4. *Journal of Solution Chemistry* 1976, *5*(4), pp.269-278.
13. Arcis. H.; Ballerat-Busserolles. K.; Rodier. L. and Coxam. J.Y. Measurement and modeling of enthalpy of solution of carbon dioxide in aqueous solutions of diethanolamine at temperatures of (322.5 and 372.9) K and pressures up to 3 MPa. *Journal of Chemical & Engineering Data* 2012, *57*(3), pp.840-855.
14. Monteiro. J.; Pinto. D.; Zaidy. S.; Hartono. A. and Svendsen. H. VLE data and modelling of aqueous N,N-diethylethanolamine (DEEA) solutions. *International Journal of Greenhouse Gas Control* 2013, 19, pp.432-440.
15. Luo. X.; Chen. N.; Liu. S.; Rongwong. W.; Idem. R.; Tontiwachwuthikul. P. and Liang. Z. Experiments and modeling of vapor-liquid equilibrium data in DEEA-CO_2-H_2O system. *International Journal of Greenhouse Gas Control* 2016, 53, pp.160-168.

Supplementary Data

Table S1a: Experimental CO_2 loading of aqueous 1 mol/L DEAE solution at different temperature and CO_2 partial pressure.

303.15 K		**313.15 K**		**323.15 K**	
P_{CO2} (kPa)	**Loading** $\left(\frac{molCO_2}{molDEAE}\right)$	**P_{CO2}** (kPa)	**Loading** $\left(\frac{molCO_2}{molDEAE}\right)$	**P_{CO2}** (kPa)	**Loading** $\left(\frac{molCO_2}{molDEAE}\right)$
0.310	0.387	0.344	0.328	0.434	0.266
1.068	0.593	1.172	0.520	1.601	0.460
5.378	0.822	4.620	0.721	5.903	0.668
12.90	0.905	17.03	0.866	15.45	0.795
26.65	0.945	47.47	0.932	32.00	0.864
51.32	0.977	90.12	0.960	61.32	0.907
92.33	0.997			90.01	0.934

Table S1b: Experimental CO_2 loading of aqueous 2 mol/L DEAE solution at different temperature and CO_2 partial pressure.

303.15 K		**313.15 K**		**323.15 K**	
P_{CO2} (kPa)	**Loading** $\left(\frac{molCO_2}{molDEAE}\right)$	**P_{CO2}** (kPa)	**Loading** $\left(\frac{molCO_2}{molDEAE}\right)$	**P_{CO2}** (kPa)	**Loading** $\left(\frac{molCO_2}{molDEAE}\right)$
0.431	0.311	0.556	0.284	0.775	0.236
0.913	0.465	1.104	0.401	1.775	0.365
3.016	0.663	3.378	0.601	5.326	0.560
11.32	0.827	8.904	0.742	12.39	0.705
26.39	0.900	25.45	0.853	31.97	0.834
47.00	0.932	51.35	0.905	62.39	0.890
105.65	0.965	88.32	0.934	84.96	0.914

Table S1c: Experimental CO_2 loading of aqueous 3 mol/L DEAE solution at different temperature and CO_2 partial pressure.

303.15 K		**313.15 K**		**323.15 K**	
P_{CO2} (kPa)	**Loading** $\left(\frac{molCO_2}{molDEAE}\right)$	**P_{CO2}** (kPa)	**Loading** $\left(\frac{molCO_2}{molDEAE}\right)$	**P_{CO2}** (kPa)	**Loading** $\left(\frac{molCO_2}{molDEAE}\right)$
0.568	0.266	0.891	0.218	1.913	0.234
1.258	0.400	1.759	0.338	4.154	0.360
2.154	0.504	2.710	0.419	7.085	0.472
3.533	0.595	4.101	0.503	10.84	0.570
5.326	0.681	9.302	0.653	20.46	0.701
10.70	0.776	19.60	0.769	42.70	0.812
18.39	0.836	39.54	0.849	80.45	0.874
35.77	0.895	63.20	0.886	80.45	0.874
81.34	0.933	85.00	0.905		

Table S1d: Experimental CO_2 loading of aqueous 4 mol/L DEAE solution at different temperature and CO_2 partial pressure.

303.15 K		**313.15 K**		**323.15 K**	
P_{CO2} (kPa)	**Loading** $\left(\frac{molCO_2}{molDEAE}\right)$	**P_{CO2}** (kPa)	**Loading** $\left(\frac{molCO_2}{molDEAE}\right)$	**P_{CO2}** (kPa)	**Loading** $\left(\frac{molCO_2}{molDEAE}\right)$
1.051	0.209	1.904	0.190	3.792	0.178
2.120	0.331	4.021	0.304	8.791	0.301
3.775	0.453	8.934	0.462	15.96	0.425
6.740	0.600	19.00	0.639	28.54	0.578
14.94	0.750	35.90	0.750	60.95	0.751

33.87	0.845	58.44	0.816	90.95	0.813
75.90	0.905	87.26	0.854		

Standard uncertainties u are u(T) = 0.05 K, u(P_1) = 0.031 kPa, u(P_2) = 0.021 kPa, u(P_{CO2}) = 0.021 kPa, and the combined extended uncertainties U are U(mol/L) = 0.001 mol/L, U(α) = 0.026 (95 % level of confidence and coverage factor, k=2).

Table S2: Estimated interaction parameter of activity coefficient model of (DEAE+CO_2+H_2O) system.

Parameters	**β (L/mol)**
$\beta_{CO_2-H^+}$	0.09622
$\beta_{CO_2-DEAEH^+}$	-0.2098
$\beta_{CO_2-OH^-}$	0.094678
$\beta_{CO_2-HCO_3^-}$	0.3105
$\beta_{CO_2-CO_3^{2-}}$	-0.16889
β_{CO_2-DEAE}	0.149557
$\beta_{H^+-OH^-}$	0.094573
$\beta_{H^+-HCO_3^-}$	0.092505
$\beta_{H^+-CO_3^{2-}}$	0.093547
β_{H^+-DEAE}	0.096638
$\beta_{DEAEH^+-OH^-}$	0.095455
$\beta_{DEAEH^+-HCO_3^-}$	0.197521
$\beta_{DEAEH^+-CO_3^{2-}}$	0.230074
β_{OH^--DEAE}	0.481559
$\beta_{HCO_3^--DEAE}$	0.099612

$\beta_{CO_3^{2-}-DEAE}$	-0.18477
$\beta_{CO_2-H^+}$	0.434174

AAD% = 3.34

$$\%AAD = \left|((\alpha_{exp} - \alpha_{cal})/\alpha_{exp})\right| * 100$$

Sentinel 2 Analysis of Turbidity Retrieval Models in Inland Water Bodies: The Case study of Jordanian Dams

Nidal M. Hussein [1,*], Mohammed N. Assaf [2,*] and Sohib S. Abohussein [3]

[1] Department of Civil Engineering, University of Petra, Amman – Jordan, ORCID:0000-0002-4188-7694;
[2] School of Natural Resources Engineering and Management, German Jordanian University, Amman, Jordan, ORCID: 0000-0002-4003-8690 ;
[3] Department of Civil Engineering, University of Petra, Amman –Jordan
***** *Corresponding authors: nidal.hussein@uop.edu.jo; m.assaf@gju.edu.jo ; 201911339@uopstd.edu.jo Tel.:00962795931416.*

Abstract: This study investigates the potential of using Sentinel 2 multispectral satellite images to develop turbidity retrieval models and further estimate the turbidity values of inland water bodies in Jordan. Traditionally, laboratory analysis has been used to assess surface water quality, which is expensive, time-consuming, and needs to access the field physically. In contrast, remote sensing technologies can detect the water contaminant level at a consistent spatial and temporal coverage. Turbidity is an essential indicator of inland water quality as it directly reflects underwater light penetration. This study was held in three Jordanian dams, King Talal Dam, Mujib Dam, and Wadi Al Arab dam, which vary in their water quality level. Twenty water samples were collected from each dam. Forty samples were used to calibrate the models, and the rest samples were used to validate the predictive models. The results show that Sentinel 2 near-infrared band to green band (B8/B3) achieved high fitting accuracies with R^2 = 0.832 and root mean square error (RMSE) = 1.123 NTU.Overall, this study has demonstrated the ability of Sentinel 2 data to estimate the turbidity in different ranges of inland water bodies quality and indicate that remote sensing can be used as an efficient tool for monitoring inland water quality. This study presents empirical data that could act as a platform to extend future work to cover more sites and contexts.

Keywords: Sentinel 2; Inland water; Turbidity; Jordan

1. Introduction

Inland waters in Jordan can be determined as a significant source for drinking and irrigation purposes. Surface water can mainly be described as rivers, dams, and reservoirs that symbolize tremendous significance to the valued environmental components (VECs). In general, it plays an essential role in providing a suitable environment for species.

They are also considered an integral element in hydrological, climate regulation, carbon cycle, and nutrient cycle. However, Jordan is dealing with a critical and severe shortage of clean water to provide a healthy and suitable environment for species. The reason behind this current massive shortage is because of the fast-growing population. The rise in the population rate in Jordan is linked with the ongoing conflicts in neighboring countries, which resulted in people migrating and taking refuge in Jordan. Statistics shared by the Ministry of Water and Irrigation show that 50% of water usage between 2008-2017 is closely linked with domestic purposes than any form of water usage [1].

According to recent studies and considering the gross domestic product (GPD) as a representation for countries' wealth and a factor for comparison, it shows that the Kingdom of Jordan is the 3rd place globally as the water poorest country in the world, and second-lowest country in the Middle East [2].

Current statistics show that the water per capita is less than one-tenth of the international water poverty line of 1,000 cubic meters annually [2]. The Pressure that the kingdom of Jordan is dealing with is tremendous and caused the kingdom to lose much more water in these recent years. However, Jordan's kingdom has shown a significant effort to integrate treating wastewater into the water budget.

Recent studies show that a massive portion of the country's inland water bodies has been mixed with treated water leaving the country's 34 wastewater treatment plants as of 2020 [3]. Treated wastewater from many treatment plants is discharged into dams and been released later to irrigate significant parts of Jordan valley.

Climate change is viewed as one of the principal challenges that amount to Jordan's water . In recent years, the kingdom of Jordan has been dealing with serious and essential issues of climate change consequences including shifting in precipitation patterns, shortage in the rainfall season, and temperature rise, which lead to an expansion in the water surface's evaporation rate [4]

A different source of pollution has been exposed to water bodies. Consequently, escalated water-quality checking of inland water bodies and water storage facilities that give reliable, consistently refreshed water-quality data for a superior water area the board turns into a significant commitment that the nation needs to meet successfully. It turns out to be much more meaningful because of the current water situation circumstance in Jordan and the various employments of putting away surface water covering a broad scope of areas including, yet not restricted to, homegrown, water system, and mechanical applications

Inland water shows high affectability and capacity to reflect ecological changes, for example, environmental change, land cover, and land uses [5]. Constant observing such changes and examples successfully and proficiently is of extreme significance [6-10]. Satellite distant detecting procedures are characterized as a strategy that gauges geophysical boundaries from the electromagnetic energy reflected or produced from the earth [11]. In light of water's optical properties, because of the presence of optically dynamic constituents, remote sensing has an extraordinary potential to be utilized for water-quality checking, particularly for Jordan with quite a severe level of its water vulnerable bodies.

Water remote detecting depends on the watercolor perception right away without taking water tests. It relates watercolor quantitatively to specific constituents that collaborate with sun-powered radiation and change the energy range of reflected radiation from water bodies. These constituents are alluded to as optical water-quality boundaries. Three unique methodologies can be utilized in distant detecting estimations to gauge water constituents' focuses [12].

Remote sensing methods have been generally used to gauge the subjective boundaries of water bodies. Gholizadeh et al. recorded eleven water-quality boundaries that can be estimated by remote sensing strategies [13]. These boundaries are turbidity, chlorophyll-a (Chl-a), colored dissolved organic matters (CDOM), Secchi disk depth (SDD), turbidity, complete suspended dregs (TSS), water temperature (WT), total phosphorus (TP), Sea surface saltiness (SSS), dissolved Oxygen (DO), biochemical oxygen interest (BOD), and compound oxygen interest (COD).

Even though the water remote technique has been widely recognized for its technicality and great potentials, its uses in remote sensing have only begun to be recognized in the early 1970s. The early endeavours of utilizing this strategy zeroed in on spectral and thermal estimations of reflected energy from ocean and inland water bodies surfaces. Experimental connections were created between the spectral properties and the water body's water-quality boundaries [14]. Pionke and Blanchard and Ritchie et al. explored the relationship of reflected sun-oriented radiation and dregs' grouping in supplies' surface water.

They built up an observational way to decide suspended silt utilizing this strategy [15, 16]. Dekker et al. utilized far-off airborne detecting for three shallow lakes with shifted trophic levels [17]. Wynne et al. evaluated lake ice separation patterns by observing ice phenology as an atmosphere pointer where satellite-inferred separation dates were contrasted and accessible ground information [18]. Latifovic and Pouliot introduced another strategy for extricating lake ice phenology occasions of 36 lakes from verifiable long-haul satellite records procured by the arrangement of cutting-edge sensors [9].

Jeffries et al. and, Gholizadeh et al. research gave a complete survey on distant observing strategies and applications for lakes and waterways [13, 19]. Scarcely any endeavors were taken in Jordan in the region of remote detecting.

As of late, Avisse et al. proposed a methodology that utilizes Landsat symbolism and digital elevation model (DEMs) to get information on Yarmouk bowl stockpiling amount varieties in an

inaccessible outskirt territory among Jordan and Syria where the common Syrian war hinders ground checking.

Their empirical data were approved against accessible in situ estimations in neighboring Jordanian supplies [8]. Al-Bakri et al. research introduced a case from Jordan, where geospatial strategies were used for water system water evaluation. Their work was restricted to surveying groundwater deliberation records comparable to inundated zones and assessed crop water utilization in three water bowls, for example, Yarmouk, Amman-Zarqa, and Azraq. Planning of flooded zones and harvest water prerequisites was done utilizing Landsat 8 images and day-by-day climate records [20].

This research aims at evaluating the utilization of the emerging multispectral image techniques monitoring turbidity. Studies show that a high concentration of turbidity particles can lead to a massive disaster to water quality and clarity. It can also be dangerous for fish and other aquatic organisms to breathe or damage their gills [21-23].

Utilizing the emerging multispectral image technique monitoring turbidity has become a useful tool to determine the turbidity's concentration and suspended particulate matter in water. Recent studies have shown the value of using remote sensing for water quality analysis to capture a whole study area's synoptic data to produce continuous surface data, often showing detailed spatial variability in water quality [24-27].

. The investigation will eventually prompt building up a numerical model fit for foreseeing turbidity concentration without the need for in situ measurement and enabling remote monitoring of turbidity concentrations of distributed inland water bodies across the kingdom of Jordan. In this recent study, multispectral satellite images (Sentinel 2) have been provided by European Space Agency institutions to structure this study's purpose. In general, the result behind this research will give us the prevailing tool to water administration agency.

2. Materials and Methods

2.1 Study area's

For this examination, three dams have been chosen for investigation. The initial two dams are situated up north of the capital city of Jordan – Amman. Al Arab (WAD) and King Talal (KTD) dam, and the third dam is situated down south of Amman called Mujib dam (MD), as demonstrated in figure 1

The reason for choosing these dams is their essential role in the Jordanian water -sector, likewise, due to the importance of their geographic location and the variation of their water quality in turbidity concentration.

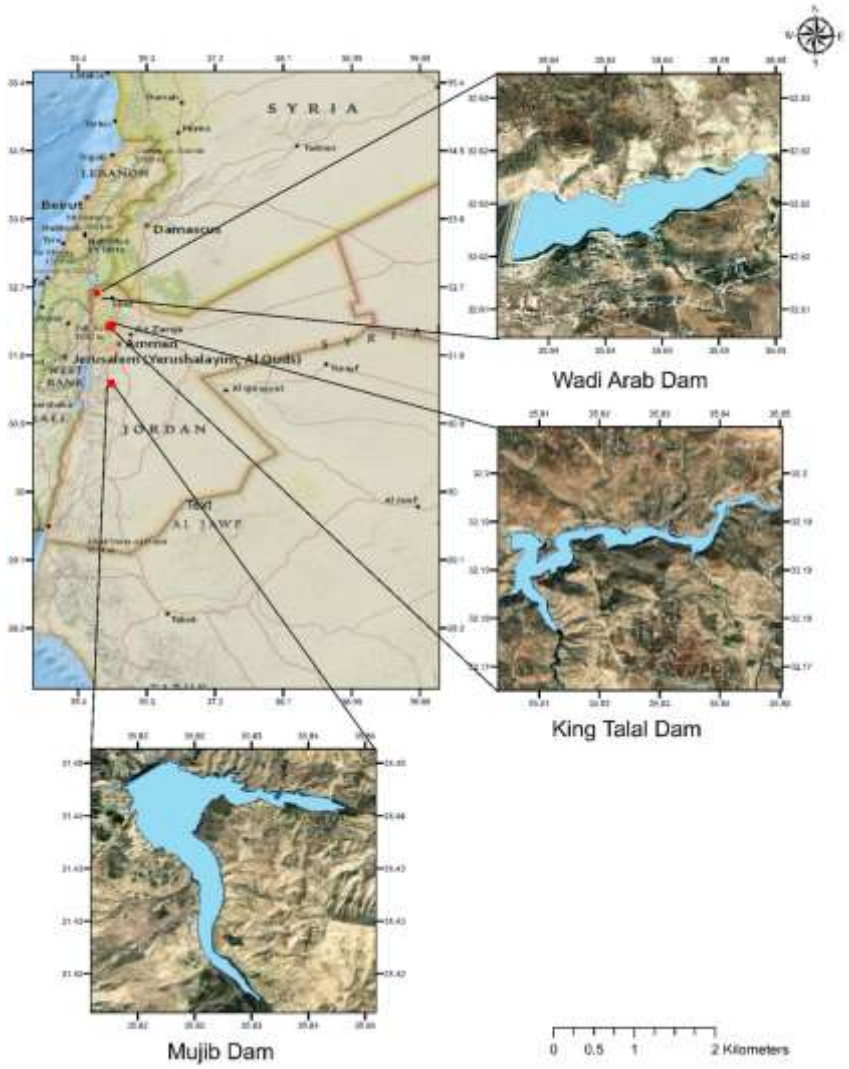


Figure 1: Dams' locations [24]

2.2 Water Sampling and analysis

Sixty water samples were gathered from these three dams. From areas distributed through, 20 examples were taken from King Talal Dam, 20 examples from Mujib dam, and 20 from Wadi al Arab dam. Water samples were gathered around 20 cm beneath the water surface. They were contained in cleaned bottles, which were transferred to analysis to the University of Petra (UOP) research facility, Amman, Jordan. The sampling points' distribution of each dam is shown in Figures 2-4. The collected water samples were analyzed using Turbidity Meter Model TB 210 IR. Each of these samples was tested using a turbidity meter three times to find the average value.

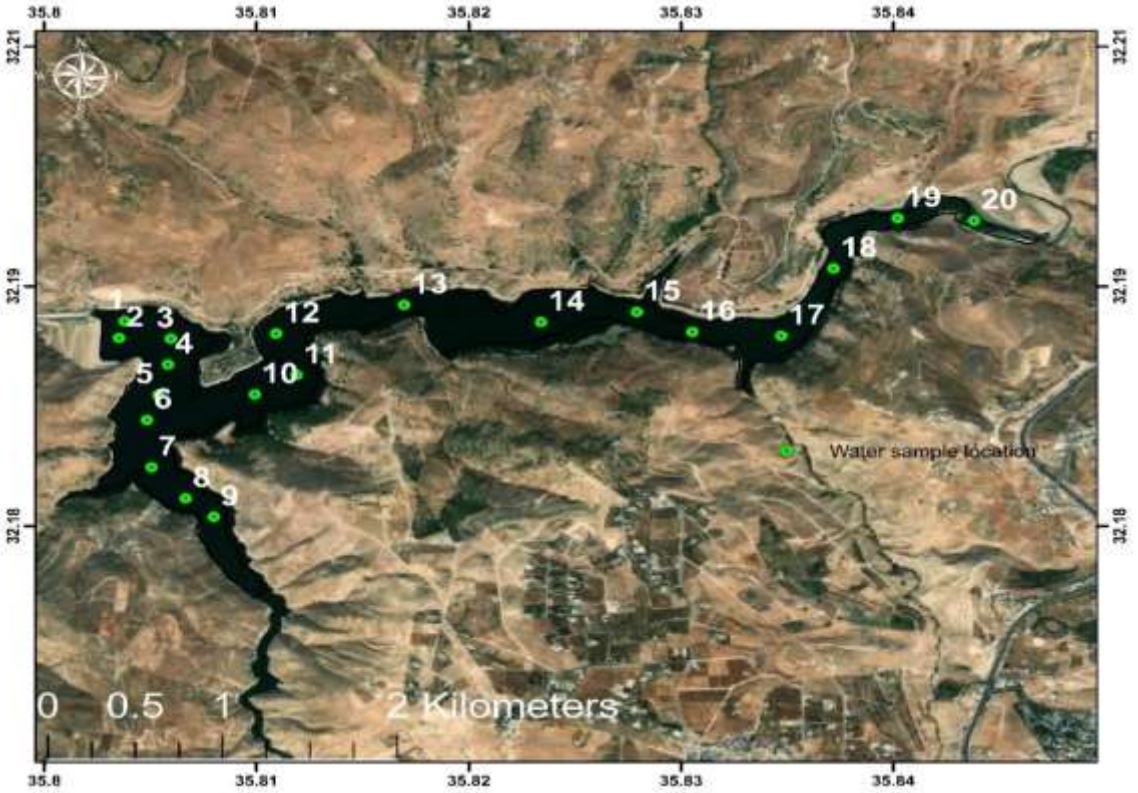


Figure 2: Sampling points distribution of king Talal dam**.**

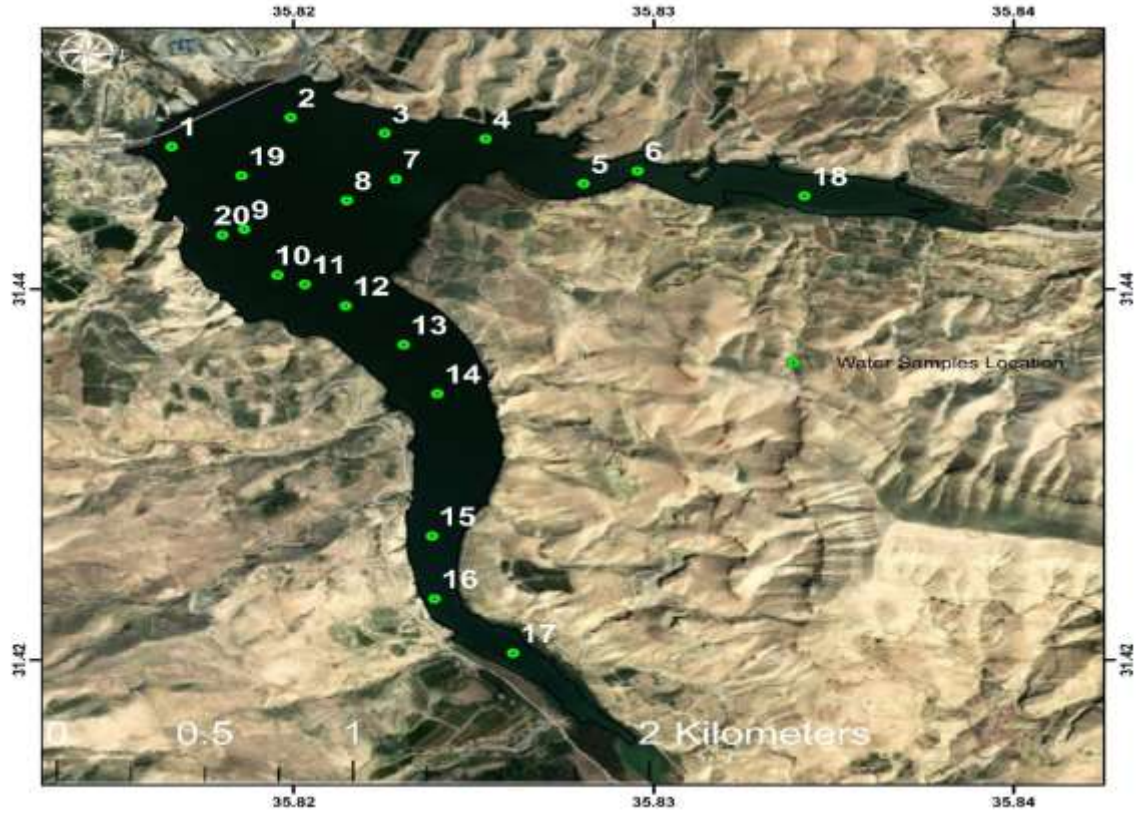


Figure 3: Sampling points distribution of Mujeb dam.

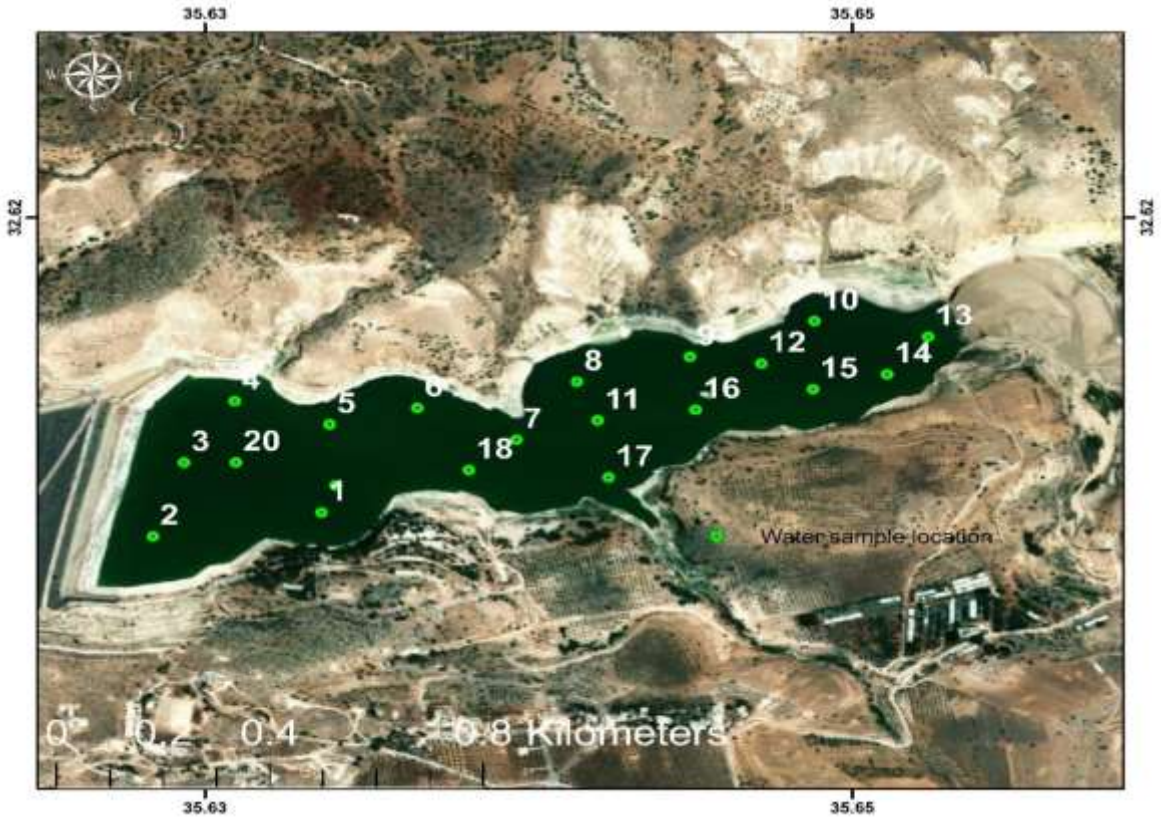


Figure 4: Sampling points distribution of Wadi Al-Arab dam

2.3 Algorithms for Turbidity Estimation

Turbidity presences in water responded with changes in optical water properties; based on that, the remote sensing algorithms can detect the turbidity concentration in water. Several researchers have used single band algorithms and two-band ratio algorithms to developed turbidity retrieval models. For the single band algorithms, the widely used algorithms are near-infrared (NIR) [28, 29] and red [30, 31]. Two-band ratio algorithms used the ratio between green and red [32-34], blue and red [35], NIR and Vegetation Red-Edge [36], and NIR and red [37]. In this work, the previously developed algorithms found in the literature were adopted to the corresponding Sentinel 2 bands.

3. Results and Discussion

Table 1-3 show measurement values for the turbidity concentration of samples that have been collected from King Talal dam, Wadi al Mujib, and Wadi al Arab. The spatial distribution of turbidity concentrations through the three dams are presented in figure 5-7.

Table 1: Turbidity concentration and corresponding sampling points' coordinates of samples collected from King Talal Dam (KTD).

Visit Data / **15/7/2019**	**Dam Name: King Talal Dam**		
site	Latitude	Longitude	Turbidity (NTU)
1	32.191214	35.802659	6.87
2	32.19017	35.802359	6.9
3	32.190125	35.80503	7.02
4	32.188527	35.80488	7.29
5	32.186657	35.804386	7.4
6	32.185104	35.803796	6.32
7	32.182171	35.804032	6.41
8	32.180246	35.805792	5.18
9	32.179102	35.80724	4.92
10	32.186675	35.809343	4.56
11	32.187883	35.811499	5.72
12	32.190443	35.810448	6.2
13	32.192213	35.817026	8.27
14	32.192267	35.820534	7.48
15	32.19115	35.824075	5.91
16	32.191776	35.829	9.74
17	32.190541	35.831865	8.11
18	32.190302	35.836436	8.95
19	32.19446	35.839118	8.56
20	32.197574	35.842423	9.26

Table 2: Turbidity concentration and corresponding sampling points' coordinates of samples collected from the Mujeeb Dam (MD).

Visit Data / **30/6/2019**	**Dam Name: Mujib**		
site	Latitude	Longitude	Turbidity (NTU)
1	31.443241	35.816654	1.66
2	31.444401	35.820263	1.2
3	31.443779	35.823117	1.31
4	31.44355	35.826175	1.2
5	31.441765	35.829147	1.38
6	31.442268	35.830789	1.32
7	31.441938	35.82345	1.37
8	31.441087	35.821969	1.61
9	31.439934	35.818858	1.04
10	31.438103	35.819867	2.75
11	31.437737	35.820693	1.83
12	31.436877	35.821938	2.83
13	31.435321	35.823697	1.26
14	31.433362	35.824716	1.1
15	31.427677	35.824555	1.31
16	31.425169	35.82463	1.11
17	31.422999	35.827012	1.11
18	31.441271	35.835853	1.09
19	31.442076	35.818773	1.63
20	31.439705	35.818194	1.33

Table 3: Turbidity concentration and corresponding sampling points' coordinates of samples collected from Wadi Al Arab.

Visit Data	Dam Name: Wadi Al Arab		
30/6/2019			
site	Latitude	Longitude	Turbidity (NTU)
1	32.617107	35.636684	2.79
2	32.616618	35.633839	2.42
3	32.618131	35.634364	3.09
4	32.619388	35.63522	3.19
5	32.618911	35.636822	2.7
6	32.619248	35.6383	2.59
7	32.618596	35.639972	2.84
8	32.619783	35.640994	3.01
9	32.620295	35.6429	3.72
10	32.621028	35.645	2.95
11	32.621993	35.648343	3.27
12	32.621272	35.648495	2.75
13	32.620707	35.646919	2.82
14	32.619935	35.646227	3.56
15	32.61963	35.644977	3.16
16	32.619212	35.642995	3.25
17	32.617827	35.641528	3.53
18	32.617977	35.639169	2.71
19	32.617667	35.636925	2.96
20	32.618134	35.635241	3.1

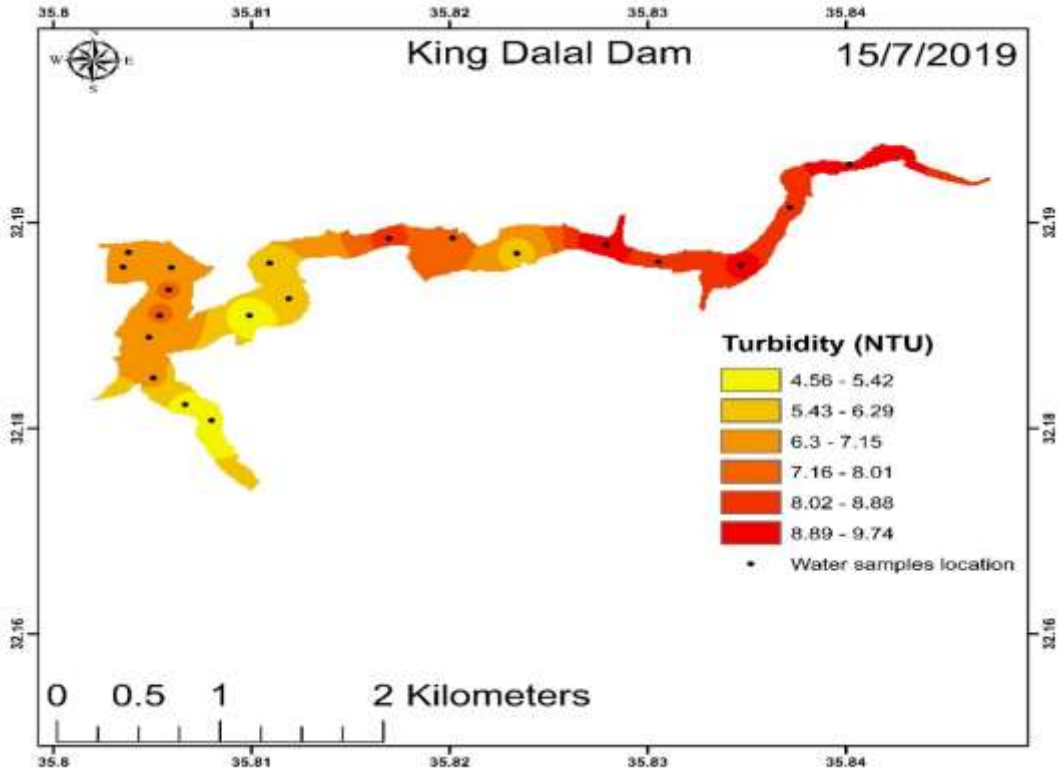


Figure 5: Spatial distribution of turbidity over KTD

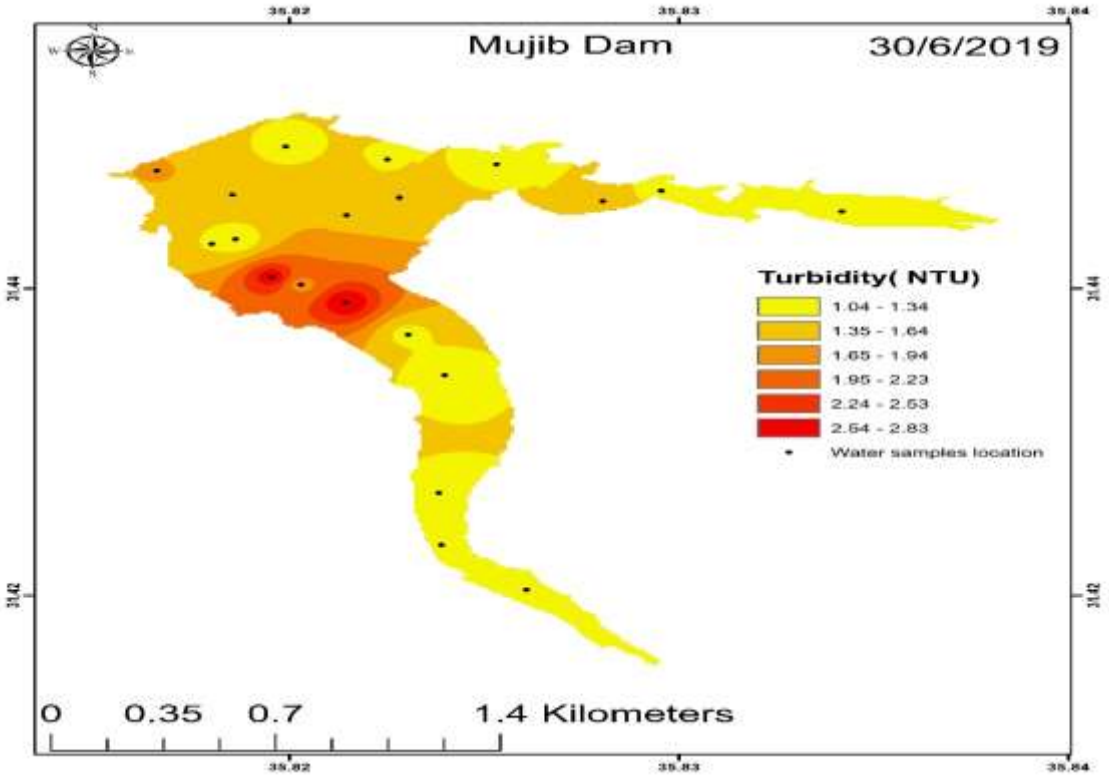


Figure 6: Spatial distribution of turbidity over Mujib dam

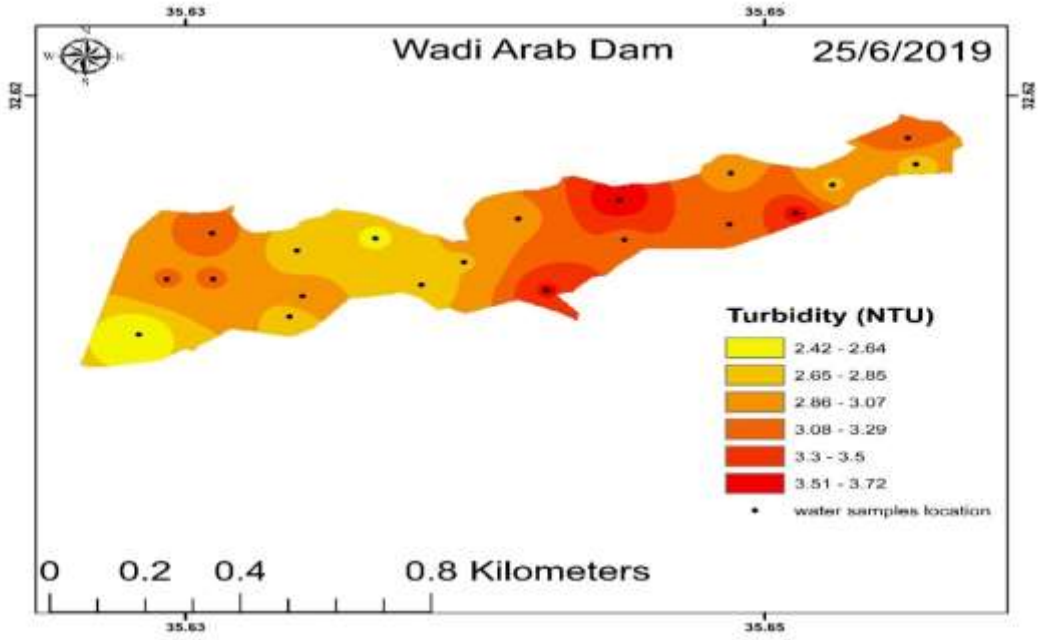


Figure 7: Spatial distribution of turbidity over Wadi Al Arab dam

4. Result Analysis and Discussion

4.1. Sentinel 2 Image Processing

To survey and explore the water quality in inland waters, Sentinel 2 satellite symbolisms were picked. Sentinel two pictures were gathered from Copernicus Open Access Hub (https://scihub.copernicus.eu) by the European Space Agency. Those photographs were taken on a similar field visit date and were collected as Level 1 C MAI data

Table 4: Sentinel 2 images used for algorithm development

Location	Sampling Date	Acquisition Date of Sentinel 2 image	Cloud cover	Number of samples
KTD	2019-07-15	2019-07-15	1.4111	20
Mujeeb	2019-06-30	2019-06-30	1.3674	20
Wadi Al Arab	2019-06-25	2019-06-25	0.0018	20

The data of L1C has been given as a digital number that can be represented as top-of-atmosphere (TOA) reflectance with 60, 20, and 10 m bands resolution, as shown in table 5. For band analysis consistency, the Sentinel Application Platform (SNAP) version 6.0 has been used to resampled the image bands to 20 m resolution using.

Table 5: Sentinel 2 spectral bands, spatial resolution, band range, and central wavelength at reference radiance used in this study

Band (spatial resolution)	Band range (nm)	Central wavelength (nm)
Band 1 coastal/aerosol (60 m)	421–457	443
Band 2 blue (10 m)	439–535	490
Band 3 green (10 m)	537–582	560
Band 4 red (10 m)	646–685	665
Band 5 VRE (20 m)	694–714	705
Band 6 VRE (20 m)	731–749	740
Band 7 VRE (20 m)	768–796	783
Band 8 NIR (10 m)	767–908	842
Band 8a NIR (20 m)	858–881	865
Band 9 WV (60 m)	931–958	945
Band 10 cirrus (60 m)	1338–1414	1375
Band 11 SWIR (20 m)	1539–1681	1610
Band 12 SWIR (20 m)	2072–2312	2190

As commonly known, TOA reflectance can significantly get affected by atmospheric conditions, leading to confusion and uncertainty in satellite data. Therefore, it's essential to run atmospheric correction protocol correction to accurately estimate the surface reflectance. One of the most used atmospheric correction models is the Atmospheric and Topographic Correction (ATCOR), which is used to convert the TOA data to remote sensing reflectance (Rrs). For the cause of this research, PCI Geomatica (2017) (ATCOR based) software has been used to prevent any issues that can lead to any miss leading data and eliminate terrain and atmospheric effects.

4.2. Algorithm Development

In this investigation, georeferenced turbidity values that are collected from the three dams and the corresponding pixels data Sentinel 2 satellite were employed to produce a predictive turbidity model. The sixty water samples that have been collected from three dams (Wadi Al-Arab Dam, King Talal Dam, and Mujib Dam) were divided into sets (40 points for calibration and 20 points for validation). The turbidity algorithms discovered in the literature were adopted to Sentinel-2 bands to create configurations using one or two-band ratios.

The performance of top-fitting regressions models between the bands' index with turbidity measured values is shown in figure 8-10. The near-infrared to green band ratio produced the best performing model (R^2= 0.854) using the exponential function.

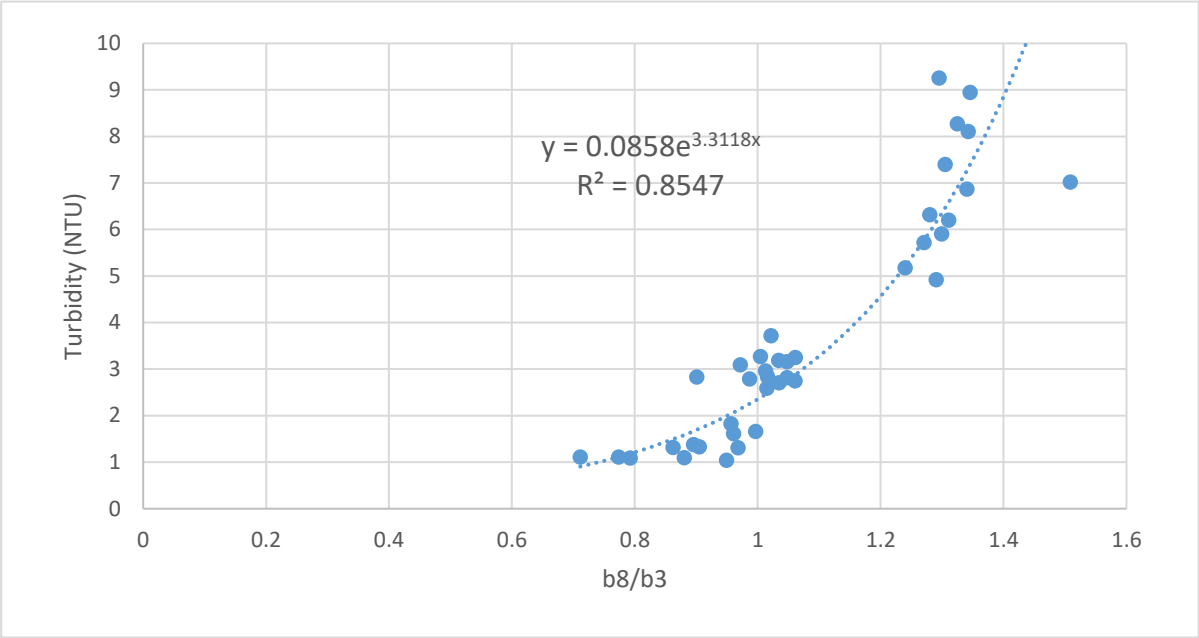


Figure 8: Regression between the Sentinel 2 band index (b8/b3) and measured turbidity**.**

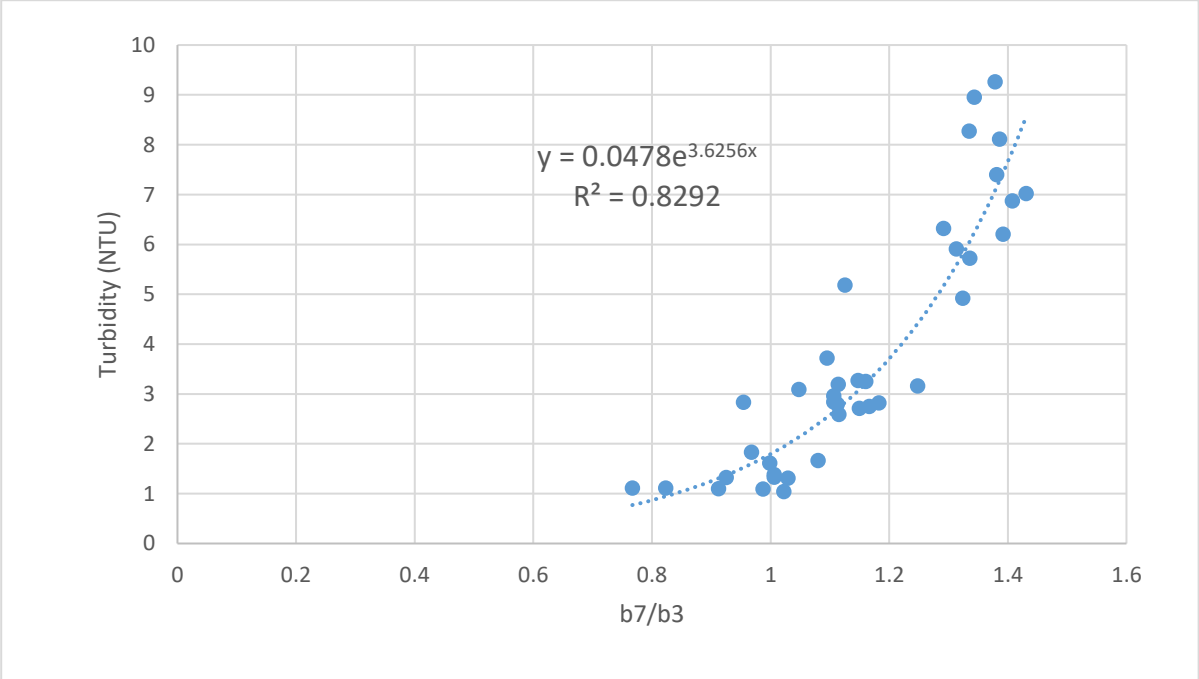


Figure 9: Regression between the Sentinel 2 band index (b7/b3) and measured turbidity.

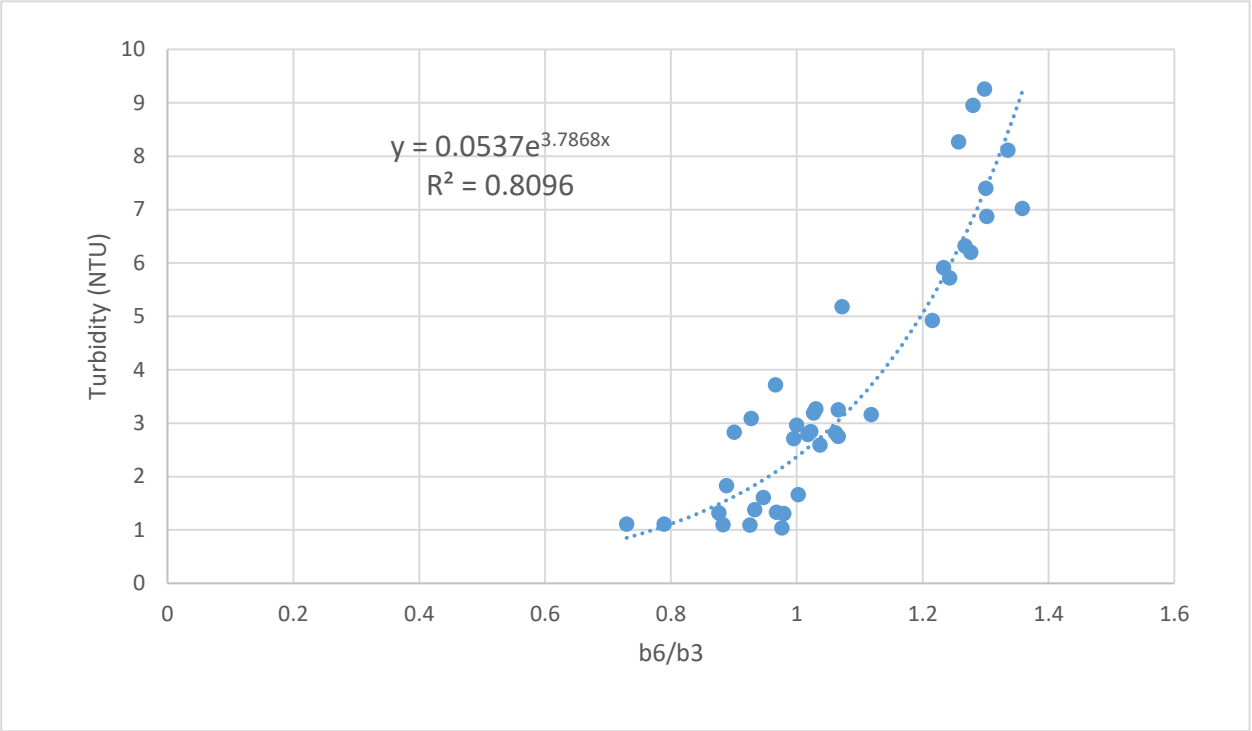


Figure 10: Regression between the Sentinel 2 band index (b6/b3) and measured turbidity.

4.3. Algorithm Validation

The validation data set, which consisted of (20) samples, was used to evaluate the calibrated models' predictive capacities indicated above. The bases for evaluation relied on the four statistical parameters; mainly determination coefficient (R^2), root mean square error (RMSE), mean absolute error (MAE), and bias values. The validation results also indicated that two bands ratio (b8/b3) was provided the best performance through the four selected statistical parameters. The predictive performance of the three calibrated models is presented in table 6. The differences between the predicted and measured turbidity concentration of the three calibrated models are illustrated in Figures 11-13.

Table 6: Validation results of Sentinel 2 turbidity models

Index	Equation	R^2	RMSE	MAE	bias
B8/B3	y = 0.0858e3.3118x	0.832	1.123	0.920	0.301
B3/B8	y = 0.0478e3.6256x	0.621	1.712	1.056	0.031
B6/B3	y = 0.0537e3.7868x	0.621	1.794	1.166	0.083

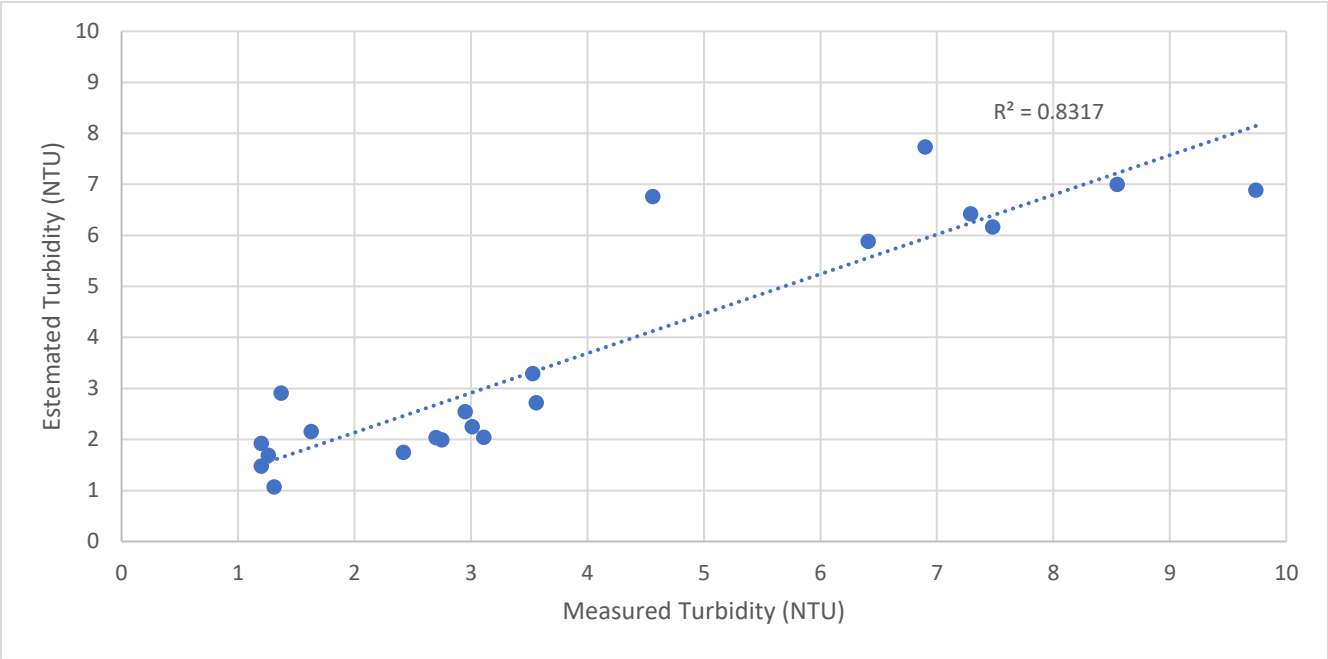


Figure 11: Regression between predicted and measured turbidity using the B8/B3 model

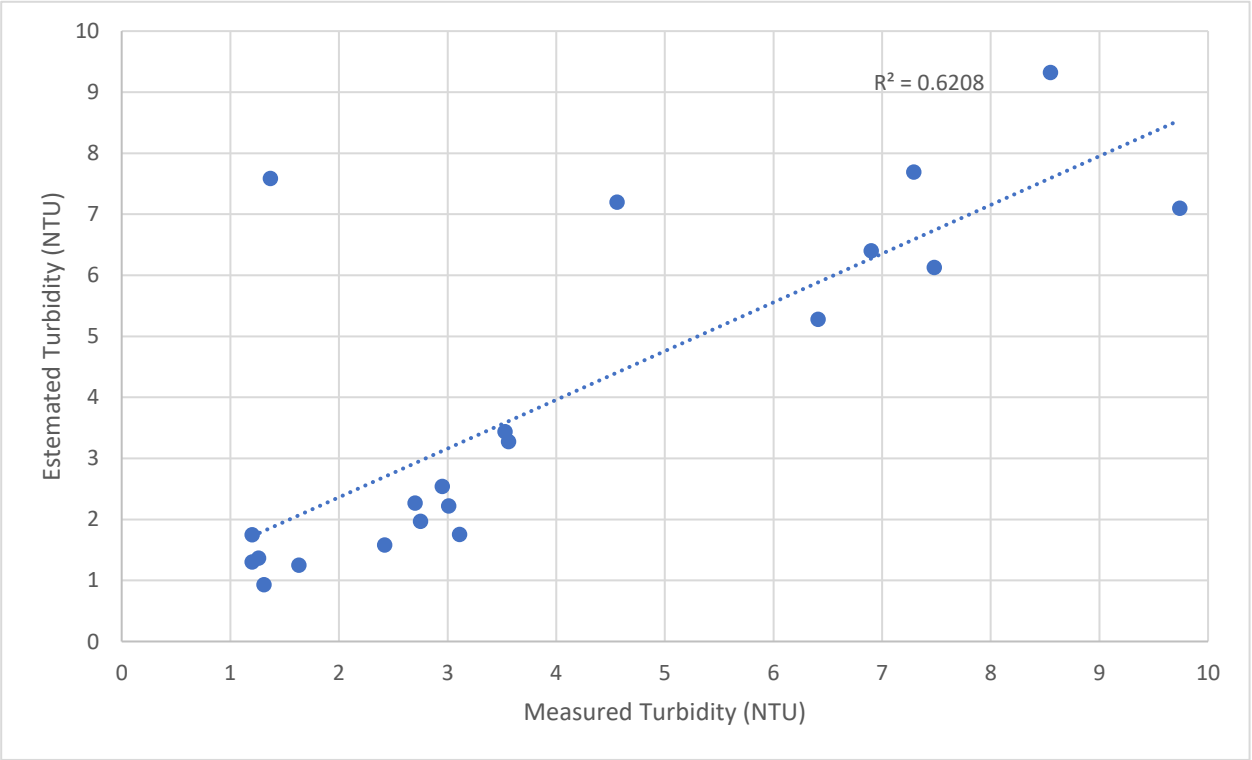


Figure 12: Regression between predicted and measured turbidity using the B3/B8 model

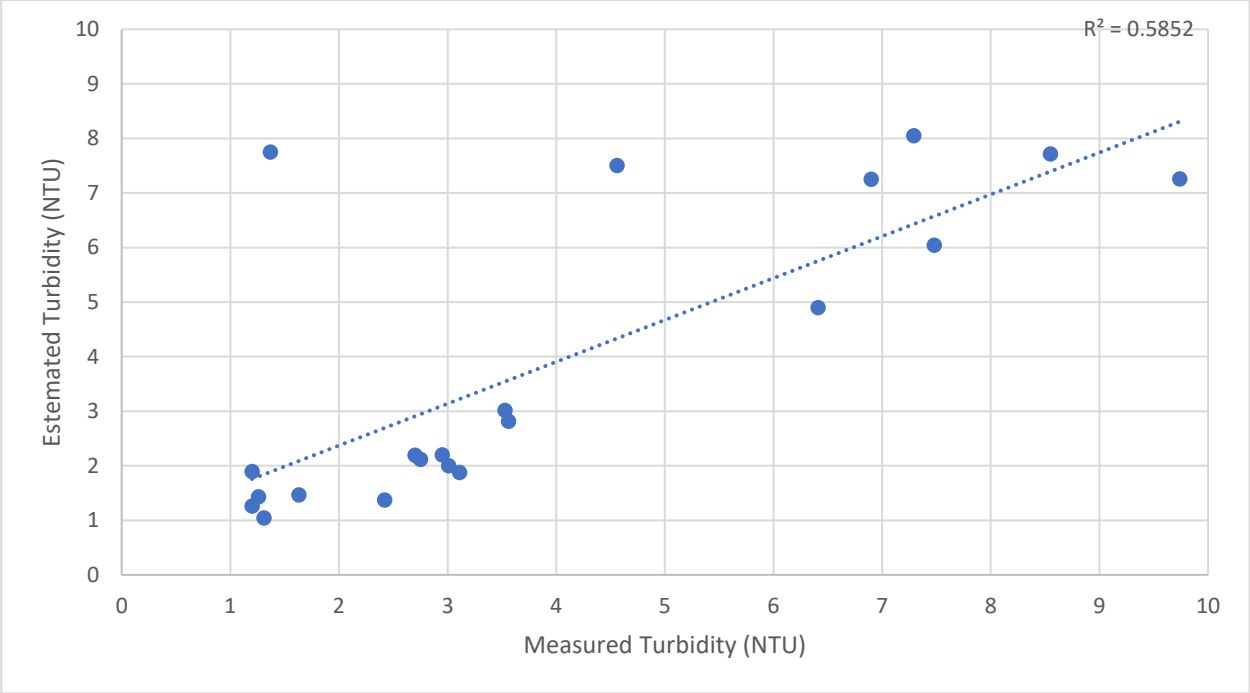


Figure 13: Regression between predicted and measured turbidity using the B6/B3 model

Two-band models have shown a substantially greater predictive ability for turbidity concentration using exponential functions. Accordingly, turbidity concentrations with the highest R2 value and the lowest mean absolute error (RMSE) were successfully predicted by the B8/B3 model (R^2 = 0.832, RMSE = 1.123 NTU).

4. Conclusions

In this research, the same-empirical model methodology was applied to construct a turbidity concentration predictive model by testing and analyzing several band-based algorithms using Sentinel 2 images in inland water. Sixty water samples were collected from three different dams in Jordan, King Talal dam, Wadi al Arab Dam, and Mujib dam. These dams have different water quality properties and massive variations in turbidity concentration. The turbidity concentration range between 2.79-3.1(NTU) in Wadi Al Arab dam, 1.66 - 1.33 (NTU) in Mujeeb dam, and finally 6.87-9.26 in King Talal Dam. To build the predictive model, about two-thirds of the samples were used for the calibration. The remaining sampling was used to validate the created models' performance by comparing the measured field data with the predicted data from developed algorithms. The determination coefficient (R^2) and the lowest root mean square error (RMSE) values have been used to estimate the predictive models capability.

One band algorithms, two-band ratios algorithm, and three-band ratios algorithm have been tested to determine the best fit model. The near-infrared to green (B8/B3) model's exponential function has shown the top fitting performance (R^2 = 0.832, RMSE = 1.123 NTU). The output results of this research appearance that Sentinal 2 data can be used efficiently to evaluate and monitor the turbidity concentrations in inland water bodies over a wide range of water quality.

Acknowledgments: authors would like to thank the Deanship of Scientific Research and Graduate Studies at University of Petra (grant no. 3/7/2019).

References

1. Jordan Water Sector Facts & Figures, 2017. 2017, Ministry of Water and Irrigation Amman, Jordan.
2. WATER MANAGEMENT INITIATIVE Review of Water Scarcity Ranking Methodologies. 2017, United States Agency for International Development Amman, Jordan.
3. Saidan, M.N., et al., Wastewater reclamation in Major Jordanian industries: a viable component of a circular economy. Water, 2020. 12(5): p. 1276.
4. Water Resources in Jordan: A Primer 2010, Water Resources Management Division Department of Environment and Conservation Government of Newfoundland and Labrador
5. Carpenter, S.R., et al., Understanding regional change: a comparison of two lake districts. Bioscience, 2007. 57(4): p. 323-335.
6. Duan, H., et al., Comparison of different semi-empirical algorithms to estimate chlorophyll-a concentration in inland lake water. Environmental monitoring assessment, 2010. 170(1-4): p. 231-244.
7. Hadjimitsis, D.G. and C. Clayton, Assessment of temporal variations of water quality in inland water bodies using atmospheric corrected satellite remotely sensed image data. Environmental monitoring assessment 2009. 159(1-4): p. 281.
8. Avisse, N., et al., Monitoring small reservoirs' storage with satellite remote sensing in inaccessible areas. Hydrology Earth System Sciences, 2017. 21(12).
9. Latifovic, R. and D. Pouliot, Analysis of climate change impacts on lake ice phenology in Canada using the historical satellite data record. Remote Sensing of Environment, 2007. 106(4): p. 492-507.
10. Chance, E., K. Cobourn, and V. Thomas, Trend detection for the extent of irrigated agriculture in Idaho's Snake river plain, 1984–2016. Remote Sensing, 2018. 10(1): p. 145.
11. Pielke Sr, R.A., Mesoscale Modeling and Satellite Simulator, in International Geophysics. 2013, Elsevier. p. 407-426.
12. Morel, A.Y. and H.R. Gordon, Report of the working group on water color. Boundary-Layer Meteorology, 1980. 18(3): p. 343-355.
13. Gholizadeh, M.H., A.M. Melesse, and L. Reddi, A comprehensive review on water quality parameters estimation using remote sensing techniques. Sensors, 2016. 16(8): p. 1298.
14. Ritchie, J.C., P.V. Zimba, and J.H. Everitt, Remote sensing techniques to assess water quality. Photogrammetric Engineering Remote Sensing 2003. 69(6): p. 695-704.
15. Pionke, H. and B. Blanchard, The remote sensing of suspended sediment concentrations of small impoundments. Water, Air, Soil Pollution, 1975. 4(1): p. 19-32.
16. Ritchie, J.C., et al., relationship of reflected solar radiation and the concentration of sediment in the surface water of reservoirs. Remote sensing of earth resources, 1975.
17. Dekker, A., et al., Remote sensing, ecological water quality modelling and in situ measurements: a case study in shallow lakes. Hydrological sciences journal, 1996. 41(4): p. 531-547.
18. Wynne, R.H., et al., Satellite monitoring of lake ice breakup on the Laurentian Shield (1980-1994). Photogrammetric Engineering Remote Sensing, 1998. 64(6): p. 607-617.
19. Jeffries, M.O., K. Morris, and N. Kozlenko, Ice Characteristics and Processes, and Remote Sensing. Remote Sensing in Northern Hydrology: measuring environmental change, 2005: p. 63.
20. Al-Bakri, J., et al., Geospatial techniques for improved water management in Jordan. Water, 2016. 8(4): p. 132.
21. Irigoien, X. and J. Castel, Light limitation and distribution of chlorophyll pigments in a highly turbid estuary: the Gironde (SW France). Estuarine, Coastal Shelf Science, 1997. 44(4): p. 507-517.
22. Fabio, N., N. Simona, and G. Francis, Turbidity retrieval and monitoring of Danube Delta watersusing multisensory optical remote sensing data: An integrated view from the delta plain lakes to the western–northwestern Black Sea coastal zone. Remote Sensing of Environment, 2013. 132(6): p. 86-101.
23. Baughman, C.A., et al., Reconstructing turbidity in a glacially influenced lake using the Landsat TM and ETM+ surface reflectance climate data record archive, Lake Clark, Alaska. Remote Sensing, 2015. 7(10): p. 13692-13710.
24. Hussein, N.M. and M.N. Assaf, Multispectral Remote Sensing Utilization for Monitoring Chlorophyll-a Levels in Inland Water Bodies in Jordan. The Scientific World Journal, 2020. 2020.

25. Ouma, Y.O., et al., Estimation of reservoir bio-optical water quality parameters using smartphone sensor apps and Landsat ETM+: review and comparative experimental results. Journal of Sensors, 2018. 2018.
26. Ouma, Y.O., K. Noor, and K. Herbert, Modelling Reservoir Chlorophyll-a, TSS, and Turbidity Using Sentinel-2A MSI and Landsat-8 OLI Satellite Sensors with Empirical Multivariate Regression. Journal of Sensors, 2020. 2020.
27. Assaf, M.N., Utilizing Landsat 8 and Sentinel 2 Satellites Images for Water Quality Evaluation in King Tala Dam. 2019, German Jordanian University.
28. Koponen, S., et al., A case study of airborne and satellite remote sensing of a spring bloom event in the Gulf of Finland. Continental Shelf Research, 2007. 27(2): p. 228-244.
29. Kallio, K., et al., Retrieval of water quality from airborne imaging spectrometry of various lake types in different seasons. Science of the Total Environment, 2001. 268(1-3): p. 59-77.
30. Miller, R.L. and B.A. McKee, Using MODIS Terra 250 m imagery to map concentrations of total suspended matter in coastal waters. Remote sensing of Environment, 2004. 93(1-2): p. 259-266.
31. Quang, N.H., et al., Spatiotemporal variation of turbidity based on landsat 8 oli in cam ranh bay and thuy trieu lagoon, vietnam. Water, 2017. 9(8): p. 570.
32. Wang, F., et al., Applications of Landsat-5 TM imagery in assessing and mapping water quality in Reelfoot Lake, Tennessee. International Journal of Remote Sensing, 2006. 27(23): p. 5269-5283.
33. Somvanshi, S., et al., Integrated remote sensing and GIS approach for water quality analysis of Gomti river, Uttar Pradesh. International Journal of Environmental Sciences, 2012. 3(1): p. 62.
34. Akbar, T., Q. Hassan, and G. Achari, A remote sensing based framework for predicting water quality of different source waters. The International Archives of Photogrammetry, Remote Sensing Spatial Information Sciences 2010. 34: p. 1-4.
35. Remote sensing methods for lake management: A guide for resource managers and decision-makers. 2009: North American Lake Management Society.
36. Sakuno, Y., et al., Evaluation of unified algorithms for remote sensing of chlorophyll-a and turbidity in lake shinji and lake nakaumi of Japan and the vaal dam reservoir of South Africa under eutrophic and ultra-turbid conditions. Water, 2018. 10(5): p. 618.
37. Bhatti, A.M., et al., Assessing the potential of remotely sensed data for water quality monitoring of coastal and inland waters. 2008.

Pyrolysis of High-Density Polyethylene: II. Artificial Neural Networks Modeling

Ibrahim Dubdub [1,*], Mohammed Al-Yaari [2]

[1] Chemical Engineering Department, King Faisal University, P.O. Box 380, Al-Ahsa 31982, Saudi Arabia; idubdub@kfu.edu.sa
[2] Chemical Engineering Department, King Faisal University, P.O. Box 380, Al-Ahsa 31982, Saudi Arabia; malyaari@kfu.edu.sa
***** *Corresponding author: idubdub@kfu.edu.sa; Tel.: 00966135896989.*

Abstract: Due to its powerful performance to predict efficiently different experimental data, developing an efficient artificial neural network (ANN) model has attracted the attention of many researchers to be used for variety of engineering applications. In this work, an ANN model was efficiently developed to predict the pyrolysis of high-density polyethylene (HDPE) under nitrogen environment at different heating rates (5, 10, 20, and 40 K/min) covering the temperature range of 300–900 K using thermogravimetric analyzer (TGA) data. A feed-forward back-propagation model, with tansig-tansig transfer function, was recommended to be used to predict the weight loss % (output parameter) during the pyrolysis of HDPE. The model input variables include heating rate (K/min) and temperature (K). The optimum architecture of the model has 10 neurons in two hidden layers. Results showed an excellent agreement between the experimental and the predicted weight loss % values with a correlation coefficient (R=1). In addition, to validate the proposed model, a highly efficient performance was reported when the proposed model was simulated using new input data (R=0.99962).

Keywords: Pyrolysis; high-density polyethylene (HDPE); Artificial Neural Network (ANN); Thermogravimetric Analysis (TGA)

1. Introduction

Artificial neural networks (ANN) modeling has attracted the attention of researchers because of its highly-efficient performance to predict or forecast data that are expensive to be collected. ANN modeling is currently used for variety of engineering applications. One of these applications, ANN models can be utilized to predict the thermogravimetric analyzer (TGA) data of the materials pyrolysis.

In 2004, Conesa et al. [1] developed for the first time an ANN model to obtain the kinetic parameters of the pyrolysis of some materials using TGA experimental data at different heating rates.

Bezerra et al. [2] investigated the TGA data of the pyrolysis of different fiber using ANN. Two input parameters (temperature and heating rate) and an output layer (mass retained) were employed. The optimum ANN topology was reported as 2-21-21-1.

Burgaz et al. [3] used ANN to measure the thermal stability of the mixture of polyethylene oxide and clay using TGA experimental data. A feed-forward back-propagation model with Levenberg–Marquardt (LM) algorithm, and tansig–logsig–purelin transfer function was developed to predict weight loss %.

Yıldız et al. [4] developed an ANN model to monitor the weight loss % during the thermal decomposition of some blends with different compositions using TGA data covering a wide temperature range (298-1273 K). Three input parameters, namely temperature, blend ratio and heating rate, were used as the input variables.

Çepelioğullar et al. [5] investigated the weight loss of a refuse-derived fuel during the pyrolysis process by developing an ANN model. Two input parameters (heating rate, and temperature) were

used. Transfer functions and number of neurons in each hidden layer were optimized to obtain the best structure of the proposed model. The best reported topology includes 7 to 8 neurons with tansig-logsig transfer functions.

Charde et al. [6] developed an ANN model to predict some of the kinetic parameters of the thermal decomposition of the mixture of polycarbonate and $CaCO_3$ using TGA experimental data. Three input parameters (temperature, conversion, and time) were used. Two statistical parameters, namely mean squared error and regression coefficient, were used to identify the best architecture of the proposed ANN model.

Chen et al. [7] developed an ANN model to predict the TGA data of the combustion of some blends at different CO_2/O_2 ratios as a function of heating rate, temperature, and CO_2/O_2 ratio.

Naqvi et al. [8] developed an ANN model using TGA data to predict the thermal decomposition of a sewage sludge has a high ash contact. Good performance of the proposed ANN model was reported.

Bong et al. [9] studied the effect of microalgae ash catalyst on the pyrolysis of a mixture of peanut shell and pure microalgae at range of heating rates (10-100 K/min). Like the rest of the previous researchers, ANN model, with heating rate and temperature as input variables, was developed to predict the weight loss % of the mixture during its thermal decomposition using TGA data.

Dubdub and Al-Yaari [10,11] and Al-Yaari and Dubdub [12] performed ANN modeling to predict the weight loss % using TGA experimental data of the pyrolysis of low-density polyethylene (LDPE), the catalytic cracking of HDPE, and pyrolysis of mixed plastic, respectively. Excellent agreement between the experimental and predicted results was reported.

Prabhakaran et al. [13] investigated the combustion of pet coke under an oxygen atmosphere at different heating rates (10, 50, 75 K/min). An ANN model with LM algorithm was developed to predict the mass loss % as a function of temperature and heating rate. Single-layer perception model (SLP) 2-6-1 and the multi-layer perception model between 2-14-6-1 to 2-14-7-6-1 with 11 different models were tested. Three statistical parameters, namely coefficient of variation, sum of deviation square, and mean residual were used to evaluate the proposed models. The best architecture model was reported as 2-14-7-6-1.

Liew et al. [14] investigated the catalytic co-pyrolysis of corn cob and HDPE at a wide range of heating rates (10-200 K/min) and temperatures (323-1173 K). An ANN model was developed to predict the co-pyrolysis behavior and to determine the thermogravimetric curves as a function of temperature, heating rate and mixing ratio.

In summary, extensive work has been performed to develop ANN models to predict the thermal decomposition data of either pure polymers/materials, where there are mainly two input variables (heating rate and temperature) and one output variable (weight loss %) [2,5,8,10,11,13], or mixed polymers/materials, where there are usually more than two input variables [3,4,6,7,9,12,14].

However, there is insufficient work aimed to develop knowledge on the pyrolysis of pure polymers and specially HDPE, which represents around 20 wt% of the municipal plastic waste, using ANN modeling. Therefore, this work aims to develop a highly-efficient ANN model to predict the TGA data of the pyrolysis of HDPE. Specifically, weight left % of the tested samples was targeted to be predicted as a function of the pyrolysis heating rate and temperature.

2. Materials and Methods

2.1. Experiments

Proximate and ultimate analysis were performed to characterize HDPE samples. Both characterization techniques were completed using PerkinElmer Simultaneous Thermal Analyzer

6000, and PerkinElmer 2400 Series II CHNS Elemental Analyzer, USA. Details of both analyses are reported elsewhere [10] and analysis data are presented in Table 1.

Table 3. Proximate and ultimate analysis of HDPE samples.

Proximate Analysis, wt%			Ultimate Analysis, wt%			
Moisture	**Volatile**	**Ash**	**C**	**H**	**N**	**S**
0.405	99.377	0.218	82.77	16.92	0.00	0.29

Then, 10 mg of HDPE powder samples were used to obtain the TGA data for each test. Thermogravimetric analysis was performed using Thermogravimetric Analyzer TGA7, produced by PerkinElmer, Waltham, MA, USA. TGA experiments were conducted under nitrogen (99.999%) gas flowing at 100 cm^3/min at four different heating rates (5, 10, 20, and 40 K/min).

2.2. Artificial Neural Networks Modeling

Based on the available experimental data, process modeling must include the influenced parameters as per their significance. However, when the process becomes more complex where relationships between input and output parameters are non-linear, simple mathematical process modeling becomes inefficient to treat such tedious tasks.

Artificial neural networks (ANN) modeling has attracted the attention of researchers because of its powerful performance in predicting and forecasting experimental data for many engineering applications. Therefore, it has been used efficiently as a promising alternative option to the simple mathematical modeling. However, ANN modeling needs computational effort [15] and sufficient, and representative experimental data for all process variables.

Usually, the experimental (raw) data are divided into three subsets: training, validation, and testing. Although the training datasets are used to create the network learning and adjust weight of each parameter as per the error function, the validation and testing datasets are used to check the performance and test the generalization of the network, respectively [16].

Generally, an ANN network has three layers of neurons: input, hidden, and output layers. In addition, each layer has a weight and a bias for each input parameter, output vector/s, and a transfer function connecting between layers [16].

However, the best ANN architecture can be generally obtained by the optimization of some network features including number of hidden layers, number of neurons in each layer, transfer functions, and learning algorithm.

To evaluate the performance of the developed ANN model, some statistical parameters, listed below, can be used [17,18]. In this work, mass left % ($W\ \%$) during the HDPE pyrolysis was aimed to be predicted.

$$\text{Average correlation factor } (R^2) = 1 - \frac{\sum\left((W\ \%)_{est} - (W\ \%)_{\exp}\right)^2}{\sum\left((W\ \%)_{est} - \overline{(W\ \%)_{\exp}}\right)^2} \quad (4)$$

$$\text{Root mean square error (RMSE)} = \sqrt{\frac{1}{N}\sum\left((W\ \%)_{\text{est}} - (W\ \%)_{\exp}\right)^2} \quad (5)$$

$$\text{Mean absolute error (MAE)} = \frac{1}{N}\sum\left|(W\ \%)_{est} - (W\ \%)_{\exp}\right| \quad (6)$$

$$\text{Mean bias error (MBE)} = \frac{1}{N}\sum((W\ \%)_{est} - (W\ \%)_{\text{exp}}) \tag{7}$$

$$\text{Correlation coefficient (R)} = \frac{\sum_{m=1}^{n}\left((W\ \%)_{exp,m} - \overline{(W\ \%)_{exp,m}}\right)\left((W\ \%)_{est,m} - \overline{(W\ \%)_{est,m}}\right)}{\sqrt{\sum_{m=1}^{n}\left((W\ \%)_{exp,m} - \overline{(W\ \%)_{exp,m}}\right)^2 \sum_{m=1}^{n}\left((W\ \%)_{est,m} - \overline{(W\ \%)_{est,m}}\right)^2}} \tag{8}$$

where

$(W\ \%)_{est}$: is the estimated value of the weight left % by the ANN model;
$(W\ \%)_{exp}$, is the experimental value of the weight left %; and
$\overline{(W\%)}$: is the average values of weight left %.

3. Results and Discussion

3.1 Thermogravimetric Analysis Raw Data

The thermogravimetric (TG) curves of the pyrolysis of HDPE at different heating rate of (5, 10, 20, and 40 K/min) are presented in Figure 1, from which the raw data of this work has been extracted. However, since the scope of this work is limited to the investigation of the performance of the developed ANN model, TGA analysis and kinetic study are described elsewhere [19].

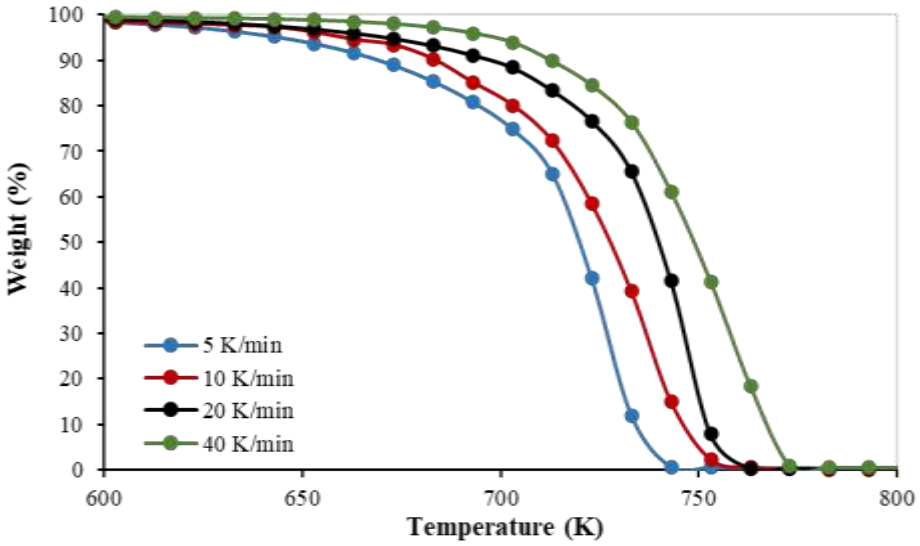


Figure 6. Thermogravimetric (TG) curves of the pyrolysis of high-density polyethylene (HDPE).

3.2 Performance of the Developed ANN model

An ANN model has been developed to predict the TGA data of the pyrolysis of HDPE. Specifically, weight left % of HDPE as a function of temperature, and heating rate, was targeted to be predicted by the proposed ANN model.

In this investigation, an ANN model with feed-forward and back-propagation scheme was developed using 160 datasets. Then, the developed model was then validated using extra 4 datasets during the simulation stage. Number of datasets used for training and simulation stages is presented in Table 2. However, Table 3 presents the predicted values of the weight left % of HDPE during the

simulation stage using the new datasets. The obtained values are exactly equal to those obtained experimentally which implies the robustness of the developed model.

Table 4. Number of Datasets used for the training and simulation stages

Heating Rate (K/min)	Training Stage	Simulation Stage
5	40	1
10	40	1
20	40	1
40	40	1
Total	**160**	**4**

Table 5. ANN-predicted weight loss values obtained during the simulation stage

ANN input variables		ANN output variable
Heating rate (K/min)	**Temp. (K)**	**Mass left (wt%)**
5	733	11.97
10	733	39.22
20	733	65.54
40	723	84.5

Using MATLAB 2021a, the datasets used for the training stage were divided randomly into three subsets: 70% for training, 15% for validation, and 15% for testing.

A high accuracy model requires a large representative experimental dataset [20]. To find to the best structure of ANN, it is required to optimize number of hidden layers, number of neurons in each layer and transfer function. Number of neurons in each hidden layer is a crucial parameter having a significant influence on the performance of the developed ANN model. Therefore, underfitting (too few neurons) and overfitting (too many neurons) should be avoided, and the optimum number of neurons must be obtained [21,22]. For this purpose, prediction performance of different ANN architectures has been checked.

Although the correlation coefficient, defined by equation (1), has been considered as the main criterion to nominate the high-efficient ANN model to predict the output variable (weight left %) for all tests, other statistical parameters, expressed by equations (2-4), have been used to evaluate the proposed structure. Then, the selected structure has been tested (simulated) with new 4 datasets.

As shown in Figure 2, the best ANN structure is (2-10-10-1) with R=1. The developed model has two hidden layers with 10 and 10 neurons, respectively. In addition, the tansig-tansig transfer functions for the two hidden layers and the linear transfer function (Pureline) for the output layer

have been recommended to be used. Moreover, among different algorithms which were checked, the Levenberg-Marquardt (LM) algorithm was recommended for this network [23]. The default training parameters in MATLAB toolbox have been used and the "goal", which is the mean square error (MSE), has been set to zero.

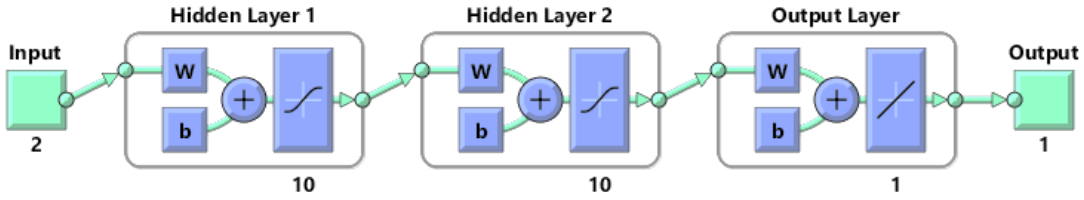


Figure 7. Topology of the selected ANN network.

Figure 3 presents the performance of the developed ANN model for all stages. Results indicate an excellent agreement between the experimental (X-axis) and the predicted (Y-axis) values of the output parameter. In addition, Figure 4 shows the performance plot through the training, validation, and test errors when predicting the experimental values. The testing stage has been stopped when validation error increased consecutively for 6 epochs. In this case, an optimum value of MSE (MSE= 0.0084557) has been obtained (i.e., the best validation performance is 0.0084557 at epoch 0). This value is very small and proves good prediction performance as well [24-26].

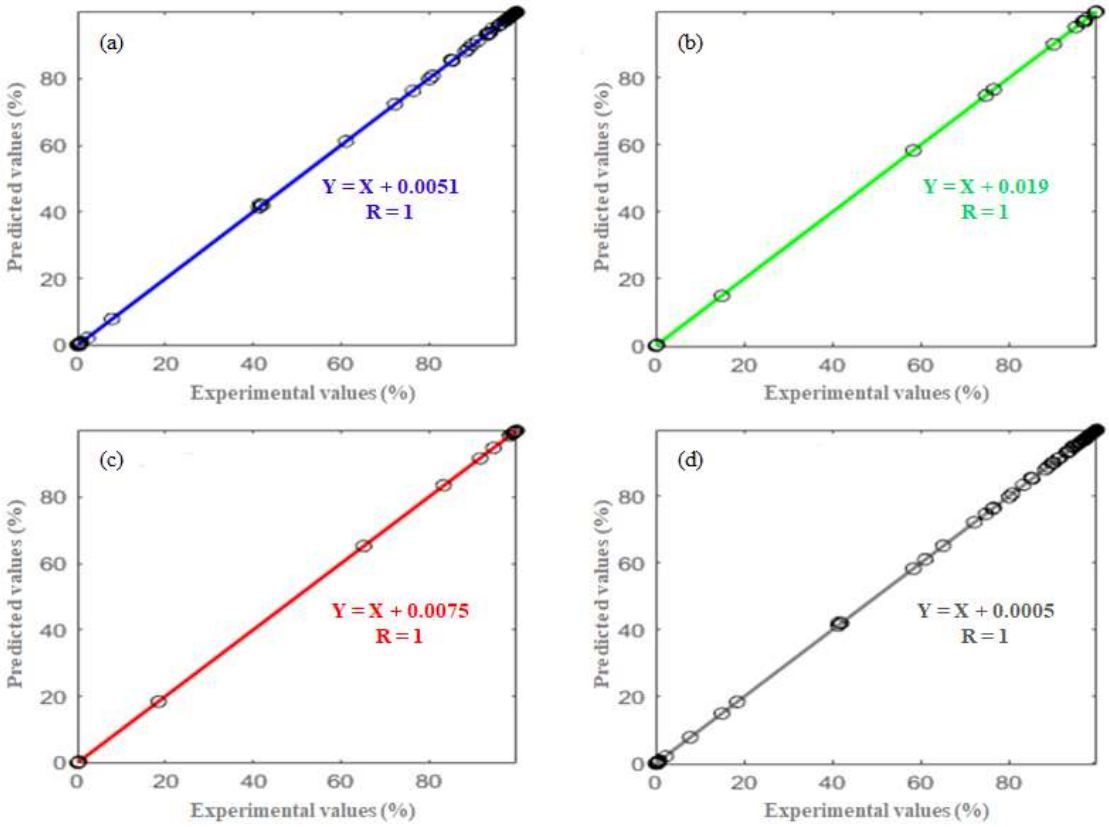


Figure 8. Regression lines of the predicted values of weight left % obtained from: (a) training data, (b) validation data, (c) testing data, (d) all data.

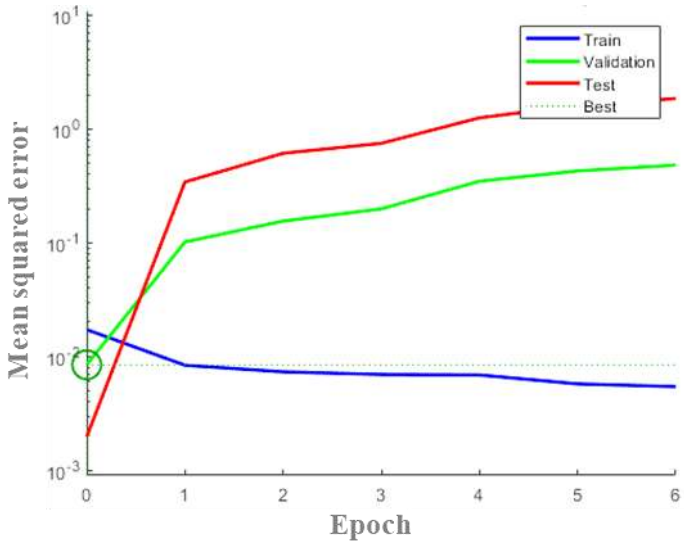


Figure 9. Optimum mean squared error

Furthermore, Figure 5 shows the error histogram for the training dataset which is drawn across the zero error. The error lies only in a narrow range (-0.717 to 0.4076) which implies a good performance of the proposed ANN model.

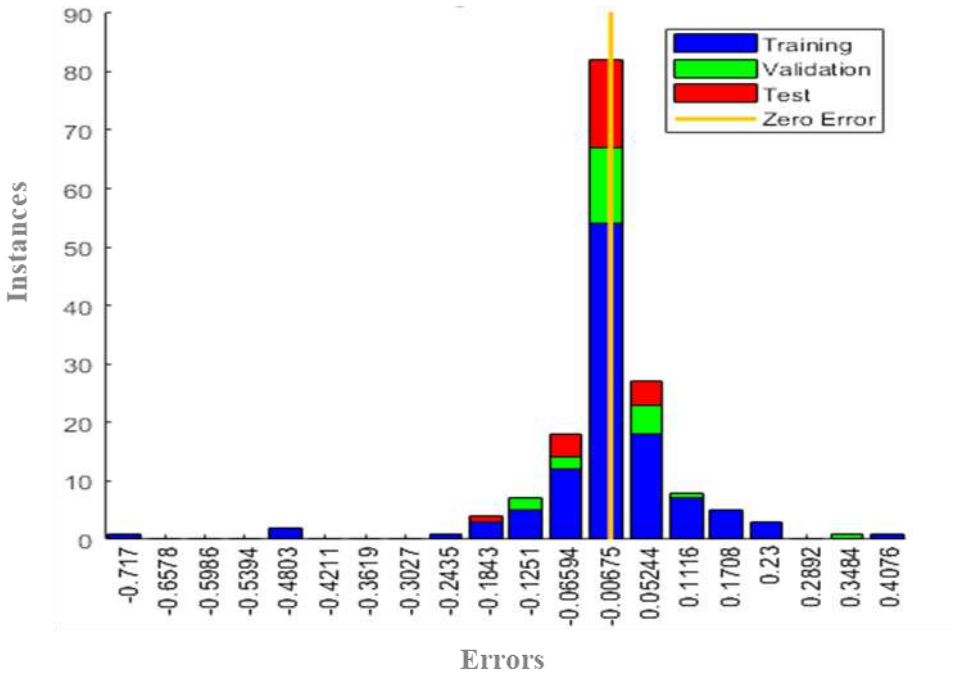


Figure 10. Error histogram of training data with 20 bis

The prediction performance of the (2-10-10-1) model has been evaluated by the values of R, MAE, RMSE, and MBE. Although the high value of R is preferable, the values of other statistical measurements (MAE, RMSE, and MBE) should be low for the high-efficient ANN model. Table 4 lists these values for the training, validation, testing and all datasets. As presented in Table 4, the developed ANN model can predict efficiently the output parameter (R=1). To validate the proposed model, it was then checked with new four datasets. Figure 6, where the predicted and experimental values are in a full agreement, proves the high-efficient performance of the ANN model as per the new simulated datasets. In addition, as presented in Table 5, the R value was very high (R=0.99962) and very low values of MAE, RMSE, and MBE were obtained. Thus, it can be easily concluded that the developed ANN model efficiently predicted the TG experiment data. Error histogram has been created for the simulation data and is shown in Figure 7. As shown in the figure, the error again lies only in a narrow small range (-0.01918 to 1.821).

Table 6. Statistical parameters of the developed ANN model

Data sets	R	RMSE	MAE	MBE
Training	1.00000	0.13125	0.07062	0.00378
Validation	1.00000	0.09195	0.05373	-0.01622
Test	1.00000	0.04437	0.02808	0.01143
All	**1.00000**	**0.11672**	**0.06171**	**0.001930**

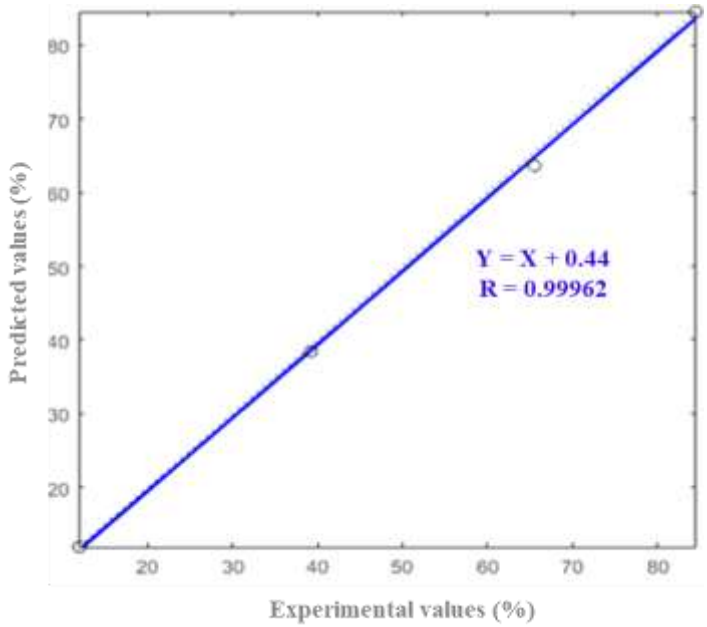


Figure 11. Regression lines of the predicted values of weight left % obtained from the simulated datasets for the (2-10-10-1) ANN model.

Table 7. Statistical parameters of the (2-10-10-1) model for the simulated data

R	RMSE	MAE	MBE
0.99962	1.01685	0.70507	-0.67127

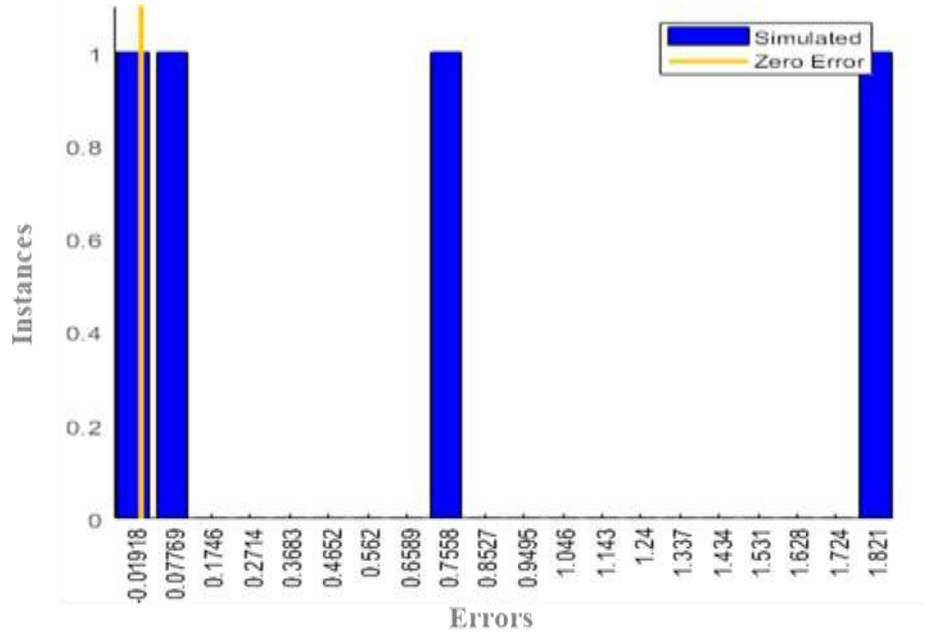


Figure 12. Error histogram of the (2-10-10-1) ANN model for the simulated datasets

4. Conclusions

Plastic waste management must be given a priority by governments to avoid the serious environmental issues caused by the disposed and incinerated wastes. Pyrolysis of different plastics has many advantages over other treatment techniques. Among different plastic wastes, HDPE products represents around 18.7 wt% of municipal waste plastic.

In this work, an efficient ANN model was targeted to be developed to predict the thermal behavior of HDPE at different heating rates (5, 10, 20, and 40 K/min). The weight left% of HDPE samples were predicted as a function of heating rate and temperature. Different ANN structures have been checked and different network parameters have been optimized.

The best ANN architecture has two hidden layers with 10 neurons in each and the *tangsig* transfer function was recommended for both layers. The (2-10-10-1) network topology showed a highly-efficient performance (R=1) to predict the TGA data of the HDPE pyrolysis. Then, the proposed network has been used to simulate new input datasets and full agreement between the experimental and predicted data has been observed (R=0.99962). In addition, very low values of MAE, RMSE, and MBE have been reported.

This proves that ANN model can efficiently predict the pyrolysis TGA data of HDPE and worthy to be checked for other complex pyrolysis process.

Author Contributions: Both authors contributed significantly to the completion of this article and have read and agreed to the published version of the manuscript.

Funding: This research and the APC were funded by the Deanship of Scientific Research at King Faisal University, Saudi Arabia, under the Research Group Support Track (Grant No. 17122013).

Acknowledgments: The authors acknowledge the Deanship of Scientific Research at King Faisal University (KFU) in Al-Ahsa for the financial support under the Research Group Support Track (Grant No. 17122013).

Conflicts of Interest: The authors declare no conflict of interest.

References

1. Conesa, J.A.; Caballero, J.A.; Reyes-Labarta, J.A. Artificial neural network for modelling thermal decompositions. *J. Anal. Appl. Pyrolysis* **2004**, 71, 343-352. https://doi.org/10.1016/S0165-2370(03)00093-7
2. Bezerra, E.M.; Bento, M.S.; Rocco, J.A.F.F.; Iha, K.; Lourenço, V.L.; Pardini, L.C. Artificial neural network (ANN) prediction of kinetic parameters of (CRFC) composites. *Computational Materials Science* **2008,** 44, 656–663. https://doi.org/10.1016/j.commatsci.2008.05.002
3. Burgaz, E.; Yazici, M.; Kapusuz, M.; Alisira, S. H.; Ozcan, H. Prediction of thermal stability, crystallinity and thermomechanical properties of poly(ethylene oxide)/clay nanocomposites with artificial neural networks. *Thermochimica Acta* **2014**, 575, 159– 166. https://doi.org/10.1016/j.tca.2013.10.032
4. Yıldız, Z.; Uzun, H.; Ceylan, S.; Topcu, Y. Application of artificial neural networks to co-combustion of hazelnut husk–lignite coal blends. *Bioresour. Technol.* **2016,** 200, 42–47. https://doi.org/10.1016/j.biortech.2015.09.114
5. Çepelioğullar, Ö.; Mutlu, İ.; Yaman, S.; Haykiri-Acma, H. A study to predict pyrolytic behaviors of refuse-derived fuel (RDF): Artificial neural network application. *J. Anal. Appl. Pyrolysis* **2016,** 122, 84-94. https://doi.org/10.1016/j.jaap.2016.10.013
6. Charde, S.J.; Sonawane, S.S.; Sonawane, S.H.; Shimpi, N.G. Degradation kinetics of polycarbonate composites: kinetic parameters and artificial neural network. *Chem. Biochem. Eng. Q.* **2018,** 32, 151–165. https://doi.org/10.15255/CABEQ.2017.1173
7. Chen, J.; Xie, C.; Liu, J.; He, Y.; Xie, W.; Zhang, X.; Chang, K.; J. Kuo, J. Sun, L. Zheng, S. Sun, M. Buyukada, F. Evrendilek, Co-combustion of sewage sludge and coffee grounds under increased O2/CO2 atmospheres: Thermodynamic characteristics, kinetics and artificial neural network modeling. *Bioresour. Technol.* **2018**, 250, 230–238. https://doi.org/10.1016/j.biortech.2017.11.031
8. Naqvi, S. R.; Tariq, R.; Hameed, Z.; Ali, I.; Taqvi, S.A.; Naqvi, M.; Niazi, M. B. K.; Noor, T.; Farooq, W. Pyrolysis of high-ash sewage sludge: Thermo-kinetic study using TGA and artificial neural networks. *Fuel* **2018**, 233, 529-538. https://doi.org/10.1016/j.fuel.2018.06.089
9. Bong, J. T.; Loy, A. C. M.; Chin, B. L. F.; Lam, M. K.; Tang, D. K. H.; Lim, H. Y.; Chai, Y. H.; Yusup, S. Artificial neural network approach for co-pyrolysis of Chlorella vulgaris and peanut shell binary mixtures using microalgae ash catalyst. *Energy* **2020**, 207, 118289. https://doi.org/10.1016/j.energy.2020.118289
10. Dubdub, I.; Al-Yaari, M. Pyrolysis of mixed plastic waste: I. kinetic study. *Materials* **2020**, 13, 4912. https://doi.org/10.3390/ma13214912
11. Dubdub, I.; Al-Yaari, M. Pyrolysis of low density polyethylene: kinetic study using TGA data and ANN prediction. *Polymers* **2020**, 12, 891. https://doi.org/10.3390/polym12040891
12. Al-Yaari, M.; Dubdub, I. Application of artificial neural networks to predict the catalytic pyrolysis of HDPE using non-isothermal TGA data. *Polymers* **2020**, 2, 1813. https://doi.org/10.3390/polym12081813

13. Sathiya Prabhakaran, S. P.; Swaminathan, G.; Viraj, V. J. Thermogravimetric analysis of hazardous waste: Pet-coke, by kinetic models and artificial neural network modeling. *Fuel* **2021**, 287, 119470. https://doi.org/10.1016/j.fuel.2020.119470
14. Liew, J. X.; Loy, A. C. M.; Chin, B. L. F.; AlNouss, A.; Shahbaz, M.; Al-Ansari, T.; Govindan, R.; Chai. Y. H. Synergistic effects of catalytic co-pyrolysis of corn cob and HDPE waste mixtures using weight average global process model. *Renewable Energy* **2021**, 170, 948-963. https://doi.org/10.1016/j.renene.2021.02.053
15. Bar, N.; Bandyopadhyay, T. K.; Biswas, M. N.; Das, S. K. Prediction of pressure drop using artificial neural network for non-Newtonian liquid flow through piping components. *J. Pet. Sci. Eng.* **2010**, 71, 187. https://doi.org/10.1016/j.protcy.2013.12.426
16. Quantrille, T. E.; Liu, Y. A. Artificial intelligence in chemical engineering, Elsevier Science, **1992**.
17. Halali, M. A.; Azari, V.; Arabloo, M.; Mohammadi, A. H.; Bahadori, A. Application of a radial basis function neural network to estimate pressure gradient in water–oil pipelines. *J. Taiwan Inst. Chem. Eng.* **2016**, 58, 189–202. https://doi.org/10.1016/j.jtice.2015.06.042
18. Govindan, B.; Jakka, S. C. B.; Radhakrishnan, T. K.; Tiwari, A. K.; Sudhakar, T. M.; Shanmugavelu, P.; Kalburgi, A. K.; Sanyal, A.; Sarkar, S. Investigation on kinetic parameters of combustion and oxy-combustion of calcined pet coke employing thermogravimetric analysis coupled to artificial neural network modeling. *Energy Fuels* **2018**, 32, 3995-4007. https://doi.org/10.1021/acs.energyfuels.8b00223
19. Al-Yaari, M.; Dubdub, I. Pyrolysis of high-density polyethylene: I. Kinetic Study. *The 9th Jordan International Chemical Engineering Conference* (JICHEC9), 12-14 Oct. **2021**.
20. Al-Wahaibi, T.; Mjalli, F. S. Prediction of horizontal oil-water flow pressure gradient using artificial intelligence techniques. *Chem. Eng. Commun.* **2014**, 201, 209. https://doi.org/10.1080/00986445.2013.766603
21. Osman, E.A.; Aggour, M.A. Artificial neural network model for accurate prediction of pressure drop in horizontal and near-horizontal-multiphase flow. *Petroleum Science and Technology* **2002**, 20, 1-15. https://doi.org/10.1081/LFT-120002082
22. Qinghua, W.; Honglan, Z.; Wei, L.; Junzheng, Y.; Xiaohong, W.; Yan, W. Experimental study of horizontal gas-liquid two-phase flow in two medium-diameter pipes and prediction of pressure drop through BP neural networks. *International Journal of Fluid Machinery and Systems* **2018**, 11, 255-264. https://doi.org/10.5293/IJFMS.2018.11.3.255
23. Beale, M. H.; Hagan, M. T.; Demuth, H. B. Neural network toolbox TM user's guide, MathWorks, **2018**.
24. Sun, Y.; Liu, L.; Wang, Q.; Yang, X.; Tu, X. Pyrolysis products from industrial waste biomass based on a neural network model. *Journal of Analytical and Applied Pyrolysis* **2016**, 120, 94-102. https://doi.org/10.1016/j.jaap.2016.04.013
25. Ahmad, M.S.; Mehmood, M. A.; Taqvi, S. T. H.; Elkamel, A.; Liu, C. G.; Xu, J.; Rahimuddin, S. A.; Gull, M. Pyrolysis, kinetics analysis, thermodynamics parameters and reaction mechanism of Typha latifolia to evaluate its bioenergy potential. *Bioresource Technology* **2017**, 245, 491-501. https://doi.org/10.1016/j.biortech.2017.08.162

26. Aydinli, B.; Caglar, A.; Pekol, S.; Karaci, A. The prediction of potential energy and matter production from biomass pyrolysis with artificial neural network. *Energy Exploration & Exploitation* **2017**, 35, 698–712. https://doi.org/10.1177/0144598717716282

speaker	corresponding author	page
Abdalla Al Jedayeh	Abdalla Al Jedayeh	805
Abdelhadi Benabdessadok	Abdelhadi Benabdessadok	998
Abdulbari A. Ahmad	Abdulbari A. Ahmad	49
Abdulhamid. Elwaer	Abdulhamid. Elwaer, Abdulroaf Shahein	804
Abdulrazaq Alzamily	Abdulrazaq Alzamily	336
Abir Berkouk	Abir Berkouk	960
Adair Gallo Junior	Adair Gallo Junior	506
Ahlam Waleed Hunaihen	Ahlam Waleed Hunaihen	852
Ahmad Alhadid	Ahmad Alhadid	178
Ahmad Rafiq Muosa Mohammad	Ahmad Rafiq Muosa Mohammad	840
Ahmed Abdala	Ahmed Abdala	471
Ala'a Omari	Ala'a Omari	526
Amrutha	Amrutha ,Gautham Jeppu	727
Anna Maria Menelaou	Patroklos Vareltzis	152
Arwa Al-Da'asen	Arwa Al-Da'asen	30
Aseel Fadhil kareem	Aseel Fadhil kareem	67
Atikah Kadri	Atikah Kadri	790
Aymen A.Awad	Aymen A.Awad	117
Azizul Azri Mustaffa	Azizul Azri Mustaffa	215
Bahia Messai	Bahia Messai	144
Basma A. Abdulmajeed	Huda Majid Hasen	693
Batoul Rhamtalla	Batoul Rhamtalla	456
Eman Sh. Awad	Eman Sh. Awad	967
Eyad AlRashaideh	Eyad AlRashaideh	335
Fayhaa Abbood Mahdi Al-Nadawi	Fayhaa Abbood Mahdi Al-Nadawi	22
Fernanda Tavares	Pedro Castano	508
German Luna-Mejías	German Luna-Mejías	253
H. boulika	H. boulika , M. el hajam , M. hajji nabih , N. idrissi kandri, A. Zerouale	360
Haitham Osman	Haitham Osman	199
Heba Alzaben	Heba Alzaben , Ali AlShquar , Ban Baniatta , Ibrahim Alzoubi and Sameer AlTawabini	540
Hendrik Kiepfer	Hans-Jörg Bart1	712
Hocine Bouleghlem	Hocine Bouleghlem	9
Hooi Kim Phang	Hooi Kim Phang	728
Hosni Ezuber	Hosni Ezuber	906

I.Kadri	I.Kadri	31
Ibrahim A. Suleiman	Ibrahim A. Suleiman	101
Ibrahim Dubdub	Ibrahim Dubdub	1084
Ilknur Kucuk	Ilknur Kucuk	685
Iman H. Gatea	Iman H. Gatea	2
Isam M. Arafa	Isam M. Arafa	81
Jalal R. Omar	Jalal R. Omar	524
Joanna Kujawa	Joanna Kujawa	831
Khairul Naim Ahmad	Wan Nor Roslam Wan Isahak	106
Kian Hong Gan	Jau Choy Lai	806
Ma'moun Al-Rawashdeh	Ma'moun Al-Rawashdeh	118
Madhusree Kundu	Madhusree Kundu	1044
Malik M. S. Salhab	Malik M. S. Salhab	337
Marah Daraghmah	Marah Daraghmah	759
Meriem Bouteraa	Meriem Bouteraa	179
Mohamad Hammoud	Zaid AlHulaybi	514
Mohammad Ali Freij	Mohammad Ali Freij	600
Mohammad Alrbaihat	Mohammad Alrbaihat	842
Mohammad Alwaqfi	Ihab H. Alsurakji , Amjad El Qanni	361
Mohammad Ashraf Ali	Mohammad Ashraf Ali	820
Mohammad Raji Abdallah Qasaimeh	Mohammad Raji Abdallah Qasaimeh	438
Mohammed Abualreesh	Mohammed Abualreesh	267
Mohammed Al-Waqfi	Mohammed Al-Waqfi	564
Mohammed Al-Yaari	Mohammed Al-Yaari	129
Mohammed Hamada Ali Ahmed	Mohammed Hamada Ali Ahmed	58
Mohammed M. A. Al-Mougher	Mohammed M. A. Al-Mougher	576
Mohammed S. El-Ali Al-Waqfi	Mohammed S. El-Ali Al-Waqfi	749
Nabeel Jarrah	Nuhu Dalhat Mu'azu and Nabeel Jarrah	198
Nidal M. Hussein	Nidal M. Hussein , Mohammed N. Assaf	933
Nidal M. Hussein	Nidal M. Hussein , Mohammed N. Assaf	1066
Nidal M. Hussein	Nidal M. Hussein	546
Noor Aljammal	Noor Aljammal	818
Nuhu Dalhat Mu'azu	Nuhu Dalhat Mu'azu	458
Nur A'ina Shafiqa Wakari	S Izhar	948
Nur Amalina Ramli	Fatmawati Adam	623
Nur Hanina Malek	Syed Shatir A. Syed-Hassan	491
Nurliyana Nasuha Binti Safie	Nurliyana Nasuha Binti Safie	1008

Obada Dwekat	Abdelrahim Abusafa	644
Omar S. Mahdy	Omar S. Mahdy	659
Praveengouda Patil	C. R Girish2	603
Rajender Dahiya	Rajender Dahiya, CSP, MIChemE	305
Rajender Dahiya	Rajender Dahiya,Priyal Dahiya	318
Rania Remmani	Rania Remmani	924
Raudh Jamal Raheem	Raudh Jamal Raheem	541
Rawan Alyasoury	Qusai Al-Najdawi , Deema Abu Al-Ruz ,RawanAlyasoury ,Ghadeer Al-Khatib	383
Rowaida M. Fahmy	Rowaida M. Fahmy	339
sabreen Mheidat	sabreen Mheidat	601
Sagheer A. Onaizi	Sagheer A. Onaizi	774
Sagheer Onaizi	Raha M. Kharabsheh , Aymen A.Awad , Mohammad A. Alhusban	417
Said Al Rabadi	Said Al Rabadi	233
Salem Alsanusi	Salem Alsanusi	297
Salman Raza Naqvi	Salman Raza Naqvi	1033
Sarra Melloul	Sarra Melloul	244
Sewar Aljarrah	Sewar Aljarrah	898
Seyedeh Parvin Moussavi	Milad Mousazadeh	369
Seyedeh Parvin Moussavi	Seyedeh Parvin Moussavi , Reza Rostami	426
Shadi Sawalha	Shadi Sawalha	1018
Shamsuddeen A. Haladu	Nuhu Dalhat Mu’azu	167
Shehab Al-Sohpany	Shehab Al-Sohpany	259
Shekhar R. Kulkarni	Pedro Castaño	141
Siti Aslina Hussain	Siti Aslina Hussain	234
Siti Shawalliah Idris	Siti Shawalliah Idris	489
Tayel El-Hasan	Tayel El-Hasan	876
Vladimir Saranchin	Vladimir Saranchin , Alexey Lykov	675
Vladimir Saranchin	Vladimir Saranchin	738
Wajdi Mohamed Ratemi	Wajdi Mohamed Ratemi	186
Waleed Mohammed Abood	Faten Hameed kamil	989
Yaprak Özbakır	Yaprak Özbakır	71
Zahraa W. Hasan	Zahraa W. Hasan, Abbas J. Sultan, Laith S. Sabri, Jamal M. Ali	490
Zakia Guebudji	Zakia Guebudji	961
Ziad Abu El-Rub	Ziad Abu El-Rub	116